

Selected Papers from the
Proceedings of Geo-Chicago 2016

GSP 269



Geo-Chicago 2016: Sustainability and Resiliency in Geotechnical Engineering

ASCE

EDITED BY Dimitrios Zekkos, Ph.D., P.E.;
Arvin Farid, Ph.D., P.E.; Anirban De, Ph.D., P.E.;
Krishna R. Reddy, Ph.D., P.E., D.GE; and
Nazli Yesiller, Ph.D.



GEO-
INSTITUTE

GEOTECHNICAL SPECIAL PUBLICATION NO. 269

GEO-CHICAGO 2016

SUSTAINABILITY AND RESILIENCY IN GEOTECHNICAL ENGINEERING

SELECTED PAPERS FROM SESSIONS OF
GEO-CHICAGO 2016

August 14–18, 2016
Chicago, Illinois

SPONSORED BY

Geo-Institute of the American Society of Civil Engineers

EDITED BY

Dimitrios Zekkos, Ph.D., P.E.
Arvin Farid, Ph.D., P.E.
Anirban De, Ph.D., P.E.
Krishna R. Reddy, Ph.D., P.E., D.GE
Nazli Yesiller, Ph.D.



Published by the American Society of Civil Engineers

Published by American Society of Civil Engineers
1801 Alexander Bell Drive
Reston, Virginia, 20191-4382
www.asce.org/publications | ascelibrary.org

Any statements expressed in these materials are those of the individual authors and do not necessarily represent the views of ASCE, which takes no responsibility for any statement made herein. No reference made in this publication to any specific method, product, process, or service constitutes or implies an endorsement, recommendation, or warranty thereof by ASCE. The materials are for general information only and do not represent a standard of ASCE, nor are they intended as a reference in purchase specifications, contracts, regulations, statutes, or any other legal document. ASCE makes no representation or warranty of any kind, whether express or implied, concerning the accuracy, completeness, suitability, or utility of any information, apparatus, product, or process discussed in this publication, and assumes no liability therefor. The information contained in these materials should not be used without first securing competent advice with respect to its suitability for any general or specific application. Anyone utilizing such information assumes all liability arising from such use, including but not limited to infringement of any patent or patents.

ASCE and American Society of Civil Engineers—Registered in U.S. Patent and Trademark Office.

Photocopies and permissions. Permission to photocopy or reproduce material from ASCE publications can be requested by sending an e-mail to permissions@asce.org or by locating a title in ASCE's Civil Engineering Database (<http://cedb.asce.org>) or ASCE Library (<http://ascelibrary.org>) and using the “Permissions” link.

Errata: Errata, if any, can be found at <http://dx.doi.org/10.1061/9780784480120>

Copyright © 2016 by the American Society of Civil Engineers.
All Rights Reserved.
ISBN 978-0-7844-8012-0 (PDF)
Manufactured in the United States of America.

Preface

Geo-engineers and geo-scientists have been playing a major role in providing, protecting, and preserving infrastructure and the environment. Many innovative technologies and practices are constantly being developed and implemented. Evolving global climate change and exploding world population are leading to major concerns such as extreme geohazards, increased environmental pollution, and rapid depletion of natural resources. These new challenges can be addressed with new and innovative concepts, materials, energy sources, technologies, and practices. Sustainability and resiliency have become essential in the development of new materials and infrastructure systems. *Geo-Chicago 2016: Sustainability, Energy, and the Environment* held in Chicago August 14-18, 2016, provided a unique opportunity to highlight recent advances, new directions, and opportunities for sustainable and resilient approaches to design and protect infrastructure and the environment.

The Geo-Chicago 2016 Conference attracted a significant amount of interest and in the end more than 350 papers were accepted for publication. The papers are divided into five Geotechnical Special Publications (GSPs) that capture the multidisciplinary aspects and challenges of sustainability and resiliency, energy and the geoenvironment.

The first GSP, *Sustainability and Resiliency in Geotechnical Engineering*, addresses major broad issues related to sustainability and resilience in geotechnical and geoenvironmental engineering, including carbon sequestration as well as characterization, analysis, monitoring, and response to geohazards and natural disasters, including earthquakes and landslides. Advances in emerging technologies and materials such as bio-mediated soils and nanomaterials are also presented.

The second GSP, *Geotechnics for Sustainable Energy*, tackles the new and innovative ways of storing and extracting energy in and from geotechnical media and structures such as shallow and deep ground, piles and foundations, and landfills. The second GSP also presents the challenges of the energy storage and extraction at the field and lab scales as well as its numerical and experimental modeling.

The third GSP, *Sustainable Geoenvironmental Systems*, addresses recent advances in landfill engineering and geosynthetics used for geoenvironmental systems, as well as advances in sustainable barrier materials and systems. The third GSP also presents studies into slopes, dikes, and embankment, the application of ground improvement in geoenvironmental applications, and the geoengineering of mine wastes and industrial byproducts.

The fourth GSP, *Sustainable Materials and Resource Conservation*, describes the properties and applications of new, recycled, and residual materials, detailed/improved characterization of soils with laboratory and field testing methods, and effects of chemicals and other environmental factors on properties and behavior of soils. The fourth GSP also presents the approaches and use of modeling and simulations in geoenvironmental engineering.

The fifth GSP, *Sustainable Waste Management and Remediation*, addresses various aspects of remediation, contaminated materials, containment, policy, and education. In addition, international perspectives are included to provide further context on challenges and innovations in geoenvironmental engineering on a global scale.

Following standards of practice of the Geo-Institute of the American Society of Civil Engineers, each paper published in these Geotechnical Special Publication (GSPs) was peer reviewed by at least two anonymous, qualified, technical reviewers (and in some cases three or four reviewers) and selected for publication by the proceedings editors. An advanced document management service was utilized in order to assure anonymity and maintain uniformity of standards. As such, the papers contained in these proceedings are eligible for discussion in the ASCE Journal of Geotechnical and Geoenvironmental Engineering and for ASCE awards.

The Editors

Nazli Yesiller, Ph.D., A.M.ASCE, Global Waste Research Institute / California Polytechnic State University, San Luis Obispo
Dimitrios Zekkos, Ph.D., P.E., M.ASCE, University of Michigan
Arvin Farid, Ph.D., P.E., M.ASCE, Boise State University
Anirban De, Ph.D., P.E., M.ASCE, Manhattan College
Krishna R. Reddy, Ph.D., P.E., D.GE, F.ASCE, University of Illinois at Chicago

Acknowledgments

The success of Geo-Chicago 2016 is credited to the session chairs and authors of the technical papers and also plenary session presenters for their valuable contributions to the geotechnical literature. The commendable quality of the Conference's technical content and these proceedings are also the result of the efforts of the hundreds of reviewers. We thank the session chairs, authors and reviewers for generously contributing their valuable time and expertise, in many cases, under time pressure and demanding deadlines.

The following individuals served as the conference program committee. They deserve special acknowledgment and recognition for their extraordinary efforts in making this Conference a reality and a resounding success:

- Conference Chair – Krishna R. Reddy, University of Illinois at Chicago
- Conference Co-Chair/Workshops Co-Chair – Nazli Yesiller, Global Waste Research Institute / California Polytechnic State University, San Luis Obispo
- Technical Program Chairs – Dimitrios Zekkos, University of Michigan; Arvin Farid, Boise State University and Anirban De, Manhattan College
- Short Courses Chair – Michael A. Malusis, Bucknell University
- Workshops Chair – James L. Hanson, California Polytechnic State University, San Luis Obispo
- Technical Tours/Social Program Co-Chairs – Doug Hermann, Independent Consultant; and Dhooli Raj, Collins Engineers, Inc.
- Sponsorships and Exhibits Co-Chairs – Carsten H. Floess, AECOM and Charles Wilk, ALLU Group, Inc.
- G-I TCC Liaison – Susan E. Burns, Georgia Institute of Technology

The Editors sincerely appreciate the help and patience of Ms. Helen Cook and Mr. Brad Keelor of Geo-Institute of the ASCE for their help in managing the paper submissions and organization of the conference.

We hope that these GSPs will serve as valuable references to all working in geoen지니어ing.

The Editors

Nazli Yesiller, Ph.D., A.M.ASCE, Global Waste Research Institute / California Polytechnic State University, San Luis Obispo

Dimitrios Zekkos, Ph.D., P.E., M.ASCE, University of Michigan

Arvin Farid, Ph.D., P.E., M.ASCE, Boise State University

Anirban De, Ph.D., P.E., M.ASCE, Manhattan College

Krishna R. Reddy, Ph.D., P.E., D.GE, F.ASCE, University of Illinois at Chicago

LIST OF SESSION CHAIRS

Dipanjan Basu	Takeshi Katsumi	Naoki Sakai
Deepankar Choudhury	Hideo Komine	Muhannad T. Suleiman
Amro El Badawy	Senro Kuraoka	Burak F. Tanyu
Kevin C. Foye	Lin Li	Binod Tiwari
Kevin Franke	Barbara A. Luke	Antonio Thome
Malay Ghose-Hajra	Brina Montoya	Joseph Wartman

LIST OF REVIEWERS

Beena Ajmera	Liangbo Hu	Anand Puppala
Ahmed Alawneh	Nick Hudyma	Krishna Reddy
Ashraf Aly Hassan	Toru Inui	Cleomar Reginatto
B. Munwar Basha Sr.	Masahiko Katoh	Jennifer Retherford
Dipanjan Basu	Takeshi Katsumi	Daniela Robertson
Sriman Battacharyya	Junichi Kawabata	John Seymour
Ryley Beddoe	Youhei Kawamura	Franz Simon
Jaqueline Bonatto	Jeffrey Keaton	Nina Stark
Omer Bozok	Golam Kibria	Timothy Stark
Pamela Burnley	Seunghee Kim	Garry Stevenson
Susan Burns	Itaru Kitahara	Takefumi Takuma
Bora Cetin	Prabir Kolay	Burak Tanyu
Halil Ceylan	Abhishek Kumar	Junliang Tao
Debarghya Chakraborty	Anitha Kumari	Thuraisamy Thavaraj
Santiram Chatterjee	Senro Kuraoka	Kuo Tian
Jiannan Chen	Lin Li	Binod Tiwari
Deepankar Choudhury	Mingdong Li	Farshid Vahedifard
Helen Cook	Zhen Liu	Stan Vitton
Mandar Dewoolkar	Barbara Luke	Joseph Wartman
Giancarlo Flores	Barbara Luke	Yasutaka Watanabe
Kevin Foye	John McCartney	Nazli Yesiller
Kevin Franke	Arif Moghal	Xinbao Yu
Madhavi Gali	Brina Montoya	Ming Zhu
Malay Ghose Harja	Nisha Naik	
Priyanka Ghosh	Yacoub Najjar	
Lawrence Gilbert	Munir Nazzal	
Kevin Gilmore	Kam Ng	
Alireza Gitipour	Michael Nicho	
Ranjiv Gupta	Sanjay Nimbalker	
Jim Hanson	Jamal Nusairat	
Karla Heineck	Kiyoshi Omine	
Georgette Hlepas	Junboum Park	
Zahid Hossain	Aravind Pedarla	
Jianying Hu	Lok Pokhrel	

Contents

Bio-Mediated Soil

A New Soil Treatment Method Using Casein from Bovine Milk	1
Jooyoung Im, Gye-Chun Cho, and Ilhan Chang	
A Stoichiometric Model for Biogeotechnical Soil Improvement	7
Sean T. O'Donnell, Nasser Hamdan, Bruce E. Rittmann, and Edward Kavazanjian Jr.	
An Environmentally-Friendly Geotechnical Approach for Soil Erosion Reduction Using Microbial Biopolymers.....	17
Ilhan Chang, Jooyoung Im, and Gye-Chun Cho	
Biotreatment of Fine-Grained Soil through the Bioencapsulation Method	25
Bing Li, Jian Chu, and Andrew Whittle	
Enhanced Germination and Growth of <i>Arabidopsis thaliana</i> Using IrO₂-Ta₂O₅ Ti as a Dimensional Stable Anode in the Electro-Culture Technique	33
G. Acosta-Santoyo, R. A. Herrada, S. de Folter, and Erika Bustos	
Erosion Reduction of Coastal Sands Using Microbial Induced Calcite Precipitation	42
Casey Shanahan and Brina M. Montoya	
Experimental Investigation of the Mechanical Properties of MICP-Treated Sands Reinforced with Discrete Randomly Distributed Fiber	52
Lin Li, Mingdong Li, Ubani Ogbonnaya, Kejun Wen, Chi Li, and Farshad Amini	
Exploring X-Ray Computed Tomography Characterization and Reactive Transport Modelling of Microbially-Induced Calcite Precipitation in Sandy Soils.....	62
Rosa Mystica Akimana, Youngwoo Seo, Lin Li, Lucas J. Howard, Mandar M. Dewoolkar, and Liang Bo Hu	
Factors Affecting the Improvement of Sand Properties Treated with Microbially-Induced Calcite Precipitation.....	72
G. G. N. N. Amarakoon and S. Kawasaki	

Particulate Simulations of Triaxial Tests on Bio-Cemented Sand Using a New Cementation Model.....	84
A. Khoubani, T. M. Evans, and B. M. Montoya	
Permeability Reduction Due to Microbial Induced Calcite Precipitation in Sand.....	94
Atefeh Zamani and Brina M. Montoya	
Sand Cementation Using the pH Dependency of Calcium Phosphate Compounds and the Addition of Various Powders	104
R. A. N. Dilrukshi and S. Kawasaki	
Sustainable Slope Stabilization Using Biopolymer-Reinforced Soil	116
Santiago Caballero, Raju Acharya, Aritra Banerjee, Tejo V. Bheemasetti, Anand Puppala, and Ujwalkumar Patil	
Using Local Soil Microbial Enrichments to Improve Sand Particle Aggregation from CaCO₃ Precipitation	127
Yu-Syuan Jhuo, Li-Hsien Chen, Hsin-Hsin Tung, Guang-Huey Lin, and Tsan-Hwei Huang	
<i>Carbon Sequestration</i>	
Chemo-Mechanical Coupling in Bonded Geomaterials: Representations in Two Scales	137
Alessandro Gajo, Francesco Cecinato, and Tomasz Hueckel	
Potential Impact of Thermal Pressurization on the Fault Response to CO₂ Injection in Carbon Capture and Storage Projects	147
Kimia Mortezaei and Farshid Vahedifard	
<i>Earthquakes</i>	
Aseismic Upgrade of an Existing Railway Embankment by Double Sheet Pile and Tubular Pile Walls	157
Takefumi Takuma, Hiroyuki Nishimura, and Shigeru Kambe	
Cyclic Shear Response of Fraser River Sand Using Cyclic Ring Shear	167
Abouzar Sadrekarimi	
Earthquake-Induced Landslide Hazard Mapping: A Case Study in Lebanon.....	177
Grace Abou-Jaoude, Angela Saade, Joseph Wartman, and Alex Grant	

Evaluation of the Liquefaction Potential for the Mega-City of Mumbai—Probabilistic Performance-Based Approach	187
K. S. Vipin and S. D. Anitha Kumari	
The Seismic Bearing Capacity Factor for Surface Strip Footings	197
Anindya Pain, Deepankar Choudhury, and S. K. Bhattacharyya	
Seismic Deformation Assessment of a Dam Founded on Low Plastic Fine-Grained Soils under Strong Earthquake Shaking	207
Thuraisamy Thavaraj, Garry Stevenson, and David Siu	
Seismic Rotational Stability of a Seawall Considering Non-Breaking Waves	217
B. Giridhar Rajesh and Deepankar Choudhury	
Site-Specific Seismic Ground Response for Mormugao Port, Goa, India.....	227
Nika S. Bhingarde and Nisha P. Naik	
<i>Geoenvironmental Engineering for Disaster Recovery</i>	
A Case Study of the Impact of Tropical Storms on the Stability of Natural Hillslopes in Macon County, North Carolina	237
Giuseppe Formetta, Alexandra Wayllace, and Ning Lu	
Characteristics of the Elemental Release from Recovered Soil Separated from Disaster Waste Generated by the Great East Japan Earthquake and Tsunami	246
Masahiko Katoh, Takuya Yamaguchi, and Takeshi Sato	
Geoenvironmental Issues for the Containment of Radioactively-Polluted Soil and Waste.....	254
Toru Inui, Takeshi Katsumi, and Atsushi Takai	
Geo-Environmental Knowledge for the Adaptation of Riverine Coastal Geo-Hazards.....	264
Kazuya Yasuhara, Van Trinh Cong, Hideo Komine, and Hemanta Hazarika	
Material Properties of Soils Recovered from Disaster Debris in Iwate Prefecture Generated by the 2011 Great East Japan Earthquake	274
Takeshi Katsumi, Atsushi Takai, Toru Inui, Masafumi Okawara, and Mitsuhiro Kawashima	
Mechanical Characteristics of Incineration Bottom Ash from Disaster Waste Caused by the Great East Japan Earthquake	284
Kenichi Sato and Takuro Fujikawa	

Radiation-Shielding Properties of Heavy Bentonite-Based Slurry for the Decommissioning of the Fukushima First Nuclear Power Plant.....292
Ema Yoshikawa, Hideo Komine, Yuma Saito, Shigeru Goto, Seiichi Narushima, Yasunori Arai, Masayuki Mizuno, Shinsuke Ujiie, Yuki Sakoda, Yasushi Nagae, Mitsugu Yoshimura, and Akihiko Suzuki

Uplift Resistance of Buried Pipelines in Dry and Unsaturated Sands: Comparison of Analytical and FE Model Results with Large-Scale Test Data298
Dilan J. Robert, N. I. Thusyanthan, and C. Q. Li

A Utilization Technique of Tsunami Sediments and Disaster Wastes Containing Salt.....310
Kiyoshi Omine and Satoshi Sugimoto

Geohazards

A Meshfree Method for Modeling the Impact of Landslide Activity318
Thanakorn Siriaksorn, Sheng-Wei Chi, and Craig Foster

Analysis of Morphometric Parameters for the Identification of Probable Landslide Occurrences329
Kishor Kumar and Yogita Garbyal

Design and Implementation of a Spatial Database for the Abu Dhabi Municipality Geohazard Management System.....339
Raghav Ramanathan, Mazen E. Adib, Walid Dawoud, Melih Demirkan, Bulent Hatipoglu, Giridhar Kolan Reddy, Michael Rosenmeier, and Cagri Cinkilic

Development of a Comprehensive Geotechnical Information Management System for Municipal Use353
Walid Dawoud, Mazen Elias Adib, Giridhar Kolan Reddy, Raghav Sarathy Ramanathan, Bulent Hatipoglu, Melih Demirkan, and Cagri Cinkilic

Effect of Hybrid Geosynthetic Layers on Soil Walls with Marginal Backfill Subjected to Rainfall362
Dipankana Bhattacharjee and B. V. S. Viswanadham

Exploring the Geomechanics of Sinkholes: A Numerical Simulation Approach372
Kishor Rawal, Zhong-Mei Wang, and Liang-Bo Hu

Feasibility Analysis of the External Electric Anode Method for Reducing Lightning Hazards382
Chao Zhang and Zhen Liu

Flood Holding Capacity: A Novel Concept to Evaluate the Resilience of Amended Soils393
Heather Kerr, Karen Johnson, David G. Toll, and Florence Mansfield

A Modified Mohr-Coulomb Model to Simulate the Response of Buried Pipes Subjected to Large Ground Displacement410
Dilan J. Robert and P. Rajeev

The Use of Neural Networks to Forecast Landslides Triggered by Rains in Mountainous Areas.....422
Eduardo M. Botero, George F. Azevedo, Hernan E. M. Carvajal, Edwin F. García, and George F. Azevedo

Nanomaterials

Bio-Nano-Cementation to Evaluate Soil Mechanical Resistance430
Jaqueline Bonatto, Karla Heineck, Antonio Thomé, Bruna DallAgnol, and Gregório Rigo Garbin

Determination of the Index Properties of Clay Soils in the Presence of Nanoparticles441
James L. Hanson, Nazli Yesiller, Amro El Badawy, Ryne Mettler, and Jared S. Stine

Enhancement of the Strength and Swelling Characteristics of Expansive Clayey Soil Using Nano-Clay Material451
Abdulla A. Sharo and Ahmed S. Alawneh

Influence of Iron Nanoparticle Concentration on the Hydraulic Conductivity of a Residual Clayey Soil.....458
Cleomar Reginatto, Iziquiel Cecchin, Ramiro L. R. Carvalho, Karla Heineck, Antonio Thomé, and Krishna R. Reddy

Potential of Soils Amended with a Nano Calcium Silicate Mixture for Lead Encapsulation in an Aqueous Medium467
Syed Abu Sayeed Mohammed, P. F. Sanaula, Munwar B. Basha, Hari Prasad Reddy, A. M. Alnuaim, and Arif Ali Baig Moghal

Prediction of the Stripping Resistance of Nanoclay-Modified Asphalts Using Their Surface Chemistries477
Zahid Hossain, Biswajit Bairgi, Musharraf Zaman, and Rifat Bulut

The Use of a Green Polymer Nanocomposite in Geo-Infrastructure.....488
Munir D. Nazzal, Tremain D. Gissentaner, Savas Kaya, and Sang Soo Kim

Zero Valent Metal (ZVI) Nanoparticles in Geotextiles and Geomembranes....498
Franz-Georg Simon, Daniela Robertson, Christine Schütt, and Volker Birke

Natural Landslides and Engineered Slopes: Monitoring and Survey Technologies

3D Model Reconstruction of Rocks on a Slope for Simulating a Rock Fall.....508
Itaru Kitahra, Shogo Atsumi, Ryo Degawa, Yohiei Kawamura, Hyongdoo Jang,
and Yuichi Ohta

**Analysis of Shear Zones of Landslides by the Numerical Simulation of
Monitored Surficial Displacement Vectors—Case Study of the Landslide at
Gunung Pass, Malaysia518**
Senro Kuraoka, Naoki Sakai, Mohamad Nazri, Suhaimi Jamaludin,
and Che Hassandi Abdullah

Design of Stable Rock Slopes for the World’s Highest Railway Bridge.....530
Gaurav Tiwari and Gali Madhavi Latha

**Development of a Landslide Observation System Using ZigBee Wireless
Communication Technology542**
Y. Kawamura, H. Jang, K. Ohta, and Y. Inagaki

McCook Reservoir Instrumentation and Monitoring551
Georgette Hlepas and William Rochford

Slope Movement in Permafrost near Fairbanks, Alaska563
Mohammadhossein Sadeghiamirshahidi and Stan Vitton

Stabilizing Walls Retained by Nailing under Additional Excavations574
Majid Taherzadeh Dorobati, Alborz Hajiannia, and Shahrzad Kasaeian

**Understanding the Behavior of Rock-Fall Motion Using Wireless Sensor
Technology.....584**
Prapti Giri, Kam Ng, Christopher Robinson, William Phillips, and Marian Phillips

The Use of LiDAR for Monitoring and Assessing Landslides596
Timothy D. Stark and Ahmed K. Baghdady

**The Use of Electrical and Geotechnical Techniques to Assess a Small Earth
Dam605**
Yara S. Maalouf, Naji N. Khoury, and Louis Junior Saad

Sustainability in Geotechnical Engineering

**Assessing the Life Cycle Benefits of Recycled Material in Road
Construction613**
Eleanor F. Bloom, Gregory J. Horstmeier, Angela Pakes Ahlman,
Tuncer B. Edil, and Gary Whited

Assessment of the Pollution Potential of an Aquifer from Surface Contaminants in a Geographic Information System: A Case Study of Pakistan	623
Yawar Hussain, Sadia F. Ullah, Adil Dilawar, Gulraiz Akhter, Hernan Martinez-Carvajal, and Henrique L. Roig	
Carbon Footprint: Liquefaction Effects on a Private Residence	633
Manasa Vijayakumar, Jennifer J. Cheng, Murat Küçükvar, Ahmed Elgamal, Kevin R. Mackie, and Omer Tatari	
Design and Construction of the Chicago Riverwalk	643
Matthew F. Hellenthal and Dan M. Gross	
Financial Sustainability as a Metric for Infrastructure Projects	653
Ranjiv Gupta, Jeremy W. F. Morris, and R. David Espinoza	
Groundwater Management for Sustainable Underground Subway Development in Manhattan, New York City	663
Chu E. Ho	
Impacts of the Design Methods of Drilled Shafts in Sand on the Environment.....	673
Mina Lee and Dipanjan Basu	
Minimization of Cost and CO₂ Emissions for Drilled Shafts under Axial Loading Using a Big Bang–Big Crunch Algorithm.....	683
Andrew Assadollahi	
State DOT Life Cycle Benefits of Recycled Material in Road Construction	693
Eleanor F. Bloom, Kelly Del Ponte, Bharat Madras Natarajan, Angela Pakes Ahlman, Tuncer B. Edil, and Gary Whited	
How Ground Improvement Contributes to the Green Building Movement.....	704
Chris Woods	
Sustainable Geotechnical Design for Al-Azhar Park, Cairo	712
Ahmed Hosny Abdel-Rahman and Salwa Yassin	
Uncertainty in the Estimates of Embodied Energy and CO₂ Emissions for Ground Improvement: The Influence of Material Haul Distance	722
Craig M. Shillaber, Annie R. Pearce, James K. Mitchell, and Joseph E. Dove	

A New Soil Treatment Method Using Casein from Bovine Milk

Jooyoung Im¹; Gye-Chun Cho²; and Ilhan Chang³

¹Graduate Student, Dept. of Civil and Environmental Engineering, Korea Advanced Institute of Science and Technology (KAIST), Republic of Korea 34141.

²Professor, Dept. of Civil and Environmental Engineering, Korea Advanced Institute of Science and Technology (KAIST), Republic of Korea 34141.

³Senior Researcher, Korea Institute of Construction Technology (KICT), Republic of Korea 10223 (corresponding author). E-mail: ilhanchang@kict.re.kr

Abstract: Methods of soil improvement that consider both the physical/mechanical properties and the environmental/geochemical aspects of soils have been studied and developed in recent years. This is due to the necessity of a nonhazardous soil improvement method that can alleviate the environmental concerns of current soil improvement methods. Several considerations such as the use of biological organisms and biopolymers have been researched for their applicability in soil improvement. In this study the use of casein proteins derived from bovine milk is purposed as a possible soil improvement material. With its biological origin and characteristics, casein treated soil is regarded to be harmless and safe to the environment. Additionally, with the large and growing amount of dairy wastes, this soil improvement method could serve as a possible sink for such wastes. Results of casein treatment have shown that a definite increase in strength is observed when casein based binders are integrated into the soil.

INTRODUCTION

In recent years environmentally friendly approaches to soil improvement have been studied and researched. Among current methods, cement is the most used soil improvement method, but the use of cement has numerous environmental drawbacks. The use of cement produces approximately 5% of the global annual CO₂ emission (Worrell et al. 2001), additionally, when cement is implemented into the soil the pH of the soil rises which can affect the local ecosystems exhibiting some detrimental effects (Hansen 2002). As a result, ecofriendly biological approaches such as the use of microbial inducing calcite precipitation (MICP) (DeJong et al. 2006; Whiffin et al. 2007) and the use of biopolymers in soil improvement has been researched (Maher and Ho 1994; Sivakumar Babu and Vasudevan 2008). However, the use of biopolymer has been shown to be sensitive to the presence of water, and as such the possible use of a soil binder with high water resistivity using casein proteins was studied.

The use of casein proteins derived from dairy products has numerous benefits. Since the binder is derived from a biological source such as dairy, its use does not have large

effects on the global emissions of greenhouse gases. Also, with the casein proteins being highly unreactive to water and hydrophobic by nature, its resistance to water will be higher than previously used biopolymers such as β -1,3/1,6-glucan (Chang and Cho 2012). In addition, numerous dairy wastes containing high concentrations of organic matters are generated (e.g., 500 m³ daily, for a typical European dairy), while wastewater treatment (e.g., anaerobic treatment) is applied only for a small portion and most of dairy wastes are dumped and disposed in ground (Capper et al. 2009; Demirel et al. 2005; Eide 2002). However, if such milk and dairy wastes could be recycled and reused in construction purposes, the amount and environmental impact of waste disposal will diminish, moreover providing a low carbon footprint eco-friendly alternative to soil treatment and improvement.

METHODS AND MATERIALS

Biopolymers and soil

Soil Type

The soil used for this study was a combination of Korean residual soil (*i.e.* *hwangtoh*) and *jumunjin* sand (*i.e.*, a common standard sand type in Korea). *Hwangtoh* is a silty clayey soil that has a mineral composition of (8.4%) quartz, (45.8%) kaolinite, (22.7%) halloysite, (14.8%) illite, and (8.3%) goethite by mass. *Jumunjin* sand is a poorly graded sand (*USCS: SP*) with an average particle size of approximately 0.6 mm. The *hwangtoh* and *jumunjin* sand were mixed at a 1 to 1 ratio by weight, and the mixed soil was used as the target soil for this study.

Casein Proteins

A technical grade of casein proteins derived from bovine milk was used as the strengthening agent of this study. Casein was purchased in the powder form from sigma Aldrich (CAS: 9000-71-9), and a binder was formed by dissolving the proteins in a solution, which was then mixed with the target soil.

Sample preparation and experimental procedure

The casein binder was prepared by dissolving the bovine casein protein in an alkaline solution (CaOH 1%), and this solution was mixed with the soil at the target water content of 25%. The soil was mixed with varying casein concentrations (by weight to the soil mass) at 0.00%, 2.00%, 2.66%, 3.33%, 4.00%, and 6.66%.

These mixtures were then molded into cubes with dimension of 40 × 40 × 40 mm and were allowed to air dry for 28 days at room temperature. After the samples were fully dried, half of the specimens were submerged into water for 24 hours before conducting unconfined compressive strength measurements to identify the strength reduction of casein-treated soils by re-wetting (saturation). Meanwhile, left-half (*i.e.*, dried) of the specimens were taken to measure the dry and undisturbed strengths of casein-treated soils.

The unconfined uniaxial compressive tests were performed using the UTM (Universal Testing Machine: Instron 5583) device. The axial strain rate was set at 0.4 mm/min, and the maximum strengths and the stress-strain behaviors were obtained from an average of three separate specimens.

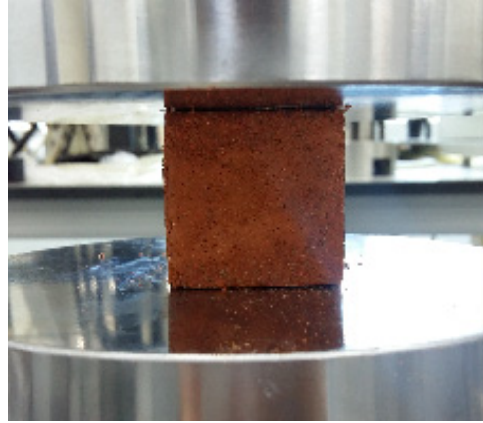


FIG. 1. Unconfined uniaxial compressive test of casein treated soils

RESULTS AND ANALYSIS

Results showed that the use of casein in the soil matrix allowed for strengthening mechanism by acting as a bonding agent between the soil particles. The compressive strengths of both the dry and wet conditions show an increase in strength with an increase in casein concentration. The increase however, is not a linear trend but instead shows a slight exponential behavior where a small increase in the casein concentration has a larger effect on the strength than in the lower concentrations. This indicates that the strengthening mechanisms of the casein binders becomes significantly more efficient at higher concentrations.

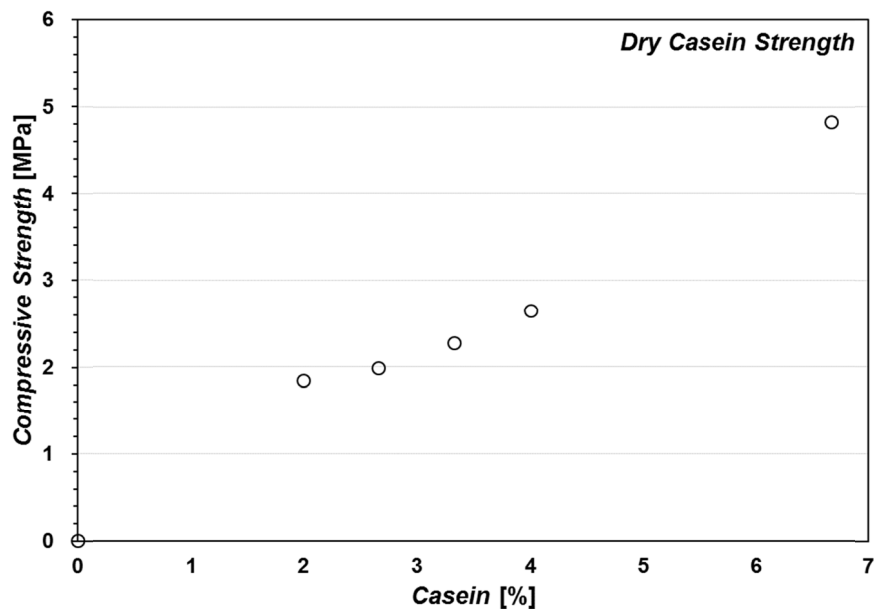


FIG. 2. Unconfined compressive strengths of various casein concentrations in the dry condition.

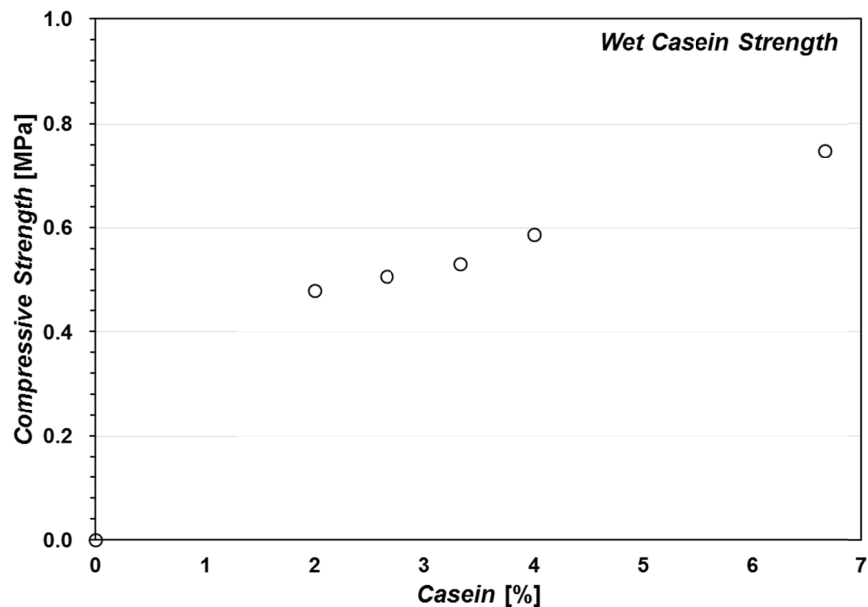


FIG. 3. Unconfined compressive strengths of various casein concentrations in the wet condition.

However, the compressive strength results showed that when the specimens were submerged in water, a significant reduction in strength was observed. Although casein proteins are hydrophobic and unreactive with water molecules, the presence of water is still shown to degrade the bonding effects of the casein binder. Approximately 1/6 to 1/4 of the dry strength was retained in the wet condition, which has a larger strength degradation than that of cement, but a lower degradation in strength when compared to that of previously used biopolymers (*1/10 to 1/20 of dry strength retained in wet condition*) (Chang et al. 2015). Table 1 shows a comparison between cemented soils and casein and gellan treated soils.

Table 1. Unconfined uniaxial compression of various binders in the dry and wet state

Binder Used	Dry Strength (MPa)	Wet Strength (MPa)
Cement 10%	2.65	1.94
Casein 6.66%	4.83	0.75
Xanthan 1%	4.94	0.00
Gellan 1%	4.61	0.23

When compared to cement, the use of biopolymers shows a more efficient strengthening effect at lower concentrations, but their resistance to water is significantly lower than that of cement. However, among the biopolymer binders used, the binder derived from casein proteins shows a much larger wet strength than its counterparts. This shows that its capabilities in water are not as low as the other biopolymers used, and its use in a water resistant biopolymer binder shows prospect.

CONCLUSIONS

The use of casein proteins for soil improvement has shown beneficial results. The compressive strengths showed that at lower concentrations than that of cement, the compressive strength of casein binder was capable of achieving a higher dry strength, but the wet strengths of casein treated soils were still lacking when compared with cement treatment. However, when the wet compressive strengths were compared with that of previously used biopolymers, an increase in the resistivity to water was observed. As such, although its resistance to water is still lacking, the use of casein proteins in a soil binder shows promise for the development of an eco-friendly soil improvement method that has a high resistivity to water.

ACKNOWLEDGMENTS

The authors appreciate the support of National Research Foundation of Korea (NRF) grant funded by the Korean government (MSIP) (No. 2015R1A2A2A03006268), by a grant from the Strategic Research Project (Development of Key Excavation Solutions for Expandable Urban Underground Space) funded by the Korea Institute of Civil Engineering and Building Technology (KICT), and by the KAIST End-Run Program (No. N01150661) supported by the Korea Ministry of Science, ICT and Future Planning (MISP).

REFERENCES

- Capper, J. L., Cady, R. A., and Bauman, D. E. (2009). "The environmental impact of dairy production: 1944 compared with 2007." *Journal of Animal Science*, 87(6), 2160-2167.
- Chang, I., and Cho, G.-C. (2012). "Strengthening of Korean residual soil with β -1,3/1,6-glucan biopolymer." *Construction and Building Materials*, 30(0), 30-35.
- Chang, I., Prasadhi, A. K., Im, J., and Cho, G.-C. (2015). "Soil strengthening using thermo-gelation biopolymers." *Construction and Building Materials*, 77(0), 430-438.
- DeJong, J., Fritzges, M., and Nüsslein, K. (2006). "Microbially Induced Cementation to Control Sand Response to Undrained Shear." *Journal of Geotechnical and Geoenvironmental Engineering*, 132(11), 1381-1392.
- Demirel, B., Yenigun, O., and Onay, T. T. (2005). "Anaerobic treatment of dairy wastewaters: a review." *Process Biochemistry*, 40(8), 2583-2595.
- Eide, M. (2002). "Life cycle assessment (LCA) of industrial milk production." *Int J LCA*, 7(2), 115-126.
- Hansen, P. J. (2002). "Effect of high pH on the growth and survival of marine phytoplankton: implications for species succession." *Aquatic microbial ecology*, 28(3), 279-288.
- Maher, M., and Ho, Y. (1994). "Mechanical Properties of Kaolinite/Fiber Soil Composite." *Journal of Geotechnical Engineering*, 120(8), 1381-1393.
- Sivakumar Babu, G., and Vasudevan, A. (2008). "Strength and Stiffness Response of Coir Fiber-Reinforced Tropical Soil." *Journal of Materials in Civil Engineering*, 20(9), 571-577.

- Whiffin, V. S., van Paassen, L. A., and Harkes, M. P. (2007). "Microbial Carbonate Precipitation as a Soil Improvement Technique." *Geomicrobiology Journal*, 24(5), 417-423.
- Worrell, E., Price, L., Martin, N., Hendriks, C., and Meida, L. O. (2001). "Carbon Dioxide Emissions from the Global Cement Industry." *Annual Review of Energy and the Environment*, 26(303-329).

A Stoichiometric Model for Biogeotechnical Soil Improvement

Sean T. O'Donnell, M.ASCE¹; Nasser Hamdan, M.ASCE²; Bruce E. Rittmann, M.ASCE³; and Edward Kavazanjian, Jr., F.ASCE³

¹Graduate Research Associate, School of Sustainable Engineering and the Built Environment, Arizona State Univ., Tempe, AZ 85287-5306.

²Staff Civil Engineer, ARCADIS U.S., Inc., 410 N. 44th St., Suite 1000, Phoenix, AZ 85008.

³Regents' Professor, School of Sustainable Engineering and the Built Environment, Arizona State Univ., Tempe, AZ 85287-5306.

Abstract: A stoichiometric model was developed for predicting the amount of carbonate precipitation and gas production from two different biogeotechnical soil improvement techniques: enzyme-induced hydrolysis of urea and microbial denitrification. Carbonate precipitation via hydrolysis of urea, or ureolysis, and via dissimilatory nitrate reduction, or denitrification, has been shown in laboratory testing to improve the shear strength and cyclic resistance of granular soils. Desaturation via denitrification has also shown the ability to improve cyclic resistance. For effective implementation of these techniques in the field, it is important to understand the material requirements necessary to achieve the desired degree of improvement. Therefore, a model for predicting carbonate precipitation and gas production from these techniques was developed using stoichiometry, thermodynamics, and microbial growth patterns and calibrated with laboratory test data. The model will facilitate the implementation of cost-effective, non-intrusive, and sustainable ground improvement.

INTRODUCTION

Microbially Induced Carbonate Precipitation (MICP) and Enzyme Induced Carbonate Precipitation (EICP) are two emerging biogeotechnical soil improvement techniques. MICP can be induced by a variety of microbial processes, the most studied of which are microbial ureolysis and microbial denitrification (DeJong et al. 2011). EICP uses plant-derived urease enzyme to facilitate carbonate precipitation via ureolysis (Hamdan 2014). Both of these biogeotechnical processes alter the geochemistry of the soil pore water by increasing the pH and alkalinity to induce precipitation of divalent cations (such as calcium) as carbonate minerals (such as calcite) (DeJong et al. 2011). Precipitation of carbonates at soil contacts can lead to cementation, and carbonate coating of soil particles can lead to particle roughening; both of which can significantly improve soil stiffness, strength, and dilatant behavior

(O'Donnell and Kavazanjian 2015; van Paassen et al. 2010). Microbial denitrification, while slower than ureolysis, has the added benefit of generating substantial amounts of biogas, which can desaturate soil, leading to improved dilatancy and cyclic resistance (He et al. 2013, Kavazanjian et al. 2015).

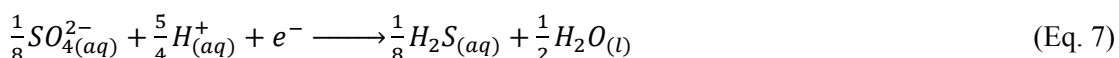
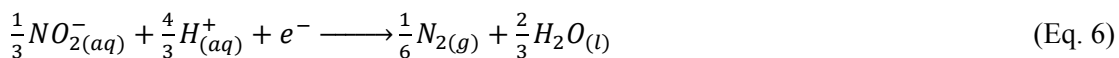
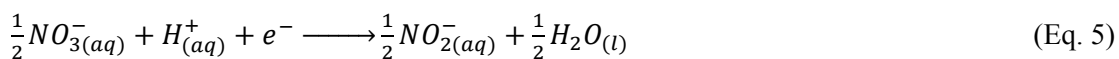
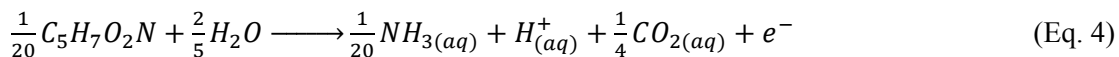
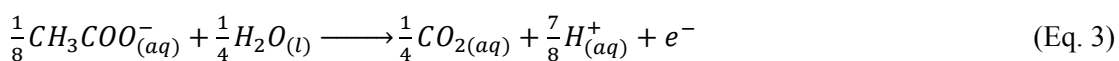
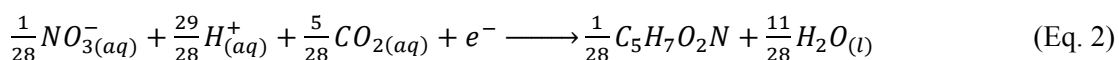
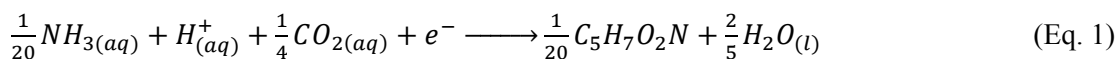
Laboratory tests have shown how carbonate precipitation and gas production can induce significant soil improvement, but the relationships between input materials (e.g., calcium chloride, calcium nitrate, urea), intermediate materials (e.g., nitrite, microbial biomass) and the outputs of interest (e.g., calcium carbonate, biogas) remain unclear. A stoichiometric model is presented herein to elucidate the interactions between inputs, intermediate products, and outputs in order to better understand the processes at work in MICP via denitrification and EICP via ureolysis.

STOICHIOMETRIC MODEL

Stoichiometric modeling of MICP and EICP involves three steps: obtaining balanced chemical equations, determining kinetic expressions, and coupling these to the thermodynamics of carbonate precipitation.

Balanced Chemical Equations

For MICP via denitrification, three types of half reactions were used to model microbial growth. Two cell synthesis half reactions were considered: ammonia (NH_3) as a nitrogen source (Eq. 1) and nitrate (NO_3^-) as a nitrogen source (Eq. 2). Two different electron donor half reactions were also considered: acetate (Eq. 3) and endogenous decay of biomass (Eq. 4). Three different electron acceptor half reactions were considered: nitrate (Eq. 5), nitrite (Eq. 6), and sulfate (Eq. 7). Sulfate was considered due to evidence for sulfate reduction in the experimental results.



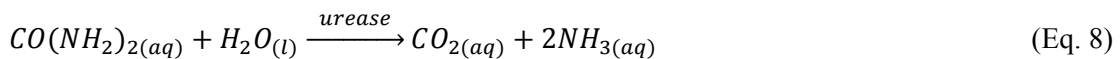
By pairing each of the two electron donor reactions and the three electron acceptor reactions, six different microbial metabolisms were identified for this work. These pairings and the coefficients used in each half reaction are presented in Table 1.

Table 1: Microbial metabolisms considered in this model including coefficients used on each of the half reactions presented in Eqs. 1-6.

Metabolism (acceptor, donor)	Coefficients						
	Eq. 1	Eq. 2	Eq. 3	Eq. 4	Eq. 5	Eq. 6	Eq. 7
Nitrate, Acetate	$f_{s,1}^0 * (1 - f_a)$	$f_{s,1}^0 * f_a$	1	0	$1 - f_{s,1}^0$	0	0
Nitrite, Acetate	$f_{s,2}^0 * (1 - f_a)$	$f_{s,2}^0 * f_a$	1	0	0	$1 - f_{s,2}^0$	0
Sulfate, Acetate	$f_{s,3}^0 * (1 - f_a)$	$f_{s,3}^0 * f_a$	1	0	0	0	$1 - f_{s,3}^0$
Nitrate, Biomass	0	0	0	1	1	0	0
Nitrite, Biomass	0	0	0	1	0	1	0
Sulfate, Biomass	0	0	0	1	0	0	1

In Table 1, the coefficient $f_{s,x}^0$ represents the fraction of electron equivalents used for cell synthesis from metabolism “x,” while the coefficient f_a represents the fraction of cell synthesis for which NO_3^- , as opposed to NH_3 , is the nitrogen source. The coefficient $f_{s,x}^0$ was calculated for each reaction based on the thermodynamic properties of the half reactions considered, as well as the efficiency of electron transfers within the cell (Rittmann and McCarty 2001). The metabolisms in which biomass is the electron donor represent the process of endogenous decay, in which cells oxidize themselves to meet energy requirements. For endogenous decay, there is no cell synthesis, so $f_{s,x}^0 = 0$. The coefficient f_a was used as a fitting parameter.

Enzyme-induced ureolysis is a much simpler process and therefore only requires the one overall balanced equation presented below in Eq. 8.



Kinetics Expressions

For MICP via denitrification and EICP via ureolysis, the systems were modeled as batch reactors, meaning there are no inputs or outputs to the system during the reaction. For microbial denitrification, a dual-limitation kinetics model was applied, giving the rate expressions for the electron donor and the biomass concentration found in Eqs. 9 and 10 below (Bae and Rittmann 1996).

$$\frac{dC_d}{dt} = -\hat{q} * \frac{C_d}{K_d + C_d} * X_a * \frac{C_a}{K_a + C_a} \quad (\text{Eq. 9})$$

C_d = concentration of electron donor (M)

\hat{q} = maximum specific rate of electron donor utilization (t^{-1})

K_d = Monod half-maximum-rate concentration of electron donor (M)

X_a = concentration of biomass (M)

C_a = concentration of electron acceptor (M)

K_a = Monod half-maximum-rate concentration of electron acceptor (M)

$$\frac{dX_a}{dt} = X_a * (\hat{q} * Y * \frac{C_a}{K_a + C_a} * \frac{C_d}{K_d + C_d} - f_d * b) \quad (\text{Eq. 10})$$

Y = true yield (mol cells/mol electron donor)

f_d = fraction of active biomass that is biodegradable

b = endogenous decay coefficient (t^{-1})

The value of \hat{q} was computed based upon the maximum electron flow to the electron acceptor and the temperature, Y was calculated based upon the $f_{s,x}^0$ values for each metabolism, and f_d was fixed at 0.8 (Rittmann and McCarty 2001). Values for C_a and C_d were calculated based upon Eq. 9 and stoichiometry from Eqs. 3-7 at each time step. The values of b, K_d , and K_a were used to fit the model to experimental data.

For enzyme-induced ureolysis, the rates of urease activity were determined based upon the studies of Fidaleo and Lavecchia (2003) with jack bean derived urease. The rate expression for urea can be found in Eq. 11 below.

$$\frac{dC_u}{dt} = -\frac{C_u * v_{max}}{(K_M + C_u) * (1 + \frac{C_a}{K_P})} \quad (\text{Eq. 11})$$

C_u = concentration of urea (M)

v_{max} = maximum reaction rate (Mt^{-1})

K_M = Monod half-maximum-rate concentration (0.0321 M)

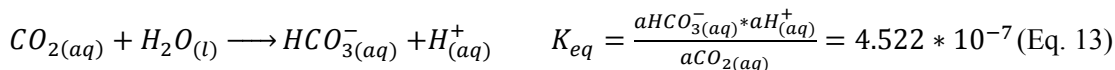
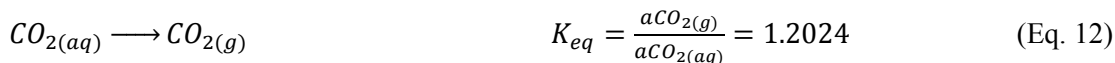
C_a = ammonium ion concentration (M)

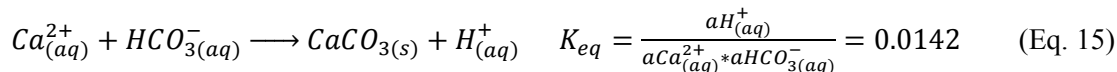
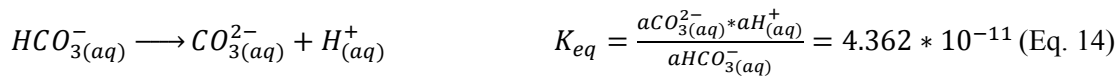
K_P = dissociation constant for enzyme-product complex (0.0122 M)

The value of v_{max} was computed at each time step based upon pH and the initial concentration of urease enzyme (Fidaleo and Lavecchia 2003).

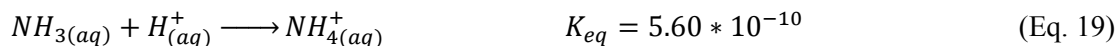
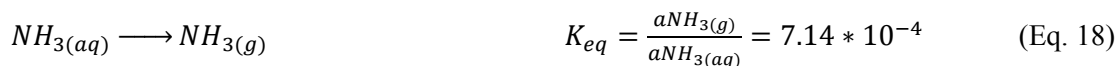
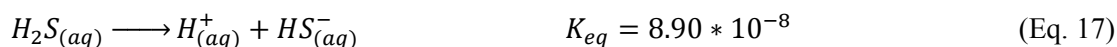
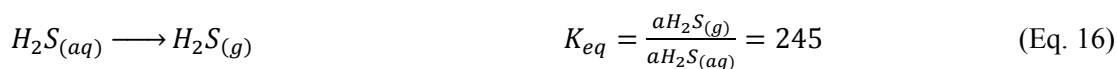
Carbonate Equilibrium and Precipitation

Once the balanced equations and kinetics expressions were established, a mass balance approach coupled with the thermodynamics of carbonate speciation and precipitation was used to determine the amount of gas production and calcium carbonate (CaCO_3) precipitation. Enzyme-induced ureolysis and microbial denitrification produce carbon dioxide (CO_2). The rate and amount of CO_2 production was determined for each process based on the kinetics and stoichiometry of the reaction. Then, the thermodynamics of carbonate speciation and CaCO_3 precipitation was used to determine how much carbon stayed in solution (as either dissolved CO_2 , bicarbonate anion (HCO_3^-), or carbonate anion (CO_3^{2-})), precipitated as CaCO_3 , or partitioned into the gas phase as gaseous CO_2 . The equations of carbonate equilibrium are presented below in Eqs. 12-15. The rate constants were obtained using the computer program CHNOSZ (Dick 2008).





As illustrated by Eqs. 12-15, inorganic carbon speciation and precipitation is intricately tied to the production and consumption of protons ($H^+(aq)$) in solution and, hence, the pH. In order to determine the equilibrium pH at each time step, a mass balance approach was used based on all of the speciation and precipitation reactions involved. So, in addition to the carbonate reactions, it was necessary to consider the speciation of hydrogen sulfide for MICP (Eqs. 16-17) and ammonia for EICP (Eq. 18-19). The rate constants for these equations were found using CHNOSZ (Dick 2008).



The activity coefficients for each of the charged chemical constituents involved in Eqs. 12-19 were determined from the ionic strength of the solution, the temperature, and the dielectric constant of water according to Davies Equation (Davies 1962).

EXPERIMENTS

Microbial Denitrification

Four specimens were prepared in 150 mm-tall, 73 mm-diameter acrylic columns equipped with a drainage port at the base, a gas collection port at the top, and sampling ports located 5 cm from the base and 5 cm from the top. Two columns contained Ottawa 20-30 crystal silica sand at a relative density of 45% while the other two contained a natural beach sand from Bolsa Chica State Beach, Huntington Beach, California at a relative density of 90%. The acrylic columns were alcohol sterilized (70% v/v ethanol) and the sand was autoclaved to minimize the potential for contamination of the columns with microbes. After sand placement, each column was purged from the top port with $N_{2(g)}$ to minimize oxygen and promote denitrification.

The columns were inoculated with a mixed culture of microbes enriched from sand and water collected from Bolsa Chica State Park. Following inoculation, each column was filled with a pore fluid solution containing $Ca(NO_3)_2$, $Ca(CH_3COO)_2$, $CaCl_2$, $MgSO_4$, and trace metals. Every two weeks, the pore fluid was drained and replaced. The details of inoculation and pore fluid makeup can be found in Kavazanjian et al. 2015. In order to monitor the amount of gas generated, dialysis bags were connected to the top ports of each column to collect gas and displaced fluid during denitrification.

During the 20th refilling cycle (42 weeks after initial inoculation), the chemistry in each column was monitored by extracting roughly 3-4 mL of pore fluid at 0, 0.75, 1.5, 3.5, 6.5, and 9.5 days after refill from both the top and bottom sampling ports. For each sample, the pH was taken immediately after extraction, the Total Kjeldahl Nitrogen (TKN) was found through the use of a Hach TNT 880 kit, and the ionic makeup of the pore fluid was determined by filtering 1 mL of the sample through a 0.2 μm filter. The filtered samples were stored at 4°C for two weeks before diluting them by a factor of 200 with DI water and analyzing the filtered, diluted samples using ion chromatography (Dionex ICS-2000). In this way, pH, TKN, nitrate, nitrite, sulfate, acetate, carbonate, ammonium, and calcium concentrations were determined at each sampling site in each column with time. The TKN data and ammonium concentrations were used to estimate the organic nitrogen content in each sample, which was used as a measure of biomass concentration.

During the 21st refilling cycle (44 weeks after initial inoculation), the amount of gas generated in each column was determined at 0, 1, 2, 3, 4, 5, 6.5, and 14 days after refill by measuring the volume change of the dialysis bag. It was assumed that the volume change was equal to the volume of gas generated.

Enzyme-Induced Ureolysis

Fifteen test tube experiments were performed to test the effects of varying the initial urea and calcium concentrations on the process of EICP via ureolysis. Triplicate tests using five different sets of initial concentrations were performed. For each set of tests, the initial concentrations of CaCl_2 was kept constant at 0.2M while the initial urea concentration was varied from 0.1-0.6M. The initial pH was adjusted to 8.0 and 0.47 g/L of jack bean derived urease was added to each tube to begin ureolysis. The details of the experimental method can be found in Hamdan 2014.

After nine days, the test tubes were opened, and approximately 9 mL from each tube was taken for sampling. The fluid was immediately filtered through a 0.2 μm syringe filter and tested for pH and total alkalinity (Hach TNT 870 kit). Each fluid sample was then stored at -20°C to halt the urease activity. Several days later, the fluid was tested using ion chromatography (Dionex ICS-2000) to determine concentrations of Ca^{2+} and NH_4^+ in each test tube.

MODEL CALIBRATION AND VALIDATION

Microbial Denitrification

The IC and pH data from the column experiments indicated that the pore fluid was super-saturated with respect to CaCO_3 , with a saturation index (SI) ranging from 10-15 at all times. This is most likely due to the high concentrations of acetate in solution, as acetate has been shown to inhibit the formation of CaCO_3 (Haile 2011; Kitano et al. 1969). The model was adjusted to reflect this finding by changing the initial SI to 10 and the long term SI to 15. The values of K_a , K_d , and b from Eqs. 9-10 were established by fitting the acetate and NO_3^- concentrations in the model to the experimental data. The fitted values for K_a , K_d , and b can be found in Table 2.

Table 2: Kinetics coefficients used to fit model output to experimental data

K_{NO_3}	K_{NO_2}	K_{SO_4}	K_{CH_3COO}	$K_{Biomass}$	b_{NO_3}	b_{NO_2}	b_{SO_4}
0.04 M	0.01 M	10^{-5} M	0.075 M	2×10^{-5} M	0.3 d^{-1}	0.3 d^{-1}	0.18 d^{-1}

The K values (K_a , K_d) for NO_3^- , NO_2^- , and acetate in Table 2 are quite high (Rittmann and McCarty 2001). It is hypothesized that the high concentrations of NO_3^- and NO_2^- found in the columns inhibited the rate of denitrification (Almeida et al. 1994). When the model was fit to the experimental data, this inhibition was reflected in the K values. The b values used to fit the data lie within the expected range (Rittmann and McCarty 2001). The fitted model output and experimental data are shown in Fig. 1.

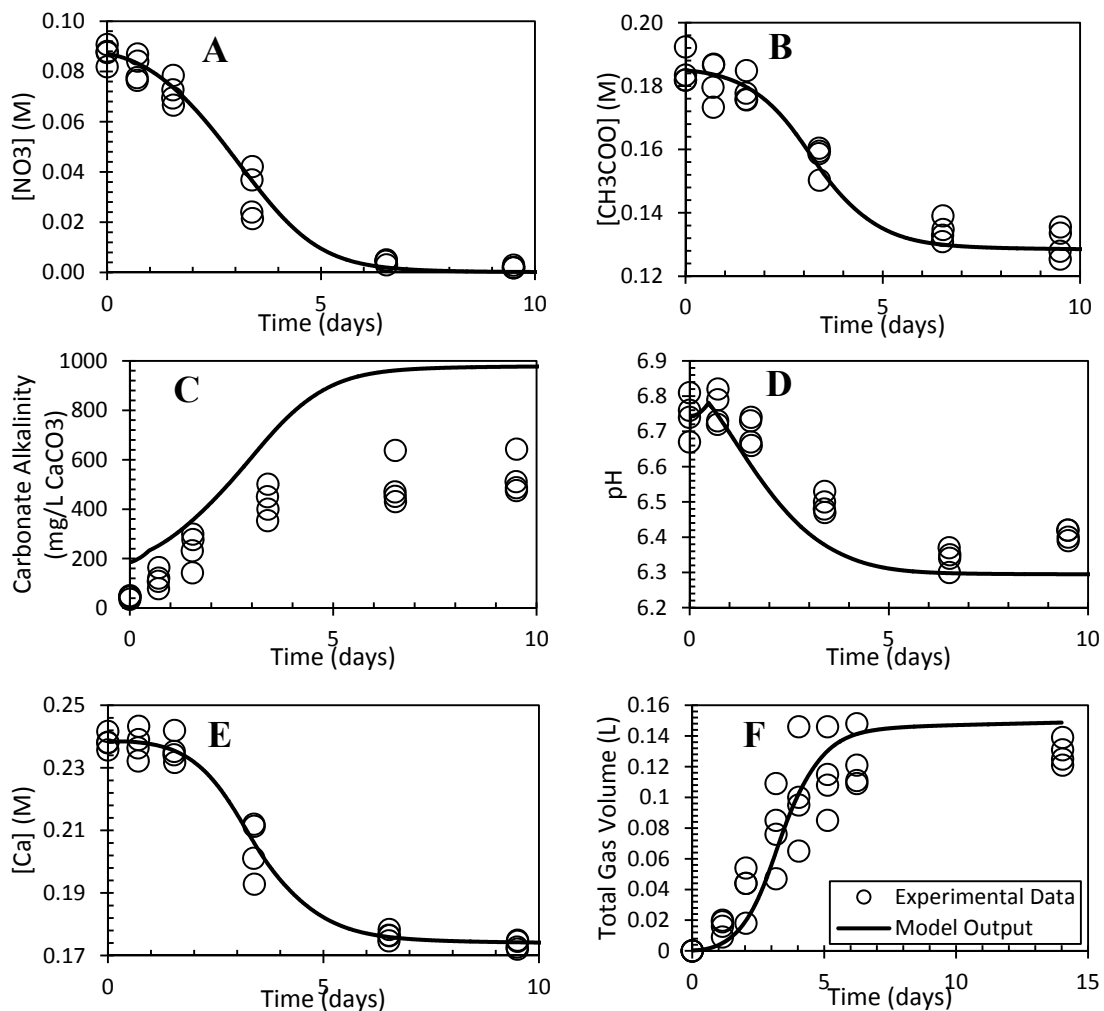


Figure 1: Model output and experimental results for nitrate (A), acetate (B), carbonate alkalinity (C), pH (D), calcium (E), and total gas volume ($N_{2(g)}$, $CO_{2(g)}$, and $H_2S_{(g)}$) (F) for microbial denitrification.

The agreement between the model output and the experimental data shown in Fig. 1 is generally good, especially with regard to Ca^{2+} concentration and total gas volume (sum of $\text{N}_{2(g)}$, $\text{CO}_{2(g)}$, and $\text{H}_2\text{S}_{(g)}$ volumes), the outputs of greatest interest for soil improvement. The amount of Ca^{2+} lost from the system is directly proportional to the amount of CaCO_3 precipitated, while the total gas volume is related to the final degree of saturation. Both of these values are necessary for determining the extent of soil improvement expected from microbial denitrification (Kavazanjian et al. 2015). The disparity between observed and expected carbonate alkalinity (Fig. 1C) is most likely due to sample preparation and subsequent IC analysis. The fluid samples taken from each column contain high amounts of dissolved CO_2 . When they are exposed to the atmosphere, even for a short time, the dissolved CO_2 will off-gas (Eq. 12). Since it was not possible to dilute and then analyze fluid samples for IC analysis without exposing them to the atmosphere, some inorganic carbon was most likely lost via this mechanism. The slight disparity between observed and expected pH is another reason why the model predicts a higher than observed carbonate alkalinity. At lower pH, much more bicarbonate can remain in solution without precipitating as calcium carbonate (Eq. 15). Since the model predicts a slightly lower pH than what was observed, it makes sense that it would also predict a slightly higher carbonate alkalinity.

Enzyme-Induced Ureolysis

The comparison between the model output and averaged experimental results for enzyme-induced ureolysis is presented in Fig. 2. Figure 2 shows fairly good agreement between the model output and the experimental results for enzyme-induced ureolysis, particularly for Ca^{2+} removal. As discussed earlier, Ca^{2+} removal is proportional to the amount of CaCO_3 precipitated. As such, it is important for assessing the amount of soil improvement achieved through EICP. The concentration of NH_4^+ ions and the pH are useful for assessing the environmental impact of EICP. The final pH values from the model and the experiments matched fairly well, but there were slight discrepancies in the NH_4^+ concentrations. The inconsistencies between the observed and predicted NH_4^+ concentrations at higher initial urea to CaCl_2 ratios is most likely due to errors in concentration measurements. When the samples were diluted with DI water before IC analysis, the pH of the samples declined and the extent of decline depended on the acid neutralizing capacity (ANC) of the samples. The decline in pH was greater for the samples with a lower initial urea to CaCl_2 ratio (and therefore lower ANC), than for the higher initial ratio samples. Essentially, the decline in pH due to DI water dilution had a greater impact in samples with less buffering capacity (ANC). This forced the ammonia equilibrium toward NH_4^+ (Eq. 19), leading to higher measured values than those predicted by the model.

CONCLUSIONS

A stoichiometric model was developed to predict the amount of CaCO_3 precipitation for MICP via denitrification and EICP via ureolysis and the amount of

gas production for denitrification. This model represents an important first step in the analysis of large scale biogeotechnical ground improvement projects. The model was formulated for batch reactors (no-flow condition). However, the model can easily be modified to account for continuous flow, making it applicable to field conditions. Overall, the stoichiometric model presented herein shows promise for understanding and predicting the complex biological and chemical interactions involved with MICP via denitrification and EICP via ureolysis.

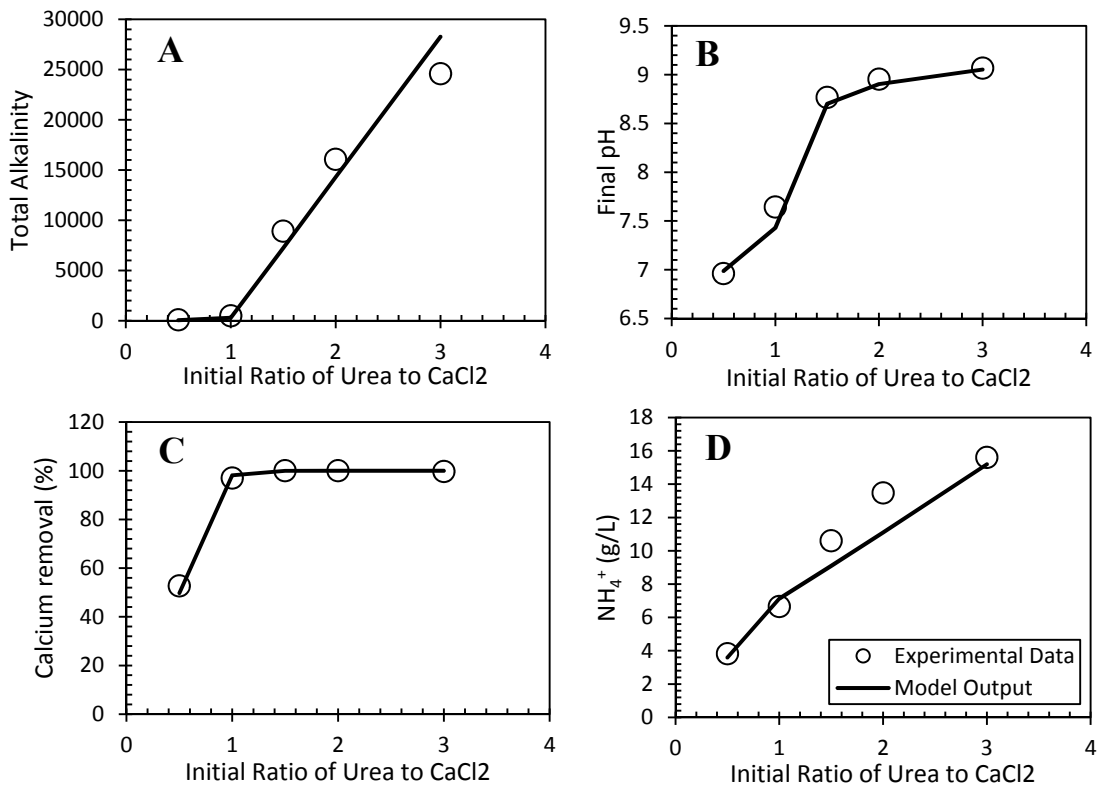


Figure 2: Model output and experimental results for total alkalinity (A), final pH (B), calcium removal (C), and final ammonium concentration (D) for enzyme-induced ureolysis.

ACKNOWLEDGEMENT

This work was funded, in part, by the Geomechanics and Geotechnical Systems, Geoenvironmental Engineering, and Geohazards Mitigation program of the United States National Science Foundation (NSF) Division of Civil, Mechanical, and Manufacturing Innovation under grants numbered CMMI-07030000 and CMMI-1233658. The authors are grateful for this support. Any opinions or positions expressed in this paper are the opinions and positions of the authors only, and do not reflect any opinions or positions of the NSF.

REFERENCES

- Almaeida, J.S., Julio, S.M., Reis, M.A.M., and Carrondo, M.J.T. (1994) "Nitrite Inhibition of Denitrification by *Pseudomonas fluorescens*." *Biotechnology and Bioengineering*, 46 (3): 194-201.
- Bae, Wookeun, and Rittmann, Bruce E. (1996) "A Structured Model of Dual-Limitation Kinetics." *Biotechnology and Bioengineering*, 49: 683-689.
- Davies, C.W. (1962). *Ion Association*. London: Butterworths. pp. 37-53.
- DeJong, J.T., Soga, K., Banwart, S.A., Whalley, R.W., Ginn, T.R., Nelson, D.C., Mortensen, B.M., Martinez, B.C., and Barkouki, T. (2011) "Soil Engineering *in vivo*: Harnessing Natural Biogeochemical Systems for Sustainable, Multi-Functional Engineering Solutions." *J. R. Soc. Interface* 8: 1-15.
- Dick, Jeffrey M. (2008) "Calculation of the relative metastabilities of proteins using the CHNOSZ software package." *Geochemical Transactions*, 9 (10): 1-17.
- Fidaleo, M. and Lavecchia, R. (2003) "Kinetic Study of Enzymatic Urea Hydrolysis in the pH Range 4-9." *Chem. Biochem. Eng. Q.* 17 (4): 311-318.
- Haile, Beyene Girma. (2011) "An Experimental Study of the Effect of Dissolved Acetate ion on the Calcite Precipitation Kinetics and its Implications for Subsurface CO₂ Storage." Master's Thesis, University of Oslo.
- Hamdan, Nasser M. (2014) "Applications of Enzyme Induced Carbonate Precipitation (EICP) for Soil Improvement." Dissertation, Arizona State University.
- He, J., Chu, J., and Ivanov, V. (2013) "Mitigation of Liquefaction of Saturated Sand Using Biogas." *Geotechnique*, 63 (4): 267-275.
- Kavazanjian, Edward Jr., O'Donnell, Sean T., and Hamdan, Nasser. (2015) "Biogeotechnical Mitigation of Earthquake-Induced Soil Liquefaction by Denitrification: A Two Stage Process." Proceedings 6ICEGE, Christchurch, NZ.
- Kitano, Yasushi, Kanamori Nobuko, and Tokyuama, Akira. (1969) "Effects of Organic Matter on Solubilities and Crystal Form of Carbonates." *American Zoologist*, 9 (3): 681-688.
- O'Donnell, Sean Thomas and Kavazanjian, Edward Jr. (2015) "Stiffness and Dilatancy Improvements in Uncemented Sands Treated through MICP." *Journal of Geotechnical and Geoenvironmental Engineering*, In publication.
- Rittmann, Bruce E. and McCarty Perry L. (2001) "Environmental Biotechnology: Principles and Applications." McGraw Hill, New York, NY.
- van Paassen, Leon A., Ghose Ranajit, van der Linden Thomas J.M., van der Star, Wouter R.L., and van Loosdrecht, Mark C.M. (2010) "Quantifying Biomediated Ground Improvement by Ureolysis: Large-Scale Biogrout Experiment." *Journal of Geotechnical and Geoenvironmental Engineering*, 136 (12): 1721-1728.

An Environmentally-Friendly Geotechnical Approach for Soil Erosion Reduction Using Microbial Biopolymers

Ilhan Chang, M.ASCE¹; Jooyoung Im²; and Gye-Chun Cho, M.ASCE³

¹Senior Researcher, Geotechnical Engineering Research Institute, Korea Institute of Civil Engineering and Building Technology (KICT), Republic of Korea 10223 (corresponding author). E-mail: ilhanchang@kict.re.kr

²Graduate Student, Dept. of Civil and Environmental Engineering, Korea Advanced Institute of Science and Technology (KAIST), Republic of Korea 34141.

³Professor, Dept. of Civil and Environmental Engineering, Korea Advanced Institute of Science and Technology (KAIST), Republic of Korea 34141.

Abstract: Global warming and unsustainable land development are known to be major triggers promoting geotechnical hazards such as farmland and coastal erosion, yellow dust, and desertification. New forestry practices, such as encouraging forests in dry land areas, are simple measures that can remove more carbon from the atmosphere and prevent the spread of deserts. Numerous global agencies and companies are thus contributing to anti-desertification movements. However, tree planting alone is not an ideal solution given that it takes approximately 2~3 years for stabilization. It is thus imperative to develop innovative technology that can promote vegetation growth and improve soil erosion resistance. In this study, a unique soil treatment and anti-desertification method is developed using environmentally friendly biogenic biopolymers. Biopolymers can effectively strengthen soil and improve durability. In particular, anionic-hydrophilic biopolymers delay water evaporation, thereby retaining a higher soil moisture condition compared to untreated soil. For technical verification, series of laboratory investigations (*i.e.* water erosion test, seed germination and growth,) were performed by applying target biopolymers to soil specimens. The results indicate that environmentally-friendly biopolymer treatment is highly effective in improving both vegetation growth (3 times faster) and soil erosion resistance (less than 2%), compared to a untreated condition.

INTRODUCTION

Annually, 12 million hectares of the Earth's landmass (the same size as the state of Mississippi) turn into new deserts (United Nations Environment Programme. 2006). Currently, more than 30% of the Earth's dry land is affected by desertification, and this trend, transforming land into deserts, is expanding into semiarid regions (Fig. 1). From the perspective of geoscience and geotechnical engineering, the critical factors affecting land erosion and desertification are limited precipitation and the removal of soil particles (especially fines < 0.002 mm) (Schlesinger et al. 1990).

The mechanism of soil erosion is generally known to be an interaction between the drag force of fluids (*e.g.*, wind or water) and soil shear resistance (Morgan 2005). Although water erosion is the largest source of global soil erosion, wind erosion is the major geomorphological force in desertified regions (Blanco and Lal 2008). Airborne particles produced by wind erosion consist of high amounts of clay minerals (Gillette and Walker 1977), and most global aeolian dust originates from North Africa (58%), the Middle East (12%), and West China (11%), regions which directly coincide with desertified areas (Tanaka and Chiba 2006; UNEP/RIVM 2004). Nonetheless, water erosion is another serious problem, because the immediate intensity of soil erosion produced by water is reported to be higher and more critical than wind erosion in areas that are undergoing desertification (*e.g.*, grasslands in semi-arid regions) (Breshears et al. 2003). Moreover, the total amount of erosion produced by water is reported to be two times larger than the amount affected by wind erosion worldwide (Lal 1995). Therefore, not only control of aeolian dust, but also enhancement of soil resistance to water erosion (*i.e.*, undrained shear strength) should be considered in desertification prevention approaches.

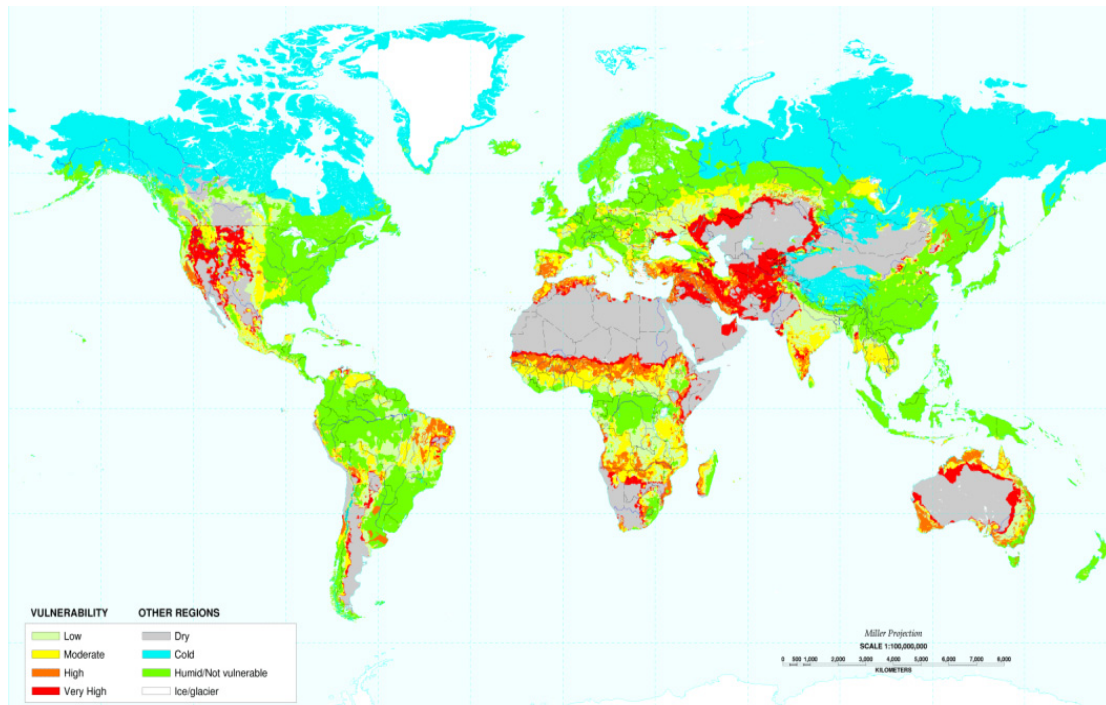


FIG. 1. World map of soil erosion and desertification (after UNEP 2006)

During the last half century the Chinese government has engaged in a large-scale (*i.e.*, 2.2 billion ha) afforestation program called the “Three North’s Forest Shelterbelt”. However, the costly effort has yielded little success, while concurrent expansion of the deserts in China has occurred, with inexorable growth ratios of 1,560 km²/yr (1950-1975), 2,100 km²/yr (1976-1988), and 3,600 km²/yr after 1998 (Wang et al. 2008; Wang et al. 2010). One of the biggest reasons for this failure is known to be that previous massive planting efforts were performed without addressing the recovery of

soil cohesion and moisture. An individual tree planted in cohesionless arid or semiarid soil can disturb the flow of air, creating turbulence and localized wind erosion on the ground around the tree trunk. As a result, trees roots were exposed and withered under the strong sunlight and limited moisture (Cao 2008). The failure of previous attempts provides a lesson about the importance of both inter-particle cohesion and soil moisture retention for soil revitalization in afforestation projects in arid and semi-arid regions.

In geotechnical engineering aspects to recover the soil strength and erosion resistance by enhancing soil cohesion is therefore very important as a countermeasure to desertification. However, in practical terms, it is impossible to supplement the sands of all arid or semi-arid regions with cohesive fine soils. As an alternative, this study presents a new concept to enrich soil cohesion using biological materials (*i.e.*, biopolymers)

EXPERIMENTAL PROGRAM

Biopolymers and soil

Beta-glucan biopolymer

Beta-1,3/1,6-glucan is a biopolymer of D-glucose monomers linked by glycosidic bonds (Bacic et al. 2009). Beta-glucan has various formations in nature such as cellulose in plants, bran of cereal grains, and cell walls of yeast, fungi, mushrooms, and bacteria.

A modified liquid type β -1,3/1,6-glucan biopolymer product (PolycanTM; Glucan Corp., Busan, Korea) produced by *Aureobasidium pullulans* SM-2001 is used in this study (Shin et al. 2007). The β -1,3/1,6-glucan content of PolycanTM is 8.9 g/L. Thus, previous study attempted the optimal β -1,3/1,6-glucan content to the mass of soil as 5 g/kg, when 1 kg of dried soil is mixed with 600 g (*i.e.* 60 % water content) of liquid phase pure PolycanTM (Chang and Cho 2012).

Xanthan gum biopolymer

Xanthan gum is an anionic polysaccharide composed of D-glucuronic acid, D-mannose, pyruvylated mannose, 6-O-acetyl D-mannose, and a 1,4-linked glucan (Cadmus et al. 1982). The best well known characteristic of Xanthan gum is pseudo plasticity (viscosity degradation depending on increase of shear rate). Moreover, Xanthan gum shows high stability under a wide range of temperatures and pH (Davidson 1980). Recently, xanthan gum biopolymer is adopted to improve the inter-particle bonding of soils through direct hydrogen bonding formation with clayey particles (Chang et al. 2015).

Korean residual soil

Korean residual soil (*i.e.* *hwangtoh*) is used in this study. *Hwangtoh* has a mineral constitution (by mass) as: quartz (8.4%), kaolinite (45.8%), halloysite (22.7%), illite (14.8), and goethite (8.3%). The natural soil was oven dried at 110°C (ASTM 2007), and was then grinded (grain size < 75 μ m) for testing. Korean residual soil has been actively adopted in several previous studies on biopolymer soil treatment (Chang and Cho 2012; Chang and Cho 2014; Chang et al. 2015)

Biopolymer-soil mixing and erosion simulation

Three different soil conditions for water erosion simulation were prepared separately as: a) natural (untreated) soil, b) 0.5% β -1,3/1,6-glucan biopolymer treated, and c) 0.5% Xanthan gum biopolymer treated. The amount of soil was fixed as 2,000 g for all cases.

For water erosion, the angle was set to be 20° using a step incliner. For a single erosion step, 500 mL of water was sprinkled which simulates raining on the soil surface. The weight of specimen was measured before and after raining. Eroded slurry was collected and its volume and mass were measured simultaneously. Slurry was dried in an oven to evaluate the absolute amount of eroded solids (Fig. 2).



FIG. 2. Laboratory precipitation simulation of soils to evaluate the erosion resistance of biopolymer treated soils.

To simulate moderate raining condition, the period between each cycle was controlled to be 48 hrs. After a single erosion process, the specimens were left in room to be naturally dried. To simulate heavy raining, the period between each cycle was shortened as 10 mins. Other procedures were same as abovementioned.

RESULTS AND ANALYSES

Biopolymers and soil

The laboratory water erosion test results are summarized in Fig. 3. Fig. 3 represents the cumulated ratio of total erosion compared to the initial amount (2,000 g) of solid soil. Biopolymer treated conditions show significant low erosion ratio (*i.e.*, 2% in average), while untreated natural soil exceeds 21.2% to 60% depending on the different rain density (*i.e.*, moderate and heavy) applied for erosion simulation.

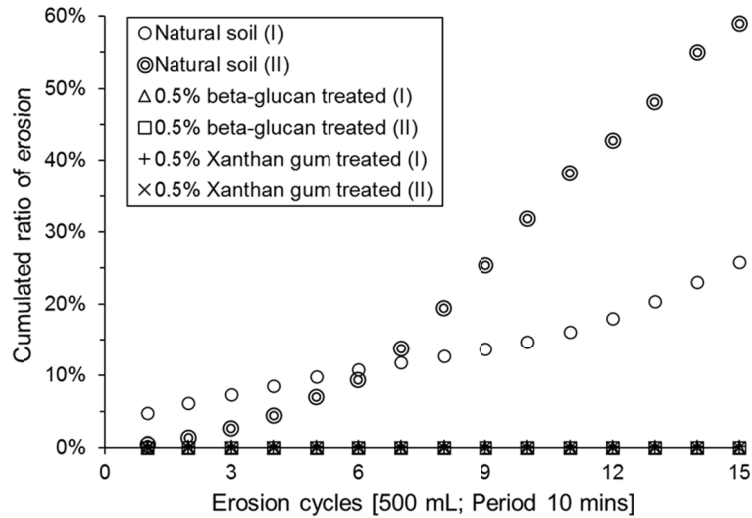


FIG. 3. Cumulated ratio of erosion with subsequent precipitation simulations.

Tables 1 and 2 summarize the erosion tendency under different rain intensities. Under moderate rain simulation, the total amount of erosion for untreated soil reaches 21.2%, while exceeds up to 60% under heavy raining for the same soil geometry (*i.e.*, untreated). However, in the case of biopolymer treated soils, biopolymer treated soils show higher erosion resistance under heavy raining, regardless of biopolymer type. For moderate rain simulation, all specimens were fully dried before the subsequent raining simulation, which render cyclic swelling and dehydration of biopolymers inside soil. Thus, the lower erosion resistance of biopolymer treated soils under moderate rain simulation seems to be affected by the structural disturbance of biopolymers which were subjected to cyclic wetting and drying, while biopolymers under heavy precipitation remained moist without extreme drying.

Table 1. Erosion result of moderate rain simulation

Soil treatment	Cumulated ratio of erosion [%]									
	1	2	3	4	5	6	7	8	9	10
Untreated	4.8	5.8	7.7	9.6	11.2	12.5	15.3	17.7	19.7	21.2
Beta-glucan	0.0	0.0	0.0	0.0	0.0	0.0	0.05	0.05	0.1	0.1
Xanthan gum	0.8	0.9	1.0	1.0	1.0	1.0	1.1	1.2	1.2	1.3

Table 2. Erosion result of heavy rain simulation

Soil treatment	Cumulated ratio of erosion [%]									
	1	2	3	4	5	6	7	8	9	10
Untreated	0.4	1.3	2.6	4.4	7.0	13.8	25.3	38.2	48.1	59.0
Beta-glucan	0	0	0	0	0	0	0	0	0	0
Xanthan gum	0.1	0.2	0.2	0.2	0.2	0.2	0.2	0.2	0.2	0.2

The higher erosion resistance under heavy rain simulation can be also recognized in Fig. 4. As totally 15 cycles of rain were applied in 140 mins, the total amount of erosion of untreated soil expands to 60%, while β -1,3/1,6-glucan treated soil shows nearly no erosion.

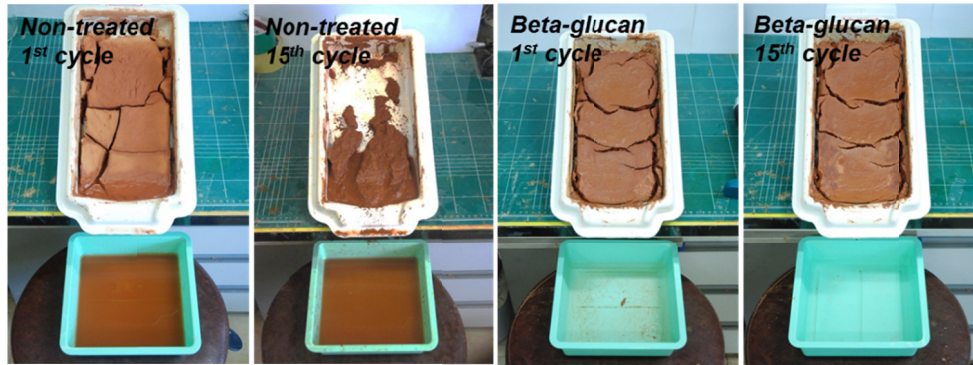


FIG. 4. Water erosion test results. Comparison between untreated and beta-glucan treated soil.

For moderate rain simulation, the period between cycles was 48 hrs. The drying tendency of untreated soil is faster than biopolymer treated soil because hydrophilic biopolymers interrupt moisture loss from soil. Thus, in the case of untreated soil, considerable amount of water infiltrates into soil at every cycle which diminishes surface rush off.

However, in the case of heavy raining, erosion accelerates after the 4th cycle. This is induced by the fully saturated condition due to continuous water supply. Meanwhile, biopolymer treated condition shows higher erosion resistance compared to moderate raining. Water sprinkled on biopolymer mixed soils suddenly flows down without any interaction with the soil surface. This indicates that the biopolymer treated soil has low permeable coats on its surface.

CONCLUSIONS

In this study, a unique soil treatment and anti-desertification method is suggested using environmentally friendly biogenic biopolymers. Biopolymers can effectively improve the strength and durability (*i.e.* stability) of soil.

In particular, anionic-hydrophilic biopolymers delay water evaporation, thereby retaining a higher soil moisture condition compared to untreated soil. Moreover, biopolymer matrices in soil enlarge soil voids which provide improved cultural environment for crops. In the aim of erosion prevention, laboratory water erosion simulation results show that environmentally-friendly biopolymer treatment is highly effective in improving soil erosion resistance (less than 2%), compared to a untreated condition.

Therefore, biopolymer treatment can be carefully concluded as an effective alternative for anti-desertification and eroded land recovery (*e.g.* revegetation). Further studies are

necessary for deeper and more theoretical understandings on the functional benefits of biopolymer treatment to prevent soil erosion and desertification

ACKNOWLEDGMENTS

The authors appreciate the support of National Research Foundation of Korea (NRF) grant funded by the Korean government (MSIP) (No. 2015R1A2A2A03006268), by a grant from the Strategic Research Project (Development of Key Excavation Solutions for Expandable Urban Underground Space) funded by the Korea Institute of Civil Engineering and Building Technology (KICT), and by the KAIST End-Run Program (No. N01150661) supported by the Korea Ministry of Science, ICT and Future Planning (MISP).

REFERENCES

- ASTM (2007). "Standard test methods for laboratory determination of water (moisture) content of soil and rock by mass (D 2216-05)." *Annual book of ASTM Standards*, ASTM International, West Conshohocken, 210-216.
- Bacic, A., Fincher, G. B., and Stone, B. A. (2009). *Chemistry, biochemistry, and biology of (1-3)-[beta]-glucans and related polysaccharides*, Academic, Amsterdam.
- Blanco, H., and Lal, R. (2008). *Principles of Soil Conservation and Management*, Springer.
- Breshears, D. D., Whicker, J. J., Johansen, M. P., and Pinder, J. E. (2003). "Wind and water erosion and transport in semi-arid shrubland, grassland and forest ecosystems: quantifying dominance of horizontal wind-driven transport." *Earth Surface Processes and Landforms*, 28(11), 1189-1209.
- Cadmus, M. C., Jackson, L. K., Burton, K. A., Plattner, R. D., and Slodki, M. E. (1982). "Biodegradation of Xanthan Gum by Bacillus Sp." *Applied and Environmental Microbiology*, 44(1), 5-11.
- Cao, S. (2008). "Why large-scale afforestation efforts in China have failed to solve the desertification problem." *Environmental Science & Technology*, 42(6), 1826-1831.
- Chang, I., and Cho, G.-C. (2012). "Strengthening of Korean residual soil with β -1,3/1,6-glucan biopolymer." *Construction and Building Materials*, 30(0), 30-35.
- Chang, I., and Cho, G.-C. (2014). "Geotechnical behavior of a beta-1,3/1,6-glucan biopolymer-treated residual soil." *Geomechanics and Engineering*, 7(6), 000-000.
- Chang, I., Im, J., Prasadhi, A. K., and Cho, G.-C. (2015). "Effects of Xanthan gum biopolymer on soil strengthening." *Construction and Building Materials*, 74(0), 65-72.
- Davidson, R. L. (1980). *Handbook of water-soluble gums and resins*, McGraw-Hill, New York ; London.
- Gillette, D. A., and Walker, T. R. (1977). "Characteristics of airborne particles produced by wind erosion of sandy soil, high plains of West Texas." *Soil Science*, 123(2), 97-110.
- Lal, R. (1995). "Global soil erosion by water and carbon dynamics." *Soils and global change*, R. Lal, K. John, E. Levine, and B. A. Stewart, eds., Lewis Publishers, Boca Raton, 440 p.

- Morgan, R. P. C. (2005). *Soil Erosion and Conservation*, Blackwell Publishing.
- Schlesinger, W. H., Reynolds, J. F., Cunningham, G. L., Huenneke, L. F., Jarrell, W. M., Virginia, R. A., and Whitford, W. G. (1990). "Biological Feedbacks in Global Desertification." *Science*, 247(4946), 1043-1048.
- Shin, H. D., Yang, K. J., Park, B. R., Son, C. W., Jang, H. J., and Ku, S. K. (2007). "Antiosteoporotic effect of Polycan, beta-glucan from *Aureobasidium*, in ovariectomized osteoporotic mice." *Nutrition*, 23(11-12), 853-860.
- Tanaka, T. Y., and Chiba, M. (2006). "A numerical study of the contributions of dust source regions to the global dust budget." *Global and Planetary Change*, 52(1-4), 88-104.
- UNEP/RIVM (2004). "The GEO-3 scenarios 2002-2032 quantification and analysis of environmental impacts." J. Potting, and J. Bakkes, eds., UNEP/DEWA/RS.03-4 and RIVM 402001022, 230.
- United Nations Environment Programme. (2006). "Deserts & Drylands." *TUNZA*, 24.
- Wang, X., Chen, F., Hasi, E., and Li, J. (2008). "Desertification in China: An assessment." *Earth-Science Reviews*, 88(3-4), 188-206.
- Wang, X. M., Zhang, C. X., Hasi, E., and Dong, Z. B. (2010). "Has the Three Norths Forest Shelterbelt Program solved the desertification and dust storm problems in arid and semiarid China?" *Journal of Arid Environments*, 74(1), 13-22.

Biotreatment of Fine-Grained Soil through the Bioencapsulation Method

Bing Li¹; Jian Chu²; and Andrew Whittle³

¹Engineer, Surbana Jurong, 168 Jalan Bukit Merah, Surbana One Singapore 150168.

²Professor, Nanyang Technological Univ., 50 Nanyang Ave., Singapore 639798.

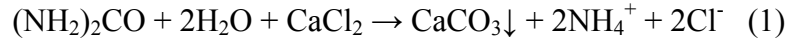
³Professor, Massachusetts Institute of Technology, 77 Massachusetts Ave., Cambridge, MA 02139.

Abstract: Treating sandy soil using a microbial induced calcite precipitation (MICP) process has been studied substantially in the past years. However, it is still a challenge to apply the MICP or other similar approach to treat fine-grained soil. In this paper, difficulties and challenges of using biocement to treat fine-grained soil such as marine clay are discussed. Different approaches adopted so far are reviewed. Some preliminary data are presented to illustrate the possibilities of improving the shear strength properties of clay using biotreatment or a MICP process through a so-call bioencapsulation method. However, the mechanisms behind the improvement in soil properties are yet to be fully understood. The cost-effectiveness is another issue that has yet to be addressed.

INTRODUCTION

Portland cement has been used to treat soft soil such as marine clay for improving its mechanical properties in the past. Usually, the best results are obtained at cement to clay ratio from 30–50% (w/w). Therefore, the use of cement to treat soft clay is expensive. Furthermore, the production of cement consumes about 5% of the total global industrial energy consumption and contributes about 5% to global anthropogenic CO₂ emission (Worrell et al. 2001). For this reason, various studies have been made to look for alternative solutions to soft soil treatment. One of them is biocementation using microorganisms.

Biocementation is a technology based on precipitation/crystallization of insoluble compounds in porous materials using enzymatic activity of natural microorganisms and some reagents. The most popular technology of biocementation is the precipitation of calcite (CaCO₃) from the solution of calcium salt and urea using enzymatic activity of urease-producing bacteria (UPB). Enzymatic hydrolysis of urea by cells of UPB (Ivanov and Chu 2008; Ivanov et al. 2015; DeJong et al. 2010; De Muynck et al. 2010) causes micro-gradient and total increase of pH and release of carbonate following with calcite crystallization and formation of a cemented product according to the following biochemical reaction:



where microbial cells are the crystallization centres due to formation of the numerous microgradients of pH and carbonate concentration in the vicinity of the particle surface.

Numerous studies on biocementation of granular soil for increasing its strength have been made before (DeJong et al. 2010; De Muynck et al. 2010; Whiffin et al. 2007; Stabnikov et al. 2011; Chu et al. 2012, 2013). The mechanism of biocementation of granular soil has been well understood. The size of bacterial cell is significantly smaller than the sizes of pores in granular soil. The minerals generated such as calcium carbonate can attach on the surface of sand grains and produce strong cementation effect. However, when the same method is used for fine-grained soil, the mechanisms become less understood. The pores in the fine-grained soil can be too small for bacterial solution to flow through it. Thus, mixing may have to be used. Assuming the binding agency such as calcium carbonate can still be produced, then how is the binding agency contributing to the cementation effect is not clear. So far, the study of the biocementation of fine-grained soil is only at a trial-and-error stage. Several different methods have been tried so far. Ng et al. (2014) attempted the use of injection method to treat residual soil using the MICP method which has a combined 62%. Some increase in shear strength and reduction in permeability were observed. Li (2015) studied the change in the undrained shear strength versus water content relationships for soil treated with the MICP process and observed that a higher undrained shear strength versus water relationship was obtained as compared with the pure clay. In other words, a higher undrained shear strength was obtained for biotreated soil given the water content the same. In this paper, a study on the use of the so-called bioencapsulation method for the treatment of soft clay is introduced. This method may become an alternative for the conventional premixing of soil cement method that has been adopted in practice (Tatsuoka 2004; Chu et al. 2009; Ivanov et al. 2015). It could also be a way to convert clay waste into value-added construction materials. The aim of the present research was to study the feasibility of bioencapsulation of soft marine clay aggregates for the production of solid construction material.

MATERIAL AND METHODS

Soil and Biocement Agents Used

The soil used in the experiments was soft marine clay obtained from an open pit excavated at a coastal area of Singapore. The soil had a specific gravity of 2.70, water content of around 55%, and pH of 7.8. The soil at the disturbed state had almost no strength. In addition, kaolin, which is silty material having homogenous properties, was also engaged for slaking test.

For the microorganisms, aerobic urease-producing alkaliphilic bacteria *Bacillus* sp. VS1 (Chu et al., 2012) were used in this study. The bacteria were cultivated under the

conditions described in Stabnikov et al. (2011). The mineral sediment was separated by gravity. The bacterial suspension was concentrated by centrifugation, re-suspended in solution of NaCl, 20 g/L, and then centrifuged again. The paste of bacterial biomass after centrifuge was dried in a freeze-dryer for two days to produce dry biomass of UPB. Urease activities of the bacterial suspension and the dry bacterial biomass were determined by the increase of electric conductivity of 1M solution of urea due to production of ammonium for 0.5 hour, which were controlled to be similar regarding to mass(g)/ml (Stabnikov et al., 2011; Ivanov et al., 2015). Original bacterial suspension was also engaged.

Sample preparation method

Small clay balls in a variance of diameter from 5 to 20mm were made from kaolin and marine clay (MC), attempting to increase the strength of biocemented clay balls. Two different preparation methods were used: one is to form a shell outside, namely “shell method”; another is to mix soil with bacteria and chemicals evenly, namely “ball method”.

Detailed procedure for shell method is described as follows:

1. Mixing clay with deionized water at 50% water content, then form small clay balls with 5 to 20mm in diameter by hand; wrap them with dry UPB powder on surface;
2. Dipping/Soaking the clay balls into 0.75M CaCl₂ and 1.5 M urea solution for two days, making sure all balls were submerged under the solution;
3. Dry the balls in a 40 degree oven overnight.

For the ball method, similar procedures as step 1 and 3 in wet method described before were involved. Clay was mixed with chemicals and different types of bacteria all together and left for drying for two days, either oven-dried at 40°C or air-dried. No dipping in chemical solution process (step 2) was involved. Similar preparation procedure was engaged for the control group, without mixing with the chemicals/bacteria.

As summarized in Table 1, eight sets of clay ball samples were made, employing different types of treatment methods and bacteria types (original wet UPB suspension and the dry UPB powder). Properties of the balls made in each group will be evaluated.

Table 1. Summary of Clay Ball Samples Prepared

	Groups No.	Mixed with Cement	Bacteria type			Treatment method		
			Dry UPB powder		Wet UPB suspension	Dipping in chemical solution	Air-dry	40 degree oven-dry
			Wrap on surface	Mixed Uniformly				
control	1	N						
	2	Y						
Shell method	3	N	√			√		
	4	Y	√			√		
	5	N		√		√		
Ball method	6	N			√	√		
	7	N		√				√
	8	N		√			√	

RESULTS AND ANALYSIS

Split test for strength measurement

In this preliminary study, the clay balls are not made to be standard in size or shape to fit any existed soil strength test. Therefore, compression tests of single clay balls were adopted to access roughly the strength properties of the clay balls. This test is similar to the split cylinder test used for concrete. As shown in Figure 1a, a single clay ball was put under UC machine for compression until it failed. A typical clay ball specimen prepared by ball method after split test is displayed in Figure 1b. Most of the clay ball split half right from the middle, as the balls are weaker in tensile strength.

Shell separated from its core was found to be formed outside the clay ball making by the shell method, as shown in Figure 1c. The outer part of clay ball contacts directly to the chemical solution, at where the reaction was supposed to happen first. This pre-formed hard shell then tended to separate from its inner part, which shrink during the drying process. Yet such shell formed was moderately thin. Noted that for samples in set 4 (marine clay plus 10% of Portland), the shells were formed, yet was inseparable from its core.

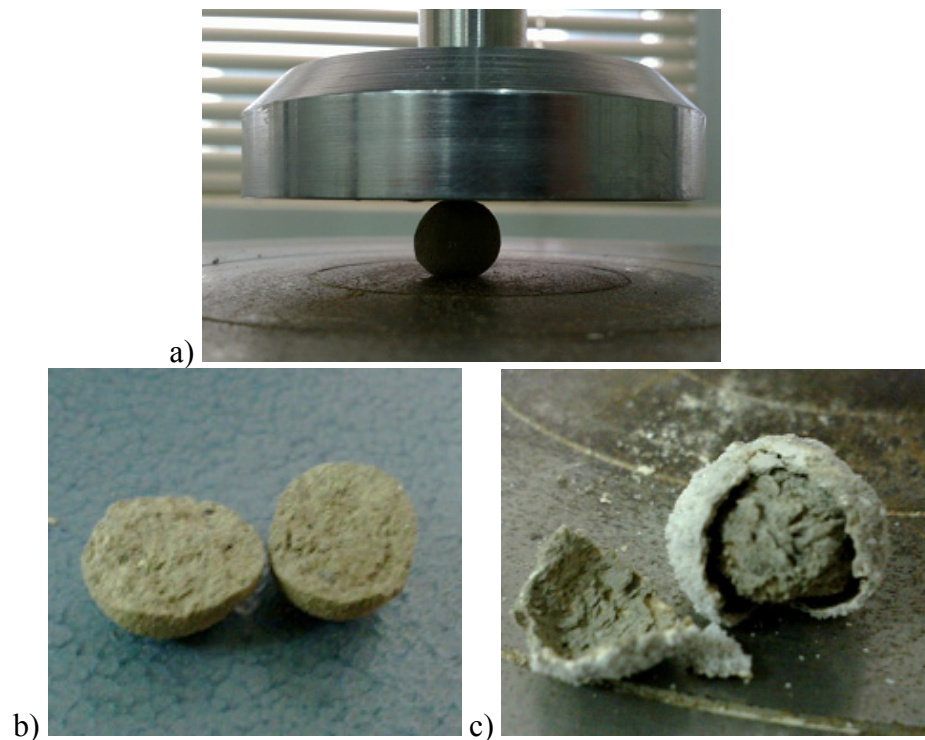


FIG. 1. Images of a) biocemented clay balls made by evenly mixing method during split test by UC apparatus, and specimens prepared by b) ball method, and c) shell method after testing.

Typical force vs. displacement curves of clay balls making by the ball method and shell method are shown in Figure 2a and 2b respectively. As shown in Figure 2b, two force peaks were detected, of which the first one was from shell breakage and the second was supposed to be from the core splitting. As the ball is considered to be failed after the breakage of shell, only the first peak is concerned. On the other hand, only one peak was detected for the balls made by the ball method as expected (Figure 2a).

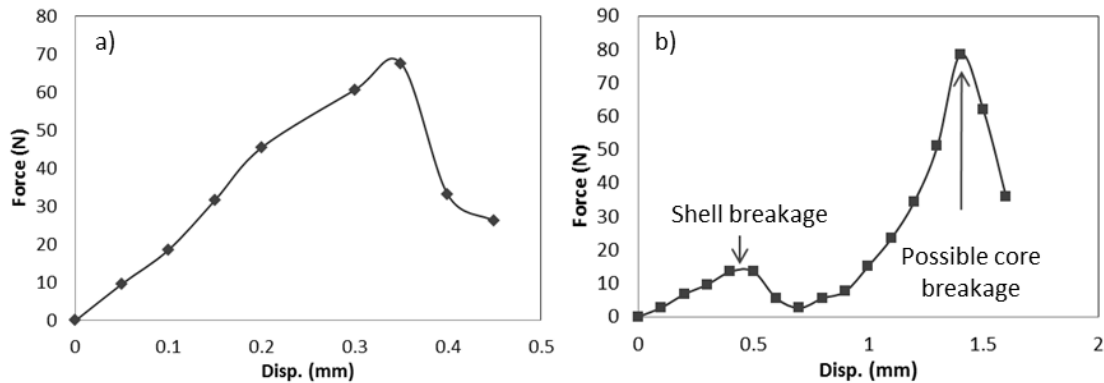


FIG. 2. Typical forces vs. displacement curve in split test of clay ball made by a) ball method, and b) shell method.

The maximum breakage forces endured by the crystal shell itself in sets 3 and 5, which was normalized by diameter square of the shell, were drawn against the ball diameter in Figure 3. The normalized forces are found to be decreased with increasing diameter. It should be noted that the strength of shell formed outside clay ball are generally very weak (enduring force less than 15 N; could be breaking by hand). Maximum normalized force endured was 0.4 N/mm² even with the smallest balls size.

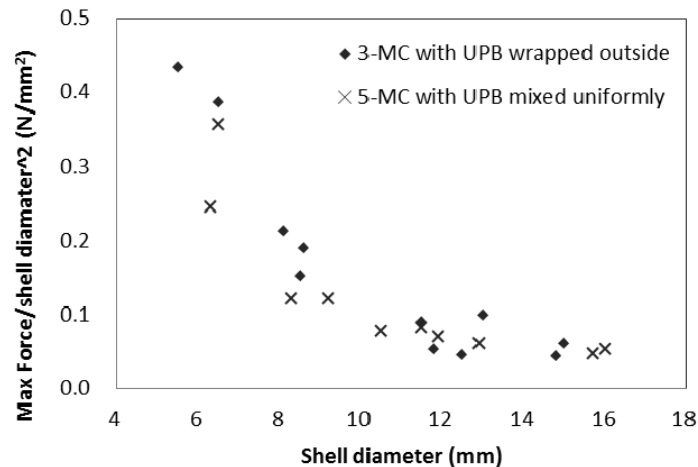


FIG. 3. Maximum normalized force from shell breakage divided by diameter² vs. diameter for clay balls prepared by shell forming method.

As shown in Figure 4, maximum forces endured by the ball method, on the other hand, could be as high as 1.5 N/mm^2 , which is around three times of the shell method. Effectiveness of ball method could be examined by the comparison of set 6, 7, 8 with control sets 1 and 2. No obvious difference was observed in sets 1, 2, and 7, 8. However, improvement was observed for specimens in set 7, engaging wet UPB instead of dry UPB powder. This might indicate the advantage of wet UPB suspension in bioencapsulation over dry UPB.

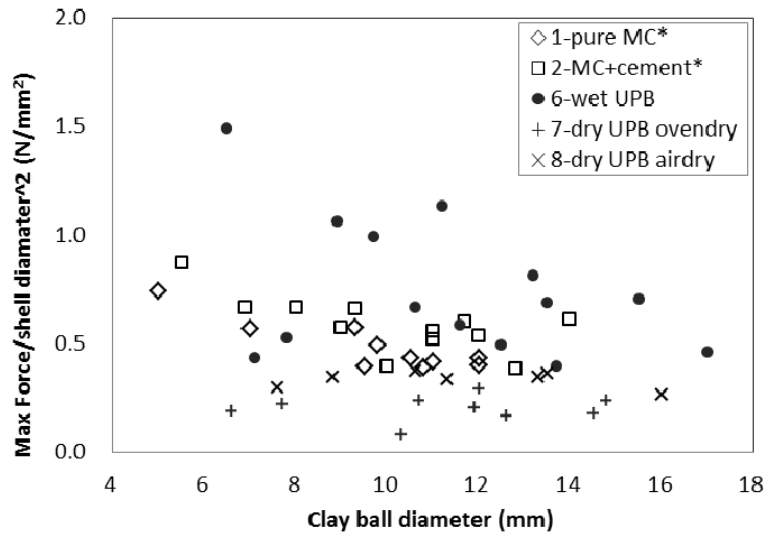


FIG. 4. Normalized maximum force vs. diameter getting from clay ball made by ball method (set 6/7/8) with control* (set 1/2).

Slaking tests

Slaking tests were conducted to assess the durability of the soil after biotreatment. Specimens for biocemented and control group were suspended into water simultaneously; photos were taken at intervals of 1, 3, 10 mins, 1, 2, 4 hr, 1, 2, 3 days, 1 week, etc., until it is fully dissolved in water. Pictures will then be tabulated and organized to see the trend.

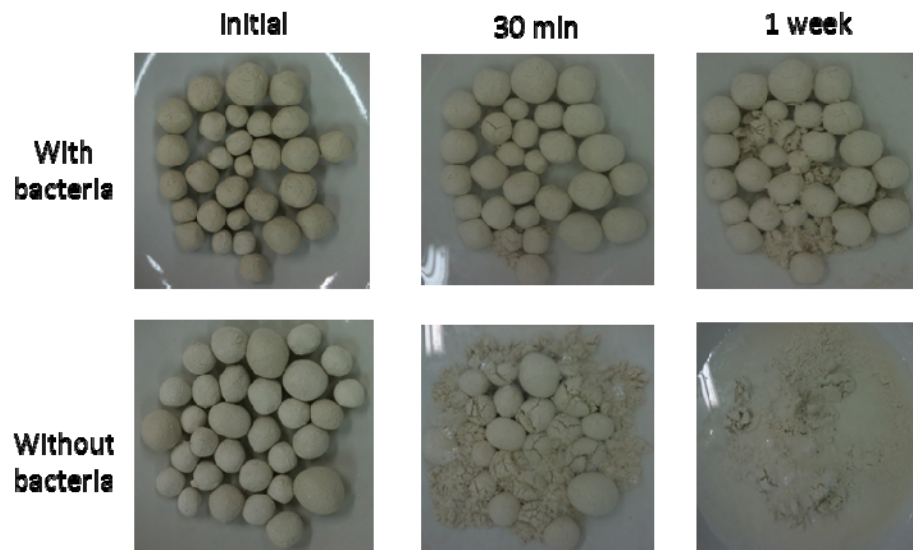


FIG. 5. Slaking test on UPB treated kaolin and pure kaolin.

Slaking tests were conducted on clay balls (5 to 20 mm in diameter) prepared with UPB and with pure kaolin mixed with distilled water, as shown in Figure 5, both employing the dry mixing method. Based on the trend of the disintegration of the kaolin balls sample, it is noted that the kaolin balls with UPB has much better resistance against being soaked in water while the kaolin balls without UPB disintegrate fastest as one can see the notable difference after 30 mins where the drastic disintegration of the kaolin balls sample starts. This endurance could be attributed to the lowering of permeability due to the re-construction of microstructure of clay particles by chemicals and bacteria added.

SUMMARY AND CONCLUSIONS

In this paper, a bioencapsulation method for the strengthening of soft clay is presented. The study has found that soft marine clay can be strengthened through encapsulation of clay aggregates with biogenic calcite produced by the treatment of clay with urease-producing bacteria in solution of calcium chloride and urea. Bioencapsulation of marine clay aggregates increase the compressive strength of marine clay aggregates from almost zero to a substantial value. Ball mixing method, which forms no shell outside the clay ball showed advantage regarding to the strength gain; on the other hand, shell method which forming crystal shell produced higher endurance of clay balls against slaking in water. The bioencapsulation method can be considered as an alternative for the conventional premixing of soil cement method for soft soil. However, the mechanisms behind the improvement in soil properties are yet to be fully understood. Suggestions to future studies were also made.

REFERENCES

- Chu, J., Varaksin, S., Klotz, U. and Menge P. (2009). "Construction processes. State-of-the-art-report". *Proceedings of the 17th International Conference on Soil Mechanics and Geotechnical Engineering*, Alexandria, Egypt, 4: 3006–3135.
- Chu, J., Stabnikov, V. and Ivanov, V. (2012). "Microbially induced calcium carbonate precipitation on surface or in the bulk of soil". *Geomicrobiology Journal* 9: 544–549.
- Chu, J., Ivanov, V. Stabnikov, V. and Li, B. (2013). "Microbial method for construction of aquaculture pond in sand". *Geotechnique* 63. doi: 10.1680=geot.SIP13.P.007
- DeJong, J.T., Mortensen, B.M. Martinez, B.C. and Nelson, D.C. (2010). "Bio-mediated soil improvement". *Ecological Engineering* 36: 197–210.
- De Muynck, W., De Belie, N. and Verstraete. W. (2010). "Microbial carbonate precipitation in construction materials: A review". *Ecological Engineering* 36: 118–136.
- Ivanov, V. and Chu, J. (2008). "Applications of microorganisms to geotechnical engineering for bioclogging and biocementation of soil in situ". *Reviews in Environmental Science and Bio-Technology* 7: 139–153.
- Ivanov, V., Chu, J., Stabnikov, V., & Li, B. (2015). "Strengthening of Soft Marine Clay Using Bioencapsulation". *Marine Georesources & Geotechnology*, 33(4), 325-329, DOI: 10.1080/1064119X.2013.877107
- Ng, W.S., Lee, M.L., Tan, C.K. and Hii S.L. (2014). Factors Affecting Improvement in Engineering Properties of Residual Soil through Microbial-Induced Calcite Precipitation, *Journal of Geotechnical and Geoenvironmental Engineering*, ASCE, ISSN 1090-0241/04014006.
- Stabnikov, V., Naemi, M. Ivanov, V. and Chu, J. (2011). "Formation of water-impermeable crust on sand surface using biocement". *Cement and Concrete Research* 41: 1143–1149.
- Tatsuoka, F. (2004). "Cement-mixed soil for Trans-Tokyo Bay highway and railway bridge abutments". *Proceedings of Geotechnical Engineering for Transportation Projects*, ASCE Special Publication GSP 126: 18–76.
- Worrell, E., Price, L., Martin, N., Hendriks, C. and Meida, L.O. (2001). "Carbon dioxide emissions from the global cement industry". *Annual Review of Energy and the Environment* 26: 303–329.
- Whiffin, V.S., Paassen, L.A. van and Harkes. M.P., (2007). "Microbial carbonate precipitation as a soil improvement technique". *Geomicrobiology Journal* 24: 417–423.

Enhanced Germination and Growth of *Arabidopsis thaliana* Using IrO₂-Ta₂O₅ | Ti as a Dimensional Stable Anode in the Electro-Culture Technique

G. Acosta-Santoyo¹; R. A. Herrada¹; S. de Folter²; and Erika Bustos¹

¹Centro de Investigación y Desarrollo Tecnológico en Electroquímica, S.C. Sanfandila, Pedro Escobedo, Querétaro, México.

²LANGEBIO, Centro de Investigación y de Estudios Avanzados del Instituto Politécnico Nacional, Km. 9.6 Libramiento Norte, Carretera Irapuato-León, 36821, Irapuato, Guanajuato, México.

Abstract: Plants are sensitive to many different forms of stimuli, and they respond to many well-known environmental conditions such as temperature, light quality, moisture, and gravity, among others. Electro-culture or electro-farming consists of stimulation by electric fields applied in the soil in order to improve the germination rate, growth rate, yields and crop quality. It has been demonstrated that the treatment also protects plants from diseases; even so, this technology remains poorly studied. Here, we study the electro-culture process for *Arabidopsis thaliana* using IrO₂-Ta₂O₅ | Ti as a dimensional stable anode (DSA) with a titanium cathode. We expect to accelerate the germination and growth rate of this plant's cotyledons, leaves, and roots in the early stages of growth. This process is beneficial due to the fact that the ions undergo electro-migration and permeate the nutrients across the seeds. Furthermore, a decrease in pH occurs nearby the DSA via electrolysis of the water during the electro-culture process (pH = 1), and we observe the generation of OH radicals during this electrolysis when the seed is exposed to low electric fields in a short time with direct currents (less than 5V in 1 hour)..

INTRODUCTION

The environmental conditions of our life has been affected negatively due to the rapid growth of the world population in recent years, which has resulted in increasing consumption of food and energy (Aladjadjiyan 2012). It is important to increase food and energy production but the tendency for satisfying growing needs has led to intensive development of plant production through the use of chemical additives, which in turn has caused more and more pollution of soil, water and air.

A fundamental property of all living organisms is their capacity to collect information from the environment and to express physiological processes that are aimed to optimize their performance under the new environmental conditions and by these means maintain homeostasis (Gurovich 2012). The application of electricity,

magnetism, monochrome light, and sound can stimulate the growth of plants to a great extent. The technology of applying electric fields to the soil in order to improve the efficiency of germination and growth of plants is called electro-culture or electro-farming which are defined as any and all applications of electricity to agriculture (Matthews 1922). This technology has been used for different purposes including seed treatment, seedling growth, plant growth, insect control, among others (Gui et al. 2013).

Electric current is broadly defined as charged particles in motion or as a flow of charge. It can be direct current (DC) or alternating current (AC), with direct current being characterized by a uniform direction of flow and amount (voltage) of electricity.

Brief exposure of seeds to electric current ends their dormancy, accelerates development throughout the period of vegetation, ultimately increases yields, and metabolism of the seedlings is stimulated. Respiration and hydrolytic enzyme activity are intensified for many types of plants (Matthews 1922; Wang et al. 2009; Artem and Albertovna 2012).

There are four main soil transportation mechanisms induced by the application of electric fields: electro-migration refers to the transportation of ions in solution in the interstitial fluid in the soil matrix towards the electrode of the opposite charge; electro-osmosis is the net flux of water or interstitial fluid induced by the electric field; electrophoresis refers to the transport of charged particles of colloidal size; and diffusion refers to the mass transport due to a concentration gradient (Cameselle and Gouveia 2013).

DSAs are currently being used in industry for the treatment of wastewater with reduced operational costs. These electrodes consist of different metal bases (titanium, zirconium, and tantalum) which are coated with different oxides: IrO_2 , RuO_2 , or SnO_2 , including $\text{RuO}_2 | \text{Ti}$ and $\text{IrO}_2 | \text{Ti}$ (Papastefanakis, Mantzavinos, and Katsaounis 2010; J. Souza, Martínez-Huitle, and Ribeiro da Silva 2011). The use of a modified anode ($\text{IrO}_2\text{-Ta}_2\text{O}_5 | \text{Ti}$) and cathode (Ti) has been reported previously by our research group, when they were used in the treatment of polluted soils in the electro-remediation technique of hydrocarbons and mercury (Pérez-Corona et al. 2013). These kinds of electrodes are resistant to extreme experimental conditions (3 A cm^{-2} at 353 K in concentrate H_3ClO_4 or $\pm 1 \text{ V}$ for 90 s in 0.5 M NaCl at 297 K) with a life span of around of 40 cycles of use under extreme conditions (Méndez et al. 2012).

Arabidopsis thaliana is a small plant in the mustard family (Brassicaceae) that has become the model system of choice for research in plant biology (Meyerowitz and Somerville 1994) and it has a natural distribution throughout Europe, Asia and North America. This plant has different accessions, or ecotypes that have been collected from natural populations, and others which have been developed in laboratories. *Arabidopsis thaliana* has several accepted standards for genetic studies and plant biology, among which is Columbia and Landsberg ecotypes, because they

can be traced for their entire life cycle including seed germination, formation of rosette plant, bolting of the main stem, flowering, and maturation of the first seeds, all in six weeks and in laboratory conditions (Meinke et al. 1998).

The aim of this work was to prove the efficiency of the electro-culture technique for a model plant using a $\text{IrO}_2\text{-Ta}_2\text{O}_5|\text{Ti}$ anode and a Ti cathode in low DC electric fields (0.1, 0.2, 0.4 and 0.8 V/cm) applied for 4 hours in a Vertisol-type soil and *Arabidopsis thaliana* Col-0 seeds to evaluate seed germination rate and early seedling development. The results obtained in this set of experiments shows that $\text{IrO}_2\text{-Ta}_2\text{O}_5|\text{Ti}$ modified electrodes used as anode and titanium cathode when a DCEF up to 0.2 V/cm is applied for 4 hours improves seed germination rate and seedling development, and that higher DCEF treatments with the same electrodes negatively affect *Arabidopsis thaliana* development.

METHODOLOGY

Vegetal material. *Arabidopsis thaliana* seeds Col-0 ecotype was obtained as a donation from Stefan de Folter, PhD from Plant Development Functional Genomics in the National Laboratory of Genomics for Biodiversity (LANGEBIO) in the National Polytechnic Institute in Mexico.

Soil sampling. Clean agricultural-purpose Pelic Vertisol-type soil was collected near a farm in Sanfandila, Queretaro, Mexico and dried in the dark according to Mexican norm NMX-12/1-1987b and United States norm from the series SW82-EPA Chapter 9. Soil samples were collected from the superficial layer of the site (between 0 and 0.2 m with respect to the natural ground level). These were transported in sterilized glass containers and kept at 277 K until used. Before experimentation, collected samples were allowed to dry for two weeks at room temperature in dark conditions; this step allowed soil moisture elimination and after that, soil samples were sieved through a 2 mm mesh for the removal of roots, gravel and non-soil components. All analytical determinations were done in triplicate in order to assure that experimental error was less than 5 % (Perez Corona et al. 2013).

Electro-culture conditions. Electro-culture was conducted as follows: low DCEF was used in all experiments (0.1; 0.2; 0.4 and 0.8 V/cm) (Bi et al. 2011; Eing et al. 2009), using a power source; 500 gr of dry and sieved soil was placed in a plastic container of 10 x 12 cm and wetted with tap water at pH 7.3 and electric conductivity 451 $\mu\text{S}/\text{cm}$; the electrodes were placed 10 cm apart in a 1D face to face arrangement (Perez Corona et al. 2013) (the anode placed in front of the cathode) using a $\text{IrO}_2\text{-Ta}_2\text{O}_5|\text{Ti}$ electrode as anode and a Ti electrode as a cathode (Méndez et al. 2012); and finally *Arabidopsis thaliana* Col-0 seeds were sown in 5 lines of 5 seeds each with a distance between the seeds of 2 cm inside the space between electrodes. Once sown, seeds were allowed a period of 24 hours of vernalization at 4° C. After the vernalization period, the electrodes were connected to a DC Power Supply GP-4303DU, which acted as a power source. The treatment was for 4 hours in each of the electric fields described above. A control without DCEF was left in every set of

experiments. After electro-culture treatments, the cells were placed in a growing chamber with artificial light in a room without windows applying a photoperiod of 8 hours of light and 16 hours of darkness; the temperature of the chamber was $26 \pm 1^\circ\text{C}$ and was maintained until the end of experiment.

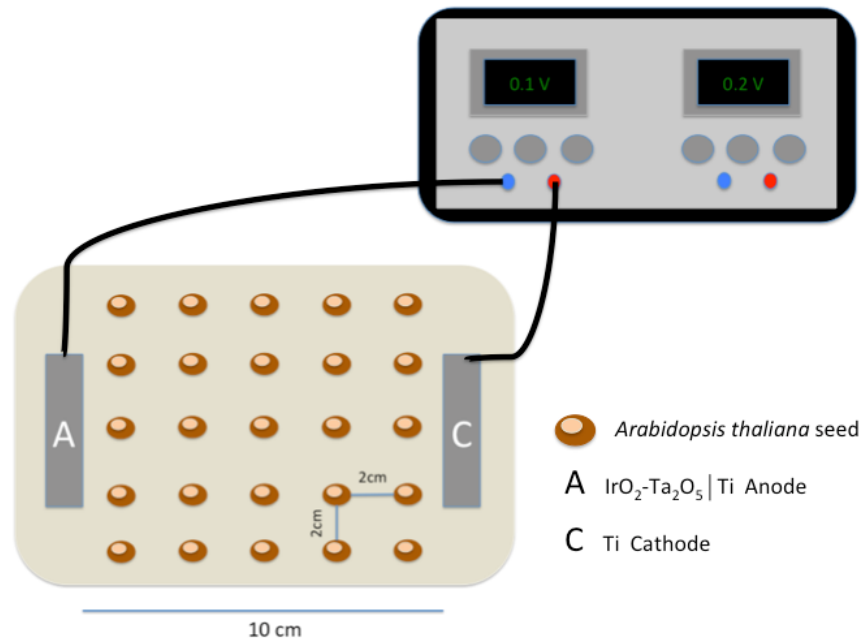


Figure 1. Arrangement of *Arabidopsis thaliana* Col 0 seeds in on the electro-culture cell. Seeds are arranged in five rows of five seeds located at 2 cm from each another in the space between anode and cathode. After a vernalization period, the electro-culture cell is connected to a power source to implement an electric field.

Germination rate. Germination rate was calculated by counting the total number of seeds that broke dormancy, that is when the epicotyl emerged. Germinated seeds were counted from the first week and every seven days until the majority of seeds had germinated, that is four weeks after treatment (Bewley 1997; A. De Souza et al. 2014; Patwardhan and Gandhare 2013).

Plantlet Development. To evaluate plantlet development after electro-culture treatment, an analogic Vernier was used to assess the diameter of the rosette of the germinated plants from tip to tip of the longest leaves for every plant in the cell. All determinations were done at least in triplicate to assure that statistical error was less than 5 % (Yang and Shen 2011; Costanzo, Catania, and Doria 2008).

RESULTS AND DISCUSSION

Germination rate. Germination rate in *Arabidopsis thaliana* was increased when using $\text{IrO}_2\text{-Ta}_2\text{O}_5 \mid \text{Ti}$ electrode as anode and Ti as cathode when compared with the Control with no DCEF applied as shown in Figure 2. As previously reported, $\text{IrO}_2\text{-Ta}_2\text{O}_5 \mid \text{Ti}$ electrodes permit the mobilization of ions in the soil due to the effect of change in pH in the anode, compared with this value in the cathode thus allowing the mobilization of ions that can contribute to the break of the dormancy of the seeds.

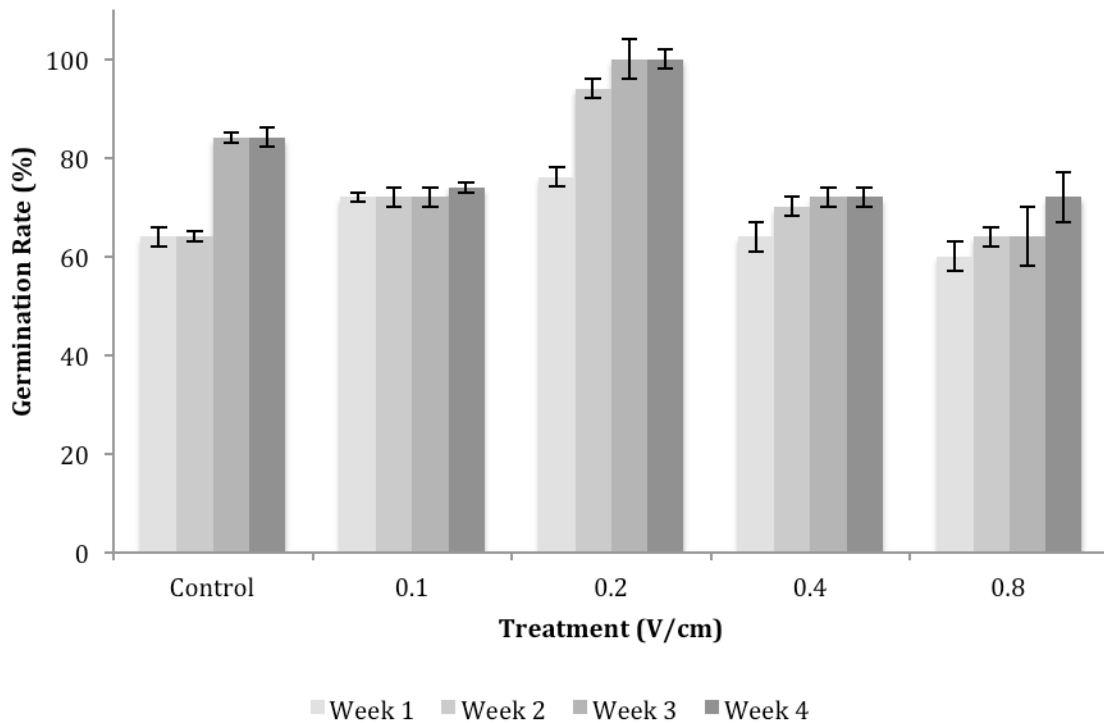


Figure 2. Germination Rate of *Arabidopsis thaliana* in four weeks with different low intensity DCEF using IrO₂-Ta₂O₅ | Ti electrodes as anode and a Ti electrode as a cathode.

Plantlet Development.

Plantlets were evaluated for rosette diameter 6 weeks after treatment with the electro-culture technique. Results showed that this electro-culture condition (IrO₂-Ta₂O₅ | Ti anode and Ti cathode) also improves plantlet development. The plants were analyzed for the rosette diameter six weeks after germination and the results showed that when we applied 0.2 V/cm direct current treatment plantlets showed a tendency to develop faster.

When plantlet development of *Arabidopsis thaliana* was assessed, we found that using IrO₂-Ta₂O₅ | Ti and Ti electrodes increased the diameter of the rosette as shown in Figure 3.

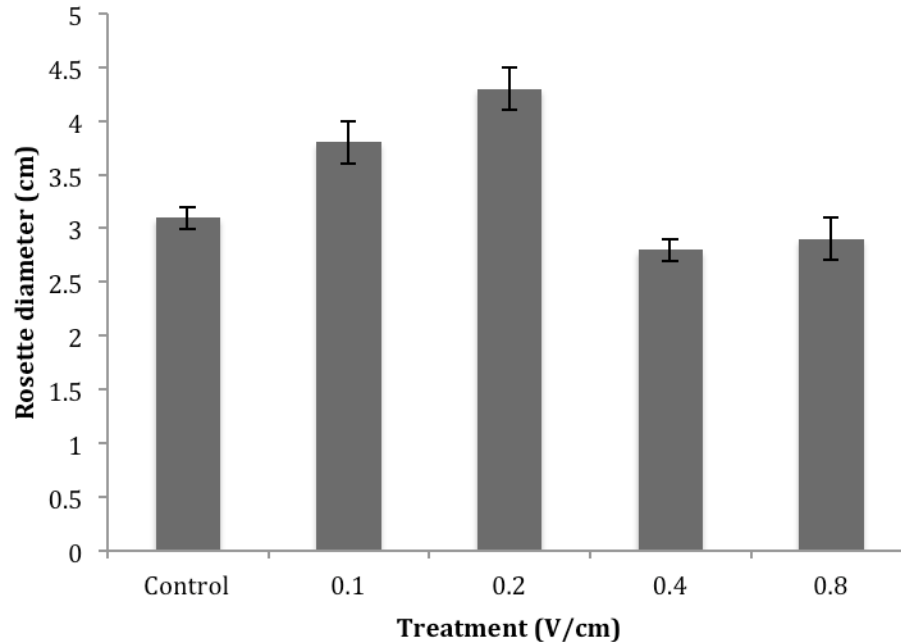


Figure 3. Rosette diameter of plants of *Arabidopsis thaliana* measured six weeks after treatment with low intensity DCEF.

After this step, we decided to evaluate the behavior of the development in three different areas of the electro-culture cell, so we analyzed the area close to the IrO₂-Ta₂O₅ | Ti anode (CA), the middle of the cell (MA) and in the area close to the Ti cathode. As previously reported (Oszust et al. 2013), when this set of electrodes is used, the middle area of the cell is the most efficient for the development of living organisms, followed by the area close to the IrO₂-Ta₂O₅ | Ti cathode. This might be due to the increase of organic carbon sources in these areas and in the mobilization of ions in the electro-culture cell as well as the increase of living bacteria and fungi in these areas after the application of the DCEF.

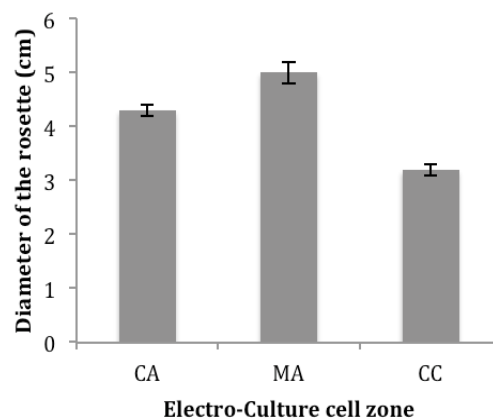


Figure 4. Diameter of the rosette of *Arabidopsis thaliana* plants after the exposure to low intensity DCEF electro-culture.

In Figure 5, we can observe the development of *Arabidopsis thaliana* plants after treatment with electro culture, and it shows that the plants treated with a 0.2 V/cm using this electrode arrangement presents better development than the plants with no treatment (control) and the plants treated with other DCEF as described in the measurements presented above.

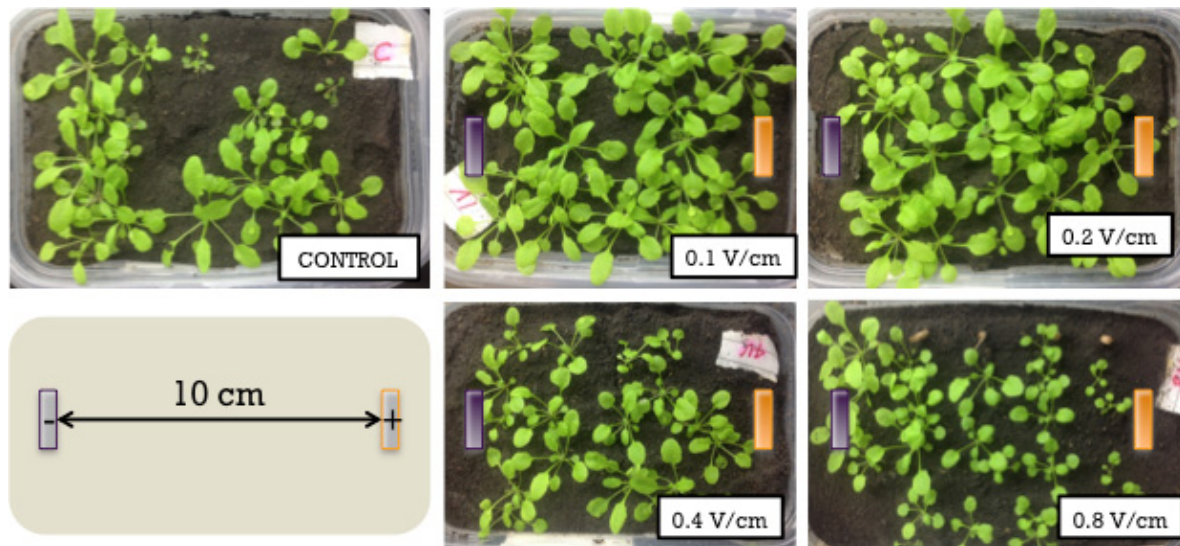


Figure 5. *Arabidopsis thaliana* plants treated with different low intensity DCEF using $\text{IrO}_2\text{-Ta}_2\text{O}_5 \mid \text{Ti}$ and Ti electrodes as an electro-culture treatment.

CONCLUSIONS

The use of a dimensionally stable anode ($\text{IrO}_2\text{-Ta}_2\text{O}_5 \mid \text{Ti}$) and a Ti cathode to generate a low intensity direct current electric field increases the germination rate and germination velocity of *Arabidopsis thaliana* seeds as well as the growth of plantlets in early stages of development. We suspect that this effect is due to the movement of ions in soil in the process called electro migration, which can lead to bioavailability of these ions, first for the germination of seeds by helping them to break dormancy, and in early stages of development helping the plantlets to synthesize organic molecules necessary to increase growth. It is imperative to complete experiments that can help us understand this effect.

ACKNOWLEDGMENTS

The authors want to thank Consejo Nacional de Ciencia y Tecnología de los Estados Unidos Mexicanos (CONACyT) for their financial support granted for the development of this investigation and Centro de Investigación y Desarrollo Tecnológico en Electroquímica, S.C. We also want to thank Dr. Stefan De Folter at LANGEBIO, Mexico for the kind donation of the vegetal material used in this project, and to Curtiss Palin, Peace Corps volunteer at CIDETEQ for the English revision of this manuscript.

REFERENCES

- Aladjadjian, Anna. 2012. "Physical Factors for Plant Growth Stimulation Improve Food Quality." *Food Production - Approaches, Challenges and Tasks*, 270. doi:10.5772/1870.
- Artem, Barinov, and Tereshkina Tatiana Albertovna. 2012. "The Effect of Electricity on Plant Growth" 1535.
- Bewley, Jd. 1997. "Seed Germination and Dormancy." *The Plant Cell* 9 (7): 1055–66. doi:10.1105/tpc.9.7.1055.
- Bi, Ran, Michael Schlaak, Eike Siefert, Richard Lord, and Helen Connolly. 2011. "Chemosphere Influence of Electrical Fields (AC and DC) on Phytoremediation of Metal Polluted Soils with Rapeseed (Brassica Napus) and Tobacco (Nicotiana Tabacum)." *Chemosphere* 83 (3). Elsevier Ltd: 318–26. doi:10.1016/j.chemosphere.2010.12.052.
- Cameselle, Claudio, and Susana Gouveia. 2013. "Advances in Electrokinetic Remediation for the Removal of Organic Contaminants in Soils." doi:10.5772/54334.
- Costanzo, Evelina, I N F N Sezione Catania, and V Andrea Doria. 2008. "The Influence of an Electric Field on the Growth of Soy Seedlings" 66: 417–20. doi:10.1016/j.elstat.2008.04.002.
- Eing, Christian J, Simone Bonnet, Michael Pacher, Holger Puchta, and Wolfgang Frey. 2009. "Effects of Nanosecond Pulsed Electric Field Exposure on Arabidopsis Thaliana," 1322–28.
- Gui, Zhibin, Antonio Piras, Limin Qiao, Kai Gui, and Boya Wang. 2013. "Improving Germination of Seeds Soaked GA3 by Electrostatic Field Treatment." *International Journal of Recent Technology and Engineering* 2 (1): 133–36.
- Gurovich, Luis. 2012. "Electrophysiology of Woody Plants." *Electrophysiology—from Plants to Heart, InTech*, no. 2009: 1–25. <http://cdn.intechopen.com/pdfs/27512.pdf>.
- Matthews, R Borlase. 1922. "Electro-Farming, or the Applications of Electricity To Agriculture." *Journal of the Institution of Electrical Engineers* 60 (311): 725–41. doi:10.1049/jiee-1.1922.0051.
- Meinke, D W, J M Cherry, C Dean, S D Rounsley, and M Koornneef. 1998. "Arabidopsis Thaliana: A Model Plant for Genome Analysis." *Science (New York, N.Y.)* 282 (5389): 662, 679–82. doi:10.1126/science.282.5389.662.
- Méndez, E, M Pérez, O Romero, E D Beltrán, S Castro, J L Corona, and A Corona. 2012. "Effects of Electrode Material on the Efficiency of Hydrocarbon Removal by an Electrokinetic Remediation Process." *Electrochimica Acta* 86: 148–56.
- Meyerowitz, EM, and CR Sommerville. 1994. *Arabidopsis*. Cold Spring Harbor, NY: Cold Spring Harbor Laboratory Press.
- Oszust, K, M Frac, B Ochoa, J Cárdenas, M Teutli, and E Bustos. 2013. "2 . Assessment of Microbial Status for an Hydrocarbon Polluted Soil after Applying an Electrokinetic Treatment." *Recent Res. Devel. Electrochem.* 9: 33–48.
- Papastefanakis, N., D. Mantzavinos, and a. Katsaounis. 2010. "DSA Electrochemical Treatment of Olive Mill Wastewater on Ti/RuO₂ Anode." *Journal of Applied Electrochemistry* 40 (4): 729–37. doi:10.1007/s10800-009-0050-9.

- Patwardhan, Mamta Samir, and Waman Ziblaji Gandhare. 2013. "High Voltage Electric Field Effects on the Germination Rate of Tomato Seeds." *Acta Agrophysica* 20 (2): 403–13.
- Perez Corona, M, B Ochoa, J Cárdenas, J Hernández, S Solís, R Fernández, M Teutli, and E Bustos. 2013. "4 . Comparison of Different Arrangements of Electrodes during the Electrokinetic Treatment of Polluted Soil with Hydrocarbons and Its Final Application in Situ." *Recent Res. Devel. Electrochem.* 661 (2): 59–80.
- Pérez-Corona, Maribel, Arturo Corona, Elías Daniel Beltrán, Jesús Cárdenas, and Erika Bustos. 2013. "Evaluation of IrO₂-Ta₂O₅|Ti Electrodes Employed during the Electroremediation of Hydrocarbon-Contaminated Soil." *Sustainable Environmental Research* 23 (4): 279–84.
- Souza, Angel De, Dagoberto García, Lilita Sueiro, and Fidel Gilart. 2014. "Scientia Horticulturae Improvement of the Seed Germination , Growth and Yield of Onion Plants by Extremely Low Frequency Non-Uniform Magnetic Fields." *Scientia Horticulturae* 176. Elsevier B.V.: 63–69. doi:10.1016/j.scienta.2014.06.034.
- Souza, J, C Martínez-Huitle, and D Ribeiro da Silva. 2011. "Electrochemical Treatment for Removing Petroleum Polycyclic Aromatic Hydrocarbons (PAHs) from Synthetic Produced Water Using a DSA-Type Anode: Preliminary Results." *Sustainable Environment* <http://140.116.228.7/download/21-5/21-5-7.pdf>.
- Wang, Guixue, Junli Huang, Weina Gao, Jiang Lu, Jian Li, Ruijin Liao, and Cheruth Abdul Jaleel. 2009. "The Effect of High-Voltage Electrostatic Field (HVEF) on Aged Rice (*Oryza Sativa* L.) Seeds Vigor and Lipid Peroxidation of Seedlings." *Journal of Electrostatics* 67 (5). Elsevier Ltd: 759–64. doi:10.1016/j.elstat.2009.05.004.
- Yang, Ling, and Hai Long Shen. 2011. "Effect of Electrostatic Field on Seed Germination and Seedling Growth of *Sorbus Puhuashanensis*." *Journal of Forestry Research* 22 (1): 27–34. doi:10.1007/s11676-011-0120-9.

Erosion Reduction of Coastal Sands Using Microbial Induced Calcite Precipitation

Casey Shanahan, S.M.ASCE¹; and Brina M. Montoya, M.ASCE²

¹Graduate Student, North Carolina State Univ., Dept. of Civil, Construction, and Environmental Engineering, Raleigh, NC 27695.

²Assistant Professor, North Carolina State Univ., Dept. of Civil, Construction, and Environmental Engineering, Raleigh, NC 27695.

Abstract: Effects of sea level rising and increasing storm severity create a more damage prone environment for coastal regions. Large storm surges can be devastating to coastal infrastructure, damaging roads, utilities, structures, and endangering the lives of local residents. Coastal sand dunes act as a primary defense to wave action, making their resiliency of the utmost importance. Microbial induced calcite precipitation (MICP) offers a potentially sustainable alternative to seawall and revetment type solutions which destroy entire ecosystems in order to protect cities or other areas of interest. Bio-cementation has been shown to improve the strength and stiffness of unsaturated sand. The study presented herein displays the behavior of MICP treated coastal sand when subjected to wave action. Two wave tank tests were conducted to assess the change in measured erosion for untreated sand and moderately cemented sand. To quantitatively measure the reduction in erosion, 3-D morphology was observed using a laser scanner before and after subjecting the sand to wave action. Acoustic wave gauges were used to monitor the input wave functions and the breaking waves on the soil surface. Further understanding of the erosion reduction potential of MICP treated sand increases the feasibility of *in-situ* application to coastal sand dunes.

INTRODUCTION

Sand dunes are geological necessities for the protection of coastal communities from the erosive effects of wind and wave action. Increases in storm severity and frequency have had significant effects on coastal geomorphology, in particular, erosion induced changes in elevation (Miller, 2015). Acting as natural defense mechanisms, coastal sand dunes dampen the effects of wave action and protect the inland infrastructure. Large storm events can lead to wave-induced overwash, which may lead to complete dune destruction if storm conditions persist (Figlus et al 2011). Erosion of the sandy coastal soils can have devastating impacts on coastal lifelines such as highways, pipe lines, and other utilities. Damages from coastal erosion may lead to extensive property damage, loss of revenue, and large repair costs. Preventing the erosion of coastal sand dunes can improve the resiliency of these coastal systems, minimizing damages and repair costs after storms. Naturally, coastal sand dunes are functional ecosystems, supporting life and providing intrastucture protection.

To successfully reinforce the sandy soil in a sustainable manner, the soil improvement methodology should not have devastating impacts on health of the preexisting ecosystem. Microbial induced calcite precipitation (MICP) has the potential to stabilize coastal sand dunes while having minimal effects on the ecology. MICP utilizes urea hydrolysis with calcium chloride to increase the alkalinity of the pore fluid and induce calcite precipitation which binds sand grains together. Studies have shown MICP can be used to successfully strengthen saturated soils (Chu et al. 2012, Chou et al 2011, Mortensen and DeJong 2011, Whiffin et al 2007, DeJong et al 2006). For proper application to the unsaturated coastal sand dunes, the MICP process must be possible in the unsaturated environment. Recent advancements in the unsaturated MICP treatment methodology have supported that unsaturated cementation is more efficient than saturated cementation in terms of shear strength for a given cementation level (Shanahan and Montoya, 2014). During unsaturated cementation, the calcite precipitation occurs at sand grain particle contacts, while under saturated conditions the cementation is more uniform throughout the soil matrix. The saturated condition commonly results in sand grain encapsulation, which occurs when the calcite cementation surrounds the entire sand grain. According to observations by Cheng and Cord-Ruwisch (2012), the most significant contribution of shear strength comes from the cementation localized at the particle contacts.

MATERIALS AND METHODS

Biological Treatment

Sporosarcina pasteurii (American Type Culture Collection, ATCC 11859) was used as the biological organism to facilitate microbial induced calcite precipitation through urea hydrolysis. Ammonium-Yeast Extract media was used to grow bacteria cultures to the desired population density ($OD_{600} = 1.0$). The nutrient broth consists of 0.13M Tris Buffer and a pH of 9.0, 10 g $(NH_4)_2SO_4$, and 20 g Yeast Extract. The Tris Buffer was created and halved, allowing for separate autoclaving of the remaining constituents. After sterilization, the solutions were combined and inoculated with *S. pasteurii* stock culture. The solution was then incubated aerobically at 80 rpm for approximately 72 hours at 30 degrees Celsius prior to soil inoculation.

Urea-calcium cementation media was used to induce ureolytic-driven calcite precipitation. The components and concentrations of the cementation media include: 0.333 M of urea, and 0.100 M of $CaCl_2$. The process overall is similar to that presented by Mortensen et al. (2011).

Cementation treatments were performed by allowing the urea-calcium media to free-drain through the soil and out the bottom of the soil boxes. In order to maintain biological activity in the unsaturated soil, micro-dosing was introduced in every flush. As discussed in Martinez (2012), micro-dosing refers to the injection of low densities of ureolytic microbes in conjunction with the nutrients required for the bacteria to precipitate calcite. Micro-dosing assisted in maintaining high levels of bacterial activity during the duration of the treatment process. Calcium chloride was excluded from the initial injection to prevent chemical crash-out. Cementation treatments were then repeated every 3 – 6 hours until the target number of flushes had been completed.

Sand Models

Soil box specimens were prepared through dry pluviation to a target void ratio of 0.70. North Carolinian Dune Sand ($D_{50}=0.23\text{mm}$, $C_u=2.0\text{mm}$, $C_c=1.0$, $G_s=2.65$) was used for this investigation to be representative of coastal erosion in North Carolina. The soil boxes were designed with an aspect ratio of 1:1 and had dimensions of 12" x 12" x 3". The bottom and side walls of the sand models are made of 1/4" PVC sheeting and structurally attached using PVC cement. The enclosure was then waterproofed using silica based caulking. To allow for free drainage, 1/4" holes were drilled at 1" centers across the entire PVC bottom plate. To prevent the loss of soil during chemical treatments, a 0.125-inch Porex filter was used beneath and on top of the soil. In an effort to prevent boundary effects at the cemented soil to uncemented soil interface in the sand dune models, the bottom 1.5" of the sand models are reinforced by 1/4" PVC sheeting. Meanwhile, a series of wooden dowels were drilled into the bottom plate and used to support a 0.012-inch thick latex membrane around the perimeter of the pluviated specimen, as shown in Figure 1. The soil was then pluviated into the membrane enclosure and topped with another Porex filter. Finally, 3 inches of pea gravel was placed on top of the second Porex filter to suppress any treatment based erosion.



FIG 1. Sand Model

Sand Dune Models

Designed for the sand models to be inserted into, the sand dune model is a wooden frame with a 2 foot by 2 foot base. The sand dune model consists of a wooden 24" x 24" box that begins with a 3" depth and increases at a fifteen degree angle from the front to the rear of the box. Fifteen degrees was selected as an angle to be representative of coastal sand dunes in North Carolina. To attempt to eliminate the boundary effects of the wooden frame, the 1 foot by 1 foot soil model is surrounded by 6 inches of uncemented North Carolinian sand in all directions. After completion of chemical treatments, the sand model is put into the partially pluviated sand dune model. More sand is added to the sand dune model until the sand model is resting at a 15 degree angle. Once the orientation of the model was corrected, uncemented sand was used to fill the remaining void around the perimeter of the sand model. The sand

was leveled and the laser morphology was obtained prior to the application of wave action.

Laser Morphology

Surface morphology was measured before and after the sand was subjected to wave action using a scanCONTROL 2600-25 line laser scanner by Micro-Epsilon. The line laser was mounted at a fifteen degree angle in order to scan the soil surface perpendicularly. This scanner is capable of taking 640 data points per profile, attributing to high precision in the generated profiles. Two six inch profiles were taken at each location and carefully matched such that the entire the soil surface could be displayed and used to accurately predict the eroded area. Laser morphology data was obtained every 2 inches in an attempt to recreate an approximate surface and estimate eroded volume.

Wave Tank

In order to produce repeatable waves with identifiable properties, the testing was conducted at the Coastal Studies Institute in an Omey Labs wave tank. The wave tank dimensions are 33' x 9.5' x 5' with an optimal operating water height of 4'-4". To physically create the waves, the Omey Labs wave maker operates through precise movements of an electrical linear planetary gear screw actuator. Due to the effects of the hydrostatic pressure of the water in the tank on the actuator, a pneumatic air spring is used for pressure equalization. Although the wave maker is capable of creating regular and irregular wave spectra, the input wave functions for this study were monochromatic. During wave generation and as shown in Figure 2, the actuator movements begin in a subtle manner and ramp up to the desired wave properties. Conversely, once the wave function has completed, the movement of the actuator lessens until coming to a complete halt. To prevent effects of wave reflection and to dampen wave energy, Omey Labs has designed a wave absorber to remove energy from breaking waves through flexing of the polycarbonate sheeting. The submerged wave absorber uses the water entrained beneath the sheeting to create the required matching force for absorption of the breaking wave.



**FIG 2. Omey Labs wave tank used for all wave tank testing
Acoustic Wave Gauges**

In order to precisely monitor the properties of the propagating and breaking waves, the software UltraLab by General Acoustics was used for data acquisition. The signal

receiver, UltraLab ULS HF416 was used in conjunction with the USS10 sensors, which operate through ultrasound pulse echoes. Ultrasonic sensors acoustically measure the number of echoes and the level. The number of echoes received by the transducer is an indication of signal quality and the level is an averaged water level, determined every ten seconds over one minute. Two wave gauges were used during experimentation – the first was located midway between the actuator and the soil specimen and the second was mounted above the soil surface to observe the effect and number of breaking waves. The wave properties observed from the first wave gauge is used herein as the input wave functions.

Mass of Calcium Carbonate Measurements

The mass of calcium carbonate was determined post-test using a gravimetric acid washing technique. The oven-dried mass of the soil sample from the sand dune model was measured before and after an acid wash (1M HCl). The dissolved calcium carbonate – acid wash solution was rinsed multiple times allowing the dissolved salts to be rinsed from the soil. The difference in the two measured masses was taken as the mass of calcium carbonate and the percentage of mass of calcium carbonate is expressed as the mass of calcium carbonate divided by the mass of soil (not including calcium carbonate).

RESULTS AND DISCUSSION

The cemented soil behaved exceptionally better than the uncemented soil when subjected to wave action. The addition of cementation lead to higher erosion resistance due to increases in shear strength and stiffness. The sand dune models were subjected to the wave input functions displayed in Figure 3a and 3c. Due to some variability controlling the exact input functions associated with differences in the ramp up and ramp down periods of the wave maker, the two input functions are not identical. Although not identical, these functions are remarkably similar. For the analysis presented, the wave functions were assumed to be equivalent to allow for a comparison of erosion. As noted by the difference in the soil surface wave functions, as shown in Figure 3d, as waves struck the surface, an insignificant amount of the cemented sand eroded away in between each successive wave. Conversely however, the soil surface wave function shown in Figure 3b, shows that after approximately 30 seconds into the wave testing, the soil surface decreases substantially in height as the wave height in between wave peaks trends in the negative direction. As noted by the initial seconds of the untreated wave test (Figure 3a), the actuator was out of position prior to the beginning of the testing which explains the sudden ramp up in wave properties.

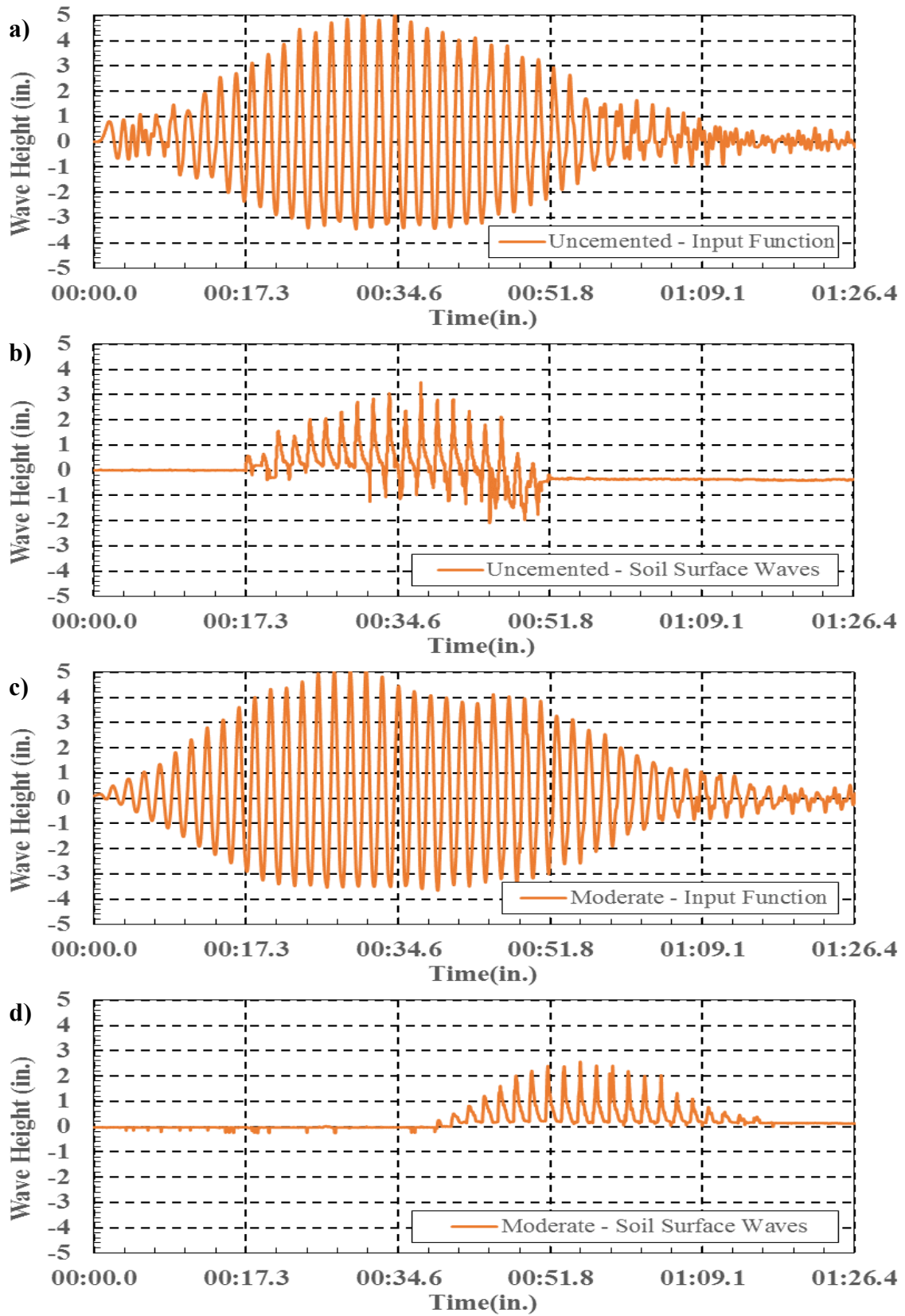


FIG. 3. Wave Functions, a) Uncemented – input function, b) Uncemented – soil surface waves, c) Moderate – input function, d) Moderate – soil surface waves

It is also shown in Figures 3a and 3c, that the presence of the sand dune model frame in the wave tank had some interference with the efficiency of the wave absorber. This phenomenon is evident by the constructive and destructive interference shown during the ramp down period and into the settling period of the wave tank. The initial and final shapes of the cemented and uncemented sand are shown below in Figure 4. Through a visual comparison of the photos in Figure 4b and 4d, the final surfaces are drastically different in terms of eroded volume. Quantitatively, the eroded areas along the centerline are displayed in Table 1. Figure 4d displays the aforementioned dowel rods, which as a result of the treatment procedure, became cemented into the sand specimen. To minimize sample disturbance, the dowels were cut at the surface of the cemented sand. Also shown in Figure 4d is the presence of pea gravel near the front face of the cemented sand. During the treatment procedure, the pea gravel particles cemented to the sand grains. Instead of potentially damaging the brittle MICP bonds, the testing was conducted with the gravel in place.

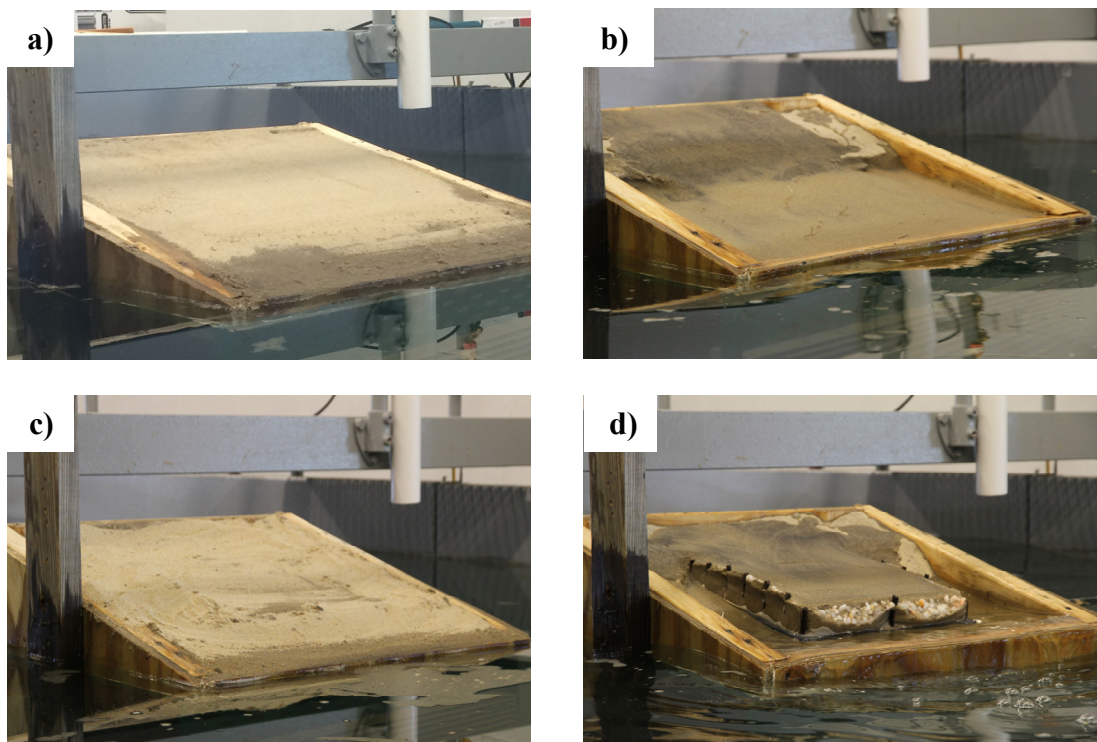


FIG 4. Photos of the initial and final stages of wave tank testing: a) Untreated - initial, b) Untreated - final, c) Moderately cemented – initial, d) Moderately cemented – final.

Upon completion of the wave testing, the surface morphology was obtained using the Micro-Epsilon line laser scanner to determine eroded area at multiple locations across the soil surface. Displayed herein are the results of the laser scanning at the centerline in the longitudinal direction. Figures 5 and 6 show the soil surfaces before and after the damaging effects of wave action. As indicated in the photos above, the final differential between surfaces after wave action was substantially greater for the

untreated sand versus the moderately cemented sand. The profiles in Figure 6 exhibits a slope change in the eroded profile at approximately 6.5-inches, which is a result of increasing and decreasing waves heights during the ramp up and ramp down phases. Due to the relatively low erosion resistance of untreated sand, erosion occurs at a rapid rate even for waves of decreasing wave heights and energies. The top of the sand model was only eroded during the peak times of the wave application.

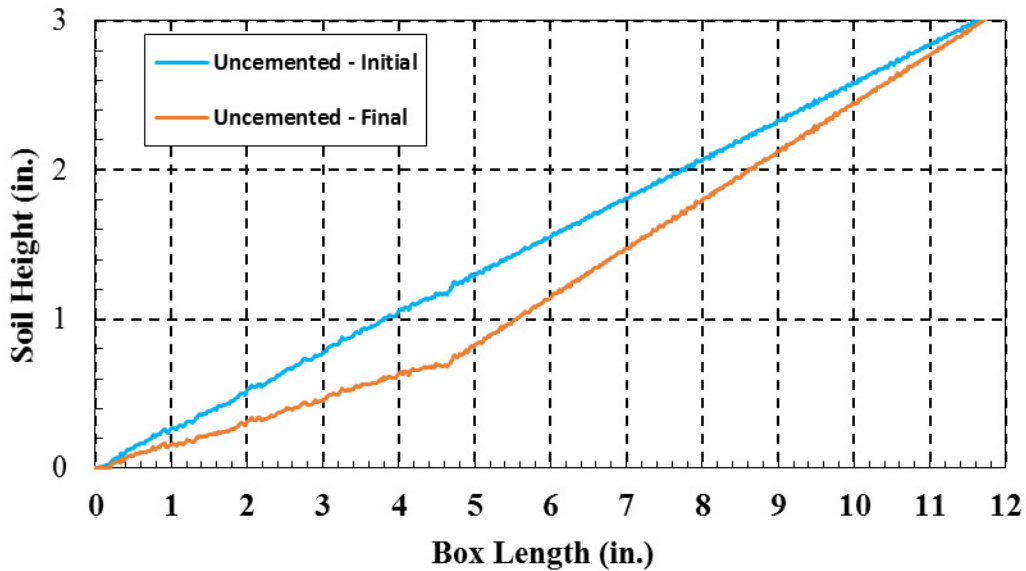


FIG 5. Laser Morphology for the Untreated sand subjected to wave action.

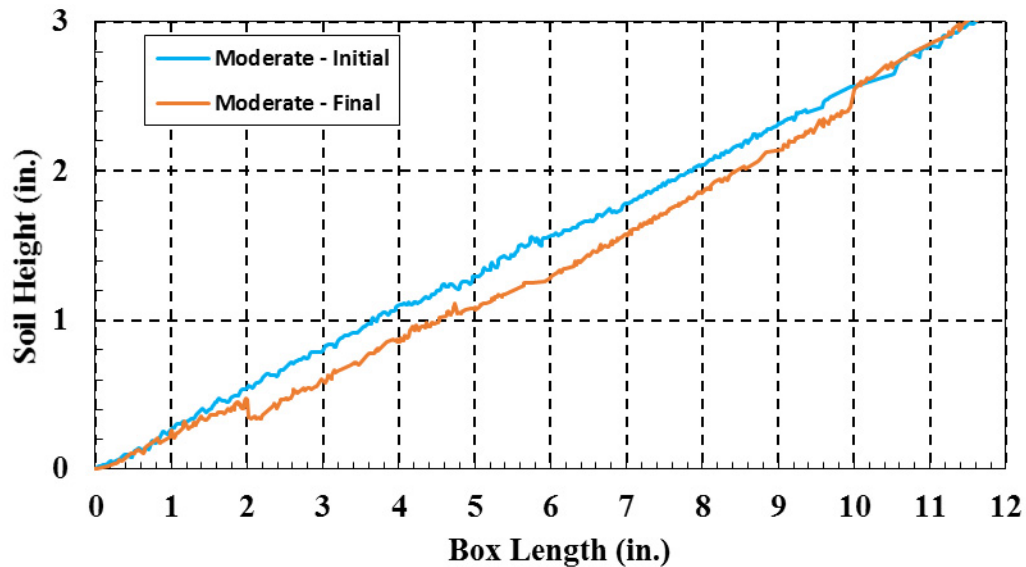


FIG 6. Laser Morphology for the Moderately cemented sand subjected to wave action.

Table 1. Model Sand Dune Summary Table

Sand Model	Number of Treatments	Eroded Area (in ²)	Estimated Eroded Mass (g)
Uncemented	0	3.0	66.7
Moderately-Cemented	30	1.6	22.2

Alternatively, there was very little erosion experienced for the moderately cemented sand model, with the expectation of a lesser cemented middle segment, as shown in the plan view cementation distribution in Figure 7. Due to the treatment methodology and the creep elongation of the latex membrane from the lateral earth pressure, the soil surface became slightly off level, resulting in preferential flow paths of the cementation media adjacent to the latex membrane during the treatment. The lateral cementation distribution is a direct function of the preferential flow, as shown in Figure 7a. As a result of the cementation differential between the outside and inside of the cemented soil specimen, the majority of the erosion occurred in the lower cementation zone.



FIG 7. Cementation Distribution: a) Plan view of soil surface, b) Profile view along centerline.

CONCLUSIONS

Unsaturated North Carolinian dune sand was successfully treated to moderate levels of cementation. The erosion reduction of the moderately cemented sand was substantial when compared to the untreated baseline model when subjected to similar wave loading. Through the application of MICP cementation to unsaturated to partially saturated sand dunes, the wave action induced erosion may be significantly reduced. Future work includes subjecting cemented sand models to fatigue loading, during which smaller and less violent waves act on the cemented and uncemented soil

surface for a significant amount of time. This study will investigate the durability of sand dunes under more typical conditions, whereas the work presented herein investigates erosion reduction during a significant storm event. Also included in future work is the interaction of the MICP process with the indigenous coastal sand dune ecology. In order for MICP to be a feasible erosion reducing methodology, the cementation durability and interference with pore space geochemistry and the effects on indigenous flora and fauna must be understood.

ACKNOWLEDGEMENTS

Funding from the National Science Foundation (EEC-1342207) is appreciated. Any opinions, findings, and conclusions or recommendations expressed in this material are those of the writer(s) and do not necessarily reflect the views of the National Science Foundation. The authors would like to thank the faculty and staff at the UNC Coastal Studies Institute, in particular: Billy Edge, Robert McClendon, Corey Adams, and Dave Sybert for all of their assistance during experimental testing.

REFERENCES

- Cheng, Liang, and Ralf Cord-Ruwisch. (2012). "In Situ Soil Cementation with Ureolytic Bacteria by Surface Percolation." *Ecological Engineering* 42: 64-72.
- Chou, C.-W., Seagren, E.A., Aydilek, A.H., and M. Lai. (2011). "Biocalcification of sand through ureolysis." *ASCE Journal of Geotechnical and Geoenvironmental Engineering*, Vol. 127, Issue 12, pp. 1179---1189.
- Chu, J., Stabnikov, V., and Ivanov, V. (2012) "Microbially induced calcium carbonate precipitation on surface or in the bulk of soil", *Geomicrobiology Journal*, Vol. 29, No. 6, 544-549.
- DeJong, J.T., Fritzges, M.B., Nüsslein, K. (2006). "Microbial induced cementation to control sand response to undrained shear". *ASCE J. Geotech. Geoenviron. Eng.* 132 (11), 1381–1392.
- Figlus, Jens, Nobuhisa Kobayashi, Christine Gralher, and Vicente Iranzo. "Wave-Induced Overwash and Destruction of Sand Dunes." *Int. Conf. Coastal. Eng. Coastal Engineering Proceedings* 1.32 (2011).
- Martinez, B.C. (2012) *Experimental and Numerical Upscaling of MICP for Soil Improvement*, Doctoral Dissertation, University of California, Davis, pp. 257.
- Miller, T. E. "Effects of Disturbance on Vegetation by Sand Accretion and Erosion across Coastal Dune Habitats on a Barrier Island." *AoB PLANTS* 7.0 (2015).
- Mortensen, B.M., Haber, M.J., DeJong, J.T., Caslake, L.F., Nelson, D.C. (2011). "Effects of environmental factors on microbial induced calcium carbonate precipitation." *Journal of Applied Microbiology*, Vol. 111, No. 2, 338-349.
- Shanahan, C. and Montoya, B. (2014) Strengthening Coastal Sand Dunes Using Microbial-Induced Calcite Precipitation. *Geo-Congress 2014 Technical Papers*: pp. 1683-1692.
- Whiffin, V.S., van Paassen, L.A., Harkes, M.P. (2007). "Microbial carbonate precipitation as a soil improvement technique." *Geomicrobiol. J.* 25 (5), 417–423.

Experimental Investigation of the Mechanical Properties of MICP-Treated Sands Reinforced with Discrete Randomly Distributed Fiber

Lin Li, M.ASCE, P.E.¹; Mingdong Li²; Ubani Ogbonnaya¹; Kejun Wen¹; Chi Li³; and Farshad Amini, F.ASCE, P.E.¹

¹Dept. of Civil and Environmental Engineering, Jackson State Univ., Jackson, MS 39217. E-mail: lin.li@jsums.edu, ogbonnayaubani@yahoo.com, kejun.wen@qq.com, famini@jsums.edu

²School of Civil Engineering, Huaihai Institute of Technology, Lianyungang, Jiangsu Province, China 222005. E-mail: ytlimd@163.com

³Inner Mongolia Univ. of Technology, College of Civil Engineering, Huhhot, China 010051. E-mail: nmglichi@gmail.com

Abstract: Microbial induced calcium carbonate precipitation (MICP) has attracted attention as a sustainable means of soil improvement in recent years. The addition of discrete randomly distributed fibers has been used in practice to stabilize soils and to improve their mechanical properties. In this study, the effect of randomly distributed discrete fiber on the mechanical properties of MICP-treated soil was investigated. Specimens were prepared at different fiber ratios. Full contact flexible molds were used to prepare the MICP-treated sand samples. Unconfined compression strength (UCS) tests were conducted. SEM images were used to analyze the binding effect of fiber. The results showed that improvements in shear strength, ductility, and failure strain were achieved with fiber addition in the MICP-treated sand. The UCS and shear strength increased with fiber content up to a fiber content of 0.3%. The UCS of MICP-treated sand at the fiber content is nearly 100% higher than that without addition of fiber. The failure strain of MICP-treated sand at the fiber content is triple higher than that without addition of fiber. Residual strengths of MICP-treated sand at the fiber content are still near 100 kPa, compared to no residual strength for that of MICP-treated sand without fiber. The inclusion of fibers increases the residual strength occurring after peak stress and decreases the brittle behavior of the MICP-treated sand.

INTRODUCTION

As one of the more promising bio-mediated soil improvement techniques, microbial-induced calcite precipitation (MICP) has been studied extensively (DeJong et al. 2006; van Paassen et al. 2010; Chou et al. 2011; Qabany et al. 2012; Burbank et al. 2013; Martinez et al. 2013; Zhao et al. 2014ab). By temporarily regulating the concentration of bacteria and nutrients in the granular soil, a cement component, such as carbonate precipitation, occurs through the bacteria ureolysis, which metabolites cause the formation of CaCO_3 in the presence of Ca^{2+} (DeJong 2006). MICP can be used as: (1) biogROUT that increases the shear strength of the soil to enhance foundation bearing capacity and slope stability, and to facilitate excavation and tunneling; (2) soil improvement against soil liquefaction during earthquakes; and (3) foundation settlement reduction (DeJong et al. 2010). Zhao et al. (2014a) developed a full contact flexible mold to prepare the sample and the results show a more uniform MICP process. The fibrous structure of non-woven geotextile mold enhances the contact between the bacteria and the cementation medium and promotes homogeneous calcium carbonate precipitation within the sand pores (Zhao et al. 2014a). However, the results of MICP-treated soils illustrate brittleness properties, which is a disadvantage for engineering applications (Zhao et al. 2014b).

Randomly distributed discrete fibers have been found to increase the shear strength and ductility of soils (Consoli et al. 2009). Yetimoglu and Salbas (2003) investigated the shear strength of sands reinforced with randomly distributed discrete fibers and found that the inclusion of fibers into soil increased the residual strength occurring after peak stress and decreased the brittle behavior of the soil. Shao et al. (2014) noted that fiber had a considerable effect on the shear strength of the sand. Fiber content had positive effects on improving the shear strength parameters (angle of internal friction and cohesion) of the mixtures. The inclusion of fibers improves the ductility of the soil by preventing the loss of post-peak strength. Addition of fiber reinforcement caused significant improvement in shear strength and ductility of fiber-reinforced soils. Addition of fiber in the MICP process has the potential to increase the ductility of the MICP-treated sand, and to prevent the loss of post-peak strength. This study is to investigate the effect of randomly distributed discrete fiber on the mechanical properties of MICP-treated soil. The soil samples were prepared using full contact flexible molds (Zhao et al. 2014a). A series of unconfined compression tests were carried out on MICP-treated sands that were prepared at different percentages of fiber content.

LABORATORY EXPERIMENTS

Experimental Materials

Uniform, clean, Ottawa silica sand (99.7% quartz) was used. The sand was uniformly graded, had a median particle size of 0.46 mm, and included no fines. It was classified as poorly graded sand on the basis of the Unified Soil Classification System. The specific gravity of the sand was

2.65. Fibermesh 150 was used, because it is one of the most commonly used fibers both by the concrete and geotechnical engineering industry. The fiber is 100% uniform homopolymer polypropylene multifilament material with a specific gravity of 0.91.

Sporosarcina Pasteurii (ATCC 11859) was used in this study due to its highly active urease enzyme. The bacteria were cultivated in an ammonium-yeast extract medium (ATCC 1376). After aerobically incubating at 30°C in a shaker at 200 rpm overnight, the bacteria and growth medium were centrifuged twice at 4000 g for 20 minutes. Then, the supernatant was removed and replaced with fresh growth medium before the bacteria were re-suspended. The bacteria and growth media were stored in the centrifuge vials at 4°C until used (Mortensen et al. 2011).

Cementation medium included 11.2 g/L urea, 27.6 g/L CaCl₂, 3.8 g/L NH₄Cl, 1.6 g/L NaHCO₃, and 4.5 g/L nutrient broth. The concentration of cementation media was selected based on Zhao et al. (2014b). The urea-Ca²⁺ molar ratio was fixed at 1:1. The pH of the cementation medium was adjusted by adding acid HCl to 6.0.

The specimens were prepared in full contact flexible molds (FCFM) as described in Zhao et al. (2014a), which were made of geotextile. The geotextile was a polypropylene, staple-fiber, needle-punched non-woven material. The geotextile have grab tensile strength of 17.6 N, apparent opening size of 0.15 mm, water flow rate of 34 mm/s, thickness of 1.5 mm, and unit mass of 200 g/m². The size of specimens was 36.8 mm in diameter and 76.2 mm in height. The mold consisted of an annular part, a bottom and a cover, as shown in Figure 1(a). Zhao et al. (2014a) found that the mechanical improvement of the MICP-treated soil using the full-contact flexible mold is one order of magnitude higher than that of the typical sample preparation method. The full-contact flexible mold enhances the contact between the bacteria and the cementation medium and promotes homogeneous calcium carbonate precipitation within the sand pores.

Experimental Methods

Following the experimental methods of Zhao et al. (2014ab), the 130 g of sand and fibers (0%, 0.1%, 0.2%, 0.3%, or 0.4% by weight of dry sand) were uniformly mixed with 45 mL bacteria solution and then air pluviated into the FCFM mold to reach a median dense condition (D_r in the range of 44%~55%). In the preparation of all samples, the required bacteria solution was first added into the dry sand to prevent floating of the fibers in the soil matrix, and then the proposed content of fibers was mixed in small increments by hand to obtain a uniform mixture. It is important to ensure that all fibers are mixed thoroughly (Shao et al. 2014). A total of 12 molds with sand samples on the shelf were immersed into 10 L cementation media in completely stirred tank reactor. All specimens were prepared in the completely stirred tank reactor. The reactor included a plastic box to contain soil specimens and cementation media, a magnetic mixer to keep the solution uniform, and an air pump to provide oxygen for bacteria (Figure 1b). A major feature of this method is to allow soil specimens fully immerse into the cementation media and to allow the cementation media to freely penetrate into the soil specimens.

Bacterial cell concentration was quantified by measuring absorbance (optical density) of the suspension using Spectrophotometer (UV-1700 UV-VISIBLE Spectrophotometer, Shimadzu) at 600 nm wavelength (OD_{600}) (Fredrickson and Fletcher 2011). OD_{600} of bacteria growth media in this research was around 0.6 at all times, with bacteria concentration of about 4.28×10^7 cells/ml. The value of OD_{600} reflects the total number of bacteria in the solution.

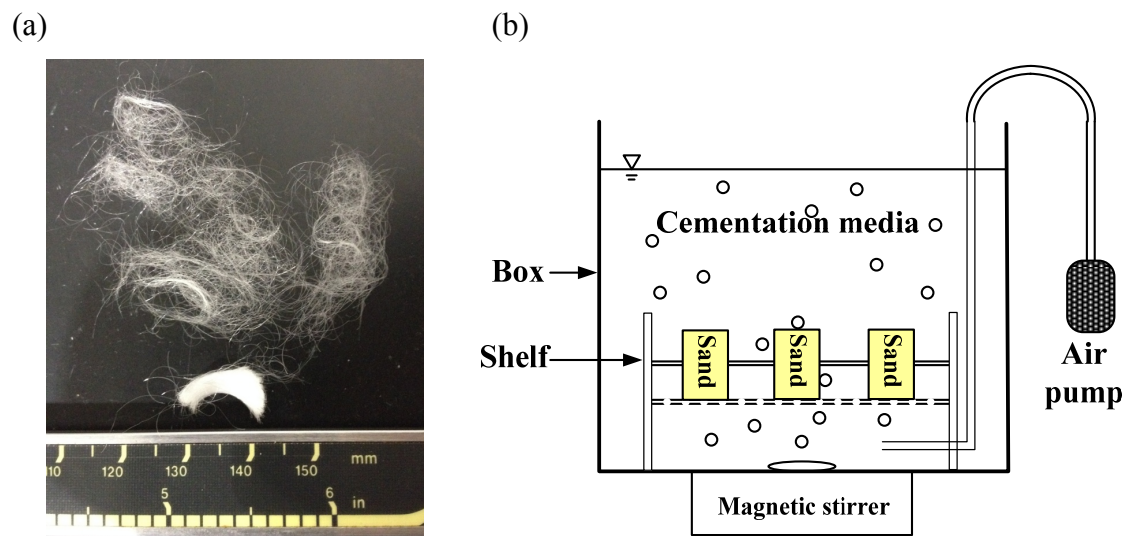


Figure 1. (a) image of synthetic fibers, and (b) schematic drawings of MICP batch reactor.

During the 7 days of reaction, only air was continuously pumped into the reactor. No bacteria, growth medium, or cementation medium was added to or pumped out of the reactor. After 7 days of reaction, the shelf was removed from the solution, each geotextile mold was cut, and the treated soil specimen was removed. The MICP sample preparation method is followed Zhao et al. (2014ab). After 7 days of reaction, the strength improvement of MICP-treated soil reached steady-state (Zhao et al. 2014b). Figure 2 shows an example of MICP-treated soil specimen. The unconfined compression tests were conducted under strain controlled conditions at a uniform loading rate of 1.5%/min in accordance with ASTM D2166. The formation of MICP was examined by scanning electron microscopy (SEM). With the bacteria concentration (OD_{600}) of 0.6 and cementation concentration of 0.5 M, the samples were prepared in the reactor for 7 days. Subsequently, these samples were sputter-coated for SEM analysis.

RESULTS AND DISCUSSIONS

The stress–strain curves obtained from UCS tests on MICP-treated sand specimens with different fiber contents (0.1%, 0.2%, 0.3%, and 0.4% by weight of sand) is shown in Figure 3a.

Although the MICP-treated samples can reach a fairly uniform state in the full contact flexible mold, there was still slightly different CaCO_3 content distributed within each sample, which may cause strength fluctuate during the tests (as shown in Table 1). At least four samples were prepared for each case to produce a representative condition. With the addition of fiber, the unconfined compression strength increases until 0.3% fiber content. When fiber content reached 0.4% by weight, unconfined compression stress-strain curves deteriorate. With the addition of fiber, the unconfined compression strength increases until 0.3% fiber content. When fiber content reached 0.4% by weight, unconfined compression stress-strain curves deteriorate.

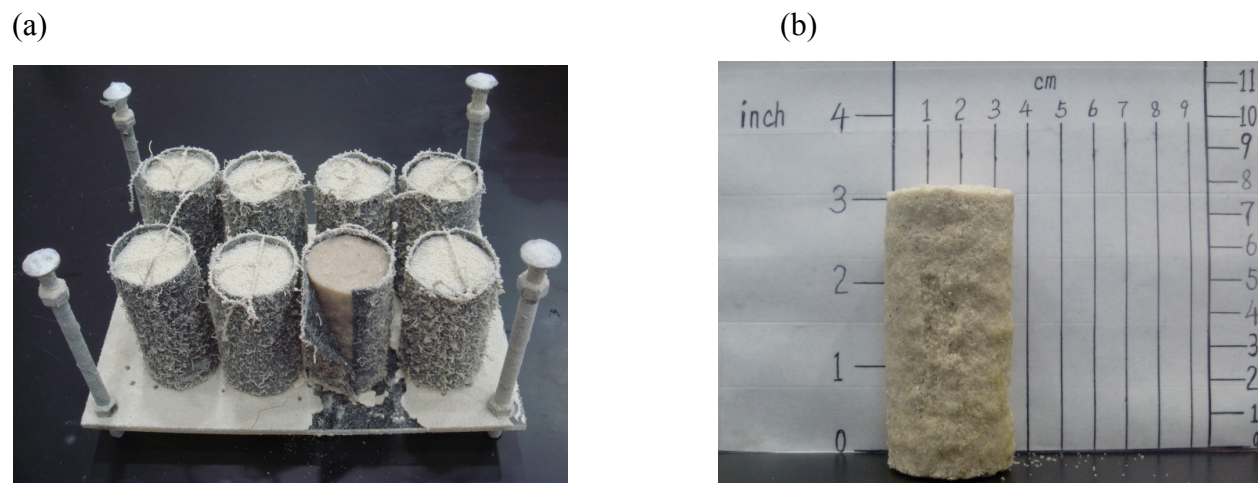


Figure 2. (a) image of specimens after the reactions, and (b) image of specimen removed from the full contact flexible mold.

Table 1. Effect of fiber content on unconfined compression strength, failure strain, and elastic modulus of MICP-treated samples.

Fiber content (%)	q_u (kPa)	ϵ_f (%)	E_{50} (MPa)	E (MPa)	q_{ur} (kPa)
0.0	68 ± 8	1.6 ± 0.4	4.3 ± 1.7	3.7 ± 0.7	0.0
0.1	90 ± 5	2.0 ± 0.3	4.9 ± 0.3	4.6 ± 0.7	50 ± 6
0.2	167 ± 2	3.5 ± 0.1	4.9 ± 0.7	4.8 ± 0.1	104 ± 10
0.3	164 ± 6	3.7 ± 0.5	4.8 ± 1.3	4.4 ± 0.6	99 ± 7
0.4	102 ± 6	3.1 ± 1.1	4.0 ± 0.8	3.4 ± 0.5	70 ± 15

Note: q_u is peak strength, ϵ_f is failure strain, E_{50} is elastic modulus at 50% of q_u , E is elastic modulus, and q_{ur} is residual strength.

Figure 3b shows the effect of fiber on UCS of MICP-treated sand. All the strengths (peak strength q_u , strength at half failure strain $q(\epsilon_f/2)$, and residual strength q_{ru} at 15% strain) increase with fiber content up to a fiber content of 0.3%. When 0.1%, 0.2%, 0.3% or 0.4% fiber was added, UCS increased by 132%, 245%, 240% and 149%, respectively. The peak strengths of MICP-treated sand at fiber content of 0.2%-0.3% are more than 2 times higher than that without addition of fiber. The strength at half failure strain of MICP-treated sand at fiber contents of 0.2%-0.3% are also approximately 2 times higher than that without addition of fiber. Residual strengths of MICP-treated sand at the fiber content of 0.2%-0.3% are more than half of their peak strengths, while the residual strength is 0 kPa for that of MICP-treated sand without fiber. When local cracks appear on MICP-treated sand with fiber, fibers across the cracks take the tension within the soil due to the fiber-soil friction, which effectively impedes further development of cracks and, thus, improves the resistance of soil to the force applied. These results indicate that fiber plays an important role on the unconfined compression strength of MICP-treated sand, and 0.2%-0.3% fiber (by weight of sand) are the most suitable fiber contents. This finding is consistent to a similar research on fiber reinforced clayey soil, with same tendency and similar optimal fiber content 0.3% (Jiang et al. 2010).

The effect of fiber on failure strain of MICP-treated sand under unconfined condition is shown in Table 1. It shows that failure strain increases with the addition of fibers. As 0.1%, 0.2%, 0.3% or 0.4% fiber were added, failure strain of MICP-treated sand increased 125%, 219%, 233% and 194% of that without fiber, respectively. The results indicate the ductility of MICP-treated sand can be significantly improved by adding suitable amount of fibers (0.2-0.3%). This finding is consistent with the results of past studies. Dos Santos et al. (2010) found that the inclusion of fibers is more effective at higher strain rates.

The effect of fiber on elastic modulus of MICP-treated sand under unconfined conditions is shown in Figure 3c. Young's modulus at the unconfined compression strength (E) and Young's modulus at 50% of the unconfined compression strength (E_{50}) increase with fiber contents up to 0.2%. The Young's modulus E reaches peak value at 0.2% fiber content and E_{50} reach peak value at 0.1% fiber content, which are 130% and 112% of that of MICP-treated sand without fiber, respectively. However, when the fiber contents exceed 0.2%, the E and E_{50} slightly decrease. At the 0.4% fiber content, the E and E_{50} are lower than the elastic modulus of MICP-treated sand without fiber. Therefore, the strengthening effect of fiber is mainly influenced by extending elastic strain range, rather than by increasing elastic modulus, which is on behalf of rigidity.

When fiber content was increased up to 0.4%, there is a drop of shear strength and UCS test. The reason is caused by the fiber impede the uniformity of bacteria distribution in the soil specimen. The non-uniformly distributed bacteria impact the distribution of calcite precipitation in the soil mixture and thus the strength of soil specimen. As the bacteria are alive and moving around in the pore among the soil mixture, the fiber can impede the bacteria movement. As more as fiber content, the more bacteria are obstructed by the fiber. The formation of calcite precipitation is around fiber, instead of around soil particle. The less bonding of soil particles by calcite precipitation causes the weak strength at the higher fiber content (0.4% of fiber content).

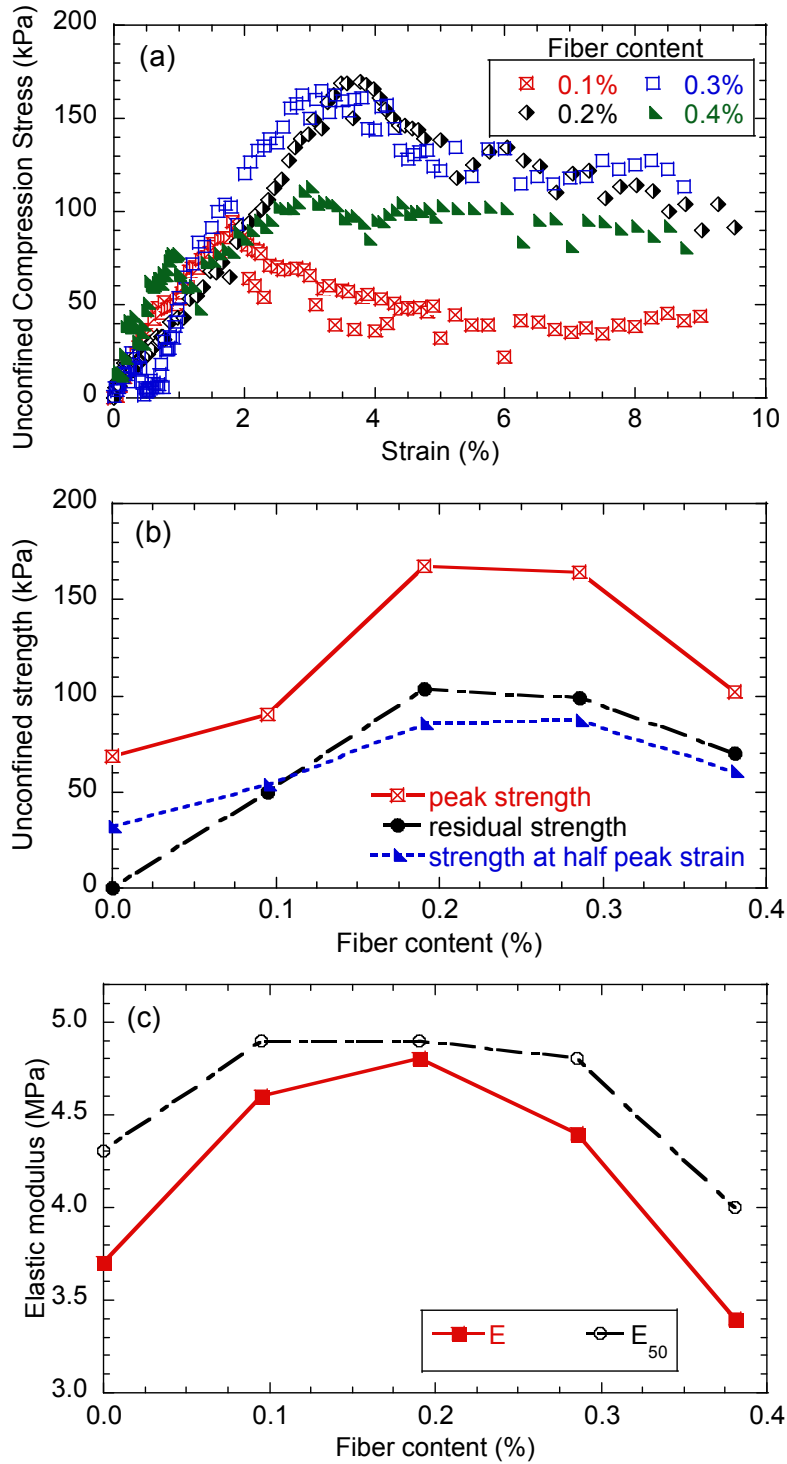


Figure 3. Effect of fiber content on: (a) unconfined compression stress, (b) unconfined compression strength, and (c) elastic modulus of MICP-treated samples.

The SEM image in Figure 4 shows that CaCO_3 crystals were mainly irregular bulk, similar to observations made by Qabany et al. (2012) and Zhao et al. (2014b). The CaCO_3 crystals tend to participate the contact segments between sand particles which result in a better bonding effect among sand particles than uniform distribution on sand particles. As a result of cementation, the strength of MICP-treated sand is improved (DeJong et al. 2010; Burbank et al. 2013). In addition, the reduction in void space due to the CaCO_3 precipitation is considered to be a secondary strengthening factor (DeJong et al. 2010).

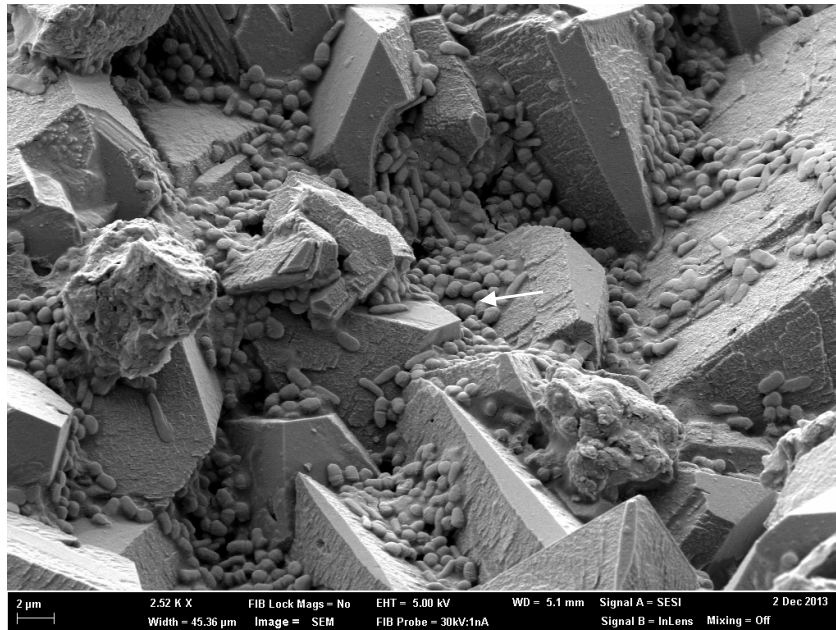


Figure 4. SEM image of MICP bonded sand particles

Conclusions

Addition of fiber in the MICP process has the potential to increase the ductility of the MICP-treated sand, and to prevent the loss of post-peak strength. In this paper, a series of unconfined compression tests were carried out on MICP-treated sand mixed with fiber contents of 0.1, 0.2, 0.3, and 0.4%, in order to study the effect of randomly distributed discrete fiber on the mechanical properties of MICP-treated soil and to investigate the corresponding mechanisms. MICP were catalyzed by *Sporosarcina Pasteurii* at the concentration of 4.3×10^7 cells/mL. The concentration of cementation media was 0.5 M. All the samples were prepared by full contact flexible molds to ensure full contact between the entire sample and the cementation media.

Under unconfined compression conditions, shear strength and failure strain were significantly improved, while elastic modulus showed a slight improvement. The results indicate various improvements achieved by adding fibers, compared with corresponding value of MICP-treated sand without fiber. Under unconfined

compressive condition, failure strain and UCS increased over 200%, and elastic modulus increased over 100%. The UCS increased gradually with an increase in fiber content up to a fiber content of 0.3%. In addition, the MICP-treated sand reinforced with fiber exhibited more ductile behavior and limited reductions in residual strength. The optimum fiber content in the MICP-treated sand was found to be 0.2%-0.3%. The UCS of MICP-treated sand at fiber content of 0.2%-0.3% is more than 2 times higher than that without addition of fiber. Residual strengths of MICP-treated sand at the fiber content of 0.2%-0.3% are near 100 kPa, while the residual strength is 0 kPa for that of MICP-treated sand without fiber. Fiber content had positive effects on improving the shear strength parameters of the mixtures. The strengthening effect of fiber is mainly characterized as extension of elastic strain scope, rather than advancing elasticity modulus, which is different from strengthening effect of calcium carbonate precipitation content. When the amount of fiber mixed with soil is too much, i.e., 0.4% by weight of sand, the fibers will inhibit the movement of bacteria in the soil matrix, which leads to an uneven distribution of bacteria in soil and thus results in non-uniform calcite precipitation. This consequently reduces the effectiveness of improvement in compressive strength and shear strength parameters.

REFERENCES

- Burbank, M. B., Weaver, T., Lewis, R., Williams, T., Williams, B., and Crawford, R. (2013). "Geotechnical tests of sands following bioinduced calcite precipitation catalyzed by indigenous bacteria." *J. Geotech. Geoenviron. Eng.*, 139, 928-936.
- Chou, C., Seagren E. A., Aydilek, A. H., and Lai M. (2011). "Biocalcification of sand through ureolysis." *J. Geotech. Geoenviron. Eng.*, 137 (12), 1179-1189.
- Consoli, N. C., Vendruscolo, M. A., Fonini, A., Dalla R. F. (2009). "Fiber reinforcement effects on sand considering a wide cementation range." *Geotextiles and Geomembrane*, 27, 196-203.
- DeJong, J. T., Fritzes, M. B., and Nusslein, K. (2006). "Microbially induced cementation to control sand response to undrained shear." *J. Geotech. Geoenviron. Eng.*, 132 (11), 1381-1392.
- DeJong, J. T., Mortensen, B. M., Martinez, B. C., and Nelson, D. C. (2010). "Bio-mediated soil improvement." *Ecological Eng.*, 36, 197-210.
- Dos Santos, A. P., Consoli, N. C., and Baudet, B. A. (2010). "The mechanics of fiber-reinforced sand." *Geotechnique*, 60 (10), 791-799.
- Jiang, H., Yi, C., and Jin, L. (2010). "Engineering properties of soils reinforced by short discrete polypropylene fiber." *J. Mater. Civ. Eng.*, 22, 1315-1322.
- Martinez, B. C., DeJong, J. T., Ginn, T. R., Montoya, B. M., Barkouki, T. H., Hunt C., Tanyu, B., and Major, D. (2013). "Experimental optimization of microbially-induced carbonate precipitation for soil improvement." *J. Geotech. Geoenviron. Eng.*, 139 (4), 587-598.
- Mortensen, B. M., Haber, M. J., DeJong, J. T., Caslake, L. F., and Nelson, D. C. (2011). "Effects of environmental factors on microbial induced calcium carbonate precipitation." *Journal of Applied Microbiology*, 111, 338-349.

- Qabany, A. A., Soga, K., and Santamarina, C. (2012). "Factors affecting efficiency of microbially induced calcite precipitation." *J. Geotech. Geoenviron. Eng.* 138, 992-1001.
- Shao, W., Li, L., Cetin, B., and Li, Y. (2014). "Experimental investigation of mechanical properties of sands reinforced with discrete randomly distributed fiber." *J. Geotechnical and Geological Engineering*, 32 (4), 901-910.
- Van Paassen, L. A., Ranajit Ghose, Thomas J. M. van der Linden, Wouter R.T. van der Star, and Mark C.M. van Loosdrecht. (2010). "Quantifying biomediated ground improvement by ureolysis: large-scale biogROUT experiment." *J. Geotech. Geoenviron. Eng.*, 136 (12), 1721-1728.
- Yetimoglu, T., and Salbas, O. (2003). "A study on shear strength of sands reinforced with randomly distributed discrete fibers." *Geotextiles and Geomembranes*, 21, 103-110.
- Zhao, Q., Li, L., Li, C., Zhang, H. and Amini, F. (2014a). "A full contact flexible mold for preparing samples based on microbial induced calcite precipitation technology." *Geotechnical Testing Journal*, ASTM, 37(5), DOI: 10.1520/GTJ20130090.
- Zhao, Q., Li, L., Li, C., Li, M., Amini, F. and Zhang, H. (2014b). "Experimental Factors on Improvement of Engineering Properties of MICP-treated Soil Catalyzed by Bacteria and Urease." *Journal of Materials in Civil Engineering*, ASCE, ASCE, 26 (12), 04014094.

Exploring X-Ray Computed Tomography Characterization and Reactive Transport Modelling of Microbially-Induced Calcite Precipitation in Sandy Soils

Rosa Mystica Akimana¹; Youngwoo Seo²; Lin Li³; Lucas J. Howard⁴; Mandar M. Dewoolkar⁵; and Liang Bo Hu⁶

¹Graduate Research Assistant, Dept. of Civil Engineering, Univ. of Toledo, Toledo, OH 43606. E-mail: RosaMystica.Akimana@rockets.utoledo.edu

²Associate Professor, Dept. of Civil Engineering, Univ. of Toledo, Toledo, OH 43606. E-mail: youngwoo.seo@utoledo.edu

³Associate Professor, Dept. of Civil and Environmental Engineering, Jackson State Univ., Jackson, MS 39217. E-mail: lin.li@jsums.edu

⁴Graduate Research Assistant, College of Engineering, Univ. of Vermont, Burlington, VT 05405. E-mail: lhoward1@uvm.edu

⁵Associate Professor, College of Engineering, Univ. of Vermont, Burlington, VT 05405. E-mail: mdewoolk@uvm.edu

⁶Assistant Professor, Dept. of Civil Engineering, Univ. of Toledo, Toledo, OH 43606. E-mail: Liangbo.Hu@utoledo.edu

Abstract: Recent interests in the bio-mediated soil alterations show a concerted focus on taking advantage of multi-physical mechanisms to seek innovative solutions to emerging challenges facing civil engineers. This paper explores the use of X-ray computed tomography (CT) to characterize the microbially induced calcite precipitation (MICP), where micro-organisms play an active role in catalyzing urea hydrolysis and inducing chemical precipitation of calcite, resulting in the reduction of porosity and permeability and improvement of strength and stiffness. The soil specimens were prepared with full contact flexible molds (FCFM). Cultured *Sporosarcina pasteurii* was used to grow biofilms. X-ray CT images of bio-treated soil specimens show its potential of characterization of spatial distribution of calcite precipitation. A macroscopic reactive-transport process was simulated focusing on the assessment and prediction of calcite precipitation. Calibrated against the experimental results of the average calcite precipitation in certain regions of the specimen, the numerical simulations indicate that modest uniformity is possible as observed in the experiments and may be addressed by conventional reactive transport modelling.

INTRODUCTION

Microbially induced calcite precipitation (MICP) has attracted strong interest as a potential soil improvement technique, where micro-organisms play an active role in

catalyzing urea hydrolysis and inducing chemical precipitation of calcite, resulting in the reduction of porosity and improvement of strength and stiffness. Despite successful implementations achieved in the laboratories and extensive research (e.g., DeJong et al. 2006, 2010; Whiffin et al. 2007; van Paassen et al. 2010; Barkouki et al. 2011; Chou et al. 2011; Qabany et al. 2012; Martinez et al. 2013; Montoya et al. 2013; Zhao et al. 2014b), there remain many critically unanswered questions as to the predictability and controllability of altered/engineered soil properties. The eventual field implementation of such technology will greatly benefit from reliable prediction of the spatial distribution and temporal evolution of bio-induced precipitation and the improved soil properties. This demands significant experimental, theoretical and modelling efforts that can enable engineers to interpret and assess laboratory results and develop effective predictive tools.

The present study aims to explore the potential of imaging techniques for better understanding the characteristics of the bio-mediated calcite precipitation process. Preliminary results of X-ray Computed Tomography (CT) of MICP-treated soil specimens are presented. These results are also assessed with numerical simulations of the reactive transport processes involved. As the sample preparation method may play an important role in achieving the effective calcite precipitation, the presented study is focused on the samples prepared using a full contact flexible mold (Zhao et al. 2013a).

SAMPLE PREPARATION

The specimens for MICP treatment were prepared by full contact flexible molds (FCFM) (Zhao et al. 2014a, 2014b), which are made of geotextile. The geotextile is a polypropylene, staple fiber and needle punched nonwoven material. The fibers are needle punched to form a stable framework that retains dimensional stability relative to each other. The selected geotextiles have an apparent opening size of 0.15 mm, maximum allowable water flow rate of 34 mm/s and thickness of 1.5 mm. This geotextile has a large number of pores, promoting penetration of chemicals from cementation media to sand pores, which is beneficial to the MICP process. The size of the mold is 51-mm diameter and 102-mm height. The molds consist of an annular part, a bottom, and a cover.

Sporosarcina pasteurii (ATCC 11 859) was used in this study because of its highly active urease enzyme. The bacteria were cultivated in an ammonium-yeast extract medium (ATCC 1376). After aerobically incubating at 30°C in a shaker at 200 rpm overnight, the bacteria and growth medium were centrifuged twice at 4000 g for 20 min. Then the supernatant was removed and replaced with fresh growth medium before the bacteria were re-suspended. The cementation medium included urea (30 g/L), CaCl₂·H₂O (73.5 g/L), NH₄Cl (10 g/L), NaHCO₃ (2.12 g/L), and nutrient broth (3 g/L). The urea-Ca²⁺ molar ratio was fixed at 1:1. The pH of the cementation medium was adjusted to 6.0.

Two types of sandy soil specimens were prepared, (1) an Ottawa silica sand (99.7 % quartz), hereafter referred to as standard sand; and (2) the same Ottawa silica sand mixed with clay. The primary purpose of using a sand with significant clay content is to assess the influence of the clay content on cementation.

As shown in Fig. 1a, 330-g of washed sand was uniformly mixed with 85 ml of bacteria and growth medium, which were then air-pluviated into a FCFM to reach an intermediate density condition (D_r in the range of 42~55 %). Eighteen molds with sand specimens on a shelf were immersed in 15 liters of cementation medium in the completely stirred tank reactor. Small holes of 5mm in diameter were punched in the shelf, and the spacing between these holes was 5 mm, which allowed the water to flow through the shelf. During the 7 days of reaction, only air was continuously pumped into the reactor. No bacteria, growth medium, or cementation medium was added to or pumped out of the reactor. After 7 days of reaction, the shelf was removed from the solution (Fig. 1b), each geotextile mold was cut, and the treated soil specimen was removed. Details of specimen preparation can be found in Zhao et al. (2014a).

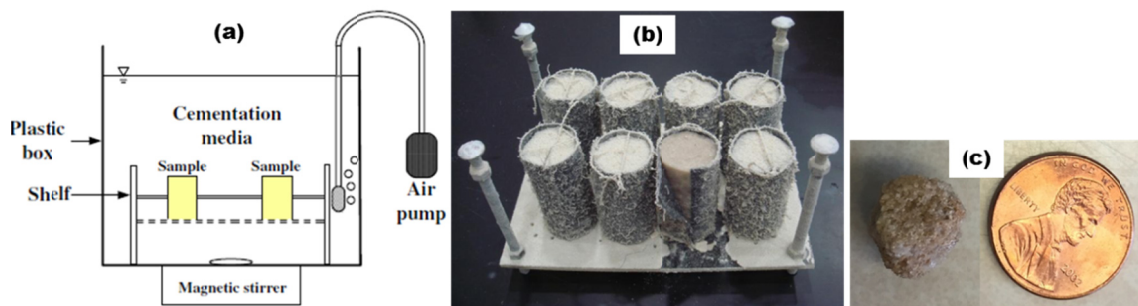


FIG. 1: (a) Schematics of the MICP batch reactor; (b) photograph of specimens after the reactions in the full contact flexible mold (and subsequently removed from the mold for X-ray CT scanning); (c) photograph of a small “cored” sample (slightly smaller than a cent coin), from the original specimen for finer X-ray scans.

X-RAY CT IMAGING

The prepared bio-treated soil specimens were subsequently subjected to X-ray CT scanning. A Skyscan 1173 scanner (Bruker micro-CT) was used. First the original roughly cylinder-shaped specimens were scanned. As the size of the specimens (~50 mm in diameter) was quite large, the resolution was set up to be about 20 micron after several attempts and adjustments. A stack of X-ray CT scans for each specimen, which was of ~100 mm long, usually contained over 1600 cross-sectional scans.

Example scanning images of the original specimens are shown in Fig. 2. For better visualization, the brightness and contrast of these images were enhanced. The presented example images were taken around the middle part of each specimen. It is noticeable that in the sand with clay (Fig. 2a), there were certain appreciably brighter areas near the center, as well as around the perimeter, indicating possible different minerals. In the standard sand (Fig. 2b), it appeared such areas only existed around the perimeter. Obviously in Fig. 2a, areas near the center might represent clay-sand mixture, which appeared much denser. Due to the large specimen size and crude resolution, an overall evaluation of calcite precipitation seems problematic.

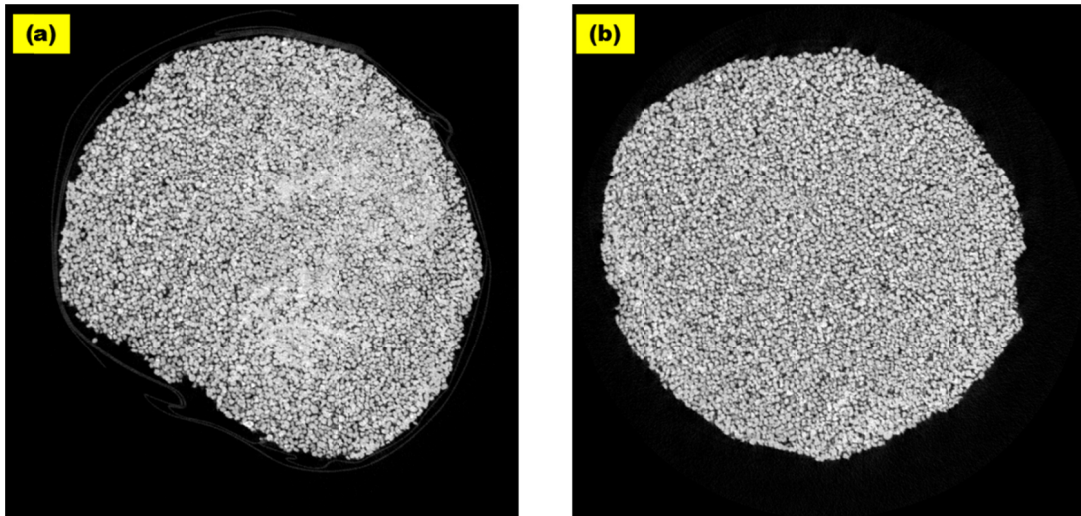


FIG. 2: (a) Example X-ray CT scan of the sand with clay, with brightness and contrast enhanced for better visualization; (b) Example X-ray CT scan of the standard sand, with brightness and contrast also enhanced.

Subsequently, a small sample was “cored” from the original specimen for X-ray scanning with finer resolution. This was carefully done by gently cutting a small piece from the specimen (Fig. 1c), because the overall strength of bio-treated soil specimens, even significantly improved, still cannot sustain a conventional coring applied to typical construction materials such as stones or concrete. The small pieces obtained were around the end and near the center of the original specimens.

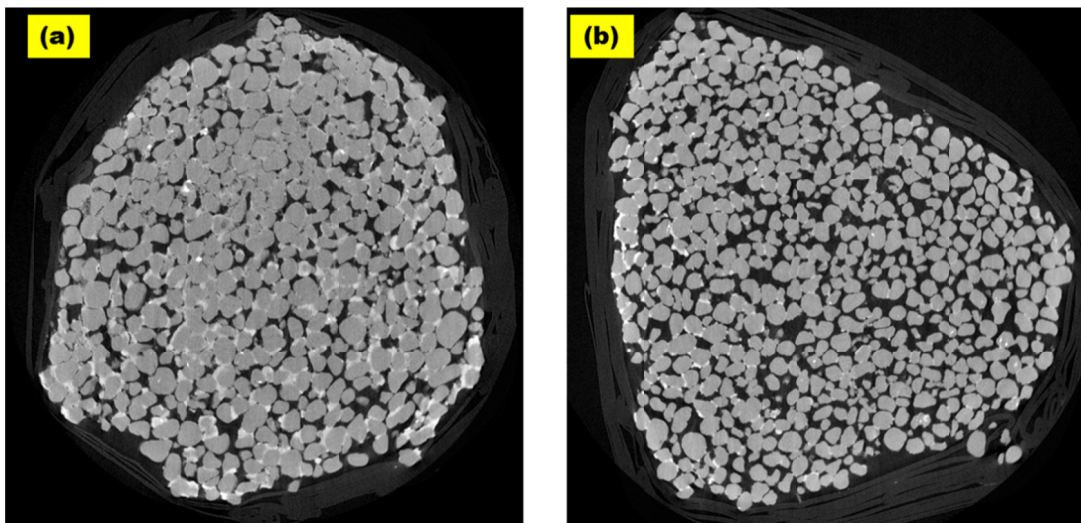


FIG. 3: (a) Example X-ray CT scan of the small core from the sand with clay, with brightness and contrast enhanced for better visualization; (b) Example X-ray CT scan of the small core from the standard sand, with brightness and contrast enhanced.

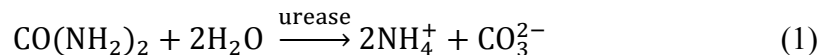
Fig. 3 shows typical X-ray scans of the two studied sandy soils. Precipitated calcites are clearly shown to primarily reside between grain contacts, while very few around the free surface of grains. In a somewhat surprise, it appears that there were more calcite precipitations in the sand with clay than in the standard sand. On the one hand, clay particles are of similar size as biofilms and therefore believed to inhibit the growth of biofilms, reducing their effectiveness in catalyzing urea hydrolysis. On the other hand, as to this particular set of experiments, the standard sand appeared much looser (Fig. 3), hence it is speculated that the greater space of pores and fewer grain contacts may have played a role in producing less calcite precipitation.

Although the small samples were not rigorously cored with a controlled geometry and in a specified positioning, it is apparent from Fig. 3 that the calcite precipitation gradually reduced towards the center, this was especially so with the standard sand where most of the precipitation appeared around the perimeter of the core.

NUMERICAL MODELLING OF REACTIVE TRANSPORT PROCESSES

The presented preliminary results of X-ray imaging are of qualitative nature but have demonstrated the potential of this technology for further MICP characterization; for example, advanced imaging tools can be used to quantify the distribution of calcite across the specimen. Some other aspects of the experimental study of MICP using FCFM as reported in Zhao et al. (2014) also provided useful information about the altered properties of treated sands. Assessment of these results can greatly benefit from quantitative simulations of the calcite precipitation process. In this section a reactive transport model for MICP (e.g., Barkouki et al. 2011; van Wijngaarden et al. 2011; Fauriel and Laloui 2012) is examined and the numerical simulations are undertaken to evaluate the spatial distribution and temporal evolution of the calcite precipitation in different scenarios.

The reactions involving the hydrolysis of urea in the supersaturated condition and the production of calcium carbonate precipitate are shown below.



The mass conservation equations are established for urea, calcium chloride and ammonium chloride, as in van Wijngaarden et al. (2011):

$$\frac{\partial(\theta C)}{\partial t} = \nabla(\theta \mathbf{D} \nabla C) - \nabla \cdot (\mathbf{q} C) + \theta m R_{\text{reac}} \quad (3)$$

where C is the mass concentration of the species under consideration (urea, NH_4^+ or Ca^{2+}), θ is the porosity, \mathbf{q} is the Darcy velocity, R_{reac} is the reaction rate and m is the stoichiometry constant. The third term in the right-handed side of eq. (3) represents the reaction term, from reaction. (1), it can be seen that $m = -1$ for C^{urea} , and $m = 2$ for $C^{\text{NH}_4^+}$; for $C^{\text{Ca}^{2+}}$, as reaction (2) is much faster than reaction (1) and thus its rate can be neglected, hence, $m = -1$. The dispersion tensor \mathbf{D} used in van Wijngaarden et al. 2011 deserves some comments. This tensor is related to the pore water (seepage) velocity \mathbf{v} (which is related the Darcy velocity, $\mathbf{v} = \mathbf{q}/\theta$), $\mathbf{D} = (\alpha_L - \alpha_T)\mathbf{v} \otimes \mathbf{v}/|\mathbf{v}| + \alpha_T|\mathbf{v}|\mathbf{I}$, α_L and α_T are the longitudinal and transverse dispersivities, respectively, \mathbf{I} is

the identity tensor. If a diffusion process rather than dispersion is considered, this tensor should be replaced with a diffusion tensor, of which each element represents a diffusion coefficient and usually assumed as a constant. If both dispersion and diffusion are considered, then an overall tensor in the form of the sum of the dispersion tensor and the diffusion tensor, $\mathbf{D}_f + \mathbf{D}_p$, can substitute \mathbf{D} in the mass conservation equation; here the formulation encompasses all the potential cases, for instance, when the flow velocity is zero, the dispersion tensor vanishes, a diffusion dominant process can be addressed accordingly. This is particularly relevant to the presented study since MICP specimens using FCFM method mainly rely on the diffusion process to induce calcite precipitation (Zhao et al. 2014a).

The reaction rate for calcite precipitation is influenced by a number of factors, including the activity of the urease, which most likely plays a dominant role. A typical formulation that has been used in previous investigations (e.g., Fauriel and Laloui 2012) is adopted here; it assumes a Monod kinetic rate,

$$R_{\text{reac}} = U_m \frac{C^{\text{urea}}}{K_m + C^{\text{urea}}} e^{-t/\tau_m} \quad (4)$$

U_m is the maximum reaction rate, K_m is the half saturation constant. The exponential term represents the decay of the micro-organisms, describing the reduction or loss of activity of bacteria. τ_m is a characteristic time at which (when $t = \tau_m$) the activity of urease is reduced by 61.2%.

The aforementioned equations comprise the core framework of the reactive transport model applied to the MICP process using FCFM. Because in this preparation method the dominant process is diffusion and the flow velocity vanishes, the second term on the right-handed side of eq. (3) also vanishes. For simplicity, infiltration from the top or bottom is neglected and axisymmetry can be reasonably assumed. Four unknown variables, C^{urea} , $C^{\text{NH}_4^+}$, $C^{\text{Ca}^{2+}}$ and R_{reac} are described by four equations discussed above, three partial differential equations as eq. (3) (for all three species) in addition to eq. (4). It should be pointed out that some variables such as the porosity do not remain constant during the process. Calcite concentration, porosity and permeability change can also be established as follows as discussed in van Wijngaarden et al. (2011).

The calcite concentration is defined in terms of mass per unit (bulk) volume,

$$\frac{\partial C^{\text{CaCO}_3}}{\partial t} = m_{\text{CaCO}_3} \theta r \quad (5)$$

m_{CaCO_3} is the molar mass of calcite. The porosity change is considered to result from calcite precipitation,

$$\frac{\partial \theta}{\partial t} = - \frac{1}{\rho_{\text{CaCO}_3}} \frac{\partial C^{\text{CaCO}_3}}{\partial t} \quad (6)$$

The porosity change also induces the permeability change based on Kozeny-Carman relationship:

$$k = \alpha \frac{\theta^3}{(1-\theta)^2} \quad (7)$$

The coefficient, α was assumed to be related to the mean particle size, d_m , in van Wijngaarden et al. 2011, $\alpha = d_m^2/180$; this relationship is also used here for simple evaluation of permeability evolution.

Fig. 4 shows the simulation of MICP process in a cylindrical specimen (50 mm in diameter and 100 mm in length as described in the preceding section) in a FCFM. The predominant mechanism is the reactive diffusion transport of each species. The values of parameters used in the present simulation are based on the calibration against the experimental measurements of the $\text{CaCO}_3\%$ in the treated specimens reported by Zhao et al. (2013), who determined that the inner core cylinder of the specimen ($0 < r < 10$ mm) had a CaCO_3 content of about 6.6% (by weight), and the outer shell ($10 \text{ mm} < r < 25$ mm)'s $\text{CaCO}_3\%$ was around 7.1%. Integrations of the distribution of CaCO_3 as shown in Fig. 3a and subsequent conversion to weight percentage yield similar values, 6.6% for the inner core and 7.3% for the outer shell. The values of the key parameters calibrated as such are: $U_m = 9 \times 10^{-6}$ kmol/(m^3s), $\tau_m = 7.38 \times 10^5$ s, $D = 1.2 \times 10^{-9}$ m^2/s , $K_m = 0.01$ kmol/(m^3).

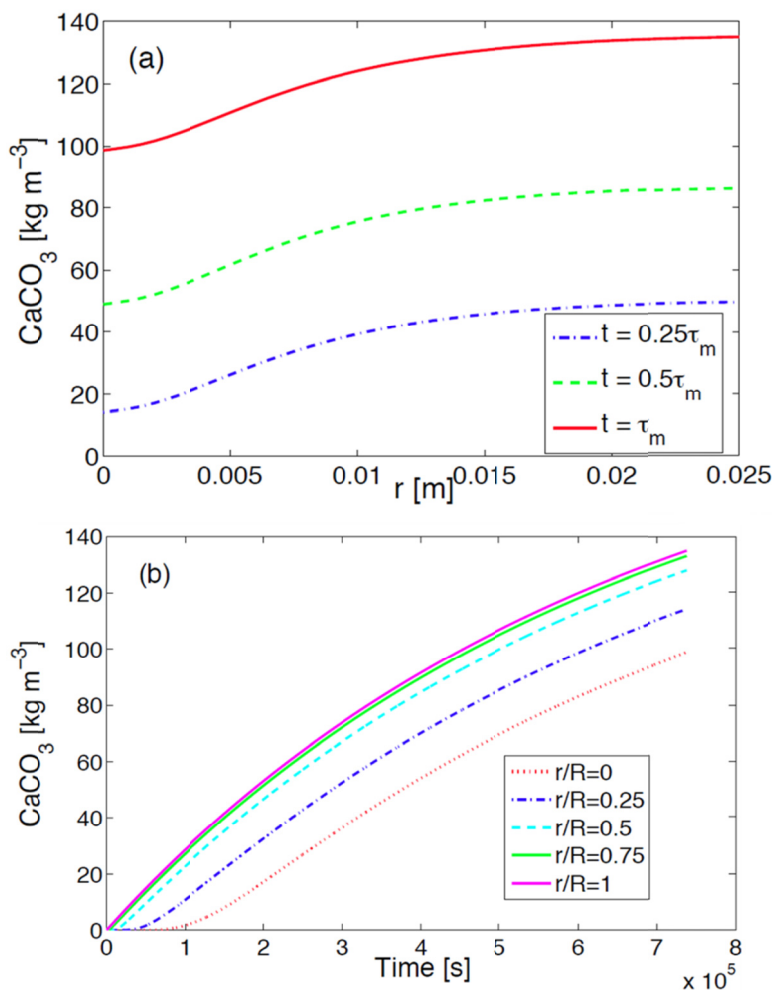


FIG. 4: (a) Radial distribution of CaCO_3 at different times; (b) evolution of CaCO_3 at different radial locations at $t = \tau_m$.

It can be seen from Fig. 4 that the spatial differences of CaCO_3 content in the specimen are quite modest in the presented simulation. As shown in Fig. 4b, calcite precipitation at the inner part of the specimen occurs after a certain period of time when supplied cementation media arrive as a result of diffusion. Fig. 5 shows the porosity

(initial $\theta=0.35$) and permeability (initial $k = 2.255 \times 10^{-11} \text{ m}^2$) evolution. Because the porosity change is directly related to the calcite precipitation, the shape of the curve resembles that of CaCO_3 content distribution. It should be noted that Fig. 5b presents the permeability in log scale, but overall the trend of each curve is still remarkably similar to Fig. 5a.

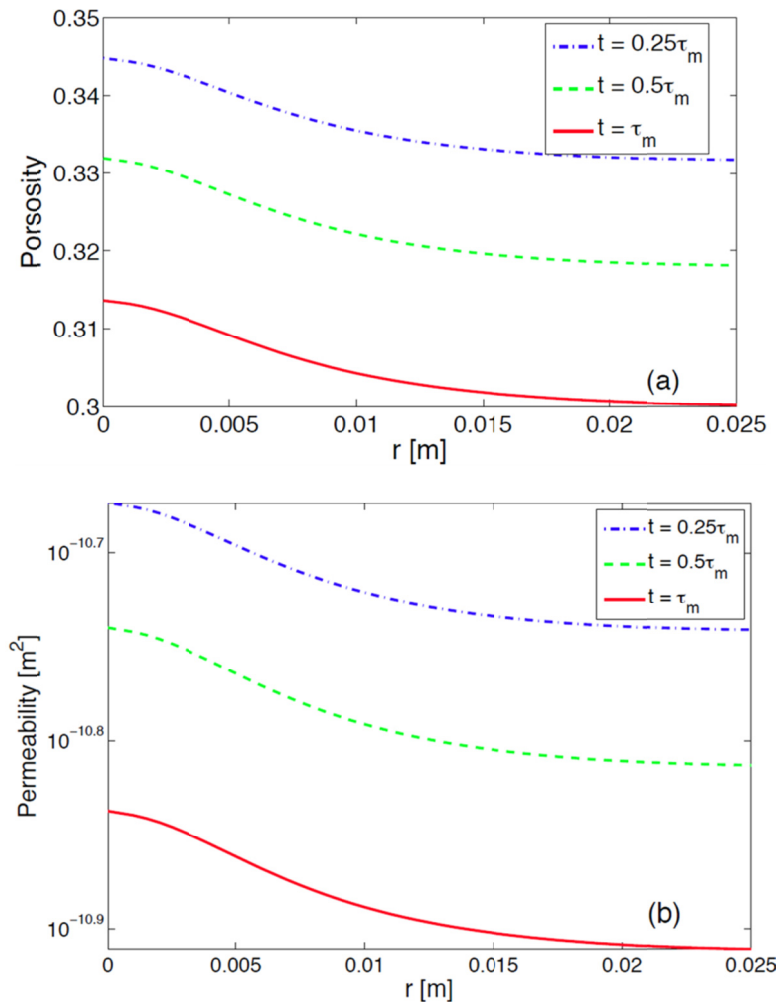


FIG. 5: (a) Radial distribution of porosity at different times; (b) radial distribution of permeability at different times.

The presented simulations provide an excellent opportunity for a parametric study to examine the roles of different mechanisms involved. It can also be extended to MICP soils prepared in injection based methods by taking into account the flow velocity and the dispersion process. In the present numerical investigation, faster reaction rate (U_m) and/or slower diffusion (D) were found to lead to higher gradient, i.e., greater non-uniformity of calcite across a specimen. The presented results are based on the experimental results previously reported on specimens prepared with FCFM in the same way. The simulation results indicate that modest uniformity is possible as observed in the experiments and may be addressed by conventional reactive transport modelling. However, it is very difficult to replicate the precise scenario as in the

laboratory experiments since boundary conditions may vary and soil heterogeneity may also play a role. Further investigation would benefit from experimental characterization of the spatial distribution of the calcite precipitation process, such as employing X-ray CT scanning and imaging analysis. X-ray CT images presented in the preceding section indicate certain differences in the amount of precipitated calcite that can be quantified to assist in assessment and numerical simulation of experimental measurements.

CONCLUSIONS

This paper presents some of the preliminary results of X-ray CT exploration of the MICP treated sandy soils. Better characterization of calcite precipitation may be achieved with properly selected specimen sizes. However, due to the practical difficulties in handling, especially removing from the mold a small specimen of limited strength (despite being improved by bio-treatment), a focus of this ongoing research is to seek a balance between the use of appropriate specimen size with proper X-ray resolution and the ability to prepare and handle suitable soil specimens of desirable improved properties.

Use of X-ray tomography gives rise to an opportunity to assess the distribution and evolution of calcite precipitation in the context of modelling of the relevant transport process. The presented conventional macroscopic reaction transport modelling attempts to mimic the scenario of a diffusion-dominant MICP process in a full contact flexible mold. Calibrated against the experimental results of the overall or average calcite precipitation in certain regions of the specimen, the simulations support the observation of modest uniformity of calcite distribution in FCFM-prepared specimens. Ongoing research includes the image analysis of X-ray scans for further characterization for numerical evaluation. However, as hydro-bio-chemo-mechanical processes are inherently interrelated and these interactions often occur across multiple scales, macroscopic simulations must be complemented with micro-scale and meso-scale investigations to gain improved understanding of MICP.

ACKNOWLEDGEMENTS

The X-ray tomography work presented in this study was supported by the U.S. National Science Foundation Award #1429252.

REFERENCES

- Al Qabany, A., Soga, K. and Santamarina, C. (2012). "Factors affecting efficiency of microbially induced calcite precipitation." *Journal of Geotechnical and Geoenvironmental Engineering*, 138(8): 992-1001.
- Barkouki, T. H., Martinez, B. C., Mortensen, B. M., Weathers, T. S., DeJong, J. T., Spycher, N. F., Ginn, T. R., Smith, R. W. and Fujita, Y. (2011). "Forward and inverse bio-geochemical modeling of microbially induced calcite precipitation in half-meter column experiments." *Transport in Porous Media*, 90(1): 23-39.

- Chou, C., Seagren, E. A., Aydilek, A. H., and Lai M. (2011). "Biocalcification of Sand through Ureolysis," *Journal of Geotechnical and Geoenvironmental Engineering*, 137(12): 1179-1189.
- DeJong, J. T., Fritzes, M. B. and Nusslein, K. (2006). "Microbially induced cementation to control sand response to undrained shear." *Journal of Geotechnical and Geoenvironmental Engineering*, 132(11): 1381-1392.
- DeJong, J. T., Mortensen, B. M., Martinez, B. C. and Nelson, D. C. (2010). "Bio-mediated soil improvement." *Ecological Engineering*, 36(2): 197-210.
- Fauriel, S. and Laloui, L. (2012). "A bio-chemo-hydro-mechanical model for microbially induced calcite precipitation in soils." *Computers and Geotechnics*, 46: 104-120.
- Martinez, B. C., DeJong, J. T., Mortensen, B. M., Barkouki, T. H., Ginn, T. R., Hunt, C., Tanyu, B. and Major, D. (2013). "Experimental optimization of microbial induced carbonate precipitation." *Journal of Geotechnical and Geoenvironmental Engineering*, 139(4): 587-598.
- Montoya, B. M., DeJong, J. T., and Boulanger, R. W. (2013). "Seismic response of liquefiable sand improved by microbial induced calcite precipitation." *Geotechnique*, 63(4): 302-313.
- van Paassen, L. A., Daza, C. M., Staal, M., Sorokin, D. Y., van der Zonb, W., and van Loosdrecht, M. C. (2010). "Potential Soil Reinforcement by Biological Denitrification," *Ecological Engineering*, 36(2): 168-175.
- van Wijngaarden, W. K., Vermolen, F. J., van Meurs, G. A. M. and Vuik, C. (2011). "Modelling biogROUT: A new ground improvement method based on microbial-induced carbonate precipitation." *Transport in Porous Media*, 87(2): 397-420.
- Whiffin, V. S., van Paassen, L. A. and Harkes, M. P. (2007). "Microbial carbonate precipitation as a soil improvement technique." *Geomicrobiology Journal*, 24 (5): 417-423.
- Zhao, Q., Li, L., Li, M., Zhang, H., and Amini, F. (2014a). "A Full Contact Flexible Mold for Preparing Samples Based on Microbial-Induced Calcite Precipitation Technology," *Geotechnical Testing Journal*, 37(5): 917-921.
- Zhao, Q., Li, L., Li, C., Li, M., Amini, F., and Zhang, H. (2014b). "Factors Effecting Improvement of Engineering Properties of MICP-treated Soil Catalyzed by Bacteria and Urease." *Journal of Materials in Civil Engineering*, 26(12): 04014094.

Factors Affecting the Improvement of Sand Properties Treated with Microbially-Induced Calcite Precipitation

G. G. N. N. Amarakoon¹ and S. Kawasaki²

¹Doctoral Student, Graduate School of Engineering, Hokkaido Univ., Kita 13, Nishi 8, Kita-ku, Sapporo, Hokkaido 060-8628, Japan.

²Professor, Faculty of Engineering, Hokkaido Univ., Kita 13, Nishi 8, Kita-ku, Sapporo, Hokkaido 060-8628, Japan.

Abstract: Bio-mineralization is an environment-friendly technology to improve soil engineering properties. One of common bio-mineralization processes is microbially induced calcite precipitation (MICP). A series of laboratory tests was conducted to produce solidification of the specimen having an estimated unconfined compressive strength (UCS) of more than several MPa, and investigate the influence of varies factors on soil properties treated with MICP. A solidification test was conducted using a syringe (30 mL) on different particle size of Mikawa sand (mean diameter: 0.6mm) and Toyoura sand (mean diameter: 0.2mm) using local ureolytic bacteria: *Parahadobactor* sp. isolated in Japan. The bacteria were grown up for 72 hours to increase the optical density (OD) of 600 nm (OD₆₀₀). The cementation media was added and the solidification test was conducted until 14 days. After that, needle penetration tests were conducted to obtain the estimated UCS value of the specimen. The results indicated that the estimated UCS value was exceeded 3 MPa for three Mikawa sand samples: (1) sample treated by 1.0g of bacteria re-injected bacterial solution after 7 days, (2) sample treated by 1.0g of bacteria without re-injection after 7 days, and (3) sample treated with 0.1g of bacteria with re-injection.

INTRODUCTION

Present soil improvement applications comprise soil replacement, preloading for consolidation, chemical admixture, and grouting stabilization. These techniques are time-consuming, expensive, and in the case of grouting and admixture stabilization are environmentally harmful (DeJong et al. 2010). In addition, coastal erosion is a significant problem throughout the world.

Breakwater construction is a method for prevention coastal erosion. Production of cement, which is a major construction material for breakwater construction, is energy

consuming and environmentally un-friendly. During the process of cement production, it releases large amount of CO₂. In addition, the process is time consuming. Therefore, additional studies into discovery alternative techniques for soil improvement are vital to achieve optimum performance, economic viability, and environmental sustainability.

Biom mineralization is a promising and environmentally innocuous technology to improve soil engineering properties. It naturally happens and is induced by nonpathogenic organisms that are native to the soil environment (DeJong et al. 2006). One common biom mineralization process is microbial induced calcite precipitation (MICP), which can bond sand grains together and improve the engineering properties of sand.

Improvement of soil mechanical properties by MICP is currently of particular interest to engineers and microbiologists, and has been demonstrated by several researchers at varying scales (DeJong et al. 2006; Whiffin et al. 2007; van Paassen et al. 2010). The technique can alter soil characteristics to increase shear strength and stiffness, while maintaining adequate permeability (Burbank et al. 2011). The technique involves introducing aerobically cultivated bacteria with highly active urease enzyme into soil, harnessing the urease enzyme to catalyze the hydrolysis of urea to produce ammonium and carbonate ions. The chemical reaction involved in this process is shown as follows (Eq. (1)):



In the presence of an introduced calcium source, often calcium chloride (CaCl₂), the calcium carbonate (CaCO₃, calcite) forms throughout the soil matrix based on the following chemical reaction (Eq. (2)):



The produced microbially induced CaCO₃ precipitates bridge adjacent soil particles by cementing the soil grains together to form cemented sand illustrative of calcareous rock (DeJong et al. 2006).

The engineering properties of MICP-treated soil may vary because MICP is a complex biochemical process, which can be effected by many factors. The MICP contains two key steps, as above equations. The urea hydrolysis is mainly dependent on the concentration of ureolytic bacteria and the available substrate (e.g., urea), whereas calcite precipitation relates to available Ca²⁺ (Mortensen et al. 2011). In accordance with the growth of nutrient concentration and incubation time, the CaCO₃ content increases. The particle size also has effect on MICP bonded soil. The efficiency of MICP is related to the permeability of the soil being sufficient to allow chemicals to flow to the bacteria and also the cement effect of CaCO₃ precipitation away particles (Mitchell and Santamarina 2005; Rebata-Landa 2007). Rebata Landa (2007) showed a relation between grain size and CaCO₃ content, and maximum carbonate deposition observed on grains was approximately 100 μm in size. Qabany et al. (2012) also found well-graded and coarser sands had a higher rate of precipitation than finer and poorly graded soils.

In this paper, we conducted a solidification test on silica sand using the ureolytic bacteria isolated from the soil near beachrock in Sumuide, Nago, Okinawa, Japan. The goal of this paper is to produce solidification of the specimen having an estimated unconfined compressive strength (UCS) of more than several MPa for soil improvement and preservation of coastal erosion and/or healing of coastal concrete structures, and investigate the influence of various factors on engineering properties of treated soil catalyzed by ureolytic bacteria.

A series of laboratory experiments was conducted to identify parameters which were affected for solidification of sample. Syringe solidification method was used for solidify sample. Needle penetration test was conducted to obtain estimated UCS value and measured pH and Ca^{2+} concentration of the outlet solution.

MATERIALS AND METHODS

Sands

Physical properties of Mikawa sand and Toyoura sand which were used in the experiments are shown in Table 1.

Table 1. Physical properties of Mikawa sand and Toyoura sand

Sand Type	Mikawa Sand	Toyouura Sand
soil particle density (ρ_s)	2.66 g/cm ³	2.64 g/cm ³
minimum density (ρ_{\min})	1.256 g/cm ³	1.335 g/cm ³
maximum density (ρ_{\max})	1.476 g/cm ³	1.645 g/cm ³
mean diameter (D_{50})	600 μm	200 μm

Bacteria

The microorganism used was *Pararhodobacter* sp., an ureolytic bacterium isolated from the soil near beachrock in Okinawa, Japan (Danjo, T. and Kawasaki, S. 2013) (Fig.1). The bacteria was cultivated in ammonium-yeast extract media (NH₄-YE) (growth media; ATCC 1376), which contained the following per liter of deionized water: (1) 0.13 M tris buffer (pH = 9.0), (2) 10 g (NH₄)₂SO₄, and (3) 20 g yeast extract. After incubating aerobically at 30°C in a shaker at 160 rpm (revolutions/ min) for 72 hours, the bacteria and growth media were centrifuged at 5000 rpm for 10 min. Then supernatant was removed and shake condense bacterial media before inject to the sample.

Cementation Media

Cementation media was used to provide chemical compositions for ureolysis, including urea, $\text{CaCl}_2 \cdot 2\text{H}_2\text{O}$, NH_4Cl , NaHCO_3 , and nutrient broth (Mortensen et al. 2011). Table 2 shows the chemical compositions of cementation media for bacteria experiments.

Table 2. Chemical compositions for cementation media

Chemical	Chemical Concentration (g/L) – 0.5M Ca
Nutrient Broth (g)	3
NH_4Cl (g)	10
NaHCO_3 (g)	2.12
$(\text{NH}_4)_2\text{CO}$ (g)	30.03
CaCl_2 (g)	55.49

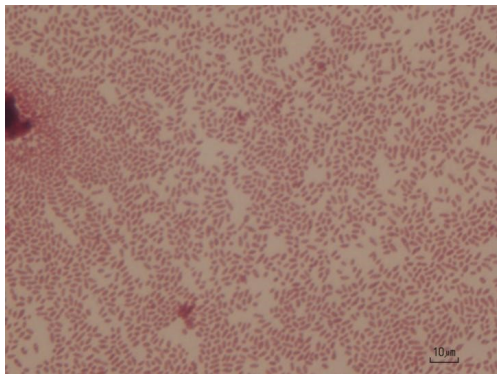


FIG. 1. Grain stain of *Pararhodobacter.sp*



FIG. 2. Syringe solidification test

Experimental Method

Syringe Solidification Test

First, 0.1g of bacterium *Pararhodobacter sp.* was shaken in with 100 mL $\text{NH}_4\text{-YE}$ medium for 3 days at 30 C. The bacteria and growth media were centrifuged at 5000 rpm for 10 min. Then, 45 g of Mikawa sand dried at 110°C for more than 2 days, was placed in a 35 mL syringe. Subsequently, 16 mL of a culture medium solution ($\text{NH}_4\text{-YE}$ solution) and 20 mL of the cementation media for consolidation (the compositions are shown in Table 1) were injected into the syringe and drained off leaving about 2 mL of solution above the top surface of the sand. This solution for consolidation was then injected and drained once a day or once every two days and the curing period was 14 days. Ca^{2+} concentration and pH value of outlet solution were measured. The syringe solidification test is shown in Fig. 2.

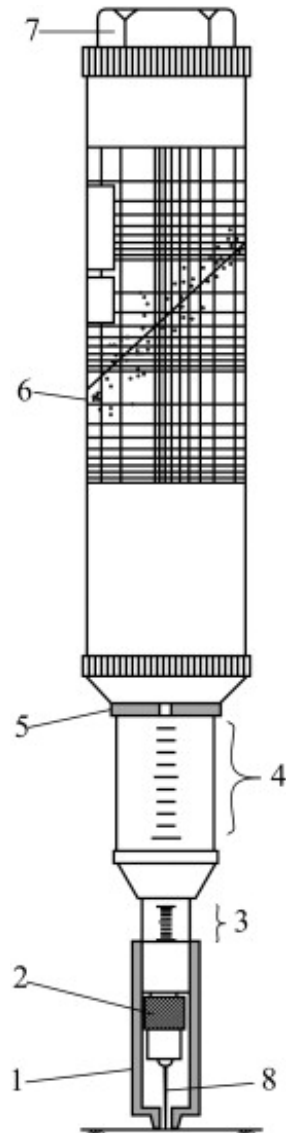
Needle Penetration Test

FIG. 3. Needle Penetrometer manufactured by Maruto Co. Ltd. (2006) and its parts: 1. presser, 2. chuck, 3. penetration scale, 4. load scale, 5. load indicating ring, 6. UCS–NPR correlation chart, 7. removable cap, and 8. penetration needle

After 14 days of curing, the needle penetration inclination (N_p) values of each sample were measured using needle penetration device (SH-70, Maruto Testing Machine Company, Tokyo, Japan) and the UCS was estimated from N_p value. The NP device consists of eight parts as shown and described in Fig. 3. Before testing, the surface, on which the test would be carried out, should be clean and smooth. The test doesn't require a specially prepared specimen. The NP can be used in any direction both in the field and laboratory. Then by holding rather tightly the removable cap and the main body, the load is perpendicularly and slowly applied to rock surface. If the test is carried

out in laboratory, the specimen should be fixed to prevent its movement during penetration. For weak and saturated rocks, the needle may be penetrated to a maximum depth of 10 mm. When this depth is reached, no more penetration could be applied and the needle is slowly pulled out. Where the rock is hard and the penetration force has come up to 100 N before the needle penetrates for 10 mm, the needle is withdrawn. After the test is completed, the needle is slowly pulled out and the penetration load and penetration depth are read from the load scale (Fig. 3, part 4) and the position of the presser on the penetration scale (Fig. 3, part 3), respectively. The strength of the sample (NPR value) was calculated from the following equation (Eq. (3)).

$$\text{NPR} = F/D \quad (3)$$

where F is the penetration load (N) and D is the depth of penetration (mm). The unit of NPR is N/mm. From the chart of UCS-NPR correlation, estimated UCS value was observed.

Experimental Conditions

To consider the effect of conditions on the UCS of a specimen, the bacterial population, reinjection of bacteria, curing temperature, particle size of the sand and viscosity were changed (as shown in Table 3).

In Case 1-3, we investigated the effect of bacterial population, Case 1, 4, 3, 5 for identify the effect of re-injection of bacteria, Case 1 and 6, we investigated the effect of particle size and Case 7 and 8 were carried for get the idea about how to effect viscosity of the culture solution for the solidification.

Table 3. Chemical compositions for cementation media

Case No.	Temp. (°C)	Population of Bacteria (g)	Shaking Time (days)	Re-injection of Bacteria (After 7 days)	Sand material with Particle Size (mm)
1	30	0.1 with centrifuge	3		Mikawa-0.6
2	30	0.3 with centrifuge	3		Mikawa-0.6
3	30	1.0 with centrifuge	3		Mikawa-0.6
4	30	0.1 with centrifuge	3	x	Mikawa-0.6
5	30	1.0 with centrifuge	3	x	Mikawa-0.6
6	30	0.1 with centrifuge	3		Toyoura-0.2
7	30	1.0 with centrifuge	3		Toyoura-0.2
8	30	1.0 without centrifuge	3		Toyoura-0.2

RESULTS AND DISCUSSION

Effect of Bacterial Population

The Fig. 4 (a) shows that the strength of the sample was increased with the increase of population of bacteria. This finding indicates that bacteria plays a key role on MICP, i.e., (1) producing enzyme to hydrolyze urea, and (2) acting as nucleation sites for formation of calcium carbonate crystals (mainly calcite; Fujita et al. 2000). More bacteria in the solution can promote more enzymes and provides more nucleation sites for the MICP.

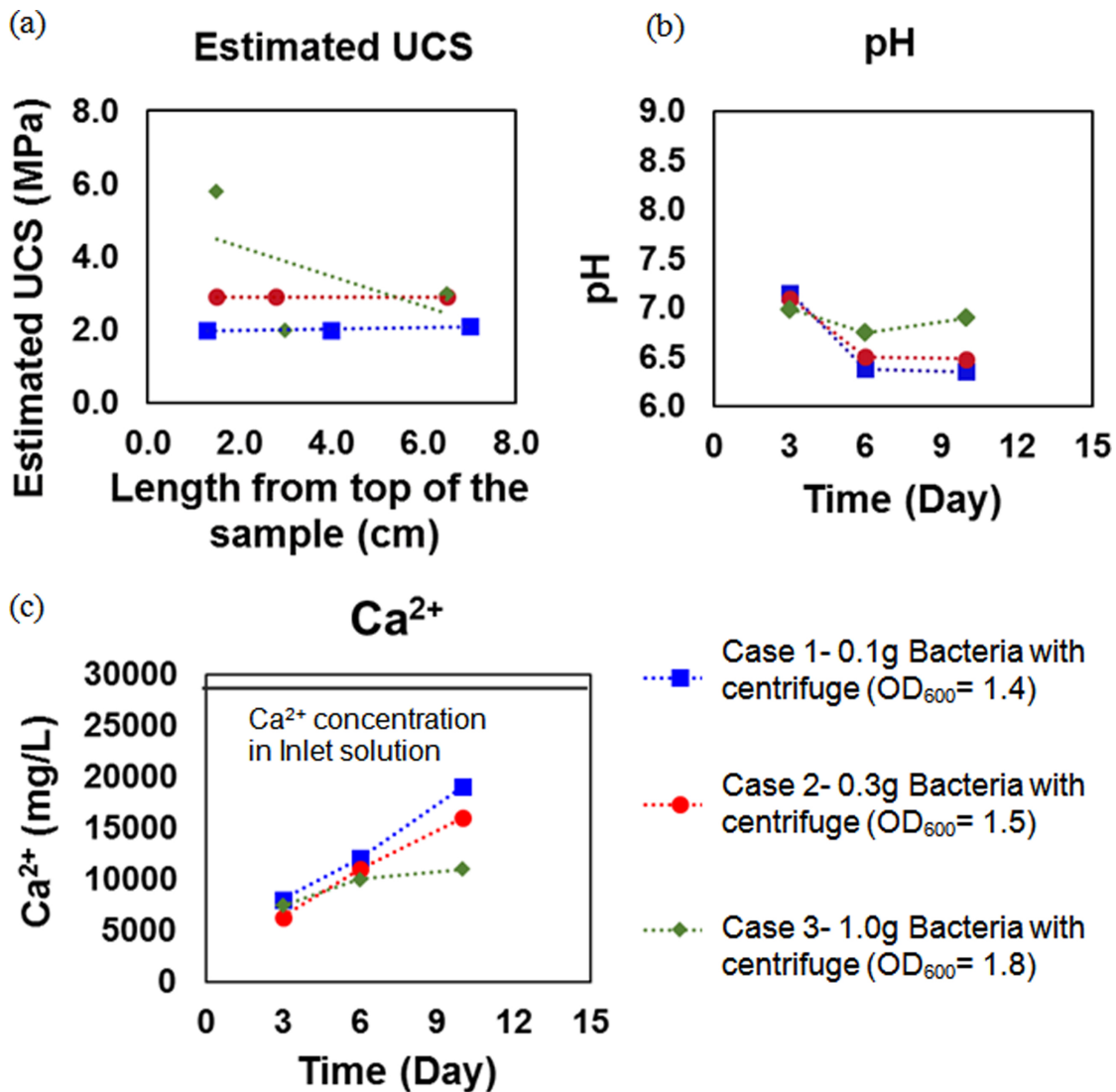


FIG. 4. Results of MICP-treated sample catalyzed by *Pararhodonactor.sp* under different bacteria concentrations: (a) Estimated UCS value with the depth of the sample, (b) pH with time and (c) Ca²⁺ concentration with time

The pH value in outlet solution was larger in high bacterial concentration sample than low bacterial concentration sample. Although, pH value was decreased with the time for all cases. The results of Ca^{2+} concentration in outlet solution were opposite to the results of pH value (Fig. 4(b) and 4 (c)).

Effect of Re-injection of Bacteria

Fig. 5 shows the results of Case 1, Case 3, Case 4 and Case 5. Here, we considered about re-injection of bacterial solution after 7 days and without re-injection. From the Fig. 5 (a) shows that the UCS value was larger when we re-injected after 7 days than without re-injection of bacterial solution.

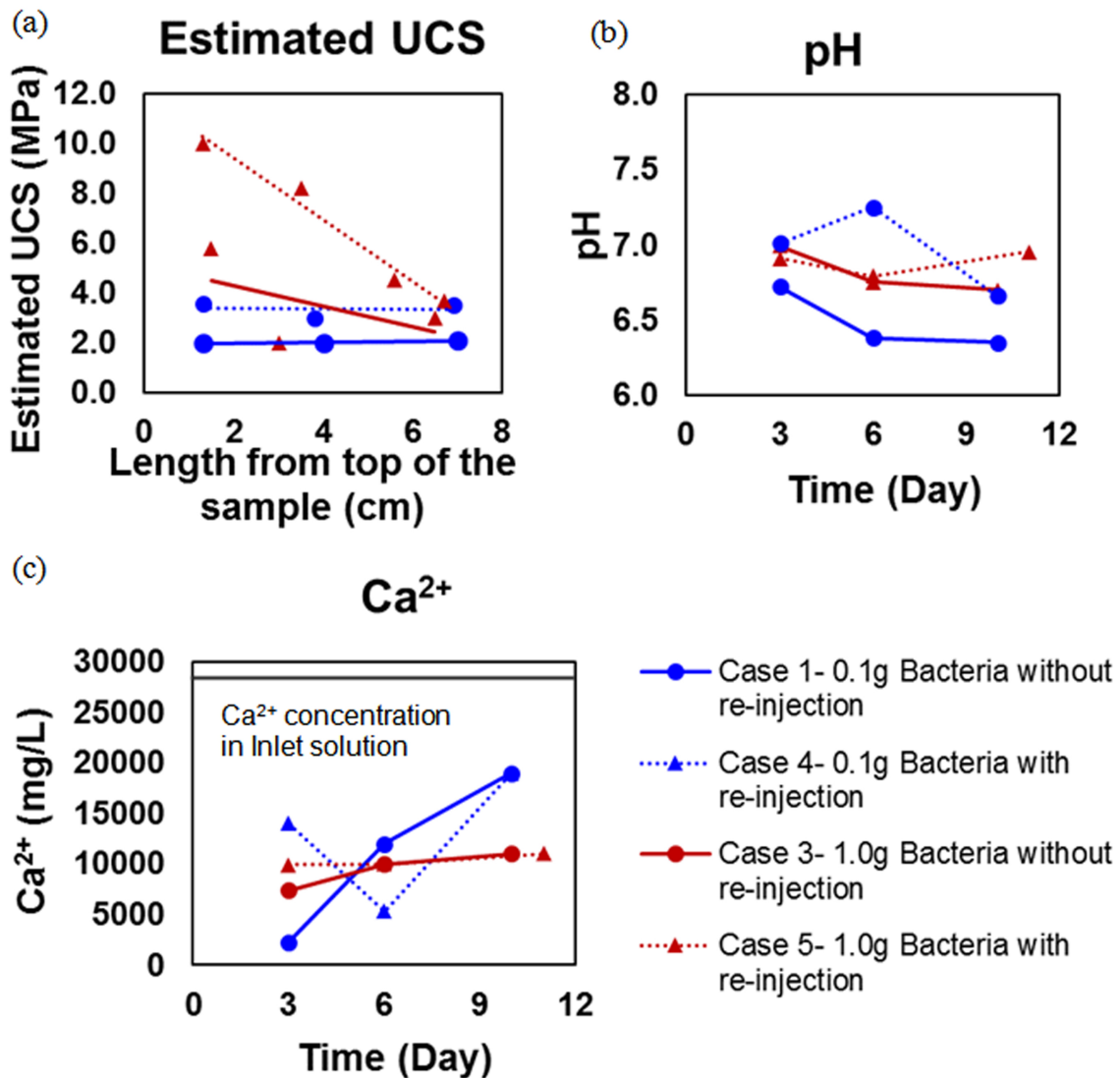


FIG. 5. Results of MICP-treated sample catalyzed by *Pararhodonactor.sp* under different injection method of bacteria: (a) Estimated UCS value with the depth of the sample, (b) pH with time and (c) Ca^{2+} concentration with time

According to Fig. 5 (b), pH value was decreased with the time without re-injection method (Case1 and 3). In case 4 and 5, the pH value was decreased until 7 days and after re-injection, pH value intended to increase and it was fluctuated around 7. The bacterial effect can optimize when pH value is maintain around 7. Because, the optimal growth for *Pararhadobacter.sp* is at 30-40 °C and pH 7.0-8.5 (Foesel B. U. et al. 2011). Ca^{2+} concentration was intended to increase with the time without added bacteria after 7 days. Moreover, Ca^{2+} concentration was decreased when re-injection of bacteria. That means, solidification process was speed up when we re-injection of bacterial solution after 7 days of curing period.

Effect of Particle Size

Two different type of silica sand with two type of particle size were used MICP-treated soil catalyzed by *Pararhadobacter.sp*. Fig. 6(a) and 6(b) show that the solidified samples after catalyzed by *Pararhadobacter.sp* for Mikawa sand specimen and Toyoura sand specimen.

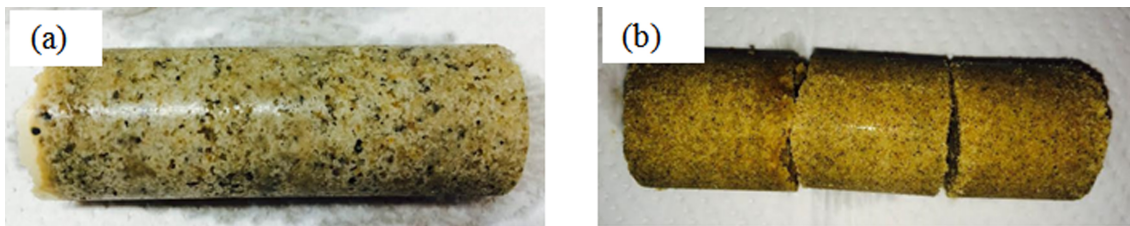


FIG. 6. (a) Solidified sample with Mikawa sand, (b) Solidified sample with Toyoura sand

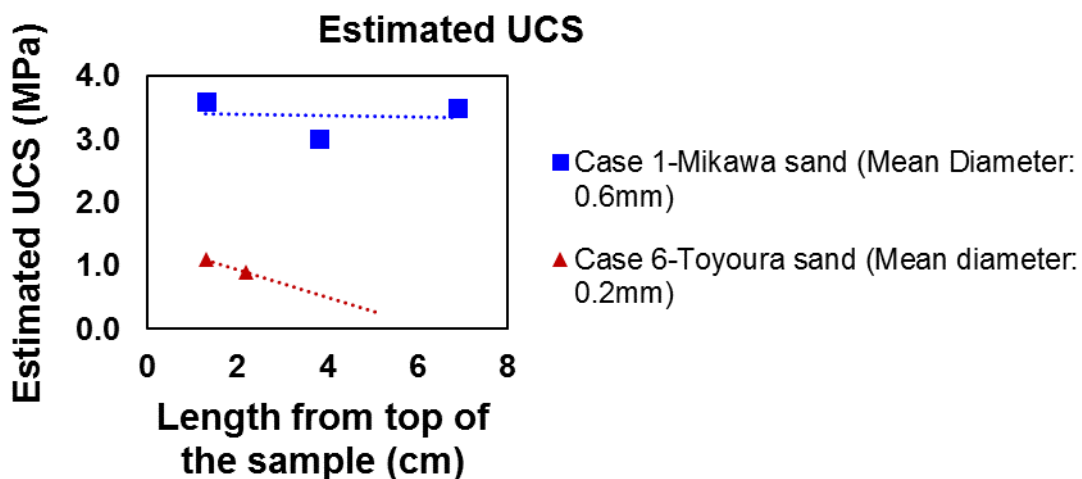


FIG. 7. Estimated UCS value of MICP-treated sample catalyzed by *Pararhadonactor.sp* under different particle size of sand samples

Fig. 7 shows the estimated UCS value at the top, middle and bottom of the sample. From the results, estimated UCS value was larger in Mikawa sand sample which has mean diameter 0.6mm than estimated UCS value in Toyoura sand sample with mean diameter 0.2mm. The reasons for less UCS value for Toyoura sand sample may happened clogging with particles.

Therefore, penetration though the sample can be restricted and effect of bacterial process can be decreased. When decrease the bacterial process, the hydrolysis process also getting slow. The results of that, CaCO_3 precipitation was decreased. Therefore, particle size of the sample was mainly effect for solidification of the sample.

Effect of Viscosity of Bacterial Culture Solution

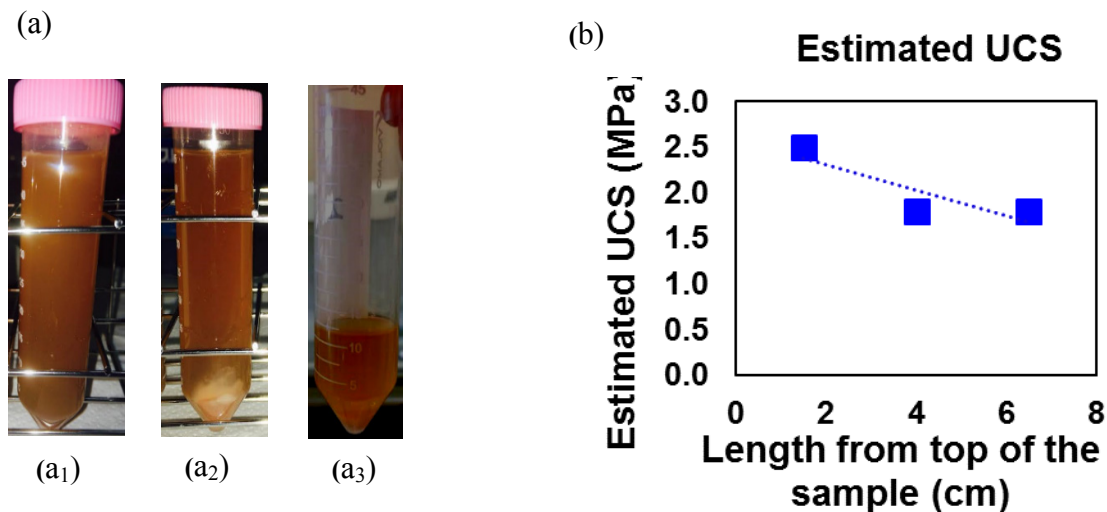


FIG. 8. (a) Bacterial solution: (a₁) before centrifuge, (a₂) after centrifuge, (a₃) condensed bacterial solution, (b) Results of Estimated UCS values for Case 8

In case 6, the test was conducted with 0.1 g of bacteria with centrifuge. The test was conducted until 14 days of curing period. After curing period, top and middle of the sample were solidified. However, the bottom part of the sample was not solidified.

Then, increased the bacterial population (1.0g) and proceeded centrifuge and condense solution with high viscosity was injected to the sand sample. However, the solution was not penetrated through the soil and not saturated. It was happened due to high viscosity of condense bacterial solution. Therefore, we could not conduct the syringe test in Case 7. Then Case 8 was conducted, 1.0 g of bacteria without centrifuge. Viscosity of this bacterial solution was less than the bacterial solution with centrifuge. Therefore, when added bacterial solution into the syringe, the solution was penetrated through the sand and saturated. After 7 days of curing period, completely solidified sand sample was obtained. The Results of estimated UCS value for Case 8 sample shows in Fig. 8(b).

Effect of Color of Test Samples

Fig. 9 shows that the color changes of the samples with the time. With the time, the sample color getting whitish color. It concluded that the CaCO_3 precipitation was happened with the time. Therefore, measure of color of the sample was a significant factor for solidification.

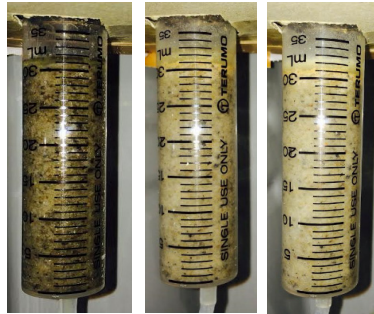


FIG. 9. Changes of color with the time for MICP-treated soil

CONCLUSIONS

Microbial induced calcite precipitation utilizing urea hydrolysis is a complex biochemical process, especially when it takes place between sand particles for improvement of soil engineering properties. There are many factors that may affect this process. Some of these factors reported in this paper included bacteria concentration, re-injection of bacteria, sand type and particle size of the sample, and viscosity of the bacterial solution.

The result of estimated UCS value show that all the studied factors have an obvious effect on the MICP treated sand. Case 3, Case 4 and Case 5 obtained the estimated UCS value more than 3 MPa: (1) Case 3-1.0g of bacteria with centrifuge but without re-injection of bacteria after 7 days, (2) Case 4- 0.1g of bacteria with centrifuge and with re-injection of bacteria after 7 days, and (3) Case 5- 1.0g of bacteria with centrifuge and with re-injection of bacteria. The estimated UCS value at top of the sample in Case 5 was 10 MPa.

Most studies on MICP soil improvement used cylindrical columns or syringes for sample preparation by pumping or injections methods. Although pumping or injections promoted cementation media penetration into soil pores under pressure to some extent, the effluent also reduces the number of bacteria as well as a portion of urease produced by bacteria, and the samples may not be uniform along the flow.

ACKNOWLEDGEMENTS

The work has been partly supported by a Grant-in-Aid for Scientific Research (No. 24300299) from the Japanese Ministry of Education, Sports, Science and Technology. This support is gratefully acknowledged.

REFERENCES

- Burbank, M.B., Weaver, T.J., Green, T.L., Williams, B.C., and Crawford, R.L. (2011). "Precipitation of calcite by indigenous microorganisms to strengthen liquefiable soils." *J. Geomicrobiology*, Vol. 28(4): 301–312.
- Danjo, T. and Kawasaki, S. (2013). "A study of the Formation mechanism of beach rock in Okinawa, Japan: Toward making Artificial Rock." *Int. J. GEOMATE*, Vol. 5 (1): 633-638.
- DeJong, J.T., Fritzges, M.B., and Nusslein, K. (2006). "Microbially induced cementation to control sand response to undrained shear." *J. Geotech. Geoenviron. Eng.*, Vol. 11(1381): 1381–1392.
- DeJong, J.T., Mortensen, B.M., Martinez, B.C., and Nelson, D.C. (2010). "Biomediated soil improvement." *Ecological Engineering*, Vol. 36(2): 197–210.
- Ehrlich, H. L. (2002). *Geomicrobiology*, Marcel Dekker, New York.
- Foesel, B.U., Darke, H.L., and Schramm, A. (2011). "Defluviimonas denitrificans gen. nov., sp. nov., and Pararhodobacter aggregans gen. nov., sp. nov., non-phototropic Rhodobacteraceae from the biofilter of a marine aquaculture." *J. Systematic and applied microbiology*, Vol. 34: 498-502.
- Fredrickson, J.K. and Fletcher, M. (2001). "Subsurface microbiology and biogeochemistry." Wiley-Liss, Hoboken, NJ.
- Fujita, Y., Ferris, E.G., Lawson, R.D., Colwell, F.S., and Smith, R.W. (2000). "Calcium carbonate precipitation by ureolytic subsurface bacteria." *J. Geomicrobiol.*, Vol. 17(4): 305–318.
- Mitchell, J.K. and Santamarina, C.J. (2005). "Biological considerations in geotechnical engineering." *J. Geotech. Geoenviron. Eng.*, Vol. 131(10): 1222–1233.
- Mortensen, B.M., Haber, M.J., DeJong, J.T., Caslake, L.F., and Nelson, D.C. (2011). "Effects of environmental factors on microbial induced calcium carbonate precipitation." *J. Appl. Microbiol.*, Vol. 111(2): 338–349.
- Qabany, A.A., Soga, K., and Santamarina, C. (2012). "Factors affecting efficiency of microbially induced calcite precipitation." *J. Geotech. Geoenviron. Eng.*, Vol. 138(8): 992–1001.
- Ramachandran, S.K., Ramakrishnan, V., and Bang, S.S. (2001). "Remediation of concrete using microorganisms." *J. ACI Mater.*, Vol. 98(1): 3–9.
- Rebata-Landa, V. (2007). "Microbial activity in sediments: Effects on soil behavior." Ph.D. thesis, Georgia Institute of Technology, Atlanta, GA.
- Van Paassen, L.A., Ghose, R., van der Linden, T.J.M., van der Star, W.R.L., and van Loosdrecht, M.C.M. (2010). "Quantifying biomediated ground improvement by ureolysis: large-scale biogrout experiment." *J. Geotech. Geoenviron. Eng.*, Vol. 136(12): 1721–1728.
- Whiffin, V.S., van Paassen, L.A., and Harkes, M.P. (2007). "Microbial carbonate precipitation as a soil improvement technique." *J. Geomicrobiol.*, Vol. 24(5): 417–423.

Particulate Simulations of Triaxial Tests on Bio-Cemented Sand Using a New Cementation Model

A. Khoubani¹; T. M. Evans, A.M.ASCE²; and B. M. Montoya, A.M.ASCE³

¹Research Assistant, School of Civil and Construction Engineering, Oregon State Univ., Corvallis, OR.

²Associate Professor, School of Civil and Construction Engineering, Oregon State Univ., Corvallis, OR. E-mail: matt.evans@oregonstate.edu

³Assistant Professor, Dept. of Civil, Construction, and Environmental Engineering, North Carolina State Univ., Raleigh, NC.

Abstract: Bio-cementation is a promising method for the natural improvement of potentially liquefiable soil deposits (e.g., loose saturated sands). In the improvement process a bacterium that can be found naturally in soil deposits is fed urea. The bacterium consumes and breaks down the urea to form ammonium and carbonate. In the presence of calcium, calcium carbonate will precipitate at particle contacts and act as a cementitious agent to solidify the deposit. Moreover, experimental tests show that bio-cemented sand exhibits more ductile behavior than chemically cemented sand. This is a desirable response from an engineering point of view, since brittle failure is often catastrophic and occurs without warning. The scope of this study is to investigate the response of bio-cemented sand using the discrete element method (DEM). This numerical method is capable of simulating behavior of granular materials based upon the basic particle-scale physics of the system of interest. A new cementation model is proposed that replicates the presence of cement between soil particles. This bond is able to capture the progressive contact dissolution between two soil particles and associated nonlinear response. Triaxial samples were built and the aforementioned bond was applied to the contact points within the assembly. Samples with and without cementation are sheared and their stress-strain responses compared in terms of soil strength and stiffness. The effects of several bonding parameters are investigated and the relative contributions of multiple physical mechanisms to system response are considered.

INTRODUCTION

Microbially-induced calcite precipitation (MICP) is a promising new method for *in-situ* cementation of loose sands. Experimental observations show that the static stiffness and shear strength of sand can be improved using MICP (Feng and Montoya, 2015; Montoya and DeJong, 2015). Moreover, MICP changes the contractive behavior of loose sand to dilative behavior upon shearing and therefore increases the liquefaction resistance of sand under dynamic loading (Montoya et al., 2013).

In addition to the physical experiments, numerical methods can be used to explain the observed behavior of bio-cemented specimens in the lab. In particular, discrete element method (DEM) simulations provide access to the microscale level information that is otherwise impossible or at least very difficult to obtain in the lab (e.g., interaction forces, bond breakage evolution, local void ratio evolution). Parallel bonds are a common approach used in DEM to effectively simulate the mechanical response of Portland cemented soils or rocks (Wang and Tonon, 2009; Evans and Ning, 2013; Ning and Evans, 2013; De Bono et al., 2014a, 2014b). However, parallel bonds fail to capture the behavior of bio-cemented sand (Evans et al. 2014; Feng et al., 2014). Bio-cemented sand tends to exhibit ductile behavior (Mortensen and DeJong, 2011; Feng and Montoya, 2015; Montoya and DeJong, 2015) while simulation of parallel bonded particles results in brittle response. Moreover, upon failure, each parallel bond disappears from the model, thus violating the requirement that mass be conserved.

Wang and Leung (2008a, 2008b) circumvented this problem in two dimensions by using separate particles for the cementation phase. A specific number of cement particles are generated in the void spaces depending on the cement content and are given random velocities until they come in contact with the sand particles. Cement particles are then attached to sand particles using parallel bonds. This model is also used to simulate Portland cemented sand with brittle behavior. In a new attempt, Evans et al. (2014) proposed a novel three-dimensional bonding model to address the aforementioned drawbacks of the parallel bond. In this model, two sand particles are connected by means of a ring of cement particles at their contact points. They showed that the progressive failure of a bond between two particles can be successfully modelled. Furthermore, after bond failure, cement particles are still present in the assembly and interact with the sand particles; this is consistent with forensic analysis of sheared physical specimens, which yield small amounts of silt-sized fines due to bond breakage (Tagliaferri et al., 2011).

The goal of the current work is to apply this bond model to an assembly of particles and study the macroscopic stress-strain behavior of the cemented specimen. The effects of varying model input parameters on specimen response are evaluated using a parametric study.

CEMENTATION MODEL

Evans et al. (2014) proposed a cementation model in which progressive failure of a bond at the contact point between two particles can be modeled. In this model two sand particles are connected through a ring that consists of several smaller cement particles (Figure 1). Cement particles are connected to each other and to the sand particles through contact bonds. A contact bond is defined by normal and shear strength. If the normal and shear forces at the sand-cement contact points exceed the corresponding strength, then the contact bond fails. The number of cement particles in a given bonding chain is an input parameter and is used (along with the radii of the sand particles in contact) to calculate the radius of the cement particles. Other input parameters of this model are the normal and shear stiffness, surface friction, and density for each of the sand and cement particles. The contact bond strength can also

be changed from one cement particle to another using a specific distribution (e.g., Weibull distribution). This model has the ability of capturing the progressive failure (ductile behavior) since sand-cement bonds do not necessarily fail at the same time. In this study the aforementioned contact model is applied to an assembly of particles and the behavior of the assembly at the macroscopic level is studied.

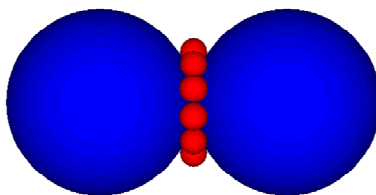


FIG. 1. Two sand particles bonded with a cement ring including 12 cement particles.

NUMERICAL SIMULATIONS

The implementation of the new model at the scale of a single particle-particle contact was demonstrated by Evans et al. (2014). Figure 2(a) compares numerical simulations for the system shown in Figure 1 to the analytical solution that may be developed based on a force balance when the system is subjected to tension or compression along its axis. If the same system now has bond strengths varying according to a Weibull distribution, failure becomes more complex, as shown in Figure 2(b).

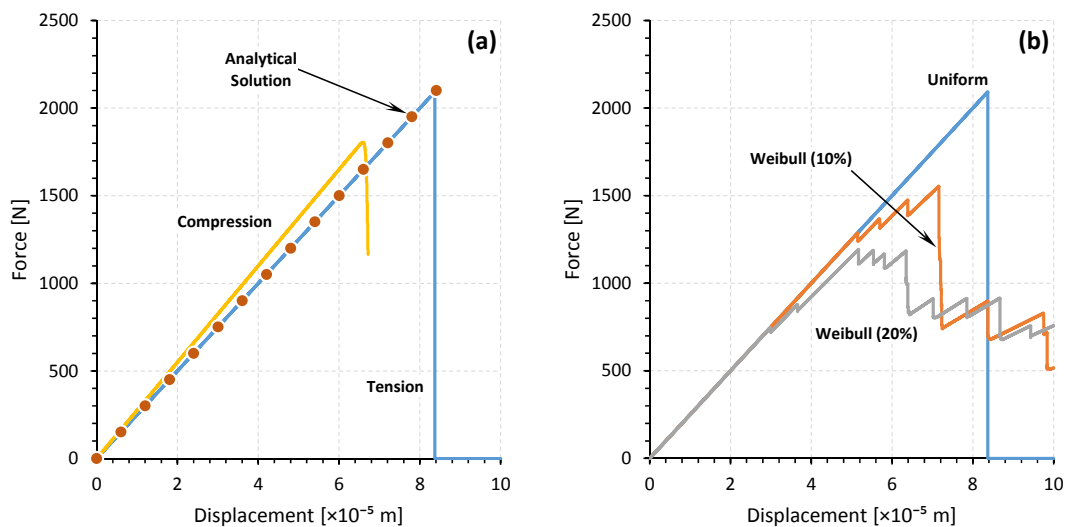


FIG. 2. Behavior of the two-particle system depicted in Figure 1: (a) uniaxial tension and compression behavior; and (b) effects of varying bond strengths. Note that all three curves have the same mean bond strength, 100 N, and that the number in parentheses is the coefficient of variation for the Weibull distributions (after Evans et al. 2014).

The behavior of the new contact bond model applied to an assembly of particles was assessed by generating approximately 2500 particles within a cube bounded by six walls (i.e., hydrostatic boundaries). These walls are used within a servo-mechanism process to bring the assembly to different states of stress. The specimen was first consolidated to a confining stress of 300 kPa by controlling wall displacement in all directions. The specimen's as-consolidated void ratio was 0.67, corresponding to a loose sample. Cementation was then applied randomly to a specific percentage of contact points among sand particles (Figure 3). The total number of particles for a 50% cementation was 53000. The sample was sheared by applying a constant rate of vertical displacement to the top and bottom walls while maintaining the lateral stresses by servo-adjusting the velocity of the lateral walls.

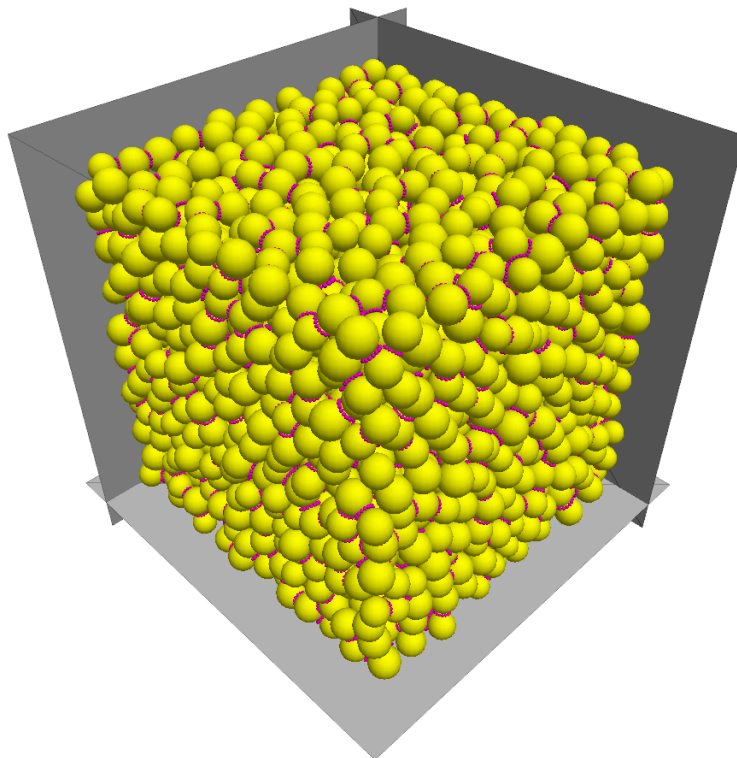
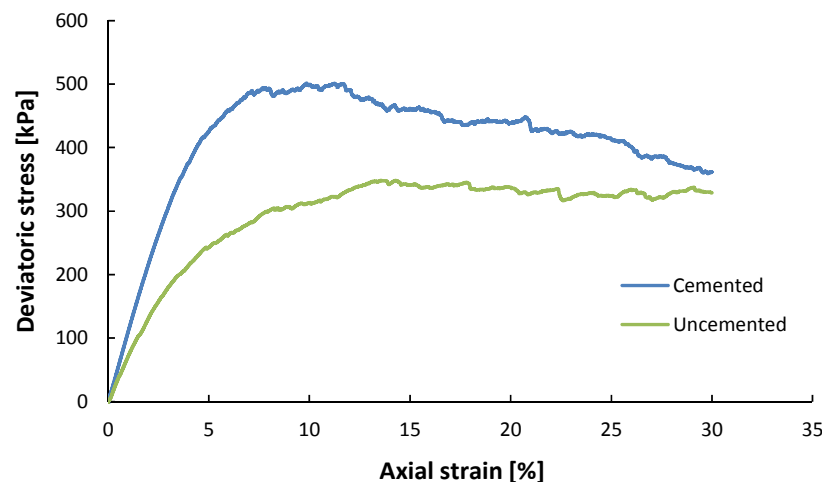


FIG. 3. A cemented assembly of particles (cement chains are installed at a random selection of 50% of sand-sand contact points).

Material properties for the specimen are shown in Table 1. Contact bond strength for the sand-cement contacts was defined as two times larger than that of the cement-cement contacts since physical experiments and surface energy measurements have shown that failure first occurs in the cement phase (Montoya and Feng, 2015). The stress-strain response of the uncemented and cemented assemblies is presented in Figure 4. Stiffness of the cemented assembly is increased considerably. Assembly behavior also changes from loose to dense type behavior (i.e., a well-defined peak stress). Deviatoric stress increases to a maximum value and then decreases. However, this decrease is not as sharp as that typically observed in parallel-bonded models, illustrating the new model's ability to effectively capture post-peak ductility. At high values of strain, when the majority of the cement chains are broken, both uncemented and cemented samples reach the same strength.

Table 1. Properties of sand and cement particles.

Parameter	Value
Sand	
Diameter, d_s	0.20 – 0.25 m
Density, ρ_s	2650 kg/m ³
Normal stiffness, k_{ns}	9×10 ⁶ N/m
Shear stiffness, k_{ss}	6×10 ⁶ N/m
Surface friction, μ_s	30°
Cement	
Diameter, d_c	0.009 – 0.015 m
Density, ρ_c	3150 kg/m ³
Normal stiffness, k_{nc}	9×10 ⁶ N/m
Shear stiffness, k_{sc}	6×10 ⁶ N/m
Surface friction, μ_c	30°
Number of particles in cement chain	15
Contact bond	
Sand-cement normal strength, $(f_n)_{s-c}$	10 ⁴ N
Sand-cement shear strength, $(f_s)_{s-c}$	10 ⁴ N
Cement-cement normal strength, $(f_n)_{c-c}$	5×10 ³ N
Cement-cement shear strength, $(f_n)_{c-c}$	5×10 ³ N
Percentage of bonded contact points	25%

**Figure 4. Effect of cementation on stress-strain response.**

PARAMETRIC STUDY

A series of parametric simulations was performed to assess the effects of changing cement properties on system macroscopic response. The fraction of cemented contacts, bond strengths, particle friction coefficients, and particle stiffnesses were all varied. The baseline parameters are shown in Table 1 (results are in Figure 4) and the

list of all of the different simulations that were performed in this parametric study is presented in Table 2. For each simulation one parameter was changed while the other parameters were kept constant.

Table 2. Parametric study simulations.

Simulation ID	% of bonded contacts	$(f_n)_{s-c}, (f_s)_{s-c}$ (N)	k_n, k_s (N/m)	μ ($^\circ$)	$(f_{n,s})_{s-c}/(f_{n,s})_{c-c}$
1	0	10^4	$9 \times 10^6, 6 \times 10^6$	30	2
2	25	10^4	$9 \times 10^6, 6 \times 10^6$	30	2
3	50	10^4	$9 \times 10^6, 6 \times 10^6$	30	2
4	25	2×10^4	$9 \times 10^6, 6 \times 10^6$	30	2
5	25	10^4	$4.5 \times 10^6, 3 \times 10^6$	30	2
6	25	10^4	$1.8 \times 10^7, 1.2 \times 10^7$	30	2
7	25	10^4	$9 \times 10^6, 6 \times 10^6$	20	2
8	25	10^4	$9 \times 10^6, 6 \times 10^6$	10	2
9	25	10^4	$9 \times 10^6, 6 \times 10^6$	30	1
10	25	10^4	$9 \times 10^6, 6 \times 10^6$	30	4

Figure 5 shows the effect of increasing the fraction of sand-sand contacts to which cementation is applied. Cementation was applied to a random selection of 25 and 50% of the sand-sand contacts. Figure 5 indicates that both the initial stiffness and ultimate shear strength of the assembly increases with an increase in the cementation percentage. Each of the two cemented specimens (Simulations 2 and 3) show post-peak response that is more ductile than it is brittle, which is a clear departure from simulations performed using parallel bonds. Nonetheless, cemented specimens still soften post-peak and at very high global strains (i.e., >25%) all four specimens reach the same final strength, indicating that cementation is no longer contributing to the shear resistance at high levels of deformation.

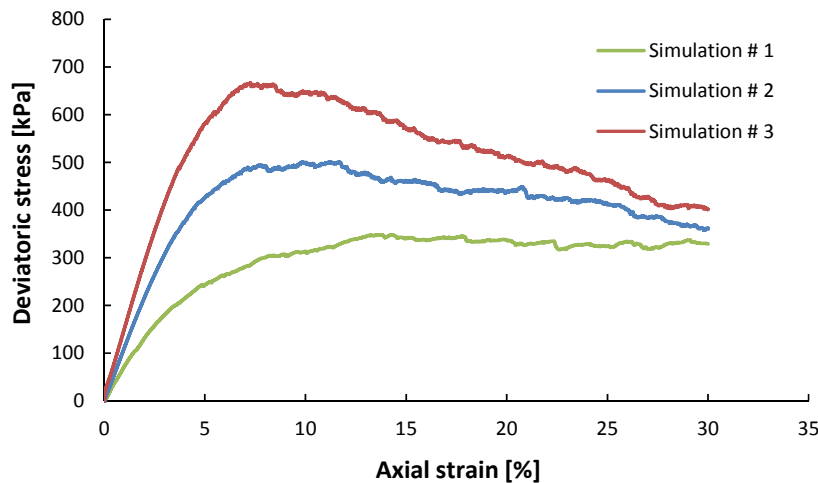


Figure 5. Effect of percentage of bonded contacts on stress-strain response.

The effects of contact bond normal and shear strength are illustrated in Figure 6. In Simulation 4, the normal and shear strength of the contact bonds is doubled compared to Simulation 2 (see Table 2). Clearly, the increase in the contact bond strength does not affect the initial stiffness but it increases the assembly's macroscale shear strength.

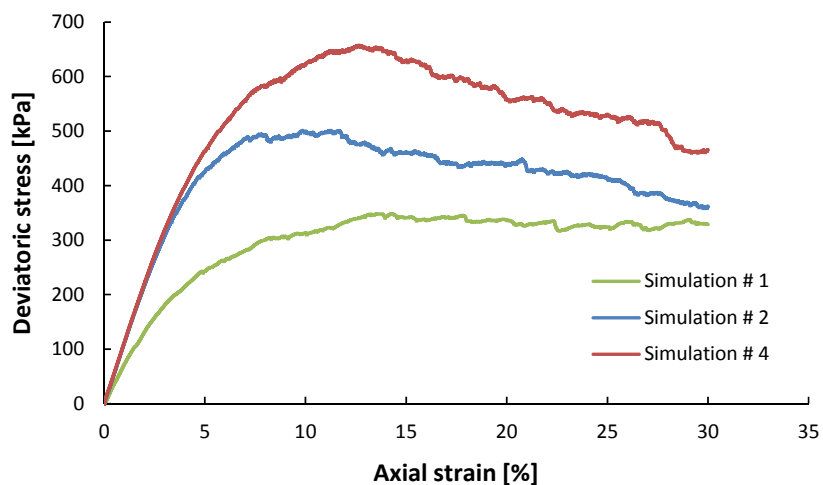


Figure 6. Effect of contact bond strength on stress-strain response.

Simulations 5 and 6 have lower and higher cement stiffness than the baseline (Table 1) values, respectively. According to Figure 7, increasing cement normal and shear stiffness has no effect on initial stiffness of the assembly. This is accompanied by a decrease in peak strength and a decrease in the strain at which peak shear strength occurs. This is intuitively satisfying because it is consistent with the idea that softer cement requires greater displacements to mobilize the force necessary for bond breakage.

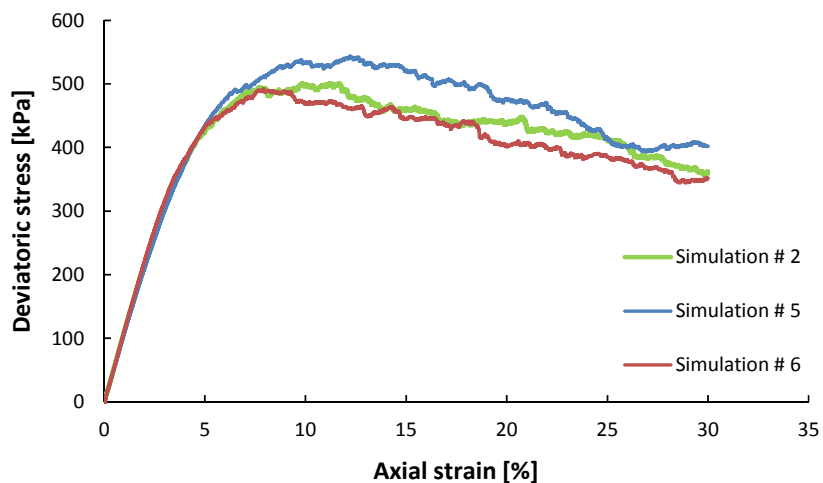


Figure 7. Effect of cement particles' stiffness on stress-strain response.

Increasing the cement particle surface friction does not change the initial stiffness of the assembly (Figure 8). Increase of surface friction from 10 to 20 degrees results in increase of peak strength but it is the same for 20 and 30 degrees. Finally, Figure 9 shows the effect of the ratio of sand-cement contact bond strength to cement-cement contact bond strength. A reduction of contact bond strength in cement chain reduces the peak strength of the assembly as cement chain rupture becomes more likely at intermediate and large strains.

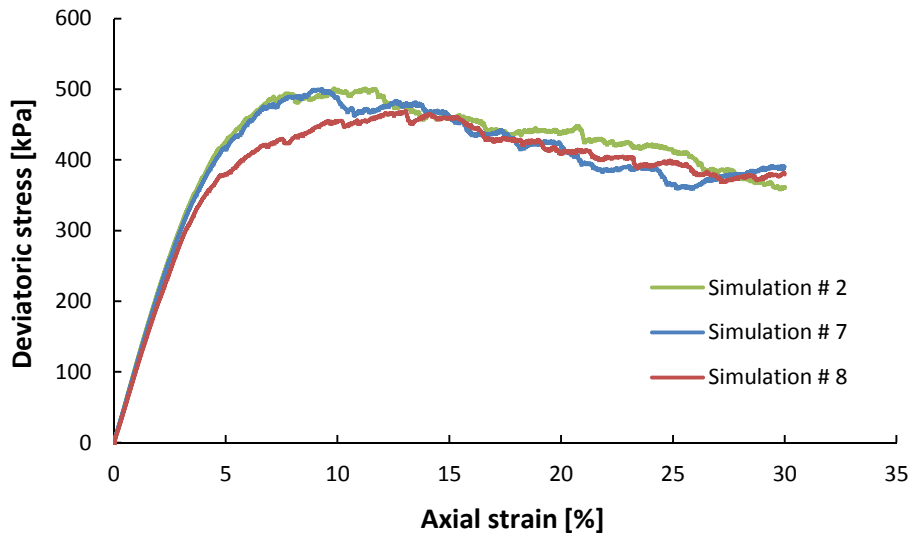


Figure 8. Effect of cement particles’ surface friction on stress-strain response.

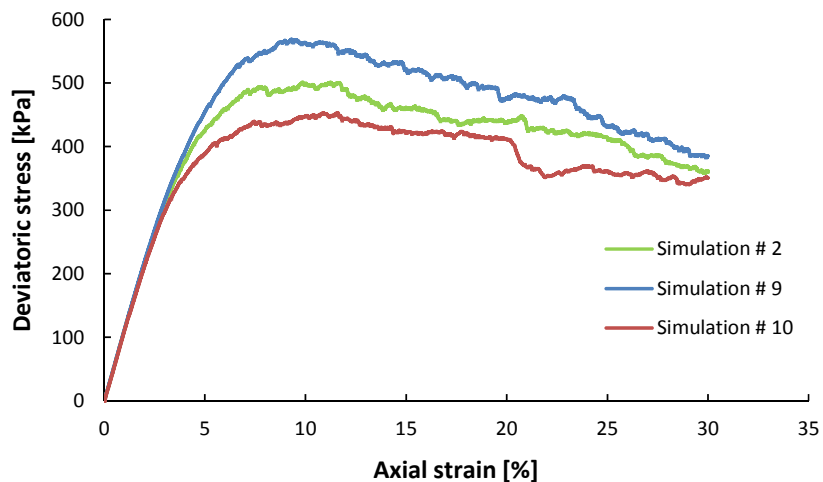


Figure 9. Effect of ratio of sand-cement contact bond strength to cement-cement contact bond strength on stress-strain response.

CONCLUSIONS

The deficiencies of current cementation models for simulating the behavior of bio-cemented sand were discussed. A new contact bond model that is capable of modeling progressive bond failure at a contact point between two particles was introduced. This model was applied to a consolidated assembly of particles which was then sheared. The macroscopic stress-strain behavior shows that the cemented specimen gains strength to a maximum value followed by decrease of strength. However, this decrease happens gradually, implying a ductile type behavior consistent with bio-cemented sand response during shearing.

In order to study the effect of each model input parameter on specimen macroscopic response, a parametric study was performed. The results revealed that as percentage of cemented contact points increases the initial stiffness and peak strength of specimen increase but the final strength of all the assemblies is the same at large strain values. An increase in bond normal and shear strength results in an increase of peak strength but no change in initial stiffness. An increase in cement particles' stiffness leads to decrease of peak strength while initial stiffness remains constant. Increase of cement particles' surface friction has no effect on specimen initial stiffness but increases the peak strength and remains the same for surface frictions of larger than 20° . If cement-cement contact bond normal and shear strength is defined smaller than that of the sand-cement, implying that the failure happens first in the cement phase, the peak strength of the specimen reduces with no change in the initial stiffness.

ACKNOWLEDGMENTS

The work described in this manuscript was supported by NSF grant number CMMI-1538460. This support is gratefully acknowledged.

REFERENCES

- de Bono, J.P., McDowell, G.R., and Wanatowski, D. (2014). "DEM of triaxial tests on crushable cemented sand." *Granular Matter*, 16(4), 563–572.
- de Bono, J.P., McDowell, G.R., and Wanatowski, D. (2015). "Investigating the micro mechanics of cemented sand using DEM." *Int. J. Numer. Anal. Meth. Geomech.*, 39(6), 655-675.
- Evans, T.M., Khoubani, A., and Montoya, B.M. (2014). "Simulating mechanical response in bio-cemented sands." *Computer Methods and Recent Advances in Geomechanics*, Oka, Murakami, Uzuoka & Kimoto (Eds.), 1569–1574.
- Evans, T.M. and Ning., Z. (2013). "Wave Propagation in Assemblies of Cemented Spheres," *Powders and Grains 2013: Proceedings of the 7th International Conference on Micromechanics of Granular Media*, 1542(1), American Institute of Physics, pp. 233-236.
- Feng, K. and Montoya, B. (2015). "Influence of Confinement and Cementation Level on the Behavior of Microbial-Induced Calcite Precipitated Sands under Monotonic

- Drained Loading.” *J. Geotech. Geoenviron. Eng.* , 10.1061/(ASCE)GT.1943-5606.0001379 , 04015057.
- Feng, K., B.M. Montoya, and T.M. Evans. (2014). “Numerical Investigation of Microbial Induced Cemented Sand Mechanical Behavior,” ASCE Geo-Congress 2014, *Geotechnical Special Publication No. 234: Geo-Characterization and Modeling for Sustainability*, Atlanta, GA, pp. 1644-1653.
- Montoya, B. and DeJong, J. (2015). “Stress-Strain Behavior of Sands Cemented by Microbially Induced Calcite Precipitation.” *J. Geotech. Geoenviron. Eng.*, 141(6), 04015019.
- Montoya, B.M., DeJong, J.T., and Boulanger, R.W. (2013). “Dynamic response of liquefiable sand improved by microbial-induced calcite precipitation.” *Géotechnique*, 63(4), 302-312.
- Montoya, B.M., Feng, K. (2015). “Deformation of Microbial Induced Calcite Bonded Sands: A Micro-scale Investigation.” *International Symposium on Deformation Characteristics of Geomaterials*, Buenos Aires, Argentina. (accepted)
- Mortensen, B.M. and DeJong, J.T. (2011). “Strength and Stiffness of MICP Treated Sand Subjected to Various Stress Paths”, *ASCE GeoFrontiers 2011: Advances in Geotechnical Engineering*, Geotechnical Special Publication 211, pp. 4012-4020.
- Ning, Z. and T.M. Evans. (2013). “Discrete Element Method Study of Shear Wave Propagation in Granular Soil,” in *Proceedings of 18th International Conference on Soil Mechanics and Geotechnical Engineering*, Paris, France pp. 1031-1034.
- Tagliaferri, F., Waller, J., Ando, E., Hall, S.A., Viggiani, G., Besuelle, P. and DeJong, J.T. (2011). “Observing strain localisation processes in bio-cemented sand using X-ray imaging.” *Granular Matter*, 13(3), pp. 247–250.
- Wang, Y. and Leung, S. (2008). ”A particulate-scale investigation of cemented sand behavior.” *Canadian Geotech. J.*, 45(1), 29-44.
- Wang, Y. and Leung, S. (2008). ”Characterization of Cemented Sand by Experimental and Numerical Investigations.” *J. Geotech. Geoenviron. Eng.*, 134(7), 992–1004.
- Wang, Y. and Tonon, F. (2009). “”Modeling Triaxial Test on Intact Rock Using Discrete Element Method with Membrane Boundary.” *J. Eng. Mech.*, 135(9), 1029–1037.

Permeability Reduction Due to Microbial Induced Calcite Precipitation in Sand

Atefeh Zamani, S.M.ASCE¹; and Brina M. Montoya, M.ASCE²

¹Graduate Student, North Carolina State Univ., Dept. of Civil, Construction, and Environmental Engineering, Raleigh, NC 27695.

²Assistant Professor, North Carolina State Univ., Dept. of Civil, Construction, and Environmental Engineering, Raleigh, NC 27695.

Abstract: Fine sands have shown that they are susceptible to liquefaction. There are many soil improvement methods that are effective in improving the shear strength and stiffness of fine sand but they often have limitations due to the soil characteristics, such as permeability. Microbial induced calcite precipitation (MICP) has been shown to be a natural and effective liquefaction mitigation method for clean fine sands. Although this method is effective, there may be limitations in implementing MICP in situ. In this study, the permeability reduction from MICP is investigated to understand its implications for field implementation of MICP treatments. Fine sand specimens have been treated to different cementation levels, estimated using nondestructive shear wave velocity measurements. Permeability of treated samples is measured using a constant head permeameter. Utilizing the permeability results of the treated specimens, numerical simulations of the MICP treatments are evaluated by creating a constant head difference between an injection and extraction well and observing the water velocity changes within the domain.

INTRODUCTION

Bio-mediated soil improvement is an emerging research field that meets societal needs for ground improvement in a more natural and sustainable manner. Bio-mediated soil improvement is a chemical reaction, mediated by bacterial activity, which improves the mechanical properties of the soil. One of the more studied methods to modify the mechanical properties of the soil with bio-geochemical reactions is microbial induced calcite precipitation (MICP). MICP uses urea hydrolysis as a chemical reaction to increase the alkalinity of the pore fluid and induce calcite precipitation, (Fujita et al. 2008; Stocks-Fischer et al. 1999). Sands cemented through the MICP process have been shown to exhibit an increase in shear strength, shear stiffness, and dilative properties (Montoya and DeJong 2015, Burbank et al. 2013, Montoya et al. 2013, Chou et al. 2011, van Paassen et al. 2010). The precipitated calcite influences the behavior of the soil by bonding the particles together and densifying the soil by decreasing the void ratio (Montoya and DeJong 2015). The research herein focuses on the change in permeability due to the

reduction of void space. The reduction in permeability may lead to an increase in treatment solution injection pressures or decrease in injection distance. In order to ultimately implement MICP in situ, changes in permeability during treatment and calcite precipitation has to be assessed.

Research has been performed for estimating permeability of samples treated using MICP. Martinez et. al. (2013) showed results of permeability tests performed on Ottawa 50-70. Results indicate a decrease in permeability of up to two orders of magnitude with an increase in shear wave velocity of about 1000 m/s (Figure 1). Figure 1 shows changes in permeability of a 0.5 meter column soil treated with MICP with changes in maximum shear wave velocity of the soil in the column. In the study presented by Martinez et al (2013), shear waves have been measured at four stations along the length of the column and the maximum shear wave is plotted in Figure 1. In the study presented herein, very fine sand is used to assess lower permeability's compared to the Ottawa Sand presented in Martinez et al. (2013).

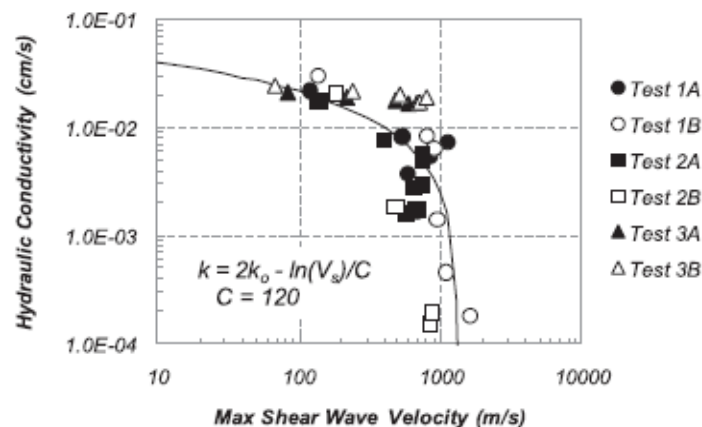


Figure 1. Changes in permeability with increase in cementation level for Ottawa 50-70 (modified from Martinez et al. 2013)

In the current study, the change in permeability from MICP cementation is experimentally assessed using Nevada sand specimens treated to varying cementation levels. Cementation levels are evaluated by using non-destructive shear wave velocity (V_s) measurements via bender elements. The bender elements are located in the middle height of 3-inch samples measuring the bulk change in shear wave velocity. After reaching the target shear wave velocity, the treatment was terminated and the sample was washed with water. Constant head permeability tests were performed on the specimens. A finite element program was also used to assess changes in velocity during the injection of the cementation media due to MICP cementation and the resulting decrease in permeability.

MATERIALS AND METHODS

Soil properties and sample preparation

The soil used for this study is a fine poorly graded sand, Nevada sand. The sand consists of a small amount of material passing the #200 sieve, which has been

removed before sample preparation. Soil properties of Nevada sand are presented in Table 1.

Table 1. Nevada sand characteristics

Name	Nevada Sand
Description	Uniformly graded Gap
D ₅₀	0.13 mm
Cu	1.7
Cc	1.24
Gs	2.65
Mineralogy	Quartz
Shape	Angular*
e _{max}	0.86
e _{min}	0.56

* - Shape based on evaluation by Mikola and Sitar (2013)

Specimen preparation

Specimens were prepared using dry pluviation to an initial void ratio of 0.7 (dry density of 1.55gr/cm³). The specimens were prepared to a height of 7cm and diameter of 7.6cm. Bender elements were placed on two sides of the cylinder to constantly measure changes in shear wave velocity during treatment. Samples were taken during the dissection of the specimen after performing the constant head permeability tests in order to determine the precipitated mass of calcite using an acid washing technique.

Biological Treatment Process

Sporosarcina pasteurii (ATCC 11589), a common alkalophilic soil bacterium with high urease activity, is used in the laboratory study to catalyze the biochemical reaction. *S. pasteurii* was grown at 30°C in an ammonium yeast extract (ATCC 1376). The ingredients were autoclaved individually and mixed together after sterilization. The growth medium was inoculated with the *S. pasteurii* stock culture and incubated aerobically at 30°C in a shaker for 40 h before harvesting at a final optical density (OD₆₀₀). Cultures were centrifuged at 4000g for 20 min in 15mL volumes. Harvested bacteria were stored in centrifuge vials at 4°C for maximum of 14 days.

Urea-calcium chloride cementation media were used to make ureolytic-driven calcite precipitation take place (Mortensen et al. 2011). Table 2 presents a summary of the cementation media components and their chemical concentrations.

The initial treatment injection inoculates the soil with bacteria suspended in the cementation media without calcium chloride, to prevent cementation during this stage. The bacteria are retained for 3 to 6 hours. Subsequent injections of cementation media (including calcium chloride) are performed every 6 to 12 hours. The injections of cementation media are continued until the target V_s is reached.

Table2. Chemical recipe for cementation media

Chemical	Chemical concentration
Urea	333 mM
NH ₄ Cl	374 mM
CaCl ₂	50 mM

The cementation process was monitored in real time with non-destructive V_s measurements. Bender elements prepared with specific techniques to operate in highly conductive environments are used to determine the V_s of soil specimens before and during treatment (Montoya et al. 2012). A 5-V, 100 Hz square wave is sent to the sending bender element and an oscilloscope is used to determine the travel time of the shear wave. The V_s is determined using equation 1:

$$V_s = \frac{\text{Distance between end of benders}}{\text{Travel time of wave}} \quad (1)$$

One untreated sample has been prepared with an initial void ratio of 0.7. The permeability and shear wave velocity of this sample is taken as the reference. Four samples were treated by MICP simultaneously. The shear wave was monitored and the target was to have samples with shear wave velocity differences of around 100m/sec. Treatment was ceased when reaching approximate predefined V_s . Once reaching the target V_s , water is passed through the sample to prepare it for permeability testing.

Permeability testing

A constant head permeameter was used to measure the permeability of soil. To perform the test, the specimen is placed in the permeameter which is set inside a tub full of water (Figure 2). The air bubble pipe is lifted to a desired elevation and its distance from the top of specimen is recorded. The bubble pipe is fixed in place so it remains stationary and the level of water in the tub is kept constant.

Vacuum is applied to the top reservoir tube and then it is filled up with water. While filling the reservoir tube, the air bubble tube should be covered by finger or a stopper to keep the pressure at the tip of the tube constant and equal to air pressure. The distance between water elevation in the tub and tip of air bubble tube is the constant head difference on the sample, which is labeled “H” in Figure 3.

To start performing the test, all tubes and vents and clamped and the stopper on top of the air bubble pipe is removed. The water level will drop from the moment the stopper has been removed leading to water passing through the sample. To measure the permeability, a chronometer is used to record the time required for water to pass through the sample leading to drop of water in the cylinder. This recording will be performed for at least three times and for different water level locations. The permeability is calculated using Darcy’s law, an expression of which is shown in Equation 2:

$$k = \frac{Q}{iAt} \quad (2)$$

Where Q is the volume of water passed through the soil which is determined using the change in water height of the reservoir tube, i corresponds to hydraulic gradient which is defined as the change in head, H , over the length of the soil specimen, L , and t is the amount of time required for the water level to drop from two reading points.

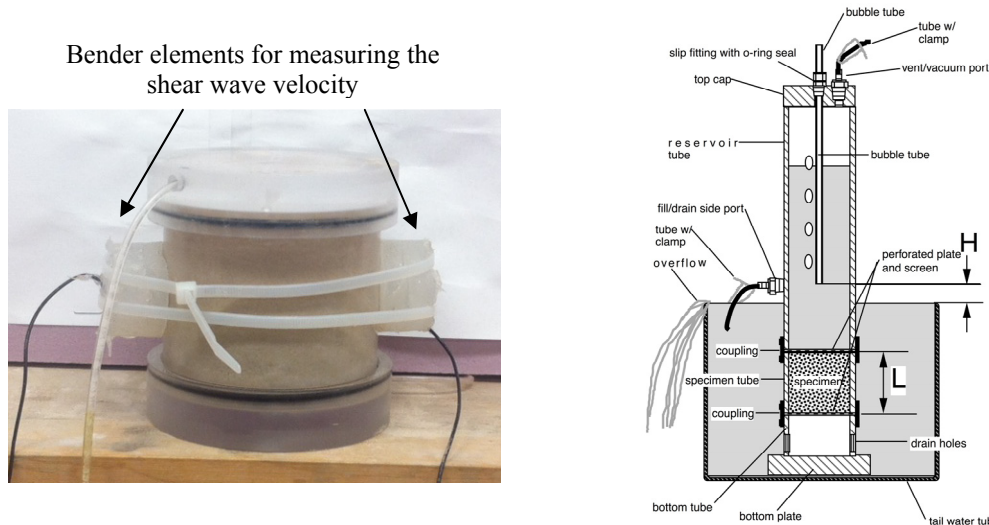


FIG 2. a) Photo of specimen set up with bender elements for measuring the shear wave velocity, and b) Constant head permeameter test set up (from Trautwein Soil Testing manual)

Numerical Modeling with Seep/W

In this study the Seep/W program has been applied to detect the effect of change in permeability with increase in cementation level when using MICP method for improving soil properties such as increase in shear strength, compressibility etc. According to the experimental results, permeability reduced with increase of cementation level. This reduction will affect the injection pressure and flow velocity the method is implemented in the field. In this study SEEP/W program has been applied to show how the reduction in permeability changes the time of treatment along with the extent of area treated by MICP method.

SEEP/W is a finite element software product for analyzing groundwater seepage and excess pore-water pressure dissipation problems within porous materials such as soil and rock. Its formulation will allow analysis of saturated steady-state problems to complicated, saturated/unsaturated time-dependent problems.

In this study, a region of fully saturated Nevada sand has been defined to estimate how changes in permeability will be affecting velocity of seepage and travel time of the cementation media in the loose Nevada sand while being treated with MICP method. The region defined is presented in Figure 3. This analysis is axisymmetric which shows an extraction well being surrounded by a number of evenly spaced injection wells. The x and y axis of the domain are 20 meter long. Four boundaries have been defined along the sides with total head of 20 meters (considering both elevation head and water pressure head). Two lines defined resembling an injection and extraction well are within a distance of 5 meters. In this analysis the head is kept constant and flow rates are obtained for different

permeability values of cemented Nevada sand referring to specific cementation levels. The maximum amount of flow rate must always be less than the permeability of the soil to prevent any kind of cavitation and soil washing.

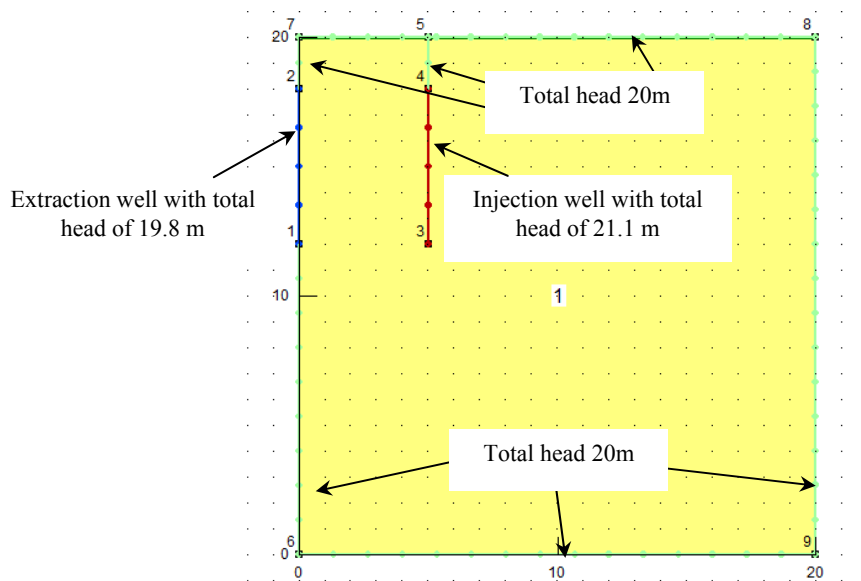


FIG 3. Boundary condition of the domain in Seep/W

RESULTS AND DISCUSSION

The specimens were prepared and treated to reach specific cementation levels. Table 3 shows the treatment levels and amount of calcite content for each specimen. One specimen is prepared without any cementation as the baseline. The results show reduction of permeability by continuing the treatment. The permeability results obtained are also plotted in Figure 4.

Based on the obtained experimental results, an increase in cementation level monitored through an increase in shear wave velocity leads to a decrease in permeability. The change in permeability is mainly due to the reduction of void space and flow paths through the soil. This reduction in permeability will lead to a longer treatment times to inject the MICP cementation media.

The permeability value of Nevada sand ($D_{50}=0.13\text{mm}$) with void ratio of 0.7 which is a fine sand compare to a coarser sand such as Ottawa 50-70 ($D_{50}=0.21\text{mm}$) with same void ratio (Martinez et al) is lower in its natural state which is due to less flow paths available as the finer soil grains clog the available paths. To compare the effect of grain size in amount of permeability reduction, results obtained in this study are compared to what obtained in Martinez et al. 2013, on a coarser sand (Ottawa 50-70). According to the results, the amount of reduction in permeability with increase in cementation level is related to the grain size of the soil. With MICP method, the cementation mostly takes place at the particle contacts, which is related to the nature of bacteria attachment (DeJong et al 2010). In addition, the suspended calcite produced in the media may also be trapped at the pore paths. This will be dependent on both size of the pore space and size of calcite. All these factors are likely to reduce

the permeability of a finer sand more compared to a coarser sand as the pore paths are smaller and number of contact points are higher.

Table 3. Permeability of Nevada sand treated with MICP to varying levels of cementation

Specimen	Initial shear wave velocity (m/sec)	Final shear wave velocity (m/sec)	Permeability*10 ⁻⁵ (m/sec)
Uncemented Sand	80	80	5.04
MICP Cemented Specimens	1	175.6	3.44
	2	337.3	3.04
	3	440.2	2.56
	4	531.2	1.41

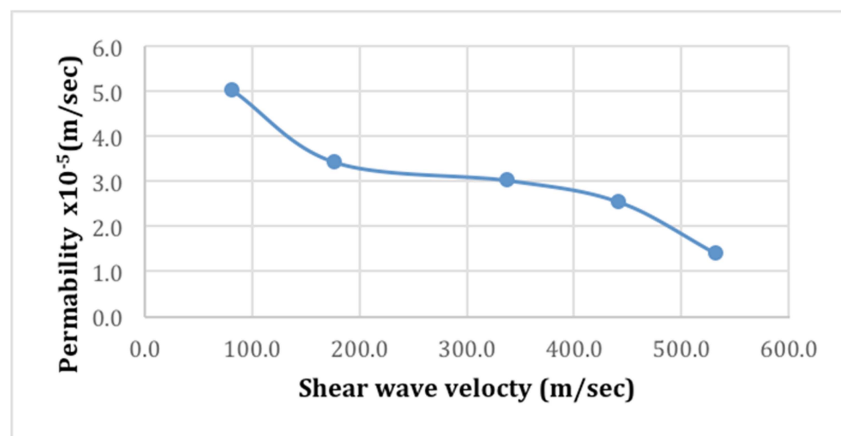


FIG 4. Change in permeability with increase in shear wave velocity resulting from MICP cementation.

In the numerical simulation, the total head of the extraction and injection are defined based on the maximum velocity of water in soil, which should not exceed its permeability values. With the heads defined for both injection and extraction wells, the maximum velocity is always lower than the permeability for all five models.

According to the results, an increase in cementation level measured with shear wave velocity will lead to a decrease in permeability. By applying a constant head for both injection and extraction well for all five models (Figure 5), the results show that the zone of influence around the injection well will decrease indicating that the cementation media will be conveyed by lower rates.

Based on the results presented in Figure 5, smaller areas will be affected by the cementation media in a specific time as the level of cementation increases. Due to this fact more time will be needed to continue injecting with a given injection/extraction well pattern so that the cementation solution reaches the desired treatment areas. In addition, if the cementation solution is not injected in a timely manner, most of the reaction will take place very close to the injection well and it will lead to clogging and prevention of additional cementation taking place farther from

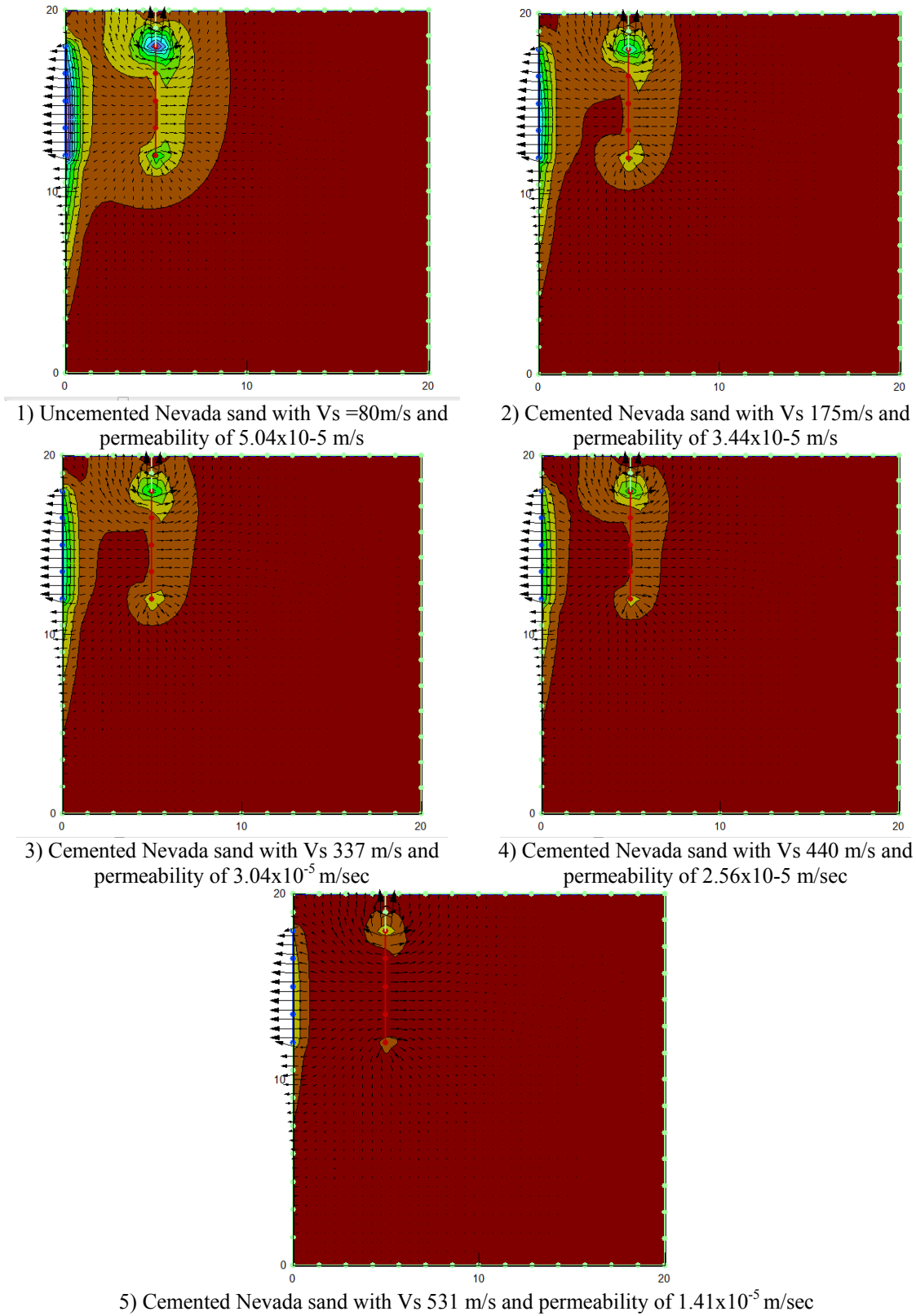


FIG 5. Seepage velocity through the domain for different cementation levels of Nevada sand

the injection well. Since it is essential to provide a uniformly distributed treatment area, it is necessary to design a pattern of wells to inject and extract the treatment media so that all desired soils will reach the target degree of cementation.

Table 4. Input values for Modeling in Seep/W

Specimen		Hydraulic conductivity*10 ⁻⁵ (m/sec)	Compressibility (M _v) (1/kPa)	Saturated volume water content (m ³ /m ³)
Uncemented Specimen		5.04	7x10 ⁻⁵	0.411
MICP Cemented Specimens	1	3.44		0.408
	2	3.04		0.404
	3	2.56		0.397
	4	1.41		0.393

Since both fine and silty sands are prone to liquefaction, the research presented here is currently being expanded to include treating silty sands, ranging in fines contents up to 35%, to equivalent levels of cementation and evaluating the changes in permeability. The resulting changes in permeability will be simulated with a modeling software in order to estimate the amount of time required to treat deposits of silty sand in situ.

CONCLUSIONS

An experimental program was established to assess the change in permeability of fine sand cemented with MICP. Fine sand specimens were cemented with MICP to varying levels of cementation, assessed using shear wave velocity measurements, and the permeability was determined as a function of cementation level. The experimental results indicate that the permeability reduces as the MICP cementation level increases; this is likely due to the decrease void space due to the precipitated calcite. The effect of the permeability reduction is initially evaluated using the Seep/W finite element program, which indicates that the reduction in permeability measured experimentally results in a decrease in the zone of influence around the injection well, indicating that the cementation media will be conveyed by lower rates.

ACKNOWLEDGMENTS

Funding and support from the National Science Foundation (EEC-1342207) and the North Carolina State University Department of Civil, Construction, and Environmental Engineering and College of Engineering are greatly appreciated. Any opinions, findings, and conclusions or recommendations expressed in this material are those of the writer(s) and do not necessarily reflect the views of the National Science Foundation.

REFERENCES

- Burbank, M., Weaver, T., Lewis, R., Williams, T., Williams, B., Crawford, R.
Geotechnical Tests of Sands Following Bioinduced Calcite Precipitation
Catalyzed by Indigenous Bacteria, Journal of Geotechnical and Geoenvironmental
Engineering, 2013, Vol.139, No.6, 928-936.

- Chou, C.W., Seagren, E.A., Aydilek, A.H., and M. Lai. Biocalcification of sand through ureolysis, *ASCE Journal of Geotechnical and Geoenvironmental Engineering*, 2011, Vol. 127, Issue 12, pp. 1179-1189.
- DeJong, J.T., Mortensen, B.M., Martinez, B.C., Nelson, D.C. (2010). "Bio-Mediated Soil Improvement." *Ecological Engineering*, 36, 197-210.
- Domenico, P. A., and Mifflin, M. D. (1965). "Water From Low-Permeability Sediments and 631 Land Subsidence." *Water Resources Research*, American Geophysical Union, vol. 1, no. 4, 632 563-576.
- Fujita, Y., et al. Stimulation of microbial urea hydrolysis in groundwater enhance calcite precipitation, *Journal of Environmental Science Biotechnology*, 2008; 42(8): 3025-3032.
- Martinez, B. C., J. T. DeJong, T. R. Ginn, B. M. Montoya, T. H. Barkouki, C. Hunt, B. Tanyu, and D. Major. "Experimental optimization of microbial-induced carbonate precipitation for soil improvement." *Journal of Geotechnical and Geoenvironmental Engineering* 139, no. 4 (2013): 587-598.
- Montoya, B.M., DeJong, J.T. Stress-strain behavior of sands cemented by microbially induced calcite precipitation, *Journal of Geotechnical and Geoenvironmental Engineering*, 2015.
- Mikola, R. G., & Sitar, N. (2013). *Seismic Earth Pressures on Retaining Structures in Cohesionless Soils*. UCB/GT-2013-01, University of California, Berkeley, Geotechnical Engineering.
- Montoya, B.M., DeJong, J.D., Boulanger, R.W. Dynamic Response of Liquefiable Sand Improved by Microbial Induced Calcite Precipitation, *Geotechnique*, 2013, Vol. 63 No.4, 302-313.
- Montoya B. M., Gerhard, R., DeJong, J.T., Weil, M., Martinez, B., Pederson, L. Fabrication, operation, and health monitoring of bender elements for aggressive environments. *ASTM Geotechnical Testing Journal*, 2012, 35(5)
- Mortensen B.M., Haber, M., DeJong, J.T., Caslake, L., Nelson, D.C. Effects of Environmental Factors on Microbial Induced Calcite Precipitation, *Applied Microbiology*, 2011.
- Stocks-Fischer, S., Galinat, J.K., and Bang, S.S. Microbiological Precipitation of CaCO₃, *Soil Biology and Biochemistry*, 1999, Vol. 31, pp. 1563-1571.
- Van Paassen, L.A., Ghose, R., van der Linden, T.J.M, van der Star, W.R.L., and van Loosdrecht, M.C.M. Quantifying biomediated ground improvement by ureolysis: Large-scale biogROUT experiment, *ASCE Journal of Geotechnical and Geoenvironmental Engineering*, 2010, Vol. 136, No. 12, 1721-1728.

Sand Cementation Using the pH Dependency of Calcium Phosphate Compounds and the Addition of Various Powders

R. A. N. Dilrukshi¹ and S. Kawasaki²

¹Doctoral Student, Graduate School of Engineering, Hokkaido Univ., Sapporo 060-8628, Japan.

²Professor, Faculty of Engineering, Hokkaido Univ., Sapporo 060-8628, Japan.

Abstract: The effect of pH increasing ability of plant-derived urease to induce the precipitation of calcium phosphate compounds (CPCs) as CPC-biogROUT (CPC-Bio) and addition of powder materials to induce the precipitation of CPCs as CPC-chemical grout (CPC-Chem) was examined separately using unconfined compressive strength (UCS) test for applying as novel, eco-friendly ground improvement methods. Initially, Toyoura sand test pieces were cemented only from CPC solutions made from stock solutions of calcium acetate and di-potassium phosphate. Subsequent sand test pieces were cemented by different concentrations of urea and CPC solution, and concentration fixed watermelon seeds extract. All test pieces were cured in an airtight container at high humidity at 25°C. Furthermore, the UCS on sand test pieces cemented with same stock solutions mentioned above with different powders such as tricalcium phosphate (TCP), magnesium phosphate (MgP), calcium carbonate (CC) and magnesium carbonate (MgC) were conducted. Maximum UCS of greater than 100 kPa was obtained after 28 days of curing for both CPC-Bio and CPC-Chem and obtained UCS was higher than the UCS of test pieces made only from CPC. pH for optimal cementation was around 8.0 and the best Ca/P ratio in CPC solutions producing the highest cementation was 0.5 for CPC-Bio.

INTRODUCTION

Some of the major challenges in the current construction industry are the incompetence of the ground to provide proper supporting capability for overlying structures, vulnerability of slopes and ground to catastrophic natural or anthropogenic events (geo-disasters) such as earthquakes, floods, landslides, embankment, and dam failures. Although, the cement-based stabilizers are widely used for ground improvement and therefore, act as countermeasures against geo-disasters, it involves major environmental issues such as large CO₂ emissions during cement production, and high

energy cost for cement production and re- excavation of cement improved ground. Therefore, innovative and sustainable ground improvement practices are necessary to withstand the stresses resulting from geo-disasters and hence to prevent or mitigate them. As a result of that, recent years, the concept of biogrouting is widely explored. It involves the biological action to induce the improvement in the ground (Van Paassen et al., 2009). Different mineral formation mechanisms are involved in the formation of biogrouts through chemical reaction series that are managed and controlled through biological activities and by products resulting from those reactions alter the properties of material in the system to produce biogROUT. Carbonate precipitation using urea and ureolytic bacteria (Harkes et al., 2010) or urea and purified/crude extracts of plant species having urease activity (Park et al., 2014; Nam et al., 2014) or using glucose and yeast (Kawasaki et al., 2006), iron/manganese compound precipitation through iron-oxidizing bacteria (Weaver et al., 2011), siloxane bond formation using glucose and yeast (Terajima et al., 2009), calcium phosphate compound (CPC) based chemical grouts (CPC-Chem) formation by its self-setting mechanism (Akiyama and Kawasaki, 2012a), CPC biogROUT (CPC-Bio) formation in relation to the addition of ureolytic microorganisms and an ammonia source to CPC-Chem (Akiyama and Kawasaki, 2012b) are some examples.

Regarding CPCs, its solubility depends on the pH of the surrounding environment (Tung, 1998). This makes it possible to utilize the mechanisms of pH adjustment by a biologic activity to control CPC precipitation and hence to form CPC-Bio. CPC-Chem is easy to obtain, safe to handle, non-toxic, and can be recycled in the form of a fertilizer and these advantages make it suitable for geotechnical applications (Akiyama & Kawasaki, 2012a). A maximum unconfined compressive strength (UCS) of 63.5 kPa was achieved after 14 days of curing period for sand test pieces cemented CPC-Chem (Akiyama & Kawasaki, 2012a).

Our aim of this study was to precipitate CPC-Bio by using a pH regulator like plant-derived urease along with urea, and improve the CPC-Chem by using two kinds of phosphate powders (tricalcium phosphate, TCP; magnesium phosphate, MgP) and two kinds of carbonate powders (calcium carbonate, CC; magnesium carbonate, MgC) and increase the UCS more than 100 kPa that is the strength required for mitigating soil liquefaction (Yamazaki et al., 1998).

Selection of a pH Regulator for the Precipitation of CPC-Bio

The enzyme having urease activity is catalyzed the hydrolysis of urea to form ammonium ion (NH_4^+) and carbonate ion (CO_3^{2-}). However, NH_4^+ ions actually start out as NH_3 . When NH_3 reacts with water, it creates OH^- ions, which raise the pH of the system. A plant species that contains urease activity other than ureolytic microorganisms was selected as a pH regulator. Three types of plant seeds such as watermelon, melon and pumpkin were used and investigated the best seed for our study by measuring pH variation of each seeds extract and urea solution. According to the pH variation in each solution, it varies from 7 to 9 in melon and watermelon seed extract and urea solutions. This range of pH is favorable for CPC precipitation. Out of them, watermelon seeds (*Citrullus vulgaris*) that leftover as food waste were selected due to its low price.

Selection of Powder Materials for CPC Precipitation

In this study, four types of powders were used as seed crystals for CPC precipitation. Physical properties and some properties of powder materials that are expected to increase the UCS are described herein. TCP is a type of CPCs and hence, it can be solidified and changed in to hydroxyapatite (HA) over time by its self-setting process (Tung, 1998). Furthermore, TCP release less phosphate ions by the process of hydrolysis when compare with other CPC powders (Chow, 1991) and therefore, neutral to weakly alkaline pH range can be expected. TCP possesses insolubility in the neutral to weakly alkaline pH range (Tung, 1998). TCP is an approved food additive in Japan, so it is non-toxic and easy to acquire (Kawasaki and Akiyama, 2013). Cost of TCP powder is about 2800 JPY/500 g. Physical properties such as mean diameter and density of TCP are 12.0 μm and 3.14 g/cm^3 respectively. Other type of phosphate powder we used was MgP. It has been used as a quick hardener for the emergency repair of roads and airport runways (Seehra et al., 1993; Mestres and Ginebra, 2011). It may produce Struvite-K ($\text{KMgPO}_4 \cdot 6\text{H}_2\text{O}$) among the sand particles after reacting with dipotassium phosphate which is the stock solution of phosphate we used in this study. Mean diameter of MgP particle is 8.2 μm and density is 2.19 g/cm^3 . MgP costs about 3200 JPY/500 g.

Two carbonate powders we selected were CC and MgC. CC is the main component of oyster and scallop shells, which are disposed as marine industrial waste (410,000 t/year in Japan; Ports and Harbors Bureau, 2004) and it is the main component of limestone. Fernandez et al. (1998) have shown that the UCS can be increased from 35 MPa to a 56 MPa by using CC crystal. It is non-toxic and inexpensive (2600 JPY/500 g). Mean diameter and density of CC are 17.1 μm and 2.93 g/cm^3 respectively. Mg-containing carbonates such as magnesite (MgCO_3) and dolomite ($\text{CaMg}(\text{CO}_3)_2$) have a lower solubility than CC (Chou et al., 2000). Therefore, strength and chemical stability can be expected when MgC and CPC-Chem are used. Hence, MgC was also selected as promising candidate to reinforce the ground along with CPC-Chem. It is also a non-toxic, recyclable material. It costs about 3800 JPY/500 g. Mean diameter of MgC particle is 20.7 μm and density is 2.16 g/cm^3 .

MATERIALS AND METHODS

Stock solutions of calcium acetate- $\text{Ca}(\text{CH}_3\text{COO})_2$ (CA), and dipotassium phosphate- K_2HPO_4 (DPP) with final concentrations of CA: DPP = 0.75 M: 1.5 M and CA = DPP = 0.75 M, which have yielded largest UCS at the initial investigation were used for this study. For CPC-Bio method, urea was selected as the ammonia source, and watermelon seeds extract having urease enzyme which was prepared by soaking crushed seeds in water or another liquid as required, about 30 min. was used for catalyzing the hydrolysis of urea. Toyoura sand, a typical clean sand found in Japan with mean diameter $D_{50} = 170 \mu\text{m}$, particle density $\rho_s = 2.64 \text{ g}/\text{cm}^3$, minimum density $\rho_{\text{min}} = 1.335 \text{ g}/\text{cm}^3$ and maximum density $\rho_{\text{max}} = 1.645 \text{ g}/\text{cm}^3$, was used for making UCS test pieces. The test pieces relevant to CPC-Chem method (hereafter, CPC- Powder method) were made using same stock solutions and sand mentioned above with TCP, MgP, CC and MgC powders.

CPC-Bio Method

As we mentioned earlier, the solubility of CPCs depends on the pH of the solution. Therefore, maintaining a favorable pH is very important to form CPC-Bio. As the pH value is closely related with urease activity, the change in urease activity with the concentration of seeds extract and urea was investigated.

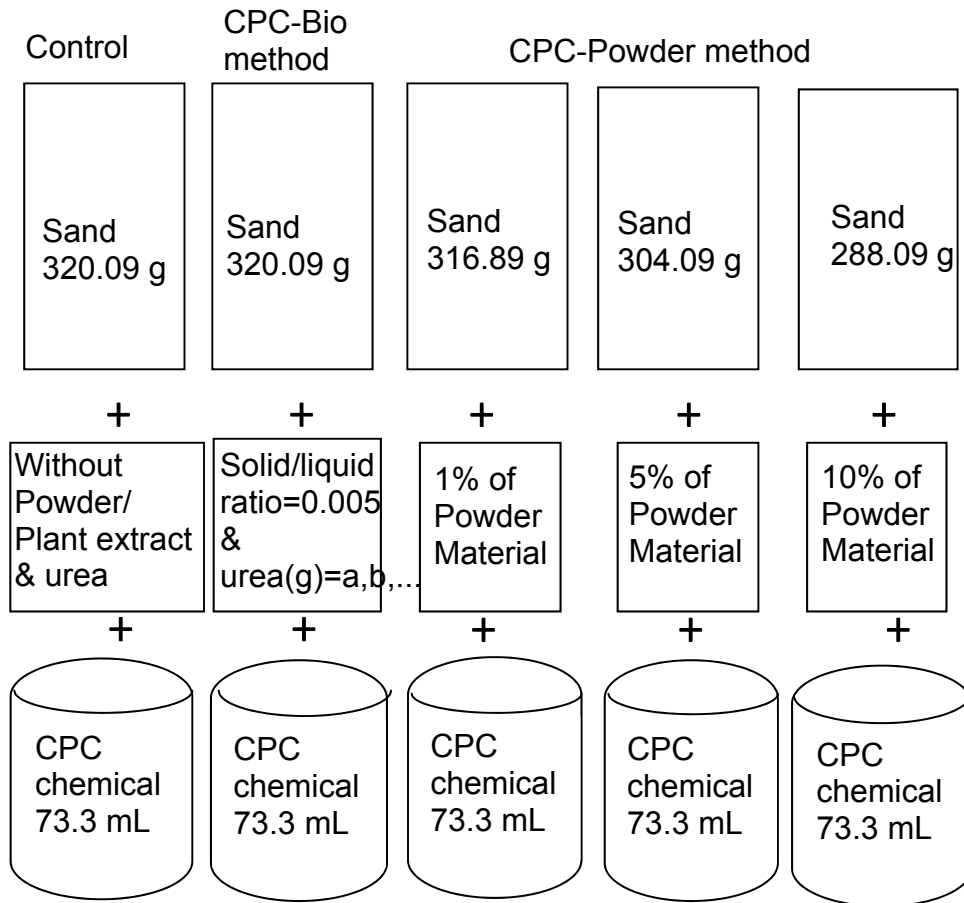


FIG. 1. Conceptual image of making test pieces

Urease activity test was conducted according to a method based on conductivity (Whiffin, 2004). The concentration of seeds extract was explained by the term “solid/liquid ratio” (dry weight of crushed seeds, (g) /volume of liquid, (mL)). Urease activity was investigated by selecting different solid/ liquid ratios of seeds extract and different concentrations of urea to understand the behavior of urease activity. Urea dissolved in 10 mL of distilled water was mixed with 10 mL of seeds extract and the final mixture with the volume of 20 mL was used for measuring conductivity. Obtained conductivity values were plotted with time (min.), and slope of the graph was used to calculate urease activity of seeds extract mixed with urea. At the same time, the variation of pH value in relation to different solid/liquid ratios (from 0.0005 to 0.005) and urea was investigated to determine optimal concentrations for maximum CPC precipitation. Weight of urea ranging from

0.08 g to 0.8 g was selected and dissolved in a DPP solution (0.75 M and 1.5 M). Small scale sample mixtures consisting of 15 g of sand, 1.72 mL of plant seed extract prepared using CA solution and 1.72 mL urea solution made by dissolving urea in 1.72 mL DPP solution were used for the pH test. The final volume of the solution mixture was 3.44 mL.

At the preparation of UCS test pieces, crushed seeds were soaked in the concentration known CA solution about 30 min. The required weight of urea weighted in advance, was then dissolved in the concentration known DPP solution. A volume of 36.65 mL from both the seeds extract in the CA solution and the urea in the DPP solution were added to 320.09 g of Toyoura sand. Conceptual image of making test pieces in this method is shown in Fig. 1. The mixture was uniformly mixed in a stainless steel ball for 2 min. and then divided into quarters. Each quarter was then placed in to a plastic mold (inner diameter $\phi=5$ cm, height $h=10$ cm). Before placing the sample into the mold, an overhead projector sheet (0.1 mm thick) was used to cover the inner wall of the mold to avoid any disturbance of the test pieces during their removal from the mold. The mixture was tamped down 30 times by a hand rammer when each quarter was filled into the mold. Finally, the upper edges of the test pieces were slightly trimmed so that they were flat, and covered with Parafilm M (Structure Probe, Inc., West Chester, PA) to avoid desiccation. The molded test pieces were cured in an airtight container at high humidity. After curing, test pieces were removed carefully from the mold, and the UCS was measured with a UCS apparatus T266-31100 (Seiken-sha Co.Ltd., Japan) at an axial strain rate of 1% /min. A temperature of 25 °C was maintained while preparing, curing and testing of the test pieces. The repeatability of measurements of UCS was studied by testing two test pieces for each test case under same condition. The pH of top, bottom, and middle of each test piece was measured and calculated as an average of three measurements using a pH Spear (Eutech Instruments Pte., Ltd., Singapore). Segments of the UCS test pieces were observed by Scanning Electron Microscope (SEM) (TM 3000 Miniscope, HITACHI) just after the UCS tests.

CPC-Powder Method

In CPC- Powder method, the UCS test pieces were made according to a weight proportion of sand and powder material. Conceptual image of making test pieces in this method is shown in Fig. 1. Initially, required weight of powder material was weighted in advance and mixed well with sand in a stainless steel ball to get an uniform mixture. A volume of 36.65 mL from both CA solution (0.75M) and DPP solution (1.5M) were added to the sand-powder mixture. Again, the mixture was uniformly mixed 2 min. and followed the same conditions and procedures described in CPC-Bio method for preparing, curing and testing of the test pieces.

RESULTS AND DISCUSSION

CPC-Bio Method

Urease activity test results for the mixture of watermelon seeds extract and urea are graphically represented by Fig. 2. When the weight of urea (g) was increased, then the urease activity was decreased and when the solid/ liquid ratio of the seeds extract was

increased, the urease activity was increased. According to the results of pH values with different amount of urea and solid/ liquid ratios, pH was gradually increased and became constant with time and it has shown favorable pH for CPC precipitation, in the mixture of 0.08 g of urea and 0.005 of solid/ liquid ratio. The value of urease activity was also high (in between 800-900 u/L) in that mixture (urea = $0.08\text{g} \times 3.44\text{mL} / 20\text{mL} = 0.465\text{ g}$, solid/ liquid ratio = 0.005)

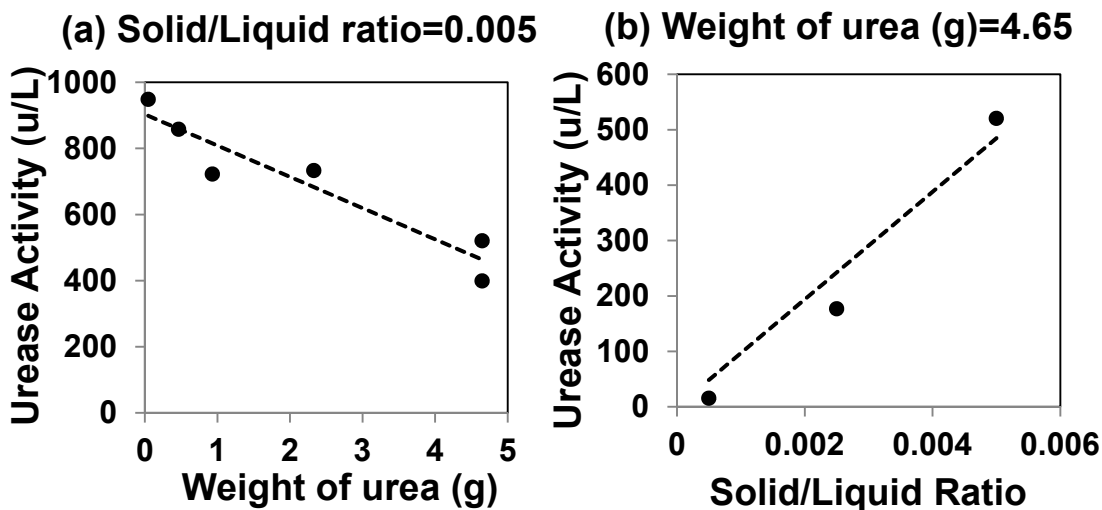


FIG. 2. The variation of urease activity (u/L) with (a) weight of urea (g) and (b) solid/liquid ratio

Therefore, the UCS test was conducted for the test pieces prepared using best combination of urea and seeds extract. A weight of 1.71 g ($0.08\text{g} \times 36.65\text{mL} / 1.72\text{mL}$) was used to prepare the initial UCS test pieces and subsequently, more test pieces were made by changing the weight of urea in the range of 1.71 g-17.07 g to observe the behavior of UCS. As shown in Fig.3 (a), the increment of UCS with the increment of urea was limited up to certain level and thereafter, the UCS was decreased. The pH change at that level was around 8 to 9. It is clear that an increase in urea causes to release more NH_4^+ ions in relation to urea hydrolysis, and hence, it was caused to increase in the pH that was unfavorable for CPC precipitation. Then, the UCS value has decreased after a certain level of urea. The maximum value of UCS (after 7 days of curing period) was obtained with 8.54 g of urea. Same behavior of UCS was observed for CA: DPP = 0.75 M: 1.5 M (Fig.3 (b)). Accordingly, temporal variation of the UCS was studied using 8.54 g of urea for both cases (CA = DPP = 0.75 M and CA = 0.75 M, DPP = 1.5 M) (Figs. 3 (c) and 3 (d)).

In the case of CA = DPP = 0.75 M (Ca/P = 1), the possible precipitates are DCPA (Dicalcium phosphate anhydrate) and/or DCPD (Dicalcium phosphate dihydrate) (Tung, 1998). The UCS value was become to decrease after 14 days. According to Fig.3 (c), the pH of the test pieces after 28 days was more than 9. That was unfavorable for precipitating CPC relevant to CA = DPP = 0.75 M. This is a possible reason to

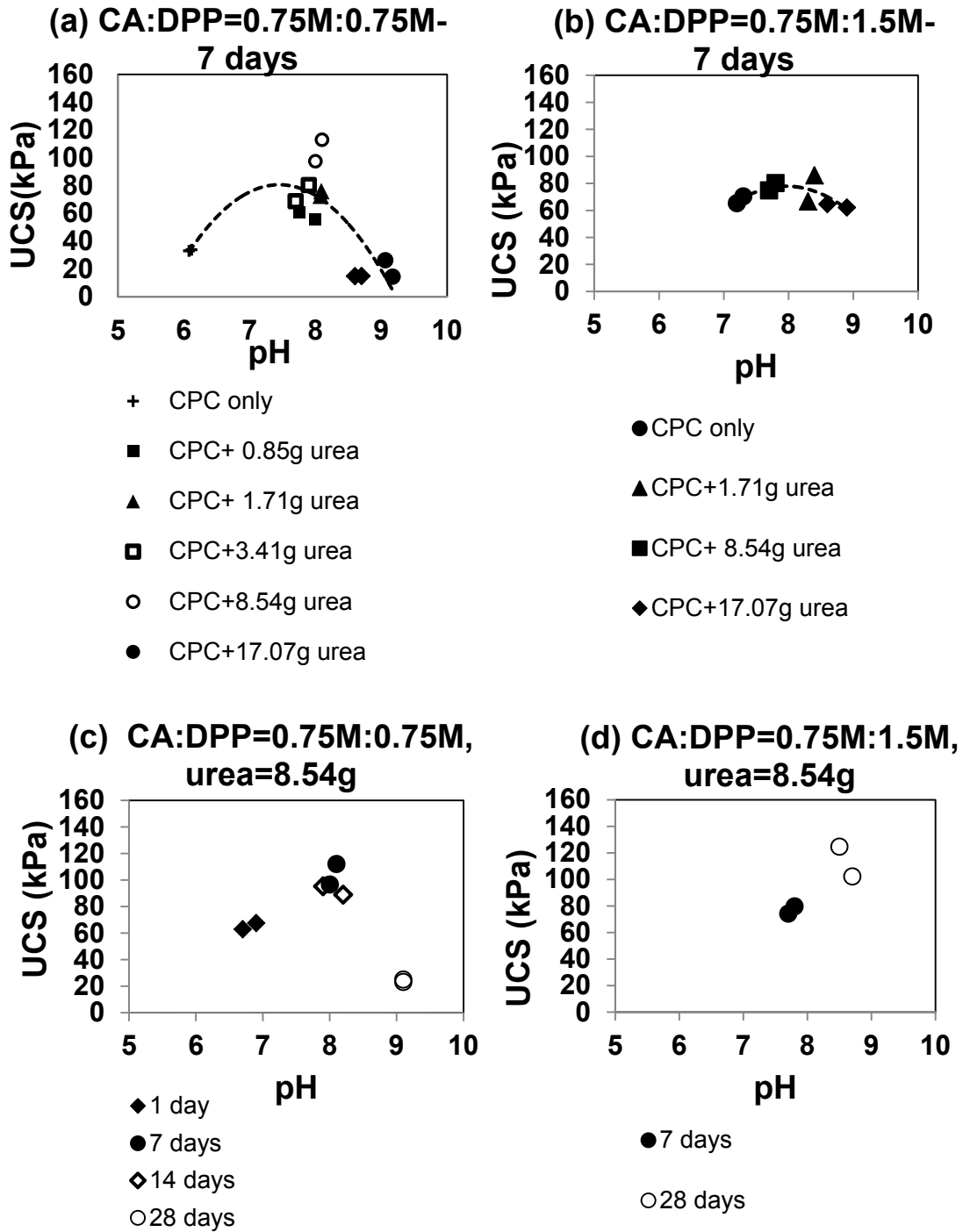


FIG. 3. Effect of pH on UCS (Solid/ liquid ratio=0.005)

decrease the UCS after 28 days. The solubility of DCPD is higher than that of DCPA for the same value of pH, and the formation of DCPD after 14 days may cause to decrease the UCS after 14 days rather than 7 days, even if both cases indicated nearly the same pH values. Regarding the CA = 0.75 M and DPP = 1.5 M, the pH value of the test pieces

increased with time and pH of around 8 was observed after 28 days. This favorable pH caused to precipitate maximum CPC. Therefore, the UCS value was increased with time and obtained a value of more than 100 kPa after 28 days. Furthermore, a specific crystal structure could not be identified from SEM observations in the segments of the test pieces in all test cases.

CPC-Powder Method

For the ease of comparison, the compressive stress (σ)–strain (ϵ) curves of test pieces made from two phosphates and two carbonates powders were plotted separately (Fig.4). For each test case, we selected the test pieces with curing period of 28 days. The two stress–strain curves obtained for each test case showed almost the same behavior in terms of shape. The stress–strain curves of the TCP-added test pieces showed a higher compressive stress (σ) than MgP-added test pieces at same weight percentage, and nearly same failure strain (ϵ) was observed in compared with the MgP-added test pieces without the test pieces with 10% TCP and 10% MgP. A specific pattern of the compressive stress (σ) of CC-added test pieces could not be observed in compared with MgC-added test pieces.

The other important thing is to notice that the test pieces made from low percentage of MgP and MgC showed compressive stresses less than or similar to the test pieces made only from CPC. Furthermore, a previous research has shown that TCP, MgP, CC, and MgC do not possess pozzolanic properties with deionized water (Kawasaki et al., 2013). Therefore, CPC chemical solutions greatly affected for the strength variation of powder added test pieces.

As shown in Fig. 5, the wet densities of the test pieces cemented with four kinds of powders and CPC-Chem increased with the amount of added powder, and UCS increased accordingly in TCP- and CC-added test pieces. This increment of UCS could not be clearly seen in MgP- and MgC-added test pieces. Even if, two identical test pieces in each case showed almost same values for wet densities, there was a little gap between UCS values in some TCP- and CC-added test pieces. pH values of those identical test pieces were nearly same. Therefore, it may be due to uneven surfaces of the test pieces. Specially, the upper face of the test pieces cemented with CC and CPC-Chem has swollen slightly after preparing the test pieces. Then, we had to prepare an even surface manually, before conducting UCS test. This is a possible reason to get uneven surfaces.

Moreover, the result shows that the addition of magnesium compounds is not effective for increasing UCS using CPC-Chem. The SEM images showed that small crystals similar to MgP and MgC were present in MgP- and MgC-added test pieces without bonding with the sand particles. Previous studies have explained that the magnesium ions are considered to be an inhibiting factor on the self-setting of CPC (Amjad et al., 1984). With reference to that, magnesium ions released from the magnesium compounds exchange with the calcium ions in the CPC stock solution and reduce the precipitation of CPC. These are the possible reasons to decrease the UCS in MgP- and MgC-added test pieces. As we mentioned earlier, because of the upper faces of the test pieces cemented with CC powder and CPC-Chem have swollen slightly after preparing the test pieces, it may provide an underestimate for UCS. The UCS may be improved by the addition of vertical

confining pressure. Therefore, it is better to apply CPC-CC Powder method for sub surface environments where considerable overburden pressures exist.

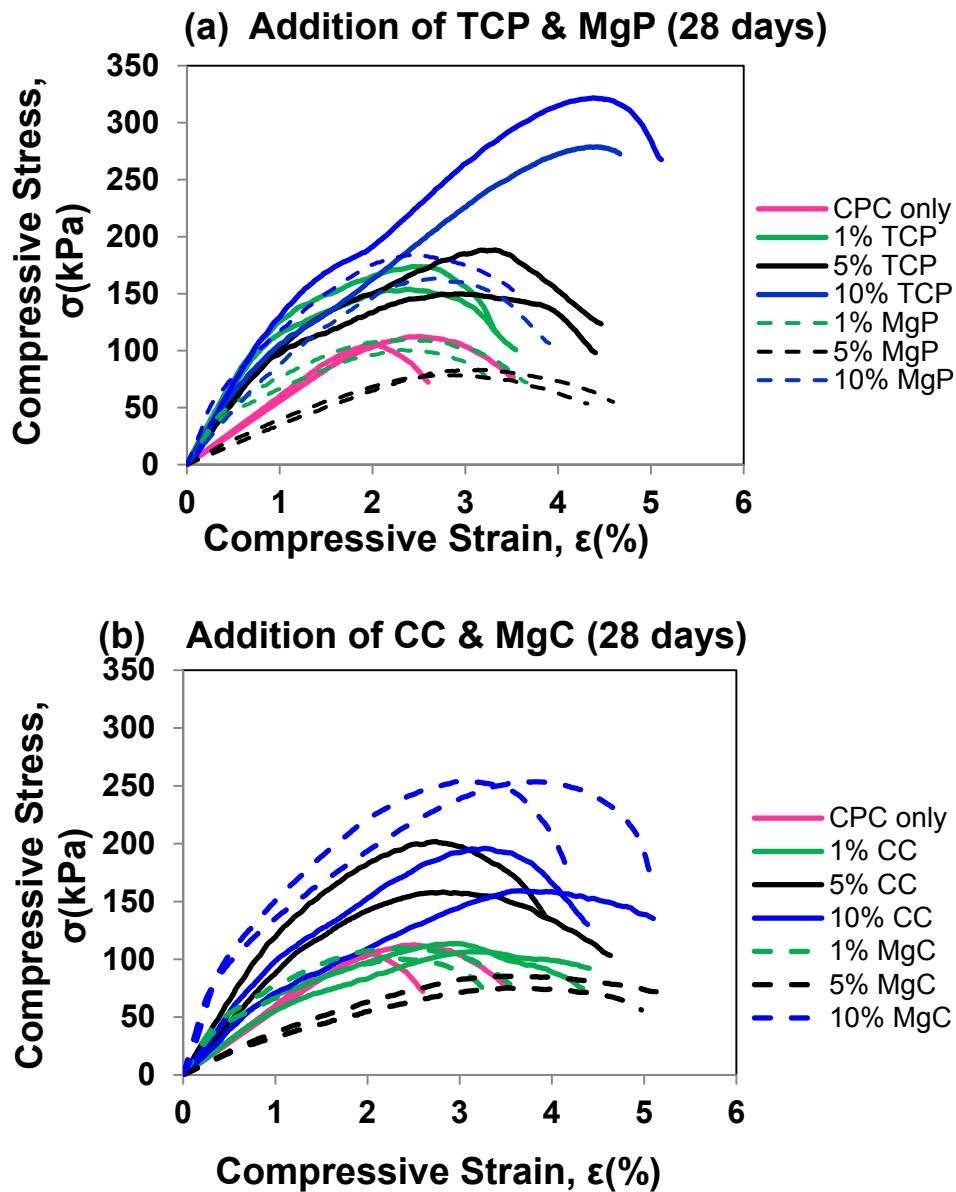


FIG. 4. Stress-strain curves. (a) addition of TCP and MgP (28 days) and (b) addition of CC and MgC (28 days)

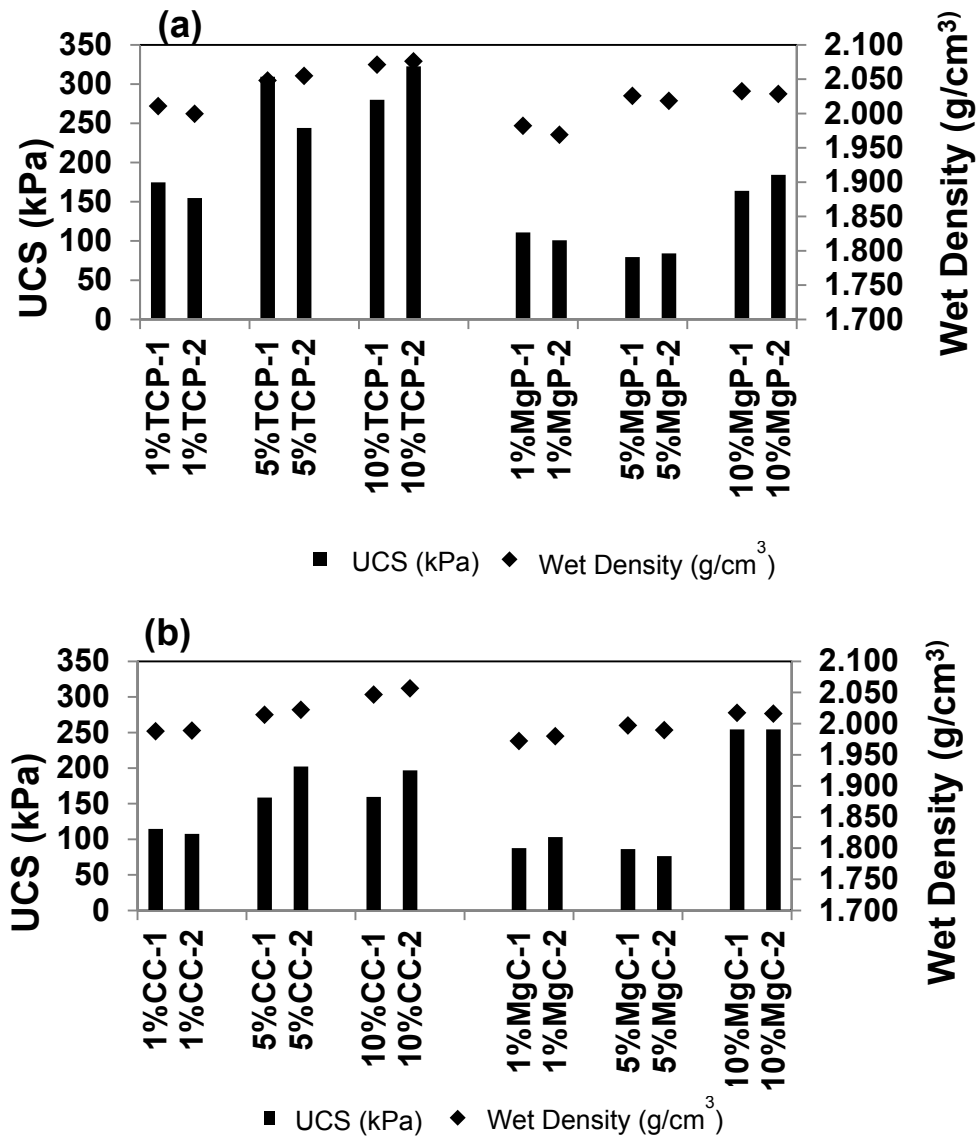


FIG. 5. Variation of UCS (kPa) with wet density (g/cm³). (a) addition of TCP and MgP (28 days) and (b) addition of CC and MgC (28 days)

CONCLUSIONS

The effectiveness of plant-derived urease enzyme (watermelon seeds extract) to induce the precipitation of CPC-Bio and addition of powder materials to induce the precipitation of CPC-Chem, and hence, to improve the UCS of sand was examined for small scale, cylindrical samples. The results are as follows.

- The UCS of more than 100 kPa was achieved after curing of 28 days, due to generated CPC-Bio with the help of CA: DPP = 0.75 M: 1.5 M in relation to the use of watermelon seeds extract at a solid-liquid ratio of 0.005 and 8.54 g of urea for 320.09 g of Toyoura sand, and best pH observed for optimal cementation was around 8.0.

The pH was the governing factor to precipitate CPC as CPC-Bio and watermelon seeds extract having urease activity helps to increase the pH by catalyzing the process of urea hydrolysis.

- The UCS of TCP-added test pieces showed clear increment with the percentage of added powder and maximum UCS values relevant to 1%, 5% and 10 % TCP were 175, 309 and 322 kPa respectively.
- The UCS of MgP-and MgC added test pieces showed UCS less than or similar to test pieces made only from CPC at low percentage of MgP and MgC. At high percentage (eg. 10% in this study) of MgP and MgC, the UCS was dramatically increased. The reason for this increment will be studied in future after conducting Energy Dispersive X-ray Analysis (EDX) and X-Ray Diffraction (XRD).

Long-term strength of test pieces in CPC-Powder method is needed in the future by understanding the long term behavior of technical solutions with accessory materials. All of the TCP- and CC-added test pieces cemented with CPC stock solutions have been showed a UCS larger than 100 kPa after 28 days. In some cases, it has reached up to about 300 kPa. This observation suggests that after studying the long term behavior of the strength, the CPC-powder method would allow for adjustment of strength over 100 kPa by controlling powder percentage according to the requirement of the liquefaction prevention and to use as a cost effective ground improvement practice.

ACKNOWLEDGMENTS

The work was partly supported by a Grant-in-Aid for Scientific Research (No. 24300299) from the Japanese Ministry of Education, Sports, Science, and Technology; this support is gratefully acknowledged.

REFERENCES

- Akiyama, M. and Kawasaki, S. (2012a). "Novel grout material using calcium phosphate compounds: in vitro evaluation of crystal precipitation and strength reinforcement." *Engineering Geology*, Vol. 125: 119–128.
- Akiyama, M. and Kawasaki, S. (2012b). "Microbially mediated sand solidification using calcium phosphate compounds." *Engineering Geology*, Vol. 137-138: 29-39.
- Amjad, Z., Koutsoukos, P.G., and Nancollas, G.H. (1984). "The crystallization of Hydroxyapatite and fluorapatite in the presence of magnesium ions." *J. Colloid Interface Sci.* 101: 250–256.
- Chou, L., Garrels, R.M., and Wollast, R. (2000). "Comparative study of the kinetics and mechanisms of dissolution of carbonate minerals." *Chem. Geol.* 78: 269–282.
- Chow, L.C. (1991). "Development of self-setting calcium phosphate cements." *Centennial Mem. Issue of Ceram. Soc. Jpn.* Vol. 99: 954–964.
- Fernandez, E., Gil, F.J., Best, S.M., Ginebra, M.P., Driessens, F.C.M., and Planell, J.A. (1998). "Improvement of the mechanical properties of new calcium phosphate bone cements in the CaHPO_4 - α - $\text{Ca}_2(\text{PO}_4)_2$ system: compressive strength and microstructural development." *J. Biomed. Mater. Res.* 41: 560–567.

- Harkes, M.P., Van Paassen, L.A., Booster, J.L., Whiffin, V.S., and Van Loosdrecht, M.C.M. (2010). "Fixation and distribution of bacterial activity in sand to induce carbonate precipitation for ground reinforcement". *J. Ecological Engrg.*, Vol. 36:112–117.
- Kawasaki, S. and Akiyama, M. (2013). "Enhancement of unconfined compressive strength of sand test pieces cemented with calcium phosphate compound by addition of various powders." *Soils and Foundations*, Vol. 53(6): 966–976
- Kawasaki, S., Murao, A., Hiroyoshi, N., Tsunekawa, M., and Kaneko, K. (2006). "Fundamental study on novel grout cementing due to microbial metabolism." *J. of the Japan Society of Engineering Geology.*, Vol. 47: 2–12 (in Japanese with English abstract).
- Mestres, G. and Ginebra, M.P. (2011). "Novel magnesium phosphate cements with high early strength and antibacterial properties." *Acta Biomater.*7: 1853–1861.
- Nam, I.H., Chon, C.M., Jung, K.Y., Choi, S.G., Choi, H., and Park, S.S. (2014). "Calcite Precipitation by Ureolytic Plant (*Canavalia ensiformis*) Extracts as Effective Biomaterials." *KSCE J. of Civil Engrg.*, (0000) 00(0): 1-6.
- Park, S.S., Choi, S.G., and Nam, I.H. (2014). "Effect of Plant-Induced Calcite Precipitation on the Strength of Sand." *J. of Materials in Civil Engrg.*: 1-5 (06014017).
- Ports and Harbors Bureau, 2004. (<http://www.mlit.go.jp/kowan/recycle/>), Recycling technology guidelines for harbor and airport construction and maintenance.
- Seehra, S.S., Gupta, S., and Kumar, S. (1993). "Rapid setting magnesium cement for quick repair of concrete pavements – Characterization and durability aspects." *Cem. Conc. Res.*23: 254–266.
- Terajima, R., Shimada, S., Oyama, T., and Kawasaki, S. (2009). "Fundamental study of siliceous biogROUT for eco-friendly soil improvement." *J. of of the Japan Society of Civil Engineers*, Ser.C (Geosphere Engineering), Vol. 65: 120–130 (in Japanese with English abstract).
- Tung, M.S. (1998). "Calcium phosphates: structure, composition, solubility, and stability, in: A. Zahid (Ed.), Calcium phosphates in biological and industrial systems." *Kluwer Academic Publishers*, Norwell: 1-19.
- Van Paassen, L.A., Harkes, M.P., Van Zwieten, G.A., Van der Zon, W.H., Van der Star, W.R.L., and Van Loosdrecht, M.C.M. (2009). "Scale up of biogROUT: a biological ground reinforcement method." *Proc. 17th Intl. Conference on Soil Mechanics and Geotechnical Engineering*: 2328-2333.
- Weaver, T.J., Burbank, M., Lewis, A., Crawford, R., and Williams, B. (2011). "Bio-induced calcite, iron and manganese precipitation for geotechnical engineering applications." *Proc. Geo-Frontiers*: 3975–3983.
- Whiffin, V.S. (2004). Microbial CaCO₃ precipitation for the production of biocement. *PhD. dissertation*, School of Biological Science & Biotechnology, Murdoch University, Perth, Australia, 154 p.
- Yamazaki, H., Maeda, K., Takahashi, K., Zen, K., and Hayashi, K. (1998). "Technical Note of Port and Harbour Research Institute", Vol. 905: 1-29 (in Japanese)

Sustainable Slope Stabilization Using Biopolymer-Reinforced Soil

Santiago Caballero¹; Raju Acharya¹; Aritra Banerjee¹; Tejo V. Bheemasetti²; Anand Puppala³; and Ujwalkumar Patil²

¹Doctoral Student, Dept. of Civil Engineering, Univ. of Texas at Arlington, Arlington, TX 76019.

²Faculty Associate - Research, Dept. of Civil Engineering, Univ. of Texas at Arlington, Arlington, TX 76019.

³Professor, Dept. of Civil Engineering, Univ. of Texas at Arlington, Arlington, TX 76019.

Abstract: Different stabilization methods for improving soil behavior are commonly used to control slope stability problems in dams, levees and embankments. The present study demonstrates the use of Biopolymer soil mixtures as a sustainable slope stabilization technique. Expansive clayey soils with low and high plasticity characteristics were collected from representative dam embankments located in the Dallas-Fort worth (DFW) area in Texas. The experimental study consists of mixing the collected soil with a commercially available biopolymer (Guar-Gum), at 0.25%, 0.5%, 1%, and 1.5% concentrations by weight. Strength and swell parameters of mixtures were obtained by direct shear test and swell pressure tests respectively. Results obtained indicate that the addition of biopolymer increases the shear strength and the swelling phenomenon of the soil. The 0.5% biopolymer soil mixture presents the optimum concentration based on its high strength and low swell potential. Strength parameters for both, non-reinforced soil and biopolymer reinforced soil (0.5% mixture) are used to conduct slope stability analysis using the limit equilibrium approach. The application of Biopolymer reinforced soil substantially increased the factor of safety against shallow slope failures. This research highlights the adaptability of biopolymers in enhancing the strength parameters and providing a safe sustainable solution.

INTRODUCTION AND BACKGROUND

Slope failures in dams, levees and embankments possess major threat to both, lives and associated civil engineering structures. Cracks, slides and depressions are signs of embankment instability which are majorly caused due to both gradual and rapid changes in the environment. The repeated wetting-drying cycles causes loss of soil strength and also results in desiccation cracking of the surface. Past researchers have stated that the infiltration of rain water have softened the embankment material and eventually triggered the shallow slope failures (Dronamraju, 2008; Le, 2013).

Traditionally, shallow landslides have been repaired by replacing the desiccation zone with new compacted material. However, repairing works are extremely expensive and the frequency and recurrence of failures increase the operation and maintenance costs (McCleskey et al. 2005). Therefore, soil stabilization methods have attracted increasing attention during the past decades. Past researchers reported that using chemical additives, fibers and composts increased the strength of the soils and mitigated the cracking of highway pavements (Puppala et al., 2000, 2004, 2006, 2013; Du et al., 2013). A stabilization method for shallow failures was proposed for by Le (2013) consisted on using an admixture with lime and fibers to the soil. Conventional soil stabilization mixing materials, such as ordinary cement or lime, have several limitations, especially from the environmental perspective. The production of cement and other stabilization materials is known as a great contributor of CO₂ to the atmosphere. It may also cause several disturbances within the soil mass, such as high PH and other problems due to the chemical reactions during mixing (Bremmer, 2001). This study introduces the use of Biopolymer as sustainable soil stabilization technique for shallow slope failures.

Biopolymer is a product mainly formed by microorganisms for their own protection and/or to make the environment more hospitable for their living (Maier et al. 2000). It is also called exopolymers or extracellular polymeric substances (EPS) (Sutherland 2001). The main source of biopolymer is plants but it can also be obtained from different types of trees and even produced by bacteria. The biopolymers are mostly high molecular weight polysaccharides. These polysaccharides contain chemically active groups with electrical charges which make them actively interact with clay minerals (Sutherland 2001). Therefore, biopolymers are likely to enhance the shear strength of soil with no side effects from the environmental perspective.

In the last decade, researchers have demonstrated the improvement of soil behavior when treated with biopolymers (Nugent et al, 2009, 2011; Larson et al, 2012, 2013; Chen et al, 2013). Nugent et al. (2009) evaluated the effect of xanthan gum and guar gum biopolymers on the liquid limit of kaolinite clay. The effectiveness of the use of biopolymers was later confirmed with the study conducted by Nguten et al. (2011), where authors evaluated the erosional resistance of the kaolinite combined with the two biopolymers. The natural benefits of biopolymers are surface adhesion, self-adhesion of cells into biofilm, formation of protective barriers, water retention around roots of vegetation, and nutrient accumulation (Larson et al. 2012). Larson et al (2012) performed experimental models in laboratory to validate the use of the biopolymer as slope stabilization technique. Results also showed that biopolymers reduce the transport of solids in runoff water, heavy metals from small arm firing ranges, and reduce the generation of dust. The study developed by Chen et al. (2013) presented the feasibility of using xanthan gum and guar gum biopolymers to stabilize mine tailings. The authors also evaluated the liquid limit and the undrained shear strength of the sun dried mine tailing mixed with the biopolymer solutions at different dosages. The authors found guar gum to be more effective than xanthan gum due to higher viscosity of the guar gum solution than the xanthan gum solution at same concentration.

The main objective of the present research is to study the feasibility of Biopolymer treated soil as a sustainable slope stabilization technique. Two different soils from Grapevine and Joe Pool lake dams were selected to perform experimental and analytical studies. Soil collected from both sites was mixed with Biopolymer (Guar-Gum) at different proportions. Strength and swell parameters are obtained from a Biopolymer treated soil mixture. The use of undrained shear strength, fully softened shear strength and residual shear strength, of both core soil and Biopolymer treated soil, were used as boundaries to conduct slope stability analysis.

LABORATORY RESULTS

Collected soil samples from both, Joe Pool and Grapevine Dams were used to conduct basic geotechnical laboratory tests such as sieve analysis; hydrometer analysis and Atterberg limit tests. Results were compared with values obtained in earlier research (McCleskey, 2005; Dronamraju, 2008) at the same sites. Table 1 shows the results from laboratory tests.

Table 1. Laboratory Results of Grapevine and Joe Pool Soils

Description	Site	
	Grapevine Dam	Joe Pool Dam
LL	30	58
PL	17	24
PI	13	34
USCS	CL	CH

Studies developed over the past years showed that guar-gum biopolymer is more effective when used as stabilizer compared with other type of biopolymers. The effect on soil properties such as liquid limit, are not representative of the benefits in terms of shear strength of compacted soil. Soils were mixed with guar-gum biopolymer at 0.25%, 0.5%, 1% and 1.5% proportions. Various tests including standard proctor compaction, direct shear, and one dimensional free swell test were conducted to study the effect of biopolymers as sustainable soil stabilizer. Surficial slope failures are mitigated when the treated soil reduces the shrinkage or swelling potential and increases the shear strength at the same time. Table 2 shows the results from one dimensional free swell tests performed on all sample mixtures from both sites. Figure 1 and 2 show the results of drained shear strength of Grapevine and Joe Pool soils respectively, obtained by conducting the direct shear test.

Table 2. One Dimensional Free Swell Pressure Test Results

Description	Maximum Swell Pressure (kPa)				
	Control Soil	0.25 % Biop.	0.50 % Biop.	1 % Biop.	1.5 % Biop.
Grapevine Dam	9.58	13.26	14.36	30.16	51.23
Joe Pool Dam	21.55	23.46	25.86	31.36	47.16

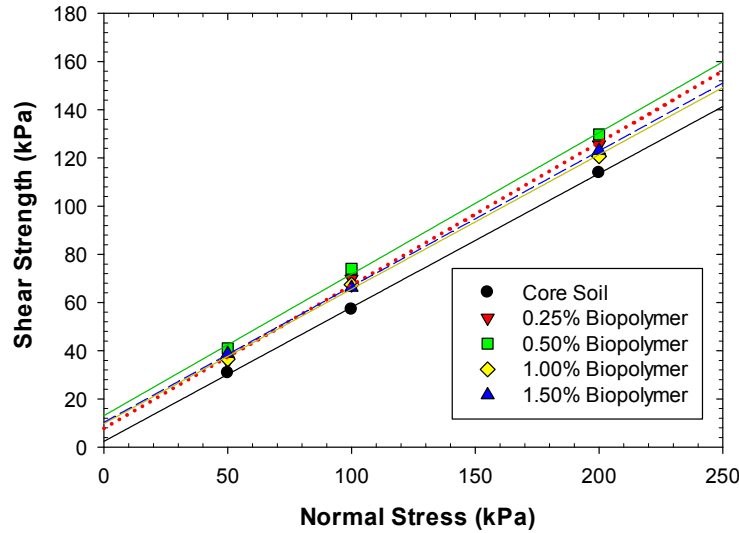


FIG. 1. Direct shear test results for Grapevine soil and biopolymer mixtures.

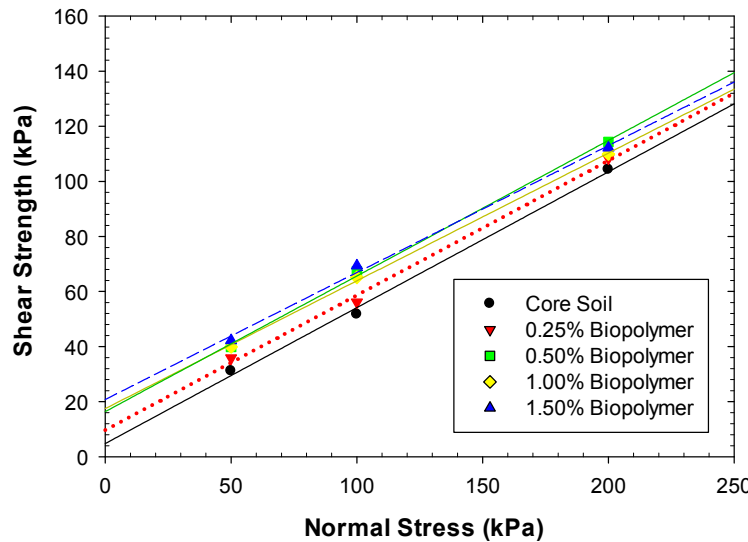


FIG. 2. Direct shear test results for Joe Pool soil and Biopolymer mixtures.

Several interpretations are discussed based on laboratory results. Swell tests results indicated that both soils are susceptible to volumetric changes as expected. However, the increase of swelling potential is proportional to the increase of biopolymer in the mixture. The soil strength increases with the increase of biopolymer in mixtures for both cases as well. Based on these results, the 0.5% biopolymer soil mixture was found to be the most effective combination with high strength and low swelling potential at the same time. Additional tests were performed on the 0.5% biopolymer soil mixtures to obtain drained and undrained shear strength parameters for soils at Grapevine and Joe Pool sites.

Torsional ring shear test and direct shear test were conducted to evaluate residual shear strength and fully softened shear strength respectively. Results will be used as

input parameters to address the stability of the dam embankments at different scenarios. Figures 3 and 4 shows the results for residual shear strength and fully softened shear strength tests conducted on 0.5% Biopolymer soil mixtures.

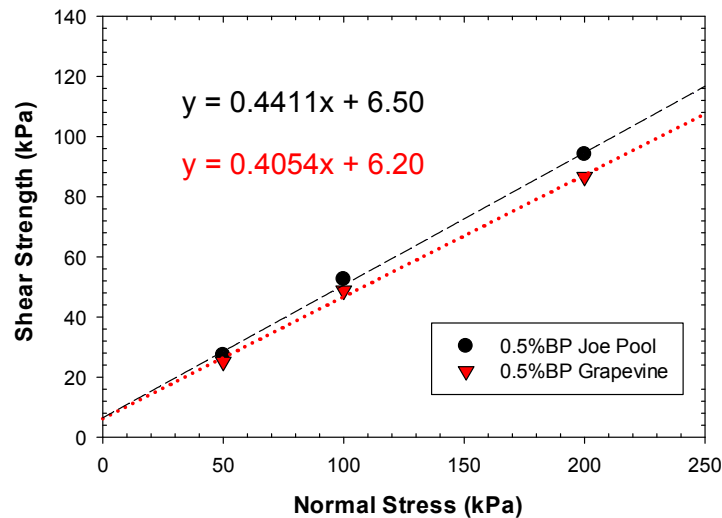


FIG. 3. Residual shear strength of 0.5% biopolymer soil mixture of Grapevine and Joe Pool Dams obtained by Torsional ring shear test

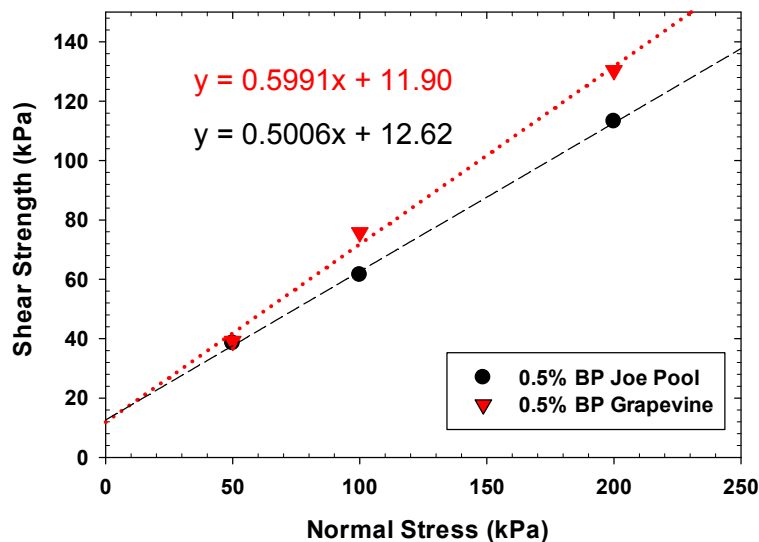


FIG. 4. Fully softened shear strength (FSS) of 0.5% biopolymer soil mixture of Grapevine and Joe Pool Dams obtained by direct shear test

SLOPE STABILITY ANALYSIS

The slope stability analysis of dam embankments at Grapevine and Joe Pool Dam is presented in this section. The study focuses on the Limit Equilibrium (LE) principles in Factor of Safety (FOS) determination. Several limit equilibrium methods have been

developed for slope stability and they are based on certain assumptions for the interslice normal and shear forces. The current study presents the application of strength parameters at three different slope stability scenarios: 1) No rainfall condition, 2) Long-Term rainfall condition and 3) under a repeated weathering cycle (drying/wetting cycles). Shallow landslides are known to have a circular or non-circular failure surface. The Spencer's method was considered for the present analysis based on the assumptions involved (e.g. it considers both interslice forces, it assumes a constant interslice force function, it can be used for circular and non-circular failures). SLOPE/W slope stability software is one component of the complete suite of the geotechnical software GeoStudio and it will be utilized to compute FOS for each scenarios. The Mohr-Coulomb material model was adopted for the analysis with basic input soil parameters such as unit weight, cohesion and friction angle of the soil.

The geometry of the dam slopes was determined by conducting field surveying. The geometry of the slope models involves three different soil regions: the compacted core soil, the 1.2 m (4 feet) top soil layer where desiccation takes place, and the treated soil region. Shallow landslides are mainly triggered due to the desiccation zone located at an average depth of 0.3 m to 1.2 m (1 - 4 feet) and their failure surface was found to be parallel to the slope face (Day, 1996). The analysis considers the maximum dry unit weight of the control and treated soils in all three cases regarding the saturation condition of soils. The change of unit weight of soil that occurs in the transition of soil from being unsaturated to fully saturated is considered to have a small impact on the slope stability analysis. Table 3 shows the maximum unit weight obtained by Standard Proctor tests performed to control soils and treated soils (0.5% Biopolymer soil mixture).

Table 3. Maximum Dry Density of Soil used in Slope Stability Analysis

Description	Maximum Dry Density kN/m^3 (pcf)	
	Control Soil	0.5 % Biop.
Grapevine Dam	17.00 (108.1)	16.10 (102.3)
Joe Pool Dam	14.70 (93.4)	14.50 (92.2)

The shear strength parameters are determined based on the slope stability scenario to be considered in the analysis: 1) No Rainfall condition, 2) Long-term rainfall condition and 3) Wetting and Drying cycles (Fully softened condition). For simplicity, Case 1 (No rainfall condition) will consider the undrained shear strength (c_u) due to the soil state in post-construction conditions. It is assumed that this analysis represent the state of the soil in a short-term condition. Both dams were constructed by compacting borrow soils at the optimum moisture content and it is assumed that there is no change in moisture content in the Case 1. The properties are also applicable to the compacted soil region within 1.2 m (4 feet) of desiccation zone by assuming that the formation of initial desiccation cracks does not affect the shear strength of the soil. The undrained shear strength for soil samples was obtained using the unconfined compression test.

Case 2 evaluates the long-term rainfall condition that leads to the saturation of the 1.2 m (4 feet) desiccation zone along the slope. Drained conditions typically prevail within this region and the residual shear strength was used in this zone to simulate the condition. Residual strength parameters were obtained using the Bromhead torsional ring shear device. It is assumed that the condition of the soil below the desiccation zone remains constant for all of the cases considered in the analysis.

Case 3 evaluated the effect of weathering process due to wetting /drying cycles expected on Grapevine and Joe Pool dams by using of the Fully Softened shear strength (FSS) parameters. Studies developed by Terzaghi (1936), Skempton (1964) and others demonstrated that factors of safety calculated using the peak strength of undisturbed stiff-fissured clay samples do not reflect the actual state of the soil in the field. Skempton (1970) initially suggested that this is caused because more swelling and softening occur in the field than in the laboratory, therefore, the strength of stiff-fissured clays should be evaluated by using the fully softened shear strength. Research studies have been developed over the years and it suggests that after several wetting and drying cycles, softening will take place in the soil reducing the peak shear strength. Therefore, the fully softened shear strength parameters are used to evaluate the 1.2 m (4 feet) desiccation zone for the weathering condition. The fully softened shear strength was obtained by direct shear tests of disturbed samples as recommended by researches in the past. Table 4 shows the soil strength parameters used in the SLOPE/W software as input to perform slope stability analysis for each scenario.

Table 4. Shear Strength parameters used in SLOPE/W to perform slope stability analysis

SOIL DESCRIPTION	SLOPE STABILITY CONDITION				
	Case 1 No Rainfall	Case 2 Long-Term Rainfall		Case 3 Wetting/Drying cycle	
	c_u (kPa)	c_r' (kPa)	ϕ_r' °	c_{fss} (kPa)	ϕ_{fss} °
<i>Control Soil - Grapevine</i>	42.2	0	18	0	34.8
<i>0.5% BP Soil mix - Grapevine</i>	56.2	6.20	22	12	31
<i>Control Soil - Joe Pool</i>	62.7	0	20	0	27
<i>0.5% BP Soil mix - Joe Pool</i>	79.8	6.50	24	12.70	27
<i>Remarks</i>	Undrained	Residual Drained		Fully softened	

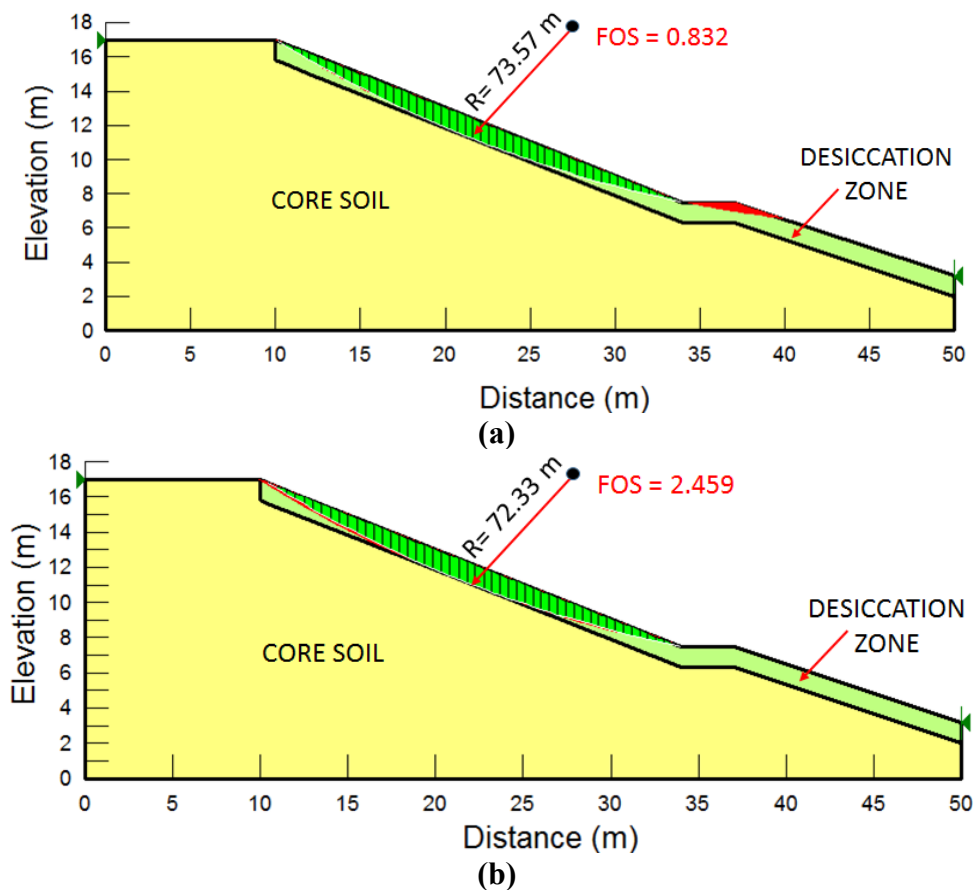


FIG. 5. Slope stability modeling for Grapevine embankment (Case 2: Long-term rainfall condition)

Figures 5(a) and (b) present the examples of the geometry of the Grapevine dam slope modeled in the SLOPE/W software corresponding to Case 2 (Long-term Rainfall condition) before and after soil stabilization respectively. Similar models were prepared to assess factors of safety of both dam embankments at different scenarios and results are summarized in Table 5.

Table 5. Factors of Safety for Different Scenarios

SOIL DESCRIPTION	Case 1 No Rainfall	Case 2 Long-Term Rainfall	Case 3 Wetting/Drying cycle
	Grapevine Dam		
<i>No stabilization</i>	8.6	0.83	1.78
<i>0.5% Biopolymer Soil mix. (1.2 m)</i>	11.9	2.46	4.30
Joe Pool Dam			
<i>No stabilization</i>	14.7	0.91	1.27
<i>0.5% Biopolymer Soil mix. (1.2 m)</i>	18.5	2.74	4.45

Results from the analysis indicates an increase of FOS for models where treated soil strength parameters were used. Case 1 shows the stability of slopes in a short-term condition when undrained parameters prevailed within the embankment. Case 2 and Case 3 are more realistic considering residual and fully softened shear strength parameters to simulate long-term rainfall conditions and weathering within the desiccation zone respectively.

The slopes of the dam embankments experienced surface failures which is validated with the computed FOS lower than 1.0 for Case 2. The analysis also indicates that slopes will be stable against weathering cycles in Case 3. However, the FOS with no stabilization at Joe Pool Dam is lower than 1.50 and it is considered to be less than the standard safety value of 1.50 for static stability. The improvement of desiccation zone with Biopolymer treated soil will significantly increase FOS for both, Case 2 and Case 3.

SUMMARY AND CONCLUSIONS

This study introduces a sustainable slope stabilization technique by improving the soil behavior with a biopolymer (guar-gum). Two representative locations at the North Texas region, Grapevine and Joe Pool Dam embankments, were selected to perform slope stability analyses at different scenarios. Both slopes have experienced a large number of surficial failures caused by desiccation cracks formed after a weathering process. Shear strength and swell tests were conducted on soil mixtures prepared at different percentages of biopolymer. The 0.5% biopolymer soil mixture showed to be the most effective based on its high strength and low swell potential.

Soil strength parameters of both, core soil and 0.5% biopolymer soil mixture were used as input parameters for slope stability analysis. The analysis was performed at three different scenarios: No rainfall, long-term rainfall condition and weathering condition. Results showed acceptable factors of safety for Case 1 (No rainfall condition). However, Case 1 simulates the short-term post-construction of each embankment and it is shown for reference only. It is notice that for Case 2 and Case 3, factors of safety increased significantly by using biopolymers as stabilization technique. These two cases consider the actual field situation of both embankments which were previously subjected to weathering cycles. The study highlights the use of residual and fully softened shear strengths for Case 2 and Case 3 respectively. Results for both cases validated the use of Biopolymers (guar-gum) as soil stabilizer on the desiccation zone. A future research is necessary to assess the durability of biopolymer soil mixtures.

ACKNOWLEDGEMENTS

The authors would like to thank the US Army Corps of Engineers for their excellent support provided throughout this research study.

REFERENCES

Ajmera, B., Tiwari, B., Shrestha, D. (2012). "Effect of Mineral Composition and Shearing Rates on the Undrained Shear Strength of Expansive Clays", *Geo-Congress conference 2012*, ASCE, San-Francisco, CA.

Chen R., Zhang L. and Budhu M. (2013). "Biopolymer Stabilization of Mine Tailings" *Journal of Geotechnical and Geoenvironmental Engineering*, ASCE: 1882

Duncan, J.M., and Wright, G.S. (2005). "Soil Strength and Slope Stability", *John Wiley & Sons*, Hoboken, N.J.

Larson S., Newman J., Beverly M. and Nestler C. (2012). "Modified Biopolymers as an Alternative to Petroleum-Based Polymers for Soil Modification". *Engineer Research and Development Center, U.S. Army Corps of Engineers*.

McCleskey, L. K Jr. (2005). "Experimental Investigations to Select Stabilization Methods to Mitigate Embankment Desiccation Cracks in order to Reduce Slope Failures." *Thesis presented to University of Texas at Arlington, Arlington, TX*.

Nugent R., Zhang G., Gambrell R. (2009). "Effect of Exopolymers on the Liquid Limit of Clays and Its Engineering Implications", *Journal of the Transportation Research Board* (No. 2101), Transportation Research Board of the National Academies, Washington, D.C: 34-33.

Puppala, J. A. and Musenda, C. (2000). "Effects of Fiber Reinforcement on Strength and Volume Change Behavior of Expansive Soils", *Proceedings of the 79th Annual Meeting of the Transportation Research Board*, January 9-13, 2000, Washington D. C.

Puppala, J. A., Banavathu, N., Qasim, R. S., Williammee, R., and Intharasombat, N. (2004). "Laboratory Investigations to Address the Use of Compost Amendments to Enhance Expansive Subsoils", ASCE, 2004, *Recycled Materials in Geotechnics*, pp. 91-104

Puppala, A., Chittoori, B., Talluri, N., Le, M., Bheemasetti, T., and Thomey, J. (2013) *Stabilizer Selection for Arresting Surficial Slope Failures: A Sustainability Perspective*. *Geo-Congress 2013*: pp. 1465-1474. doi: 10.1061/9780784412787.147

Skempton, A.W, (1970). "First-time slides in over-consolidated clays", *Geotechnique Vol. 20* (3): 320-324.

Skempton, A.W (1977). "Slope stability of cuttings in brown London Clay", *Proc. 9th International Conference on Soil Mechanics and Foundation Engineering*, Tokyo, Vol. 3: 261-270.

Skempton, A.W. (1985). “Residual Strength of Clays in Landslides, Folded Strata and the Laboratory”, *Geotechnique*, Vol. 35 (1): 3-18.

Tiwari, B., Brandon, L.T., Marui, H.T. and Gyanu R. (2005). “Comparison of Residual Shear Strengths from Back Analysis and Ring Shear Tests on Undisturbed and Remolded Specimens”, *Journal of Geotechnical and Geoenvironmental Engineering*, Vol. 131 (9): 1071-1079.

Yan-Jun Du., Ning-Jun Jiang., Song-Yu Liu., Fei Jin., Singh D.N., Puppala A.J. (2013) “Engineering properties and microstructural characteristics of cement-stabilized zinc-contaminated kaolin”, *Canadian Geotechnical Journal*, 2014, 51:289-302, 10.1139/cgj-2013-0177.

Using Local Soil Microbial Enrichments to Improve Sand Particle Aggregation from CaCO₃ Precipitation

Yu-Syuan Jhuo¹; Li-Hsien Chen²; Hsin-Hsin Tung³; Guang-Huey Lin⁴; and Tsan-Hwei Huang⁵

¹Ph.D. Student, Dept. of Civil Engineering, Nat'l Taiwan Univ., Taiwan. E-mail: ymca0777@gmail.com

²Associate Professor, Dept. of Civil Engineering, Nat'l Taipei Univ. of Technology, Taiwan. E-mail: lhchen@mail.ntut.edu.tw

³Associate Professor, Graduate Institute of Environmental Engineering, Nat'l Taiwan Univ., Taiwan. E-mail: htung@ntu.edu.tw

⁴Associate Professor, Dept. of Microbiology, Tzu Chi Univ., Taiwan. E-mail: guanghuey@gmail.com

⁵Professor, Dept. of Civil Engineering, Nat'l Taiwan Univ., Taiwan. E-mail: thuang@ntu.edu.tw

Abstract: The study uses microbial enrichment cultures to enhance CaCO₃ precipitation around soil particles for strength augmentation. Soil samples were collected from a landslide site near PinKuang River, Hsindian. Enrichment cultures from soil samples using *Thermus* medium can generate alkaline products, which raised the pH from 7.8 to 9.3 and kept there for over a month. Bacteria strains isolated from these enrichments can also increase the surrounding pH from 7.8 to 9.0 in average. Calcium was discovered on the surface of bio-treated sample by electron spectroscopy for chemical analysis system (ESCA), and the treated specimens reduced almost a half of the penetration depth in penetration test. The results from this study may be applied to ground improvement of natural slope in the future.

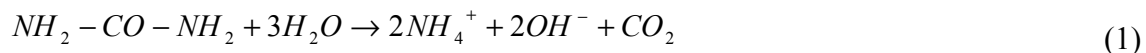
INTRODUCTION

Pores plugged by microbe-induced chemical cements are common in natural world. The phenomena begin early in geological evolution. Sulfur, calcium carbonate, magnetite, greigite, polyphosphate, apatite, technetium oxide have been confirmed to be the direct or indirect products of corresponding bacteria (Castanier et al. 1999; Cavanga et al. 1999; Earlish 1999), which are part of the formation process of sedimentary rocks. Microbes distribute widely, among which the species of microbes in soils are the most diverse population. Every soil microbe has its special capability, such as decomposing plastic or degrading oil contamination. With current environmental concern, it can be considered as a better sustainable option that applying microbial augmentation for geotechnical related issues (Mitchell and Santamarian. 2005). *Bacillus pasteurii* has been used to strengthen

foundation and concrete by CaCO₃ precipitation enhancement (DeJong et al. 2010; Wang et al. 2014). Taiwan lies in subtropical regions and is located in a complex tectonic area between two plates, rainfall and earthquakes happen frequently. The natural environment and human activity together cause frequent landslide and debris flow. Therefore, the objectives of this study were: 1) isolate soil microbes capable of inducing CaCO₃ precipitation from local a landslide site; and 2) apply microbial enrichments to strengthen sand specimens. This technology can be applied to future applications in the natural field for ground improvement.

MECHANISM OF MICROBIOLOGICAL INDUCED PRECIPITATION

The mechanism of microbiological induced precipitation was found in *Bacillus pasteurii*. The chemical equations were shown in equations (1) and (2). The bacteria uses urea as a nutrient, decompose it by urease and produce NH₃ and CO₂, which is called urea hydrolysis. NH₃ is an alkaline substances, when released the pH of surroundings increases. Ca²⁺ and CO₃²⁻ can precipitate in the form of CaCO₃ easily. Since pH is the key factor that influences CaCO₃ production, this study used pH as the detection target to find a proper medium for microbial enrichments in the following experiments.



MEDIUM SELECTION AND pH VARIATIONS

From the mechanism mentioned above, the higher the pH is, the easier Ca²⁺ and CO₃²⁻ ions are to form CaCO₃. The study prepared 5 different media, soil extraction (abbreviated as SE, refer to Lorenz et al. 1991), M9 medium, M9 medium with 100 ml SE, Thermus medium (Ramaley and Hixson 1970) and modified UF medium (Kulkarni and Gadre, 2002). The modified UF medium which is replaced fructose with glucose to facilitate the absorption of microbes and deleted peptone, yeast extract and castor oil to insure that microbes utilize urea as the single source of nitrogen nutrient. 1 g of soil sampled from a landslide site in PingKuang River, Hsindian was placed into every medium and incubated for 3 days and the pH of each culture was measured by pH meter (Figure 1). The initial soil pH is 5.0. For microbial enrichments incubated in SE, Thermus and modified UF, the pH increased. The pH reached an exceptionally high value of 9.3 in Thermus medium. The pH of the other two medium reduce slightly after microbial metabolism. Therefore, the Thermus medium was used in all the experiments hereafter.

To confirm the soil microbes have the same metabolic performance in the same region, four different locations in the landslide site were randomly selected to collect soils. Incubated in medium for 1, 14 and 30 days, the pH variation of four samples are similar, as shown in Figure 2. This verified that the soil microbes in the region of Hsindian landslide site have the same characteristic on producing alkaline substances. As the incubation time increases, pH doesn't change a lot and there is no significant decline, which means that the soil microbes can maintain the preferred alkaline environment for CaCO_3 formation. After tracking for four months, the pH remains at about 9.3 to 9.5.

Figure 3 presents the pH of each separated bacteria in Thermus medium incubated for 3 days. The pH of most bacteria grown in Thermus medium increased to 9.1 in average. Except for T3-5 and T4-6, which lead to relatively lower pH. Comparing with Figure 1, the pH of in microbial enrichments is higher than pure cultures in Thermus medium.

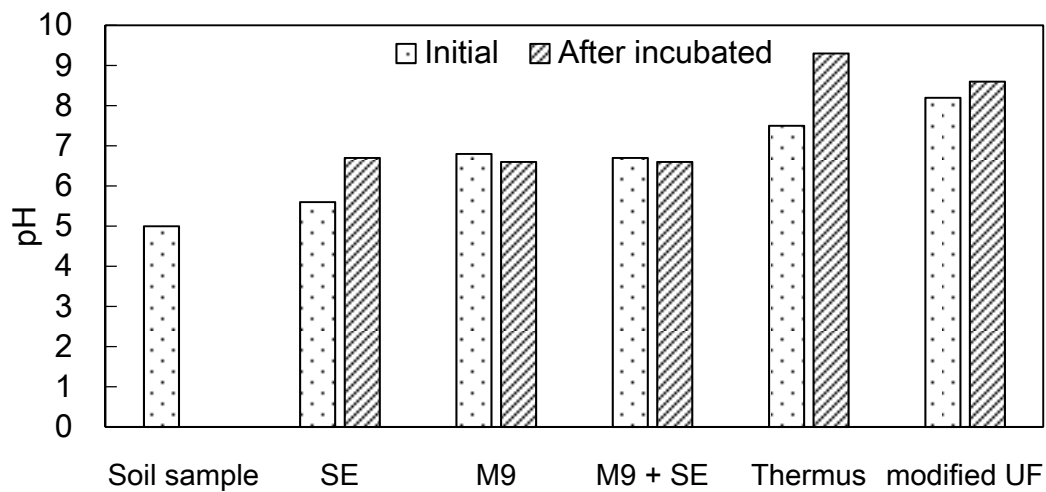


FIG. 1 pH variation of microbial enrichments incubated in 5 different medium for 3 days.

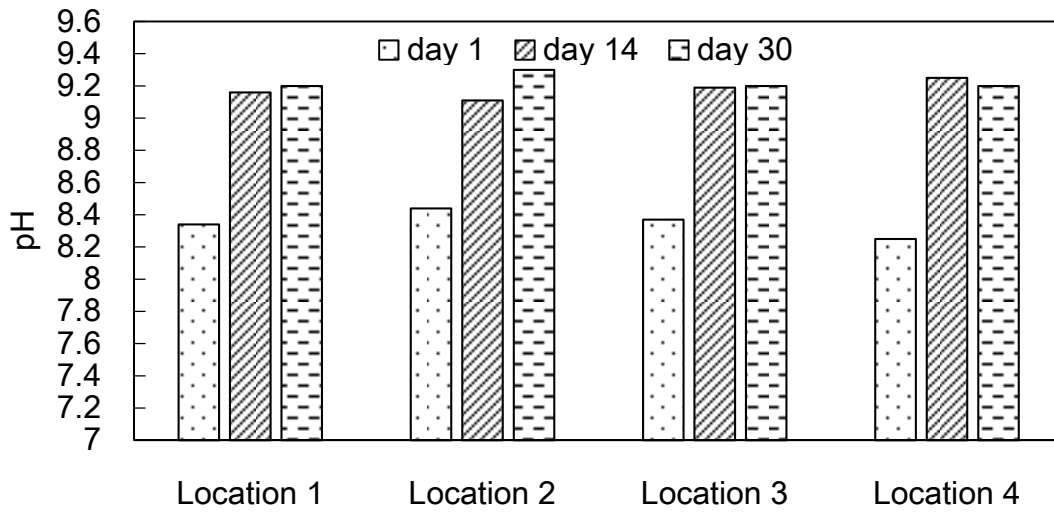


FIG. 2 pH variation of microbial enrichments from 4 different locations soil samples incubated in *Thermus* medium for 1, 14, and 30 days.

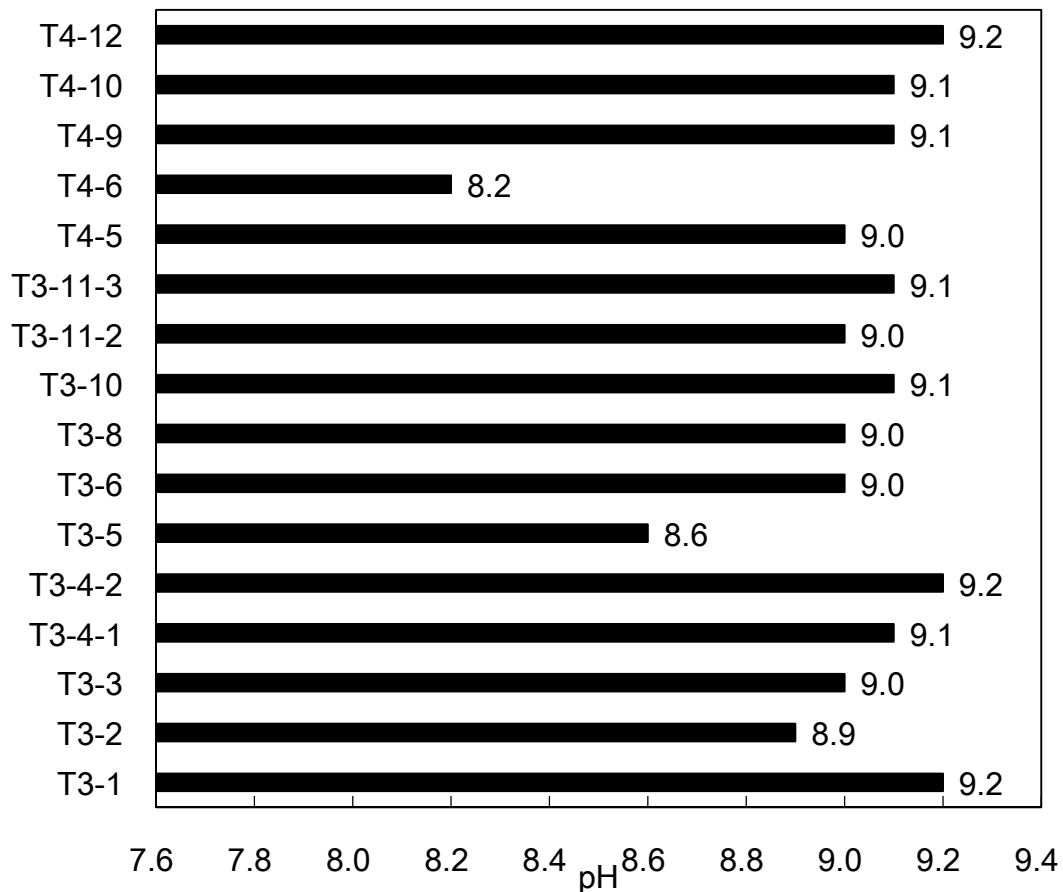


FIG. 3 pH of each separated bacteria incubated in Thermus medium for 3 days.

RELATIONSHIP OF pH AND DIFFERENT SOIL CONTENTS

Since the final goal for this study is to use microbial enrichments to improve strength of natural slope, considering the ratio of soil and medium is important. Figure 4 presents the patterns of pH versus time at different soil contents, pH were increased substantially within 2 days, then remained constant thereafter. When soil content is greater than 20%, the pH values were lower than the soil content which is less than 20% significantly. This indicated that the medium need to be excess in order to provide microbial metabolic need which resulted in desired pH.

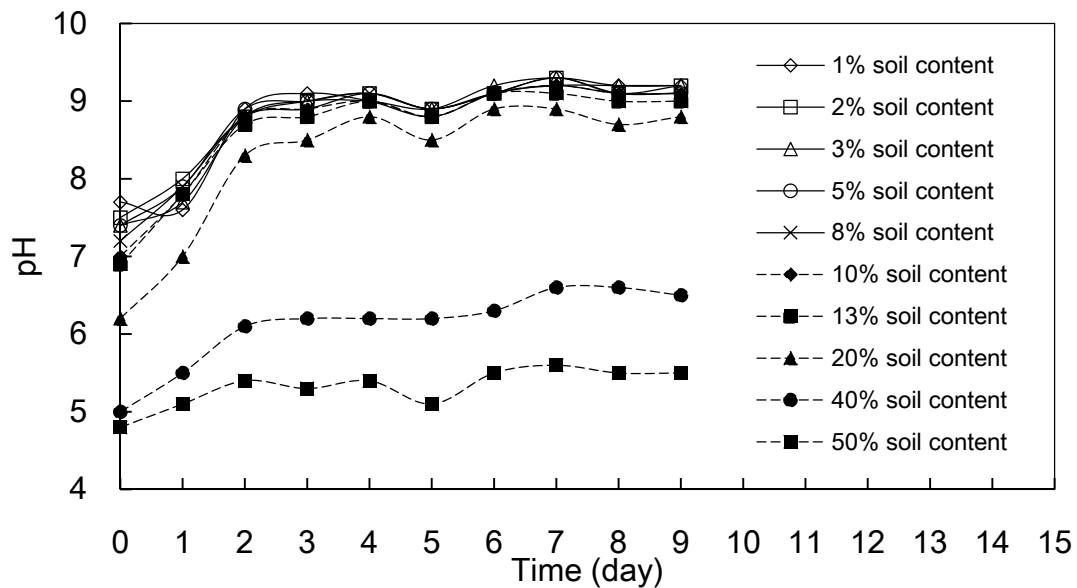


FIG. 4 The relationship of pH and different soil contents in *Thermus medium* versus time.

CONCENTRATION OF TOTAL INORGANIC CARBONATE

CO_3^{2-} in solution can be obtained by adding carbonate compounds, or from CO_2 which is generated from microbial metabolism dissolve in water then transform to HCO_3^- and CO_3^{2-} at pH greater than 8.5. Considering improve sand specimens without adding NaHCO_3 or NaCO_3 , the concentration of total inorganic carbonate (TIC) generated through microbial metabolism need to be monitored, to understand the concentration of CO_3^{2-} which directly affect the formation of CaCO_3 under experimental conditions. Figure 5 shows the TIC concentrations of blank, incubated 7 days and 30 days are 40, 260 and 230 ppm respectively. The pH of culture medium achieved to 9.2, which indicated that the CO_2 in the solution was transformed to HCO_3^- and CO_3^{2-} . However, CaCl_2 concentration can affect microbial growth, reduce metabolism, the pH value cannot further improved.

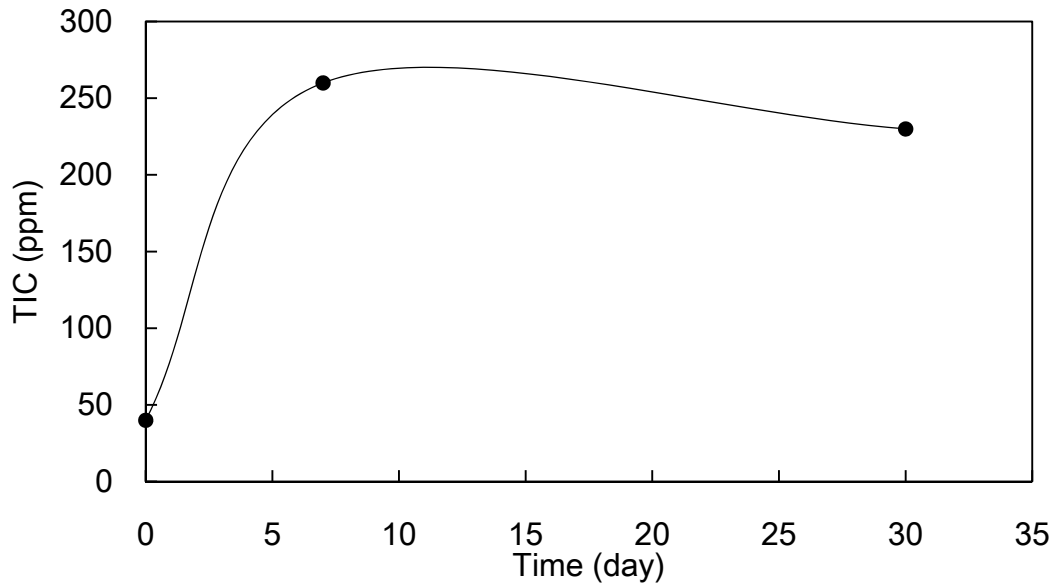


FIG. 5 The total inorganic carbon (TIC) concentrations in enrichment culture

ESCA ANALYSIS AND PENETRATION TEST

ESCA is a machine that analysis chemical elements of sample surface, sample needs to be dried, ESCA can detect three chemical elements simultaneously. This study chose C, O and Ca. The culture medium in the bio-treated samples were removed and placed in 60 °C oven until the samples were completely dry. Figure 6 (a) shows element C and O were detected on untreated samples, Ca was identified from the surface of bio-treated sample with 50 mM CaCl₂. This indicated that the product on the sand surface was CaCO₃ precipitate, which were induced by microbial enrichments. Penetration tests were conducted on both the untreated and bio-treated specimens. Table 1 presents different treatment of each specimen additives and results of penetration tests. The sand samples were sterilized before the experiment. The untreated specimen was sand with ddH₂O and was used as control group. In order to explore the effect of CO₃²⁻ in sand strength improvement, NaCO₃ was added to sample 003. The results showed that the average penetration depth for experimental groups was 8.465 mm, which was nearly only a half of control group. The penetration depth of 003-1 and 003-2 were similar, and the addition of NaCO₃ did not exhibit significant difference. However, all the treated specimens cannot be improved evenly, this problem need to be solved in the future.

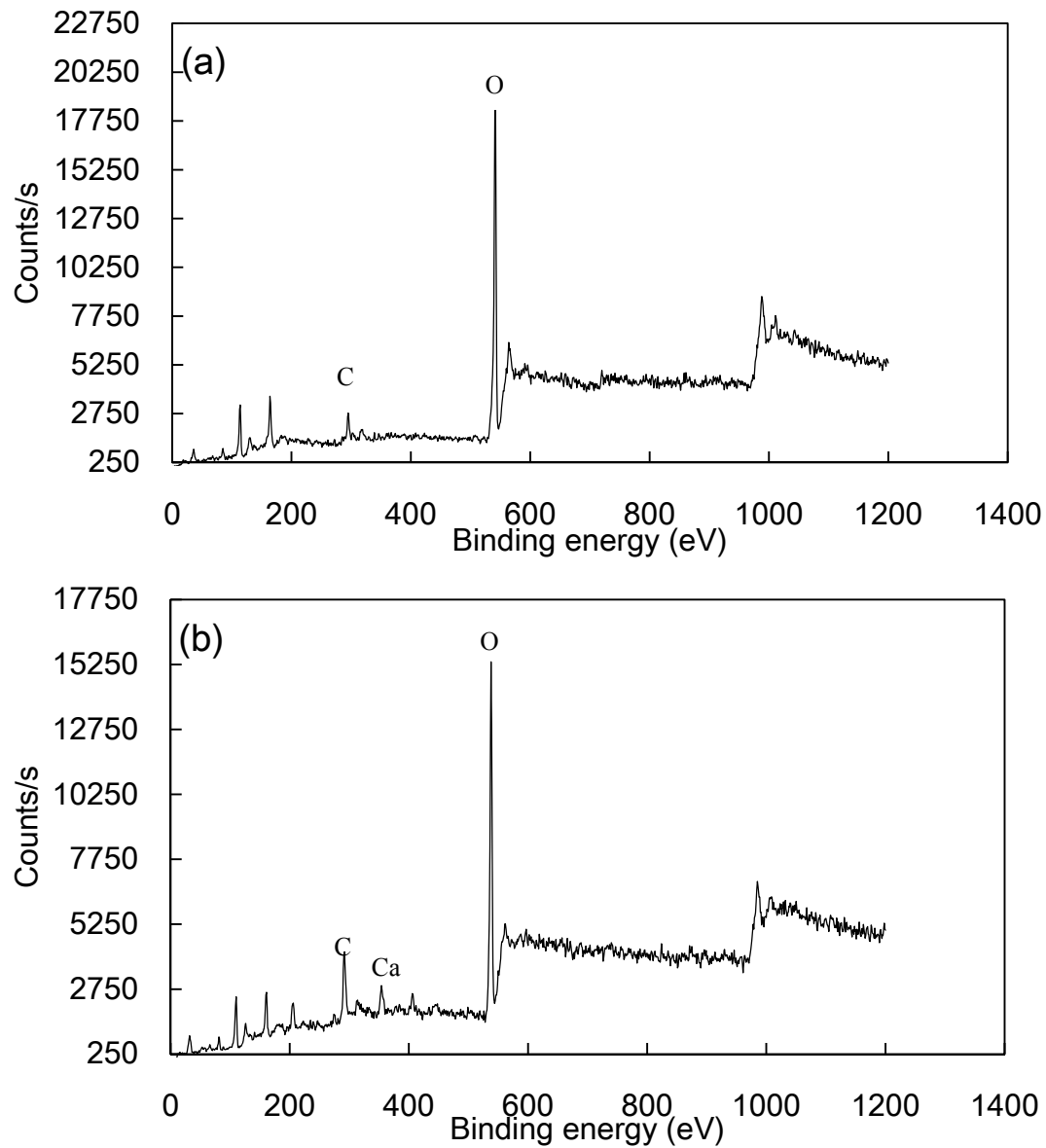


FIG. 6 Chemical elements on the samples surface were detected by ESCA. (a) untreated sand, (b) bio-treated sand with 50 mM CaCl₂.

Table 1 Penetration test results

NO.	Specimen treatment	Average settlement (mm)
000	Sand + ddH ₂ O	15.33
001-1	Sand + microbial medium + 50 mg/L CaCl ₂	8.36
001-2	Sand + microbial medium + 100 mg/L CaCl ₂	8.60
002-1	Sand + microbial medium + 50 mg/L CaCl ₂ + 50 mg/L Na ₂ CO ₃	9.76
002-2	Sand + microbial medium + 100 mg/L CaCl ₂ + 100 mg/L Na ₂ CO ₃	7.14

CONCLUSIONS

Among the five mediums tested, soil microbes of Hsindian landslide incubated in *Thermus* medium produced the highest alkaline substance and increased the pH to 9.3 - 9.5. In the same region, the pH variations in different soil microbial enrichments were the same; the pH in each culture was increased and remained consistent for over a month. The elevated pH can provide a proper environment for CaCO₃ precipitation. The pH of most of the isolated pure culture bacteria incubated in *Thermus* medium can be over 9.0, which was slightly lower than the pH of microbial enrichments. The results exhibit the advantages of mixed cultures. When soil to medium ratio was over 20%, the pH was decreased substantially, which indicated adequate nutrient from the medium might be needed for better metabolic activities. The concentration of TIC produced during the incubation was 260 mg/L, which was ideal for CaCO₃ formation. Ca, C and O were detected on the surface of bio-treated sand sample; this indicated that the product on the sand surface was CaCO₃ that may be induced by microbes. The penetration depths of bio-treated specimens declined one half compared to specimens without treatment. However, the improvement was primary on the surface of sand sample, which may need further exploration. The technology from this study can be a reference for in-situ ground improvement applications. Using the local soil microbial enrichment cultures can be an added benefit for reducing the possible ecological intrusion.

ACKNOWLEDGMENTS

This study was under the sponsorship of the Ministry of Science and Technology (MOST) of Republic of China, under the project (102-2221-E-002-181-).

REFERENCES

- Castanier, S., Merayer-Levrel, G. L. and Perthuisot, J. P. (1999) "Ca-carbonates precipitation and limestone genesis—the microbiogeologist point of view," *Sediment. Geol.*, Vol.126 (1-4): 9-23.

- Cavanga, S. and Clari, P. and Martire, L. (1999). "The role of bacteria in the formation of cold seep carbonates: geological evidence from Monferrato (Tertiary, NW Italy)," *Sediment. Geol.*, Vol.126 (1-4): 253-270.
- DeJong, J. T., Fritzes, M. B. and Nusslein K. (2006). "Microbially induced cementation to control sand response to undrained shear," *J. Geotech. Geoenviron.*, Vol.132 (11): 1381-1392.
- DeJong, J. T., Mortensen, B. M., Martinez, B. C. and Nelson, D. C. (2010). "Bio-mediated soil improvement," *Ecol. Eng.*, Vol. 36 (2): 197-210.
- Ehrlich, H. L. (1999). "Microbes as geologic agents: Their role in mineral formation," *Geomicrobiol. J.*, Vol. 16 (2): 135-153.
- Fischer, S. S., Galinat, K. J. and Bang, S. S. (1999). "Microbiological precipitation of CaCO_3 ," *Soil Biol. Biochem.*, Vol. 31 (11): 1563-1571.
- Gray, D. H. and Sotir, R. B. (1996). "Biotechnical and soil bioengineering slope stabilization: A practical guide for erosion control." *John Wiley & Sons*, New York.
- Jhuo, Y. S., Huang, T. H., Lin, G. H. and Chen, L. H. (2012). "Apply microbiological mineralization of rock formation to granular soil improvement." *Proc., the 25th KKCNN Symp. on Civil Eng.*, Busan, KR, 379-382.
- Kroll, R. G. (1990). Alkalophiles. In: Edwards, C. (Ed.), *Microbiology of Extreme Environments*. McGraw-Hill, New York, pp. 55-92.
- Kulkarni, N., Gadre R. V. (2002). "Production and properties of an alkaline, thermophilic lipase from *Pseudomonas fluorescens* NS2W." *J. Ind. Microbiol. Biotechnol.*, Vol. 28 (6):344-348.
- Mitchell, J. K. and Santamarian, C. J. (2005). "Biological considerations in geotechnical engineering," *J. Geotech. Geoenviron.*, Vol. 131 (10): 1222-1233.
- Muynck, W. D. and Debrouwer, D., Belie, N. D. and Verstraete, W. (2008). "Bacterial carbonate precipitation improves the durability of cementitious materials." *Cement Concrete Res.*, Vol. 38 (7): 1005-1014.
- Ramaley, R. F. and Hixson, J. (1970). "Isolation of a nonpigmented, thermophilic bacterium similar to Thermophilic bacterium similar to *Thermus aquaticus*." *J. Bacteriol.*, Vol. 103 (2):527-528.
- Riding, R. (2000). "Microbial carbonates: the geological record of calcified bacterial-algal mats and biofilms." *Sedimentology*, Vol. 47 (1): 179-214.
- Wang, J. Y., Snoeck, D. and Vlierberghe, V. S., Verstraete, W. and Belie, N. D. (2014). "Application of hydrogel encapsulated carbonate precipitating bacteria for approaching a realistic self-healing in concrete." *Constr. Build Mater.*, Vol. 68: 110-119.

Chemo-Mechanical Coupling in Bonded Geomaterials: Representations in Two Scales

Alessandro Gajo¹; Francesco Cecinato¹; and Tomasz Hueckel²

¹Dept. of Civil, Environmental and Mechanical Engineering, Univ. of Trento, Trento, Italy.

²Dept. of Civil and Environmental Engineering, Duke Univ., Durham, NC.

Abstract: Chemo-mechanical couplings in geomaterials have received increasing attention in recent years for a number of applications, ranging from the stability of slopes and coastal structures to geological CO₂ sequestration. Chemical processes may result in strengthening or weakening effects, the latter being particularly critical for safety assessment in civil and energy engineering applications. In this work, coupling of chemical and mechanical processes in cemented soils and rocks is investigated by means of a micro-structure inspired model, consisting of an assembly of grains and bonds undergoing dissolution or deposition of mineral mass, affecting geometrical characteristics of the system and thus determining the evolution of specific surface area and of bond cross-sectional area at the micro-scale, and of porosity at the macro-scale, which become key variables linking the micro-scale and macro-scale mechanisms. The resulting micro- to macro-scale model is validated against the available experimental evidence, consisting of a number of different chemo-mechanical experiments on calcarenite. The model is thus shown to provide a flexible framework for consistent interpretation of experimental loading paths, and can be readily extended to more complex materials or to incorporate additional effects.

INTRODUCTION

Terzaghi (1950) in his paper on Mechanism of Landslide discusses the chemical weathering affecting rock of any kind which “weakens intergranular bonds” leading to a decrease in cohesion and to a progressive decrease in Factor of Safety, due to chemical weathering. Also in the case of loess, water from external reservoirs is identified as responsible for removing soluble binders and destroying intergranular bond(s), with the same macroscopic effect of a decreasing cohesion. In a more modern day context one needs to add that the dissolution of cementation bonds may be dramatically enhanced by an increase in acidity of the run-off water, namely from an acid rain (e.g. see Zhao et al. 2011).

Further, the recent interest in geological CO₂ sequestration brings challenges in predicting the effectiveness of injections since CO₂, upon being injected, reacts with

brine producing a weak acid, which can in turn react with the surrounding geomaterial, especially if the reservoir rock has fully carbonate composition (e.g. limestone, see Andre et al. 2010 and Grgic 2011), or is carbonate-cemented (e.g. calcite cemented sandstone, see Canal et al. 2014). On the other hand, the technique of acid softening of rocks prior to hydraulic fracturing in unconventional gas and oil recovery or heat recovery from geothermal reservoirs poses interesting questions in ensuring the control of the process (Hu & Hueckel 2011).

The aim of this work is to investigate coupling of chemical and mechanical processes involved in weakening or strengthening of bonded geomaterials by means of a micro-structure inspired model. The micro-scale model is calibrated on (but it is not limited to) a regular array of grains and bonds undergoing dissolution or deposition of mineral mass, which both affect geometrical characteristics of the system. Simple reactions of dissolution and deposition between pore fluid and solid minerals are considered, thus complex phenomena involving solid-solid mass exchange are neglected for the sake of simplicity. Variable geometrical characteristics are used to determine the evolving specific surface area and the bond resisting cross-sectional area at the micro-scale, and variable porosity at the macro-scale, which become key variables linking the micro-scale and macro-scale mechanisms. At the macro-scale, a reactive chemo-plasticity model (e.g. Loret et al. 2002) is combined with a model for bonded geomaterials (e.g. Gens & Nova 1993), while kinetic rate equations must be adapted for dissolution/precipitation accounting for their acidity sensitivity (e.g. Sjoberg 1976).

Schematically, based on the kinetics of dissolution/deposition reaction of different minerals, two main cases are discussed, namely the case of both reactive grains and reactive bonds (e.g. calcarenite, where both grains and bonds are made of calcium carbonate) and the case of non-reactive grains and reactive bonds (e.g. silicic sand with carbonate bonds). While in the former case the timescales of dissolution/deposition of grains and bonds are comparable, in the latter case the timescale of reaction of bonds is negligibly small compared to that of the grains. Both cases are relevant to typical CO₂ sequestration problems, depending upon composition of the host rock. Further, the proposed framework could be easily extended to situations involving the presence of different families of cementation bonds characterized by different strengths and chemical dissolution properties (e.g., in the context of CO₂ sequestration, see Hangx et al. 2013).

MODEL OUTLINE

Two types of information can be obtained from the existing literature: information on the material strength change and on stiffness change, due to mechanical loading and chemical dissolution - that is typically provided by macro-scale experiments; and information about the chemical processes of dissolution and precipitation of the key minerals, which is obtained from micro-scale information. Consequently, we construct a two-scale model, which includes: (i) a macro-scale chemo-elasto-plastic model, where both the apparent preconsolidation stress and the apparent isotropic tensile strength depend on the material microstructural features, and (ii) an integrated

model for mass change of minerals, in the framework of an idealized evolving micro-scale structure of grains and bonds, subject to removal or addition of mineral mass, localized mechanical failure and chemical healing.

The macro-scale, in the considered case, is described by continuum variables of (elastic and plastic) strain and stress tensors, continuum free energy, and compressive and tensile strength. Such variables all depend on a series of macro-scale variables, such as the mass change of the minerals, and on micro-structural quantities (as the geometry of bonds and grains). The macroscopic continuum variables depend through phenomenological functions on micro-structural variables.

The macroscopic constitutive model is developed assuming a yield function along the lines of an existing approach for bonded geomaterials (e.g. Gens & Nova 1993), in which an isotropic tensile strength function is included, as an extension of the modified Cam Clay model. An associated flow rule is adopted for the sake of simplicity. The expression of the yield locus includes two macroscopic quantities, p_{tens} and p_{comp} , representing the increase of tensile and compressive strength, compared to uncemented soil, due to the presence of cementation bonds (Gajo et al. 2015). Coupling with the micromechanical behavior is introduced by assuming that p_{tens} and p_{comp} depend on the mean specific cross section area a_b of all mechanically active cementing bonds (corresponding to unbroken bonds, thus ‘actively’ contributing to the macroscopic strength).

Further, a simplified hardening relationship similar to that of Cam Clay is adopted, assuming negligible elastic compressibility (Gajo et al. 2015). However, the proposed constitutive framework is not limited to the above outlined simple assumptions.

The macroscopic strain tensor is decomposed into additive elastic and plastic parts. The macroscopic elastic behavior of the material is described in the framework of hyperelasticity and elasto-plastic coupling (Hueckel 1976), and can thus be deduced upon defining a suitable elastic free energy density function. To account for the presence of both mechanically and chemically interacting bonds, the standard linear elasticity form of the free energy function of the uncemented solid skeleton (i.e. the unbonded soil) $\varphi_g = \varphi_g(\boldsymbol{\varepsilon}_e)$ is modified, based on phenomenological interpretations, into a more general function:

$$\varphi = \varphi(\boldsymbol{\varepsilon}_e, \boldsymbol{\varepsilon}_p, m_b) \quad (1)$$

A macroscopic variable m_b is the time-integrated mass change of all mechanically active cementing bonds per unit volume, from a reference configuration m_{b0} ($\Delta m_b > 0$ implies an increase of bond mass with respect to the reference configuration).

From the chemical point of view, for the case of only reacting bonds, during cement dissolution a fraction of cement bonds, which in a general situation carries a fraction of the overall stress, disappears, causing the reduction of a_b . This leads to a stress increase in the remaining fractions of the bonds, thus inducing strains at constant stress level. As a result, cement dissolution induces a decrease of soil stiffness with

associated strains (if dissolution occurs at constant stress) or a decrease of soil stiffness with an associated decrease of applied stress (if dissolution occurs at constant strain). On the other hand, cement deposition induces an increase of material stiffness, at constant stress and strain. This behavior is taken into account with a step-wise form of the elastic energy (Gajo et al. 2015).

In the case of both reactive solid grains and bonds, the additional consideration must be made that if the number of cementing bonds is negligible, grain dissolution implies some macroscopic volumetric strain. In fact, in the limit of null active cementing bonds, grain dissolution is associated to volume compression (due to the decrease of grain volume). The volumetric effect of grain dissolution in uncemented soil is completely analogous to the volumetric effect of a decrease of temperature in the grain material, in contrast with the effect of deposition, which is assumed to produce no volumetric strain.

From the macroscopic point of view, the net mass change \dot{m} within the REV due to dissolution and/or deposition is controlled by chemical kinetics. The rate at which the minerals aggregate or dissociate is proportional to the specific reactive surface area a_r per unit volume of the reacting materials. The macroscopic quantity a_r (with units m^2/m^3) corresponds to the area per unit volume of all interfaces of the porous skeleton that are exposed to chemical interaction, i.e. the areas that are actually in contact with the pore fluid.

Further, a chemo-mechanical rate equation is defined via an empirical function, expressing the rate of change of mechanically active bonds per unit volume, \dot{N}_{ba} , including the two mechanisms of destructuration and cement deposition, $\dot{N}_{ba} = f(\dot{m}_b, \dot{\epsilon}_p)$. As a result, in general cement dissolution/deposition \dot{m}_b affects soil's mechanical strength in two ways, namely (i) through the restoration of previously broken bonds and (ii) through the reduction/increase of the bond cross sections. In fact, in general cement dissolution/deposition is expected to affect both porosity and the thickness of bonds.

The constitutive concepts described above are based on two key macroscopic quantities, the cross section of active bonds a_b and the reactive surface area a_r , which must be defined in terms of microscopic variables. To relate the evolution of microscopic variables with the macroscopic chemo-mechanical description of the material, reference is made to a simplified microscopic geometry. As an example, in Figure 1a, a 2D schematic of the considered geometry at the microscopic scale inspired from microscope photographs of thin sections of calcareous rocks is shown, in the general case where grains might not be in direct contact, but they are linked by cementation bonds that are assumed to be isotropically distributed. In a large porosity configuration such as that illustrated in Figure 1, the geometry of bonds can be approximated with that of a cylinder, and the geometry of grains can be represented by that of a sphere. In Figure 1b, a 2D schematic is shown of the case where, regardless of the size of bonds, grains remain in direct contact, resulting in a simplification of the bonds' geometry.

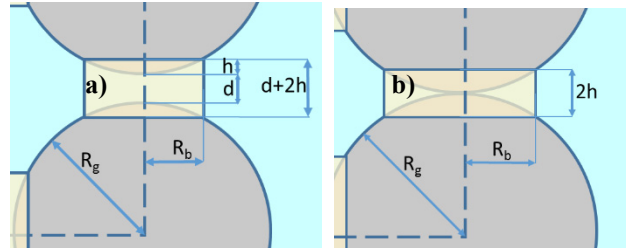


FIG. 1. Schematic of the considered simplified geometry at large porosity, (a) in a general case where the spherical grains are not in direct contact, but they are linked by cylindrical bonds, and (b) in the case where the spherical grains are in direct contact, and bonded by cylindrical bonds.

The key cross-scale functions that are developed by considering the material microstructure are the expressions of $a_r = f(R_b, R_g, L_b, d, v_b, v_g, \boldsymbol{\varepsilon})$ and $a_b = f(R_b, \boldsymbol{\varepsilon}_p, a_r)$, where R_b, R_g are the mean bond and grain radii, L_b the mean bond length, d the mean distance between grain edges, v_b, v_g the bond and grain specific volume and $\boldsymbol{\varepsilon}, \boldsymbol{\varepsilon}_p$ the total and plastic strain tensor. The interested reader is referred to Gajo et al. (2015) for further details.

MODEL VALIDATION

The above described model was numerically integrated through a fully implicit, backward Euler integration scheme, showing adequate convergence.

The model capabilities to reproduce the experimental chemo-mechanical behavior of bonded geomaterials were tested by simulating a series of loading paths along the lines of experimental datapoints reported in the literature, after having deduced the relevant parameters as much as possible from published data.

As a first example, the model is tested by simulating unconfined compression tests on saturated calcarenite, by first reproducing an acid weathering phase and subsequently a mechanical loading phase, and comparing the simulations with the experimental data of Ciantia et al. (2014). In this context, a variable expressing the ‘degree of dissolution’ can be introduced as $\xi = M_{dis}/M_0$, where M_{dis} represents the dissolved mass and M_0 the initial mass of reacting solids, so that $\xi=0$ for the unweathered material and $\xi=1$ at complete dissolution of the reacting solids.

As discussed in section 2, the equivalent elastic modulus of the bonded material E depends on both the elastic properties of calcite cement and of the unbonded granular material, and is calculated upon taking the second derivative of the free elastic energy density with respect to elastic strain. Thus, we obtain an expression of the form

$$E = E_g (1 - a_b^\alpha) + E_b a_b^\alpha \quad (2)$$

where E_g and E_b the elastic moduli of uncemented solid skeleton and of completely cemented soil (which is approximated with that of pure calcite) respectively, and parameter $\alpha = 1.8$. It should be noted that eqn. (2) is also consistent with mixture theory-based rules to obtain the equivalent parameters of a composite mass, typically employed in soil improvement calculations (e.g. see Ou et al. 1996). Moreover, eqn. (2) includes elasto-plastic coupling, because the cross section of active bonds a_b depends on plastic strains, which may induce damage of elastic stiffness.

In Figure 2a, simulations of stress-strain curves during unconfined compression tests are plotted at different values of ξ , together with analogous experimental data. To adequately reproduce experimental conditions, the simulation consisted of two steps, namely of a first step reproducing exposure to an acid solution up to the target value of ξ , and of a second step simulating the unconfined compression test in the weathered material. The reproduction of experimental data is especially accurate until the ultimate strength is attained. After the peak, simulations exhibit a smaller amount of softening than experiments, overall showing a less markedly fragile behavior. Since the post-peak response is typically deeply affected by shear or compaction banding which leads the conventional behavior to be much different from that of a homogeneously deforming sample, additional ad-hoc constitutive assumptions were not introduced for more accurate reproduction of this phenomenon.

Further, oedometer tests on calcarenite samples previously subjected to different degrees of weathering (Ciantia et al. 2014) were reproduced. In Figure 2b, satisfactory oedometer test simulations are shown in terms of vertical strain versus vertical stress, at different degrees of dissolution. Experimental data from Ciantia et al. (2014) are also reported in the graph for comparison.

Finally, in Figure 3 the stress path of Castellanza and Nova (2004)'s oedometer test on calcarenite in the (p, q) plane is simulated, and fittingly compared to experimental data. The path A-B represents the mechanical loading phase. Upon reaching point B, the vertical load is kept constant and the acid weathering phase starts, gradually causing an increase of radial stress, revealing as a linear decrease of deviatoric stress with increasing mean stress (path B-C).

In all of the above described examples, satisfactory agreement between the model prediction and the experimental data is obtained, after adequate parameter calibration. The slight over-prediction of elastic stiffness for increasing dissolution that can be observed in Figure 2 is due to the adoption of a unique parameter set to reproduce all of the considered experiments (cf. Gajo et al. 2015, Table 1 therein). These results suggest that the presented model provides a powerful and flexible framework for adequately reproducing different experimental chemo-mechanical loading paths.

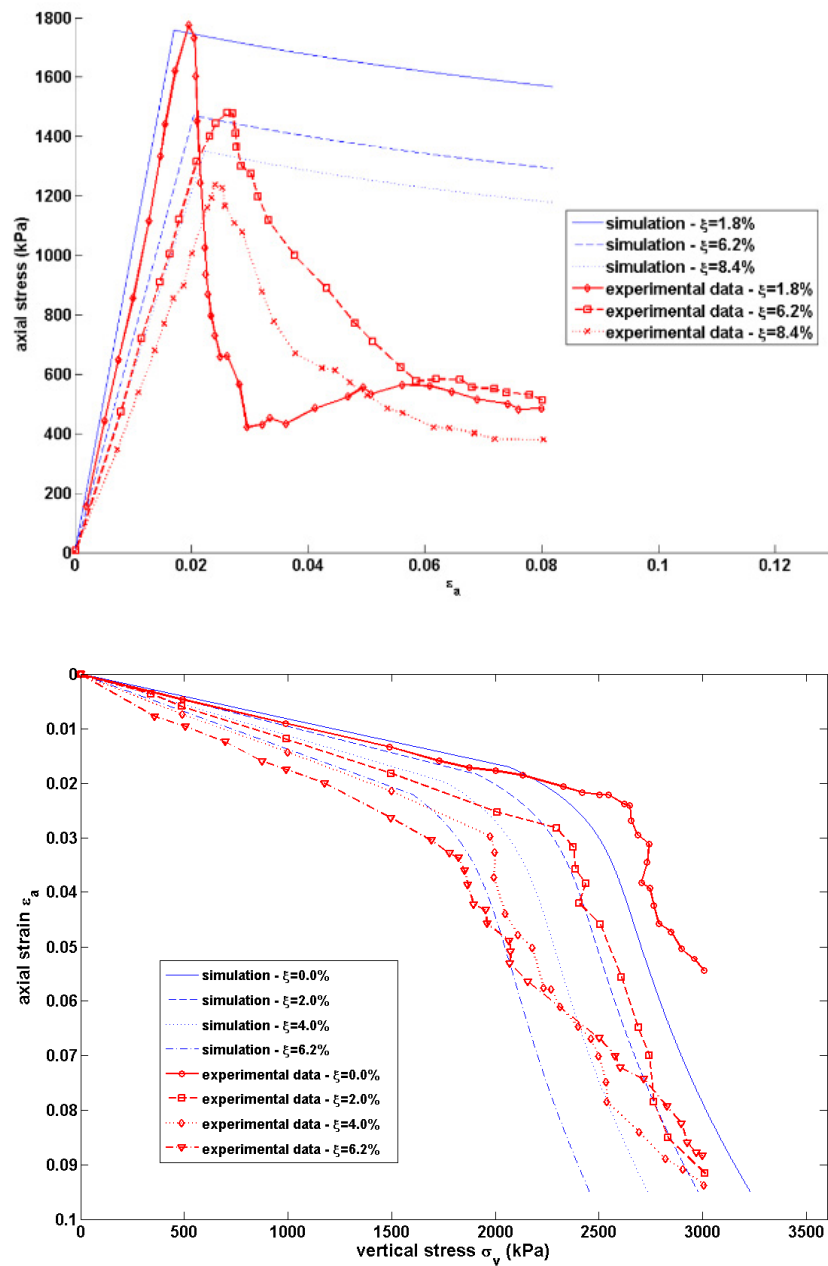


FIG. 2. Comparison of simulations and experimental data in terms of (a) deviatoric (axial) stress versus axial strain in unconfined compression tests on calcarenite, (b) axial strain versus vertical stress in oedometer tests on calcarenite, carried out after weathering up to different values of degree of dissolution. Experimental data from Ciantia et al. (2014)

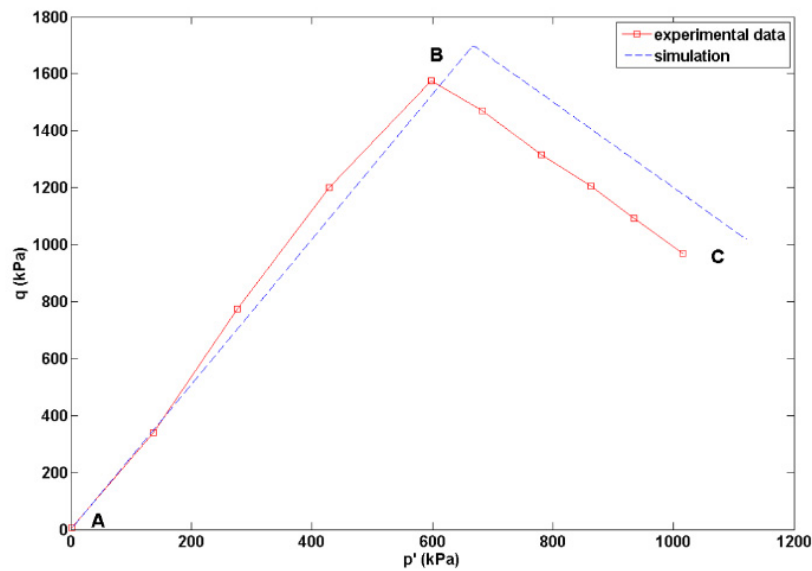


FIG. 3. Comparison of simulations and experimental data in terms of deviatoric stress versus mean effective stress in an oedometer test on calcarenite. Path A-B represents the loading phase in unweathered conditions, path B-C represents the acid weathering phase at constant applied load. Experimental data from Castellanza and Nova (2004).

CONCLUSIONS

In this work an innovative, general two-scale modelling framework able to account for the key aspects of the coupled chemo-mechanical behavior of bonded granular materials is presented, and validated against experimental evidence. The proposed framework includes an integrated model for mass change of minerals, in the frame of an idealized evolving micro-scale structure of grains and bonds, subject to removal or addition of mineral mass, localized mechanical failure and chemical healing, and a macro-scale chemo-elasto-plastic model, where both the yield stress under isotropic compression and the isotropic tensile strength depend on the material microstructural features, incorporating elasto-plastic coupling to describe the degradation of elastic properties due to mechanically induced debonding.

For the sake of simplicity, the distribution of bonds and their cross sections are assumed isotropic and the model presentation is based on simple linear isotropic elasticity and Cam Clay yield function. The proposed constitutive framework is not, however, limited to these simple assumptions and could be straightforwardly applied to more complex elasticity models and yield functions. Moreover, the proposed framework could be easily extended to situations involving the presence of different families of cementation bonds characterized by different strengths and chemical dissolution properties.

It can be concluded that the presented model provides a powerful and flexible framework for adequately reproducing different experimental chemo-mechanical loading paths. It is worth remarking that the model is to be intended as an open

framework rather than being specialized on a particular material type. Different additional effects, such as mechanical anisotropy, could easily be incorporated depending on modeling needs.

ACKNOWLEDGMENTS

The first two authors gratefully acknowledge financial support from European Union FP7 project under contract number PIAPP-GA-2013-609758-HOTBRICKS.

The third author gratefully acknowledges financial support from the “Visiting Professor 2013” programme of the University of Trento.

Dr. Matteo Ciantia of UPC and Prof. Riccardo Castellanza of the University of Milan, Bicocca are acknowledged for kindly providing some of their data for our calibrations.

REFERENCES

- Andre L, Azaroual M, Menjot A. (2010) Numerical Simulations of the Thermal Impact of Supercritical CO₂ Injection on Chemical Reactivity in a Carbonate Saline Reservoir Transport in porous media; 82 (1):247-274
- Canal J, Delgado-Martin J, Barrientos V, Juncosa R, Rodriguez-Cedrùn B, Falcon-Suarez I (2014) “Effect of supercritical CO₂ on the Corvio sandstone in a flow-thru triaxial experiment”, in *Rock Engineering and Rock Mechanics: Structures in and on Rock Masses*, Alejano, Peruchó, Olalla & Jimenez (Eds), Taylor & Francis, London.
- Castellanza R and Nova R. (2004) Oedometric tests on artificially weathered carbonatic soft rocks, *J. of Geotechnical and Geoenvironmental Eng. ASCE*; 130(7): 28 – 739
- Ciantia MO, Castellanza R and di Prisco C. (2014) Experimental study on the water-induced weakening of calcarenites, *Rock Mech. Rock Eng.*; DOI 10.1007/s00603-014-0603-z
- Gajo A., Cecinato F., Hueckel T. (2015) A micro-scale inspired chemo-mechanical model of bonded geomaterials; submitted to *International Journal of Rock Mechanics and Mining Sciences*.
- Gens A, Nova R. (1993) “Conceptual bases for a constitutive model for bonded soils and weak rocks”, in *proc. International Symposium on Geotechnical Engineering of Hard Soils - Soft Rocks*; Athens, Greece.
- Grgic D. (2011) Influence of CO₂ on the long-term chemomechanical behavior of an oolitic limestone, *Journal of Geophysical Research*; 116, B07201, doi:10.1029/2010JB008176.
- Hangx S J T, Spiers C J, Peach C J (2010) Creep of simulated reservoir sands and coupled chemical-mechanical effects of CO₂ injection, *Journal of Geophysical Research*; 115, B09205, doi:10.1029/2009JB006939.
- mechanical effects of CO

- Hu LB and Hueckel T. (2011) “Coupled chemo-mechanics in evolving permeability in geomaterials”, *Computational Geomechanics (ComGeo II)*; edited by Pietruszczak and Pande, Cavtat-Dubrovnik, 599-608
- Hueckel T. (1976) Coupling of elastic and plastic deformations of bulk solids; *Meccanica* 11(4): 227-235
- Loret B, Hueckel T, Gajo A. (2002) Chemo-mechanical coupling in saturated porous media: elasto-plastic behaviour of homoionic expansive clays, *International Journal of Solids and Structures*; 39: 2773-2806
- Ou C, Wu T and Hsieh H. (1996) Analysis of deep excavation with column type of ground improvement in soft clay. *Journal of Geotechnical Engineering*; 122(9): 709–716.
- Sjoberg EL. (1976) A fundamental equation for calcite dissolution kinetics. *Geochim. Cosmochim. Acta*; 40: 441–447.
- Terzaghi K. (1950) Mechanism of landslides; *Geol. Soc. Am. Engineering Geology*; Berkeley, pp.89-123.
- Zhao Y, Cui P, Hu LB, Hueckel T. (2011) Multi-scale chemo-mechanical analysis of the slip surface of landslides in the Three Gorges, China. *Science China Technological Sciences*; 54: 1757-1765

Potential Impact of Thermal Pressurization on the Fault Response to CO₂ Injection in Carbon Capture and Storage Projects

Kimia Mortezaei, S.M.ASCE¹; and Farshid Vahedifard, M.ASCE²

¹Ph.D. Student, Dept. of Civil and Environmental Engineering, Mississippi State Univ., Mississippi State, MS 39762. E-mail: km1745@msstate.edu

²Assistant Professor, Dept. of Civil and Environmental Engineering, Mississippi State Univ., Mississippi State, MS 39762. E-mail: farshid@cee.msstate.edu

Abstract: In this study, we investigated the impact of thermal pressurization (TP) on temperature and pore pressure changes within the shear zone of a slipping fault under supercritical CO₂ injection. Injecting CO₂ into the subsurface increases pore pressure in the reservoir that may cause slip on a pre-existing fault leading to seismic events. As a weakening mechanism, TP of fault fluid during slip tends to reduce frictional resistance by increasing pore pressures along the fault shear zone. We employed a coupled thermo-hydro-mechanical finite element model to compare the response of fault shear zone during CO₂ injection with and without considering the TP effect. The CO₂ injection was simulated using a poroelasticity model. For the model with the TP effect, a simple constitutive law was implemented in the poroelasticity model to couple pore pressure changes with temperature rise due to frictional heating. The results indicated that, in general, TP can lead to a significant increase of pore pressure built up during CO₂ injection. The effects of hydraulic diffusivity and slip velocity on pore pressure and temperature changes were evaluated.

INTRODUCTION

Over the past decade or so, induced seismicity due to high pressure fluid injection has been a point of controversy for emerging energy geo-technologies such as unconventional hydrocarbon reservoirs, enhanced geothermal systems, and carbon capture and storage (CCS) projects (NRC 2013). There are many unanswered questions regarding the induced seismicity potential associated with CO₂ injection for storage purposes, primarily due to lack of large-scale injection experience and some unique characteristics of CCS operations (NRC 2013).

When CO₂ is injected, pore pressure in the reservoir increases and effective stress decreases. The changes in effective stress and pore pressure cause expansion in the reservoir leading to deformation of the overburden (Harjes, 1997). This phenomena may threaten the storage integrity by creating new fractures and reactivating existing faults (e.g., Rutqvist 2012). In the presence of an existing fault combined with favorable injection characteristics, fault slip occurs which may increase the leakage risk and can induce low-magnitude seismic events (Bachu 2008, NRC 2013).

Once fault slip initiates, two mechanisms with opposite impacts compete to control slip and rate of slip (Segall and Bradly 2012). On one hand, shear-induced dilatancy of the fault core tends to increase the fault permeability helping the fault zone to be increasingly undrained and consequently, to decrease the fluid pressure. On the other hand, if the fault slip occurs fast enough, it becomes harder for the fluid flow to keep up with dilatancy. . Consequently, frictional heating is generated leading to a fault weakening mechanism which increases fault fluid pressure and decreases frictional resistance within the fault shear zone (Rice 2006, Segall and Bradly 2012). An earthquake occurs if the thermal weakening process during the fault's early slip takes over the shear-induced dilatancy due to the release of tectonic stress driving the fault motion (Wibberley and Shimamoto 2005).

Recently, several CCS operations have been conducted in faulted areas (e.g., Castelletto et. al. 2013, Teatini et. al. 2014). There is very limited, if any, information on the impact of TP on the response of fault shear zone during CO₂ injection in the vicinity of a stressed fault. This paper presents results of series 2D coupled Thermo-Hydro-Mechanical (THM) simulations using the finite element method to investigate the effects of TP on pore pressure and temperature changes within the shear zone of a stressed fault during CO₂ injection.

NUMERICAL SIMULATION

We developed a coupled THM finite element model in COMSOL Multiphysics 5.1 to numerically monitor pore pressure and temperature changes within the fault core during CO₂ injection. To evaluate the impact of TP, comparative studies were performed between two sets of models for each parameter of interest: one set without TP and the second set with TP. The CO₂ injection was simulated using a poroelasticity model. For the model with the TP effect, a simple constitutive law for TP developed by Rice (2006) was implemented in the poroelasticity model to couple pore pressure changes with temperature rise due to frictional heating. For this purpose, the TP equation was incorporated in COMSOL's PDE interface and was coupled with the poroelasticity module of the software.

It is noted that this study is not dealt with the nucleation phase but rather with the coseismic period after that the thermal weakening dominates rate and state dependent friction. Similar approach has been used in other TP studies (e.g., Andrew 2002, Rempel & Rice 2006). Thermal pressurization can be analyzed in two phases: earthquake nucleation and high slip rate. The study of the interaction between TP and rate- and state-dependent friction through an entire earthquake from nucleation to ceasing stage is still an open issue. While some studies (e.g., Kanamori and Heaton, 2000; Andrews 2002) indicated that TP is significant during the coseismic period and

major earthquakes, recent considerations suggest that TP has a substantial contribution to earthquake nucleation, as well (Segall & Rice 2006, Schmitt et. al. 2011). Here, we studied the TP effect after slip initiation and after sufficient shear heating has occurred to dominate rate- and state-dependent friction.

The following sections briefly present the constitutive equations which were used to simulate TP followed by a description of the numerical model which was developed. Due to space limitation, we do not present the governing equations of single phase flow and geomechanics associated with the poroelasticity theory but they can be found in literature (e.g., Mortezaei & Vahedifard 2015).

Thermal Pressurization Constitutive Model

Generally, the following factors affect pore pressure during slip: 1) shear heating; 2) porosity change; 3) heat flow; 4) fluid flow and 5) dehydration reaction (Sulem et al., 2007). In this study, we ignored the dehydration reaction factor as well as porosity changes. Such an assumption is consistent with that used in similar TP simulations (e.g., Andrews 2002; Bizzarri & Cocco 2006; Rice 2006). Also, due to small diffusion distance perpendicular to the fault compared to the parallel direction as well as small variations in properties and forces, it is reasonable to assume that fluid flow in the direction perpendicular to the fault is one dimensional (Andrews 2002; Bizzarri & Cocco 2006; Rice & Cocco 2007; Rice 2006; Segall & Rice 2006). The fault-normal stress (σ_n) is assumed to remain constant during the earthquake slip, as previously assumed in similar studies (e.g., Bizzarri & Cocco, 2006; Rice & Cocco 2007). The coupled shear heating and pore pressure variations can be expressed as:

$$\frac{\partial P}{\partial t} = \frac{\alpha_f}{\beta_f} \frac{\partial T}{\partial t} + \omega \frac{\partial^2 P}{\partial y^2} \quad (1)$$

$$\frac{\partial T}{\partial t} = \frac{\tau_f v}{\rho_{bulk} C_{bulk} w} + c_{th} \frac{\partial^2 T}{\partial y^2} \quad (2)$$

where P is pore pressure, T is temperature, t is time, β_f is fluid compressibility, α_f is fluid expansivity, ω is the hydraulic diffusivity and is defined as $\omega = K/(\mu\beta_f\phi)$, K is permeability, μ is dynamic viscosity of fluid, ϕ is porosity, y is the spatial coordinate normal to the fault, τ_f is the shear strength which can be expressed as $\tau_f = f(\sigma_n - P)$, σ_n is normal stress, f is frictional coefficient, v is slip rate (velocity), ρ_{bulk} is the density of bulk composite, C_{bulk} is the specific heat of the bulk composite at constant pressure, w is the slip zone width, and C_{th} is thermal diffusivity. The detailed derivation of the above equations can be found in Andrew (2002), Rice (2006) and Bizzarri & Cocco (2006).

Geometry and Input Parameters

The main objective of this study is to simulate the response of a fault shear zone during CO₂ injection. Several field observations have shown that slipping takes place

within an extremely thin shear zone of 1 mm thick or less (Rice 2006). The shear zone is embedded in a finely granulated fault core with thickness ranging from 10 mm to 10 cm and that core itself lies within the damage zone of granulated rock having thickness of 1 to 10 m (Rice 2006). Based on the aforementioned dimensions, we numerically simulated a plan view of a vertical strike-slip faulting regime in which the blocks are sliding horizontally along the vertical fault. Fig. 1 depicts the plan view model of the strike-slip fault which was used in the numerical simulation. The base model represents a fault shear zone with thickness of $w = 1$ mm within the fault core of 5 cm thick, and is located at the depth of 1,500 m, a representative depth for CCS operations. CO₂ injection was simulated by a point source in the center of the fault zone considering that the injection well breaks into the fault. We selected reasonable annual injection rates for a full-scale injection site and then scaled them down based on the size of the numerical model and used the scaled injection rates in our simulations. Here if we assume that CO₂ is injected at the rate of 1 million tons/year per well, it corresponds to an average injection rate of 32 kg/s per well. For a 1000 m long horizontal well, the rate of injection for one centimeter would be 0.00032 kg/s/cm. Therefore, the injection rate becomes 0.0016 kg/s for the current numerical model (i.e., 5 cm width \times 0.00032 Kg/s/cm). Three injection rates were examined in this study: 0.001 (base model), 0.0015, and 0.002 kg/s/m.

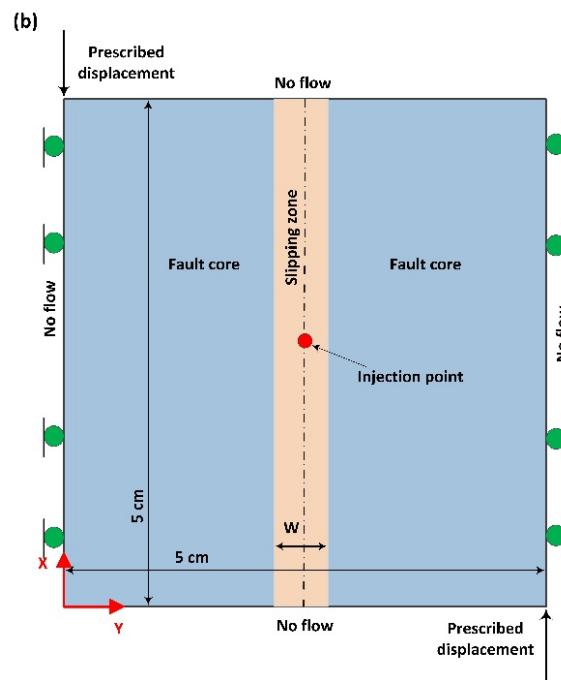


FIG 1. Model geometry used in numerical simulations, plan view

We set the initial conditions assuming linear pore pressure and temperature gradients (9.81 MPa/km and 25°C/km depth, respectively), with the no-flow condition applied at all four boundaries (Fig. 1). Mechanical boundary conditions are rollers at the top and bottom of the model. Since we modeled the plan view of the strike-slip fault, both major and minor principal stresses (i.e., S_1 and S_3) are

horizontal. We assumed a principal stress ratio of $S_1/S_3 = 0.6$ to generate initial stresses in the model. This stress ratio corresponds to a dynamic friction coefficient of 0.5 which is reported in similar studies (e.g., Bizzarri & Cocco 2006; Rice 2006) and is also used in the current study. As shown in Fig. 1, prescribed displacements, depending upon the designated slip velocity, were applied to the top-left and bottom-right corners of the model. Since this study aims to model the response of a stressed fault during the coseismic period, the fault slip velocity needs to be representative of high slip velocity. Different ranges have been defined to consider slip velocity as “fast”. For example, Di Toro et al. (2004) defined high slip velocity to be in the range of 0.1-2 m/s. Several researchers (e.g., Andrews, 2002; Rice, 2006; Sulem et al. 2007) considered the velocity of 1 m/s for investigating TP. In this study, three fault slip rates of 0.1 m/s (base model), 0.5 m/s and 1 m/s were examined. It was assumed the slip rate remains constant during the event. Note that the slip rate profile across the slipping zone is linear and is a function of time and position ($V(y,t) = V_{slip} y/(0.5w)$). Velocity of zero was assigned to the outside of this zone.

Table 1 shows input parameters which were used in the model. The fault properties such as porosity and permeability as well as the geometry of the fault shearing zone were selected based on those reported in Bizzarri & Cocco (2006) and Rice (2006). The fluid parameters such as compressibility, density, and dynamic viscosity were selected based on those reported for supercritical CO₂ in the literature (e.g., Law & Bachu 1996; Span & Wagner 1996; Vilarrasa et al. 2010; Burke 2011). The material is considered to be homogeneous and isotropic and its properties are constant during time.

Table 1. Input parameters

Material	Symbol	Value	Unit
Permeability (base)	K	10^{-19}	m^2
Porosity	ϕ	0.025	1
Thermal expansivity of the fluid	α_f	2.5×10^{-3}	K^{-1}
Fluid compressibility	β_f	1.2×10^{-4}	Pa^{-1}
Dynamic viscosity of the fluid	μ	2×10^{-5}	Pa s
Fluid density	ρ_f	600	$Kg m^{-3}$
Density of bulk composite	ρ_{bulk}	2700	$Kg m^{-3}$
Thermal conductivity	k	1.35	$J m^{-1} s^{-1} K^{-1}$
Dynamic frictional coefficient	f	0.5	1
Young's modulus	E	10	GPa
Poisson's ratio	ν	0.25	-
Initial temperature	T_0	50	$^{\circ}C$

RESULTS

Previous investigations (e.g., Andrews 2002; Noda and Shimamoto 2005; Wibberley & Shimamoto 2005) show that several factors such as the slip rate, the depth and the width of the shear zone can influence the TP mechanism. Rate of frictional heating and the rate of fluid pressure build-up are significantly affected by slip rate. The hydraulic transport properties can be determined by the depth as well as

the normal stress. Rate of frictional heating and the rate of TP are controlled by the width of the slip zone (Kurz et al. 2008). Here we discuss the parametric study results for various values of hydraulic diffusivity (ω) as well as slip velocity (v). In order to illustrate the effect of TP, two set of models were developed and compared for each parameter of interest. In the first set of models, only poroelasticity was taken into account whereas in the second set, poroelasticity was coupled with the TP model.

Effect of Hydraulic Diffusivity

Hydrodynamic properties of faults can be primarily defined in terms of hydraulic diffusivity (ω), which is related to K and storage capacity per unit sample volume (β_f). In the current study, we investigated three different values of $K = 10^{-19}$, 10^{-18} and 10^{-17} m^2 which correspond to $\omega = 10^{-9}$, 10^{-8} and $10^{-7} \text{ m}^2/\text{s}$, respectively. Fig. 2 depicts shear resistance and pore pressure evolutions for the base model ($w = 1 \text{ mm}$, $\omega = 10^{-9} \text{ m}^2/\text{s}$). As shown, since the normal stress was assumed to remain constant during slip, the strength will reduce to 7 MPa and pore pressure approaches 25 MPa. Fig. 3 presents the comparative results of pore pressure evolution for three cases of ω for the models with and without TP effects. For each case, a comparison should be performed at the time when the pore pressure reaches the residual state in the model with the TP effect. This time varies from 0.23 to 0.56 seconds for the models with $\omega = 10^{-9}$ and $10^{-7} \text{ m}^2/\text{s}$, respectively. As expected, a higher hydraulic diffusivity value leads to a lower pore pressure build up in both sets of models. This is due to the fact that higher ω leads to a higher rate at which fluid diffuses from the shear zone and subsequently, to a lower pore pressure build up. Comparison of two sets shows that accounting for TP will increase pore pressure by about 50%. This difference corresponds to 8.7, 8 and 9.6 MPa for $\omega = 10^{-9}$, 10^{-8} and $10^{-7} \text{ m}^2/\text{s}$, respectively. It is shown that pore pressure response is very similar for the low values of ω (i.e., 10^{-8} and $10^{-9} \text{ m}^2/\text{s}$). Furthermore, increasing ω reduces the effect of TP, and therefore reduces the time needed to reach the residual state. In other words, the effective normal stress reduction is larger for smaller values of hydraulic diffusivity.

In Fig. 4 temperature change is illustrated versus time for three different ω values. As shown, as ω increases the temperature field exhibits lower increase during injection. Because higher ω improves drainage capacities of the shear zone, it corresponds to a higher fault strength and a decreased maximum temperature. While temperature develops significantly by increasing ω to $10^{-7} \text{ m}^2/\text{s}$, it is very close for the other two cases of $\omega = 10^{-8}$ and $10^{-9} \text{ m}^2/\text{s}$. The maximum temperature of 530 °C was reached in the lowest ω ($10^{-9} \text{ m}^2/\text{s}$). Temperature decreases to 526 and 491 °C for $\omega = 10^{-8}$ and $10^{-7} \text{ m}^2/\text{s}$, respectively.

Effect of Slip Velocity

Fig. 5 shows pore pressure changes at different slip velocity (v), ranging from 0.1 to 1 m/s. It is noted that the slip velocity had no significant impact on the results for the model without the TP effect. As expected, pore pressure build up for the coupled poroelasticity-TP model is highly affected by slip velocity. As shown in Fig. 5, a reduction in the slip velocity from 1 to 0.1 m/s resulted in a decrease of pore pressure

from 25 MPa to 23 MPa. All of the coupled poroelasticity-TP models led to higher pore pressure levels than that in the poroelasticity without TP model. For example, for the model with $v = 1$ m/s, the pore pressure difference between the models with and without TP becomes approximately 8 MPa at the instability time of the coupled poroelasticity-TP model. It is evident from Fig. 5 that the instability time becomes shorter and the fault is weakened faster for larger slip velocities. For $v = 0.1$ m/s, the maximum pore pressure is reached after 0.23 s whereas it becomes 0.08 and 0.05 s for the slip rates of 0.5 and 1 m/s, respectively. These results can be explained by considering the fact that a higher velocity generates higher frictional heat leading to a greater pore pressure buildup. Temperature changes for different v values are illustrated in Fig. 6. As expected, a larger v yields a higher temperature increase. In the model with $v = 1$ m/s, the maximum temperature of 537 °C was attained compared to 526 °C and 491 °C for the slip velocity values of 0.5 and 0.1 m/s.

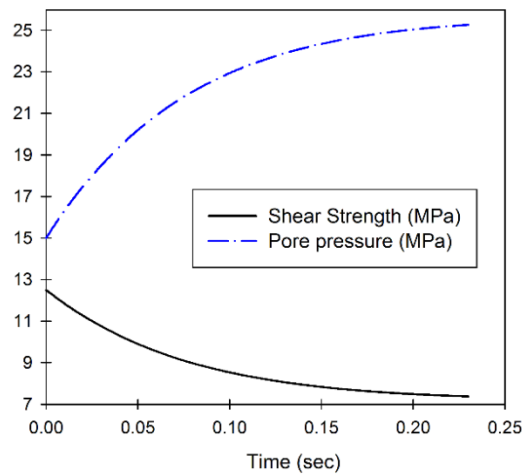


FIG 2. Shear resistance and pore pressure versus time.

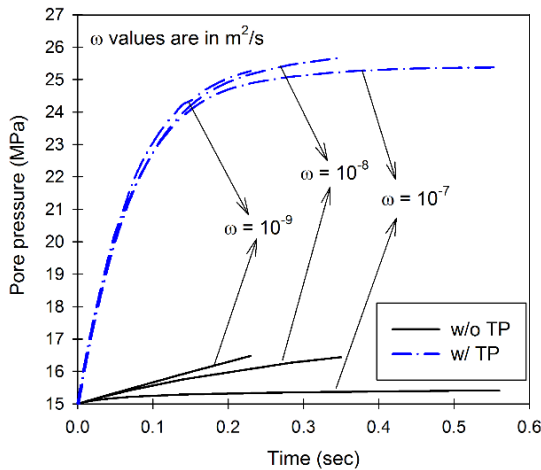


FIG 3. Pore pressure versus time at the center of the fault shear zone.

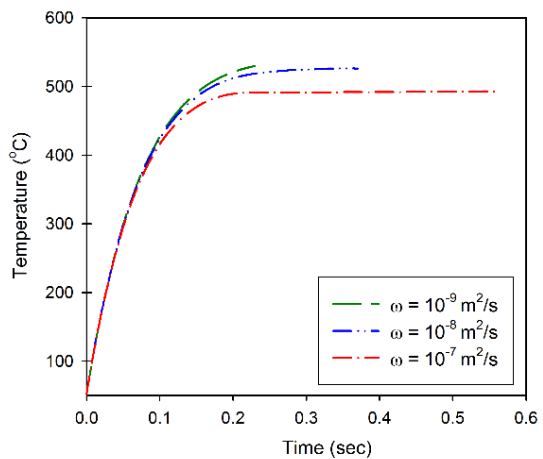


FIG 4. Temperature versus time for different slipping zone thicknesses.

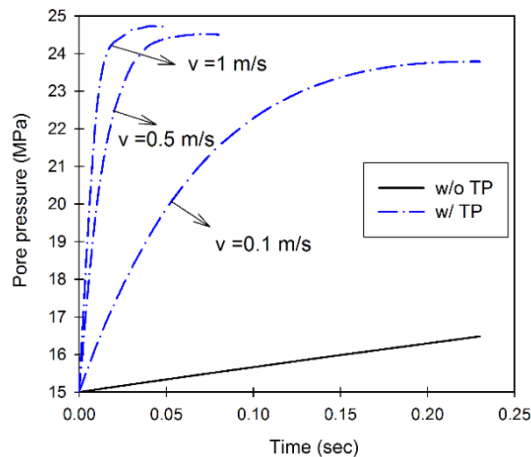


FIG 5. Pore pressure versus time for various slip velocities.

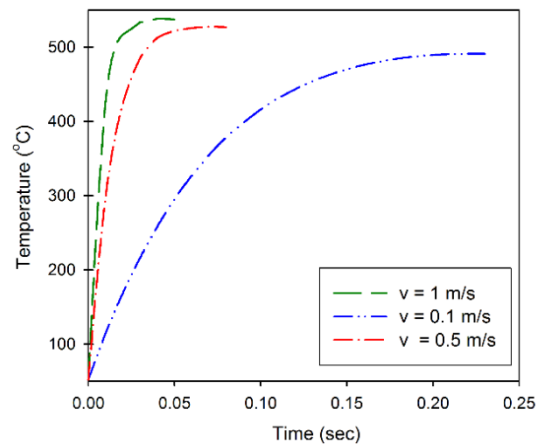


FIG 6. Temperature change versus time for various slip velocities.

SUMMARY AND CONCLUSIONS

In this paper, we investigated the impact of thermal pressurization (TP) on fluid behavior and temperature rise within the fault shear zone in CCS projects. Once fault slip initiates, it generates frictional heating which increases pore pressure and decreases effective normal stress along the fault. We developed a coupled Thermo-Hydro-Mechanical (THM) model using a simple TP constitutive model coupled with poroelasticity to capture pore pressure development as a result of both shear heating-induced TP and fluid injection. In this model, porosity, friction and normal stress changes were assumed to be constant during slip. The model was aimed to capture the response of the fault shear zone after the nucleation phase and during domination of TP, and when a seismic slip speed of 0.1 m/s was attained. Two sets of models, with and without TP effect, were built and compared. We conducted the simulations for various values of hydraulic diffusivity and slip velocity. The following conclusions can be drawn from the numerical simulation results:

1. The comparative simulation study of two models, with and without the TP effect, indicated that in all cases ignoring the TP role can lead to a significant underestimation of the pore pressure buildup during CO₂ injection.
2. We found that as hydraulic diffusivity decreases, reduction in the effective normal stress and effect of TP becomes larger. Considering TP, pore pressure develops as much as 50% more than in the model without TP. Temperature rise decreases about 39 °C by increasing hydraulic diffusivity from 10⁻⁷ to 10⁻⁹ m²/s.
3. Regarding slip velocity, a reduction of 2 MPa in pore pressure was observed by altering the velocity rate from 1 to 0.1 m/s as a result of higher frictional heating. For the velocity of 1 m/s, temperature increases ten times higher than its initial value.

ACKNOWLEDGEMENT

This material is based upon work partially supported by the National Strategic Planning & Analysis Research Center (nSPARC) at Mississippi State University.

REFERENCES

- Andrews, D. J. (2002). "A fault constitutive relation accounting for thermal pressurization of pore fluid." *Journal of Geophysical Research: Solid Earth (1978–2012)*, 107(B12), ESE-15.
- Bachu, S. (2008). "CO₂ storage in geological media: role, means, status and barriers to deployment." *Progress in Energy and Combustion Science*, 34(2), 254-273.
- Bizzarri, A., & Cocco, M. (2006). "A thermal pressurization model for the spontaneous dynamic rupture propagation on a three-dimensional fault: 1. Methodological approach." *Journal of Geophysical Research: Solid Earth (1978–2012)*, 111(B5).
- Castelletto, N., Teatini, P., Gambolati, G., Bossie-Codreanu, D., Vincké, O., Daniel, J.-M., Battistelli, A., Marcolini, M., Donda, F., Volpi, V., (2013), "Multiphysics modeling of CO₂ sequestration in a faulted saline formation in Italy." *Advances in Water Resources*, 62:570-587.
- Di Toro, G., Goldsby, D. L., & Tullis, T. E. (2004). "Friction falls towards zero in quartz rock as slip velocity approaches seismic rates." *Nature*, 427(6973), 436-439.
- Harjes, H. P. (1997). "Injection-induced earthquakes and crustal stress at 9 km depth at the KTB deep drilling site, Germany." *Journal of Geophysical Research*, 102(B8), 18-477.
- Heaton, T. H. (1990). "Evidence for and implications of self-healing pulses of slip in earthquake rupture." *Physics of the Earth and Planetary Interiors*, 64(1), 1-20.
- Kanamori, H., & Heaton, T. H. (2000). "Microscopic and macroscopic physics of earthquakes." *Geophysical Monograph-American Geophysical Union*, 120, 147-164.
- Kurz, W., Imber, J., Wibberley, C. A. J., Holdsworth, R. E., & Collettini, C. (2008). "The internal structure of fault zones: fluid flow and mechanical properties." *Geological Society, London, Special Publications*, 299(1), 1-3.
- Law, D. H. S., & Bachu, S. (1996). "Hydrogeological and numerical analysis of CO₂ disposal in deep aquifers in the Alberta sedimentary basin." *Energy Conversion and Management*, 37(6), 1167-1174.
- Mortezaei, K., & Vahedifard, F. (2015). "Numerical simulation of induced seismicity in carbon capture and storage projects." *Geotechnical and Geological Engineering*, 33(2), 411-424.
- NRC (2013). "Induced Seismicity Potential in Energy Technologies." *National Research Council, National Academies Press*, Washington, DC, pp. 300.
- Noda, H., & Shimamoto, T. (2005). "Thermal pressurization and slip-weakening distance of a fault: An example of the Hanaore fault, southwest Japan." *Bulletin of the Seismological Society of America*, 95(4), 1224-1233.
- Rempel, A. W., & Rice, J. R. (2006). "Thermal pressurization and onset of melting in fault zones." *Journal of Geophysical Research: Solid Earth (1978–2012)*, 111(B9).
- Rice, J. R. (2006). "Heating and weakening of faults during earthquake slip." *Journal of Geophysical Research: Solid Earth (1978–2012)*, 111(B5).
- Rice, J. R., & Cocco, M. (2007). "Seismic fault rheology and earthquake dynamics." *Tectonic Faults: Agents of Change on a Dynamic Earth*, 99-137.
- Rutqvist, J. (2012). "The geomechanics of CO₂ storage in deep sedimentary formations." *Geotechnical and Geological Engineering*, 30(3), 525-551.

- Schmitt, S. V., Segall, P., & Matsuzawa, T. (2011). "Shear heating-induced thermal pressurization during earthquake nucleation." *Journal of Geophysical Research: Solid Earth (1978–2012)*, 116(B6).
- Segall, P., & Bradley, A. M. (2012). "The role of thermal pressurization and dilatancy in controlling the rate of fault slip." *Journal of Applied Mechanics*, 79(3), 031013.
- Segall, P., & Rice, J. R. (2006). "Does shear heating of pore fluid contribute to earthquake nucleation?." *Journal of Geophysical Research: Solid Earth (1978–2012)*, 111(B9).
- Sulem, J., Lazar, P., & Vardoulakis, I. (2007). "Thermo-poro-mechanical properties of clayey gouge and application to rapid fault shearing." *International journal for numerical and analytical methods in geomechanics*, 31(3), 523-540.
- Span, R., & Wagner, W. (1996). "A new equation of state for carbon dioxide covering the fluid region from the triple-point temperature to 1100 K at pressures up to 800 MPa." *Journal of physical and chemical reference data*, 25(6), 1509-1596.
- Teatini, P., Castelletto, N., & Gambolati, G. (2014). "3D geomechanical modeling for CO2 geological storage in faulted formations. A case study in an offshore northern Adriatic reservoir, Italy." *International Journal of Greenhouse Gas Control*, 22:63-76.
- Vilarrasa, V., Bolster, D., Dentz, M., Olivella, S., & Carrera, J. (2010). "Effects of CO2 compressibility on CO2 storage in deep saline aquifers." *Transport in porous media*, 85(2), 619-639.
- Wibberley, C. A., & Shimamoto, T. (2005). "Earthquake slip weakening and asperities explained by thermal pressurization." *Nature*, 436(7051), 689-692.

Aseismic Upgrade of an Existing Railway Embankment by Double Sheet Pile and Tubular Pile Walls

Takefumi Takuma, A.M.ASCE¹; Hiroyuki Nishimura²; and Shigeru Kambe³

¹Senior Manager - Engineering, Giken America Corp., 5770 Hoffner Ave., Suite 101, Orlando, FL 32822.

²Manager, Japan Press-in Assoc., 2-4-12 Konan, Minato-ku, Tokyo, 108-0075 Japan.

³Manager, Giken America Corp., 5770 Hoffner Ave., Suite 101, Orlando, FL 32822.

Abstract: The East Japan Railway Company, which owns and operates major long distance and commuting lines in and north of Tokyo, is upgrading existing track embankments per the new aseismic guidelines so they will be resilient to withstand strong earthquakes in the future. Some of the embankment retrofit projects are installing double sheet pile walls with tie-wires or tie-rods that connect them to minimize the possibility of liquefaction of the embankments. The construction next to live railway tracks, especially those on embankments, requires extremely low vibration and allows for no ground settlement as part of special attention to railway safety. In addition, the work space is often quite limited due to steep slopes of the embankment, neighboring structures, overhead catenary lines, and/or overcrossing bridges with minimal distance from the tracks. The press-in piling method has been successfully adopted to drive sheet piles and tubular piles to meet these requirements for pile installation within a few meters of the rail company's busy commuter lines.

INTRODUCTION

During Japan's 143 years of railway history, there have been numerous earthquake-caused damages to the railway tracks recorded. The railway embankments have been especially vulnerable to seismic motions due to the fact that many of them were built during the latter half of 19th century and the first half of 20th century without taking seismic effects into account. The 1968 Tokachi-oki Earthquake (Magnitude M=7.8) in northern Japan caused extensive embankment damage at many locations on the Tohoku line, which prompted the government's railway agency to do thorough investigation on the factors involved in the damage. Yamamoto (1985) summarized the findings and categorized the embankment damage in the following 5 types (Figure 1 can also be referred to).

- (1) Type I Sliding slope – most commonly found and caused by earthen structures of loose slope surfaces with well-compacted embankment and/or seismic vibration with pore pressure.
- (2) Type II Collapsed embankment – caused by topographical conditions of sloped subgrades, geological conditions of very soft subgrades and/or existence of “water pockets”.
- (3) Type III Vertically cracked embankment - caused by structural conditions of insufficient compaction and/or liquefaction of subgrades.
- (4) Type IV Settlement of embankment – caused by conditions of very soft subgrades.
- (5) Type V Failure due to liquefaction – caused by materials of pure sand and/or vibration and pore pressure.

Solid Lines: Shape after an Earthquake

Hatched Areas: Lost Embankment due to an Earthquake

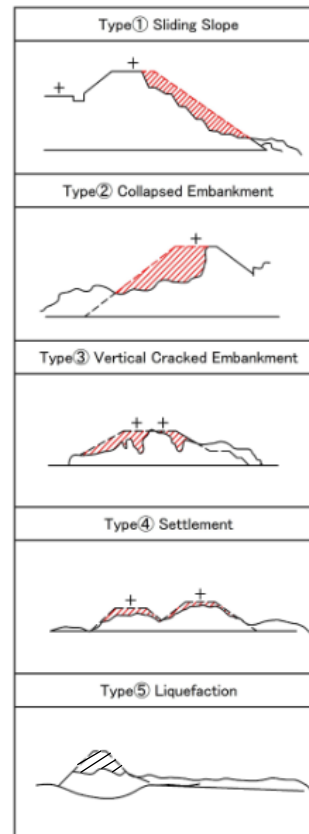


FIG. 1 Five Types of Railway Embankment Failures (Yamamoto, 1985)

Not so many aseismic upgrades on earthen structures had been conducted compared to those on concrete structures such as viaducts and bridge abutments due to the fact that earthen structures could be reconstructed with relative ease. However, many embankment failures caused by the East Japan Great Earthquake of March 11, 2011 prompted the railway company to start upgrading the existing high embankments (more than 6 m) of high traffic lines in the southern Tokyo area, where another strong earthquake is expected any time soon.

Kanda and Tateyama (2014) summarized aseismic design guidelines for railroad structures in Japan. Based on the guidelines, the railway company recently prepared a design manual for their aseismic upgrades of earthen structures with input from outside experts before a series of aseismic retrofit projects. It specifies the maximum design settlement amounts and the factors of safety for a Level 1 earthquake (the seismic level that a structure to be designed is expected to encounter at least once during its service life). It has separate figures for general fill and fill behind bridge abutments, which tend to suffer from elevation gaps between embankments and abutments in addition to lateral movement due to an earthquake (Kitsunai, 2015).

The typical retrofit methods for embankments are as follows. Figure 2 also illustrates them.

- (1) Placing soil nails in an embankment (see also Figure 3).
- (2) Placing ground anchors in an embankment.

- (3) Placing double sheet pile walls in both slopes of an embankment with tie-rods or tie-wires connecting them (this will be discussed more in details later).
- (4) Placing in-situ piles or tubular piles through the slope of an embankment.
- (5) Ground improvement.

Method	Section Views
Soil Nails	
Ground Anchors	
Sheet Pile + Tie Rods or Tie Wire	
Driving Piles	
Ground Improvement	

FIG. 2 Typical Embankment Aseismic Reinforcement Methods



FIG. 3 Soil Nails with Concrete Grids on an Embankment Slope (East Japan Railway Co., 2014)

PRESS-IN PILING METHOD

The press-in piling method utilizes a reaction force derived from a few previously installed piles to push in the next pile by hydraulic force. The press-in piling equipment of this type operates on top of previously-installed piles and moves forward on its own; Figure 4 shows this sequence. Due to the fact that this method is not using vibratory or percussive force to drive the pile, it is regarded as an environmentally-friendly piling method.

Its advantages are:

- (1) Low noise and practically vibration free (White, et al., 2002).
- (2) The equipment size is relatively small and its clamping point is much lower than those of other piling methods. This fact enables the equipment to work in physically tight working conditions, horizontally and vertically.
- (3) With attachments, it can drive piles into hard soil effectively.
- (4) It can achieve much more accurate pile installation due to a combination of better control of the piles and lower clamping points compared with other piling methods.

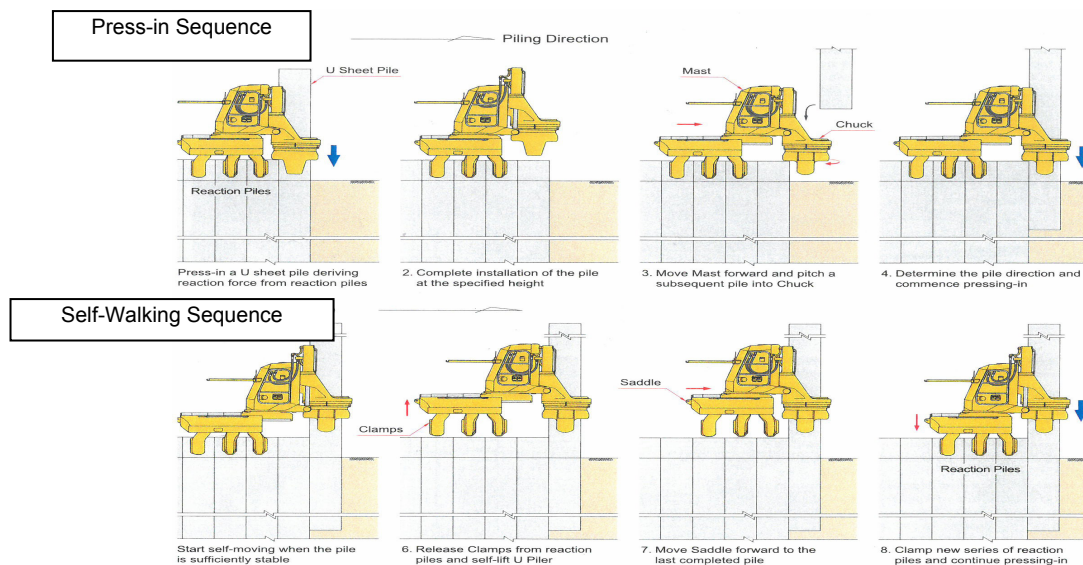


FIG. 4 Sequence of the Press-in Piling and its “Self-Walking”

GRB SYSTEM

The GRB (Giken Reaction Base) system comprises of a few auxiliary equipment in addition to the press-in pile driver to transport, pitch, and drive piles all on previously driven piles. In other words, this system makes pile driving possible even without any access roads to the piling location. Figure 5 illustrates how the system works all on top of the already-driven piles.

For example, it can construct sheet pile walls on a slope sandwiched by live railway tracks and buildings where a service crane could not be brought in. Figure 6 shows an example of very tight site conditions along a railway prior to mobilization of the GRB system.

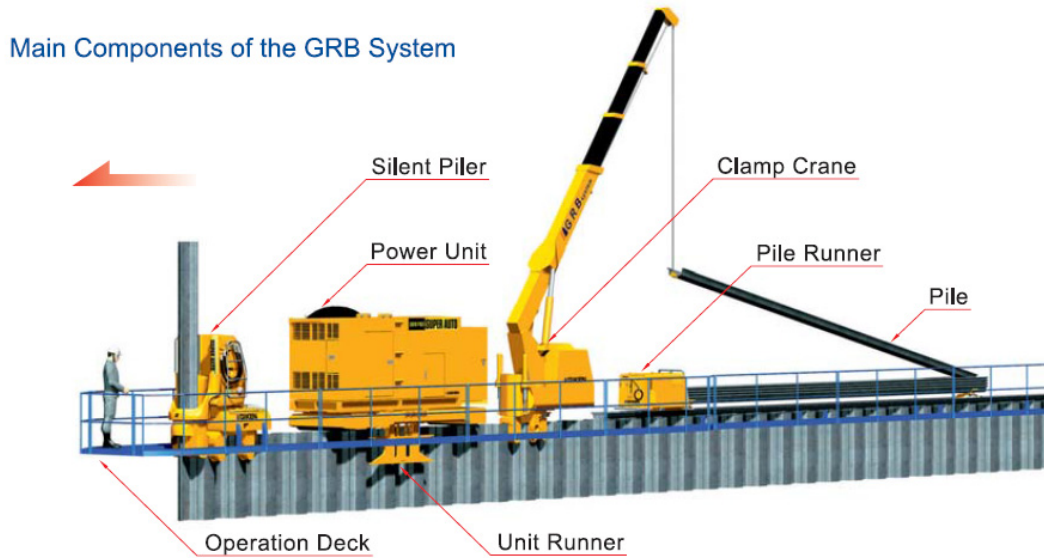


FIG. 5 Concept of the GRB System



FIG. 6 Embankment Retrofit Project Site Prior to Sheet Pile Installation (Takadanobaba-Mejiro Section of Yamanote Line)

CASE STUDY 1: OTSUKA-SUGAMO EMBANKMENT UPGRADE PROJECT

The Yamanote Line is a 34.5 km long mostly quad-tracked electrified loop circulating the heart of Japan's governmental, business, and commercial centers. 11-car electric trains are running as frequently as every 2 minutes during rush hour. Its Otuska-Sugamo section is sandwiched by buildings and very narrow roads. Therefore, the use of the GRB system for the aseismic upgrade work with the double sheet pile walls was the only practical choice to meet the project schedule. Mobilization of the pile driver and ancillary equipment required detailed planning and execution because

of the very tight access, which was only available for a few hours per night when the overhead catenary lines were de-energized.

While the soil was generally soft except the gravel layer with the STP value of about 50 as shown in the boring profile in Figure 7, there was an undocumented non-reinforced concrete retaining wall which had to be pre-drilled prior to sheet pile driving. The integrated auger attachment was used with the press-in pile driver to install 15.5-meter long Type VL U-shaped sheet piles in both slopes of the embankment. With the GRB system, the sheet pile driving work was successfully done on a 24-hour basis without stopping for trains passing by. Figure 8 shows the press-in sheet pile driving with the GRB system on the steep slope of the project.

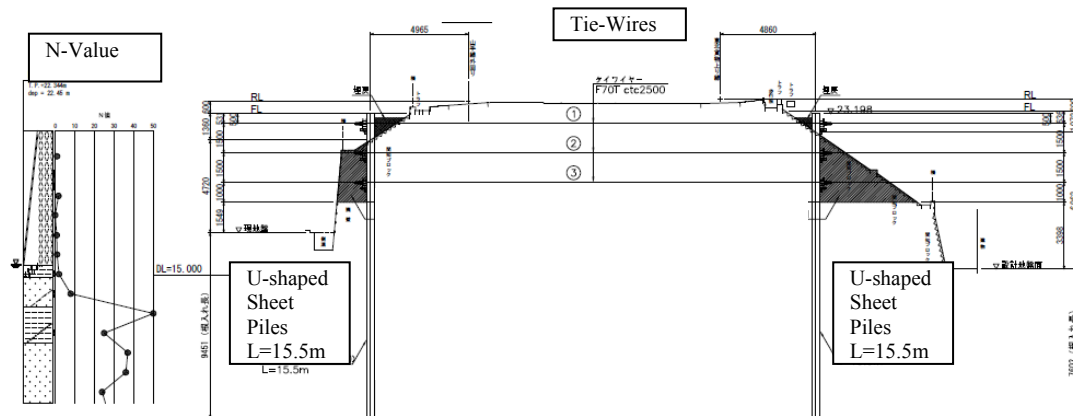


FIG. 7 Typical Section of Otsuka-Sugamo Section of Embankment Upgrade



FIG. 8 Sheet Pile Installation by the Press-in Driver with GRB System

CASE STUDY 2: HODOGAYA-HIGASHITOTSUKA RETAINING WALL RETROFIT PROJECT

The Yokosuka Line is a 73.3 km long, all electrified, and double-tracked commuter line connecting Tokyo with the Navy port of Yokosuka. The Hodogaya-Higashitotsuka section is around the mid-point of the line and just south of the densely populated Yokohama area.

The project was to retrofit an existing concrete retaining wall for the elevated tracks at Higashitotsuka station by installing ground anchors. However, nearby buildings were found to be too close to the retaining wall for the type of equipment needed as shown in Figure 9. Therefore, a combination of vertically driven pipe piles and soil improvement between the piles and the retaining wall was designed instead. Not only was there minimal horizontal clearance between the train track and the pile line (as little as 3.5 meters between the track's center line and the closest pile on one end of the project), the overhead clearance was also quite limited due to overhead power lines and the station concourse bridge as shown in Figures 10 and 11. The soil there was loose sand fill underlain by medium to dense silt and competent mudstone as a bearing layer.



FIG. 9 Retaining Wall and Adjacent Buildings Prior to Construction

Obviously, vibration by pile driving was a major concern for the railroad since the pile line was so close to the heavily traveled tracks. A rotary press-in pile driver with the GRB system was chosen to install 13 to 14 m long, 600 mm diameter tubular piles. Cutter bits were welded to toe circumference of each pile in order to facilitate the driving. The pile driver rotated and simultaneously pushed the pipe piles in the ground without causing measurable vibration or ground settlement (the ground movement was constantly monitored). The railroad allowed the piling to be done during the day time after having verified that the rotary press-in piling had caused no ground settlement in the test section at night when the trains were not running. Further, in order to make hoisting and pitching of the piles safer and to minimize the risk of a crane falling on the tracks, a Y-shaped boom crane was mounted onto the pile driver as shown in Figure 11.

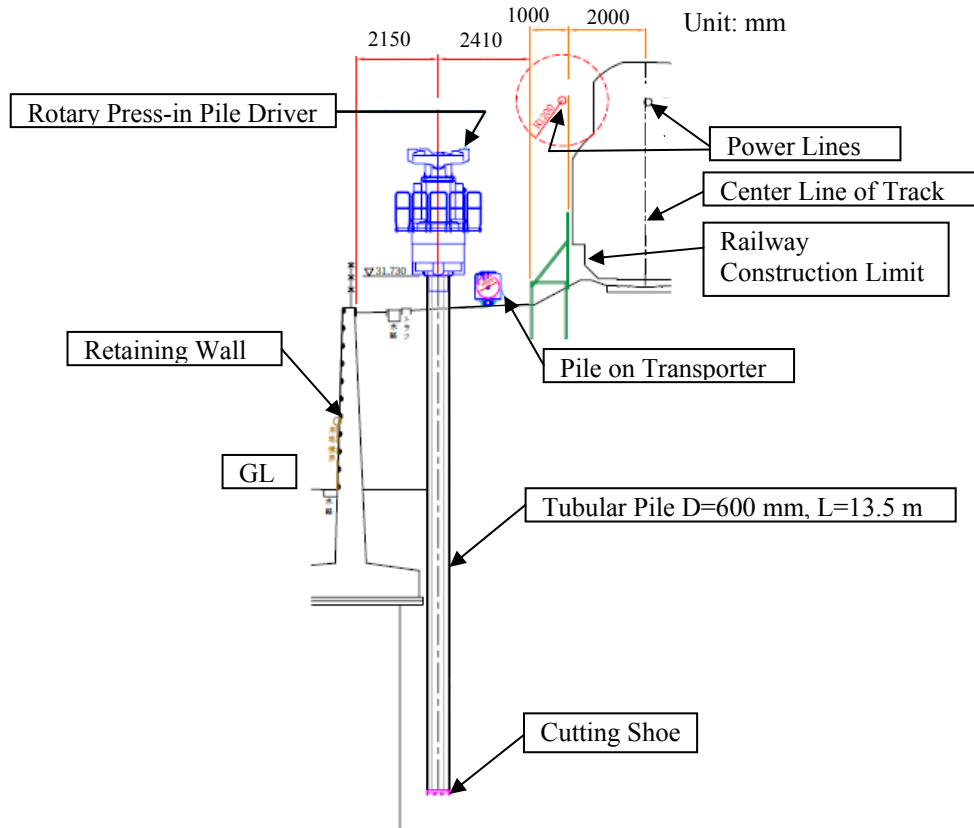


FIG. 10 Typical Section



FIG. 11 Rotary Press-in Driving with Limited Overhead and Horizontal Clearance (Next to Running Trains)

Mechanical joints were used to expedite the pile splicing in order to avoid time-consuming on-site welding. As shown in Figure 12, the joints (the middle section of the pipe pile) were coupled with each other by load conveying keys and key-setting bolts. These type of joints were shown to be as strong as or stronger than the rest of the pipe pile section in terms of tension, compression, bending moment, and shear.



FIG. 12 Mechanically-spliced Tubular Pile

CONCLUSIONS

Railway embankments need to be upgraded in earthquake-prone areas based on the newer aseismic standards for earthen structures in the light of numerous collapses caused by a recent strong earthquake in Japan. Sheet piles with tie-rods or cables are one of the highly effective methods for the aseismic retrofit. The press-in piling with the GRB system can provide a high degree of safety and reliable solutions for driving sheet piles and tubular piles for railway-related construction, especially with minimal distance from the heavily traveled tracks, power lines and/or nearby structures. Ground settlement can be eliminated by the rotary press-in method for tube piles since it does not remove or vibrate the surrounding soil. The press-in and rotary press-in methods have been successfully utilized on multiple aseismic embankment upgrade projects.

ACKNOWLEDGMENTS

The authors appreciate the support of Japan Press-in Association.

REFERENCES

- Anderson, D., Martin, G., Lam, I., and Wang, J.N. (2008), "Chapter 8 Slopes and Embankments", *Seismic Analysis and Design of Retaining Walls, Buried Structures, Slopes and Embankments* (NCHRP Report 611), National Cooperative Highway Research Program, Transportation Research Board, Washington/D.C.: 96-104

- East Japan Railway Company (2014), "Overview of FY2015.3 JR East (Non-consolidated) Capital Expenditure Plan", *Press Release Package dated April 30, 2014*, East Japan Railway Company, Tokyo/Japan: 3
- Kanda, M., Tateyama, M., (2014), "Aseismic Techniques for Foundations and Earthen Structures", *Railway Research Review* Vol. 71, No. 3, Railway Technical Research Institute, Tokyo/Japan: 20-23 (in Japanese)
- Kitsunai, S. (2015), "Aseismic Reinforcement of Railway Earthen Structures – Aseismic Reinforcement Work of Cut Slopes and Embankments of East Japan Railway Company", *Journal of Civil Engineering*, July 2015, Vol. 56, No. 7, Office Space, Tokyo/Japan: 65-68 (in Japanese)
- Murashita, T., Kunitomi, K., Morishita, A., and Uchida, R. (2014), "Anti-seismic Reinforcement of Existing Railway Embankment by Micropiling", *Technical Research Report of Konoike Construction Co., Ltd., 2014*, Konoike Construction Co., Ltd., Osaka/Japan: 9-16 (in Japanese)
- Ohashi, K. and Nasu, M. (1980), "A Seismic Reinforcement of Existing Railway Embankment", *Journal of the Japanese Geotechnical Society*, August 1980, No. 1192, Tokyo/Japan: 37-44 (in Japanese)
- Seki, M., Ohki, M., Shoji, T., Nagao, T., and Arashika, T. (2009), "Experimental Study on the Failure of the Embankment and the Effect of Countermeasures on Earthquakes", *Proceedings of the Japanese Geotechnical Society Chubu Branch 21st Annual Symposium, 2009*, Nagoya/Japan: 75-82 (in Japanese)
- White, D., Finlay, T., Bolton, M., and Bearss, G. (2002), "Press-in Piling: Ground Vibration and Noise During Piling Installation", *Proceedings of Deep Foundations 2002 Conference (GSP 116)*, ASCE, Reston/VA: 363-371
- Yamamoto, T. (1985), "Countermeasures for Earthquake of Railway Structures", *Proceedings of Japan Society of Civil Engineers*, No. 355, VI-2, Tokyo/Japan: 164-173 (in Japanese)

Cyclic Shear Response of Fraser River Sand Using Cyclic Ring Shear

Abouzar Sadrekarimi, Ph.D., P.Eng., M.ASCE

Assistant Professor, Dept. of Civil and Environmental Engineering, Western Univ.,
London, ON, Canada N6A 5B9.

Abstract: Cyclic triaxial, direct simple shear, torsional shear, resonant column, and cyclic ring shear apparatuses have been used for evaluating cyclic shear strength and liquefaction resistance of cohesionless soils. In this study cyclic shear response of Fraser River sand is investigated using constant-volume cyclic ring shear tests. The effects of sample preparation method, vertical stress, number of loading cycles to liquefaction (N_L), cyclic stress ratio (CSR), and relative density (D_{rc}) on the liquefaction behavior of Fraser River sand are investigated. Fraser River sand specimens are prepared by different sample preparation methods and tested under stress-controlled, constant-volume, plane-strain shearing condition. The ring shear specimens are consolidated to vertical stresses of 100, and 200 kPa prior to the application of uniform, sinusoidal, shear stress cycles. The specimens are then subjected to cyclic shear stress ratios (CSR) of 0.08, 0.10, 0.12, 0.15 and 0.20. Cyclic shear strain and effective vertical stress respectively increase and decrease with increasing the number of loading cycles. Larger cyclic shear strains and greater reductions in effective vertical stress are also produced at higher CSR. It is found that saturated water-pluviated samples exhibit significantly higher cyclic shearing resistance compare to dry air-pluviated and saturated moist-tamped samples. Compared to cyclic direct simple shear tests, cyclic shearing resistance measured in ring shear experiments is higher due to the rigid boundaries of the specimen chamber which impose a perfect plane strain shearing condition.

INTRODUCTION

In the past 45 years, cyclic shear response and liquefaction resistance of loose to medium-dense cohesionless soils has been among the vital concerns related to the performance of structures located in high seismic zones. Recent evidences of ground failure in cohesionless soils during strong earthquake loading has demonstrated the need for understanding the cyclic shear response of loose to medium-dense sand under cyclic loading. Cyclic liquefaction failure can occur when a cohesionless soil is subjected to cyclic loading in undrained (or constant-volume) shearing. Past researchers (Seed and Idriss, 1971) have highlighted the fact that earthquake loading can trigger the development of cyclic liquefaction and loss of shear strength of cohesionless soils. Seed et al. (1971) used cyclic triaxial testing with uniform cyclic

shear stresses to simulate earthquake loading on soil samples in the laboratory. Seed and his co-workers presented a simplified procedure to evaluate liquefaction potential through stress-controlled testing, where the stresses induced by earthquake loads are compared to the cyclic shear strength of soil. Various important parameters influence liquefaction resistance of cohesionless soils such as relative density, cyclic stress ratio, ground motion characteristics and vertical effective stress. These and other parameters have been investigated by various researchers (Ishihara and Okada, 1982, Seed and Lee, 1966, Wijewickreme, et al., 2005). These studies often suggest that the liquefaction risk of saturated sands is determined by its void ratio (higher the void ratio the more easily liquefaction will occur), effective confining pressure (the higher the confining pressure the more easily liquefaction will occur), and the magnitude of cycle stress or strain (fewer number of cycles are required to induce liquefaction at higher cyclic stress or strains).

Cyclic shear response of Fraser River sand has been studied in constant-volume cyclic simple shear (Wijewickreme, et al., 2005) and undrained cyclic triaxial tests (Vaid and Thomas, 1995). These studies have compared the cyclic behavior of Fraser River sand prepared by either air pluviation or water pluviation sample preparation techniques. They have found that Fraser River sand samples prepared by pluviation through air often present higher liquefaction susceptibility (Wijewickreme, et al., 2005). Besides cyclic direct simple shear and triaxial shear tests, ring shear tests have also been used for investigating cyclic shearing response and liquefaction behavior of soils (Sassa, et al., 2005, Suzuki, et al., 2013, Trandafir and Sassa, 2005). In this study, a comprehensive laboratory research program is carried out to study the cyclic shear response and liquefaction behavior of Fraser River sand using constant-volume cyclic ring shear tests. Similar to direct simple shear testing, a ring shear specimen is subjected to zero lateral strains (K_0) during consolidation and a plane-strain simple shearing condition with cyclic rotation of principal stresses (ASTM, 2007). The effects of specimen preparation method, relative density, vertical stress, and boundary conditions are evaluated.

TESTED MATERIAL

The Fraser River sand used in this research was obtained from a site located at the Fraser River delta in British Columbia, Canada. The specific gravity of sand particles (G_s), maximum (e_{max}), and minimum (e_{min}) void ratios of respectively 2.69, 0.96, and 0.63 were determined following ASTM standard guidelines (ASTM, 2006a, ASTM, 2006b, ASTM, 2006c). The particles of this sand are generally sub-angular to angular based on scanning electron microscopic (SEM) images and they are composed of 55% orthoclase feldspar, 35% quartz, and 10% muscovite based on X-ray diffraction analysis conducted in this study. Fig. 1 presents the grain size distribution of the Fraser River sand used in this study.

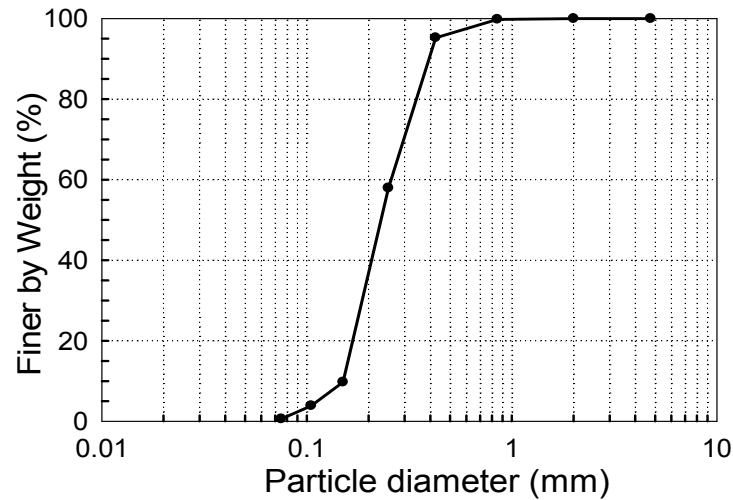


FIG. 1. Average grain size distribution of the Fraser River sand used in this study

EXPERIMENTAL PROCEDURE

A number of methods are available for reconstituting laboratory sand specimens. These include, dry air pluviation, water pluviation, and moist tamping methods. Dry air-pluviation sample preparation technique closely replicates the particle fabric of aeolian sands, and water-pluviated samples replicate the particle fabric of fluvial and hydraulic fill sands (Mulilis, et al., 1977, Vaid and Thomas, 1995). Water-pluviation technique is essentially similar to the air-pluviation method except that the sand particles are pluviated through water rather than air, thus ensuring sample saturation. Moist tamping sample preparation technique on the other hand replicates the particle fabric of moist-dumped fill sands.

Several researchers (Casagrande, 1975, Ladd, 1974, Lee and Seed, 1967, Mulilis, et al., 1977, Oda, et al., 1978, Tatsuoka, et al., 1986, Vaid, et al., 1999, Wijewickreme, et al., 2005) have studied the effect of specimen preparation techniques on cyclic liquefaction behavior and cyclic resistance of sands. Based on cyclic triaxial tests on three sands, Ladd (1974) observed that specimens prepared by dry-vibration were significantly weaker than those prepared using moist-tamping during cyclic loading. It was determined that the cyclic strength of moist-tamped specimens was approximately twice as large as those of the dry-vibrated specimens. Similar results are also reported by Mulilis et al. (1977) for Monterey No. 0 sand samples in cyclic triaxial tests. On the other hand, based on cyclic direct simple shear (DSS) tests Vaid et al. (1999) found that the cyclic resistance of water pluviated Fraser River sand samples was very close to those of undisturbed samples obtained by ground freezing. Wijewickreme et al. (2005) also carried out cyclic DSS tests on a Fraser River sand similar to that used in this study. They found that air pluviated samples were more susceptible to cyclic liquefaction compared to those prepared by water pluviation. A number of other studies (Sriskandakumar, et al., 2012, Vaid and Thomas, 1995) have also observed that air pluviated samples are more susceptible to liquefaction compared to water pluviated specimens.

The laboratory testing program for this study was designed to analyze the cyclic liquefaction behavior of Fraser River sand specimens prepared by different specimen preparation methods and subject to different cyclic stress ratios (CSR). A cyclic ring shear device (from GCTS, Arizona, USA) was used in the experiments. The ring shear device accommodates ring-shaped specimens with external and internal diameters of 152.2 mm, and 96.6 mm, respectively and a height of 30 mm. A combined force-torque sensor measured the vertical force and the shearing torque applied on the soil sample. The vertical displacement and the angular rotation of the upper platen were separately measured by a high resolution LVDT and an angular encoder, respectively. Both stress-controlled and strain-controlled cyclic shearing tests can be conducted with this apparatus. Fig. 2 shows a photograph and a schematic diagram of the shearing mode applied in the cyclic ring shear device.

In this study, ten specimens were prepared using different specimen preparation method (i.e. dry air pluviation, saturated water pluviation, and saturated moist tamping). Dry air pluviated Fraser River sand samples were pluviated using a funnel and the drop height was used to obtain the desired relative density. In saturated water-pluviation sample preparation method, the sand was pluviated through de-aired water rather than air in order to obtain saturated samples. In the saturated moist tamping method, the Fraser River sand was thoroughly mixed with 5% water, and then poured and gently tamped in 3 layers (of 10 mm height) into the annular ring shear chamber and then subsequently saturated by flushing water.

The specimens were subsequently consolidated to vertical stresses of $\sigma'_{vc} = 100$, and 200 kPa. The amount of vertical compression and thus specimen's volume change were carefully measured during the application of σ'_{vc} and the specimen void ratio was subsequently calculated at the end of consolidation. Constant-volume cyclic shearing was then carried out by subjecting the specimens to different levels of uniform sinusoidal cyclic shear stresses (τ_{cyc}) at a cyclic shearing frequency of 0.1 Hz. In order to replicate an undrained shearing condition, a constant specimen volume was maintained by continuously adjusting the normal force to prevent changes in specimen height during shear through a computer-controlled and feedback system. Excess pore pressure during shear was inferred from the change in total stress required to maintain constant volume (i.e. height) conditions. This technique is analogous to undrained shearing of a saturated specimen (ASTM, 2007, Dyvik, et al., 1987). The cyclic ring shear machine used in this study was fine-tuned at various cyclic shearing frequencies and it was found that the cyclic shearing frequency of 0.1 Hz gave uniform and much better sinusoidal response. A cyclic shearing frequency of 0.1 Hz has been also used by several other researchers (De Alba, et al., 1976, Sanin and Wijewickreme, 2006, Srisankandakumar, et al., 2012, Wijewickreme, et al., 2005) to investigate cyclic shearing and liquefaction behavior. In cyclic ring shear (as well as in simple shear) tests, cyclic stress ratio (CSR) is defined as the ratio of cyclic shear stress to the initial (consolidation) vertical effective stress, i.e. τ_{cyc}/σ'_{vc} . Uniform cyclic shear stress ratios of 0.08, 0.10, 0.12, 0.15 and 0.20 were applied in the cyclic ring shear tests in this study until a double-amplitude cyclic shear strain, γ_{cyc} of 7.5% was developed. Similar to the liquefaction criterion used in cyclic direct simple shear tests, the occurrence of cyclic liquefaction was determined when a double-amplitude cyclic shear strain, $\gamma_{cyc} = 7.5\%$ was reached. This failure criterion is essentially

equivalent to the development of 5% double-amplitude axial strain in cyclic triaxial tests (Idriss and Boulanger, 2008, Mulilis, et al., 1977).

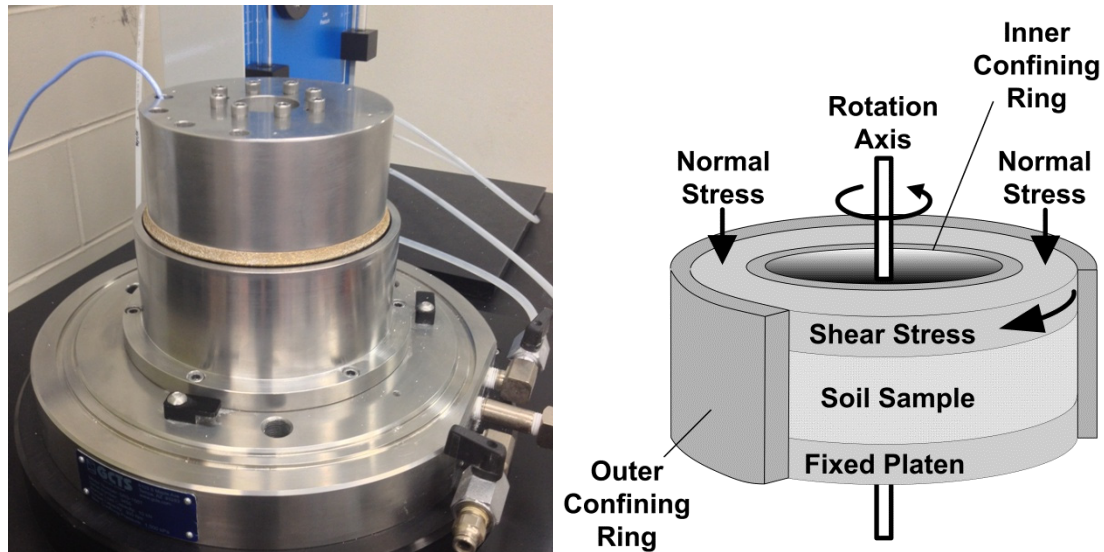


FIG. 2. A photograph and the schematic mode of shearing applied in the cyclic ring shear apparatus at Western University

RESULTS AND DISCUSSION

Figs. 3 and 4 show typical cyclic stress-strain and stress path relationships obtained from the ring shear tests performed on Fraser River sand specimens. While all the specimens exhibit gradual increase of shear strain with increasing the number of loading cycles, the amount of vertical stress (σ_v) reduction (corresponding to the generation of excess pore water pressure) increases with the number of cycles.

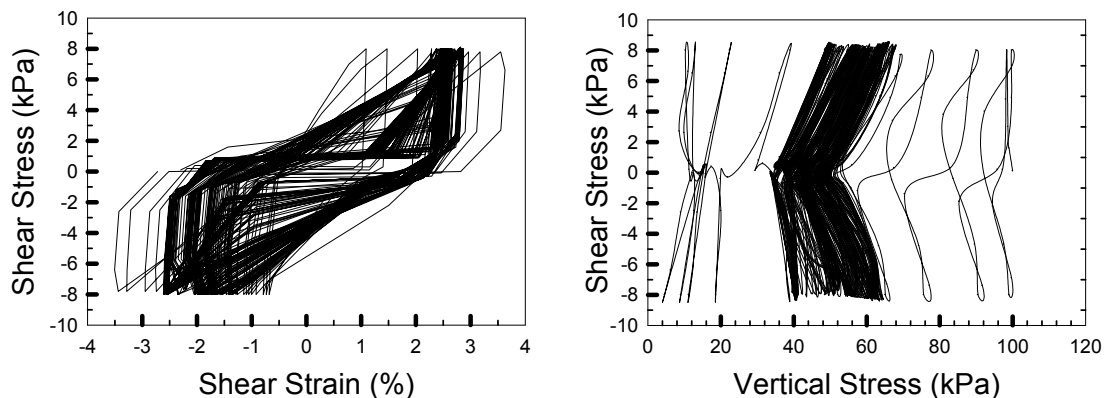


FIG. 3. Stress-strain and stress-path responses of Fraser River sand in constant-volume cyclic ring shear test ($\sigma'_{vc} = 100$ kPa; CSR = 0.08; $D_{rc} = 34\%$, prepared by air pluviation)

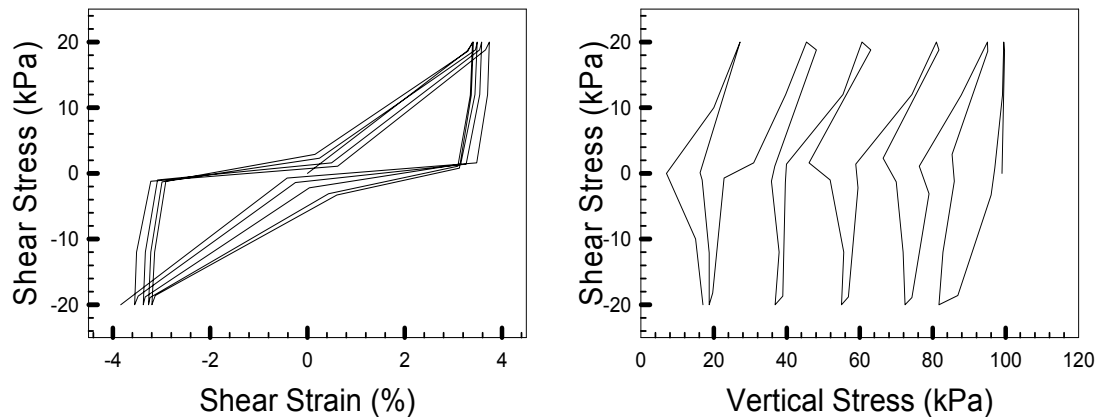


FIG. 4. Stress-strain and stress-path responses of Fraser River sand in constant-volume cyclic ring shear test ($\sigma'_{vc} = 100$ kPa; CSR = 0.20; $D_{rc} = 34\%$, prepared by saturated moist-tamped)

It was the primary interest of this study to examine the cyclic shear resistance of Fraser River sand specimens under different cyclic loadings and sample preparation methods. In order to facilitate this comparison, the number of loading cycles required to reach liquefaction (at $\gamma_{cyc} = 7.5\%$) for a given applied CSR is defined as N_L . Resistance to cyclic loading is usually determined as the CSR that produces cyclic liquefaction in 15 cycles of uniform loading, termed cyclic resistance ratio (CRR). This is equivalent to earthquake loading of magnitude (M) of 7.5 (Idriss and Boulanger, 2008).

Figs. 5 and 6 compare CSR and CRR for each of the specimen preparation methods. While Fraser River sand specimens prepared using water pluviation and moist tamping display nearly the same cyclic resistance in ring shear tests, they present significantly higher CRR compared to those for specimens prepared using dry air pluviation. A similar difference between CRR of air and water pluviated samples is also observed in cyclic DSS tests (Wijewickreme, et al., 2005). Fabric studies and electrical conductivity measurements (Mulilis, et al., 1977) indicate that the orientation and arrangement of the contacts between sand grains are probably the primary reasons for the observed differences in the cyclic strength of sand prepared using different techniques. Fig. 6 also presents the ranges of CRR from cyclic simple shear tests on undisturbed specimens of Fraser River sand (Robertson, et al., 2000). These samples were taken from depths of 10.5 m and 14.5 m by ground freezing using liquid nitrogen. The undisturbed samples present liquefaction resistances between those from specimens reconstituted by air pluviation and water pluviation techniques. In order to directly apply cyclic shear test results to field conditions, a specimen with a fabric similar to the in-situ soil should be tested. However, obtaining high-quality undisturbed frozen samples of saturated cohesionless soils can be very difficult and expensive. The cyclic shear testing results of Fig. 6 suggest that the average CRR of air pluviated and water pluviated reconstituted specimens would provide a better estimate of the in-situ liquefaction resistance.

The results developed from the cyclic ring shear tests are also compared with the cyclic behavior of Fraser River sand samples in cyclic DSS tests (Wijewickreme, et

al., 2005). According to Figs. 5 and 6, cyclic shear resistance from the ring shear tests is considerably higher than those from cyclic DSS tests irrespective of the specimen preparation method. The available cyclic DSS experiments on Fraser River sand have been carried out on specimens confined by a wire-reinforced membrane (Sivathayalan and Vaid, 2004, Wijewickreme, et al., 2005). Because of its flexibility, a wire-reinforced membrane allows radial strains in a DSS specimen and hence produces imperfect plane-strain and constant-volume shearing conditions. In particular, soil particles adjacent to the membrane will not experience a plane-strain (zero lateral strain) deformation. This has been demonstrated to induce a greater vertical strain and enhanced strain-softening behavior in DSS experiments (Baxter, et al., 2010, Marachi, et al., 1981, McGuire, 2011). For the medium-dense ($D_{rc} = 38 - 44\%$) specimens of Fig. 5, a deviation from constant-volume shearing would produce specimen densification and increased cyclic resistance. Therefore, the higher resistance observed in cyclic ring shear tests is possibly associated with the rigid boundaries (steel rings) imposing a perfect plane-strain shearing condition in the ring shear tests. The ASTM (2007) standard practice for DSS testing also allows a stack of Teflon-coated rigid rings for confining a specimen. Although a latex membrane is still used for forming a specimen, this technique can minimize radial deformation of the DSS specimen and improve plane-strain and constant-volume shearing conditions (Baxter, et al., 2010, McGuire, 2011).

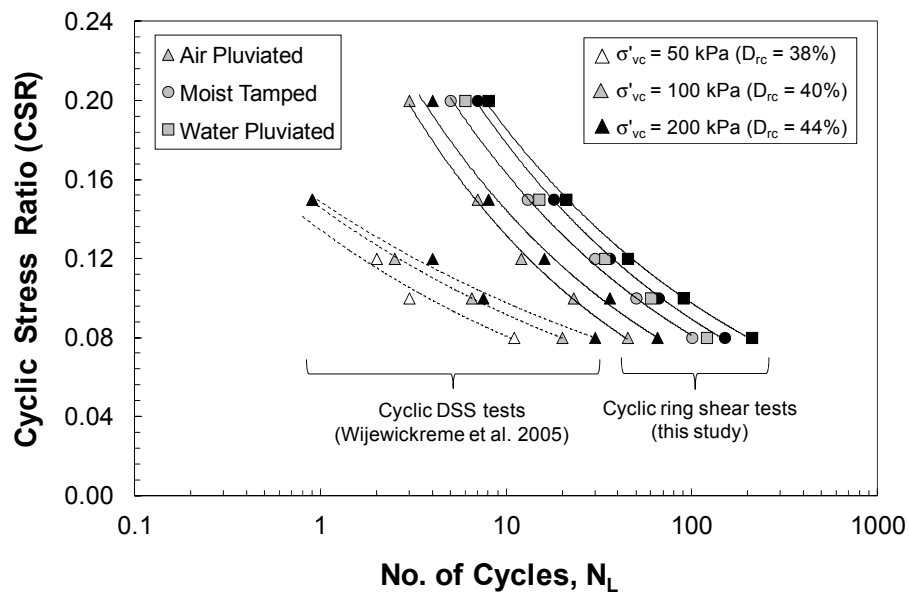


FIG. 5. CSR versus number of cycles required to reach $\gamma_{cyc} = 3.75\%$ from constant-volume cyclic ring shear (this study) and cyclic direct simple shear (Wijewickreme, et al., 2005) tests on Fraser River sand specimens

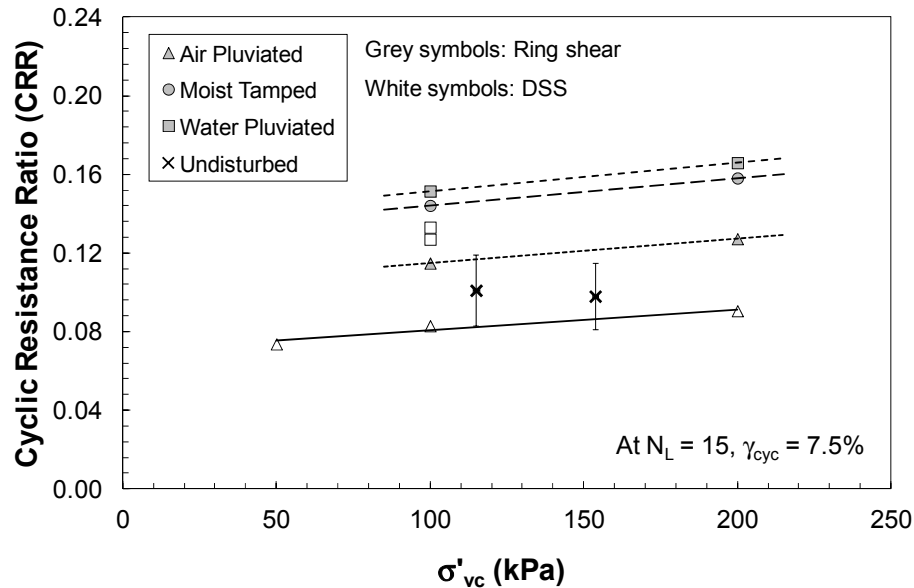


FIG. 6. CRR of Fraser River sand samples from constant-volume cyclic ring shear (this study) and cyclic DSS (Robertson, et al., 2000, Wijewickreme, et al., 2005) tests

CONCLUSIONS

The cyclic behavior and liquefaction response of Fraser River sand was investigated in this study for samples prepared by different methods, and at different cyclic stress ratios. In all tests, higher cyclic stress ratios appear to reduce the cyclic shear strength of Fraser River sand observed in ring shear tests. Fraser River sand specimens prepared by water pluviation and moist tamping methods exhibited higher cyclic resistances than those prepared by air pluviation. These findings reinforce that sample preparation method can greatly affect the cyclic shear resistance and liquefaction behavior of Fraser River sand. These further highlight the importance of sand fabric in the assessment of the cyclic response of sands. Comparison with the liquefaction resistance of undisturbed samples suggested that the liquefaction resistance of an in-situ sandy soil can be better represented by the average liquefaction resistance of specimens reconstituted by air pluviation and water pluviation techniques. Larger cyclic resistances were also measured in ring shear tests compared to those from cyclic direct simple shear experiments on Fraser River sand. This is likely associated with the effect of different boundary conditions imposed in these apparatuses.

ACKNOWLEDGEMENT

The laboratory research program of this study was funded by the Natural Sciences and Engineering Research Council of Canada (NSERC) and Fraser River sand samples were provided by GeoPacific Consultants (Vancouver, BC). The author is grateful for both of these supports.

REFERENCES

- ASTM (2006a). "Standard D854: Standard Test Methods for Specific Gravity of Soil Solids by Water Pycnometer." *Annual Book of ASTM Standards*, ASTM International, West Conshohocken, PA.
- ASTM (2006b). "Standard D4253: Standard test methods for maximum index density and unit weight of soils using a vibratory table." *Annual Book of ASTM Standards*, ASTM International, West Conshohocken, PA.
- ASTM (2006c). "Standard D4254: Standard test methods for minimum index density and unit weight of soils and calculation of relative density." *Annual Book of ASTM Standards*, ASTM International, West Conshohocken, PA.
- ASTM (2007). "Standard D6528: Standard Test Method for Consolidated Undrained Direct Simple Shear Testing of Cohesive Soils." *Annual book of ASTM Standards*, ASTM International, West Conshohocken, PA.
- Baxter, C. D. P., Bradshaw, A. S., Ochoa-Lavergne, M., and Hankour, R. (2010). "DSS test results using wire-reinforced membranes and stacked rings." *GeoFlorida 2010: Advances in Analysis, Modeling & Design (GSP 199)*, D. O. Fratta, A. J. Puppala, and B. Muhunthan, eds., American Society of Civil Engineers (ASCE), Reston, VA, 600-607.
- Casagrande, A. (1975). "Liquefaction and cyclic deformation of sands: a critical review." *Proc., 5th Pan-American Conf. on Soil Mechanics and Foundation Engineering*, 80 - 133.
- De Alba, P., Seed, H. B., and Chan, C. K. (1976). "Sand liquefaction in large-scale simple shear tests." *Journal of Soil Mechanics and Foundations Division, ASCE*, 102(GT9), 909 - 927.
- Dyvik, R., Berre, T., Lacasse, S., and Raadim, B. (1987). "Comparison of truly undrained and constant volume direct simple shear tests." *Geotechnique*, 37(1), 3 - 10.
- Idriss, I. M., and Boulanger, R. W. (2008). *Soil liquefaction during earthquakes*, Earthquake Engineering Research Institute, San Francisco.
- Ishihara, K., and Okada, S. (1982). "Effects of large pre-shearing on cyclic behaviour of sand." *Soils and Foundations*, 22(3), 109 - 125.
- Ladd, R. S. (1974). "Specimen preparation and liquefaction of sands." *Journal of Soil Mechanics and Foundation Division, ASCE*, 100(10), 1180 - 1184.
- Lee, K., and Seed, H. B. (1967). "Dynamic strength of anisotropically consolidated sand." *Journal of Soil Mechanics and Foundations Division, ASCE*, 93(5), 169 - 190.
- Marachi, N., Duncan, J., Chan, C., and Seed, H. (1981). "Plane-strain testing of sand." *Laboratory Shear Strength of Soils, ASTM STP 740*, R. N. Yong, and F. C. Townsend, eds., American Society for Testing and Materials, 294 - 302.
- McGuire, S. T. (2011). "Comparison of direct simple shear confinement methods on clay and silt specimens." Master of Science, University of Rhode Island.
- Mulilis, J. P., Arulanandan, K., Mitchell, J. K., Chan, C. K., and Seed, H. B. (1977). "Effects of sample preparation on sand liquefaction." *Journal of Geotechnical Engineering Division, ASCE*, 103(GT2), 91 - 108.
- Oda, M., Koishikawa, I., and Higuchi, T. (1978). "Experimental study of anisotropic shear strength of sand by plane strain test." *Soils and Foundations*, 18(1), 25-38.

- Robertson, P. K., Wride, C. E., List, B. R., Atukorala, U., Biggar, K. W., Byrne, P. M., Campanella, R. G., Cathro, D. C., Chan, D. H., Czajewski, K., Finn, W. D. L., Gu, W. H., Hammamji, Y., Hofmann, B. A., Howie, J. A., Hughes, J., Imrie, A. S., Konrad, J. M., Kupper, A., Law, T., Lord, E. R. F., Monahan, P. A., Morgenstern, N. R., Phillips, R., Piche, R., Plewes, H. D., Scott, D., Segoo, D. C., Sobkowicz, J., Stewart, R. A., Watts, B. D., Woeller, D. J., Youd, T. L., and Zavodni, Z. (2000). "The CANLEX project: summary and conclusions." *Canadian Geotechnical Journal*, 37(3), 563-591.
- Sanin, M. V., and Wijewickreme, D. (2006). "Cyclic shear response of channel-fill Fraser River Delta silt." *Soil Dynamics and Earthquake Engineering*, 26(9), 854 - 869.
- Sassa, K., Wang, G., Fukuoka, H., and Vankov, D. A. (2005). "Shear-Displacement-Amplitude Dependent Pore-Pressure Generation in Undrained Cyclic Loading Ring Shear Tests: An Energy Approach." *Journal of Geotechnical and Geoenvironmental Engineering, ASCE*, 131(6), 750 - 761.
- Seed, H. B., and Idriss, I. M. (1971). "Simplified procedure for evaluating soil liquefaction potential." *Journal of the Soil Mechanics and Foundations Division, ASCE*, 97(SM9), 1249 - 1273.
- Seed, H. B., and Lee, K. L. (1966). "Liquefaction of saturated sands during cyclic loading." *Soil Mechanics and Foundations Division, ASCE*, 92(SM6), 105-134.
- Sivathayalan, S., and Vaid, Y. (2004). "Cyclic resistance and post liquefaction response of undisturbed in-situ sands." *13th World Conference on Earthquake Engineering*, Vancouver, Canada, August 1-6, 2004, Paper No. 2940.
- Sriskandakumar, S., Wijewickreme, D., and Byrne, P. M. (2012). "Multiple cyclic loading response of loose air-pluviated Fraser River Delta silt." *15th World Conference on Earthquake Engineering* Lisbon, Portugal, 24 - 28 September 2012.
- Suzuki, M., Takahara, H., and Umezaki, T. (2013). "Dynamic Ring Shear Characteristics of Artificially Cemented Sand." *International Symposium on Earthquake-Induced Landslides*, K. Ugai, H. Yagi, and A. Wakai, eds., Springer-Verlag Berlin Heidelberg, Kiryu, Japan, 445 - 453.
- Tatsuoka, F., Ochi, K., Fujii, S., and Okamoto, M. (1986). "Cyclic undrained triaxial and torsional shear strength of sands for different sample preparation methods." *Soils and Foundations*, 26(3), 23 - 41.
- Trandafir, A. C., and Sassa, K. (2005). "Seismic triggering of catastrophic failures on shear surfaces in saturated cohesionless soils." *Canadian Geotechnical Journal*, 42(1), 229-251.
- Vaid, Y. P., Sivathayalan, S., and Stedman, D. (1999). "Influence of specimen-reconstituting method on the undrained response of sand." *Geotechnical Testing Journal*, 22(3), 187-195.
- Vaid, Y. P., and Thomas, J. (1995). "Liquefaction and postliquefaction behavior of sand." *Journal of Geotechnical Engineering, ASCE*, 121(2), 163 - 173.
- Wijewickreme, D., Sriskandakumar, S., and Byrne, P. (2005). "Cyclic loading response of loose air-pluviated Fraser River sand for validation of numerical models simulating centrifuge tests." *Canadian Geotechnical Journal*, 42(2), 550-561.

Earthquake-Induced Landslide Hazard Mapping: A Case Study in Lebanon

Grace Abou-Jaoude, M.ASCE¹; Angela Saade²; Joseph Wartman, M.ASCE, P.E.³; and Alex Grant⁴

¹Assistant Professor, ASCE, Dept. of Civil Engineering, Lebanese American Univ., Lebanon.

²Undergraduate Research Assistant, Dept. of Civil Engineering, Lebanese American Univ., Lebanon.

³H.E. Berg Associate Professor, ASCE, Dept. of Civil and Environmental Engineering, Univ. of Washington, Seattle.

⁴Graduate Student, Dept. of Civil and Environmental Engineering, Univ. of Washington, Seattle.

Abstract: Located in a seismic zone with a rugged topography, Lebanon is classified as highly vulnerable to earthquake and landslide hazards. According to Keefer (1984), even small magnitude earthquakes may trigger landslides leading to significant damages. Regional seismic hazard assessment for landslides has been done using methods based on the traditional infinite slope stability analysis following Newmark (1965). This approach provides a quick assessment of co-seismic landslides but has several disadvantages. In particular, the predefined failure surface leads to overestimated values of the critical accelerations of the slopes and underestimates the hazardous areas. Two newly proposed methods are implemented over a representative region of Lebanon with the use of the geographic information systems (GIS). Data including geological maps, high-resolution digital elevation models of the topography, site investigations and geotechnical data for the different geological units, earthquake peak ground acceleration maps, and a preliminary landslide inventory database are collected for the analysis. A co-seismic landslide hazard map for the country is then produced and the results are presented for a representative area. This hazard assessment represents the initial warning system that identifies high-risk sloping zones. Focus is particularly on densely populated urban areas where the landslide hazard greatly affects currently existing structures.

INTRODUCTION

Co-seismic landslide hazard assessment has been traditionally done using Newmark's (1965) sliding block method combined with an infinite slope analysis. It typically starts with the determination of the critical acceleration ($a_{critical}$) of the slope based on the slope angle and the strength parameters of the slope. Slope displacement is then calculated using this $a_{critical}$ value and the corresponding peak ground acceleration (PGA) of the slope that is typically obtained from a probabilistic seismic hazard analysis. Often, the resulting displacement predictions are regarded as an index measurement for the expected performance of a slope during an earthquake. Hazard levels are usually set for displacement predictions greater than a certain threshold, usually 5cm. A major disadvantage of the sliding block approach is the resulting overestimation of $a_{critical}$ due to the underlying assumption of a predefined slope failure plane, and consequently the underestimation of hazard areas prone to sliding.

In fact, earthquake reconnaissance studies reveal that earthquake-induced landslides occur in both soil and rock units. Modeling the slope as a sliding block resting on an inclined infinite plane does not account for the material heterogeneity and slope geometry encountered in the field. In rock, weathering, fracturing, bedding, and jointing often control the sliding mode of a slope, and soils do not necessarily have a pre-defined weak sliding plane. Many other factors, such as vegetation and weight distribution, play an important role in the stability of slopes. Keefer (1984) showed that an earthquake event can trigger more than one mode of slope failure. Fourteen types of landslides were identified in his study of forty world-wide earthquakes and were grouped into three major categories – namely, disrupted falls, coherent slides and lateral spreads. Disrupted falls, such as rock slides, detach from steep slopes, are generally shallow, and constitute the majority of the mapped landslides. Coherent slides are deep near circular failure surfaces and mainly occur on moderate slopes. Lateral spreads involve fluid-like flow and move on gentle slopes. Accordingly, the infinite planar mode of slope failure may not be always applicable for regional-scale assessment of earthquake-induced landslides.

In this paper, we present two new approaches for assessing seismic slope instabilities that were developed as part of a project based in Lebanon. In the first approach, we assess the seismic instability of a slope through $a_{critical}$ values derived from a parametric study based on Bishop's (1955) limit equilibrium method. Bishop's method uses circular slip surfaces with no restriction to any predefined slope failure plane. In the second approach, we use a multi-modal analysis to independently capture the $a_{critical}$ values corresponding to the different modes of failure in soil and rock slopes. Then, we test these two approaches versus the sliding block model in a regional scale assessment of earthquake-induced landslide hazards for Lebanon. We highlight the hazard levels for a region in the northern part of Lebanon characterized with a high rate of slope failures due to its topography and geology.

CRITICAL ACCELERATION OF A SLOPE

Newmark's sliding-block theory

The sliding-block theory consists of modeling a slope as a rigid frictional block sliding on an infinite inclined plane (Newmark 1965) to identify $a_{critical}$. Permanent displacement of the sliding mass accumulates when the acting inertial forces, generated by the earthquake motion, exceed the yield resistance of the ground surface (Jibson et al., 2000). In the infinite slope-rigid block calculation, the factor of safety is calculated based on the material properties, namely cohesion, c , friction angle, ϕ , unit weight, γ , and the unit weight of water, γ_w , the slope angle, β , the thickness of the failure surface, t , and the proportion of saturated failure surface, m .

At limit equilibrium, $a_{critical}$ (expressed in terms of g) is computed using:

$$a_{critical} = (FS - 1) \sin \beta \quad (1)$$

Permanent slope displacement can be either calculated for a specific earthquake event through double integration or using empirical regression equations that have been developed based on Newmark's (1965) model. In this study, we adopt the well-known Jibson (2007) equation for displacement prediction that is based on the PGA values:

$$\log D_N = 0.215 + \log \left[\left(1 - \frac{a_{critical}}{a_{max}} \right)^{2.341} \left(\frac{a_{critical}}{a_{max}} \right)^{-1.348} \right] \pm 0.510 \quad (2)$$

where D_N is the displacement prediction in cm , $a_{critical}$ is the critical acceleration (in g 's), a_{max} is the peak or maximum ground acceleration (in g 's).

Limit equilibrium approach

Limit equilibrium analysis has been used to assess the seismic stability of slopes. Loukidis et al., (2003) and Li et al., (2008) have developed simplified solutions to assess the seismic stability of soil and rock slopes using the Mohr-Coulomb (MC) failure criterion and the 2002 generalized Hoek-Brown (HB) failure criterion, respectively. The MC criterion, defined using a cohesion term c and a friction term ϕ , is widely used in geotechnical engineering for modeling both cohesionless and cohesive soil material. The HB criterion, defined using the geological strength index GSI , the material constant m_i , and the unconfined compressive strength σ_{ci} , is often used for modeling the strength of a wide range of rock masses. Li et al. (2008) showed that the MC criterion resulted in good agreement between the limit analysis and limit equilibrium solutions for slopes less than 45° , but significantly overestimated the safety of steep slopes when compared to numerically bounded solutions. They also found that results are significantly improved when the HB criterion was used for steep slopes, greater than 45° . Moreover, Loukidis et al. (2003), among others, showed that Bishop's (1955) limit equilibrium model for circular slip surfaces provides reasonably good results when compared to rigorous

numerical upper and lower bound solutions for a range of slope inclinations and material strength conditions.

Saade et al. (2016) conducted a parametric assessment that considers material strength and slope inclination as variables in a limit equilibrium analysis to develop generalized equations for $a_{critical}$. A plane strain slope model implemented in the Rocscience code *SLIDE* (Version 6.0) was used to conduct simulations of slopes with height H inclined between 15° and 70° using both the MC and HB criterion. General equations for $a_{critical}$ of a slope and for a set of strength parameters were generated in a two-step regression analysis. An advantage of this approach is that it is based on the limit equilibrium analysis of a generalized slope geometry. Having equations proposed for two yield criteria enhances the methods versatility and allows the user to define the strength parameters of a geologic unit using the most appropriate strength criteria. For slopes less than 45° and the MC criteria, $a_{critical(MC)}$ values were plotted against the non-dimensional cohesion term $c/\gamma H$ for different friction angles and fitted into functions of the form:

$$a_{critical(MC)} = C1_{(MC)} \frac{c}{\gamma H} + C2_{(MC)} \quad (3)$$

For slopes greater than 45° and the HB criteria, the values of $a_{critical(HB)}$ were plotted against the non-dimensional term of unconfined compressive strength $\sigma_{ci}/\gamma H$ for every $GSI-m_i$ combination and fitted into functions of the form:

$$a_{critical(HB)} = C1_{(HB)} \ln\left(\frac{\sigma_{ci}}{\gamma H}\right) + C2_{(HB)} \quad (4)$$

Detailed tables of regression coefficients for use in Eqs. (3) and (4) are provided in Saade et al. (2016). After calculating the $a_{critical}$ values for the region under investigation, slope displacements can be obtained using Eq. (2). This approach was validated through a regional co-seismic landslide hazard analysis for the Val Verde quadrangle in Northridge, CA (Saade et al. 2016). Out of a total of 5.714 km^2 actual landslide area in Val Verde quadrangle, the proposed model correctly predicted a sliding area of 0.37 km^2 , whereas the traditional infinite slope analysis only predicted 0.057 km^2 . The accuracy of the proposed model, defined as the ratio of the total area correctly predicted over the total area of the quadrangle, was equal to 95% with an efficiency of capture of 5.73%, compared to almost the same accuracy for the traditional approach but for an efficiency of only 0.925%.

Multi-Modal Slope Analysis

Grant et al., (2014) presented a preliminary framework for the separation of co-seismic landslide hazard into four key modes of failure, namely rock failures, disrupted soil slides, coherent soil slides, and lateral spreads. Slope angle was used to separate the terrain into areas susceptible to each mode of failure based on published case studies (here, rock-slope failures, $35-90^\circ$; disrupted soil slides, $20-50^\circ$; coherent slides, $20-35^\circ$, lateral spreads, $0-6^\circ$), and stability of each type of failure was assessed with a unique

geotechnical model. Disrupted soil slides were assessed via infinite slope analyses, rock failures by the Culmann method for wedges, coherent soil failures were assumed to exhibit a circular slip surface and a simplified stability model was derived and implemented, and lateral spreading was assessed based on the work of Hamada et al., (1987). The main advantage of this approach is that it allows the user to use independent methods to assess co-seismic stability for the different modes of failure.

LANDSLIDE HAZARDS IN LEBANON

Situated in the central part of the Eastern Mediterranean, Lebanon is a mountainous country with two mountain chains and a valley in between running along a north-south axis. It is bounded to the West by the Mount Lebanon Thrust fault and bisected by a compressional bend along the left-lateral strike-slip Dead Sea Fault (Figure 1). The recent discovery of the offshore active thrust fault system located close to the Lebanese coastline (Elias et al., 2007) led to the re-evaluation of the country's seismic hazard. Huijer (2010) produced new *PGA* contour maps for the purpose of seismic design of structures. No studies have ever explicitly linked the occurrences of mass movements in Lebanon to its seismicity.

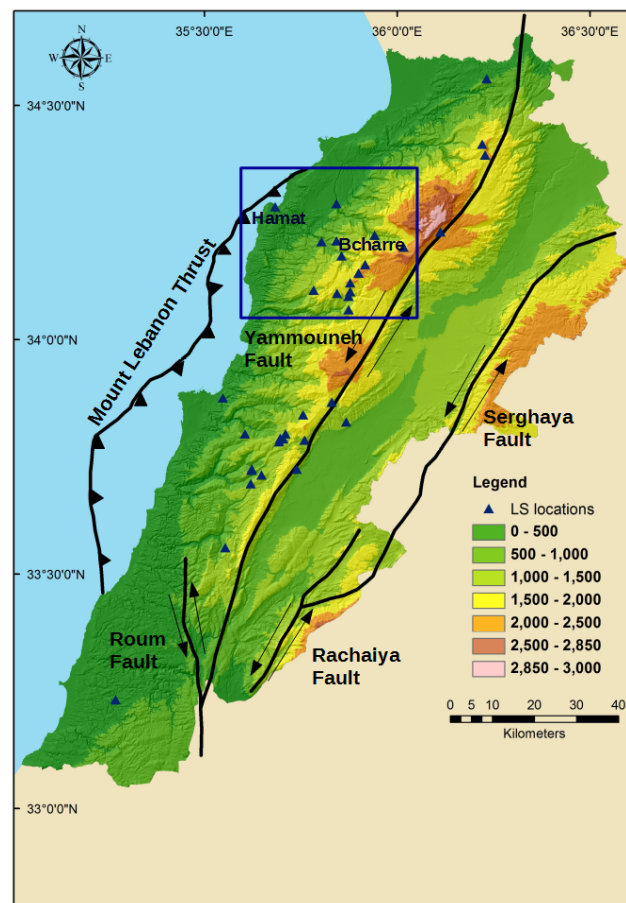


FIG. 1: Topography, major fault systems, and mapped landslide locations

Lebanon's rapid population growth during the 20th century resulted in the accelerated occupation of the coastal strip and its extension on the hillsides of the western mountain range, also known as Mount Lebanon. This massive expansion led to the exposure of the population to higher risks due to landslide hazards. According to a 2006 study conducted by The World Bank to identify global landslide hazard, Lebanon was categorized among countries that have "medium to high," "high," and "very high" landslide hazard ratings.

We took a closer examination of the locations where mass movements occur across Lebanon by reviewing literature records (e.g. Khawlie and Hassanain 1984; Abdallah et al. 2005) and news coverage. Figure 1 shows several sliding locations across the country, with numerous records in the northern part of Lebanon. In particular, the area that extends from the coastline of Batroun to the village of Bcharre in the western Mountain Range, (box in Figure 1), is greatly affected.

DATA COLLECTION AND ANALYSIS

Data collection

The following terrain factors were considered in this study: geological formation and lithology, structural geology, slope angle, peak ground acceleration, and groundwater table. The data sets used in this analysis were: 1) the 1:50,000-scale geologic mapping of the country based on Dubertret (1945), 2) the PGA map based on a probability of exceedance of 10% in 50 years obtained from Huijjer (2010), and 3) the 15-m digital elevation model (DEM) of the topography based on the latest map produced by the CNRS. Figure 2 shows that the main geologic units, which are predominantly Jurassic limestone and Cretaceous sandstones.

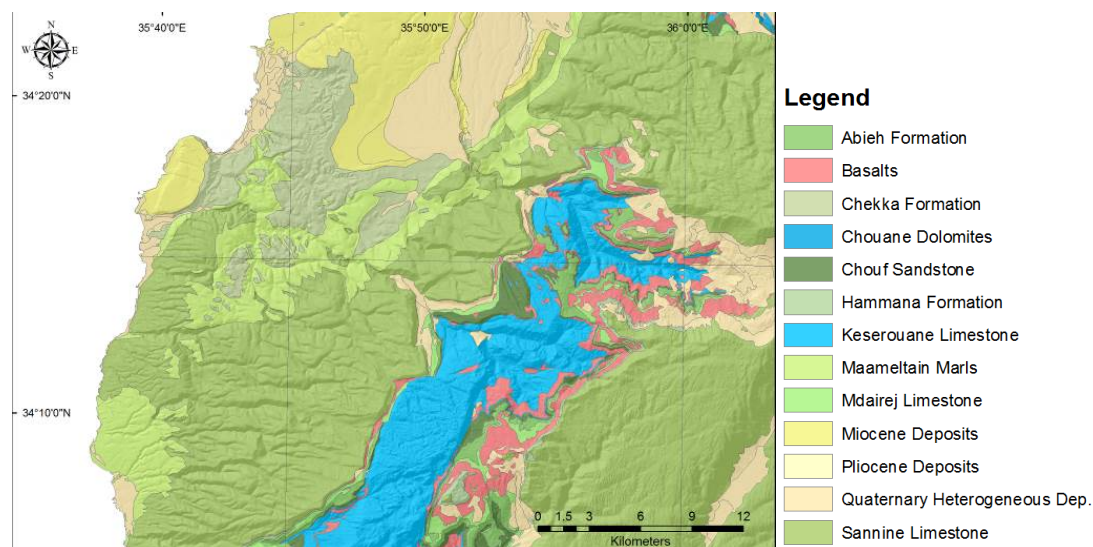


FIG. 2: Geologic map of the study area

We assigned representative HB strength parameters to the geologic units using site investigation data from engineering design projects that we were able to access and field visits that we conducted in the selected region. Table 1 lists the geologic units and the corresponding final soil properties that were used in our analysis.

Table 1 – Estimated strength parameters of geologic units in the study area

Geologic Unit	Cohesion (kPa)	Friction Angle (deg.)	Unit Weight (kN/m ³)	GSI	mi	UCS (kPa)
Abieh Formation	42	20	23	20	10	1000
Basalts	52	25	23	20	20	1000
Chekka Formation	48	20	23	20	15	1000
Chouane Dolomites	61	25	23	40	10	1250
Chouf Sandstone	48	20	23	20	15	1000
Hammana Formation	48	20	23	20	15	1000
Keserouane Limestone	61	25	23	40	10	1250
Maameltain Marls	59	25	23	40	10	1000
Mdairej Limestone	77	34	23	50	10	2000
Miocene Deposits	48	20	23	20	10	1000
Pliocene Deposits	57	25	23	40	5	2000
Quaternary Heterogeneous Dep.	15	30	23	0	0	0
Sannine Limestone	59	25	23	40	10	1000

Newmark's sliding-block analysis

Raster maps were generated in ArcGIS© for the strength parameters and the factor of safety for every 15-m grid cell was calculated. Based on Jibson et al. (2000), the failure surface depth for the infinite sliding-block was assumed constant ($d = 3.33\text{m}$) and dry soil conditions were considered ($m = 0$). The critical accelerations for each grid cell were then calculated using Eq. (1). The PGA map was rasterized and the slope displacements were calculated from Eq. (2). Figure 3 shows the 15mx15m pixels where displacements were greater than 5cm.

Limit Equilibrium Analysis

Calculations were performed in ArcGIS© using Eqs. (3) and (4). Slope displacements were then calculated using Eq. (2). Displacements less than 5cm were neglected in the final maps. Figure 4 shows the produced displacement maps for the selected regions.

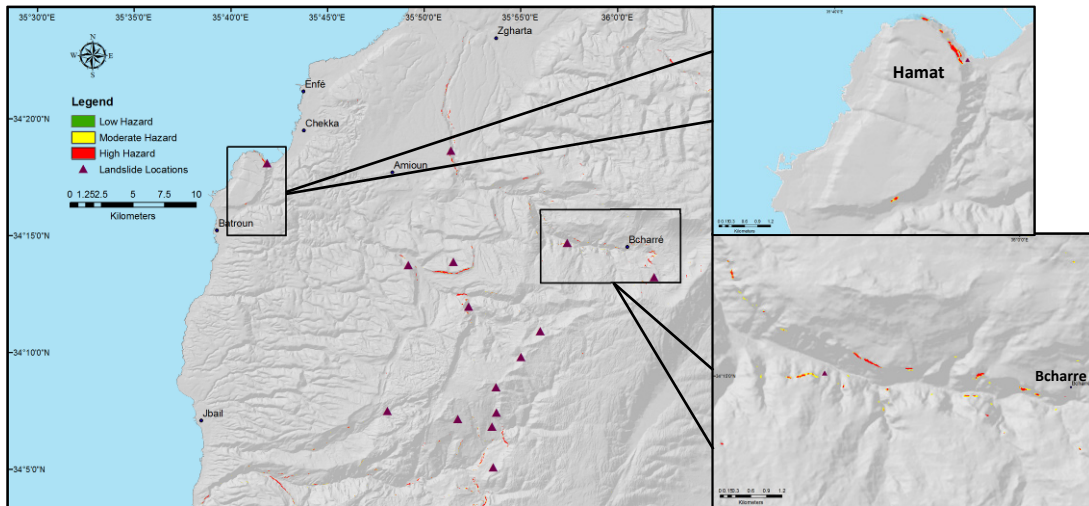


FIG. 3: Hazard predictions based on Newmark's sliding block analysis

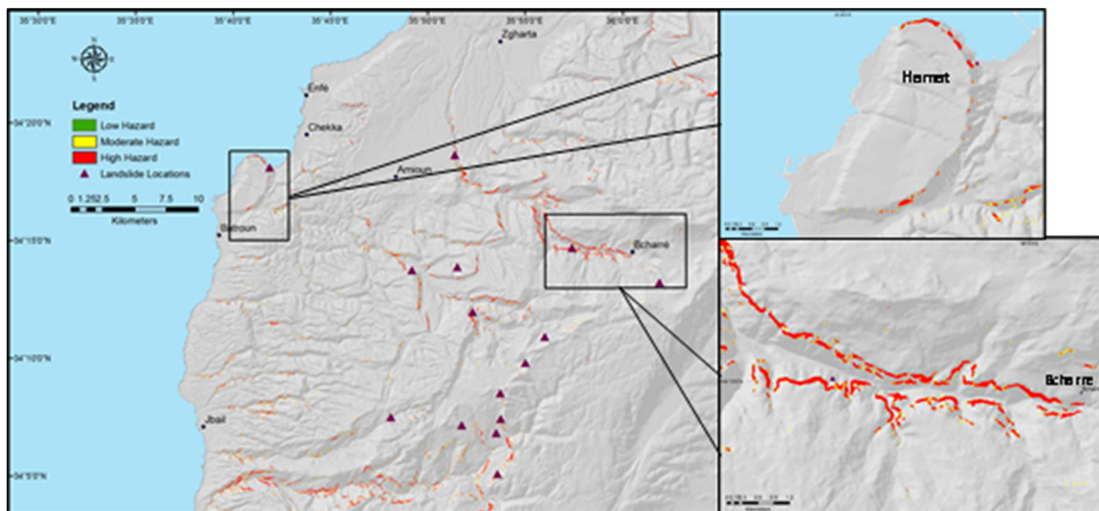


FIG. 4: Hazard predictions based on limit equilibrium analysis

Multi-Modal Slope Analysis

Slope susceptibility to coseismic failure was assessed based on the terrain classification and the governing mode of failure. A low-medium-high hazard classification system was applied to the failure modes but at different thresholds. Disrupted failures need less displacement to trigger a hazard when compared to coherent soil failures. Lateral spreading potential was classified into low and high displacement categories. Figure 5 shows the corresponding displacement predictions for the different modes in the selected regions.

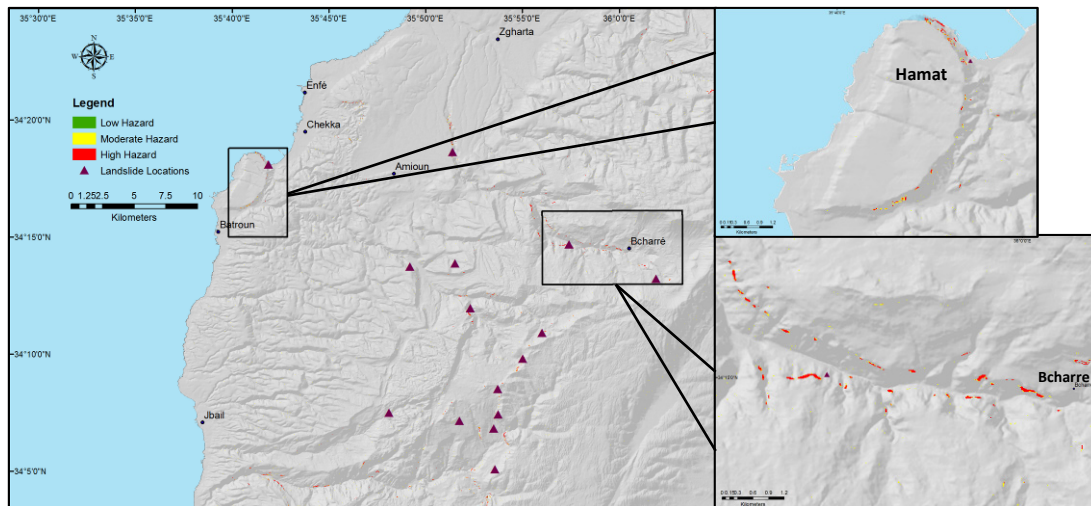


FIG. 5: Hazard predictions based on multi-modal slope analysis

CONCLUSION

Lebanon is a country that is located in a relatively high seismic zone and has a rugged topography making it vulnerable to coseismic landslide hazards. In this paper, we presented three approaches to assess coseismic landslide hazard at a regional scale, and highlighted the zones having the highest potential for sliding during an earthquake with the goal of producing for the first time a landslide hazard classification map for Lebanon. Although Lebanon does not have a published landslide inventory map, we collected data from the literature about landslide locations in Lebanon. This allowed us to check the results we obtained against the observed/mapped mass movements with respect to Lebanon's geologic units and slopes. Additionally, high hazard locations that showed repeatedly predicted using the three approaches indicate the need to conduct further field assessments and verify the extent of the hazard. Potential consequences to structures and humans due to coseismic landsliding should also be considered and vary depending on the area. For example, a high coseismic slope hazard region where failure will have only limited consequences on homes or people corresponds to a low risk area. Conversely, if a rockfall runout is capable of striking a village and pose risk to life-safety, then the high hazard area will also be mapped as a high risk area.

ACKNOWLEDGEMENTS

The authors acknowledge the support of USAID (Grant No. AID-OAA-A-11-00012), NAS (Sub-Grant No. PGA-2000001933), and NSF (Grant No. CMMI-1156413) for funding the project that resulted in this work. Any opinions, findings, conclusions, or recommendations expressed in this article are those of the authors alone, and do not necessarily reflect the views of these agencies.

REFERENCES

- Abdallah, C., Chorowicz, J., Kheir, R. B., and Khawlie, M. (2005). "Detecting major terrain parameters relating to mass movements' occurrence using GIS, remote sensing and statistical correlations, case study Lebanon." *Remote Sensing of Environment*, Vol. 99 (4): 448-461.
- Dubertret, L., (1945). "Cartes géologiques à l'échelle de 1/50 000 (Hamidieh, Halba, Batroun, Tripoli, Sir El Dannieh, Jbail, Qartaba, Baalbeck, Beirut, Zahle, Rayak, Saida, Jezzine, Rachaya)." *République Libanaise, Ministère des Travaux Publics, Beyrouth, Liban.*
- Elias, A., Taponnier, P., Singh, S. C., King, G. C. P., Briais, A., Daeron, M., Carton, H., Sursock, A., Jacques, E., Jomaa, R., and Klinger, Y. (2007). "Active thrusting offshore Mount Lebanon: Source of the tsunamigenic A.D. 551 Beirut-Tripoli earthquake." *Geology*, Vol. 35 (8): 755-758.
- Grant, A. R., Wartman, J., and Abou-Jaoude, G. (2014). "A Terrain classification system for coseismic landslide hazard analysis: Lebanon, A Case Study". *Presented at the 2014 GSA Annual Meeting in Vancouver, British Columbia.*
- Hamada M, Towhata I, Yasuda S, Isoyama R (1987). "Study on permanent ground displacement induced by seismic liquefaction." *Computers and Geotechnics*, Vol. 4 (4): 197-220
- Huijter, C.E. (2010). "Implications of the recent mapping of the offshore thrust fault system on the seismic hazard of Lebanon." *Dissertation, American University of Beirut*
- Jibson, R.W. (2007) "Regression models for estimating coseismic landslide displacement." *Engineering Geology* Vol. 91 (2): 209-218.
- Jibson, R.W., Harp E.L., Michael J.A. (2000). "A method for producing digital probabilistic seismic landslide hazard maps." *Engineering Geology*, Vol. 58 (3): 271-289.
- Keefer, D.K. (1984). "Landslides caused by earthquakes." *Geological Society of America Bulletin* Vol. 95 (4): 406-421.
- Khawlie M.R. and Hassanain H.I. (1984). "Failure phenomena and environmental control of the relatively unstable Hammana area, Lebanon." *Engineering Geology*, Vol. 20 (3): 253-264
- Kim, J. and Sitar N. (2004). "Direct estimation of yield acceleration in slope stability analyses." *J. Geotechnical & Geoenviron. Engrg.*, Vol. 130 (1): 111-115.
- Li, A.J., Merifield R.S., Lyamin A.V. (2008). "Stability charts for rock slopes based on the Hoek-Brown failure criterion." *International Journal of Rock Mechanics and Mining Sciences*, Vol. 45 (5): 689-700
- Newmark, N. M. (1965). "Effects of earthquakes on dams and embankments." *Geotechnique*, Vol. 15 (2): 139-160.
- Saade, A., Abou-Jaoude, G., and Wartman, J. (2016). "Regional-scale co-seismic landslide assessment using limit equilibrium analysis", *Engineering Geology*, Vol. 204: 53-64

Evaluation of the Liquefaction Potential for the Mega-City of Mumbai— Probabilistic Performance-Based Approach

K. S. Vipin¹ and S. D. Anitha Kumari²

¹Earthquake Specialist, SwissRe, Bangalore 560027. E-mail: ks.vipin@gmail.com

²Associate Professor, M.S. Ramaiah Univ. of Applied Sciences, Peenya, Bangalore 560058. E-mail: anithakumari.ce.et@msruas.ac.in

Abstract: Most urban centers in India are prone to earthquakes and hence the assessment of seismic hazard and its secondary effects play a major role in mitigating the hazard for these cities. In India, the sub-standard quality of buildings and inadequate assessment of hazard pose a major risk in hazard mitigation. One of the best ways to tackle this issue is to identify seismic vulnerable regions in the country and take adequate measures for hazard mitigation. This paper addresses the issue of identifying the liquefaction susceptible areas in Mumbai city based on a probabilistic method. Mumbai, being a coastal city and situated on a deep soft soil deposit, the level of saturation and the soil conditions can worsen the seismic effects. The method adopted in this study uses an end-to-end probabilistic approach both for seismic hazard modeling and liquefaction potential evaluation. The use of probabilistic methods in liquefaction potential evaluation will help in quantifying the uncertainties involved in seismic hazard and soil parameters. The liquefaction return period curve and the factor of safety against liquefaction at various locations in Mumbai along with maps showing spatial variation of factor of safety against liquefaction are developed in the study.

INTRODUCTION

Earthquakes are one of the devastating natural hazards, which results in liquefaction of soft soils. The harmful effects of liquefaction were observed during various deadliest earthquakes viz. Niigata (1964), Kobe (1985), Loma Prieta (1989), Bhuj (2001), Christchurch (2011) and Tohoku (2011). The heavy damages that occur during these liquefaction events has prompted the scientific community to extend research on the liquefaction susceptibility of major urban centres. Liquefaction susceptibility can be evaluated using in-situ or laboratory tests. Some of the most commonly used field tests for the evaluation of liquefaction susceptibility include standard penetration test (SPT), cone penetration test (CPT), shear-wave velocity test (V_s) and the Becker penetration test (BPT) (Youd et al. 2001). The most widely adopted liquefaction evaluation method includes the one suggested by Seed et al. (1985). The liquefaction assessment correlations based on the in situ penetration tests

help to estimate the triggering or initiation of seismically-induced soil liquefaction. Initial research on liquefaction susceptibility was mainly based on SPT and CPT data. These tests are widely used because they are having an advantage of correlating the liquefaction potential with relative density and also plenty of test data was available. Recently large amount of shear wave velocity (V_s) profile is available and it is relatively easy to collect this data for a large area. Moreover, V_s is less sensitive to the problems associated with penetration resistance when fines are present. Hence, in this study, a new performance based liquefaction potential evaluation method is developed based on shear wave velocity (V_s) values.

However, all the liquefaction potential evaluation methods based on shear wave velocity is using a single magnitude and single ground acceleration value. Kramer and Mayfield (2007) put forward another method wherein the entire range of ground motion and magnitude levels for the evaluation of liquefaction potential based on SPT values. Vipin and Sitharam (2012) proposed an approach for the assessment of liquefaction potential based on CPT data. In the present study, a similar method is developed for assessing performance based liquefaction susceptibility for Mumbai. This technique is built on the probabilistic liquefaction assessment suggested by Kayen et al. (2013).

STUDY AREA

Mumbai is the second most populous Indian city situated on the western coastal region. Mumbai which is considered as the financial capital of India, is situated on soft soil. The city covers an area of around 600km^2 and is lying within a latitude of $18^\circ 53' \text{ N}$ to $19^\circ 20' \text{ N}$ and longitudes if $72^\circ 45' \text{ E}$ to 73° N . Fig 1 shows the study area. According to the seismic zonation map prepared by Bureau of India Standards (IS – 1893 Part I, 2002), Mumbai is in seismic zone III which classifies it as a moderate seismic risk area. Several studies by researchers (Mohan et al. 2007; Mhaske and Choudhury, 2010) have indicated the vulnerability of the region to seismic hazards. Due to the rapid and uncontrolled rise in urban sprawl, the need to provide additional residential and industrial areas has resulted in an increased vulnerability to liquefaction hazard in various parts of Mumbai which is formed as a reclaimed and amalgamated island. Due to the proximity to sea and other water bodies, the depth of ground water table in Mumbai is relatively shallow (Dixit et al. 2012).

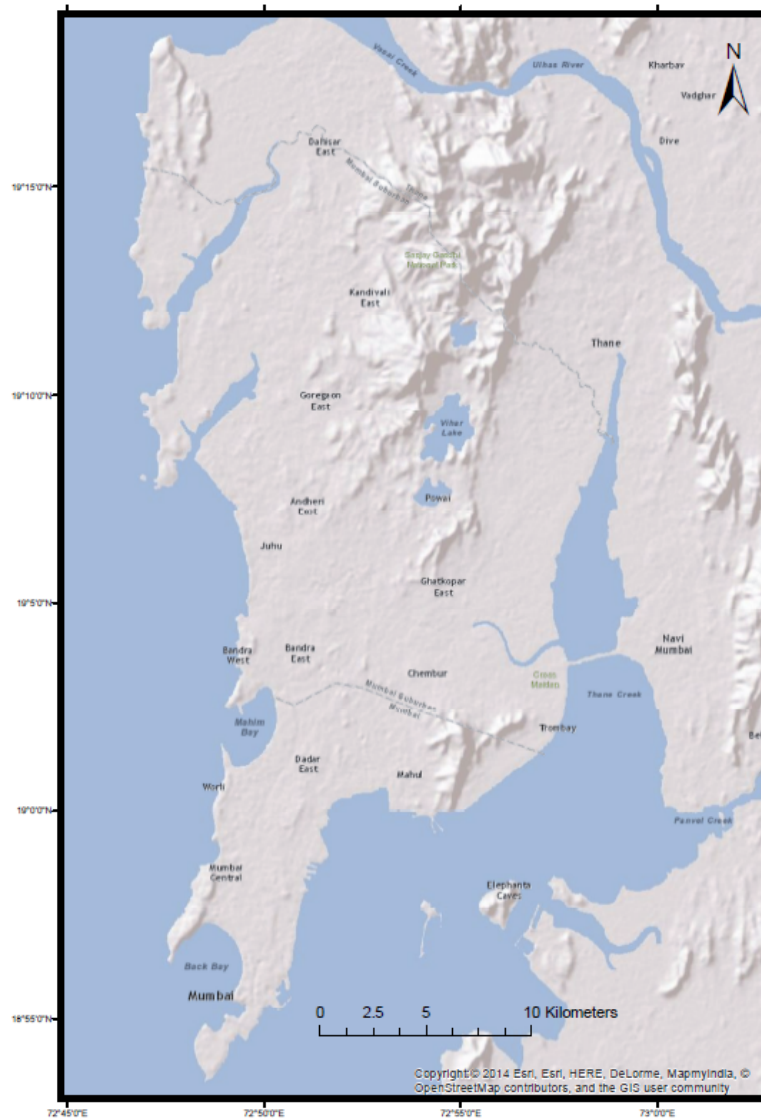


FIG. 1. Study area

SEISMIC HAZARD ASSESSMENT OF MUMBAI

Various studies were done in the past to assess the seismic hazard of Mumbai. A uniform hazard response spectra was developed by Raghukanth and Iyengar (2006) for Mumbai which is valid for different site conditions. Deterministic seismic hazard analysis of Mumbai which considers only a particular scenario has been reported by Desai and Choudhury (2014). The study on the spatial variation of probabilistic seismic hazard for Mumbai reported by Sarika and Choudhury (2014) indicates that seismic values were higher when compared with non-probabilistic zoning studies. In the present study, the method adopted for assessing the seismic hazard is similar to the one used by Vipin et al. (2009) and Sitharam and Vipin (2011). The earthquake catalogue, seismic sources and the seismicity parameters were taken from Vipin et al. (2009). All the seismic sources within a radial distance of 350km from Mumbai have

been considered in the analysis. The ground motion prediction equation (GMPE) reported by Raghukanth and Iyengar (2007) for South India is used for this study as it is the only relation available for this region. This relation gives the peak ground acceleration (PGA) at the bed rock level. To calculate the surface level PGA values, the site classification of Mumbai was done based on NEHRP (BSSC, 2001) provisions. The surface level ground acceleration values are evaluated using the site amplification factors for the respective site classes suggested by Raghukanth and Iyengar (2007). Based on these inputs, a complete probabilistic seismic hazard analysis is done for Mumbai and the surface level PGA values are calculated.

PERFORMANCE BASED EVALUATION OF LIQUEFACTION POTENTIAL

Liquefaction potential refers to a measure of earthquake loading and the corresponding soil resistance to liquefaction. This is generally expressed as a ratio of cyclic stress ratio (CSR, for loading) to cyclic resistance ratio (CRR, for resistance). The earthquake loading is characterized by peak ground surface acceleration and earthquake magnitude whereas the cyclic resistance or CRR is correlated to the values of various in-situ tests like SPT, CPT or shear wave velocity (V_s). Adopting SPT values, a large number of studies are reported based on deterministic and probabilistic approaches for evaluating liquefaction resistance. (Seed and Idriss 1971, Seed et al. 1985, Youd et al. 2001, Liao et al. 1988, Juang and Jiang 2000, Cetin et al. 2004).

While evaluating liquefaction potential, the uncertainties associated with earthquake loadings were not considered in the previous studies. When liquefaction potential is evaluated adopting deterministic CRR curves, only a single ground motion hazard and a single earthquake magnitude is used. On the other hand, performance based approach adopts probabilistic CRR curves. This method includes all ground motion hazards and earthquake magnitudes. The fundamentals for this approach were laid by Cornell (1968) in the procedure of seismic risk analysis. The performance-based approach to evaluate the return period of seismic soil liquefaction was integrated by Kramer and Mayfield (2007) into the method suggested by Cetin et al. (2004). They considered the entire range of ground motion and magnitude levels for the evaluation of liquefaction potential. The conventional methods of evaluating liquefaction potential provide a reliable prediction of different sites when subjected to a particular level of loading. However, performance based approach provides the liquefaction probability at various sites when subjected to different levels of loading.

Assessment of liquefaction potential based on shear wave velocity (V_s) value

In the present study, liquefaction potential is evaluated based on shear wave velocity (V_s). One of the latest work to assess the probability of liquefaction based on shear wave velocity is Kayen et al. (2013). According to their study, the probability of liquefaction is given by:

$$P_L = \Phi \left[-\frac{(0.0073V_{S1})^{2.8011} - 1.946 \ln CSR - 2.6168 \ln M_w - 0.0099(\ln(\sigma'_{v0}) + 0.0028FC)}{0.4809} \right]$$

where P_L is the probability of liquefaction; Φ is the standard normal cumulative distribution function; V_{S1} is the shear wave velocity at a given depth; CSR is the cyclic stress ratio without magnitude scaling factor; M_w is the moment magnitude of earthquake, σ'_{v0} is the effective vertical pressure at the given depth; FC is the fineness content in percentage. The value of depth reduction factor, which is used in calculating CSR is obtained using the method suggested by Cetin et al (2004). Adopting the above probabilistic relation, a performance based approach was developed to evaluate the liquefaction susceptibility using V_s values and is given below.

$$P\left[FS_L < FS_L^* \mid a_i, m_j\right] = \Phi \left[-\frac{(0.0073V_s)^{2.8011} - 1.946 \ln CSR_{eq,i} FS_L^* - 2.6168 \ln m_j - 0.0099(\ln(\sigma'_{v0}) + 0.0028FC)}{0.4809} \right]$$

FS_L is the factor of safety against liquefaction, FS_L^* is the targeted value of factor of safety against liquefaction, $CSR_{eq,i}$ is the cyclic stress ratio without any magnitude scaling factor computed for acceleration value a_i , a_i and m_j (moment magnitude) is obtained from the probabilistic deaggregated seismic hazard curve with respect to the magnitude.

PROBABILISTIC EVALUATION OF LIQUEFACTION RETURN PERIOD FOR MUMBAI

This study is broadly classified into two parts: (i) probabilistic seismic hazard assessment of Mumbai and (ii) probabilistic assessment of liquefaction potential using V_s values. The methodology adopted for the seismic hazard assessment is similar to the studies reported by Vipin et al. (2009) and Sitharam and Vipin (2011). To assess the liquefaction potential, shear wave velocity is the additional input required. Since measured V_s values are not available for the entire city, the V_s values were obtained from USGS (2015). However, this data gives the average V_{s30} values with a grid size of 1km x 1km. In the present study, the liquefaction potential is assessed for a depth of 3m. Since the V_s values for such shallow depths are not available it was calculated based on the method suggested by Boore et al. (2011). The depth of water table is taken as 1m and the density of soil as 16kN/m³. The percentage of fines is assumed to be 35%. The above assumptions are made based on Dixit et al. (2012).

RESULTS AND DISCUSSIONS

The entire analysis – probabilistic seismic hazard assessment and probabilistic liquefaction potential evaluation were done using MATLAB programs developed by the authors. Curves showing the variation of factor of safety against mean annual rate of exceedance at a depth of 3 m for four different locations in Mumbai are shown in Fig. 2. It can be seen that Nariman point, Worli and Jawaharlal Nehru Port (JN Port) are highly susceptible to liquefaction than Kandivali East. From Fig.2, the liquefaction return period for any given factor of safety can be obtained. If the factor of safety value of "1" is considered as a threshold for liquefaction, then the return period of liquefaction at Kandivali East will be around 72,000 years, whereas the

same for the other three locations will be in the range of 100 – 200 years. Figures showing the spatial variation of Factor of safety values against liquefaction for return periods of 475 and 2500 years (probability of exceedance of 10% and 2% in 50 years) are shown in Fig. 3 and 4. Those regions, which are having FS values less than or equal to 1 are highly susceptible to liquefaction, whereas those regions with FS greater than 2 can be considered as safe against liquefaction. It can be seen that most of the southern parts of the city are highly susceptible to liquefaction, whereas the northern parts of the city, mainly the regions near Sanjay Gandhi National Park are less susceptible to liquefaction. Trombay, which is the location of Nuclear power plant, is also less susceptible to liquefaction.

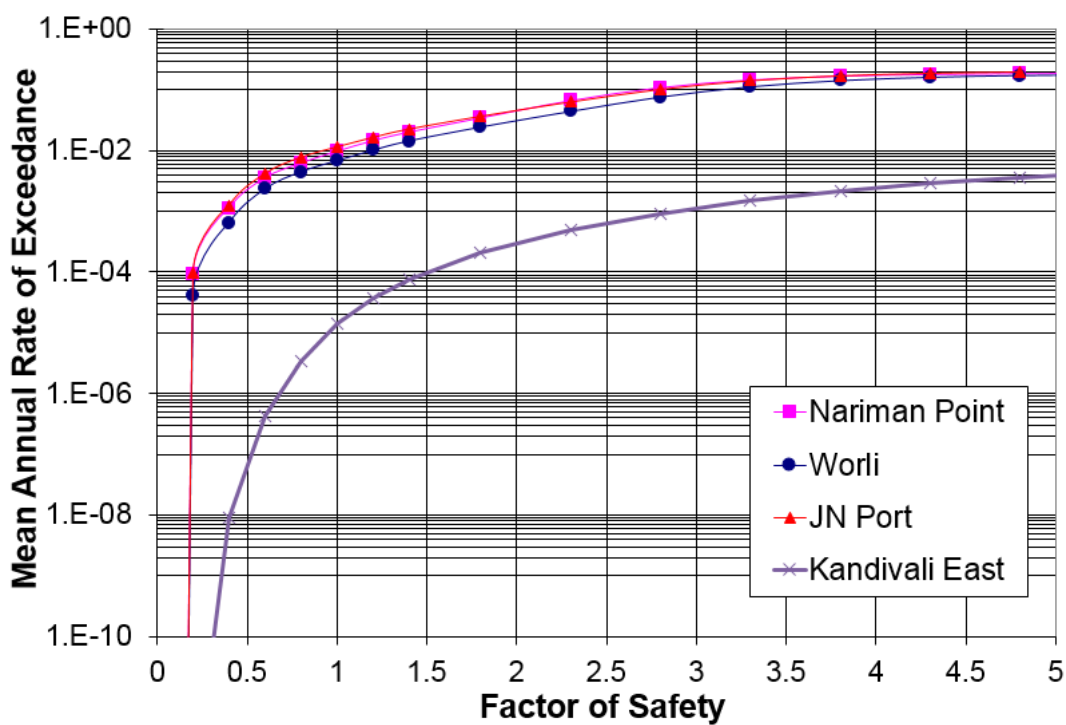


FIG.2. Factor of safety against mean annual rate of exceedance at a depth of 3m for various locations in Mumbai

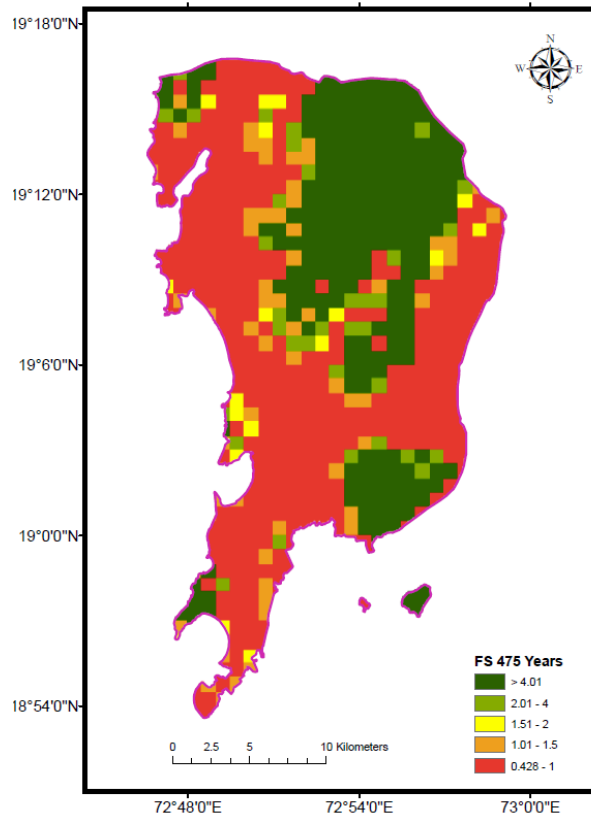


FIG.3. Factor of safety against liquefaction for a return period of 475 years at 3m depth

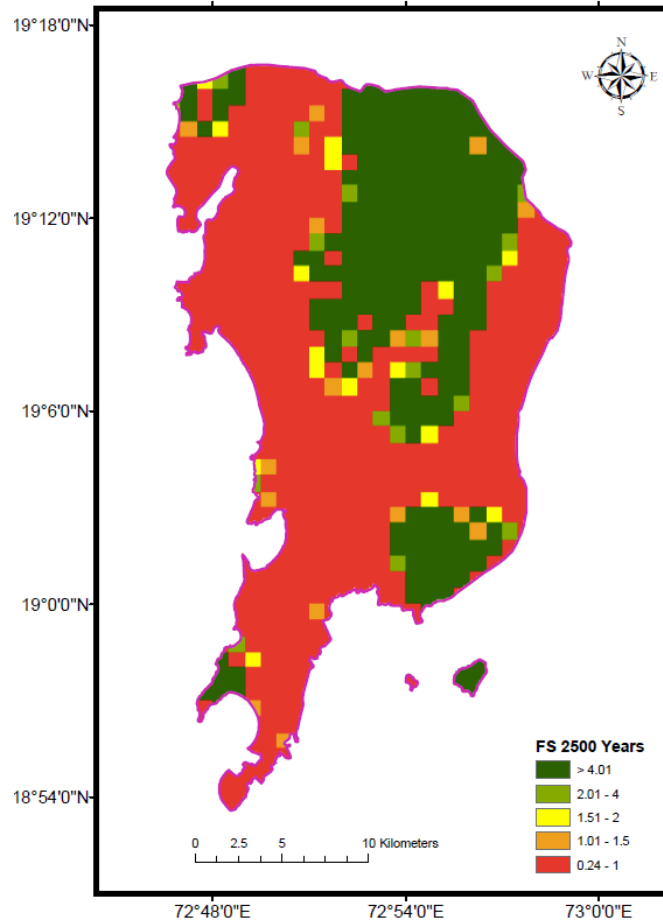


FIG.4. Factor of safety against liquefaction for a return period of 2500 years at 3m depth

Even though, some studies on liquefaction potential evaluation of Mumbai were done earlier, all these works considered scenario earthquakes. Hence, it may not be a good idea to compare the results of this study with those studies. The northern region of Mumbai as well as a small region on the south eastern side of Mumbai is having a hilly terrain. These regions are expected to have low liquefaction susceptibility and this is clearly visible in the variation of Factor of safety values.

CONCLUSIONS

The method adopted for liquefaction potential evaluation in this study considers the uncertainties in earthquake loading and soil strength. One of the main outcome of this work is the development of liquefaction return period curves. This will help in finding out the liquefaction return period for any factor of safety values under consideration. The factor of safety values against liquefaction reported in this study can be used in delineating liquefaction susceptible areas. The locations, which are having factor of safety against liquefaction greater than two, can be considered safe against

liquefaction for the given return period. For those regions, which are having factor of safety less than 2, it is recommended to do a detailed site specific study.

REFERENCES

- Boore, D. M., Thompson, E.M. and Cadet, H. (2011). "Regional Correlations of VS30 and velocities averaged over depths less than and greater than 30m." *Bulletin of the Seismological Society of America*, Vol. 101 (6): 3046–3059.
- Building Seismic Safety Council, BSSC (2001). *NEHRP recommended provisions for seismic regulations for new buildings and other structures*.
- Cetin, K. O. et al. (2004). "Standard penetration test-based probabilistic and deterministic assessment of seismic soil liquefaction potential." *J. Geotechnical & Geoenv. Engrg.*, Vol. 130 (12): 1314–1340.
- Cornell, C.A. (1968). "Engineering seismic risk analysis." *Bulletin of the Seismological Society of America*, Vol.58 (5): 1583–1606.
- Desai, S. S. and Choudhury, D. (2014). "Deterministic Seismic Hazard Analysis for Greater Mumbai, India." *Geo-Congress 2014*, ASCE: 389-398.
- Desai, S. S. and Choudhury, D. (2014). "Spatial Variation of probabilistic seismic hazard for Mumbai and surrounding region." *Natural Hazards*, Vol. 71:1873-1898.
- Dixit, J., Dewaikar, D.M. and Jangid, R.S. (2012). "Assessment of liquefaction potential for Mumbai City." *Natural Hazards*, Vol. 12: 2759-2768.
- IS 1893(Part I) (2002). *Indian standard criteria for earthquake resistant design of structures, Part 1—general provisions and buildings*.
- Juang, C. H., and Jiang, T. (2000). "Assessing probabilistic methods for liquefaction potential evaluation." *Soil dynamics and liquefaction*, R. Y. S. Pak and J. Yamamuro, eds., Geotechnical Special Publication, ASCE, 107:148–162.
- Kayen, R. et al. (2013). "Shear-wave-velocity based probabilistic and deterministic assessment of seismic soil liquefaction potential." *J. Geotechnical & Geoenv. Engrg.*, Vol. 139 (3):407-419.
- Kramer, S. and Mayfield, R.T. (2007). "Return period of soil liquefaction." *J. Geotechnical & Geoenv. Engrg.*, Vol.133 (7): 802–813.
- Liao, S. S. C., Veneziano, D., and Whitman, R. V. (1988). "Regression models for evaluating liquefaction probability." *Journal of Geotechnical Engrg.*, Vol.114 (4): 389–411.
- Mhaske, S.Y. and Choudhury, D. (2010). "GIS-based soil liquefaction susceptibility map of Mumbai city for earthquake events." *J. Appl. Geophys.*, Vol. 70: 216–225.
- Mohan, G., Surve, G. and Tiwari, P. (2007). "Seismic evidences of faulting beneath the Panvel flexure." *Current Science*, Vol. 93: 991–996.
- Raghukanth, S. T. G. and Iyengar, R. N. (2006). "Seismic hazard estimation for Mumbai city." *Current Science*, Vol. 91 (11):1486-1494.
- Raghukanth, S. T. G. and Iyengar, R. N. (2007). "Estimation of seismic spectral acceleration in peninsular India." *J Earth Syst Sci.*, Vol.116 (3):199–214.
- Seed, H.B. and Idriss, I.M. (1971). "Simplified procedure for evaluating soil liquefaction potential." *Journal of Soil Mechanics and Foundation Engineering*, Vol. 97: 1249-1273.

- Seed, H. B., Tokimatsu, K., Harder, L. F. and Chung, R. M. (1985). "Influence of SPT procedures in soil liquefaction resistance evaluations." *Journal of Geotechnical Engrg.*, Vol. 111 (12): 1425–1445.
- Sitharam, T.G. and Vipin, K.S. (2011). "Evaluation of spatial variation of peak horizontal acceleration and spectral acceleration for South India: A probabilistic approach." *Natural Hazards*, Vol. 59 (2): 639-653.
- USGS. "<http://earthquake.usgs.gov/hazards/apps/vs30/>." Last accessed on 10th Aug, 2015.
- Vipin, K.S., Anbazhagan, P. and Sitharam, T.G. (2009). "Estimation of peak ground acceleration and spectral acceleration for South India with local site effects: Probabilistic approach." *Natural Hazards and Earth System Sciences*, Vol. 9: 865-878.
- Vipin, K.S. and Sitharam, T.G. (2012). "A performance based framework for assessing liquefaction potential based on CPT data." *Georisk*, Vol.6 (3): 177-187.
- Youd T. L. et al. (2001). "Liquefaction resistance of soils: Summary report from the 1996 NCEER and 1998 NCEER/NSF workshops on evaluation of liquefaction resistance of soils." *J. Geotechnical & Geoenv. Engrg.*, Vol. 127 (10): 817–833.

The Seismic Bearing Capacity Factor for Surface Strip Footings

Anindya Pain¹; Deepankar Choudhury, M.ASCE²; and S. K. Bhattacharyya³

¹Ph.D. Student, Academy of Scientific and Innovative Research (AcSIR), New Delhi 110001, India; Scientist, CSIR-Central Building Research Institute, Roorkee 247667, India. E-mail: pain_anindya@yahoo.co.in

²Professor, Dept. of Civil Engineering, Indian Institute of Technology Bombay, Powai, Mumbai 400076, India; Adjunct Professor, Academy of Scientific and Innovative Research (AcSIR), New Delhi 110001, India. E-mail: dc@civil.iitb.ac.in

³Professor, Dept. of Civil Engineering, Indian Institute of Technology Kharagpur, West Bengal 721302, India; Former Director, CSIR-Central Building Research Institute, Roorkee 247667, India. E-mail: srimankb@gmail.com

Abstract: In earthquake prone areas, computation of bearing capacity under seismic condition is very important for the safe design of foundations. In previous years, attempts were made to use pseudo-static approach and a very few investigators used pseudo-dynamic approach to compute the seismic bearing capacity. Using the limit equilibrium method, the values of bearing capacity factor for surface strip footings resting on cohesionless soil are obtained by considering simple planar rupture surfaces under seismic conditions. The seismic forces are computed using the modified pseudo-dynamic method in which dry cohesionless soil is assumed as visco-elastic medium subjected to harmonic base shaking. Width of the footing, seismic wave velocities and angular frequency of the input motion influence the value of seismic bearing capacity. Comparisons of the proposed method with available theories in the seismic case are also presented to highlight the advantages of the present method for the design of surface strip footings considering seismic waves.

INTRODUCTION

Determination of the seismic bearing capacity of surface foundation is an important topic of research for the safe design of any superstructures in earthquake prone areas. Over the years attempts were made to use limit equilibrium method, limit analysis method, numerical methods, and numeric methods to compute bearing capacity under static and seismic conditions. Meyerhof (1963) is among the earliest, where the seismic forces were applied at the structure only as pseudo-static loads. Effect of the seismic forces on the inertia of the supporting soil was not considered in the analyses. Correcting this error, Sarma and Iossifelis (1990), Richards et al. (1993), Budhu and Al-Karni (1993), Choudhury and Subba Rao (2005) and Choudhury and Subba Rao (2006) considered the seismic forces both on the superstructure and on the supporting soil mass.

Kumar and Rao (2002) carried out the analysis for seismic bearing capacity of shallow foundations by using method of characteristics ignoring the vertical component of seismic acceleration. Soubra (1999) investigated the bearing capacity under static and seismic conditions using the upper-bound limit analysis theory. Kumar and Ghosh (2006) proposed the bearing capacity factors for the embedded footings on sloping ground using upper bound limit analysis. Ghosh (2008) applied pseudo-dynamic seismic forces for seismic bearing capacity of a strip footing using upper bound limit analysis. Author computed the values of the unit weight component of bearing capacity factor $N_{\gamma d}$ for different magnitudes of soil friction angle and soil amplification factor. Ghosh and Choudhury (2011) used limit equilibrium method to compute seismic bearing capacity factors with pseudo-dynamic seismic forces. Recently, Kumar & Chakraborty (2013) applied the lower bound theorem of the limit analysis in conjunction with finite elements and nonlinear optimization to compute the bearing capacity factor N_{γ} for a rough strip footing by incorporating pseudo-static horizontal seismic body force. This method of analysis is very rigorous as there is no requirement of assumption of failure mechanism.

In pseudo-static approach, the dynamic nature of the earthquake is considered in a very approximate way, whereas the pseudo-dynamic approach considers the vertically propagating shear and primary waves. The existing pseudo-dynamic method presents certain aspects which are open to criticism. First, the existing pseudo-dynamic method does not satisfy the zero stress boundary condition at the ground surface (Bellezza, 2014). Second, the existing pseudo-dynamic method assumes that the acceleration value amplifies linearly towards the ground surface which requires the assumption of an amplification factor (Pain et al., 2015).

Using the limit equilibrium method, the values of bearing capacity factor ($N_{\gamma d}$) for surface strip footings resting on dry cohesionless soil are obtained by considering simple planar rupture surfaces under seismic conditions. The seismic forces are computed using the modified pseudo-dynamic method in which the dry cohesionless soil is assumed as visco-elastic medium subjected to harmonic base shaking. The effects of both vertical and horizontal accelerations are considered in the present study. Comparisons of the proposed method with available theories in the seismic case are also presented.

METHODOLOGY

Yuan et al. (2006) proposed the equation of motion of stress waves travelling through visco-elastic medium. In vector form the equation of motion may be written as:

$$\rho \frac{\partial^2 \bar{u}}{\partial t^2} = \left\{ (\lambda + G) + (\eta_l + \eta_s) \frac{\partial}{\partial t} \right\} grad(\kappa) + \left(G + \eta_s \frac{\partial}{\partial t} \right) \nabla^2 \bar{u} \quad (1)$$

where ρ = density; λ = Lamé constant; G = Shear modulus; η_l and η_s = Viscosities; \bar{u} = Displacement vector and $\kappa = div(\bar{u})$

Bellezza (2015) proposed the solution of a plane wave propagating vertically in a Kelvin-Voigt homogeneous medium for the calculation of active thrust under seismic

condition. The proposed simplified form of eqn.(1) is given below

$$\rho \frac{\partial^2 u_h}{\partial t^2} = G \frac{\partial^2 u_h}{\partial z^2} + \eta_s \frac{\partial^3 u_h}{\partial t \partial z^2} \quad (2)$$

$$\rho \frac{\partial^2 u_v}{\partial t^2} = (\lambda + 2G) \frac{\partial^2 u_v}{\partial z^2} + (\eta_l + 2\eta_s) \frac{\partial^3 u_v}{\partial t \partial z^2} \quad (3)$$

Soil is modeled as Kelvin–Voigt solid assumed as a purely elastic spring and a purely viscous dashpot connected in parallel. In a Kelvin–Voigt material, the resistance to shearing deformation is given by the sum of an elastic component and a viscous component:

$$\tau = \gamma_s G + \eta_s \frac{\partial \gamma_s}{\partial t} \quad (4)$$

where τ = Shear stress; γ_s = Shear strain; η_s = Viscosity; G = Shear modulus

For a horizontal harmonic base shaking of angular frequency ω ; $\eta_s = \frac{2G\xi}{\omega}$ where ξ = damping ratio.

Solving the eqn.(2) for harmonic horizontal shaking and applying the boundary condition i.e. shear stress at the free surface ($z = 0$) is zero and assuming a base displacement $u_{hb} = u_{h0} \cos(\omega t)$, one can get the horizontal displacement as

$$u_h(z, t) = \frac{u_{h0}}{C_s^2 + S_s^2} \left[(C_s C_{sz} + S_s S_{sz}) \cos(\omega t) + (S_s C_{sz} - C_s S_{sz}) \sin(\omega t) \right] \quad (5)$$

where,

$$C_{sz} = \cos\left(\frac{y_{s1}z}{H}\right) \cosh\left(\frac{y_{s2}z}{H}\right) \quad (6a)$$

$$S_{sz} = -\sin\left(\frac{y_{s1}z}{H}\right) \sinh\left(\frac{y_{s2}z}{H}\right) \quad (6b)$$

$$C_s = \cos(y_{s1}) \cosh(y_{s2}) \quad (7a)$$

$$S_s = -\sin(y_{s1}) \sinh(y_{s2}) \quad (7b)$$

$$y_{s1} = \frac{\omega H}{V_s} \sqrt{\frac{\sqrt{1+4\xi^2}+1}{2(1+4\xi^2)}} \quad (8a)$$

$$y_{s2} = -\frac{\omega H}{V_s} \sqrt{\frac{\sqrt{1+4\xi^2}-1}{2(1+4\xi^2)}} \quad (8b)$$

Now differentiating eqn. (5) twice with respect to time, one can get the horizontal acceleration as:

$$a_h(z, t) = \frac{k_h g}{C_s^2 + S_s^2} \left[(C_s C_{sz} + S_s S_{sz}) \cos(\omega t) + (S_s C_{sz} - C_s S_{sz}) \sin(\omega t) \right] \quad (9)$$

where, $k_h g = -\omega^2 u_{h0}$

Equation (3) can be written in a form similar to eqn.(2) provided that u_h , G and η_s are replaced by u_v , $E_c (= \lambda+2G)$ and $\eta_p = (\eta_r+2\eta_s)$. And in the similar manner solving the eqn.(3) for harmonic vertical shaking and applying the boundary condition i.e. normal stress at the free surface ($z = 0$) is zero and assuming a base displacement $u_{vb} = u_{v0} \cos(\omega t)$, one can get the vertical displacement as

$$u_v(z,t) = \frac{u_{v0}}{C_p^2 + S_p^2} \left[(C_p C_{pz} + S_p S_{pz}) \cos(\omega t) + (S_p C_{pz} - C_p S_{pz}) \sin(\omega t) \right] \quad (10)$$

where,

$$C_{pz} = \cos\left(\frac{y_{p1}z}{H}\right) \cosh\left(\frac{y_{p2}z}{H}\right) \quad (11a)$$

$$S_{pz} = -\sin\left(\frac{y_{p1}z}{H}\right) \sinh\left(\frac{y_{p2}z}{H}\right) \quad (11b)$$

$$C_p = \cos(y_{p1}) \cosh(y_{p2}) \quad (12a)$$

$$S_p = -\sin(y_{p1}) \sinh(y_{p2}) \quad (12b)$$

$$y_{p1} = \frac{\omega H}{V_p} \sqrt{\frac{\sqrt{1+4\xi^2} + 1}{2(1+4\xi^2)}} \quad (13a)$$

$$y_{p2} = -\frac{\omega H}{V_p} \sqrt{\frac{\sqrt{1+4\xi^2} - 1}{2(1+4\xi^2)}} \quad (13b)$$

Now differentiating eqn. (10) twice with respect to time, one can get the vertical acceleration as:

$$a_v(z,t) = \frac{k_v g}{C_p^2 + S_p^2} \left[(C_p C_{pz} + S_p S_{pz}) \cos(\omega t) + (S_p C_{pz} - C_p S_{pz}) \sin(\omega t) \right] \quad (14)$$

where, $k_v g = -\omega^2 u_{v0}$

Consider a surface strip footing, AE, of width B resting on dry cohesionless soil as shown in Fig.1(a). One way failure mechanism is considered under seismic condition. Hence, the failure zone is divided into two parts viz. active planar wedge, ADE and passive planar wedge EDF. The depth of both wedges is H . The inclination of the failure wedges are α_a and α_p with horizontal respectively for active and passive wedges. The depth of the wedge is a function of width of the footing B and α_a . At depth z , the mass of thin element of the failure active wedge [$m_a(z)$] (Fig.1(b)) and the mass of a thin element of the failure passive wedge [$m_p(z)$] (Fig.1(c)) may be computed as:

$$m_{a,p}(z) = \frac{\gamma}{g} \frac{H-z}{\tan \alpha_{a,p}} dz \quad (15)$$

where γ is the unit weight of the soil. From eqn. (15), the total weight of the failure active (W_a) and passive (W_p) wedge may be computed by integrating over the entire depth $H = B \tan(\alpha_a)$.

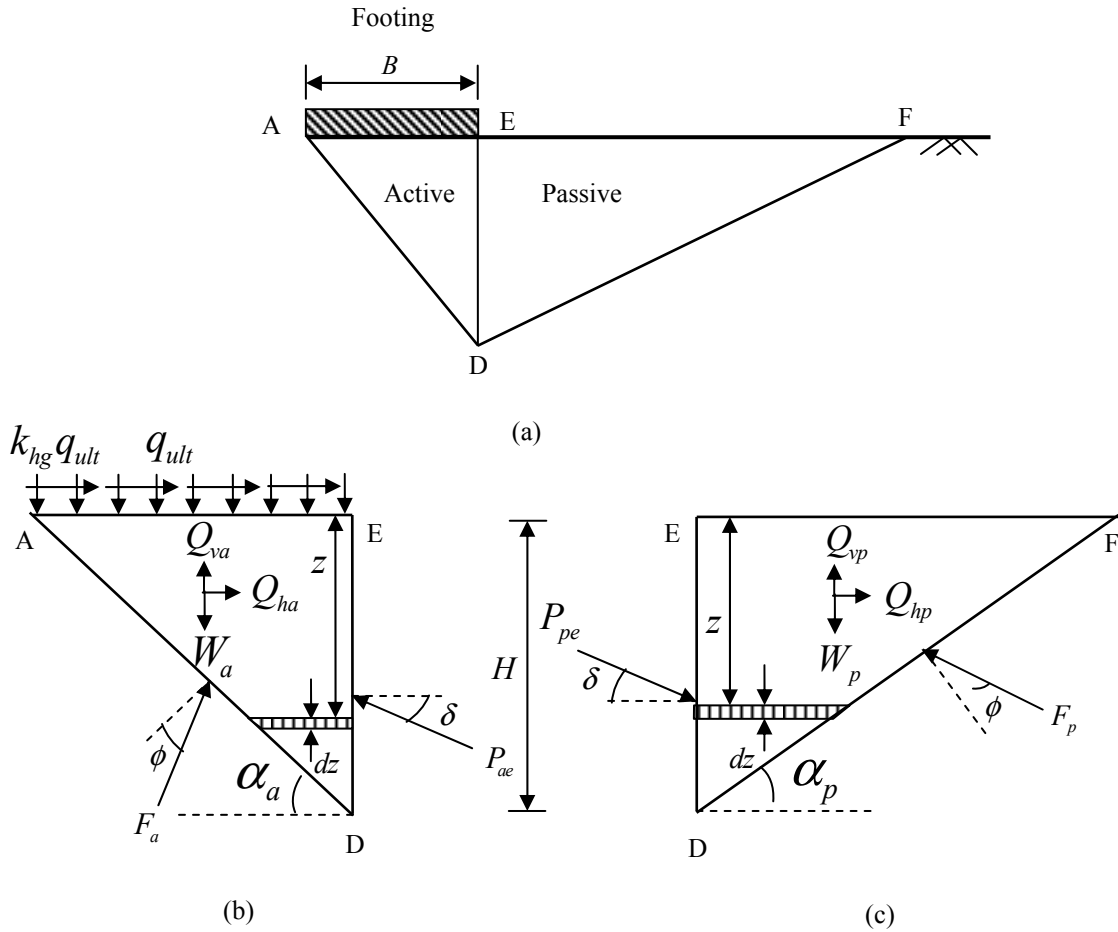


FIG.1. (a) Strip footing with different failure zones; (b) Forces acting in the active wedge; (c) Forces acting in the passive wedge

The total horizontal and vertical seismic inertia forces acting within the active failure wedge (Q_{ha}) and the total horizontal seismic inertia force within the passive failure wedge (Q_{hp}) can be obtained as:

$$Q_{ha, hp} = \int_0^H m_{a,p}(z) a_h(z, t) \tag{16a}$$

$$Q_{va, vp} = \int_0^H m_{a,p}(z) a_v(z, t) \tag{16b}$$

The most critical direction of the seismic inertia forces are shown in the Fig.1 to obtain the minimum value of bearing capacity. The total active thrust and passive resistance may be obtained by considering the force equilibrium of the failure wedges as shown in Fig.1.

$$P_{ae, pe}(t) = \frac{W_{a,p} \sin(\alpha_{a,p} \mp \phi) \pm Q_{ha, hp} \cos(\alpha_{a,p} \mp \phi) - Q_{va, vp} \sin(\alpha_{a,p} \mp \phi)}{\cos(\phi + \delta \mp \alpha_{a,p})} \tag{17}$$

where ϕ is the soil friction angle and δ is the interface friction angle between two failure wedges.

The seismic active earth pressure coefficient (K_{ae}) and the seismic passive earth pressure coefficient (K_{pe}) are defined as:

$$K_{ae,pe} = \frac{2P_{ae,pe}(t)}{\gamma H^2} \quad (18)$$

Bearing Capacity of Surface Strip Footing Under Seismic Condition

From Fig.1(c), the components of the total seismic passive resistance, in the horizontal and vertical directions may be obtained as:

$$M_{pe} = \frac{1}{2} \gamma H^2 K_{pe} \cos \delta$$

(19a)

$$N_{pe} = \frac{1}{2} \gamma H^2 K_{pe} \sin \delta \quad (19b)$$

Similarly, from Fig.1(b), by considering the equilibrium of all the forces, the components of the total seismic active thrust (P_{ae}) in the horizontal and vertical direction can be obtained as:

$$M_{ae} = q_{ult} H K_{ae} \cos \delta + \frac{1}{2} \gamma H^2 K_{ae} \cos \delta$$

(20a)

$$N_{ae} = q_{ult} H K_{ae} \sin \delta + \frac{1}{2} \gamma H^2 K_{ae} \sin \delta \quad (20b)$$

where q_{ult} is the seismic bearing capacity of the footing.

Now considering the equilibrium of forces along face DE, it may be written that:

$$M_{ae} = M_{pe} \text{ and } N_{ae} = N_{pe} \quad (21)$$

The most crucial decision in this analysis is the selection of proper value of δ . The value of δ selected for the present analysis is $\phi/2$ as suggested by Richards et al. (1993) and Ghosh and Choudhury (2011). From eqn. (21) one may write:

$$q_{ult} = \frac{1}{2} \gamma B \tan \alpha_a \left(\frac{K_{pe}}{K_{ae}} - 1 \right) \quad (22)$$

A non-dimensional bearing capacity factor $N_{\gamma e}$ may be written as:

$$N_{\gamma e} = \frac{2q_{ult}}{\gamma B} = \tan \alpha_a \left(\frac{K_{pe}}{K_{ae}} - 1 \right) \quad (23)$$

RESULTS AND DISCUSSIONS

Results of the analysis are presented in graphical form for seismic bearing capacity factor ($N_{\gamma d}$). Input parameters considered in the present analysis are as follows: $B = 1$ to 2.5 m; $\phi = 20, 30$ and 40° ; $\delta = 0.5\phi$; $k_v = 0.0k_h$ and $0.5k_h$; $T = 0.2$ to 0.5 sec; $V_s =$

100, 150 and 200 m/s for $\phi = 20, 30$ and 40° respectively; $V_p/V_s = 1.87$ for $\nu_s = 0.3$ (where ν_s = Poisson's ratio of the backfill soil) and damping ratio $\xi = 10\%$.

Table 1 shows the values of α_a and α_p associated with the critical failure surfaces for which the value of bearing capacity factor is minimum. The values of α_a are found to be decreasing with the increase in the seismic acceleration coefficient values. The depth of the failure surface is more for higher ϕ values. It is also observed that the depth of the failure surface steadily reduces with the increase in the seismic acceleration coefficient values.

Table 1. Values of α_a and α_p corresponding to the critical failure surface for $B = 2\text{m}$, $k_v = 0.5 k_h$, $T = 0.3$ sec, $V_s = 150$ and 200 m/s for $\phi = 30$ and 40° respectively, $V_p/V_s = 1.87$ and $\xi = 10\%$

ϕ	k_h	α_a	α_p	H/B
30°	0.00	44°	21°	0.966
	0.05	41°	20°	0.869
	0.10	38°	20°	0.781
	0.15	34°	19°	0.674
	0.20	29°	18°	0.554
40°	0.00	53°	14°	1.327
	0.05	50°	14°	1.192
	0.10	47°	14°	1.072
	0.15	44°	14°	0.966
	0.20	40°	13°	0.839

The variation of $N_{\gamma d}$ with k_h for various ϕ and k_v values is given in Fig.2. $N_{\gamma d}$ is decreasing with increase in both horizontal and vertical seismic accelerations. For example, $N_{\gamma d}$ decreases by about 83% for a change in k_h from 0.0 to 0.3 when $k_v = 0.0k_h$ and $\phi = 30^\circ$, similarly when k_h changes from 0.0 to 0.3 for $k_v = 0.5k_h$ and $\phi = 30^\circ$, $N_{\gamma d}$ decreases by about 89%. It is also observed that, higher the ϕ value, more is the influence of both k_h and k_v . Fig.2 shows a significant influence of the vertical seismic acceleration particularly for $k_h > 0.1$.

Ghosh (2008) reported that the seismic bearing capacity continuously decreases with increase in the soil amplification factor value. But there is no clear guideline for the selection of a proper amplification factor value. Selection of an appropriate amplification value is very crucial for safe and economic design of foundations. The amplification of acceleration in the present methodology is a function of normalized frequencies ($\omega H/V_s$ and $\omega H/V_p$) and damping ratio (Pain et al., 2015). So, for a particular soil, if we assume a constant value of damping ratio, under a particular period of base shaking T , the amplification of acceleration depends on the depth of the critical failure surface (H). And this depth is a function of α_a and the width of the footing, B . To understand the effect of footing width on the $N_{\gamma d}$, a parametric study is done on different width of the footings. Table 2 shows the variation of $N_{\gamma d}$ with B for $k_h = 0.10$, $k_v = 0.5k_h$, $T = 0.3$ sec and $\xi = 10\%$. Very marginal decrease in the value of $N_{\gamma d}$ is observed for comparatively bigger strip footings.

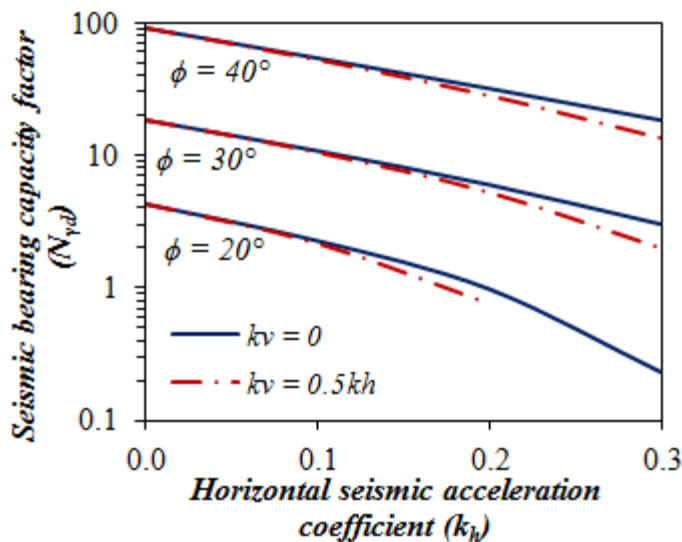


FIG.2. Variation of $N_{\gamma d}$ with k_h and k_v for $B = 2\text{m}$, $T = 0.3\text{ sec}$, $\xi = 10\%$, $V_s = 100, 150$ and 200 m/s for $\phi = 20, 30$ and 40° respectively and $V_p/V_s = 1.87$

The decrease in the value of $N_{\gamma d}$ may be attributed to the increase in the value of normalized frequencies ($\omega H/V_s$ and $\omega H/V_p$). The amplification of acceleration increases as the normalized frequency approaches $\pi/2$, which is the normalized fundamental frequency of the soil deposit (Pain et al., 2015). If the footing width is such that the normalized frequencies are close to $\pi/2$, a sharp reduction in the bearing capacity is observed.

Table 2. Variation of $N_{\gamma d}$ with B for $k_h = 0.10$, $k_v = 0.5k_h$, $T = 0.3\text{ sec}$ and $\xi = 10\%$

$B(m)$	<i>Seismic bearing capacity factor ($N_{\gamma d}$)</i>		
	$\phi = 20^\circ$	$\phi = 30^\circ$	$\phi = 40^\circ$
1.0	2.189	10.496	52.624
1.5	2.182	10.467	52.471
2.0	2.172	10.426	52.256
2.5	2.159	10.372	51.976

Table 3 shows the variation of $N_{\gamma d}$ with T for $k_h = 0.10$, $k_v = 0.5k_h$, $B = 2\text{m}$ and $\xi = 10\%$. $N_{\gamma d}$ is increasing with increase in period of shaking T . The angular frequency ω decreases when the period of shaking increases. The value of normalized frequency decreases for higher values of T while the other parameters are constant. The increase in the value of $N_{\gamma d}$ is because of the decrease in the value of the normalized frequencies. $N_{\gamma d}$ increases by only 2.56% for a change in T from 0.2 to 0.5 sec. The change is very insignificant from the application point of view. But a designer should keep in mind that individually B , T or seismic wave velocities may not have that much impact on the value of $N_{\gamma d}$, but the critical combination of these parameters may have serious consequence. A check should be made to ensure that the normalized frequencies are not close to $\pi/2$.

Table 3. Variation of N_{yd} with B for $k_h = 0.10$, $k_v = 0.5k_h$, $T = 0.3$ sec and $\xi = 10\%$

$T(sec)$	<i>Seismic bearing capacity factor (N_{yd})</i>		
	$\phi = 20^\circ$	$\phi = 30^\circ$	$\phi = 40^\circ$
0.2	2.130	10.255	51.364
0.3	2.166	10.404	52.139
0.4	2.179	10.454	52.406
0.5	2.185	10.478	52.529

Comparison of Results

In Fig.3, the present values of N_{yd} are compared with pseudo-static results reported in the literature. It is clear from the figure that the present results compare well with the existing analytical results. The results using the method of characteristics (Kumar and Rao, 2002) are very conservative. The present values are in good agreement with those reported by Choudhury and Subba Rao (2005). Results are on the higher side as compared to those reported by Kumar and Chakraborty (2013), which may be due to difference in the method of analysis. However, the present study considers the dynamic properties of the soil and characteristic of the input motion more realistically compared to the literature mentioned above.

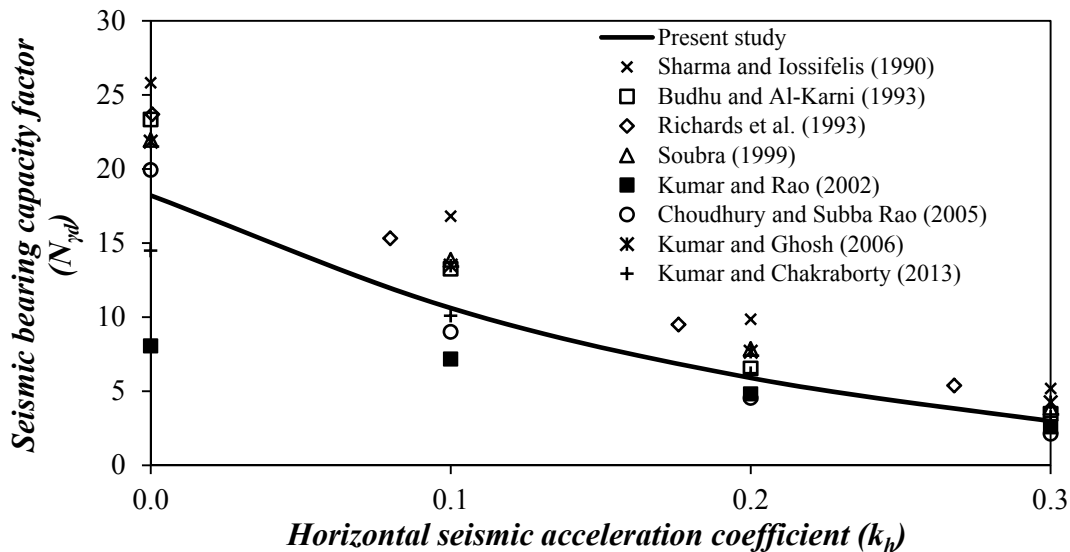


FIG.3. Comparison of N_{yd} with $B = 2m$, $\phi = 30^\circ$, $k_v = 0.0k_h$, $T = 0.3$ sec, $V_s = 150$ m/s, $V_p = 280$ m/s and $\xi = 10\%$

CONCLUSIONS

Seismic bearing capacity for design of surface strip footing is obtained using modified pseudo-dynamic seismic forces. Proposed method satisfies the boundary conditions. Amplification of acceleration depends on the dynamic properties of the

soil and characteristics of the input motion. Soil friction angle and seismic acceleration coefficients has profound influence on the seismic bearing capacity. The width of the footing, seismic wave velocities and period of shaking have some influence on the value of seismic bearing capacity. Comparison of the present method with the available literature is reported.

REFERENCES

- Bellezza, I. (2014). "A new pseudo-dynamic approach for seismic active soil thrust." *Geotechnical and Geological Engineering*, Vol. 32 (2): 561-576.
- Bellezza, I. (2015). "Seismic active soil thrust on walls using a new pseudo-dynamic approach." *Geotechnical and Geological Engineering*, Vol. 33 (4): 795-812.
- Budhu, M. and Al-Karni, A. (1993). "Seismic bearing capacity of soils." *Géotechnique*, Vol. 43 (1): 181-187.
- Choudhury, D. and Subba Rao, K.S. (2005). "Seismic bearing capacity of shallow strip footings." *Geotechnical and Geological Engineering*, Vol. 23 (4): 403-418.
- Choudhury, D. and Subba Rao, K. S. (2006). "Seismic bearing capacity of shallow strip footings embedded in slope", *International Journal of Geomechanics, ASCE*, Vol. 6 (3): 176-184.
- Ghosh, P. (2008). "Upper bound solutions of bearing capacity of strip footing by pseudo-dynamic approach." *Acta Geotechnica*, Vol. 3 (2): 115-123.
- Ghosh, P. and Choudhury, D. (2011). "Seismic bearing capacity factors for shallow strip footings by pseudo-dynamic approach." *Disaster Advance*, Vol. 4 (3): 34-42.
- Kumar, J. and Rao, V.B.K.M. (2002). "Seismic bearing capacity factors for spread foundations." *Géotechnique*, Vol. 52 (2): 79-88.
- Kumar, J. and Ghosh, P. (2006). "Seismic bearing capacity for embedded footing on sloping ground." *Géotechnique*, Vol. 56 (2): 133-140.
- Kumar, J. and Chakraborty, D. (2013). "Seismic bearing capacity of foundations on cohesionless slopes." *J. Geotech. Geo-environ. Eng.*, Vol. 139 (11): 1986-1993.
- Meyerhof, G.G. (1963). "Some recent research on the bearing capacity of foundations, The ultimate bearing capacity of foundations." *Can. Geotech. J.*, Vol. 1 (1): 16-26.
- Pain, A. Choudhury, D. and Bhattacharyya, S. K. (2015). "Seismic stability of retaining wall-soil sliding interaction using modified pseudo-dynamic method." *Géotechnique Letters*, Vol. 5 (1): 56-61.
- Richards, R. Jr. Elms, D. and Budhu, M. (1993). "Seismic Bearing Capacity and Settlements of Foundations." *J. Geotech. Geo-environ. Eng.*, Vol. 119 (4): 662-674.
- Sarma, S.K. and Iossifelis, I.S. (1990). "Seismic bearing capacity factors of shallow strip footings." *Géotechnique*, Vol. 40 (2): 265-273.
- Soubra, A.H. (1999). "Upper bound solutions for bearing capacity of foundations." *J. Geotech. Geo-environ. Eng.*, Vol. 125 (1): 59-69.
- Yuan, C. Peng, S. Zhang, Z. Liu, Z. (2006). "Seismic wave propagation in Kelvin-Voigt homogeneous visco-elastic media." *Sci. China, Ser. D Earth Sci.*, Vol. 49 (2): 147-153.

Seismic Deformation Assessment of a Dam Founded on Low Plastic Fine-Grained Soils under Strong Earthquake Shaking

Thuraisamy Thavaraj¹; Garry Stevenson²; and David Siu³

¹Senior Geotechnical Engineer, Klohn Crippen Berger Ltd., 500-2955 Virtual Way, Vancouver, BC, V5M4X1, Canada. E-mail: tthavaraj@klohn.com

²Manager, GeoStructures, Klohn Crippen Berger Ltd., 500-2955 Virtual Way, Vancouver, BC, V5M4X1, Canada. E-mail: gstevenson@klohn.com

³Engineering Team Lead, Geotechnical Group (Team A), BC Hydro, 6911 Southpoint Dr., Edmonds A02, Burnaby, BC, V3N4X8, Canada. E-mail: David.Siu@bchydro.com

Abstract: This paper presents the seismic assessment of a central core embankment dam partially founded on relatively weak, low plastic fine-grained soils. Characterization of low plastic fine-grained soils, especially their cyclic and post-cyclic behavior was critical in assessing the seismic performance of the dam. A site investigation and laboratory testing program was undertaken to characterize the low plastic fine-grained soils and their behavior under the cyclic loading. An effective stress based constitutive model UBCSAND, developed at the University of British Columbia, Canada and implemented in the computer program FLAC, was shown to be able to capture the characteristic cyclic behavior observed in the laboratory cyclic direct simple shear tests. Seismic deformation analyses using the model showed that, although the low plastic fine grained soils will not behave like loose sand, it can still cause significant displacements due to accumulation of strains during cyclic loading.

INTRODUCTION

Seismic assessment of a central core embankment dam partially founded on low plastic fine grained soils is the focus of this study. The dam was built immediately downstream of the original hydraulic fill dam. The upper part of the original dam was largely removed but the lower part of the dam was retained and was incorporated into the new dam with very flat slopes. The crest of the new dam is 288 m long and is cambered from El 131 m at the centre to El 130.5 m at the abutments. The new dam has relatively wide central core, filter and drain zones. The filter and drain zones are each 2.5 m wide. The maximum normal reservoir level is El 125.5 m.

The methods for assessing liquefaction potential of cohesionless soils such as clean sand and non-plastic silts are well established, and they are usually determined using Standard Penetration Test (SPT) or Cone Penetration Test (CPT) data. Their post-liquefaction residual strengths are determined based on SPT or CPT data and empirical correlations. However, application of these methods and correlations to low

plastic fine-grained soils may lead to an overly conservative design or assessment. There have been significant developments in the liquefaction assessment of low plastic fine-grained soils in recent years. According to the recent methods, these low plastic soils are initially screened for liquefaction susceptibility using their plasticity index and their water content with respect to the liquid limit. If found to be susceptible, advanced laboratory tests on undisturbed samples are recommended, in addition to in situ testing, to confirm their liquefaction susceptibility and to characterize their cyclic and post-cyclic behavior.

The site investigation program should include in situ shear vane, SPT or CPT testing and undisturbed sampling; the laboratory program should include constant volume cyclic direct simple shear tests (CDSS) and consolidation tests. The CDSS tests should include tests with and without initial static bias and both cyclic and post-cyclic monotonic phases. The cyclic loading phase is to study the response under cyclic loading and the post-cyclic monotonic loading phase is to assess the post-earthquake or post-liquefaction residual shear strength of the material. The post-cyclic monotonic loading phase may be replaced with a post-consolidation phase, if the post-consolidation due to dissipation of pore-pressure developed during cyclic loading is of interest.

FOUNDATION CONDITIONS

The present dam was built in a valley which was infilled with sand and gravels from bedrock to between El 105 m and El 110 m. Fine grained soils overlie sands and gravels between the abutments and the mid-valley. They are absent at the mid-valley. Bedrock was not encountered during any of the field investigation and is believed to be below El 40 m. The foundation soils at the dam site can be divided into the following units. Unit 1: Sand and gravel, very dense; Unit 2: Sand, fine to medium, well graded, dense, often interbedded with silts and gravels; Unit 3: Silt, some to trace clay, soft to firm, some very fine sand; Unit 4: Silt, some very fine sand, stiff to firm; and Unit 5: Silt, sandy gravelly, some cobbles, hard (Till-like). The seismic behaviour of the low plastic fine grained soils of Unit 3 is of particular interest.

GROUND MOTIONS AND LIQUEFACTION ASSESSMENT

The ground motions for the seismic assessment were defined by Uniform Hazard Response Spectrum (UHRS) with PGA of 0.64 g. The earthquake magnitude for the assessment was taken as a moment magnitude M_w 7.5. During the initial stages of the study, a liquefaction assessment was performed using site investigation data from the early 1980s assuming that all foundation soils including the low plastic fine grained soils behaved as granular soils following Seed's simplified method (Idriss and Boulanger, 2008). The liquefaction assessment showed that the SPT $(N_1)_{60-cs}$ required to prevent liquefaction (with FOS=1.0) is high, ranging between 20 and 30 blows/ft. The hydraulic fill within the original dam will liquefy; however, liquefaction will not be triggered in the dense to very dense predominantly sand Units 1 and 2. The mid-valley section of the dam is founded on these dense units. However, the dam between

the right abutment and the mid-valley is founded Units 3 and 4, which overlie the dense Units 1 and/or 2.

Soil Unit 3 is a predominantly fined-grained low plastic silt or clay. This unit is generally soft, with low blow counts, and will trigger liquefaction under the earthquake with PGA of 0.64 g, if treated as “sand-like” material according to Seed’s simplified method. Unit 4 is stiffer than Unit 3 and will not trigger liquefaction, even when treated as “sand-like” material. The Unit 3 soil layers were screened for liquefaction using the screening criterion proposed by Idriss and Boulanger (2008) and Bray et al. (2004). The screening showed that the Unit 3 soil layers are susceptible to liquefaction and laboratory tests are required to determine their liquefaction potential and evaluate their cyclic behavior.

Post-earthquake stability analysis of a dam section between the right abutment and mid-valley section of the dam was conducted using post-liquefaction residual shear strength ratio, S_{ur}/σ_{vo}' of 0.12 (where σ_{vo}' is the initial effective overburden stress) for Unit 3. The correlation between S_{ur}/σ_{vo}' and SPT $(N_1)_{60-cs}$ proposed by Idriss and Boulanger (2008) for granular soils was used to estimate the strength. The analyses showed that the dam will not be stable and will undergo failure. However, treating low plastic fine-grained soil layers as granular soils and using the strength correlation meant for granular soils is inappropriate. Therefore, a field investigation program was under taken to extract samples from Unit 3 and to conduct in situ and laboratory testing to characterize its cyclic behavior under seismic loading.

SITE INVESTIGATION, LABORATORY TESTING AND LIQUEFCTION SCREENING

The site investigation program consisted of mud rotary drill holes with SPTs, Nilcon vane shear tests, Shelby tube sampling and installation of piezometers. The laboratory program consisted of cyclic direct simple shear tests (CDSS), isotropically consolidated undrained (CIU) triaxial tests, oedometer consolidation tests, moisture content, grain size and Atterberg limits tests. Thavaraj et al. (2013) presents the details, results and interpretation of the site investigation and laboratory testing.

Liquefaction screening and liquefaction assessment using the Seed’s simplified method meant for granular soils based on the 2008 data are shown in Figure 1 for a soil column taken through the dam. It shows that the fine-grained low plastic soil layers in Unit 3 will trigger liquefaction according to the Seed’s simplified method and will be susceptible to liquefaction, according to the plasticity based screening criteria; however, further laboratory tests are required.

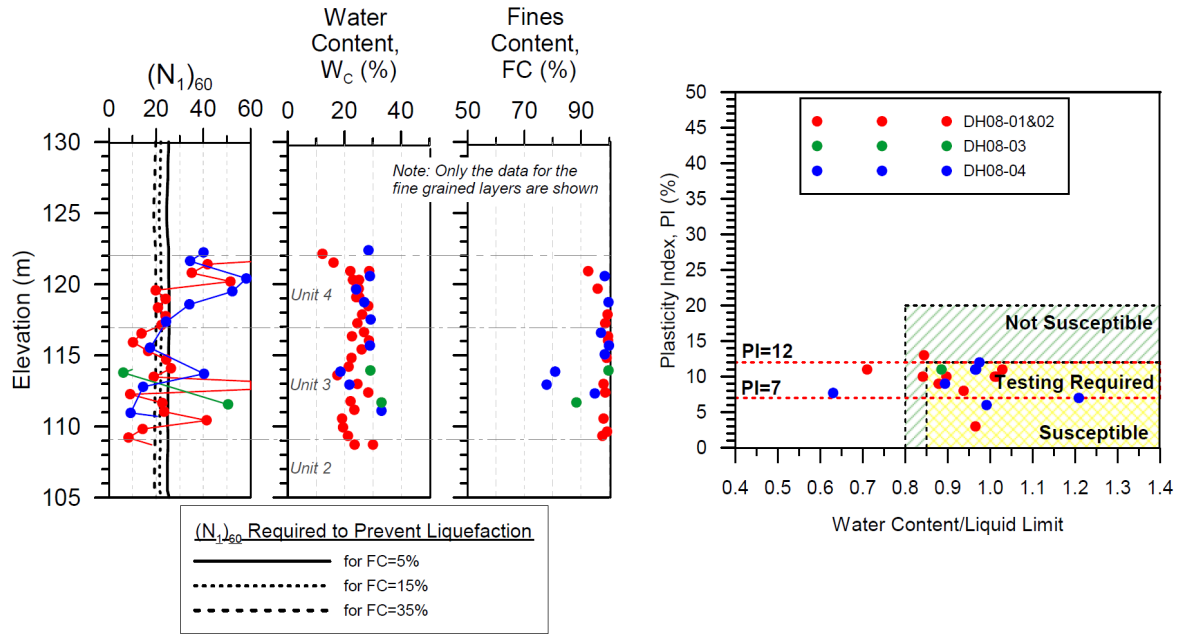


FIG. 1. Liquefaction assessment of fine-grained soils based on 2008 data.

CYCLIC SIMPLE SHEAR TESTS

Nine constant volume cyclic direct simple shear tests were conducted on Shelby tubes samples on the NGI simple shear test apparatus. The samples were initially consolidated to approximately the in situ vertical effective stress prior to the cyclic loading and the cyclic loading phase was followed by a post-cyclic monotonic loading in all but one test. Post-cyclic consolidation was conducted in one test. An initial static bias of 0.1 was applied in steps to the samples in two tests prior to cyclic loading. The applied cyclic stress ratio (CSR) ranged between 0.15 and 0.30. Table 1 summarizes CDSS test parameters and results (adopted from Thavaraj et al., 2013).

Test results showed (Thavaraj et al., 2013) that, under cyclic loading, low plastic fine grained soils accumulate shear strain in a gradual manner without any abrupt loss in stiffness or increase in shear strain. This behavior is similar to that of dense sand. The excess pore water pressure ratio initially increases rapidly under high cyclic stress ratios and for subsequent cycles of loading, it follows the same pattern of dilation and contraction. The corresponding stress-strain curve is “concave upwards” during dilation rather than “convex upwards”. The shear strain accumulates gradually during each subsequent dilation part of loading with the reduction in the stiffness. Data from the post-cyclic testing (Thavaraj et al., 2013) showed that the lower bound value of the post-cyclic undrained strength ratio of 0.20, much greater than the ratio 0.12 estimated using the granular soils correlation proposed by Idriss and Boulanger (2008).

Table 1 Summary of the Nine CDSS Test Parameters and Results

Test No	Drill Hole No	Depth	w_{ave}	σ_{vc}'	e_c	τ_h/σ_{vc}'	Cyclic					Post-Cyclic Monotonic		Ave. OCR	PI
							CSR τ_{cy}/σ_{vc}'	N for $\gamma=3.75\%$	N_{Total}	γ_{max}	$\Delta u_r/\sigma_{vc}'$	S_{ur}/σ_{vc}'	γ_f		
		(m)	(%)	(kPa)						(%)		(%)			
1	DH08-02	10.1	23	151	0.584	0	0.30	0.73	1	5	0.61	0.77	16	2.6	10
2	DH08-02	10.1	25	150	0.641	0	0.15	58	125	15	0.98	-	-	2.6	10
3	DH08-02	10.1	26	150	0.687	0	0.22	7	15	7	0.88	0.43	17	2.6	10
4	DH08-02	16.8	23	249	0.592	0	0.22	1	7	16	0.98	0.14	15	1.3	3
5	DH08-04	8.2	23	122	0.616	0	0.22	4	15	11	0.91	0.44	15	2.7	9
6	DH08-04	6.7	19	110	0.516	0	0.24	3.8	46	16	0.98	0.31	21	2.3	8
7	DH08-04	6.7	19	110	0.507	0.1	0.24	2.2	27	16	0.96	0.55	21	2.3	8
8	DH08-04	11.0	21	150	0.539	0	0.24	1.27	14	16	0.96	0.21	20	1.6	12
9	DH08-04	11.0	21	150	0.542	0.1	0.24	1.23	14	15	0.94	0.39	20	1.6	12

Notes: In Test No. 2, post-cyclic consolidation was carried out and the post cyclic consolidation strain was 3.76%. w_{ave} -average initial water content from trimmings; σ_{vc}' - Initial effective vertical consolidation stress; e_c - Void ratio after consolidation estimated assuming fully saturated soil; τ_h - Initial static shear stress; N- Number of cycles; γ_{max} – Maximum shear strain reached during consolidation; Δu_r - Residual pore water pressure after cyclic loading; S_{ur} - Maximum shear strength reached during the post-cyclic monotonic loading phase; γ_f – Maximum shear strain reached during post-cyclic monotonic loading phase; Ave. OCR: Estimated average OCR of sample using the consolidation test data; and PI- Plasticity Index.

Seismic deformation analyses can be expected to predict realistic deformation of the dam, if the constitutive model used for the low plastic fine grained soils capture the characteristic behavior observed in the CDSS testing and described above at the element level.

SEISMIC DEFORMATION ANALYSES

Seismic deformation analyses of a critical section the earthfill dam were carried out using the computer program FLAC (Fast Lagrangian Analysis of Continua; Itasca, 2008) to estimate seismic displacements. The FLAC model, layering and SPT $(N_1)_{60}$ values used for the dam are shown in Figure 2.

Methodology

The analyses were carried out in two steps: an initial static analysis was carried out using an elastic-plastic model with Mohr-Coulomb failure criterion to establish in situ stresses in the model; and it was followed by a time domain dynamic analysis using an effective stress based constitutive model called UBCSAND developed at the University of British Columbia by Dr. Byrne and his co-workers (Byrne et al., 2004). The dynamic analyses were conducted simulating undrained conditions. The input motions were applied as velocity time history at the base of the model, located at

El 95 m within a dense foundation sand layer. The “within” motion extracted at El 95 m in a 1-D site (ground) response analysis using the computer program Proshake (Edupro, 2005) was used as input and the base was conservatively treated as a rigid base. A small amount of Rayleigh damping (1%-2%) was also used in addition to the hysteretic damping in the dynamic analysis.

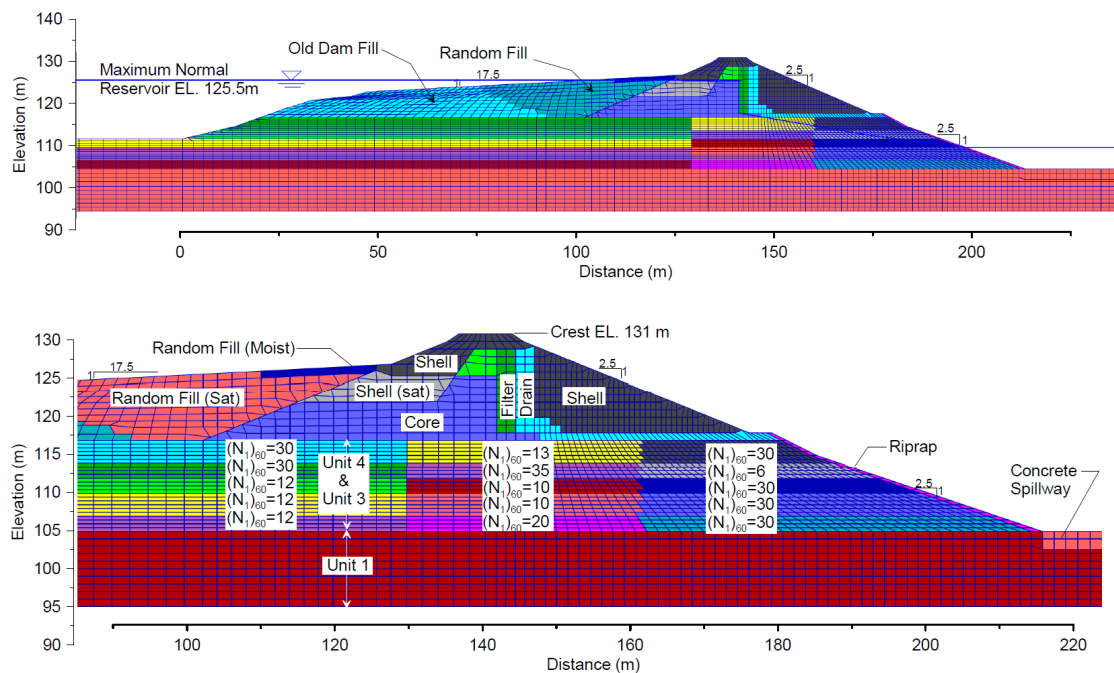


Fig. 2. Finite difference mesh and material units, foundation layering and SPT $(N_1)_{60}$ used in the FLAC analysis.

UBCSAND Model, Model Parameters and Simulation of CDSS Tests

The UBCSAND model is capable of capturing the monotonic, pre-liquefaction and post-liquefaction behavior of granular and low plastic fine grained soils due to cyclic loading. The model was verified by a series of laboratory tests, centrifuge tests and a field test (Byrne et al., 2004, Puebla et al., Yang et al., 2004). The model was modified slightly to capture the behavior of fine grained soils with an initial static bias in this study. UBCSAND model uses both elastic and plastic parameters (Byrne et al. 2004). The elastic modulus, G^e is considered as stress level dependent and expressed in terms of the shear modulus constant as $G^e = k_g^e P_a (\sigma'/P_a)^{n_e}$ where k_g^e is an elastic shear modulus constant, σ' is the mean stress in the plane of loading, P_a is atmospheric pressure and n_e is the elastic exponent. For low plastic fined grained soils k_g^e is taken in terms of SPT $(N_1)_{60}$ as $k_g^e = 217 (N_1)_{60}^{1/3}$ and n_e is taken as 0.5. The bulk modulus B^e is related to G^e as $B^e = cG^e$ where c depends on the Poisson's ratio and is taken as 0.92; and G_i is the elastic shear modulus at low stress level. The plastic shear modulus, G_i^p is expressed as $G_i^p = k_g^p (\sigma'/P_a)^{n_p-1}$ where k_g^p is a plastic shear modulus constant and n_p is the plastic exponent. k_g^p is expressed in terms of k_g^e and SPT $(N_1)_{60}$ as $k_g^p = k_g^e (N_1)_{60}^2 * 0.003 + P_a$ and n_p is taken as 0.6. The measured

SPT $(N_1)_{60}$ blow counts from the site investigations were used for $(N_1)_{60}$. The plastic shear stiffness in the UBSCAND model is controlled by three calibration factors and a fourth factor controls the post-trigger response of fine grained soils. These four calibration factors were obtained with calibration of the model to the CDSS tests described in Thavaraj et al. (2013).

The nine CDSS tests conducted on the low plastic fine grained soils were simulated using the UBSCAND model. Figures 3 and 4 show the simulation of the four CDSS tests (Tests # 3, 4, 6 and 8) by UBSCAND. The close agreement shown on the stress-strain loops, shear strain, stress path and excess pore water pressure accumulation with number of cycles demonstrate the capability of the model in capturing the simple shear behavior observed in the laboratory. Similar agreement was observed in all the other tests.

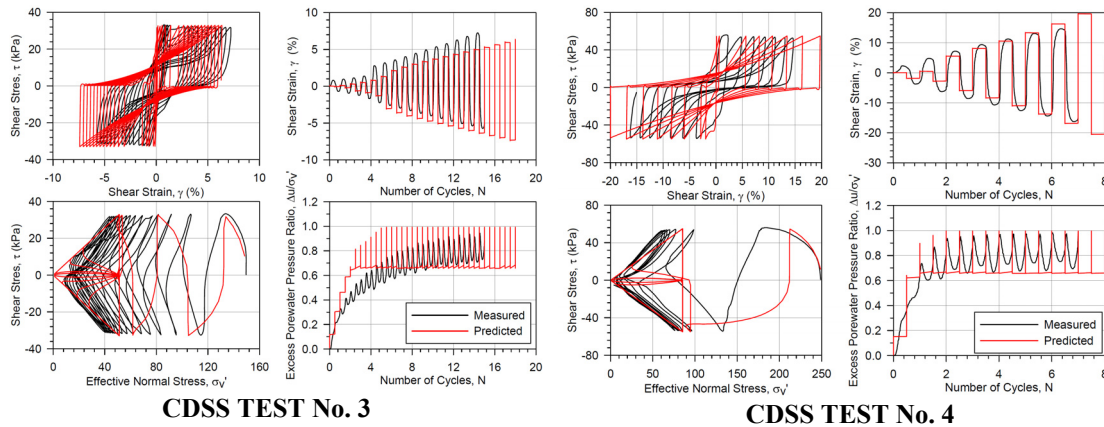


Fig. 3. Simulation CDSS tests 3 and 4 using UBSCAND.

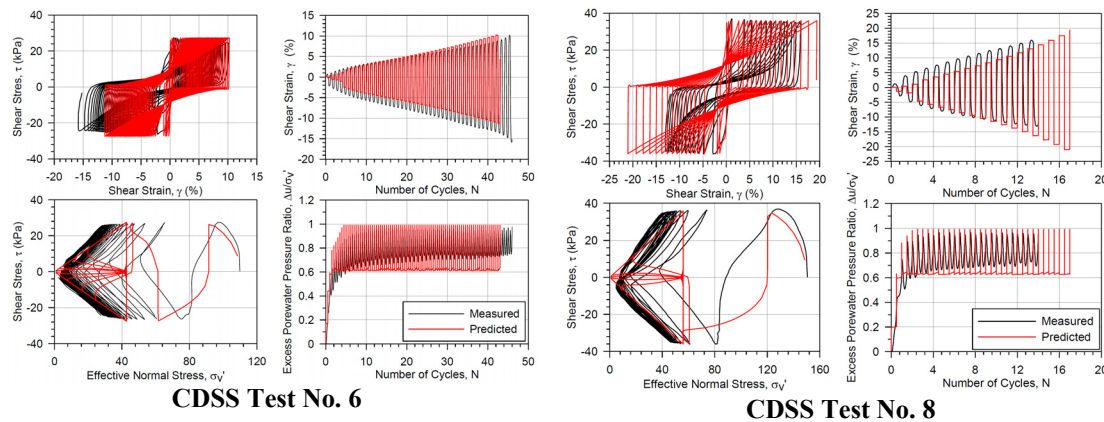


Fig. 4. Simulation of CDSS tests 6 and 8 using UBSCAND.

Input Motions

A suite of seven natural records representative of the scenario earthquake were selected and uniformly scaled to approximately match the UHRS in the period range of interest. The period range of interest was taken as 0.5 to 1 second. Figure 5 shows the target spectra and the spectra of the uniformly scaled records. Table 2 lists the earthquake and intensity parameters for these earthquakes.

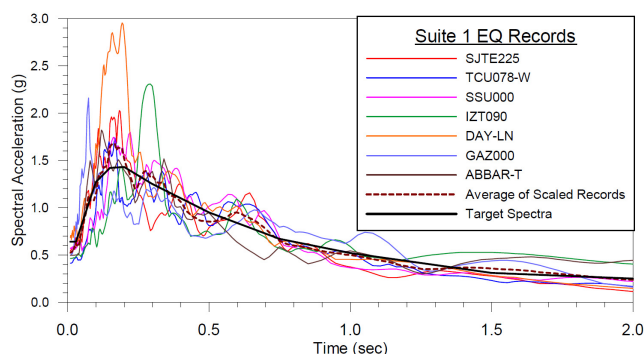


Fig. 5. Response spectra of uniformly scaled seven records.

Table 2. Earthquake Record Parameters and Predicted Displacements

Number	Earthquake	Record	M	PGA (g)	Duration (sec)	I _a (m/s)	Scaling Factor
1	1989 Loma Prieta, CA	SJTE225	6.9	0.53	10.1	4.9	1.9
2	1999 Chi-Chi, Taiwan	TCU078-W	7.6	0.41	25.9	4.9	0.9
3	1994 Northridge, CA	SSU000	6.7	0.56	7.3	3.4	2.0
4	1999 Kocaeli, Turkey	IZT090	7.4	0.46	13.2	3.6	2.1
5	1978 Tabas, Iran	DAY-LN	7.4	0.66	12.3	5.7	2.0
6	1976 Gazil, USSR	GAZ000	6.8	0.49	6.4	3.1	0.8
7	1990 Manjil, Iran	ABBAR-T	7.4	0.50	30.6	7.6	1.0

Note: M- Earthquake Magnitude; PGA- Peak Ground Acceleration; Duration- Effective duration taken as time interval between 5% and 95% in Husid plot; and I_a- Arias Intensity.

Results of Seismic Deformation Analyses

Figure 6 shows the horizontal and vertical time histories of the crest and Figure 7 shows the deformed shape and the displacement vectors. The results showed that the weak layers in the foundation with SPT (N_1)₆₀ of less than or equal to 12 generated significant strains and caused movements in both the downstream and upstream directions, and, as a result, the centre of the dam settled significantly; however, the crest did not move horizontally by any significant amount. The average horizontal and vertical displacements of the crest are 0.13 m and 1.36 m, respectively. The deformations within the dam core/filter/drain are primarily vertical; the average and maximum displacements are about 5% and 20% of the filter thickness. The estimated post-earthquake consolidation settlement under the crest is approximately 0.32 m, corresponding to 4% strain. When this is added to the undrained settlement, the average settlement of the top of the core is approximately 1.7 m.

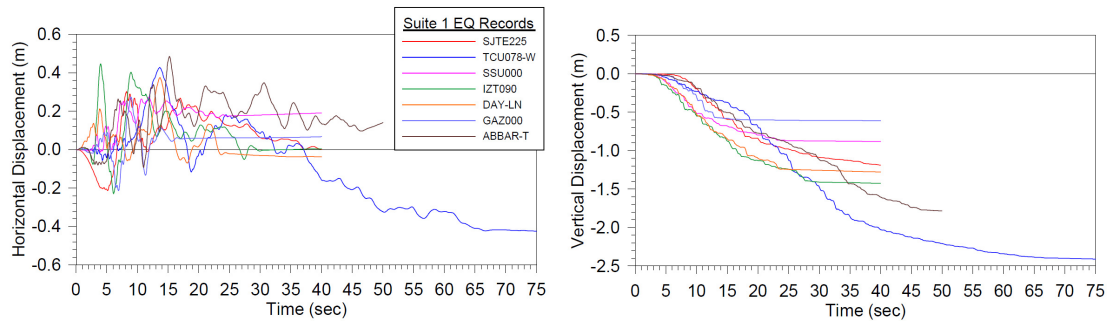


Fig. 6. Seismic displacements of the crest using the seven records.

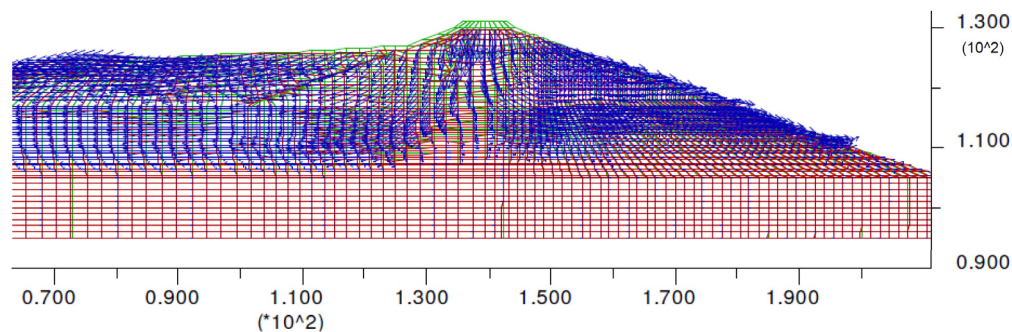


Fig. 7 Deformed (red), undeformed (green) shapes of the dam and displacement vectors at the end of earthquake: SJTE225.

SUMMARY AND CONCLUSIONS

Low plastic fine grained soils behave similar to dense sands, exhibiting gradual build-up in shear strain without any abrupt loss in stiffness or increase in shear strain which are characteristics of loose sands. They cannot be treated as loose sand using the methodologies and correlations developed for loose sand. Their behaviour can be studied by conducting CDSS tests on undisturbed samples. The seismic deformation analyses should incorporate a constitutive model which is able to capture the characteristic behaviour of these soils observed in the laboratory CDSS tests, at the element level. Only then can the analyses be expected to reliably predict seismic displacements.

Seismic deformation analyses of a dam founded on low plastic fine grained soils was performed using the UBCSAND model. The model was shown to be able to capture the characteristic cyclic behavior observed in the laboratory CDSS tests. The analyses showed that, although the low plastic fine-grained soils will not behave similar to loose sand, they can still cause significant displacements due to accumulation of strains due to cyclic loading.

ACKNOWLEDGMENTS

The authors would like to acknowledge Dr. P.M. Byrne for the review of the study presented in this paper and BC Hydro for permission to publish this paper.

REFERENCES

- Bray, J.D., Sancio, R.B., Riemer, M.F. and Durgunoglu, T. (2004). "Liquefaction Susceptibility of Fine-Grained Soils". *Proc. of the 11th Intl. Conf. on Soil Dynamics and Earthquake Engineering*, Berkeley, CA, Jan. 7-9, 2004.
- Byrne, P. M., Park, S. S., Beaty, M., Sharp, M., Gonzalez, L., and Abdoun, T. (2004). "Numerical modeling of Liquefaction and Comparison with Centrifuge Tests", *Canadian Geotechnical Journal*, Vol. 41, pp. 193-211.
- Edupro, 2005. "PROSHAKE-Ground Response Analysis Program", EduPro Civil Systems Inc., Redmond, WA.
- Idriss, I. M. and Boulanger, R.W. (2008). "Soil Liquefaction During Earthquakes", Monograph No. MNO-12 (First Edition), Earthquake Engineering Research Institute (EERI), Oakland, CA. p.243.
- Itasca (2008). FLAC2D ver5. Fast Lagrangian Analysis of Continua. A finite difference program for the dynamic deformation analysis. Itasca Consulting Group Inc., Minneapolis, MN, USA.
- Puebla, H. Byrne, P. M. and Phillips, R. (1997). "Analysis of CANLEX Liquefaction Embankments: Prototype and Centrifuge Models", *Canadian Geotechnical Journal*, Vol. 34, pp. 641-657.
- Thavaraj, T., Stevenson, G., Williams, J. and Siu, D. (2013). "Characterizing Low Plastic Fine-Grained Foundation Soils under Strong Earthquake Shaking". *Proc., Geo-congress 2013: Stability and Performance of Slopes and Embankments III*, Geotechnical Special Publication No. 231, pp. 211-220.
- Yang, D. Naesgard, E., Byrne, P. M., Adalier, K. and Abdoun, T. (2004). "Numerical Model Verification and Calibration of George Massey Tunnel Using Centrifuge Models", *Canadian Geotechnical Journal*, Vol. 41, pp. 921-942.

Seismic Rotational Stability of a Seawall Considering Non-Breaking Waves

B. Giridhar Rajesh, S.M.ASCE¹; and Deepankar Choudhury, M.ASCE²

¹Ph.D. Research Scholar, Dept. of Civil Engineering, Indian Institute of Technology Bombay, Mumbai 400076, India. E-mail: bgrajesh@iitb.ac.in

²Professor, Dept. of Civil Engineering, Indian Institute of Technology Bombay, Mumbai 400076, India. Also, Adjunct Professor, Academy of Scientific and Innovative Research (AcSIR), New Delhi, India. E-mail: dc@civil.iitb.ac.in

Abstract: Simple analytical solutions to predict the rotational displacements of seawall supporting cohesionless backfill under the combined action of earthquake forces, non-breaking wave force, hydrostatic and hydrodynamic forces for active earth pressure condition has been presented. The seismic forces are calculated by using the pseudo-static method. The excess pore pressures generated due to seismic shaking has been incorporated in the calculation of earth pressure in terms of excess pore pressure ratio. The amount of tilt has been calculated for both during and after the earthquake. A detailed parametric study has been conducted by varying parameters, such as height of non-breaking wave, depth of submergence of backfill, soil friction angle, backfill and wall inclinations and excess pore pressure ratio. It has been observed that, the rotational displacement of the wall is increasing by 48% as the ratio of height of non-breaking wave to the total height of seawall increases from 0.00 to 0.60. The results obtained in the present study are in good agreement when compared to the specific cases in available literature.

INTRODUCTION

The behavior of waterfront structures such as seawalls, bulkheads and caisson quay walls under geo-hazards such as earthquakes and tsunamis is an important topic of research in earthquake geotechnical engineering. During many earthquakes, numerous waterfront retaining structures failed with substantial outward rotational displacements. The prediction of seismic rotational displacement of simple retaining wall with dry backfill soil itself is complex and the complexity increases with the presence of water in front of wall and backfill soil. The most popular method for sliding stability analysis of retaining walls is Newmark's (1965) sliding block method. Siddharthan et al. (1992) proposed a simple rigid plastic model for determining sliding and tilting displacements of rigid walls. Zeng and Steedman (2000) proposed rotating block method to determine rotational displacement of rigid gravity retaining walls. All the above mentioned studies are only applicable for dry backfills and without the presence of water in front of the wall. Ebeling and Morrison

(1992) detailed the separate methodology for seismic design of waterfront retaining structures. Choudhury and Ahmad (2007, 2008), Chakraborty and Choudhury (2014) and Kang et al. (2014) studied the combined effects of earthquake and tsunami on the stability of waterfront retaining wall. Choudhury and Ahmad (2010) presented the seismic design factors for vertical waterfront retaining wall considering partially submerged backfill. But these studies explain only seismic displacements of waterfront retaining walls, not the rotational displacements of wall. Moreover, these studies considered a simple vertical waterfront retaining wall with horizontal backfill, but in practice they can be inclined also. Ahmad and Choudhury (2010) studied the rotational stability of waterfront retaining structures but they have not considered the wave forces from seaward side. Rajesh and Choudhury (2015, 2016) studied the stability of seawall under the combined action of non-breaking wave force but those are force based approaches and displacements have not been addressed. When the non-breaking wave trough is at the wall, the total water pressure acting on the wall from seaward side will be less than the hydrostatic water pressure and the wall may tilt seaward by creating active state of earth pressure in the backfill. To the authors' knowledge till date, no study considered this aspect along with earthquake forces to evaluate seismic rotational stability. The probability of occurrence of non-breaking wave from seaward side along with the earthquake main shock may be unlikely but there is always a possibility of occurrence of moderate non-breaking wave along with earthquake main-shock or consequent fore shocks or aftershocks. The recent 2015 Lamjung and 2011 Tohoku earthquakes show the importance of aftershocks which are of comparable magnitude with main-shocks along with non-breaking wave. In the light of above discussion, in the present study, the rotational stability of a non-vertical gravity type waterfront seawall with sloping submerged backfill under the combined action of seismic forces from earthquake or consequent aftershocks, non-breaking wave force, hydrostatic and hydrodynamic forces from both sides of the wall are examined in active state of earth pressure.

METHODOLOGY

A typical rigid non-vertical gravity type seawall with sloping submerged backfill as shown in Fig. 1 is considered in the present study. The wall height is h and top width is b . The inclination of wall and backfill are θ and β , respectively. The non breaking wave of height H and wave length L with its wave trough at the wall is considered. The water levels on seaward and landward sides are d_S and d_L , respectively. The details of various forces considered in the present analysis are summarized in Table 1.

Determination of threshold seismic acceleration coefficient (k_{tr})

Assuming that the base of the foundation is rigid and wall is prone to pure rotation about toe (point O) as shown in Fig 1, the threshold seismic acceleration k_{tr} can be obtained following the approach of Zeng and Steedman (2000) by equating summation of the driving and resisting moments (M_D and M_R) i.e.,

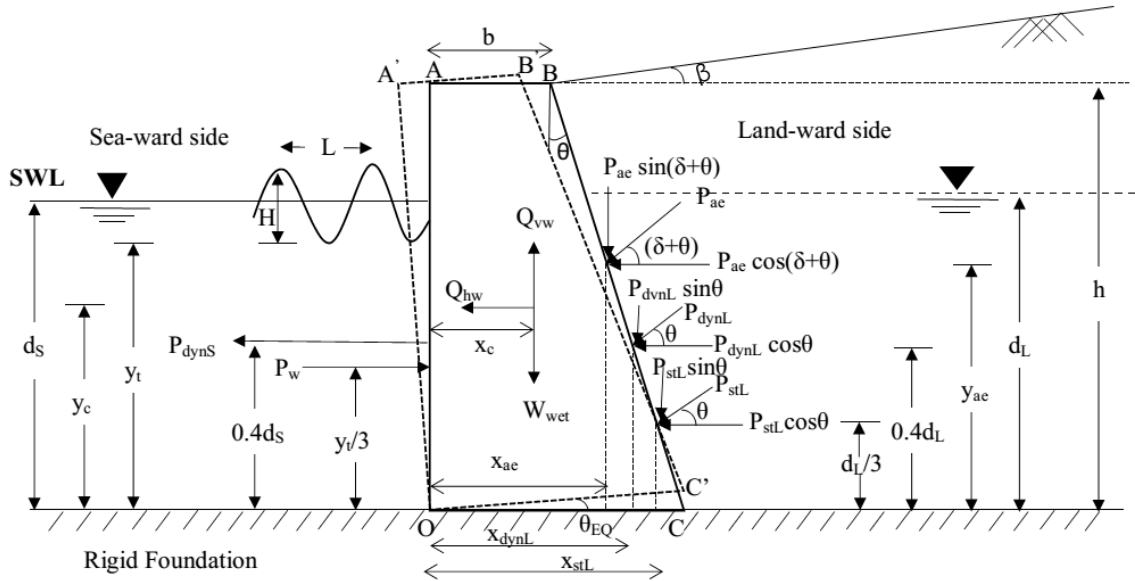


FIG. 1. A typical sketch of seawall under rotational mode of active state of earth pressure subjected to different forces during an earthquake

Table 1. Forces considered in the present study for seawall

Force	Used formulae	Reference
Total seismic active earth pressure force	$P_{ae} = \frac{1}{2} K_{ae} \bar{\gamma} h^2 (1 - k_v)$	Ebeling and Morrison (1992)
Hydrodynamic force on landward and sea-ward sides	$P_{dynL}, P_{dynS} = \frac{7}{12} k_h \gamma_w (d_L, d_S)^2$	Westergaard (1933)
Hydrostatic force on landward side*	$P_{stL} = \frac{1}{2} \gamma_{we} (1 - k_v) d_L^2$	Ebeling and Morrison (1992)
Non-breaking wave force on seaward side*	$P_w = \frac{1}{2} (\gamma_w (1 - k_v) d_S - P_1) (d_S + h_o - H)$ $P_1 = \frac{\gamma_w H}{\cos(2\pi d_S / L)}$	Miche (1944) and Rundgren (1958)
Where		
$\psi = \tan^{-1} \left(\frac{\gamma_d k_h}{\gamma (1 - k_v)} \right), \bar{\gamma} = \left(\frac{d_L}{h} \right)^2 (\gamma_{sat} - \gamma_w) (1 - r_u) + \left(1 - \left(\frac{d_L}{h} \right)^2 \right) \gamma_d, \gamma_{we} = \gamma_w + (\gamma_{sat} - \gamma_w) r_u$		
K_{ae} is seismic active earth pressure coefficient; γ_w is unit weight of water; γ_{sat}, γ_d are saturated and dry unit weight of soil; $\gamma_{we}, \bar{\gamma}$ are modified unit weight of water and soil due to submergence; r_u is excess pore pressure ratio; ψ is seismic inertia angle; h_o is height of mean water level above still water level		
*Modified to consider hydrodynamic force due to vertical seismic excitation as per Chwang (1979)		

$$\begin{aligned}
& P_{stL} \cos \theta \frac{d_L}{3} + P_{dynL} \cos \theta 0.4d_L + P_{dynS} 0.4d_S + P_{ae} \cos(\delta + \theta)y_{ae} + Q_{hw}y_c - P_w \left(\frac{d_S + h_o - H}{3} \right) = \\
& P_{stL} \sin \theta x_{stL} + P_{dynL} \sin \theta x_{dynL} + P_{ae} \sin(\delta + \theta)x_{ae} + (W_{wet} - Q_{vw})x_c
\end{aligned} \tag{1}$$

where, y_{ae} , y_c , x_{stL} , x_{dynL} , x_{ae} , and x_c are lever arm distances of corresponding forces as shown in Fig. 1. The limiting value of k_h which satisfies equation (1) can be computed by trial and error method and is known as coefficient of threshold seismic acceleration coefficient (k_{tr}). The seawall will start rotating about toe once the value of k_h exceeds the threshold seismic acceleration coefficient k_{tr} .

Rotational displacement of the seawall during the earthquake (θ_{EQ})

The equation of motion of seawall, once the seismic acceleration exceeds the threshold acceleration can be written as

$$M_o = -y_c \left(\frac{W_{wet}}{g} \right) a_c(x) + x_c \left(\frac{W_{wet}}{g} \right) a_c(y) + J_c \alpha \tag{2}$$

where,

$a_{c(x)}$ and $a_{c(y)}$ are accelerations of centroid of seawall in x and y directions, respectively and can be determined as

$$a_c(x) = a_g - \alpha y_c - \omega^2 x_c \tag{3}$$

$$a_c(y) = \alpha x_c - \omega^2 y_c \tag{4}$$

M_o is summation of all the moments about point O ; J_c is polar moment of inertia of seawall; α is angular acceleration; ω is angular velocity; a_g is ground acceleration. The angular acceleration of seawall α can be obtained by solving equations (2), (3) and (4) as

$$\alpha = \frac{M_D - M_R}{\frac{W_{wet}}{g} (x_c^2 + y_c^2) + J_c} \tag{5}$$

The angular velocity of seawall for the duration of earthquake (t_{EQ}) considered can be computed as

$$\omega = \int_0^{t_{EQ}} \alpha dt \tag{6}$$

Finally, the rotational displacement (θ_{EQ}) of seawall can be obtained by integration of angular velocity of rotation over the time t_{EQ} , i.e.,

$$\theta_{EQ} = \int_0^{t_{EQ}} \omega dt \quad (7)$$

Rotational displacement of the seawall after the earthquake (θ_f)

Once the earthquake has stopped, the seawall start decelerating and comes to rest after some time. The non-breaking wave force has been considered only during the earthquake as the present study focused on the combined effects of non-breaking waves and earthquake forces. The angular acceleration (α_f) of the seawall after the earthquake has been stopped can be easily obtained by neglecting earthquake forces and non-breaking waves force in equation (5). The time required for seawall to come to rest after the earthquake has been stopped (t_f) can be determined by equating angular velocity (ω_f) of seawall after the earthquake has stopped i.e.

$$t_f = \frac{-\omega}{\alpha_f} + t_{EQ} \quad (8)$$

The final rotational displacement (θ_f) of seawall can be expressed as,

$$\theta_f = \theta_{EQ} + \omega(t_f - t_{EQ}) + \frac{1}{2} \alpha_f (t_f - t_{EQ})^2 \quad (9)$$

RESULTS AND DISCUSSIONS

Typical results are presented in tabular forms to show the design application of present methodology. Threshold seismic acceleration coefficient (k_{π}) is determined using the equation (1). If the obtained k_{π} is greater than the k_h , the seismic displacements during the earthquake θ_{EQ} and after the earthquake θ_f are computed using equations (7) and (9). Rotational displacements are calculated for a typical set of input parameters in non-dimensional form for different horizontal seismic acceleration coefficients, which would be helpful for design engineers. Parameters are chosen following the approach of Ebeling and Morrison (1992) to avoid possible shear fluidization. It is to be noted that the value of r_u is neglected in the parametric variations as r_u changes with horizontal seismic acceleration and depth. However, to demonstrate the effect of r_u one typical result (Table 7) is presented with crude assumption of constant r_u with depth and seismicity. In the present study the non-existence of solution when $k_h < k_{\pi}$ is denoted as “-” and if it is due to shear fluidization it is represented as “--”. It is to be specified that, the larger values of rotational displacements indicate worst case scenarios and may not be possible in field. The analysis does not consider the permanent seismic induced displacements and also the acceleration in the backfill has been assumed as constant.

Effect of non-breaking wave height (H)

The effect of non-breaking wave height (H) on the rotational stability of wall is shown in Table 2. The values of θ_{EQ} , t_f and θ_f are increasing significantly with the increase in value of H/d_S as expected, because the increase in non-breaking wave force, decreases the resisting moment. The value of k_{tr} is reducing with increase in H/d_S i.e., small values of k_h are enough to rotate the wall if non-breaking wave hit the wall during the earthquake. For example, for $k_h=0.20$, when H/d_S changes from 0.0 to 0.60, the values of θ_{EQ} increases from 2.13° to 3.16° . Hence, the rotational displacement during the earthquake increased by about 48%. For the same data, the values of t_f and θ_f increases from 0.85s to 1.16s and 4.06° to 7.37° , respectively.

Effect of submergence of backfill (d_L)

Table 3 shows the effect of submergence of backfill (d_L) on the rotational stability of seawall. As can be seen from Table 3, the values of θ_{EQ} and θ_f are increasing with the increase in value of d_L/h , which is due to the fact that the increase in submergence of backfill increases the driving moment. For a typical values of $k_h=0.25$, When d_L/h changes from 0.0 to 1.0 i.e., as the backfill changes from completely dry state to fully submerged state the value of θ_{EQ} increases from 0.20° to 3.98° . Hence, the rotational stability of the seawall will become more critical as the submergence level in the backfill increases.

Effect of soil friction angle (ϕ)

It can be observed from Table 4 that the value of k_{tr} increases as the value of friction angle (ϕ) increases i.e., the value of k_h required to tilt the seawall increases with backfill friction angle. For example, for increase in ϕ from 30° to 40° , the value of k_{tr} is increased from 0.196 to 0.240. For the same data with a typical value of $k_h=0.25$, the values of θ_{EQ} is reduced by about 66%. Similar trend has been observed for t_f and θ_f also. The reason behind this trend can be attributed to the fact that the seismic active earth pressure decreases as the soil friction angle increases, which in turn reduces the rotational displacements.

**Table 2 Effect of H/d_S on rotational displacement of seawall for $b = 3$ m,
 $h = 10$ m, $\theta = 10^\circ$, $\beta = 10^\circ$, $\phi = 30^\circ$, $\delta = \phi/2$, $d_L/h = 1.00$, $d_S/h = 0.75$,
 $d_S/L = 0.15$, $h_o/H = 0.5$, $t_{EQ} = 0.5$ s, $k_v = k_h/2$**

k_h	$H/d_S = 0.0$			$H/d_S = 0.30$			$H/d_S = 0.60$		
	calculated $k_{tr} = 0.120$			calculated $k_{tr} = 0.094$			calculated $k_{tr} = 0.067$		
	$\theta_{EQ}(\circ)$	$t_f(\text{s})$	$\theta_f(\circ)$	$\theta_{EQ}(\circ)$	$t_f(\text{s})$	$\theta_f(\circ)$	$\theta_{EQ}(\circ)$	$t_f(\text{s})$	$\theta_f(\circ)$
0.10	-	-	-	0.21	0.54	0.23	0.64	0.64	0.81
0.15	0.66	0.64	0.84	1.28	0.77	1.98	1.70	0.86	2.92
0.20	2.13	0.95	4.06	2.75	1.08	5.95	3.16	1.17	7.37
0.25	3.17	1.17	7.41	3.77	1.30	9.79	4.17	1.38	11.52

Table 3 Effect of d_L/h on rotational displacement of seawall for $b = 3$ m, $h = 10$ m, $\theta = 10^\circ$, $\beta = 10^\circ$, $\phi = 30^\circ$, $\delta = \phi/2$, $d_S/h = 0.75$, $H/d_S = 0.40$, $d_S/L = 0.15$, $h_o/H = 0.5$, $t_{EQ} = 0.5$ s, $k_v = k_h/2$

k_h	$d_L/h = 0.0$			$d_L/h = 0.75$			$d_L/h = 1.00$		
	calculated $k_{tr} = 0.240$			calculated $k_{tr} = 0.195$			calculated $k_{tr} = 0.081$		
	$\theta_{EQ}(\circ)$	t_f (s)	$\theta_f(\circ)$	$\theta_{EQ}(\circ)$	t_f (s)	$\theta_f(\circ)$	$\theta_{EQ}(\circ)$	t_f (s)	$\theta_f(\circ)$
0.20	-	-	-	-	-	-	-	-	-
0.25	0.20	0.52	0.21	1.98	0.75	2.97	3.93	1.33	10.44
0.30	1.44	0.65	1.87	2.90	0.86	5.02	--	--	--
0.35	2.68	0.78	4.15	3.85	0.98	7.56	--	--	--
0.40	3.55	0.86	6.13	--	--	--	--	--	--

Table 4 Effect of ϕ on rotational displacement of seawall for $b = 3$ m, $h = 10$ m, $\theta = 10^\circ$, $\beta = 10^\circ$, $\delta = \phi/2$, $d_L/h = 0.75$, $d_S/h = 0.75$, $H/d_S = 0.40$, $d_S/L = 0.15$, $h_o/H = 0.5$, $t_{EQ} = 0.5$ s, $k_v = k_h/2$

k_h	$\phi = 30^\circ$			$\phi = 35^\circ$			$\phi = 40^\circ$		
	calculated $k_{tr} = 0.196$			calculated $k_{tr} = 0.220$			calculated $k_{tr} = 0.240$		
	$\theta_{EQ}(\circ)$	t_f (s)	$\theta_f(\circ)$	$\theta_{EQ}(\circ)$	t_f (s)	$\theta_f(\circ)$	$\theta_{EQ}(\circ)$	t_f (s)	$\theta_f(\circ)$
0.20	0.49	0.56	0.54	-	-	-	-	-	-
0.25	1.98	0.75	2.97	1.04	0.62	1.30	0.67	0.58	0.77
0.30	2.90	0.86	5.02	2.56	0.81	4.13	1.62	0.69	2.22
0.35	3.85	0.98	7.56	3.51	0.92	6.46	2.82	0.83	4.65
0.40	--	--	--	4.49	1.04	9.31	4.09	0.97	7.97
0.45	--	--	--	--	--	--	5.10	1.09	11.12

Effect of the ground inclination (β)

Table 5 shows the effect of ground inclination (β) on rotational stability of seawall. It can be observed that for a typical value of $k_h=0.3$, as the value of β is increased from 0° to 10° the values of θ_{EQ} and θ_f are increased by about 37% and 57%, respectively. This increase is expected, because increase in β increases the value of seismic active earth pressure force leading to increase in rotational displacements. However, the changes in threshold seismic acceleration coefficient k_{tr} due to change in ground inclination β is marginal.

Effect of the wall inclination (θ)

The effect of change in the wall inclination (θ) on rotational displacements of the wall is shown in Table 6. It can be observed that, for a typical value of $k_h = 0.3$, as the wall inclination (θ) increases from 0° to 10° , the value of θ_{EQ} is decreased from 6.18° to 1.30° . Hence, about 79% decrease in the value of θ_{EQ} occurs for an increase in wall

inclination angle (θ) from 0° to 10° . For the same data, the value of k_{tr} is increased from 0.106 to 0.285; thereby indicating that the seawall would start rotating at higher values of k_h for larger values of wall inclination (θ). Similar trend is observed for θ_{EQ} also.

Table 5 Effect of β on rotational displacement of seawall for $b = 3$ m, $h = 10$ m, $\theta = 10^\circ$, $\phi = 30^\circ$, $\delta = \phi/2$, $d_L/h = 0.75$, $d_S/h = 0.75$, $H/d_S = 0.40$, $d_S/L = 0.15$, $h_o/H = 0.5$, $t_{EQ} = 0.5$ s, $k_v = k_h/2$

k_h	$\beta = 0^\circ$			$\beta = 5^\circ$			$\beta = 10^\circ$		
	calculated $k_{tr} = 0.212$			calculated $k_{tr} = 0.205$			calculated $k_{tr} = 0.196$		
	$\theta_{EQ}(\circ)$	t_f (s)	$\theta_f(\circ)$	$\theta_{EQ}(\circ)$	t_f (s)	$\theta_f(\circ)$	$\theta_{EQ}(\circ)$	t_f (s)	$\theta_f(\circ)$
0.20	-	-	-	-	-	-	0.49	0.561	0.54
0.25	1.10	0.64	1.39	1.29	0.66	1.71	1.98	0.75	2.97
0.30	2.11	0.76	3.20	2.90	0.86	5.00	2.90	0.86	5.02
0.35	3.45	0.93	6.38	3.85	0.98	7.53	3.85	0.98	7.56

Table 6 Effect of θ on rotational displacement of seawall for $b = 3$ m, $h = 10$ m, $\beta = 10^\circ$, $\phi = 30^\circ$, $\delta = 2\phi/3$, $d_L/h = 0.5$, $d_S/h = 0.75$, $H/d_S = 0.40$, $d_S/L = 0.15$, $h_o/H = 0.5$, $t_{EQ} = 0.5$ s, $k_v = k_h/2$

k_h	$\theta = 0^\circ$			$\theta = 5^\circ$			$\theta = 10^\circ$		
	calculated $k_{tr} = 0.106$			calculated $k_{tr} = 0.185$			calculated $k_{tr} = 0.285$		
	$\theta_{EQ}(\circ)$	t_f (s)	$\theta_f(\circ)$	$\theta_{EQ}(\circ)$	t_f (s)	$\theta_f(\circ)$	$\theta_{EQ}(\circ)$	t_f (s)	$\theta_f(\circ)$
0.15	1.04	0.68	1.42	-	-	-	-	-	-
0.20	2.22	0.88	3.89	0.65	0.58	0.76	-	-	-
0.25	3.70	1.13	8.40	1.87	0.74	2.74	-	-	-
0.30	6.18	1.56	19.29	3.72	0.97	7.23	1.30	0.63	1.64

Effect of excess pore pressure ratio (r_u)

The value of excess pore pressure ratio (r_u) has a major effect of on the rotational stability of the wall. It can be observed from Table 7 that, for a typical value of $k_h = 0.25$, when excess pore pressure ratio (r_u) changes from 0.0 to 0.4, the values of θ_{EQ} and θ_f increase by about 9% and 15%, respectively. This observation is expected, because increase in r_u increases the water thrust on wall generating higher rotational displacements. So, the value of r_u in seismic design of seawall should be chosen carefully. However, as can be seen from Table 7 that, the effect of r_u on k_{tr} and t_f is marginal.

Comparison of Results

Considering that the rotating block method of Zeng and Steedman (2000) is in agreement with the centrifuge modelling results for dry soils, the present study results are compared with those results. Table 8 shows the comparison between the present

study results and the results obtained by Zeng and Steedman (2000) for the particular set of input parameters mentioned. It can be observed that the values of k_{tr} , θ_{EQ} , t_f and θ_f are exactly same for dry case. It can also be observed further that the values of θ_{EQ} , t_f and θ_f obtained for submerged backfill are on higher side due to the extra destabilizing wave and water forces considered in the present study.

Table 7 Effect of r_u on rotational displacement of seawall for $b = 3$ m, $h = 10$ m, $\theta = 10^\circ$, $\beta = 10^\circ$, $\phi = 30^\circ$, $\delta = \phi/2$, $d_L/h = 0.75$, $d_S/h = 0.75$, $H/d_S = 0.40$, $d_S/L = 0.15$, $h_o/H = 0.5$, $t_{EQ} = 0.5$ s, $k_v = k_h/2$

k_h	$r_u = 0.0$			$r_u = 0.2$			$r_u = 0.4$		
	calculated $k_{tr} = 0.196$			calculated $k_{tr} = 0.187$			calculated $k_{tr} = 0.176$		
	$\theta_{EQ}(^\circ)$	t_f (s)	$\theta_f(^\circ)$	$\theta_{EQ}(^\circ)$	t_f (s)	$\theta_f(^\circ)$	$\theta_{EQ}(^\circ)$	t_f (s)	$\theta_f(^\circ)$
0.20	0.49	0.56	0.54	0.69	0.59	0.82	1.00	0.64	1.27
0.25	1.98	0.75	2.97	2.07	0.77	3.18	2.15	0.79	3.41
0.30	2.90	0.86	5.02	3.00	0.89	5.33	3.09	0.92	5.68
0.35	3.85	0.98	7.56	--	--	--	--	--	--

Table 8 Comparison of the rotational displacement θ for $b = 5$ m, $h = 10$ m, $\beta = 10^\circ$, $\phi = 40^\circ$, $\delta = \phi/2$, $d_L/h = 0.75$, $d_S/h = 0.50$, $d_S/L = 0.15$, $H/d_S = 0.40$, $h_o/H = 0.5$, $t_{EQ} = 0.5$ s, $k_h = 0.5$, $k_v = 0$

Parameter	Zeng and Steedman (2000)	Present study	
		Dry Backfill	Wet Backfill
k_{tr}	0.383	0.383	0.249
$\theta_{EQ}(^\circ)$	1.52	1.52	4.26
t_f (s)	0.69	0.69	1.17
$\theta_f(^\circ)$	2.09	2.09	10.00

Conclusions

The seismic rotational stability of a rigid non-vertical gravity type seawall with inclined backfill under the combined action of non-breaking wave force, hydrostatic force and hydrodynamic forces from both seaward and landward sides was investigated. The seismic forces are evaluated by using the widely accepted Mononobe-Okabe pseudo-static approach. The proposed methodology describes the determination of threshold seismic acceleration coefficient, seismic rotational displacements during and after the earthquake in a simple way, which will be helpful for practicing engineers in the design of seawall against rotational mode of failure. A detailed parametric study, investigating the effects of non-breaking wave height, depth of submergence level in backfill, soil friction angle, wall and backfill inclinations and excess pore pressure ratio has been conducted. The effect of non-breaking wave during the earthquake main shock or foreshocks and aftershocks has significant effect on rotational stability of seawall. The increase in non-breaking wave

height, depth of submergence of backfill increases the rotational displacements of the seawall. It is also observed further that, the increase in excess pore pressure ratio increases the rotational displacements, so one should choose appropriate value of excess pore pressure ratio in the design of seawall.

REFERENCES

- Ahmad, S. M., and Choudhury, D. (2010). "Seismic rotational stability of waterfront retaining wall using pseudodynamic method." *International Journal of Geomechanics, ASCE*, 10(1), 45–52.
- Chakraborty, D., and Choudhury, D. (2014). "Stability of non-vertical waterfront retaining wall supporting inclined backfill under earthquake and tsunami." *Ocean Eng*, 78, 1–10.
- Choudhury, D., and Ahmad, S. M. (2007). "Design of waterfront retaining wall for the passive case under earthquake and tsunami." *Applied Ocean Research*, 29(1–2), 37–44.
- Choudhury, D., and Ahmad, S. M. (2008). "Stability of waterfront retaining wall subjected to pseudodynamic earthquake forces." *J. Waterway, Port, Coastal, Ocean Eng., ASCE*, 134(4), 252–260.
- Choudhury, D., and Ahmad, S. M. (2010). "Pseudostatic design factors for stability of waterfront retaining wall during earthquake." *J. Earthquake and Tsunami*, 4(4), 387–400.
- Chwang, A.T. (1979) "Hydrodynamic pressure on an accelerating dam and criteria for cavitation." *J. Eng. Math.*, 13(2), 143–152.
- Ebeling, R. M., and Morrison, E. E., Jr. (1992). "The seismic design of waterfront retaining structures." U.S. Army Technical Rep. No. ITL- 92-11, Washington, D.C.
- Kang, G. C., Kim, D. S., and Kim, T. H. (2014). "Quay wall stability considering earthquake and tsunami overtopping forces together in the active condition." *Natural Hazards Review*, 15(4), 04014011.
- Miche, M. (1944). "Mouvements ondulatoires des mers en profondeur constante on décroissante." *Ann. Ponts chaussées*, 114, 1-4.
- Newmark, N. (1965). "Effects of earthquakes on dams and embankments." *Geotechnique*, 15(2), 139–160.
- Rajesh, B. G., and Choudhury, D. (2015). "Stability of seawalls by considering non-breaking wave forces during earthquakes." *Disaster Adv.* 8, 1–15.
- Rajesh, B. G., and Choudhury, D. (2016). "Influence of non-breaking wave force on seismic stability of seawall for passive condition." *Ocean Eng.*, (in press) <http://dx.doi.org/10.1016/j.oceaneng.2016.01.006>
- Rundgren, L. (1958). *Water wave forces: a theoretical and laboratory study*, Kungl. Tekniska Högskolan, Stockholm, S.E.
- Siddharthan, R., Ara, S., and Norris, G. M. (1992). "Simple rigid plastic model for seismic tilting of rigid wall." *J. Struct. Engrg.*, ASCE, 118(2), 469–487.
- Westergaard, H. M. (1933). "Water pressures on dams during earthquakes." *Trans. Am. Soc. Civ. Eng.*, 98, 418–433.
- Zeng, X., and Steedman, R. S. (2000). "Rotating block method for seismic displacement of gravity walls." *J. Geotech. Geoenviron. Eng.*, 126(8), 709–717.

Site-Specific Seismic Ground Response for Mormugao Port, Goa, India

Nika S. Bhingarde, S.M.ASCE¹; and Nisha P. Naik²

¹Student Member, ASCE, PG Student, Goa College of Engineering, Farmagudi, Ponda, Goa 403401, India. E-mail: nikabhingarde@yahoo.com

²Associate Professor in Civil Engineering, Goa College of Engineering, Farmagudi, Ponda, Goa 403401, India. E-mail: nisha@gec.ac.in

Abstract: Ports are lifeline structures, which play an important role in the economic growth of any country. Hence these structures should necessarily be designed for earthquakes. Mormugao port in the south west region of Goa state, which lies on the west coast of India is located at about 250 km from Koyna and 350 km from Latur which, in the past have experienced earthquakes of magnitude $M_w=6.3$ and $M_w=6.2$ respectively. In this paper, seismic ground response study is carried out for Mormugao port of Goa state. Data of ten borelogs were obtained from the port site. The bedrock depth was found to vary from 10.50 to 16.50 m. The shear wave velocity (V_s) was evaluated using two established correlations developed between V_s and field SPT ' N '. Earthquake time histories were developed for the port site using three methods: (i) generating synthetic accelerograms, (ii) generating artificial accelerograms, both by using *SeismoArtif 2.1.0* software, and by (iii) matching the Indian seismic codal bedrock target spectra using *SeismoMatch 2.1.0* software, by considering seed accelerograms of real earthquakes. One dimensional equivalent linear ground response analysis was carried out using *DEEPSOIL v6.0* software using generated accelerograms. The influence of local soils on the bedrock motion (for 8 time histories) was represented in the form of surface acceleration time history, amplification spectra, response spectra, and ground motion parameters. The site at the Mormugao port was found to be amplifying type with a maximum amplification (Fourier amplitude) of 12.69.

INTRODUCTION

The Indian sub continent is one of the most earthquake prone areas in the world. The damage patterns of many earthquakes around the world, have demonstrated that, local soil conditions can have a major effect on the level of ground shaking. When seismic waves are produced at the bedrock, travel to the ground surface after passing through soil layers. The characteristics of the waves get changed depending upon the soil profile. Seismic Ground Response Analysis (SGRA) aims at determining the effect of soils at the site, in amplification or de-amplification of seismic waves and

hence, estimating the design ground response spectra at the site under consideration. Severe damage was observed during the 2001 Bhuj earthquake in the epicentral region, which also destructed Ahmedabad city located 250 km away from the epicenter, due to amplification of ground motion through soft alluvium. Ports play a very important role in the economic growth of any country. To reduce destructions in the event of earthquake, site specific seismic hazard analysis is essentially required to be carried out for Ports. Seismic design requires evaluation of regional seismicity, site specific ground motions and involves various geotechnical earthquake engineering aspects. India has 13 major ports, 200 minor and intermediate ports, and Mormugao port located in Goa state is one such major port of India. In the present study, one dimensional equivalent linear SGRA was carried out for the lone port of Goa state using different methods of selection for obtaining input motions essential for SGRA.

STUDY AREA

The study area is the Mormugao port located at 15.25°N and 73.98°E and is Goa's main port. Goa falls in the intra-plate Stable Continental Region (SCR) of Indian Peninsula and hence is an ideal location for a port structure. However, recent devastating earthquakes in the Indian Peninsular region have created concerns about the seismic stability of this structure under scanner. Recent studies on the Indian Peninsular have indicated that Indian Peninsula can no longer be considered stable or aseismic. Seismic studies for Mumbai City were carried out by Raghukanth and Iyengar (2006) and Desai and Choudhury (2014a) developed seismic hazard maps and design response spectra for Mumbai city. In another study by Desai and Choudhury (2014b), probabilistic seismic hazard analysis for two sea ports of Mumbai region. Seismo-tectonic maps developed for the state of Goa (Naik and Choudhury, 2014) showed the occurrence of 105 earthquakes events in the seismic influence zone of Goa state. Hence, in the present study site seismic ground response analysis is undertaken for the Mormugao Port, Goa. There have been reports of a large tsunami with no known source in Vasco da Gama in 1524 near Daibul (Bilham and Gaur, 2011), thus the need to carry out the present study.

SEISMIC SITE CLASSIFICATION

Seismic site classification is essential for seismic analysis and design of structures. It is important to define the site class so that it complies with the provisions in National Earthquake Hazards Reduction Program (NEHRP, 2009). Dynamic soil properties such as shear wave velocity and maximum shear modulus of soil are important parameters for seismic ground response study. Shear wave velocity (V_s) is one of the most important parameters of a geological model to assess the site effect and the ground response. It is also increasingly recognized that the V_s profile could potentially reveal valuable information on the stiffness and associated geotechnical properties at the near surface (Xia et al., 1999). Due to lack of field data of actual shear wave velocity from the site, shear wave velocity was obtained by using correlations between SPT 'N' value and shear wave velocity ' V_s '. Two established correlations of Mhaske and Choudhury (2011) and Naik (2015) were adopted in this

study. Engineering bedrock was considered at a level where SPT ' N ' value is greater than or equal to 50. The mean shear wave velocity of the overburden soil $V_{s(OBS)}$ for all boreholes and their seismic site classification as per NEHRP (2009) is given in Table 1. The variation of $V_{s(OBS)}$ for various boreholes is depicted in Fig.1. It is seen that the typical overburden soil above rock comes under soil class E (soft clay) as per NEHRP (2009) for seismic design for all, except MBH-B4 boreholes and class c for MBH-B4 borehole.

Table 1. Site specific classification based on NEHRP 2009 for the study area

Borehole Name	Location		Mean $V_{s(OBS)}$ (m/s)	Category (As per NEHRP, 2009)
	Latitude (N)	Longitude (E)		
LH-1	15°24'39.31"	73°47'48.79"	166.36	E
MBH-A1	15°24'42.23"	73°47'53.03"	115.93	E
MBH-A2	15°24'38.83"	73°47'57.41"	117	E
MBH-A3	15°24'41.64"	73°47'58.30"	146.54	E
MBH-A4	15°24'44.97"	73°47'54.13"	124.49	E
MBH-B1	15°25'00.83"	73°47'27.75"	163.08	E
MBH-B2	15°25'03.04"	73°47'28.92"	130.74	E
MBH-B3	15°25'05.21"	73°47'30.17"	87.63	E
MBH-B4	15°25'05.32"	73°47'39.06"	600	C
MBH-C1	15°24'35.50"	73°48'07.94"	94.65	E

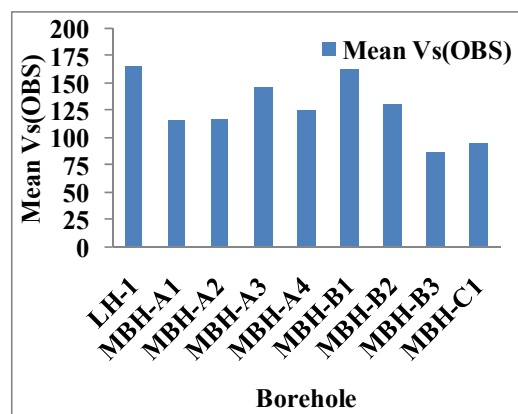


FIG. 1. A chart showing the variation of Mean $V_{s(OBS)}$ at all the borehole locations.

SELECTION OF INPUT MOTIONS

It is a known fact that time history signals recorded at a given site constitute a random process which is impossible to reproduce. Selecting an appropriate set of records that can be used for dynamic analysis of structural systems is important for

performance based design. In the present study, selection of input motion is based on three criteria's, as follows:

- 1) Criteria 1- Generating two synthetic time histories using *SeismoArtif 2.1.0* software. Out of the two synthetic time histories, one is generated for near field condition and the other is generated for far field condition and are designated as Synthetic 1 and Synthetic 2 EQ. respectively.
- 2) Criteria 2- Generating two artificial time histories using *SeismoArtif 2.1.0* software. One artificial time history is generated for low duration (20 sec) and the other is generated for high duration (60 sec), which are designated as Artificial 1 and Artificial 2 EQ. respectively.
- 3) Criteria 3- Matching time histories of various selected earthquake with IS code spectra for zone III using *SeismoMatch 2.1.0* software. The earthquake time histories chosen for the present study for matching are 1995 Kobe, 1999 Kocaeli, 2001 Bhuj and 1940 El Centro earthquakes.

The accelerograms are matched to a Indian seismic codal (IS1893- 2002, Part I) spectrum for zone III and for rocky sites using different calculation methods. In all, 8 time histories were considered, which are shown in the Fig.2.

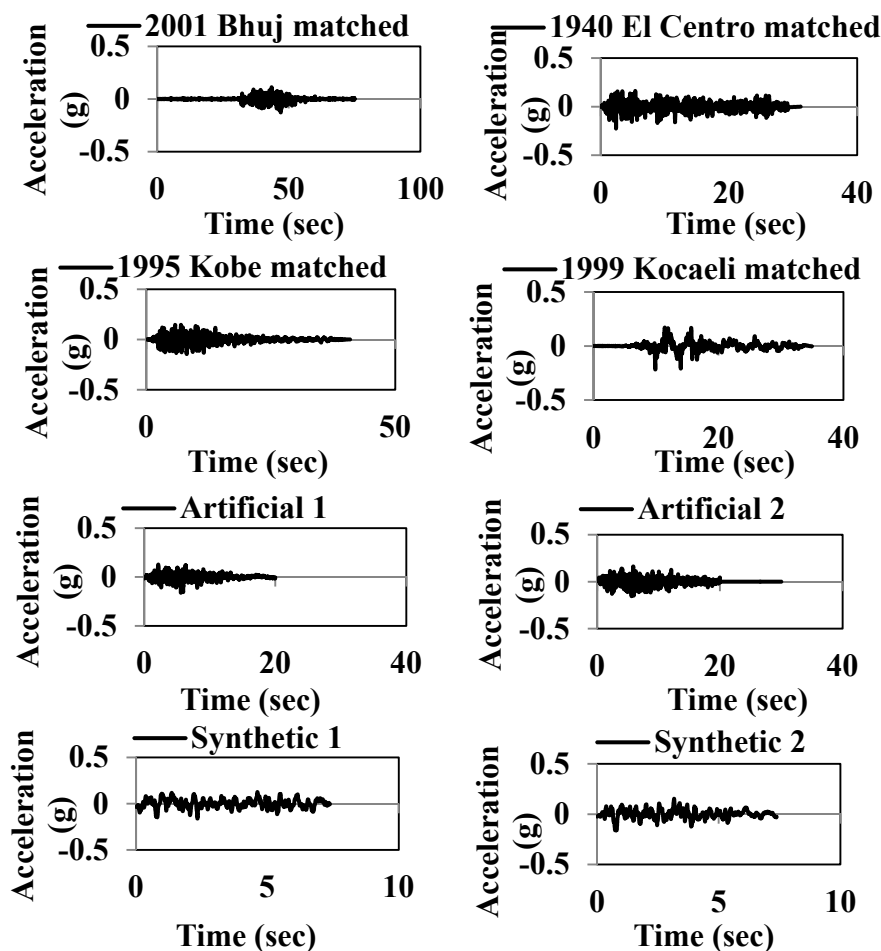


FIG. 2. Time histories generated by considering Indian seismic code IS 1893-2002 (Part I) spectrum.

Ground motion parameters of the earthquake time histories considered were obtained using *SeismoSignal 2.1.0* software. Some of the parameters are given in Table 2 giving a range of values obtained for all the input motions.

Table 2. Ground motion parameters for the generated time histories at bedrock

Parameter	Minimum	Maximum
Max. Acceleration (g)	0.018	0.346
Sustained Maximum Acceleration (g)	0.015	0.171
Effective Design Acceleration (g)	0.017	0.212
Predominant Period (sec)	0.020	0.300
Mean Period (sec)	0.215	2.077
Bracketed duration (sec)	7.340	69.860

RESULTS OF SGRA

The results of seismic SGRA using IS Code spectrum for zone III for the borehole LBH-1 are displayed below. The response spectra and the amplification spectra for eight different input motions considering IS code spectrum is shown in the Fig. 3(a) and Fig.3(b) respectively. The maximum amplification ratio for the borehole LBH-1 considering IS code spectrum was found to be 5.34. It is to be noted that, in all the cases, Artificial 2 input motion showed a distinctive feature in the amplification graph, as its duration is high (60 sec) as compared to the other input motions. The surface acceleration time history obtained from the SGRA using IS code spectrum is shown in the Fig. 4(a). The variation of PGA with the depth is also developed and shown in the Fig. 4(b).

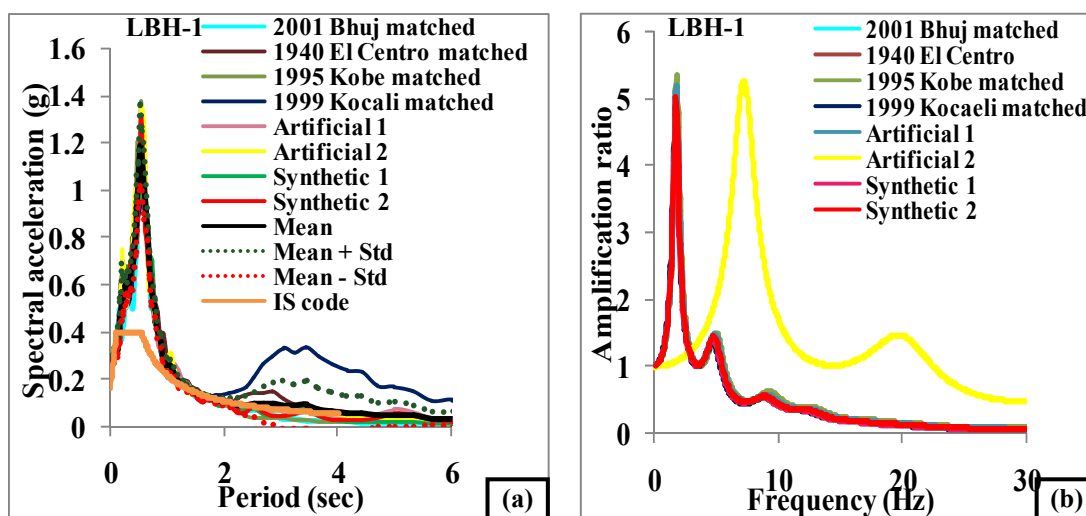


FIG. 3. (a) Response spectrum and (b) Amplification spectra for borehole LBH-1 by considering IS code spectrum for zone III.

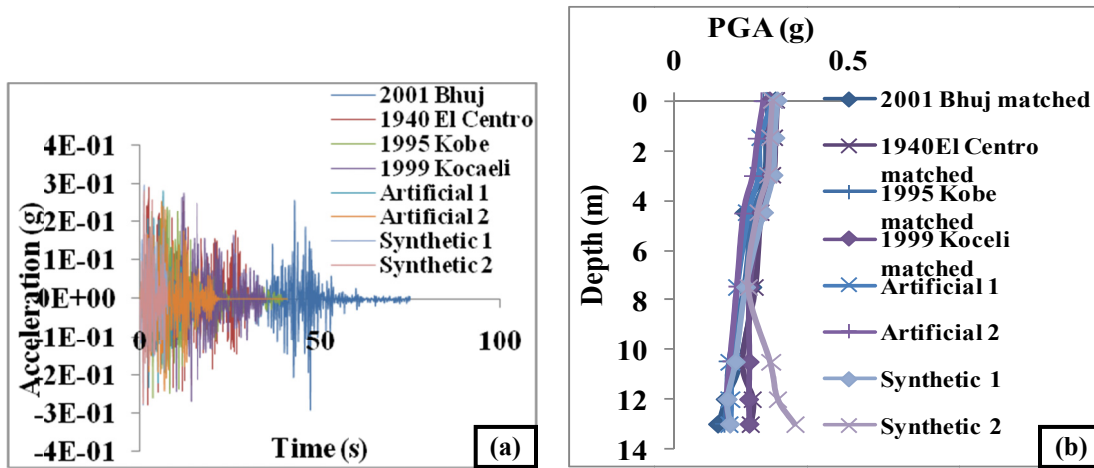


FIG. 4. (a) Surface accelerogram for borehole LBH-1 (b) Graph for LBH-1 showing variation of depth with PGA by considering IS code spectrum.

The results of seismic GRA using IS Code spectrum for zone III for the borehole MBH-A1 are displayed below. The response spectra and the amplification spectra for eight different input motions considering IS code spectrum is shown in the Fig. 5(a) and Fig. 5(b) respectively. The maximum amplification ratio for the borehole MBH-A1 considering IS code spectrum was found to be 6.61. The surface acceleration time history and variation of PGA with the depth obtained is shown in the Fig. 6(a) and Fig.6(b). Similar analysis was carried out for all the boreholes. The response spectra obtained for boreholes MBH-A2, MBH-A3, MBH-A4, MBH-B1, MBH-B2, MBH-B3 and MBH-C1 are shown in Fig. 7(a to g). The maximum amplification ratio for the borehole MBH-A2, MBH-A3, MBH-A4, MBH-B1, MBH-B2, MBH-B3 and MBH-C1 by considering IS code spectrum was found to be 4.86, 12.69, 7.22, 5.62, 6.43, 3.75 and 4.08 respectively.

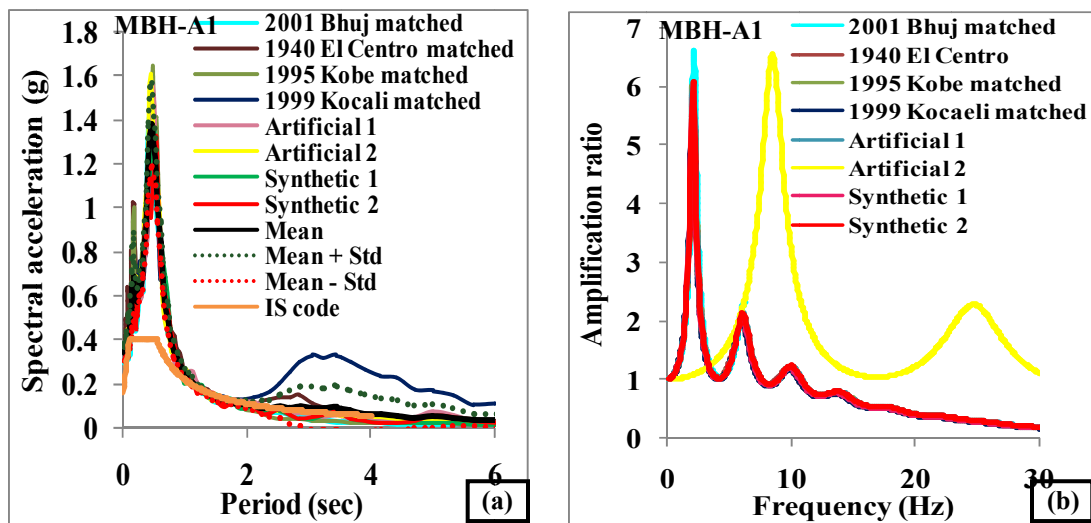


FIG. 5. (a) Response spectrum and (b) Amplification spectra for borehole MBH-A1 by considering IS code spectrum for zone III.

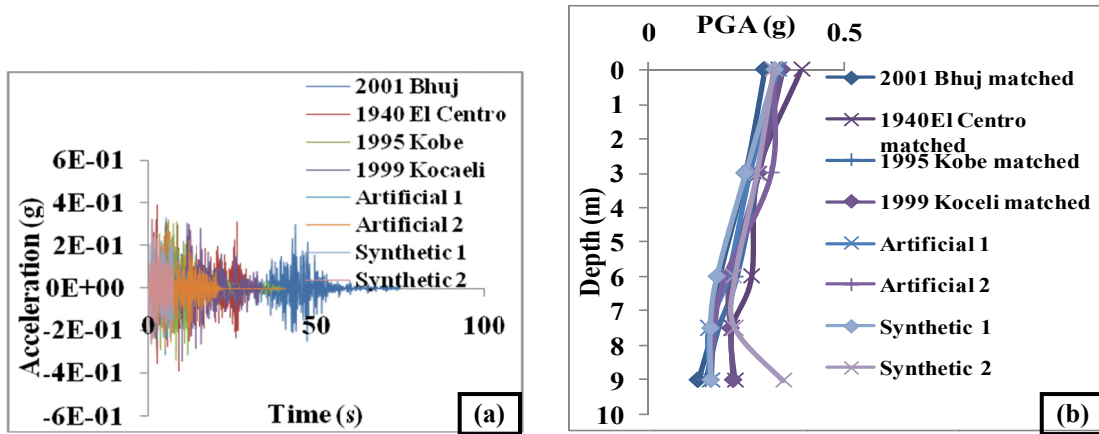
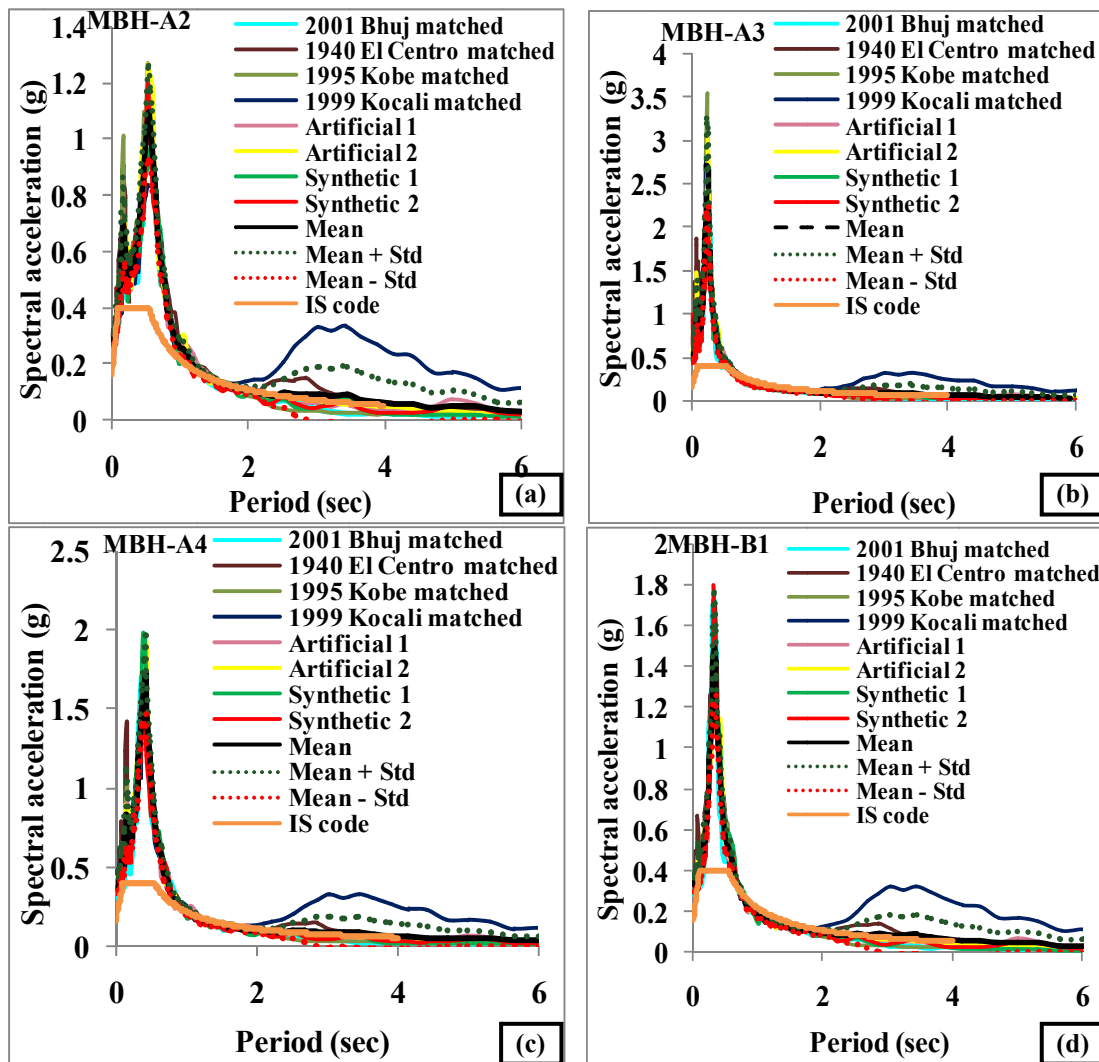


FIG. 6. (a) Surface accelerogram for borehole MBH-A1 (b) Graph for MBH-A1 showing variation of depth with PGA by considering IS code spectrum.



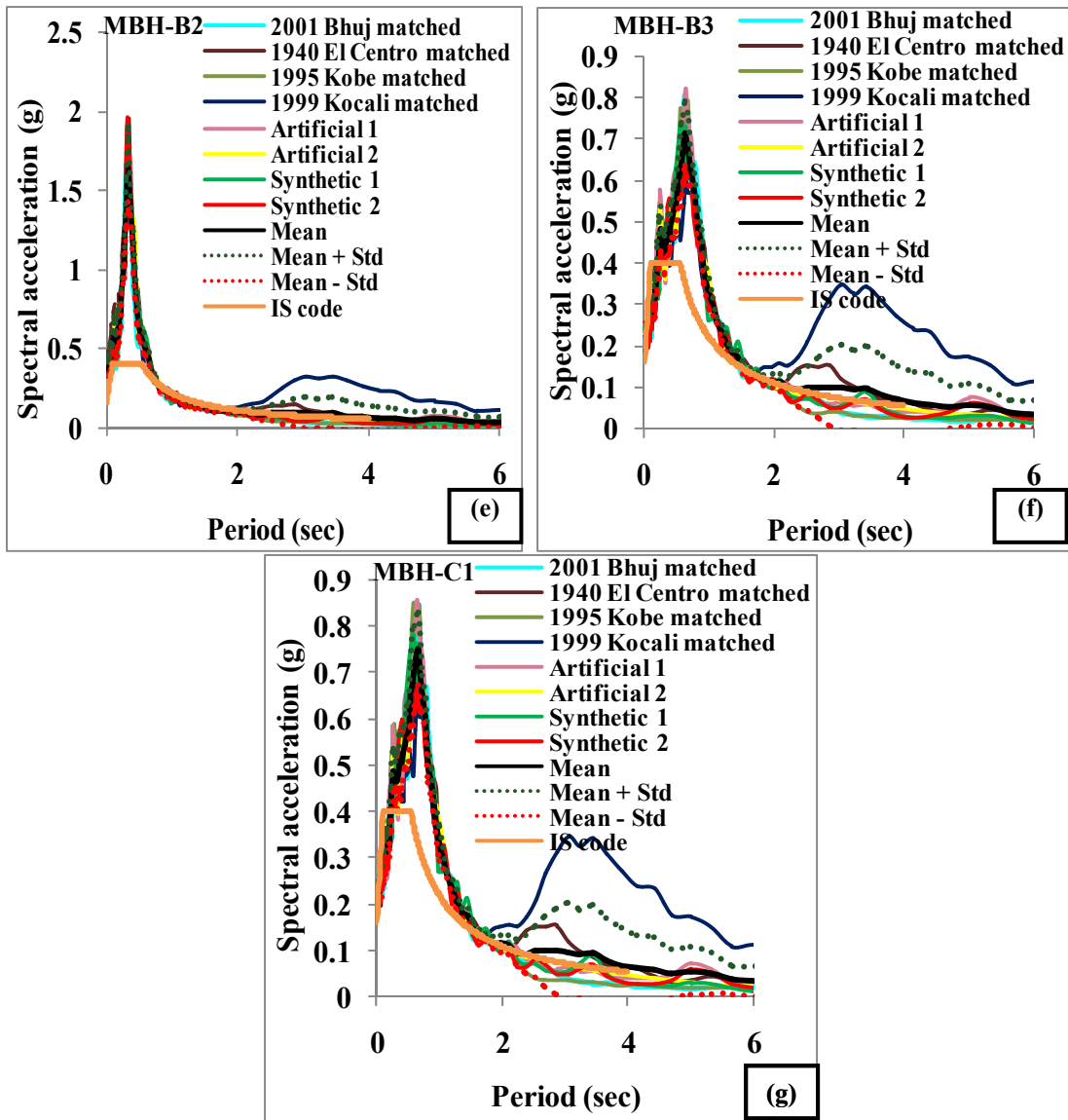


FIG. 7. Response spectrum obtained by GRA for the boreholes (a) MBH-A2, (b) MBH-A3, (c) MBH-A4, (d) MBH-B1, (e) MBH-B2, (f) MBH-B3 and (g) MBH-C1.

The surface time histories obtained from SGRA using *DEEPSOIL v6.0* software (Hashash et al., 2014) were further analyzed to find out the ground motion parameters at the surface. Ground motion parameters at the surface for the generated time histories by considering Indian seismic codal spectrum (IS code spectrum) were analyzed using *SeismoSignal 2.1.0* software. The ground motion parameters at the surface for the generated time histories for the boreholes LBH-1 and MBH-A1 are presented in Table 3. Similar analysis was done for all the remaining borehole locations at the port site. The influence of the local soils in modifying the characteristics of the bedrock motion is distinctively seen in the ground motion parameters. In the work carried out by Naik (2015), other sites located in the same

city as that of the port, having pre-dominantly silty soils were found to be amplifying type with an amplification factor between 6 to 7.

Table 3. Ground motion parameters at the surface for generated time histories.

BH	Parameter	Time history							
		2001 Bhuj	1940 El Centro	1999 Kobe	1995 Kocaeli	Art 1	Art 2	Syn 1	Syn 2
LBH-I	Max. Acceleration (g)	0.29	0.29	0.26	0.28	0.28	0.26	0.3	0.28
	Sustained Maximum acceleration (g)	0.19	0.24	0.24	0.26	0.22	0.24	0.18	0.26
	Effective design acceleration (g)	0.29	0.29	0.26	0.27	0.28	0.25	0.3	0.28
	Predominant Period (sec)	0.52	0.54	0.52	0.52	0.54	0.54	0.54	0.54
	Mean Period (sec)	0.59	0.57	0.56	0.97	0.58	0.58	0.58	0.57
	Bracketed Duration (sec)	66.2	30.46	37.7	28.16	19.8	21.1	7.26	7.3
MBH-AI	Max. Acceleration (g)	0.3	0.39	0.34	0.34	0.33	0.32	0.32	0.32
	Sustained Maximum acceleration (g)	0.23	0.31	0.31	0.3	0.25	0.27	0.23	0.24
	Effective design acceleration (g)	0.3	0.4	0.34	0.34	0.33	0.32	0.33	0.32
	Predominant Period (sec)	0.44	0.46	0.46	0.46	0.46	0.44	0.46	0.52
	Mean Period (sec)	0.5	0.47	0.47	0.83	0.52	0.49	0.49	0.5
	Bracketed Duration (sec)	54.9	29.6	35.6	26.28	19.7	20.6	7.26	7.3

CONCLUSIONS

Seismic ground response analysis was carried out for the Mormugao port in Goa, India. The analysis was conducted on nine boreholes using 8 input motions selected based on three criteria's of selection. The input motions were matched with the Indian seismic codal spectrum. The conclusions of the study can be briefly stated as follows:

1) Earthquake time histories were obtained by matching actual earthquake time histories with Indian seismic codal spectrum for zone III and rock sites, artificial and synthetic earthquakes were also generated. A suite of 8 input motions matching the codal spectrum were developed. The generated time histories were analyzed and ground motion parameters at the bedrock were evaluated using *SeismoSignal 2.1.0*. The predominant period at the bedrock was observed to vary from 0.02 to 0.3 sec and the maximum horizontal acceleration varied from 0.018 to 0.346 g.

2) SGRA was carried out for the nine locations using *DEEPSOIL v6.0* software. The response spectrum obtained from GRA was compared with the response spectrum given by Indian seismic code IS1893 (Part1): 2002 for soft soil sites. It was seen that higher spectral accelerations were obtained as compared to IS code spectrum. The GRA considering IS code spectrum gave maximum amplification ratio (considering Fourier amplitude) of 12.69. Based on the study, it was observed that time histories with higher duration gives more amplification as compared with time histories with lower duration.

3) Ground shaking is stronger where shear wave velocity is lower as the soil stiffness is directly related to the shear wave velocity. It was also observed that soft soils amplify more. It has been observed that borehole MBH-A3 gives maximum amplification among all the boreholes.

4) Time period plays a very important role in the seismic ground response analysis. Depending upon the input motion period and the individual soil layer period, amplification and de-amplification was observed, as can be noted in the plot of variation of PGA with depth.

ACKNOWLEDGMENT

The authors would like to thank the Mormugao Port Trust (MPT), Goa for providing the borehole data from the port site.

REFERENCES

- Bilham, R. and Gaur, V. K. (2011). "Historical and future seismicity near Jaitapur, India." *Current Science*, Vol.101: 1275-1281.
- Desai, S.S. and Choudhury, D. (2014a). "Spatial variation of probabilistic seismic hazard for Mumbai and surrounding region." *Natural Hazards*, Vol. 71(3):1873–1898.
- Desai, S.S. and Choudhury, D. (2014b). "Deaggregation of seismic hazard for two ports in Mumbai metropolitan region." in International conference on geotechnical engineering, *GeoShanghai 2014: Advances in Soil Dynamics and Foundation Engineering*, GSP 240, ASCE, 62–71.
- Hashash, Y.M.A, Groholski, D.R., Phillips, C. A., Park, D. and Musgrove, M. (2014) *DEEPSOIL v6.0*, User Manual and Tutorial.,107 p.
- IS1893 (2002). "Criteria for earthquake resistant design of structure." *Bureau of Indian Standards*, New Delhi, Part I.
- Mhaske, S. and Choudhury, D. (2011). "Geospatial contour mapping of shear wave velocity for Mumbai city." *Natural Hazards*, Vol. Vol. 59: 317 – 327.
- Naik, N. P.(2015). "Site specific seismic hazard studies for the state of Goa." *Ph.D thesis*, IIT Bombay.
- Naik, N.P. and Choudhury, D. (2014). "Development of Fault and Seismicity Maps for the State of Goa, India." *Disaster Advances*, Vol. 7(6):12-24.
- NEHRP, (National Earthquake Hazard Reduction Program) (2009), Recommended provisions for seismic regulations for new buildings and other structures – Part 1: Provisions, Prepared by the Building Seismic Safety Council for the Federal Emergency Mangement Agency (Report FEMA 450), Washington DC.
- Raghukanth, S. T. G. and Iyengar, R. N. (2006). "Seismic hazard estimation for Mumbai city." *Current Science*, Vol. 91(11):1486.
- SeismoArtif version 2.1.0, www.seismosoft.com.
- SeismoMatch version 2.1.0, www.seismosoft.com.
- SeismoSignal version 2.1.0, www.seismosoft.com.
- Xia, J., Miller, R. D., Park, C. B. (1999). "Estimation of near-surface shear-wave velocity by inversion of Rayleigh waves." *Geophysics*, Vol. 64(3): 691-700.

A Case Study of the Impact of Tropical Storms on the Stability of Natural Hillslopes in Macon County, North Carolina

Giuseppe Formetta¹; Alexandra Wayllace²; and Ning Lu, F.ASCE³

¹Postdoctoral, Dept. of Civil and Environmental Engineering, Colorado School of Mines, Golden, CO 80401. E-mail: formetta@mines.edu

²Teaching Associate Professor, Dept. of Civil and Environmental Engineering, Colorado School of Mines, Golden, CO 80401. E-mail: awayllac@mines.edu

³Professor, F.ASCE, Dept. of Civil and Environmental Engineering, Colorado School of Mines, Golden, CO 80401. E-mail: ninglu@mines.edu

Abstract: Rainfall-induced shallow landslides are one of the most significant hazards in mountain areas. In order to analyze and eventually predict the timing and locations of landslides triggering, we use a recent established USGS Hillslope FS2 model to simulate the hillslope hydrology and stability. Stresses, soil moisture, and soil suction are concurrently simulated by a coupled variably saturated flow and stress fields finite element model. The hydro-mechanical framework is applied to a hillslope in Macon County, North Carolina. Here, extensive failure of hillslopes often occurs after heavy tropical storms. In recent years, we conducted site monitoring of soil moisture and suction at different depths in some landslide-prone hillslopes. The objectives of the case study were: i) to simulate the stability conditions of the monitored slopes during hurricanes Frances and Ivan and ii) to identify a possible rainfall scenario for slope failure. The application involved the calibration of the hillslope hydro-mechanical properties by using the measured soil moisture and suction data. Results show that the hillslope was stable under the rainfall of hurricanes Frances and Ivan. However, it would fail if the intensity of the rainfall increased by a factor of 1.3.

INTRODUCTION

Precipitation-induced landslides are one of the most serious environmental hazards and constitute a serious threat to public safety. In subtropical climatic regions, with mountainous topography, rainfall is generally the most common cause of landslides. Geo-environmental factors such as geology, land-use, vegetation, climate, increasing population may increase the landslides occurrence (Sidle and Ochiai 2006).

To improve the predictability of shallow landslides, many authors (Montgomery and Dietrich 1994; Baum et al. 2008) developed physically based slope-stability models that synthesize the interaction between hydrology, geomorphology, and soil

mechanics (Lu and Godt, 2013). In general, they include a hydrological component to simulate infiltration and groundwater flow processes and a soil-stability component to simulate the safety factor of the slope. Several models are available in literature with different degrees of complexity. Typical hydrological components range from steady state (Montgomery and Dietrich, 1994) to transient groundwater flow (Simoni et al., 2008). Common slope stability components are based on limit-equilibrium methods (Fellenius, 1936; Janbu, 1973) or shear strength reduction analysis (Smith and Griffiths, 2004). Recently the framework proposed by Lu et al., 2012 allows to compute a scalar field of factor of safety defined for each point of the hillslope differently from limit-equilibrium method that defines a single stability indicator for the entire hillslope.

Western North Carolina (Fig. 1) is an area particularly exposed to heavy-rainfall induced landslides especially because of the concentration of orographic precipitations and hurricanes, the presence of steep slopes and thin soil depths (Witt, 2005). Landslides in this area are triggered by subtropical storm systems (Wooten et al., 2008) and are predominantly influenced by antecedent soil moisture condition. One recent example is Hurricanes Frances and Ivan, which caused 5 deaths, and destroyed 27 homes.

In this paper we conducted a 2D slope stability analysis of a hillslope located in Western North Carolina (Fig. 1) under the Hurricanes Frances and Ivan. We used the recently established USGS Hillslope FS2 model to simulate the hillslope hydrology and stability based on the framework presented in Lu et al. (2012). The model computes soil moisture and soil suction fields solving the 2D Richards equation and soil total stress solving the 2D linear elasticity equation. Finally, effective stress and local factor of safety are computed based on the suctions stress theory (Lu and Likos, 2004).

The model application involves three steps. First, to identify the hillslope hydro-mechanical properties we calibrated the model parameters using on site measurements of pressure head and soil moisture at three different depths (0.4, 0.9, and 1.35 m). Then we performed the hillslope stability analysis using the rainfall measured during the hurricanes Frances and Ivan. Finally, to establish which rainfall scenario would cause instability, we iteratively increased the rainfall intensity until the hillslope fails.

STUDY AREA

The case study Mooney-Gap (Fig. 1) is located in the Southern Appalachian Mountains of Macon County, North Carolina (southeastern USA). The Macon County (Wooten et al. 2008), has an extension of 1350 km², and elevation ranges between 500 and 1650 m. Average annual precipitation varies between 1800 and 2400 mm and average annual air temperature ranges from 11 to 14 °C. In September 2004, this area was damaged by heavy rainfall from the remnants of the Hurricanes Frances (September, 7-8) and Ivan (September, 16-17). These events caused catastrophic consequences: 155 triggered landslides, 5 deaths, 27 homes destroyed (Wooten et al 2008).

The monitoring site was located in a hill that did not fail during the Hurricanes Frances and Ivan. A monitoring system was installed on the hillslope in order to

collect hourly measurements of rainfall, and soil suction and soil water content at three different depths (0.4, 0.9 and 1.35 m). The collected data covers a two months period, from 01-11-2014 to 01-01-2015. The altimetric profile of the two analyzed hillslopes (Fig. 1 - black triangle and black circle) was extracted from a 6 meters resolution LIDAR digital elevation model provided by North Carolina Department of Transportation. The geological profile reported in Fig. 1 was drawn on the basis of on site stratigraphy measurements.

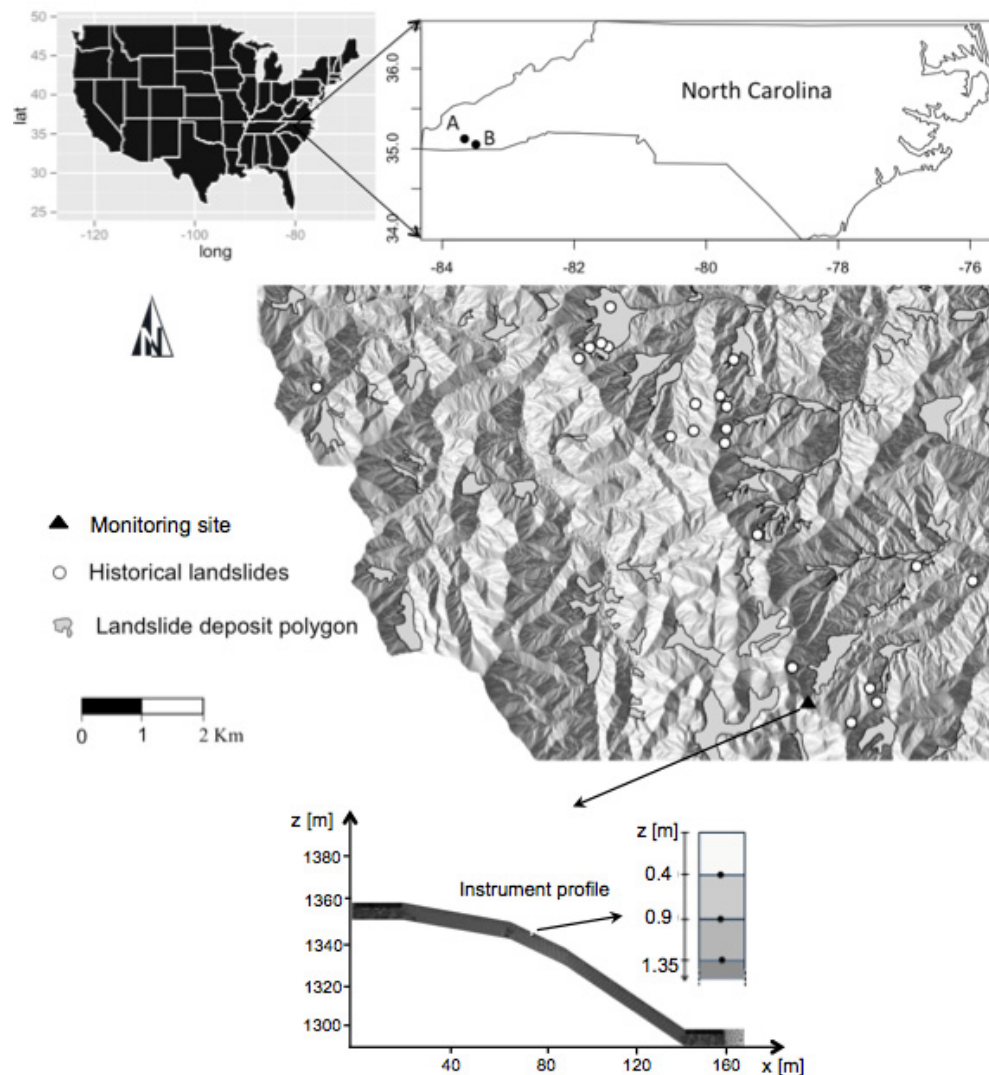


FIG. 1. Mooney-Gap study area localization: historical landslides and monitored site.

HYDRO-MECHANICAL FRAMEWORK

The stability analysis of the monitored hillslope was carried out according the framework presented in Lu et al., 2012. It involves the computation of soil moisture,

soil suction, and gravity induced soil total stress fields. The use of the suction stress theory allows the computation of the effective stress ensuring a mathematically consistent description of transition between saturated-unsaturated states. Finally, the potential unstable areas are detected using the field of local factor of safety (Lu et al., 2012) that is capable of capturing the shifting of stress paths toward the failure state due to transient rainfall infiltration.

The model implements one way coupling of two existing finite element codes. The first is based on FEM2D (Reddy, 1985) and solves the governing equations for plain strain linear elasticity. The second program is based on the hydrological model SWMS-2D (Simunek et al., 1994) which solves Richards equation for unsaturated flow.

Estimation of the on site Van Genuchten and Mualem parameters was performed using the automatic model parameters optimization (MPO) integrated in the software HYDRUS-2D. This optimization implements the Levenberg-Marquardt optimization algorithm in order to find the parameter set that minimizes the difference between modeled and observed data.

RESULTS

The MPO-HYDRUS component was used to estimate the model parameter set that minimizes the differences between observed and simulated values of soil moisture and soil suction. The model initial conditions were computed using an infiltration process with a low rainfall rate (0.0001 m/h) until the soil water content and soil suction dynamic reached a stationary state close to the initial measured values. No flow boundary conditions were set at the bottom and at the upper-left side of the hillslope. Seepage boundary conditions were set at the lower-right side of the hillslope and this was justified by the presence of a creek. Atmospheric boundary conditions were applied at the top of the hillslope.

The optimization process was carried out at the three locations (0.4, 0.90, and 1.35 m depth). We split the two months soil moisture and pressure head measured data in half and we used one month for model parameter calibration and one month for model simulation. The estimated optimal parameter set is presented in Table 1 where θ_r is the residual water content, θ_s is the saturated water content, α and n are Van Genuchten parameters, and k_s is the saturated hydraulic conductivity. Parameter values determined by using the inverse modeling procedure have typical values of the soil in site classified as silty sands and silty clays (Lewis et al., 2013). Figure 2 presents the comparison between modeled and measured soil moisture and pressure head at the three different depths. The model is able to mimic the dynamic behavior of both soil moisture and soil suction in the three sensor locations (at 0.40, 0.9, and 1.35 m depth) both in calibration and simulation periods. For this reason we used the estimated optimal parameter set to carry out the stability analysis.

Table 1. Optimal parameters estimated for each soil layer.

	θ_r [-]	θ_s [-]	α [1/m]	n [-]	k_s [m/h]
Layer 1	0.24	0.40	4.0	1.70	0.10
Layer 2	0.26	0.42	4.2	1.55	0.12
Layer 3	0.23	0.45	4.3	1.85	0.04

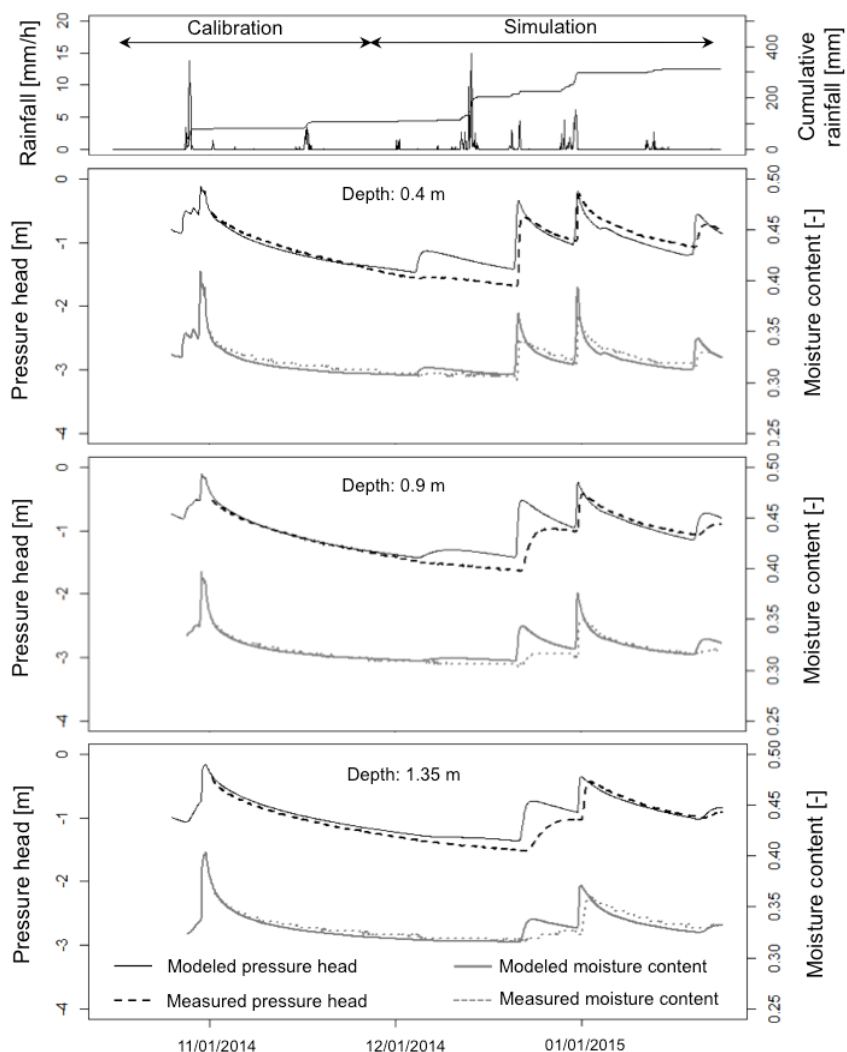


FIG. 2. Comparison between modeled (solid line) and measured (dashed line) moisture content (in gray) and pressure head (in black). Results are provided at the three different depths: 0.4, 0.9, and 1.35 m.

Boundary conditions for the mechanical model were rollers at the hillslope bottom and sides. Therefore vertical displacement is zero at the base and horizontal displacement is zero at the sides. Mechanical properties used for the stability analysis are presented in Table 2 where c' is effective cohesion, ϕ' is the effective friction angle, E is the Young modulus, μ is the Poisson's ratio, and γ is the dry unit weight of the soil.

The rainfall that occurred during hurricanes Frances and Ivan was measured in the Mooney Gap station (RG31 at 1364 m) and was used as input of the hydro-mechanical framework in order to simulate the stability conditions of the hillslope. Moreover, in order to define the rainfall scenario that would cause failure, we iteratively increased the measured rainfall that occurred during Hurricanes Frances and Ivan stopping the analysis when the safety factor decreased to less than 1.0. We found that increasing the rainfall occurred during hurricanes Frances and Ivan by 30% would cause the hillslope failure. Suction stress and field of local factor of safety are reported in Fig. 3 for the measured Frances and Ivan rainfall, and in Fig. 4 for the 30% increased rainfall.

Table 2. Parameters used for the mechanical model.

	c' [kPa]	ϕ' [°]	E [MPa]	μ [-]	γ [kN/m ³]
Layer 1	15	38	10.0	0.33	16.0
Layer 2	12	40	10.0	0.33	16.0
Layer 3	12	40	10.0	0.33	16.0

Results are presented at three different times: before the hurricanes, after the peak of hurricane Frances, and after the peak of hurricane Ivan. Figures 3 and 4 show that during the hurricanes Frances and Ivan suction stress decreases mainly near the soil surface up to 1.5 m in depth. Suction stress near the crest and the toe of the hillslope decreases to values between 1-2 kPa for the measured Frances and Ivan rainfall and to values between 0-1 kPa for scenario with 30% increased rainfall.. Fig. 3 shows that the hillslope was stable during hurricanes Frances and Ivan. Local factor of safety decreases in the top-soil due to the infiltration process and corresponding decreasing of suction stress. Fig. 4 shows the failure evolution of the hillslope for the 30% increased rainfall scenario. In black is depicted the area with local factor of safety lower than 1 and a black line delineates the surface of failure. The failure surface depth is about 0.8 m which is consistent with observations of landslides that occurred during Frances and Ivan in the area (Wooten et al. 2008). A small area presenting safety factor lower than 1 is observed in the upper gentle slope section of the hillslope. This is probably due to a combination of being close to a boundary and having a sudden change in slope.

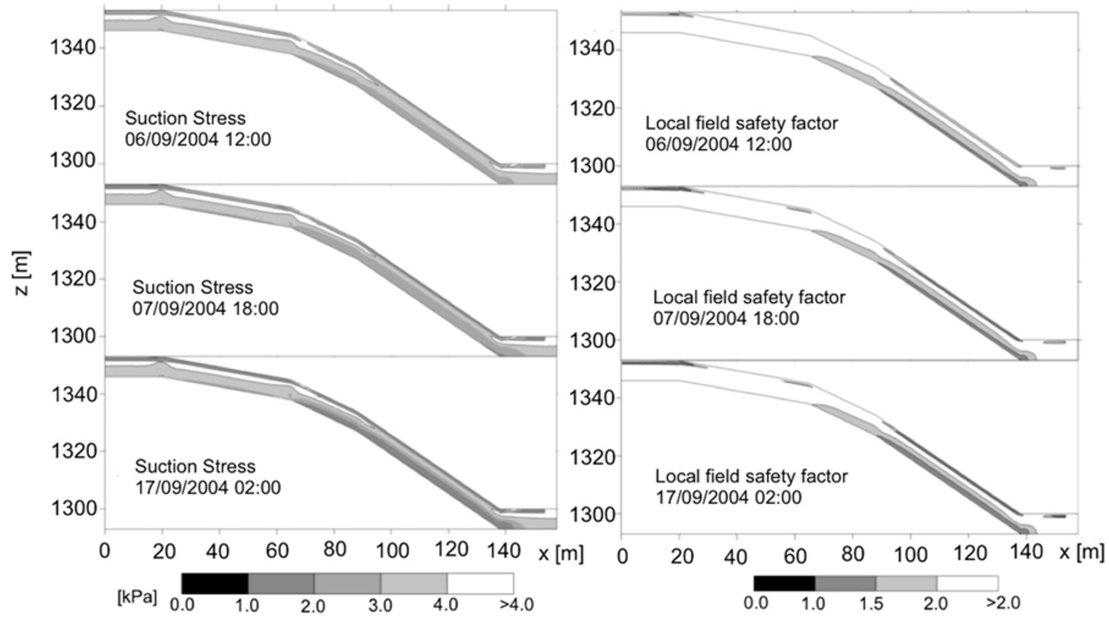


FIG. 3. Suction stress and local factor of safety during the Frances and Ivan rainfall at three different times: before the hurricanes, after the Frances peak, and after the Ivan peak.

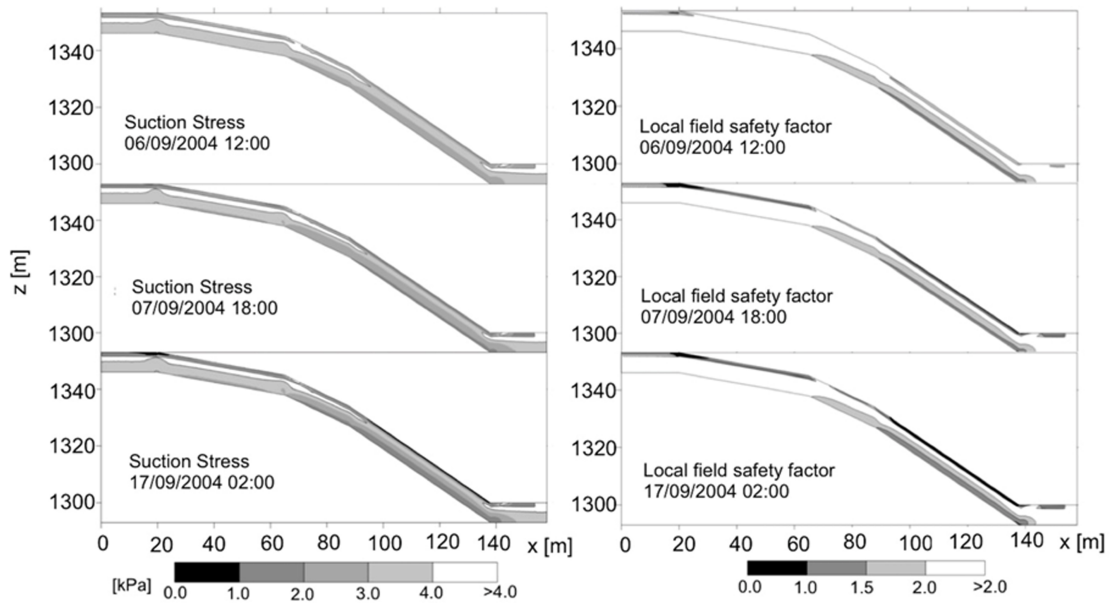


FIG. 4. Suction stress and local factor of safety during the 30% increased Frances and Ivan rainfall at three different times: before the hurricanes, after the Frances peak, and after the Ivan peak.

CONCLUSIONS

In this paper we evaluated the impact of the hurricanes Frances and Ivan on hillslope stability for a slope located in Western North Carolina. We used a hydro-mechanical model that captures the main physical mechanisms in the hillslope and calculates a local factor of safety without the need of assuming a failure surface. The framework implements a unified effective stress theory which is later used in the slope stability analysis. Hydro-mechanical parameters were obtained by inverse modeling using measured soil moisture and pressure head data.

Results indicate that the monitored hillslope was stable when subjected to a rainfall equivalent to hurricanes Frances and Ivan. The zone with lower local factor of safety (1.33) was located in the lower area of the hillslope. Finally, we iteratively increased the rainfall intensity until hillslope instability was reached. Failure occurs at a rainfall 30% larger than the one measured during Frances and Ivan. A failure surface is first observed at the toe of the hillslope, later evolving to the area near the crest.

ACKNOWLEDGMENTS

The authors appreciate the support of a NASA grant (NNX12AO19G) to NL.

REFERENCES

- Baum, R. L., Godt, J. W., & Savage, W. Z. (2010). Estimating the timing and location of shallow rainfall-induced landslides using a model for transient, unsaturated infiltration. *Journal of Geophysical Research: Earth Surface* (2003–2012), 115(F3).
- Fellenius, W. (1936), Calculation of the stability of earth dams, in *Transactions of the 2nd Congress on Large Dams*, vol. 4, pp. 445–463, Int. Comm. on Large Dams, Washington, D.C.
- Janbu, N. (1973), Slope stability computations. *Embankment-dam engineering*, in Casagrande, vol. R, edited by C. Hirschfeld and S. J. Poulos, pp. 49–86, John Wiley, New York.
- Lewis, Y. W., Wayllace, A., Lu, N., Godt, J. W., and Wooten, R. M. (2013) “Hydro-Mechanical Properties and Stability Analysis of Four Landslide-Prone Hillslopes in Western North Carolina.” *GSA Annual Meeting in Denver*. 2013.
- Lu, N., & Godt, J. W. (2013). *Hillslope hydrology and stability*. Cambridge University Press.
- Lu, N., Sener-Kaya, B., Wayllace, A., & Godt, J. W. (2012). Analysis of rainfall-induced slope instability using a field of local factor of safety. *Water Resources Research*, 48(9).
- Lu, N., & Likos, W. J. (2004). *Unsaturated soil mechanics*. Wiley.
- Montgomery DR, Dietrich WE (1994) A physically based model for the topographic control on shallow landslide. *Water Resour Res* 30:83–92
- Reddy, J. N. (1985), *Introduction to the Finite Element Method*, McGraw-Hill, New York.

- Ochiai, H. (2006). *Landslides: processes, prediction, and land use* (Vol. 18). American Geophysical Union.
- Simoni, S., Zanotti, F., Bertoldi, G., and Rigon, R. (2008): Modeling the probability of occurrence of shallow landslides and channelized debris flows using GEOTOP-FS, *Hydrol. Process.*, 22, 532-545.
- Simunek, J., T. Vogel, and M. T. van Genuchten (1994), The SWMS-2D code for simulating water flow and solute transport in two-dimensional variably saturated media, Version 1.21, Res. Rep. 132, USDA-ARS U.S. Salinity Lab., Riverside, Calif.
- Nakhaei, M., & Šimunek, J. (2014). Parameter estimation of soil hydraulic and thermal property functions for unsaturated porous media using the HYDRUS-2D code. *Journal of Hydrology and Hydromechanics*, 62(1), 7-15.
- Smith, I. M., and D. V. Griffiths (2004), *Programming the Finite Element*, 4th ed., John Wiley, West Sussex, U. K.
- Witt, A. C. (2005). A brief history of debris flow occurrence in the French Broad River Watershed, western North Carolina. *NC Geogr*, 13, 58-82.
- Wooten RM, Gillon KA, Witt AC, Latham RS, Douglas TJ, Bauer JB, Fuemmeler SJ, Lee LG (2008) Geologic, geomorphic, meteorological aspects of debris flows triggered by hurricanes Frances and Ivan during September 2004 in the southern Appalachian Mountains of Macon County, North Carolina (southeastern USA). *Landslides* 5(1):31-44

Characteristics of the Elemental Release from Recovered Soil Separated from Disaster Waste Generated by the Great East Japan Earthquake and Tsunami

Masahiko Katoh¹; Takuya Yamaguchi²; and Takeshi Sato³

¹Senior Assistant Professor, Meiji Univ., 1-1-1 Higashimita, Tama, Kawasaki, Kanagawa 214-8571, Japan.

²Master Course Student, Gifu Univ., 1-1 Yanagido, Gifu, Gifu 501-1193, Japan.

³Professor, Gifu Univ., 1-1 Yanagido, Gifu, Gifu 501-1193, Japan.

Abstract: The physicochemical characteristics of the recovered soil separated from disaster waste and tsunami sediment generated by the Great East Japan Earthquake can be significantly different from those of the non-affected soil because the recovered soil contains unavoidable contamination such as pieces of concrete and wood debris as well as sea water. This study investigated elemental release from the recovered soil with water percolation using a column leaching test in order to investigate changes in the elemental release characteristics of the recovered soil. The electrical conductivity (EC) in the leaching water was constant at the initial stage of testing and gradually decreased at the middle stage of the test. The main contributors to the high EC value were calcium and sulfate ions, and the effect of sea water on elemental release was limited. Copper and zinc concentrations were relatively high during the early part of the leaching test, and subsequently, the concentrations of these elements decreased. In contrast, low levels of fluoride, lead, and arsenic in the leaching water were detected initially; however, the concentrations dramatically increased with the decrease in calcium and sulfate concentrations. These results indicate that the characteristics of elemental release altered with water percolation.

INTRODUCTION

A total of 17 million MT of disaster waste and 11 million MT of tsunami sediment were generated by the Great East Japan Earthquake and the subsequent tsunami in Iwate, Miyagi, and Fukushima prefectures, where the disaster caused by the earthquake and tsunami was worst. In Miyagi Prefecture, the total amount of disaster waste and tsunami sediment was 11 million MT, corresponding to the amount of general waste generated over a period of 12–13 years. One-third (w/w) of the disaster waste and tsunami sediment comprised soil and sediment. The disaster waste and tsunami sediment have been treated by separation, incineration, and reuse (Yamane et al. 2015).

In this study, the soil and sediment separated in the treatment are defined as recovered soil. The physicochemical characteristics of the recovered soil can be quite different from those of the non-affected soil because the recovered soil contains unavoidable

contamination such as pieces of concrete, wood debris, and sea water. For example, as a result of sea water contamination, the recovered soil has a wide range and high values of electrical conductivity (EC), from dozens to 5,000 mS/m; the values for the non-affected soil are a few mS/m (Takai et al. 2013). The elemental behavior of soil, such as dissolution–precipitation, sorption–desorption, and ion-exchange reactions, is in equilibrium between solid and liquid phases under a relatively low water-percolation rate. Thus, if the recovered soil is reused, elemental leaching from the recovered soil as a result of water percolation would cause disturbance of the chemical equilibrium of elemental behavior, which would result in changes in the elemental release characteristics. In particular, the recovered soil may contain harmful elements derived from industry; furthermore, the tsunami sediments also contain heavy metal(loid)s derived from rock affected by hydrothermal alteration. Therefore, a change in the elemental release characteristics may enhance heavy metal(loid) leaching, although initial evaluation of elemental release before reuse may have been acceptable, without leaching of harmful elements. However, little information is available about the characteristics of elemental release from the recovered soil affected by water percolation.

This study investigated elemental release from the recovered soil with water percolation by means of column leaching tests. The aim of this study was to determine the changes in the elemental release characteristics in the recovered soil with water percolation. The results obtained can provide important information to facilitate reuse of the recovered soil.

MATERIALS AND METHODS

Preparation of Recovered Soil

Two types of recovered soils sampled from Iwate Prefecture were used for the column tests: recovered soils were separated from disaster waste mainly containing combustible and incombustible wastes, respectively (hereafter RS-A and RS-B, respectively). Air-dried recovered soil samples were passed through a 2-mm sieve prior to use in the column tests. Tables 1 and 2 list the main chemical properties of the recovered soil. The pH and EC values of the recovered soil samples were measured in ultra-pure water with a solid:liquid ratio of 1:10 using a pH meter (MM-60R; DKK-TOA Co., Japan). The total carbon (TC) content of the recovered soil samples was determined using a carbon, hydrogen, and nitrogen (CHN) elemental analyzer (MT-6; Yanaco New Science Inc., Japan). The water-soluble elements were extracted using ultra-pure water with a solid:liquid ratio of 1:10 and were analyzed using an ion chromatograph (IC; 881 Compact IC Pro; Metrohm AG, Switzerland) equipped with a cation column for calcium, magnesium, potassium, and sodium ion analysis (IC YS-50; Showa Denko K.K., Japan), an anion column for sulfate, fluoride, and chloride ion analysis (IC SI-90 4E; Showa Denko K.K., Japan), and using an inductively coupled plasma mass spectrometer (ICP-MS; 7500cx; Agilent Technologies Inc., USA) for copper, zinc, lead, cadmium, and arsenic analysis.

Setup of the Column Test

Figure 1 shows a schematic of the up-flow saturated column leaching test. A clay plate was placed at the bottom of the column (diameter of column 20 mm, height 120 mm), and 46.2 g of the recovered soil sample was placed on the plate. The packing density of the recovered soil layer was 1.47 Mg/m^3 , calculated on the basis of the height of the recovered soil layer (100 mm). The pore volume (PV) of the recovered soil (14.1 cm^3) in the column was calculated using the volume of recovered soil (31.4 cm^3), the density of soil particles (2.67 Mg/m^3), and the mass of recovered soil (46.2 g). Each recovered soil column was prepared in triplicate. Ultrapure water was pumped from the bottom of the column using a constant flow pump at a rate of 0.1 ml/min . The flow rate corresponded to 19.1 mm of precipitation. The leached solution was collected from the top of the column at a rate of 2 PV per day, and the test continued until the water volume reached 60 PV. The solution sample was passed through a $0.45\text{-}\mu\text{m}$ filter; the pH and EC were determined using a pH meter, and the elemental concentrations were measured using IC and ICP-MS.

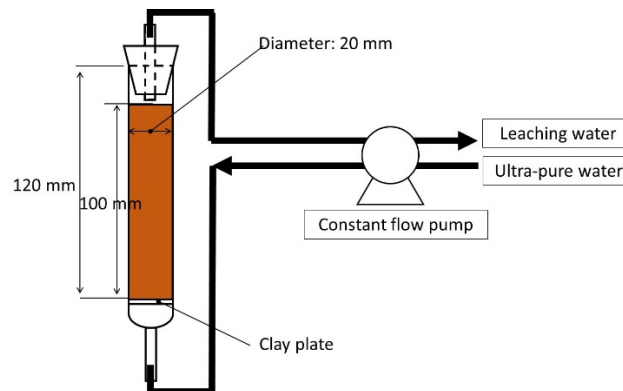


FIG. 1. Schematic of the up-flow saturated column leaching test.

RESULTS AND DISCUSSION

Chemical Properties of Recovered Soil

The EC values of RS-A and RS-B were 220 and 260 mS/m, respectively (Table 1), markedly higher than those of the non-affected soil. The elements that enhanced the EC value in the recovered soil were not sodium and chloride, but calcium and sulfate, suggesting that a large proportion of the water-soluble elements in the recovered soil used in this study was not derived from sea water, but instead from other sources. One of these sources would have been gypsum. The amounts of water-soluble calcium and sulfate in the recovered soil were 5.2 and 14.3 g/kg for RS-A and 6.1 and 16.6 g/kg for RS-B, respectively, which were converted to 0.13 and 0.15 mmol/kg for RS-A and 0.15 and 0.17 mmol/kg for RS-B, respectively. The molar ratios of calcium and sulfate as water-soluble phases in RS-A and RS-B were 0.87 and 0.88, respectively, comparable with the values of calcium sulfate. The levels of water-soluble harmful elements in RS-A and RS-B were relatively low; however, the levels of water-soluble lead and

cadmium in both recovered soils were slightly higher than 0.1 mg/kg, a value equivalent to the Japanese environmental standard (converted using the standard value of 0.01 mg/L and the solid:liquid ratio of the water extraction).

Table 1. Chemical Properties of Recovered Soil Used in This Study (Air-Dried Basis)

Recovered soil	pH	EC (mS/m)	TC (g/kg)	Water-soluble (g/kg)					
				Ca	Mg	Na	K	Cl	SO ₄
RS-A	7.7	220	37	5.2	0.1	0.4	0.1	0.4	14.3
RS-B	7.8	260	47	6.1	0.2	0.6	0.2	0.7	16.6

Table 2. Water-Soluble Harmful Elements of Recovered Soil Used in This Study (Air-Dried Basis)

Recovered soil	Water-soluble (mg/kg)					
	Cu	Zn	Pb	Cd	As	F
RS-A	0.2	0.1	0.2	0.2	0.02	7.2
RS-B	0.3	0.3	0.2	0.3	0.02	7.4

Values of pH and EC of Leaching Water

Figure 2 shows the pH and EC values of the leaching water. The variations in pH and EC between RS-A and RS-B with increasing leaching water volume were very similar, and these values were not significantly different between the recovered soils. The pH of the leaching water from both soils ranged between 7.7 and 8.2 during the leaching test; thus, the pH of the leaching water was stable and neutral. The EC values at the first sampling were very high, more than 400 mS/m, and were then stable at 222–256 mS/m until 16 PV; subsequently, the EC values dramatically decreased to 20 mS/m from 18 to 44 PV. After 46 PV, the EC values were stable at 13–20 mS/m. The EC results for the leaching water indicate that contaminant elements in the recovered soil were dissolved and leached till 44 PV.

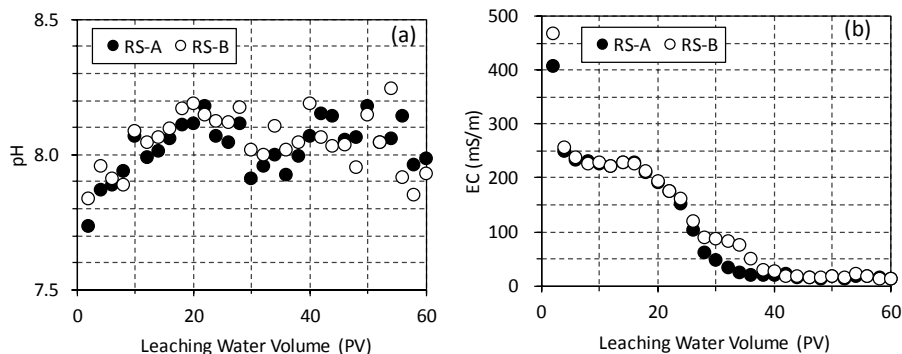


FIG. 2. (a) pH and (b) EC of leaching water from recovered soil.

Concentrations of Dominant Positive and Negative Ions in Leaching Water

The concentrations of the dominant positive and negative ions in the leaching water are shown in Figs. 3 and 4, respectively. The concentrations of calcium and sulfate ions in the leaching water of both soils followed a trend same that of the variations in EC. The highest concentrations were detected at the beginning of the test, and subsequently, the concentrations altered to the first stable state. After the first stable state, the concentrations rapidly dropped at 20 PV and 30 PV for RS-A and RS-B, respectively, until general concentrations of calcium and sulfate ions were observed. The only difference in calcium and sulfate concentrations between RS-A and RS-B was the point at which the decrease in the concentration began: 18 PV for RS-A and 28 PV for RS-B. The concentrations of sodium and chloride ions in both soils rapidly decreased from the beginning of the test to 6 PV, gradually reduced to 28 PV, and were then less than 1 mg/L. Similarly, the magnesium and potassium concentrations decreased with increasing leaching water volume; however, the magnitude of the decrease in the concentration was gentle compared to that of the concentrations of sodium and chloride ions.

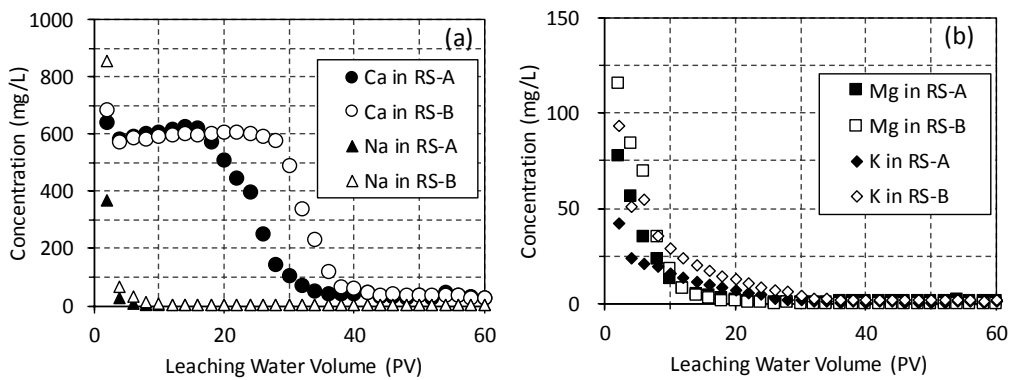


FIG. 3. Concentrations of (a) calcium and sodium ions and (b) magnesium and potassium ions in leaching water from recovered soil.

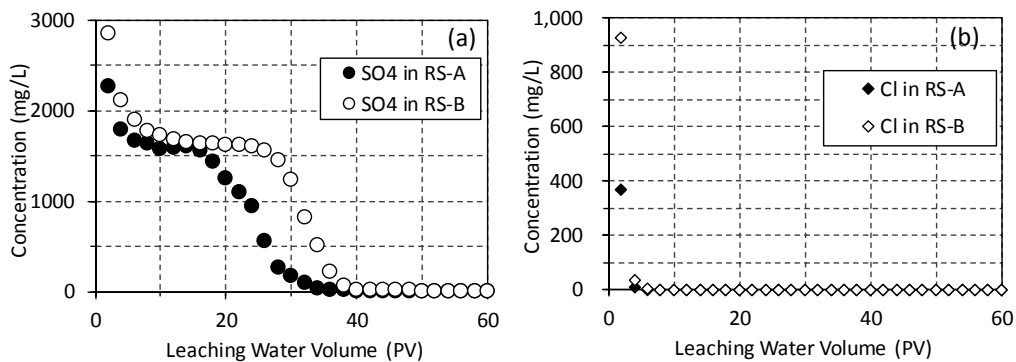


FIG. 4. Concentrations of (a) sulfate ions and (b) chloride ions in leaching water from recovered soil.

High concentrations and rapid decreases at the beginning of the test were observed for sodium and chloride ions. The recovered soil had been separated from disaster waste, which contained various waste materials, including tsunami sediment affected by sea water. Therefore, dissolution of sodium and chloride from tsunami sediment in RS-A and RS-B would have been responsible for the flush decrease in concentrations of sodium and chloride ions. Furthermore, it is suggested that the elements derived from sea water would have been washed out within a relatively short time. From the results of calcium and sulfate ions, the trend in the EC values with water percolation was explained by the high levels of calcium and sulfate in the recovered soil. The molar ratio of calcium and sulfate concentrations was almost 1 during the leaching test, suggesting that gypsum waste was concentrated in the recovered soil and dissolved into the leaching water. Stable calcium and sulfate concentrations were observed from the initial to the middle stages of testing. This would have been because the leaching water was oversaturated with regard to gypsum till the middle stage of the test, and subsequently, the concentrations started to decrease as the gypsum content decreased with the progress of water percolation. The turning point at which the concentration decrease commenced was the only difference between the recovered soils, which would have resulted from the initial differences in the gypsum content of the recovered soil (Table 1). The amounts of water-soluble calcium and sulfate in RS-B were higher than those in RS-A, implying a higher content of gypsum in RS-B. Thus, the higher content of gypsum in RS-B would have caused the delay in the concentration decrease.

Concentrations of Harmful Elements in Leaching Water

The concentrations of harmful elements in the leaching water are illustrated in Fig. 5. The variations in elemental concentrations with increasing leaching water volume showed almost the same trend despite the differences in the recovered soil. Cadmium was not detected in the leaching water during the test. High concentrations of copper and zinc were measured in the leaching water from both soils at the initial stage of testing; however, the elemental concentrations gradually decreased with increases in the leaching water volume. In contrast, the lead and arsenic concentrations in the leaching water were low until 20 PV except for the first and second samplings; however, after around 20 PV for RS-A and 30 PV for RS-B, the concentrations of both elements gradually but linearly increased until the end of testing. The fluoride concentration increased at around 20 PV for both soils, and peaks in concentration were observed at 28 PV for RS-A and 36 PV for RS-B. The PV values at which the concentrations of lead, arsenic, and fluoride increased were comparable with the PV at which the levels of calcium and sulfate decreased. Therefore, the dissolution of large quantities of elements such as calcium and sulfate would have caused a disturbance in the chemical equilibrium of elemental behavior, which resulted in the enhancement of fluoride, lead, and arsenic concentrations. Fluoride, lead, and arsenic are present as various phases in soil, such as ion-exchangeable and bound to soil particles. Some of these phases are calcium fluoride, lead sulfate, and calcium arsenate when large quantities of calcium and sulfate are present in the soil, because the solubility constants of calcium fluoride, lead sulfate, and calcium arsenate are lower than that of gypsum. These minerals can certainly be dissolved by water percolation; however, during the

initial stage of the test, the high concentrations of calcium and sulfate derived from gypsum in the recovered soil would have inhibited the dissolution of calcium fluoride, lead sulfate, and calcium arsenate due to chemical equilibrium (Bothe, Jr. and Brown 1999; Ahn et al. 2003), causing the low concentrations of fluoride, lead, and arsenic. As the concentrations of calcium and sulfate decreased with water percolation, the chemical equilibrium would have altered to the dissolution reactions of calcium fluoride, lead sulfate, and calcium arsenate, resulting in enhancement in their concentrations. Furthermore, the low content of fluoride compared to those of lead and arsenate would have caused a reduction in the fluoride concentration. These results indicate that the elemental release characteristics changed with the leaching of other elements by water percolation. Furthermore, note that in the case of reuse of the recovered soil, continuous and careful monitoring of soil and groundwater near the site at which the recovered soil is reused is necessary to determine whether harmful elements are being dissolved out of the recovered soil.

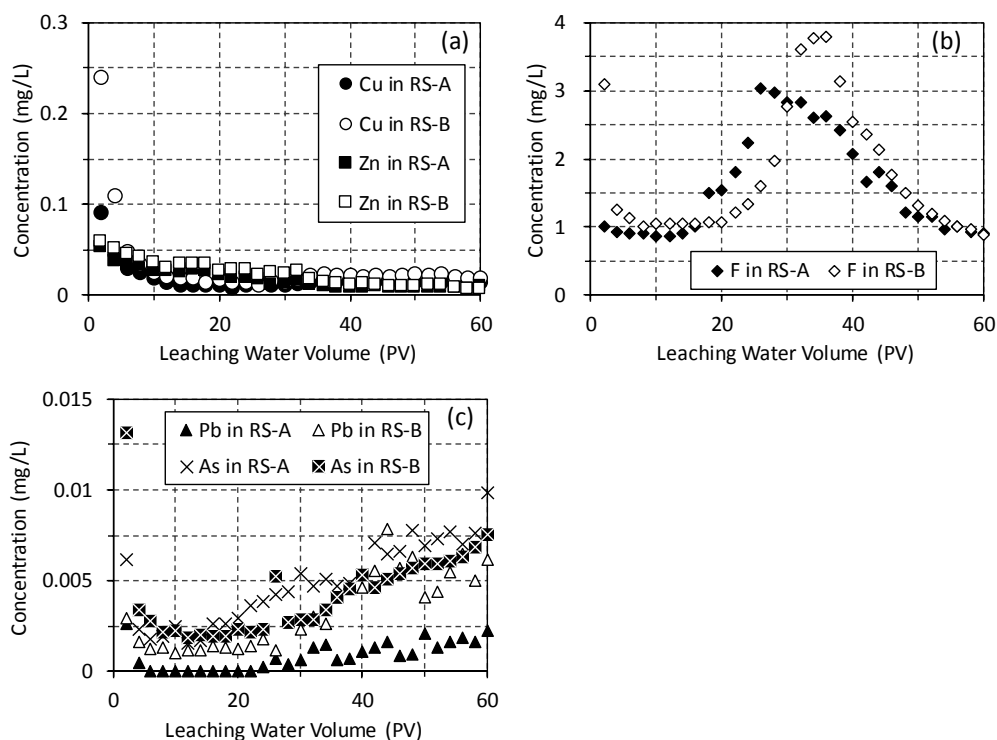


FIG. 5. Concentrations of (a) copper and zinc, (b) fluoride, and (c) lead and arsenic in leaching water from recovered soil.

CONCLUSION

This study investigated elemental release from recovered soil with water percolation in a column leaching test. The recovered soil was separated from the disaster waste and tsunami sediment generated by the Great East Japan Earthquake and tsunami. Two types of recovered soil were subjected to testing. The pH in the leaching water of both soils was neutral during the test. The EC in the leaching water from both soils was

constant and high during the initial stage of testing and gradually decreased in the middle of the test. The main contributors to the high EC value were calcium and sulfate ions, and the effect of sea water on elemental release was limited compared to the effects of calcium and sulfate ions. Copper and zinc concentrations were relatively high initially, and their concentrations decreased with increasing leaching water volume. In contrast, the fluoride, lead, and arsenic concentrations in the leaching water from both soils remained at a low level during the early stage of the test; however, their concentrations dramatically increased with the decrease in calcium and sulfate concentrations. These results indicate that the characteristics of elemental release altered with water percolation. Therefore, continuous, careful monitoring of soil and groundwater near sites where the recovered soil is reused is essential.

ACKNOWLEDGMENTS

The CHN elemental analyzer instruments used in the chemical analyses were made available by the Division of Instrumental Analysis at Gifu University. The authors are grateful to Prof. F. Li and Prof. K. Hirooka (Gifu University) for allowing the use of ICP-MS. This study was supported by the Environment Research and Technology Development Fund (3K133003) of the Ministry of the Environment, Japan.

REFERENCES

- Ahn, J.S., Chon, C.M., Moon, H.S. and Kim, K.W. (2003). "Arsenic removal using steel manufacturing byproducts as permeable reactive materials in mine tailing containment systems." *Water Res.* Vol. 37: 2478–2488.
- Bothe Jr., J.V. and Brown, P.W. (1999). "Arsenic immobilization by calcium arsenate formation." *Environ. Sci. Technol.* Vol. 33: 3806–3811.
- Takai, A., Yasutaka, T., Endo, K. and Katsumi, T. (2013). "Distribution and physicochemical properties of tsunami deposits generated by the 2011 Great East Japan Earthquake." *Japanese Geotechnical J.* Vol. 8 (3): 391–402.
- Yamane, K., Takai, A., Katsumi, T., Inui, T., Mikata, K., Okawara, M. and Kawashima, M. (2015). "Characterization of recovered soils in Iwate Prefecture generated by the Great East Japan Earthquake." *Proc. 11th JGS Symposium on Environmental Geotechnics*, JSS, Fukushima, Japan: 93–98.

Geoenvironmental Issues for the Containment of Radioactively-Polluted Soil and Waste

Toru Inui¹; Takeshi Katsumi²; and Atsushi Takai³

¹Associate Professor, Kyoto Univ., Sakyo, Kyoto, Japan. E-mail: inui.toru.3v@kyoto-u.ac.jp

²Professor, Kyoto Univ., Sakyo, Kyoto, Japan. E-mail: katsumi.takeshi.6v@kyoto-u.ac.jp

³Assistant Professor, Kyoto Univ., Sakyo, Kyoto, Japan. E-mail: takai.atsushi.2s@kyoto-u.ac.jp

Abstract: This manuscript briefly introduces technical solutions for containment of the low-level radioactively contaminated soil and waste generated by the accident of Fukushima Daiichi nuclear power plants. Two technical concerns in designing and constructing the lining system are addressed and analyzed in the laboratory experiments. Firstly, hydraulic integrity of GCLs, which is installed as a barrier layer in the cover system, was investigated. The focus was placed on barrier performance of GCL overlap subjected to slippage and low overburden pressure, caused by differential settlement of waste layer. GCL overlap maintained its hydraulic integrity even against the overlap slippage up to 100 mm, although there were some variations in apparent hydraulic conductivity values, relating to overlap treatments. Secondly, a series of batch sorption tests was conducted to assess the effects of cations in the landfill leachate on the cesium sorption characteristics of mineral sorption layer, which is installed beneath the contaminated wastes and soils. Calcium and potassium ions in the leachate most significantly lowered the cesium sorption by sodium bentonite and decomposed granite soil, respectively.

INTRODUCTION

A mega-thrust earthquake and the subsequent huge tsunami, which occurred in March 2011 at off the Pacific coast of Tohoku, Japan, caused severe accidents at the Fukushima Daiichi Nuclear Power Plant. In the affected area, radioactive contamination of surface environment occurred by fall-out of radioactive chemicals such as ¹³⁴Cs and ¹³⁷Cs. Accordingly, a large quantity of radioactively polluted soil and waste was generated in the affected area through remediation works as well as public works such as water treatment and municipal solid waste incineration. Contaminated soils and wastes have been collected and stored at temporary storage yards (Fig. 1) as of early 2015. Table 1 shows estimated amounts of polluted soils and wastes generated in Fukushima Prefecture. It is estimated that more than 20 million m³ of soils and wastes need to be stored properly for future final disposal. Soil and waste contaminated with relatively low concentrations (less than 100,000 Bq/kg) will be disposed of or temporarily stored in containment facilities similar to typical engineered landfills.

Although typical engineered landfilling will be executed, there are some technical issues specific to storage of these radioactively contaminated soils and wastes. Basically, water solubility of radioactive cesium is very high. Particularly, radioactive cesium in incinerator fly ash will easily leach out (National Institute for Environmental Studies 2013). In addition, it should be noted that MSW landfills in Japan basically allow the rainfall infiltration into the waste layer to accelerate the biodegradation, as well as to wash out the soluble contaminants in the waste. Thus, when radioactively contaminated soils and wastes is disposed of in storage facilities, installing a hydraulic barrier in the cover system and a sorption layer in the bottom lining system is considered to prevent infiltration and leakage of radioactive cesium (Fig. 2).



FIG. 1. Soil Bags Containing Radioactively Polluted Wastes and Soils Piled at a Temporary Storage Yard in Fukushima (March 2015).

TABLE 1. Estimated Amounts of Radioactively Polluted Soils and Wastes Generated in the Affected Area, Fukushima Prefecture (Data from the Ministry of the Environment, Japan).

Category		Volume (x 10 ³ m ³)
Soil, Non-combustible	≤ 8,000 Bq/kg	10,060
	8,000 - 100,000 Bq/kg	10,350
	> 100,000 Bq/kg	10
Incineration ash of combustible wastes		1,550
Wates contaminated in more than 100,000 Bg/kg		20

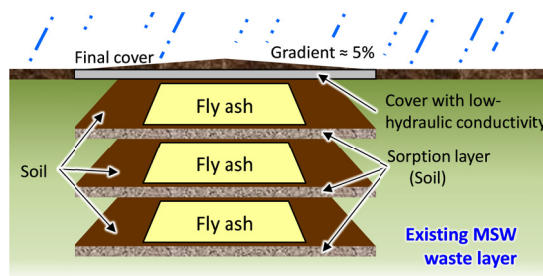


FIG. 2. Schematic View of Disposal of Radioactively Contaminated MSW Fly Ash in Existing Landfills.

Geosynthetic clay liners (GCLs) are expected to act as a hydraulic barrier in the final cover system of containment facilities because of their limited thickness, low hydraulic conductivity and ease of installation with simple overlapping (Estornell and Daniel, 1992). However, compressibility of these wastes and soils layers is relatively high due to degradation of organic fraction (leaf, plant, etc.) and deliquescence of incinerator ash, and may cause differential settlement. Generally, 150 to 200 mm was employed as the conventional GCL overlap in Japan to accommodate drying shrinkage and installation variations. However, when the GCL overlap is subjected to differential settlement, slippage of GCL overlaps and reduced overburden pressure adversely affect hydraulic integrity of GCL overlaps (Katsumi et al. 2014).

Another concern is cesium sorption performances of mineral reactive barriers such as compacted soil and bentonite amended soil, which act as sorption layers against radioactive cesium leaching from soil and waste. Generally, clayey soils have high distribution coefficients for radioactive cesium (National Institute for Environmental Studies 2013). However, when incinerator ash is landfilled, high concentrations of cations dissolved in the leachate may limit the sorption capacity of mineral barriers.

This manuscript summarizes the laboratory testing results to overcome these technical issues for containment of radioactively polluted soil and waste with low concentrations, which were generated in the area affected by the accident of Fukushima Daiichi nuclear power plants. Firstly, hydraulic barrier performance of GCL overlap subjected to slippage of up to 100 mm due to differential settlement was evaluated by conducting flow box tests for three needle-punched GCL products. Also, this manuscript addresses the results on a series of batch sorption/desorption tests to assess the effects of major cations in the landfill leachate on the cesium sorption/desorption characteristics of sodium bentonite and decomposed granite soil.

FLOW BOX TEST FOR EVALUATING THE HYDRAULIC BARRIER PERFORMANCE OF GCL OVERLAP

Materials

Three different needle-punched GCL products with three layers (bentonite layer sandwiched by geotextiles) were examined. Basic properties of three GCL products are summarized in Table 2. GCL-1 consisted of a uniform sodium bentonite powder layer sandwiched with a polypropylene nonwoven geotextile and a polypropylene woven geotextile. Nonwoven geotextile was pre-filled with sodium bentonite powder, which is expected to act as a sealing for the interface after hydration. GCL-2 comprised of a uniform granular sodium bentonite layer sandwiched with a polypropylene nonwoven geotextile and a polypropylene woven geotextile. In overlap section of GCL-2, 4 kg/m² of granular sodium bentonite (mean diameter = 1.2 mm) was uniformly placed on the interface between upper and lower GCLs. GCL-3 contained a uniform granular sodium bentonite layer with polypropylene nonwoven geotextiles on both sides. Overlapping treatment was similar to that for GCL-2 except the mean diameter of granular bentonite used (0.6 mm).

TABLE 2. Basic Properties of Three different GCL Products

GCL	Thickness (mm)	Geotextiles (Upper / Lower)	Bentonite	Bentonite mass (g/m ²)	Overlap treatment
1	7	Nonwoven incl. bentonite powder / Woven	Na bentonite, Powder	5,000	Simple overlapping
2	6	Nonwoven / Woven	Na bentonite, Granular	≥ 4,000	Lay granular bentonite in 4 kg/m ²
3	6	Nonwoven/ Nonwoven	Na bentonite, Granular	5,900	Lay granular bentonite in 4 kg/m ²

Methods

Figure 3 shows a flow box test equipment used for evaluating the hydraulic barrier performance of the GCL overlap, which was previously developed by the authors (Ogawa et al. 2013). A similar testing device was also developed and employed by Kendall and Austin (2014) to assess hydraulic performance of GCL overlaps.

A pair of GCLs was overlapped and set at the bottom of the tank with 150 mm in overlap, which was a typical setting in many field applications of GCLs in Japan. In addition, 50 mm of overlap was set to simulate the decreased overlap induced by differential settlement. In both cases, the center of the overlap section corresponded to the center of base plate of the equipment, and the length of overlap section was 300 mm as shown in Fig. 3. Non-permeable rubber boards (5 mm in thickness) were placed to prevent the permeation through the non-overlap section.

Figure 4 shows an enlarged view of the GCL overlap with possible flow paths during permeation; 1) flow through the interface between overlapped GCLs and 2) vertical flow through the overlap section. A 300 mm thick silica sand layer with its wet density of 1.6 Mg/m³ and moisture content of 13% was filled above the GCLs, which were left for 24 hours to allow them to be hydrated. Then, a constant water head of 450 mm was applied on the GCL overlap. Accordingly, vertical effective stress acting on the GCL overlap was 2.6 kPa, which was lower than the effective overburden pressure expected in the field.

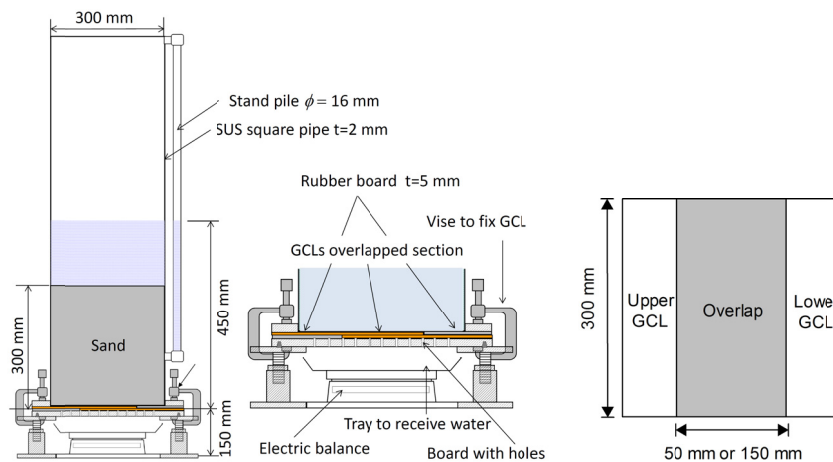


FIG. 3. Schematic View of a Flow Box Test Equipment (Ogawa et al. 2013).

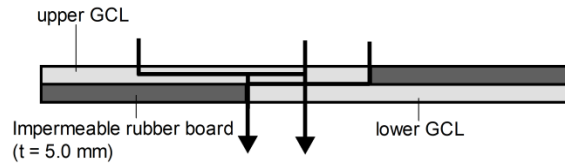


FIG. 4. Enlarged View of the GCL Overlap in a Flow Box Test with Possible Flow Paths (Ogawa et al. 2013).

Results and Discussion

As shown in Fig. 4, a couple of possible flow paths were considered in this study; 1) flow through the interface between overlapped GCLs and 2) vertical flow through the overlap section. However, contributions of each flow path to the total leakage cannot be separated. Thus, hydraulic barrier performance was evaluated using two different indices. The one is the leakage rate per unit length of the overlap, q ($\text{m}^3/\text{s}/\text{m}$), and the other is the apparent hydraulic conductivity, k_a (m/s), which was determined based on Darcy's law, assuming that the area of permeation was limited to the area of the overlap and the height of the permeable media is the thickness of the overlap, which is a double of the thickness of GCL. Profiles of q and k_a are plotted in Fig. 5(a) and (b). Note that no effluent was observed for GCL-3 even after 30 days of permeation, in both cases (50 mm and 150 mm in overlap), probably because finer granular bentonite was dosed to the interface and bentonite mass per unit area was larger comparing to GCL-2 with a similar structure and overlap treatment.

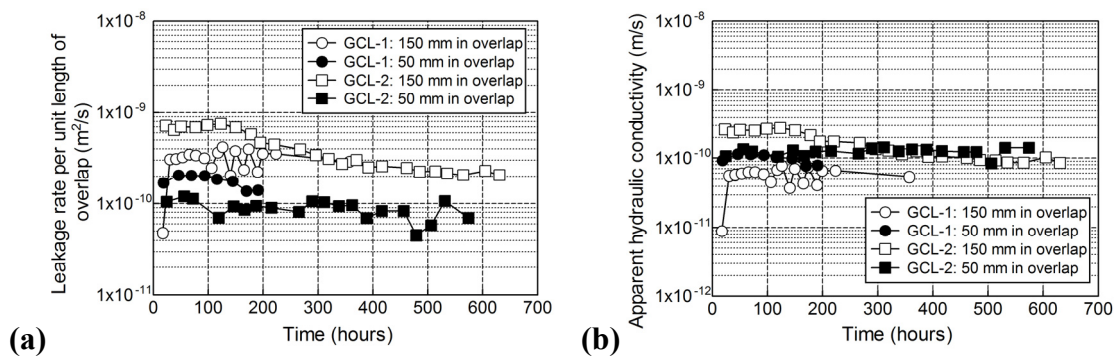


FIG. 5. Results of the Flow Box Test for GCL overlaps; (a) Leakage Rate per Unit Length of Overlap with Time, and (b) Apparent Hydraulic Conductivity with time.

Fig. 5(a) indicates that q was gradually decreased particularly in GCL-2. It took longer for granular bentonite on the interface to be fully hydrated and seal the gap between upper and lower GCLs. 50 mm overlap provided the lower q for both GCL-1 and GCL-2 than 150 mm overlap. This indicates that vertical flow contributed to the total leakage considerably, taking into account that the area of permeation in 150 mm overlap was three times larger than that in 50 mm overlap.

Fig. 5(b) indicates that the effect of overlap (50 mm and 150 mm) on k_a was not confirmed for both GCL-1 and GCL-2. k_a values were approximately 1×10^{-10} m/s for GCL-1 and in the order of 10^{-11} m/s for GCL-2, respectively. As a reference, Table 3 shows hydraulic conductivity values of GCLs-1 to 3, which were determined by using

the flexible wall hydraulic conductivity tests (ASTM D 5887) under the confining pressure of 30 kPa. These values can be regarded as hydraulic conductivity when only vertical flow is allowed, although the confining pressure is much higher than in this flow box test.

k_a values were 3 to 10 times higher in GCL-1, and 2 to 3 times higher in GCL-2, comparing with hydraulic conductivity values of intact GCLs shown in Table 3. These differences were induced by the flow through the interface between the overlapped GCLs. Particularly in GCL-1, contribution of the interface flow was relatively larger since no granular bentonite was placed at the interface. However, absolute k_a values obtained were low enough to act as hydraulic barrier in the final cover. From these observations, overlapped GCLs, even when the slippage up to 100 mm was induced by differential settlements, maintain its hydraulic integrity if the contact between upper and lower GCLs was kept in this flow box test.

TABLE 3. Hydraulic conductivity of double layered GCL.

GCL	Hydraulic conductivity(m/s)
GCL-1	1 to 3×10^{-11}
GCL-2	2 to 5×10^{-11}
GCL-3	3 to 4×10^{-11}

BATCH TEST FOR EVALUATING THE EFFECTS OF CATIONS ON CESIUM SORPTION CHARACTERISTICS OF MINERAL SORPTION LAYER

Materials

Two soil samples, sodium bentonite and decomposed granite soil, were selected for the sorption tests. Sodium bentonite (particle density: 2.88 Mg/m^3 , natural water content: 10%) was extracted from a needle-punched geosynthetic clay liner (GCL) Bentofix® BFG 5000, and then sieved with a $75 \mu\text{m}$ -opening sieve. Decomposed granite soil (particle density: 2.70 Mg/m^3 , natural water content: 10%, Cation exchange capacity: 9.3 cmol/kg) was sieved with a 2 mm-opening sieve.

Solutions containing various types and concentrations of cations were prepared for the batch sorption tests. Firstly, solutions with sodium, potassium or calcium ion concentrations ranging from 0 to 500 mg/L were prepared by using the chloride chemicals. The simulated leachate from MSW incinerator fly ash (MSWIFA) was also prepared as follows. MSWIFA was collected in a certain incineration facility for municipal solid waste in Japan. The ash was mixed with distilled water in a ratio of 1 to 10 in mass basis. The solution was filtered by using a membrane filter with $0.2 \mu\text{m}$ opening. In addition, the solutions after diluting this leachate by 10 times and 100 times were used. Table 4 shows the chemical properties of the simulated leachate.

TABLE 4. Chemical properties of the simulated leachate used.

pH	E.C. (mS/m)	Al (mg/L)	Ca (mg/L)	Fe (mg/L)	K (mg/L)	Na (mg/L)	Pb (mg/L)	Zn (mg/L)
12.4	3.6×10^3	1	5.3×10^3	1	3.5×10^3	2.7×10^3	1	2

Methods

Cesium concentration of each solution was adjusted to 100 $\mu\text{g/L}$ by using the standard cesium chloride solution. The tests were performed by mixing 0.05, 0.1, 0.2, 0.3 or 0.5 g of dried soil sample with 100 mL of the solution in a 250 mL polyethylene bottle. The mixture was subjected to 24 hours of horizontal shaking on an incubator shaker at 150 rpm and under 20°C. After shaking, the mixture was centrifuged and then filtered using a 0.20 μm -opening filter. Concentrations of cesium were analyzed by a graphite furnace atomic absorption spectrophotometer. A sorption isotherm is described by calculating the amount of cesium sorbed with the equilibrium cesium concentration, and the distribution coefficient K_d was determined from a slope of the sorption isotherm. Also, concentrations of major cations were analyzed through the inductively coupled plasma (ICP) analysis.

Results and Discussion

Figure 6 shows the sorption isotherms and the K_d values for the sodium bentonite obtained when the tests were performed for distilled water, and the three simulated leachate solutions shown in the previous section. K_d values for the three simulated leachate were one to three order of magnitude lower than K_d for distilled water. Major differences between these solutions are concentrations of cations and pH values. According to Khan et al. (1994), cesium sorption capacity of the bentonite is pH-dependent and increased under the low-mid alkaline condition, while K_d values are not increased if pH is higher than 9. Considering the pH values of these simulated leachate solutions (pH 9.3 to 12.4), pH value did not contribute to the decreasing K_d values. These observations indicate that existence of the cations in the simulated leachate is a main factor affecting the cesium sorption capacity.

Figure 7 shows concentration changes of cesium ion (Cs^+) and three cations after sorption test affected by the dose of bentonite for the 10 times-dilution leachate case. Potassium (K^+) and calcium (Ca^{2+}) ions as well as Cs ion were sorbed to the sodium bentonite according to the dose of bentonite. These concentration profiles clearly support that some coexisting cations in the simulated leachate were selectively sorbed to the bentonite and lowered the Cs sorption capacity.

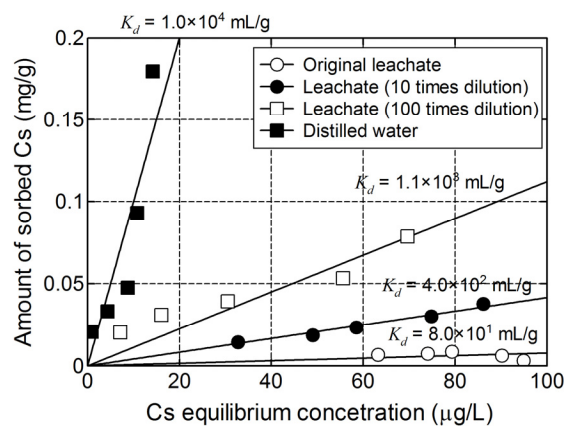


FIG. 6. Sorption Isotherms of Sodium Bentonite for the Simulated Leachate Solutions and Distilled Water.

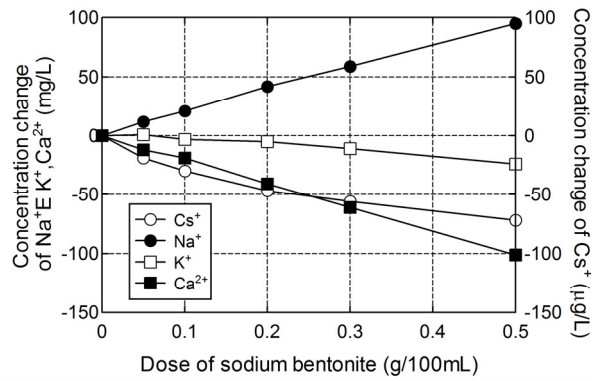


FIG. 7. Concentration Change of Cs and Three Cations after Sorption Tests (10 Times-Diluted Leachate Cases) Affected by the Dose Of Sodium Bentonite.

Figure 8(a) shows the relationships between the cation concentrations (equivalent concentration basis) and the K_d values obtained for the sodium bentonite. Overall, the lower K_d values were obtained for a certain cation concentration in the order of Ca^{2+} , K^+ , Na^+ . This means that calcium ion was most likely to prevent the sodium bentonite from sorbing Cs ion rather than potassium and sodium. This order corresponds well to the general preference of cation exchange equilibria in soil; highly charged cations (Ca^{2+}) tend to be held more preferentially than cations with less charge ($Na^+ < K^+$) and secondly, cations with a small hydrated radius ($Na^+ < K^+$) are less likely to be removed from the exchange complex. It can be concluded that the combined influence of these two criteria is important for the adverse effect of the coexisting cations on the Cs sorption ability. The K_d values determined for the 10 times and 100 times diluted leachates were also plotted on Figure 8(a), based on the concentration of Ca^{2+} , which is proved most influential to the Cs sorption. The K_d values for these leachate cases were similar to those for the cases with the equivalent Ca^{2+} concentration, even though these leachates contain considerable concentrations of Na^+ and Ca^{2+} as shown in Table 4. This result support the effect of Ca ion on Cs sorption is dominant even when other influential cations exist, since the cation with a higher valence and larger ionic radius are more likely to be held by the bentonite.

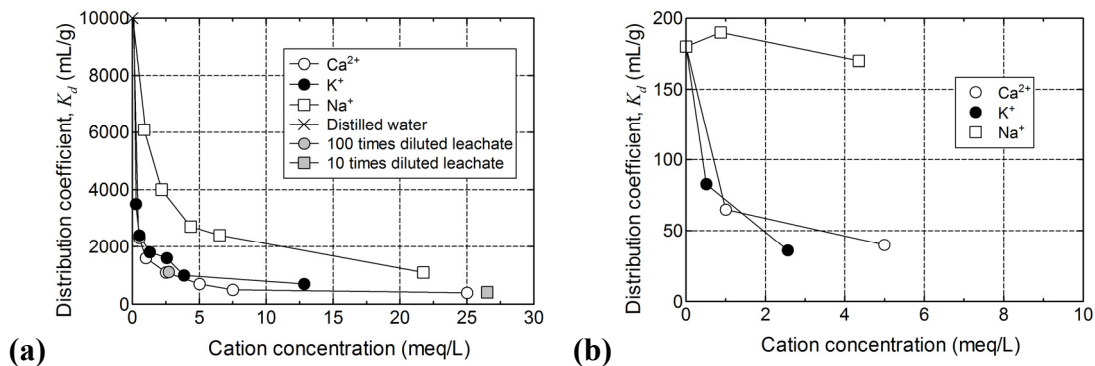


FIG. 8. K_d values affected by the cation concentrations in the solution: (a) Sodium Bentonite and (b) Decomposed Granite Soil.

Figure 8(b) shows the relationships between the cation concentrations and the K_d values for the decomposed granite soil. Comparing with the sodium bentonite, the K_d values were much smaller for a certain cation concentration. In addition to this, there are two main differences from the sodium bentonite. Na^+ has no effect on the K_d values for the decomposed granite soil under the testing conditions in this study, probably because it has a very low concentrations of exchangeable sodium. Also, potassium ion was most likely to prevent the decomposed granite soil from sorbing Cs ion rather than calcium. Many previous studies confirmed that potassium ions compete with cesium ions for sorption to the clayey soil (National Institute for Environmental Studies 2013). Anyway, this different trend suggests that sorption processes different from those of the sodium bentonite lies behind the decomposed granite soil. Further study is necessary to verify how the soil type relates to the effect of cations in the leachate on the cesium sorption/desorption characteristics of mineral barriers.

CONCLUSIONS

This manuscript briefly summarizes the current state on containment of low-level radioactively contaminated soil and waste generated by the accident of Fukushima Daiichi nuclear power plants. In addition, laboratory experiments were conducted to address two technical concerns in designing and constructing the lining system for containment facilities. Firstly, hydraulic integrity of GCLs, which is installed as a barrier layer in the cover system, was investigated using a flow box test. Hydraulic barrier performance of GCL overlap, which is subjected to slippage and low overburden pressure due to differential settlement of waste layer, was examined. GCL overlap maintained its hydraulic integrity even against the overlap slippage up to 100 mm, although there were some variations in apparent hydraulic conductivity values, which depended on overlap treatments. Also, a series of batch sorption tests was conducted to assess the effects of cations in the landfill leachate on the cesium sorption characteristics of mineral sorption layer, which is installed beneath the contaminated wastes and soils. Although some differences existed among sodium bentonite and decomposed granite soil, calcium and potassium ions in the leachate most significantly lowered the distribution coefficients for cesium.

ACKNOWLEDGMENTS

The authors appreciate the supports from Mr. Shota Kihara and Mr. Shotaro Ogawa, former Graduate Students of Kyoto University, in conducting laboratory tests. A part of this work was supported by JSPS KAKENHI Grant Number 25289134.

REFERENCES

- Estornell, P. and Daniel, D.E. (1992). "Hydraulic conductivity of three geosynthetic clay liners", *Journal of Geotechnical Engineering*, ASCE, 118: 1592–1606.
- Katsumi, T., Inui, T., Takai, A. and Ogawa, S. (2014). "Containment of nuclide contaminated MSW incinerator ash in landfills: Effect of differential settlement", *Proc. 10th International Conference on Geosynthetics*, M. Ziegler, G. Bräu, G. Heerten, and K. Laackmann (eds.), German Geotechnical Society, Essen, Germany: on USB.

- Kendall, P.M. and Austin, R.A. (2014). "Investigation of GCL overlap techniques using a large scale flow box", *Proc. 7th International Congress on Environmental Geotechnics*, A. Bouazza, S.T.S. Yuen, and B. Brown (eds.), Engineers Australia (EA): 746-753.
- Khan, S.A., Raiz-ur-Rehman, and Khan, M.A. (1994). "Sorption of cesium on bentonite", *Waste Management*, 14(7): 629-642.
- National Institute for Environmental Studies (2013). *Technical Report on Proper Waste Treatment and Disposal Considering the Fate and Transport of Radionuclide*, 3rd Edition, http://www.env.go.jp/jishin/attach/haikihyouka_kentokai/10-mat_3.pdf (browse on March 6, 2014), in Japanese.
- Ogawa, S., Sumoto, S., Inui, T., Takai, A. and Katsumi, T. (2013). "Hydraulic barrier performance of overlapped geosynthetic clay liners subjected to differential settlements", *Geosynthetics Engineering Journal*, Japan Chapter of International Geosynthetics Society, 28: 103-108.

Geo-environmental Knowledge for the Adaptation of Riverine Coastal Geo-hazards

Kazuya Yasuhara¹, Van Trinh Cong², Hideo Komine³, and Hemanta Hazarika⁴

¹Ph.D., Professor Emeritus, Institute for Global Change Adaptation Science, Ibaraki University, 2-1-1 Bunkyo, Mito, Ibaraki, 310-8512, Japan

e-mail: kazuya.yasuhara.0927@vc.ibaraki.ac.jp

²Ph. D, Director, Institute of Water and Environment Research, 2 Street Truongsa, District Binhthanh, Ho Chi Minh City, Vietnam

³Ph.D., Professor, Department of Civil and Environmental Engineering, Waseda University, 3-4-1 Ohkubo, Shinjyuku-ku, Tokyo, 169-8555, Japan

⁴Ph.D., Professor, Graduate School of Engineering, Kyushu University, 744 Motooka, Nishi-ku, Fukuoka, 819-0395, Japan

ABSTRACT: The paper proposes eco-friendly adaptive techniques using locally available materials and industrial by-products. Used automobile tires, as an industrial by-product, were combined with palm fibers to construct reinforced dyke systems as a multiple protective measure. The tires used with a mangrove plantation inside can work together with mangroves to protect against impacts from such severe climate events as storm surges. The addition of the palm fibers plays a role in increasing dyke stability, particularly when mixed with cement and dyke soils.

1. INTRODUCTION

An attempt has been made to propose multiple protection that combines traditional techniques, locally conventional methodology, and the advanced technology in Mekong Delta, Vietnam. In addition, this new adaptation is also characterized by cost-saving aspects because locally available natural materials are expected to be adopted and low-cost natural and artificial geosynthetic materials are expected to be prepared by the local private sector. This strategy has just started pilot tests in Vietnam. The Japanese group is included to undertake improvements and advancement of pilot tests under planning. The paper is intended to present an outline of the pilot tests and the expected results to be obtained through the internationally collaborative research project, particularly with the inclusion of aspects of environmental geotechnology.

2. SEVERITY OF COASTAL EROSION IN VIETNAM: HAI HAU COAST

Coastal retreat in Vietnam has been severe, mainly because of climate change. As an example, Mai et al. (2009) reported that the respective annual amounts of retreat during 1905–1960, 1960–1973, and 1973–1992 were 30–50 m, 20–35 m and 10 m on the Hai Hau coast of northern Vietnam. Because of that severe retreat, coastal dyke collapse has occurred frequently, about once every 7–10 yr, as depicted in Fig. 1.

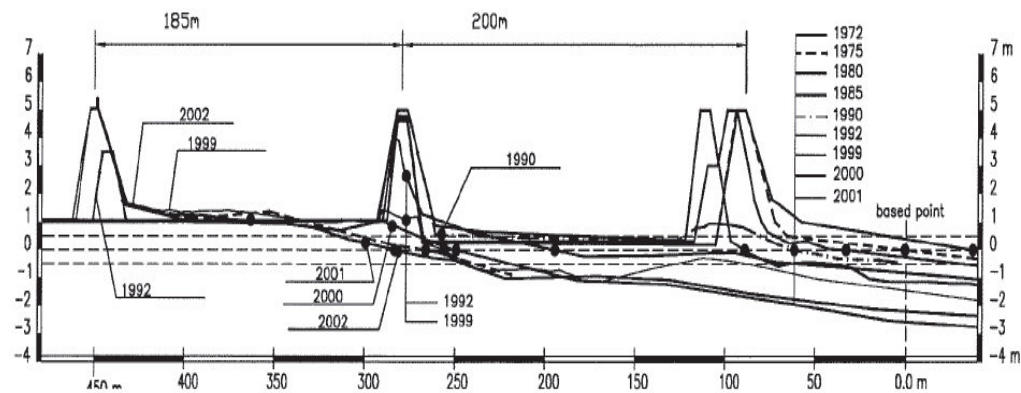


FIG. 1 Overlapping cross-shore profiles from 1972 to 2003 at Hai Lay/ Hai Trieu section (After Cong V., Mai et al. 2009)



FIG. 2 History of erosion process in Hai Hau coast, Vietnam (Vu, L.G., 2003)

Figure 2 shows that devoting attention to old churches as symbolic monuments can illustrate the destruction caused by the progressive retreat of the Hai Hau coast. Unfortunately, the remaining symbolic churches finally collapsed in 2010.

3. MULTIPLE-PROTECTION AGAINST COASTAL EROSION

The Mekong Delta in the lower part of Mekong River is the largest granary of Asia, but is nevertheless a region that is vulnerable to climate change. That vulnerability is likely to affect residents' lives and natural environments strongly in numerous ways related to infrastructure, industries (agriculture and fisheries), and ecology. Those impacts are not mutually independent but rather are expected to share strong mutual correlation. Regarding disasters particularly, difficult situations have arisen. So-called "compound disasters" that occur as a consequence of combinations of multiple causes are classifiable as climate change-associated events or climate change-independent events. Unfortunately, however, it seems that many projects related to adaptation to climate change inside and outside of countries associated with the Mekong Delta have been conducted individually. Few achievements have been integrated internally and internationally to proceed to the next stage.

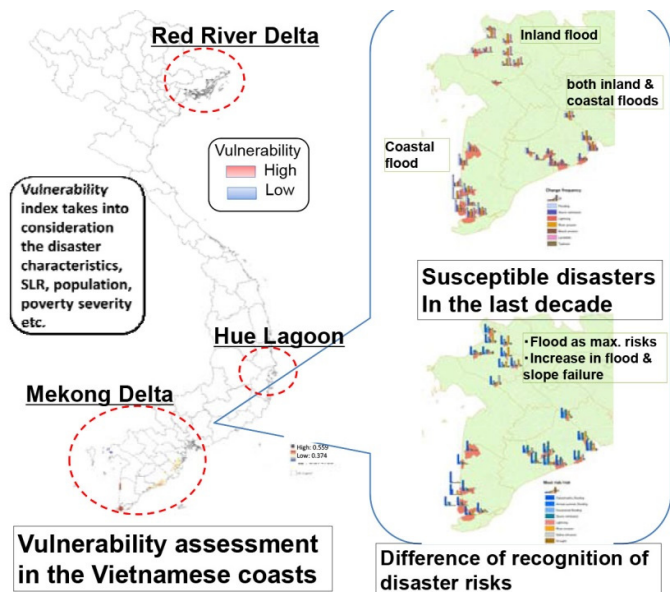
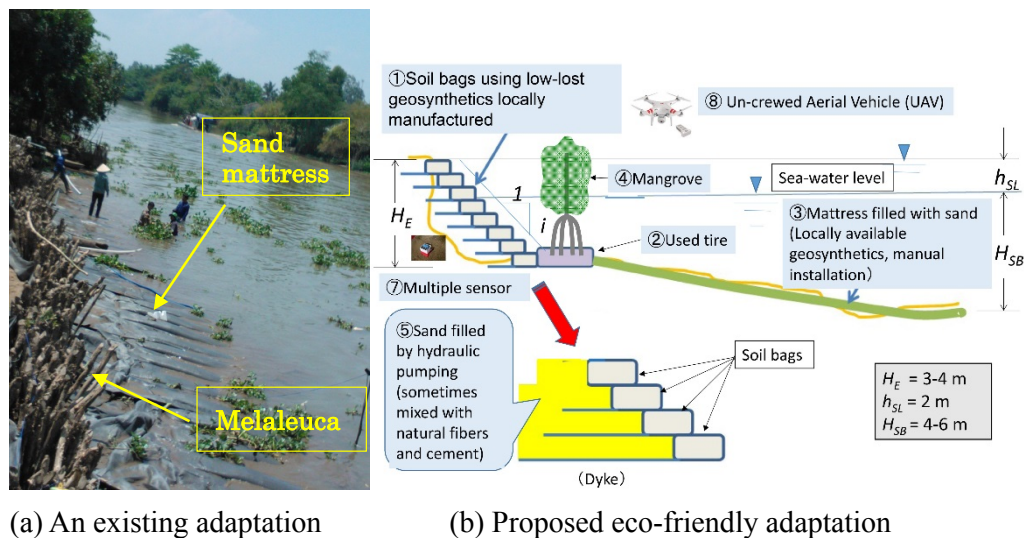


FIG. 3 Objective areas for adaptation to disasters caused by climate change



(a) An existing adaptation (b) Proposed eco-friendly adaptation

FIG. 4 A comparison between present and proposed adaptation in Mekong delta

To overcome these difficulties, it is necessary to confront obstacles against proper solutions not only from inter-disciplinary aspects but also from trans-disciplinary aspects in which many stakeholders such as local residents, governments, researchers, and industries are involved.

The second important feature of the Mekong Delta is the proposal of concrete adaptation, which is able to endow the resilience of stakeholders to climate change by considering not only natural but also social and human backgrounds. This adaptation is also necessary to maintain good harmony with industries (agriculture and fisheries, mainly) and ecologies in the objective region (Fig. 3). Given this background, we first propose “smart adaptation,” which is highly resilient and which constitutes multiple protective dykes as depicted in Fig. 4. This multiple protection is characterized by the following:

- i) resilient dykes improved and reinforced with a mixture of natural fibers and cement, as previously proposed by Sato et al. (2013);
- ii) locally available and cost-saving soil bags protecting dykes proposed by Institute of Innovate Water Resources in Vietnam (IIWR, 2015);
- iii) mangrove protection using used tires, as proposed by Hazarika et al. (2014);
- iv) cost-saving sand mattresses used for reducing erosion and for increasing accumulation in river and sea beds proposed by IIWR; and
- v) a monitoring system adopted as a soft adaptive measure using un-crewed aerial

vehicles (UAVs) to measure the behavior of dykes and water surfaces in rivers and coasts, in addition to multi-purpose sensors embedded in dykes.

This multiple protection adaptation measure includes not only disaster prevention aspects but also ecological and environmental aspects related to geotechnical engineering. This paper outlines knowledge of environmental geotechnical engineering that is necessary for the multiple protection proposed herein, although application of this multiple technique has just started. Therefore it is in its initial stages.

4. GEOTECHNICAL STABILIZATION OF DYKES

Among the impacts of global warming, sea-level rise (SLR) poses the greatest threat to the stability of human settlements along coastlines, particularly in vulnerable areas in Asia–Pacific regions. Areas along coasts and rivers have been affected recently by SLR, underscoring the need to assess the vulnerability of coasts and riverbanks. It is therefore necessary to develop countermeasures to mitigate the influences of strong and persistent SLR for coasts and river levees. Among the alternatives available for countering these threats, applying earth reinforcement and soil improvement are promising strategies, not only for coastal structures but also for river levees that must sustain wave action that is sometimes so severe that it produces storm surges. Furthermore, combinations of conventionally used techniques are an anticipated geotechnology for reducing climate change-induced disasters, as presented in Table 1.

Table 1. Geotechnical stabilization of dykes

Improvement/ Reinforcement	Examples of Technique	Remarks
Mechanical improvement/ Reinforcement	<ul style="list-style-type: none"> ● Well-graded soils ● Well-compacted soils ● Inclusion of fiber materials 	<ul style="list-style-type: none"> ● Inexpensive ● Durable ● Locally available material or traditionally used material
Chemical improvement /reinforcement	<ul style="list-style-type: none"> ● Mixture of cement, quicklime and adhesive materials 	<ul style="list-style-type: none"> ● Attention to contamination
Mechano-chemical improvement /reinforcement	<ul style="list-style-type: none"> ● Admixture of fiber materials with cement ● Sandwiched-structure using Non-woven fabrics with quicklime ● Placement of geosynthetics with soils stabilized by cement 	<ul style="list-style-type: none"> ● Hybrid ● Cost/benefit analysis

Important issues for attaining this purpose are how to reduce costs for construction practices intended to mitigate disasters and to reduce environmental impacts. Therefore, finding techniques that satisfy engineering effectiveness, eco-friendliness, and cost savings simultaneously is a challenging task. This paper therefore starts to outline the past; then it presents current circumstances and future prospects for geotechnical engineering as a means of protecting Vietnamese coastal riverine dykes.

According to fundamental knowledge in geotechnical engineering, dykes and levees typically have (i) well-graded distribution of soil particles, (ii) adequate compaction, (iii) protective measures against water seepage, and (iv) sufficient drainage systems. Soil improvement and earth reinforcement are added to stabilize banks which are endangered to resist excessive external forces in the context of climate change.

As one option that enables practical application at the actual site in Vietnam for increasing stability of banks, in cases of shortage of stability of banks, addition of palm fibers (mechanical stabilization), a locally available natural material in Vietnam, to sandy soils increases friction force. The addition of cement increases cohesion force (chemical stabilization) as illustrated schematically in Fig. 5. Both additions can increase bank stability. Furthermore, combined usage of palm fiber and added cement to sandy soils is expected to increase stability more than in the case of adding palm or cement individually or separately.

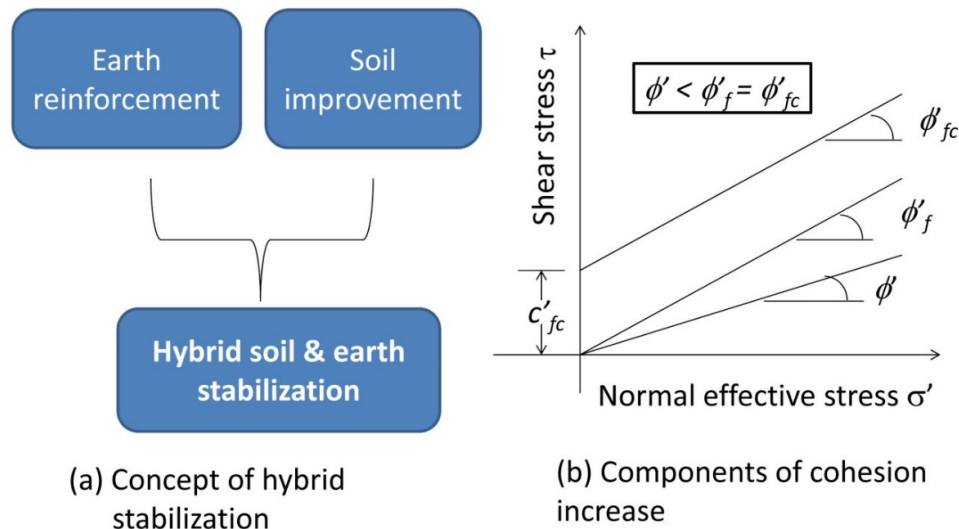


FIG. 5 Soil and earth stabilization mixed with palm fibers and added by cement

Sato et al. (2013) conducted laboratory tests of both seepage failure and permeability tests on sandy soils with and without a mixture of palm fibers. Results show that utilization of the mixture of soil and palm fiber for banks is expected to improve both the reinforcement to seepage failure and the drainage potential, particularly for banks that constitute sand-rich and coarser soils. Whether increased friction and cohesion are expected to contribute to bank stability remains an open question.

5. PROTECTION OF DYKES

Along with conventional countermeasures to protect water-frontal dykes against wave actions such as construction of wall structures and placements of concrete blocks, plantation of mangroves is often adopted as a typical conventional usage in Asia-Pacific regions as a protective measure for dykes undergoing climate change. Measures of this kind are called “Green Infrastructure.” However, because impacts of climate change have recently worsened, it is increasingly necessary to protect mangrove forests, which are extremely important from viewpoints of both ecological maintenance and disaster mitigation. To attain this purpose, the current paper presents a proposal of the use of used passenger car tires based on the achievements of Hazarika et al. (2014) who attempted to grow two plants, Kirinsou and Dechondra inside of disused tires, as presented in Fig. 6. Both plants are robust against seawater. In the present paper, instead of those plants used by Hazarika et al., plantation of mangroves is proposed as depicted in Fig. 7.



FIG.6 Plants inside used tires

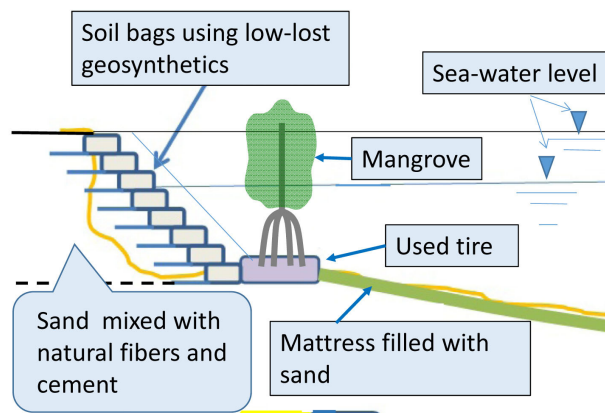


FIG. 7 Protection of mangrove by sand mattress and used tire

The system of used tires with mangroves described above is regarded as a hybrid structure from the viewpoint that the used tire structure functions both for protection of dykes and for the growth and maintenance of mangroves.

6. PROTECTION OF MANGROVES

The river bank composition in the Mekong Delta region is mostly young alluvium with low erosion resistance (critical velocity of 0.5–0.8 m/s). As a result, erosion occurs mostly on canal and river systems even though the flow velocity in this region is not high. Sand mattresses have been developed (Trinh Cong Van, 2002;2010) and tested on the Saigon River. They will be applied for river erosion protection as a low-cost solution (see Fig. 4 (a), Fig. 8 and Fig. 9).



FIG.8 Sand mattresses installation (left) and after 18 months (right)

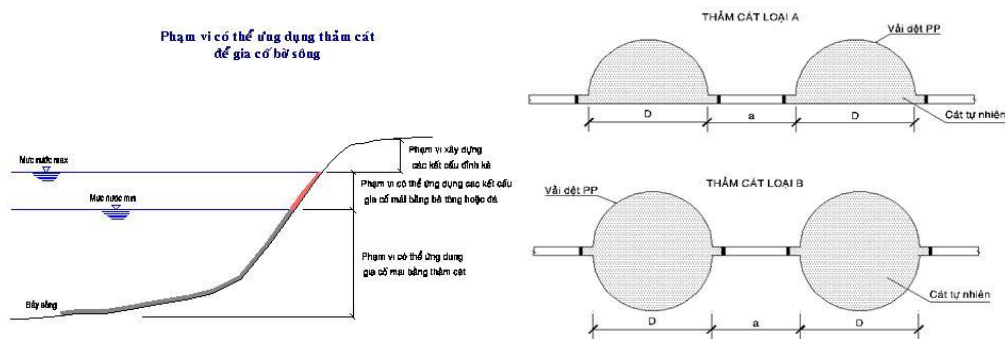


FIG. 9 River bank protection design (left) and cross-section of mattresses (right)

The sand mattress size can be determined based on the hydraulic condition of the rivers. In small and medium rivers, mattresses of 30–50 cm diameter are applicable. Sand mattresses can also be installed through simple construction by a householder or householder group.

By summarizing the previous chapter and the present chapter, it can be understood that the multiple adaptive system previously depicted in Fig. 4 comprises two measures for protecting mangroves against severe climate: used tires with mangrove plantation inside and sand mattresses. This system of used tires and sand mattresses is placed along the coast and is connected perpendicularly to the direction of incident waves.

7. GEO-ENVIRONMENTAL ASPECTS IN PROPOSED ADAPTATION

Geo-environmental aspects are pointed out as:

- i) The locally available and naturally originated material is used for reinforcement of dykes
- ii) Protection of mangroves is emphasized as the ecological maintenance by adopting the local available sand mattress technique and utilizing the used passenger car tires.

Those lead to development of cost saving geo-techniques based on our philosophy that environmental impact reduction by successful utilization of waste materials be co-existed with disaster mitigation.

8. CONCLUSION

The paper presents a proposal of eco-friendly multiple adaptive measure for protecting water fronts under severe external forces induced in the context of climate change which includes (i) stabilization of dykes using the techniques of soil improvement and earth reinforcement, (ii) protection of dykes using the units of used tires placed parallel along the coastal line as a breakwater, and (iii) protection of mangroves using a sand mattress placed in front of the mangroves surrounded by used tires.

The proposed technique is characterized by eco-friendliness and cost-saving because attempts are made to (i) take not only engineering aspects but also ecological aspects into consideration and (ii) use the locally available materials and industrial waste materials for dyke stabilization. In this sense, the new technique proposed herein can be regarded as green infrastructure.

Last but not least, the technique will work well in vulnerable waterfront areas in the Asia–Pacific regions, although it emphasizes the Vietnamese waterfronts.

ACKNOWLEDGEMENT

This study was and has been carried out under the supports by the strategic project of Ministry of Environment, Japan, (FY2010-FY2014), and the Grant-in-Aid from Ministry of Education, Sport, Science and Tourism (MEXT) (FY2015-FY2018).

REFERENCES

- Hazarika, H. and Hara, T. (2014). Resilient and sustainable geotechnical solution- Lessons learned from the 2011 Great East Japan Disaster –, Proc. Intern'l Conf. on Sustainable Civil Infrastructure, Keynote Paper, Hyderabad, India, Springer.
- Mai, C. V., Stive, M. J. F. and Van Gelder, F. H. A. J. M. (2009). Coastal protection strategies for the Red River Delta, *Journal of Coastal Research*, 25(1), 105–116
- Sato, K., Komine, H., Murakami, S. and Yasuhara, K. (2013). An experimental Evaluation on Effects on Seepage Failure Using a Natural Fiber Mixed with Soils for River Dykes Proc. International Conf. on Geotechnics for Sustainable Development – Geotech Hanoi, (CD ROM), 2013
- Tamura, M. (2012). Vulnerability assessment to climate change in the Asa-Pacific regions: issues and perspectives, *Memoir of Human Science*, Ibaraki University, 53, 25-36, (in Japanese).
- Trịnh, C. V. (2002). Design and Installation of Sand mattresses for river bank protection in Mekong delta region, MARD study, 2002 (in Vietnamese).
- Trịnh, C. V. (2010). Shore Erosion in the South of Vietnam, Applied protection Measures and Study Needs, Mito, Japan 2010.
- Yasuhara, K., Van, T.C. and Duc, D.M. (2012). Geosynthetics-aided adaptation against coastal instability caused by sea-level rise, Proc. Geosynthetics Asia 2012, Bangkok, Thailand, 1-15, Dec., 2012.
- Yasuhara, K., Komine, H., Satoh, K. and Duc, D.M. (2013). Geotechnical response to climate change-induced disasters in the Vietnamese coasts and river dykes: A Perspective, Proc. Second International Conf. Geotechnics for Sustainable Development, Geotech – Hanoi 2013, 3-21, Hanoi, Vietnam.

Material Properties of Soils Recovered from Disaster Debris in Iwate Prefecture Generated by the 2011 Great East Japan Earthquake

Takeshi Katsumi¹; Atsushi Takai²; Toru Inui³; Masafumi Okawara⁴; and Mitsuhiro Kawashima⁵

¹Professor, Kyoto Univ., Yoshida-Honmachi, Sakyo, Kyoto 6068501.

²Assistant Professor, Kyoto Univ., Yoshida-Honmachi, Sakyo, Kyoto 6068501.

³Associate Professor, Kyoto Univ., Yoshida-Honmachi, Sakyo, Kyoto 6068501.

⁴Associate Professor, Iwate Univ., 4-3-5 Ueda, Morioka 0208551.

⁵Iwate Prefectural Government, 10-1, Uchimarui, Morioka 0208570.

Abstract: This paper focuses on material properties of more than 400 soils recovered from disaster debris in Iwate Prefecture generated by the 2011 Great East Japan earthquake and tsunami. Analyses in this study verified that recovered materials basically have sufficient quality as geomaterial from the viewpoint of chemical and physical properties, being expected to be utilized in geotechnical applications though additional processes such as mixing of steel slag and crushed concrete affect material properties. Some results raised an experimental concern regarding applicability of existing test standards for assessment of recovered materials.

INTRODUCTION

An earthquake of magnitude 9.03 (M_w), referred to as the 2011 earthquake off the Pacific coast of Tohoku, occurred at 14:46 on March 11, 2011. This was one of the five most powerful earthquakes in the world since modern record-keeping started. The earthquake triggered a tsunami that reached heights of up to 39.5 m at the maximum in Miyako city, Iwate Prefecture, and travelled up to 10 km inland in the Sendai plain in Miyagi Prefecture (Katsumi et al. 2014). This earthquake caused various geotechnical and geoenvironmental problems in East Japan, as summarized by Inui et al. (2012).

Soils recovered from disaster debris which occupied one-third of approximately 30 million-ton disaster debris and tsunami deposit was strongly expected to be utilized as geomaterial after the 2011 Tohoku earthquake and tsunami for reduction of waste amount disposed at landfill sites. Recovered materials generally contain a number of small wood originated in disaster debris, showing different properties as geomaterial site by site due to difference in characteristics of soil fraction including tsunami deposits, composition of disaster debris, and machines and their combination used for treatment. As disaster debris treatment in Iwate and Miyagi Prefectures has completed at the end of March, 2014, quality of recovered materials over the entire projects should be figured out by analyzing data accumulated for quality management. Understanding

of material properties of recovered materials can contribute to acceleration of utilization of recovered materials as well as adequate and prompt disaster debris treatment during future catastrophes.

Given such backgrounds, this study assessed quality of recovered materials and its influencing factors. In particular, after disaster debris treatment at each site was summarized, frequency distributions of each property were analyzed by site. Practical records in Iwate Prefecture were used, since all data throughout the projects were fully accumulated and summarized.

DISASTER DEBRIS TREATMENT IN IWATE PREFECTURE

Immediately after the 2011 earthquake off the Pacific coast of Tohoku and subsequent tsunami, the government estimated that approximately 20 million tons of disaster debris and 10 million tons of tsunami deposit had been generated through this disaster mostly in Iwate, Miyagi, and Fukushima Prefectures (see Figure 1(a) for the locations of these prefectures). Tsunami deposits are the soils transported by the tsunami and also require proper treatment as well as the disaster debris. It was geographically and economically unrealistic to construct new landfill facilities with sufficient capacities to accept these wastes, since they are several times larger than the annual generation of municipal solid waste in each local municipality. For example, disaster debris generation in Iwate prefecture corresponded to 12-year municipal solid waste generation in the whole prefecture and, in a more particular case, it corresponded to 280-year municipal solid waste generation in Rikuzentakata city, Iwate prefecture. Reuse of these materials was therefore required.

Treatment of the disaster debris has been a big challenge, since a large amount of soil-waste mixtures had never been generated in Japan before. While the detailed processes of disaster debris treatment vary by site, a basic flow in Iwate Prefecture can be illustrated in Figure 2 as indicated in a *Guideline for utilization of treated wastes for the recovery works* published by Iwate Prefecture (2013). After the debris was cleared

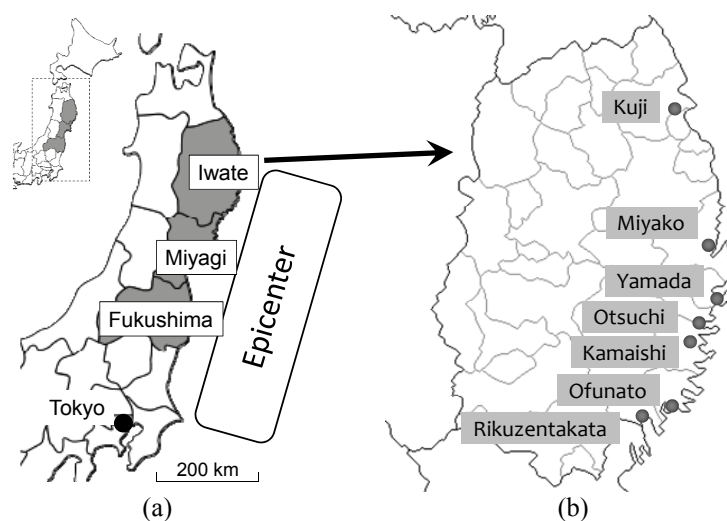


FIG. 1. Location of: (a) Iwate, Miyagi, and Fukushima Prefectures, and (b) treatment sites in Iwate Prefecture.

at the affected sites, transported to temporary storage sites, and stockpiled depending on the separation into tsunami deposits, soil-dominant debris, and waste-dominant debris after manual and rough separation at primary temporary storage sites. Amount of waste remained in these deposits and debris increased in this order. The deposits and debris were passed through advanced mechanical treatment systems consisting of several processes of crushing and separating. Tsunami deposits were recovered as “Recovered Soil Class A” through this treatment, and soils separated from soil-dominant debris with quality satisfying the criteria for utilization were recovered as “Recovered Soil Class B.” Although Recovered Soil Class B contains wood fraction relatively more than Recovered Soil Class A due to crushed wooden debris, these two recovered soils has been utilized as geomaterial in civil engineering applications. “Separated Fine Fractions” and “Residue” which were obtained from soil-dominant and waste-dominant debris with low quality were incinerated or disposed in existing facilities. “Recovered Soil Class B” originated in waste-dominant debris was also expected to be utilized as geomaterial (a gray arrow in Figure 2), but all of soil fraction through the treatment was treated as “Separated Fine Fractions” or “Residue” in practice because effect of inclusion of wood fraction was unrevealed.

For classification of soils generated through the treatment into recovered soil or waste, Iwate Prefectural Government issued a certificate regarding 17 properties listed

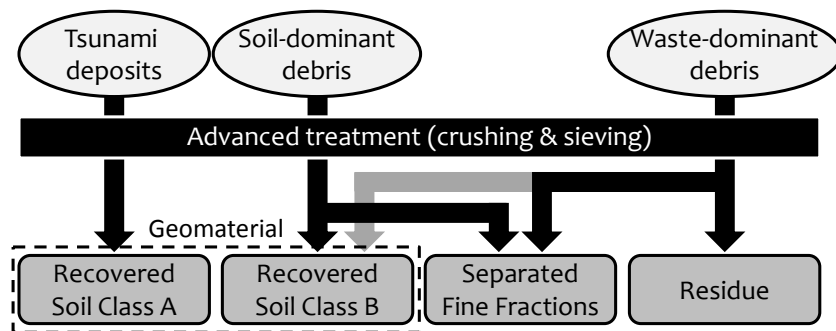


FIG. 2. Basic flow of disaster debris treatment and classification of recovered materials in Iwate Prefecture.

Table 1. Properties of recovered materials certified by Iwate Prefecture.

Environmental suitability			
Cd	Cr(VI)	Hg	Se
Pb	As	F	Br
Physical properties (and standard)			
Particle density (JIS A 1202)		Water content (JIS A 1203)	
Particle size (JIS A 1204)		Soil consistency (JIS A 1205)	
Cone index (JIS A 1228)			
Chemical properties (and standard)			
pH (JGS 0241)		EC (JGS 0212)	
Salinity (JGS 0241)		Ignition loss (JIS A 1226)	

Properties in boldface were analyzed in this study.

Table 2. Criteria for recovered materials in the guideline (MLIT 2012).

Item	Criteria
Maximum grain size	< 300 mm
Cone index	> 400 kN/m ²
Salinity	< 1 mg/g
Electrical conductivity	< 200 mS/m
pH	6 – 9
Swelling (at CBR soaking)	> 3%

in Table 1 with respect to each 3,000 m³ of generated soil from the viewpoints of environmental aspect following the Japanese standard for soil contamination and basic quality as geomaterial. This study analyzed 6 properties indicated by boldface in the table. The guideline of Iwate Prefecture refers to the material criteria proposed by the Ministry of Land, Infrastructure, Transport and Tourism for fill embankments, as shown in Table 2 (MLIT 2012).

SITE SPECIFIC TREATMENT AND DATA USED IN THIS STUDY

In this study, practical data collected from totally 7 treatment sites—Kuji, Miyako, Yamada, Kamaishi, Ofunato, and Rikuzentakata districts, from north to south—were used. Each site is located as shown in Figure 1(b). While tsunami deposits and disaster debris were generally treated with processes consisting of crushing and separating under dry condition, some distinctive treatments were additionally conducted in Kamaishi, Ofunato, and Rikuzentakata districts for further improvement.

Table 3 summarizes distinctive points of treatment at each site. In Kamaishi and Ofunato districts, steel slag and crushed concrete, which were surplus by-products, were mixed up with generated recovered materials, respectively in anticipation of strength increase and further separation of soil fraction from debris. In Ofunato district and Rikuzentakata district, wet processing was used on some tsunami deposits and

Table 3. Summary of distinctive treatment at each site.

Site name	Distinctive points about treatment
Kamaishi	- Steel slag was mixed up with Recovered Soil Class A and Class B.
Ofunato	- Crushed concrete was mixed with Recovered Soil Class B. - After some of deposits and debris were treated by wet processing for desalting, sand and clay fractions were separately obtained by wet cyclones using difference in specific gravity. Then, lime was mixed for dehydration.
Rikuzentakata	- Recovered materials were mainly utilized in farmland. - Tsunami deposits on farmland were separately removed from affected areas. - After some of deposits and debris were treated by wet processing, particle size of generated materials were adjusted by mixing with clean soil.

Table 4. The type and number of samples analyzed in this study.

Site name	Recovered Soil Class A	Recovered Soil Class B	Separated Fine Fractions	Residue	Others	Subtotal
Kuji	20	5				25
Miyako	69	13	2	1		85
Yamada	15	8	3	1		27
Otsuchi	52	16		1		69
Kamaishi	16	34				50
Ofunato	2	36		8	15	61
Rikuzentakata	77				29	88
Subtotal	251	112	5	11	44	405

disaster debris to lower salinity. In Rikuzentakata district, the treatment system was designed to utilize the recovered materials in agricultural applications. The total number of materials analyzed in this study was 405 which can be categorized into five types indicated in Table 4. “Others” includes soils through wet processing in Ofunato and Rikuzentakata districts, sand and clay fractions through wet cyclones in Ofunato district, and tsunami deposit on farmlands in Rikuzentakata district.

RESULTS AND DISCUSSION

Particle Density

Regardless of types of recovered material, the mode value of particle density was around 2.7 g/cm^3 at Kuji, Miyako, Otsuchi, and Otsuchi districts where no additional processes were applied, as shown in Figure 3. The particle density of Recovered Soil Class B was relatively smaller than that of Recovered Soil Class A due to larger amount of wood fraction. The fact that the distribution peak shifted to right from north to south indicates that original seabed sediments had locally different characteristics. In Kamaishi district, while the particle density of the recovered soils without additional treatment ranged within 2.8 g/cm^3 as same as the four districts, the recovered soils improved by steel slag showed particle density over 2.90 g/cm^3 . This result is adequate considering that the steel slag with particle density of $3.3\text{--}3.6 \text{ g/cm}^3$ was added to recovered soils in a mass ratio of approximately 30%. In Ofunato district where sand and clay fractions were separately obtained through wet cyclones, sand fraction was larger than clay fraction, which ranged from 2.4 to 2.6 g/cm^3 .

Clay content

Clay content was evaluated as shown in Figure 4 to verify relationships with chemical properties. In the four districts where no additional processes were applied, recovered materials basically contained clay fraction of less than 20%, regardless of types of recovered material. In Kamaishi district, fine particles seem to be removed or scattered during treatment because clay content of all materials was less than 10%; however in fact, this result attributes to large particle density mentioned above. Since steel slag is mainly composed of sandy fraction having heavy particles, mass content of fine fractions became relatively smaller compared to other districts. Correspondingly in

Ofunato district, as coarse crushed concrete was added for improvement, clay content was relatively low below 10%. Clay materials which were separately obtained through wet cyclones in this district surely showed high clay content over 25% up to 52%. In Rikuzentakata district, clay content was relatively high because sand and clay fractions were intentionally mixed up for agricultural purpose.

Cone index

In Japan, limitation of available natural resources, as well as land spaces for landfills, has strongly promoted the reuse of surplus soil after classification into five levels of 1st- to 4th-class soils and muddy soil (Katsumi 2015). Cone index is specified as one of the parameters for the classification, and soils with cone index higher than 200 kN/m² has been actively utilized in geotechnical applications. Cone index of recovered materials showed large values ranging mostly within 12000 kN/m², as indicated in Figure 5. Such large cone index is due to inclusion of wood fractions which act as a reinforcing material. Thus, the cone index of Recovered Soil Class B containing a high proportion of wood fractions was larger than that of Recovered Soil Class A containing less amount of wood. In Kamaishi district, the minimum cone index increased to 1800 kN/m², which was comparatively higher than that in other districts, attributed to mixing of steel slag. Similarly, the recovered soils in Ofunato district showed relatively large cone indices due to inclusion of coarse crushed concrete though clay and sand fractions separately obtained through wet cyclones showed low values as “Others” indicated in the figure because these materials are poorly graded.

Regardless of material types, 395 of the 397 recovered materials showed cone indices higher than 200 kN/m² corresponding to the 4th-class soil, and 337 materials of

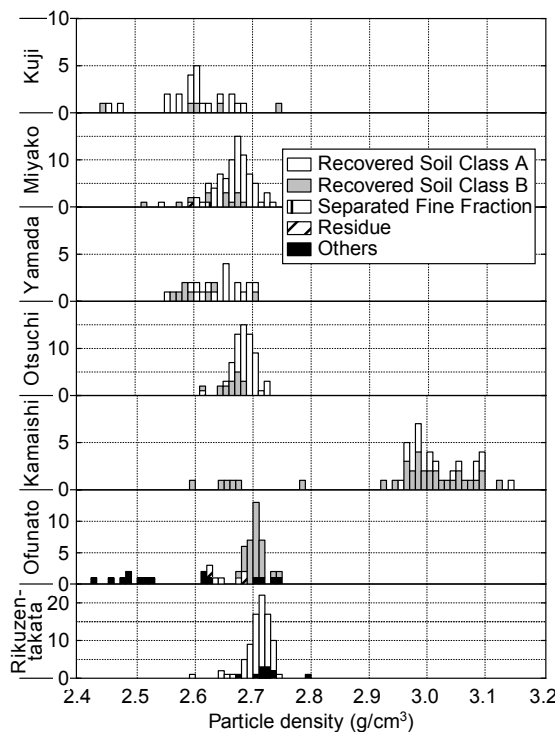


FIG. 3. Frequency distribution of particle density.

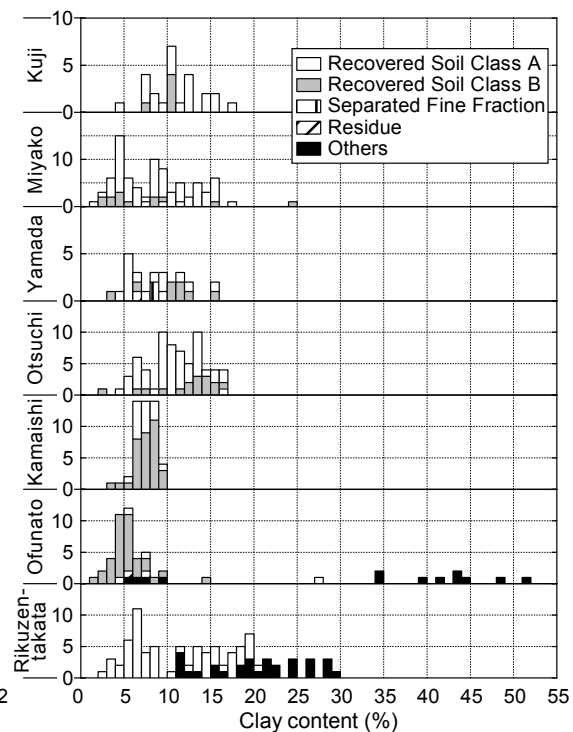


FIG. 4. Frequency distribution of clay content.

them, furthermore, showed that higher than 800 kN/m^2 corresponding to the 1st-class soil in the Japanese standard. The values of only 2 samples collected at Rikuzentakata district were below the 4th-class standard, but high strength was not required at this site because the recovered materials were generated for agricultural applications. These results clearly prove that recovered materials have sufficient strength as geomaterial except when being generated for agricultural purpose. However, it should be noted that the test standard for measurement of cone index can be applied on granular materials in principle. Thus, additional tests such as triaxial test and CBR test should be selected according to application for comprehension of strength characteristics.

Ignition loss

Figure 6 shows frequency distributions of ignition loss. In Japan, ignition loss refers to the mass loss in a sample heated to 750°C in the field of geotechnical engineering. In the four districts where no additional treatment was done, the ignition loss of Recovered Soil Class B was relatively higher than that of Recovered Soil Class A due to larger amount of wood fraction included, but most of materials showed the values lower than 10% regardless of types. In Kamaishi district where steel slag was used, the ignition loss was apparently small compared to other districts due to the large particle density of samples because the mass of incombustible matters includes the mass of steel slag. In Ofunato district the values were widely varied. Many materials showed the ignition loss higher than 10% due to cement hydrates by crushed concrete as well as organic matters. The ignition loss values of clay fraction separately obtained through wet cyclones were larger than 15%, since hydrated water generated by addition of lime for water content regulation greatly affected the values. These observations

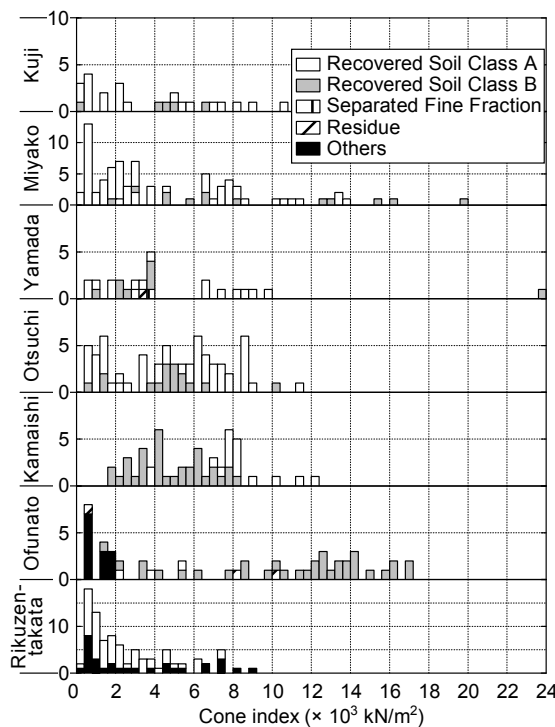


FIG. 5. Frequency distribution of cone index.

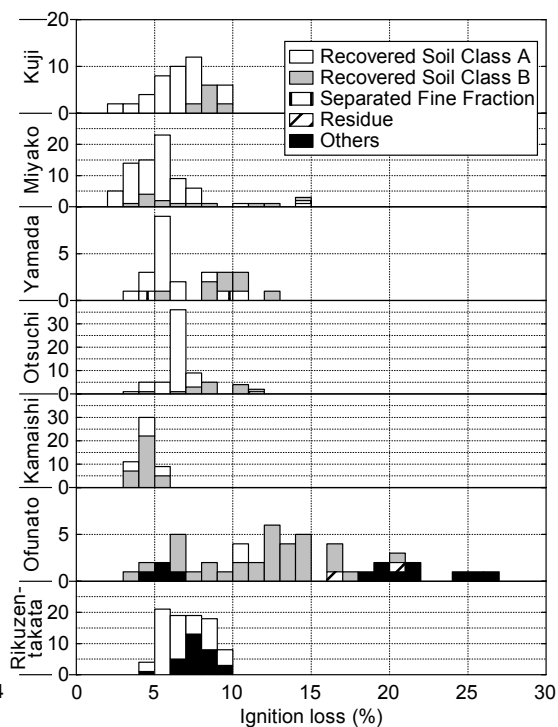


FIG. 6. Frequency distribution of ignition loss.

demonstrate that additive agents for significantly affects the ignition loss of recovered materials. Although ignition loss is often referred as an index of organic matter content that means purity of recovered materials in this case, a distinctive test method, e.g. heating at 330°C (Takai et al. 2014), has to be newly established for adequate measurement of organic matter remained in recovered materials.

pH

Figure 7 illustrates frequency distributions of pH. This result demonstrates that the pH of recovered materials mostly ranges below 9 in the four districts without additional treatment and in Rikuzentakata district. In Kamaishi district, calcium oxide mainly consisting in steel slag increased pH with a reaction with water to produce calcium hydroxide. In Ofunato district, the pH of recovered materials increased due to mixing of crushed concrete whose pH ranges between 12 and 13. These observations confirm that additive agents affect pH value. However, as indicated in the above-mentioned guideline published by Iwate Prefecture, recovered materials with relatively high pH should be also aggressively utilized in geotechnical applications because cement-based materials have been widely applied for ground improvement, and it is empirically well known that the pH of improved parts can be lowered to a value similar to the adjacent ground with time. When recovered materials are utilized in a public water area or a marine area where inflow of leachate from geomaterial must be concerned, some measures such as cover soil are required; however, utilization of recovered materials should not be judged based only on pH values. The lowest pH among all of materials was 6.4 in Kuji district. Considering the fact that pH of tsunami deposits left on farmland for 9 months after the earthquake was lower than 4.0 due to oxidation by sulfide ion derived from seawater (Takai et al. 2013), pH of recovered materials was neutralized during removal, transportation, storage, and treatment.

Salinity

Figure 8 shows frequency distributions of salinity. As seen from this figure, 35 of the 405 recovered materials exceeded 1.0 mg/g which is a criteria for utilization in the guideline published by Iwate Prefecture. Outside the range of this figure, Recovered Soil Class A showed 6.6 mg/g in Otsuchi district, 5.1 mg/g in Ofunato district, and 7.4 mg/g in Rikuzentakata district. By region, whereas the salinity of all materials was below 1.0 mg/g in Kamaishi district, 18.4% of materials in Miyako district exceeded the criteria. However, in Kamaishi district, salinity was underestimated owing to the large particle density as same as clay content and ignition loss. The fact that 23 of the totally 167 Recovered Soil Class A (= 13.8%) showed salinity higher than 1.0 mg/g indicates that saline matter remained in soil fraction even after treatment. Since electrical conductivity (EC) is an index representing electrolyte concentration of the solution, the tendency of EC was almost similar with that of salinity except Kamaishi district where dissolution of calcium and magnesium compounds consisting in steel slag significantly affected. Although salinity and EC of geomaterial are generally concerned for steel corrosion and plant growth, coastal region ought to have relatively high salinity even before the earthquake. Thus, even if there is a concern of steel corrosion, recovered materials should be aggressively utilized with the aid of existing corrosion-resistant materials and technologies.

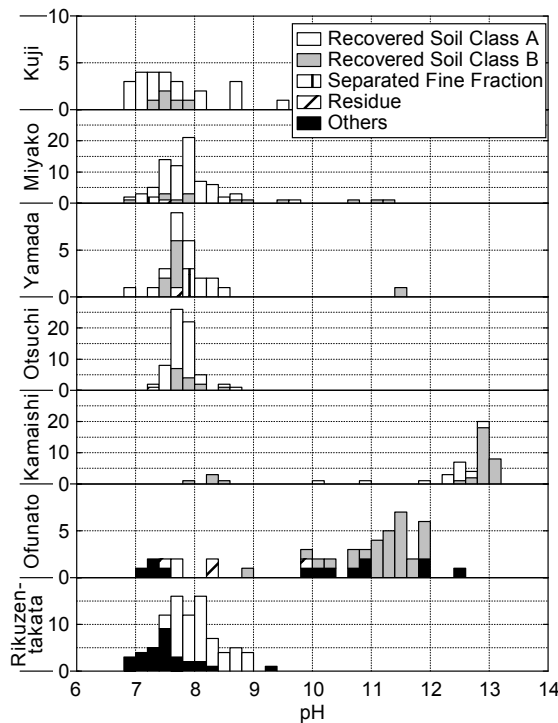


FIG. 7. Frequency distribution of pH.

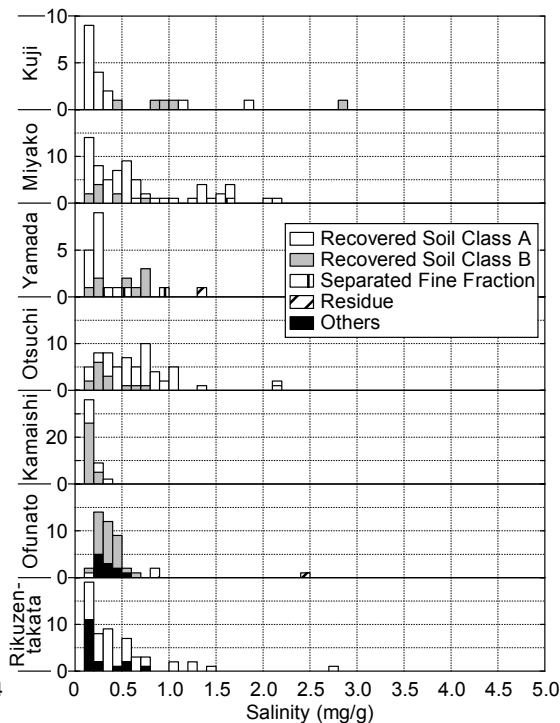


FIG. 8. Frequency distribution of salinity.

CONCLUSIONS

In this study, material properties of recovered materials generated by the 2011 East Japan earthquake was analyzed throughout the projects in Iwate Prefecture. Recovered materials basically have high quality similar to general geomaterial from the viewpoint of chemical and physical properties, being expected to be utilized in geotechnical applications. Additional processes affect material properties of recovered materials as summarized in Table 5. Mixing of steel slag leads to increases in particle density, cone index, pH, and EC, while leading to decreases in ignition loss, clay content, and salinity which are affected by large particle density. Mixing of crushed concrete increases cone index, ignition loss, and pH. Recovered materials for agricultural applications have relatively high clay content, high plastic index, and low cone index. Some results raised an experimental concern regarding applicability of existing test standards especially for ignition loss, particle size distribution, and the mass-related parameters.

Table 5. Summary of effects of additional processes on material properties.

Additional process	Effect on properties
Mixing of steel slag	Increase in particle density, cone index, pH, and EC Decrease in ignition loss, clay content, and salinity
Mixing of crushed concrete	Increase in cone index, ignition loss, and pH
Agricultural utilization	Increase in clay content and plastic index Decrease in cone index

As discussed and summarized above, additional processes using other solid agents lead to changes in material properties of recovered materials. Thus, it is important to determine which additional processes and materials should be selected in consideration of acceptable criteria and cost for each application.

ACKNOWLEDGMENTS

The authors acknowledge to Mr. Shin-ichi Iwashita (Oyo Corporation., Ltd.), Dr. Yoshikazu Otsuka (Okumura Corporation., Ltd.), Ms. Kaori Yamane (formerly Kyoto University), and the members of Department of Environment and Residential Life, Iwate Prefectural Government for their considerable support and contributions.

REFERENCES

- Inui, T., Yasutaka, T., Endo, K., and Katsumi, T. (2012). "Geo-environmental issues induced by the 2011 off the Pacific Coast of Tohoku Earthquake and tsunami." *Soils and Foundations*, Vol.52, Issue 5 (Special Issue on Geotechnical Aspects of the 2011 off the Pacific Coast of Tohoku Earthquake), 856-871.
- Iwate Prefecture (2013). "Guideline for Utilization of Treated Wastes for the Recovery Works (Revised version)." http://www.pref.iwate.jp/dbps_data/_material/_files/000/000/003/225/manual.pdf (accessed on August 1, 2015, in Japanese)
- Katsumi, T. (2015). "Soil excavation and reclamation in civil engineering: Environmental aspects." *Soil Science and Plant Nutrition*, Taylor & Francis, Vol.61, No.S1, 21-29.
- Katsumi, T., Endo, K., Imanishi, H., Inui, T., Kazama, M., Nakashima, M., Okawara, M., Otsuka, Y., Sakamoto, H., Sakanakura, H., Suzuki, H., Takai, A., and Yasutaka, T. (2014). "Environmental geotechnics for the recovery from 2011 East Japan earthquake and tsunami." *Proceedings of the 7th International Congress on Environmental Geotechnics*, A. Bouazza, S.T.S. Yuen, and B. Brown (eds.), Engineers Australia, 170-189.
- Ministry of Land, Infrastructure, and Transport (2012). "Basic Concepts on the Utilization of Recycled Materials in Constructing Fill Embankment to Accelerate the Revitalization from the Earthquake Disaster." <http://www.mlit.go.jp/common/00208618.pdf> (access on August 1, 2015, in Japanese).
- Takai, A., Endo, K., Yasutaka, T., Inui, T., and Katsumi, T. (2013). "Characterization of tsunami deposits toward utilization followed by the 2011 East Japan Earthquake and tsunami." *Proceedings of the Congrès GEsED (Gestion Environnementale des Sédiments de Dragage)*, O21. (on CD).
- Takai, A., Uddin, M.N., Inui, T., and Katsumi, T. (2014). "Mechanical properties of geomaterial recovered from disaster debris after the 2011 earthquake." *Proceedings of the 7th International Congress on Environmental Geotechnics*, A. Bouazza, S.T.S. Yuen, and B. Brown (eds.), Engineers Australia, 1602-1609.

Mechanical Characteristics of Incineration Bottom Ash from Disaster Waste Caused by the Great East Japan Earthquake

Kenichi Sato¹ and Takuro Fujikawa²

¹Professor, Fukuoka Univ., 8-19-1 Nanakuma Jonan, Fukuoka, Japan. E-mail: sato@fukuoka-u.ac.jp

²Assistant Professor, Fukuoka Univ., 8-19-1 Nanakuma Jonan, Fukuoka, Japan. E-mail: takuro-f@fukuoka-u.ac.jp

Abstract: The Great East Japan Earthquake resulted in extensive damage and left a vast amount of debris. The debris from the disaster has been incinerated to reduce the volume. This study focused on the predicted future demand of land soil, for example, to use in post-disaster reconstruction works. In order to examine the availability to recycle and utilize the incineration bottom ash from the disaster debris, the material properties of the incineration bottom ash was evaluated by soil experiments. Features of incineration bottom ash recycled material were compared with general incineration bottom ash from F City. A modified CBR test (JIS A 1211) was adapted to evaluate the availability of using the material as subgrade and roadbed material. A constant pressure direct shear test was employed to assess the shear properties. The results show that the incineration bottom ash recycled material has equivalent shear properties with regard to physical composition compared to general incineration bottom ash. The study reports that there is a possibility for incineration bottom ash recycled material to be effectively utilized as a roadbed material and used as a soil material with varied strengths.

1. INTRODUCTION

Processing of disaster debris generated in the Great East Japan Earthquake was completed in March 2014 with the exception of the Fukushima Prefecture. In the Miyagi Prefecture, about 1.37 million tons of flammable disaster debris has been incinerated in an intermediate processing facility to reduce the volume. However, it was difficult to cover the entire volume of incineration bottom ash generated by incineration processing for final disposal sites within prefectures. Therefore, in order to recycle and utilize the incineration bottom ash as a post disaster reconstruction material, chemical agents and water were added to improve the quality and develop a high quality recycled material. This is expected to become a major example of bottom ash utilization because there are not many cases of use of general waste incineration bottom ash as a construction material in Japan. This study evaluates the material properties of the incineration bottom ash from disaster debris processed in Sendai City by soil experiments (physical testing, modified CBR test, direct shear test). It also

reports studies on disaster debris management for the future and the possibility of utilizing the bottom ash from disaster debris and general bottom ash as a civil engineering material.

2. TEST OUTLINE

2-1 Incineration bottom ash

In this research, a sample of incineration bottom ash recycled material was taken from a temporary incineration facility of earthquake debris at Watari-cho in Sendai, Miyagi Prefecture (Figure.1) and adjusted to a particle size of 13mm or less. To compare with the targeted material, incineration bottom ash from general waste taken in May and July of 2012 from an incineration facility of F City was used (hereinafter referred to as incineration bottom ash A (BA-A), incineration bottom ash B (BA-B), respectively). Foreign components (remaining burnt wood, scrap metal, etc.) were removed by vibration sieve after stoker type incinerator emissions. Then, high quality incineration bottom ash recycled material (BA-RM) was developed and stored on site



FIG. 1. Temporary incineration facility of earthquake debris.

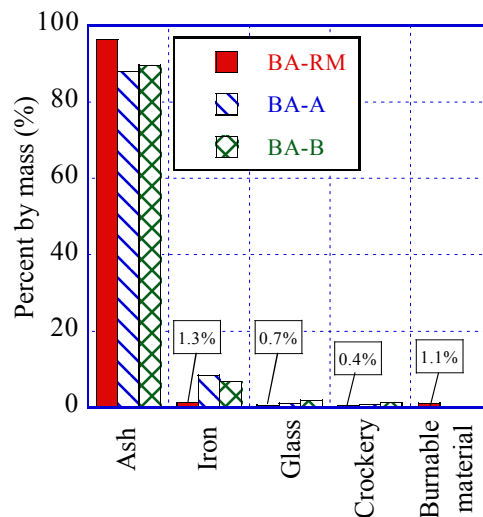


FIG. 2. Main physical composition of bottom ash

after 15% by wet weight ratio of magnesium solidifying agent was added for heavy metal stabilization processing. Figure 2 shows the physical composition of the bottom ash, Figure 3 shows the grain size distribution curve, and Table 1 shows the physical properties including the physical properties of decomposed granite soil as a common ground material. It was found that both of the incinerator bottom ashes include 90% or more of ash in total and 15% to 25% of fine fraction.

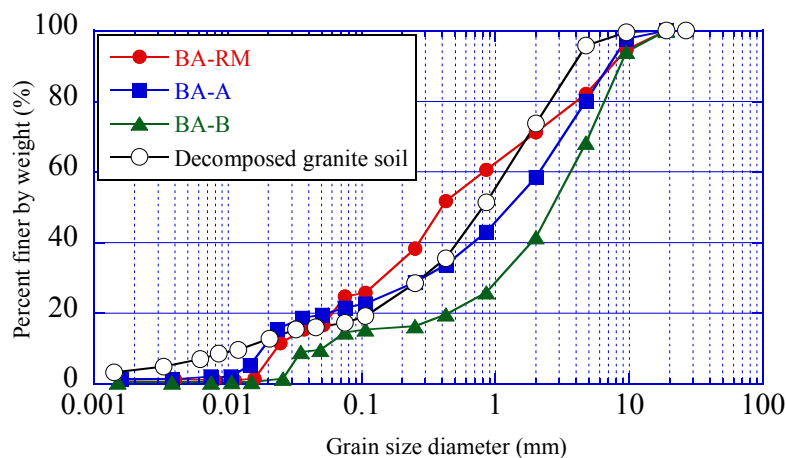


FIG. 3. Grain size distribution curve

Table 1. Physical property including the physical properties of decomposed granite soil as a common ground material

Sample	Discharged time	Soil particle density ρ_s (g/cm ³)	U_c	U_c'	Fine-grained fraction content F_c (%)	Maximum dry density ρ_{dmax} (g/cm ³)		Optimum water content w_{opt} (%)	
						A-b method	E-b method	A-b method	E-b method
BA-RM	Aug, 2013	2.433	117.9	2.1	24.7	1.274	1.405	30.0	22.6
BA-A	May, 2013	2.581	69.6	2.1	21.6	1.370	1.501	29.2	14.9
BA-B	Jun, 2012	2.588	105.7	11.1	14.6	1.460	1.493	22.0	18.0
Decomposed Granite soil	—	2.720	166.7	2.4	17.7	1.819	—	15.3	—

2-2 Test Overview

1) Evaluation as a subgrade and roadbed material

A modified CBR test (JIS A 1211) was carried out to examine the applicability as a subgrade and roadbed material of incineration bottom ash recycled material.

2) Assessment of Shear properties

A constant pressure direct shear test was carried out to examine the applicability as an embankment material and landfill embankment material of incineration ash bottom

recycled material. In addition, an examination was carried out focusing on the effects of the difference in the density of compaction on the shear properties by changing the density ($D_c = \rho_d / \rho_{dmax}$):80%, 90%, and 95%. Compared with the soil material, incineration bottom ash recycled materials contains various particle sizes of more than 2mm. We used a measurable medium-sized direct shear test with 20cm diameter and 7cm height specimens, and 50 kN and 30 kN maximum shear load and maximum vertical load respectively. Specimens were prepared from the experimental conditions shown in Table 2. In this experiment, the loading pressure was $\sigma_v = 50, 100, 150\text{kPa}$, and shear velocity was 0.3 mm / min.

Table 2. Experimental conditions

Sample	Rammer	Drop	Condition of sample	Degree of compaction $D_c(\%)$	Load pressure (kPa)
BA-RM	2.5 kg	300 mm	wetting (Optimum water content)	80, 90, 95	50, 100, 150

3. RESULTS AND DISCUSSIONS

3-1 Evaluation as a subgrade and roadbed material

Figure 4 shows the modified CBR test results and Table 3 shows the modified CBR value. Compared to the required value from the Road Association, incineration bottom ash recycled material fully satisfied the required value and showed that it can be applied as an upper and lower roadbed material. This indicates that the incineration bottom ash recycled material is available for reconstruction work in disaster areas. In addition, it shows that the modified CBR value of incineration bottom ash from disaster debris is almost equivalent to the incineration bottom ash of general waste of F City.

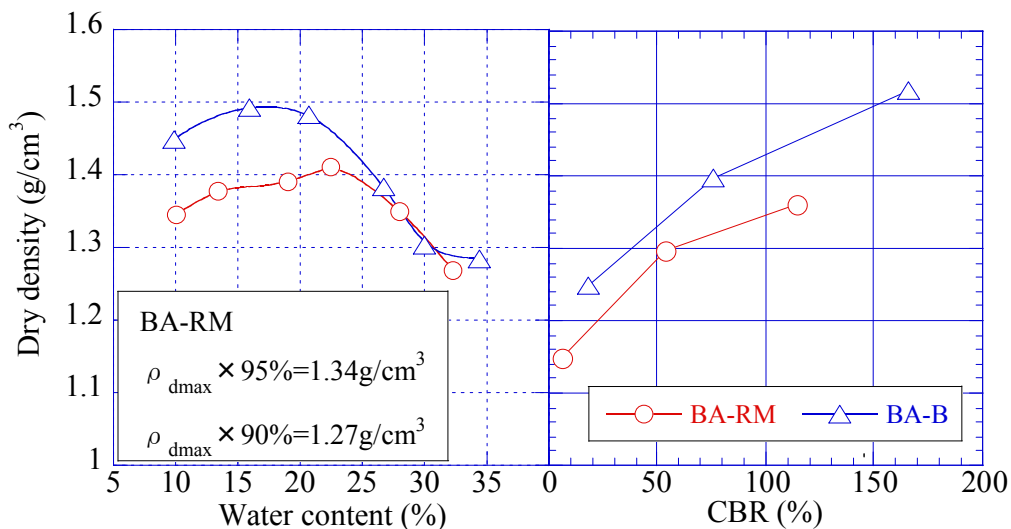


FIG. 4. Modified CBR test results

Table 3. Modified CBR value

	Modified CBR (%)	
	D _c =90%	D _c =95%
BA-RM	43	86
BA-A	44	75
BA-B	56	85
Requirement value (Japan Road Association)	Base course	More than 80
	Sabbase course	Less than 80

3-2-1 Shear characteristics

Figure 5 shows the direct shear test results for the three different compaction densities (D_c = 80, 90, 95%). For the shear behavior of incinerator bottom ash recycled materials, with increasing specimen density, the shear stress caused by shearing tends to increase. Also, when D_c = 90, 95%, it reached the residual strength after the shear stress reaches the peak intensity. The incineration bottom ash shows a tendency to expand with compaction. Figure 6 shows the relationship between the compaction density and strength constant of incineration ash bottom recycled material obtained from the direct shear test. It is found that, when compaction density increases, strength parameters tend to increase. Also, it shows that the shear resistance angle is around 50 degrees which is considered large even compared to the ground material. Thus, it is suggested that incineration bottom ash recycled material is expected to have reasonable frictional strength and is sufficiently good to be used as an alternative material to soil.

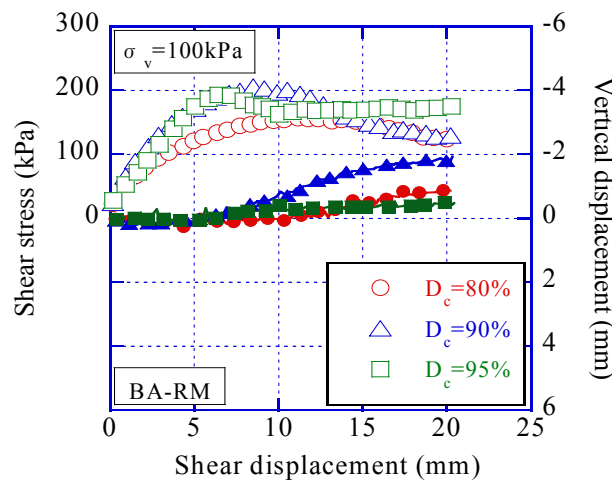


FIG. 5. Direct shear test results from three types of different compaction densities

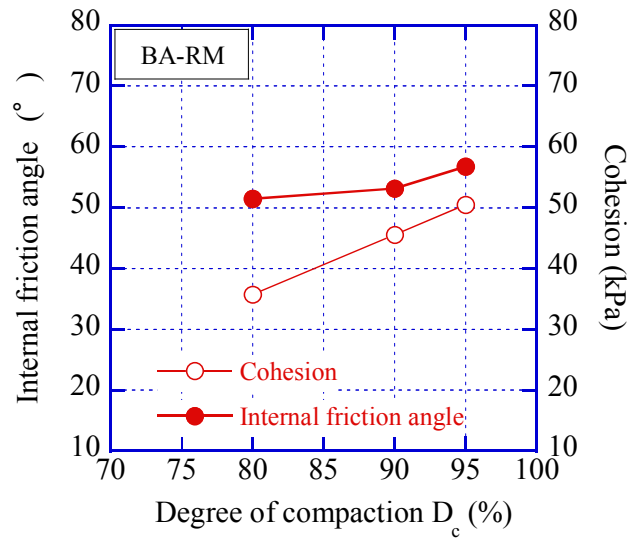


FIG. 6. Relationship between the compaction density and strength constant of incineration ash bottom recycled material obtained from direct shear test.

3-2-2 Comparison with the incineration bottom ash from municipal solid waste

Figure 7 represents the direct shear test results of compaction density $D_c = 90\%$ of incineration bottom ash recycled materials and incineration bottom ash A for the vertical stresses $\sigma_v = 50, 100, 150\text{kPa}$ to (a) (b). It is understood that the clear peak intensity is no longer seen in the shear behavior with the increase of normal stress in any of the bottom incineration ash tests. In addition, the vertical displacement amount decreases with increasing normal stress. The reason may be the compressibility and friability of ash appearing in the experimental results.

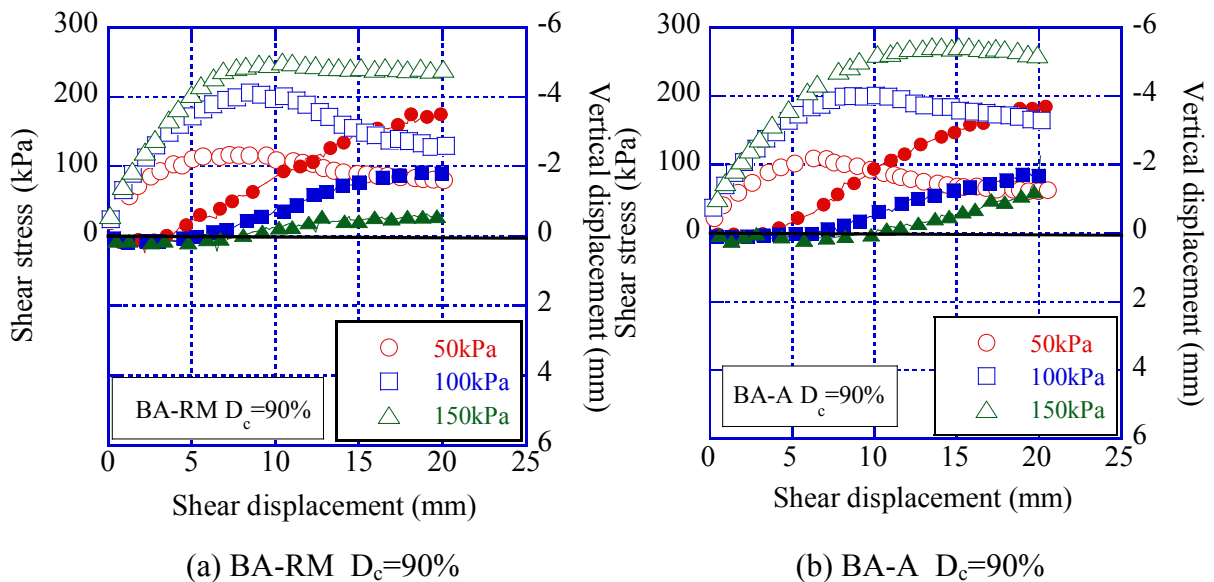


FIG. 7. Direct shear test result of compaction density $D_c = 90\%$

Figure 8 shows the relationship between the maximum shear stress and the normal stress σ_v of the decomposed granite soil as a comparative material and for each of the bottom ash materials at $D_c = 90\%$. Internal friction angle for either of the incinerator bottom ash materials is more than 50° and shows a higher strength constant than that of the decomposed granite soil. In addition, the shear characteristics of bottom ash from incineration of disaster debris and general waste are shown to be almost the same. Therefore, the ash generated in the processing of disaster debris is sufficiently available for the reconstruction of the earthquake areas as a ground material.

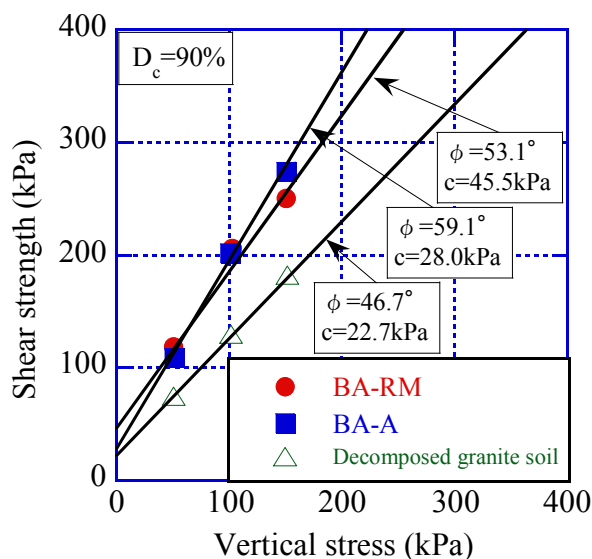


FIG. 8. Relationship between the maximum shear stress and the normal stress

4. CONCLUSIONS

- 1) There is a potential for incineration bottom ash recycled material to be effectively used as a roadbed material, rather than as an underlying roadbed material, without issues associated with collection time.
- 2) Incineration bottom ash recycled material is proposed as a soil material for various required strengths. It has equivalent shear properties to incineration bottom ash from municipal solid waste with similar physical composition. Incinerated bottom ash is known to have a self-hardening feature that solidifies the material over time due to mixing with coal at the time of incineration. A further study of the self-hardening features is also suggested.

ACKNOWLEDGMENTS

The authors appreciate the support of Environmental Research Fund of the Ministry of the Environment (3K133003) for this study.

REFERENCES

- Hirofumi Sakanakura, Kazuki Ozawa, Toshihiko Miura, Toru Inui, Hiroyuki Sakamoto, Takeshi Sato, Masaki Nkano, Hiroyuki Yoshino (2013) . "Proposal of physical property evaluation scheme intended for utilization of ground material by incineration bottom ash recycled materials from disaster debris as a raw material." *10th Environmental Geotechnical Engineering Symposium Proceedings*, pp.419-426.
- Japanese Geotechnical Society (2000). "The method of soil test and commentary. (2012)." *Japanese Geotechnical Society*, p.280.
- Shota Kumamoto, Kenichi Sato, Takuro Fujikawa, Chikashi Koga (2012). "Study of applicability of the crushing processed incineration ash as a ground material. " *the Japan Society of Civil Engineers western branch*, pp.529-530.
- Syogo Miyata, Kenichi Sato, Takuro Fujikawa, Chikashi Koga (20113). "Examination of effective use of general waste incineration ash,as a ground material. " *10th Environmental Geotechnical Engineering Symposium Proceedings*, pp191-194.

Radiation-Shielding Properties of Heavy Bentonite-Based Slurry for the Decommissioning of the Fukushima First Nuclear Power Plant

Ema Yoshikawa¹; Hideo Komine¹; Yuma Saito¹;
Shigeru Goto¹; Seiichi Narushima²; Yasunori Arai²;
Masayuki Mizuno³; Shinsuke Ujiie³; Yuki Sakoda³; Yasushi Nagae⁴;
Mitsugu Yoshimura⁵; and Akihiko Suzuki⁵

¹Dept. of Civil and Environmental Engineering, School of Creative Science and Engineering, Waseda Univ., Japan.

²Seibu Construction Co., Ltd.; ³Hojun Co., Ltd.; ⁴TELNITE Co., Ltd.;

⁵Soil and Rock Engineering Co., Ltd.

Abstract: The 2011 off the Pacific coast of Tohoku earthquake has impacted Japan, and it made serious damage to nuclear power plant in Fukushima. At present, Japanese government and engineers proceed decommissioning of the power plant, and ensuring safety of workers is the most important matter especially in fuel debris retrieval. On these backgrounds, the authors focus on heavy bentonite based slurry for filling material of nuclear reactor. Heavy slurry is capable of shielding gamma ray and neutron beam from its high specific gravity and water content. The purpose of this research is to investigate and define the properties of heavy bentonite based slurry by soil mechanics experiment. That is, the research described in this paper is a proposal to use it for decommissioning of the Fukushima I nuclear power plant. For quantifying the radiation shielding properties, the authors measured the transmitted radiation dose through heavy slurry. The result shows the heavy slurry has definite radiation shielding properties. In conclusion, the heavy bentonite based slurry may be useful for radiation shielding, and save workers health in particular.

1. INTRODUCTION

Whole of Japan was impacted by the 2011 off the Pacific coast of Tohoku earthquake. There has been severe situation because of the radioactive contamination around and inside of the nuclear reactors in Fukushima I nuclear power plant. Moreover, there must be some people who struggle to cope with difficult problems on the surrounding spot. Under such circumstance, radiation shielding material is necessary from the point of view of reducing the possibility of exposure to the workers in fuel debris retrieval and construction of soil covered facility of radioactive waste. Since the accident occurred, Nuclear Emergency Response Headquarters had decided the medium- and long-term roadmap for decommissioning of Units 1 to 4. FIG.1 shows one of the methods to protect workers from radiation in fuel debris retrieval proposed in the roadmap. It makes a suggestion that filling a reactor vessel with water to cooling a reactor and radiation shielding. However, the radiation shielding by water is not fully effective.

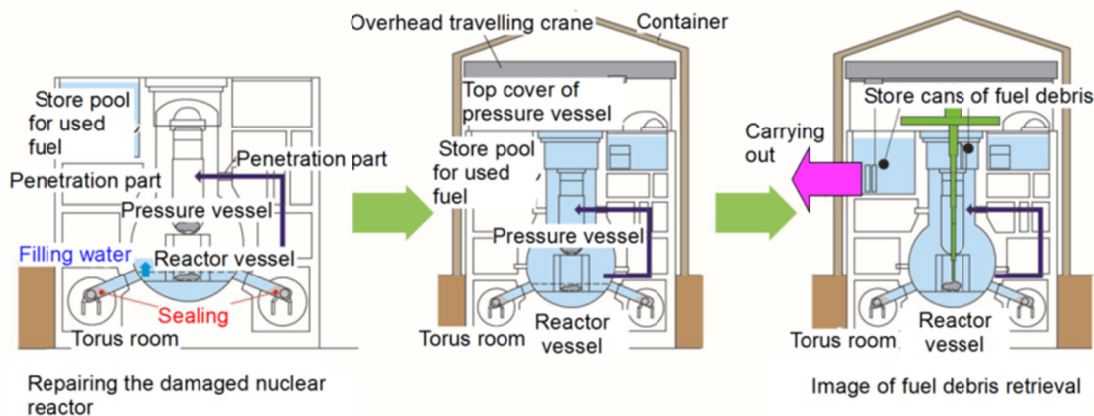


FIG.1. Method of fuel debris retrieval that filling the nuclear reactor with water according to medium- and long-term roadmap

Water can shield only neutron beam as almost same mass as hydrogen atom. Consequently, the authors focus on heavy bentonite based slurry for filling material of nuclear reactor, because of its exceptional shielding properties. It was confirmed that the high specific gravity material shows excellent characteristic of radioactive reduction related to gamma ray. In addition, if the high specific gravity material has high water content, shielding effect of neutron beam increases. As a familiar fact, gamma ray and neutron beam have prominent penetration of substance in comparison with alpha and beta rays. Note that such radiation shielding concerned with gamma ray and neutron beam is indispensable to the construction of decommissioning. Accordingly, based on the previous research (Komine, 2015), the heavy slurry can be used for radiation shielding.

2. PRODUCT HEAVY SLURRY

2.1 Materials of heavy bentonite based slurry

Heavy slurry is composed of water, sodium pyrophosphate, barite and sodium-type bentonite. Barite is a mineral composed mainly of barium sulfate and the high specific gravity that is the greatest feature of heavy slurry is due to barite. Particle density of barite is about 4.21. Sodium pyrophosphate is dispersing agent and bentonite is added to heavy slurry for preventing precipitation of particles. Table 1 and 2 show fundamental parameter of bentonite and mixing ratio of heavy bentonite based slurry.

Table 1. Fundamental parameter of bentonite (Super clay)

Soil particle density (Mg/m^3)	2.62
Liquid limit (%)	547.0
Plastic limit (%)	47.39
Plasticity index	499.61

Table 2. Mixing ratio of heavy bentonite based slurry

Case	Water (g)	Sodium pyrophosphate (g)	Barite (g)	Bentonite (Super clay) (g)	Specific gravity
A	100	0.2	400	7	2.5
B	100	0.2	140	10	1.8
C	100	0.2	10	12	1.1

2.2 Method of producing heavy bentonite based slurry

The method of manufacturing the heavy bentonite slurry is presented as below. An electric stirrer is used to production of heavy slurry. FIG.2 shows a method of producing heavy bentonite based slurry and FIG.3 is a picture of heavy bentonite based slurry .

- 1) Required amount of water in stirring vessel is stirred 2 minutes on about 400rpm after added sodium pyrophosphate.
- 2) The slurry is stirred 2 minutes on 400rpm after added bentonite.
- 3) The slurry is stirred 2 minutes on 400rpm after added barite.

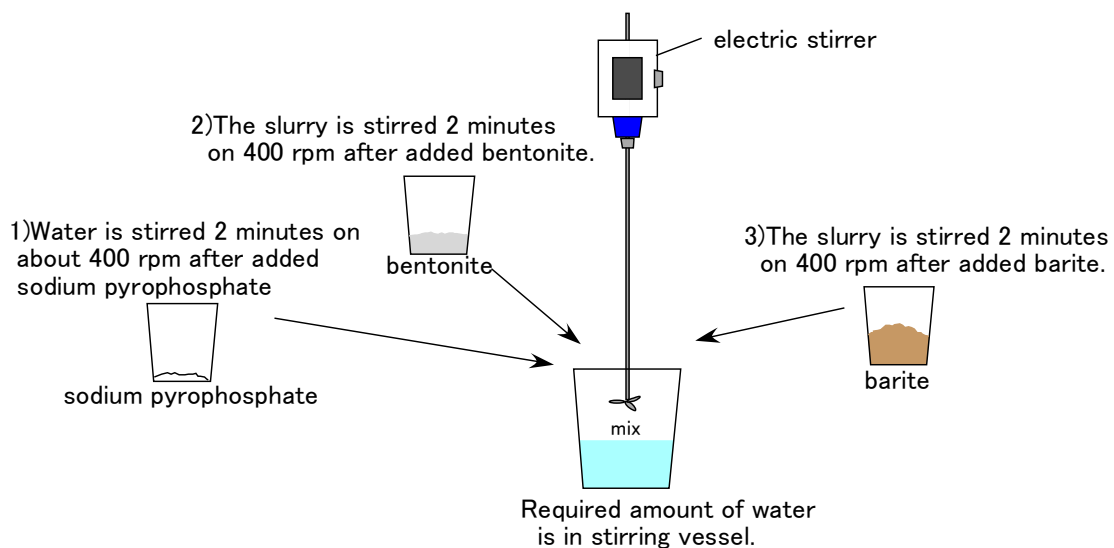
**FIG.2. Method of producing heavy bentonite based slurry**



FIG.3. Picture of heavy bentonite based slurry

3. RADIATION SHIELDING PROPERTIES TEST

3.1 Method of experiment

Measurement method of transmitted radiation dose is presented the below. Gamma ray source and neutron beam source are used in the test. Main theme of the test is to confirm a relation between specific gravity of heavy slurry and effect of radiation shielding. FIG.4 and 5 show the setup of the experiment of gamma ray test and neutron beam test.

- 1) After preparing the heavy bentonite based slurry, acrylic containers filled up with heavy slurry. (Inside dimensions of acrylic container is 300mm x 300mm x 100mm.)
- 2) A source of gamma ray or neutron beam is put on the side of acrylic container, and survey meter is put on the contrast side. The distance between radiation source and detector is fixed to 150 mm both of gamma ray and neutron beam test.
- 3) When measured value becomes steady, record the transmitted radiation dose.
- 4) When a case of test has been completed, the test passes next case.

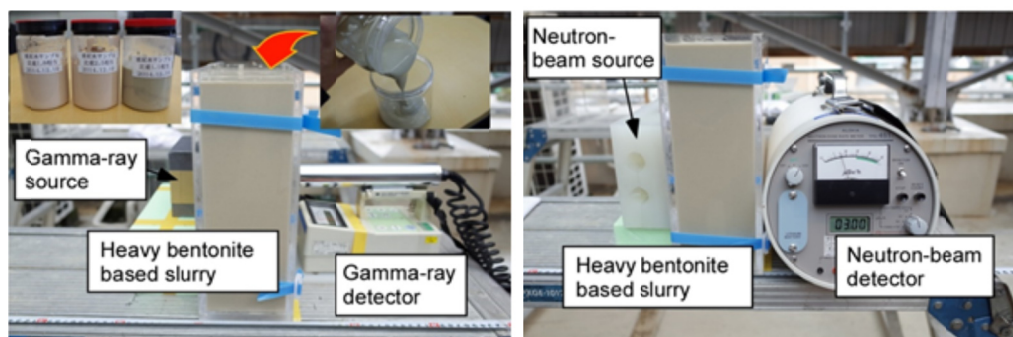


FIG. 4. Picture of setup of radiation shielding properties test (left: gamma ray test, right: neutron beam test)

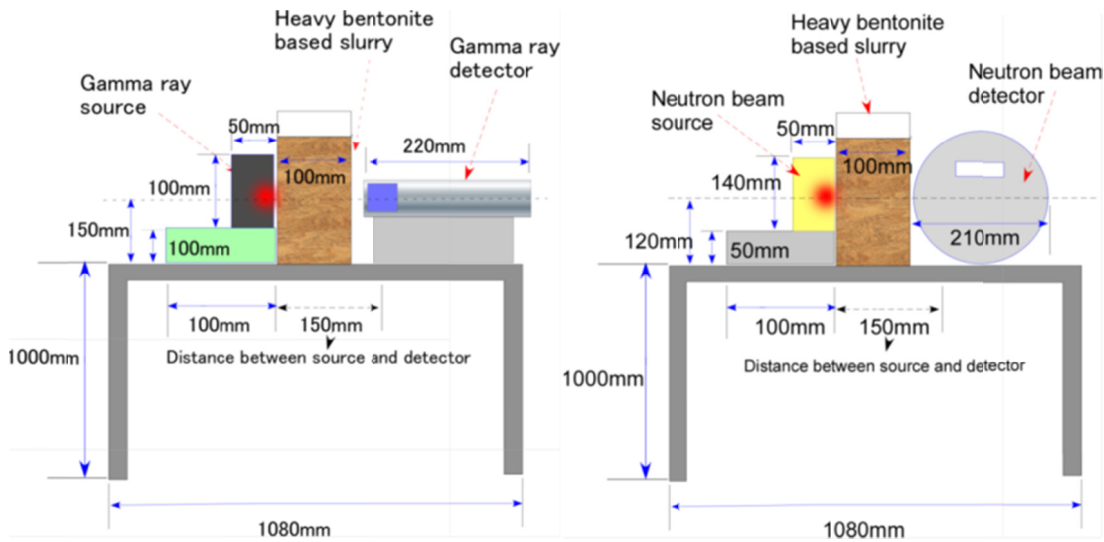


FIG.5. Image of setup of radiation shielding properties test (left: gamma ray test, right: neutron beam test)

3.2 Test Result and discussion

FIG.6 shows the relation between the gamma ray dose and the specific gravity of heavy slurry in case of heavy slurry thickness is 100mm fixed.

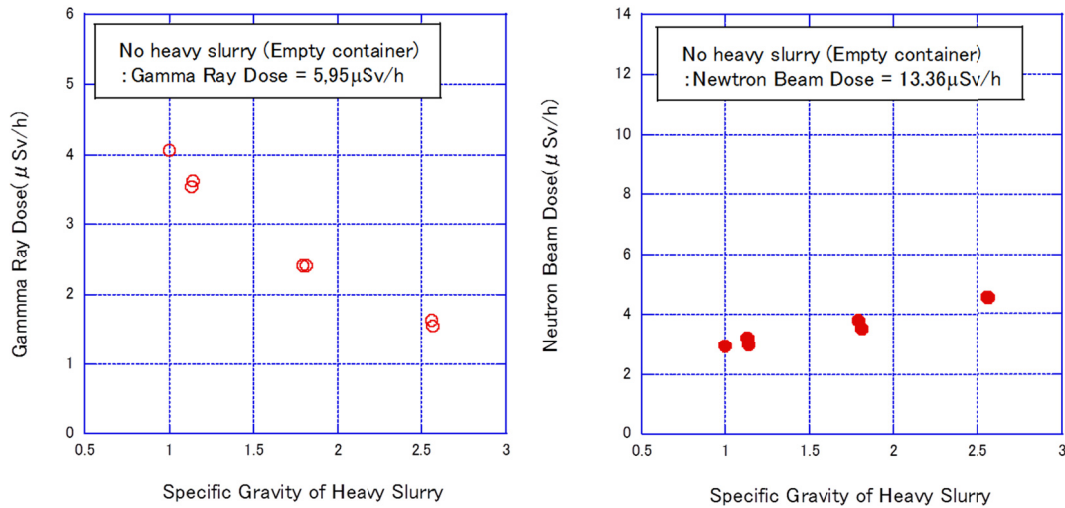


FIG.6. Relation between the gamma ray dose (left graph) or the neutron beam dose (right graph) and the specific gravity of heavy slurry

Following the study, it is clarified that gamma ray shielding is due to specific gravity of the heavy slurry. Gamma ray dose decreases with increasing of specific gravity. On the other hand, neutron beam dose increases with increasing of specific gravity because neutron beam dose is caused by water content. That is penetrated material has high neutron beam shielding property when it has low specific gravity. The test result shows specific gravity of heavy slurry has opposite effect between gamma ray and neutron beam shielding. Based on the study, the authors will pursue the most suitable mixing ratio of heavy slurry with the perspective of the shielding properties of gamma ray and neutron beam.

4. CONCLUSIONS

In this paper, author describes fundamental data to confirm the radiation shielding properties of bentonite based heavy slurry. The following conclusions were drawn from this study.

- 1) Gamma ray shielding is due to high specific gravity of the heavy slurry.
- 2) Neutron beam dose is caused by water content and it means material has high neutron beam shielding property when it has low specific gravity.
- 3) The specific gravity of heavy slurry must be considered from a point of view of difference shielding effect between gamma ray and neutron beam. On the actual construction, a balance of each radiation shielding is a matter of great importance.

5. REFERENCES

- Komine, H., (2015). "Radiation shielding experiments of geo-material for recovery from the Fukushima I nuclear power plant accident", *Geo-Environmental Engineering 2015* (to be published).
- Suzuki, A., (2014). "The absorption/capture of the neutron ray to emit from Californium 252", *50th JGS Symposium (in Japanese)* (to be published).
- Ujie, S., (2014). "The development of high-radiation-shielding and flexible materials", *11th JGS Symposium on Environmental Geotechnics (in Japanese)* :471-478.
- Saito, Y., (2014). "Radiation shielding properties of heavy slurry which assumed fuel debris retrieval", *11th JGS Symposium on Environmental Geotechnics (in Japanese)*: 483-488.
- Nuclear Emergency Response Headquarters ., (2015) "Mid-to-Long Term Roadmap (RM) on decommissioning of Fukushima Daiichi Nuclear Power Station"

Uplift Resistance of Buried Pipelines in Dry and Unsaturated Sands: Comparison of Analytical and FE Model Results with Large-Scale Test Data

Dilan J. Robert¹; N. I. Thusyanthan²; and C. Q. Li³

¹Lecturer, School of Engineering, RMIT Univ., Melbourne, VIC 3001, Australia. E-mail: dilan.robert@rmit.edu.au

²Principal, Geotechnical Engineer, Consulting Services Dept., Saudi Aramco, Dhahran 31311, Saudi Arabia. E-mail: it206@cantab.net

³Professor, School of Engineering, RMIT Univ., Melbourne, VIC 3001, Australia. E-mail: chunqing.li@rmit.edu.au

Abstract: Pipelines are commonly buried underground to provide environmental stability, temperature insulation and mechanical protection. These pipelines are frequently subjected to earthquake induced upward displacements, which can cause significant social-economic loss to consumers and utility management. Further, high thermal and pressure of the conveying medium can induce differential stresses on the axial restrained pipe to result upward buckling of the pipeline that can disturb the serviceability conditions. The uplift resistance from soil cover protects the pipe against such unwanted movements, representing it as a vital design parameter, in that pipeline integrity under operating conditions relies on its value. The paper presents full-scale uplift results and finite-element parametric studies conducted to investigate the effects of dimensionless cover heights (soil cover height to diameter ratio), soil relative density and moisture content on the peak uplift resistance of pipes. The results showed that the available analytical models could predict realistic peak uplift resistance for pipes buried at shallower depths, however, they can substantially under-predict the pipe loads/uplift resistance especially when buried at deeper embedded depths and non-dry soil conditions. The results of the current study are useful for pipe designs against earthquakes and/or severe operating conditions induced uplift displacements in sandy soils.

Keywords: Pipelines, Earthquakes, Upward buckling, Uplift resistance, Non-dry soil, Analytical models.

INTRODUCTION

Pipelines are commonly buried underground to provide environmental stability, temperature insulation and mechanical protection. These pipelines are frequently subjected to earthquake induced upward displacements, which can cause significant social-economic loss to consumers and utility management. Further, high thermal and pressure of the conveying medium can induce differential stresses on the axial restrained pipe to result upward buckling of the pipeline that can disturb the

serviceability conditions. The uplift resistance from soil cover protects the pipe against such unwanted movements, representing it as a vital design parameter, in that pipeline integrity under operating conditions relies on its value.

Design of a buried pipeline requires a minimum depth of soil cover to provide the sufficient uplift resistance against upward displacements. Due to the severe operating conditions of oil and gas transport lines, the depth of soil cover needs to be calculated on the basis of pipeline operating conditions and soil mobilization resistance. Further, burial depth requirement stands a significant portion of the total construction cost of the pipeline. Therefore, the proposal of soil cover height in high pressure and high temperature (HPHT) pipelines requires a compromising decision which provides sufficient soil cover height while minimizing the unwanted construction costs making the design economically viable. Thus, an accurate estimation of peak uplift resistance from soil cover is vital in the design phase of HTHP pipelines. The paper presents full-scale uplift results and finite-element parametric studies conducted to investigate the effects of dimensionless cover heights (soil cover height to diameter ratio), soil relative density and moisture content on the peak uplift resistance of pipes subjected to vertical displacement in coarse-grained soils. Full scale experimental results were compared with the FE results for validation. The results from the current study are compared to ASCE design guidelines as well as available analytical models which predict the uplift resistance of soil.

LITERATURE REVIEW

Substantial analytical and numerical works have been conducted by previous researchers to investigate the uplift resistance and failure mechanisms of soil during upward displacement of pipes (Trautmann et al, 1985; Ng and Springman 1994; Bransby et al, 2001; White et al, 2001; Vanden Berghe et al, 2005; Chin et al, 2006; Schupp et al, 2006; Cheuk et al, 2008). Previous observations from model tests suggest that the uplift mechanism (i.e. inclination of the shear zone) depends on the initial state of the sands. A localized shear with a flow-around mechanism was observed in model tests conducted by Bransby et al. (2001) for very loose sands (Fig. 1c). A similar mechanism was also observed by White et al. (2001) for initially dense sand after the peak resistance is achieved. Such mechanism has also been numerically predicted by Vanden Berghe et al. (2005) for very loose sand. For medium to dense soil, inclined slip surface model (Fig. 1b) was experimentally proven to be a closer approximation for the real deformation mechanisms (Thusyanthan et al, 2010). Cheuk et al. (2008) showed that the average inclination of the shear zones is influenced by the soil density, with denser soil being more dilatant.

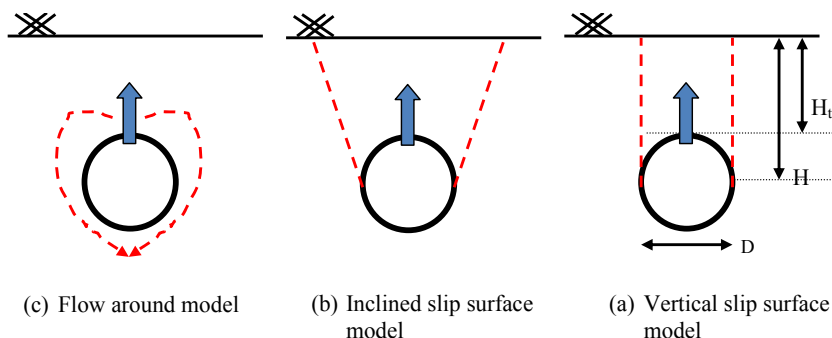


Fig. 1. Different uplift mechanisms of buried pipes in granular soils

Several prediction models have been reported in literature to assess the peak uplift resistance of pipes buried in granular soils. Schaminée et al. (1990) have proposed a limit equilibrium solution (known as vertical slip model; Fig. 1c) to estimate the uplift resistance (Eq. 1) due to shear resistance along the vertical slip surface and weight of the soil block. Vermeer and Sutjiadi (1985) described a solution (Eq. 2) with straight shear bands extending to the soil surface considering the normality condition [i.e. friction angle (ϕ) = Dilation angle (ψ)]. Ng and Springman (1994) also proposed a solution similar to vertical slip model for the case of earth pressure coefficient, $K=1$ (Eq. 3). White et al. (2001) proposed an alternative limit equilibrium solution (Eq. 4) which considers Bolton's flow rule (Bolton, 1986) to infer the angles of friction and dilation linked to relative density (γ' - effective unit weight of backfill soil) and stress levels.

$$P = \gamma' HD + \gamma' H^2 K \tan \phi \quad \text{Eq. 1}$$

$$P = \gamma' HD + \gamma' H^2 K \tan \phi_{\max} \cos \phi_{\text{crit}} \quad \text{Eq. 2}$$

$$P = \gamma' HD + \gamma' H^2 \tan \phi_{\max} \quad \text{Eq. 3}$$

$$P = \gamma' HD + \gamma' H^2 \tan \psi + \gamma' H^2 (\tan \phi_{\max} - \tan \psi) [(1 + K_o) - (1 - K_o) \cos 2\psi / 2] \quad \text{Eq. 4}$$

Cheuk et al. (2008) argued that vertical slip model does not capture the deformation at the peak resistance, while the solution based on inclined planes with normality (Eq.2) overestimates the dilation (thus width of soil block lifted). The limit equilibrium solutions which capture the realistic shear band inclination via flow rules (such as in Eq. 4) have been reported to predict accurate uplift resistance.

OVERVIEW OF THE FULL SCALE EXPERIMENTS

Full scale experiments were carried out using a steel pipeline of 3m in length and 200mm in diameter. A full scale test tank of 2250mm width, 2500mm height and 5000mm length was used in the experiment. The backfill cover was loose fine sand (similar to Fraction E sand) with bulk unit weight of 15kN/m^3 (relative density ~ 35%, Thusyanthan et al, 2010). Firstly, the pipeline, which was attached with load

cells (capacity 20 tons) and vertical side bars with a tape measure, was lowered down to the full scale test tank using an overhead crane. Then, it was covered with layers of soil (each ~30cm in thickness) with uniform compaction of each layer using Rammers. Having finished the test box preparation, the pipe was raised using manual pulleys at the two ends of the pipe at uniform rate of ~10mm/min. The readings of the load cell were recorded by a digital camera, and the displacement readings were measured by survey teams using the tape measure on the vertical side bars. A series of uplift experiments were carried out at various cover heights. In this paper, results of only H_t/D ratios of 6 and 8 are presented for comparison with FE modeling. These tests were conducted at in-situ moisture content (approximately 5% moisture).

FE MODELING OF UPLIFT PIPE DISPLACEMENT

Overview

FE modelling of uplift pipe displacement was undertaken in ABAQUS with geometric non-linearity and large strain formulation. This ensures that the large strains induced in the elements around the pipe during uplift of the pipe are modeled correctly. The non-linear geometry option (NLGEOM) in ABAQUS considers the changes in geometry during the analysis, and thus the equilibrium is achieved using the current configuration (i.e. current nodal position) of the model. All the analyses were performed under plane strain conditions and the model uses soil and pipe elements with 8-noded biquadratic, plane strain, reduced integration (CPE8R) elements (ABAQUS, 2007). Figure 2 shows the geometry and the mesh discretisation of the FE model used to simulate the vertically loaded pipeline experiments. The wall boundaries were assumed to be smooth and supported only in the normal direction. The pipe was pulled vertically by imposing equal uplift displacement on all pipe nodes and was set to move freely in the lateral direction. Adaptive meshing has been incorporated in the analyses to control the mesh distortions that result from large deformations of the soil caused by upward pipe displacements. The behaviour of the pipe is assumed to be linear elastic, whereas non-linear elasticity is assumed for the behaviour of soil surrounding the pipe.

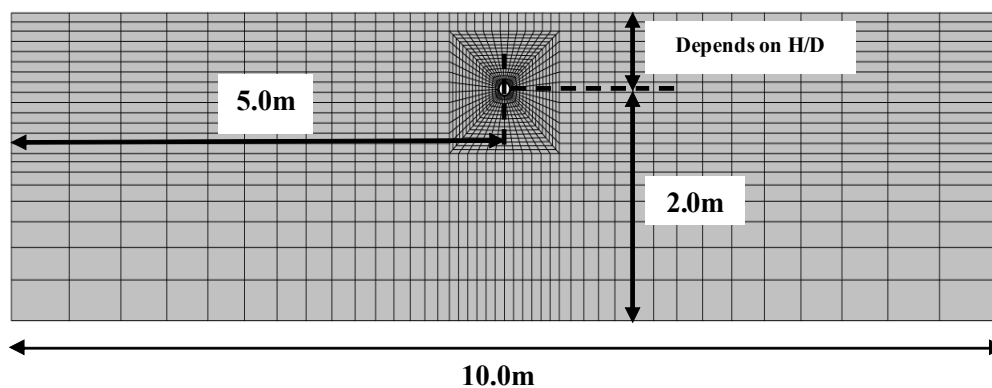


Fig. 2. Geometry and mesh discretisation of the model used for the FE analyses

The interaction between the pipe and soil has been modeled on the basis of Coulomb friction model which relates the maximum allowable frictional shear stress (τ_{crit}) across the interface to the contact pressure (σ_n') between the pipe and soil. The allowable frictional stress is given by $\mu\sigma_n'$ where $\mu(\tan\phi_\mu)$ is the interface friction coefficient. The contacting surfaces will stick together and the behaviour remains elastic when $\tau < \tau_{crit}$. The slipping along the interface between the buried pipe and surrounding soil takes place once τ produced in the interface reaches τ_{crit} . This behaviour was modelled using the finite movement solution available in ABAQUS (ABAQUS, 2007). In the current study, ϕ_μ was set to equal to half of the peak frictional angle of soil (Cheong, 2006 & Yimsiri et al, 2004).

Constitutive Models

Pipe model

The pipe was assumed to have a Young's modulus of 204 GPa with a Poisson's ratio, of 0.3, for all the analyses conducted in this paper. Nevertheless, since the pipe was displaced as a rigid body, the pipe stiffness is essentially infinity, and thus, the soil stresses imposed on the pipe and the pipe deformations are negligible (Cheong, 2006).

Soil model

Soil behavior was modeled using Nor-Sand model. Nor-Sand model is a generalised Cambridge-Type constitutive model for sand, developed on the basis of the critical state theory. It uses the state parameter concept (Been & Jefferies, 1985) and attempts to accurately reproduce dilation and softening on the dry side of the critical state. This is achieved by postulating infinite isotropic normal consolidation loci (NCL), which allows a separation of the intrinsic state from the over-consolidation state. A main feature of Nor-Sand model is the use of rate-based hardening using the state parameter to size the yield surface. The original Nor-Sand model was proposed by Jefferies (1993) and was implemented into STANDARD finite elements by Dasari and Soga (2000). In order to enhance the model performance, three modifications were made by Cheong (2006). They include (i) a new definition for the critical state, (ii) lode angle dependency on the critical state parameter and (iii) the evolution of yield surface with respect to plastic shear strain. Nor-Sand code was implemented into explicit finite elements in order to be benefited by explicit simulations (Robert, 2010).

The calibration of the Nor-Sand model was performed on the basis of sand type (i.e. Chiba sand) having similar particle size gradation with sand used in large scale tests (Fig. 3). Chiba sand was previously calibrated by Robert (2010) for both saturated and unsaturated states through a series of triaxial laboratory tests.

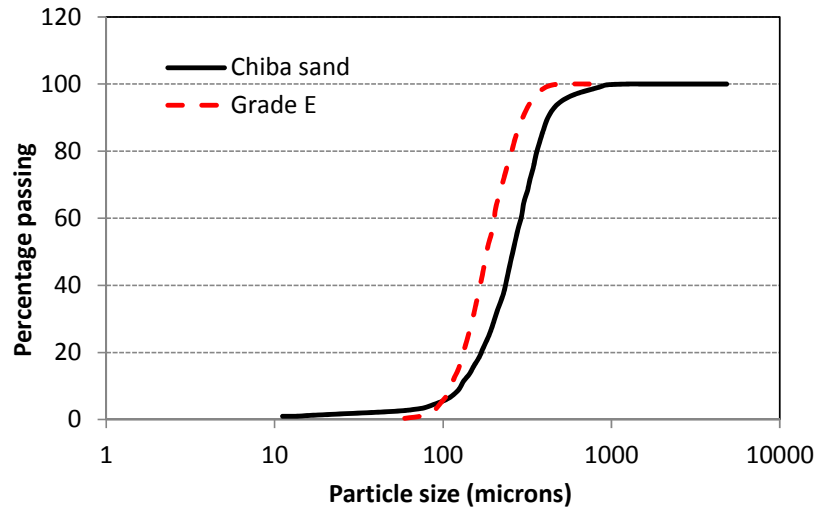


Fig. 3. Particle size distribution of sands used in the study

RESULTS

Simulating large scale tests

Analyses were performed to simulate the large scale tests using above modeling methodology. Simulations were performed on the basis of assuming the initial state of the sand as in dry condition. This is because the large scale tests were conducted at in-situ moisture content at which the water saturation of the sand (i.e. ~15%) is even lower than residual degree of saturation for Chiba sand. Figure 4 illustrates the soil moisture test data for Chiba sand obtained at dry density of 1.47g/cm³ (~48% relative density). The initial dry density of the soil used in large scale tests is ~1.4g/cm³.

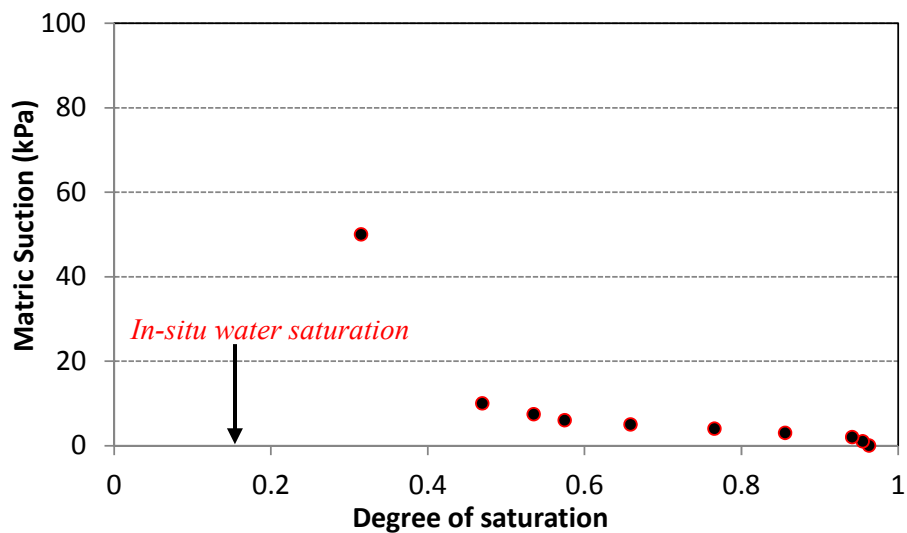


Fig. 4. Soil moisture test data at dry density of 1.47g/cm³ (Robert, 2010)

Fig.5 shows the load (uplift resistance)-displacement plots obtained from the analyses in comparison with the FE results for H_t/D case 6 and 8. The deformation mechanisms of the FE model at ~ 0.5 dimensionless displacement (i.e. displacement/diameter) were showed in Fig. 6a&b (plastic deviatoric strains are shown). Larger pipe loading was resulted for deeply embedded pipes due to larger confinement effects from soil. i.e. The larger/broader shear band evolution induces higher pipe uplift resistance in $H_t/D=8$ case compared to smaller/narrower shearing of soil at $H_t/D=6$ (Fig.6).

FE model, which assumes dry sand behavior, predicts similar peak loading as compared to uplift resistance observed in large scale test for $H_t/D=8$, whereas the model under-predicts the experimental uplift resistance by $\sim 8\%$ for $H_t/D=6$. This slight under-prediction of peak uplift resistance at shallower depth could be due to the effects of suction and apparent cohesion of sand particles at the in-situ moisture content. The effect of suction and apparent cohesion diminishes (i.e. relatively low) at larger confining stresses (i.e. $H_t/D=8$) and hence the dry Nor-Sand model simulates similar peak uplift resistance when pipe is buried at deeper depths. The models predict stiffer response at lower pipe displacements in both H_t/D cases. This can be due to slightly coarseness (i.e. higher elastic stiffness) of the calibrated Chiba sand compared to grade E sand used in the large scale tests.

The prediction of the peak dimensionless uplift resistance ($F/\gamma HDL$, F – Peak uplift resistance, γ – Unit weight of soil, H – Soil cover height, L - Pipe length) from FE model was compared to the experimentally observed values and ASCE (1984) predictions in Fig. 7. It can be seen that the FE model prediction follows the ASCE guideline for pipe loading at $\phi'=36^\circ$ (ϕ' at $1.4\text{g}/\text{cm}^3$ for Chiba sand is $\sim 35^\circ$). The slight increase in the peak dimensionless load from large scale test at $H_t/D=6$ could be due to the suction and apparent cohesion effect of sand at in-situ moisture condition.

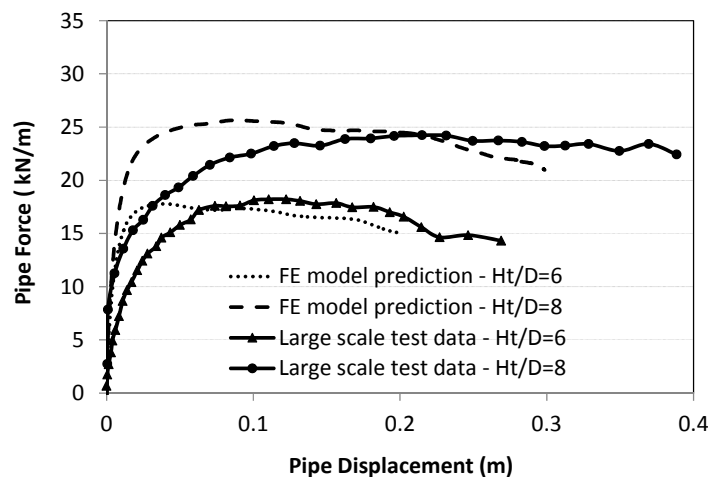


Fig. 5. FE model prediction of the pipe uplift resistance -displacement in comparison with test data

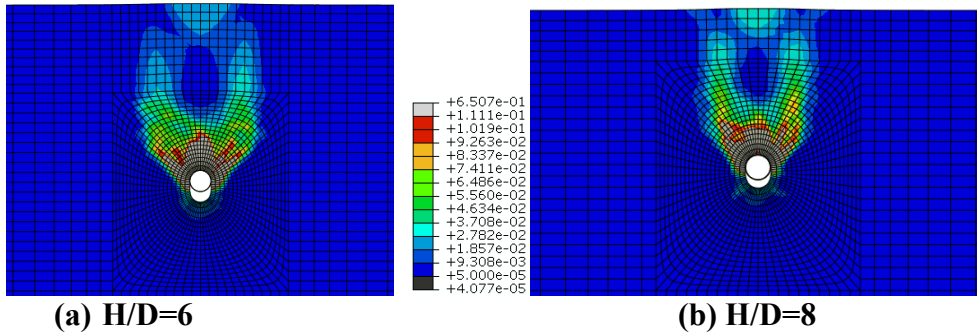


Fig. 6. Deformation mechanism of the FE model at (a) H/D=6 & (b) H/D=8 at peak pipe mobilization (Shear strain contours are shown).

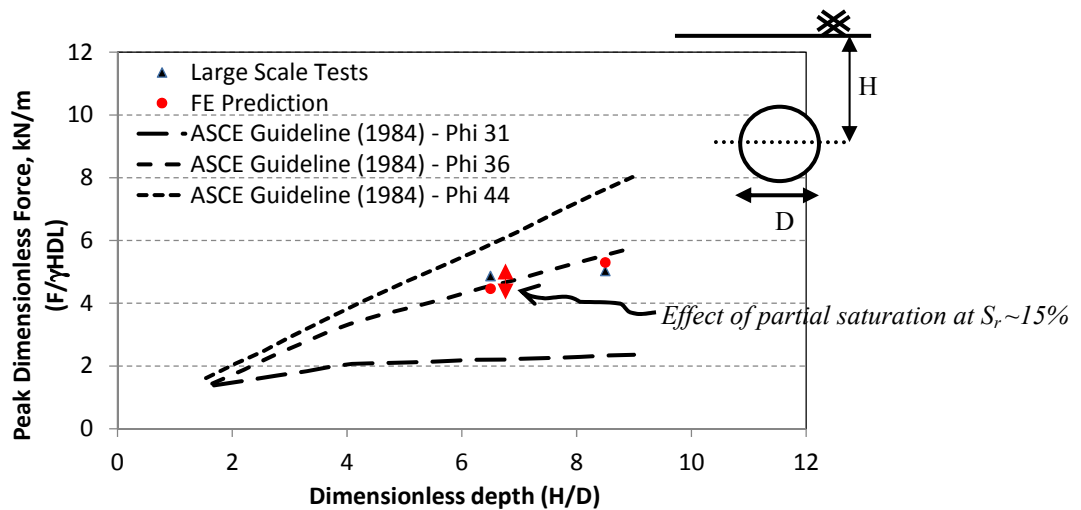


Fig. 7. Comparison of large scale test data and FE model predictions with ASCE guidelines for peak dimensionless force vs dimensionless depth

Response prediction for pipes buried in different sand initial densities

Further FE analyses were conducted on the basis of Chiba sands at different dry densities and pipe embedded depths to investigate the uplift resistance of soils. Dry densities were selected at effective friction angles of 36° and 44° from triaxial test data obtained from Robert, 2010. The triaxial test data showed that the corresponding dry densities are 1.43g/cm^3 and 1.55g/cm^3 at the relative dilatancy indices (Bolton, 1986) of 0.6 and 3 (at mean effective stress of 10kPa) respectively.

The results of FE analyses are compared with previous analytical solutions as well as to ASCE (1984) guideline predictions in Fig.8 a & b for different dry densities. It can be noted that the peak dimensionless load obtained from FE analyses agree well with ASCE predictions in general. However, the peak soil resistance for denser soils (i.e. $\phi'=44^\circ$) shows a decrease in the increase of uplift resistance for deeply embedded

pipe. This is because the different soil failure mechanisms at deep embedded pipes (deep-seated failure) in contrast to general shear failure of soil at shallow embedded pipes.

The predictions from the analytical models show a substantial difference when compared to ASCE guideline prediction and current FE analysis results. None of the analytical solutions are capable in capturing the non-linear increase of uplift soil resistance induced by different failure mechanisms at shallow and deeply embedded pipes in Chiba sand. The solutions proposed by White et al. (2001) and Schaminee et al. (1990) over-predict and under-predict the peak dimensionless force respectively, compared to ASCE and FE analysis results. The solution by Vermeer and Sutjiadi (1985) predicts similar peak dimensionless loads to ASCE and FE predictions for pipes buried at shallow depths, however it is unable to capture the different uplift resistances induced by varying soil failure mechanisms at deep embedded pipes.

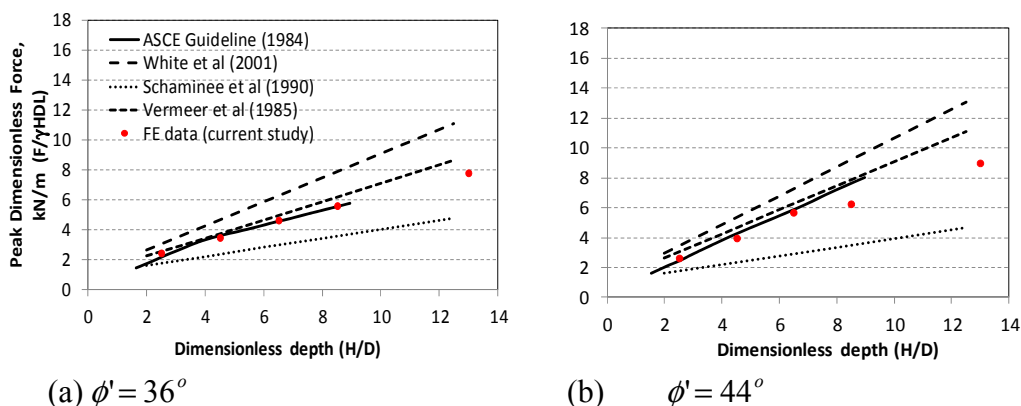


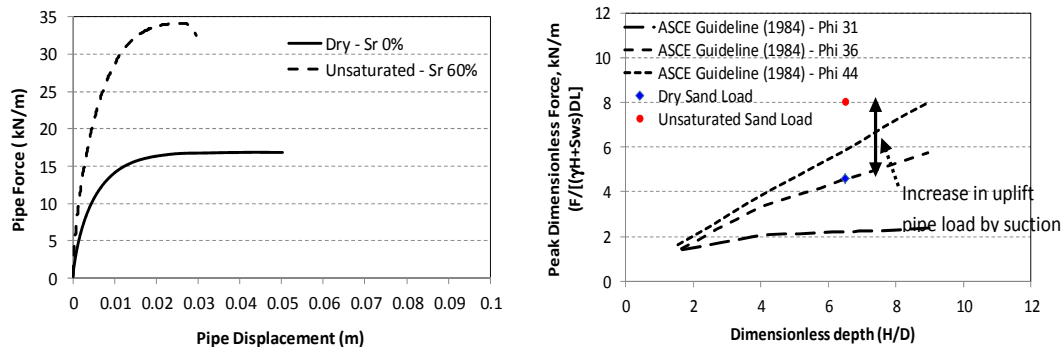
Fig. 8. Peak dimensionless force vs dimensionless depth

Response prediction for pipes buried in unsaturated soils

Previous studies have showed that the pipe behavior in lateral soil displacement under unsaturated condition can be substantially different when compared with the behavior under dry soil conditions (Robert, 2010; Robert and Soga, 2013; Robert et al, 2015). These studies showed that the lateral pipe loading under unsaturated condition can be substantially higher (more than a factor of 2) when compared to the loading in dry sand when tested at similar dry densities.

Analyses were conducted to investigate the behavior of pipes under uplift displacement in unsaturated soils. The initial dry density assumed for the soils is based on $\phi' = 36^\circ$ at a water saturation of 60%. Analyses were performed at $H/D = 6$. Unsaturated Nor-Sand model was developed and calibrated for unsaturated Chiba sand (Robert, 2010; Robert and Soga, 2013; Robert et al, 2015). The results of the analyses are showed in Fig. 9-10.

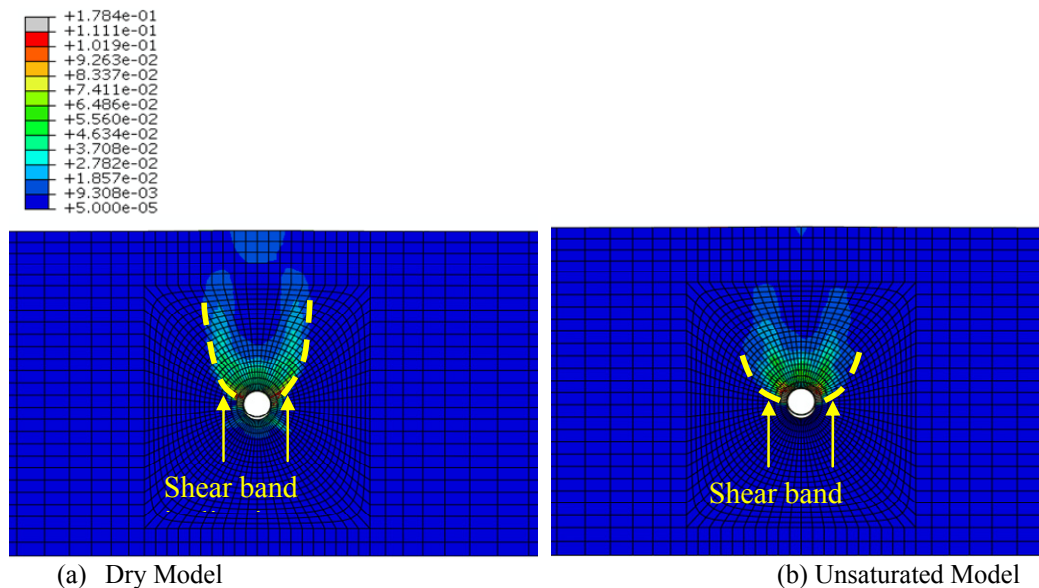
The uplift resistance of the pipeline under unsaturated sand condition (i.e $S_r=60\%$) has resulted significantly higher load when compared to the pipe loading obtained under dry sand condition as showed in Fig. 9. The suction induced apparent cohesion effect of Chiba sand has dramatically increased the uplift resistance of the pipeline when compared to dry condition (Robert, 2010). This can be further elaborated using the comparison of the deformation mechanisms between dry and unsaturated sand models. The deformation mechanism observed for unsaturated sand model showed broader shear band inclination compared to the soil deformation observed for dry sand model (Fig.11). This resulted for the peak dimensionless load to increase by a factor of ~ 2 for uplift loading in unsaturated sand (at 60% water saturation) when compared to the loading in dry sand at the same dry density of soil (Fig. 9b).



(a) Uplift resistance Vs displacement

(b) Peak Dimensionless Force Vs Dimensionless depth

Fig. 9. Loading response of pipes buried in dry and unsaturated (60% water saturation) soils – H/D=6.0



(a) Dry Model

(b) Unsaturated Model

Fig. 10. Deformation mechanisms (shear strains) of dry and unsaturated ($S_r=60\%$) FE model (H/D=6)

CONCLUSION

The uplift resistance from the soil cover is a vital design parameter for HTHP pipelines as well as for the pipelines with high risk of exposure to earthquakes. This is due to the significant cost associated with the burial depth requirement in addition to the socio-economic losses that could result in the event of pipeline failures. Hence, for effective asset design and management, it is important to determine the accurate estimation of the uplift resistance from the soil cover above the pipeline. This paper presents full-scale uplift results and finite-element parametric studies conducted to investigate the effects of dimensionless cover heights (soil cover height to diameter ratio), soil relative density and moisture content on the peak uplift resistance of pipes subjected to vertical displacement in coarse-grained soils. Full scale experimental results were compared with the FE results for validation. The results from the current study are compared to ASCE design guidelines as well as available analytical models which predict the uplift resistance of soil.

Results from the current study revealed that the uplift resistance for pipes buried in dry soils agrees well with ASCE predictions in general. However, the uplift resistance of deeply embedded pipes ($H/D > 6$) in denser soils are lower than the ACSE prediction. This is due to the different soil failure mechanism that occurs during the uplift of deeply embedded pipelines (deep-seated failure) in contrast to general shear failure of soil at shallow embedded pipes. None of the analytical solutions are capable in capturing the non-linear path of uplift soil resistance vs pipeline displacement or the transition of failure mechanisms at shallow and deeply embedded pipes.

The uplift resistance of the pipeline under partially-saturated sand condition ($S_r = 60\%$) is significantly higher when compared to the identical dry sand condition. The suction induced apparent cohesion effect of Chiba sand dramatically increases the uplift resistance of the pipeline when compared to dry condition. The peak dimensionless uplift load was increased by a factor of ~ 2 for uplift loading in partially saturated sand when compared to the uplift resistance in dry sand and ASCE guideline prediction at the same dry density of soil. The current study is being continued to investigate and quantify the partial saturation effects, burial depths and pipeline diameters on uplift resistance of soils.

REFERENCES

- ABAQUS, Inc. (2007), ABAQUS V.6.7 User's Manual, Providence, Rhode Island.
- ASCE-Guidelines (1984). "Guidelines for the seismic design of oil and gas pipeline systems", committee on gas and liquid fuel lifelines of the ASCE technical council on lifeline earthquake engineering.
- Been, K. and Jefferies, M.G. (1985). "A state parameter for sands", *Geotechnique*, Vol.35(2); pp.99-112.
- Bolton, M.D. (1986). "The strength and dilatancy of sands", *Geotechnique*, Vol.36 (1): 65-78.

- Bransby, M. F., Newson, T. A., Brunning, P., and Davies, M. C. R. (2001). "Numerical and centrifuge modeling of the upheaval resistance of buried pipelines." *Proc., 20th Int. Conf. on Offshore Mechanics and Arctic Engineering*, Rio de Janeiro, Brazil.
- Cheuk C. Y., White D. J. and Bolton M. D (2008). "Uplift Mechanisms of Pipes Buried in Sand." *Journal of Geotechnical and Geoenvironmental Engineering*, Vol. 134 (2): 154-163.
- Cheong, T.P. (2006). "Numerical modelling of soil-pipeline interaction", *PhD Thesis*, University of Cambridge.
- Chin, E. L., Craig, W. H., and Cruickshank, M. (2006). "Uplift resistance of pipelines buried in cohesionless soil." *Proc., 6th Int. Conf. on Physical Modelling in Geotechnics*. Ng, Zhang, and Wang, eds., Vol. 1, Taylor & Francis Group, London, 723–728.
- Ng, C. W. W., and Springman, S. M. (1994). "Uplift resistance of buried pipelines in granular materials." *Centrifuge 94*, Leung, Lee, and Tan, eds., 753–758.
- Robert, D.J. (2010). "Soil-pipeline interaction in unsaturated soils", *PhD Thesis*, University of Cambridge.
- Robert, D.J. and Soga, K. (2013). "Chapter 13: Soil–Pipeline Interaction in Unsaturated Soils." *Mechanics of Unsaturated Geomaterials*, L. Laloui (editor), John Wiley and Sons, 303-325.
- Robert. D. J., Soga. K, and O'Rourke. T. D. (2015). "Pipelines Subjected to Fault Movement in Dry and Unsaturated Soils." *International Journal of Geomechanics*, ASCE (Accepted).
- Schaminée, P. E. L., Zorn, N. F., and Schotman, G. J. M. (1990). "Soil response for pipeline upheaval buckling analyses: Full-scale laboratory tests and modeling." *Proc., 22nd Annual Offshore Technology Conf.*, OTC6486, 563–572.
- Schupp, J., Byrne, B. W., Eacott, N., Martin, C. M., Oliphant, J., Maconochie, A., and Cathie, D. (2006). "Pipeline unburial behaviour in loose sand." *Proc., 25th Int. Conf. on Offshore Mechanics and Arctic Engineering*, Hamburg, Germany, OMAE2006-92541.
- Thusyanthan, N.I, Sultan M, J. Wang & S.K, Haigh (2010), "Uplift resistance of buried pipelines and DNV guidelines", *OPT 2010*, Feb 2010, Amsterdam.
- Trautmann, C. H., O'Rourke, T. D., and Kulhawy, F. H. (1985). "Uplift force-displacement response of buried pipe." *J. Geotech. Engrg.*, 111 (9); 1061–1076.
- Vanden Berghe, J. F., Cathie, D., and Ballard, J. C. (2005). "Pipeline uplift mechanisms using finite element analysis." *Proc., 16th Int. Conf. of Soil Mechanics and Foundation Engineering*, Osaka, Japan, 1801–1804.
- Vermeer, P. A., and Sutjiadi, W. (1985). "The uplift resistance of shallow embedded anchors." *Proc., of 11th Int. Conf. of Soil Mechanics and Foundation Engineering*, Vol. 3, San Francisco, 1635–1638.
- White, D. J., Barefoot, A. J., and Bolton, M. D. (2001). "Centrifuge modeling of upheaval buckling in sand." *Int. J. Physical Modeling in Geotechnics*, 2(1); 19–28.
- Yimsiri, S., Soga, K., Yoshizaki, K., Dasari, G. R., and O'Rourke, T. D. (2004). "Lateral and Upward Soil-Pipeline Interactions in Sand for Deep Embedment Conditions", *Journal of Geotechnical and Geoenvironmental Engineering, ASCE*, Vol. 130(8); 830-842

A Utilization Technique of Tsunami Sediments and Disaster Wastes Containing Salt

Kiyoshi Omine¹ and Satoshi Sugimoto²

¹Professor, Graduate School of Engineering, Nagasaki Univ., Japan. E-mail:

omine@nagasaki-u.ac.jp

²Assistant Professor, Graduate School of Engineering, Nagasaki Univ., Japan.

Abstract: In this study a geo-environmental approach was used for the restoration of the farmed land that was damaged by salinity, due to tsunami water in the pacific coast of Tohoku region in Japan. In order to confirm the effect of the organic fertilizer with salt-tolerance bacteria, laboratory tests of the tsunami sediments and the soils separated from disaster wastes were performed. The organic fertilizer can be easily increased by mixing rice bran, oil cakes, grinds of fish bones and water. Electric conductivity, EC, of the tsunami sediments mixed with the organic fertilizer was measured continuously. The value of EC decreases with increase in curing period and becomes almost a half after one month. The potting cultivation test for rice plants was conducted. The soils separated from disaster wastes also contain salt from seawater. The organic fertilizer was also mixed with the separated soils and its applicability was confirmed by laboratory tests.

INTRODUCTION

The great east Japan Earthquake (Higashi Nihon Daishinsai in Japanese) of magnitude 9.0 was an undersea mega thrust earthquake off the coast of Japan that occurred at 14:46:23 JST on Friday, 11 March 2011. The location of the epicenter of this earthquake was 70 kilometers east of the Oshika Peninsula of Tohoku and the hypocenter at an underwater depth of approximately 32 km. It was the most powerful known earthquakes to have hit Japan, and one of the five most powerful earthquakes in the world since modern record keeping began in 1900.

The earthquake triggered extremely destructive tsunami waves of around 40 m in height in Miyako, Iwate and Tohoku, in some cases traveling up to 10 km inland. In addition to loss of life and destruction of infrastructure, the tsunami caused a number of nuclear accidents in the power plant in Fukushima that caused evacuation zones affecting hundreds of thousands of residents. The seawater inundated large areas of agricultural land and turned soil saline.

The mega earthquake and consequent tsunami caused a great damage to, not only human life and infrastructure, but also the agricultural land and crops in Tohoku region, Japan. The after math of the tsunami has created many problems to environment and geo-environment of the affected areas. A large amount of disaster wastes were caused

by the great east Japan Earthquake. Soil pollution with high salinity, which made the farmland unusable for cultivation, is also one of the major geo-environmental problems. The objective of this study is to know soil chemical property due to tsunami and to apply an innovative approach to control the salinity of the agricultural land (Omine et al., 2012a). In order to confirm effectiveness of the organic fertilizer with salt-tolerance bacteria, laboratory tests of the tsunami sediments and the soils separated from disaster wastes are performed in this study.

METHODS OF RESTORATION OF SALINE SOIL

The aim of soil salinity control is to prevent soil degradation by salinization and to reclaim already degraded soils. Various attempts are now being tested to control salinity of the agricultural land.

The primary method of controlling soil salinity is to permit 10-20% of irrigation water to leach through the soil; the leached water is then drained and discharged through an appropriate drainage system. The salt concentration of the drainage water normally becomes 5 to 10 times higher than that of the irrigation water. National Federation of Agricultural Corporative Associations in Japan has suggested the following primary salt removal method for paddy fields (ZEN-NOH, 2011);

Step 1: Removal of mud and wastes by Tsunami

Step 2: Plowing (turning over) Step 3: Watering

Step 4: Soil puddling

Step 5: Dewatering

Step 6: Repeat of Step 2 ~ 5 (2 ~ 6 times) until EC is less than 0.3~0.6 mS/cm.

In case of high salt concentration, hydrated lime or calcium carbonate will be mixed.

However, it cannot be applied to land area without water supply and dewatering system immediately.

Another method is to establish salt tolerant plants for reducing the salinity of soil biologically. In this study, an innovative idea was tested for reducing the salt concentration from the agricultural soils. Mr. Usugami who is a researcher of Fukushima produced special organic fertilizer containing salt tolerant bacteria or halo bacteria for many years. The volume of the organic fertilizer can be increased by mixing rice bran, oil cakes, grinds of fish bones and water. Figure 1 shows the extension method of the organic fertilizer. The rice bran of 30 kg, oil cake of 10 kg, fish lees of 2 kg and water of 35 kg are mixed with the original organic fertilizer of 2 kg using mixer. After mixing each material, temperature of the organic fertilizer was increased to 48°C for 2 days and turned over for aeration. It is considered that almost same organic fertilizer can be obtained by this method, because the original organic fertilizer has been increased by this method. Figure 2 shows processing of the organic fertilizer after 3 days. The authors increased 2 kg of the organic fertilizer up to 300 kg by this extension method. The organic fertilizer containing the salt tolerant bacteria was made ready for application in the tsunami affected large areas of Rikuzentakata for the purpose of reducing salinity of the agricultural land (Omine et al., 2012).

The sample was collected separately in sterile plastic sheets, and brought to the laboratory for microbiological analysis. The salt-tolerance was determined in LB agar supplemented with NaCl. The growth was monitored after 72 hours incubation at 30°C.

Finally, six types of salt-tolerance bacteria were isolated from the organic fertilizer (Omine et al., 2012b).

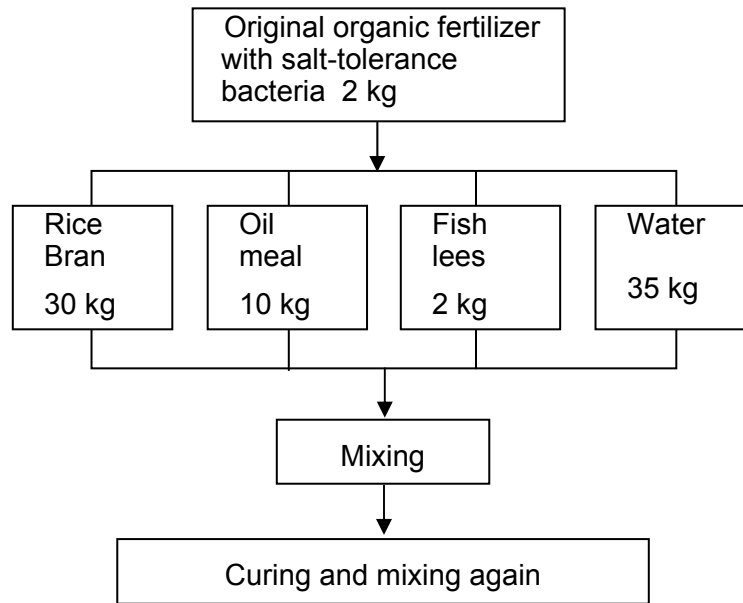


FIG. 1. Extension method of the organic fertilizer.



FIG. 2. Processing of the admixture of organic fertilizer after 3 days.

For improving the agricultural land damaged by Tsunami, the organic fertilizer of 10 kg per 1000 m² and the rice bran of 100 kg per 1000 m² are needed. The rice bran is nutrition for increasing the salt-tolerance bacteria on site. Finally, 1 ton of the organic fertilizer was made and it was brought to Rikuzentakata city together with 4 tons of the rice bran. These materials (organic fertilizer and rice bran) were disseminated at the agricultural land of 6 ha together with rapeseed or rye as green manure crop.

Soil investigation at the site was performed on March 2012. Due to the rail fall and vegetation of sunflower, the salt concentration decreased gradually and the highest EC at the site was 0.25 mS/cm on September 2011. The value of EC decreased furthermore on March 2012. Therefore, it was difficult to distinguish the effect of the organic fertilizer with salt-tolerance bacteria clearly. It is considered that the organic fertilizer contains necessary nutrition and the soil is improved.

LABORATORY TESTS ON TSUNAMI SEDIMENTS

In order to confirm the effect of the organic fertilizer with salt-tolerance bacteria, laboratory tests of the tsunami sediment were performed.

For making clear the effect, table salt of 400mg/100g-dry soil was added to a soil sampled from agricultural field at Rikuzentakata city. The organic fertilizer of 1g and rice bran of 10g were mixed with the soil of 330g. Another saline soil from Souma city at Fukushima Prefecture is also used and the sample is prepared by mixing the organic fertilizer of 4g and rice bran of 40g into the soil of 800g. Electric conductivity of the sample was measured continuously as shown in Fig.3. Value of EC decreases with increase in curing period and becomes less than a half after two months.

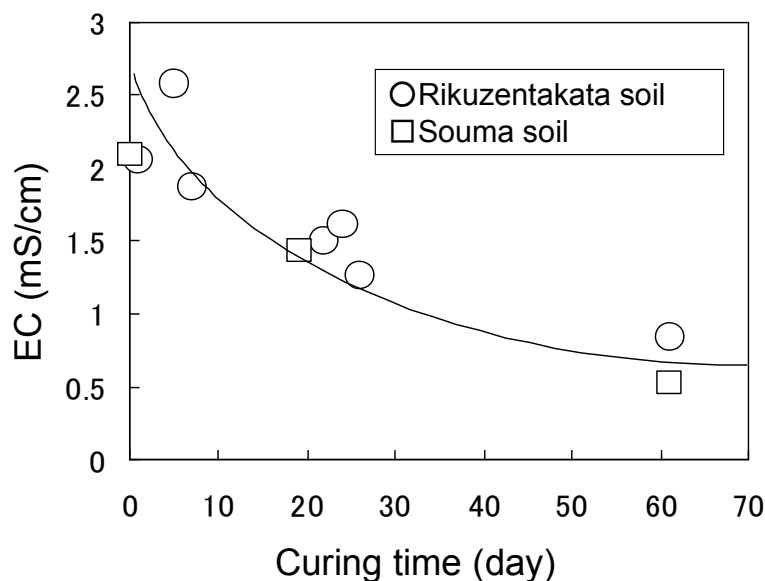


FIG. 3. Relationship between EC and curing period on tsunami sediments.

The farmers in Rikuzentakata city are not able to start a cultivation of rice, because the agricultural land has contained a large size of disaster wastes in the soil and tractor cannot work correctly.

It was therefore that the potting cultivation test for rice plants was conducted. Figure 4 shows the test result after one month. In the case of control without the organic fertilizer, rice plants were died during one week. On the other hand, the plants using the organic fertilizer have grown steadily.

An image of effect on restoration of saline soil by salt-tolerance bacteria is shown in Fig.5. The salt-tolerance bacteria cannot decompose or remove salt in the soil.

However, when the bacteria increase, those absorb nutrition together with salt into the body. The bacteria also excrete organic acid and it will chelate salt. It is therefore that effect of the bacteria is not to reduce concentration of salt, namely control elution of salt into water. This effect will continue a long time, because it is considered that bacteria do not decompose soon after they died. Usually, there are many useful microorganisms such as lactic acid bacteria, yeast and bacillus subtilis in the organic fertilizer. Those microorganisms will also contribute reducing soil salinity.

Thus, the organic fertilizer with salt-tolerance bacteria can reduce the soil salinity and it is also confirmed that the organic fertilizer is effective for growth of rice plants and restoration of agricultural land.

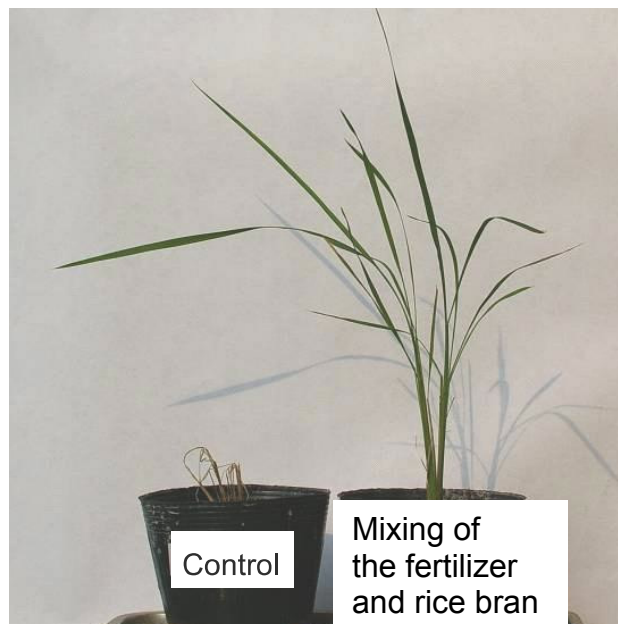


FIG. 4. Result of potting cultivation test for rice plants.

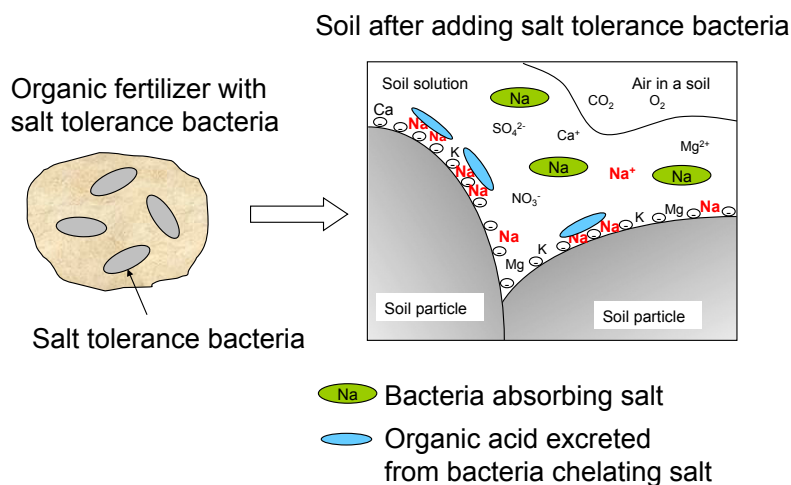


FIG. 5. Image of effect on restoration of saline soil by salt-tolerance bacteria.

LABORATORY TESTS ON DISASTER WASTES

Huge amounts of disaster wastes were generated on the Tohoku coastal areas. The disaster wastes containing various matters, such as woods, plastic pieces, glass chips, and soils, are being treated and large amount of separated soil are generated.

There are two types of separate soils obtained from disaster wastes (Yamane et al., 2013). Type-B of separate soil means the incombustible mixed disaster waste with crushed and sieving less than 20 mm. Type-C of separate soil means the combustible mixed disaster waste without crushing and with sieving less than 20 mm. These samples are obtained from Iwate Prefecture.

Type-B of the separate soil (Yamada Town) is used in this study. Ignition loss of the soil was 9.1% and a value of pH was 7.6. A content of combustible material larger than 2 mm was 4.8% in weight. The separated soil may be used as a vegetation base material. However, the separate soil contains salt from seawater.

In order to confirm usefulness of the separate soil as vegetation base soil, the organic fertilizer is mixed with Type-B of the separate soil. Figure 6 shows a sample of the separate soil. It is found that many wood chips contains in the soil. Initial EC of the original separate soil was 1.98 mS/cm. The organic fertilizer of 3 g and rice bran of 30 g were mixed with the separate soil of 700 g with water content of 29.0%. Change of EC on the separate soil with the organic fertilizer is shown in Fig.7. The value of EC decreases with increase in curing period.

Potting cultivation test for rapeseed was conducted. Figure 8 shows the test result after one month. In the case of control without the organic fertilizer, the rapeseed did not grow sufficiently. On the other hand, the rapeseed mixing the organic fertilizer and rice bran has grown steadily. As another case, the organic fertilizer and rice bran were sprinkled on the soil surface. It is found that sprinkling method of the organic fertilizer on the surface is also effective for growing the rapeseed.



FIG. 6. Type-B of the separated soil (Ymada town).

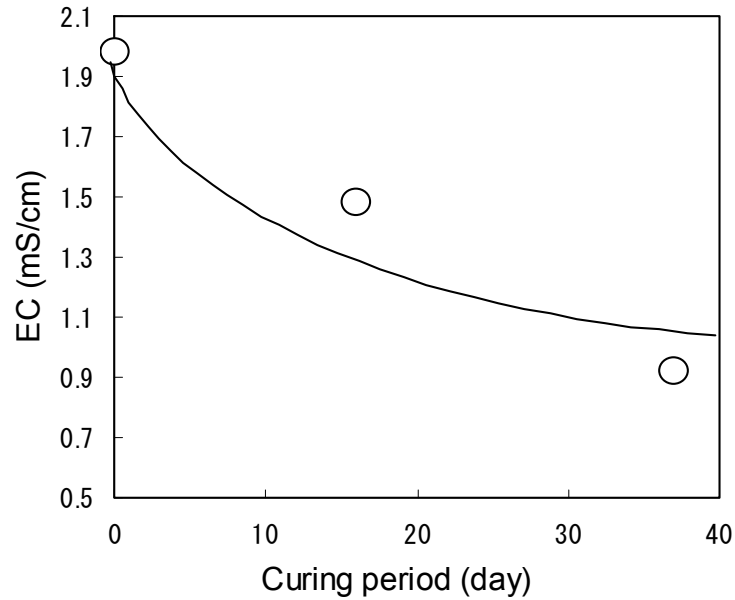


FIG. 7. Relationship between electric conductivity and curing period on separated soils.

Thus, the organic fertilizer with salt-tolerance bacteria can reduce the soil salinity and it is also confirmed that the organic fertilizer is effective for growth of plants and restoration of saline soil and separate soil.

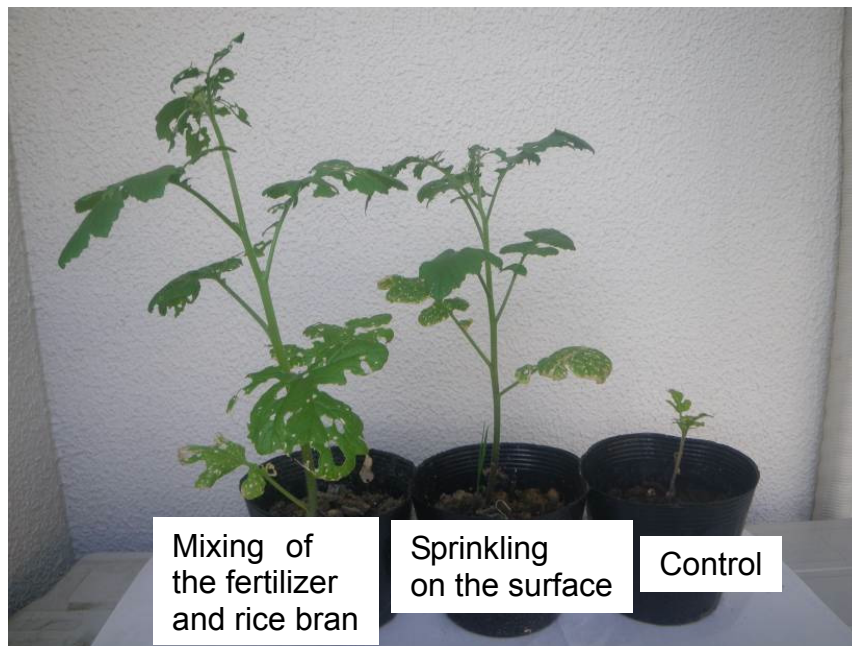


FIG. 8. Result of potting cultivation test for rapeseed.

CONCLUSIONS

The organic fertilizer containing salt-tolerance bacteria was used at the agricultural land damaged by Tsunami for restoration of the saline soil. The laboratory tests of chemical properties and potting cultivation were also performed on the Tsunami sediments and the separated soil from disaster wastes. From the test results, the organic fertilizer containing salt-tolerance bacteria can reduce the excessive salts from the soil and consequently reduced the salinity problem. It was also confirmed that the organic fertilizer is effective for growth of rice plant and rapeseed. It is also expected that the organic fertilizer provided necessary nutrients to the soil and plant.

ACKNOWLEDGMENTS

The authors wish to acknowledge the financial support by Grant-in-Aid for Scientific Research (15H04039) from Japan Society for the Promotion of Science and the Environmental Sciences Research Grants (3K133003).

REFERENCES

- Omine, K., Fujikawa, T., Sugimoto, S., and Maeda, H. (2012a). "Investigation of Rikuzentakata city of Iwate prefecture and geo-environmental Approach - Ground settlement, waste materials and restoration of saline agricultural land -", *Japanese Geotechnical Journal*, 7(1): 231-241 (in Japanese).
- Omine, K., Azizul Moqsud, M., and Edward Raja, C. (2012b) "Soil Restoration of Agricultural Land Damaged by Sea Water in Tohoku Earthquake 2011", *International Journal of Environment*, 2(2): 128-134.
- ZEN-NOH (2011). http://www.zennoh.or.jp/press/topic/PDF/20110329_1.pdf (in Japanese) [Accessed 30 August 2015].
- Yamane, K., Morita, K., Takai, A., Inui, T., Katsumi T., and Otsuka, Y. (2013). "Physical properties of the soils separated from disaster wastes", *Proceedings of the 13th Geo-Environmental Engineering 2013*, Seoul, Korea:130-136.

A Meshfree Method for Modeling the Impact of Landslide Activity

Thanakorn Siriaksorn¹; Sheng-Wei Chi²; and Craig Foster³

¹Ph.D. Candidate, Dept. of Civil and Materials Engineering, Univ. of Illinois at Chicago, IL 60607. E-mail: tsiria3@uic.edu

²Assistant Professor, Dept. of Civil and Materials Engineering, Univ. of Illinois at Chicago, IL 60607.

³Associate Professor, Dept. of Civil and Materials Engineering, Univ. of Illinois at Chicago, IL 60607.

Abstract: This paper presents a two-field semi-Lagrangian reproducing kernel particle method for landslide simulations. The method combines advantages of Eulerian and Lagrangian formulations in that state variables follow material points while the approximation functions are updated in the current configuration to allow extreme deformation and material separation. The Biot theory is employed to describe poromechanics of geomaterials. A Drucker-Prager model with damage is adopted to represent constitutive model of solid phase of porous media. In addition, a variationally consistent integration (VCI) scheme is employed in the two-field semi-Lagrangian formulation to enhance solution accuracy. The proposed method is verified with several numerical examples and its applicability of simulating landslide events is validated with an experimental result.

INTRODUCTION

The prediction and assessment of environmental impacts caused by landslide activities requires accurate predictions for both slope stability analysis and run-out. Due to distinctive characteristics in each landslide process, different numerical techniques are usually employed to model different landslide processes. Continuum-based methods with a Lagrangian formulation, such as finite element method (FEM), are preferable before crack initiation in slope stability analysis (Cho and Lee 2001; Borja and White 2010; Conte et al. 2014; Duncan 1996). On the other hand, discontinuum-based methods, such as the discrete element method (DEM), are common for addressing fluid-like behaviors in run-out simulation (Campbell et al. 1995; Tang et al. 2009; Cleary and Campbell 1993; Cleary 2004). However, the bulk modulus for the contact models in DEM is difficult to calibrate.

This paper presents a semi-Lagrangian Reproducing Kernel Particle Method (RKPM) to consistently simulate entire landslide processes. The present method analyze slope stability effectively as FEM and high-order solution accuracy can be readily achieved through the consistency conditions in the approximation functions (Liu et al. 1995; Chen et al. 1996). Extreme deformation and material separation in

the run-out simulation is naturally handled by the semi-Lagrangian RKPM since the approximation functions of the method are constructed in the current configuration (Guan et al. 2009; Guan et al. 2011). Domain integration required in the Galerkin formulation is carried out by the Modified Stabilized Non-conforming Nodal Integration (MSNNI) for efficiency and stability (Chen et al. 2007). In addition, the Variationally Consistent Integration (VCI) is employed to improve solution accuracy (Chen et al. 2013). Further, the saturated two-phase deforming porous media model following Biot theory (Biot 1941; Zienkiewicz and Shiomi 1984; Zienkiewicz et al. 1999) is incorporated into the framework to represent poromechanics of geomaterials.

MECHANICS OF SATURATED DEFORMABLE POROUS MEDIA

To account for the coupling effect between solid and fluid phases, the saturated two-field formulation, extended from Biot theory (Zienkiewicz et al. 1999), is adopted with the assumption of no phase change and isothermal conditions. In this paper, only two fields are considered: displacement and pore water pressure.

The governing equations of the two-field formulation, consisting of the equation of motion and continuity equation, can be respectively expressed by

$$\left. \begin{aligned} \sigma_{ij,j} + b_i &= \rho \ddot{u}_i && \text{in } \Omega \\ \alpha \dot{u}_{i,i} + \frac{\dot{P}}{M} + q_{i,i} &= 0 && \text{in } \Omega \end{aligned} \right\} \quad (1)$$

where σ_{ij} is the total stress, b_i is the body force, ρ is the total density of porous medium, u_i is the displacement of solid skeleton, Ω is the domain of the problem, α is the Biot coefficient, P is the pore water pressure, and q_i is the superficial velocity of water flow. M is the Biot compressibility modulus.

The Biot coefficient α serves as a means of effective stress reduction, and hence the total stress σ_{ij} can be decomposed as

$$\sigma_{ij} = \bar{\sigma}_{ij} - \alpha P \delta_{ij} \quad (2)$$

where $\bar{\sigma}_{ij}$ is the effective stress of solid phase, and δ_{ij} is the second-order identity tensor. Unless otherwise noted, Drucker-Prager with damage model (Ju 1989; Simo and Ju 1987a; Simo and Ju 1987b) is employed to calculate $\bar{\sigma}_{ij}$ as it is fully decomposed from fluid phase.

In this paper we assume an isotropic porous medium, adopting Darcy's law to describe the superficial velocity of water

$$q_i = -\frac{k_w}{\mu_w} (P_{,i} - \rho_w g_i) \quad (3)$$

where k_w is the intrinsic permeability, μ_w is the dynamic viscosity of water, ρ_w is the water density, and g_i is the gravitational acceleration.

SEMI-LAGRANGIAN RKPM

Conventional mesh-based methods suffer from mesh distortion in large deformation problems, causing poor solution accuracy or non-convergent results. Meshfree methods were introduced to relieve the strong tie between the mesh quality and solution accuracy (Belytschko et al. 1994; Liu et al. 1995; Chen et al. 1996). Nonetheless, the Lagrangian meshfree methods, which require the mapping between the initial/reference configuration and current configuration, break down in extreme deformation problems, such as landslide simulations. The semi-Lagrangian RKPM circumvents such issue by constructing the approximation functions in the current configuration (Guan et al. 2009; Guan et al. 2011) while state variables follow material. The unique properties of semi-Lagrangian RKPM can be demonstrated by Figure 1.

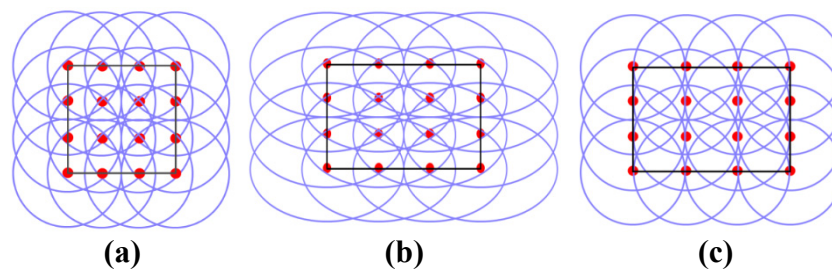


FIG. 1. Comparison between the 2-D RK shape functions in (a) initial configuration, (b) current configuration of Lagrangian RKPM, and (c) current configuration of semi-Lagrangian RKPM.

The shape function of semi-Lagrangian RKPM is expressed by

$$\Psi_I(\mathbf{x}) = C(\mathbf{x}; \mathbf{x} - \mathbf{x}_I) \Phi_a(\mathbf{x} - \mathbf{x}_I) \quad (4)$$

where $\Psi_I(\mathbf{x})$ is the shape function of node I in the current configuration $\mathbf{x}_I = \mathbf{x}(\mathbf{X}_I, t)$ and \mathbf{X}_I are the nodal position of node I in the current configuration and the initial configuration, respectively. $C(\mathbf{x}; \mathbf{x} - \mathbf{x}_I)$ is the correction function and $\Phi_a(\mathbf{x} - \mathbf{x}_I)$ is the kernel function with a support measure a . In this work, a normalized support size of 1.5 is used with the cubic spline function as the kernel function.

The correction function is introduced to ensure the specified order of consistency n in the approximation,

$$C(\mathbf{x}; \mathbf{x} - \mathbf{x}_I) = \sum_{|\alpha|=0}^n (\mathbf{x} - \mathbf{x}_I)^\alpha b_\alpha(\mathbf{x}) \tag{5}$$

where $\alpha = (\alpha_1, \alpha_2, \dots, \alpha_m)$ designates the m-dimensional index, with $|\alpha| \equiv \sum_{i=1}^m \alpha_i$; $(\mathbf{x} - \mathbf{x}_I)^\alpha \equiv (x_1 - x_{1I})^{\alpha_1} (x_2 - x_{2I})^{\alpha_2} \dots (x_m - x_{mI})^{\alpha_m}$; $b_\alpha \equiv b_{\alpha_1, \alpha_2, \dots, \alpha_m}$; $b_\alpha(\mathbf{x})$ are the corresponding coefficient of the monomials $(\mathbf{x} - \mathbf{x}_I)^\alpha$. The coefficients $\mathbf{b}(\mathbf{x})$ are obtained by satisfying the n^{th} order reproducing condition

$$\sum_{I=1}^{NP} \Psi_I(\mathbf{x}) \mathbf{x}_I^\alpha = \mathbf{x}^\alpha \quad ; \quad |\alpha| \leq n \tag{6}$$

where NP is the total number of nodes. By imposing the reproducing condition (6) the coefficient $b_\alpha(\mathbf{x})$ in the correction function can be determined and the shape function is derived as

$$\Psi_I(\mathbf{x}) = \mathbf{H}^T(\mathbf{0}) \mathbf{M}^{-1}(\mathbf{x}) \mathbf{H}(\mathbf{x} - \mathbf{x}_I) \Phi_a(\mathbf{x} - \mathbf{x}_I) \tag{7}$$

where $\mathbf{H}(\mathbf{x} - \mathbf{x}_I)$ is the vector of $\mathbf{x}^\alpha - \mathbf{x}_I^\alpha$ and

$$\mathbf{M}(\mathbf{x}) = \sum_{I=1}^{NP} \mathbf{H}(\mathbf{x} - \mathbf{x}_I) \mathbf{H}^T(\mathbf{x} - \mathbf{x}_I) \Phi_a(\mathbf{x} - \mathbf{x}_I) \tag{8}$$

SEMI-LAGRANGIAN RKPM FOR SATURATED POROUS MEDIA

Using Galerkin weak formulation and applying boundary conditions, the variational equations of the governing equations (1) are obtained as

$$\int_{\Omega} \delta u_{i,j}^h \bar{\sigma}_{ij}^h d\Omega - \int_{\Omega} \delta u_{i,j}^h \alpha P^h \delta_{ij} d\Omega + \int_{\Omega} \delta u_i^h \rho \ddot{u}_i^h d\Omega = \int_{\Gamma_h} \delta u_i^h h_i d\Gamma + \int_{\Omega} \delta u_i^h b_i d\Omega \tag{9}$$

$$\int_{\Omega} \delta P^h \alpha u_{i,i}^h d\Omega + \int_{\Omega} \delta P^h \frac{\dot{P}^h}{M} d\Omega + \int_{\Omega} \delta P_{,i}^h \frac{k_w}{\mu_w} P_{,i}^h d\Omega = \int_{\Gamma_s} \delta P^h v_s^w d\Gamma + \int_{\Omega} \delta P_{,i}^h \frac{k_w}{\mu_w} \rho_w g_i d\Omega \tag{10}$$

Using semi-Lagrangian RKPM, the approximations of displacement and pore water pressure are defined as

$$u_i^h(\mathbf{x}, t) = \sum_{I=1}^{NP} \Psi_I(\mathbf{x}) d_{iI}(t) \tag{11}$$

$$P^h(\mathbf{x}, t) = \sum_{I=1}^{NP} \Psi_I^w(\mathbf{x}) P_I(t) \tag{12}$$

where $d_{il}(t)$ and $P_I(t)$ are generalized displacement and pore water pressure, respectively. $\Psi_I(\mathbf{x})$ and $\Psi_I^w(\mathbf{x})$ are the shape functions of displacement and pore water pressure, respectively. The semi-discrete equations can be derived by applying Eqs. (11) and (12) into the variational equations (9) and (10).

In time domain, the central difference scheme is employed for displacement and the forward Euler method is employed for pore pressure

$$\left. \begin{aligned} d_{il}^{n+1} &= d_{il}^n + \Delta t v_{il}^n + 0.5 \Delta t^2 a_{il}^n \\ v_{il}^{n+1} &= v_{il}^n + 0.5 \Delta t (a_{il}^n + a_{il}^{n+1}) \\ P_I^{n+1} &= P_I^n + \Delta t \dot{P}_I^n \end{aligned} \right\} \tag{13}$$

where Δt is time step size.

Applying temporal discretizations, the fully discrete equations read

$$\left. \begin{aligned} (\mathbf{M} + 0.5 \Delta t (\mathbf{C} + \mathbf{G})) \mathbf{a}^{n+1} &= \mathbf{F}^{\text{ext}} - \mathbf{F}^{\text{int}} - (\mathbf{C} + \mathbf{G}) \hat{\mathbf{v}}^{n+1} \\ \mathbf{S} \dot{\mathbf{P}}^{n+1} &= \tilde{\mathbf{F}}^{\text{ext}} - \tilde{\mathbf{F}}^{\text{int}} \end{aligned} \right\} \tag{14}$$

with

$$\left. \begin{aligned} M_{IJ} &= \int_{\Omega} \Psi_I \rho \Psi_J d\Omega, \quad G_{IJ} = \int_{\Omega} \Psi_I \rho \bar{\Psi}_J d\Omega, \quad F_{il}^{\text{ext}} = \int_{\Gamma_h} \Psi_I h_i d\Gamma, \\ F_{il}^{\text{int}} &= \int_{\Omega} \Psi_{I,j} \bar{\sigma}_{ij}^h d\Omega - \int_{\Omega} \Psi_{I,j} \alpha \Psi_{J,i} \delta_{ij} d\Omega P_J^{n+1} - \int_{\Omega} \Psi_I \rho g_i d\Omega, \\ S_{IJ} &= \int_{\Omega} \Psi_I^w \frac{\Psi_J^w}{M} d\Omega, \quad \tilde{F}_I^{\text{ext}} = \int_{\Gamma_s} \Psi_I^w v_s^w d\Gamma, \\ \tilde{F}_I^{\text{int}} &= \int_{\Omega} \Psi_I^w \alpha \Psi_{J,i} d\Omega v_{ij}^{n+1} + \int_{\Omega} \Psi_{I,i}^w \frac{k_w}{\mu_w} \Psi_{J,j}^w d\Omega P_J^{n+1} - \int_{\Omega} \Psi_{I,i}^w \frac{k_w}{\mu_w} \rho_w g_i d\Omega \end{aligned} \right\} \tag{15}$$

In this paper, 5% mass proportional damping is used for \mathbf{C} . The convective term \mathbf{G} is from the change of the semi-Lagrangian RK shape function with respect to time, which is negligible in nodal integrations (Chi et al. 2015; Guan et al. 2011). The lumped mass scheme using the row summation method is used for \mathbf{M} and \mathbf{S} to obtain diagonal matrices to avoid solving system of equations, which improves efficiency.

VARIATIONALLY CONSISTENT INTEGRATION

When numerical integration is performed in the Galerkin weak formulation, it causes numerical inconsistency, which impairs the accuracy of solutions (Chen et al. 2013). In order to recover the consistency, VCI modifies the approximations of the test functions to satisfy the specified order of integration constraint, thus achieving the desired order of exactness (Chen et al. 2013). The gradient of the test function is modified to satisfy the following equation

$$\int_{\Omega} \delta \tilde{u}_{i,j}^h \sigma_{ij}^h d\Omega = - \int_{\Omega} \delta u_i^h \sigma_{ij,j}^h d\Omega + \int_{\Gamma} \delta u_i^h \sigma_{ij}^h n_j d\Gamma \quad (16)$$

where $\delta \tilde{u}_i^h$ is the modified version of the test function δu_i^h . $\int_{\Omega} \cdot d\Omega$ and $\int_{\Gamma} \cdot d\Gamma$ indicate numerical integrations of the domain and boundary, respectively.

By enforcing Eq. (16) to achieve linear exactness (i.e., $\sigma_{ij}^h = \text{constant}$ and $\sigma_{ij,j}^h = 0$), the integration constraints can be derived as

$$\int_{\Omega} \tilde{\Psi}_{I,j} d\Omega = \int_{\Gamma} \Psi_I n_j d\Gamma \quad (17)$$

where $\tilde{\Psi}_I$ is the shape functions of $\delta \tilde{u}_i^h$. The shape functions can be expressed by

$$\tilde{\Psi}_{I,j} = \Psi_{I,j} + R_I \xi_{jI} \quad (18)$$

where R_I is a local function that has the same domain of influence of Ψ_I for computational efficiency. ξ_{jI} is the corresponding coefficient, which can be solved by substituting Eq. (18) into Eq. (17)

$$\xi_{jI} = \left(\int_{\Gamma} \Psi_I n_j d\Gamma - \int_{\Omega} \Psi_{I,j} d\Omega \right) / \int_{\Omega} R_I d\Omega \quad (19)$$

NUMERICAL EXAMPLES

Single-Field Semi-Lagrangian RKPM for Slope Stability Analysis

To verify the result from semi-Lagrangian RKPM with MSNNI and VCI (VC-MSNNI) for a single-field formulation, the slip surface calculated from the proposed method is compared with that from FEM (Zienkiewicz et al. 1975) by using the critical value of cohesion when slope is unstable from the paper (Table 1). The slip surface is represented by fully damaged points. Figure 2 shows the schematic of the

model and comparison of the results from FEM and semi-Lagrangian RKPM. The black lines and arrows illustrate the displacement and slip surface from FEM, while the color and nodal points show the results from semi-Lagrangian RKPM. From Figure 2b, the locations of the slip surface from the two methods are similar.

Table 1. Material properties of the landscape

Young's Modulus (Pa), E	2×10^8
Poisson's Ratio, ν	0.25
Cohesion (Pa), c	2000
Friction Angle ($^\circ$), ϕ	20
Density (kg/m^3), ρ	2039

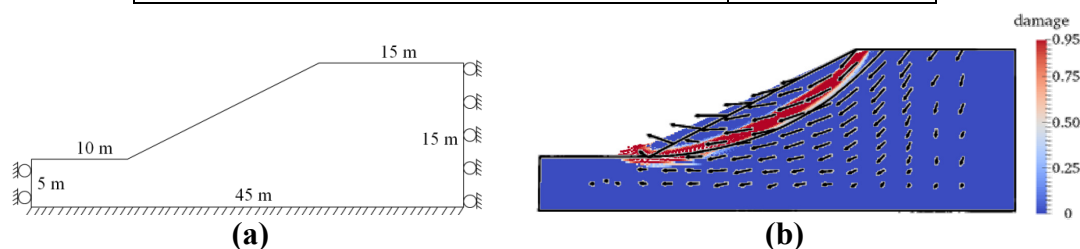


FIG. 2. (a) Schematic of the landscape simulation. (b) Numerical results from semi-Lagrangian RKPM (color) and FEM (Zienkiewicz et al. 1975) (black).

One-Dimensional Consolidation

Table 2. Specification of the 1-D consolidation problem

Young's Modulus (Pa), E	3×10^7
Poisson's Ratio, ν	0.2
Saturated Density (kg/m^3), ρ	1700
Biot Coefficient, α	1
Biot Compressibility Modulus (Pa), M	3.33×10^8
Permeability ($\text{m}^2/(\text{Pa} \cdot \text{s})$), k_w/μ_w	1.02×10^{-6}
Load (Pa), T_0	$1000 \sin(0.5\pi t/t_f)$ (Full load at $t = t_f = 0.1$ s)

The performance of semi-Lagrangian RKPM with VC-MSNNI for saturated porous media is tested by a consolidation problem subjected to a step load (Figure 3a). Table 2 shows the specifications of the problem. In this problem, a linear elastic constitutive model is used. Linear basis is used for shape functions of displacement and pore pressure. An impermeable boundary is imposed on all sides except the top, where water can flow in and out freely. The pore pressure is evaluated at the points of

interest: A and B (Figure 3a), from 0 to 30 seconds. The results from the proposed method are compared with the results from FEM using implicit Newmark algorithm (Zienkiewicz and Shiomi 1984), and analytical solutions. From Figure 3, the semi-Lagrangian RKPM using explicit method exhibits oscillations at the beginning but the results are in good agreement with FEM and the analytical solutions, after the oscillations taper off.

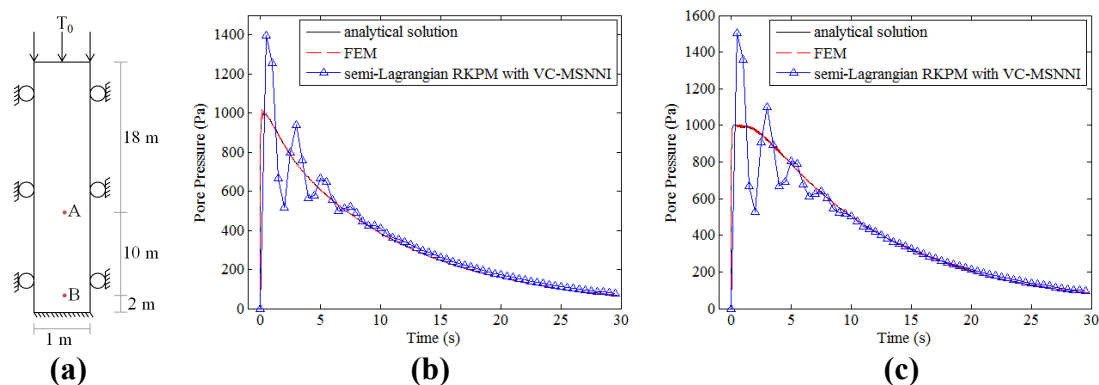


FIG. 3. (a) Schematic of the 1-D consolidation problem. (b)-(c) Comparison of the results from semi-Lagrangian RKPM with explicit temporal discretization and FEM with Newmark scheme and analytical solutions at points A and B.

Two-Field Semi-Lagrangian RKPM for Landslide Simulation

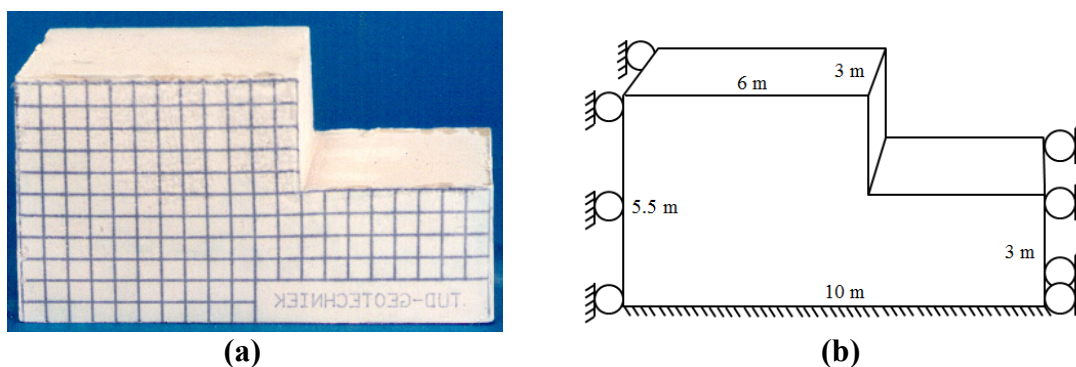


FIG. 4. (a) Experimental setup for a centrifuge test (grid size is 5 mm) (Allersma 2004). (b) Schematic and boundary conditions of the model.

A two-field semi-Lagrangian RKPM with VC-MSNNI is validated by the experimental results from the vertical-cut slope in a centrifuge test (Allersma 2004) (Figure 4a). The schematic and boundary conditions of the model, where the rightmost, bottom, and left boundaries are impervious, are shown in Figure 4b. Identical semi-Lagrangian RK shape functions with linear basis of displacement and pore pressure is employed. The material parameters used are calibrated from (Allersma 2004) and are given in Table 3. The damage contour and the progressive

deformations of the slope are illustrated in Figure 5. As can be seen in Figure 5, the numerical simulation shows similar failure surface and deposition in comparison with the experimental result.

Table 3. Material parameters of the vertical-cut slope

Young's Modulus (Pa), E	2.2×10^7
Poisson's Ratio, ν	0.2
Saturated Density (kg/m^3), ρ	2900
Biot Coefficient, α	1
Biot Compressibility Modulus (Pa), M	3.33×10^7
Permeability ($\text{m}^2/(\text{Pa} \cdot \text{s})$), k_w/μ_w	1.0×10^{-6}
Cohesion (Pa), c	5×10^4
Friction Angle ($^\circ$), ϕ	15

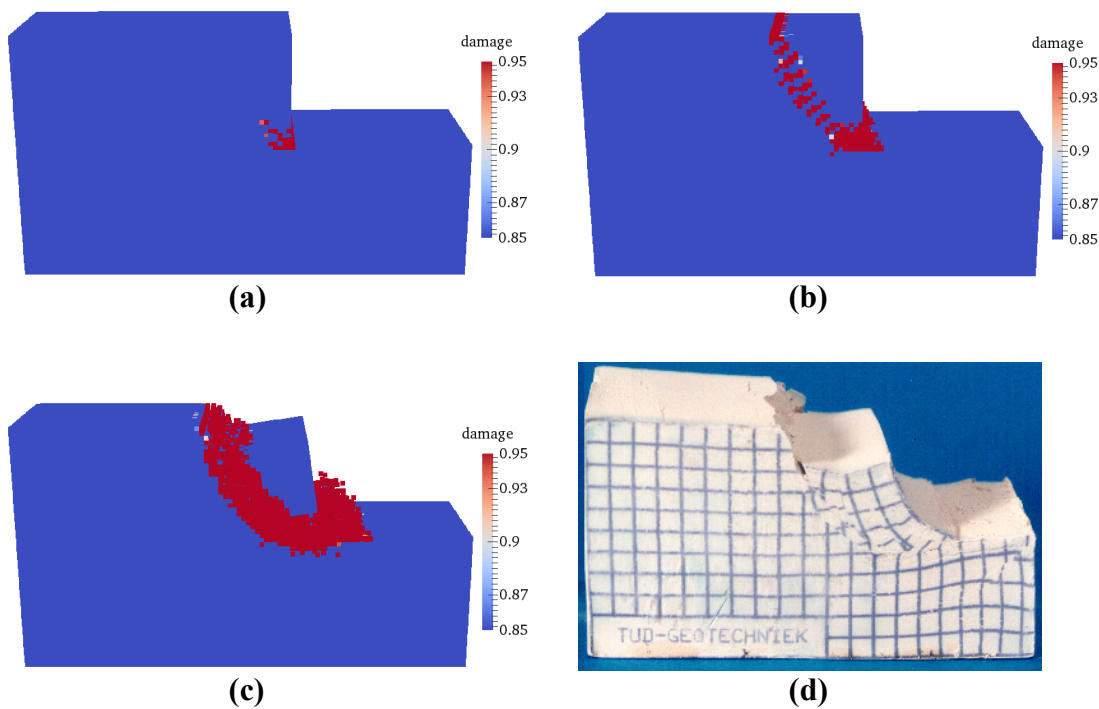


FIG. 5. (a)-(c) Damage contours and progressive deformations from the simulation. (d) Final deformation in experiment.

CONCLUSIONS

This paper presents a two-field semi-Lagrangian RKPM to effectively model landslide activities within one mathematical framework. Solid constitutive models developed for FEM can be readily incorporated into the present method with capability of modeling extreme deformation and separation. A saturated two-field deforming porous media model following Biot theory with the use of Drucker-Prager and damage models for solid phase is formulated in the framework to represent geomaterials behaviors. A stabilized nodal integration that recovers the Galerkin exactness (VC-MSNNI) is employed in the present formulation to improve accuracy and stability. The numerical examples demonstrate that the slip surface and pore water pressure from the proposed method qualitatively agree well with FEM and experimental results. In addition, equal-order interpolation for displacement and pore pressure can be used in the proposed method without experiencing instability.

REFERENCES

- Allersma, H.G.B. (2004). "Physical Modelling of Large Granular Systems in a Centrifuge." In *Symposium on Traffic and Granular Flow (TFG03), Delft*. <http://geo.citg.tudelft.nl/~allersma/pap160.doc>.
- Belytschko, T., Lu, Y.Y., and Gu, L. (1994). "Element-Free Galerkin Methods." *International Journal for Numerical Methods in Engineering*, 37 (2), 229–56.
- Biot, M.A. (1941). "General Theory of Three-Dimensional Consolidation." *Journal of Applied Physics*, 12 (2), 155–164.
- Borja, R.I. and White, J.A. (2010). "Continuum Deformation and Stability Analyses of a Steep Hillside Slope under Rainfall Infiltration." *Acta Geotechnica*, 5 (1), 1–14.
- Campbell, C.S., Cleary, P.W., and Hopkins, M. (1995). "Large-Scale Landslide Simulations: Global Deformation, Velocities and Basal Friction." *Journal of Geophysical Research: Solid Earth (1978–2012)*, 100 (B5), 8267–8283.
- Chen, J.S., Hillman, M., and Rüter, M. (2013). "An Arbitrary Order Variationally Consistent Integration for Galerkin Meshfree Methods." *International Journal for Numerical Methods in Engineering*, 95 (5), 387–418.
- Chen, J.S., Hu, W., Puso, M.A., Wu, Y., and Zhang, X. (2007). "Strain Smoothing for Stabilization and Regularization of Galerkin Meshfree Methods." In *Meshfree Methods for Partial Differential Equations III*, 10.1007/978-3-540-46222-4_4.
- Chen, J.S., Pan, C., Wu, C.T., and Liu, W.K. (1996). "Reproducing Kernel Particle Methods for Large Deformation Analysis of Non-Linear Structures." *Computer Methods in Applied Mechanics and Engineering*, 139 (1), 195–227.
- Chi, S.W., Lee, C.H., Chen, J.S., and Guan, P.C. (2015). "A Level Set Enhanced Natural Kernel Contact Algorithm for Impact and Penetration Modeling." *International Journal for Numerical Methods in Engineering*, 102 (3-4), 10.1002/nme.4728/full.

- Cho, S.E. and Lee, S.R. (2001). "Instability of Unsaturated Soil Slopes due to Infiltration." *Computers and Geotechnics*, 28 (3), 185–208.
- Cleary, P.W. (2004). "Large Scale Industrial DEM Modelling." *Engineering Computations*, 21 (2-4), 169–204.
- Cleary, P.W. and Campbell, C.S. (1993). "Self-Lubrication for Long Runout Landslides: Examination by Computer Simulation." *Journal of Geophysical Research: Solid Earth (1978–2012)*, 98 (B12), 21911–21924.
- Conte, E., Donato, A., and Troncone, A. (2014). "A Finite Element Approach for the Analysis of Active Slow-Moving Landslides." *Landslides*, 11 (4), 723–731.
- Duncan, J.M. (1996). "State of the Art: Limit Equilibrium and Finite-Element Analysis of Slopes." *Journal of Geotechnical Engineering*, 122 (7), 577–596.
- Guan, P.C., Chen, J.S., Wu, Y., Teng, H., Gaidos, J., Hofstetter, K., and Alsaleh, M. (2009). "Semi-Lagrangian Reproducing Kernel Formulation and Application to Modeling Earth Moving Operations." *Mechanics of Materials*, 41 (6), 670–683.
- Guan, P.C., Chi, S.W., Chen, J.S., Slawson, T.R., and Roth, M.J. (2011). "Semi-Lagrangian Reproducing Kernel Particle Method for Fragment-Impact Problems." *International Journal of Impact Engineering*, 38 (12), 1033–1047.
- Ju, J.W. (1989). "On Energy-Based Coupled Elastoplastic Damage Theories: Constitutive Modeling and Computational Aspects." *International Journal of Solids and Structures*, 25 (7), 803–833.
- Liu, W.K., Jun, S., and Zhang, Y.F. (1995). "Reproducing Kernel Particle Methods." *International Journal for Numerical Methods in Fluids*, 20 (8-9), 1081–1106.
- Simo, J.C. and Ju, J.W. (1987a). "Strain-and Stress-Based Continuum Damage models—I. Formulation." *International Journal of Solids and Structures*, 23 (7), 821–840.
- Simo, J.C. and Ju, J.W. (1987b). "Strain-and Stress-Based Continuum Damage models—II. Computational Aspects." *International Journal of Solids and Structures*, 23 (7), 841–869.
- Tang, C.L., Hu, J.C., Lin, M.L., Angelier, J., Lu, C.Y., Chan, Y.C., and Chu, H.T. (2009). "The Tsaoling Landslide Triggered by the Chi-Chi Earthquake, Taiwan: Insights from a Discrete Element Simulation." *Engineering Geology*, 106 (1), 1–19.
- Zienkiewicz, O.C., Chan, A.H.C., Pastor, M., Schrefler, B.A., and Shiomi, T. (1999). *Computational Geomechanics*, Wiley Chichester. <http://tocs.ulb.tu-darmstadt.de/92000215.pdf>.
- Zienkiewicz, O.C., Humpheson, C., and Lewis, R.W. (1975). "Associated and Non-Associated Visco-Plasticity and Plasticity in Soil Mechanics." *Geotechnique*, 25 (4), 671–689.
- Zienkiewicz, O.C., and Shiomi, T. (1984). "Dynamic Behaviour of Saturated Porous Media; the Generalized Biot Formulation and Its Numerical Solution." *International Journal for Numerical and Analytical Methods in Geomechanics*, 8 (1), 71–96.

Analysis of Morphometric Parameters for the Identification of Probable Landslide Occurrences

Kishor Kumar¹ and Yogita Garbyal²

¹Chief Scientist, Geotechnical Engineering Division, CSIR-Central Road Research Institute, P.O. - CRRI, Mathura Rd., New Delhi 110025, India.

²Research Intern, Geotechnical Engineering Division, CSIR-Central Road Research Institute, P.O.-CRRI, Mathura Rd., New Delhi 110025, India.

Abstract: Himalaya is an active mountain belt where high tectonic activities, since its formation, have been one of the major inherent and internal factors for some of the major landslide hazards. In this study, a watershed named as Patalganga located in NW Himalayan region of Garhwal between longitude 79°29'15" E-79°29'30" E and latitude 30°29'25" N- 30°29'15" N has been selected for morphometric analysis of certain parameters relevant to landslide hazard. The watershed is highly vulnerable to such phenomena because of its fragile geoenvironmental setting and a large number of landslides of different shapes and sizes have already been reported within the basin. These landslide activities have been correlated with the morphometric parameters through calculation of their areal, linear, relief and hydrological characteristics in GIS platform. Some of these morphometric indices have been capable of identifying the landslide signatures and even predict the future landslide activities. Slope length gradient index is one of the tools which has been taken as a major point of discussion in the paper which highlights the role of knickpoints in the probability of developing landslides and even the landslide dams on the river. Out of fourteen numbers of knickpoints identified, ten were found to have direct correlation with the landslide activity which has been verified from the landslide inventory maps of the area.

1. INTRODUCTION

The youngest mountain chain, Himalaya, is tectonically active, covering about 16.25% of the total geographic area of the country, is inherently vulnerable and prone to different natural hazards (Joshi et al. 2006). It measures for about 2400km in length and 370km in width which lies to the north of the Indo- Gangetic Plain and extends between latitudes 26°20' and 35°40' N and between longitudes 74°50' and 95°40' E. The Himalaya has diverse morphology yet it is characterized by mainly steep hill slopes and narrow valleys. Extreme rainfall, landslides, flash floods, debris flows, landslide dams and glacial lakes outburst and consequent flooding etc. are the main type of hazards other than its high vulnerability to the earthquake hazards.

Himalaya have experienced changes in its ecosystem and landforms, mainly due to growing population and overexploitation of natural resources in these areas. The

unplanned residential and commercial buildings, misplanned road construction, mining etc. has resulted in increasing landslide activities. Among all the natural hazards, landslides are the most common and widespread phenomena which can be predicted and controlled unlike other hazards, if properly studied.

While studying Himalayan Rivers, it was observed that their tributary watersheds possess very high steep slopes and narrow valleys with deep incision resulting in high discharge which makes the area more prone to landslide. As studied in the north-western Himalaya, hillslope adjustment to a lowering river bed via landsliding is one of a significant response (Burbank et al. 1996). In this paper, Patalganga watershed, which is a tributary of one of the prominent Himalayan Rivers i.e. Alaknanda is studied. Patalganga basin has faced big landslides resulting in damming the river in the past and still holds the fear of repetition of the likewise hazards. Such damming was experienced in 1970 on Patalganga River, on breaching of which Alaknanda River had been blocked at the confluence with Patalganga. Breaching of the dam on Alaknanda had resulted in widespread devastation on downstream (Kumar et al. 2009). Srinagar city, about 100 km downstream, was heavily inundated and filled with sand and silt. Many villages were either completely washed away or badly damaged. Landslides developed during 1970 in Patalganga valley still reactivate almost every year during monsoon however, magnitude of such damages have so far been smaller but has the potential to become disastrous.

The use of satellite images has become very useful these days especially for geomorphology, in obtaining the quantitative measurements and performing geomorphic analysis (Hayden et al. 1886; Ulrich et al. 2003). It gives reliable solutions when needed quickly. ASTER DEM is most widely used for its easy availability. Despite being less accurate than higher resolution data, the knowledge of geomorphic setting and accurate use of threshold values can give efficient results. Himalaya being tectonically active, the morphometry plays an important role in quantifying various aspects that govern landscaping of the basin. Further implication of morphometric parameters for identifying the existing and most susceptible landslide prone areas which affects the drainage system is also investigated. Two geomorphic indices viz. SL Index and River profile have been used in several studies to identify active tectonic deformations in an area. Landsliding may have significant impact on the drainage network of mountainous areas, where pronounced knickpoints can develop along the stream thalweg, influencing long-profile shape and trends (Galve et al. 2014). It is studied that, if the extreme conditions such as extreme rainfall, earthquakes are excluded and only stream incision is considered as the main triggering mechanism, then knickpoint and landslide show a significant relationship. When incision varies in a systematic way, for example, which results in the upstream knickpoint migration, the majority of landslides will occur downstream of the knickpoint showing the relationship between knickpoints and landslides. Stream incisions are driven by migrating knickpoints which can impose a spatial and temporal pattern on landslide distribution (Bigi et al. 2006).

Historically, Alaknanda River had caused flash flooding due to breaching of several landslide dams on its course or on its tributaries in the Alaknanda valley. Such flooding has claimed many lives and destroyed property worth several billions in the past. The

potential for future events of damming remains, as there are many landslides directly intercepting the connected major streams and rivers that can form dams and lakes. So identifying these vulnerable areas prone to formation of hazardous landslides and consequent dams/ lakes in the stream path is a step towards quick mitigation or forewarning to prevent immediate loss of life. Knickpoints relate with landslide probable areas which could directly discharge onto river with a potential of damming it. The damming also causes the local change in the equilibrium and thus can also form a new knickpoint.

2. STUDY AREA

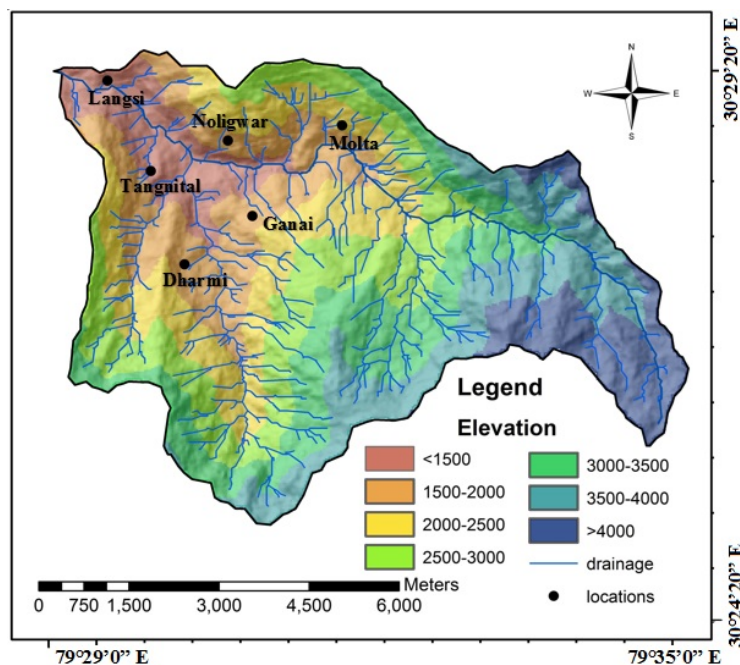


FIG. 1 Location map of Patalganga watershed using DEM.

A Patalganga basin located in NW Himalayan region of Garhwal under Chamoli district, between longitude 79°29'15" E-79°29'30" E and latitude 30°29'25" N-30°29'15" N. covers an area of 48.69 sq. km. The altitude between the mouth of the basin and highest point on it ranges from 1289m to 4186m (**FIG. 1**). The mouth of the basin ends with a narrow valley over which a major highway i.e. NH-58, connecting to this region from rest of the country runs. The highest rainfall usually occurs during the monsoon period from May to September. The average annual rainfall in this region

recorded as 500–600 mm. As per the seismic zonation map of India (IS 1893-2002) the area falls in the category of seismic zone V.

The higher reaches of the basin which have steep slopes are thinly populated whereas the habitation is mostly confined to the valley regions. Slope instability in the area is mainly controlled by valley slopes, their orientational relationship with the attitude of discontinuity surfaces, amount and nature of loose deposits on these slopes, rainfall pattern, nature of rocks exposed, and structural and tectonic features present, besides human interaction in the terrain (CGWB, Chamoli district report). However, the main triggering factors for landslides are the intense rainfall, earthquakes and anthropogenic activities. when, within a basin a new landslide develops or older get reactivated, it may have its toe at streambed or away from it in both the cases the debris discharges onto the

river bed which has the potential to generate the knickpoints, epigenetic gorges and even stream blockages (Galve et al. 2014). Such blockade on the river Patalganga had been experienced during 1970 which later breached and blocked the main Alaknanda at the junction on breaching of which there was wide scale devastation up to 100 km downstream.

3. GEOLOGY AND GEOMORPHOLOGY

Catchment of Patalganga, comprises of both Lesser and Higher Himalayan rocks. Broadly, the rock types exposed in the area belong to Pre-Cambrian-Late Paleozoic age (Kumar et al. 2009). The two main lithological units Garwal Group and the Central Crystallines are separated by the Main Central Thrust (MCT). Except the major thrust belts like MCT, several local faults also govern the tectonic setting of the area. The lithology of this area mainly comprises of Garhwal Group of rocks like dolomites, quartzites and slates, while in some higher elevations gneisses, schists and high grade metabasics of Central Crystalline Group of rocks are also found. Rocks are often highly sheared and weathered. Quartzites seem to be jointed and thickly bedded, slates on the other hand are thinly bedded. Shearing in some areas caused the filling of gauge materials in the jointed rock mass. The gneisses are hard and massive but in few locations these are observed as loose boulders. Quaternary sediments, mainly composed of assorted moraines and hill wash materials of Pliocene glacial period, also covers a huge thickness in the basin.

4. METHODOLOGY

For extracting Hydrological features, Digital Elevation Model (DEM) data have been used to serve as inputs to various models. DEM are elevation data collected by remote sensing methods or by transforming the contour maps to raster format by digitizing and surface analysing (Hosseinzadeh 2011). Currently, the availability of high-resolution DEMs and more frequent use of GIS software in quantitative analysis of geomorphic methods have caused substantial improvement of studying large areas in a short time cost-effectively. In this paper, the ASTER DEM satellite data is used for calculating the geomorphometry of the area. ASTER DEM, with a 30m*30m grid cell size in raster format, received from Terra satellite, is used to extract the drainages and the watershed area. ArcGIS software, version 9.3 (ESRI 2008) having hydrological tools was used to extract drainage channels. Different geomorphic indices are used to analyse drainage networking system. Due to high sensitivity of river channels to minor changes in channel morphology or slope gradient, the quantitative results could decipher recent tectonic activity. These changes lead to formation of new equilibrium conditions in short span and thus these new equilibrium, different from the past, discards the anomalies in river network and can be considered recent tectonic activity in cases other factors as lithology or climate are discarded (Galve et al. 2014).

The morphometric parameters like areal, linear, stream network, relief and topographical are calculated to have a general idea about the tectonic activity of

Patalganga watershed. Quantitative analysis for all the parameters was done using Arc GIS, however, detailed study was carried out only on few parameters which are helpful in identifying the landslide. Some of the parameters like Valley Floor index ratio (Vf), Drainage density (Dd), Elongation ratio (Re), Hypsometric integral (HI) and Slope length gradient index (SL) give an idea about the river erodibility strength for knowing whether the river can discharge debris enough to create natural damming. These parameters also give information about the river valley incision which is an important phenomenon for this study to locate landslide through knickpoint migrations. The Stream Length-Gradient index, has been demonstrated for detecting homogeneous lithological anomalies on stream-profiles related to active tectonics and other sub-surface and surface processes (Doranti-Tiritan et al. 2014). The correlation between the active landslides and the location of anomalies in the SL Index graph for the Patalganga watershed tests the suitability of it to support landslide detection. The longitudinal profile of a channel determines the gradient of a river and their behaviour along the channel from the headwater to mouth (Doranti-Tiritan et al. 2014). A graph is prepared in semi-logarithmic scale showing both SL index and longitudinal profile such that the knickpoints are demarcated. The knickpoints present are further marked on the DEM to find the location on the watershed. The landslide inventory map has already been prepared, also through GSI landslide zonation and Google Earth, the present landslide areas are digitized. The location of knickpoints and the existed landslides are correlated. The importance of the study of knickpoint, for identification of landslides and subsequent strategy for prediction and prevention has been proved useful as a tool for preliminary studies of landslide hazard in the Himalaya.

5. RESULTS AND INTERPRETATIONS

The calculated values for the important indices as shown in the (**Table No. 1**) suggest that the watershed has high stream incision than lateral erosion with V shaped valleys, high erosional activities with more overland flow than infiltration and tectonically uplifting areas. The high incision activity in the area are significant to knickpoints as well as the landslide formation of the area. High erosional activity with overland flow suggest that the area is prone to erosional activities with the potential of high discharge and thus forming natural dams in the extreme conditions.

Graph of slope length gradient vs. flowlength gives the areal distribution of anomalies. The values has been filtered to discard background values related to the different outcropping lithologies and finally, the anomaly map has been obtained. Using longitudinal profile and the slope length gradient index by plotting on the same graph shows that the anomalous index values and the sharp changes in the profile elevation demarcates the knickpoints. Locations of the knickpoints when

TABLE No. 1 Morphometric indices used for the landslide investigation.

Morphometric indices	Formulas	Result	Comments
Drainage density (Dd) Hortan, (1945)	$Dd = \frac{L}{A}$ <p>where, L=Total length of stream, A= Area of basin.</p>	1.009	High Dd ¹
Elongation ratio (Re) Schumn (1956)	$Re = \frac{\sqrt{\frac{A}{\pi}}}{Lb}$ <p>where, A=Area of basin, $\pi=3.14$, Lb=Basin length</p>	0.705	Elongated ²
Asymmetric factor (AF) Hare and Gardner (1984)	$AF = \frac{Ar}{A}$ <p>where, Ar is area right to the main drainage, A is total catchment area</p>	25.48	Tilted ³
Hypsometric integral (HI) Strahler (1964)	$HI = \frac{(\text{mean elevation} - \text{min. elevation})}{(\text{max. elevation} - \text{min. elevation})}$	0.424	Mature stage ⁴
Stream length index ratio (SL) Hack (1973)	$SL = \frac{\Delta h}{\Delta L} * L$ <p>where, L is the total channel length from the midpoint of the reach upstream to the highest point on the channel, and $\Delta H/\Delta L$ is the channel slope, ΔH is change in elevation for a particular channel of the reach with respect to ΔL that symbolizes the length of the reach</p>	14099-11.65 Average-1231.3	Active uplift ⁵
Valley floor width to height ratio (Vf) Miller (1991)	$Vf = \frac{2Vfw}{(Eld - Esc) + (Erd - Esc)}$ <p>where, Vfw is valley floor width, Eld is elevation of left drainage divide, Erd is elevation of right drainage divide, Esc is elevation of valley bottom</p>	0.07	Active region ⁶

¹More overland flow than infiltration, tectonically active; ²Incision more than lateral erosion. ³Prominent Tilting on the left facing downstream; ⁴More erosion than tectonic uplift; ⁵Knickpoints are present showing tectonic control; ⁶Area of uplift and deep stream incision, v-shaped valley.

plotted in the DEM are correlated with the locations of the identified landslide among which the major Patalganga landslide location show very high anomalous values for S.L. index and profile break for forming knickpoints (**FIG. 2**). These points/areas have been checked by a detailed landslide inventory map of Patalganga watershed and, the 90% of the identified anomalies (10 out of 14 anomalies) resulted to be connected to stream modifications due to active or partially reactivated landslides (**FIG. 3**).

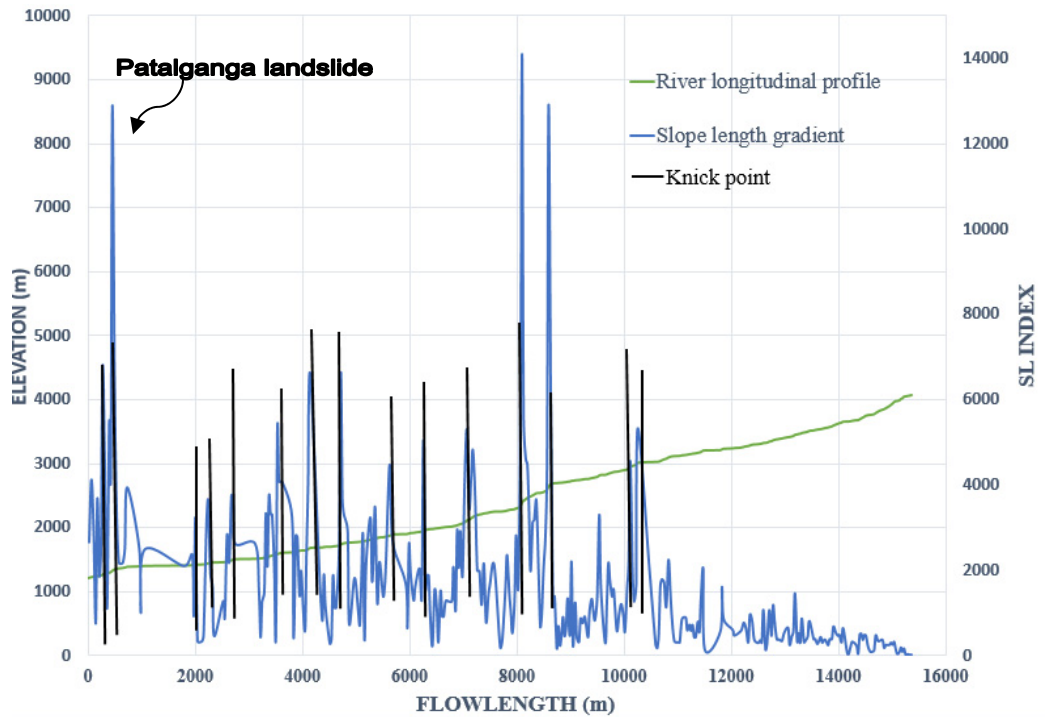


FIG. 2 Showing the anomalous values for slope length index and slope break in the river profile together used to mark knickpoints.

These pronounced landslides in relation to knickpoints are those which affect the drainage system directly by discharging onto the river or by the action of stream incision, knickpoint migration and by forming landslide damming. Generally, at the main stream and regional scale the knickpoints marks the tectonic structures like faults, however, through the correlation of the present landslide areas and the knickpoints it is very well understood that in tributary areas the knickpoints and the landslides show a good relationship.

The knickpoints of a watershed can also be used as a primary action for knowing the landslide hazard potential areas. Once the potential areas are known the detailed investigation, as per the requirement, can be carried out for detailed analysis and design of preventive/controlled measures for disastrous landslides.

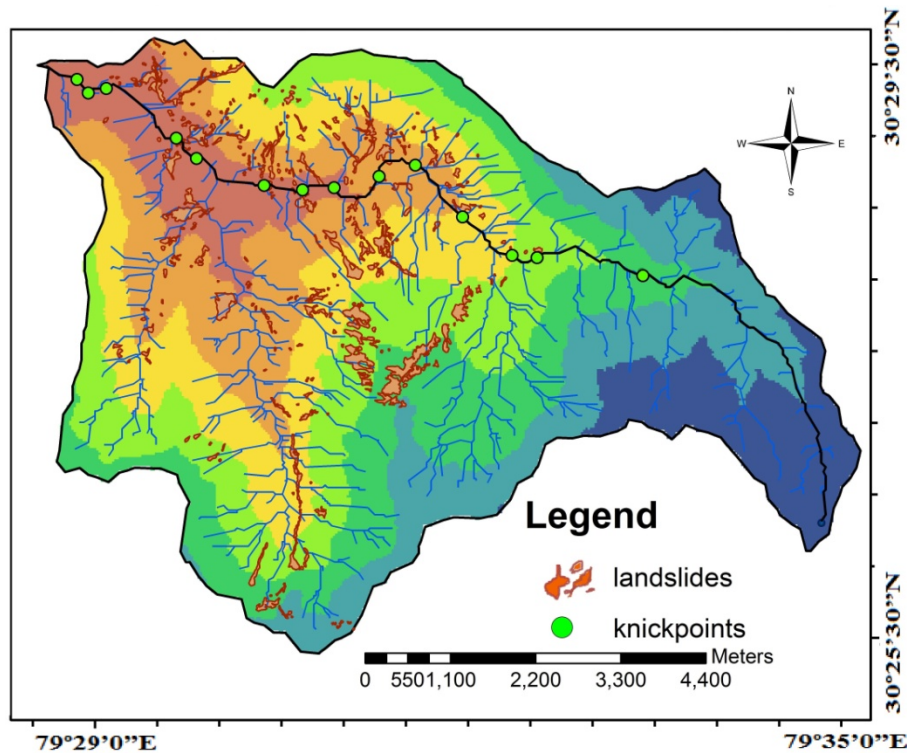


FIG. 3 Knickpoints on the main stream and landslides affecting the channel in the area show the similar nature of their occurrences.

6. DISCUSSION AND CONCLUSION

Generally, morphometric indices have been used for finding the tectonic activity on a regional scale, however, when used to smaller scale, as in the case of present study, same can be used for demarcating the landslide prone areas. Utilization of the data should be done according to the need of the study. Since the digital elevation map (DEM) is used, the degree of quality and accuracy of DEMs and the nature of algorithms are basic questions for authenticity. It is said that a better resolution data is most appropriate however the non-availability or the high pricing of these high resolution images for research purpose makes the other easily available ASTER data high on need. The precautions for using data is kept in knowledge, to minimise the errors. It is important to choose the appropriate use of threshold value according to the area which makes the errors minimum and enough to take a first fair idea about the peculiar characteristic locations with knickpoints and landslide. ASTER DEMs have an enough resolution for extracting first and second-order Rivers in mountainous areas with 25 threshold values without of resampling elevation data (Hosseinzadeh 2011). At this threshold the drainages of the mountainous areas extracted from ASTER DEM show best agreement among different geomorphic units. Once the quality of the data is satisfactory the morphometric indices are calculated using the Arc GIS platform.

This study mainly focuses on the use of knickpoints for identifying landslide risk areas. For Patalganga watershed the slope length index and river profile are used to find knickpoints. The locations of the knickpoints show a significant relationship with the locations of the landslides present in this area. Hence, when a landslide is affecting the drainage system directly by discharging huge amount of sediment to form stable natural damming or those landslides which are formed due to stream incision or knickpoint propagation making the slopes of the valley unstable, they will have an impact on the drainage system and an anomalous character is noticed. Using the quantitative approach of morphometry, one can suggest that knickpoints, rather than being an indicator of tectonic setting in regional scale, can also help to infer the landslide locations in tributaries scale, which are not generated on extreme natural conditions like earthquake or cloudburst. Some of the knickpoint locations which are identified through graph (FIG. 2) having no present activities of landsliding can be taken as a risk prone areas where probability of failures are much more than the surrounding locations. Hence these risk prone areas can be highlighted to give more emphasis during the field investigation. The detailed mapping of the identified knickpoints should be used to minimise the probable risk and also as forewarning to the people.

7. REFERENCES

- Bigi, A., Hasbargen, L. E., Montanari, A., and Paola, C. (2006). "Knickpoints and hillslope failures: Interactions in a steady-state experimental landscape." *Geological Society of America Special Papers*, 398: 295-307.
- Burbank, D. W., Leland, J., Fielding, E., Anderson, R. S., Brozovic, N., Reid, M. R., and Duncan, C. (1996). "Bedrock incision, rock uplift and threshold hillslopes in the northwestern Himalayas." *Nature*, 379(6565): 505-510.
- CGWB (Central Ground Water Board). "Report on Chamoli district at a glance." http://www.cgwb.gov.in/District_Profile/Uttarakhand/Chamoli.pdf
- Doranti-Tiritan, C., Hackspacher, P.C., De Souza, D.H. and Siqueira-Ribeiro, M.C. (2014). "The Use of the Stream Length-Gradient Index in Morphotectonic Analysis of Drainage Basins in Pocos de Caldas Plateau, SE Brazil." *International Journal of Geosciences*, 5(11): 1383.
- Galve, J.P., Piacentini, D., Troiani, F. and Della Seta, M. (2014). "Stream Length-Gradient Index mapping as a tool for landslides identification." *Mathematics of Planet Earth* (pp. 343-346). Springer Berlin Heidelberg.
- Hack, J.T. (1973). "Stream-profile analysis and Stream-gradient index." *U.S. Geological Survey Journal of Research*, 1: 421-429.
- Hare, P.W. and Gardner, T.W. (1985). "Geomorphic indicators of vertical neotectonism along converging plate margins, Nicoya Peninsula, Costa Rica." *Allen and Unwin, Boston*: 75-104.
- Horton, R.E. (1945). "Erosional development of streams and their drainage basins; hydro physical approach to quantitative morphology." *Geological society of America bulletin*, 56(3): 275-370.

- Hosseinzadeh, S.R. (2011). "Drainage Network Analysis, Comparison of Digital Elevation Model (DEM) from ASTER with High Resolution Satellite Image and Aerial Photographs." *International Journal of Environmental Science and Development*, 2(3): 194.
- Joshi, V. and Kumar, K. (2006). "Extreme rainfall events and associated natural hazards in Alaknanda valley, Indian Himalayan region." *Journal of Mountain Science*, 3(3): 228-236.
- Kumar, K., Prasad, P. S., Kimothi, S., and Mathur, S. (2009). "A Geomorphological Appraisal of Patalganga Landslide on National Highway-58, Garhwal Himalaya, Uttranchal." *Indian Geotechnical Conference*, IGS Guntur Chapter, Guntur 2009.
- Kumar, K., Devrani, R. and Mathur, S. (2010). "Landslide Hazard Potential Analysis using GIS, Patalganga valley, Garhwal, Western Himalayan region of India." *European Journal of scientific Research*, Vol. 45, No.3: 346-366.
- Miller, J. R., Ritter, D.F. and Kochel, R.C. (1990). "Morphometric assessment of lithologic controls on Drainage Basin evolution of the Crawford Upland, South-Central Indiana." *American Journal of Science*, v. 290: 569-599.
- Schumm, S.A. (1956). "Evolution of drainage systems and slopes in badlands at Perth Amboy, New Jersey." *Geological Society of America Bulletin*, v. 67: 597-646.
- Strahler, A.N. (1964). "Quantitative geomorphology of drainage basins and channel networks." *Handbook of Applied Hydrology*, McGraw Hill Book Cooperation, New York: 4-76.

Design and Implementation of a Spatial Database for the Abu Dhabi Municipality Geohazard Management System

Raghav Ramanathan¹; Mazen E. Adib²; Walid Dawoud¹; Melih Demirkan²; Bulent Hatipoglu¹; Giridhar Kolan Reddy²; Michael Rosenmeier¹; and Cagri Cinkilic¹

¹RIZZO Associates, 500 Penn Center Boulevard, Suite 100, Pittsburgh, PA 15217.

²Abu Dhabi City Municipality, Town Planning Sector, Abu Dhabi City Municipality P. O. Box 263, Abu Dhabi, UAE.

Abstract: One of the major driving forces behind the recent popularization of spatial information is the increasing availability of spatial data from governmental and commercial sources. A large number of spatial data depots, digital geolibraries and spatial data warehouses have been developed or are under development in all sectors of modern society. The Municipality of Abu Dhabi City (ADM) recently developed a GIS portal that works as a focal point of information and spatial data-related assets. An important component of this GIS portal is the geohazard information management system (GHIMS), a spatial database system that stores and manages geotechnical, hydrogeological and geophysical data along with interpreted geology, lithology and geohazard risk maps. This paper discusses the approach towards the design and implementation of a spatial database that forms the backbone the GHIMS. All relevant data and information were initially stored in an ESRI geodatabase using a feature based model to maintain consistency and conformity to projection and resolution standards. Configuration controls, attribute domains and topology elements were applied to appropriate feature classes to ensure and maintain data quality standards. Key factors influencing the geodatabase design were data volume, data format and extent of analyses. The geodatabase has feature datasets and raster catalogs that provide geotechnical, geological, and hydrogeological information, and damages related to buildings and infrastructure. The geodatabase also stores intermediary information necessary for generation of geohazard risk maps, such as reclassified rasters, distribution maps, model-builder toolboxes, and tools. The geodatabase was then migrated to the Oracle® Spatial environment. Key assumptions, constraints, and decisions taken during the geodatabase design are also discussed along with factors that may affect the database performance, extensibility, and maintainability.

INTRODUCTION

In the last few decades, the city of Abu Dhabi has witnessed rapid infrastructure development and urbanization (UPC, 2007). The Abu Dhabi Municipality (ADM) is responsible for sustainable development of the region and has implemented a significant number of projects to establish modern infrastructure for the city. These projects have resulted in acquisition of large volumes of geotechnical and geological data from site investigations. The ADM also has amassed massive amounts of spatial data related to city planning and satellite imagery. This extensive volume of data acquired is routinely accessed by internal and external users for various purposes (Geotechnica, 2014).

The ADM recently developed a GIS portal – ‘Makani’ to archive existing data and to manage continuous influx of newer data. The GIS portal works as a focal point for accessing all spatial data related assets. Makani also facilitates exchange of spatial data and GIS services to public and private entities that are involved with the ADM. The spatial data accessible through Makani is predominantly used in planning, designing and construction of various infrastructure projects. The Makani integrates different spatial data assets such as survey stations, seismic hazards, planning and welfare and geohazards (ASM, 2011).

An important component of Makani is the Geohazard Information Management System (GHIMS) – a spatial database system that stores and manages geotechnical, hydrogeological and geophysical data along with interpreted geology, lithology and geohazard risk maps. The primary purpose of the GHIMS is to serve as an inventory for all data that provides information on the local geohazards in the Abu Dhabi Municipality such as borehole locations, logs, interpolated subsurface information, groundwater contours, subsurface void locations, buildings and infrastructure damaged due to the prevailing geohazards. The GHIMS also stores a variety of hazard maps developed using geospatial and statistical techniques based on pattern analysis of a range of parameters contributing to hazard.

The subsurface conditions in the Abu Dhabi City pose a variety of engineering problems (Tose and Taleb, 2000). Much of the urbanized Abu Dhabi City including majority of the coastal islands are reclaimed land covered by backfill material placed in an uncontrolled manner (Price et al., 2012). Geotechnical boring logs also indicate presence of karst topography. The subsurface conditions along with fluctuations in groundwater levels and the local lithology pose a variety of geohazards such as development of solution cavities, cavity collapse, ground surface subsidence and settlement, presence of loose and soft soil and perched groundwater conditions. Significant damage to infrastructure and buildings that is attributed to local geohazards has been observed throughout the municipality. The GHIMS enables engineers, consultants and ADM officials to make decisions related to city planning, sanctioning new construction projects and assessing risk, reviewing ground conditions and accessing existing reports. This paper discusses the design decisions and working aspects of the comprehensive geohazard management system developed.

DESIGN OF GEODATABASE

In the last decade, GIS and database management systems have been widely developed to manage and analyze spatial data relating to geologic, geotechnical and karstic features (Cooper et al. 2007; Lei et al. 2001, Gao et al. 2005). Spatial data manipulation in GIS environments is a key function of any GIS application (Demers, 1997). There are numerous advantages to manage spatial information and GIS data layers in a geodatabase environment as it allows for coordinated relationships between feature classes, which enable the creation of domains thereby reducing errors during data entry (Orrnsby and Burke, 2004). A geodatabase enables storage in a single file or folder and is more efficient for storage of large datasets (FLNRO, 2013). The geodatabase supports a model of topologically integrated feature classes, similar to the coverage model. It also extends the coverage model with support for complex networks, relationships among feature classes, and other object-oriented features (MacDonald et al., 2001).

Design Considerations

An ESRI geodatabase called Geohazard Information Management System (GHIMS) was developed to store, manage, and analyze data relating to karstic features, such as cavities, surface subsidence, and presence of soluble bedrock formations, in addition to other information contributing to local geohazards. All data storage and management were performed in ArcCatalog and all data manipulations were performed in ArcMap. The GHIMS geodatabase is a tool developed to analyze regional geohazards within the ADM. The geodatabase contains a specific set of feature datasets, feature classes, raster catalogs, and raster classes together with feature attributes, subtypes, and domains; suitable for a variety of geologic, hydrogeologic, and risk assessment maps. In addition to basic geology (lithology, cavity location, etc.), the geodatabase includes damaged buildings and roads survey data, susceptibility of cavity to collapse, and geohazard risk assessment.

The following design standards were established for the GHIMS geodatabase based on review of industry practices (Geomatics Yukon, 2011; Lovell John Ltd, 2005): (i) All feature classes should be stored within relevant feature datasets, (ii) Feature datasets may be used to separate data into logical groups when many feature classes are being distributed as a package inside a single database, (iii) Feature datasets must conform to the projection, cluster tolerance and resolution, and naming conventions of ADM, (iv) All feature classes must conform to configuration, naming conventions, and metadata standards of ADM, (v) All feature classes must have descriptions, (vi) Where appropriate, feature classes should have attribute domains and topology elements applied to them and (vii) Model-Builder models used in the creation of data should be stored in toolboxes within the databases.

General standards relating to naming conventions were also established. A general standard is applicable for all entities of the geodatabase. Some entities might have additional standards applicable to specific entity types. These standards were applied for data production, publication and distribution. Some of the standards established were: (i) Only alphanumeric characters are used, (ii) Underscore character would be used to separate words, (iii) special characters are not allowed, and (iv) if abbreviations are to be used, standard abbreviations will be used. If letters are to be removed to form an ad-hoc abbreviation, removal-of-vowels-first method will be applied. An additional standard for feature classes stored within feature datasets is the inclusion of a 2 letter abbreviation of the respective feature dataset the feature class will be stored in. Table 1 shows the major components of the GHIMS geodatabase. Also, since the data in the geodatabase is to be published to Spatial Database Engine (SDE) a 32- character limit is applied to feature class names. All data was Geo-referenced to the following ADM standard coordinate reference system.

Table 1. Details of all feature datasets stored within the GHIMS geodatabase

Name	Abbreviation	Type	No. of Datasets
BOREHOLES	BH	Feature Dataset	2
CUT/FILL	CF	Feature Dataset	2
DAMAGE SURVEY	DS	Feature Dataset	8
GEOLOGY_MODEL	GM	Feature Dataset	8
HYDROGEOLOGY	HG	Feature Dataset	6
KARST CAVITY	KC	Feature Dataset	6
SABKHA DISTRIBUTION	SD	Feature Dataset	2
CAVITY PROBABILITY	CP	Raster catalog	3
CUT FILL DISTRIBUTION	CD	Raster catalog	2
GEOLOGY_ADM	GA	Raster catalog	54
HYDROGEOLOGY LAYERS	HR	Raster catalog	6
INTEGRATED RISK	IR	Raster catalog	2

The key factors influencing geodatabase design depend on current industry practices and the project specific goals. The GHIMS geodatabase was designed with the ultimate plan for streamlining three important facets of a database, namely (i) Project oriented design, (ii) Data format, and (iii) Data volume and analysis. The GHIMS geodatabase houses datasets providing information relating to three different aspects of the sub-surface environment: geotechnical, geological, and hydrogeological information. Therefore, it was important to categorize and group datasets based on the information provided by each dataset. Beside the broad classification established above, there are project specific components or groups that house certain intermediary files that are vital in generating the final project deliverables.

The GHIMS geodatabase houses both vector and raster datasets contributing information on the same aspect. Owing to the difference in data formats, these datasets cannot be grouped together based on the project oriented design structure. Therefore, vector datasets for a particular aspect are grouped together as feature datasets while raster datasets contributing information on the same aspect are grouped together in raster catalog format separate from the vector datasets owing to ArcGIS geodatabase limitations relating to grouping different data types.

The geospatial information collected and analyzed covers a wide aerial extent, and the distribution of data is scattered over the study area. Not all regions within the ADM extent have the same data density. Also, the spatial extent of the source data is not common for all datasets. Therefore, the current project extent of the geodatabase was decided based on the data distribution of all datasets. Regions with poor data coverage were not included in the extent. It should be understood that, not all regions within the geodatabase extent have good data coverage. Some of these regions were included either, for maintaining a spatially continuous study area rather than discretized parcels or to meet certain project objectives despite poor data coverage.

Database Architecture

Feature Datasets

The “BOREHOLES” dataset has 2 feature datasets. The first feature class “BH_GIMS”, stores location information relating to 22,000 boreholes within the Abu Dhabi Municipality. These boreholes include legacy data with drilling dates ranging from 1978 to as recent as 2013 with provision to update for further addition of boreholes. Primary source for the data stored in this feature class is a gINT based borehole database maintained by the ADM called Geotechnical Information Management System (GIMS). The second feature class is a subset of “BH_GIMS,” in that it contains only those boreholes that were qualified based on borehole data quality and spatial distribution for use in subsurface 3D modelling. Additions or updates to this feature class have to be manual and performed on a project-by-project basis.

The “CUT_FILL” dataset stores two feature classes; namely, “CF_ANTH_CHNG” and “CF_DRDG_LN.” The “CF_ANTH_CHNG” feature class provides the spatial extent of various types of anthropogenic changes to the landscape such as excavation, backfilling and dredging. “CF_DRDG_LN” feature class provides location of the dredged channels along the Abu Dhabi coast. Both these feature classes were derived from satellite images.

The “DAMAGE_SURVEY” dataset stores eight feature classes. “DS_ASPHLT_CR” feature class stores the location of cracks observed on asphalt pavements and is derived from Global Positioning System (GPS) waypoints recorded by during field visits to regions with damaged buildings, roads, pavements, and infrastructure. “DS_DMGD_BLDNG” feature class provides the locations of damaged houses identified from public housing reports and inspection.

“DS_DMGD_RD” feature class provides the locations of Damaged Roads identified within the ADM extent from various forensic geotechnical reports and inspections performed at locations of distress. “DS_DPRSSION” feature class provides the locations of surface depressions identified from forensic geotechnical reports. “DS_RPRD_DPRSS” feature class provides the locations of surface depressions identified in within the ADM extent that were remediated or rectified. “ERRSNL_FSSR” feature class contains the locations of erosional fissures observed within the ADM extent. “DS_INSPCTD_HS” feature class provides the locations of damaged houses identified from Public Housing reports that were inspected in detail by qualified engineers on site. “DS_RD_CLLPS_LN” feature class contains the locations of GPS waypoints along collapsed roads observed during field visits. All information for these feature classes is obtained from forensic geotechnical reports provided by ADM and inspections performed on site during field visits as part of damage survey assessments of buildings, roads, pavements, and infrastructure. Additions or updates to this feature class can only be made if a recently damaged housing plot was inspected by a qualified team of engineers. The updates/additions will have to be made manually.

The “HYDROGEOLOGY” dataset contains six feature classes related to hydrogeological condition within the ADM. “HG_DWTRNG_LOC” This feature class is a point dataset, which provides the locations of dewatering projects based on dewatering permit applications and reports provided to ADM for approval by local and international consultants and contractors. “HG_EAD_WLL” feature class provides the locations of monitoring wells maintained by the Environmental Agency of Abu Dhabi (EAD). This point dataset is derived from information provided by the EAD and is presented in a GIS format. “HG_EAD_VES” feature class provides the locations of wells maintained by the EAD with Vertical Electrical Sounding results. “HG_STTC_GWL” is a point feature class that stores the elevation of static groundwater level along with location information obtained from the GIMS database. “HG_GWL_CNTR” is a polyline feature class that stores information on the static groundwater elevation in 5m contour intervals. This file is derived from interpolation between points stored in the “HG_STTC_GWL.” The “HG_PND_WTLND” is a polygon feature class that provides the location of surface water bodies or wetlands. The polygons are derived from satellite imagery by the process of digitization.

The “KARST_CAVITY” feature dataset contains six feature classes related to karstic topography and features. “KC_CVT_CLLPSB” is a point feature class that shows the distribution of stable or unstable cavities. The stability of cavities depends on a series of stability charts produced from geotechnical modelling and analysis. Updates or additions to this layer is an elaborate process and involves geotechnical interpretations and intensive modeling and post processing efforts. “KC_HALITE_BH” is a point feature class that provides the locations of boreholes that have halite or rock-salt listed in the geology description of the boring log. “KC_OLD_RSK_MP” is a polygon feature class that represents the cavity risk map developed by a consulting firm based on geophysical studies. “KC_SLT_LR” is a polygon feature class that provides the possible spatial extent of sub-surface soluble

halite zones. “KC_VD_DPTH” is a point feature class, which stores information relating to the presence of cavities or voids, and the depth to these cavities or voids based on data from borehole log descriptions from the GIMS database.

The “SABKHA_DISTRIBUTION” feature dataset contains two feature classes; namely “SD_SABKHA” and “SD_SOFT_SOIL”. The SD_SABKHA feature class is a polygon dataset that provides the spatial extent of coastal and inland sabkha. Sabkhas are a flat area prone to periodic inundation and evaporate depositions, dominated by carbonates or sulphates (Al-Farraj, 2005). This is derived from geology maps developed by the Abu Dhabi Ministry of Energy (MoE). The SD_SOFT_SOIL is a point feature class that stores the cumulative thickness of soils with a field N (Standard Penetration Test [SPT] Blow count) value of less than ten. This feature class is derived from post processing the GIMS database and then converting the post processed data into a point feature class.

Raster Catalogs

“GEOLOGY_ADM” is a catalog of rasters providing top elevations, bottom elevations, and cumulative thickness values for each subsurface lithology as extracted from subsurface 3D modeling results. HYDROGEOLOGY (HR) raster catalog is a collection of all rasters that provide information relating to the local hydrogeology. These raster provide surface elevations of groundwater level, top of bedrock, and groundwater flow velocity (calculated from numerical models). INTEGRATED_RISK (IR) is a raster catalog of intermediary raster files and the final raster file that provides the classification of the ADM into Very High Risk (raster values ranging from 50 – 100), High Risk (raster values ranging from 30 – 50) and Moderate to High Risk (raster values ranging from 10 – 30) based on the risk score calculated. Each raster pixel denotes the risk score calculated for that particular pixel. CAVITY_PROBABILITY (CP) raster catalog consists of intermediary cavity probability files and the final cavity probability map, which is stored as an integer raster file. Regions of low probability, low to moderate probability, moderate to high probability, high probability, and very high probability areas are delineated in the probability map, thereby providing information on the zones more susceptible to cavity formation. Figure 1 shows the GHIMS geodatabase architecture.

IMPLEMENTATION OF WEB-BASED SYSTEM

Web based GIS systems or web map applications enable access to data and information from any location (Kimmance et al., 1999). Web-based central database is used to enable effective data collection, data maintenance and communication (Lan et al., 2009). To enable information stored in the GHIMS geodatabase to be accessible via the web, the data stored in the geodatabase needs to be uploaded onto the ADM GIS web portal, Makani. The Makani web portal is supported by Oracle® 11g, a Relational Database Management System (RDBMS) for data management and

storage on ADM servers, therefore the geodatabase needs to be migrated to a relational database format. To effectively implement the geodatabase into a relational database all relational spatial tables have the same name as its corresponding feature class as given in Table 2. For data consistency and to simplify the data upsizing process into oracle database; field names in both oracle spatial tables and in the geodatabase feature class were kept the same. For the end user; each feature class was provided by detailed description also each field was provided by descriptive alias

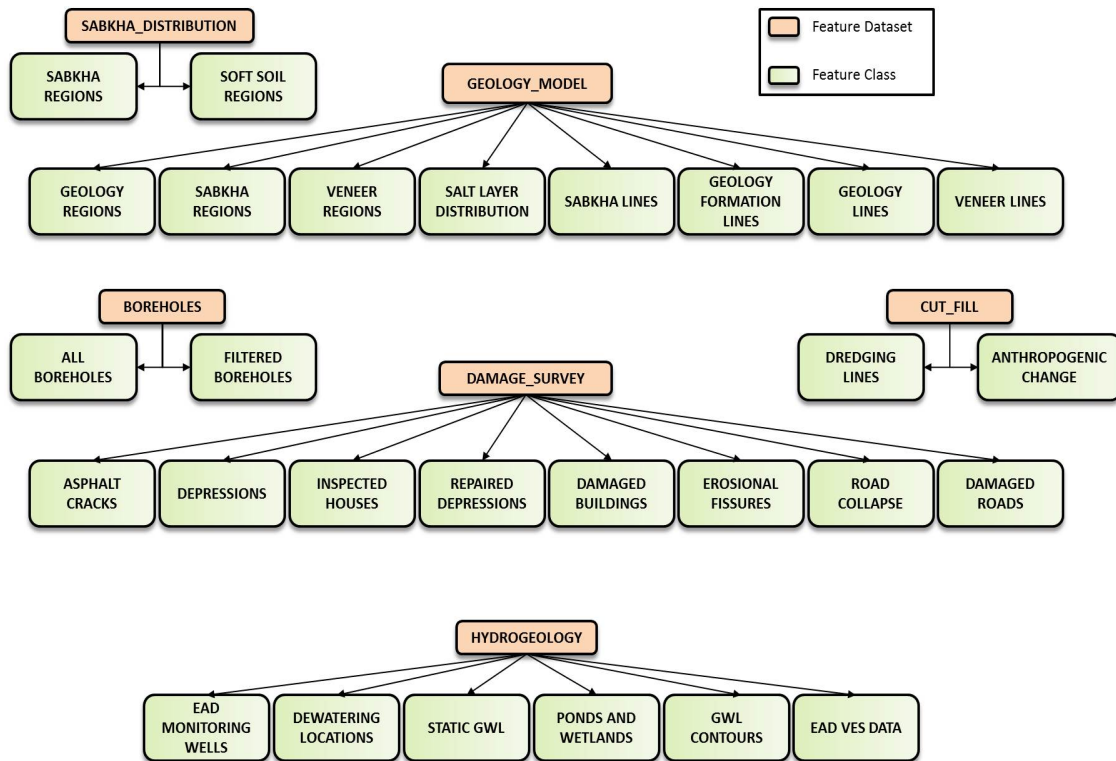


FIG.1. The GHIMS geodatabase architecture showing some of the feature datasets and respective feature classes along with the raster catalogs

Table 2: Oracle© spatial tables and GHIMS geodatabase mapping

Oracle© Spatial Table Name	Feature Class Name	
	Feature Dataset Name	Feature Class Name
BH_GIMS	BOREHOLES	BH_GIMS
CF_ANTH_CHNG	CUT_FILL	CF_ANTH_CHNG
CF_DRDG_LN	CUT_FILL	CF_DRDG_LN
DS_ASPHLT_CR	DAMAGE_SURVEY	DS_ASPHLT_CR
DS_DMGD_BLDNG	DAMAGE_SURVEY	DS_DMGD_BLDNG
DS_DMGD_RD	DAMAGE_SURVEY	DS_DMGD_RD
DS_DPRSSION	DAMAGE_SURVEY	DS_DPRSSION
DS_ERRSNL_FSSR	DAMAGE_SURVEY	DS_ERRSNL_FSSR
DS_INSPCTD_HS	DAMAGE_SURVEY	DS_INSPCTD_HS
DS_RPRD_DPRSS	DAMAGE_SURVEY	DS_RPRD_DPRSS
DS_RD_CLLPS_LN	DAMAGE_SURVEY	DS_RD_CLLPS_LN
GM_FRMTN_LN	GEOLOGY_MODEL	GM_FRMTN_LN
GM_GEOL_LN	GEOLOGY_MODEL	GM_GEOL_LN
GM_GEOL_RGN	GEOLOGY_MODEL	GM_GEOL_RGN
GM_SBKHA_LN	GEOLOGY_MODEL	GM_SBKHA_LN
GM_SBKHA_RGN	GEOLOGY_MODEL	GM_SBKHA_RGN
GM_SLT_DBI	GEOLOGY_MODEL	GM_SLT_DBI
GM_VNR_LN	GEOLOGY_MODEL	GM_VNR_LN
GM_VNR_RGN	GEOLOGY_MODEL	GM_VNR_RGN
HG_DWTRNG_LOC	HYDROGEOLOGY	HG_DWTRNG_LOC
HG_EAD_VES_DT	HYDROGEOLOGY	HG_EAD_VES_DT
HG_EAD_WLL_DT	HYDROGEOLOGY	HG_EAD_WLL_DT
HG_GWL_CNTR	HYDROGEOLOGY	HG_GWL_CNTR
HG_PND_WTLND	HYDROGEOLOGY	HG_PND_WTLND
HG_STTC_GWL	HYDROGEOLOGY	HG_STTC_GWL
KC_CVT_CLLPSB	KARST_CAVITY	KC_CVT_CLLPSB
KC_HALITE_BH	KARST_CAVITY	KC_HALITE_BH
KC_OLD_RSK_MP	KARST_CAVITY	KC_OLD_RSK_MP
KC_SLT_LR	KARST_CAVITY	KC_SLT_LR
KC_VD_DPTH	KARST_CAVITY	KC_VD_DPTH
KC_WTR_LOSS	KARST_CAVITY	KC_WTR_LOSS
SD_SABKHA	SABKHA_DISTRIBUTION	SD_SABKHA
SD_SOFT_SOIL	SABKHA_DISTRIBUTION	SD_SOFT_SOIL

Each table has a shape column that is defined as SDO_GEOMETRY type which stores the spatial component of the table. Each table also has a surrogate primary key that is used as a unique identifier as shown in Figure 2.

SYSTEM.BH_BH3DMDL		SYSTEM.GM_VNR_RGN		SYSTEM.CF_DRDG_LN	
P	INTERNALID	NUMBER (10)	NUMBER (10)	P	INTERNALID
U	OBJECTID	NUMBER (38)	NUMBER (38)	U	OBJECTID
	SHAPE	SDO_GEOMETRY	SDO_GEOMETRY		SHAPE
	FID	VARCHAR2 (40 BYTE)	NUMBER (4)		DRNAME
	POINTID	VARCHAR2 (100 BYTE)	MCUAE_ID		FOLDER_PATH
	HOLEDEPTH	NUMBER (10.3)	MCUAE_CODE		SYMBOL_ID
	HOLE_STARTD	DATE	MCUAE_LAYER		ALT_MODE
	HOLE_ENDD	DATE	MCUAE_AGE		BASE
	EAST	NUMBER (12.3)	MCUAE_GROUP		CLAMPED
	NORTH	NUMBER (12.3)	MCUAE_DPST_TYP		EXTRUDED
	GIMS_EL	NUMBER (10.3)	MCUAE_FRMT		SNIPPET
	BHSRCE	VARCHAR2 (254 BYTE)	MCUAE_MBER_AGE		POPUF_INFO
	CONTRACTOR	VARCHAR2 (100 BYTE)	MCUAE_EXPLIB		CF_DRDG_LN_OBJID_UK (OBJECTID)
	GIMS_FILL	NUMBER (10.3)	MCUAE_LITH		CF_DRDG_LN_PK (INTERNALID)
	MOE_EL	NUMBER (10.3)	GM_VNR_RGN_OBJID_UK (OBJECTID)		CF_DRDG_LN_PK (INTERNALID)
	DC_EL	NUMBER (10.3)	GM_VNR_RGN_PK (INTERNALID)		CF_DRDG_LN_OBJID_UK (OBJECTID)
	MOE_EXTENT	VARCHAR2 (100 BYTE)	GM_VNR_RGN_OBJID_UK (OBJECTID)		
	FILL_DIFF	NUMBER (10.3)	GM_VNR_RGN_PK (INTERNALID)		
	EL_DIFF	NUMBER (10.3)	GM_VNR_RGN_OBJID_UK (OBJECTID)		
	GIMS_EL_UP	NUMBER (10.3)			
	BH_BH3DMDL_OBJID_UK (OBJECTID)				
	BH_BH3DMDL_PK (INTERNALID)				
	BH_BH3DMDL_PK (INTERNALID)				
	BH_BH3DMDL_OBJID_UK (OBJECTID)				
SYSTEM.GM_FRMTN_LN		SYSTEM.DS_DPRSSN		SYSTEM.GM_SBKHA_RGN	
P	INTERNALID	NUMBER (10)	NUMBER (10)	P	INTERNALID
U	OBJECTID	NUMBER (38)	NUMBER (38)	U	OBJECTID
	SHAPE	SDO_GEOMETRY	SDO_GEOMETRY		SHAPE
	LINETYPE	VARCHAR2 (50 BYTE)			UAE_SBKHA_SED
	GM_FRMTN_LN_OBJID_UK (OBJECTID)		DS_DPRSSN_OBJID_UK (OBJECTID)		MCUAE_ID
	GM_FRMTN_LN_PK (INTERNALID)		DS_DPRSSN_PK (INTERNALID)		MCUAE_CODE
	GM_FRMTN_LN_PK (INTERNALID)		DS_DPRSSN_PK (INTERNALID)		MCUAE_LAYER
	GM_FRMTN_LN_OBJID_UK (OBJECTID)				MCUAE_AGE
					MCUAE_GROUP
					MCUAE_DPST_TYP
					MCUAE_FRMT
					MCUAE_MBER_AGE
					MCUAE_EXPLIB
					MCUAE_LITH
					GM_SBKHA_RGN_OBJID_UK (OBJECTID)
					GM_SBKHA_RGN_PK (INTERNALID)
					GM_SBKHA_RGN_PK (INTERNALID)
					GM_SBKHA_RGN_OBJID_UK (OBJECTID)
SYSTEM.CF_ANTH_CHNG		SYSTEM.BH_GIMS			
P	INTERNALID	NUMBER (10)	NUMBER (10)		
U	OBJECTID	NUMBER (38)	NUMBER (38)		
	SHAPE	SDO_GEOMETRY	SDO_GEOMETRY		
	CHANGE_CLA	VARCHAR2 (50 BYTE)	POINTID		
			HOLEDEPTH		
			HOLE_STARTD		
			EAST		
			NORTH		
			ELEVATION		
			BH_GIMS_OBJID_UK (OBJECTID)		
			BH_GIMS_PK (INTERNALID)		
			BH_GIMS_PK (INTERNALID)		
			BH_GIMS_OBJID_UK (OBJECTID)		

FIG. 2. Contents and properties of some spatial database tables. Suffix “_PK” indicates the primary key for each table.

Once the Oracle spatial tables are created, the geodatabase was migrated into the Oracle database and the uploaded onto ADM servers. A series of maps documents were prepared using ArcMap and uploaded onto ADM's ArcServer. These maps define the symbology, scales of display and color ramps for raster catalogs along with labels and annotations. Figures 3 and 4 are screenshots showing the graphic user interface of the web map application.

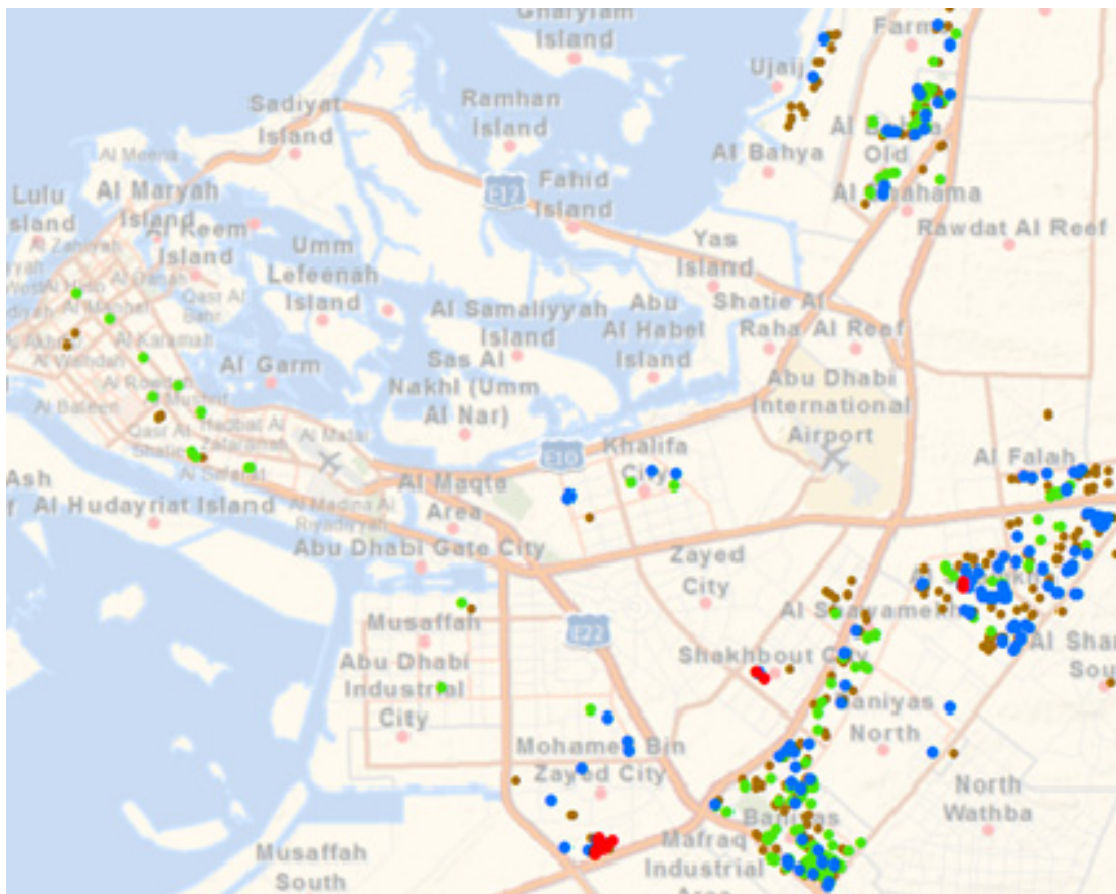


FIG. 3. A screenshot of the web map application shows the locations of damaged houses, roads and infrastructure, data stored in the “DAMAGE_SURVEY” feature dataset

CONCLUSIONS

A geodatabase was designed and populated with geotechnical, hydrogeological information. The geodatabase was then implemented on a Relational Database Management System in Oracle Spatial 11g edition. The data stored in the database is seamlessly integrated with an existing web mapping application – Makani, thus



FIG. 4. The web mapping application also has the provision for overlaying satellite orthoimages over GHIMS layers

integrating vital subsurface spatial information with other core organizational data. The migration from ESRI geodatabase to Oracle 11g platform enables direct interoperability across GIS products and allows standard SQL access to spatial data and operations. Increased scalability in terms of size is another advantage. It must be noted that the system is a static system, meaning that there is no provision for real time updates to the database. But considering the nature of data and information store and delivered through the database, the key components require several iterations of interpretive analysis and engineering judgement, thus eliminating the need for a dynamic data delivery and update system.

ACKNOWLEDGMENTS

The authors appreciate the support of the Spatial Data Division of the ADM and the cooperation offered by all agencies that provided assistance and contributed data towards the completion of this study.

REFERENCES

- Abu Dhabi: Urban Planning Council [UPC], (2004). "Abu Dhabi Urban Planning Vision 2030." [cited 2007]. p. 22. Available from: <http://www.upc.gov.ae/template/upc/pdf/abu-dhabi-vision-2030-revised-en.pdf>
- Asian Surveying and Mapping Magazine, (April 2011). "ADM Launches 'Makani' GIS Portal in Abu Dhabi." Available from: <https://asmmag.com/news/headlines/1033-adm-launches-makani-gis-portal-in-abu-dhabi.html>
- Cooper AH. (2007). "The GIS approach to evaporate-karst geohazards in Great Britain." *Engineering Geology* 53: 981-992. DOI 10.1007/s00254-007-0724-8
- Demers MN. 1997. "Fundamentals of geographic information systems." Wiley, New York, p. 486
- Gao Y, Alexander EC Jr., Tipping G. R., (2002). "The development of a karst feature database for Southeastern Minnesota." *Environmental Geology*, 54(5): 945-956.
- Geomatics Yukon, Department of Environment, Dept. of Energy, Mines and Resources and Pacific GeoTech Systems North Inc. (2011) "Corporate Spatial Data Infrastructure Standards, Ver. 2.4," *Standards Report*, Available from: http://geomaticsyukon.ca/Downloads/CSDI_Standards_v2.4_Nov10_2011.pdf
- Kimance, J. P., Bradshaw, M. P., & Seetoh, H. H. (1999). "Geographical Information System (GIS) application to construction and geotechnical data management on MRT construction projects in Singapore." *Tunnelling and underground space technology*, 14(4), 469-479
- Lan, H. X., Martin, C. D., Froese, C. R., Kim, T. H., Morgan, A. J., Chao, D., & Chowdhury, S. (2009). "A web-based GIS for managing and assessing landslide data for the town of Peace River, Canada." *Natural Hazards and Earth System Science*, 9(4), 1433-1443.
- Lovell Johns Ltd. (2005) "Guidelines for Geographic Data Intended for the GISCO Reference Database." *Copyright 2005, Eurostat, Witney, UK*. Available from: <http://ec.europa.eu/eurostat/documents/4311134/4366152/guidelines-geographic-data.pdf>
- MacDonald A, Brown T, Andrade J, Hoel E, Bailey J. (2001). "Building a Geodatabase: GIS by ESRI." *ESRI User Manual 2001*.
- Ministry of Forests, Lands and Natural Resource Operations [FLNRO]. (2013) "File geodatabase standards for data creation, publication, and distribution." *British Columbia p. 5*. Available from: http://www.data.gov.bc.ca/local/dbc/docs/geo/services/standards-procedures/file_geodatabase_standards.pdf
- Ormsby T, Napoleon, E, Burke, R, Groesl C, Bowden, L. (2008). "Getting to know ArcGIS Desktop: Basics of ArcView, ArcEditor and ArcInfo" *2nd Edition*, p. 592.
- Price SJ, Farrant AR, Leslie A, Terrington RL, Merrit J, Entwisle D, Thorpe S, Horabin C, Gow H, Self S, and McCormick T. (2012). "A 3D superficial and bedrock geological model of the Abu Dhabi urban area, United Arab Emirates." *British Geological Survey Commercial Report, CR/11/138*

- Tennant EW. (2007). "A sample geodatabase structure for managing archaeological data and resources with ArcGIS." *Technical Briefs in Historical Archaeology* 2: 12-23
- The Geotechnica. (2004). Equipe Group, p. 27. Available from: http://www.equipegroup.com/pdfs/theGeotechnica_August_2014.pdf
- Tose JA, Taleb A, 2000. "Khalifa city 'b' ground conditions program." In: Mohamed & Al Hosani, editors. *Georngineering in Arid Lands.* Balkerna, Rotterdam. p. 75-81

Development of a Comprehensive Geotechnical Information Management System for Municipal Use

Walid Dawoud¹, Mazen Elias Adib², Giridhar Kolan Reddy², Raghav Sarathy Ramanathan¹, Bulent Hatipoglu¹, Melih Demirkan¹, Cagri Cinkilic¹

¹RIZZO Associates, 500 Penn Center Boulevard, Suite 100, Pittsburgh, PA-15217

²Abu Dhabi City Municipality, Town Planning Sector, Abu Dhabi City Municipality P. O. Box 263, Abu Dhabi, UAE

ABSTRACT: The Municipality of Abu Dhabi City (ADM) routinely commissions and manages projects where large volumes of data from site investigations are archived by internal and external users. The data includes legacy information from site investigation projects such as borehole logs, interpretive reports, cross sections, and field and lab test data. The information was either in image or paper format. The extensive volume and the format of the data made it impossible to query for specific needs. Also, due to its large quantity, storage and filing systems were cumbersome for users with potential for documents to be misplaced. The Spatial Data Division within the Abu Dhabi Municipality developed the Geotechnical Information Management System (GIMS) as a comprehensive data storage and management solution that enables easy access to all geotechnical data. The geotechnical information from the legacy data were digitized and effectively archived so that it could be made accessible internally and externally. Information relating to the subsurface from 21,257 hardcopy borehole logs and reports were extracted and stored in a gINT® database which is compatible with the Association of Geotechnical and Geoenvironmental Specialists (AGS) 3.1 data interchange standard. The GIMS database consists of 93 tables; however for the most commonly used field and laboratory tests, a subset database consisting of 30 tables to address specific geotechnical data submittal requirements was developed as well. Strict procedures and standards for geotechnical data submittal applicable to contractors and consultants were also defined to ensure streamlined updates to the database. The GIMS was also designed to interact with other software such as existing GIS and civil design software. A custom geotechnical Web Map Application (WMA) was developed to handle dynamic data delivery to the end user through the web. This GIS integration enables access to existing geotechnical data via the internet or the ADM's intranet. This paper discusses in detail the design decisions, various aspects of implementation and the challenges faced during development of the entire GIMS application.

INTRODUCTION

The Abu Dhabi Municipality (ADM) is responsible for commissioning and managing various infrastructure and developmental related projects within the city of Abu Dhabi. During the last few decades the ADM has accumulated large volumes of data from numerous site investigation projects. The Municipality also has extensive legacy information such as borehole logs, interpretive reports, cross sections and other such data relating to subsurface conditions. Majority of this information was in paper or image format which made it very cumbersome to archive and retrieve leading to underutilization of existing geotechnical data (Geotechnica, 2011).

A simple solution to enable efficient utilization of existing geotechnical data is to centralize and validate all subsurface information using a centralized database application (Kunapo et al., 2005). In many regions, multiple databases have been developed to act as a comprehensive data management tool for site investigation data (Koike et al., 1996). Geotechnical software has made significant advances over the recent years and several geotechnical database management applications are available in the industry (Toll et al., 2003). gINT is one such application that provides centralized data management and reporting for geotechnical subsurface projects of all types.

A comprehensive geotechnical database used in conjunction with GIS greatly improves efficiency of storing, managing and retrieving geotechnical subsurface information at any time using the internet (Kunapo et al., 2005). Such a system was designed and developed to handle ADM's geotechnical data storage and management needs. An enterprise gINT database was designed, consisting of 93 tables capable of storing geotechnical and hydrogeological lab and field data. A Web Map Application (WMA) called Geotechnical Information Management System (GIMS) was developed to provide internal and external access to the data stored in the geotechnical database. This paper discusses the design and implementation of the system.

DATABASE DESIGN

Currently, the ADM has a repository of 21,258 boreholes obtained from around 3000 site investigation reports. The spatial extent of the databases covers an area of approximately 11,000 sq. km. Figure 1 shows the spatial distribution of all 21,258 boreholes. The geotechnical database was designed based on the publically available Association of Geotechnical and Geoenvironmental Specialists (AGS) standards. The AGS is a non-profit organization established to improve the profile and quality of geotechnical and geo-environmental engineering. The purpose of the AGS Format is to provide a means of transferring geotechnical and geo-environmental data between users and stakeholders. In order to ensure the widest possible level of acceptance, AGS Format uses the American Standard Code for Information Interchange (ASCII).

The AGS Format file is a text file, containing tables of information on all aspects of the geotechnical site investigation. Each table comprises a Group name, column

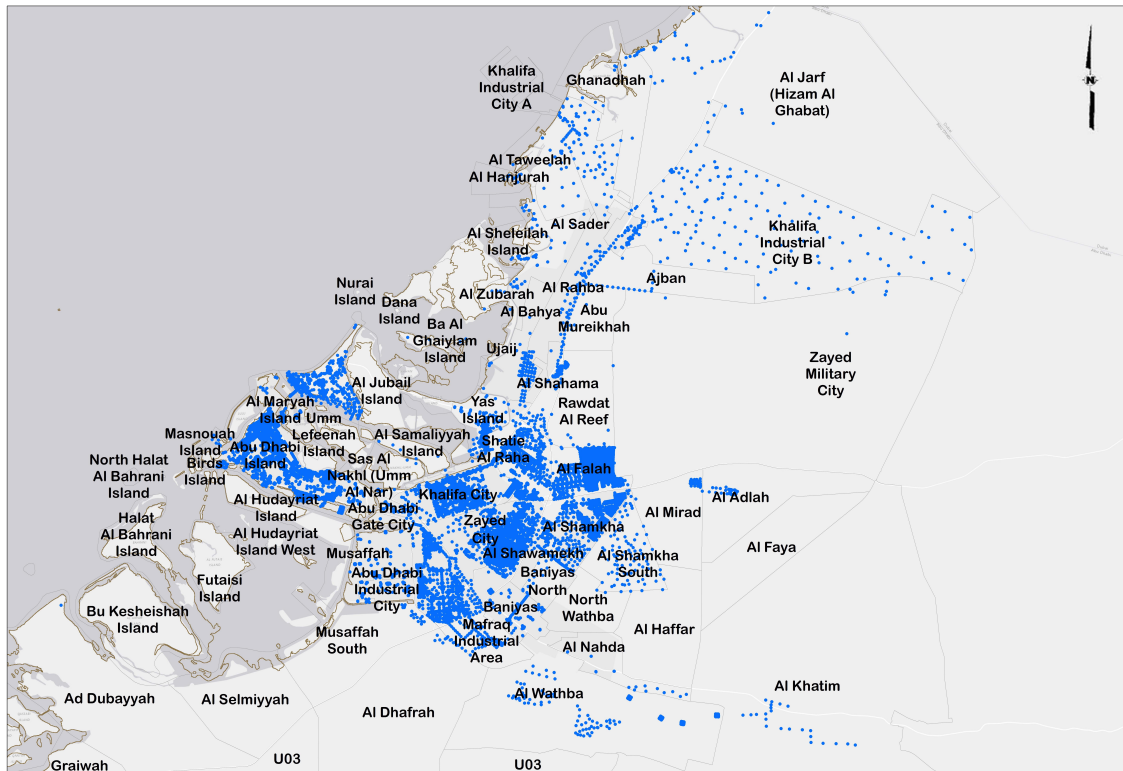


FIG. 1. The spatial extent of all boreholes within the ADM obtained from various sources and projects.

headings and data Variables. Since the GIMS data structure is based on the AGS 3.1 data interchange format it uses similar table and field naming conventions to AGS. The AGS naming convention makes use of abbreviated table and field names for data storage. A total of 93 tables exist in the current GIMS design although only a subset of the comprehensive database (30 tables) is used on a regular basis. This subset includes the most commonly used lab and field data parameters that are recorded during field investigations. After each update, the subset database is upsized into the master GIMS database.

The GIMS database follows a parent-child structure. In this structure each record in one table can be associated with multiple records in another table. In table design, each row in the child table refers to a row in the parent table. It follows a one to many relationships, for example, a borehole may have many different samples recovered or SPT N value readings at different depths. The parent record must always be defined before its child record. Figure 2 shows the entire database structure of the GIMS database.

The primary table is the “PROJECT” table which consists of details relating to the site investigation project different sets of boreholes belong to. This table has a child table called the “POINT” table which stores information relating to the borehole locations and elevations among other data. The “POINT” table has a unique field – “PointID” which acts as the primary key and all children tables are linked with the “POINT” table using this particular field, which acts as a unique ID for each borehole. All tables besides “PROJECT” and its children are either direct or indirect

children of the “POINT” table. Table 1 shows the relationship between the 30 tables of the subset database.

Table 1. Database table direct relations for ADM Subset Database

Parent Table	Direct Children Tables
PROJECT	EXTERNAL PROJECT REPORT FILES, POINT
POINT	CDIA, CORE, DETL, EXTERNAL BOREHOLE REPORT FILES, FLSH, GEOL, HDIA, IPRM, ISPT, SAMP, STCN, WSTK
GEOL	LITHOLOGY SOIL, LITHOLOGY ROCK, DETL
SAMP	LAB SPECIMEN
LAB SPECIMEN	ATTERBERG, CNMT, HYDROMETER, SIEVE, UNCONF COMPR, DIRECT SHEAR, WC DENSITY
ATTERBERG	ATTB READINGS
DIRECT SHEAR	DSHR READINGS
HYDROMETER	HYD READINGS

There are various advantages to using the parent-child structure such as (i) only predefined records can be entered, thus reducing the possibility of typographical errors, (ii) Mistakes corrected in the “parent” record automatically updates the corresponding records in the children tables, (iii) when a parent table is deleted, all the child records are also automatically deleted.

DATABASE IMPLEMENTATION

Among the 21,258 boreholes available to the ADM, majority boreholes were in image format, some boreholes were available in digital format (MS Excel sheets) and in PDF formats. Boreholes available in image and PDF formats were digitized manually. Data entry and database was performed in 3 stages. The first set of data was imported from from Excel files which consisted of borehole log information stored in the AGS 3.1 data interchange format. The total number of boreholes entered as part of this phase was 4,516. The second set of data consists of information from scanned versions of site investigations reports. A total of 15,517 boreholes were entered during this phase of the project. The third phase consists of boreholes available in PDF formats, a total of 1225 boreholes were entered in this phase.

Data entry was carried out by a number of operators, under the supervision of Senior Geotechnical Engineers. Important remarks and comments, such as drilling fluid loss and drops in drilling rods were provided in the appropriate data tables. The input data were checked using data checking rules and procedures available in the gINT® program. In addition to this automatic checking procedure, the data were also checked manually. Data entry was carried out on a table by table approach. Data for a particular table was entered for all boreholes within a report or project before proceeding to the next table. Figure 3 illustrates the data entry process.

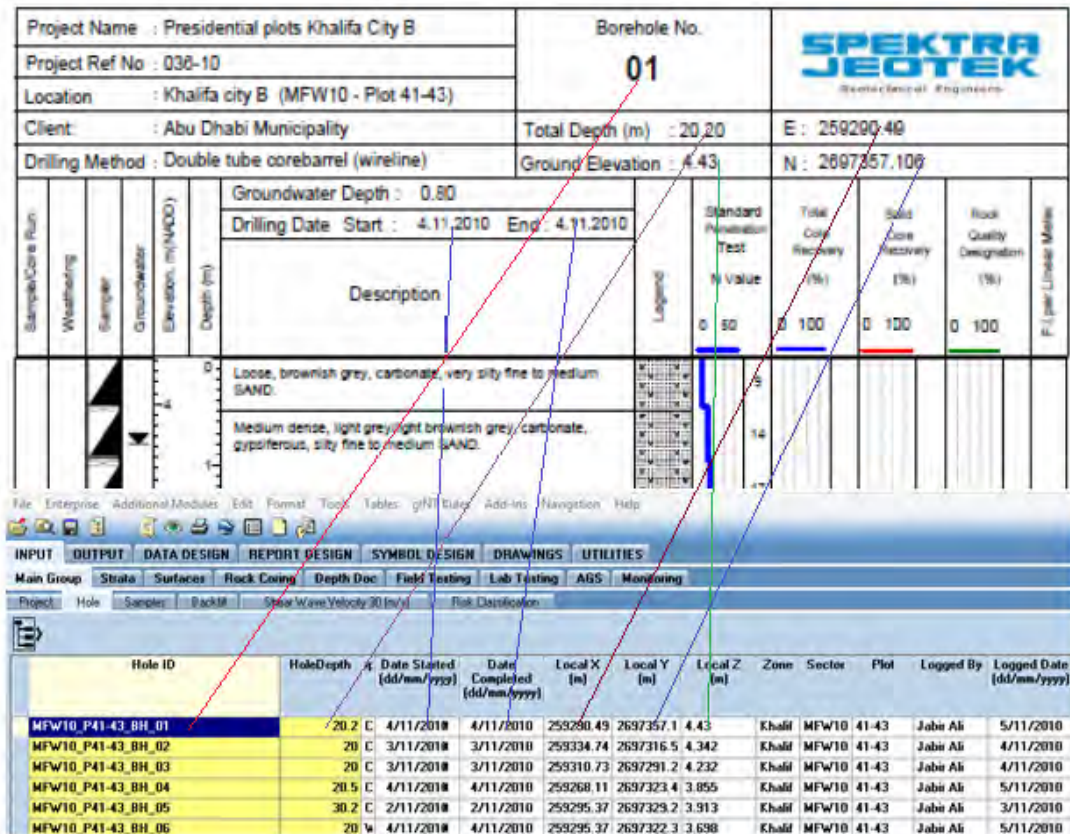


FIG. 3. Borehole data entry process

Comparisons were performed between entered data and source data to confirm that the required data is correctly and completely entered. The checking takes into consideration the AGS 3.1 data standards. The final checking covers geologic structure, comparing databases to ensure gINT® fields requirements (Type, format, etc.), relation between different fields in the same table, illogical data for boreholes or test results, and logic between fields and tables. This final review ensures consistency of data through queries and validation rules based on geotechnical aspect.

GIMS was integrated with the Municipality’s GIS web portal by creating a custom geotechnical web map application for gINT. The GIS integration allows access to the existing geotechnical data at any time, from anywhere, via the Internet or the Municipality’s intranet. The robust geotechnical data submission standards ensure the uniformity and quality of data that is submitted. By providing geotechnical data templates in gINT, Microsoft Access, and AGS 3.1 format, GIMS also enables the exchange of geotechnical data between stakeholders.

The GIMS WMA was developed using Microsoft Visual Studio.NET with WCF, SILVERLIGHT, and ESRI SOAP Toolkits. MS SILVERLIGHT is the major tool responsible for the user interface. It is used to design the front end of the WMA. Figure 3 shows a screenshot of the user interface.

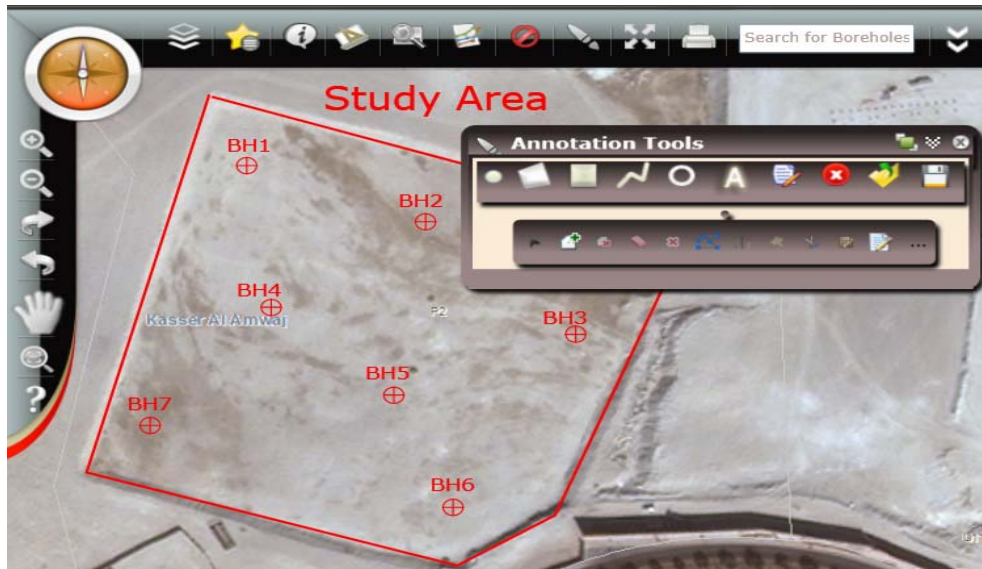


FIG. 4. GIMS WMA user interface.

ESRI SOAP Toolkits is a set of components that are added to the WMA to provide a host of spatial capabilities like spatial search and buffering annotations. The user is also able to query for borehole specific information using SQL scripts or based on geotechnical parameters as shown in Figures 4 and 5.

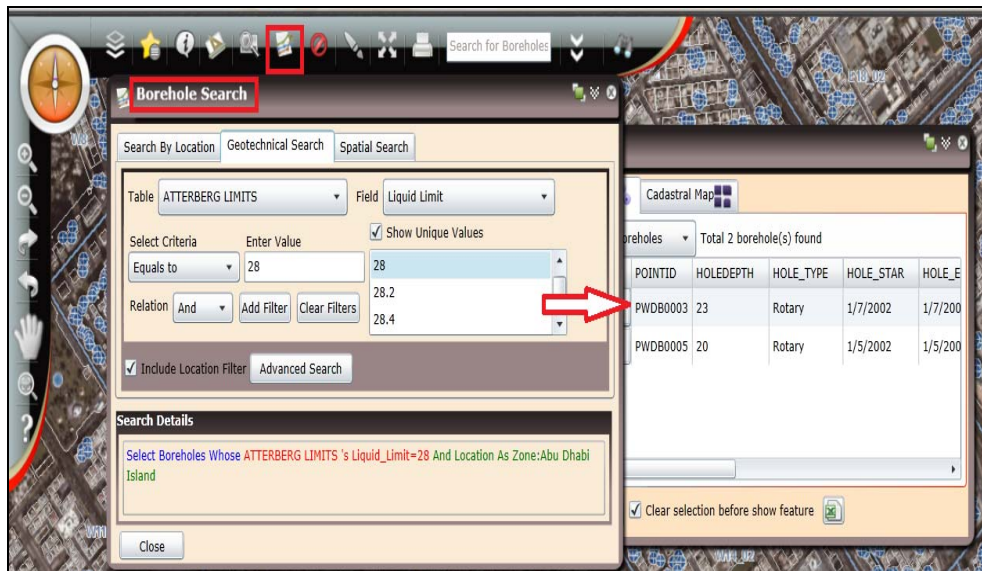


FIG. 5. GIMS Borehole specific search provisions.

The WMA also has the provision to view generate and download corresponding borehole logs or entire site investigation reports on the fly as shown in Figure 6.

ACKNOWLEDGMENTS

The authors appreciate the support of the Spatial Data Division of the ADM and the cooperation offered by all agencies that provided assistance and contributed data towards the completion of this study.

REFERENCES

- Koike, K., Minta, T., Ishizaka, S., & Ohmi, M. (1996). Hydrogeological and ground-water resource analysis using a geotechnical database. *Nonrenewable Resources*, 5(1), 23-32. Chicago
- Kunapo, J., Dasari, G., Phoon, K., and Tan, T. (2005). "Development of a Web-GIS Based Geotechnical Information System." *J. Comput. Civ. Eng.*, 19(3), 323–327.
- The Geotechnica. (2004). Equipe Group, p. 27. *Available from: http://www.equipegroup.com/pdfs/theGeotechnica_August_2014.pdf*
- Toll, D. G., & Cubitt, A. C. (2003). Representing geotechnical entities on the World Wide Web. *Advances in Engineering Software*, 34(11), 729-736.

Effect of Hybrid Geosynthetic Layers on Soil Walls with Marginal Backfill Subjected to Rainfall

Dipankana Bhattacharjee¹ and B. V. S. Viswanadham²

¹Research Scholar, Dept. of Civil Engineering, Indian Institute of Technology Bombay, Powai, Mumbai 400 076, India. E-mail: dipankanabhattacharjee@gmail.com

²Professor, Dept. of Civil Engineering, Indian Institute of Technology Bombay, Powai, Mumbai 400 076, India (corresponding author). E-mail: viswam@civil.iitb.ac.in

Abstract: The objective of this paper is to examine the influence of hybrid geosynthetic layers in dissipating pore water pressures in geogrid reinforced soil walls with marginal backfill subjected to rainfall. In this regard, numerical modelling was carried-out using a finite-element based software SEEP/W by subjecting the soil wall to different rainfall intensities, ranging from 10 mm/hr to 80 mm/hr. For selected sections, static global stability of the soil wall with and without hybrid geosynthetic layers was carried-out using SLOPE/W. The number of hybrid geosynthetic layers was varied to arrive at the optimum number of layers needed to maintain stability against different intensities of rainfall simulated, and the results were compared with equivalent number of conventional sand drainage layers. The results indicated that, the hybrid geosynthetic layers placed at bottom half were more effective in reducing the pore water pressures developed during rainfall, and in improving the stability of the reinforced wall section than identical number of sand layers.

INTRODUCTION

Mechanically stabilized earth (MSE) walls reinforced with geogrids have seen a tremendous growth over the past thirty years. However, along with this growth, numerous failures of reinforced soil walls and slopes were reported simply due to infiltration of rainwater into an otherwise stable structure. Koerner and Koerner (2011) reported that, of the 82 cases of wall failure in their database, improper drainage control during rainfall was the cause of failure in 68% of them, due to presence of marginal fills in reinforced soil zones. This may be attributed to the primary assumption made while designing MSE walls, which states that, hydrostatic pressures are non-existent. This assumption is valid only if well graded, freely draining soil is used in the reinforced zone. The Federal Highway Administration allows up to 35% of fines in the reinforced zone, provided proper measures are adopted to address various design issues related to drainage and deformation (FHWA, 2009). However, the unavailability of good quality granular material has recently led to the use of low permeability backfill soils, leading to development of excess positive pore water pressures during rainfall, reduction in shear strength at the

interface of soil-reinforcement and excessive deformations. The use of low permeable backfill was reported as the cause of major serviceability problems by Mitchell and Zornberg (1995), Koerner and Soong (2001, 2005) and Yoo and Jung (2006). Yoo and Jung (2006) carried out seepage studies numerically on a segmental retaining wall of height 7.4 m with low permeable backfill using SEEP/W. It was reported that, the factor of safety reduced drastically due to seepage, and investigations revealed that relatively high percentage fines coupled with insufficient drainage measures were the prominent reasons. The instability arises due to the inefficiency of the marginal backfill soil to dissipate the excess pore water pressure generated within soil walls during the rainfall event, resulting in development of destabilizing seepage forces behind the reinforced zone. However, marginal backfills comprising of silts and/or clays can be used in the reinforced soil zone, provided proper drainage components are incorporated in the design, and potential savings could be in the range of 20-30% of current reinforced soil wall costs. The use of permeable inclusions as an effective alternative to relieve the pore pressure buildup was discussed by Mitchell and Zornberg (1995) and Raisinghani and Viswanadham (2011). Geocomposites that combine drainage and reinforcement properties were recommended as a remedial measure by Chen et al. (2007) for improving the stability of a vertical geosynthetic reinforced earth wall with clayey backfill. Koerner and Soong (2005) reported that, the seepage forces behind the reinforced zone was reduced to half on provision of geocomposite layers. Based on the above literature review, it can be inferred that, the ideal technique required for maintaining stability of the soil wall against rainfall infiltration requires both reinforcement and drainage criteria to be satisfied simultaneously. Such a dual-function geosynthetic material, possessing good in-plane drainage capabilities of a non-woven geotextile, coupled with the reinforcement strength of a woven geogrid is herein referred to as a hybrid geosynthetic. Till date, studies on the potential use of hybrid geosynthetics in reducing pore water pressures in a low permeable backfill soil wall subjected to rainfall is limited.

In the present paper, an attempt has been made to evaluate the effect of inclusion of hybrid geosynthetic layers and sand drainage layers separately on the drainage capability of reinforced earth (RE) walls constructed with low-permeability backfill soil subjected to rainfall. For this purpose, numerical modelling was carried out on a 6 m high reinforced soil wall subjected to five different rainfall intensities, ranging from 10 mm/hr to 80 mm/hr, using a finite element based software SEEP/W (Geostudio, 2012). For selected sections, static global stability analysis with and without hybrid geosynthetics was carried out using the limit equilibrium based software SLOPE/W. The number of hybrid geosynthetic layers was varied to optimize the height up to which provision of these layers proved effective under various intensities of rainfall simulated. The analyses was repeated with identical number of sand drainage layers, and the pore water pressures and factor of safety values obtained with identical number of hybrid geosynthetic layers and sand layers were compared.

DETAILS OF THE REINFORCED SOIL WALL SECTION

The polymeric strip reinforced soil wall section having 6 m height used in the present study is shown in Fig. 1, which is an existing structure along NH-17 in the

state of Karnataka, India. The properties of marginal soil within the reinforced zone and backfill zone were maintained as identical. The wall was designed with nine layers of polymeric strip reinforcements of length 5.1 m, connected with precast reinforced concrete panels. The tensile load values of the reinforcement layers are summarized in Table 1, obtained after deducting for relevant factors related to creep, installation damages, etc. The fill material used during construction (Table 2) was prepared by blending river sand and locally available soil in equal proportions, and was reported to have a permeability of 1.64×10^{-7} m/s with fines $\geq 30\%$.

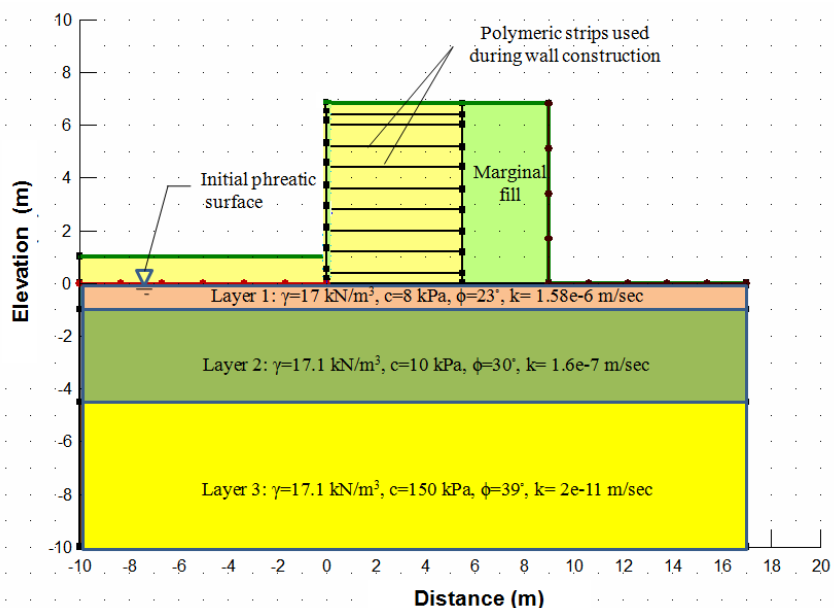


FIG. 1. Schematic diagram of RE wall section adopted in the analysis.

The hybrid geosynthetic layers (or sand layers) were placed from the bottom of the wall, midway between the existing polymeric strip layers, and were considered to be 2 m longer than the length of the polymer strip reinforcement layers (i.e. 7.1 m). The hybrid geosynthetic selected in the study was a combination of woven geogrid and nonwoven geotextile, having properties as summarized in Table 3, adopted on the basis of published data compiled by Iryo and Rowe (2005). The unsaturated hydraulic conductivity functions and volumetric water content functions for the marginal fill material and non-woven geotextile component of hybrid geosynthetic were approximated using the van Genuchten (1980) equation as follows:

$$\theta_w = \theta_r + \frac{\theta_s - \theta_r}{\left[1 + \left(\frac{\Psi}{a}\right)^n\right]^m} \quad (1)$$

where, θ_w is the volumetric water content, θ_s is the saturated volumetric water content, θ_r is the residual water content, Ψ is the negative pore-water pressure, and a , n , m are curve-fitting parameters. The soil-water characteristic curves and hydraulic conductivity functions thus developed for the soils and nonwoven geotextile are

presented in Figs. 2a-2b. For the marginal fill, the van Genuchten parameter α' (kPa⁻¹) was calculated as 0.22 for wetting cycle, and 0.11 for drying cycle, while n parameter was approximated as 1.47 for backfill soil and 3.16 for sand.

Table 1. Tensile load values of polymeric strips used in the RE wall

Layer No. (from top)	Tensile load (kN/m)	Layer No. (from top)	Tensile load (kN/m)
Layer 1	25.2	Layer 5	50.39
Layer 2	30.23	Layers 6,7	62.99
Layer 3	37.79	Layer 8	75.59
Layer 4	47.24	Layer 9	88.18

Table 2. Properties of backfill soil and sand used in construction of the RE wall

Soil Type	γ (kN/m ³)	k (m/sec)	c (kPa)	ϕ (°)
Marginal fill	22.17	1.64×10^{-7}	0	32
Sand	20.00	1.2×10^{-5}	0	34

γ = Unit weight; Coefficient of permeability = k ; Cohesion = c ; Angle of internal friction = ϕ

NUMERICAL MODELLING OF THE REINFORCED SOIL WALL SUBJECTED TO RAINFALL

For the RE wall section with marginal backfill subjected to rainfall, seepage analysis was carried out using the finite element program SEEP/W and stability analysis was performed using SLOPE/W (Geostudio, 2012). To analyze the unsteady transient flow through the unsaturated soil mass taking place during rainfall, the theory suggested by Tsaparas *et al.* (2002) was incorporated in SEEP/W in the form of Equation (2):

$$\frac{\partial}{\partial x} \left(k_x \frac{\partial h}{\partial x} \right) + \frac{\partial}{\partial y} \left(k_y \frac{\partial h}{\partial y} \right) + \frac{\partial}{\partial z} \left(k_z \frac{\partial h}{\partial z} \right) + q = m_w^2 \rho_w g \frac{\partial h}{\partial t} \quad (2)$$

where h is the hydraulic head, k_x and k_y are the coefficients of permeability of the soil with respect to water along x and y axes, q is the applied flux in the domain, m_w is the coefficient of volumetric water change with respect to a change in suction (and is equal to the slope of the soil water characteristic curve), ρ_w is the density of water and g is gravitational acceleration. The soil wall with marginal fill was initially subjected to different rainfall intensities varying from 10 mm/hr to 80 mm/hr for a duration of 24 hours, and the development of pore pressures and changes in suction of the unsaturated soil during this period, and upto 24 hr after completion of duration of rainfall were monitored numerically. Afterwards, the effect of inclusion of hybrid geosynthetic layers and sand drainage layers of 0.2m thickness within the soil wall subjected to rainfall were analyzed and compared. The number of sand and hybrid geosynthetic layers (n) was varied from 1 to 6, and the corresponding sections were analyzed to obtain pore pressures and safety factors with the progress of rainfall.

During seepage analysis, the flux boundary q equal to the desired rainfall intensity was applied at the surface of the soil wall to create rainfall numerically. In addition, non-ponding boundary condition was adopted in order to prevent excessive accumulation of rainfall on the slope surface. In the present analysis, five typical rainfall intensities were selected, viz, 10 mm/hr (moderate rainfall), 22 mm/hr (heavy rainfall), 36 mm/hr (very heavy rainfall), 50 mm/hr and 80 mm/hr (torrential rainfall), as per the classification of rainfall event on the basis of average hourly intensity suggested by Llasat (2001). As the present paper is intended to evaluate the effect of rainfall of medium to high intensity with short duration on the performance of soil wall with marginal fill with and without hybrid geosynthetics, a rainfall of 24 hours duration was considered for each intensity of rainfall simulated. An initial ground water table was assumed to be located near the base of the wall at the onset of rainfall.

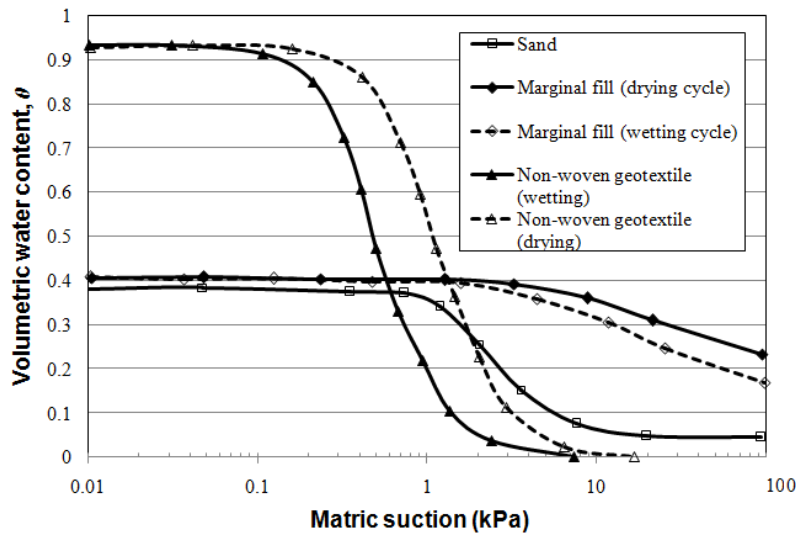
Table 3. Properties of hybrid geosynthetic material adopted

k_{ng} (m/sec)	k_{tg} (m/sec)	Thickness (mm)	T_{ug} (kN/m) ^a	f_b (kPa) ^b
2.3×10^{-2}	3.5×10^{-3}	3.7	55.35	12.49
k_{ng} = Saturated normal coefficient of permeability; k_{tg} = Saturated tangential coefficient of permeability; T_{ug} = Ultimate tensile load of geogrid reinforcement layer (non-woven geotextile tensile load component is not considered); For non-woven geotextile, the van Genuchten parameter, α' (kPa ⁻¹) was adopted as 3.00 for wetting cycle, and 1.50 for drying cycle; n was taken as 3.00; ^a Wide-width tensile test; ^b Bond skin friction value obtained from modified direct shear test.				

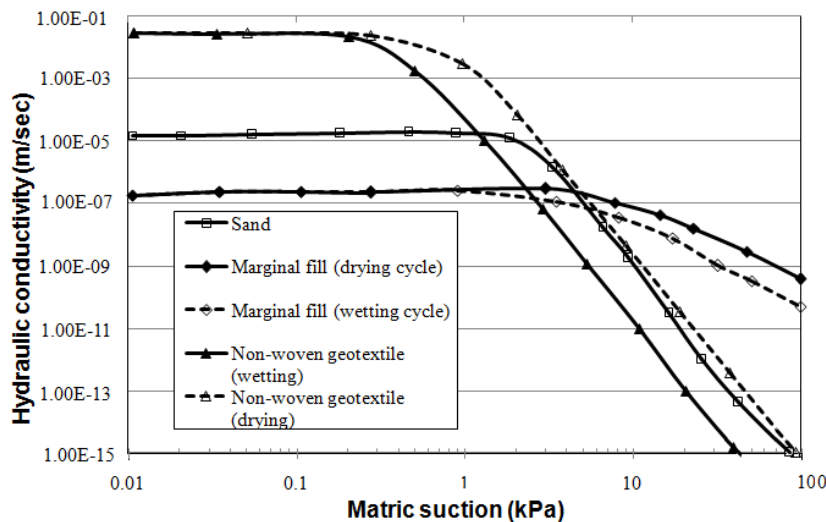
A series of numerical trials was conducted with different mesh configurations and time steps to establish a suitable numerical scheme. Based on this study, the analysis was carried out with an approximate global element size of 0.25 m, with 3597 nodes, and 3582 elements. The marginal fill and foundation soil layers were modelled considering triangular and quadrilateral elements, while the hybrid geosynthetics were modelled as interface material model in conjunction with interface elements added to the mesh to represent the thickness of the geosynthetics. The ‘Saturated/Unsaturated model’ was used as the constitutive material model for predicting the response of the soil during rainfall infiltration, without considering capillary barrier effects created by non-woven geotextiles in unsaturated soil-geotextile system. However, this is not a major limitation to the present study, because as pointed out by Iryo and Rowe (2004), as in the case considered in the present analysis, where $k_{sat-geotextile} > k_{sat-soil}$, and the rainfall flux (q) is greater than the saturated soil permeability ($k_{sat-soil}$), capillary barrier effects do not pose as a significant threat.

Figs. 3a-3c illustrate the typical results of seepage analysis for the RE wall section subjected to 22 mm/hr rainfall with marginal fill alone, and after the inclusion of three number of hybrid geosynthetic layers and sand drainage layers respectively, in terms of development of phreatic surfaces at the end of 24 hrs (when rainfall stopped). As can be noted from Figs. 3a-3c, the phreatic surface had risen to a considerable height within the reinforced zone in presence of the marginal fill alone, which is detrimental for the stability of the wall section. However, the phreatic surface lowered with the provision of drainage layers, and the reduction was more pronounced with the

provision of hybrid geosynthetic layers, as compared to identical number of sand drainage layers. The variation of pore water pressure (u) in kPa along the base of the RE wall for the above three cases are shown in Fig 4, monitored at the end of 24 hrs of rainfall. As evident from Fig 4, the marginal fill alone depicted high values of pore water pressure at the end of rainfall, thereby indicating inefficiency of the fill material to dissipate the generated pore pressures during rainfall. On the other hand, the pore pressure values in the reinforced zone reduced by almost 40% and 72% with the inclusion of three layers of sand and hybrid geosynthetic respectively, ensuring enhanced stability of the RE wall section against rainwater infiltration.



(a) Soil-water characteristic curves



(b) Hydraulic conductivity functions

FIG. 2. Hydraulic properties for soils and nonwoven geotextile developed on the basis of van Genuchten (1980) equation and database of Iryo and Rowe (2005).

The normalized pore water pressures $u/\gamma h$ (defined as a ratio of pore water pressure at half reinforcement length from toe of the wall to the product of unit weight of the soil and height of the wall) was calculated at the wall base, mid-way of the reinforced zone to assess the reduction in pore water pressure with increase in number of sand and hybrid geosynthetic layers. Figure 5 gives the variation of $u/\gamma h$ obtained for various rainfall intensities at the end of rainfall. The value of $u/\gamma h$ was found to reduce significantly with the inclusion of hybrid geosynthetic layers as compared to identical number of sand layers for all intensities of rainfall ranging from 10 mm/hr to 80 mm/hr. Moreover, increase in number of sand or geocomposite layers beyond four ($n = 4$ in Fig 5) was found to have marginal influence on $u/\gamma h$, thereby implying that the provision of such layers, introduced from the bottom of the wall, midway between the existing polymeric strip layers, proved to be effective upto about mid-height of the RE wall. Hence, the drainage layers provided in the lower half of the wall section played a significant role in lowering pore water pressures and maintaining stability of the RE wall subjected to rainfall.

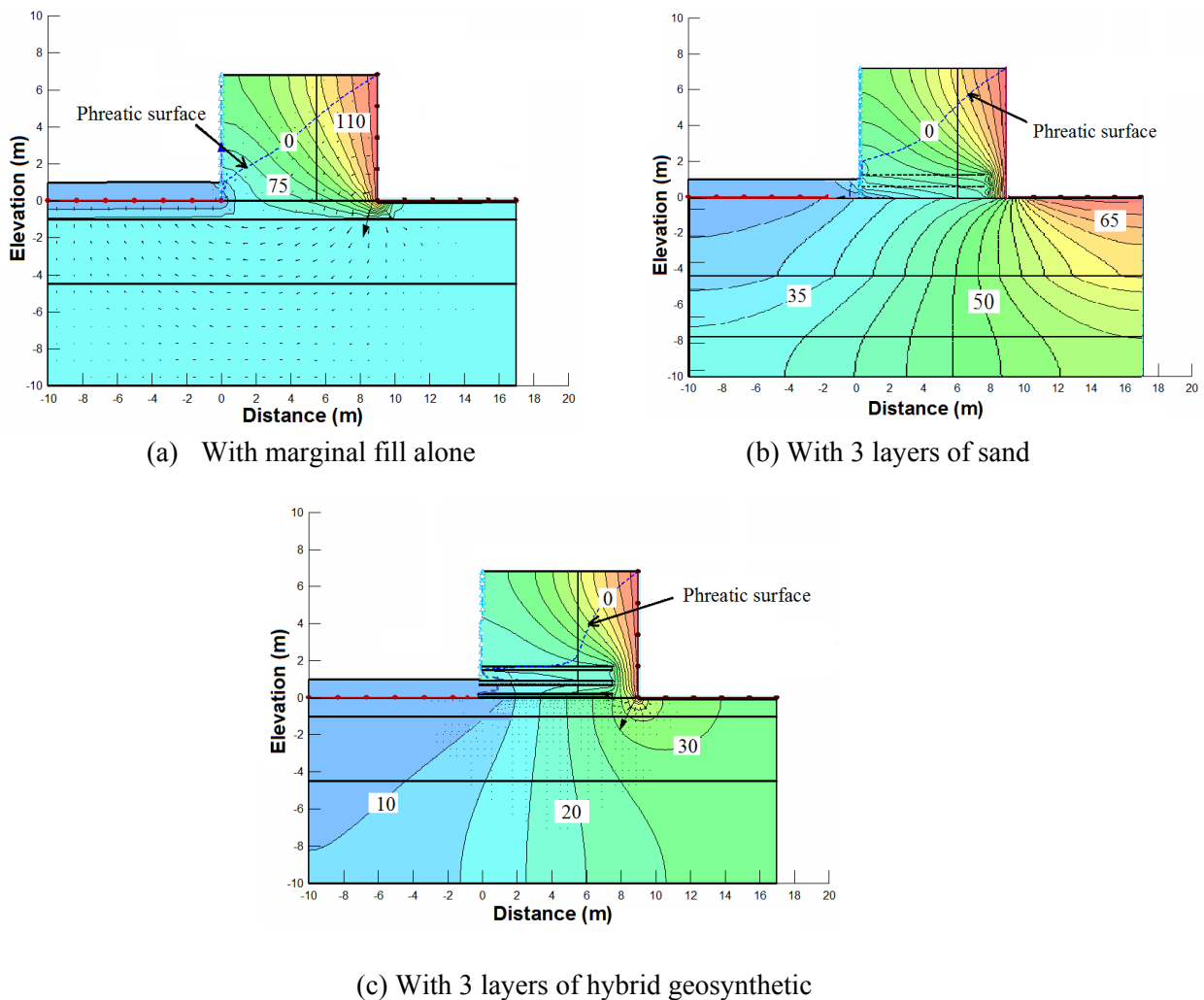


FIG. 3. Seepage analysis results of RE wall for 22 mm/hr rainfall at the end of 24 hrs [Numericals along the contours represent pore water pressure values in kPa].

STABILITY ANALYSIS USING SLOPE/W

The phreatic surfaces obtained from SEEP/W analyses during various stages of rainfall were incorporated into the limit equilibrium based software SLOPE/W for performing the stability analysis of the soil wall under rainfall condition, using modified Bishop's method of slices. The variation of negative pore pressures in the unsaturated zone above the water table was incorporated in the slope stability analysis, by utilizing the modified Mohr-Coulomb failure criterion. While performing the stability analysis, the reinforcement functions of hybrid geosynthetic layers were considered together with their in-plane drainage capability. The tensile load (kN/m) and bond skin friction values of the hybrid geosynthetic layers as presented in Table 3 were considered as input values in the analyses, along with the values of unit weight, cohesion and internal friction of the marginal fill, as presented in Table 2.

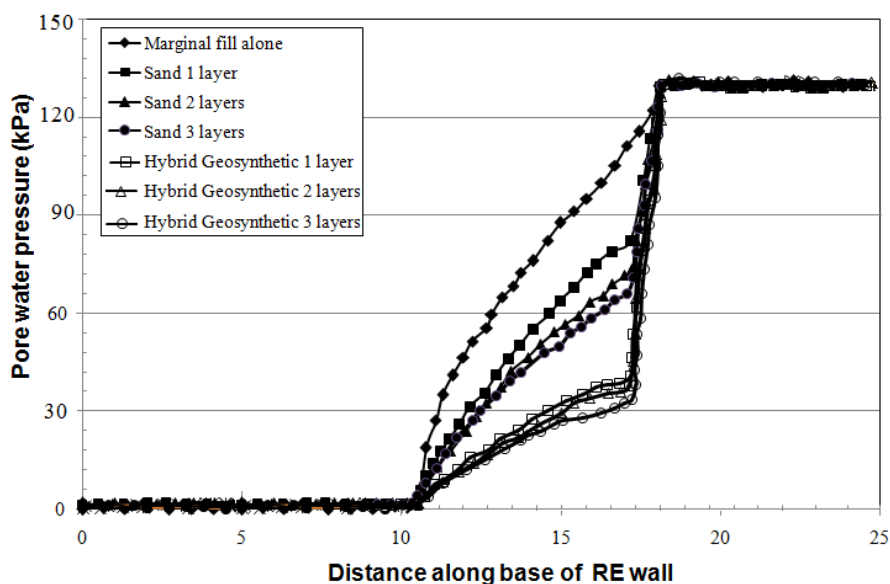


FIG. 4. Pore water pressure developed at the end of 24 hrs of 22 mm/hr rainfall.

Figure 6 presents the values of factor of safeties obtained by incorporating four layers of hybrid geosynthetic and sand within the RE wall subjected to five different rainfall intensities. In general, the factor of safety reduced with the progress of rainfall, but started improving once the rainfall stopped with the inclusion of drainage layers. The hybrid geosynthetic reinforced section exhibited higher factor of safety values compared to identical number of sand drainage layers for all intensities of rainfall, and was observed to be stable even under a torrential rainfall intensity of 80 mm/hr. Figure 6 reveals that, beyond a rainfall intensity of 22 mm/hr, the rainfall intensity did not affect factor of safety values significantly, implying that, the reinforced soil wall section has already reached its capacity to receive rainwater.

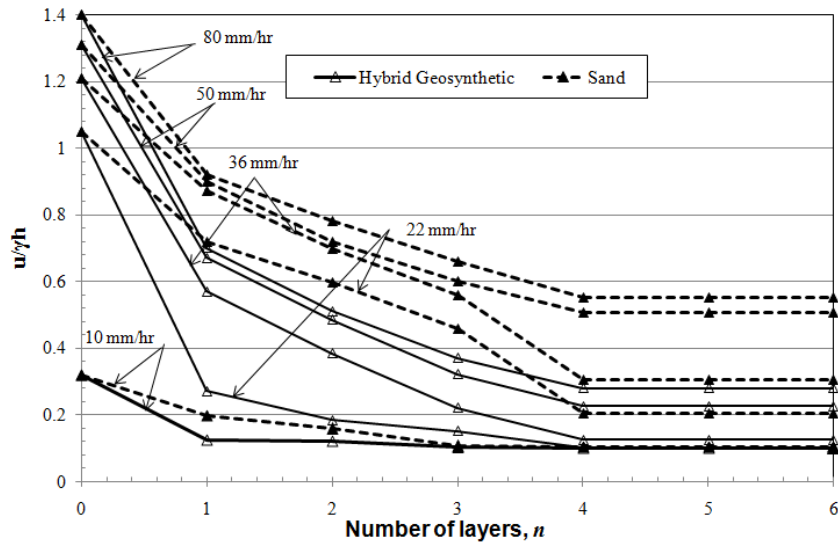


FIG. 5. Variation of $u/\gamma h$ with number of sand and hybrid geosynthetic layers for different rainfall intensities at the end of 24 hrs.

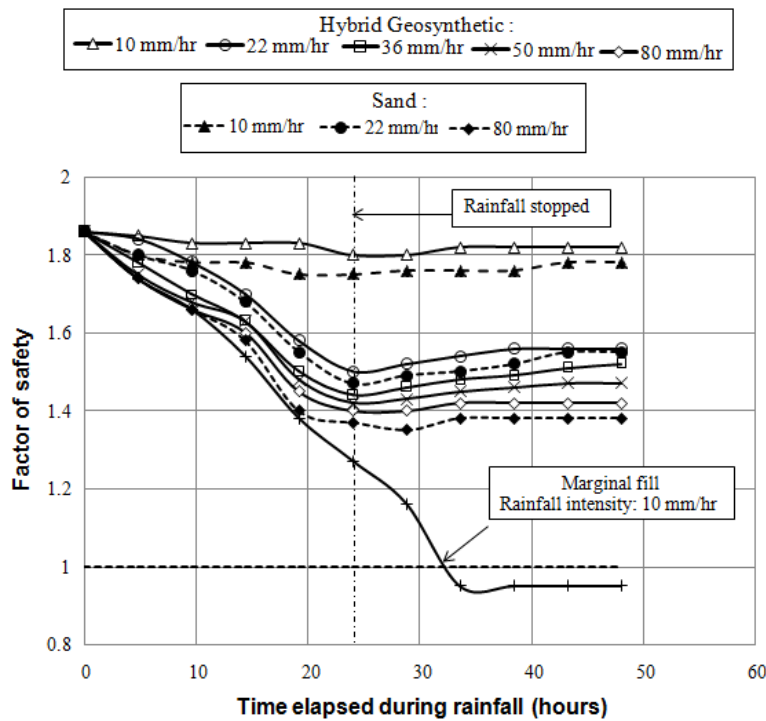


FIG. 6. Variation of factor of safety with hybrid geosynthetic and sand layers ($n=4$).

CONCLUSIONS

Based on the interpretation of seepage and stability analyses results of wall section with marginal fill subjected to rainfall, it can be concluded that the pore water pressure generated within the reinforced zone due to rainfall reduced by 40% and

72% respectively with the inclusion of sand and hybrid geosynthetic layers. In general, the hybrid geosynthetic layers were found to be more effective as a better drainage measure and reinforcing element than identical number of sand layers for different intensities of rainfall simulated. The drainage layers provided in the upper half of the wall section were observed to be less significant in lowering pore water pressures as well as in improving the global stability. Hence, the provision of hybrid geosynthetic layers is a viable option to alleviate the problems posed by low permeability backfill in reinforced soil wall construction.

REFERENCES

- Chen, H-T., Hung, W-Y., Chang, C-C., Chen, Y-J., and Lee, C-J. (2007). "Centrifuge modeling test of a geotextile-reinforced wall with a very wet clayey backfill". *Geotextiles and Geomembranes*, 25(6): 346–359.
- FHWA-NHI-10-024. (2009). "Design and construction of mechanically stabilized earth walls and reinforced soil slopes", Vol 1: 94-101.
- Geostudio 2012: SLOPE/W, SIGMA/W and SEEP/W, Ver. 7.15, User's Guide, *Geo-Slope International Ltd*, Calgary, Canada.
- Iryo, T. and Rowe, R.K. (2004). "Numerical study of infiltration into a soil-geotextile column". *Geosynthetics International*, 11(5): 377 – 389.
- Iryo, T. and Rowe, R.K. (2005). "Hydraulic behaviour of soil-geocomposite layers in slopes". *Geosynthetics International*, 12(3): 145 – 155.
- Koerner, R.M. and Soong, T-Y. (2001). "Geosynthetic reinforced segmental retaining walls". *Geotextiles and Geomembranes*, 19(6): 359–386.
- Koerner, R. M., Soong, T.-Y., and Koerner, G. R. (2005). "Back drainage design and geocomposite drainage materials". *Proc. of NAGS Conference, GRI-19*, Las Vegas, Nevada, USA, GII Publication, Folsom, PA: 51-86.
- Koerner, R. M. and Koerner, G. R. (2011). "The importance of drainage control for Geosynthetic reinforced mechanically Stabilized earth walls". *Journal of Geoengineering*, 6(1): 3-13.
- Llasat, M.C. (2001). "An objective classification of rainfall events on the basis of their convective features". *International J. of Climatology*, 21(1): 1385-1400.
- Mitchell, J.K. and Zornberg, J.G. (1995). "Reinforced soil structures with poorly draining backfills. Part II: Case Histories and Applications". *Geosynthetics International*, 2(1): 265-307.
- Raisinghani, D.V. and Viswanadham, B.V.S. (2011). "Centrifuge model study on low permeable slope reinforced by hybrid geosynthetics". *Geotextiles and Geomembranes*, 29(6): 567-580.
- Tsaparas, I., Rahardjo, H., Toll, D.G. and Leong, E.C. (2002). "Controlling parameters for rainfall-induced landslides". *Computers and Geotechnics*, 29(1): 1-27.
- Van Genuchten, M. Th. (1980). "A closed-form equation for predicting the hydraulic conductivity of unsaturated soils". *Soil Science Society of America J.*, 44 (5):892-898.
- Yoo, C.A, Jung, and H.Y. (2006). "Case History of Geosynthetic Reinforced Segmental Retaining Wall Failure". *J. Geotechnical and Geoenvironmental Engrg.*, 132(12): 1538-1550.

Exploring the Geomechanics of Sinkholes: A Numerical Simulation Approach

Kishor Rawal¹; Zhong-Mei Wang²; and Liang-Bo Hu³

¹Graduate Research Assistant, Dept. of Civil Engineering, Univ. of Toledo, Toledo, OH 43606. E-mail: Kishor.Rawal@rockets.utoledo.edu

²Associate Professor, College of Resources and Environmental Engineering, Guizhou Univ., Guiyang, Quizhou Province 50025, China. E-mail: re.zmwang@gzu.edu.cn

³Assistant Professor, Dept. of Civil Engineering, Univ. of Toledo, Toledo, OH 43606. E-mail: Liangbo.Hu@utoledo.edu

Abstract: Sinkhole is a hazardous geological phenomenon which in recent years has occurred with an alarmingly increased frequency around the world. Although the conceptual nature of the involved key mechanisms of formation of the sinkhole is well-known and is believed to be related to the interaction between the underlying limestone rock layer and the groundwater subsequently leading to the accumulated deformation in the soil overlaying the weakened rocks, there has not been an adequate amount of geomechanical research devoted to the study of sinkholes in a quantitative manner. This paper presents some of the preliminary results of an ongoing research aimed to explore a geo-mechanical modelling approach and to understand the behavior of geo-materials around sinkholes. The finite difference program, FLAC, is used to model the behavior of geo-materials involved and simulate the deformation and stress characteristics of sinkholes. A parametric study is conducted to examine the results with different sizes of cavity, overburden thickness and pressure. The potential scenario of water drawdown is also examined. The results demonstrate some key characteristics of sinkhole subsidence and the feasibility of a geomechanical approach manifested in numerical modelling to improve the understanding of the process of sinkhole development.

INTRODUCTION

Sinkholes are a spectacular yet devastating geo-hazard which has recently occurred with an alarmingly rising frequency around the world. It poses a significant threat to the environment, infrastructure and human lives. The conceptual nature of the involved key mechanisms is well-known, as it is usually related to the formation or development of a cavity as a result of the interaction between the underlying limestone rock layer and the groundwater, which subsequently leads to the accumulated deformation in the soil overlaying the weakened rocks. However, there are many possible causes or triggering events behind the collapse of sinkholes, including loosening of soil layers, dissolution of limestone bedrock (Martinez et al. 1998; Galloway et al. 1999; Gutierrez

and Cooper 2002), lowering of the water table (Kiernan 1989; Sowers 1996), loss of buoyant support (Newton 1984), blasting (Pazuniak 1989; Iqbal 1996), and leakage of sewer system and water pipelines (Goering and Sayed 1989; Scarborough 1996).

Solution sinkholes form by the dissolution of limestone bedrock by the ground water leading to early small depressions and subsequently a possible collapse of soil-rock layers over time (White 1988; Sowers 1996). Subsidence sinkholes are similar to solution sinkholes except that the limestone bedrock is covered by a thin layer of soils. It generally occurs in clay and sand areas where soils are not knitted or bonded well together (Waltham et al. 2007). Cover collapse sinkholes are another type of sinkholes characterized by the growth and propagation of a void in the bedrock above the cavity, as the bedrock is gradually eroded and fractures or cracks develop, facilitating the water flow; an arch begins to propagate upwards through the cover and eventually collapses when the limit of mechanical stability is exceeded.

Numerous studies have been devoted to understanding the mechanism of failure of sinkholes. An early study by Drumm et al. (1990) used the classic plasticity theory to evaluate the stability of soils in a cylindrical void and developed the lower bound solution for the overburden loading causing instability. Abdulla and Goodings (1996) examined the stability of cemented sand layer overlying the cylindrical shaped cavity, with or without overburden. Tharp (1999) introduced a simplified hemispherical model to examine the mechanics of upward propagation of cover collapse sinkholes, including the effects of pore water pressure changes. Vaziri et al. (2001) developed an analytical model for the stability of the axisymmetric region of caprock above a cavity. Augarde et al. (2003) used finite element limit analysis to obtain upper and lower bound loading values in studying the undrained stability of submerged cavities. A recent study of Shalev and Lyakhovsky (2012) developed a two-dimensional viscoelastic damage numerical model to explore the mechanical formation of collapsed sinkholes by viscous flow and brittle fracture failure.

Geomechanics has an important role to play in understanding the behavior of geomaterials involved in sinkhole formations and collapses. The core of the problem at hand may involve multi-physics phenomena of hydro-chemo-mechanical interactions to be understood, formulated and modelled at their proper scales. This paper presents some of the preliminary results of an ongoing research aimed to explore a geomechanical modelling approach to better understand the sinkhole processes. The early stage of this research mainly focuses on the mechanics around a cavity/opening in rock formation underlying a weaker soil layer. Traditional geotechnical analyses have been usually conducted with an aim to identify the limit or maximum load as a function of the geometric configuration of soil layer and cavity size and strength properties. Geotechnical research of sinkholes can certainly be enhanced by theoretical, analytical and numerical efforts to explore the progressive nature of the sinkhole process. In the present study, a parametric study is undertaken to investigate the characteristics of deformation and stress as influenced by various factors, including overburden pressure, thickness and size of the cavity. However, the formation of a sinkhole is a complicated scenario which is triggered or affected by the complex hydrological events. Hence, a coupled hydro-mechanical simulated model is needed to explain the intricate processes involved during the formation of sinkhole. Thus, the latter section presents the preliminary couple model to show the effect of water drawdown scenario.

BASICS OF NUMERICAL MODELLING

As discussed in the preceding section, eventually the mathematical modelling will have to consider complex, and most likely coupled geo-mechanical behavior such as carbonate or dolomite dissolution reaction and associated chemical softening. The simulations presented are restricted to purely mechanical responses of soil and rock layers. The main goal of the present investigation is to understand the characteristics of deformation and stress around a cavity that may facilitate the formation or growth of a sinkhole and explore the feasibility of this modelling approach before more complicated mechanical constitutive models can be introduced and non-mechanical processes considered. Hence, the geometry and material behavior are kept simple in the current simulations. Moreover, a hydro-mechanical model is also presented in the latter section to study the intricate processes during the formation of a sinkhole and explore the effect of ground water table in drawdown scenarios.

Geometry of the Model and Material Properties

A typical conceptual cavity model in FLAC2D is shown in Fig. 1, in which the materials are represented by the elements or the zones; and the grids and meshes are adjusted to make the desired circular cavity. In this model, the bottom layer represents the limestone whilst the upper layer represents the clay overlying the limestone rock. The thickness of clay and limestone is assumed as 5m each while the width is assumed to be 20m. Initially, a small circular cavity throat is assumed to form in the limestone layer. Also, an overburden downward pressure is applied from the top.

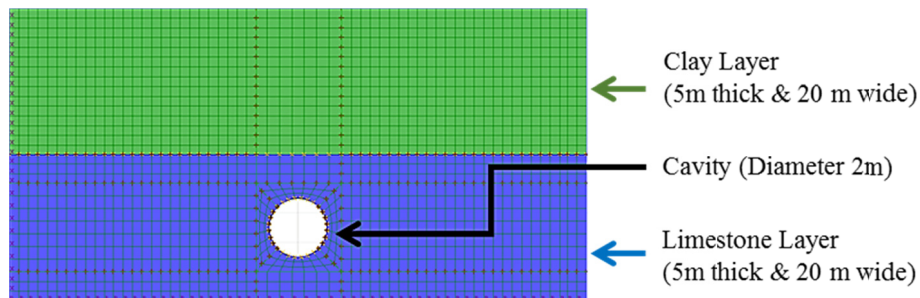


FIG. 1. Geometry of the model.

Table 1: Input sinkhole model parameters

Input Parameters	Clayey Soil	Limestone Rock
Density (ρ)	2000 kg/m ³	2700 kg/m ³
Friction angle (ϕ)	27°	30°
Cohesion (c)	15 kPa	1 MPa
Modulus of Elasticity (E)	30 MPa	5 GPa
Poisson's ratio (ν)	0.3	0.3

Mohr-Coulomb plasticity model is used for both layers. The model parameters are taken based on typical ranges of soil or rock properties and shown in Table 1, where ρ

is the density, ϕ is the friction angle, c is the cohesion intercept, E is the modulus of elasticity, and ν is the Poisson's ratio.

NUMERICAL RESULTS

Parametric Study in FLAC

A number of factors are investigated at this point including soil and rock geometrical configuration (thickness) and properties (cohesion and angle of friction), cavity/opening size (diameter) and location (depth). The presented simulations focus on three critical factors in a parametric cavity size (D), overburden pressure (p) and thickness (H).

Overburden Pressure

For a cavity of a constant size ($D = 2\text{m}$), the overburden pressure is increased step by step and the vertical displacement and stress at the cavity are evaluated through the numerical analysis. Vertical displacements at the surface and at the top of the cavity are shown in Fig. 2a. The values are expressed as normalized non-dimensional quantities. With increasing overburden pressure ($p/\gamma H$), the vertical deformation (u/H) at the cavity first increases with a small slope as the material deforms elastically at the beginning, followed by the plastic deformation. A greater slope of the deformation around the cavity as influenced by overburden pressure is observed while the displacement at the ground surface seems still stable. The characteristic of deformation at the top of the cavity is confirmed in part by the vertical stress (σ) as shown in Fig. 2b. The trend for the generated stress becomes much steeper when the overburden pressure applied is increased significantly, i.e., when $p/\gamma H$ exceeds 100.

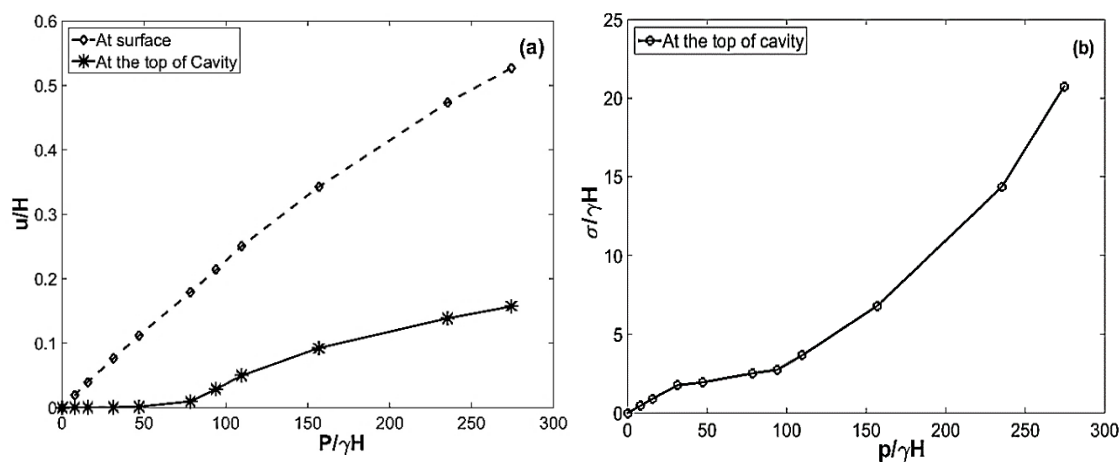


FIG. 2. Influence of increase in overburden pressure (p) on (a) the vertical deformation at the top of the cavity and surface; (b) the vertical stress (σ) at the top of the cavity, where γ represents the specific weight of clay, u represents the vertical deformation and H represents the thickness over a cavity.

Cavity Size

For a constant overburden thickness of clay (5 m) over the limestone layer of 5m thick, the diameter of the cavity varying from 0 to 3 m is increased step by step and the vertical deformation at the node points is evaluated through the numerical analysis. Vertical deformation is calculated at the cavity for each case as shown in Fig. 3. It is found that with increasing cavity diameter, the vertical deformation increases more dramatically when D exceeds 2 m, which is around half of the limestone rock's thickness. Below that the deformation appears to increase quite modestly as influenced by the cavity size.

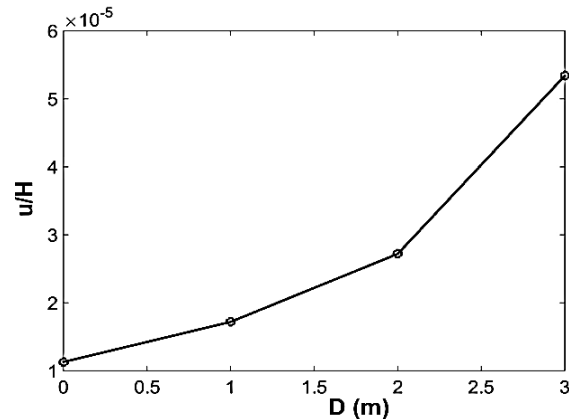


FIG. 3. Influence of increase in diameter of the cavity (D) on the vertical deformation (u) at the cavity; note that the overburden thickness remains constant ($H=5$ m).

Layer Thickness

For a cavity of a constant size, simulations of varying clay layer thickness over a rock formation produce similar results at the top of the cavity as those influenced by overburden pressure as already presented earlier; this is quite understandable as the thicker overlay soil results in higher vertical pressure. Therefore, a minor change is introduced: a single clay layer or a single limestone layer is simulated instead of two layers (clay and limestone). It should be noted that in the early section on overburden pressure, the gravity of the layers has been intentionally ignored in order to separate the effects of the loading (overburden pressure) and the layer thickness. In essence, the behavior investigated here is affected by both the weight of overlying layer and the geometry of the configuration.

Still similar trends can be seen. The overburden thickness above cavity (H) is plotted with the resulting vertical deformation at the cavity (u) in Fig. 4. Obviously, the deformation in a stronger limestone layer is much smaller. The trends of the graphs in Fig. 4a and 4b are similar, but it appears that the deformation at the top of a cavity in a softer layer would increase more dramatically with the increase in the layer thickness.

In summary, although some aspects of the presented results are quite expected, overall they provide some details of the influence of important factors. It is worth noting that the interplay of overburden thickness and cavity size can be quite intricate, as while the increase in overburden thickness increases the overall applied pressure, it also increases the distance from the cavity to the ground surface, thus potentially

alleviates the effects of the cavity (e.g., Augarde et al. 2003). This characteristic may not be directly reflected by the deformation or stress development, but may be potentially explored by the identification of critical levels of (overburden) load.

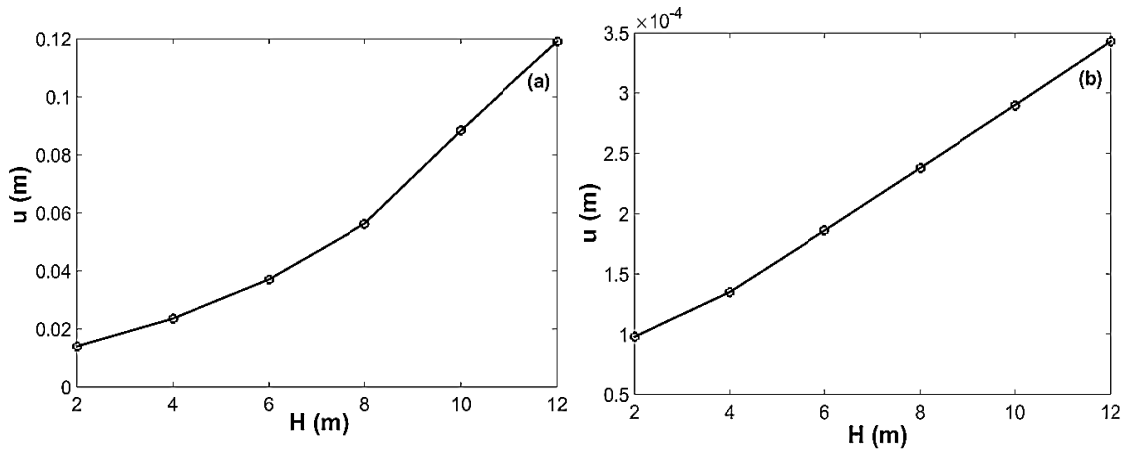


FIG. 4. Influence of increase in overburden thickness (H) at a constant cavity size on the vertical deformation (u) at the top of the cavity (a) in a clay layer; (b) in a “stronger” limestone layer.

Vertical Stress Profile

A typical stress distribution is shown in Fig. 5. Fig. 5b re-plots the values of the vertical stresses along the depth on A-A” and B-B”. As can be seen, higher vertical stresses occur away from the cavity than above or below the cavity. Along B-B”, the vertical stresses first increase as the depth increases, but when the depth approaches the cavity, the vertical stress starts to decrease because the circumferential stress just around the cavity is significant which mitigates the increase in vertical stresses at the top of the cavity. Obviously, the effect of the circumferential stress becomes negligible away from the cavity.

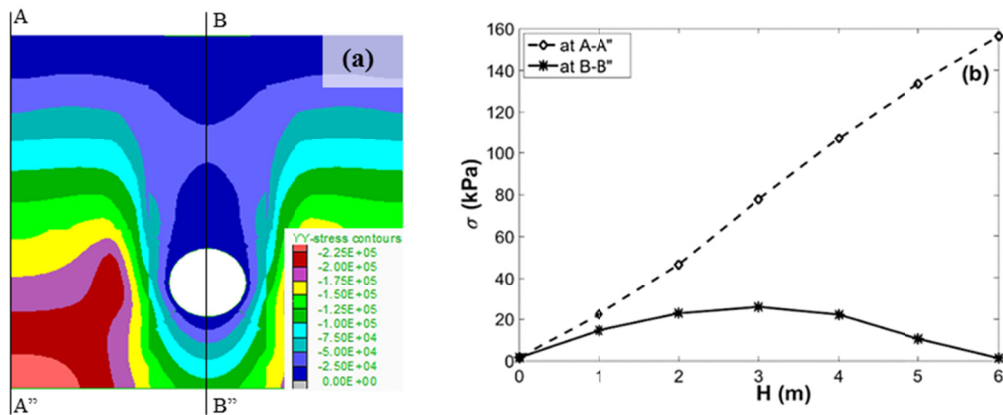


FIG. 5. (a) A typical color map of vertical stress (σ) contours; (b) distribution of vertical stress (σ) at A-A” and B-B” from ground to the cavity.

A Scenario of Water Drawdown

Lowering of the water table as a result of drawdown has become a primary cause for a more frequent occurrence of sinkholes. So, it is of interest to tentatively simulate this scenario in a coupled analysis in FLAC, in which both the mechanical process and the groundwater flow are considered. A drawdown scenario is initiated by imposing different water pressure decreases at the top and the bottom, inducing a downward water flow that eventually lowers the water table by approximately 6 m, as shown in Fig. 6a. It is observed that the vertical deformation in a coupled simulation is larger than that of mechanical simulation. In addition, a parametric study is conducted to show the influence of the groundwater table (GWT) as shown in Fig. 6b. When the GWT is at 9m, the vertical deformation (u) is measured as 0.158 m but as the GWT is lowered to 1m, it increases up to 0.174m. Hence, decreasing the water table increases the vertical deformation in the hydro-mechanical analysis. Studying this type of water drawdown scenario and the effects of GWT change provides further opportunities to understand the extent to which how permeation of water potentially facilitates and accelerates the sinkhole development.

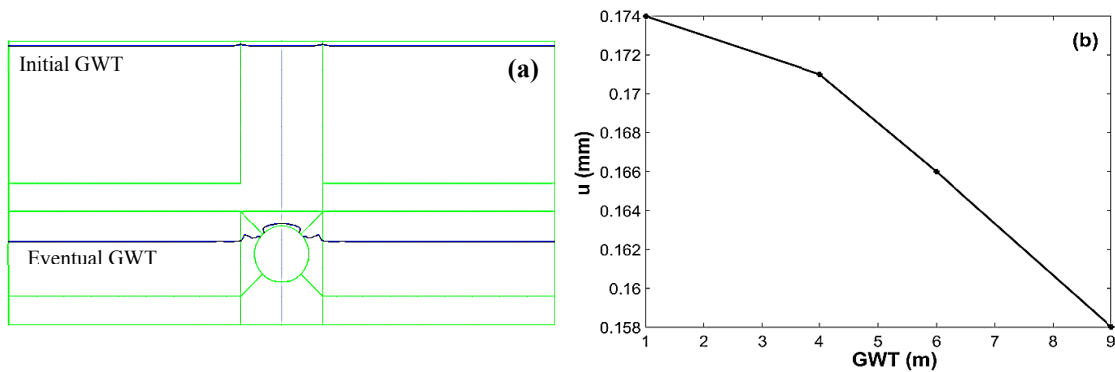


FIG. 6. (a) Simulated lowering of the water table; (b) Influence of groundwater table (GWT) on the vertical deformation (u) at the top of the cavity, zero is at the bottom of the rock.

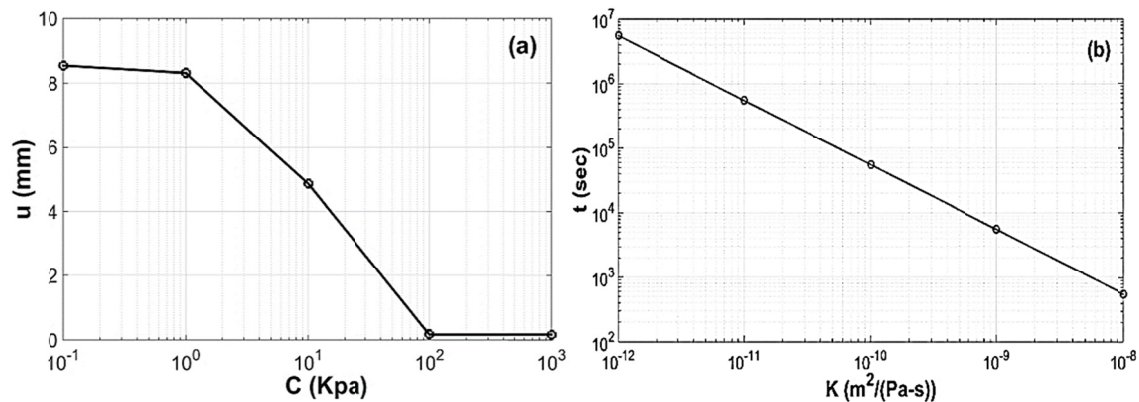


FIG 7. (a) Effect of cohesion (c) on the vertical deformation of the limestone layer; (b) Effect of permeability (K) with the time of collapse (t).

The effect of cohesion can be observed using either single or double layer; however, a single layer is more explainable and easier to show the precise relationship. The following presentation is based on a single-layered (limestone) hydro-mechanical model implemented in FLAC with varying the strength parameter (cohesion) at a constant friction angle. Higher the cohesion, shear strength of the material also becomes higher. Fig. 7 shows that the increasing the cohesion of the material (c), the vertical deformation (u) decreases abruptly up to a certain limit (100 kPa in this case) due to increase in shear strength. Beyond that, the limestone gained the sufficient strength and the vertical deformation remains constant without any application overburden pressure. Fig. 7b shows the time needed for this collapse (t) at different permeability, indicating a linear relationship as the high permeable soil collapse in a short period of time and vice versa. It means the low permeable soils are more resistant to collapse and takes longer time to cause abrupt collapse. The collapse of the model is defined by the plasticity indicator which forms around the cavity at the beginning similar to Fig 7a, spreads out and finally leads to huge deformation.

DISCUSSION

The preceding sections present the results mainly focused on the vertical deformation and stress in the soil and rock formations. The yielding or the failure of material is not solely governed by the level of stress components but whether the criterion is met. For all the simulation cases, especially those with very high stress or large deformation, it is interesting to observe the plastic deformation around the cavity. Fig. 8a is a typical contour of plasticity indicators which indicate the occurrence of plastic deformation. It suggests that the material yields initially at the periphery of the cavity (red sign around the cavity in Fig. 8a). Subsequently, the plastic failure occurs in other zones primarily rising from a cavity to the top surface. The region which lies over the cavity is the weakest zone in which the fracture or damage may occur to facilitate the water flow and dissolution activities. Fig. 8b shows an inverted conical shape of the contour of vertical deformation; details of these results deserve further investigation as it is widely speculated that the failure surface is usually formed in such shape and region.

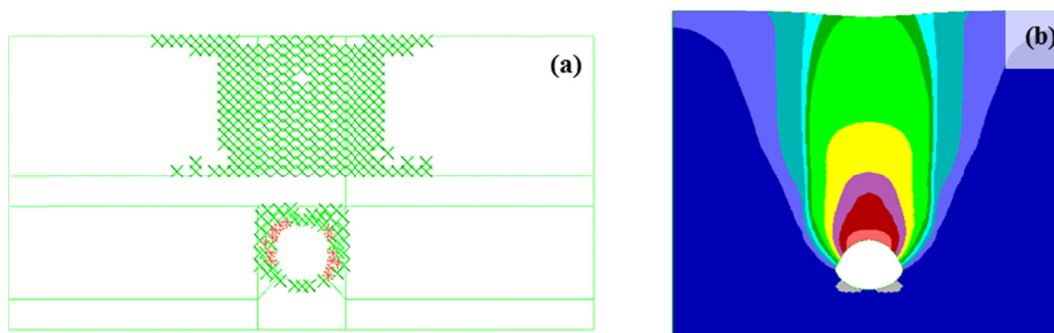


FIG. 8. (a) Plasticity indicator around the cavity in a typical simulation; (b) Vertical deformation contours forming the inverted conical shape of potential failure surface.

CONCLUSIONS

This paper presents some of the results in the early stage of an ongoing research focused on a geomechanical modelling approach to better understand the sinkhole geo-hazard. While it is believed that natural processes of sinkholes may be associated with dissolution dominated mechanisms and thus require an extended period (even geological scale) of time, the increased anthropogenic activities, especially those related to the energy exploitation and resulting in the deterioration of our ecological system, may potentially significantly intensify the hydro-chemo-geomechanical interactions and accelerate the originally prolonged processes. Geomechanics plays an important role in understanding the relevant mechanisms and eventually developing effective simulation or prediction tools.

The presented study mainly focuses on the characteristics of deformation and stress around a cavity in a traditional mechanical analysis and a hydro-mechanical analysis of water drawdown scenarios. Several important factors are considered. The presented results so far suggest that this approach is feasible, but needs more sophisticated refinements and significant advances in order to explore many intricacies and complexities of the mechanisms involved. Clearly future models may have to consider complex, coupled geomechanical processes such as carbonate or dolomite dissolution reaction and associated chemical softening and damage, as well as complicated hydro-geo-mechanical processes involved.

REFERENCES

- Abdulla, W. A. and Goodings, D. J. (1996). "Modeling of sinkholes in weakly cemented sand." *Journal of Geotechnical Engineering*, 122(12): 998-1005.
- Augarde, C. E., Lyamin, A. V. and Sloan, S. W. (2003). "Prediction of undrained sinkhole collapse." *Journal of Geotechnical and Geoenvironmental Engineering*, 129(3): 197-205.
- Drumm, E. C., Kane, W. F. and Yoon, C. J. (1990). "Application of limit plasticity to the stability of sinkholes." *Engineering Geology*, 29(3): 213-225.
- Galloway, D., Jones, D. R. and Ingebritsen, S. E. (1999). *Land subsidence in the United States*. Reston, VA: US Geological Survey.
- Goering, R. L. and Sayed, S. M. (1989). "Mann road sinkhole stabilization: a case history." *Proc. 3rd Multidisciplinary Conf. on Sinkholes and the Engineering and Environmental Impacts of Karst*. Balkema, Rotterdam, 319-325.
- Gutiérrez, F. and Cooper, A. H. (2002). "Evaporite dissolution subsidence in the historical city of Calatayud, Spain: damage appraisal and prevention." *Natural Hazards*, 25(3): 259-288.
- Iqbal, M. A. (1996). "Engineering experience with limestone." *International Journal of Rock Mechanics and Mining Sciences and Geomechanics Abstracts*. 2(33): 85A.
- Kiernan, K. (1989). "Sinkhole hazards in Tasmania." *Proceedings of the 3rd Multidisciplinary Conference on Sinkholes and the Engineering and Environmental Impacts of Karst*, 123-128.

- Martinez, J., Johnson, K. and Neal, J. (1998). "Sinkholes in Evaporite Rocks Surface subsidence can develop within a matter of days when highly soluble rocks dissolve because of either natural or human causes." *American Scientist*, 86(1): 38-51.
- Newton, J. G. (1984). "Sinkholes resulting from ground-water withdrawals in carbonate terranes - an overview." *Reviews in Engineering Geology*, 6: 195-202.
- Pazuniak, B. L. (1989). "Subsurface investigation response to sinkhole activity at an eastern Pennsylvania site." *Proceedings of the 3rd Multidisciplinary Conference on Sinkholes*. St. Petersburg, FL, 263-269.
- Scarborough, J. A. (1996). "Risk and reward: pipes and sinkholes in east Tennessee." *International Journal of Rock Mechanics and Mining Sciences and Geomechanics Abstracts*, 2(33): 97A.
- Shalev, E. and Lyakhovsky, V. (2012). "Viscoelastic damage modeling of sinkhole formation." *Journal of Structural Geology*, 42: 163-170.
- Sowers, G. (1996). *Building on Sinkholes: Design and Construction of Foundations in Karst Terrain*. ASCE, Reston, VA.
- Tharp, T. M. (1999). "Mechanics of upward propagation of cover-collapse sinkholes." *Engineering Geology*, 52(1): 23-33.
- Vaziri, H. H., Jalali, J. S. and Islam, R. (2001). "An analytical model for stability of rock layers over a circular opening." *International Journal of Solids and Structures*, 38 (21): 3735-3757.
- Waltham, T., Bell, F. G. and Culshaw, M. (2007). *Sinkholes and Subsidence: Karst and Cavernous Rocks in Engineering and Construction*. Springer-Verlag, Berlin.
- White, W. B. (1988). *Geomorphology and Hydrology of Karst Terrains*. Oxford University Press, New York.

Feasibility Analysis of the External Electric Anode Method for Reducing Lightning Hazards

Chao Zhang, S.M.ASCE¹; and Zhen Liu, M.ASCE²

¹Graduate Research Assistant, Dept. of Civil and Environmental Engineering, Michigan Technological Univ., 1400 Townsend Dr., Houghton, MI 49931.

²Assistant Professor, Dept. of Civil and Environmental Engineering, Michigan Technological Univ., 1400 Townsend Dr., Houghton, MI 49931 (corresponding author).
E-mail: zhenl@mtu.edu

Abstract: Lightning rods are usually employed to reduce lightning hazards in facilities such as power distribution lines through transmitting the lightning to the ground. The high electrical conductivity of the surrounding soils is the prerequisite for the effectiveness of the lightning rod. In general, the electrical conductivity increases with increasing the degree of saturation. Therefore, the surrounding soils with a low moisture content may possess a relatively low electrical conductivity, which increase the lightning hazards. It is thus desirable to main a high moisture content in soils surrounding the lightning rod. The water flow in the soils induced by external electrical field is usually referred as electro-osmosis flow, which has been widely used in ground remediation in geotechnical engineering. Based this physical phenomenon, an external anode method is proposed in this paper to maintain the high moisture content around the grounding rod by inserting an anode around the grounding rod. The feasibility analysis of the proposed external electric anode method was carried out through numerical simulations. The physical phenomenon underlying the proposed method was a typical coupled electro-saturated-unsaturated water flow process in porous media. In order to model this complex coupled process, a multi-physical framework is proposed to solve this problem numerically. The coupled electro-saturated-unsaturated water flow is decoupled by introducing a series of physical relationships which could be directly obtained through specific geotechnical experiments. At last, two comprehensive parametric studies were conducted to preliminarily assess the feasibility of the proposed method. Results of the case studies reveal that the external anode method has the potential to reduce the lightning hazards.

INTRODUCTION

Lightning is a major natural hazard that may cause numerous casualties and tremendous economic loss (Gomes and Ab Kadir 2011). As illustrated in Figure 1, in practice, a lightning rod is employed to conduct the lightning to the ground, which represents a common method to reduce lightning hazards. The high electrical conductivity of the surrounding soils is a key factor to the effectiveness of the lightning rod. According to Ancn (1942), the electrical conductivity of the soils could be expressed as a equation of degree of saturation. In general, the electrical conductivity increases with an increasing degree of saturation. As a result, surrounding soils with a low moisture content may possess a relatively low electrical conductivity, which may increase the lightning hazards.

Hence, it is desirable to maintain enough water content in the soils around the grounding rod. This is of great interest in power distribution lines, in which lightning arrestors/rods are widely used while their coupling with ground has been barely understood from the perspective of geotechnical engineering.

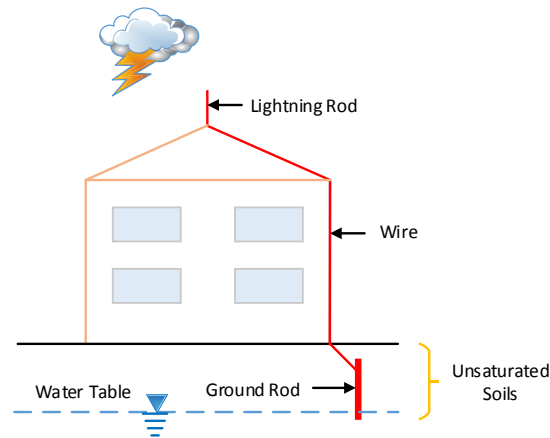


FIG. 1. Schematic plot of the lightning rod.

As for the water flow in soils, there are mainly four types of physical potentials governing this process, i.e. water head, chemical gradient, thermal gradient and electric gradient (Mitchell and Soga 2005). It is not easy to modify the local water head permanently by adjusting water head, chemical gradient and thermal gradient, whereas it may be convenient to modify the local water head permanently by inserting an anode around the grounding rod. In this paper, an external anode method is proposed to maintain the high moisture content around the grounding rod.

The water flow in the soils induced by external electric gradients is usually referred as electro-osmosis flow, which has been widely used in ground remediation in geotechnical engineering. In recent years, in order to apply electro-osmosis flow to electrokinetic remediation, the complex physical phenomena underlying the water flow in soils under an external electrical field have been extensively investigated (Acar and Alshawabkeh 1993; Acar et al. 1989; Virkutyte et al. 2002). Besides altering the pore water pressure regime by inducing a time-dependent coupled flow and deformation (consolidation) process in the soil mass, the application of an electrical field to a fine-grained soil promotes complex electro-chemical phenomena, such as hydrolysis reactions at the electrodes, ion migration, changes in pore water pH, aqueous phase reactions, precipitation and dissolution, adsorption and desorption. These phenomena can, in turn, induce permanent modifications to the mechanical properties of the soil (Esrig and Gemeinhardt 1900; Gray 1970). As a result, the electro-osmosis phenomena is a complex multi-physical process.

In this paper, the feasibility analysis of the proposed external anode method is conducted via numerical simulations. From physical perspective, this problem involves a coupled electro-saturated–unsaturated water flow process. In order to depict this complex coupling process, a multi-physical framework is proposed to formulate this problem mathematically. The coupled electro-saturated-unsaturated water flow is decoupled by introducing a series of physical relationships which could be directly measured using some geotechnical experiments. Then the proposed framework is implemented with

FlexPDE (, a commercial platform for solving partial differential equations. Two case studies with a two-dimensional and axisymmetric geometries are conducted as in this preliminary investigation. The results will help draw conclusions regarding whether the proposed external anode method could significantly help maintain high water moisture content around the grounding rod, which will reduce the lightning hazards.

MULTI-PHYSICAL FRAMEWORK

Basic Concepts and Assumptions

If the water table is below the grounding rod, the soils surrounding the grounding rod will have relatively a low moisture content. As a result, the surrounding soils may process low electrical conductivity, which may reduce the effectiveness of the grounding rod. As depicted in Figure 2, an external anode is installed around a grounding rod. It is expected that the anode will modify the local water head and help maintain a high moisture content in the soils around the grounding rod.

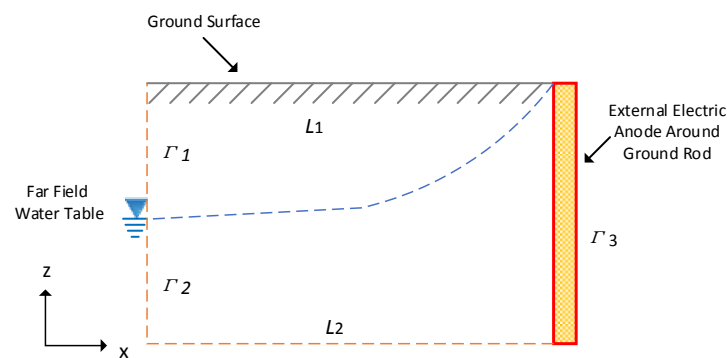


FIG. 2. Schematic plot of the proposed external electric anode method.

In Figure 2, one could observe that saturated and unsaturated soils coexist in the physical domain of interest, which means that coupled saturated and unsaturated water flow should be taken into consideration. Meanwhile, the electrical conductivity of unsaturated soils varies with the degree of saturation. As a result, the water flow will influence the electrical field while the electrical field will in turn change the water flow. Therefore, it is concluded that the major physical mechanisms behind the proposed external electric anode method is a coupled electro-saturated-unsaturated water process.

In order to describe this problem mathematically, a multi-physical framework is proposed for this coupled electro-saturated-unsaturated water flow process. For simplicity's sake, the following assumptions are made.

(1) The computational domain of interest is assumed to be under isothermal conditions (Tamagnini et al. 2010; Yuan and Hicks 2015).

(2) The coupled water flow could be expressed as a linear combination of the water flow induced independently by the water head and electric gradient (Esrig 1968; Hu and Wu 2013).

(3) Electrophoresis and streaming currents are negligible (Tamagnini et al. 2010);

(4) The effect of chemical reactions (precipitation, dissolution, aqueous phase reactions and sorption) could be neglected (Tamagnini et al. 2010; Yuan and Hicks 2014).

(5) The effect of change in pH and ionic concentrations of dissolved species in soils is negligible (Tamagnini et al. 2010).

(6) The effect of consolidation and deformation of soils on the hydraulic and electric conducting behavior is negligible.

(7) Darcy's law and Ohm's law are valid (Hu and Wu 2013; Yuan and Hicks 2015).

Governing Equations

According to Richard's equation (Richards 1931), the coupled unsaturated-saturated water flow in soils could be expressed as:

$$n \frac{\partial S_w}{\partial H} \frac{\partial H}{\partial t} + \nabla \cdot \mathbf{v} = 0 \quad (1)$$

where S_w is the degree of saturation; t is the time; n is the porosity; H is the hydraulic pressure head; \mathbf{v} is the velocity of water flow. In this case, two physical potentials would contribute to the overall water flow: one is the water head and the other one the electrical field. According to Esrig (1968), the overall water flow could be expressed as the combination of the two water flows induced by the two physical potentials. Thus, the velocity of water flow could be written as:

$$\mathbf{v} = -\mathbf{k}_w k_{rw} \nabla(H+z) - \mathbf{k}_{eo} k_{reo} \nabla V \quad (2)$$

where \mathbf{k}_w is the intrinsic hydraulic conductivity; k_{rw} is the coefficient of relative hydraulic conductivity; z is the vertical coordinate; \mathbf{k}_{eo} is the intrinsic electro-osmosis conductivity; k_{reo} is the coefficient of relative electro-osmosis conductivity; V is the electrical potential. Substituting Equation (2) into Equation (1), the coupled electro-saturated-unsaturated water flow could be described as:

$$n \frac{\partial S_w}{\partial H} \frac{\partial H}{\partial t} = \nabla \cdot [\mathbf{k}_w k_{rw} \nabla(H+z) + \mathbf{k}_{eo} k_{reo} \nabla V] \quad (3)$$

According to Ohm's law, the electrical current density could be expressed as (Ohm 1827):

$$\mathbf{j} = -k_{r\sigma e} \mathbf{k}_{\sigma e} \nabla V \quad (4)$$

where $\mathbf{k}_{\sigma e}$ is the intrinsic electrical conductivity; $k_{r\sigma e}$ is the coefficient of relative electrical conductivity. Due the conservation of electrical charge, the governing equation for the electrical potential could be expressed as:

$$\nabla \cdot \mathbf{j} = C_p \frac{\partial V}{\partial t} \quad (5)$$

where C_p is the soil capacitance per unit volume which is negligible. Substitute Equation (5) into Equation (4), the governing equation for the electrical potential could be written as:

$$\nabla \cdot (k_{r\sigma e} \mathbf{k}_{\sigma e} \nabla V) = 0 \quad (6)$$

Therefore, the final governing equations for this problem could be written as:

$$\begin{cases} n \frac{\partial S_w}{\partial H} \frac{\partial H}{\partial t} = \nabla \cdot [\mathbf{k}_w k_{rw} \nabla(H+z) + \mathbf{k}_{eo} k_{reo} \nabla V] \\ \nabla \cdot (k_{rse} \mathbf{k}_{se} \nabla V) = 0 \end{cases} \quad (7)$$

Boundary Conditions

The physical domain shown in Figure 2 could be selected as a typical computational domain for this study. The boundary conditions along the ground surface can be expressed as:

$$\frac{\partial H}{\partial z} = 0, \text{ at } L_1 \quad (8)$$

$$\frac{\partial V}{\partial z} = 0, \text{ at } L_1 \quad (9)$$

In the far field, the influence of the electrical field is assumed to be negligible. As a result, the water flow will be only governed by the water head. Therefore, the boundary conditions along vertical far field cross section can be expressed as:

$$\begin{cases} \frac{\partial H}{\partial x} = 0 & \text{at } \Gamma_1 \\ H = h_w - z & \text{at } \Gamma_2 \end{cases} \quad (10)$$

$$\frac{\partial V}{\partial x} = 0, \text{ at } \Gamma_1 \text{ and } \Gamma_2 \quad (11)$$

where h_w is the height of the far field water table. The external electric anode is assumed to be impermeable. The boundary conditions along the external electric anode can be expressed as:

$$\frac{\partial H}{\partial x} = 0, \text{ at } \Gamma_3 \quad (12)$$

$$V = V_a, \text{ at } \Gamma_3 \quad (13)$$

Physical Relationships

One big challenge of the problem is the nonlinearity in the materials properties, that is, the descriptions of the undetermined parameters in Equation (7), the relationships between these parameters and their dependence on dependent and independent variables. Mostly of these physical relationships are associated with the consideration of the unsaturated regime in the computational domain. The relative hydraulic conductivity, electro-osmosis conductivity and electrical conductivity could be expressed as a function of the degree of saturation (Van Genuchten 1980). In this study, the model adopted by Tamagnini et al. (2010) and Yuan and Hicks (2014) is selected to depict these physical relationships due to their simplicity. The degree of saturation could be expressed as an equation of the hydraulic pressure head:

$$S_w = \left[1 + (-\alpha H)^n \right]^{-m} \quad (14)$$

where $\alpha = 0.00851 \text{ kPa}^{-1}$, $n = 1.31$ and $m = 1 - \frac{1}{n}$.

In terms of the relative hydraulic conductivity, it could be expressed as an equation of the degree of saturation:

$$k_{rw} = a_w (S_w)^{b_w} \quad (15)$$

where $a_w = 1.0$ and $b_w = 5$.

The electro-osmosis conductivity could be expressed as a function of the degree of saturation:

$$k_{reo} = a_{eo} (S_w)^{b_{eo}} \quad (16)$$

where $a_{eo} = 1.0$ and $b_{eo} = 3.2$.

The relationship between electrical conductivity and degree of saturation could be expressed as:

$$k_{r\sigma e} = a_{\sigma e} (S_w)^{b_{\sigma e}} \quad (17)$$

where $a_{\sigma e} = 1.0$ and $b_{\sigma e} = 2$.

NUMERICAL EXAMPLES

The proposed multi-physical framework of this problem is implemented with FlexPDE. As a preliminary study, two simple case studies were carried out to investigate the feasibility of the proposed external anode method in this section.

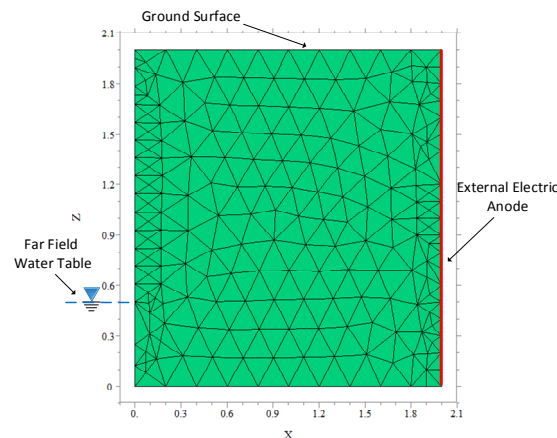


FIG. 3. Finite element mesh and geometry in Case 1.

Case 1: Two-Dimensional Study

As illustrated in Figure 3, a two-dimensional computational domain was utilized for this study. An external electric anode was placed at the right edge of the computational domain. The height and width of the computational domain were 2.0 m. The right edge of the computational domain was assumed to comply with the far field condition so that the electrical field has no effect on the water flow at that region. The height of the free field water table was assumed to be 0.5 m. The upper edge of the computational domain was assumed to be the ground surface. The boundary conditions of each edge were set as Subsection *Boundary Conditions*.

A series of simulations were conducted on the computational domain by varying the anode voltage. The distribution of the degree of saturation in the computational domain without an external electric potential is illustrated in Figure 4 (a). It could be observed that the distribution of the moisture content around the grounding rod is consistent with that of far field. As a result, there is a significant unsaturated region around the grounding rod, which may reduce the effectiveness of grounding rod. From Figure 4 (b) to (d), the voltage of the external electric anode decreases from -0.25 V to -1.0 V. Compared with Figure 4 (a), the presence of an external electrical field could significantly modify the distribution of the degree of saturation around the grounding rod. With a decreasing voltage of the electric anode, the moisture content of the soils around the electric anode will increase remarkably. One could see that the soils around the grounding rod are totally saturated with a voltage of -1.0 V as illustrated in Figure 4 (d). The degree of saturation along the grounding rod is illustrated in Figure 5. It could be observed that the local water table increases with the decreasing anode voltage. In terms of this two-dimensional study, the external electric anode has a remarkable potential to modify the local water head.

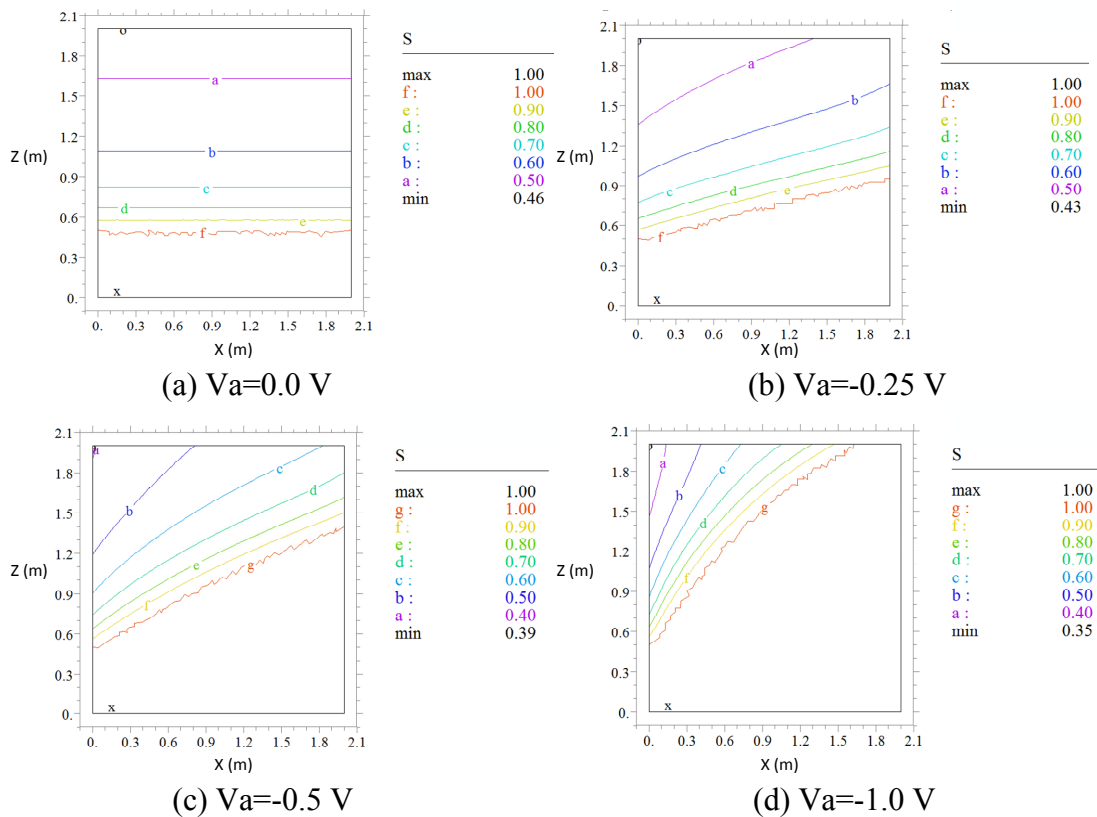


FIG. 4. Distribution of degree of saturation in the computational domain of Case 1 at different anode voltages.

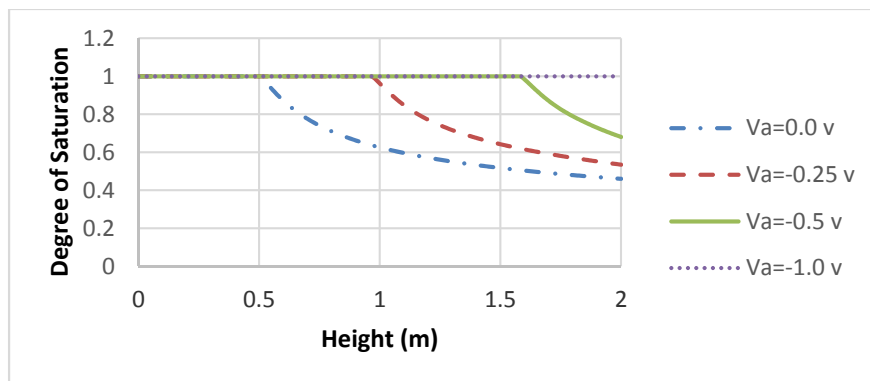


FIG. 5. Degree of saturation along the grounding rod at different anode voltages in Case 1.

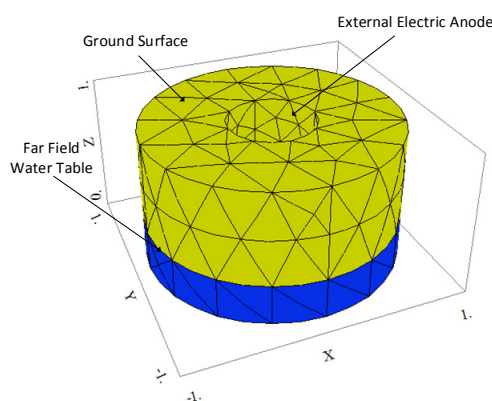


FIG. 6. Finite element mesh and geometry in Case 2.

Case 2: Axisymmetric Study

In this case study, a cylindrical simulation domain was adopted as illustrated in Figure 6. It was assumed that the grounding rod locates at the center of the computational cylinder domain and an electric anode was placed at the center of the simulation domain to construct the external electrical field. The height of the computational domain was 1.0 m. The radius of the simulation cylinder domain was 1.0 m. It was assumed that the boundary along the external circle of the simulation domain satisfies the far field assumption and that the anode at the center has no effects on the water head at that area. As a result, the water head along the external circle of the simulation domain was consistent with that of far field. The height of the free field water table was assumed to be 0.3 m. The upper surface of the computational domain was assumed to be ground surface. The boundary conditions of each surface were set as Subsection *Boundary Conditions*.

In this case study, the anode voltage was also selected as a parameter to investigate the feasibility of the proposed external anode method. The degree of saturation in the cross section of the computational domain is shown in Figure 7. There is an obvious unsaturated soil region around the grounding rod, which is consistent with the observation of Case 1 as illustrated in Figure 7 (a). This observation confirmed the importance of holding high moisture content around the grounding rod. From Figure 7 (b) to (d), the voltage of the external electric anode decreases from -0.2 V to -0.6 V. Trends similar with Case 1 are observed in this case study. The presence of an external electrical field could significantly

change the local moisture content around the grounding rod. This effect would become more significant with a decreasing voltage at the electric anode. The degree of saturation along the grounding rod is illustrated in Figure 8. It could be observed that the local water table increases with the decreasing anode voltage. During the simulation process, the degree of saturation around the grounding rod increased with adding the anode and the water tended to flow towards the anode. Therefore, results from this axisymmetric study also support the utilization of the proposed external anode method.

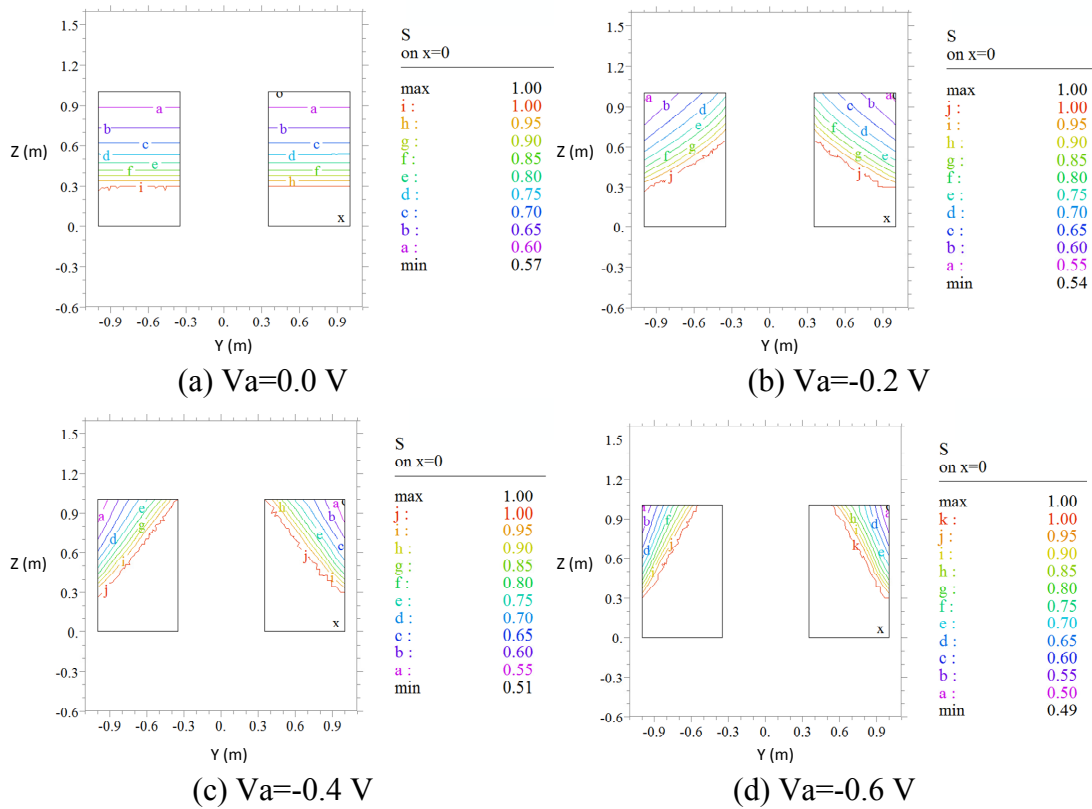


FIG. 7. Distribution of degree of saturation in a cross section of the computational domain at different anode voltages.

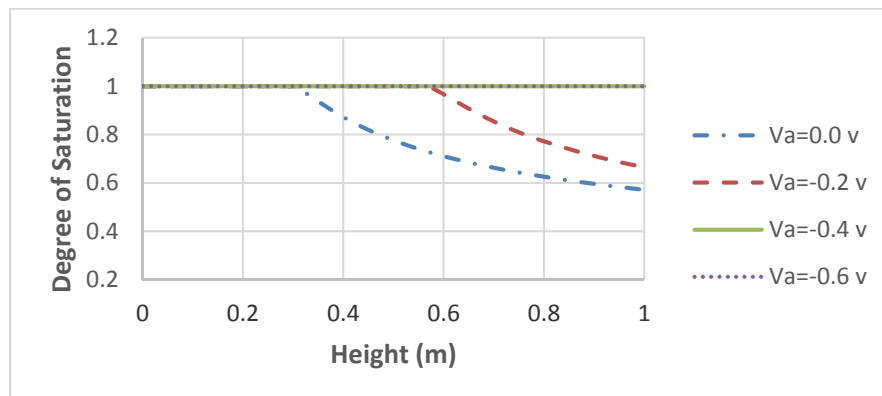


FIG. 8. Degree of saturation along the grounding rod at different anode voltages in Case 2.

SUMMARY AND CONCLUSIONS

In this study, an external anode method was proposed to reduce the lightning hazards by increasing the electrical conductivity in the soils surrounding the grounding rod by means of maintaining a high moisture content. For the purpose, the efficiency of the external electrical field in modifying the local water potential needs to be clarified. The primary underlying mechanism is a coupled electro-saturated-unsaturated water flow. Based on the understanding, a multi-physical framework was proposed to investigate this problem numerically. A series of physical relationships as a function of the degree of saturation was introduced to decouple the governing equations. The numerical simulation results of two typical cases were presented and discussed. The results confirmed that the external electric anode method has the potential to reduce the lightning hazards significantly. As a preliminary study, this investigation shows the potential of applying the proposed method to mitigating the lightning hazards associated with distribution lines in the power industry.

REFERENCES

- Acar, Y.B. & Alshawabkeh, A.N. 1993. Principles of electrokinetic remediation. *Environ Sci Technol*, **27**, 2638-2647.
- Acar, Y.B., Gale, R.J., Putnam, G. & Hamed, J. 1989. Electrochemical processing of soils: its potential use in environmental geotechnology and significance of pH gradients. *2nd International Symposium on Environmental Geotechnology*. ENVO Publishing Company, Incorporated, 14-17.
- Ancn, G. 1942. The electrical resistivity log as an aid in determining some reservoir characteristics. I. *Pet Tech*, **5**.
- Esrig, M. & Gemeinhardt, J. 1900. Electrokinetic stabilization of an illitic clay. *Journal of Soil Mechanics & Foundations Div*, **92**.
- Esrig, M.I. 1968. Pore pressures, consolidation, and electrokinetics. *Am Soc Civil Engr J Soil Mech*.
- FlexPDE, P. Solutions Inc. URL <http://www.pdesolutions.com>.
- Gomes, C. & Ab Kadir, M. 2011. A theoretical approach to estimate the annual lightning hazards on human beings. *Atmospheric Research*, **101**, 719-725.
- Gray, D.H. 1970. Electrochemical hardening of clay soils. *Geotechnique*, **20**, 81-93.
- Hu, L. & Wu, H. 2013. Mathematical model of electro-osmotic consolidation for soft ground improvement. *Geotechnique*, **64**, 155-164.
- Mitchell, J.K. & Soga, K. 2005. *Fundamentals of soil behavior*. John Wiley & Sons.
- Ohm, G.S. 1827. *Die galvanische Kette, mathematisch bearbeitet*. Riemann.
- Richards, L.A. 1931. Capillary conduction of liquids through porous mediums. *Journal of Applied Physics*, **1**, 318-333.
- Tamagnini, C., Jommi, C. & Cattaneo, F. 2010. A model for coupled electro-hydro-mechanical processes in fine grained soils accounting for gas generation and transport. *Anais da Academia Brasileira de Ciências*, **82**, 169-193.
- Van Genuchten, M.T. 1980. A closed-form equation for predicting the hydraulic conductivity of unsaturated soils. *Soil Science Society of America Journal*, **44**, 892-898.

- Virkutyte, J., Sillanpää, M. & Latostenmaa, P. 2002. Electrokinetic soil remediation-critical overview. *Science of the Total Environment*, **289**, 97-121.
- Yuan, J. & Hicks, M. 2014. Numerical modelling of electro-osmosis consolidation of unsaturated clay at large strain. *Proc. of the 8th European Conf. on Numerical Methods in Geotechnical Engineering*.
- Yuan, J. & Hicks, M.A. 2015. Numerical simulation of elasto-plastic electro-osmosis consolidation at large strain. *Acta Geotechnica*, 1-17.

Flood Holding Capacity: A Novel Concept to Evaluate the Resilience of Amended Soils

Heather Kerr¹; Karen Johnson¹; David G. Toll¹; and Florence Mansfield¹

¹School of Engineering and Computing Sciences, Durham Univ., Lower Mountjoy, South Rd., Durham, DH1 3LE.

Abstract

The term water holding capacity (WHC) has long been used to help researchers determine how soils respond to typical wetting under rainfall. However the term WHC is insufficient as a measurement to describe how soil responds to flooding events. This paper aims present a novel method for WHC testing that also incorporates the volume change, shear strength, erosional resistance and hydraulic conductivity of the soil under saturated conditions. The qualitative combination of these parameters will be used to outline a soil's ability to withstand flooding, or its 'flood holding capacity'. Data from recent testing that uses both compost and recycled minerals from the treatment of drinking water to amend soil to improve its 'flood holding capacity' (FHC) is presented in this paper to highlight the shortcomings of using WHC alone. At this stage of research the idea of flood holding capacity is only conceptual, however the premise of flood holding capacity is examined using this experimental data.

List of Notations

WHC – Water Holding Capacity
FHC - Flood Holding Capacity
WTR – Water Treatment Residual
OM – Organic Matter
SOM – Soil Organic Matter

INTRODUCTION

In recent years the UK has experienced remarkable flash flooding, caused by intense rainfall that generates overland flow, fuelling the popular opinion that flooding is a direct consequence of enhanced climate change, (Muchan *et al.*, 2015). Many hypothesize that it is likely that flash-flooding events will become more prevalent e.g. Madsen *et al.* (2014). As such there is growing concern for how we prepare for and mitigate the effects of these events (Hopkins & Warburton, 2015) as flooding detrimentally affects soils, increasing greenhouse gas emission, soil erosion and degradation of soil structure (Lal, 2003). Consequently water-holding capacity, a measure of how much water can hold under typical conditions, is no longer sufficient to describe a soil's ability to accommodate water during a flood event. During flooding,

water flow is likely to increase in velocity and turbulence the consequences of which will rely on the soil's relationship with water (depending on parameters such as hydraulic conductivity), its shear strength and resistance to erosional forces. This paper builds on the concept of water holding capacity in order to develop the concept of 'flood-holding capacity'. Anderson & Gregorich (1984) proposed the definition of soil quality as "the sustained capability of a soil to accept, store and recycle water, nutrients and energy". This definition encompasses the fundamental indicators upon which 'flood-holding capacity' is based. This new term aims to qualitatively integrate the key soil properties that determine how a soil copes with and mitigates the deleterious effects of rapidly onset floodwaters on soil.

Soil conditions such as structure, texture, organic matter content and bulk density (the density of the total mass of air, water and matter) (Krull, *et al.*, 2004; Rawls *et al.*, 2003) all have a critical role in determining how much water a body of soil can hold, which in turn affects water retention and runoff in flooding events. Not only can soils play a crucial role in reducing the severity of floods, they are an extremely important carbon sink; to date the one-way exchange of organic matter with soil, i.e. removal of crops from the land without the return of organic wastes to the soil, has resulted in the loss of carbon dioxide and been the cause of one third of all anthropogenic green house gas emissions (Lal, 2004). This consequently leads to a negative spiral of soil organic matter loss and physical degradation, greater release of greenhouse gases, increased severity and frequency of storm events due to climate change, leading to further flooding and soil degradation (Lal, 2003). Therefore the maintenance of 'soil quality' or 'soil health' in respect to this important soil ecosystem service is critical to environmental sustainability, particularly how soil reacts to water. There is little clarity in the choice of soil properties and appropriate monitoring techniques to determine soil health, meaning its definition is often qualitative. To date there has been slow progress in quantitative monitoring of soil quality relevant to this key role due to soil's inherent chemical, physical and biological complexities in combination with the multifaceted nature of environmental concerns (Arshad & Martin, 2002). It is well known that in the assessment of flood hazard and mitigation there are countless large scale factors that affect the severity of flooding, such as topography, land cover, geology and land use, however the storage of water in soil is often overlooked.

DEVELOPING THE CONCEPT OF 'FLOOD HOLDING CAPACITY'

There are a number of crucial parameters that dictate how flooding will affect soils and indeed vice versa for how soils could influence flooding. These are broadly split into three parts: firstly the water holding capacity, secondly the infiltration rate & hydraulic conductivity, and thirdly shear strength and erosional resistance. The subsequent section will briefly outline why is it important to include not only water holding capacity in an assessment of soil, but also the other identified parameters in order to develop an

understanding of how these will change the ‘flood holding capacity’ of a soil, a concept defined as:

“The ability or capacity of a soil to take up and store flood water upon submersion without significant soil erosion or loss of shear strength, and resistance to the detrimental impacts of flooding on soil structure and critical ecoservice functions”

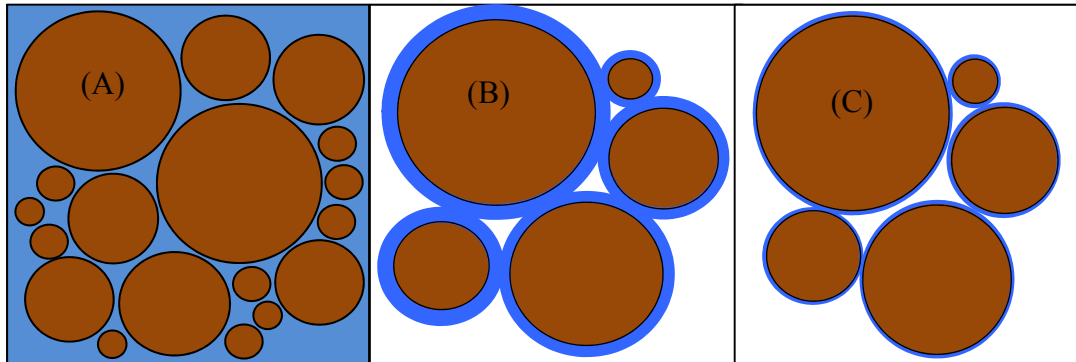


Figure 1: Stages of water retention in the soil matrix. (A) Complete saturation, no air present (θ_{SAT}) (B) Unsaturated soil, both air and water present between soil particles (θ_{FC}) (C) Permanent wilting point, only water adsorbed to soil surface remains (θ_{PW})

Water holding capacity

Figure 1 presents the stages of water retention in the soil matrix. These characteristics of soil are needed to determine how soil water content changes with increasing and decreasing suction experienced over wetting and drying cycles. The ability of soil to hold water is essential to its variety of ecosystem functions, and for this research particularly critical to how a soil reacts to flooding. The amount of water in a soil affects important soil parameters, and is generally singled out as the most important influence on soil strength (Hamza & Anderson, 2005; Soane, 1990), affecting susceptibility to compaction and in turn the bulk density, soil strength and structure which subsequently influences how water can move through the soil mass (Saffih-Hdadi *et al.*, 2009). It is key to note here that despite the significance of water content, there is an important co-dependence between water content, organic matter content and bulk density as they all affect each other. Water content is governed by the other properties of the soil but vice versa the water content affects the characteristics of the soil. For example, organic matter content will affect the water content of a soil, as OM acts a retardant for compaction, making the soil less dense and therefore making the infiltration process faster in addition to the water holding properties of the organic matter itself.

Greater water content increases compaction susceptibility, to a point of maximum density (Figure 2) where increasing moisture content then reduces the density achievable. Compaction increases bulk density, reduces permeability, infiltration rate,

rooting, water storage and porosity of the soil while increasing soil strength (Soane & Van Ouwerkerk, 1994; Raper & Kirby, 2006; Whalley et al, 1995; Meek et al 1991)

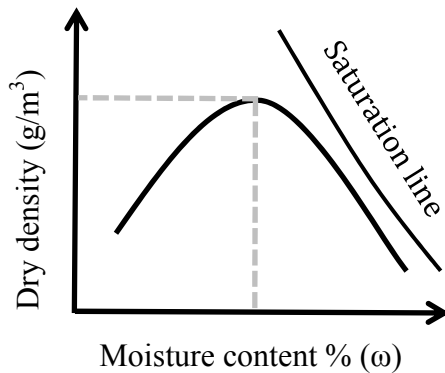


Figure 2: Simplified compaction curve showing the relationship between density and compaction at different moisture contents. Grey dashed line indicates the point of maximum dry density. This curve is achieved by performing a Proctor compaction test (BS 1377:1990 Part 4).

It is clear from this discussion that in general, higher water content encourages detrimental changes to soil structure under loading forces.

Angers *et al.*, (1987) stress the need “to increase the volume of pore space a soil can retain under a given load, through the use of soil amendments”. It essentially states that the amendment of soils must aim to reduce a soil’s compactibility at saturation by strengthening aggregate bonds in the soil matrix. Close to saturation point, soil in the aggregated state is able to retain more water quantities in comparison to the same soil in a compacted state. In a dry state the soil water characteristic is almost the same for aggregated and compacted soils. It is well known by agricultural soil scientists that it is therefore fundamental to include organic matter as a soil amendment as it acts to resist compacting forces by improving the mechanical and physical properties of the soil (a further discussion on this follows) (Franklin *et al.*, 1973), despite civil engineers regarding organic matter as an undesirable material as it acts to the detriment of required engineering qualities. Consideration for other amendments, such as recycled wastes or bio-solids must therefore include their affect on these critical soil properties.

Measurement of water holding capacity & volume change

The water content of a soil is typically expressed using the gravimetric or volumetric water content (or may be represented in terms of degrees of saturation), where the relationship between water content and suction is shown using a soil water retention curve (SWRC, figure 3). When soil dries from a saturated state it follows the primary drying curve until the point of residual suction, from which it follows the primary wetting curve as wetting occurs. The final volumetric content after wetting may be lower than the content at initial saturation due to irrecoverable shrinkage or air trapped within the soil. Should the wetting or drying cycle be reversed at any point during saturation or desaturation, soil follows scanning curves. Although providing a detailed overview of how soils respond to wetting and drying the SWRC does not directly account for any volume change during the sample’s wetting or drying cycles despite providing the volumetric water content. Toll *et al.*, (2015, in press) among others stress the importance

of measuring volume change as the volumetric response of a soil has a significant impact on the interpretation of results.

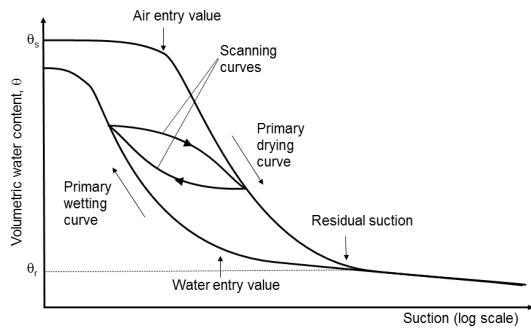


Figure 3: (left) Typical Soil Water Retention Curve (after Toll, 2012)

Figure 4 provides a schematic of this important difference, giving an example of the need for the quantification of volume change when measuring the change of water content in a soil. Sample 1 provides a baseline value of the volume of soil and of water. To indicate change under wetting,

samples 2 and 3 both have the same increase in water volume, 25 cm^3 to 37.5 cm^3 . There are two responses to the same addition of water; due to swelling the volume of sample 2 has increased to 150 cm^3 whereas sample 3 has increased to twice the original volume to 200 cm^3 with the same addition of water. Sample 4 has taken up twice as much water as sample 3 and tripled in volume compared to the original sample. Although both samples 1 and 2 have both taken up the same quantity of water, the volumetric water contents are 0.25 and 0.19 respectively, providing a misleading indication of the water uptake of each sample if only the volumetric water content is known. Similarly sample 4 has the same volumetric water content as sample 3 (0.25), despite a tripling of both water and volume against the original sample. This highlights that volumetric water content will be the same if the ratio of water to volume remains constant, regardless of the change between the two.

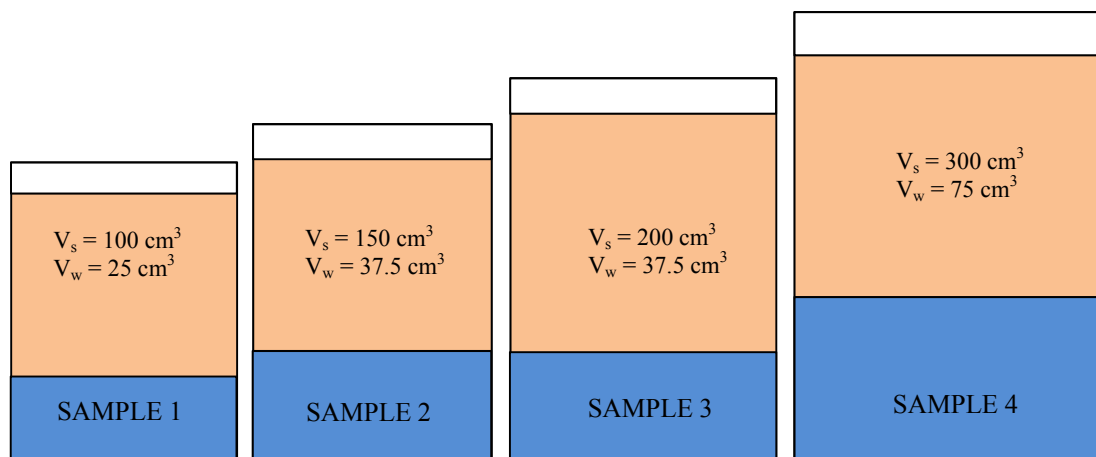


Figure 4: Volumetric water content of four samples. Sample 1 represents the original sample, where samples 2-4 present different changes during wetting. The volumetric content for 1, 2 & 4 = 0.25, the volume of sample 3 = 0.19

The overarching principal is that a greater volume of soil is desirable in flooding scenarios, as the soil body therefore has a larger area within which to store water. It is therefore important to know the gravimetric water content (as this provides an indication of how much water is held in the soil matrix compared to the dry soil mass) and volume change of a soil in order to assess a soil's suitability to act as a storage medium. The 'water holding capacity' of a soil with reference to the 'flood holding capacity' needs to therefore include not just a strict value of how much water a soil can hold at a specific suction but encompasses the volume change of a soil.

A novel method for water holding capacity

In order to quantify the gravimetric water content and volume change of soil under wetting, a novel method is presented. The research compares the performance of soil alone with soil amended using compost and water treatment residual (WTR) in a variety of proportions. Three components were used in testing: low organic content topsoil (classified as silt loam), high-grade (PAS 100) compost and dried water treatment residual (WTR). To briefly outline the rationale for WTR amendment: water treatment residual is the bi-product of drinking water processing that uses an iron based (FeCl_3 or $\text{Fe}[\text{SO}_4]_3$) coagulant to remove particulates from water (Ippolito *et al.*, 2011). The addition of iron coagulant to the water treatment process enables a reaction that produces the amorphous hydrous oxide of iron. The final residual is therefore a combination of hydrous iron oxides and the suspended solids removed from the water such as silty sediments and other organic materials (Makris *et al.*, 2004). The similarity in texture of WTR to fine soil and the total organic carbon (30g/kg) may enable good structure and subsequent water holding capacity; typically WTR is ~80% water, attributed to the presence of organic matter (Cox *et al.*, 1997; Walpole, 2012). Fe oxides in the soil may interact with SOM to enhance macro-aggregate stability via their flocculation capacity i.e. the binding of clay particles to organic fractions (Zhang & Horn, 2001). Currently

WTR is disposed of via landfills or on-site storage (Basta *et al.*, 2000), however increasingly limited storage space and resulting higher disposal charges have encouraged the water treatment facilities to look for other options (Butkus *et al.*, 1998). Preliminary research shows that WTR/compost 1:1 amendments provide a cost-effective way to remediate contaminated land, however the use of WTR/compost amendments to increase water holding capacity and increase resilience to flooding has not yet been thoroughly investigated.

Sample #	Soil %	Compost %	WTR %	Sand %
1	100			
2	50	50		
3	50		50	
4	50			50
5	50	25	25	
6	50	25		25
7	60	40		
8	60		40	
9	60			40
10	60	20	20	
11	60	20		20
12	70	30		
13	70		30	
14	70			30
15	70	15	15	
16	70	15		15

Table 1: (left) Sample amendments percentage by dry weight.

Soil was processed through a 6.3 mm sieve and stored at field moisture content (~12%). WTR was air dried for several days to remove water and also passed through a 6.3 mm sieve. Compost was not processed before use. Samples were mixed proportionally by dry weight as seen in Table 1. Sand was used in place of WTR as an inert substrate to simulate WTR’s structural effect without the potential geochemical effect of WTR.

Once mixed, samples without compost were either air dried or wetted to achieve 12% water content. Samples with compost were all made to 20% water content. This was the driest point at which samples could be compacted and remain sufficiently cohesive to use for further testing. Samples were compacted using normal Proctor compaction (BS1377) and extruded forming samples 38 x 76 mm. Once extruded the samples were painted with three coats of liquid latex (excluding the end faces), designed to hold the samples together while having the flexibility to allow free swelling. At each stage in the following method samples were weighed and measured at 24 hour periods: Samples were placed upright on a bed of saturated sand in order to soak up water from the base, expelling any air trapped in the sample. Once the samples had reached a steady weight, they were submerged fully with a 5 cm head of water above the sample columns; this was to simulate flooding conditions on soil near saturation. Again these were monitored until no further water was taken up; however in some cases the samples lost mass due to disintegration of the end faces.

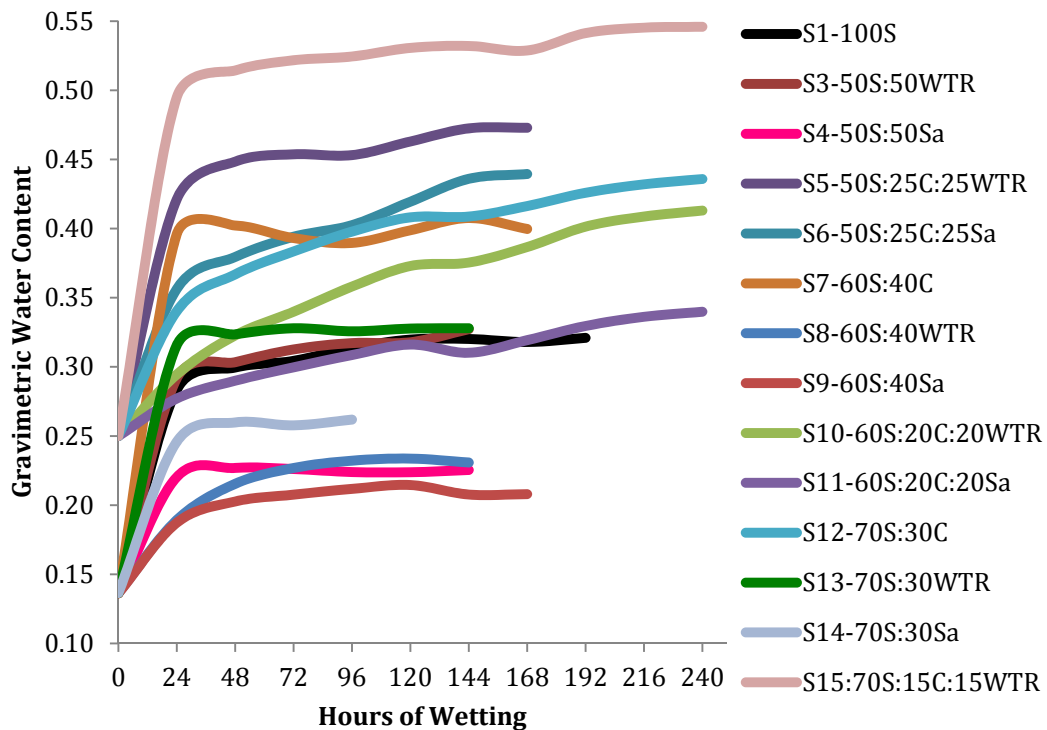


Figure 5: Gravimetric water content change over time for 14 samples. N=8

Figure 5 presents the gravimetric water content of samples over time, calculated using the equation below giving the ratio of grams of water to grams of dry soil.

$$(1a) \theta_g = \frac{M_w - M_d}{M_d} \quad \text{or} \quad (1b) \theta_g = \left(\frac{M_w}{M_d}\right) - 1$$

Equation 1: Gravimetric water content where M_w is wet mass of sample and M_d is the dry mass of the sample

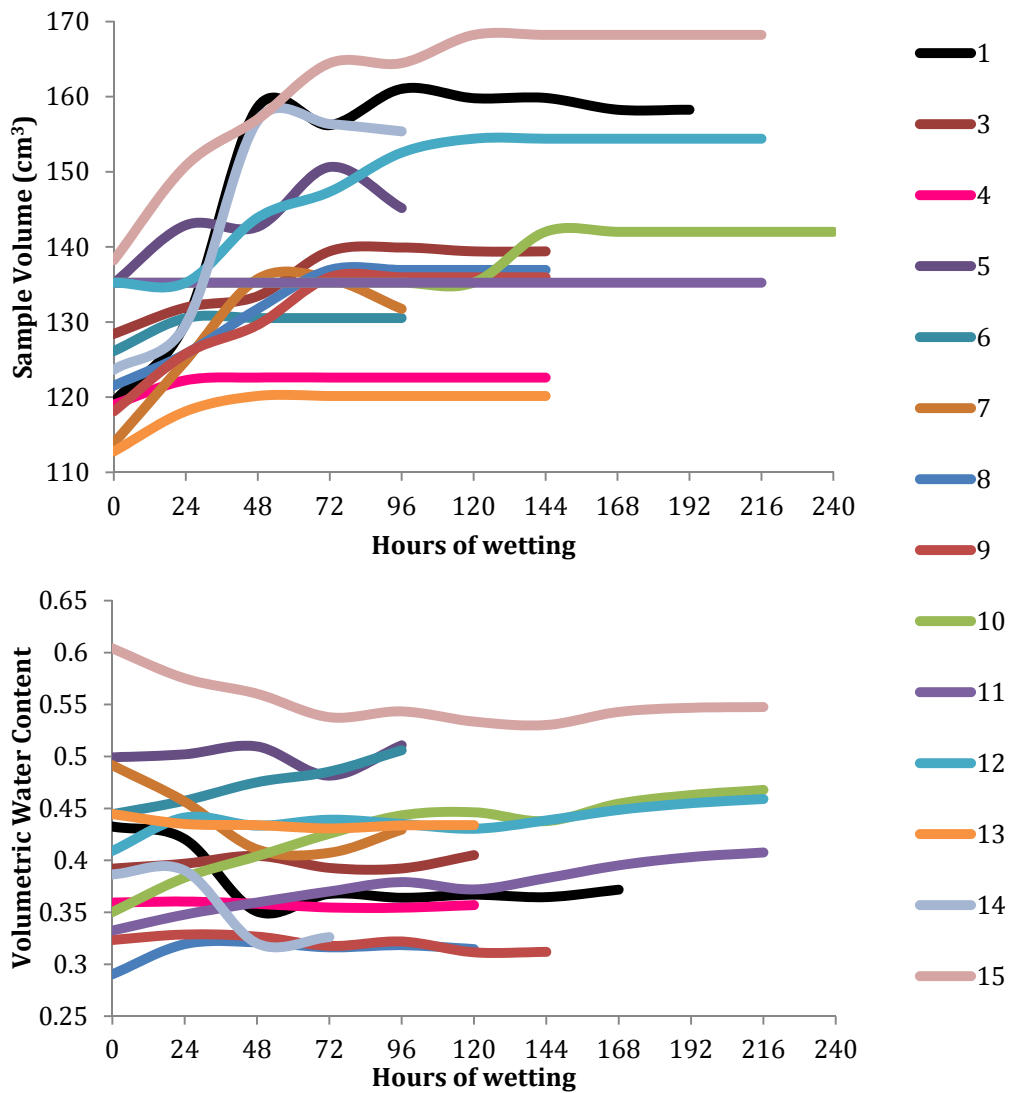


Figure 6: (top) Sample volume change over time. $N = 8$; (bottom) Volumetric water content of samples over time. $N = 8$

Figure 5 presents the gravimetric water content over time and provides an excellent indicator of how well soils take up and store water once exposed to water. It is clear that samples containing compost, as expected, hold a greater mass of water per gram of soil than their counterparts without compost. This may however be partly attributed to the higher initial gravimetric water content and lower density of samples compared to the samples containing only soil and WTR or sand. Importantly, of the amendments, those with compost and WTR performed better than compost alone. Those with WTR amendment alone, with the exception of sample 3, had a lower gravimetric water content than unamended soil, however this may be due in part to a density difference between soil and WTR. Figure 6 is a strong example of how the same volumetric data can give different results depending on how they are presented. Should one take only the volumetric water content of the samples over time it would appear that they are following a primary drying curve, whereas the reality is that the samples were taking up water at a proportionally slower rate than the increase in volume of the samples, with the exception of samples that did not swell (these were the samples with higher proportions of WTR). Figure 6 indicates that samples swelled to varying degrees before reaching a plateau.

Infiltration rate & hydraulic conductivity

A soil's infiltration rate (also called percolation rate) is simply a measure of how quickly precipitation enters the soil profile, measured in unit volume crossing the air/soil interface into a unit area of soil per unit time (Philips & Kitch, 2011). It is dependent on the antecedent conditions, rainfall regime, site attributes such as slope and vegetation cover, and physical properties of the soil (such as structural stability, bulk density and pore structure). Hydraulic conductivity (k , also called permeability) describes the intrinsic ability of a soil to transmit fluid, and is typically higher parallel to the soil surface than perpendicular movement downwards through the soil profile. Infiltration rate is a function of k , hydraulic gradient and infiltration area following Darcy's Law (1856).

It is well known that the movement of water through the soil matrix is essential to its health and that hydraulic conductivity is therefore an extremely important geotechnical parameter (Boyle *et al.*, 1988; Sezer *et al.*, 2009). It is imperative to consider in the context of 'flood holding capacity' as it introduces the speed of water movement, critical to how a soil responds to flooding. Soils need to accept and hold water while rapidly transmitting it downward through the soil profile in order to avoid topsoil saturation and generate overland flow. However it is unavoidable in intense precipitation events that as a soil accepts greater volumes of water, the infiltration rate slows with increasing soil saturation to a point at which water supply exceeds the rate of infiltration and runoff is generated. Given the same starting moisture content, soils allowing a high infiltration rate and a greater capacity to hold water within their matrix will allow more water to infiltrate before runoff occurs. However soils with an excessively high k soils may suffer from slaking, the breakdown of large soil aggregates (<2.5 mm) to microaggregates (<0.25 mm) due to the creation of high internal pressure of air trapped in the soil matrix

upon rapid immersion in water (Zaher & Caron, 2008). The breakdown of weak aggregates in this manner damages soil structure reducing shear strength, increasing risk of erosion and limiting infiltration rate as microaggregates block soil pores and effectively seal the soil surface.

Particle size distribution, particle shape and texture, voids ratio, and the degree of soil saturation are all important factors in the hydraulic conductivity of a soil (Head, 1982). A soil with high hydraulic conductivity and rate of infiltration (at which slaking is not induced) would be favorable in a flooding event. Hydraulic conductivity is typically measured using the Falling Head Test (BS1377-5; 1990). A full procedure description is not necessary for this review, however fundamentally water flows through a soil sample of known dimensions driven by the pressure of a water head and the rate of flow is determined and presented as the coefficient of permeability (k), typically in cm/hr. It can also be derived empirically from grain size distribution and cone penetrometer testing (Lunne, 1997). Here, the rate of uptake by samples can be used as a simple proxy for infiltration rate and associated hydraulic conductivity.

Shear strength and erosional resistance

A major cause of soil degradation across the globe is soil erosion, affecting ~1094 million ha, a vast proportion of which is specifically affected by water erosion i.e. runoff and raindrop erosion (Lal, 2003). When soil is wetted it is vulnerable to erosion which has a number of deleterious affects on the health of a soil, including but not limited to: breakdown of SOC by slaking and disruption of aggregates, preferential removal of C in runoff water due to its low density and mineralization of SOM (Lal, 2003). Rapid immersion underwater causes slaking due to surface disruption as a result of compressed entrapped air, impact of the rainfall itself, and shearing force of the immersion or collision of aggregates. The breakdown of aggregates then releases C upon wetting.

Soil erosion occurs through water drop impact and entrainment of particles by runoff (Nearing *et al.*, 1999). Drag and lift forces occurring in turbulent bursts resulting from runoff causes the detachment of soil particles (Cleaver & Yates, 1973), with hydraulic shear stress governing the initial motion of particulates (Leonard & Richard, 2004). One of the main factors affecting substrate movement is the shear strength of the soil (Terzaghi *et al.*, 1996), i.e. the resistance to movement and detachment between particles in the soil matrix created by physical and chemical bonds or cementation that enable cohesion (Craig, 2004). Saturated soil shear strength can be used to predict the critical shear stress required to erode soil (Leonard & Richard, 2004). Soil aggregate stability in topsoil has also been correlated closely with susceptibility to runoff (Barthes & Roose, 2002; Zhang *et al.*, 2007) and soil erodibility (Le Bissonnais *et al.*, 2007). Research examining the relationship between erosion and shear strength such as Cruse & Larson (1977) and Al-Durrah & Bradford (1982) who developed a force-resistance model for soil detachment by water drop impact derived from shear strength measured using a fall cone penetrometer, have both observed significant relationships between soil shear strength and splash detachment. Similarly and more recently, Ghidley & Alberts (1997),

Frei *et al* (2003), Fattet *et al.*, (2011) found that soil aggregate stability was correlated with shear strength, where higher values for stability and strength also correlated with a decrease in erodibility. Generally, soils that exhibit higher saturated shear strength and have greater aggregate stability are better able to resist the erosional forces of water drop impact and runoff generated shear forces. In addition greater soil aggregate stability is positively correlated with infiltration rate (Fattet *et al*, 2011).

The effect of vegetation and SOM is well known on the stability of soil; root biomass physically reinforces soil matter (Stokes *et al.*, 2009) in addition to the contribution of SOM, which binds microaggregates (>250um) into macroaggregates (several mm) (Gale *et al.*, 2000). The production of macroaggregates by SOM increases the amount of water that a soil can hold as the OM alone can hold up to 10 times its weight in water (Lal, 2009) in addition to the geotechnical improvements that the creation of macroaggregates promotes: increase in shear strength, lowering of bulk density, and increased permeability significant geotechnical improvements it can bring (Puppala *et al.*, 2007). A number of studies cite that water retention is a major hydraulic property that dictates a soil's ability to resist erosion and that soil with high infiltration rates, high levels of OM and good soil structure will resist erosion most successfully (Bot & Benites, 2005; Rawls *et al*, 2003; Wall, 2003). However excessive application of organic matter leads to a variety of negative impacts on the geotechnical characteristics of soil and phosphorous concentrations in water (causing eutrophication), e.g. Puppala *et al.*, (2007) determined that an increase of soil organic matter from 20% to 40% yielded a significant enhancement of soil strength, however amendment beyond 40% resulted in a decrease in these properties.

Fattet *et al.*, (2011) state that although aggregate stability tests may be used as an adequate indicator of a soil's stability, they cannot replicate triaxial or direct shear tests. In the laboratory triaxial testing (BS1377-7; 1990) is a reliable and accurate method that has the ability to control drainage and pore water pressure in the sample. Briefly, a cylindrical specimen typically 38 x 76 mm sealed in a rubber membrane is saturated, consolidated and sheared in a tri-axial testing apparatus. During these processes the soil response is observed by plotting the effective principal stress ratio against the axial strain, until specimen failure occurs. This type of tri-axial testing is appropriate to quantify the shear strength and point of failure of a soil under flooding conditions. A Fall Cone Penetrometer Test (BS 1377-7:1990) is a viable alternative due to its simplicity and efficiency (Hazell, 2008). The test in essence requires a cone apparatus to be dropped into a sample under its own weight from a predetermined height, where the penetration resistance values can be correlated to shear strength parameters (Tanaka *et al.*, 2012).

DISCUSSION AND CONCLUSIONS

Traditional methods to describe how water is held in soil are inadequate to provide an indication of how soils react to flash flooding. Firstly, we need to include the important

volume change of soil in our definition water holding capacity in addition to the volume or mass of water it can hold. Secondly it is critical that we also consider the shear strength and hydraulic conductivity in addition to the water holding capacity, to determine the capacity of a soil to withstand and perhaps dampen the adverse affect of flooding.

Shear strength (fall cone) and aggregate stability (drop impact) data collected in addition to water holding capacity data provides a key example of why we need to consider not just the WHC but all three components (WHC, shear strength and hydraulic conductivity) when assessing a soil. In order to have good ‘flood holding capacity’ soils need to exhibit high maximum gravimetric water content, high shear strength and aggregate stability and high hydraulic conductivity (rate of uptake provided as a proxy for this data). Examining water holding capacity (figure 5) indicates that amendment yields a marginal improvement for maximum gravimetric water content, where eight samples have a higher WHC than soil alone and one sample has a higher volume change than soil after wetting. In general, amendment with WTR and compost gives the highest maximum gravimetric content and rate of uptake and amendment with compost at any ratio gives a greater volume change. However, considering the insignificant difference between amendment with only compost vs WTR and compost, what is the rationale for including WTR? Based on WHC alone, there is little to separate the different amendments. Figure 7 answers this question, where it is clear that amendment with WTR and compost increases the shear strength and aggregate stability. Sample 1 (soil alone) clearly has low saturated shear strength and aggregate stability in comparison with amended samples despite a high maximum gravimetric water content and volume change. WTR amendment alone provides improvements in shear strength and aggregate stability, but reduces the maximum gravimetric water content and volume change. WTR and compost amendment increase shear strength and aggregate stability in addition to the improvement in maximum gravimetric water content and volume change.

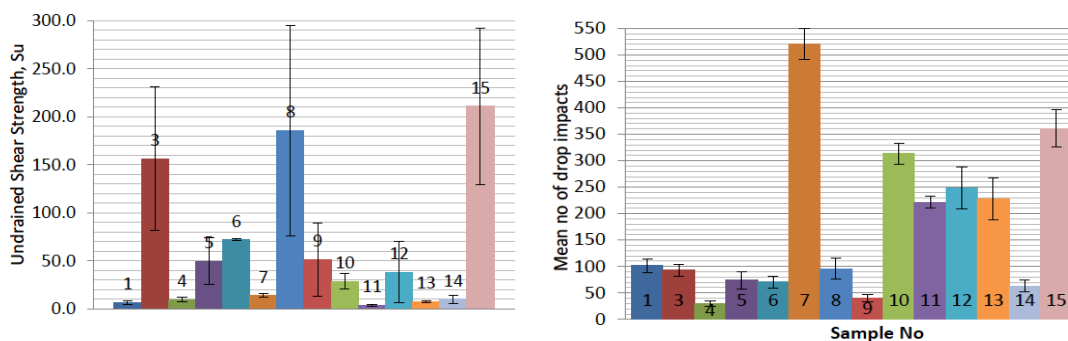


Figure 7: (left) Undrained shear strength of samples based on fall cone penetrometer test (right) Mean number of drop impacts to cause disaggregation for each sample

In summary, researchers and agricultural engineers need to understand the importance of shear strength and hydraulic conductivity in addition to water holding capacity in their assessment of soil when evaluating their ability or capacity to take up and store flood water upon submersion without significant soil erosion and resistance to the detrimental impacts of flooding on soil structure and critical ecoservice functions, termed here as 'flood holding capacity'. Amendments to soil intended to improve the flood holding capacity are required not only to increase the maximum gravimetric water content, but enhance the volume change of a soil to provide a greater volume within which to hold water, improve the speed of movement of water through the soil matrix and enable resistance to erosive forces when wetted. This is highlighted using an amendment with WTR and compost, where only amendment with both components improves all three components of 'flood holding capacity'

REFERENCES

- Anderson, D. W., & Gregorich, E. G. (1984). Effect of soil erosion on soil quality and productivity. In *Soil erosion and degradation. Proceedings of 2nd ann. western provincial conf. rationalisation of water and soil research and management*, Saskatoon, Saskatchewan (pp. 105-113).
- Al-Durrah, M. M., & Bradford, J. M. (1982). The mechanism of raindrop splash on soil surfaces. *Soil Science Society of America Journal*, 46(5), 1086-1090.
- Angers, D. A., Kay, B. D., & Groenevelt, P. H. (1987). Compaction characteristics of a soil cropped to corn and brome grass. *Soil Science Society of America Journal*, 51(3), 779-783.
- Arshad, M. A., & Martin, S. (2002). Identifying critical limits for soil quality indicators in agro-ecosystems. *Agriculture, Ecosystems & Environment*, 88(2), 153-160.
- Barthes, B., & Roose, E. (2002). Aggregate stability as an indicator of soil susceptibility to runoff and erosion; validation at several levels. *Catena*, 47(2), 133-149.
- Basta, N. T., Zupancic, R. J., & Dayton, E. A. (2000). Evaluating soil tests to predict bermudagrass growth in drinking water treatment residuals with phosphorus fertilizer. *Journal of environmental quality*, 29(6), 2007-2012.
- Bot, A., & Benites, J. (2005). Creating drought-resistant soil. The importance of soil organic matter: key to drought-resistant soil and sustained food and production. *FAO Soils Bulletin*, 80, 35-40.
- Boyle, M., Frankenberger, W. T., & Stolzy, L. H. (1989). The influence of organic matter on soil aggregation and water infiltration. *Journal of Production Agriculture*, 2(4), 290-299.

- Butkus, M. A., Grasso, D., Schulthess, C. P., & Wijnja, H. (1998). Surface complexation modeling of phosphate adsorption by water treatment residual. *Journal of environmental quality*, 27(5), 1055-1063.
- Cleaver, J. W., & Yates, B. (1973). Mechanism of detachment of colloidal particles from a flat substrate in a turbulent flow. *Journal of Colloid and Interface Science*, 44(3), 464-474.
- Craig, R. F. (2004). *Craig's soil mechanics*. CRC Press.
- Cruse, R. M., & Larson, W. E. (1977). Effect of soil shear strength on soil detachment due to raindrop impact. *Soil Science Society of America Journal*, 41(4), 777-781.
- Cox, A. E., Camberato, J. J., & Smith, B. R. (1997). Phosphate availability and inorganic transformation in an alum sludge-affected soil. *Journal of Environmental Quality*, 26(5), 1393-1398.
- Darcy, H. (1856). *Les fontaines publiques de la ville de Dijon: exposition et application...* Victor Dalmont.
- Fattet, M., Fu, Y., Ghestem, M., Ma, W., Foulonneau, M., Nespoulous, J., Le Bissonnais, Y. and Stokes, A., (2011) Effects of vegetation type on soil resistance to erosion: Relationship between aggregate stability and shear strength. *Catena*, 87(1), pp.60-69.
- Franklin, A. G., Orozco, L. F., & Semrau, R. (1973). Compaction and strength of slightly organic soils. *Journal of the Soil Mechanics and Foundations Division*, 99(7), 541-557.
- Frei, M., Boll, A., Graf, F., Heinimann, H.R., Springman, S., (2003). Quantification of the influence of vegetation on soil stability. *Proceedings of the International Conference on Slope Engineering: 8–10 December 2003, Hong Kong, China*.
- Gale, W.J., Cambardella, C.A., Bailey, T.B., 2000. Root-derived carbon and the formation and stabilization of aggregates. *Soil Science Society of American Journal* 64, 201–207.
- Ghidey, F., & Alberts, E. E. (1997). Plant root effects on soil erodibility, splash detachment, soil strength, and aggregate stability. *Transactions of the ASAE*, 40(1), 129-135.
- Hamza, M. A., & Anderson, W. K. (2005). Soil compaction in cropping systems: a review of the nature, causes and possible solutions. *Soil and tillage research*, 82(2), 121-145.

- Hazell, E (2008). Numerical and experimental studies of shallow cone penetration in clay. Oxford : University of Oxford . 9-28.
- Head, K. (1982) Manual of soil laboratory testing, Vol 2. Pentech Press.
- Hopkins, J., & Warburton, J. (2015). Local perception of infrequent, extreme upland flash flooding: prisoners of experience? *Disasters*.
- Ippolito, J. A., Barbarick, K. A., & Elliott, H. A. (2011). Drinking water treatment residuals: A review of recent uses. *Journal of environmental quality*, 40(1), 1-12.
- Krull, E. S., Skjemstad, J. O., & Baldock, J. A. (2004). Functions of soil organic matter and the effect on soil properties. *Cooperative Research Centre for Greenhouse Accounting*.
- Lal, R. (2003). Soil erosion and the global carbon budget. *Environment international*, 29(4), 437-450.
- Lal, R. (2004). Soil carbon sequestration impacts on global climate change and food security. *Science*, 304(5677), 1623-1627.
- Lal, R. (2009). Soils and sustainable agriculture: A review. *In Sustainable agriculture* (pp. 15-23). Springer Netherlands.
- Le Bissonnais, Y., Blavet, D., De Noni, G., Laurent, J. Y., Asseline, J., & Chenu, C. (2007). Erodibility of Mediterranean vineyard soils: relevant aggregate stability methods and significant soil variables. *European Journal of Soil Science*, 58(1), 188-195.
- Léonard, J., & Richard, G. (2004). Estimation of runoff critical shear stress for soil erosion from soil shear strength. *Catena*, 57(3), 233-249.
- Lunne, T., Robertson, P. K., & Powell, J. J. M. (1997). Cone penetration testing. *Geotechnical Practice*.
- Madsen, H., Lawrence, D., Lang, M., Martinkova, M., & Kjeldsen, T. R. (2014). Review of trend analysis and climate change projections of extreme precipitation and floods in Europe. *Journal of Hydrology*, 519, 3634-3650.
- Makris, K. C., Harris, W. G., O'Conno, G. A., & Obreza, T. A. (2004). Phosphorus immobilization in micropores of drinking-water treatment residuals: Implications for long-term stability. *Environmental science & technology*, 38(24), 6590-6596.
- Meek, B. D., Rechel, E. R., Carter, L. M., DeTar, W. R., & Urie, A. L. (1992). Infiltration rate of a sandy loam soil: effects of traffic, tillage, and plant roots. *Soil Science Society of America Journal*, 56(3), 908-913.

- Muchan, K., Lewis, M., Hannaford, J., & Parry, S. (2015). The winter storms of 2013/2014 in the UK: hydrological responses and impacts. *Weather*, 70(2), 55-61.
- Nearing, M. A., Norton, L. D., Bulgakov, D. A., Larionov, G. A., West, L. T., & Dontsova, K. M. (1997). Hydraulics and erosion in eroding rills. *Water Resources Research*, 33(4), 865-876.
- Philips, C. E., & Kitch, W. A. (2011). A review of methods for characterization of site infiltration with design recommendations. In *Proceedings: 43rd Symposium on Engineering Geology and Geotechnical Engineering*, University of Las Vegas, NV, March (pp. 23-25).
- Puppala, A. J., Pokala, S. P., Intharasombat, N., & Williammee, R. (2007). Effects of organic matter on physical, strength, and volume change properties of compost amended expansive clay. *Journal of Geotechnical and Geoenvironmental Engineering*, 133(11), 1449-1461.
- Raper, R. L., & Mac Kirby, J. (2006). Soil compaction: how to do it, undo it, or avoid doing it. *American Society of Agricultural and Biological Engineers*.
- Rawls, W. J., Pachepsky, Y. A., Ritchie, J. C., Sobecki, T. M., & Bloodworth, H. (2003). Effect of soil organic carbon on soil water retention. *Geoderma*, 116(1), 61-76.
- Ritz, K., Black, H. I., Campbell, C. D., Harris, J. A., & Wood, C. (2009). Selecting biological indicators for monitoring soils: a framework for balancing scientific and technical opinion to assist policy development. *Ecological Indicators*, 9(6), 1212-1221.
- Saffih-Hdadi, K., Défossez, P., Richard, G., Cui, Y. J., Tang, A. M., & Chaplain, V. (2009). A method for predicting soil susceptibility to the compaction of surface layers as a function of water content and bulk density. *Soil and Tillage Research*, 105(1), 96-103.
- Sezer, A., Göktepe, A. B., & Altun, S. (2009). Estimation of the Permeability of Granular Soils Using Neuro-fuzzy System. In *AIAl Workshops* (pp. 333-342).
- Soane, B. D. (1990). The role of organic matter in soil compactibility: a review of some practical aspects. *Soil and Tillage Research*, 16(1), 179-201.
- Soane, B. D., & Van Ouwerkerk, C. (1994). Soil compaction problems in world agriculture. In *Soil compaction in crop production* (Vol. 11, pp. 1-26). Elsevier Amsterdam.

- Stokes, A., Atger, C., Bengough, A.G., Fourcaud, T., Sidle, R.C., (2009). Desirable plant root traits for protecting natural and engineered slopes against landslides. *Plant and Soil* 324, 1–30.
- Tanaka, H. Hirabayashi, H. Matsuoka, T. Kaneko, H. (2012). Use of fall cone test as measurement of shear strength for soft clay materials. *Soils and Foundations* . 52 (4), 590-599
- Terzaghi, K., Peck, R. B., & Mesri, G. (1996). Soil mechanics in engineering practice. *John Wiley & Sons*.
- Toll, D.G. (2012) The behaviour of unsaturated soils. *Chapter 5 in A Handbook of Tropical Residual Soil Engineering*, (eds. Huat, B.B.K., Toll, D.G. & Prasad, A.) London: Taylor and Francis, ISBN: 9780415457316.
- Toll D.G., Asquith, J., Fraser, A., Hassan, A., Liu, G., Lourenco, S.D.N., Mendes, J/, Noguchi, T., Osinski, P. and Stirling, R. (2015) Tensiometer techniques for determining soil water retention curves. *Conference proceedings: Asia-Pacific Conference on Unsaturated Soil, China*.
- Wall, G., Baldwin, C. S., & Shelton, I. J. (2003). Soil erosion-causes and effects. *Ontario Institute of Pedology*.
- Walpole, A. M. (2012) Treating PTE contaminated soil with Fe-based Drinking Water Treatment Residual: An investigation into the effects on plant growth. Durham University MEng Research Project (unpublished).
- Whalley, W. R., Dumitru, E., & Dexter, A. R. (1995). Biological effects of soil compaction. *Soil and Tillage Research*, 35(1), 53-68.
- Zaher, H., & Caron, J. (2008). Aggregate slaking during rapid wetting: Hydrophobicity and pore occlusion. *Canadian Journal of Soil Science*, 88(1), 85-97.
- Zhang, B., & Horn, R. (2001). Mechanisms of aggregate stabilization in Ultisols from subtropical China. *Geoderma*, 99(1), 123-145.
- Zhang, G. S., Chan, K. Y., Oates, A., Heenan, D. P., & Huang, G. B. (2007). Relationship between soil structure and runoff/soil loss after 24 years of conservation tillage. *Soil and Tillage Research*, 92(1), 122-128.

A Modified Mohr-Coulomb Model to Simulate the Response of Buried Pipes Subjected to Large Ground Displacement

Dilan J Robert¹ and P. Rajeev²

¹Lecturer, School of Engineering, RMIT Univ., Melbourne, VIC 3001, Australia. E-mail: dilan.robert@rmit.edu.au

²Senior Lecturer, Dept. of Civil and Construction Engineering, Swinburne Univ. of Technology, VIC 3122, Australia. E-mail: prajeev@swin.edu.au

Abstract: At the present time, it is very common in practice (industry as well as in research) to utilize Mohr-Coulomb to simulate the soil behaviour in the application of soil-structure interaction problems. The model is often chosen considering its simplicity, ease of use, reasonable computational time and the high level of understanding among the engineers. However, the linear elastic-perfectly plastic Mohr-Coulomb model is unable to predict the softening behaviour of material and hence to predict the pipe load accurately when subjected to large soil movements such as from landslides or earthquakes. A user defined modified Mohr-Coulomb model is developed to capture the strain softening behaviour of soil and to simulate the pipeline response subjected to large ground deformation. The softening behaviour of the model has been calibrated on the basis of direct shear test data, and triaxial test data have been used for calibrating the yielding and flow characteristics of the model. The calibrated model has been applied to simulate the response of HDPE pipeline undergoing different ground displacements. Finally, the model response was used to develop a strain demand model for buried pipelines facilitating the risk assessments.

Keywords: Pipelines, Earthquakes, Modified Mohr-Coulomb model, Triaxial test, Direct shear test, HDPE pipe, Risk assessment.

INTRODUCTION

The development of numerical analysis and its application to geotechnical engineering problems over the past 20 years have provided geotechnical engineers with an extremely powerful analysis tool. The most recent research work conducted in the area of numerical modelling of soil-pipeline interaction problems has been able to highlight the development of proper numerical tools to capture the real behaviour of pipelines when subjected to lateral movements.

The accurate prediction of pipeline response during large ground deformation mainly depends on capturing the realistic soil behavior during its state change (such as void ratio) as well as at different mean normal stresses. The advanced constitutive models, such as Nor-Sand (Jefferies, 1993) and Cam-Clay (Schofield et al., 1968) are

well equipped to capture such complexities in soil behaviour. However, these models are required to be calibrated using advanced soil testing programs. On the other hand, it is very common in practice to utilize standard material models such as linear elastic-perfectly plastic Mohr-Coulomb to simulate the soil behaviour in the application of soil-structure interaction problems. Such models are readily available in commercial finite element programs such as ABAQUS.

However, the linear elastic-perfectly plastic Mohr-Coulomb model is unable to predict the softening behaviour of material and hence to predict the pipe load accurately when subjected to large soil movements such as from landslides or earthquakes. A user defined modified Mohr-Coulomb model is developed to capture the strain softening behaviour of soil and to simulate the pipeline response subjected to large ground deformation. The softening behaviour of the model has been calibrated on the basis of direct shear test data, and triaxial test data have been used for calibrating the yielding and flow characteristics of the model. The calibrated model has been applied to simulate the response of HDPE pipeline undergoing different ground displacements. Finally, the model response was used to develop a strain demand model for buried pipelines facilitating the risk assessments.

MOHR COULOMB MODEL

Model details

Mohr-Coulomb model is a simple linear elastic-perfectly plastic model which is widely used for the design applications in geotechnical engineering to simulate material response under monotonic loading. The model is widely popular in the community for modelling the behaviour of soils due to its relative simplicity and the requirement of the basic soil properties (such as friction and dilation of soils).

Within the Mohr-Coulomb framework, the soil is modelled as an isotropic dilatant elastic-perfectly plastic material. Elastic behaviour is modelled assuming linear isotropic elasticity of which the stress is defined from the elastic strain as;

$$\sigma = D_E \varepsilon^e \quad (1)$$

Where σ is the stress, D_E is the fourth-order elasticity tensor, and ε^e is the elastic strain.

The model behaves elastically and obeys Hooke's law until the onset of yielding which is determined by the Mohr-Coulomb yield criterion. For general states of stress, the yield criterion of the model in terms of three stress invariants is defined as (p : compression negative) (ABAQUS, 2011);

$$F = R_{mc} q - p \tan \phi' - c' = 0 \quad (2)$$

where

$$R_{mc}(\Theta, \phi') = \frac{1}{\sqrt{3} \cos \phi'} \sin(\Theta + \pi/3) + \frac{1}{3} \cos(\Theta + \pi/3) \tan \phi'$$

ϕ' is the friction angle (slope of the yield surface in p - $R_{mc}q$ stress planes)

c' is the cohesion of the material

Θ is the deviatoric polar angle defined as $\cos(3\Theta) = \left(\frac{r}{q}\right)^3$

$$p = -1/3(\sigma_{11} + \sigma_{22} + \sigma_{33}) \quad (3)$$

$$q = \sqrt{\frac{3}{2} S_{ij} S_{ij}}, \text{ or}$$

$$q = \sqrt{\frac{3}{2} \sqrt{S^2_{11} + S^2_{22} + S^2_{33} + S^2_{12} + S^2_{21} + S^2_{23} + S^2_{32} + S^2_{31} + S^2_{13}}} \quad (4)$$

where $S = \sigma + pI$ (stress: tension positive)

S = Stress deviator

$$\begin{pmatrix} S_{11} \\ S_{22} \\ S_{33} \\ S_{12} \\ S_{13} \\ S_{23} \end{pmatrix} = \begin{pmatrix} \sigma_{11} \\ \sigma_{22} \\ \sigma_{33} \\ \sigma_{12} \\ \sigma_{13} \\ \sigma_{23} \end{pmatrix} + p \begin{pmatrix} 1 \\ 1 \\ 1 \\ 0 \\ 0 \\ 0 \end{pmatrix}$$

$$r = \left(\frac{9}{2} S : S : S\right)^{1/3} = \left(\frac{9}{2} S_{ij} S_{jk} S_{ki}\right)^{1/3} \quad (5)$$

The strain response follows a non-associative flow rule. A flow function is defined with a smooth elliptic function, proposed by Menétrey and Willam (1995) in the deviatoric stress plane as;

$$P = \sqrt{(\varepsilon c' \tan \psi)^2 + (R_{mv} q)^2} - p \tan \psi \quad (6)$$

where,

$$R_{mv}(\Theta, e) = \frac{4(1-e^2)\cos^2\Theta + (2e-1)^2}{2(1-e^2)\cos\Theta + (2e-1)\sqrt{4(1-e^2)\cos^2\Theta + 5e^2 - 4e}} R_{mc}(\pi/3, \phi')$$

$$R_{mc}(\pi/3, \phi') = \frac{3 - \sin\phi'}{6 \cos\phi'}$$

where ϕ' and ψ are the friction angle and the dilation angle measured in the p - $R_{mv}q$ plane, respectively. c' is the initial cohesion yield stress; Θ remains as defined in yield criterion; ε is a parameter which is referred to as meridional eccentricity which

defines the rate at which the hyperbolic function approaches the asymptote (the flow potential becomes a straight line in the meridional stress plane as the meridional eccentricity becomes zero); and e is a parameter referred to as the deviatoric eccentricity that describes the ‘out-of-roundedness’ of the deviatoric section in terms of the ratio between shear stress along the extension meridian ($\Theta = 0$) and shear stress along the compression meridian ($\Theta = \frac{\pi}{3}$).

Addition of material softening

The original Mohr-Coulomb model has been modified to capture the strain softening behaviour of the material at large deformations. The softening behaviour has been captured by reducing the mobilized friction and dilation angle with an increase in plastic deviatoric shear strains (Anastasopoulos *et al.*, 2007) as shown in Fig.1. A user subroutine (VUMAT, ABAQUS 2011) has been developed using FORTRAN to capture the full response of the Mohr-Coulomb model including strain softening behavior of the material.

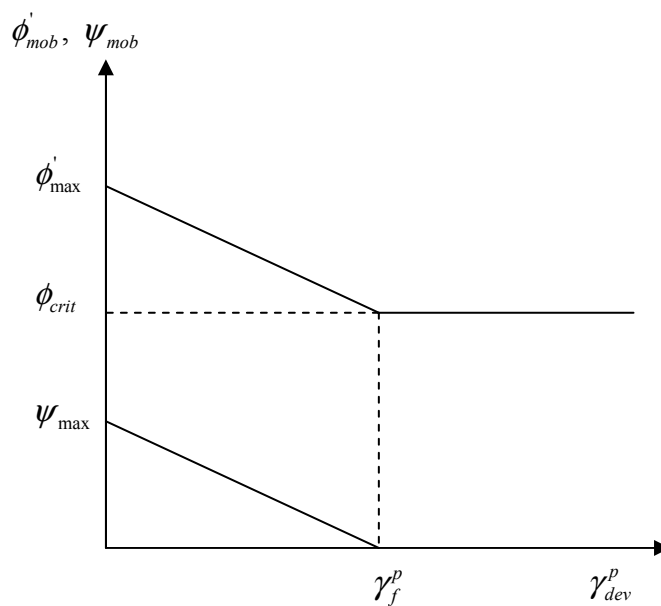


FIG.1. Typical variation of mobilized friction and dilation angles with plastic deviatoric strains

where ϕ'_{max} and ϕ'_{crit} are the peak friction angle and critical state friction angle, respectively, and ψ_{max} is the ultimate dilation angle, ψ_{res} residual dilation angle, γ_f^p is the plastic deviatoric shear strain when the softening is completed.

Calibration for mesh sensitivity (i.e. γ_f^p calibration)

Calibration of γ_f^p is required on the basis of direct shear tests in order to obtain a mesh-independent solution. The procedure introduced by Anastasopoulos *et al.* (2007) has been adopted when deriving plastic shear strain at the completion of softening (γ_F^p) based on direct shear test data.

$$\gamma_F^p = \gamma_p^p + \frac{\delta x_f - \delta x_p}{16d_{50}} = \frac{\delta x_p - \delta x_y}{D} + \frac{\delta x_f - \delta x_p}{d_{FE}} \quad (7)$$

where

d_{FE} -size of the element.

D – thickness of the sample in direct shear test

δx_y , δx_p and δx_f are the horizontal displacements at yielding, peak and completion of softening, respectively

A parametric study has been carried out to validate the mesh independence of the modified Mohr-Coulomb model in application to the lateral pipeline analyses. The analyses were carried out in ABAQUS/STANDARD to analyse the behaviour of a laterally moving pipeline in dry sand, located at H/D=4, using original Mohr-Coulomb (MC) and modified Mohr-Coulomb model (MMC). The model parameters for Mohr-Coulomb (MC) and Modified Mohr-Coulomb (MMC) models are listed in Table 1. Three different mesh discretised models having the minimum mesh sizes of 8.0mm, 10.0mm and 12.0mm, are considered. A typical finite element mesh used for the study is shown in Fig.2. Table 2 shows the strain output derived from typical direct shear test data. A shear band width is assumed to be 8mm. The variation of ϕ' and ψ with the calculated deviatoric strain is shown in Fig.3. The pipeline is assumed to be a linear elastic material (ASTM Grade A-36 steel). The results of the study are showed in terms of computed pipe load-displacement curves (Fig. 4). It can be seen that the modified Mohr-Coulomb model can effectively simulate the softening behaviour irrespective of the mesh size dependence. The conventional linear elastic-perfectly plastic Mohr-Coulomb model was not capable in producing the strain softening behaviour of the soil.

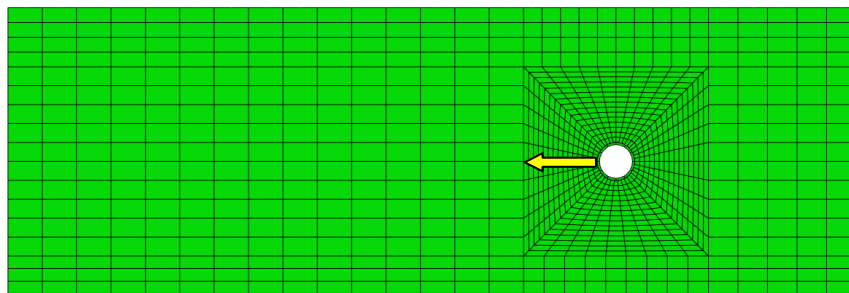


FIG. 2. Typical FE mesh (minimum size-8mm) used for the study

Table 1. Model parameters for MC and MMC models

Parameter Model	γ_d (kg/m^3)	E (kPa)	ν	c' (kPa)	ϕ'_{max} (degrees)	ψ (degrees)	γ_f^p	ϕ_{crit} (degrees)
MC	1640	1745	0.3	0.5	39	18.9	-	-
MMC-8mm	1640	1745	0.3	0.5	39	18.9	0.2715	33
MMC-10mm	1640	1745	0.3	0.5	39	18.9	0.2172	33
MMC-12mm	1640	1745	0.3	0.5	39	18.9	0.1889	33

Table 2. Strain quantities based on typical direct shear data

Horizontal Displacement (mm)	Shear Stress (kPa)	Verticle Dispalcement (mm)	Elastic Shear Strain	Total Shear Strain	Plastic Shear Strain	Deviatoric Strain	Mobilized ϕ' (deg)	Mobilized ψ (deg)
0	0	0	0	0	0	0	0	0
0.01271941	2.2305494	0.014	0.000962747	0.000962747	0	0	10.581635	0
0.055965403	4.400127	0.0152	0.001899177	0.001899177	0	0	20.229843	0
0.099211397	6.0006351	0.015221987	0.002589986	0.002589986	0	0	26.682536	0
0.17044009	8.0025405	0.027906977	0.00259	0.00259	0	0	33.831161	0
0.24166879	8.9425214	0.058350951	0.00259	0.004833376	0.002243376	0.001295214	36.831555	6.9
0.35614347	9.4302953	0.093868922	0.00259	0.007122869	0.004532869	0.002617053	38.301925	14.3
0.48588146	9.516672	0.14968288	0.00259	0.009717629	0.007127629	0.004115139	38.556289	16.5
0.78605953	9.6284535	0.25623679	0.00259	0.015721191	0.013131191	0.007581296	38.882814	18.5
0.97176291	9.6843442	0.32219873	0.00259	0.019435258	0.016845258	0.009725614	39.044959	18.97
1.1727296	9.6030486	0.37801268	0.00259	0.044555836	0.041965836	0.024228987	38.808865	13.9
1.4296617	9.4861861	0.44397463	0.00259	0.076672349	0.074082349	0.042771464	38.466718	12.3
1.6738743	9.3134328	0.49217759	0.00259	0.107198924	0.104608924	0.06039599	37.954925	9.7
1.8875604	9.1457606	0.54291755	0.00259	0.133909686	0.131319686	0.075817456	37.45127	8.5
2.1444925	8.9730073	0.58604651	0.00259	0.166026199	0.163436199	0.094359933	36.92516	6.9
2.5184431	8.8561448	0.63424947	0.00259	0.212770024	0.210180024	0.121347493	36.565092	6
3.0043246	8.6884725	0.70021142	0.00259	0.273505211	0.270915211	0.15641297	36.042549	4
3.4469601	8.4852334	0.73572939	0.00259	0.328834649	0.326244649	0.188357436	35.399736	3.5
3.8768761	8.2870753	0.77885835	0.00259	0.382574149	0.379984149	0.219383951	34.762965	2.5
4.2482829	8.2006986	0.80676533	0.00259	0.428999999	0.426409999	0.246187928	34.482279	1.5
4.7341643	8.0025405	0.8422833	0.00259	0.489735174	0.487145174	0.281253397	33.831161	0
5.1360977	7.9415688	0.86257928	0.00259	0.539976849	0.537386849	0.310260442	33.628793	0
5.4489952	7.8602731	0.87019027	0.00259	0.579089036	0.576499036	0.332841874	33.357483	0
5.7644365	7.8297872	0.88541226	0.00259	0.618519199	0.615929199	0.355606889	33.255303	0
6.1231239	7.6875198	0.88541226	0.00259	0.663355124	0.660765124	0.381492922	32.775293	0
6.4792674	7.885678	0.89302326	0.00259	0.707873061	0.705283061	0.407195365	33.44245	0
6.809972	7.885678	0.90063425	0.00259	0.749211136	0.746621136	0.431061914	33.44245	0
7.1661155	7.9161639	0.90570825	0.00259	0.793729074	0.791139074	0.456764357	33.544191	0

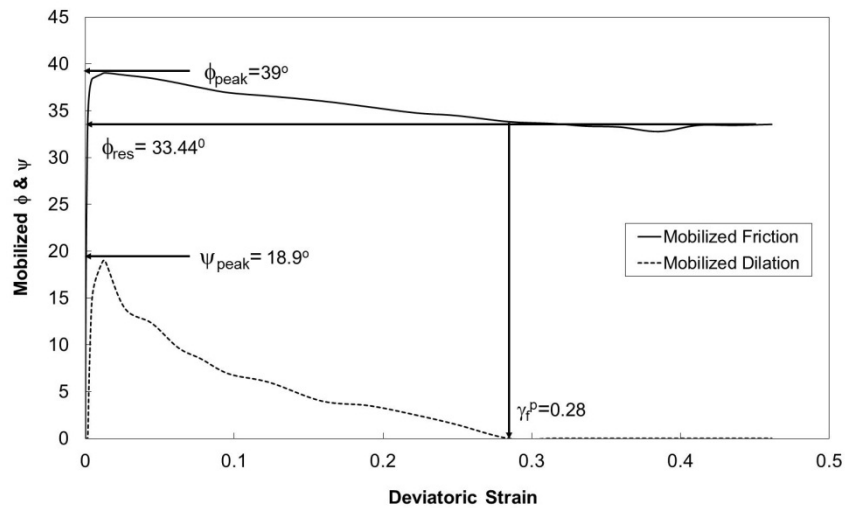


FIG. 3. Mobilized friction and dilation angle with deviatoric strain

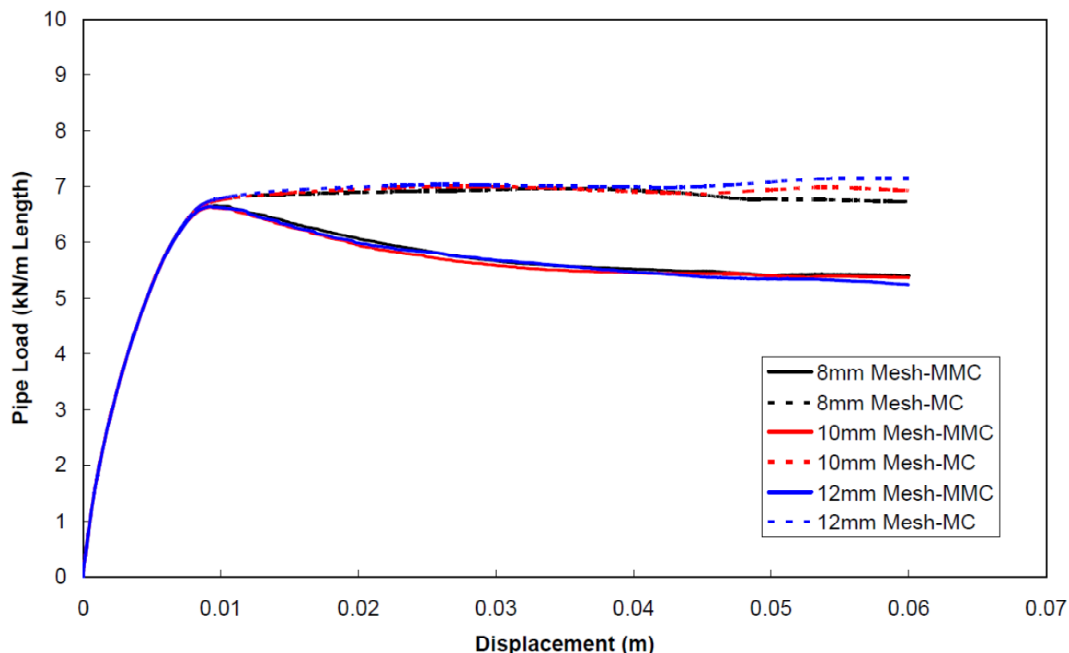


FIG. 4. Pipe Load-displacement plot using MC and MMC models

Calibration for material properties

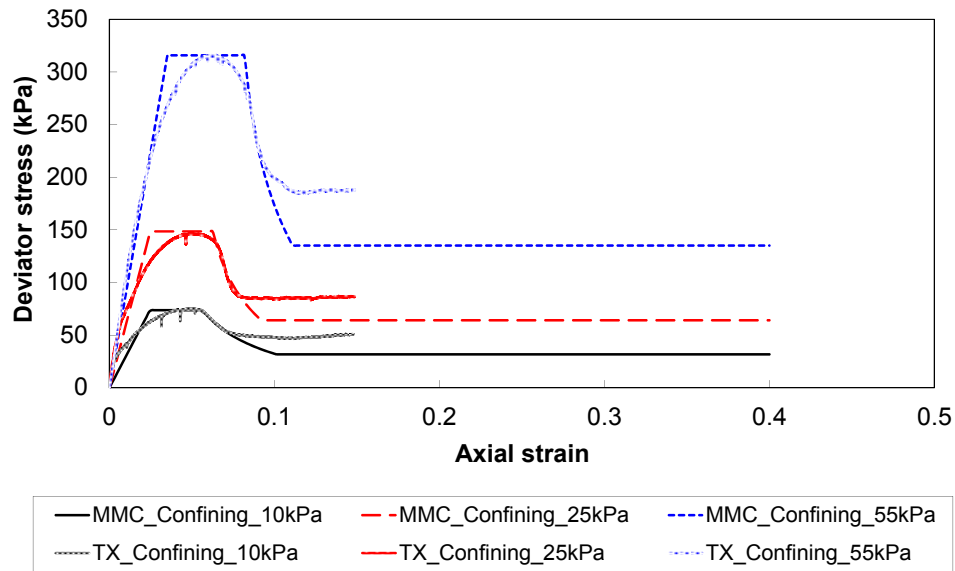
The modified Mohr-Coulomb model has been further calibrated using triaxial compression test data for yielding and flow characteristics. Triaxial compression tests were performed on different types of sand at various initial states, moisture contents and confining stresses (Robert, 2010). The results of a finer sand at dry density of 1.6g/cm^3 with varying confining stresses ($p'=10\text{kPa}, 25\text{kPa}$ & 55kPa) are showed and discussed in this paper. Table 3 shows the calibrated material properties of the full model.

Table 3. Modified Mohr-Coulomb input parameters based on triaxial compression tests

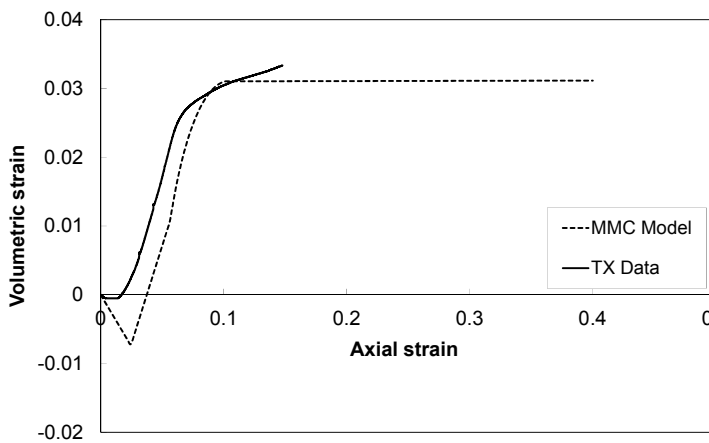
γ_d (g/cm^3)	p' (kPa)	E (kPa)	ν	c' (kPa)	ϕ'_{max} ($^\circ$)	ψ_{max} ($^\circ$)	ϕ_{crit} ($^\circ$)	γ_f^p
1.6	10	3000	0.35	0.5	47.5	15.04	33	0.102
	25	6000	0.35	0.5	47.5	14.41	33	0.092
	55	9000	0.35	0.5	47.5	13.64	33	0.108

Figures 5 shows the results of the FE analyses conducted to simulate the drained triaxial compression tests on saturated sands having initial density of 1.6g/cm^3 at

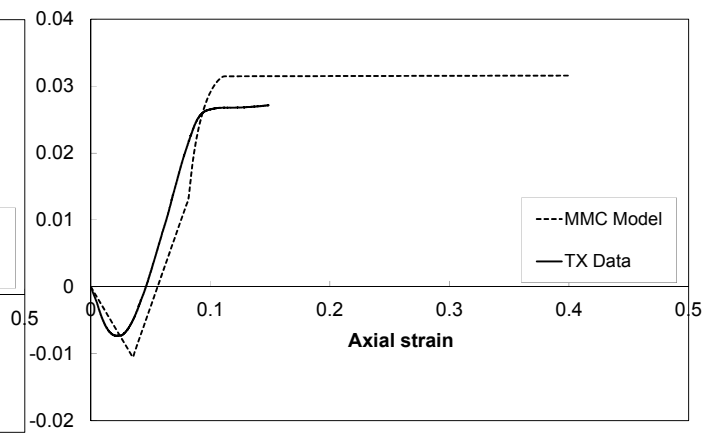
different net confining stresses (see Robert, 2010 for the results of other tests and calibration). The computed results are compared to the experimental results, in terms of stress-strain and volumetric strain plots at different confining pressures. The model predicts realistic stiffness, peak strength, softening and dilatancy behaviour in comparable to the experimental results under different confining stress levels.



(a) Stress-strain plot



(b) Volumetric strain plot- $p' = 10kPa$



(c) Volumetric strain plot- $p' = 55kPa$

FIG. 5. FE simulation of saturated Tokyo Gas sand, $\gamma_d = 1.6g/cm^3$

BURIED HDPE PIPELINE RESPONSE UNDER EARTHQUAKE

The model has been applied to predict the response of buried (at 0.8m depth) high density polyethylene (HDPE) pipeline (diameter=0.35m, thickness=34mm) subjected to an earthquake displacement in granular soil (initial density~1.6g/cm³). The simulated scenario is based on an earthquake induced strike-slip fault displacement of 0.5m. The pipeline is located far from the fault plane. The displacement rate of the earthquake was selected at 0.0625m/s. The response of the model for buried steel pipelines subjected to lateral soil displacement has been discussed elsewhere (Robert, 2010; Robert and Soga, 2013; Robert et al, 2015).

Simulating HDPE material behaviour

The calibration of HDPE material response has been conducted on the basis of pure tension test (O'Rourke *et al.*, 2006). The measured stress-strain curves are shown in Fig. 6 at different strain rates (at 21°C). The current FE modelling simulates the strain rate dependence of HDPE pipe material at the temperature of 21°C (Fig. 6), using von Mises' plasticity.

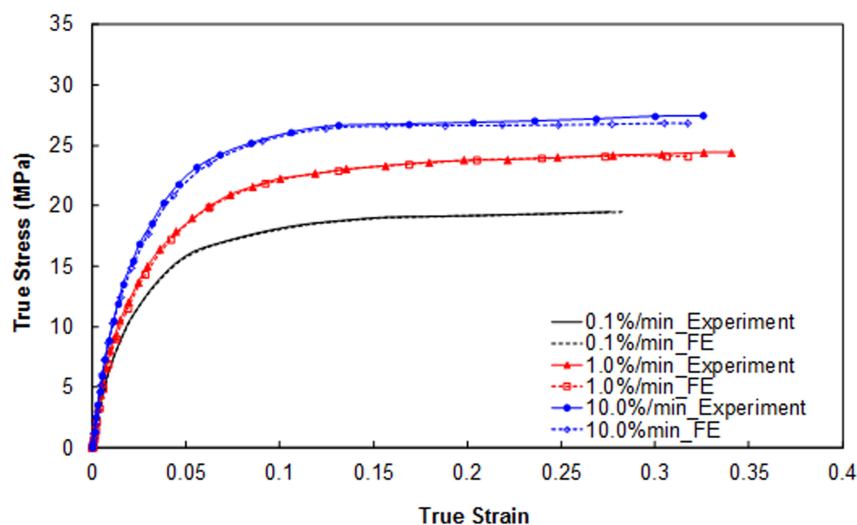


FIG. 6. Calibration of HDPE model in comparison with pure tension data (Robert et al, 2015)

FE model

3D FE analyses were carried out using ABAQUS (ABAQUS, 2011) with geometric non-linearity and large strain formulation. Soil and pipe were represented by 3-D solid continuum elements (C3D8R). The pipe was assigned with 90 elements in the circumferential direction and 70 elements in the longitudinal direction. The mesh density adopted for the soil box can be referred to as the intermediate mesh, in which finer meshes concentrated at the locations where the pipeline was located. This resulted in a total of 6300 elements to model the pipeline and approximately 31,200 elements to model the soil. The wall boundaries were assumed to be smooth and supported only in the normal direction. Earthquake displacement was applied to the

side walls of the model. Adaptive meshing has been incorporated in the analyses to control the mesh distortions that result from large deformations of the soil caused by lateral pipe displacements. The geometry and mesh discretization of the model was shown in Fig. 7.

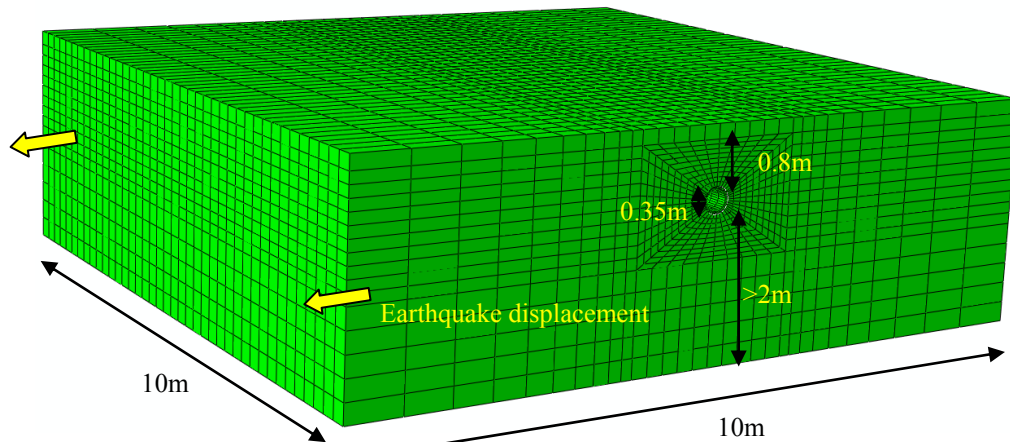


FIG. 7. FE mesh model for soil

Results and discussion

The results of the analysis are showed from Figs. 8-10. The earthquake induced fault displacement has significantly deformed the HDPE pipe (Fig. 8). Maximum deformation has occurred in the pipe around $\sim 2\text{m}$ from the pipe ends (Fig. 9) which have fixed displacement boundary condition to simulate far field condition. The middle of the pipe has experienced the least deformation due to near zero relative displacements of the mid-pipe.

The maximum strain response along the buried pipeline length is further investigated in order to evaluate the effect of ground displacement on pipe performance. The allowable tensile strain of HDPE pipe is about 0.30 (Palermo, 1983). The resulted maximum strain along the pipe at 0.5m fault displacement is ~ 0.025 (Fig. 9) which is well below the allowable strain limit of HDPE. Hence, the considered pipeline is safe at 0.5m fault displacement under the simulated conditions. However, the compression strain limit for short-term loading, such as in earthquake, is around 0.028 (McGrath and Sagan, 2010).

Further, the lateral strain response of a critical element within the pipeline with fault displacement was analyzed and showed in Figure 10. It can be seen that the lateral strain are very close to the allowable strain at the fault displacement of 0.5 m for the critical element. The strain in the critical element is a compressive strain, hence, this can cause buckling crack in pipe surface and eventually lead to the failure. The behaviour of strain in the critical element with fault displacement (as in Figure 10) can be used as the demand model for buried pipes subjected to large ground displacement due to earthquake or landslide. However, the effect of variability in different ground condition and frequency content of earthquake loading can change the response significantly. Therefore the demand model has to incorporate these effects to determine the response and its variability for the risk assessment of buried pipe.

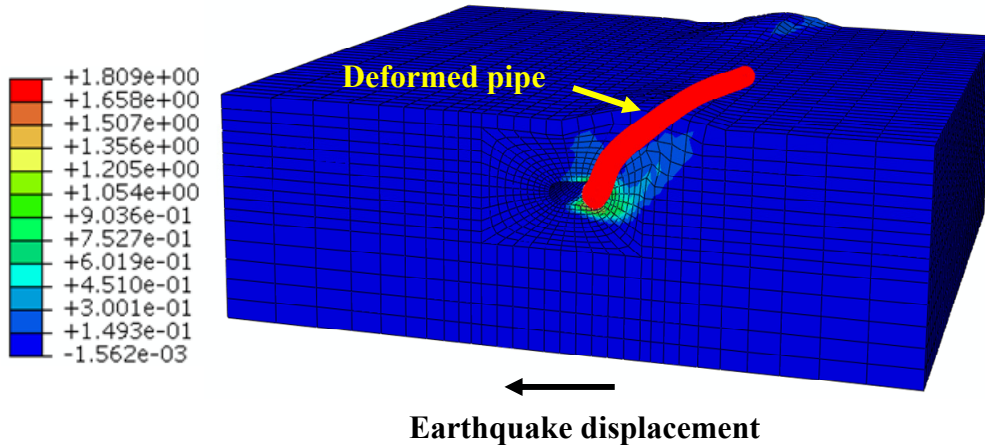


FIG. 8. Soil and pipe deformation (max principal strains) due to earthquake

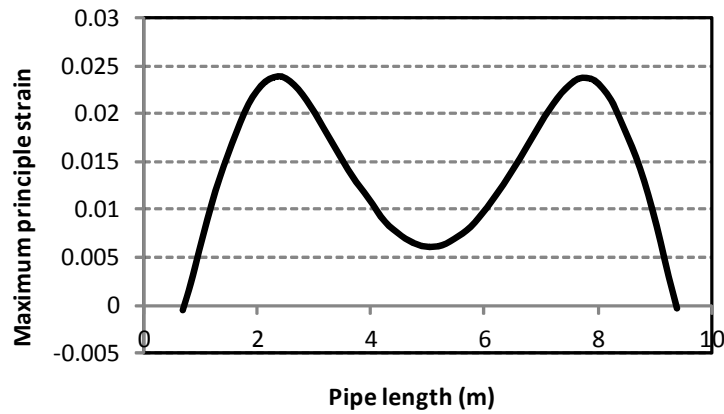


FIG. 9. Maximum strain response of the pipeline at 0.5 m of fault displacement

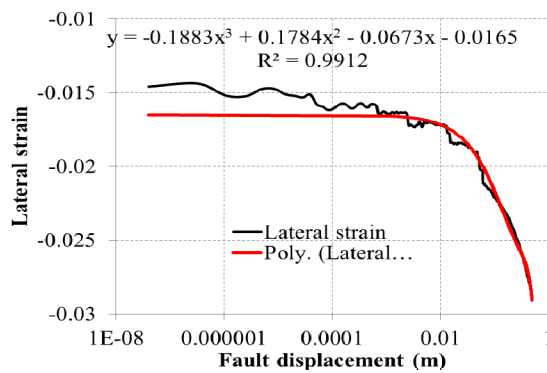


FIG. 10. Lateral strain response of critical element within the the pipeline with fault displacement

SUMMARY AND CONCLUSION

In this paper, the application of modified Mohr-Coulomb model to analyze a pipeline subjected to large ground displacement (such as earthquake) has been discussed. A user defined modified Mohr-Coulomb model is developed to capture the strain softening behaviour of soils undergoing large deformation. The strain softening parameter has been calibrated using direct shear test data, and triaxial compression test data has been used to calibrate the other modeling parameters. The calibrated model was utilized to simulate the behavior of HDPE pipeline undergoing earthquake displacement and to propose a typical strain based demand model. The model is based on the maximum strain in the pipe which can cause cracking in the pipe surface due to compression with fault displacement. Developed model can be used for risk assessment of buried flexible pipe subject to large ground deformation. However, the effect of variability in different ground condition and frequency content of earthquake loading can change the response significantly. Hence, the demand model is currently being extended to incorporate these effects to determine the response and its variability for the risk assessment of buried pipe.

REFERENCES

- ABAQUS, Inc. (2011), ABAQUS V.6.7 User's Manual, Providence, Rhode Island.
- Anastasopoulos, Gazetas, G., Bransby, M.F., Davies, M.C.R. and Nahas, A.E. (2007), "Fault rupture propagation through sand: Finite-Element analysis and validation through centrifuge experiments", *Journal of Geotechnical and Geoenvironment Engineering*, Vol.133, Issue 8, pp.943-958.
- McGrath, T.J. and Sagan, V.E. (2010). Recommended LRFD Specifications for Plastic Pipe and Culverts. Washington, DC: National Academy Press.
- O'Rourke, T. (2006). "NEESR Annual Report", Cornell University, Rensselaer Polytechnic Institute and Sciencenter Discovery Centre.
- Palermo, E.F. (1983), Rate Process Method as a Practical Approach to a Quality Control Method for Polyethylene Pipe, Proceedings of the Ninth Plastics Fuel Gas Pipe Symposium
- Robert, D.J. (2010). "Soil-pipeline interaction in unsaturated soils", *PhD Thesis*, University of Cambridge.
- Robert, D.J. and Soga, K. (2013). "Chapter 13: Soil-Pipeline Interaction in Unsaturated Soils." *Mechanics of Unsaturated Geomaterials*, L. Laloui (editor), John Wiley and Sons, 303-325.
- Robert, D. J., Soga, K., and O'Rourke, T. D. (2015). "Pipelines Subjected to Fault Movement in Dry and Unsaturated Soils." *International Journal of Geomechanics*, ASCE (Accepted).

The Use of Neural Networks to Forecast Landslides Triggered by Rains in Mountainous Areas

Eduardo M. Botero¹; George F. Azevedo¹; Hernan E. M. Carvajal²; Edwin F. García³; and George F. Azevedo¹

¹Ph.D. Student, Dept. of Civil and Environmental Engineering/FT, Univ. of Brasilia.

²Professor, Dept. of Civil and Environmental Engineering/FT, Univ. of Brasilia.

³Professor, Environmental School/Univ. of Antioquia.

Abstract: In this work, it has been verified the ability of a computational tool known as artificial neural networks to predict landslides triggered by rains in mountainous areas. The neuronal model was trained and verified for a tropical mountainous location in the city of Medellin - Colombia. The construction of the database, composed by 2054 samples, consisted in obtaining nine representative slopes and twenty typical rains of the study site, characterized by their duration and return period. There have been combined data of nine slopes and twenty rainfalls, there by obtaining the fluid pressure profile in a finite element code, in order to get the safety in each of the analyzed cases. To obtain shear strength values for the simulations, the parabolic envelope proposed by Lade (2010) was used. Thus, the input data to the neural network are the slope and the precipitation and the output is the safety factor. It has been verified the ability of the neural networks to learn specific information of the studied problem and give an answer, with minimum error, for any other condition, generalizing the problem and allowing the application of the tool in a location with similar conditions.

INTRODUCTION

Mass movements are one of the most frequent causes of human and economic losses around the world, that is why the determination of the threat of mass movements and the ability to predict these events have been a subject of great interest to the scientific community (Aleotti & Chowdhry 1999; Chacón et al. 2006). For tropical environments characterized by deep weathering profiles and high rate of rainfall, an important number of researchers are concentrated on understanding the rain as a key factor in the occurrence of such mass movements (Crosta 1998; Terlien 1998; Polemio & Petrucci 2000; Iverson 2000; Larsen 2008).

In the case of the Aburrá Valley (Medellin - Colombia), with a total of 3.4 million inhabitants, the mass movements correspond to 3 of every 10 disasters that occur in the region and they correspond to 75% of the total victims per year. Mass movements alone were responsible for 1390 fatalities and economic losses exceeding \$ 10 million in the period of 1880-2007 (Aristizábal & Gómez 2007). In Colombia, were recorded, during the last century, 36 disasters generated by mass movements of considerable magnitude, and the most catastrophic was Villatina's disaster, in Medellín, which occurred on September 27th of 1987, with an estimated number of 640 fatalities (Aristizabal et al 2010).

METHODOLOGY

The methodology used focused on creating a database that trains an Artificial Neural Network that is able to predict landslides caused by rains. The construction of the database consisted of obtaining nine representative slopes and twenty typical rains of the study area, characterized by its duration and intensity. The nine slopes were combined with the twenty rains, therefore, the pore pressure profile was obtained by a finite element code that calculates the factor of safety for several depths. Once trained, this network makes possible the map's creation with landslides prediction caused by rain for several scenarios.

An area of 1.5 km² was chosen as the study area. This area is located in the northwestern coast of the city of Medellín (Fig. 1), and it is located in the Aburrá Valley, in which there are five other cities besides Medellín forming the so-called Metropolitan Area of Medellín.

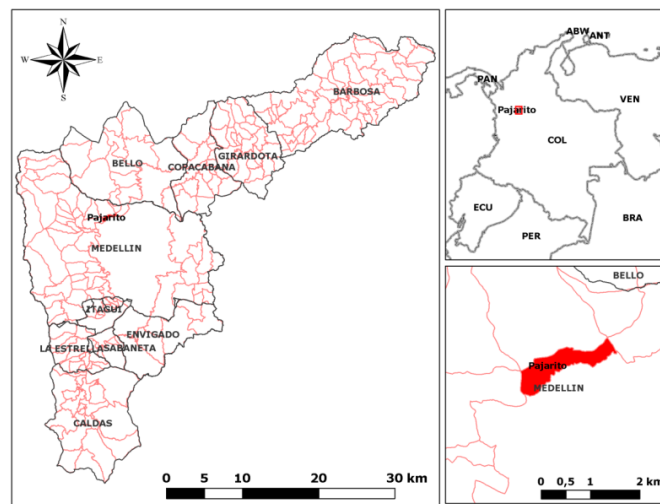


FIG. 1. Location of the study area.

Using the topography of the study area, a digital elevation model (DEM) of slopes was prepared with a pixel size of 10 m. Taking into account the classification of slopes made by Garcia (2004), in which is presented the relationship between the occurrence of landslides and the inclination value of the land, the decision was to create a histogram with nine kinds of slopes that, according to the author, give the highest probability to have landslides. Once the intervals were fixed, the slopes were chosen, for which the numerical analysis of infiltration and slope stability were made. The chosen slopes were the upper limit of each class of slope histogram.

Using the Intensity Duration Frequency (IDF) curve of the San Cristobal rainfall station (INTEGRAL, 2011), located within the study area, a set of five times of duration (20,40,60,80 and 100 minutes) and another set of four return periods (Tr) (2.33, 10, 50 and 100 years) were established and the correspondent Intensity (I) was obtained for each of the several combinations. The amount of rain time duration and return periods

were set in order to explore all the IDF curves, to see the possible rain scenarios in the area of study and also to train the neural network with all possible rain cases.

The Geotechnical characterization made by Lobo (2012) and INTEGRAL (2011) was used, in which is obtained the water retention curve parameters and shear test, and these results are presented in Tables 1 and 2.

Table 1. Water retention curve parameters.

$\alpha = 0,035 \text{ kPa}^{-1}$	$n' = 1,26$	$m = 0,206$	$k = 3e-5 \text{ m/seg}$
-----------------------------------	-------------	-------------	--------------------------

Table 2. Shear test.

Test No	1	2	3
Shear Strength, S (kPa)	72,51	89,42	139,65
Effective stress, σ' (kPa)	50	100	200

After that, a numeral analysis of the infiltration was made, from where the pore pressure in the chosen slopes, characterized by the inclination, at the end of each twenty rains was obtained. For this purpose, the finite element code prepared in the laboratory of Geomechanics of Kyoto University, presented by Garcia (2010), was used.

From the previously described Numerical analysis of infiltration, the variation of the pore pressure is obtained in each of the slopes at the end of each precipitation taken from the IDF curve.

Considering the geometry of the nine slopes, characterized by the inclination, coming from the histogram suggested by Garcia (2004), and adding strength parameters, it is also possible to calculate the relationship between the acting stresses (τ) and those shear stresses (s) for each of the scenarios of combinations among slope and rain, resulting in a safety factor, as shown in Eq. 1 proposed by Lade (2010).

$$FS = \frac{s}{\tau} = \frac{aP_a \left(\frac{\sigma'}{P_a}\right)^b}{\tau} \quad (1)$$

Where a and b are dimensionless numbers, σ' is the effective stress and P_a is the atmospheric pressure in the same units as s and σ' .

Lade (2010) proposes an rupture envelope without effective cohesion, which can be modeled by a potential function in the same form of the Eq. 2

$$\left(\frac{s}{P_a}\right) = a \left(\frac{\sigma'}{P_a}\right)^b \quad (2)$$

In order to calculate the values of a and b, the logarithm of both sides was taken in the Eq. 2 and an expression that represents a straight line on the logarithm scale was produced (Eq. 3).

$$\log\left(\frac{s}{P_a}\right) = \log(a) + b \log\left(\frac{\sigma'}{P_a}\right) \quad (3)$$

Creating a relationship between s and τ , the equation that determines the safety factor of an infinite slope is shown in Eq. 4.

$$FS = \frac{a P_a \left[\frac{\gamma_{sat} h (\cos \alpha)^2 - u}{P_a} \right]^b}{\gamma_{sat} h \cos(\alpha) \sin(\alpha)} \quad (4)$$

Where 'a' and 'b' are dimensionless numbers obtained from Eq. 3, P_a is the atmospheric pressure in kPa, γ_{sat} is the saturated specific weight in kN/m³, h is the depth in m, u is the pore pressure in kPa, α is the inclination of the slope in degrees. The equation of the factor of safety previously shown in Eq. 4 was applied to h (depth) with increments of 0,30m until a depth of 4,20m is reached in each one of the geometries obtained, changing the pore pressure according to each precipitation studied.

Once you have a database of safety factors varying with depth according to the pore pressure generated by each rainfall, a neural network is trained.

The working platform Weka was used to train the network. This is a software for experimentation and testing of different algorithms of automated learning; in particular, the methods of regression are: IBk, LinearRegression, REPTree and MultilayerPerceptron. In all these cases the input parameters that the software has as default were used.

RESULTS:

The map of slopes was made with a pixel size of 10m, the study area has 1,0km x 1,5km, so that it results in 15000 pixels. In the Fig. 2 the Map of slopes is shown.

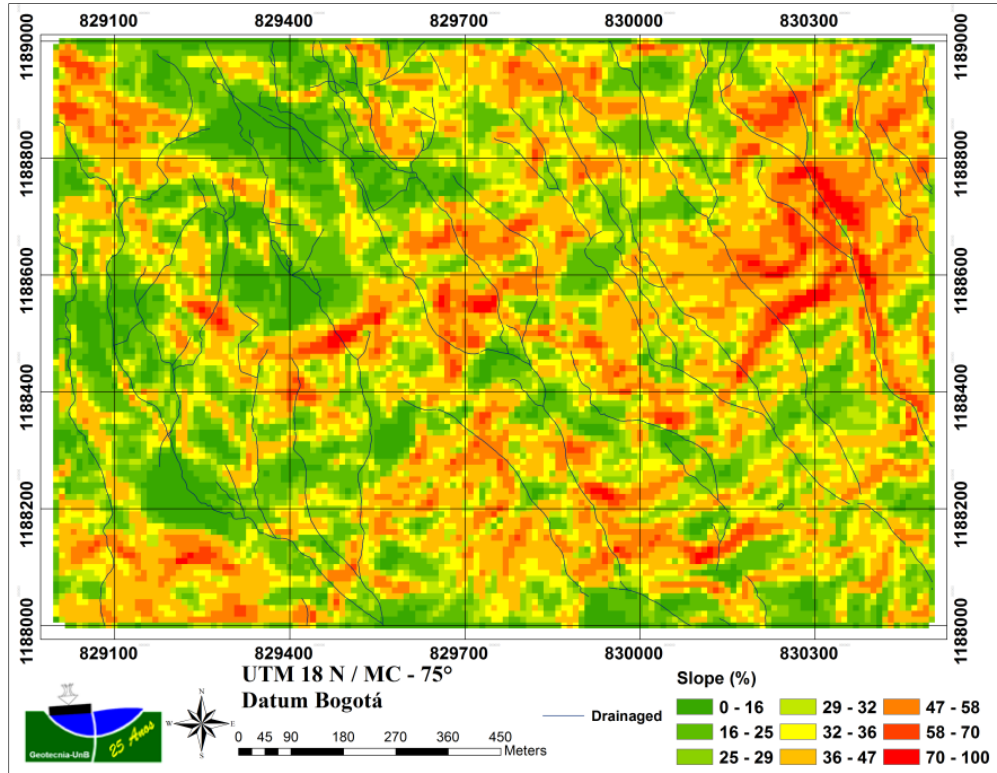


FIG. 2. Map of slopes.

With the obtained data in the map of slopes of the Fig. 2, the histogram of slopes was built and is shown in Fig. 3.

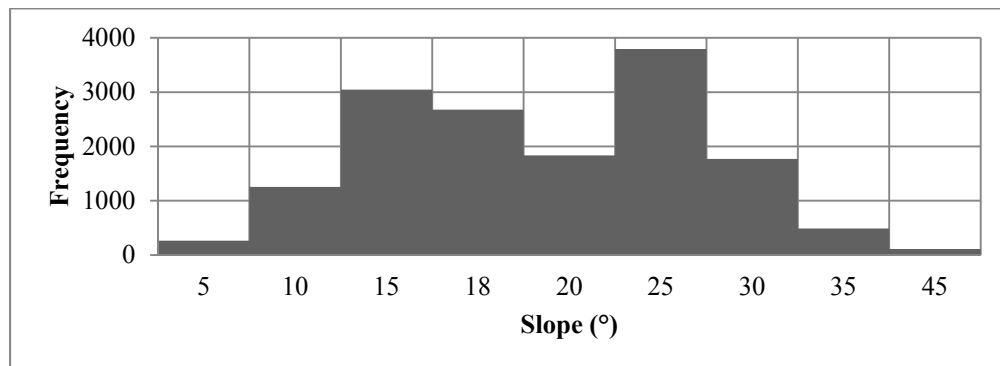


FIG. 3. Histogram of slopes.

The geometry of the cases to be analyzed for the network training was defined as the upper limit of each group of the slope histogram.

The intensity of the rain for each of the four return periods and twenty rains, presented in Table 3, was obtained from the IDF curve.

Table 3. Rains adopted

I (mm/h)	D (min)	Tr (Years)	I (mm/h)	D (min)	Tr (Years)
75	20	2,33	140	20	50
55	40		90	40	
42	60		66	60	
34	80		54	80	
28	100		45	100	
105	20	10	160	20	100
70	40		100	40	
52	60		74	60	
43	80		58	80	
35	100		48	100	

With the hydraulic and geometrical parameters defined, presented in Table 1, Table 2 and in Fig. 3, the infiltration analysis is done, and it was obtained the curve of pressure of pores for each of the nine slopes, characterized by the inclination, at the end of each of the rains characterized by their intensity.

In this way, we have computed the factor of safety and we have now a database composed of slopes, rain, depth as inputs and the factor of safety as an output.

The network was trained using the software Weka and using the four implemented approximation methods with the software's default parameters.

Validation with 10 partitions is used to perform experiments. To calculate the approximated error, the absolute average error was used, and that corresponds to the average of the differences between the set point and the one produced by the method, and the correlation coefficient that indicates the correlation between the actual values and the values estimated by each method. The Table 4 shows the results obtained.

Table 4. Neuronal network errors

Method of approximation in Weka	Absolute average error	Correlation coefficient
Linear Regression	0.9995	0.8615
REPTree	0.3086	0.9748
Ibk	0.0566	0.9992
Multilayer Perceptron	0.2879	0.9881

The results of the experimental study show a good behavior of Multilayer Perceptron, and it was decided to conduct another study in order to obtain the best topology and adapt the model to the best parameters performance so that they can solve the problem described with a better error while maintaining or improving the correlation factor.

The better network performance was obtained using a learning rate of 0.3, a value of momentum of 0.07, and a network topology of 2 hidden layers with 8 neurons in the first layer and 2 neurons in the second layer. Furthermore, with the increasing number of iterations, much lower error rates are obtained.

Using the trained neural network, it is now possible to create a safety factor map for any depth and any rain of the study area as presented in Fig. 4. To use the neuronal network, the same slopes already calculated are used, the intensity and duration of rainfall are defined from the IDF curve and a depth is chosen to evaluate the safety factor.

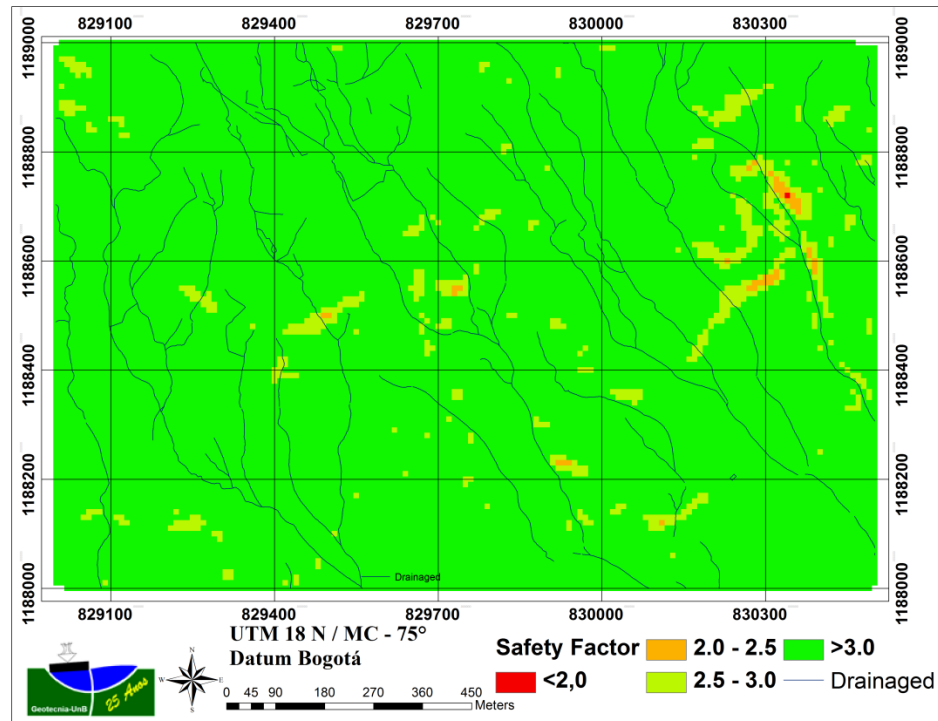


FIG. 4. Safety factor map for $I = 53\text{mm/h}$, $D = 90\text{ min}$, $h = 3.5\text{m}$.

CONCLUSIONS:

The neural network showed an easy and fast processing, allowing this to be a possible tool in predicting landslides that can be triggered by rains.

The use of neural networks proved to be a powerful methodology that can evaluate the susceptibility of mass movements in zones of big areas, such as the zone of the present study, in which the analytical estimation of the safety factor becomes impossible due to the large amount of pixels.

In this work, the presented methodology should be validated with other methods or landslides inventory so that the landslide prediction capacity triggered by rains can be determined.

Neural networks technique showed an excellent ability to interpolate the data of the problem addressed. Once you already have an initial database, you can increase the number of inputs and improve the network performance.

This methodology can be extrapolated to other zones, other soil types and other distributions of rain in order to obtain the safety factors and the potential depths slope failure under rainfall infiltration processes.

REFERENCES:

- Lade, Poul V. (2010). The mechanics of surficial failure in soil slopes. *Engineering Geology*, 114, 57-64.
- Aleotti P. ; Chowdhury R. (1999). Landslide hazard assessment: summary review and new perspectives. *Bulletin of Engineering Geology and the Environment*.58 (1). 21-44
- Chacón, J., Irigaray, C., Fernandez, T., El Hamdouni, R. (2006). Engineering geology maps: landslides and geographical information systems. *Bulletin of Engineering Geology and the Environment*. 65(1), 341-411.
- Crosta, G., (1998). Regionalization of rainfall threshold: an aid for landslide susceptibility zonation. *Environmental Geology*. 35(2-3), 131-145.
- Terlien, M. T. J., (1998). The determination of statistical and deterministic hydrological landslide-triggering thresholds. *Environmental Geology* 35 (2-3), 124-130.
- Polemio M., Petrucci O. (2000). Rainfall as a Landslide Triggering Factor: An Overview of Recent International Research. *Landslides in research, theory and practice. Proceedings of the 8th International Symposium on Landslides, Carraiff*.1219-1226.
- Iverson, R., (2000). Landslide triggering by rain infiltration. *Water Resources Research*. 36 (7).1897-1910.
- Larsen, M., C., (2008).Rainfall-triggered landslides, anthropogenic hazards, and mitigation strategies. *Advances in Geosciences*. 14, 147-153.
- Aristizábal, E., Martinez, H., Gómez, J. (2010),, Uma breve revisión sobre el estudio de movimientos em masa detonados por lluvias. *Revista de la Academia Colombiana de Ciencias Exactas, físicas y Naturales*. 34 (131), 209-227.
- Aristizábal, E., Gómez, J., (2007), Inventario de emergencias y desastres en el Valle de Aburrá: originados por fenómenos naturales y antrópicos en el periodo 1880-2007. *Revista Gestión y Ambiente*, 10(2), 17-30.
- Garcia, H.A.G. (2004). Avaliação da Susceptibilidade aos Movimentos de Massa Usando Sistemas de Informação Geográfica e Redes Neurais Artificiais.
- INTEGRAL (2011), Elaboración de estudios geológicos geotécnicos, hidrogeotécnicos, análisis de la vulnerabilidad estructural, y diseños de obras en las zonas de riesgo de la ciudad de Medellín, 178 p
- Lôbo, B. R. H. (2012). Efeito do avanço da frente de umidade na redução da sucção e da resistência ao cisalhamento de um perfil de solo coluvionar em Medellín-Colômbia.
- Garcia, E. (2010). Numerical Analysis of the Rainfall Infiltration Problem in Unsaturated Soil, Ph.D. Thesis, Kyoto University.

Bio-Nano-Cementation to Evaluate Soil Mechanical Resistance

Jaqueline Bonatto

Universidade Federal do Rio Grande do Sul, Porto Alegre, Brazil. E-mail: jaquebonatto@yahoo.com.br

Karla Heineck

Universidade Federal do Rio Grande do Sul, Porto Alegre, Brazil. E-mail: karla@ppgec.ufrgs.br

Antonio Thomé

Universidade de Passo Fundo, Passo Fundo, Brazil. E-mail: thome@upf.br

Bruna DallAgnol

Universidade de Passo Fundo, Passo Fundo, Brasil. E-mail: brunab_d@hotmail.com

Gregório Rigo Garbin

Universidade de Passo Fundo, Passo Fundo, Brazil. E-mail: greggarbin@gmail.com

Abstract: The demand of infrastructure investment in the world has led to invest high financial values to solve problems related to population growth. The rehabilitation and expansion of civil infrastructure are required to serve the growing needs of society and is directly limited by the availability of competent soils upon which construction can occur. Parallel to this, environmental degradation of ecosystems is occurring in an exponential level, thus contributing to problems such as pollution of groundwater, soil and air. From the socio-economic point of view, the infrastructure activity is shown to be divergent. Even though, on the one hand, represent development, the benefit ultimately achieve environmental problems and may cause health risks for people and for the environment. Most soil improvement techniques, which are used worldwide, involve the addition of mechanical energy and/or synthetic material, both of which have substantial energy cost associated with their production, however, the bio-cementation technique has as order to improve the mechanical properties in a sustainable way. Bio-cementation is the formation of particulate material attached to the soil by microorganisms. The various microbiological processes have the potential to modify the behavior of the soil. Many bacteria such as the species: *Bacillus*, *Sporosarcina*, *Sporolactobacillus*, *Clostridium* and *Desulfotomaculum* have potential for biological cementation. Nanoparticles are usually coated in order to enable obtaining properties of higher performance, however, it appears as a potential using nano-calcium to increase the soil resistance in bio-cementation process.

Keywords: Cementation, Microorganisms, Contaminated areas.

1 INTRODUCTION

The demands of infrastructure investment in the world, led to invest large amounts of money to solve problems related to population growth. The rehabilitation and expansion of civil infrastructure are required to serve the growing needs of society and is directly limited by the availability of competent soils upon which construction can occur (MONTROYA, 2012).

Parallel to this, environmental degradation of ecosystems is occurring in an exponential level, thus contributing to problems such as pollution of groundwater, soil and air. From the socio-economic point of view, the infrastructure activity is shown to be divergent. Even though, on the one hand, represent development, the benefit ultimately achieve environmental problems and may cause health risks for people and for the environment. Besides the development generates contaminated areas which carry risks to human health, devalue properties and entail limitations for urban development, it is in this context that arise the remediation techniques for contaminated soils which can promote the complete rehabilitation of contaminated areas, enabling again activities formerly developed.

Microbial geotechnology is an emerging branch of Geotechnical Engineering. Although there are many potential applications of microorganisms for this area, promising applications are found in bio-cementation technique of contaminated soils (IVANOV and CHU, 2008).

The natural and sustainable solution is needed to improve soil conditions and allow the continued growth of the country's infrastructure. New soil improvement techniques have used biological processes to remediate soil properties (DeJong et al., 2013).

The improvement of the soil mechanical properties can vary widely among bio-cementation processes in soil. The main properties that can perform a change of 10 times or more include permeability, rigidity, compressibility, cut resistance, and volumetric behavior. These changes in the properties provide numerous application possibilities.

The objective was to review the main aspects involved in bio-nano-cementing of soil and to verify the main microorganisms involved in the process as well as their microbial activity in sandy soil.

2 LITERATURE REVIEW

2.1 *Bio-cementation technique*

Microbial cementation or bio-cementation is the formation of particulate material attached to the soil through microorganisms present in the ground (CHU, 2012).

Most soil improvement techniques that are used involve the addition of mechanical energy and/or synthetic materials to the soil both of which have substantial energy costs associated with their production (DeJong et al., 2010).

The artificial cementation occurs through the use of Portland cement, which provides the addition of high alkalinity into the soil, which may damage the soil structure (FRITZGES, 2005).

Due to these factors, there is a need to develop a new alternative for soil remediation and improving. The use of bio-cementation for soil improvement presents a relatively new and environmentally friendly option for geotechnical engineering.

Montoya (2012) points out that the bio-cementation technique requires significant progress in science, and fundamentally on engineering about heterogeneity, soil structure and spatial distribution system of pores, the fluid in movement and transport, and biodiversity.

Currently, the potential of biological soil techniques is being investigated by DeJong et al. 2006; Whiffin et al. 2007; Thawadi, 2008, Ivanov and Chu 2008; Montoya in 2012.

Bio-cementation consists of microorganisms catalyzing chemical reactions in the soil, by providing some substrates, resulting in precipitation (or dissolution) of inorganic minerals that change the mechanical properties of the soil.

Kucharski et al. (2005) applied a patent for microbial bio-cementation for cement formation with a high strength in a permeable material using the combination of this material with urea biomass produced by microorganisms, urea, calcium and soluble salts. The microorganisms provided rapid hydrolysis in the urea, the pH increased during the hydrolysis of urea to ammoniac and formed calcite in the soil. The cement produced has a resistance to compression greater than 5 MPa. Also the author points out that the materials treated by bio-cementation can be rocky, sand, sandstone, silt, limestone, gypsum, peat, clay and sediments. The fundamental microorganisms in this process are the *Bacillus*, *Sporosarcina*, *Sporolactobacillus*, *Clostridium* and *Desulfotomaculum*.

2.1.1 Enhancers microorganisms in the process

Yang et al. (1993) highlights that exopolysaccharides producing bacteria can be used to modify the soil matrix in situ. After growth of these bacteria in the soil, its permeability is reduced. This technique can be used for different geotechnical applications such as bioremediation, control levees, minimizing erosion, the construction of the reactive barrier and a long-term stabilization of contaminated soils.

The main factors that affect the application of microorganisms into the geotechnical engineering include the selection and identification of microorganisms suitable for different applications and in different environments, the optimization of microbial activity in situ, application of bio-security, profitability and stability of soil properties after bio-modification (THAWADI, 2008).

The various microbiological processes have the potential to change the behavior of soil. Several mechanisms have been identified to produce precipitated (either inorganic or organic) or generate gas within the soil matrix. In the study of Montoya (2012), the author uses the hydrolysis of urea to increase the alkalinity of the pore fluid and to induce the calcite precipitation. The precipitated calcite generates cemented grains, which increases the resistance and rigidity of the sand. The process of microbiologically induced precipitated calcite (MICP) has the potential to be used as an alternative to traditional methods of soil improvement as more environmentally friendly.

The ureolytic bacteria are commonly encountered in the underground, though, the subsoil has microbial communities that need to be stimulated or increased (FUJITA et al, 2008, DEJONG et al 2009). If ureolytic bacteria are present in the underground, stimulating the population size and/or urease activity, providing adequate nutrients, it shows to be ideal because it uses native organisms and reduces the engineering challenges of controlling the underground transport cells (DEJONG et al 2009). However, if there is no presence of ureolytic bacteria in the soil, bio-augmentation of the microorganisms can be performed, which experience has proven satisfactory.

Many bacteria such as species: *Bacillus*, *Sporosarcina*, *Sporolactobacillus*, *Clostridium* and *Desulfotomaculum* have potential for biological cementation as shown by studies of DeJong et al. 2009; Ivanov and Chu 2008 Montoya in 2012.

Sporosarcina pasteurii is a gram-positive bacterium and not pathogen, the length of the rod shaped between 1-4 microns in diameter. This bacterium is movable with its polar flagellum. Breathing of this microorganism is optional anaerobic (MOBLEY and Haussinger 1989 cited GIRINSKY, 2009), regarding the production of enzymes, it produces two types of important enzymes in this process: oxidase and nitrate reductase. Furthermore, Bacillus bacteria are capable of degrading urea.

Sporosarcina pasteurii is widely used as a source of urease enzyme in bio-cementation reactions (Equation 01). It produces intracellular urease, which is close to 1% of the cell dry weight (THAWADI, 2013), showing to possess great potential for use. Bacteria of the genus *Sporosarcina* are the most frequent used microorganism in studies.



Also, Thawadi (2013) points out that bacteria of the genus *Bacillus* are urease positive bacteria which offers specific advantages such as higher specific activity of urease, more stable (robust), increased tolerance to high concentrations of ammonium and more consistent production of urease.

The microbiological process can be complicated by the transport of microbial cells in the soil, which depends on the cell size, surface properties of the cells, and physiological state of the cell (MURPHY and GINN, 2000 and cited IVANOV and CHU, 2008).

The microorganisms grown for the bio-cementation technique were to resist high concentrations of calcium and alkaline pH, between 7.5 to 10 (GIRINSKY, 2009).

2.1.2 Factors that interfere in the bio-cementation process

Whiffin (2004) highlights two main processes for bio-cementation: the first is the phase of bacterial growth and second is the cementation stage. This sequence of bio-cementation to prevent premature precipitation of CaCO_3 .

Calcium and carbonate concentrations can have a positive or negative effect on the rate of precipitation and/or an inhibitory effect on the production of CaCO_3 by bacteria. Hydrolysis of urea produces carbonate ions in a molar ratio of 1: 1. Thus, with increasing urea, carbonate concentration may be increased in order to facilitate the saturation of CaCO_3 (HENRIQUES, 2011).

The chemical cementation of the soil in the nature is due to the precipitation of the material in the spaces between soil particles and connection of these particles. Microorganisms are often associated with cemented sediments containing calcium, magnesium, iron, manganese and aluminum, which are crystallized as carbonates, silicates, phosphates, sulfides and hydroxides, especially iron hydroxides (DEJONG et al. 2006).

Chemical transformations of metal ions in the soil are mediated by soil microorganisms. Example of sand cementation in nature is the formation of pores in ferrihydrite (ROSS et al. 1989). Iron hydroxides, depending on their crystallization may also be an important cementation agent of soils (DNIKER et al. 2003).

The biological cementation with iron hydroxides can be detected in the roots of all wetland plants, where Fe (II), produced by iron reducing bacteria, reacts with the oxygen released by the roots (Johnson-Green and Crowder 1991; Weiss et al. 2005 cited Thawadi, 2008). To form ferric hydrates, through oxidation and hydrolysis of Fe (II) and Fe (III) iron, must be reduced by the reduction of harmful bacteria. Oxidation of ferrous ions and chelates in soil is chemically performed or catalyzed by neofilicas or acidophilic iron-oxidant bacteria (THAWADI, 2008). Another well-known example of natural cementation is the silicon dioxide precipitation, which fills the pores and glues the soil particles together. It is also known as natural soil calcification due to the deposition of calcium carbonate from above groundwater flow, increased evapotranspiration from the soil, or calcium and calcium carbonate formation in areas of high alkalinity formed by the decomposition of carbonate organic matter (MOZLEY DAVIS, 2005).

The calcium carbonate precipitation rate is an important variable of the process. Compared with the traditional soil reinforcement methods, that have gel times in the order of minutes (KAROL, 2003), microbial processes are usually slow, this is advantageous, since the rate should be low enough to avoid rapid precipitation and subsequent clogging near the entrance of the injection system. However, the conversion rate should not be too low.

Figure 01 shows chemical reactions in the process of soil bio-cementation.

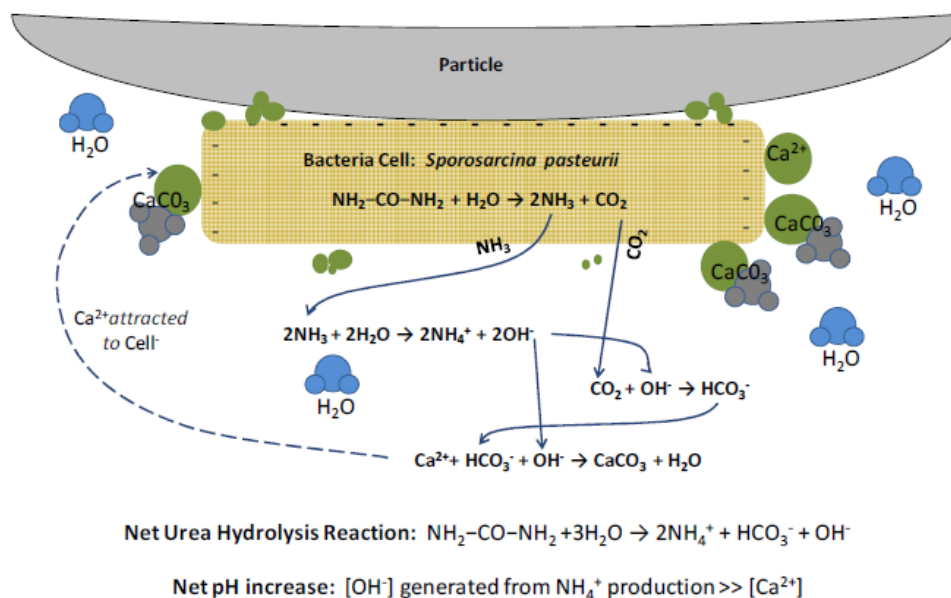


Figure 01. Chemical reactions in bio-cementation (DEJONG et al, 2008).

The calcium ions in the solution fed to the bacteria are free to bind with the carbonate to form a cementation level in each soil particle. This causes the binding within the soil matrix to become more reactive. During the reaction process, the ammonia plays an important role because it helps to increase the pH, causing the bacteria to feed on urea and to precipitate calcite (DEJONG et al, 2008).

2.1.3 Nano-calcium as precipitator agent

The use of nanoparticles in bioengineering practices offers advances in technology in the issue of preserving the environment and quality of life. Nanomaterials are being used in several areas: feeding, medicine, technologies and in the environment.

The performance of cement based materials is heavily dependent on the formation of resistant chemicals such as hydrated calcium particles and also the quality of the interfacial transition zone between the paste and the aggregate particles. Innovations involving nanotechnology and more specifically the nano modifications of Portland cement based materials, promise amplification in these two aspects of cementitious materials. This is the function of nano modification, to manipulate the nanoscale cement composites, in order to enable improved properties. For types of nanoparticles have been investigate in concrete, carbon nanotubes, nano CaCO_3 (calcium carbonate), the nano SiO_2 (silicon dioxide) and nano TiO_2 (dioxide titanium). Importantly, nanoscience is inherently multidisciplinary, and its application includes all the areas of science with strong and multiple interactions between them (chemistry, physics, materials and engineering) (GLEIZE, 2010). Nanotechnology began to be evaluated on this purpose, and has attracted considerable scientific interest in the potential use of new chemical compounds, in the form of particles of extremely small scale (HENCHE, 2013).

Calcium carbonate is a chemical substance with formula of CaCO_3 original from calcareous rocks, and according to the particle size was considered inert, participating in the mixture with the voids filling effect. Dal Molin (2010) points out that when nanoparticles of nano calcium carbonate are introduced in mixtures and mortars, they can further accelerate the hydration rate of the cement compounds. The effect of dispersed nano CaCO_3 provides action on the hydration rate of the compounds and gain of compressive strength, as found by Surendra et al (2012).

3. MATERIALS AND METHODS

3.1 Soil

The sand used in this study comes from a field in the municipality of Osório, Rio Grande do Sul, Brazil. This material is characterized as a thin, clean and uniform particle size sand. According to Girardello (2013), the soil has specific weight of $26.3 \text{ kN} / \text{m}^3$, and a void ratio between 0.6 to 0.9.

The analyzes of grain size and physical indexes were performed by Girardello (2013). Figure 02 shows the grain size distribution of the studied soil.

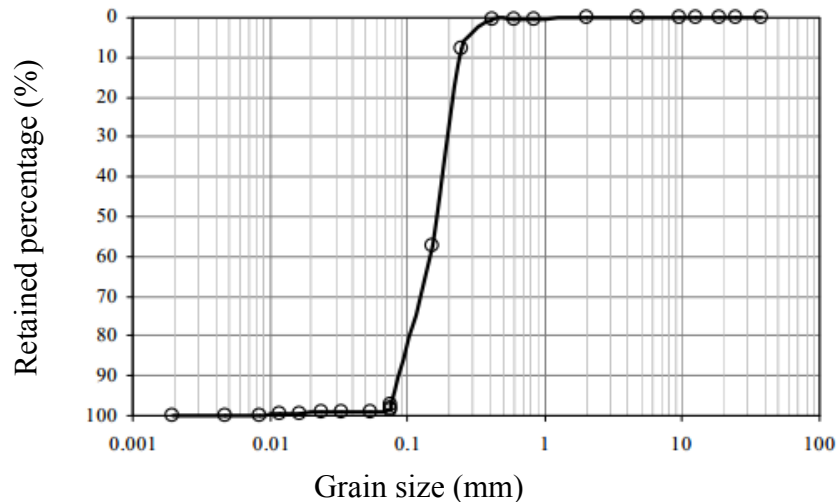


Figure 02. Grain size distribution
Source: Girardello, 2013.

Table 01 shows the physical indexes of the sand used in the experiment.

Table 01. Physical indexes of the sand.

Physical Indexes	Osório Sand
Real specific weight of grains	26.3 kN/m ³
Uniformity coefficient	2.1
Curvature coefficient	1.0
Effective diameter, D10	0.09 mm
Average diameter, D50	0.16 mm
Minimum void ratio	0.60
Maximum void ratio	0.90

Source: GIRARDELLO, 2013.

3.1.1 Sampling

Natural drying of soil was carried out, so that there was no death of microorganisms in the microbiota of soil. After moisture was added through a nutritional environment until corresponding to 10% moisture, and molded at a relative density of 60%.

The samples were molded into cylindrical specimens of 10 cm high and 5 cm in diameter. Figure 03 shows the samples molded for testing.



Figure 03. Samples molded for testing.

3.1.2 Growing environments

3.1.2.1 Preparation of nutritional growth environment A

The environment A was designated as proposed by Lee (2003) and employed by Valencia (2009), Gomez (2009), Valencia (2010) Muneton (2013), where good results were obtained with the inductor of CaCO_3 precipitation. The composition for the preparation of the environment is 15 g of calcium acetate 4 g of yeast extract, 5 g of glucose per 1000 ml of distilled water with a pH of approximately 8.

3.1.2.2 Preparation of growth environment B

The environment B was proposed by Siddik et al. (2013) which has the following composition for preparation: 7 g agar, 3 g of nutrient environment with peptone, 20 g urea, 10 g NH_4Cl , 2.12 g NaHCO_3 in 1000 ml of distilled water.

Figure 04 presents the nutritional environments prepared.



Figure 04. Nutritional environments prepared.

3.2 Measurement of CO₂ Formation

The evolution method of CO₂, respirometry test or C mineralization was performed to determine how much CO₂ is breathed by soil microbiota with the environments A and B. By the determination of breathing rates during an incubation period, one can determine the maximum rate of breath, associated with the existing biomass of that soil. This method consists in capturing CO₂-C, emitted from a soil sample in NaOH solution and by titrating the dosage of HCl.

In each hermetically sealed container was added a sample body (derived from study treatments), a flask with 30 ml of 0.5 mol/L NaOH solution (to capture CO₂-C) and another containing 30 ml H₂O (to keep moisture).

After 24 hours of incubation, the containers were opened and NaOH flasks removed, taking care to leave open each container containing soil for 15 minutes to allow air exchange (this time was uniform for all samples). It was pipetted 10 mL of NaOH solution (previously incubated with the soil) into a 125 ml Erlenmeyer flask, then it was added 10 ml of BaCl₂ solution of 0.05 mol/L and 3 drops of 1% phenolphthalein then titrate- with HCl 0.25 mol/L solution. The turning point is clear passing from violet to colorless. After the time required for air exchange of the soil, another flask with 30 mL of NaOH solution of 0.5 mol/L was added to each system, and then sealed and incubated again. The procedure was repeated for 28 consecutive days.

4. RESULTS

The evolution of CO₂ obtained during the period of 28 days, in Figure 05 evaluates the microbiological activity during bio-cementation process.

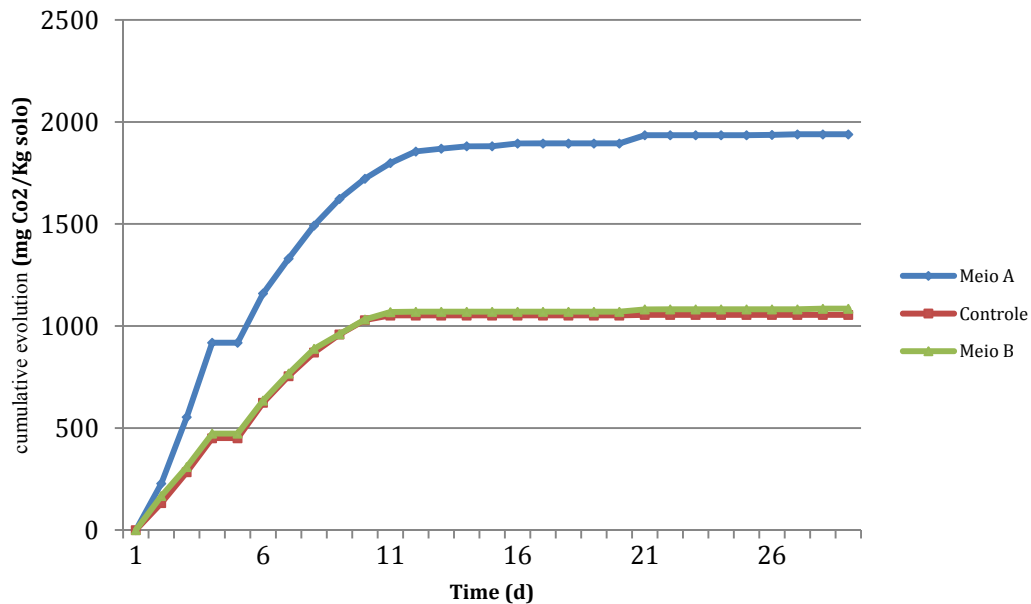


Figure 05. CO₂ Evolution (mg/kg) accumulated during the 28 days, from Bio-cementation technique.

It is observed that the environment A showed a significant increase when compared to other environments and to the control. The control peaked until the tenth day, and then to this day, remained practically constant until the 28 days of trial. The test with environment A proved satisfactory because there was a production of CO₂ until the eleventh day, subsequent to that, there was a constancy of the experiment. The test with the environment B did not show satisfactory results when compared to the control.

The increase in microbial activity evidenced in the test of CO₂ evolution shows that the environment A had a significant increase when compared to other experiments, with accumulated values of 1939.5 mg CO₂ /kg of soil, while the environment B obtained 1084, 5 mg CO₂ /kg and the control 1054.5 mg of CO₂ /kg of soil tested.

As shown in the literature, up to 15 days is when bio-cementation process can occur because it is at this time that bacteria have their exponential growth (Gonzalez, 2009, Li et al, 2011, Li et al, 2013 Muneton, 2013).

5. FINAL CONSIDERATIONS

The respirometry test showed the presence of microorganisms enhancers of bio-cementation process in the soil. The environment A was more efficient than the middle B. Bio-nano-cementation technique has proved to be very interest in the scientific world by reducing environmental impacts with the production of cement, and remediating contaminated areas, as well as improving the mechanical properties of the soil.

Thus, we noted the importance of using new techniques for remediation of contaminated sites and soil improvement. In addition, the bio-nano-cementation technique is interesting in the field of geotechnical engineering, to solve many environmental and geotechnical problems occurred frequently.

REFERENCES

- Dal Molin, D.C.C. Técnicas experimentais para estudo da microestrutura. In: ISAIA, G. C. 2 ed. Materiais de construção civil e princípios de ciencia e engenharia de materiais. V.1 cap. 14, pg 105-438. São Paulo: IBRACON, 2010.
- DeJong, Jason et al [2008]. “Bio-Mediated Soil Improvement,” 1st International Conference on Bio-Geo-Civil Engineering. Delft, The Netherlands.
- DeJong, J.T., Mortensen, B.M., Martinez, B.C., Nelson, D.C. (2010). Bio-mediated soil improvement. *Ecological Engineering*, Vol 36, 197-210.
- DeJong, J.T., Fritzges, M.B., Nusslein, K., 2006. Microbial induced cementation to control sand response to undrained shear. *Journal of Geotechnical and Geoenvironmental Engineering*, ASCE, Vol. 132, No. 11, 1381–1392.
- DeJong, J. D., Soga, K. S., Kavazanjian, E. et al. (2013). Biogeochemical processes and geotechnical applications: progress, opportunities, and challenges. *Geotechnique* 63, No. 4, 287–301.
- Dniker SW, Rhoton FE, Torrent J, Smeck NE, Lal R (2003) Iron (hydr)oxide crystallinity effects on soil aggregation. *Soil Sci Soc Am J* 67:606–611.

- Fujita, Y., Taylor, J.L., Gresham, T.T., Delwiche, M., Colwell, F., McLing, T.L., Petzke, L.M., Smith, R.W. (2008). Stimulation of microbial urea hydrolysis in groundwater to enhance calcite precipitation. *Environ. Sci. Technol.* 42, 3025–3032.
- Girinsky, Olivier. Pre-industrialisation d'un procede de consolidation de sol par biocalcification in situ. These de doctorat in Microbiologie. Universite D'Angers, 2009.
- Gleize, P. J. P. Nantecnologia e Materiais de Construção. Capitulo 53 do livro Materiais de construção civil e principios de ciencia e engenharia de materiais. Ed. G. C Isaia. 2 ed. São Paulo, IBRACON, 2010. 2 v.pg 1719-1745.
- Henche, D. Composto cimenticio de alta resistencia com adição de nanotubos de carbono. Universidade Federal do Paraná. Curitiba, 2013, p. 223. Programa de Posgraduação em Engenharia de Construção Civil.
- Ivanov, V.; Chu, J. Applications of microorganisms to geotechnical engineering for bioclogging and biocementation of soil in situ. *Rev Environ Sci Biotechnol*, 2008.
- Karol, R.H. (2003). *Chemical Grouting and Soil Stabilization*. Marcel Dekker, New York, NY, 558.
- Kucharski ES, Winchester W, Leeming WA, Cord-Ruwisch R, Muir C, Banjup WA, Whiffin VS, Al-Thawadi S, Mutlaq J (2005) Microbial biocementation. Patent Application WO/2006/066326; International Application.
- Montoya, Brina Mortensen. Bio-Mediated Soil Improvement and the Effect of Cementation on the Behavior, Improvement, and Performance of Sand. Dissertation: Civil and Environmental Engineering. University of California, 2012.
- Mozley PS, Davis JM (2005) Internal structure and mode of growth of elongate calcite concretions: evidence for small-scale, microbially induced, chemical heterogeneity in groundwater. *Geol Soc Am Bull* 117:1400–1412.
- Ross CW, Mew G, Childs CW (1989) Deep cementation in late quaternary sands near Westport, New Zealand. *Aust J Soil Res* 27:275–288.
- Surendra, P. S., Shiho, K., Pengkun, H., Corr, D. Application of nanoparticles. 3^o International Symposium on UHPC and Nanotechnology for High Performance Construction Materials- HiperMat Kassel, Alemanha- Março, 2012.
- Thawadi, Salwa. High Strength in-situ biocimentation of soil by calcite precipitating locally isolated ureolytic bacteria. Doctor of Biological sciences and biotechnology. Murdoch University, 2008.
- Whiffin, V.S., van Paassen, L.A., Harkes, M.P. (2007). Microbial carbonate precipitation as a soil improvement technique. *Geomicrobiol. J.* 25 (5), 417–423.
- Yang IC, Li Y, Park JK, Yen TF (1993) Subsurface application of slime—forming bacteria in soil matrices. In: *Proceedings of the 2nd international symposium in situ and on site bioreclamation*, April 1993, San Diego.

Determination of the Index Properties of Clay Soils in the Presence of Nanoparticles

James L. Hanson, M.ASCE, Ph.D., P.E.¹; Nazli Yesiller, A.M.ASCE, Ph.D.²; Amro El Badawy, A.M.ASCE, Ph.D.³; Ryne Mettler, S.M.ASCE⁴; and Jared S. Stine⁴, S.M.ASCE

¹Professor, Dept. of Civil and Environmental Engineering, California Polytechnic State Univ., San Luis Obispo, CA 93407.

²Director, Global Waste Research Institute, California Polytechnic State Univ., San Luis Obispo, CA 93407.

³W.M. Keck Foundation Postdoctoral Fellow, Global Waste Research Institute, California Polytechnic State Univ., San Luis Obispo, CA 93407.

⁴Research Assistant, Dept. of Civil and Environmental Engineering, California Polytechnic State Univ., San Luis Obispo, CA 93407.

Abstract: This investigation was conducted to evaluate index properties of clay soils in presence of nanoparticles, which applies to assessing both risks (containment system integrity and environmental impacts) and benefits (potential use in geotechnical applications). Atterberg limits, swell index, pH, total dissolved solids (TDS), and electrical conductivity of soil-nanoparticle mixtures were determined. Tests were conducted on CL soil, CH soil, and bentonite. Metallic nanoparticles (SiO_2 and Ag) were used in the analysis. Nanoparticles were added to the test soils at mixture ratios ranging from 0.1% to 1.0% (by weight). The results of the test program indicated that the index properties measured generally were affected by presence of nanoparticles. Atterberg limits for soil-nanoparticle mixtures typically were lower compared to data for baseline soils. Swell tests generally were not sensitive to nanoparticle addition. The SiO_2 had relatively high dissolution in DI water as indicated by the measured high TDS and electrical conductivity, whereas the Ag nanoparticles had minimal dissolution. The observed increases in TDS and conductivity in the soil-nanoparticle mixtures likely resulted from pH- and ligand-driven dissolution of the SiO_2 and Ag nanoparticles, respectively. The dissolution processes were time-dependent varying with soil and nanoparticle type.

INTRODUCTION

Engineered nanomaterials (ENMs) exhibit unique physicochemical, optical, catalytic, and antimicrobial properties compared to their bulk counterparts (Petosa et al. 2010, El Badawy et al. 2010). As a result, nanotechnology has been used extensively in recent years to develop breakthrough innovations in a range of industries including electronics, energy, automotive, clean technologies, and consumer products as well as medical applications (Muller and Nowack 2008).

Common nanomaterials in consumer products include silver, titanium, zinc, gold, other heavy metals, carbon, and silicon/silica. Products containing nano size particles (1 to 100 nm, ASTM E2456) have been increasing at a high rate, from tens to over several hundreds in just a few years, with over 1300, 1500, and 1800 consumer products on the market in 2011, 2013, and 2015, respectively as listed by the PEN Consumer Products Inventory (PEN 2015). Discarded consumer products containing nanoparticles are inevitably disposed of in conventional waste containment facilities. Approximately 50% of nanomaterials produced is estimated to be eventually disposed of in landfills based on life cycle analyses (Mueller and Nowack 2008). Most waste streams are expected to contain nanomaterials or nanotechnology products in future (USEPA 2006). USEPA (2006, 2007) indicated the need for reevaluation and revalidation of methods for waste treatment and assessment of current containment technologies for nanowastes. Nanotechnology was identified as an opportunity for proactive waste management aligned with product development (USEPA 2006). Potential risks arise from adverse interactions between wastes containing nanoparticles and the containment systems. Performance and durability of barrier systems against nanomaterials need to be evaluated to ensure long-term safety of containment systems.

In similarity to beneficial applications in numerous industries and the medical field, potential use of nanoparticles has been assessed in geotechnical engineering. Effectiveness of nanoparticle amendments to soils for ground improvement was investigated through laboratory studies. Majeed and Taha (2012) investigated the use of copper nanoparticles, magnesium nanoparticles, and nano clay at ratios ranging from 0.05 to 1% (w/w) for improving the geotechnical properties of soft soil samples. The results of the study indicated that the addition of nanomaterials to the soft soil samples decreased the liquid limit, plastic limit, plasticity index, and linear shrinkage; increased the compressive strength; and increased the compacted dry density and optimum moisture content of the soft soil with increasing effects observed with increasing weight fractions of added nanomaterials. Taha and Taha (2012) reported the use of nano clay, nano alumina, and nano copper to reduce shrinkage and swell strains as well as to decrease the development of desiccation cracks on the surface of compacted soil samples for soils mixed with different ratios of bentonite (0, 5, 10, and 20% w/w). Pham and Nguyen (2014) reported that polyethylene glycol (PEG) coated silica nanoparticles caused inhibition of swelling of montmorillonite clay in the presence of electrolytes. The addition of SiO₂ nanoparticles to cement treated residual soil samples resulted in improvements in compaction, and increased the compressive strength of soil by up to 80% with the addition of 0.4% SiO₂ nanoparticles (Bahmani et al. 2014). As ground improvement applications that incorporate nanomaterials are further developed and implemented, both the effectiveness of the ground improvement and long-term stability of the system need to be considered.

This investigation was conducted to determine the influence of nanomaterials on fine-grained soils to provide baseline assessment of both risks (containment system integrity) and benefits (ground improvement) of soil-nanoparticle interactions. Laboratory tests were conducted to determine index properties and to assess behavior of soils in presence of nanomaterials as well as identify the potential mechanisms associated with interactions between soils and nanoparticles.

EXPERIMENTAL TEST PROGRAM

The laboratory experimental test program included determination of basic index tests on soils alone, nanomaterials alone, and on soil-nanomaterial mixtures to establish baseline behavior and to assess interactions between the test soils and nanomaterials. The testing program included determination of Atterberg limits (LL, PL), swell index, pH, total dissolved solids (TDS), and electrical conductivity. Details of the test materials and test procedures are presented in this section.

Materials

Three soils were tested: low plasticity clay (CL), high plasticity clay (CH), and bentonite. The soils were selected to provide a wide range of behavior for fine-grained soils. The CH and CL soils were natural soils obtained from San Luis Obispo, California. The bentonite was in granular form and was obtained from a GCL manufacturer. Properties of the soils are provided in Table 1. Two commercially available uncoated engineered nanomaterials were used in the test program: silicon dioxide (SiO₂) and silver (Ag). The silica was selected as the ground improvement additive due to its relatively low cost (e.g., in comparison to titanium dioxide and zinc oxide). The silver nanoparticles were selected as the potential waste stream, as they are the most common type of nanomaterial used in consumer products and thus, have high potential for release into the environment. The average particle sizes that were reported by the manufacturer were 20 nm and 20 to 30 nm for SiO₂ and Ag, respectively. When the particle size of SiO₂ approaches the nanoscale, the ratio of O to Si becomes less than 2. The SiO₂ terminology is used herein.

Table 1. Soil Properties

Property	CL	CH	Bentonite
LL	47	58	358
PL	24	24	80
PI	23	34	278
<i>w</i>	4.3	16.3	9.3 ^a
Percent clay fraction (by weight) ^b	30.9	28.1	68.3
Activity	0.74	1.21	4.07
pH	7.54	7.92	9.14
<i>G_s</i>	2.78	2.73	2.75

^aas-received moisture content

^bclay size defined as < 0.005 mm

Test Procedures

Atterberg limits (ASTM D4318) and swell index (ASTM D5890) tests were conducted on soils and soil-nanomaterial mixtures. For mixtures containing SiO₂, the rates of addition were 0.1, 0.2, 0.5, and 1.0% on a dry mass basis. For mixtures containing Ag, the rates of addition were 0.1 and 1.0% on a dry mass basis. Atterberg limits tests were conducted on all three soils and all nanoparticle mixture ratios. Swell

tests were conducted on bentonite and all nanoparticle mixture ratios. Preparation of the soil for all tests included grinding dry soil (oven dried at 105°C) with mortar and pestle to obtain a specimen that passed No.100 sieve. Deionized (DI) water was used in all tests. For Atterberg limits tests, the nanomaterials were added to the soil in aqueous form to assure uniform mixing. First, the soil was prepared to a moisture content higher than the liquid limit and then the nanomaterial was added to the wet soil in the aqueous form. The soil/nanomaterial mixture was allowed to hydrate for 16 hours prior to testing. For swell index tests, two methods of preparation were used: a dry method and a wet method. For the dry method, the nanomaterials were added to the dry soil at the appropriate mass based ratio for the individual mass increments (0.2 g) used in the tests. For the wet method, nanomaterials were added to the soil in aqueous form (similar to the process for Atterberg limits specimen preparation), the soil/nanomaterial mixture was allowed to hydrate for 16 hours, and then the mixture was dried and repulverized prior to conducting the swell index test. This method for adding nanomaterials assured that the nanomaterials had sufficient time for reaction with the clay soils prior to conducting swell tests.

The pH testing procedure (ASTM D4972) included an air dried soil sample passed through a No. 10 sieve mixed with DI water at a liquid to soil ratio that provided sufficient amount of liquid to fully submerge the pH probe. For CL and CH soils, a liquid to soil ratio of 30 mL DI water to 30 g soil was used. Because of the high affinity of bentonite to water, a liquid to soil ratio of 120 mL DI water to 20 g soil was used. This provided sufficient liquid volume for measuring the pH. For the soil/nanomaterial mixtures, a nanomaterial ratio of 1% of the total dry mass of the soil sample was used for a conservative assessment. For the soil/nanomaterial mixtures, the nanoparticles were added to the oven dried soil samples and the mixture was stirred using a small plastic spoon to ensure sufficient distribution of the nanoparticles in the soil matrix before mixing with DI water. After measuring the pH of the samples, a TDS/conductivity meter was used to measure the TDS and electrical conductivity of the samples. To monitor the dissolution of nanomaterials and soils over time, the measurements of the TDS and electrical conductivity were repeated at 1, 2, 4, 8, 16, and 34 days. TDS and electrical conductivity were measured through day 16 for the bentonite-nanomaterial mixtures and the CH soil-Ag mixture. For these cases, the water was completely absorbed by the soil preventing the use of the TDS probe for measurements. Control samples including only DI water and DI water-nanomaterial mixtures also were prepared and tested for pH, TDS, and electrical conductivity for comparison to the test specimens with soil.

RESULTS AND DISCUSSION

The results of the Atterberg limits tests are presented in Table 2. The Atterberg limits were affected by addition of nanomaterials. In all cases tested, the LL, PL, and PI decreased with nanoparticle addition. For the case of 1% SiO₂ addition, decreases in LL were 7, 6, and 19 percentage points for CL, CH, and bentonite, respectively. For the case of 1% Ag addition, the decreases in LL were 4, 4, and 16 percentage points for CL, CH, and bentonite, respectively. The lower values of LL indicate a

tendency for higher hydraulic conductivity (e.g., Benson and Trast 1995); lower compressibility (Holtz et al. 2011); and higher shear strength (Terzaghi et al. 1996).

Table 2. Summary of Results of Atterberg Limits Tests

Soil Type	Addition Rate	SiO ₂			Ag		
		LL	PL	PI	LL	PL	PI
CL	<i>0.0</i>	47	24	23	47	24	23
	0.1	46	22	24			
	0.2	43	22	21			
	0.5	42	21	21			
	1.0	40	20	20	43	22	21
CH	<i>0.0</i>	58	24	34	58	24	34
	0.1	55	22	33			
	0.2	54	22	32			
	0.5	54	22	32			
	1.0	52	20	32	54	22	32
Bentonite	<i>0.0</i>	358	80	278	358	80	278
	0.1	354	79	275			
	0.2	350	77	273			
	0.5	342	75	267			
	1.0	339	73	266	342	75	267

– Not available

Italics font represents baseline soil conditions without nanoparticle addition

Swell index values are reported for 2 methods of sample preparation (dry method and wet method). The values for swell index for bentonite alone (baseline condition) were 25 and 31 for dry and wet preparations, respectively. For the case of SiO₂ addition, the swell values were 25, 24, 24, and 22 for dry preparation and 31, 30, 30, and 28 for wet preparation for mixture ratios of 0.1, 0.2, 0.5, and 1.0%, respectively. For the case of Ag addition, the swell values were 24 and 31 for mixture ratio of 1% for dry and wet preparations, respectively. Swell tests generally were not sensitive to nanoparticle addition and significant differences were not observed between soils with and without nanoparticles. Swell index tests may not provide sufficient resolution to evaluate changes in behavior of bentonite due to addition of nanoparticles.

The pH, total dissolved solids, and electrical conductivity test results (Table 3) were used to assess the dissolution characteristics of the soil, nanomaterials, and the soil-nanomaterial mixtures. The pH of the investigated clay soils was nearly neutral (7.54) for CL soil, slightly alkaline (7.92) for CH soil, and alkaline (9.14) for bentonite (Table 3). At the pH levels of the investigated clay soils, the Ag and SiO₂ nanoparticles as well as the particles of the test soils are expected to have negatively charged surfaces (El Badawy et al. 2010, Tso et al. 2010). These charged surfaces would limit the physical nanoparticle-soil particle interactions due to repulsive forces. The resulting high surface areas of nanomaterials would promote dissolution, if favorable conditions (e.g., pH) existed in the soil/aqueous system. Dissolution of ions from the three test soils was indicated by the significantly higher TDS and electrical conductivity of the soils compared to those of the DI water control (Table 3). The pH of the SiO₂ and Ag nanomaterial controls one hour after addition to deionized water

were 10.7 and 7.04, respectively. The TDS and electrical conductivity data for the nanomaterial tested alone indicated that, compared to the deionized water control, a significant dissolution in deionized water occurred for SiO₂ while Ag exhibited minimal dissolution. These results suggested a pH-dependent dissolution of the nanomaterial controls. SiO₂ nanomaterials were reported to dissolve significantly in aqueous solution at pH \geq 9.5 and were reported to be typically synthesized at pH values between 10.5 and 11.5 for high stability (Rimer et al. 2007). The pH value of 10.7 obtained in this study for the SiO₂ control was in the range of the pH values of highly stabilized silicon oxide nanoparticles and therefore, the SiO₂ nanomaterials were likely stable and conducive to dissolution. The Ag nanomaterials had minimal dissolution at neutral pH as indicated by the low TDS and electrical conductivity. Dissolution of silver nanomaterials is promoted at acidic pH levels as reported by Li and Lenhart (2012).

Table 3. pH, TDS, and Electrical Conductivity 1 Hour after DI Water Addition

Category	Matrix	pH	TDS (mg/L)	Electrical Conductivity (μ S/cm)
DI Water Control	Water	6.22	2.40	5.84
Soil Control	CL	7.54	288	601
	CH	7.92	156	501
	Bentonite	9.14	755	1514
Nanomaterial Control	SiO ₂	10.7	107.40	213.00
	Ag	7.04	2.90	14.44
Soil – Nanomaterial Mixtures	CL-1% SiO ₂	8.96	326	669
	CL-1% Ag	7.64	310	638
	CH-1% SiO ₂	8.96	193	599
	CH-1% Ag	8.7	257	531
	Bentonite-1%SiO ₂	9.46	990	1972
	Bentonite-1%Ag	9.40	911	1822

The addition of SiO₂ nanomaterials increased the pH of the CL-SiO₂ mixture to 8.96 as compared to the pH of 7.54 for CL clay only conditions (Table 3). The TDS and electrical conductivity of the mixture increased as a result of the dissolution of the SiO₂ nanomaterials at the alkaline pH of the CL-SiO₂ mixture. The changes in pH, TDS, and electrical conductivity between CL control and CL-Ag mixture were modest and less than the changes in these parameters with SiO₂ addition. The relatively low increase in TDS and electrical conductivity may indicate a ligand-assisted dissolution of Ag nanomaterials in CL clay or may result from the variability between soil samples without dissolution effects. For the CH soil, the addition of SiO₂ or Ag nanomaterials resulted in an increase in the pH of the mixtures towards more alkaline values than the soil alone conditions (Table 3). The increase in TDS and electrical conductivity of the CH-SiO₂ mixture compared to CH clay only indicated that pH-dependent dissolution of SiO₂ nanomaterials occurred in the mixture. Minimal dissolution was expected for Ag nanoparticles at alkaline pH. However, the TDS and electrical conductivity of the CH-Ag mixture was higher than those of CH

only suggesting a ligand-driven dissolution of Ag nanomaterials. Similar to the CL soil, the differences in TDS and electrical conductivity may have resulted from the variability between soil samples and not indicate dissolution. The pH of bentonite was alkaline (9.14) and the addition of the SiO₂ or Ag to the bentonite resulted in a modest increase (which was lower than the increases for CL and CH soils) in the pH of the mixtures (Table 3). However, the TDS and the electrical conductivity for the bentonite-SiO₂ and the bentonite-Ag mixtures were significantly higher compared to bentonite clay only. These trends also may be explained as pH-dependent dissolution of SiO₂ in the bentonite-SiO₂ mixture and as ligand-driven dissolution of the Ag nanomaterials in the bentonite-Ag mixture. Overall, for all test soils, the neutral to alkaline pH range of the soils was not favorable for the dissolution of Ag nanoparticles to ionic silver where the Ag dissolution likely resulted from a ligand-driven process. The dissolution of SiO₂ nanoparticles on the other hand resulted from alkaline pH conditions in the test soils.

The potential long-term interactions between the fine-grained soils and nanoparticles (for containment or stabilization applications) were assessed by analyzing the variations in TDS and electrical conductivity over time. As the TDS and electrical conductivity data exhibited the same trends, only the electrical conductivity data are presented in the paper (Figures 1 and 2). The SiO₂ control continued to steadily dissolve over time until the conclusion of the experiment, whereas the Ag control exhibited minimal dissolution (Figures 1 and 2). All specimens demonstrated increasing trends of conductivity (and TDS) with time (consistent with presence of dissolution). SiO₂ control, CH-SiO₂ and bentonite specimens (control and mixtures with SiO₂ and Ag) demonstrated trends of increasing conductivity that extended to long durations, whereas the remaining specimens stabilized asymptotically after between 4 and 8 days. Allowing time for dissolution to be completed may be required as a function of soil type and nanoparticle type for soil stabilization applications. For all soil types with SiO₂, the electrical conductivity was higher for the mixtures than for the soil control, suggesting that dissolution of the SiO₂ had occurred (Figure 1). The SiO₂ dissolution generally was higher for the CH clay than the CL clay and bentonite as indicated by the greater difference in conductivity between control soil tests and soil-SiO₂ tests. The Ag nanomaterials exhibited minimal or no dissolution in the investigated soil mixtures over time as indicated by the small differences between control soil tests and soil-Ag tests (Figure 2).

Overall, the relatively high dissolution of the SiO₂ in the tested soil-nanoparticle mixtures indicates high potential for interactions between the soils and the particles. The silicon ions going into solution have high potential for interacting with the clays for stabilization applications. The high valence silicon may replace the lower valence cations in the clays improving strength properties and providing a beneficial solidification application. The relatively low dissolution of the Ag in the tested soil-nanoparticle mixtures indicates low potential for interactions between the soils and the particles. Integrity of a containment system with clay particles may not be highly impacted by the silver nanoparticles. Further determination of the engineering properties of nanomaterial-amended soils would be required to quantify potential benefits and risks. The index testing program described herein permits evaluation of general trends that will impact risks and benefits.

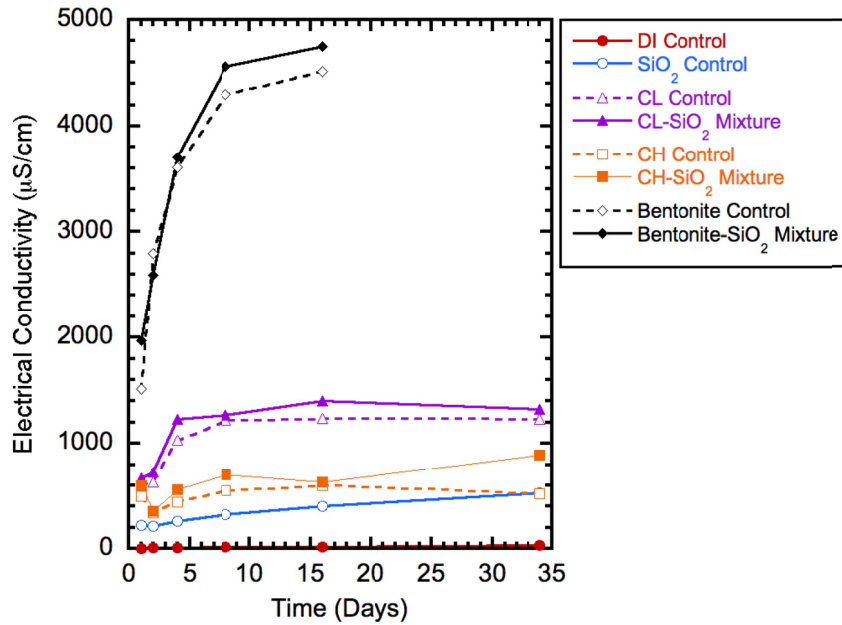


FIG 1. Electrical conductivity versus time for SiO₂ nanoparticles.

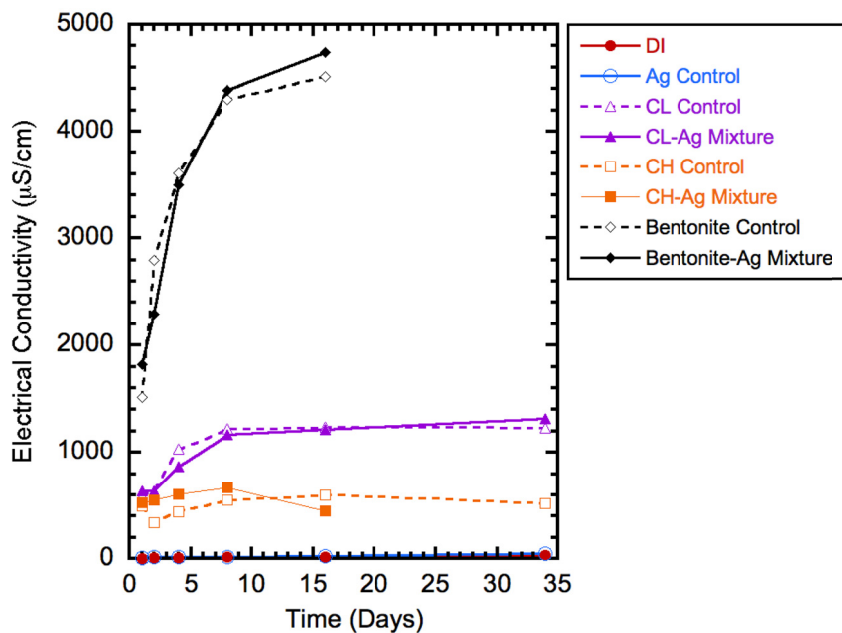


FIG 2. Electrical conductivity versus time for Ag nanoparticles.

CONCLUSIONS

This investigation was conducted to evaluate index properties of clay soils in presence of nanoparticles, for assessing both risks (containment system integrity) and benefits (soil stabilization). The testing program included determination of Atterberg

limits, swell index, pH, TDS, and electrical conductivity. The soils tested were CL, CH, and bentonite. The engineered nanomaterials tested were SiO₂ (stabilization) and Ag (waste stream). Based on the investigation, the following conclusions were drawn:

- 1) For the case of SiO₂ addition, decreases in LL were up to 7, 6, and 19 percentage points for CL, CH, and bentonite, respectively. For the case of Ag addition, the decreases in LL were up to 4, 4, and 16 percentage points for CL, CH, and bentonite, respectively. Higher addition rates caused higher decreases in LL.
- 2) Swell tests on bentonite generally were not sensitive to nanoparticle addition and significant differences were not observed between soils with and without nanoparticles. Swell index values were more sensitive to method of preparation (dry versus wet) as opposed to addition of nanomaterials.
- 3) The soil pH data suggested that minimal pH-driven dissolution occurred for Ag nanoparticles in the test soils, whereas higher pH-driven dissolution of SiO₂ nanoparticles was observed. The increased TDS and electrical conductivity in the soil-nanoparticle mixtures likely resulted from pH-driven and ligand-driven dissolution of the SiO₂ and Ag nanoparticles, respectively.
- 4) Long-term dissolution of SiO₂ suggested that allowing time for dissolution to be completed may be required for soil stabilization applications. In contrast to the SiO₂ nanomaterials, the Ag nanomaterials exhibited minimal or no dissolution in the investigated soil mixtures over time.
- 5) The Atterberg limits, pH, TDS, and electrical conductivity measurements generally demonstrated trends consistent with greater dissolution of SiO₂ than Ag in soil mixtures resulting in interaction with clay microstructure and correspondingly greater influence on soil consistency.
- 6) Application-specific testing of soil-nanoparticle systems is required to assess type and duration of potential interactions.

ACKNOWLEDGMENTS

This study was partly supported by the Global Waste Research Institute. Mr. Mettler was supported by NSF REU Site Grant No. 1263337.

REFERENCES

- ASTM D4318-10E1 (2010). "Standard test methods for liquid limit, plastic limit, and plasticity index of soils." *Annual Book of ASTM Standards*, Vol. 04.08 - Soil and Rock (I): D 420 to D 5779, ASTM International, West Conshohocken, PA.
- ASTM D4972 (2013). "Standard test method for pH of soils." *Annual Book of ASTM Standards*, Vol. 04.08 - Soil and Rock (I): D 420 to D 5779, ASTM International, West Conshohocken, PA.
- ASTM D5890 (2011). "Standard test method for swell index of clay mineral component of geosynthetic clay liners." *Annual Book of ASTM Standards*, Vol. 04.13 - Geosynthetics, ASTM International, West Conshohocken, PA.
- ASTM E2456-06 (2012). "Standard terminology relating to nanotechnology." *Annual Book of ASTM Standards*, Vol. 14.02 - General Test Methods; Forensic Sciences;

- Terminology; Conformity Assessment; Statistical Methods, ASTM International, West Conshohocken, PA.
- Bahmani, S.H., Huat, B.B., Asadi, A., and Farzadina, N. (2014). "Stabilization of residual soil using SiO₂ nanoparticles and cement." *Construction and Building Materials*, Vol. 64: 350-359.
- Benson, C.H. and Trast, J.M. (1995). "Hydraulic conductivity of thirteen compacted clays." *Clays and Clay Minerals*, Vol. 43 (6): 669-681.
- El Badawy, A.M., Luxton, T.P., Silva, R.G., Scheckel, K.G., Suidan, M.T., and Tolaymat, T.M. (2010). "Impact of environmental conditions (pH, ionic strength, and electrolyte type) on the surface charge and aggregation of silver nanoparticles suspensions." *Environmental Science and Technology*, Vol. 44 (4): 1260-1266.
- Holtz, R.D., Kovacs, W.D., and Sheahan, T.C. (2011). *An Introduction to Geotechnical Engineering*, Second Edition. Pearson, Upper Saddle River, NJ.
- Li, X., and John J. Lenhart. (2012). "Aggregation and dissolution of silver nanoparticles in natural surface water." *Environmental Science and Technology*, Vol. 46 (10): 5378-5386.
- Majeed, Z.H., and Taha. M.R. (2012). "Effect of nanomaterial treatment on geotechnical properties of a Penang soft soil." *Journal of Asian Scientific Research*, Vol. 2 (11): 587-592.
- Mueller, N.C., and Nowack, B. (2008). "Exposure modeling of engineered nanoparticles in the environment." *Environmental Science and Technology*, Vol. 42 (12): 4447-4453.
- PEN (2011). The Project on Emerging Nanotechnologies, Woodrow Wilson International Center for Scholars, <http://www.nanotechproject.org/cpi/products/>, last accessed August 29, 2015.
- Petosa, A.R., Jaisi, D.P., Quevedo, I.R., Elimelech, M., and Tufenkji, N. (2010). "Aggregation and deposition of engineered nanomaterials in aquatic environments: role of physicochemical interactions." *Environmental Science and Technology*, Vol. 44 (17): 6532-6549.
- Pham, H., and Nguyen, Q.P. (2014). "Effect of silica nanoparticles on clay swelling and aqueous stability of nanoparticle dispersions." *Journal of Nanoparticle Research*, Vol. 16 (1): 1-11.
- Taha, M.R., and Taha, O. (2012). "Influence of nano-material on the expansive and shrinkage soil behavior." *Journal of Nanoparticle Research*, Vol. 14 (10): 1-13.
- Rimer, J.D., Trofymuk, O., Navrotsky, A., Lobo, R.F., and Vlachos, D.G. (2007). "Kinetic and thermodynamic studies of silica nanoparticle dissolution." *Chemistry of Materials*, Vol. 19 (17), 4189-4197.
- Terzaghi, K., Peck, R.B., and Mesri, G. (1996). *Soil Mechanics in Engineering Practice*, Third Edition. Wiley, New York, NY.
- Tso, C., Zhung, C., Shih, Y., Tseng, Y., Wu, S., and Doong, R. (2010). "Stability of metal oxide nanoparticles in aqueous solutions." *Water Science and Technology*, Vol. 61 (1): 127-133.
- USEPA (2007). "Nanotechnology White Paper," EPA 100/B-07/001, February, 2007, Office of the Science Advisor, Science Policy Council, Washington, DC.
- USEPA (2006). *Nanotechnology and OSWER Symposium: New Opportunities and Challenges*, July 12-13, 2006, Washington, DC.

Enhancement of the Strength and Swelling Characteristics of Expansive Clayey Soil Using Nano-Clay Material

Abdulla A. Sharo¹ and Ahmed S. Alawneh²

¹Ph.D., Assistant Professor, Dept. of Civil Engineering, Jordan Univ. of Science and Technology, P.O. Box 3030, Irbid 22110, Jordan. E-mail: aasharo@just.edu.jo

²Professor, Dept. of Civil Engineering, Jordan Univ. of Science and Technology, P.O. Box 3030, Irbid 22110, Jordan. E-mail: asshslash@just.edu.jo

Abstract: The main goal of this work is to investigate the effect of addition of nano-clay material on the improvement of strength and swelling potential of an expansive clayey soil. The geotechnical properties of a selected expansive clayey soil obtained from Irbid city were determined for soil classification purposes. Free swelling and unconfined compressive strength UCS were conducted on soil samples with different percentages of nano-clay added at about 0.1% to 3.0% by weight and compared to samples free of nano-clay material. The results showed that the addition of nano-clay may increase the strength of expansive soil at low doses, however, swelling potential decreased with the addition of nano-clay.

INTRODUCTION

With the newly increased attention for the nanotechnology applications in geotechnical engineering, soil stabilization becomes a common approach used to enhance soils to accomplish the specifications of different projects (Kolias *et al.*, 2005).

Expansive soil, also known as shrink-swell soil, will show a volume increases if exposed to water during the wet season. This increase in volume will produce uplift pressure under the foundations of the structure resting on such a soil. During the dry seasons, expansive soil will shrink and consequently its volume will decrease. As a result, a severe damage may occur to the structure if this type of soil is not treated to lower its expansive amount. Soil treatment, which includes soil stabilization by additives, is a well know method in this field. As a new practice, the addition of finer particles such as nanomaterials, even at low doses, could improve the expansive soil properties (Taha, 2009).

In a more recent study, (Nikookar *et al.*, 2013) showed that early strength of problematic silt has effectively improved by using nano-clay particles as stabilizing additive.

This paper pronounces a study conducted on an expansive clayey soil to improve its engineering properties by the addition of nanomaterial. The improvement achieved is dependent on the type of nanomaterials. Nano clay, Fig. 1, was used in this study as an additive material. The effect of Nano-Clay on swelling potential and unconfined compressive strength of the studied expansive clayey soil was examined in this work. The results showed that the addition of Nano-Clay particles at a nano scale will significantly reduce the amount of expansion of the shrink-swell soil and also may slightly increase the strength of such a soil. It could be summarized that the Nano-Clay particles in the vicinity of moisture can cause soil stabilization by fastening the particles together.

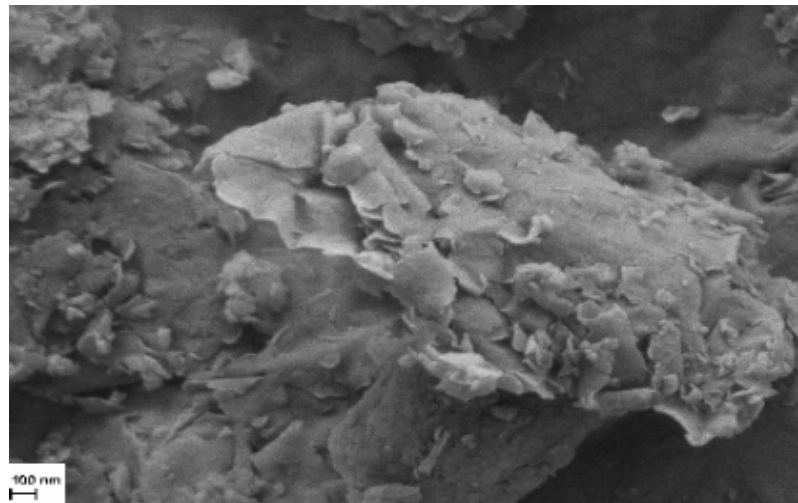


FIG. 1. The Nanomaterial used in this study, Nano Clay.

GEOTECHNICAL PROPERTIES OF THE SELCTED EXPANSIVE SOIL

In this study, the soil tested was obtained from northern region of Jordan and specifically, from the eastern part of Irbid City (Fig. 2). Like most of the populated areas of Jordan, Irbid soil is a very well known to be highly expansive clayey soil with a smectite as a dominant mineral. A disturbed soil samples from the bottom of a 2m borrow bit was collected from the eastern part of Irbid city.

The physical properties were estimated according to American Society for Testing and Materials specifications (ASTM D 7263–09) and (ASTM D 854-02). Based on the results, the solid unit weight of the clay was approximately 17.0 kN/m^3 and the specific gravity of soil solids was in the order of 2.77.

Atterberg limits were estimated according to American Society for Testing and Materials specifications (ASTM D 4318-00). In relation to the results, the clayey soil samples showed a Liquid Limit (LL), Plastic Limit (PL), and Plasticity Index (PI) of about 58%, 25%, and 33% respectively.

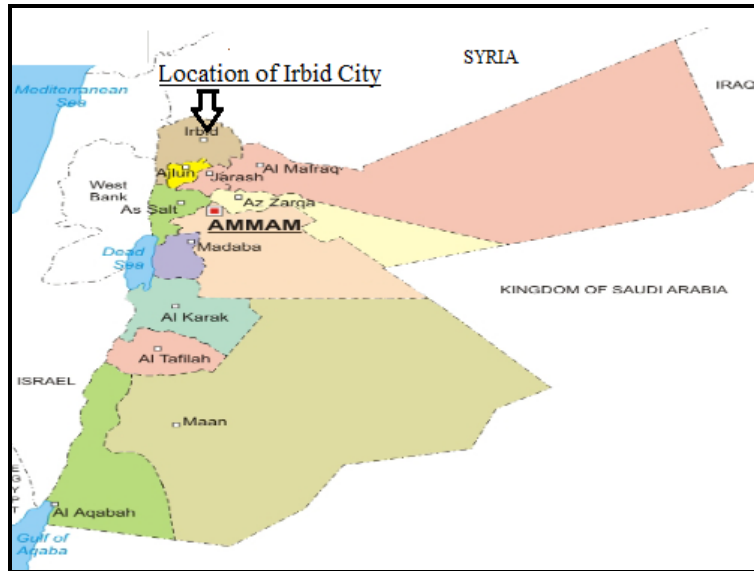


FIG. 2. Jordan map showing the location of Irbid city from which the samples was collected.

Soil sample physical properties findings, including Atterberg limits, are summarized in table 1. In line with the Unified Soil Classification System (USCS), the soil was classified as high plasticity clay (CH).

Table 1. Physical properties of soils

Characteristic	Standard	value
Specific Gravity	ASTM D 854-02	2.77
Unit weight (kN/m ³)	ASTM D7263-09	17.0
Liquid Limit (LL)	ASTM D 4318-00	58%
Plastic Limit (PL)	ASTM D 4318-00	25%
Plasticity Index (PI)	ASTM D 4318-00	33%

THE NANOCCLAY AND METHOD OF ADDTION

The Nanoclay (Fig. 1) was used as an additive material in this study. The specifications for the Nanoclay used are as in Table 2.

Table 2. Properties of Nanoclay

Property	Standard
Appearance (Color)	Light tan to brown
Appearance (form)	Powder
Aspect ratio	300-500
Specific Gravity	2.6

The addition of Nanoclay particles was carried out at different percentages by weight. In order to mix the Nanoclay particles with the expansive soil samples the Nanoclay was first solved in water. The solution, then, was treated under the Sonicator machine for about 15 minutes for dispersion purposes to ensure that all Nanoclay particles are standing as individual particle within the solution. Then after, the solution was mixed with soil samples at different dosages.

EFFECT OF NANO CLAY ON UNCONFINED COMPRESSIVE STRENGTH

The effect of Nanoclay on the strength of the expansive soil was examined by measuring the unconfined compressive strength of soil without and with Nanoclay additive at different percentages (0.1%, 0.4%, 0.6%, 0.7%, 1.0%, 2%, 3%). The UCS test was done according to ASTM (D2166-65). Figure 3, (a) & (b), below shows the effect of different clay percentages on the unconfined compressive strength of expansive soil studied.

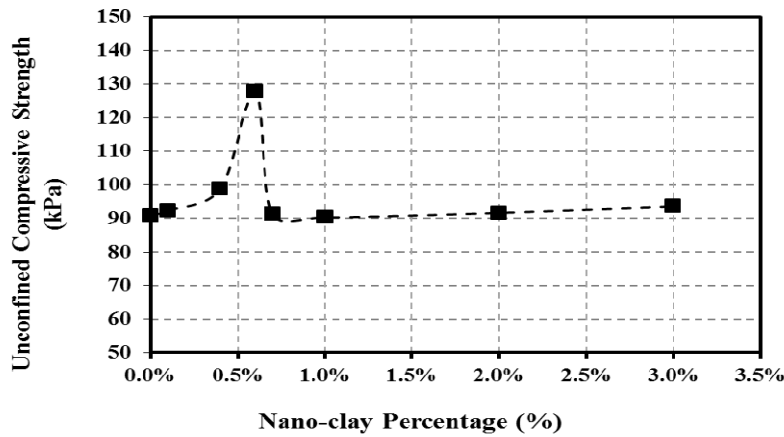


Fig. 3(a)

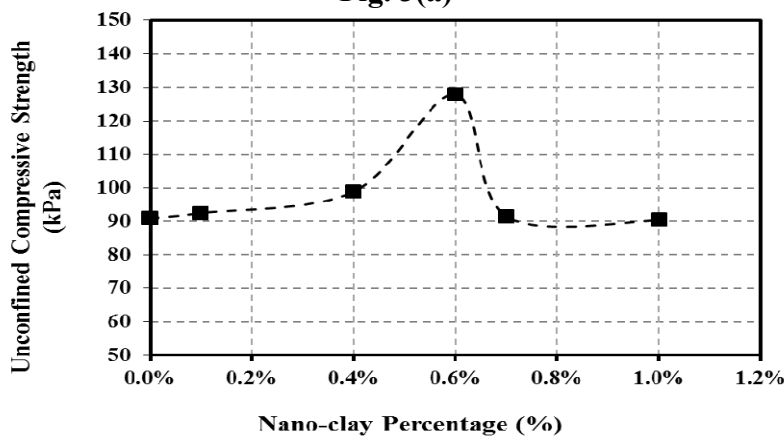


Fig. 3(b)

FIG. 3. Effect of different Nanoclay percentage and unconfined compressive strength (a) Nano-clay percentages between 0.1% to 3.0% (b) Nano-clay percentages effect exemplified around the peak.

From the figure above, it can be illustrated that the addition of a small dosage of Nanoclay particles, up to 0.6%, is associated with about 45% increase in the values of the unconfined compressive strength of soil. This can be explained by saying that the Nanoclay acts as a fastening agent that ties soil particles together. However, at higher dosages, Nanoclay will be surrounded by higher amount water which may prevent, to some extent, the Nanoparticles from functioning as a fastening agent and this could explain the return of the unconfined compressive strength value to about the initial value examined without the addition of Nanoclay.

Also, it can be illustrated from Fig. 3 (a) that a slight increase in UCS strength is allied with higher dosages of Nanoclay which can be attributed to the possible decrease in the intraparticle voids and consequently the increase in soil unit weight.

EFFECT OF NANO CLAY ON SWELLING POTENTIAL

The main theme for this study was to investigate the capability of Nanoclay addition in reducing the swelling potential of expansive soils. The swelling potential was measured as per ASTM (D 4546-14) and was presented as a percentage according to the following equation;

$$\text{Swell percentage} = \Delta H/H\%$$

Where ΔH is the swelling amount (increase in height of the tested soil sample); and H is the original height of soil sample. Figure 4, which illustrates the effect of different Nanoclay percentage with the amount of swell percent, shows that a significant reduction in swelling amount is associated with the addition of Nanoclay. The rate of reduction is decrease with the higher percentages of Nanoclay.

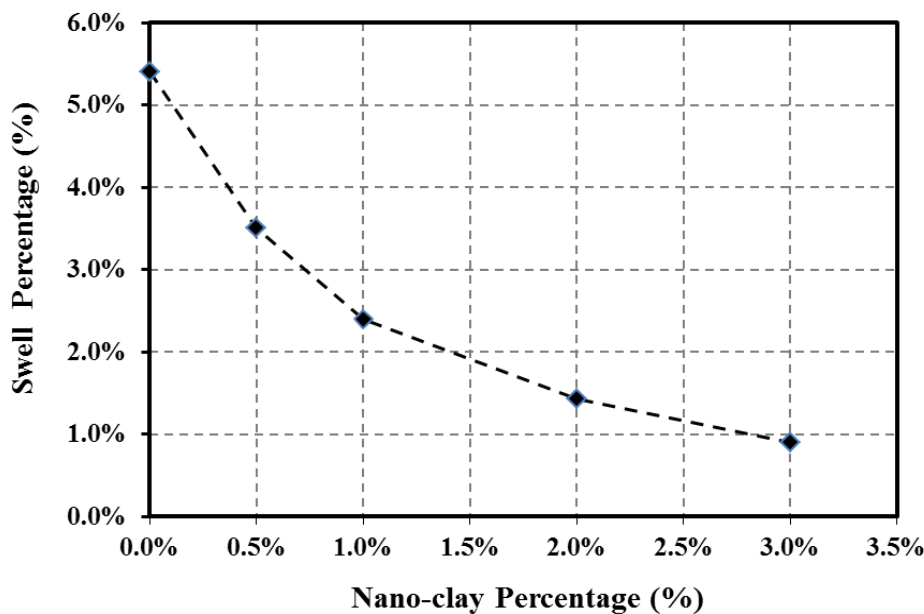


FIG. 4. Effect of different Nanoclay percentage and swell percentage.

A possible explanation for the enhancement of swelling potential is that the Nanoclay particles will lay in the soil intraparticle voids. By addition of water, the Nanoclay particles, which has a high affinity to water by its nature, will adsorb most of the water and prevent it from interacting with the soil particles. Nanoclay particles will expand within the soil intraparticle voids. So that most of the increase in volume due to water addition will be within the intraparticle voids. The rest of water reaches the soil particle causing it to show some expansion.

Also, it should be pointed out that a higher ratio of surface to volume exists at the nanoscale which causes the nano particles to interact very actively with the other soil particles.

CONCLUSIONS

This study was conducted to investigate the possibility of improving expansive clay properties by the addition of nano material. Mainly, the effect of Nanoclay addition to expansive soils on the unconfined compressive strength and on the amount of soil expansion measured as a percentage.

Based on the test results, the following conclusion may be drawn.

- Nanoclay addition at low percentages, i.e., less than about 0.7%, to expansive soil may improve its strength while a higher percentage may affect unconfined compressive strength negatively.
- Nanoclay addition to expansive soil will reduce the swelling potential. The more Nanoclay the less swelling potential.
- The Nanoclay particle addition to soil particles is another factor for the increase in water accumulation capability associated with a lesser volume increase.

Drawn from the results above, authors believe that nanoscale could be considered as a promising area for future research for further improvements in soil strength and other soil properties.

ACKNOWLEDGMENTS

The authors appreciate the assistance of Eng. Bashar Bani-Khaled and Yousef Al-Houidi for their efforts during the lab tests.

REFERENCES

ASTM (American Society for testing and Materials), D7263-09, (1988). Standard Test Methods for Laboratory Determination of Density (Unit Weight) of Soil Specimens, "Annual Book of ASTM Standards, Section 4, Vol. 04.09, Soil and Rock; Building Stones," ASTM, Philadelphia.

ASTM (American Society for testing and Materials), D4318-00, (1988). Standard Test Methods for Liquid Limit, Plasticity Limit, and Plasticity Index of Soils, "Annual Book of ASTM Standards, Section 4, Vol. 04.08, Soil and Rock; Building Stones," ASTM, Philadelphia.

ASTM (American Society for testing and Materials), D854-02, (1988). Standard Test Methods for Specific Gravity of Soils, "Annual Book of ASTM Standards, Section 4, Vol. 04.08, Soil and Rock; Building Stones," ASTM, Philadelphia.

ASTM (American Society for testing and Materials), D4546-14, (2003). Standard Test Methods for One-Dimensional Swell or Collapse of Soils, "Annual Book of ASTM Standards, Section 4, Vol. 04.08, Soil and Rock; Building Stones," ASTM, Philadelphia.

ASTM (American Society for testing and Materials), D2166-65, (2003). Standard Test Method for Unconfined Compressive Strength of Cohesive Soil. "Annual Book of ASTM Standards, Section 4, Vol. 04.08, Soil and Rock; Building Stone," ASTM, Philadelphia Volume 04.08.

Kolias, S., V. Kasselouri-Rigopoulou and A. Karahalios, (2005). "Stabilisation of clayey soils with high calcium fly ash and cement." *Cement Concrete Comp.*, 27(2): 301-313.

Nikookar M., Bahari, M., Nokookar, H., and Arabani, M, (2013). "The Strength Characteristics of Silty Soil Using Nano-Clay." 7th SASTech 2013, Iran, Bandar-Abbas. 7-8 March, 2013.

Taha, M.R., (2009). "Geotechnical Properties of Soil-ball Milled Soil Mixtures." In: Bittnar, Z., P.M. Bartos, J. Nemecek, V. Šmilauer and J. Zeman (Eds.), *Nanotechnology in Construction*. Springer, Berlin, Heidelberg, 3: 377-382.

Influence of Iron Nanoparticle Concentration on the Hydraulic Conductivity of a Residual Clayey Soil

Cleomar Reginatto¹; Iziquier Cecchin¹; Ramiro L. R. Carvalho²; Karla Heineck³; Antonio Thomé⁴; and Krishna R. Reddy⁵

¹Ph.D. Student, Engineering, UFRGS, Porto Alegre RS; ²Undergraduate Student, Environmental Engineering, UPF, Passo Fundo, Brazil; ³Professor UFRGS, Porto Alegre, Brazil; ⁴Professor UPF, Passo Fundo, Brazil; ⁵Professor, UIC, Chicago.

Abstract: The development of new remediation techniques is needed due to the great diversity of contaminated areas. Nanomaterials, especially zero valent nanoiron particles, have been most frequently used because of their higher reactivity, lower toxicity, and lower cost than other metallic nanoparticles. Even though the nanoparticles' size is smaller than soil pores, clogging may happen over time, reducing the permeability of the soil. When residual clay soil is used, the suitable zero valent nanoiron concentration that must be used for remediation is unknown. This concentration can interfere with the permeability of and the reactivity with the contaminant. Thus, the objective of this work was to evaluate the hydraulic conductivity in residual clay soil for different nanoiron concentrations (1 g/L, 4 g/L, 7 g/L, and 10 g/L). Undeformed specimens were molded with a 5-cm diameter and 5-cm height. Percolation tests were performed using a column apparatus while observing the variation in conductivity over time. The results showed that the concentrations of 1 and 4 g/L do not affect the soil conductivity. However, beyond these values, there is a change to the natural values of the conductivity, affecting the process of the migration of zero valent nanoiron in the soil.

INTRODUCTION

Soils and groundwater are contaminated by toxic pollutants from either natural or anthropogenic sources at concentrations capable of posing great risk to human health and the environment. The problems of contaminated soils have raised great concern among environmental agencies due to the existence of a large number of polluted sites, mainly in urban and industrialized areas (Hu et al. 2006; Thome et al. 2015).

Technologies that make use of nanoscale materials for the remediation of contaminated areas have been rapidly developed in recent years, mainly in North America and Europe (USEPA 2014; NANOREM 2013). The studies are being carried out, for the most part, on a bench scale. However, some nanomaterials (NMs) are already being applied on a field scale (Karn et al. 2011; Mueller et al. 2011).

The remediation realized for NMs has the potential to reduce the costs to large areas and through in situ treatment, reduce the time of decontamination, dispense the need for treatment, dispose of contaminated soil, and reduce the concentration of the contaminant to values close to zero (Karn et al. 2011).

Several types of nanoparticles (NPs) are used for environmental remediation, but the nanoscale zerovalent iron particles (zNIP) is more studied and used, mainly because of its characteristics of non-toxicity and ease of obtainment (Zhang et al. 2003; Sun et al., 2006; Klaine et al. 2008). It has also excelled because the small size of the particles and a large surface to volume ratio makes nanoscale iron particles (NIP) more reactive than that of microscale zerovalent iron particles (Reddy, 2010; Reddy et al. 2011).

Zero valent nanoiron is widely used for the decontamination of groundwater, but few studies have been conducted on the reactivity of NIP for soils, as there is a big difference due to the adsorption and immobilization of recalcitrant chemicals by minerals and organic matter.

The particles need to have a high reactivity to remove contaminants, as well as enough mobility in the porous medium and a low toxicity (Crane et al. 2012). The low mobility of NPs is attributed to a high surface energy, leading to the agglomeration of the particles. The particles become denser than water and settle down quickly in solutions, limiting their transport in soils during in situ remediation applications. (Darko-kagya et al. 2010; Thomé et al. 2015).

Considering the necessity of the dispersion of NPs in the soil, favored mobility mechanisms are proposed, including the involvement of these particles with materials that become less reactive, called stabilizers or “coating” (Reddy et al. 2014; Schrick et al. 2002).

For the use of a stabilizer, the preferred method uses compounds that have a negative charge; thus, the reactivity with soil particles (usually negatively charged) is reduced and the agglomeration of the particles decreases due to the repulsion between them, ensuring the dispersion (Petosa et al. 2010).

The concentration of nanoiron particles that is more suitable for use in soil remediation has not yet been identified, as this influences the permeability of the soil and the availability of the reducing agent in the middle. The NPs have a size less than the pores, but over time, retention may occur, causing the formation of aggregates that simulate a filter, reducing the permeability (Saleh et al. 2007).

The objective of this work was to evaluate the hydraulic conductivity of clayey soil through the percolation of different nanoiron concentrations with the presence of a stabilizer in the composition.

METHODOLOGY

Soil and research location

The research was conducted in the Laboratory of Environmental Geotechnics, situated in the Centre of Technology (CETEC) at the University of Passo Fundo, in the city of Passo Fundo, southern Brazil. Un-deformed soil samples of clay soil were molded. These samples were collected at 1.2 m in depth (horizon B) from an open trench in the soil of the experimental field of Geotechnics.

The soil is derived from basaltic rock, and its main physical-chemical and geotechnical characteristics are presented in Table 1.

Table 1. Physical-chemical and geotechnical characteristics of the soil under study

Parameter	Valor
Clay (%)	68
Silt (%)	5
Sand (%)	27
Natural moisture (%)	34
Specific weight (kN/m ³)	16.03
Void ratio	1.24
Degree of Saturation (%)	73.5
Porosity (%)	54
pH	5.4
Organic matter (%)	< 0.8
CTC- (cmole/dm ³)	8.6
Hydraulic conductivity (m/s)	1.39×10^{-5}

The pedological classification is oxisol and the geotechnical classification is a clay with a high plasticity (CH), (Streck et al. 2008).

The soil presents an acidic pH, a high clay content, a low content of organic matter, and a low cationic exchange capacity (CEC), typical of soils with a predominance of the mineral kaolinite (Streck et al. 2008).

Column apparatus

The experiments were carried out in a flexible wall column assembled according to the ASTM D4874 (1995). The column test allowed evaluations of the hydraulic conductivity at different concentrations of a soil component (particles, solutions, contaminants...), as well as an interaction of this component with the environment.

In this test, the specimen is confined by flooding the reservoir where the specimens are placed. The specimens are saturated with deionized water followed by the suspension with a reducing agent. The suspension is forced to percolate in an upstream flow through the body test, allowing for an evaluation of the hydraulic conductivity at the same time.

Figure 1 shows the detail of the specimen in the assembly process and in Figure 2, it is possible to see the column equipment used in the experiment.



FIG. 1. Column apparatus used in tests (sample details)

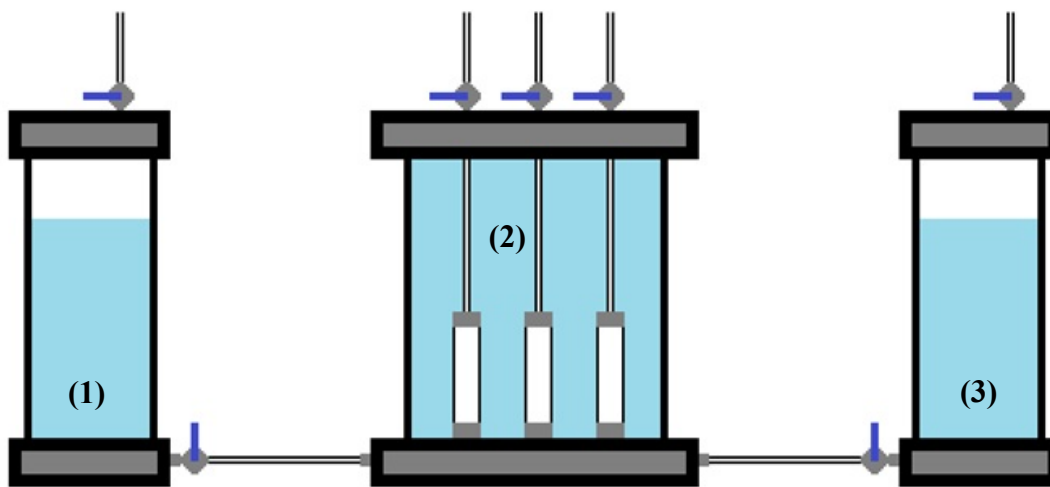


FIG. 2. Column apparatus used in the experiment (general view)

The three columns (1) shown in the right of Figure 2 are filled with a nano iron suspension and it is plugged to the specimens through which receive the suspension. In the image, (2) represents the reservoir in which the specimens are inserted, and (3) is the water column through which the confining pressure is applied.

During the test, the specimens lie wrapped in a membrane that at the same time waterproofs the body and allows the transfer of the confining pressure to the specimens, holding the internal pressure for suspension seepage without body deformation.

Nanoiron

A type of nanoiron has been tested with the presence of a surfactant donated by NANOIRON, an s.r.o company (NANOIRON, 2014), with the commercial name Nanofer 25S. The nanoiron suspension is composed of 14 to 18% iron (Fe), 2 to 6%

magnetite (Fe_3O_4), 0 to 1% carbon (C), 77% water, and 3% of a stabilizer. The average size of nanoiron particles is 50 nm.

Experimental Design

Several tests were performed in different suspension concentrations: 1 g/L, 4 g/L, 7 g/L, and 10 g/L of nanoiron to evaluate the concentration that does not interfere with the soil's natural conductivity. The values used were based on studies already carried out for other soils and waters, testing a range of values that can remediate a contaminated site and that do not interfere with its natural characteristics.

The suspension was percolated through the specimen in an upward flow. The specimen has the dimensions of 5 cm in diameter and 5 cm in height. The confining pressure was 30 kPa, while the internal pressure for the flow was 10 kPa. Due to the specimen height, the hydraulic gradient was 20.

Different samples of the percolated nanoiron suspension were collected at different times during the test. The percolated collection ended after spending 18 void ratio of the specimens.

RESULTS AND DISCUSSION

Figures 3 to 6 show the values of the hydraulic conductivity in a logarithmic range in relation to the time with the concentrations of 1 g/L, 4 g/L, 7 g/L, and 10 g/L, respectively.

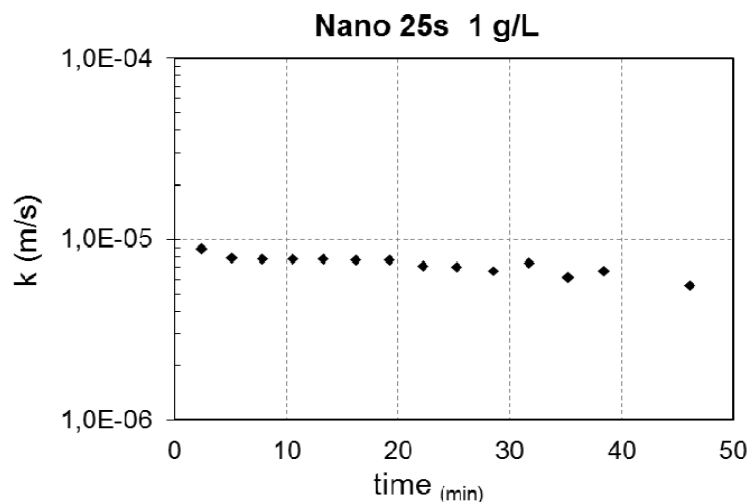


FIG. 3. Hydraulic conductivity with nanoferro 1 g/L

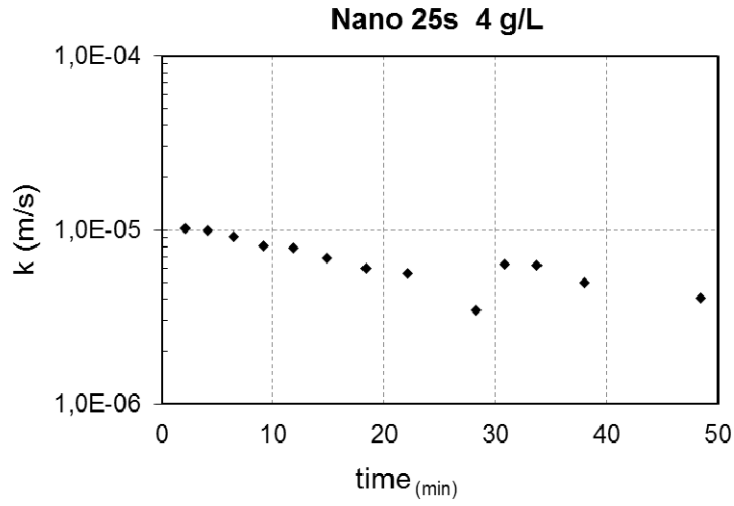


FIG. 4. Hydraulic conductivity with nanoiron 4 g/L

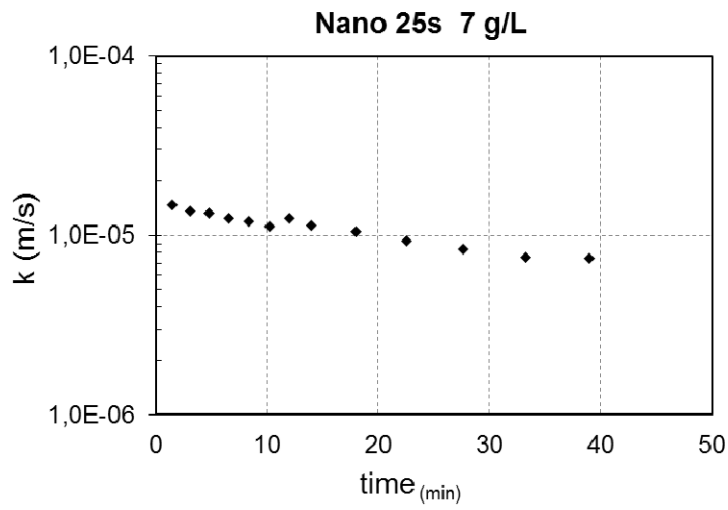


FIG. 5. Hydraulic conductivity with nanoiron 7 g/L

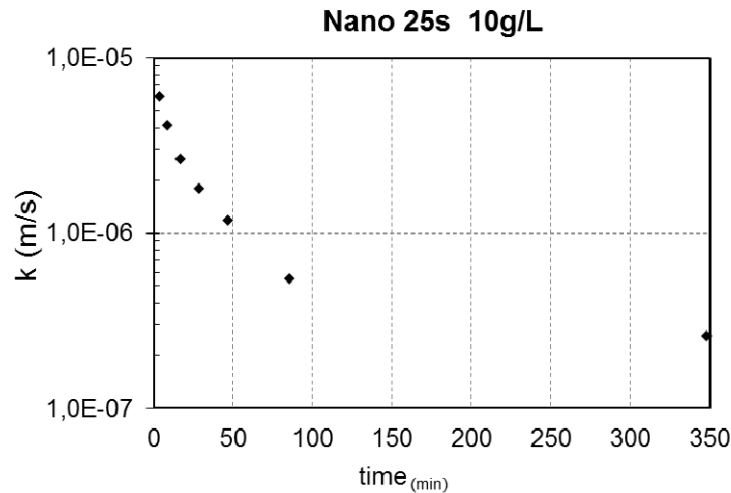


FIG. 6. Hydraulic conductivity with nanoiron 10 g/L

In relation to the results, it can be seen that for the concentrations of 1 g/L and 4 g/L, there was no change in the natural conductivity of the soil, and both were the same order of magnitude, around 1.10^{-6} m/s. For the concentration of 7 g/L, there was a decrease in the conductivity from $1.5E-5$ m/s to $7.4.E-6$ m/s. As well, for the concentration of 10 g/L, in the short test time, a bridging of the soil was already noted, resulting in a sharp fall in conductivity of $6.1E-6$ m/s to $2.5E-7$ m/s in a few void ratio percolated. The concentration of nanoparticles influence on flow properties in the soil. Some phenomena can influence of soil proprieties: Linear reversible attachment: when particle-particle and particle-collector interaction energies are similar, the deposition is not limited nor affected anyhow by the amount of deposited particles; Blocking phenomenon: when particle-particle interaction energies are repulsive, deposited particles exclude the immediate vicinity of the collector surface from further deposition of suspended colloids that approach the soil grain; Ripening phenomenon: when particle-particle interaction energies are attractive, deposited particles tend to attract the suspended ones. A progressive increase of the attachment kinetics is found, that leads to higher and higher concentrations of attached colloids, until the porous medium is completely clogged. (Saleh et al., 2007; Tosco et al. 2014).

In case of blocking, the presence of a layer of attached colloids do not affect significantly the pore flow. On the contrary, in case of ripening, the influence of attached and suspended particles on the fluid and porous medium properties (porosity, conductivity, fluid density, etc.) cannot be neglected, and clogging occurs, leading to a progressive reduction in porosity and permeability. Consequently, flow and transport problems are coupled. (Tosco and Sethi, 2010; Reddy, 2010)

CONCLUSIONS

The results showed that concentrations of up to 4 g/L could be used for in situ remediation for the soil tested, because it did not change the natural conductivity of the soil.

The use of concentrations of 7 g/L and 10 g/L caused reductions in the natural hydraulic conductivity caused by soil filling and the forming of clusters, and this would not be suitable for use in remediation processes.

ACKNOWLEDGMENTS

The authors appreciate the support of the CNPQ, FAPERGS, and CAPES and the research group on Environmental Geotechnics UPF/UFRGS.

REFERENCES

- ASTM: American Society for Testing and Materials –. *D4874: Standard Test Method for leaching solid material in a Column Apparatus*. Philadelphia, 1995.
- Crane, R.A. and Scott, T.B. (2012). “Nanoscale zero-valent iron: Future prospects for an emerging water treatment technology”. *Journal of Hazardous Materials* Vol. 211-212: 112-125.
- Hu, N.; Li, Z.; Huang, P.; Tao, C. (2006). “Distribution and mobility of metals in agricultural soils near a copper smelter in South China”. *Environmental Geochemistry and Health*. Vol. 28: 19-26.
- Karn, B.; Kuiken, T.; Otto, M. (2009). “Nanotechnology and in situ remediation: a review of the benefits and potential risks”. *Environmental Health Perspectives*. Vol. 117(12): 1813-1831.
- Klaine, S.J.; Alvarez, P.J.J.; Batley, G.E.; Fernandes, T. E.; Handy, R.D.; Lyon, D.Y.; Mahendra, S.; Mclaughlin, M.J.; Lead, J.R. (2008). “Nanoparticles in the Environment: Behavior, Fate, Bioavailability, and Effects”. *Environmental Toxicology and Chemistry*. Vol. 27: 1825-1851.
- Mueller, N.C.; Braun, J.; Bruns, J.; Cerník, M.; Rissing, P.; Rickerby, D.; Nowack, B. (2012). “Application of nanoscale zero valent iron (nZVI) for groundwater remediation”. *European Environmental Science and Pollution*. Vol. 19: 550-558.
- NANOIRON s.r.o. (2014). “Nanoiron, Future technology”. Available on <<http://www.nanoiron.cz>>. Accessed in: 25/07/ 2014.
- NANOREM (2013). “Nanotechnological Remediation Processes from Lab Scale to End User Applications for the Restoration of a Clean Environment”. Available on: <<http://www.nanorem.eu/index.aspx>>. Accessed in 31/06/2014.
- Petosa, R.; Jaisi, D.P.; Quevedo, I.R.; Elimelech, M.; Tufenkji, N. (2010). “Aggregation and deposition of engineered nanomaterials in aquatic environments: role of physicochemical interactions”. *Environmental Science Technology*. Vol. 44: 6532-6549.
- Reddy, K.R.; Darko-kagya, K.; Cameselle, C. (2011). “Electrokinetic-enhanced transport of lactate-modified nanoscale iron particles for degradation of dinitrotoluene in clayey soils”. *Separation and Purification Technology*. Vol. 79: 230-237.
- Reddy, K.R.; Darnault, C.; Darko-kagya, K. (2014). “Transport of lactate-modified nanoscale iron particles in porous media”. *Journal of Geotechnical and Geoenvironmental Engineering*. Vol. 140 (2). doi: 10.1061.

- Reddy, K.R. (2010). "Nanotechnology for site remediation: dehalogenation of organic pollutants in soils and groundwater by nanoscale iron particles". In: *Proceedings of the 6th International Congress on Environmental Geotechnics*. New Delhi, India, Vol. 1: 163-180.
- Saleh, N., Sirk, K., Liu, Y., Phenrat, T., Dufour, B., Matyjaszewski, K., Tilton, R.D.; Lowry, G.V. (2007). "Surface modifications enhance nanoiron transport and napl targeting in saturated porous media". *Environmental Engineering Science*, Vol. 24: p.45-57.
- Schrick, B.; Blough, J.L.; Jones A.D.; Mallouk, T.E. (2002): "Hydro dechlorination of trichloroethylene to hydrocarbons using bimetallic nickel-iron nanoparticles". *Chemical Materials*. Vol. 14: 5140-5147.
- Streck, E.V. Rio Grande do Sul soils. 2. ed. Porto Alegre: EMATER/RS, Brazil, 2008.
- Sun, Y.-P.; Li, X.-Q; Cao, J.; Zhang, W.-X.; Wang, H.P. (2006). "Characterization of zerovalent iron nanoparticles". *Advanced Colloid Interface Science*. Vol. 120: 47-56.
- Thomé, A.; Reddy, K.R.; Reginatto, C.; Cecchin, I. (2015). "Review of nanotechnology for Soil and Groundwater Remediation: Brazilian Perspectives". *Water, Air, & Soil Pollution*. Vol. 226: 2-20.
- Tosco, T., Sethi, R., 2010. Transport of non-newtonian suspensions of highly concentrated micro- and nanoscale iron particles in porous media: a modeling approach. *Environ. Sci. Technol.* Vol.44, 9062e9068.
- Tosco, t.; Papini, M. P.; Viggi c. c.; Sethi, R. (2014) Nanoscale zerovalent iron particles for groundwater remediation: a review. *Journal of Cleaner Production*, Vol.77: 10-21.
- USEPA: U.S. Environmental Protection Agency. (2012). "Nanotechnology: Applications for Environmental Remediation". Available on: <http://www.cluin.org/techfocus/default.focus/sec/Nanotechnology:_Applications_for_Environmental_Remediation/cat/Application/#3>. Accessed in 06/12/2014.
- Zhang, W.-X. (2003). "Nanoscale iron particles for environmental remediation: An overview". *Journal of Nanoparticle Research*. Vol. 5: 323-332.
- Zhang, Y., Li, Y.M., Zheng, X.M. (2011). "Removal of atrazine by nanoscale zero valent iron supported on organobentonite". *Science of the Total Environment*. Vol. 409: 625-630.

Potential of Soils Amended with a Nano Calcium Silicate Mixture for Lead Encapsulation in an Aqueous Medium

Syed Abu Sayeed Mohammed¹; P. F. Sanaulla²; Munwar B. Basha³; Hari Prasad Reddy⁴; A. M. Alnuaim⁵; and Arif Ali Baig Moghal, M.ASCE⁶

^{1,2}HKBK College of Engineering, Bangalore 560045, India.

³Dept. of Civil Engineering, IIT Hyderabad, Yeddumailaram 502205, India.

⁴Dept. of Civil Engineering, NIT, Warangal 506004, India.

^{5,6}Dept. of Civil Engineering, College of Engineering, King Saud Univ., Riyadh 11421, Saudi Arabia. E-mail: reach2arif@gmail.com

Abstract

Lead (Pb^{2+}) contamination in soils leads to its leaching and release which in turn, poses significant environmental and health risks. In lieu of this, a number of studies are available for solidification and stabilization as a remediation technique for brown fields typically contaminated with Pb^{2+} . In this study, the performance of two soils in retaining Pb^{2+} has been evaluated. Two tropical soils were selected and amended with nano calcium silicate (potential stabilizing material) in small percentages to enhance the Pb^{2+} fixation. Batch adsorption studies, leaching tests and kinetic studies were conducted. The experimental data was then used to plot adsorption isotherms. Langmuir isotherm was found to be more suitable than Freundlich isotherm for both soil mixtures. Kinetic data was fitted on selected four models viz., pseudo first order, second order, Elovich and intra particle diffusion. Correlation coefficients obtained by all models fitted well with the following ranking: Elovich > Intraparticle diffusion > Pseudo second order > Pseudo first order. Qualitative measurements were also made using SEM and EDS. The leachable heavy metal concentrations were reduced following soil-nano calcium silicate treatment to concentrations lower than the TCLP standard regulatory threshold of $< 5 \text{ mg L}^{-1}$ for Pb^{2+} even after a curing period of more than 90 days. Results suggest that the soil nano-metallic Ca/CaO mixture is suitable for use in immobilization of Pb^{2+} contaminated soil under normal moisture conditions.

INTRODUCTION

Lead contamination in soils is of major concern due to not only its toxicity to humans and animals, but also to its ease of exposure through ingestion or inhalation. Activities such as mining, manufacturing and the use of synthetic products (e.g., pesticides, paints, batteries, and industrial waste) have resulted in many Pb-contaminated sites. Over time, the Pb loading rate in soil exceeds its natural removal rate by more than 20- folds. Soil is generally considered contaminated with Pb when its total Pb concentration exceeds 400 mg/ kg and remediation is required at this level, various remediation technologies have been developed to clean up Pb-contaminated soils. Among those, in situ Pb stabilization using binding agents is a promising approach due to its sustainability and cost effectiveness. Other remediation technologies, including excavation, solidification, and chelation/extraction, are either very costly or only partially effective (Covelo, Vega 2007; Moirou et. al., 2001).

Lead exposure may also cause weakness in fingers, wrists, or ankles. Lead exposure also causes small increases in blood pressure, particularly in middle-aged and older people. Lead exposure may also cause anemia. At high levels of exposure, lead can severely damage the brain and kidneys in adults or children and ultimately cause death. In pregnant women, high levels of exposure to lead may cause miscarriage. High-level exposure in men can damage the organs responsible for sperm production. EPA has determined that lead is a probable human carcinogen.

Hence the properties of soils have to be studied so that a sustainable remediation method can be devised in order to make these contaminated sites safe for human habitation. Most of the naturally available soils can be used as liner materials to retain heavy metals which will entrap the contaminants in their soil matrices and make them immobile. Also to enhance its retention capacity a number of soil amendments are available such as lime, cement, fly ash etc. Mohammed and Moghal (2014).

These amendments have their own advantages and disadvantages. In this study the use of Nano calcium silicate (NCS) in small concentrations is proposed to be used as a soil amendment. Nano-sized particles have large surface areas relative to their volumes and may have enhanced chemical and biological reactivity. They can be manipulated for specific applications to create novel properties not commonly displayed by particles of the same material at macroscale. Behavior of materials at nanoscale is not necessarily predictable from what we know at macroscale. At the nanoscale, often highly desirable, properties are created due to size confinement. Nano calcium silicate (NCS) is a proprietary new material produced by the reaction of silica with calcium ions. NCS comprises of single platelets of 5-10 nm thick and upto 300 nm across. These self assemble into particles of about 1 – 5 μm in size with a 3 dimensional open framework “gypsum desert rose” type structure. The particles have high pore volume and a high readily accesible surface area of upto about $600\text{m}^2\text{g}^{-1}$. The surface of nano size platelets contains both silanol (Si-OH) groups and Ca^{2+} ions which collectively provide bonding sites for the adsorption of and functionalisation of NCS by various cations. The advantage of using NCS is its ability to encapsulate heavy metals in its newly formed aggregates because of aggregation of soil particles and enclosure / binding with Ca- associated immobile salts so as to render it inert and keep it permanently. It is hypothesized that the addition of NCS

would reduce the heavy metal leaching potential from contaminated soil because of its high reduction potential and high surface area. In this study heavy metal lead (Pb^{2+}) and its interaction with NCS amended soil have been considered (Srinivasa et. al., 2012).

MATERIALS AND METHODS

Soils

Two tropical soils were collected directly from their natural locations namely, red earth soil (RS) of Bangalore, India from the campus of Hazrath Kutubuddin Baqtia Kaki College of Engineering (HKBK) ($13^{\circ}02'26.02''$ N and $77^{\circ}37'40.22''$ E) and black cotton soil (BCS) of Belgaum, India from the campus of Visvesvaraya Technological University (VTU) ($15^{\circ}47'7.93''$ N and $74^{\circ}28'12.53''$ E). At both these sites, excavation was carried out for a depth of 2 m. The soil was air dried and sieved through 2mm, sub samples of air dried soil were ground and sieved to obtain aggregates that were less than 0.1mm in order to ensure uniformity of the material. The physicochemical properties of soils were determined the natural pH of soils was found to be 7.5 and 8.3 respectively and the USCS (Unified Soil Classification System) classified both soils as CH (clay with high plasticity) and A-2-7 is the AASHTO classification.

Solutions used

The nitrate salts of Pb^{2+} (Merck Limited, Mumbai, India), of analytical grade type have been used to prepare standard solutions using deionized double distilled water of known concentrations (10, 15, 20, 25, 30, 100, 200 and 1000 mg L^{-1}). Nano calcium silicate (NCS) was synthesized using a proprietary method of the authors and used in three different low concentrations with a range of 0.5 to 2 % by weight of soil and notated as X1, X2 and X3. Pb concentrations were determined using Atomic absorption spectrophotometer (AAS) supplied by PerkinElmer Inc. model Analyst AA400 (Mohammed and Sanaulla 2015).

Batch Sorption Tests

Batch sorption tests were in accordance with ASTM D4646 (2008). This test method is meant to allow for a rapid (24-h) index of a geomeedia's sorption affinity for given chemicals or leachate constituents. Samples with solid to liquid (S/L) ratios of 1:20, 1:30, 1:40, 1:100, 1:200, were taken and shaken for 24 hours. Then, 100 mgL^{-1} of contaminant was added proportionally to all samples and again shaken for 24 hours. The samples were then removed, filtered and the filtered liquid was analyzed for its concentration. For pH dependent tests, similar procedure was employed, where the pH of the contaminant which was first adjusted to the required level and then the adsorbent was added while maintaining a constant S/L ratio of 1:20 throughout the procedure. All pH adjustments were made using 0.1 N HCl and 0.1 N NaOH.

Leaching Tests

A known weighed percentage of heavy metal was mixed as a contaminant with soil or soil mixture with two load ratios of 50 and 100 mg/kg respectively and allowed to dry naturally for 7 and 28 days. This soil mixture was subjected to leaching tests by shaking a small amount of this soil in distilled water maintaining an S/L ratio of 1:20 for about 24 hours and determining the concentration of leached contaminant from water in accordance with ASTM D3987(2012).

Sorption kinetics

The kinetic study of metal ions which is helpful in determining the time necessary to arrive at maximum removal capacity, is of paramount importance. For these studies, batch experiments were carried out for predetermined time intervals in different polyethylene bottles maintained at similar conditions. At the end of each fixed time interval, the soil slurry was filtered and the concentration of metal ions was determined. This procedure was repeated till the concentration of metal ions in the filtrate remained unchanged with time.

RESULTS AND DISCUSSIONS

Soil pH plays a very important role in the sorption of heavy metals. At very low pH, sorption is very low due to the presence of more H^+ ions and these positively charged ions cannot react with positively charged sorbents. However, with the increase in pH, the number of negatively charged sites increase and these act as active sites available for sorption. In order to classify the different processes taking place in course of contaminant sorption, synthetic solution of Pb^{2+} with an initial concentration of 100 mgL^{-1} , were taken and the pH of this solution was made in the order of 4, 6, 8 and 10. At each pH, the solution was filtered and subjected to chemical analysis in order to determine its concentration. It was found that, for Pb^{2+} , the concentration was almost 90% at a pH range of 4 to 6 and it decreased to less than 10% at a pH of 10. This data gives us an idea about the behavior of Pb^{2+} at various pH ranges. Hence, from these tests it was decided to maintain a working pH range of 5 for all the experiments so as to make sure that the system is subjected only to pure sorption and interference from other processes such as precipitation, ion exchange, diffusion is avoided to the maximum Heike (2004). pH plays a major role in sorption and it was observed that, there is a gradual increase in the amount sorbed with the rise in pH. This process can be explained by the changes taking in the sorbate (soils and their oxide surfaces) and the formation of hydroxides of metal complexes due to the variations brought out by pH. The pH of the solution affects the protonation of the functional group on the adsorbent surface of soils as well as metal complexation. To elaborate at low pH values, adsorbed protons that are exchanged on surface can form proton bonds between surface and metal complexes. The sorbed protons, also, generate positive charges at the surface repelling or attracting positively or negatively charged metal complexes respectively.

In order to study the sorptive behavior of soils at different conditions, batch sorption studies were conducted at different initial concentrations (10, 20, 30 and 40 mgL⁻¹ with a S/L ratio of 1:20), dilution ratios (ranging from 1:20 to 1:400 of soil : solution ratio with a concentration of 500 mgL⁻¹) and at varying pH (maintaining an initial concentration of the solution at 100 mg/l and keeping a S/L ratio of 1:20). It can be seen that the amounts of Pb²⁺ retained by the two soils and NCS amended soils, were influenced by initial concentration, dilution ratios (Fig. 1) and pH. For both the soils and soils amended with NCS the amount of metal ions that were sorbed were found to increase almost linearly with increase in the initial concentration, dilution ratios and pH. There was a marginal increase in its sorption capacity for amended soils than pure soils.

The initial concentration of metal provides an important driving force to overcome all mass transfer resistance of metal ion between the aqueous and solid phases. Hence, a higher initial concentration of Pb²⁺ will increase the sorption rate. Also, there is hardly any competition from competing ions resulting in increased sorption efficiency. An increase in soil amount increases the number of active sites that are available for sorption. However, as dilution ratio increases (Fig. 1), more amounts of metal ions become available for sorption. Only stable metal ions get sorbed leading to an effective and permanent sorption. Gharbi (2004) reported that an increase in the solid support weight results in an increase in retention. This is attributed to an increase in the available surface area and thus an increase in active sites. The increase in heavy metal retention with the solid support is not proportional. This can be explained by the decrease in the mass transfer gradient as the remaining concentration of heavy metal diminishes. In the above study it was found that the degree of sorption for black cotton soil (BCS) was more compared to red soil (RS) due to higher cation exchange capacity, specific surface area and alkaline nature of BCS. (Moirou et. al., 2001; Coles and Yong 2006; Kumpiene et. al., 2008; Nemr 2009).

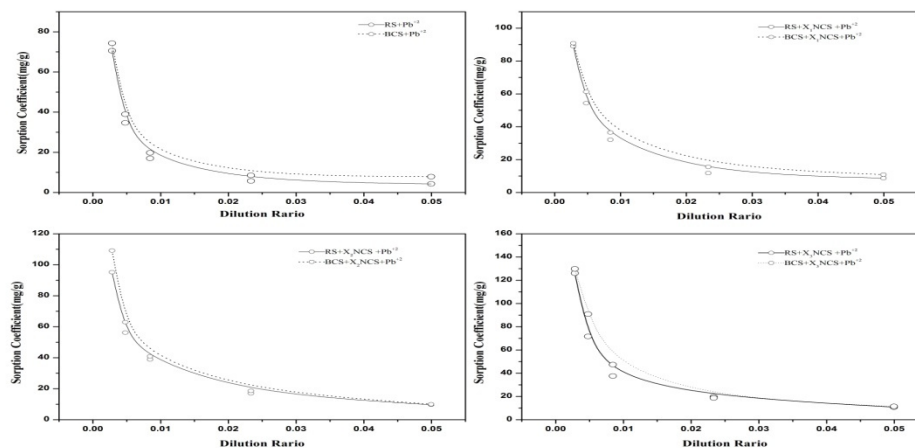


Fig. 1 Sorption at different dilution ratios

Leaching Studies

Batch leaching tests were performed as per ASTM D3987(2012), and readings were taken over different curing periods of 7, 14, 28 and 90 days at two load ratios

(50 and 100 mg/kg). There was a gradual increase in concentration of leached contaminants (Fig. 2). Also, the amount of leaching was more for higher load ratio. It was observed that over a period of time due to presence of many chemically active elements in soil react and produces acidic pH which leaches out already sorbed heavy metal species back into the solution. It was observed that red soil and BCS effectively curtailed the movement of Pb^{2+} in the short term but over a period of 90 days the sorbed Pb^{2+} was leached, where as the addition of NCS in small concentrations to soil drastically reduced the movement of Pb^{2+} onto aqueous medium. This proves the efficacy of NCS as an effective amendment to retain heavy metals in soils over long terms. This may be probably due to encapsulation of Pb^{2+} into the soil NCS matrix which renders it inert. Sawell et. al., (1988).

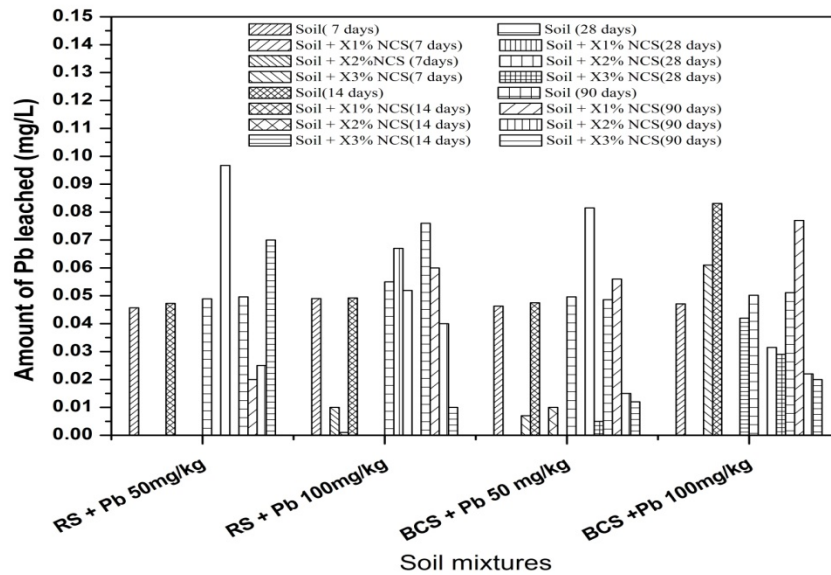


Fig.2 Leaching of Pb^{2+} at different load ratios

Kinetic studies

Time dependent studies give us an idea of sorption behavior of soils with metals at different time intervals, and helps to understand the time required to stabilize an element. Sorption increased linearly and was directly proportional to time and initial concentration. This time dependent experimental data was used to test different kinetic models such as pseudo first order, pseudo second order, Elovich and intraparticle diffusion. The results obtained are enumerated in tables 1 and 2. It was observed from regression analysis that pseudo second order kinetic model was better than first order as its value was closer to one. Also for a heterogeneous material like soil, monolayer sorption does occur in a limited way. Instead, a number of processes are involved such as chemi-sorption, ion exchange and precipitation. Pseudo second order being a better model for this mixture reinforces this idea further, and this is in confirmation with the work of Ho and Mc Kay (1999). Elovich kinetic model tries to deal with the process of desorption and chemisorption. It can be seen from the regression analysis, as given in Table 2, that it is closer to 1 which proves that

chemisorption is also taking place, where the α and β values represent sorption and desorption. Further, sorption is directly proportional to concentration and desorption is inversely proportional to concentration Covelo and Vega (2007).

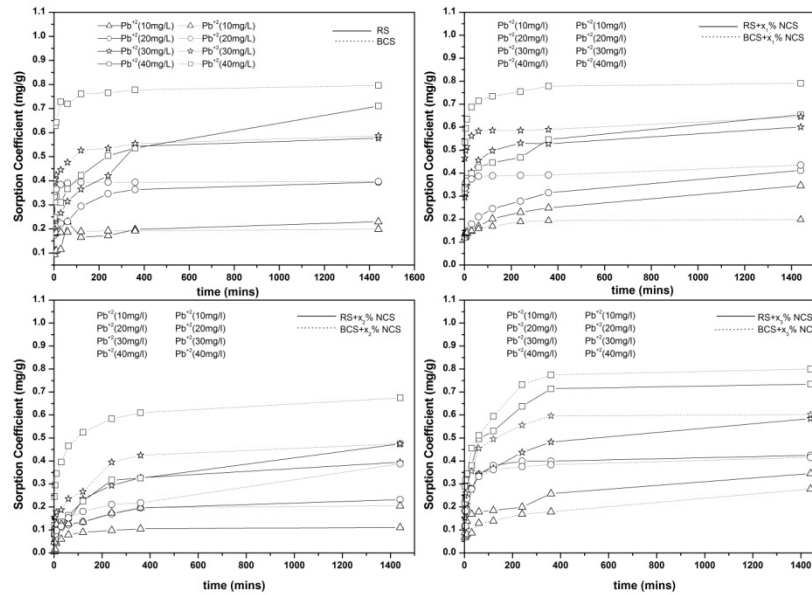


Fig. 3 Time dependent sorption at different concentrations

Table 1 Pseudo first order and second order model parameters

Parameters		Pseudo first order		Pseudo second order	
Sorbent	Initial Conc. (mg/L)	$k_1 \text{ min}^{-1}$	R^2	$k_2(\text{gmg}^{-1}\text{min})$	R^2
RS +Pb	10	0.0164	0.9913	1.31E-08	1.0000
	20	0.0055	0.9886	1.30E+00	1.0000
	30	0.0058	0.9947	0.00E+00	1.0000
	40	0.0024	0.9926	5.78E-08	1.0000
BCS + Pb	10	0.0026	0.9577	1.23E-08	1.0000
	20	0.0182	0.9799	8.86E-10	1.0000
	30	0.0105	0.9287	5.08E-09	1.0000
	40	0.0059	0.9157	2.94E-09	1.0000
RS +X1% NCS +Pb	10	0.0151	0.9726	1.13836e	1.0000
	20	0.0098	0.9685	8.49E-08	1.0000
	30	0.1220	0.9624	1.25E-08	1.0000
	40	0.0117	0.9618	2.97E-10	1.0000
BCS + X1% NCS +Pb	10	0.0049	0.9354	6.34E-09	1.0000
	20	0.0059	0.9539	1.27E-08	1.0000
	30	0.0075	0.9435	2.29E-08	1.0000
	40	0.0024	0.9781	1.46E-10	1.0000
RS + X2% NCS +Pb	10	0.0300	0.9790	9.06E+00	1.0000
	20	0.0038	0.9950	4.34E+00	0.9900
	30	0.0040	0.9889	2.55E+00	0.9990
	40	0.0028	0.9590	6.76E+00	1.0000
BCS + X2% NCS +Pb	10	0.0200	0.9800	8.98E+00	1.0000
	20	0.0290	0.9640	3.38E+00	0.9900
	30	0.0250	0.9687	2.26E+00	0.9990
	40	0.0360	0.9940	1.88E+00	0.9992

Table 2 Elovich and intraparticle diffusion model parameters

Parameters		Elovich			Intra Particle Diffusion		
Sorbent	Initial Conc. mg/L	β gm g^{-1}	α m $g g^{-1} min$	R^2	k_{dif} mg g $^{-1} min^{-0.5}$	C mg/g	R^2
RS	10	5.0E+01	5.3E-01	0.9437	8.4E-03	8.9E-02	0.9535
	20	3.2E+01	5.6E+00	0.9481	5.1E-03	2.0E-01	0.9961
	30	1.5E+01	4.4E-01	0.9700	1.1E-02	2.5E-01	0.8476
	40	1.8E+01	2.4E+00	0.9192	1.1E-02	3.0E-01	0.2973
BCS	10	3.8E+02	1.4E+27	0.9744	4.2E-04	1.8E-01	0.9741
	20	2.4E+02	2.8E+36	0.9854	1.3E-03	3.7E-01	0.8870
	30	1.1E+02	1.3E+24	0.9493	2.6E-03	5.4E-01	0.8559
	40	4.1E+01	3.6E+09	0.9768	4.5E-03	6.7E-01	0.8005
RS + X1%NCS	10	1.0E+03	2.6E-03	0.9732	1.8E-04	1.9E-01	0.9673
	20	7.2E+02	3.8E-03	0.9804	2.3E-04	3.9E-01	0.8783
	30	4.3E+02	6.3E-03	0.9814	3.7E-04	5.9E-01	0.8409
	40	2.7E+02	1.0E-02	0.9703	5.9E-04	7.8E-01	0.8165
BCS + X1%NCS	10	5.5E+02	4.9E-03	0.9684	3.2E-04	1.9E-01	0.9177
	20	3.0E+02	9.2E-03	0.9693	5.3E-04	3.8E-01	0.8568
	30	2.5E+02	1.1E-02	0.9869	6.7E-04	5.7E-01	0.8718
	40	2.1E+02	1.3E-02	0.9801	7.9E-04	7.7E-01	0.8555
RS + X2%NCS	10	5.6E+01	4.8E-02	0.9800	2.7E-03	3.3E-02	0.8150
	20	4.2E+01	6.5E-02	0.9600	4.4E-03	8.4E-02	0.9587
	30	1.9E+01	1.4E-01	0.9810	9.2E-03	9.9E-02	0.9349
	40	1.8E+01	1.5E-01	0.9200	1.1E-02	9.4E-02	0.9595
BCS + X2%NCS	10	5.6E+01	4.8E-02	0.9550	3.1E-03	2.1E-02	0.8742
	20	3.4E+01	8.1E-02	0.9200	6.1E-03	8.9E-02	0.9670
	30	2.6E+01	1.1E-01	0.9100	8.2E-03	1.5E-01	0.9860
	40	1.5E+01	1.8E-01	0.9300	1.3E-02	8.0E-02	0.9600
RS + X3%NCS	10	5.6E+01	4.9E-02	0.9470	2.9E-03	1.2E-01	0.9485
	20	1.9E+01	1.4E-01	0.9804	5.3E-02	8.5E-02	0.9460
	30	1.5E+01	1.8E-01	0.9898	5.3E-02	8.2E-02	0.9460
	40	1.0E+01	2.6E-01	0.9794	2.3E-02	3.6E-02	0.9712
BCS + X3% NCS	10	4.4E+01	6.1E-02	0.9710	2.3E-02	3.6E-02	0.9710
	20	2.6E+01	1.1E-01	0.9700	7.3E-03	2.1E-01	0.9697
	30	2.5E+02	1.1E-02	0.9869	1.2E-02	2.7E-01	0.9569
	40	1.1E+01	2.5E-01	0.9760	1.8E-02	3.2E-01	0.9650

Isotherm data analysis

The adsorption of Pb ions was carried out at different initial concentrations ranging from 10 to 40 mg/l at a pH of 5 at a shaking rate of 30 rpm. Analysis of this data is important and can be used to describe how solute interacts with adsorbent and is critical in optimizing the use of adsorbent. Langmuir and Freundlich are the most widely accepted surface adsorption models for single solute systems. The Langmuir model represents one of the first theoretical treatment of nonlinear sorption and suggests that the uptake occurs on a homogeneous surface by monolayer sorption without interaction between adsorbed molecules. In addition the model assumes uniform energies of adsorption onto the surface and no transmigration of the adsorbate. Estimation of maximum adsorption capacity corresponding to complete monolayer coverage on soil and NCS was calculated (Table 3) explains the high applicability of Langmuir model. The maximum monolayer capacity obtained from Langmuir isotherm was 34.1mg/g for a combination of BCS with X3% NCS. Similarly Freundlich isotherm was validated through the experimental data and it was

found that Freundlich isotherm is less applicable to soil than Langmuir, the correlation coefficients obtained from experimental data fitted well. The adsorption intensity (n) values are lower than 1 indicating that Pb^{2+} is not favourably adsorbed (Nemr 2009).

Table 3 Isotherm parameters for different soil NCS mixtures

Parameters		Langmuir isotherm			Freundlich Isotherm		
Name of the soil	Initial Conc. mg/L	Monolayer Adsorption Capacity (mg/g)	k	R ²	K _f	n adsorption intensity	R ²
RS +Pb	10	4.5320	0.1550	0.9600	0.8400	0.3923	0.9800
	20	3.0808				0.2440	
	30	2.0000				0.1771	
	40	1.3830				0.1390	
BCS + Pb	10	6.8800	0.1330	0.9600	0.5880	0.4292	0.9900
	20	5.2500				0.2732	
	30	3.2370				0.2004	
	40	3.3023				0.1582	
RS +X1% NCS +Pb	10	1.4391	2.3205	0.9350	0.5760	-4.1619	0.9990
	20	1.5391				-7.6469	
	30	1.6988				-10.9151	
	40	1.8016				-14.0500	
BCS+ X1%NCS +Pb	10	19.0840	3.6778	0.9970	0.0105	-40.8080	0.9800
	20	0.9401				-79.0125	
	30	1.0900				-116.2590	
	40	1.0578				-152.9090	
RS +X2% NCS + Pb	10	18.9710	0.1200	0.9300	0.6090	-1.0850	0.9100
	20	16.1020				-1.3733	
	30	10.8400				-1.5763	
	40	8.8500				-1.7384	
BCS+ X2%NCS + Pb	10	5.4050	0.1630	0.8300	1.0400	-0.0469	0.9940
	20	9.0360				-0.0495	
	30	9.2330				-0.0511	
	40	7.1200				-0.0523	
RS +X3% NCS + Pb	10	26.1850	0.1528	0.9658	0.5804	-2.0297	0.9921
	20	17.4788				-3.0169	
	30	11.9459				-3.8040	
	40	4.6194				-4.4842	
BCS+ X3%NCS + Pb	10	33.7289	0.1187	0.9924	0.1070	-9.1820	0.9949
	20	22.6941				-14.0491	
	30	20.6456				-18.0176	
	40	14.1009				-21.4961	

CONCLUSIONS

Nano calcium silicate (NCS) amended with soils is identified as an effective adsorbent to retain Pb^{2+} permanently in soils. The adsorption process is pH dependent and the optimum pH was 5. The kinetic studies proved that the second order kinetic model was applicable. Furthermore isotherm equilibrium studies confirmed that Langmuir model is best fitted for the sorption process of Pb^{2+} . NCS- soil mixtures exhibited high adsorption capacity under several initial and sorbent dose concentrations. The sorption process was found to be controlled by more than one

mechanism such as ion exchange, precipitation, complexation, diffusion and encapsulation. The proposed NCS soil amendment is efficient and can reduce the huge amount of toxic Pb^{2+} from soils leaching into our ground water.

ACKNOWLEDGMENT

This paper is part of a research project supported by Science and Engineering Research Board (SERB), Department of Science and Technology (DST), Govt. of India, Project No. SR/S3/MERC/0111/2012. The authors would also like to thank Mr. Kotresha K, Junior Research Fellow (JRF) for his assistance in conducting the experiments.

REFERENCES

- American Standard Testing Methods (ASTM). (2008). "Standard Test Method for 24-h Batch-Type Measurement of Contaminant Sorption by Soils and Sediments." *D4646*. West Conshohocken, PA.
- American Standard Testing Methods (ASTM). (2012). "Standard Practice for Shake Extraction of Solid Waste with Water." *D3987*. West Conshohocken, PA.
- Coles, C. Yong, R. (2006). "Use of equilibrium and initial metal concentrations in determining Freundlich isotherms for soils and sediments." *J. Engg, Geo*, 85:19-25.
- Covelo, E. (2007). "Heavy metal sorption and desorption capacity of soils containing endogenous contaminants". *J. Hazardous. Mat.*, 143(1-2): 419-430.
- Heike, B. (2004). "Adsorption of Heavy metal ions on soils and soils constituents." *J. Colloid and Interface Sci.*, 277: 1 -18.
- Ho, Y. Mc Kay, G. (1999). "Pseudo – second order model for sorption processes". *J. Process Biochem*, 34: 451 – 465.
- Kumpiene, J. Lagerkvist, A. Maurice, C. (2008). "Stabilization of As, Cr, Cu, Pb and Zn in soil using amendments": a review. *J. Waste Manag*, 28 (1):215 – 225.
- Mohammed, S. A. S. and Sanulla,P.F.(2015)."Nano calcium silicate A – soil based mineral amendment as liners for hazardous waste containment facilities." *Indian Patent CBR No. 10983, PCT No. 2765/CHE/2015*.
- Mohammed, S. Moghal, A. (2014). "Soils Amended with Admixtures as Stabilizing Agent to Retain Heavy Metals." *ASCE Geotechnical Special Publication No. 234*: 2216-2226.
- Moirou, A. Xenidis, A. Paspaliaris, I. (2001). "Stabilization Pb, Zn, and Cd-Contaminated Soil By Means of Natural Zeolite". *J. Soil. and Sed. Cont*, 10(3): 251-267.
- Nemr, A. (2009). "Potential of pomegranate husk carbon for Cr (VI) removal from wastewater: Kinetic and Isotherm studies." *J. Hazardous, Mat*, 161: 132- 141.
- Sawell, S. Bridle, T. and Constable, T. (1988). "Heavy metal leachability from solid waste incinerator ashes." *J. Waste Manag & Res.*, Vol. 6(3): 227-238.
- Srinivasa, R. Yoshiharu, M. Tetsuji,O.(2012). "Enhanced heavy metal immobilization in soil by grinding with addition of nanometallic Ca/CaO dispersion mixture." *J. Chemosphere*, Vol. 89: 717-723.

Prediction of the Stripping Resistance of Nanoclay-Modified Asphalts Using Their Surface Chemistries

Zahid Hossain, Ph.D., M.ASCE¹; Biswajit Bairgi, M.Sc., S.M.ASCE²; Musharraf Zaman, Ph.D., F.ASCE³; and Rifat Bulut, Ph.D., F.ASCE⁴

¹Assistant Professor, Dept. of Civil Engineering, Arkansas State Univ., P.O. Box 1740, LSW#239, State University, Arkansas 72467 (corresponding author). E-mail: mhossain@astate.edu

²Former Graduate Research Assistant, Arkansas State Univ., P.O. Box 1740, State University, AR 72467. E-mail: biswajit.bairgi@smail.astate.edu

³David Ross Boyd Professor and Aaron Alexander Professor of Civil Engineering, 202 W. Boyd ST, #334, Univ. of Oklahoma, Norman, OK 73019. E-mail: zaman@ou.edu

⁴Associate Professor of Civil Engineering, Oklahoma State Univ., 207 Engineering South, Stillwater, OK 74078. E-mail: rifat.bulut@okstate.edu

Abstract: Polymers are often used to modify base asphalt binders to withstand heavy traffic loads and extreme weather conditions. However, polymer-modified asphalts are about 75% more expensive than the base binders. On the other hand, nanoclays are naturally abundant, environmentally friendly, and very inexpensive. Nanoclays can potentially be an alternative of highly expensive polymers to modify asphalt binders. To this end, this study evaluated moisture resistance (stripping) of nanoclays-modified binders through the surface free energy (SFE) technique. A commonly used performance grade (PG 64-22) binder modified with different dosages of four types of commercial nanoclays was evaluated in the laboratory. The adhesive energies, an indicator of bond strength, of nanoclay-modified binders and five different aggregates were also evaluated. It was observed that the work of cohesion increased when the asphalt binder was modified with nanoclays. A small amount (about 4%) nanoclays seemed to be effective in maintaining good wetting ability with different aggregates. Also, smaller nanoclays were found to be more compatible than relatively larger nanoclays.

INTRODUCTION

About 96% of 2.4 million miles paved roadways in the U.S. are paved with asphalt mixes, and 85% of the asphalt binders are produced for paving applications (Bahia, 1996). Nationwide, the annual construction and maintenance cost of asphalt pavements is over \$5 billion (Anderson *et al.* 2015). Though, asphalt binder make up 4-8% (by weight) of total pavement mixtures, it provides structural bonding strength, load bearing capacity, absorbance, resilience etc. to an asphalt concrete (AC)

pavement (FHWA, 2015). However, the AC pavements are prone to various types of damages. Among various pavement damages, moisture induced damages are the most common types of pavement damages in asphalt pavement. Moisture induced damage or stripping is basically a progressive deterioration of asphalt mixes through loss of cohesion of asphalt binder and loss of adhesion at binder-aggregate interface due to presence of water (Lu and Harvey, 2005). The mechanism of moisture damage is encompassed by a series of factors such as materials properties, mix composition, drainage condition, and environmental characteristics. Due to existing air-void system in asphalt mixes, no pavement is impermeable to moisture (Huang *et al.* 2001). An asphalt mix is typically designed at 4% air voids in laboratories. However, it varies from 6% to 12% in the field condition, which is referred as a pessimum range. Moisture can ingress into an asphalt mix in the pessimum range but cannot escape freely, thereby getting trapped into the asphalt mix. The trapped moisture in the asphalt mix causes loss of cohesion, loss of adhesion, development of pore pressure, hydraulic scouring, etc. and results in moisture damages such as stripping, cracking, rutting, raveling, bleeding, and shoving (Lu and Harvey, 2005). Various transportation agencies use several commonly used additives such as lime, liquid anti-stripping agents to demonstrate their potential in eliminating moisture damage problem (Al-qadi *et al.* 2014). Even though the maintenance and reconstruction work of moisture damaged pavement costs billions of dollars annually, no highway agencies addressed a specific procedure of moisture susceptibility evaluation in their design manual and specifications (Hicks *et al.* 2003). About 10% of highway agencies do not consider the moisture damages in their pavement design and specifications at all (Lu and Harvey, 2005).

In recent years, polymer-layered silicate nanocomposites, also known as organoclays or nanoclays (NCs), has drawn interest in asphalt technology due to their enhanced physical and mechanical properties such as quantum effects, structural features, high surface work, large fraction of surface atoms, and spatial confinement (Yao *et al.* 2012). Previous studies (e.g., Uddin, 2008; Jahromi *et al.* 2009) showed that NCs consist of various layered silicate minerals with a 2:1 ratio of the tetrahedron to octahedron, which is commonly referred as montmorillonite (MMT), as shown in Figure 1. The tetrahedron and octahedron layers unite into a single layer through interlayer cations and van der Waals forces (Uddin, 2008).

The various types of NCs (i.e. Cloisite[®]) have high potentials to be used as a micro-scale filler reinforcement of asphalt binder and produce modified binder with improved mechanistic properties i.e. stiffness, indirect tensile strength, fatigue resistance, shear modulus, compressive strength, and softening point (Ghile, 2015; Yao *et al.* 2015). You *et al.* (2010) illustrated that asphalt binder, when modified with NCs, exhibited improved low-temperature cracking resistance. Another study (Liu *et al.* 2012) revealed that the NC improved the durability and reduced the volatilization of oily components of asphalt binders. Yazdani and Pourjafar (2012) showed that a small amount of NC addition resulted in a significant amount of binder properties compared to commonly used polymer modifiers i.e. SBS, polypropylenes, etc. However, these limited researches on NC-modified binders are not adequate to justify

the NCs in an implementable stage (Ghile, 2015). Particularly, there is a lack of research findings on moisture susceptibility of NC-modified asphalt binder.

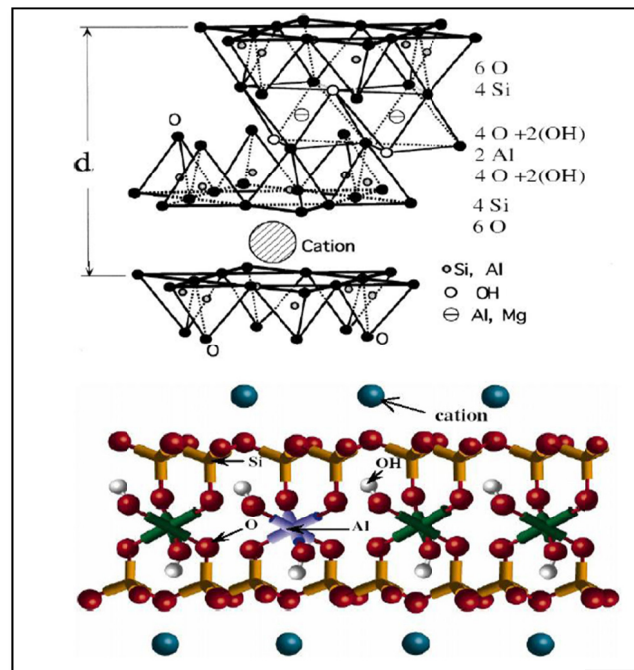


FIG. 1: Molecular structure of montmorillonite (Jahromiet *al.* 2009).

The objective of this study is to evaluate the moisture damage resistance of NC-modified asphalt binders through the Sessile Drop (SD) method. Detail objectives of this study are to: (i) determine the contact angle of various probe liquids on NC-modified binders; (ii) estimate the corresponding surface free energy components, total SFE, and work of cohesion; (iii) determine work of adhesion in the presence of water and absence of water; and (iv) estimate the compatibility strengths of different binder-aggregate systems.

THEORY OF SFE AND COMPATIBILITY ANALYSIS

A molecule of a liquid, inside the liquid body, never subjects to any force as it is effected by equal attraction force from all direction. However, the molecule, located on the surface of liquid, subjects to an inward attraction force due to absence of neighbor molecules in the direction of air. This phenomenon yields an unbalanced energy named as surface free energy (SFE) (Fini *et al.* 2011). The SFE of a material has three components: a mono-polar acidic component (Γ^+), a mono-polar basic component (Γ^-), and an apolar Lifshitz-van der Waals (Γ^{LW}) component (Cheng *et al.* 2001). While expressing the total SFE (Γ^{total}) (Eq. 1), Γ^+ and Γ^- are combined into a single term called the acid-base component (Γ^{AB}), and total SFE is the summation of Γ^{AB} and Γ^{LW} (Eq. 2). The Γ^{total} is also related with the work of cohesion or cohesive energy (W_C) of a material as shown in Eq. 3. Thus, the work of adhesion (ΔG_{ad}) between a liquid (L) and a solid (S) is the summation of its Lifshitz-van der Waals

(ΔG_{ad}^{LW}) and acid-base (ΔG_{ad}^{AB}) components (Eq. 4). The expressions of ΔG_{ad}^{LW} and ΔG_{ad}^{AB} are shown in Equations 5 and 6, respectively. Again, ΔG_{ad} between a liquid and a solid is related with Γ^{total} of the liquid and the contact angle (θ) of the liquid over the solid surface (Eq. 7). The ΔG_{ad} is also termed as adhesive energy in the absence of water or under the dry condition termed as ΔG_{dry}^{ad} . The adhesive energy in the presence of water or under the wet condition (ΔG_{wet}^{ad}) can be expressed as shown in Equation 8. In Eq. 8, parameters A, B, and W denote aggregates, binder, and water, respectively. The ratio of ΔG_{dry}^{ad} and ΔG_{wet}^{ad} is referred as the compatibility ratio (CR) as shown in Eq. 9, which quantifies the moisture resistance of an asphalt-aggregate system (Bhasin *et al.* 2006).

$$\Gamma^{AB} = 2\sqrt{\Gamma^+\Gamma^-} \quad (1)$$

$$\Gamma^{total} = \Gamma^{LW} + \Gamma^{AB} \quad (2)$$

$$W_c = 2\Gamma^{total} \quad (3)$$

$$\Delta G_{ad} = \Delta G_{ad}^{LW} + \Delta G_{ad}^{AB} \quad (4)$$

$$\Delta G_{ad}^{AB} = -2\left(\sqrt{\Gamma_L^+\Gamma_S^-} + \sqrt{\Gamma_L^-\Gamma_S^+}\right) \quad (5)$$

$$\Delta G_{ad}^{LW} = -2\sqrt{\Gamma_L^{LW}\Gamma_S^{LW}} \quad (6)$$

$$G_{dry}^{ad} = \Gamma_L^{total}(1 + \cos \theta) = 2\left(\sqrt{\Gamma_L^{LW}\Gamma_S^{LW}} + \sqrt{\Gamma_L^+\Gamma_S^-} + \sqrt{\Gamma_L^-\Gamma_S^+}\right) \quad (7)$$

$$\Delta G_{wet}^{ad} = \left\{2\Gamma_W^{LW} + 2\sqrt{\Gamma_B^{LW}\Gamma_A^{LW}} - 2\sqrt{\Gamma_B^{LW}\Gamma_W^{LW}} - 2\sqrt{\Gamma_A^{LW}\Gamma_W^{LW}} + 4\sqrt{\Gamma_W^+\Gamma_W^-} + 2\sqrt{\Gamma_B^+\Gamma_A^-} - 2\sqrt{\Gamma_B^-\Gamma_A^+} + 2\sqrt{\Gamma_B^+\Gamma_W^-} - 2\sqrt{\Gamma_B^-\Gamma_W^+} - 2\sqrt{\Gamma_A^+\Gamma_W^-}\right\} \quad (8)$$

$$CR = \frac{\Delta G_{dry}^{ad}}{\Delta G_{wet}^{ad}} \quad (9)$$

MATERIALS AND METHODOLOGIES

This study used a commonly used performance graded (PG) asphalt binder (PG 64-22) from a local refinery located in Memphis, TN and four different types of commercial NCs namely: Cloisite[®] 15 (C-15), Cloisite[®] 20 (C-20), Cloisite[®] Na⁺ (C-Na), Cloisite[®] Ca⁺⁺ (C-Ca). These NCs are nonhazardous, odorless, off white colored and natural MMT typed nanocomposites (ALTANA, 2015). For binder-aggregate compatibility analysis, this study used SFE data (Koc and Bulut, 2014) of five

different aggregates, namely, Davis Limestone (DL), Snyder granite (SG), Dolese Cooperation limestone (DCL), Hanson-Davis rhyolite (HDR), and Martin-Marietta-Mill-Creek granite (MMMCG), all from different quarries in Oklahoma.

A laboratory mixing protocol of NCs-modified asphalt binder has been employed in this study by following through the past experience of the research team of the current study (e.g., Hossain *et al.* 2013). Three different contents (2%, 4%, and 6%) of NC have been blended with the PG 64-22 binder. Firstly, about 150 gm of liquid asphalt binder heated in a container at 160°C for 2 hours, as followed in previous studies by the research team (Hossain *et al.* 2013). Three different percentages (2%, 4%, and 6%) of NC samples were added into the hot asphalt binder. The mixture was stirred with a stainless steel stirrer for 1 minute and it was then put into the oven at 160°C for 10 minutes. The interior wall of the sample container was scrapped after a regular interval in order to prevent the sticking of NC particles to the wall. The heating and stirring cycle was continued for 1 hour and the resulted blend is allowed to stay about 30 minutes to make sure the chemical reactions are completed.

Among multiple SFE techniques, this study utilized the Sessile Drop method for evaluating SFE for both binders and aggregates. In the SD method, an optical contact angle (OCA) device (Figure 2a) is use for measuring contact angles of different probe liquids on binder substrate. The contact angle is determined through analysis of the video images by the OCA software. Based on probe liquid selection criteria found in Little and Bhasin (2006), this study selected water, ethylene glycol, diiodomethane, and formamide for OCA tests of binders and aggregates.

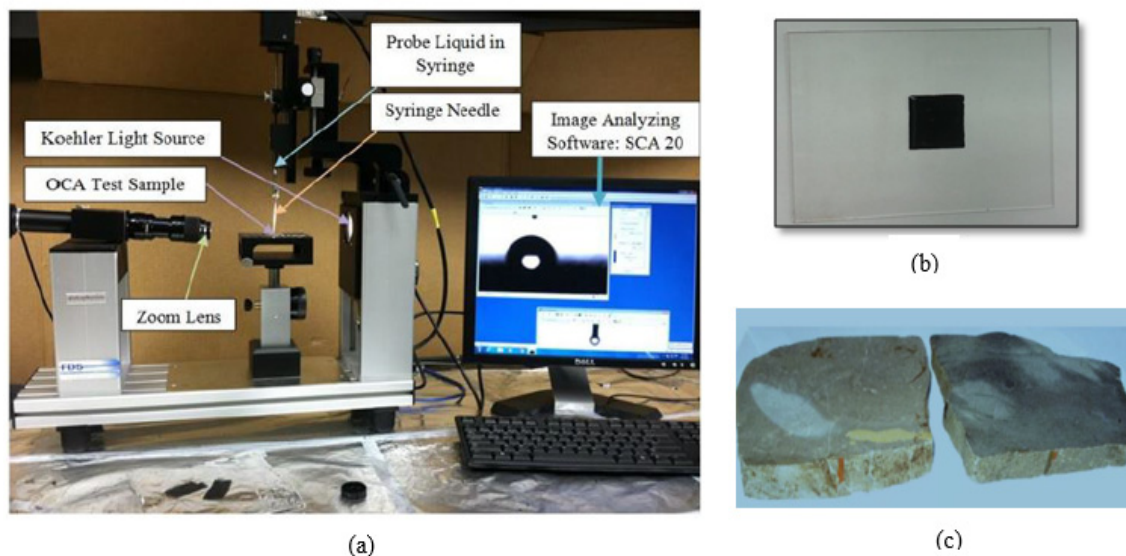


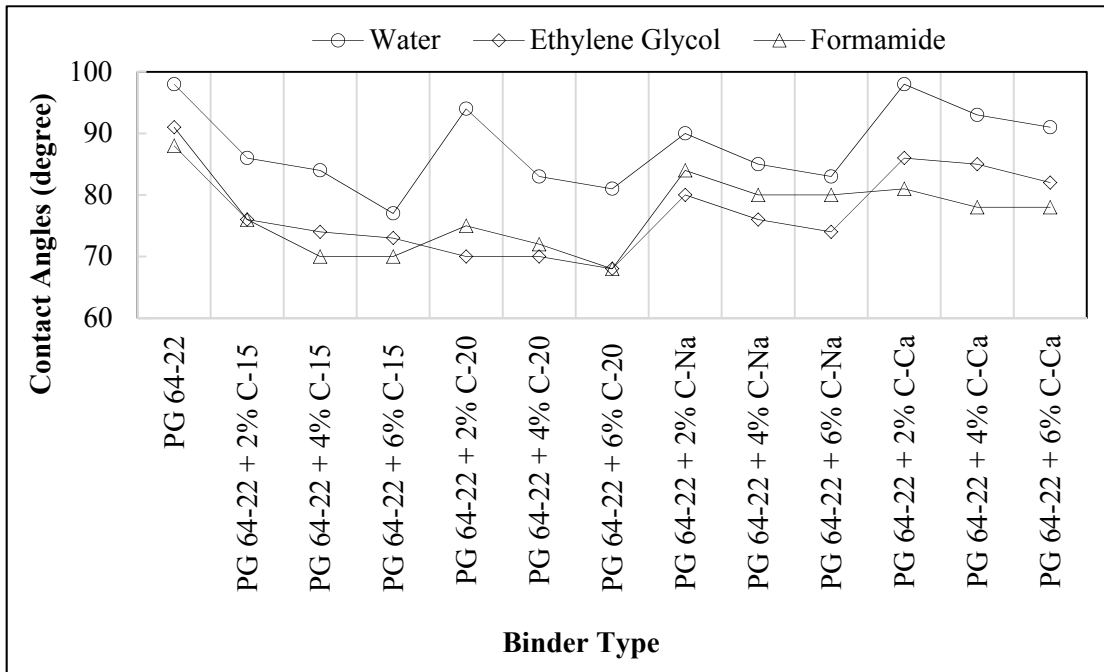
FIG. 2. (a) An OCA Device, (b) OCA Test Sample of unmodified and NC-modified binder, and (c) OCA Test Sample of aggregates.

While preparing SD test samples, this study followed a technique recommended by Tarefder and Arifuzzaman (2011). In this process a glass slide with dimensions 57 mm x 70 mm x 1.5 mm was quickly run in a flame to ensure the glass slide is free from any dust. Then the glass slide was wrapped on all sides with tape and a drop of binder sample was dispensed on the remaining rectangular portion at the middle of glass slide. The liquid binder was leveled into a smooth surface by rubbing with another clean glass slide. The binder coated glass was then allowed to cool down and finally the tapes were peeled off as shown in Figure 2b. As described in Koc and Bulut (2014), the aggregate specimens were cut using a mechanical saw to create a flat surface with 2 cm in thickness and about 7 cm x 8 cm cross section. The plate shaped aggregate is then processed through repeated washing, grinding and polishing in order to prepare the OCA test sample of aggregate as shown in Figure 2c.

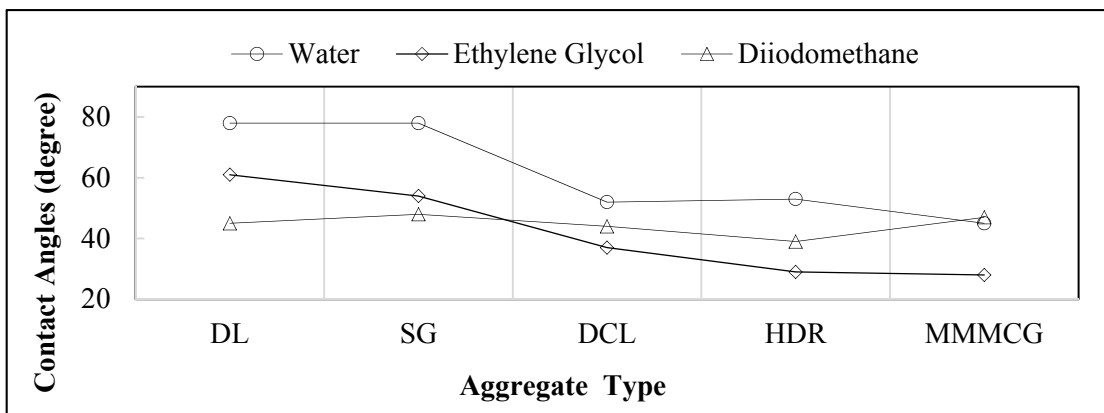
RESULTS AND DISCUSSIONS

Figure 3a shows the measured contact angles of various probe liquids on the binders and aggregates samples. Contact angle, the angle between liquid-vapor interface and solid-liquid interface, is a combined effect of cohesion, adhesion, and wettability. A contact angle of greater than 90° indicates poor wetting, and the wetting ability increases when the contact angle decreases from higher value to lower value (Buddhala *et al.* 2012). It is seen that contact angle decreases with an addition of higher content of NCs in binder, indicating an increase of wetting ability of binder with NCs incorporation. Among four different NCs, C-20 showed highest value of contact angles, followed by C-Ca, C-Na, and C-15. This could possibly be due to the less dense particles in C-20 with a loose bulk density of 1.15 kN/m^3 and packed density of 2.13 kN/m^3 and lower moisture content (less than 2%) compared to the other tested NCs (Nuntrino, 2016). As contact angle is an inverse measure of degree of wetting or wettability, the obtained trend of contact angles indicates that C-15 has the highest wettability among these four NCs, followed by C-Na, C-Ca, and C-20. In regards of aggregates, DL showed the highest contact angle, followed by SG, DCL, HDR, and MMMCG (Figure 3b). In order to SFE estimation of NC-modified binders, SFE components of probe liquids have been utilized from Van Oss *et al.* (1998).

Figure 4 shows SFE components, total SFE, and W_C of all tested binders and aggregates. As shown in Figure 4a, Γ^{LW} values are significantly higher than Γ^+ and Γ^- values for all binder samples. Thus, Γ^{LW} is found most significant contributory component to total SFE, which is consistent with previous research (Little and Bhasin, 2006). An increasing trend of SFE components, total SFE, and work of cohesion is found with addition of NCs in the binder. Lu and Harvey (2005) illustrated that loss of cohesion is one of the reasons of premature failure of pavement due to presence of water. Thus, increasing trend of W_C primarily indicates an improved moisture resistance of NC-modified binders. A better understanding of the moisture damage is obtained through compatibility analysis, which is discussed next.



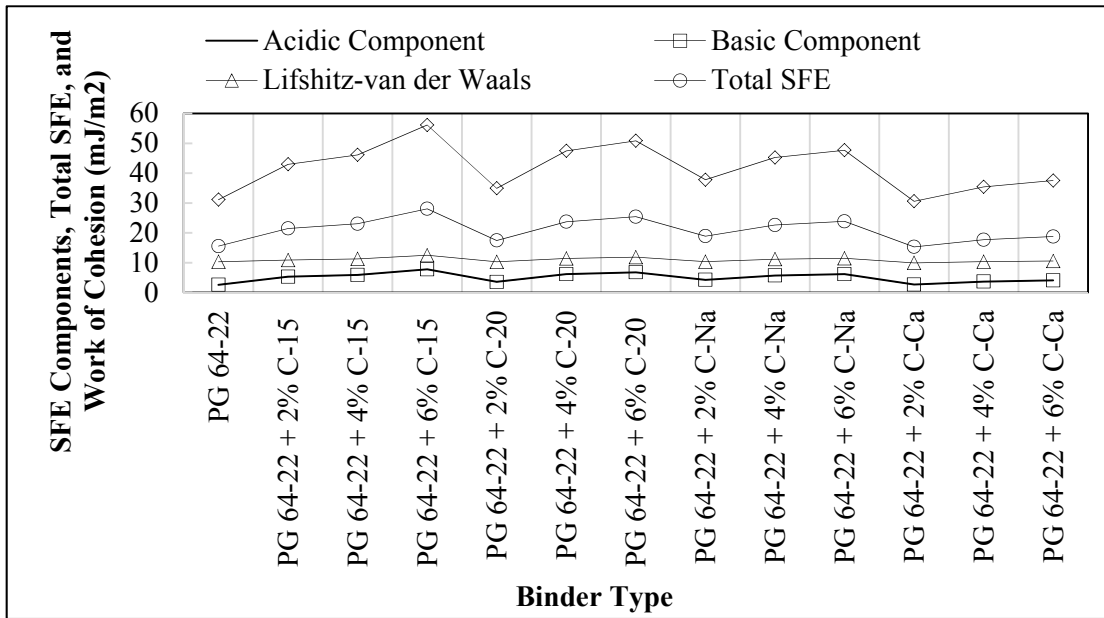
(a)



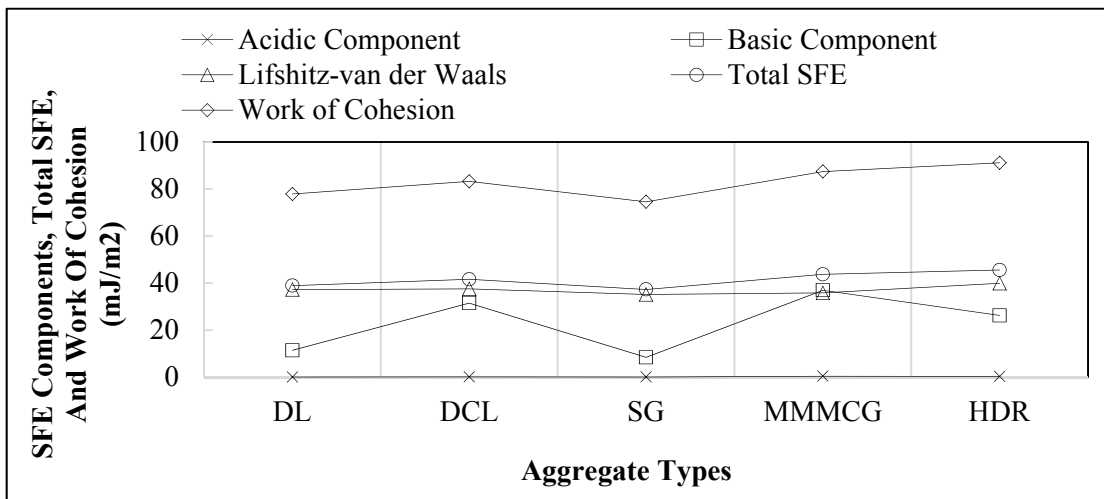
(b)

FIG. 3. (a) Contact Angles of Probe Liquids on (a) Binders, and (b) Aggregates.

The plot of ΔG_{dry}^{ad} and ΔG_{wet}^{ad} data (Figure 5) revealed that ΔG_{dry}^{ad} increases with the addition of higher content of NCs in cases of all aggregates, indicating an improved compatibility strength. Again, ΔG_{wet}^{ad} (negative value) decreased with an addition of higher content of NCs. The negative value of ΔG_{wet}^{ad} indicates the de-bonding energy at the binder-aggregate interface in the presence of water or a wet condition indicating the lower value of ΔG_{wet}^{ad} indicates a higher resistance to moisture damage of pavement. Thus, it appears that the addition of NC improves the adhesive energy between the aggregate and binder in both dry and wet condition, consequently provides more resistance to moisture damages.



(a)



(b)

FIG. 4. (a) SFE Components, total SFE, and (b) Work of Cohesion of Binders and Aggregates.

A CR analysis has been performed in order to determine the best performing binder-aggregate combination. Based on the CR guidelines found in Bhasin *et al.* (2006), moisture resistance increase with an increase of CR values and a CR value, when greater than 1.5, provides a desirable moisture resistance to pavement and. As shown in Table 1, NCs addition results in a significant increase of the CR value. It is also seen that all NC-modified binder shows a CR value greater than 1.5, which indicates that an addition of NCs provides the desired moisture resistance to pavement. Table 1 also shows that among four NCs, C-15 provides the most desirable moisture resistance and it was followed by C-20, C-Na, and C-Ca in both dry and wet

conditions. Among five aggregates, MMMCG shows the most desirable adhesive energy with all binders, and it was followed by DCL, HDR, DL, and SG in both dry and wet conditions.

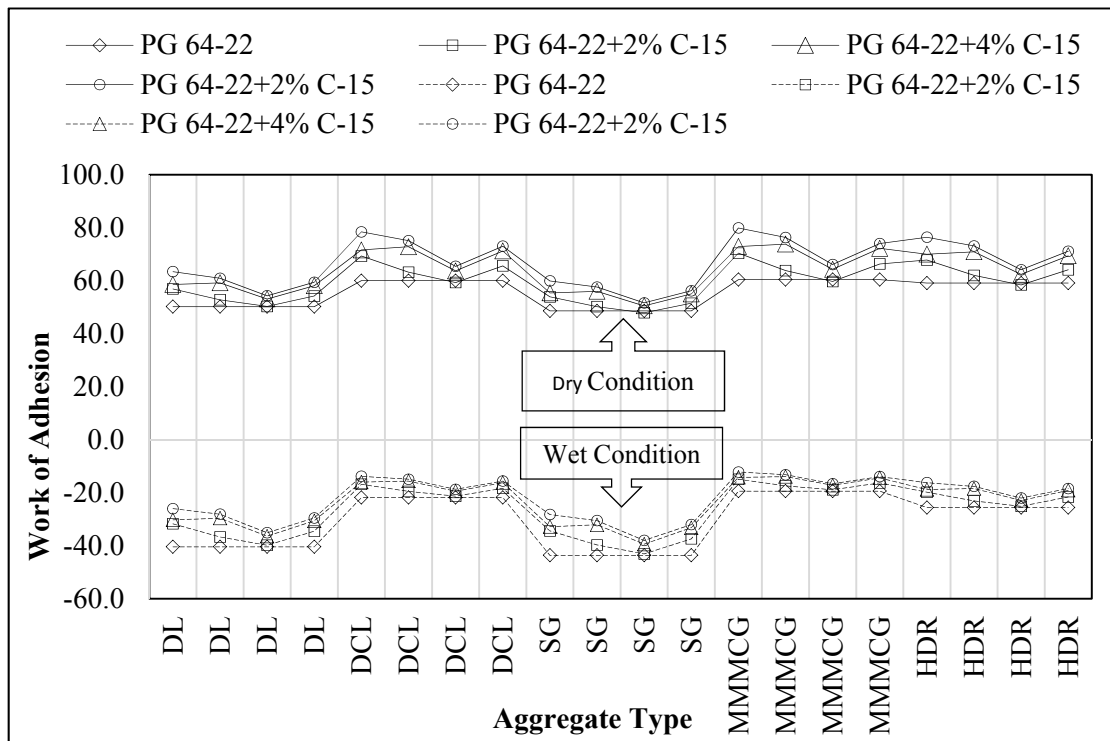


FIG. 5. Work of Adhesion of all Binder-Aggregate Combinations.

Table 1: Compatibility Ratio of All Binder-Aggregates Combinations

Types of Binder	Types of Aggregates				
	DL	DCL	SG	MMMCG	HDR
PG 64-22	1.2	2.8	1.1	3.1	2.3
PG 64-22+2% C- 15	1.8	4.1	1.6	4.7	3.4
PG 64-22+4% C- 15	1.9	4.5	1.7	5.1	3.7
PG 64-22+6% C- 15	2.4	5.7	2.1	6.5	4.7
PG 64-22+2% C- 20	1.4	3.2	1.3	3.7	2.7
PG 64-22+4% C- 20	2.0	4.7	1.7	5.3	3.9
PG 64-22+6% C- 20	2.2	5.0	1.9	5.8	4.2
PG 64-22+2% C-Ca	1.3	2.8	1.1	3.2	2.3
PG 64-22+4% C-Ca	1.5	3.3	1.3	3.7	2.7
PG 64-22+6% C-Ca	1.5	3.5	1.4	4.0	2.9
PG 64-22+2% C-Na	1.6	3.6	1.4	4.1	3.0
PG 64-22+4% C-Na	1.9	4.4	1.7	5.0	3.6
PG 64-22+6% C-Na	2.0	4.7	1.8	5.3	3.9

CONCLUSIONS

This study followed the surface free energy (SFE) approach to evaluate the moisture damage resistance of nanoclay (NC)-modified binders. To this end, four commercial NCs namely, Cloisite[®] 15 (C-15), Cloisite[®] 20 (C-20), Cloisite[®] Na⁺ (C-Na), Cloisite[®] Ca⁺⁺ (C-Ca) were tested in laboratory. SFE data of five different aggregates namely, Davis Limestone (DL), Snyder granite (SG), Dolese-Cooperton limestone (DCL), Hanson-Davis rhyolite (HDR), and Martin-Marietta-Mill-Creek granite (MMMCG) were used for a compatibility analysis. It is revealed that an addition of NC results in an increase in total SFE and work of cohesion, which primarily indicates an improved moisture resistance of NC-modified binders. The compatibility analysis showed that an addition of NC also results in a significant increase of work of cohesion and compatibility ratio, which is desired for an asphalt mixes to be more resistive to moisture damage. Among five aggregates, MMMCG showed the highest compatibility strength with all binders and it was followed by DCL, HDR, DL, and SG. Among four NCs, C-15 exhibited highest compatibility with the aggregates, and it was followed by C-20, C-Na, and C-Ca.

REFERENCES

- ALTANA Management (2015). "Technical Data Sheet and Material Safety Data Sheet," <http://www.byk.com/en/additives/additives-by-name/cloisite-20.php>.
- Al-qadi, I. L., Abuawad, I. M., Dhasmana, H., and Coenen, A. R. (2014). "Effects of Various Asphalt Binder Additives/Modifiers on Moisture Susceptible Asphaltic Mixtures." Illinois Center for Transportation, Report No. FHWA-ICT-14-004, Urbana, IL.
- Anderson, D. A., Youtcheff, J., and Zupanick, M. (2009). "Transportation in the New Millennium, 2009." <http://onlinepubs.trb.org/onlinepubs/millennium/00006.pdf>. Accessed July 5, 2015.
- Bahia (1996). "Wisconsin Transportation Bulletin: Asphalt Hand Book." Wisconsin Transportation Information, Madison, WI 53706.
- Bhasin, A., Masad, E., Little, D., Lytton, R. (2006). "Limits on adhesive bond energy for improved resistance of hot-mix asphalt to moisture damage." *Journal of the Transportation Research Board*, Vol. 1970, No. 3, 2006, pp. 3-13.
- Buddhala, A., Hossain, Z., Wasiuddin, N. M., Zaman, M., and O'Rear, E. A. (2012). "Effects of an Amine Anti-Stripping Agent on Moisture Susceptibility of Sasobit and Asphamin Mixes by Surface Free Energy Analysis. *Journal of Testing and Evaluation*, 40 (1), 2012, pp. 1-8.
- Cheng, D. X., Little, D. N., Lytton, R. L., Holste, J. C. (1998). "Surface Free Energy Measurement of Asphalt and Its Application to Predicting Fatigue and Healing in Asphalt Mixtures." *J. of Transportation Research Board*, No. 1810, pp. 44-53.
- FHWA (2015). "Warm Mix Asphalt," U. S. Department of Transportation. <http://www.fhwa.dot.gov/everydaycounts/technology/asphalt/faqs.cfm>.
- Fini, E. H., Al-qadi, I. L., Abu-lebdeh, T., and Masson, J. F. (2011) "Use of Surface Energy to Evaluate the Adhesion of Bituminous Crack Sealants to Aggregates." *American Journal of Engineering and Applied Science*, 2011, 4(2): 244-251.

- Hicks, R. G., Santucci, L., and Aschenbrener, T. (2003) "Introduction and Seminar Objectives." Moisture Sensitivity of Asphalt Pavements, A National Seminar, *Transportation Research Board Miscellaneous Report, Journal of Transportation Research Board*, Washington D. C., 3–36.
- Hossain, Z., Lewis, S., Zaman, M., Buddhala, A., and O'Rear, E. (2013). "Evaluation for Warm Mix Additive-Modified Asphalt Binders Using Spectroscopy Techniques." *Journal of Materials in Civil Engineering*, 25(2), pp. 149-159
- Huang, W., and Qian, Z. D. (2011). "Theory and Methodology of Advanced Asphalt Pavement Design," *Science Publishing House*, Beijing, China.
- Jahromi, S. G., Andalibizade B., and Vossough S. (2009). "Engineering Properties of Nanoclay Modified Asphalt Concrete Mixtures." *The Arabian Journal of Science and Engineering*, Volume 35, No. 1B, pp. 89-103.
- Koc, M., Bulut, R. (2014). "Assessment of a Sessile Drop Device and a New Testing Approach Measuring Contact Angles on Aggregates and Asphalt Binders." *Journal of Materials in Civil Engineering*, Vol. 26, No. 3, pp. 391-398.
- Little, D.N. and Bhasin, A. (2006). "Using Surface Energy Measurements to Select Materials for Asphalt Pavement." Texas Transportation Institute, Project 9-37, National Cooperative Highway Research Program, Washington, D.C.
- Liu G., Van de Ven, M. F. C. Molennar, A. A. A. (2012). "OrganoMontmorillonite Nanoclay: Alternative Modifier to Sustain Durability of Asphalt Pavement." Alternative Binders for Sustainable Asphalt Pavement, Workshop in Transportation Research Board, Washington D.C., pp. 37-48.
- Lu, Q. and Harvey, J. T. (2005). "Investigation of Conditions for Moisture Damage in Asphalt Concrete and Appropriate Laboratory Test Methods." California Department of Transportation, Research Report: UC-RR-2005-15.
- Tarefder, R., Arifuzzaman, M. (2011). "A Study of Moisture Damage in Plastomeric Polymer Modified Asphalt Binder Using Functionalized AFM Tips." *Systemics, Cybernetics and Informatics*, 9(6), pp. 23-24.
- Uddin, F. (2008). "Clays Nanoclays, and Montmorillonite Minerals." *Metallurgical and Materials Transactions A*, Volume 39(12), 2008, pp. 2804-2814.
- Nuntrino (2016). "Typical Physical Properties Bulletin," Neutrino Corporation, <http://www.neunano.com/>, Last Accessed, January 18, 2016.
- Van Oss, C. J., Chaudhury, M. K., and Good, R. J. (1998). "Interfacial Lifshitz-van der Waals and Polar Interactions in Macroscopic Systems." *Chemical Reviews*, 88(6), pp. 941-972.
- Yao H., You, Z., Li, L., Shi, Z., Goh, S. W., Mills-Beale, J., and Wingard, D. (2012). "Performance of Asphalt Binder Blended with Non-modified and Polymer Modified Nanoclay." *J. of Construction and Building Mat.*, 35, pp. 159-170.
- Yazdani A. and Pourjafar, S. (2012). "Optimization of Asphalt Binder Modified with PP/SBS/Nanoclay Nanocomposite Using Taguchi Method." *World Academy of Science, Engineering and Technology*, International Scholarly and Scientific Research & Innovation, Vol. 6, No. 7, pp. 16-20.
- You, Z., Mills-Beale, J., Foley, J. M., Roy, S., Odegard, G. M., Dai, Q., and Goh, S., W. (2010). "Nanoclay-modified Asphalt Materials: Preparation and Characterization." *J. of Construction and Building Mat.*, 25, pp. 1072-1088.

The Use of a Green Polymer Nanocomposite in Geo-Infrastructure

Munir D. Nazzal¹; Tremaine D. Gissentaner²; Savas Kaya³; and Sang Soo Kim⁴

¹Associate Professor, Dept. of Civil Engineering, Ohio Univ., Athens, OH 45701. E-mail: nazzal@ohio.edu

²Graduate Student, Dept. of Civil Engineering, Ohio Univ., Athens.

³Professor, Electrical Engineering and Computer Science, Ohio Univ., Athens, OH.

⁴Associate Professor, Dept. of Civil Engineering, Ohio Univ., Athens, OH.

Abstract

In recent years, there has been a great interest in using eco-friendly polymers in construction of geo-infrastructures to help in reducing their carbon footprint and enhancing their sustainability. Green polymers are one of these materials. Green polymers are polymers derived from plants that consist of starches, sugars, and cellulose. One of the green polymers that have received attention is polylactic acid (PLA). PLA is a hydrophobic, aliphatic polyester that can be extracted from most commonly from corn starches. This paper explores the use of PLA and PLA nanocomposites as an alternative polymer to fabricate geosynthetics. To this end, PLA nano-composite materials were prepared using different carbon nanofibers contents. The mechanical properties of the produced nanocomposites samples were examined and compared to a geogrid material typically used in reinforcement of geomaterials in highway embankments and pavement structures. The results indicated that the carbon nanofibers enhanced the elastic modulus of PLA, but reduced its failure strain. Although the PLA carbon nanocomposites had higher tensile modulus than the geogrid materials tested in this study, they had lower tensile strength and strain. It is recommended that plasticizers used with the PLA nanocomposites to enhance their ductility.

INTRODUCTION

In 2012, the United States Environmental Protection Agency (EPA), recorded that 6,526 million metric tons of greenhouse gas (GHG) were emitted, with more than a quarter of those emissions generated from transportation structures (EPA, 2014). Carbon dioxide (CO₂) is one of the main greenhouse gases that its concentration has been significantly increasing due to human related activities such as the burning of fossil fuels. For example, in April of 2014, the average CO₂ concentration in the

Northern Hemisphere was higher than 400 parts per million (ppm) (Piccirillo, 2014). The increase in the CO₂ and other GHG emissions have contributed to constant thinning of the ozone layer and global warming, which is thought to increase the occurrence of natural disasters. As such there has been a growing interest in using construction materials that can reduce the carbon footprint of transportation structures.

Geosynthetics have been used extensively in the reinforcement of embankment and pavement layers during the past four decades. Different types of geosynthetics have been used such as geogrids and geotextiles. All of these types were fabricated from synthetic (petroleum and other oil based substances) polymers of polypropylene, polyester, or polyethylene. However, in recent years, chemists and engineers have searched for fruits and vegetables that they can potentially develop into bioplastics, better known as green polymers (Adeosun et al., 2012; Mülhaupt, 2014). Green polymers can most commonly be defined as polymers derived from plants that consist of starches, sugars, and cellulose (Mittal, 2011; Adeosun et al., 2012). One of the green polymers that have received attention in recent years is Polylactic Acid (PLA). PLA is a hydrophobic, aliphatic polyester that can be extracted from most commonly from corn starches (Henton et al., 2005; Jamshidian et al. 2010). PLA's have been found to be a very suitable alternative to petroleum based polymers in the construction of plastics (Jamshidian et al. 2010). PLA is abundant because of its close relationship to lactic acid, which can be derived by way of the hydrolysis and fermentation (Jamshidian et al. 2010, Misra et al., 2010, Gibson 2010). PLA has been found to be relatively strong, showing good stiffness which is of much importance with regard to civil engineering applications (Ozkoc and S. Kemaloglu, 2009).

The production of the PLA requires 20 to 50% less fossil fuel than that of oil based plastic resins; which means that up to 2 to 5 times more PLA can be produced within a given amount of fossil fuel than oil based plastics (Jamshidian et al. 2010, Henton et al, 2005). Likewise, the energy that is required to manufacture PLA is much lower than other synthetic polymers. PLA generates much less greenhouse emissions than conventional polymer. Figure 1 compares the greenhouse gas contribution to the environment for different plastic types. It is noted that the PLA can actually reduce greenhouse gases as it is produced from field wastes or other biomass. Thus, PLA currently serves as one of the most appealing green polymers for sustainable material alternatives.

Studies have been conducted during the past five years to investigate the use of different nano-fillers to improve the mechanical properties of PLA. To this end, PLA nano-composites developed with clay and cellulose fibers were prepared and evaluated (e.g. Kaci and Zaidi, 2012; Cheng et al., 2011; Jonoobi et al., 2010, Qu et al. 2010). Jonoobi et al. (2010) conducted a study to evaluate the effect of cellulose nanofiber on PLA stiffness and strength properties. The PLA nanocomposites were fabricated using the extrusion method. Jonoobi et al. (2010) found that the PLA tensile modulus and strength increased by more than 20% when 5% by weight of the

cellulose nanofibers were used. The dynamic mechanical analysis results showed that the storage modulus increased for all nano-composites compared to neat PLA. Kaci and Zaidi (2012) evaluated the effects of the loading rates on morphology and mechanical properties of PLA clay nanocomposites. Organically modified montmorillonite was introduced at various loading rates: 1, 3 and 5 % by weight. The nanocomposites were prepared by melt intercalation in a Brabender Plasticorder mixer. Their results showed a significant improvement in modulus, hardness, and tensile strength with the increase of the clay content.

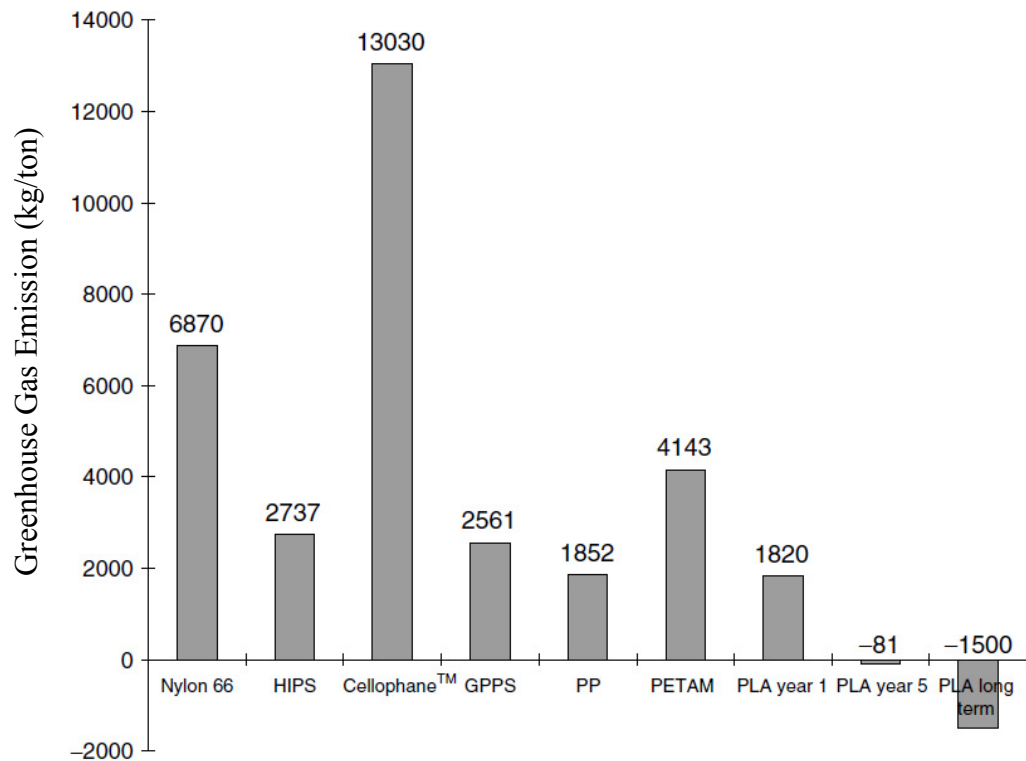


FIG. 1. Greenhouse Gas Emission for different types of Polymer (Henton *et al*, 2005).

In this paper PLA nanocomposites were prepared by mixing carbon nanofibers using melt compound process. Three carbon nanofibers loading rates were used: 1%, 3% and 5% by weight. The tension properties were determined and compared to those of a geogrid material typically used in reinforcement of soil in highway embankment.

OBJECTIVES

The main objective of this paper is to investigate the use of PLA and PLA nanocomposites as an alternative polymer to fabricate geosynthetics. Another objective of this paper is to evaluate the effect of using carbon nano-fibers on the mechanical properties of PLA.

LABORATORY TESTING PROGRAM

Materials

The PLA material used in this study was a Ingeo™ 3001D polylactide biopolymer, which was obtained from NatureWorks™ (Minnetonka, MN). Figure 2 presents a picture of the obtained PLA pellets. This type of PLA is designed for injection molding applications. Table 1 presents the main properties of the PLA used in this study. In addition a vapor-grown Pyrograf®- PR-19-XT-LHT carbon nanofibers from Applied Sciences Inc. was used in this paper. Table 2 summarizes the properties of this carbon nanofiber (CNF). The PR-19-XT-LHT fiber is produced by heat-treating at 1500°C, which converts any chemically vapor deposited carbon present on the surface of the fiber to a short range ordered structure that increases the inherent conductivity of the fiber. This nanofiber was selected to enhance the mechanical as well as the electric properties of the PLA. The electrical conductivity of PLA nanocomposites was also investigated but not reported in this paper. Three CNF loading rates were used: 1, 3 and 5% by weight.



FIG. 2. Picture of PLA pellets used in this study.

Table 1. Properties of PLA Material Used in This Study

Property	Value
Thermal conductivity	0.160 J/m-°K-s (at 25 °C)
Specific heat, Cp	25 °C 1.20 J/g °C
Glass Transition Temperature, Tg	55 - 60°C
Peak Melt Temperature, Tm	145 - 170°C
Specific Gravity, ρ	1.24 - 1.25 g/cc
Melt Density (200°C), ρ melt	1.12 g/cc
Pellet Bulk Density, ρ bulk	0.79 - 0.85 kg/liter (49 - 53 lb/ft ³)
Typical Flake Bulk Density, ρ flake	0.593 kg/liter (37 lb/ft ³)

A uniaxial geogrid material typically used in reinforcement of roadway embankment was obtained. The obtained geogrid material was manufactured from select grades of high-density polyethylene (HDPE) resins that are highly oriented and resist elongation (creep) when subjected to heavy loads for long periods of time. The obtained geogrid material were cut to make samples for tensile tests in accordance with ASTM standard test method for determining tensile properties of plastics (ASTM-D638).

Table 2. Properties of Used Carbon Nanofibers (Pyrograf Inc., 2011)

Property	Value
Fiber diameter, nm (average):	150
CVD carbon overcoat present on fiber:	No
Surface area, m ² /gm:	20-30
Dispersive surface energy, mJ/m ² :	120-140
Moisture, wt%:	<5
Iron, ppm	<14,000
Polyaromatic hydrocarbons, mg PAH/gm fiber:	<1

FABRICATION PLA-CNF NANOCOMPOSITES

The PLA-CNF nanocomposite were developed via melt compound process. The first step in the melt compound process was to create neat PLA and PLA CNF nanocomposites (PLA-1% CNF, PLA-3% CNF, and PLA-5%-CNF) resin using Leistritz Micro 18 co-rotating twin extrusion device. The step involved heating each of the five zones of the extruder to 165 °C, 190 °C, 190 °C, 195 °C, and 200°C respectively for PLA polymer. After the environment for extrusion was established in each zone, CNF and PLA resin (IngeoTM 3001D pellets) were mixed with a spoon and fed into the extruder, coming out as polymers reels on the other side. Spoon mixing of material used for feeding into the extruder. The reels were cooled in an ice bath, and fed into an extruded polymer cutter to produce resin. The resin was pressed by a Carver Inc., hydraulic hot press at 190°C to produce sheets for tensile test specimens for macroscale testing. Figure 3 presents a picture of some of the neat PLA sample as well as the PLA carbon nanocomposite samples that were prepared and tested in this paper. It is noted that all samples were made in accordance with ASTM standard tests method for determining tensile properties of plastics.

RESULTS OF MECHANICAL TESTING

Tensile tests were conduct on the prepared neat PLA and PLA carbon nanocomposites as well as the obtained geogrids. A loading rate of 0.1 in/ min were used in these test in accordance with ASTM D638 D. MTS QTest universal testing device was used to conduct all tensile tests. A minimum of two samples were tested for each case. Figure 4 presents typical stress-strain curves obtained for the PLA, PLA-1 CNF, PLA-3% CNF, PLA-5% CNF, and geogrid samples. It is noted that PLA

and PLA carbon nanocomposites samples fractured at relatively low strains (less than 2.5%). The neat PLA exhibited the most ductile behavior having a maximum elongation of 2.43%. In addition, all PLA nanocomposite material developed little or no plastic deformation and showed no necking as shown in Figure 5. At strain levels less than 2%, the nanocomposite samples had a slightly higher tensile stresses as compared to the tested geogrid material. However, the geogrid material had much higher tensile strength and failure strain.



FIG. 3. PLA and PLA nanocomposites samples.

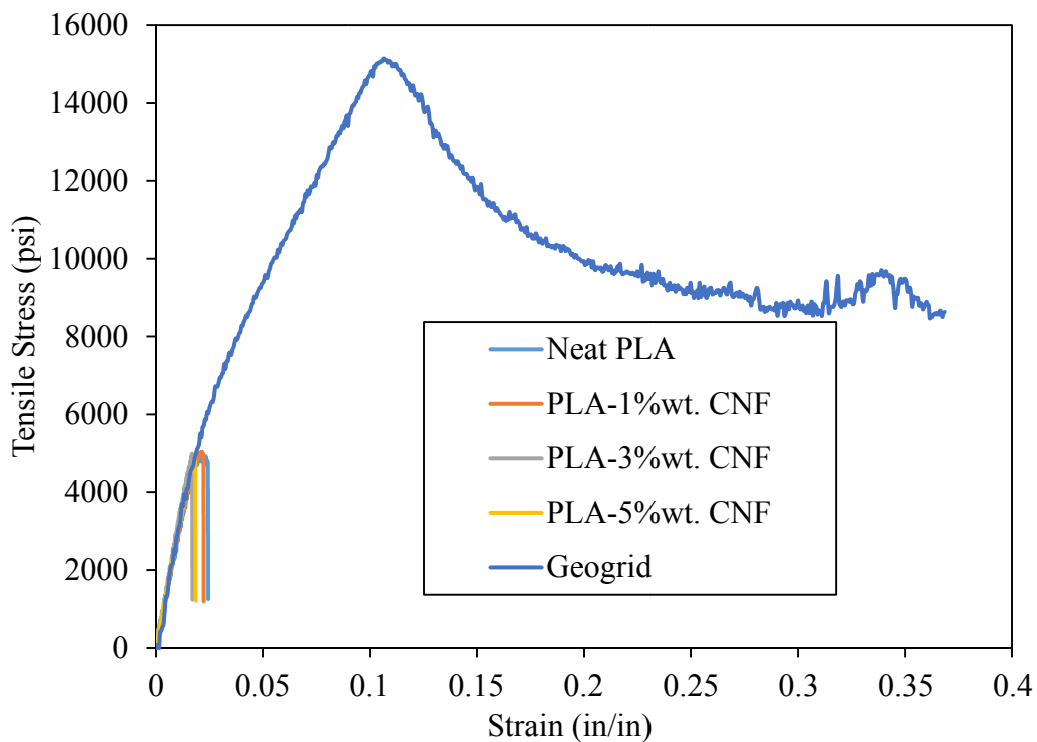


FIG. 4. Typical stress-strain curves for tested material.

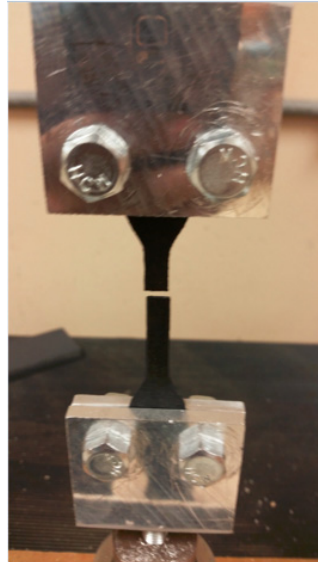


FIG. 5. Picture of tested PLA nanocomposite sample at failure.

Based on the results of the tensile tests conducted on the neat PLA, PLA carbon nanocomposite and geogrid samples, the 1.5% secant modulus, tensile strength were computed. Figure 6 presents the average secant modulus values for the neat PLA, PLA carbon nanocomposites, and geogrid samples. It is noted that the carbon nano-fibers increased the secant modulus of the PLA material. In addition, the secant modulus increased with the increase of the carbon nano-fiber content up to 3%, but the modulus values dropped after that. This may indicate that the optimum content of the carbon nano-fiber is 3% or less. The neat PLA and PLA nanocomposite samples exhibited higher elastic secant modulus values than the geogrid reinforcement materials considered in this study. The average elastic modulus of PLA carbon nanocomposite with 3% carbon nano-fiber content was about 30% higher than that of tested geogrid material.

Figure 7 presents the average tensile strength of PLA, PLA carbon nanocomposites, and geogrid samples. In general, the addition of the carbon nano-fibers did not significantly enhance the tensile strength of the PLA material. It is clear that the geogrid material had much higher tensile strength than the neat PLA and PLA carbon nano-composites.

The obtained results suggest that a plasticizer should be added to the PLA nano-composite to enhance their ductility, which may also help in enhancing their tensile strength as well. Polyethylene glycol (PEG) is one of the plasticizers that have been used to enhance the PLA nanocomposites ductility. The results also suggest that for cases where the reinforcement is not expected to be subjected to strains high than 2% then the PLA carbon nanocomposite can be used to fabricate the reinforcement material. The PLA carbon nanocomposite with 3% carbon nano-fiber content will be the recommended to be used as it had the best performance. However, full-scale tests should be performed to validate the resulted of this study.

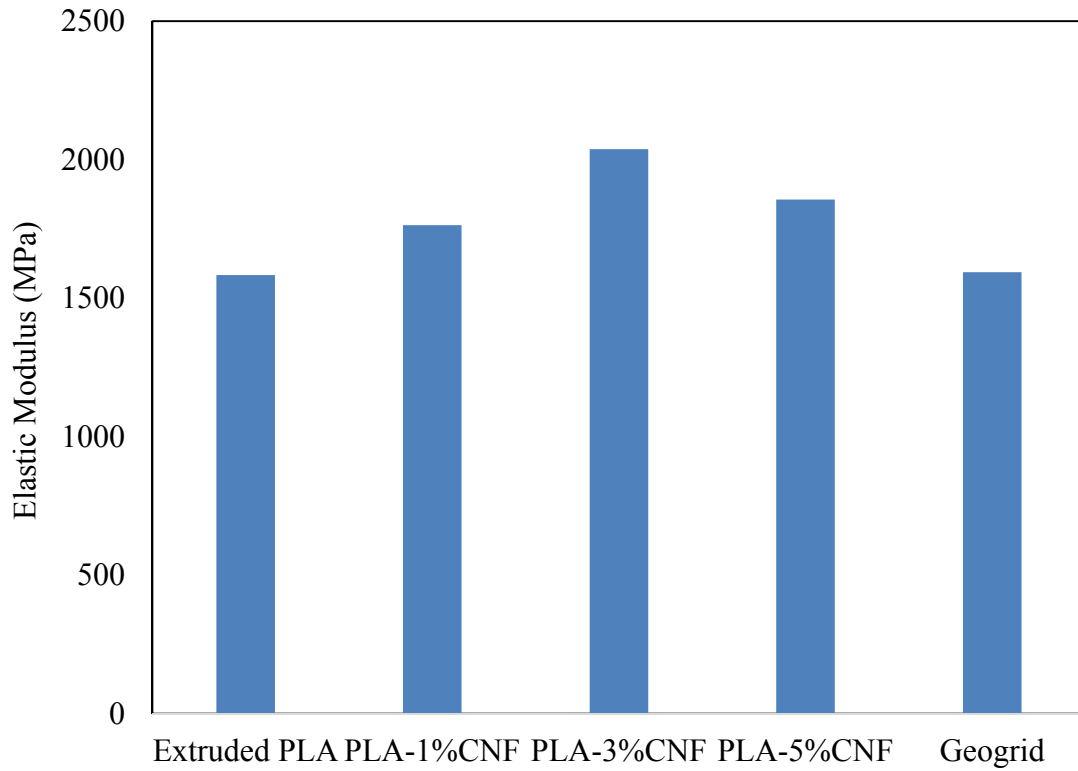


FIG. 6. Elastic modulus data for tested samples.

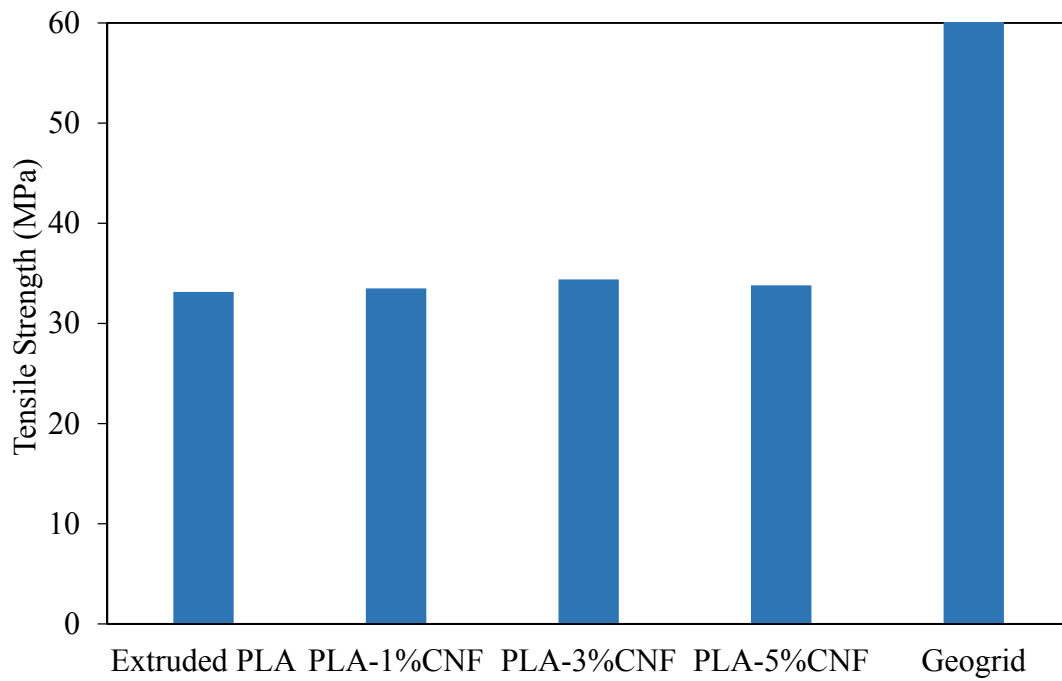


FIG. 7. Tensile strength data for tested samples.

CONCLUSIONS

In this paper, the use of PLA and PLA nano-composites as an alternative polymer to fabricate geosynthetics was explored. PLA nano-composite materials were prepared using different carbon nanofibers contents. The mechanical properties of the produced nanocomposites samples were examined and compared to a geogrid material typically used in reinforcement of geomaterials in embankments and pavement structures. Based on the results of this paper, the following conclusions can be drawn:

- Carbon nanofibers enhanced the elastic modulus of PLA. The highest improvement was achieved when 3% CNF was used by weight.
- The carbon nanofibers did not affect the tensile strength of PLA, but they slightly reduced its failure strain.
- PLA carbon nanocomposites had higher tensile modulus than the geogrid materials tested in this study.
- PLA carbon nanocomposites they had much lower tensile strength and strain than considered geogrid material.
- It is recommended that plasticizers used in a PLA carbon nanocomposite to enhance its ductility and potentially the tensile strength and strain.

ACKNOWLEDGMENT

The work upon which this study is based is in part supported by the National Science Foundation through a GK-12 grant, NSF: 0947813 in the Department of Civil Engineering at Ohio University. Contents of this study do not necessarily reflect the views or policies of National Science Foundation or Ohio University.

REFERENCES

- Adeosun, S. O., Lawal, G. I., Balogun, S. A., & Akpan, E. I. (2012). "Review of green polymer nanocomposites." *Journal of Minerals and Materials Characterization and Engineering*, Vol. 11, No. 4: 385.
- Cheng, Q., DeVallance, D., Wang, J., & Wang, S. (2011). *Advanced Cellulosic Nanocomposite Materials*. INTECH Open Access Publisher.
- D. Henton et al. (2005) "Polylactic Acid Technology." *Natural Fibers, Biopolymers, and Biocomposites*: 528-563
- G. Ozkoc and S. Kemaloglu, (2009) "Morphology, biodegradability, mechanical, and thermal properties of nanocomposite films based on PLA and plasticized PLA," *Wiley Interscience*: 2481-2487,.
- Gibson, Ronald F. (2010) "A review of recent research on mechanics of multifunctional composite materials and structures." *Composite structures*, Vol. 92, No. 12: 2793-2810.
- Habibi, Y., Lucia, L. A., & Rojas, O. J. (2010). "Cellulose nanocrystals: chemistry, self-assembly, and applications." *Chemical reviews*, Vol. 110, No. 6: 3479-3500.

- Henton, D. E., Gruber, P., Lunt, J., & Randall, J. (2005). "Polylactic acid technology." *Natural Fibers, Biopolymers, and Biocomposites*, Taylor & Francis, Boca Raton, FL: 527-577.
- Jamshidian, M., Tehrany, E. A., Imran, M., Jacquot, M., & Desobry, S. (2010). "Poly-Lactic Acid: production, applications, nanocomposites, and release studies." *Comprehensive Reviews in Food Science and Food Safety*, Vol. 9, No. 5: 552-571.
- Jonoobi, M., Harun, J., Mathew, A. P., & Oksman, K. (2010). "Mechanical properties of cellulose nanofiber (CNF) reinforced polylactic acid (PLA) prepared by twin screw extrusion." *Composites Science and Technology*, Vol. 70. No. 12: 1742-1747.
- Kumar, B., Castro, M., & Feller, J. F. (2012). "Poly (lactic acid)-multi-wall carbon nanotube conductive biopolymer nanocomposite vapour sensors." *Sensors and Actuators B: Chemical*, Vol. 161, No. 1: 621-628.
- Misra, M., Seydibeyoglu, M. O., & Mohanty, A. K. "Multifunctional Structural Green Nanocomposites: An Overview." University of Guelph, Guelph, Canada: 3-4.
- Mülhaupt, R. (2013). "Green polymer chemistry and bio-based plastics: dreams and reality." *Macromolecular Chemistry and Physics*, Vol. 21, No. 2: 159-174.
- N. De La Pena, (2007). "Sifting the Garbage for a Green Polymer" [Online]. Available: <http://www.nytimes.com>
- Naturework (2015). <http://www.natureworkslc.com/>. Accessed April 2015.
- Pyrograf Products, Inc., (2011). Pyrograf®-III Carbon Nanofiber [Online]. Available: <http://pyrografproducts.com>
- Qu, P., Gao, Y., Wu, G., & Zhang, L. (2010). "Nanocomposites of poly (lactic acid) reinforced with cellulose nanofibrils." *BioResources*, Vol. 5, No. 3: 1811-1823.
- Tabone, M. D., Cregg, J. J., Beckman, E. J., & Landis, A. E. (2010). "Sustainability metrics: life cycle assessment and green design in polymers." *Environmental science & technology*, Vol. 44, No. 21: 8264-8269.
- Mittal, V. (2011). "Bio-nanocomposites: future high-value materials." *Bionanocomposites: Future High-value Materials*: 1-27.

Zero Valent Metal (ZVI) Nanoparticles in Geotextiles and Geomembranes

Franz-Georg Simon¹; Daniela Robertson²; Christine Schütt³; and Volker Birke⁴

¹Head of Division, BAM Federal Institute for Materials Research, 12200 Berlin, Germany.

²Research Scientist, BAM Federal Institute for Materials Research, 12200 Berlin, Germany.

³Research Engineer, Ostfalia Univ. of Applied Sciences, Faculty of Civil and Environmental Engineering, Campus Suderburg, 29556 Suderburg, Germany.

⁴Head of Environmental Chemistry Group, Ostfalia Univ. of Applied Science, 29556 Suderburg, Germany.

Abstract: Reactive geomembranes and geotextiles are an innovative approach to control the migration of contaminants in geotechnical applications. Within a joint research project in cooperation with a medium-sized enterprise, the preparation and characterization of “reactive” geomembranes and geotextiles modified by the addition of zero-valent metal nanoparticles was performed. Zero-valent iron (ZVI) nanoparticles were added to polyethylene or to the fillings of geo-containers or geosynthetic clay liners. These geosynthetic products consist of mixtures of sand with clay or bentonite, typically embedded in geotextile nonwovens or geomats. The permeability of these geo-containers can be adjusted by the ratio of clay or bentonite to sand. ZVI nanoparticles were also added as reactive material to geomembranes made of polyethylene with additives like the antioxidant Irganox 1010 or glycerin. These additives prohibit oxidation of the nanoparticle and act as hydrogen donor in the dechlorination of chlorinated hydrocarbons. Contaminates such as chlorinated hydrocarbons and toxic heavy metal compounds are either decomposed or converted to less toxic species (e.g. Cr-(VI) reduction to Cr-(III)). The paper reports the first experimental results from manufacturing of the reactive geomembrane model materials and characterization of the products with microscopic techniques. First breakthrough measurements of the ZVI modified geomembrane compared to a reference sample are presented.

INTRODUCTION

Geomembranes and geotextiles are widely used in geotechnical applications for separation, filtration and geosynthetic barriers to control contaminant migration. It is commonly accepted that such polymers, mostly polyolefin materials, used for the production of geosynthetic products have a high performance and a long service life time. For example, geomembranes with BAM certification for applications in

municipal solid waste landfills have a very low permeability for organic and inorganic contaminants and fulfill the requirements for a minimum service lifetime of 100 years (Müller and Saathoff 2015). However, chlorinated hydrocarbons, e.g. from landfill leachates, are able to diffuse through the geomembrane, thereby possibly causing contamination of groundwater (Kalbe et al. 2001). It is known that chlorinated hydrocarbons can be degraded by elemental iron in permeable reactive barriers (Powell et al. 1998). Therefore research has been conducted to combine low permeability of geomembranes and the capability of iron to decompose chlorinated hydrocarbons (Shimotori et al. 2006). The reactivity of iron can even be enhanced by addition of other metals such as palladium (Kim et al. 2012). The nanoparticles can also be added to the fillings of geo-containers or geosynthetic clay liners (GCL). In GCLs clay in contact with seepage water reduces the permeability. Likewise in the geomembrane ZVI acts as reactive material.

EXPERIMENTAL

MATERIALS

Two commercial ZVI nanoparticle powders were evaluated: ZVI 1 (BASF, Germany) and ZVI 2 (NANO IRON s.r.o., Czech Republic). The ZVI nanoparticles were used as received. Per the specifications from the manufactures ZVI 1 has an iron content of 97% and ZVI 2 has approx. 65-80 % ZVI and 20-35 % iron oxides (Fe_2O_3 , FeO) after the production process. The particle size of ZVI 1 product was denoted as approximately 5 μm and of ZVI 2 of approximately 50 nm. Both ZVI nanoparticle products are applicable for groundwater remediation.

Linear-low-density polyethylene (LLDPE) was used as the polymer matrix. Naue GmbH & Co KG supplied this polymer and Polyplast Müller GmbH blended the polymer with ZVI nanoparticles and additives. The LLDPE has a melting flow index of 0.75 g/ 10 min (190°C/2.16 kg), a melting point of 130°C, a crystallization point of 109°C and a density of 0.938 g/cm³.

The polymer-ZVI-composites were prepared by mixing the polymer and ZVI particles in a roll mill (Collin, Germany). The roll mill temperature was fixed at 150°C and the holding time of the polymer-ZVI-mixture was approximately 8 to 9 minutes. The resulting products (plates 116 x 148 mm in size) were melt pressed with a hydraulic press at a temperature of 190°C for 10 min and were allowed to cool to room temperature.

The pristine sodium activated calcium bentonite (Na-bentonite) powder was a product of S & B Industrial Minerals GmbH (supplied by Naue GmbH & Co KG). The particle size distribution of the product was measured by laser granulometry (Mastersizer 2000, Germany) with the following values of d_{10} (2.815 μm), d_{50} (16.532 μm) and d_{90} (59.637 μm). The water content was measured of 10 weight percent. The X-ray fluorescence analysis (RFA) shows that the Na-bentonite consists of SiO_2 (53.68 %), Fe_2O_3 (4.49 %), TiO_2 (0.73 %), Al_2O_3 (16.49 %), MnO (0.07 %), CaO (5.51 %), Na_2O (2.76 %), K_2O (0.89 %), P_2O_5 (0.18 %) and SO_3 (2.05 %). Loss of ignition was 8.54 %. The natural iron content in Na-bentonite is relatively high (approximately 4.5 %) and the differentiation between natural iron and iron nanoparticle cannot be carried out. For the calculation of the amount of added iron

nanoparticles to the bentonite matrix a calibration curve with different amounts (0 % to 12 wt-% of ZVI) was used.

Table 1. Properties of ZVI particles

Properties	ZVI 1	ZVI 2
Adsorption isotherm BET (specific surface m ² /g)	0.42	16,92 25 ¹
Solid density (g/cm ³) (He-pycnometer)	7.70	6.49
Particle size (μm)	5.2 ¹	0.05 ¹
Laser granulometry (μm)	4.4 ²	1.013 ²
SEM image (μm)	1.4 ³	0.097 ³

¹ manufacturer information

² agglomerates

³ single particle analysis of SEM

Table 2. ZVI-polymer model material

	Polym er	ZVI 1	ZVI 2	Glycerin
Sample 1	94%	2%	-	4%
Sample 2	94%	-	2%	4%

METHODS

The size and morphology of two ZVI nanoparticles were determined using Scanning Electron Microscopy (SEM) on a ZEISS SUPRA 40 (ZEISS, Germany) with energy dispersive X-ray microanalysis unit (EDX-detector: Thermo NSS 3.1, 10kV high voltage) to verify the chemical composition of the particle surface. The ZVI powder was spread over a carbon substrate on a sample holder used for SEM and EDX analysis. The nanocomposite and microcomposite structures were further evaluated by characterizing the ZVI-modified geomembrane samples using SEM analysis performed on 40 μm thin polymer films, sputtered with carbon to avoid charging of the polymer matrix. The polymer film was prepared by a microtome CM1950 (Leica, Germany). ZVI nanoparticle distribution in the polyethylene matrix was imaged using a digital microscope VHX 1000 (Keyence, Germany). The polymer films were placed on a glass plate used for microscopic analysis.

The XRF measurements were performed with an energy dispersive X-ray analyzer XEPOS (Spectro Analytical Instruments GmbH, Germany) with X-LabPro software, Germany). XRF measurements were applied to analyze the iron content in bentonite matrix of the geotextile product and in the polyethylene matrix of the geomembrane

samples. The measurements were made on powders or directly on the polymer surface. Before XRF measurement the bentonite powder was dried in an oven at a temperature of 105°C for 5 hours and stored permanently in a desiccator.

Surface areas of the ZVI nanoparticles were determined by a nitrogen adsorption BET (Brunauer–Emmett–Teller) test using Micromeritics ASAP 2010 (USA) after degassing the samples according to DIN ISO 9277.

Particle size distribution and aggregate analysis were measured with laser granulometry (Mastersizer 2000, Malvern Instruments, UK). The nanoparticles were dispersed in 0.003 mol/l sodium pyrophosphate solution and sonicated by an ultrasonic device of type Sonopuls HD 2200 and a VS 70 t sensor (BANDELIN electronics GmbH & Co. KG, Germany).

RESULTS AND DISCUSSION

CHARACTERIZATION OF NANOPARTICLES

The morphology of the samples was investigated using SEM analysis. The micrographs of the ZVI 1 particle are shown in **FIG. 1**. It can be observed that the particle morphology is spherical and polydisperse. The histogram evaluates the particle size distribution and an particle size average of 1.4 μm was calculated. Partially “steady” aggregates of ZVI nanoparticles were observed and the size of the aggregates was between 5 to 8 μm as shown in **FIG. 1b**. In the EDX spectrum of the ZVI particle surface (**FIG. 1f**), no further element other than iron was detected. A small amount of carbon was measured, but this is a result of the sample preparation technique of the SEM method. The particles size distribution was evaluated in suspension measured by laser granulometry. The characteristic values of d_{10} (2.14 μm), d_{50} (4.40 μm) and d_{90} (8.79 μm) were determined.

The SEM imaging of ZVI 2 particles revealed aggregates of primary ZVI of approximately 50-150 nm diameters (**FIG. 2a and c**). The ZVI 2 product was received as powder and the production process was performed in suspension followed by a drying process. As a result the ZVI nanoparticles were composed to aggregates in size of > 500 nm. The aggregate size was evaluated in suspension measured by laser granulometry. The characteristic values of d_{10} (0.5 μm), d_{50} (1.013 μm) and d_{90} (6.56 μm) were determined. A re-dispersion to primary particles was not possible.

In this work, specific surface area (a_s) of both products was measured by BET test method. The ZVI 1 has an a_s of 0.42 m^2g^{-1} and the ZVI 2 has an a_s of 16.92 m^2g^{-1} . From the reactivity perspective, surface area is a more important parameter than the particle size alone. Contaminant degradation reactions are usually regarded as mediated by available ZVI surface area.

The surface of ZVI 1 and ZVI 2 particle was analyzed by EDX method. **FIG. 2f** and **FIG. 3f** show the results of measured element on the particles surface. Only iron was detected on the particles surface of ZVI 1 particle. Carbon arises from the sample preparation technique. The spectrum from the ZVI 2 product (**FIG. 2f**), on the other hand, shows also C and O with an increased content beside Fe. During the production process stabilization agents, e.g. surfactants are used for stabilization of the nanoparticles. This is confirmed with the SEM images in **FIG. 3(c, e)**, showing an organic matrix surrounding the ZVI nanoparticles and the formation of aggregate structures.

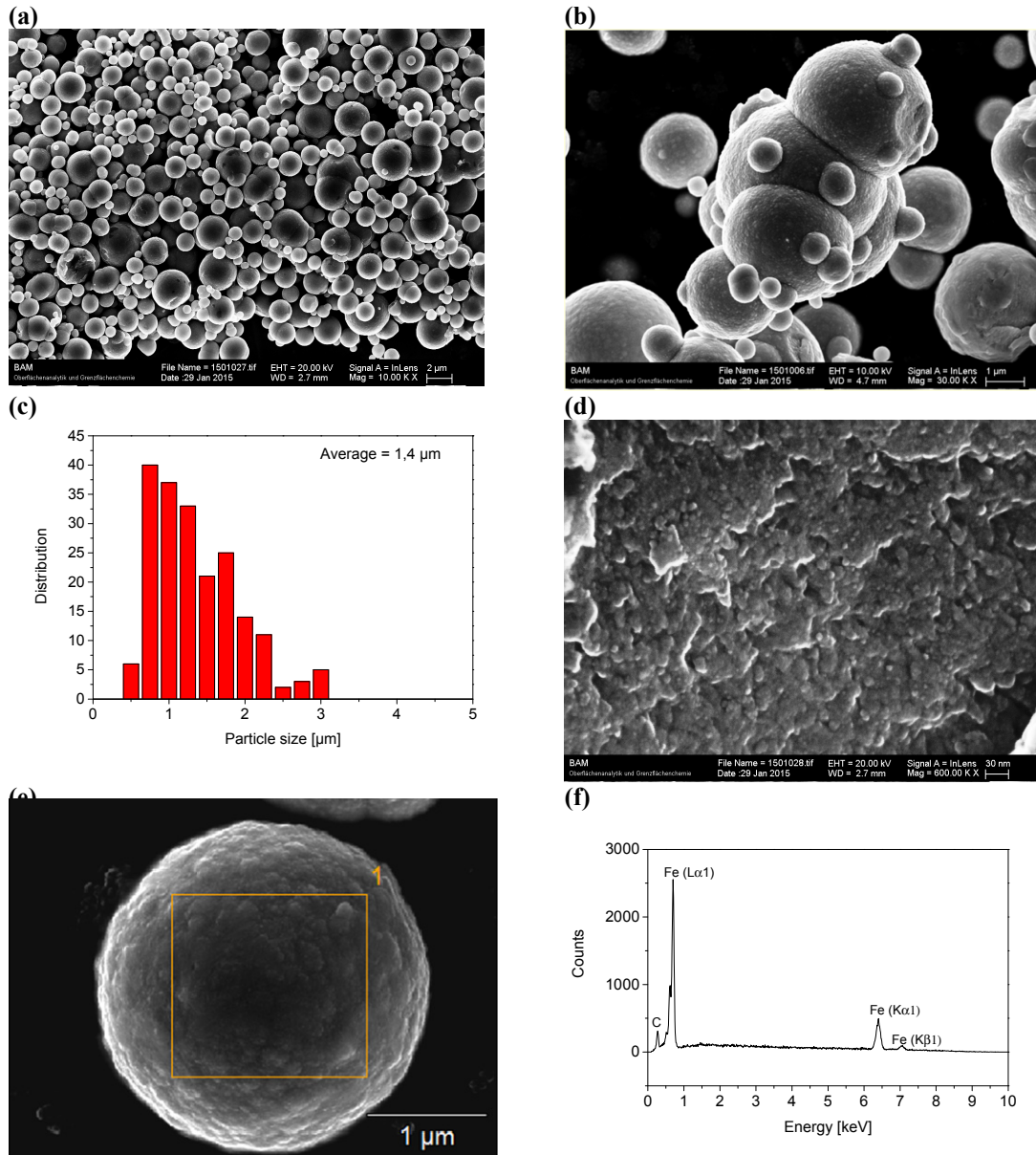


FIG. 1. SEM analysis of ZVI1 particles (a) overview screen of particle morphology, (b) ZVI particle aggregate, (c) histogram of the particle size distribution, (d) particle surface and (e, f) EDX-analysis of the particle surface

POLYETHYLENE ZVI MODEL MATERIAL

The morphology of the geomembrane sample 1 and 2 (see Table 2) were investigated using digital microscopy and SEM analysis. The images of the samples are shown in **FIG. 3**. The digital image (**FIG. 3a**, 200 times magnification) of a thin polymer film of sample 1 shows a homogenous distribution of the ZVI 1 particle in the polymer matrix. The dispersion of the nanoparticles of ZVI 2 product in the polymer matrix is considerable homogeneous than observed for the ZVI 1 particles.

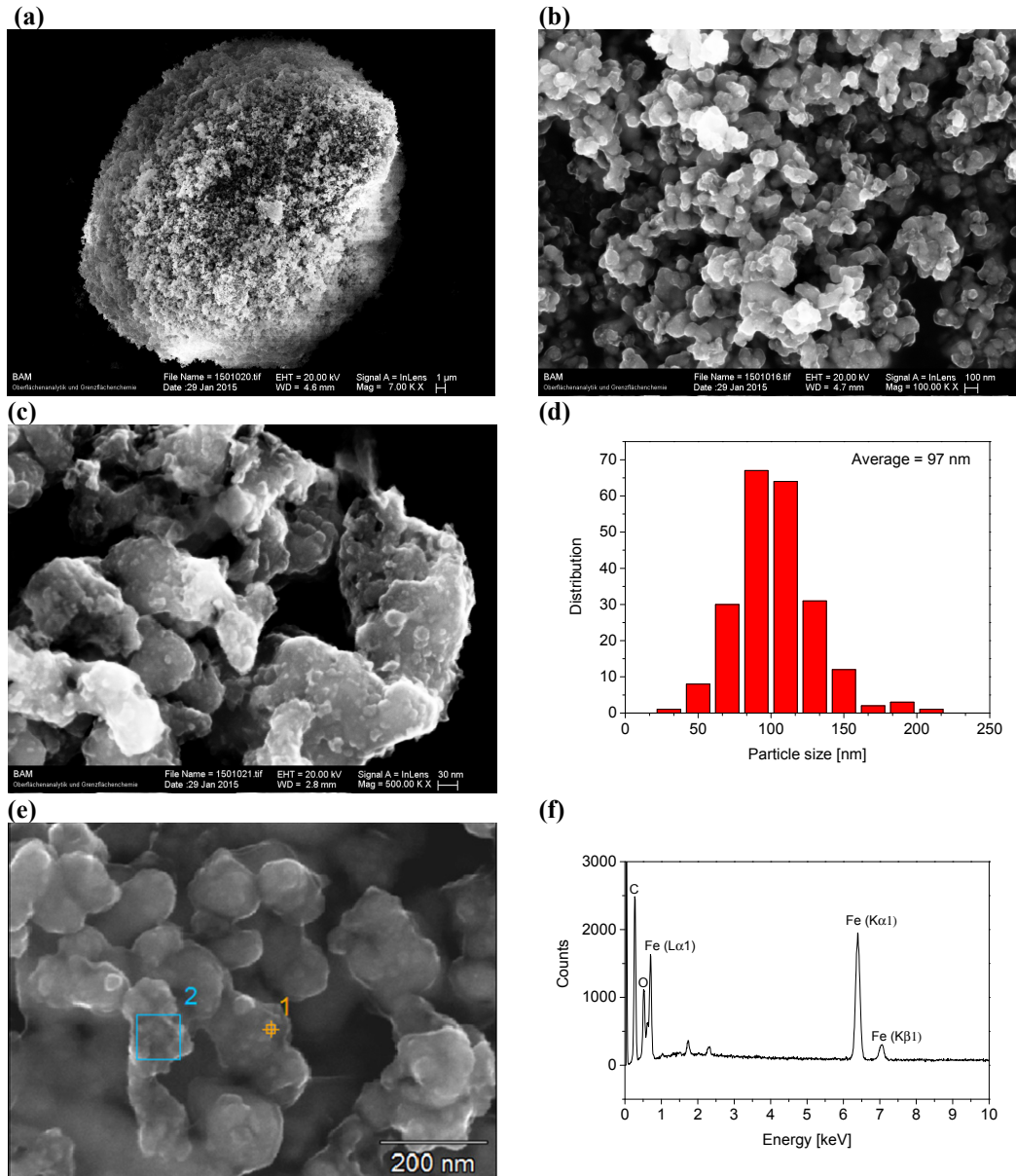


FIG. 2. SEM analysis of ZVI 2 nanoparticles (a) aggregate of primary particles, (b) aggregated ZVI nanoparticle, (c) histogram of the nanoparticle size distribution, (d) nanoparticle surface and (e, f) EDX analysis of the nanoparticle surface

However, in the SEM image (magnification of 10,000 times) it can be observed that the primary nanoparticles and aggregates are located in “hollow” spaces. **FIG. 3c** shows the digital microscopic image of geomembrane sample 2 (100 times magnification). The investigated polymer film of the geomembrane samples shown large nanoparticle aggregates (irregular black dots).

The ZVI content was determined by energy dispersive XRF measurements on 32 mm large disks. For geomembrane sample 1 a ZVI content of 1.89% and for

geomembrane sample 2 a ZVI content of 1.95 % were observed. Target value for the investigation was a concentration of 2 wt-% ZVI particles.

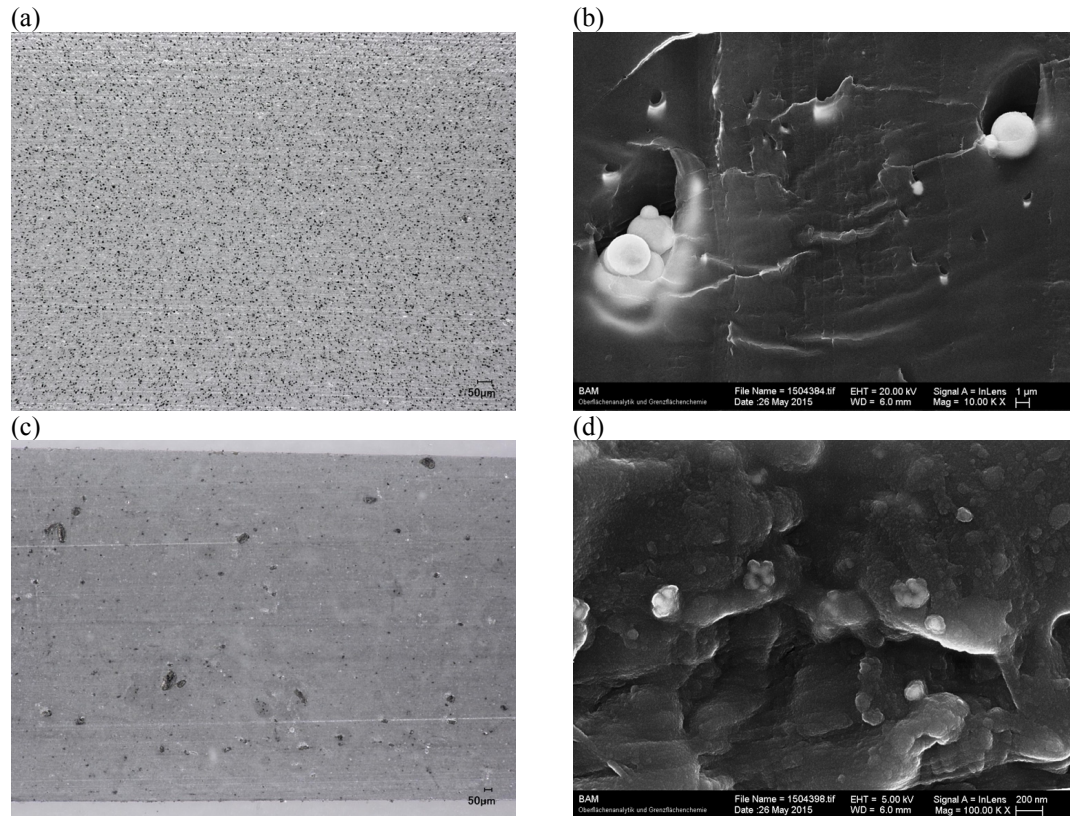


FIG. 3. Digital microscope image and SEM image of the ZVI 1 modified polyethylene matrix (a and b) and of the ZVI 2 modified polyethylene matrix (c and d)

DETERMINATION OF THE ZVI CONTENT IN BENTONITE

For ZVI content calibration in ZVI-Bentonite mixtures, a series of standards containing varying concentrations from 0 % to 12 % by weight of ZVI particles were prepared. The calibration was performed using peak intensity analysis of X-ray fluorescence spectra of Fe $K_{\alpha}1$ (6.40384) and Fe $K_{\beta}1$ (7.05798) peak at various ZVI particle amounts. For the elimination of the ZVI matrix effect, e.g. particle size differences between ZVI 1 and ZVI 2 and effects from different ZVI amounts, Compton peak normalization was carried out. **FIG. 4** shows the results of the calibration curve.

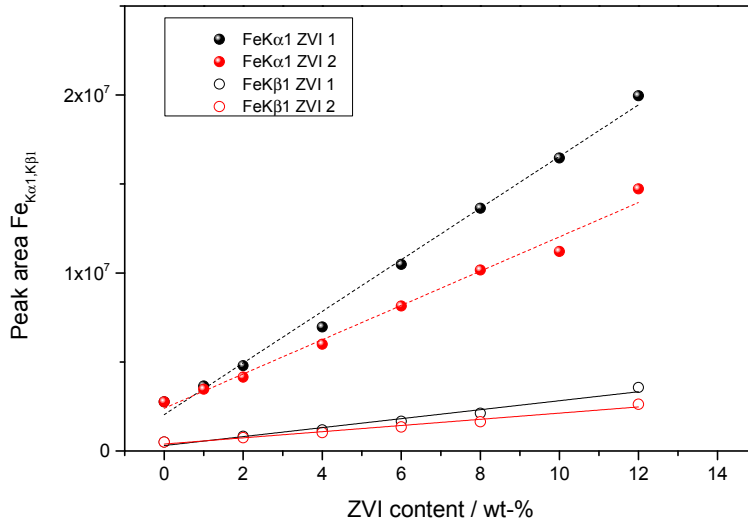


FIG. 4. Calibration curves for ZVI content in bentonite-iron samples

MEASUREMENT OF BREAKTHROUGH CURVES

Experiments with the geomembranes were performed in diaphragm cells similar to those described by Shimotori et al. (Shimotori et al. 2006). **FIG. 5** shows the experimental setup of the measurement cell (sketch and photographic image displaying the location of the membrane). The larger vessel (equivalent to larger volume) is called upstream volume and the aqueous solution is charged with 100 mg/L PCE before the test started. A smaller volume of aqueous solution (downstream volume) is separated from the larger volume by the PE geomembrane.

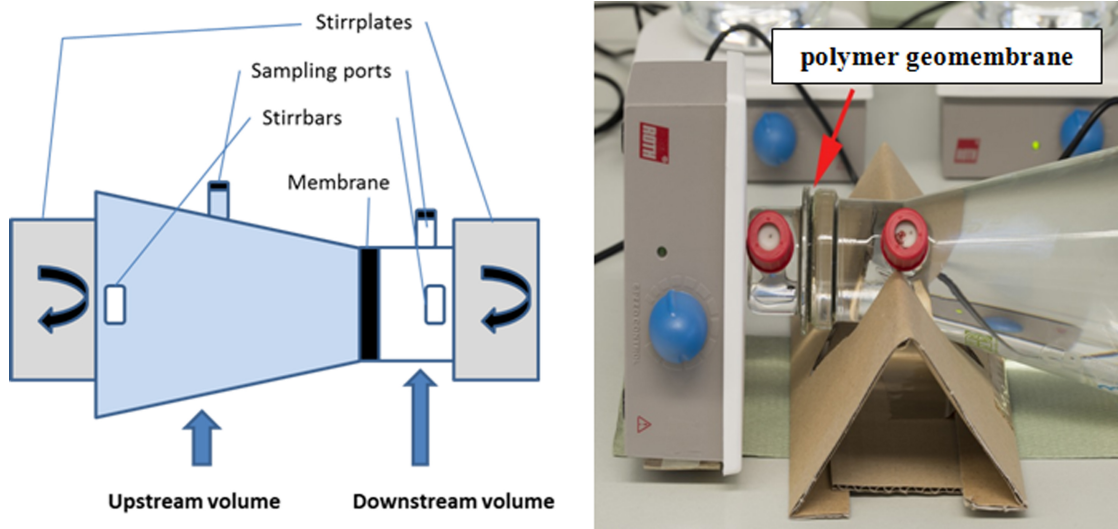


FIG. 5 Illustration of the measurement cell according to Shimotori (Shimotori et al. 2006) (left) and measurement cell with installed polymer geomembrane (right)

Geomembrane tests were conducted with thin films of polyethylene 1.) without any modifications and 2.) modified with ZVI and glycerin (see Table 2). It is important that a hydrogen donor is present (either glycerin or Irganox 1010) if chlorinated hydrocarbons are to be degraded. In the dechlorination reaction the chlorine atoms are replaced by hydrogen. In PRB applications the contaminated groundwater acts as H-donor (Reardon 1995). In the present work glycerin and Irganox 1010 (a phenolic compound) were added on manufacturing of the geomembrane. Although geosynthetic clay liners exhibit low permeability's enough water to act as H-donor is expected to be always present. For the conversion of toxic Cr-VI to Cr-III no additional reacting agent than ZVI is necessary.

FIG. 6 shows first results of breakthrough curves of a PE reference membrane (no ZVI) and a PE membrane modified with nanoscale iron particles (ZVI 2) and glycerin. The thicknesses of the tested membranes were in the same size range (PE reference 890 μm , PE membrane modified with iron particles 880 μm). The PCE concentration of the upstream and downstream volume was measured by headspace gas chromatography and the results are plotted versus the test duration.

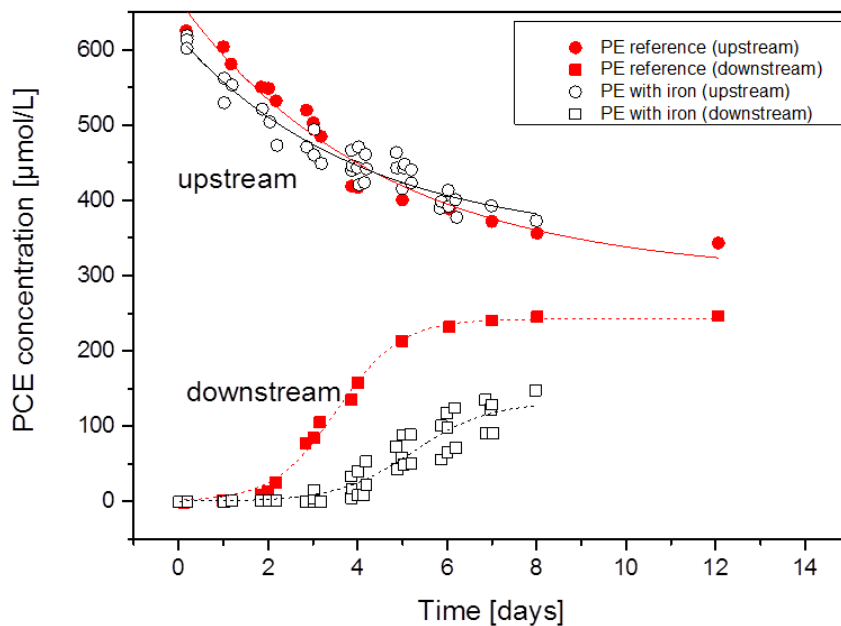


FIG. 6 Breakthrough curves of a PE reference sample (thickness 890 μm) and PE membrane modified nanoscale iron particles (thickness 880 μm)

Measurements using the membrane containing iron and glycerin gave different results compared to the measurement of the reference membrane. The lag time of the breakthrough for the modified PE membrane was twice as long as that for the PE reference membrane. It is evident that the permeability of PCE through the modified membrane is lower than that of the PE reference membrane, most probably as a result of the presence of ZVI particles in the membrane. However, at that time the primary degradation products were not observed in the downstream and upstream volume.

Further measurements of breakthrough curves with reactive geotextiles will be conducted in percolations columns (Kalbe et al. 2013; Krüger et al. 2012).

CONCLUSIONS

For our experiments two commercial zero valent iron products were used as received. The ZVI nanoparticle size was characterized with SEM and laser granulometry. Furthermore, the specific surface (BET method) and the solid density (Helium pycnometer) were measured.

Polyethylene geomembrane model sample containing zero valent iron was developed as a reactive barrier, and tested against PCE as a model contaminant in breakthrough experiments. First breakthrough experiments with a ZVI modified geomembrane in a diaphragm cell compared to a reference sample were performed. The lag time of the modified PE membrane was increased compared to the reference sample. The results demonstrate that the breakthrough of PCE through a PE membrane is decelerated by adding zero valent iron and glycerin as H-donor into the polymer. To enhance the reactivity of the nanoscale ZVI particle combinations of iron with magnesium or aluminum will also be tested.

ACKNOWLEDGMENTS

The authors appreciate the support within the ZIM program by Federal Ministry of Economic Affairs and Energy on the basis of a decision by the German Bundestag (KF2201080EB4).

REFERENCES

- Kalbe, U., Krüger, O., Wachtendorf, V., Berger, W., and Hally, S. (2013). "Development of Leaching Procedures for Synthetic Turf Systems Containing Scrap Tyre Granules." *Waste and Biomass Valorization*(4), 745-757.
- Kalbe, U., Müller, W. W., Berger, W., Tatzky-Gerth, R., and Eckardt, J. (2001). "Transport of organic pollutants in composite liners." The exploitation of natural resources and the consequences, R. W. Sarsby and T. Meggyes, eds., Thomas Telford Ltd., London, 141-147.
- Kim, Y.-k., Shin, J.-y., Lee, K.-k., Cho, H. S., Jeon, H. Y., and Kim, J. Y. (2012). "Mass transfer of trichloroethylene through the palladized iron coated reactive geomembrane." *Journal of Hazardous Materials*, 201–202, 7-15.
- Krüger, O., Kalbe, U., Berger, W., Nordhauß, K., Christoph, G., and Walzel, H. P. (2012). "Comparison of Batch and Column Tests for the Elution of Artificial Turf System Components." *Environmental Science & Technology*, 46, 13085-13092.
- Müller, W. W., and Saathoff, F. (2015). "Geosynthetics in geoenvironmental engineering." *Science and Technology of Advanced Materials*, 16, 034605 (20pp).
- Powell, R. M., Puls, R. W., Blowes, D. W., Vogan, J. L., Gilham, R. W., Schultz, D., Powell, P. D., Sivavec, T., and Landis, R. (1998). "Permeable Reactive Barrier Technologies for Contaminant Remediation." *EPA/600/R-98/125*, US Environmental Protection Agency, Washington DC.
- Reardon, E. J. (1995). "Anaerobic corrosion of granular iron: Measurement and interpretation of hydrogen evolution rates." *Environmental Science & Technology*, 29, 2936-2945.
- Shimotori, T., Cussler, E. L., and Arnold, W. A. (2006). "High-density polyethylene membrane containing Fe⁰ as a contaminant barrier." *Journal of Environmental Engineering*, 132(7), 803-809.

3D Model Reconstruction of Rocks on a Slope for Simulating a Rock Fall

Itaru Kitahra^{1,2}; Shogo Atsumi¹; Ryo Degawa¹;
Yohiei Kawamura¹; Hyongdoo Jang³; and Yuichi Ohta¹

¹Dept. of Intelligent Interaction Technology, Univ. of Tsukuba, Tennoudai 1-1-1, Tsukuba, Ibaraki 305-8573.

²Center for Computational Science, Univ. of Tsukuba, Tennoudai 1-1-1, Tsukuba, Ibaraki 305-8573.

³Dept. of Mining Engineering and Metallurgical Engineering, Curtin Univ., Locked Bag 30, Kalgoorlie, WA 6433.

Abstract: For reducing damage of rock fall, it is important to estimate the route, leap height and velocity of the rock. Although research about estimation of falling motion of rocks are actively conducted, there are still unsolved issues, since rock fall is a complex phenomenon affected by position, size, or shape of rocks and angle of slope. This paper proposes a method of rock fall simulation using a 3D model of rock and slope reconstructed by merging multiple-view images. The proposed method requires only a mobile camera to generate a 3D model, so that more practical rock fall simulation can be realized. In addition, reconstructing textured 3D model makes inspectors visually confirm how the rock falls on the slope. Due to the difficulty capturing multiple images of both of rocks and a slope at a same time, rocks and a slope are individually captured, and then, they are merged in the post process. There are two problems to be solved for merging them accurately. One is the significant difference in their spatial resolution; the other is the difference in the appearance caused by perspective projection. We conduct an experiments using multiple images of rocks and slopes captured at actual landslide site.

1. INTRODUCTION

The prevention of rock fall needs to estimate the route, height of leap and velocity of the rock. Rock fall is a complex phenomenon caused by the position, size, or shape of the rock and angle of slope. Researches about estimation of falling motion of rocks (rock fall simulation) are actively conducted in a wide range of fields (Stock G.M. et al, 2011; Nguyen H.T, 2011). Since, in these most simulations, the shape of a slope is considered as the 2D vertical-cross-section, it is difficult to estimate the 3D route, (i.e., height of leap and velocity of the rock) at the time of fall.

Some researches attempts to expand the target space into 3D. Although such simulation tries to acquire the shape of slopes by GIS information (Charalambous, S. and Sakellariou, M., 2008), it is difficult to realize highly accurate measurement

required for precise rock fall simulation. Moreover, in order to precisely estimate the collision with rocks and ground, the shape of rocks should be represented as accurately as possible. By using a laser scanner (LiDAR), shape of slope and rock can be acquired accurately. However, it is not feasible to bring and install such heavy and delicate equipment on a steep slope where fall rocks exist.

As FIG. 1 shows, we propose a method of rock fall simulation using the 3D model of rock and slope reconstructed by merging multiple-view images (Image-Based Modeling). Since our proposed method needs only mobile camera to generate 3D model, it can realize more practical rock fall simulation than using a laser scanner. In addition, inspectors can visually confirm how the rock falls on the slope, since 3D models having texture are reconstructed.

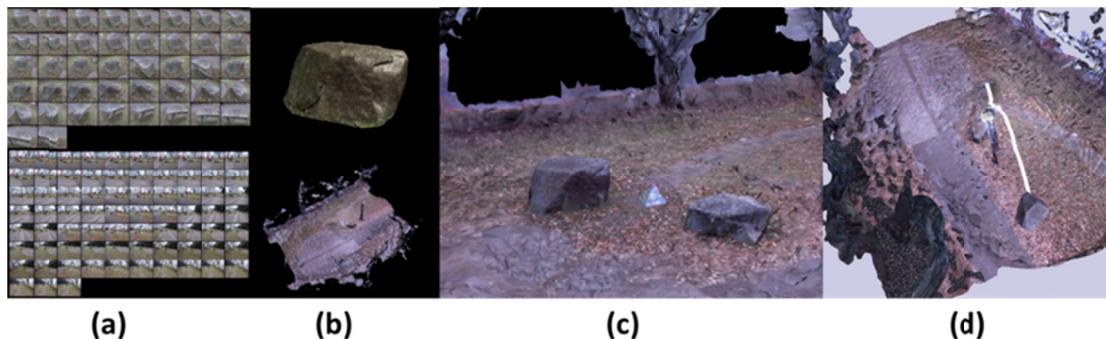


FIG. 1. Overview of our proposed method ((a): An example of multi-view images of rock and slope, (b): 3D models of rock and slope reconstructed from multi-view images, (c): A result of merging rock and slope 3D models, (d): An example of rock fall simulation using merged 3D models).

2. RELATED WORKS

Christen M. et al (Christen M. et al, 2012) conduct on 3D rock fall simulation using slope shape scanned by a laser scanner. A laser scanner enables us to accurately measure 3D shape using Time-of-Flight technology (Curless B. 2000). On the other hand, the laser scanner is designed to measure relatively large-scale space, so it is difficult to bring and install it on a slope where there are falling rocks. As the result, the previous method does not accurately measure the shape of falling rock, but approximates the shape as simple shape such as sphere or cube. Thus, it is not difficult to estimate the complex behavior of falling rocks adequately.

There are some researches to reconstruct 3D Models using multi-view images. Structure from Motion (SfM) (Snavely N., 2006) is one of the most popular and actively developing method to reconstruct 3D point cloud from multiple-view images by estimating 3D position of the feature points and pose of the capturing cameras using a factorization method (Tomas C. and Knade T., 1992). The reconstructed point cloud is sparse. So Patch-based Multi-View Stereo (PMVS) (Furukawa Y. and Ponce J., 2009) is developed to reconstruct dense point cloud. Applying Poisson Surface Reconstruction (PSR) (Kazhdan M. et al, 2006) to the reconstructed dense point cloud generates 3D models which have surface information.

In order to realize fall rock simulation, it is necessary to merge multiple 3D models of rock and slope, which are individually reconstructed. Iterative Closest Point (ICP) (Besl P.J. and Mckav N.D., 1992) is well known as the alignment method of 3D models. ICP estimates 3D rigid transformation matrix to minimize the vertex distance between two 3D models. However, ICP is intended for 3D models that have comparable spatial resolution. In other words, the target 3D models have to have similar spatial resolution. However, our target 3D models have definitely different spatial resolution. The 3D rock model, which is reconstructed from images captured close to the rock, has high spatial resolution. The 3D slope model, which is reconstructed from images captured away from the rock, has low resolution.

Since we generate the 3D model using Image-Based Modeling technique, the model has texture information. Thus, it is possible to calculate the alignment using the correspondence between the 3D models. Scale-Invariant Feature Descriptor (SIFT) (Lowe D.G., 1999) is well known as a method to detect correspondence between images by using an image feature description that robust to the appearance variation caused by rotation, scale and illumination fluctuation. However, if images are deformed by perspective projection, the matching accuracy of SIFT is significantly reduced. Although, there are other researches, which are motivated by SIFT, aim to improve the descriptive performance of image features (Rublee, E., et al., 2011.; Alahi, A., et al., 2012.), the perspective distortion problem is still unsolved.

In this paper, in order to solve the distortion problem, we focus on the property that an accurate 3D model having close to real shape and texture can generate arbitrary appearance. By rendering an image of rock similar as the appearance in a slope image, it is possible to estimate the corresponding points between the rendering rock-image and the captured slope-image. As the result, the 3D rigid transformation between two (i.e., rock and slope) 3D models can be estimated.

3. RECONSTRUCTING 3D MODELS OF ROCK AND SLOPE FROM MULTI-VIEW-IMAGES

3.1. Capturing Multiple-View Images of Rock and Slope

While capturing a rock, we get closer to the target rock and go around it, at the same time we record the orientation information of capturing pose. This information is used to merge 3D models of a rock and an environment. The required number of images to reconstruct the fine shape of the whole rock is about thirty at least; it is dependent on the size and complexity of the rock, though. To reconstruct the 3D model, the entire slope is also captured using multiple cameras. While capturing the slope, the target rock has to be observed at the center of the each captured multiple images so that the orientation information of capturing pose can be accurately acquired.

3.2. Reconstructing 3D Models of Rock and Slope

FIG. 2 shows the series of processes to reconstruct 3D model of a rock. A sparse point cloud is reconstructed by applying SfM to captured multiple-view images. By applying PMVS to the output of SfM, it is possible to increase the density of the point cloud. In order to execute the physical simulation, we need surface information of the 3D model. So, we reconstruct the surface information by applying PSR to the dense points cloud.

Since, multiple images capturing a rock have high spatial resolution because they are captured at close range to the real rock, the 3D rock model has an accurate shape and texture to the real one. On the other hand, multiple images capturing a slope have so low spatial resolution that the reconstructed 3D slope model has rough and uneven shape. Thus, we apply Laplacian smoothing (Nealen A. et al, 2006) to the 3D slope model

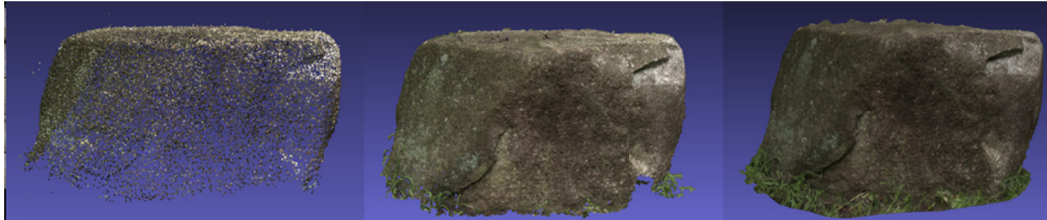


FIG. 2. Processing flow of reconstructing 3D model from multi-view images (left): Sparse points reconstructed by SfM, (center): Dense Points reconstructed by PMVS, (right): 3D model reconstructed by PSR.

3.3. Correspondence between Rock and Slope 3D Models

As discussed in Section 2, it is difficult to estimate a 3D rigid transformation matrix using ICP, due to the two problems, one is the significant difference in their spatial resolution, and the other is the difference in the appearance caused by perspective projection. We solve the first problem to find out corresponding points through 2D image processing instead of directly finding them on the 3D models. The second problem is solved by generating an appropriate appearance using the 3D rock model that has fine texture and shape information.

As showed in FIG. 3, if we put a virtual camera at beside a camera capturing the target slope, it is possible to render a virtual image using 3D rock model, in which the rendered appearance of the rock is similar as the real appearance in the image actually capturing the slope. In this situation, the virtual and real appearances of rock are almost same, so that correct corresponding points can be detected using image feature such as SIFT. However, the 3D position and orientation of a camera capturing the target slope are unknown. We solve this problem by a greedy approach. At first, we generate virtual images at various viewpoints. As the initial setting, we use positional information given by GPS (Global Positioning System). The orientation information given by an electronic compass is also used as the initial orientation. It is known that the measurement error of GPS is about 10m on average and the orientation information obtained by an electronic compass has a few degrees of error (Yun X. et al, 1999). Thus, we shift and swing the virtual camera within the error distribution and render the virtual appearance as shown in FIG. 4 (left). We rotate the virtual camera from -10 to 10 degree in y-axis and z-axis respectively and move the virtual camera from 0 to 5 to the direction away from the rock. We estimate the 3D position and orientation of the camera capturing the target slope by assuming that the virtual image, which put at the most appropriate 3D position and orientation among the variance, gives the maximum number of the matching points.



FIG. 3. An image of slope (left), A rendering image of 3D rock model (right)

3.4. Merging Reconstructed 3D Models

In order to calculate a 3D rigid transformation matrix, we need four corresponding points between the 3D rock models at least. Here, we estimate the 3D coordinate from the correspondences given in the previous section. Since the virtual image is generated using a 3D rock model, the 3D coordinate of the 2D matching points can be easily calculated.

As shown in FIG. 4 (right), we calculate 3D coordinate of the corresponding points of 3D slope model using ray casting. When the 2D matching point in the virtual image is (u, v) , the equation of a ray is given as follow.

$$\lambda \begin{pmatrix} u \\ v \\ 1 \end{pmatrix} = \mathbf{P} \begin{pmatrix} X \\ Y \\ Z \\ 1 \end{pmatrix} \quad (\lambda: \text{Constant scalar, } \mathbf{P}: \text{Transformation matrix}) \quad (1).$$

The equation is modified is

$$\lambda' \begin{pmatrix} X \\ Y \\ Z \\ 1 \end{pmatrix} = \mathbf{P}^* \begin{pmatrix} u \\ v \\ 1 \end{pmatrix} \quad (\lambda': \text{Constant scalar, } \mathbf{P}^*: \text{Pseudo-inverse matrix}) \quad (2).$$

Here, the 3D point on the 3D slope model is explained as 3D_obj (X, Y, Z) (3).

From the equation (2) and (3), the intersection (X, Y, Z) of the ray and the 3D model is obtained.

Generally, the transformation matrix to merge two models is calculated by using the N corresponding points between the 3D rock model and the 3D slope model. When corresponding points of 3D rock model are $\mathbf{X} = \{\mathbf{x}_1, \mathbf{x}_2, \dots, \mathbf{x}_N\}$ and the corresponding points of 3D slope model are $\mathbf{Y} = \{\mathbf{y}_1, \mathbf{y}_2, \dots, \mathbf{y}_N\}$, \mathbf{X} and \mathbf{Y} are expressed as follow by using a transformation matrix \mathbf{H} .

$$\mathbf{y}_i = \mathbf{H}\mathbf{x}_i \quad (i = 1, \dots, N), \quad \mathbf{H} = \begin{bmatrix} \mathbf{SR} & \mathbf{t} \\ \mathbf{0} & \mathbf{1} \end{bmatrix} \quad (4)$$

The Matrix \mathbf{S} is expressed as $\mathbf{S} = s\mathbf{I}$ by using a unit matrix \mathbf{I} and the scaling factor s . It is possible to obtain the factor s by comparing a distance between two points in the corresponding points. After obtaining a center of gravity of the point X and points Y , a translation vector \mathbf{t} is calculating by taking the difference between the Euclidean distance of the two points. A rotation matrix \mathbf{R} is obtained by singular value decomposition (Kanatani K., 1994).

Finally, by calculating the rigid transformation matrix from the corresponding points, it is possible to locate 3D rock model on the 3D slope model.

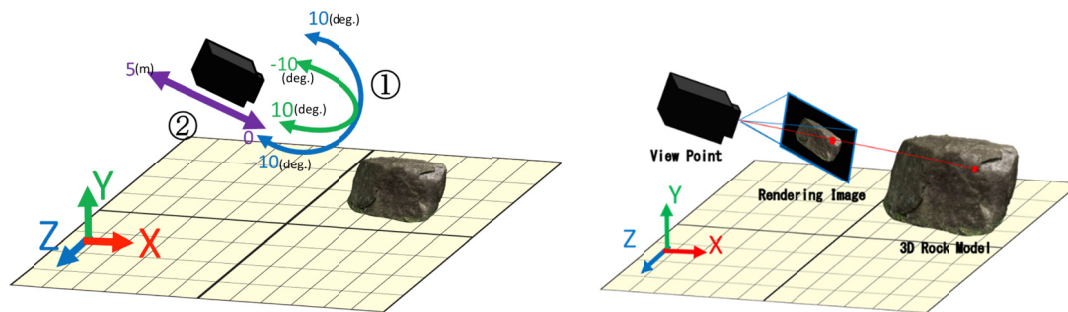


FIG. 4. Variation of virtual camera's position and orientation (left), Calculating 3D coordinate by ray casting (right).

4. EVALUATION OF ACCURACY OF RECONSTRUCTED 3D MODELS

4.1. Estimation of Scaling Factor Using a Square Pyramid

In order to estimate a scaling factor of the 3D reconstruction, a square pyramid, which the size is known, is captured with a target rock together. This square pyramid is composed of four equilateral triangles (one side is 0.5m). We attach textures to get many image features on each surface (Metaio, 2014) (Krystian Mikolajczyk, 2014) to improve the accuracy of the 3D reconstruction.

4.2. Evaluation of Accuracy of Reconstructed 3D Models

We conducted an experiment of measuring the scale of the 3D model around University of Tsukuba in Japan. Images which have 3,456 pixels \times 2,592 pixels resolution were captured by using RICOH CX2. As FIG. 5 (left) shows, the square pyramid was located near Rock A and Rock B. The number of images capturing Rock A is 52 and Rock B is 32. FIG. 6 shows captured images and reconstructed 3D models. When the average of the four Euclidean distances from the apex to the vertex of the base of 3D model is 0.5m since the real length is 0.5m, the scale of reconstructed 3D model can be measured.

FIG. 5 (right) shows the position where we measure the actual size. Table 1 shows the result of scale measurement of the generated 3D models comparing with the actual size. As Table 1 shows, the average error is 8.29×10^{-3} m and the max error is 1.50×10^{-2} m. From this result, we see that the 3D model can be reconstructed close to the actual size.

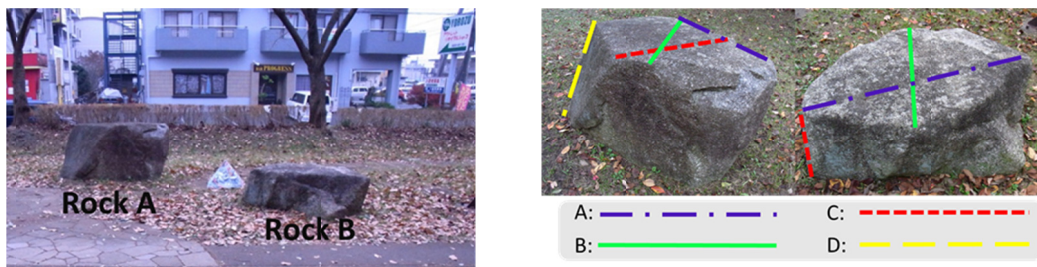


FIG. 5. Spatial relationship among rocks and a quadrangular pyramid (left), We measure the actual size at 7 spots (right).

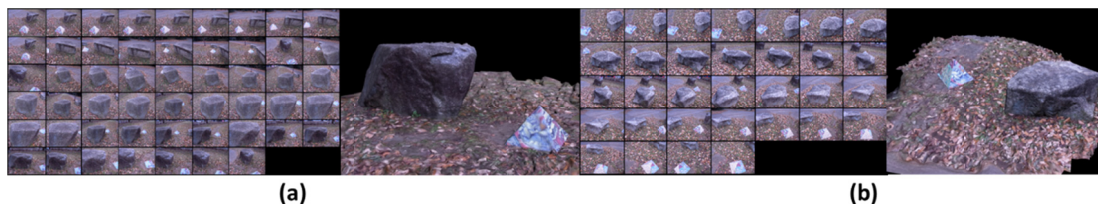


FIG. 6. Multiple-view images of two rocks and the reconstructed 3D models.

Table 1. A result of scale measurement of 3D models comparing with actual size.

	Measured Position	Scale of 3D model [m]	Actual size [m]	Error [m]
RockA	A	1.134	1.137	3.00×10^{-3}
	B	1.225	1.223	2.00×10^{-3}
	C	0.8770	0.8620	1.50×10^{-2}
	D	0.8500	0.8650	1.50×10^{-2}
RockB	A	1.3950	1.384	1.10×10^{-2}
	B	0.7800	0.7740	6.00×10^{-3}
	C	0.4260	0.4320	6.00×10^{-3}

4.3. Evaluation of Alignment accuracy of 3D Models

We captured images of a slope to reconstruct the 3D model, and merged the 3D models with the 3D models of Rock A and Rock B generated in Section 4.2. 162 images of the slope that had $3,456 \text{ pixels} \times 2,592 \text{ pixels}$ resolution were captured with RICOH CX2. FIG. 7 (left) shows the reconstructed 3D slope model. The orientation information is obtained by an electronic compass at same time. While rendering a virtual image, the camera’s position and orientation captured from 92 degree are applied to the initial position of the viewpoint. FIG. 7 (right) shows a result of merging 3D models after calculating rigid transformation matrix from the obtained corresponding points. The number of the corresponding points of Rock A and Rock B is 52 and 60, respectively.

When the apex of the square pyramid is A and the each vertex of the base is B, C, D and E, Table 2 shows the position error of the pyramid included in the 3D rock model and the pyramid included in the 3D slope model. As Table 2 shows, we confirmed 3D models of Rock A and Rock B is precisely merging with an error of about 7.35cm and 10.5cm on average, respectively.

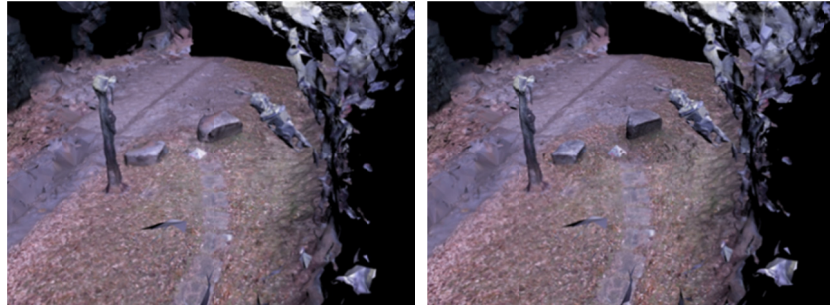


FIG. 7. Result of merging 3D rock model and 3D slope model (left: before merging, right: after).

Table 2. Error of quadrangular pyramid's position after merging two models..

Rock A		Rock B	
Measured Position	Error [cm]	Measured Position	Error [cm]
A	10.9	A	13.0
B	4.40	B	8.54
C	5.34	C	12.4
D	11.9	D	10.0
E	4.22	E	8.70

5. EXPERIMENTS AT ACTUAL LANDSLIDE SITE

We capture multiple images of rocks and slopes at actual some rock fall sites to reconstruct 3D model and merge two models. The location of capturing experiments is Syosenkyo in Yamanashi city, Kofu prefecture of Japan. The 29 images of a roc were captured using CANON EOS 5D MarkII with 5,616 pixels \times 3,744 pixels resolution. A movie of slope was shoot at frame rate of 60 fps using SONY FDR-AX1 and captured at a frame with 3840 pixels \times 2160 pixels resolution. 169 frames of the movie were used to reconstruct 3D slope model. FIG. 8 shows the images captured at the site and the reconstructed 3D models.



FIG. 8. Multiple-view Images and the reconstructed 3D models at Syosenkyo ((a): rock, (b): slope).

6. ROCK FALL SIMULATION USING RECONSTRUCTED 3D MODELS

As a physics engine for rock fall simulation, we use Bullet physics (Bullet Physics Library, 2014) that is one of the most popular open source library. The result of the Bullet Physics is drawn using OpenGL. We set density of 3D space as $2,500\text{km}/\text{m}^3$, coefficient of dynamic friction to 0.35 and coefficient of restitution to 0.4 (Japan Road Association, 2000). In simulating, 3D model of slope whose mass is zero is static rigid body and that of rock is dynamic rigid body. We use a PC (DELL Studio XPS) to

reconstruct 3D model and simulate rock fall, which is installed the following elements, CPU:3.07[GHz](Intel Core i7), GPU:NVIDIA GeForce GTS 240).

FIG. 9 shows a result of rock fall simulation by using 3D models reconstructed from images captured at Syosenkyo and merged. We also simulated rock fall by using sphere and cube that has a comparable size. The each trajectory of the center of gravity is drawn with white, red and green line to make easily understand the trajectory of CG objects.

As the simulation result, we confirm 3D rock model's motion of flying-jumping, sliding and tumbling on the 3D slope model (white line) is completely different from the one of sphere (red line) and cube (blue line) model as shown in FIG. 9. Thus, we confirmed the shape of rock was important parameter that determined fall path in simulation with physics engine.

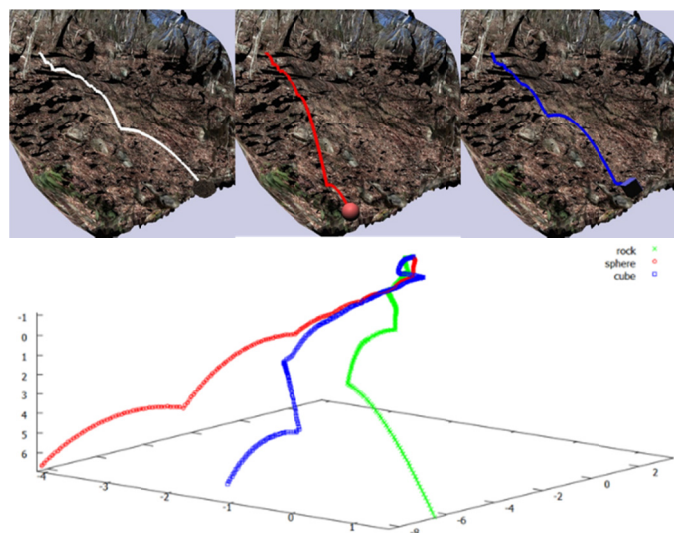


FIG. 9. A result of rock fall simulation using CG objects (From left to right: 3D rock model (a plot of 3D trajectories (green)), Sphere (red), Cube (blue)).

CONCLUSIONS

We proposed a method to simulate rock fall by using 3D model reconstructed from multiple-view images. By detecting the correspondence between the models of rocks and a slope utilizing free-viewpoint image technique, we can merge two 3D models. In addition, we realized a rock fall simulation without modeling a motion of flying-jumping, sliding and tumbling. In the experiment, we confirmed that the shape of generated 3D models and the alignment of 3D rock and slope models are enough accurate for conducting on rock fall simulation.

ACKNOWLEDGMENTS

We are grateful to Keiichi Ohta, Yasumasa Tanaka and Yuji Hasegawa of Nippon Kouei Corporation who cooperated to the experiment in this paper.

REFERENCES

Alahi, A., et al., (2012). Freak: Fast retina keypoint. Computer Vision and Pattern Recognition (CVPR), Rhode Island, America, pp. 510-517.

- Besl, P.J., McKay, N.D., (1992). A Method for Registration of 3D Shapes. IEEE Transactions on Pattern Analysis and Machine Intelligence, Vol.14, No.2, pp.239-256.
- Bullet Physics Library, (2014), <http://bulletphysics.org/wordpress/>
- Charalambous, S. and Sakellariou, M., (2008). GIS-Based Rockfall Hazard Assessment in Support of Decision Making. Laboratory of Structural Mechanics School of Rural and Surveying Engineering, National Technical University of Athens. Athens, Greece.
- Chen, Y., Medioni, G., (1992). Object modeling by registration of multiple range images. Image and Vision Computing, Vol.10, No.3, pp.145-155.
- Christen, M. et al, (2012). Integral hazard management using a unified software environment: numerical simulation tool" RAMMS" for gravitational natural hazards. 12th Congress INTERPRAEVENT, Grenoble, France, pp. 23-26.
- Curless, B., (2000). From Range Scans to 3D Models. ACM SIGGRAPH Computer Graphics, Vol.33, No.4, pp.38-41.
- Furukawa, Y., Ponce, J., (2009). Accurate, Dense, and Robust Multi-View Stereopsis. IEEE Transactions on Pattern Analysis and Machine Intelligence, Vol. 32, No. 8, pp. 1362-1376.
- Japan Road Association, (2000). Handbook of preventatives against rock falls. Maruzen, Japan. (in Japanese)
- Kanatani, K., (1994). Analysis of 3-D rotation fitting. IEEE Trans. on Pattern Analysis and Machine Intelligence, Vol. 16, No. 5, pp. 543-549.
- Kazhdan, M., et al, (2006). Poisson surface reconstruction. Symposium on Geometry processing, pp.61-70.
- Krystian Mikolajczyk Homepage, (2014), <http://lear.inrialpes.fr/people/mikolajczyk/>
- Lowe D.G., (1999). Object recognition from local scale invariant features. The proceedings of the Seventh IEEE International Conference on Computer Vision, Vol. 2, pp.1150-1157.
- Metaio Homepage, (2014), <http://www.metaio.com/research/>
- Nealen, A., (2006). Laplacian mesh optimization. ACM SIGGRAPH, pp. 381-389.
- Nguyen, H.T. et al, (2011). Use of terrestrial laser scanning for engineering geological applications on Volcanic rock slopes an example from Madeira Island (Portugal). Natural Hazards and Earth System Sciences, Vol.11, pp.807-817.
- Rublee, E., et al., (2011). ORB: an efficient alternative to SIFT or SURF. International Conference of Computer Vision (ICCV), Barcelona, Spain, pp. 2564-2571.
- Snavely, N. et al, (2006). Photo tourism: Exploring photo collections in 3D. ACM SIGGRAPH Transactions on Graphics, Vol.25, No.3, pp.835-846.
- Stock, G.M. et al, (2011). High-resolution three-dimensional imaging and analysis of rock falls in Yosemite Valley. California Geosphere, Vol.7, No.2, pp.573-581.
- Tomasi, C., Kanade, T., (1992). Shape and motion from image streams under orthography: a factorization method. International Journal of Computer Vision, Vol.9, No. 2, pp. 137-154.
- Yun, X., et al, 1999. Testing and evaluation of an integrated GPS/INS system for small AUV navigation. Oceanic Engineering, IEEE Journal, Vol.24, No.3, pp.396-404.

**Analysis of Shear Zones of Landslides by the Numerical Simulation of Monitored
Surficial Displacement Vectors—
Case Study of the Landslide at Gunung Pass, Malaysia**

Senro Kuraoka, Ph.D., P.E.¹; Naoki Sakai, Ph.D.²; Mohamad Nazri³; Suhaimi
Jamaludin⁴; and Che Hassandi Abdullah, Ph.D.⁵

¹Chief Engineer, Nippon Koei Co., Ltd., Tsukuba Ibaraki, Japan. E-mail: a4982@n-koei.co.jp

²Senior Researcher, National Research Institute for Earth Science and Disaster Prevention, Tsukuba, Ibaraki Japan. E-mail: nsakai0505@gmail.com

³Senior Researcher, Slope Engineering Branch, Ministry of Works, Malaysia.

⁴Principal Assistant Director, Slope Engineering Branch, Ministry of Works, Malaysia.

⁵Director, Slope Engineering Branch, Ministry of Works, Malaysia.

Abstract: Planning and designing countermeasures for a specific landslide require geotechnical and geological investigations of the landslide area. In particular, assessment of the extent of unstable zones and/or sliding surfaces of the landslide is essential for designing countermeasures. While borehole logging is the effective way to identify the sliding surface and shear zones, installation of the drilling systems can be prohibiting, depending on the accessibility and budgetary conditions. Past research, on the other hand, suggests that the surficial displacements may be utilized to estimate the shear zones. This paper presents the predictive analysis of the subsurface shear zone of the landslide along the highway passing the north mountain range of Malaysia. A marked failure occurred in 2003, followed by gradual continuous movements that have been monitored by 17 reflective prisms and the two total stations. No bore logging has been performed, and therefore, sliding surfaces are not well known. For the purpose of estimating the depth profile of the sliding surface, directions and magnitudes of the displacement vectors have been examined and subsequently numerical analysis of the displacement vectors was performed. The monitored displacements were reproduced by stepwise strength reduction, which yielded a band of cumulative shear failure zone that may represent the potential sliding surface.

INTRODUCTION

Assessment of the extent of unstable zones and/or sliding surfaces of the landslide is essential not only for designing structural countermeasures but also for estimating the impact of the failure. While borehole logging is the effective way to identify the sliding surface and/or the shear zone between the unstable and stable zones, installation of the drilling systems can be prohibiting, depending on the accessibility, size of the landslide, and budgetary conditions. Past research, on the other hand, suggests that the surficial displacement vectors, obtained by total stations and/or Global Navigation Satellite System (GNSS), may be utilized to estimate the shear zones (PWRI, 2013).

This paper presents the predictive analysis of the subsurface shear zone of the landslide in Gunung Pass area which is located roughly 170 km north of the capital, Kuala Lumpur located at the 44th kilometer of the Simpang Pulai – Kuala Berang Highway of Malaysia (Figure 1). In this paper, the terms ‘shear zone’ and ‘sliding surface’ are interchangeably used. The latter term implies a highly sheared zone with formation of slickenside surface, whereas the former term implies a band of area undergoing shear deformation. It is not known which of these qualitative descriptions fit the condition of this landslide, since no borehole logging has been performed.

A marked failure occurred in 2003, followed by gradual continuous movements that have been monitored by 17 reflective prisms and the two total stations. In this research work, trends of the magnitudes and directions of the displacement vectors of the prisms have been assessed and subsequently numerical simulation of the measured displacement was performed in order to estimate the depth and shape of the shear zone. The monitored displacements were reproduced by stepwise strength reduction computation, yielding a band of cumulative shear failure zone that may represent the potential sliding surface. The results are expected to be useful in planning the borehole loggings and early warning method.

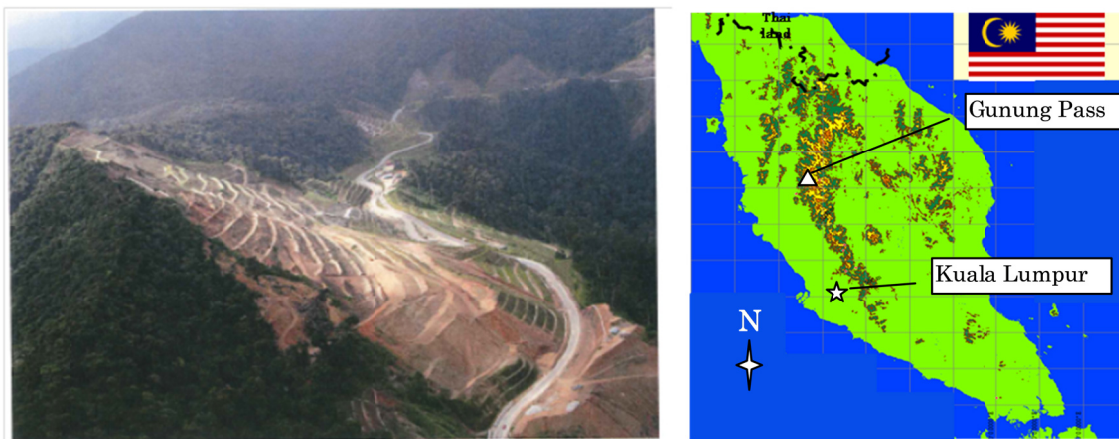


FIG. 1. View and location of the cut slope along the 44th kilometer of the Simpang Pulai – Kuala Berang Highway of Malaysia.

GEOLOGICAL FEATURES OF THE LANDSLIDE

The landslide at Gunung Pass area is 190 m high and 300 m wide with slope gradient of approximately 34 degrees (Andrew Malone Ltd, 2006 and Malone et al. 2008). The rocks of the Gunung Pass area consists of metasedimentary rocks, which have been highly deformed with metamorphism during the late Paleozoic (Suhaimi et al., 2008). The outcrops visible on the slope surface indicate that the main rock types are quartz mica schist, graphite schist, and phyllite. The rocks are grouped into two units: the central and upper part of the slope consists of the quartz mica schist, whereas the lower part of the slope along the road consists of graphite schist. The quartz mica schist shows fine micaceous foliations. The graphite schist outcrops along the road, showing fine interlayers of phyllite, quartz mica schist, and some thin micaceous quartzite.

There are three markedly large faults, designated as A, B, and C in Figure 2, that extends across the landslide, striking NS and dipping 65 to 75 degrees towards the east. The foliations of the schist tend to dip at around 18 degrees towards east, striking 335 degrees in average from North (Othman et al., 2006). Other predominant discontinuity sets were identified by the past field investigation as indicated in Table 1, where the strike is in degrees from North. Othman et al. (2006) proposed that joint sets, J2 and J3, are affecting the stability and movements of the landslide. As illustrated in the stereonet in Figure 2, however, J2 is dipping against the direction of slide and therefore combined effect of these two joint sets needs further assessment.

Table 1. Average Strike and Dip of the Discontinuities (Othman et al., 2006)

Discontinuity set	Central area of the main landslide (CH 23+900 – CH24+000) Strike/Dip (degrees)	Remarks
J1	115/75	Faults, major joints
J2	335/18	Foliations
J3	170/40	Faults and/or major joints
J4	210/75	Major joints and/or localized faults
J5	22/42	Joints

MOVEMENTS OF THE LANDSLIDE

Comparative analysis of photographs, taken by the helicopter in 2005, and the As-Built survey in 2003 was performed (Andrew Malone Ltd., 2006 and Malone et al. 2008). Movements of approximately 150 objects, such as the berm edges and drainage structures, were identified to estimate the displacement vectors. The relative size of the vectors indicated by line segments in Figure 2 is proportional to the magnitude of the horizontal displacement components. The numbers above the line segments and the contour indicate the magnitude including the vertical components. The vectors tend to be perpendicular to the topographic contour and the magnitude of the displacement decreases from the head scarp towards the road. No obvious effects of the faults, A, B, and C on the direction of displacement vectors can be seen. The displacement vectors are also superposed on the central cross section, using the horizontal and vertical components (Figure 3). The vectors near the head scarp are dipping at steep angles and tend to become gentle near berm 11, where compressive outward movements were observed in 2003(Andrew Malone Ltd., 2006).

Currently, two total stations, installed in 2007, are automatically monitoring hourly displacements of 17 prisms. The time variation plots of these displacements were made from 1st January, 2008 to 4th November 2014. As an example, the displacement of prism VP8 is shown in Figure 4 together with the daily rainfall of the site, where the displacement is the combined magnitude of the horizontal and the vertical components and it is the incremental value since 1st January, 2008. Figure 4 shows that the displacement rate tends to increase during the rainy seasons; it is several mm per month during the dry period and increases to approximately 10 mm during the rainy period.

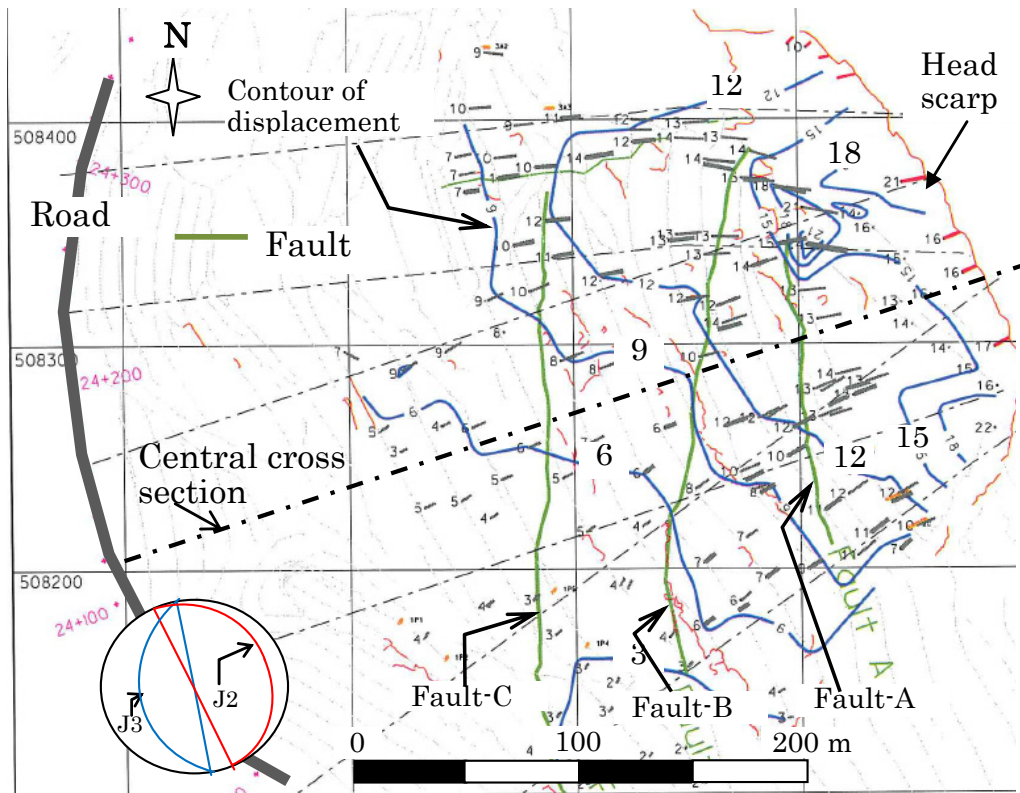


FIG. 2. Plan view of displacement vectors (grey line segments). Numbers above the lines indicate magnitude in meter and the dark blue lines are the displacement contour, ranging from 18 m to 3m (Andrew Malone Ltd., 2006).

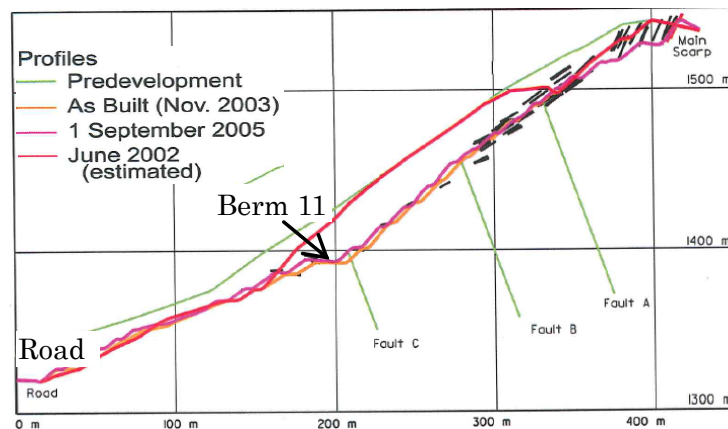


FIG. 3. Displacement vectors (back line segments) estimated by photogrammetry are plotted the on central cross section (Figure 2). The displacements near the head scarp are between 16 m to 18 m (Andrew Malone Ltd., 2006).

The displacement vectors of the prisms were calculated, using the horizontal incremental components from 1st January, 2008 to 4th November 2014 except P14 to P21 which start on March 27, 2008. As shown in Figure 5(a), the resulting vectors are magnified by 20 times and superposed on the digital elevation map (DEM) with 5 m contour interval. The actual magnitude of VP14 in Figure 5(a) and (b) is 2.6 m. As were

shown in Figure 2, the vectors tend to orient perpendicular to the topographic contour, showing no obvious effects of the faults A, B, and C on the direction of movements.

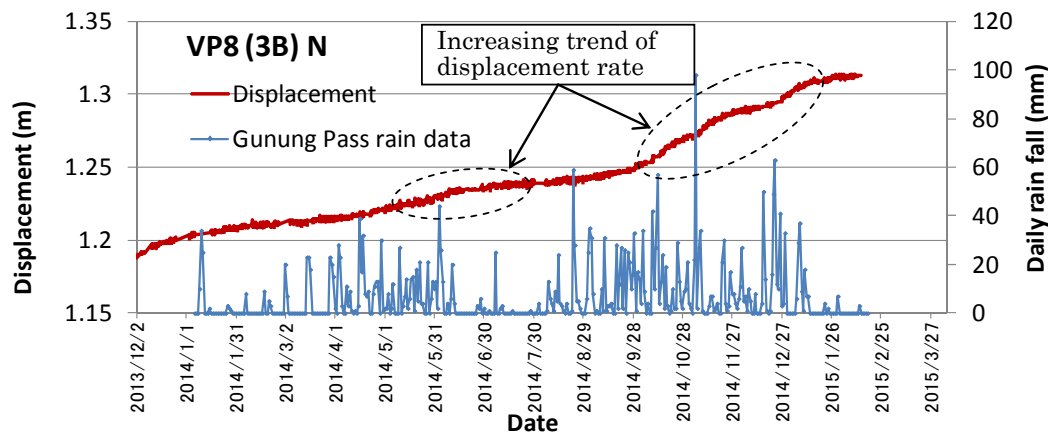


FIG. 4. An example of the displacement (VP8) obtained by the total station.

The cross section adjacent to prisms VP14, VP8, VP9, and VP11 was defined in order to assess the dipping trend of the vectors and also to be used as the cross section for the two dimensional numerical simulation. The displacement vectors of these four prisms are magnified by 20 times and superposed on the cross section, using the horizontal and vertical components (Figure 6(b)). Figure 6(b) indicates that, except VP14, the vectors tend to become smaller and more horizontal towards berm 11. However, VP14, below berm 11, shows relatively large displacement, which is different from the trend shown in Figure 2 and 3, i.e., the displacements during 2003 and 2005 tend to become small towards berm 11. Additional field investigation was performed on 13th April, 2015 in order to examine the cause of relatively large displacement at VP14. A distinct cleavage was found on the ground surface near VP14, indicating that VP14 is being affected by the localized surficial failure (Figure 5). Hence, it is inferred that the landslide mass, that is inducing the displacements of VP11, VP9, and VP8, is different from the localized landslide that is reflected by the displacements of VP14. These results imply that, while the shear zone of the landslide that occurred in 2003 may have been enlarging, it has not extended throughout the slope and the compression zone still exists near berm 11.

ESTIMATION OF SHEAR ZONE WITH MEASURED DISPLACEMENTS

Past research suggests that depth and shape of the shear zone or the sliding surface may be estimated, for preliminary assessment purpose, if sufficient surficial displacement vectors are obtained, noting that surficial vectors tend to be parallel to the dip of the segment of the sliding surface as illustrated in Figure 7(a) (PWRI, 2013).

Theoretical study has been performed to use a system of quadratic equations to approximate the sliding surface (PWRI, 2013). The landslide mass is divided into slices by the vertical line placed at the midpoint between the origin of two adjacent vectors. Then systems of simultaneous equations are derived for each slice section, assuming that the tangent of the quadratic equation evaluated at the coordinate directly below surficial vector is equal to the gradient of the surficial vectors. This method, however, suffers from erroneous solutions, yielding wavy sliding surfaces, when there are too

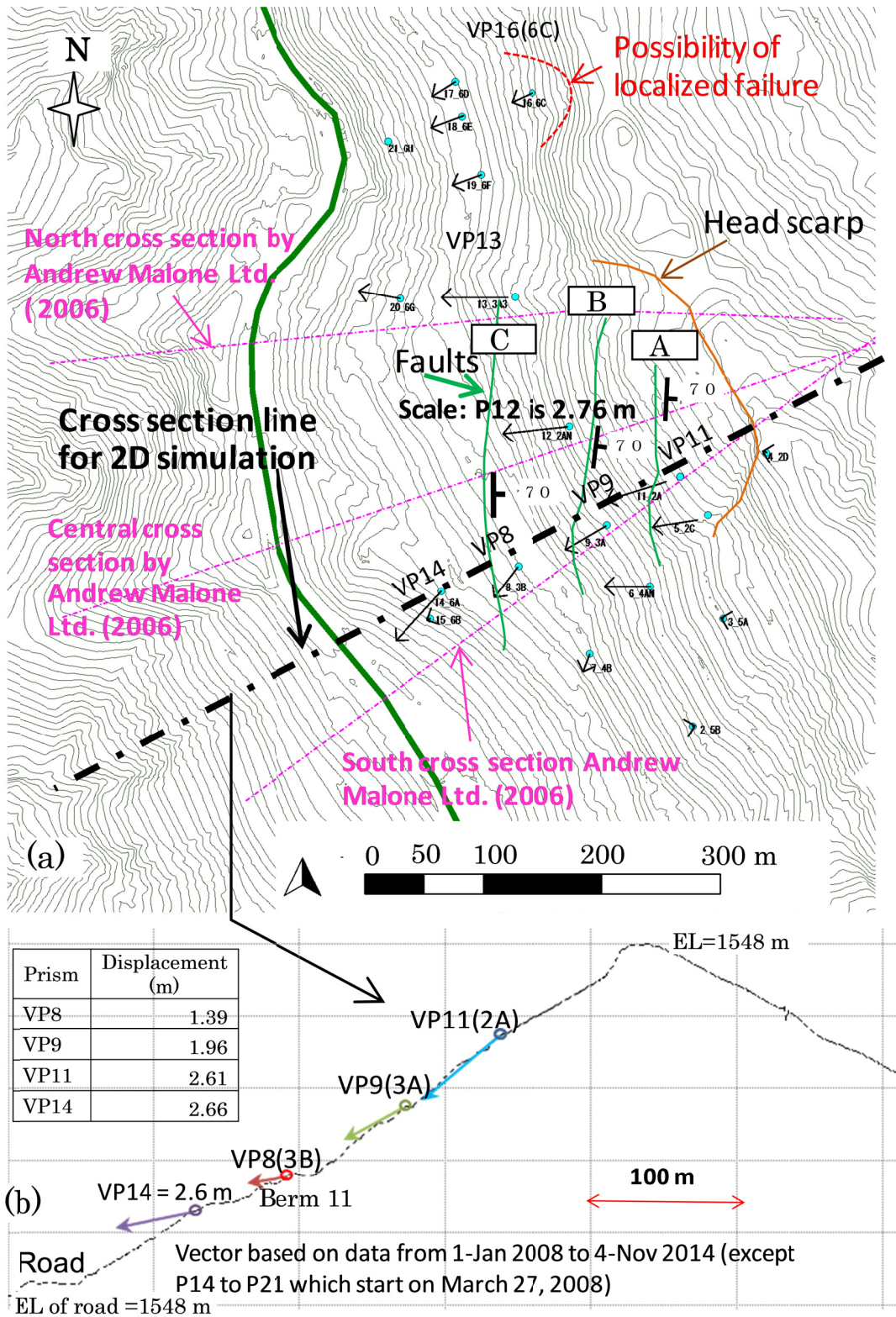


FIG. 5. Displacement vectors of reflecting prisms; (a) vectors using horizontal components (elevation contour interval at 5 m), (b) vectors on cross section adjacent to prisms VP14, VP8, VP9, and VP11.

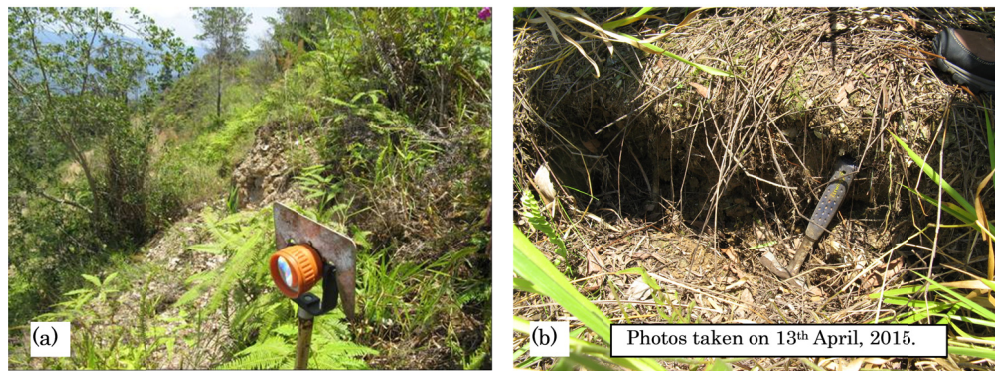


FIG. 6. (a) Reflecting prism VP14 in the front and the localized surficial failure shown in the back. (b) Distinct cleavage approximately 1 m behind VP14.

many vectors or when the direction of the vectors are not consistent with the assumed quadratic function.

A simple graphical method is also proposed (PWRI, 2013). In this graphical method, landslide is divided into slices as mentioned above. A linear line, parallel to the surficial vector of the corresponding slice, is drawn from the head scarp or the cleavage up to the boundary of the slice (Figure 7(b)). Subsequent lines are drawn in a similar fashion. If the final line that intersects the surface does not agree with the observed distress found at the toe of the landslide, the same procedure will be repeated, starting from the end point of the toe of the landslide up to the head of the landslide (PWRI, 2013). Then, as shown in Figure 7(b), the final line is drawn from the head scarp to the mid-point of the ascending and descending curves and finally connected to the end point at the toe. This procedure is applied in this research to estimate the sliding surface for partitioning the weak zone where shear failure zone is assumed to occur.

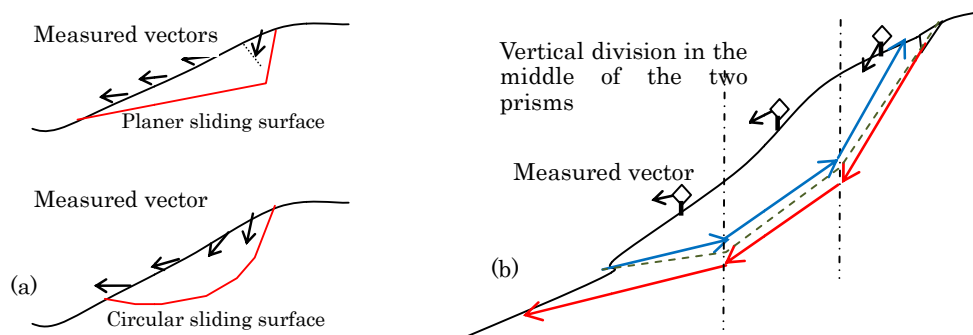


FIG. 7. (a) Examples of patterns of displacement vectors in case of planer sliding surface and circular surface, (b) Illustration of the graphical method to estimate the sliding surface.

As will be explained in the section titled ‘Numerical simulation of the monitored displacements’, the monitored displacements were simulated by progressive shear failure: the shear strength of the upper layer, assumed to be weak and prone to development of landslide, was reduced to induce shear failure zone. Hence, the modeled upper layer had to be made deeper than the potential sliding surface, in order to eliminate the effects of the boundary between the upper and lower layers on the generation of shear failure zone. For this purpose, the sliding surface was graphically

estimated before making the numerical model. As shown in Figure 8, the estimated depth of the sliding surface is between 25 to 30 m. The upper layer of the numerical model was made thick enough with reference to the results shown in Figure 8.

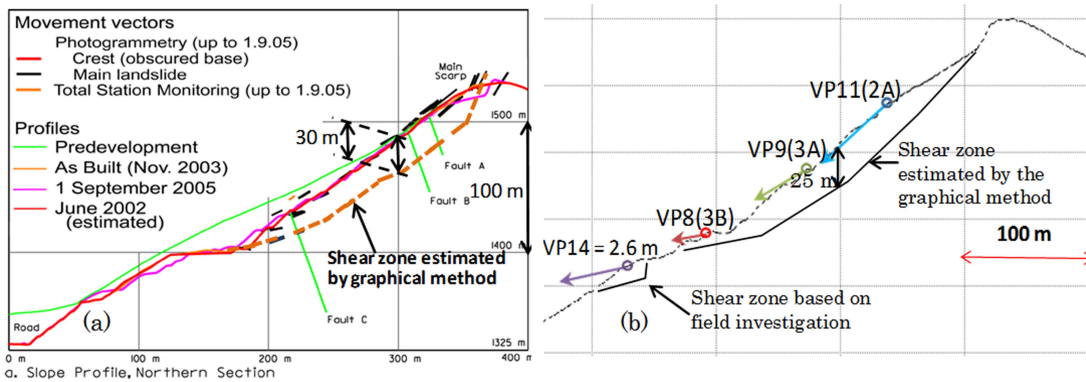


FIG. 8. Shear zones drawn by the graphical method: (a) drawn with the displacement vectors which were obtained by the photogrammetry in 2005, (b) drawn with the vectors obtained by total station from 2008 to 2014.

ASSESSMENT OF MECHANICAL PROPERTIES BY ROCKMASS CLASSIFICATION

Mechanical properties of the rock mass were assessed to estimate the input properties for the numerical simulation. The elasto-plastic model with Mohr-Coulomb yield function was adopted for the numerical simulation, which requires density, cohesion, angle of internal friction, elastic modulus, and Poisson’s ratio. These properties, except the density and the Poisson’s ratio, were estimated by the Geological Strength Index (GSI), (Hoek et al. 1997). Field investigation was performed in April of 2015 to evaluate GSI. Observation of the outcrops and surficial materials above berm 11, indicate that the rock mass falls within the GSI category of ‘Disintegrated’ or ‘Foliated/laminated’ with surface condition of either ‘Fair’ or ‘Poor’. An example is shown in Figure 9.

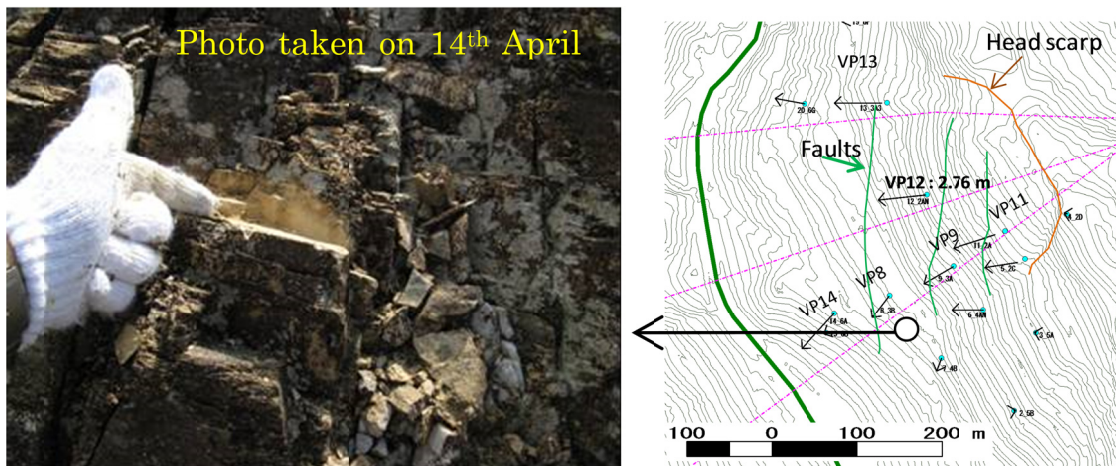


FIG. 9. Example of moderately weathered schist classified as ‘Disintegrated’ and ‘Fair’ to ‘Poor’ surface condition, giving GSI between 20 to 30.

Mechanical properties were calculated, using the equations given by Hoek et al. (1997). The equations require Hoek and Brown constant, m_i , and the uniaxial compression strength (σ_i) of intact rock pieces. Other parameters, m_b , s , and a , of the Hoek-Brown failure criterion for jointed rock mass are computed with m_i and GSI. The constant, m_i , is set to 8, based on the table of m_i given for different types of rock (Hoek et al, 1997). The uniaxial compressive strength of intact rock piece is set to 5 MPa, using the table that gives ranges of σ_i with respect to degree of weathering and the strength characterized by blow of geological hammer (Hoek et al. 1997). The unit weight of the rock mass was set to 24 kN/m³ which is on the lower side of the range of representative values for schist (Look, 2014). The Poisson's ratio was set to 0.3, which is an estimate for highly fractured rock given by Look (2014). The other parameters, m_b , s , and a were calculated with the equations given by Hoek et al. (1997).

Summary of the mechanical properties and parameters are given in Table 2 for GSI between 10 and 30. The properties for the simulation were varied from high to low strengths, shown in Table 2, in order to find the properties that can reproduce the trends of the measured displacements.

Table 2. Possible Ranges of GSI and Corresponding Properties

GSI	Hoek and Brown constant		Uniaxial compressive strength (MPa)	Cohesion (kPa)	Internal friction angle (degrees)	Elastic modulus (kPa)
	For intact rock piece m_i	Jointed rock mass m_b				
30	8	0.66	5	82	34	700,000
25	8	0.55	5	61	33	530,000
20	8	0.46	5	49	30	400,000
15	8	0.38	5	40	27	300,000
10	8	0.32	5	31	24	220,000

NUMERICAL SIMULATION OF THE MONITORRED DISPLACEMENTS

Numerical simulation of the measured displacement from 2008 to 2014 was performed in order to estimate the depth and shape of the shear zone that is likely formed between the moving mass and the stable bed rock.

Simulations were performed by the numerical simulation code, UDEC, which is a widely used code for simulation of landslides and rock tunnels (e.g., Jaboyedoff et al. 2012). Although UDEC may be classified as the distinct element method, which is a method to model assemblies of rigid blocks and/or particles, UDEC has the option to discretize the block by finite difference elements such that the block is deformable and stresses and strain distributions within the block can be obtained.

The predicted shear zones along the boundary of the deforming mass and the stable area are identified by the stretch of high maximum shear strain zones and the boundary along which the displacements become negligible relative to those in the deforming zone. These cumulative strains and displacements are produced by stepwise strength reduction, which represents, effects of material degradation and also apparent effects of reduction in effective stress as water pressure increases. The effects of water pressure could not be directly modeled, since ground water level is not measured.

The block and the finite difference mesh are generated, using the cross section along the line shown in Figure 6(a). The mesh is comprised of triangular elements, varying in the size from 5 m to 10 m. The mesh is generated up to the axis of assumed symmetry shown in Figure 10(b), where the mesh is partitioned into upper and lower layers. The thicknesses of the upper layer vary between 40 m to 50 m so that the boundary between the upper and lower layers will be deeper than the potential sliding surface which is was graphically estimated as shown in Figure 8. The left side boundary of the mesh is generated up to origin of the horizontal axis.

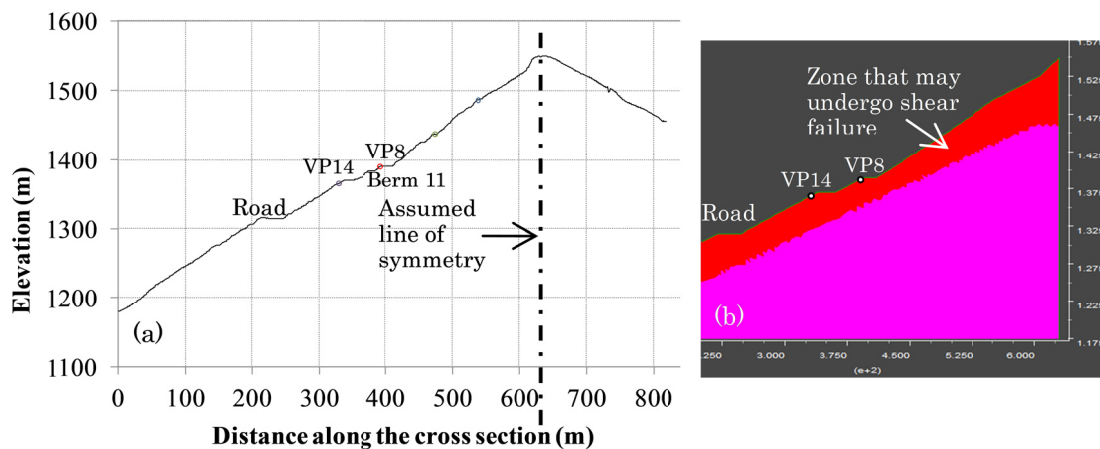


FIG. 10. (a) Cross section along the line shown in Figure 6 and the partitioned zones where different mechanical properties are set based on GSI, (b) Mesh for the simulation is generated up to the line of symmetry.

The simulations were performed without setting discrete joint models, noting that the mechanical properties based on GSI include the effects of joints and foliation. The shear strengths of the upper layer were gradually reduced from the high values to low values in Table 2, whereas the lower layer was kept as an elastic material with elastic modulus of 8 GPa which is calculated with GSI of 60 and uniaxial compression strength of 25 MPa that is for medium strength rock (Hoek et al. 1997).

Although the simulated displacements near VP8 are smaller than the measured displacement, the trend of the measured displacement is reasonably reproduced, when cohesion and internal friction angle were reduced to 49 kPa and 28 degrees, respectively (Figure 11(a) and (b)). It is also noted that steep and distinctively large displacements are generated near the head of the model, implying that mechanisms of the head scarp is successfully simulated. No convergence was reached when the angle of internal friction is further reduced to 27 degrees, which corresponds to GSI of 15. Consequently, the simulations suggest that GSI of the landslide mass is about 20.

The thickness of the deforming area is approximately 30 m which is close to the graphically estimated thickness (Figure 11(c)). Hence, it is confirmed that modeled thickness of the upper layer was adequate such that the simulated displacements are not influenced by the boundary between the two layers.

The band of high maximum shear strain is the zone where the shear failure tends to concentrate and is regarded as the potential sliding surface (Figure 11(d)). The maximum shear strain is pronounced near the head, indicating the formation of scarp.

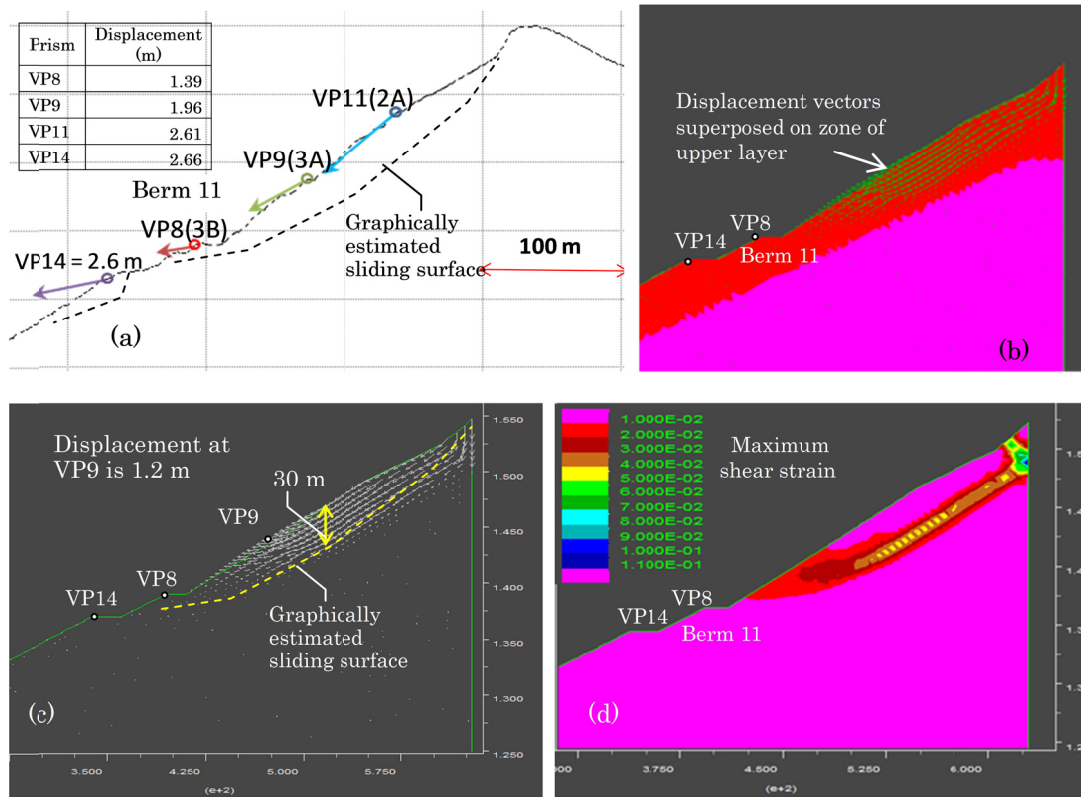


FIG. 11. (a) Cross section that shows the displacement measured from 2008 to 2014, (b) Simulated displacement superposed on the model mesh, (c) Simulated displacement vector due to reduction in strengths, (d) maximum shear strain generated by reduction in shear strengths.

CONCLUSIONS

The numerical simulation, without directly modeling discrete joints, was not only successful in reproducing the measured displacement but also showed distinct trend of steep and large displacement at the head scarp, indicating that the estimated mechanical properties are within the possible range of actual values. The strengths properties, back calculated from the simulation were found comparable to those obtained by GSI, suggesting that GSI can be a practical method in estimating mechanical properties at the preliminary stage of investigation. It is, however, recommended that reliability of the mechanical properties, obtained by GSI, be examined by monitoring and subsurface exploration as a second stage of investigation.

The depth profiles of the sliding surface are consistent among those obtained by the graphical method and the numerical simulations, suggesting that the sliding surface may have actually formed at the depth around 30 m and may be gradually expanding. Future investigation with borehole loggings will help confirm the state of the sliding surface and the ground water, which in turn will provide valuable data for further analysis in planning the methods for early warning and control works.

ACKNOWLEDGMENTS

Authors wish to express sincere appreciation for the support provided by the SATREPS project which is jointly managed and financed by the Japan Science and Technology Agency (JST), and the Japan International Cooperation Agency (JICA).

REFERENCES

- Andrew Malone Ltd. (2006). "Final report Landslide Study at Ch 23+800 to Ch 24+460, Simpang Pulai – Lojing Highway." Unpublished.
- Hoek, E and Brown, E.T. (1997). "Practical estimates of rock mass strength." *International Journal of Rock Mechanics and Mining Sciences*, Vol. 34, No 8: 1165-1186.
- Jaboyedoff, M., Derron, M., Jakubowski, J., Oppikofer, T., and Pedrazzini, A. (2012). "The 2006 Eiger rockslide, European Alps. " *Landslides Types, Mechanisms and Modeling* Cambridge University Press: 282-296.
- Look, B.G. (2014). "Handbook of Geotechnical Investigation and Design Tables." Second Edition, Balkema Book.
- Malone, A.W., Hansen, A., Hencher, S.R., and Fletcher, C.J.N. (2008). "Post-failure movements of a large slow rock slide in schist near Pos Selim, Malaysia." *Proceedings of the 10th International Symposium on Landslides and Engineered Slopes*, Xi'an, China: 457–461.
- Othman, M.A, Low, T.H., Jamaluddin, T.A. and Komoo, I. (2006). "Characteristics of a geological controlled landslide at the Simpang Pulai – Blue Valley Road." *Proceeding of International Conference on Slopes, Malaysia*: 75-88.
- PWRI (2013). "Cooperative Research Report of PWRI." No.451, January 2013, in Japanese.
- Suhaimi Jamaldin, Kamal Bharin Jaafar, Che Hassandi Abdullah and Ashaari Mohamad (2008). "Landslide warning system for Mount Pass, Malaysia Based on surface monitoring technique." *Proceeding of International Conference on Management of Landslide Hazard in the Asia-Pacific Region*: 354-365.

Design of Stable Rock Slopes for the World's Highest Railway Bridge

Gaurav Tiwari, Ph.D.¹; and Gali Madhavi Latha, Ph.D.²

¹Ph.D. Student, Dept. of Civil Engineering, Indian Institute of Science, Bangalore, India. E-mail: gaurav@civil.iisc.ernet.in

²Associate Professor, Dept. of Civil Engineering, Indian Institute of Science, Bangalore, India. E-mail: madhavi@civil.iisc.ernet.in

Abstract: Stability analysis of the two abutment slopes of a railway bridge proposed at about 359 m above the ground level, crossing a river and connecting two huge hillocks in the Himalayas, India, is presented in this paper. The rock slopes are composed of highly jointed rock mass and the joint spacing and orientation are varying along the elevation of the slopes. Geological mapping was carried out to characterise discontinuities present along different elevations of the slopes. Rock mass present along both the slopes was classified using rock mass rating (RMR) and geological strength index (GSI). Strength and deformation properties of intact rock and rock mass were estimated using different laboratory tests, in-situ tests and empirical relations. Since, the slope sections support bridge piers, bearing capacity was estimated with the help of in-situ tests and various empirical and analytical relations. Global stability and stability of individual sections of slopes were checked using different methods i.e. finite element, stereographic projections and wedge failure analysis. It was observed that slopes were globally stable however there was a possibility of wedge failure at some slope sections. Suitable rock anchors were installed at unstable slope sections. In addition to the stability analysis of the slopes, various challenges encountered during excavation and stabilisation of the suggested slope profile such as transportation of rock mass debris without allowing it to fall into the river and slope monitoring is discussed.

INTRODUCTION

A railway line is being laid in Jammu and Kashmir, India and this line is crossing the river Chenab at a height of about 359 m. A bridge is proposed at the site and once completed; this will be the world's highest railway bridge at present. The bridge connects two big hillocks of Himalayas, forming a deep gorge in a V shaped valley in this area. Among the 18 piers of the bridge, 4 piers (S10-S40) are resting on left abutment and the other 14 piers (S50-S180) are resting on right abutment. One of the important challenges of the project is the stability of abutment slopes during and after the construction. The section of the bridge and abutments along with the foundations that could affect the stability of the slope is given in Fig 1. Figure 2 shows the designer's view of the Chenab bridge.

Stability of rock mass slopes is primarily governed by the number of joint sets, joint orientations, joint shear strength, depth and steepness of the excavated slope face and its orientation with reference to the orientation of the joints. These parameters govern the failure mode of the rock slopes like circular failure, planar failure, wedge failure and toppling failure. Hence, stability analysis of a rock slopes is very complex and there is a need of using different methods for analysing the stability of slopes.

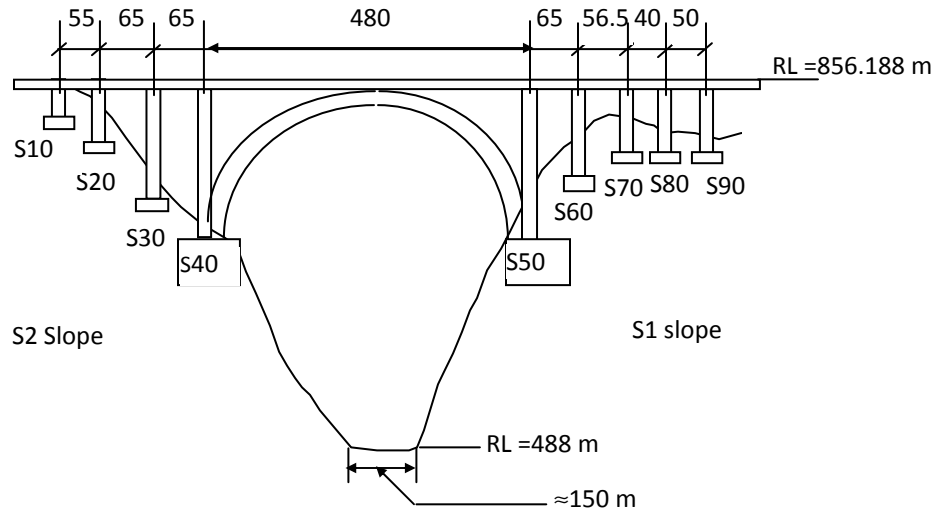


FIG. 1. Bridge details and section of the gorge with pier foundations along the slope



FIG. 2. Designer's view of the Chenab railway bridge

Different techniques have been developed over the years such as limit equilibrium method, numerical techniques (continuum and discontinuum) like finite element, discrete element, finite difference which made possible the analysis of the rock slopes with complex geometries and having variable material properties. Eberhardt et al. (2004) investigated the concept of progressive failure and the numerical modelling of rock mass strength degradation in natural rock slopes using the Ranada rockslide as a working example. Gurocak et al. (2008) performed stability analysis of rock slopes at a dam site in Turkey using finite element analysis. Latha and Garaga (2010a) and Latha and Garaga (2010b) performed static and seismic stability analyses of Himalayan rock slopes using an equivalent continuum approach incorporated in the finite difference based numerical program FLAC. Kanungo et al. (2013) performed stability analysis of some Himalayan slopes using finite element and limit equilibrium methods. Pain et al. (2014) analysed the stability of some blocky rock slopes using the finite element method.

Though the number of studies on jointed rock slope stability are numerous, every case study on this topic is unique because of the varying rock types and unique structural features present in them. The importance of the lifeline project being built on the Chenab slopes and the size of it make the case of rock slope stability at this site unique and extremely crucial. Stability analysis of the rock slopes supporting Chenab bridge piers under static and seismic conditions is presented in this article.

GEOLOGY OF THE SITE

Intensive geological investigation was carried out at the site which included mapping of joints and their structural and geomorphological features. The area of the study comes within the sub-Himalayan zone, with outcrops of unfossiliferous limestone, Sirban limestone of Hazara of presumably Permian or Permo-Carboniferous/Meso-Proterozoic age as inliers. The river Chenab forms about 350 m deep gorge in a V-shaped valley in this area. Major rock types in the area are dolomitic limestone with different degrees of fracturing; boulders of dolomitic limestone, brecciated limestone and siliceous limestone. Since, the pier locations are expected to be much deeper than the exposed rock surface, drifts and pits were excavated along different elevations of slopes for joint mapping. A total of 2 drifts and 8 pits were excavated at the site along different elevations of the slopes. Several boreholes were also drilled to explore the subsurface and to obtain samples for geotechnical testing.

Quantitative description of discontinuities such as orientation, persistence, roughness were estimated using ISRM suggested methods (ISRM, 1981). Around 1000 discontinuities were measured along the slopes using drifts, pits and exposed surface and dominant joint sets were obtained using stereographic projections. Joint mapping results yielded that the strata are characterised by three major discontinuities. One sub-horizontal and two sub-vertical joints were present at the site. The sub-horizontal joint set was named J1 while the other two joint sets were named J2 and J3. Few random joints were also present along both the slopes. The attitudes of the discontinuities along both the slopes are given in Tables 1 and 2. Since the joint attitude was varying with the slope elevation, slopes were divided into different zones on the basis of varying joint orientations. Fig. 3 shows the left and right abutment slopes and the zones created based on joint orientations. Within a specific zone, the orientations of different joints remain the same. In this figure, S1 and S2 represent right and left abutment slopes respectively and A1-J1 and A2-J2 represent various slope sections that constitute the slopes. All joint sets were found to be highly persistent. J1 joint set was closely spaced while spacing of J2 and J3 was varying from very close to wide. Joint surfaces were rough with tight to open aperture. Joints J1 and J3 were occasionally filled with clay gouge and calcic material. The lithological conditions of rock and discontinuities were more or less similar along both the slopes. Because of the variation in rock mass fracturing a range of RMR and GSI values were obtained. The estimated range of the RMR and GSI is given in Table 3.

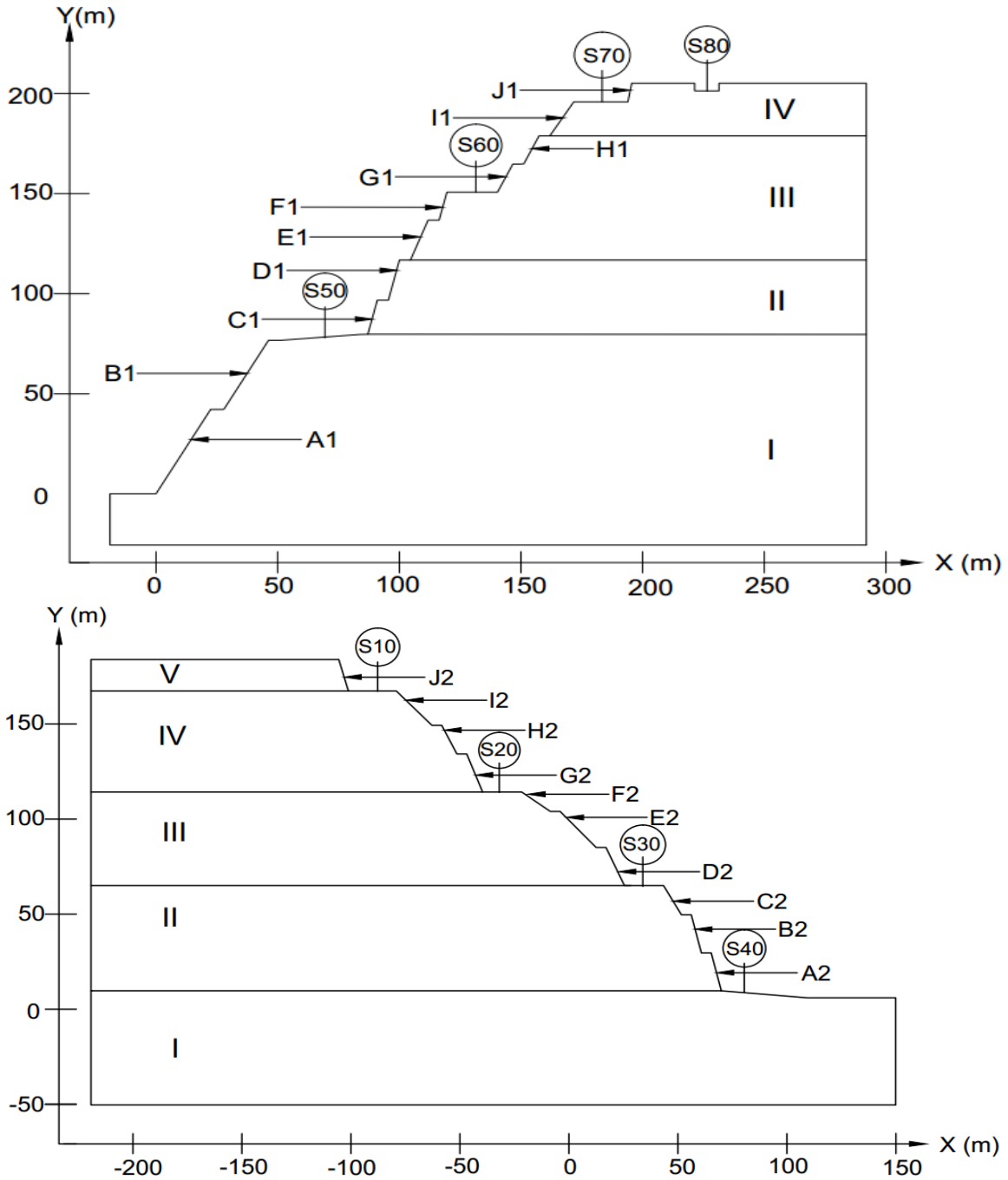


FIG. 3. Abutment slopes with the zones based on joint orientations

TABLE 1. Dip and Dip Directions of Joint Sets along Slope S1

Joint Set	Dip/Dip Direction (degrees)			
	I	II	III	IV
J1	52/N038	41/N053	38/N048	47/N067
J2	48/N242	48/N235	56/N240	47/N244
J3	63/N149	71/N152	70/N153	71/N131

TABLE 2. Dip and Dip Directions of Joint Sets along Slope S2

Joint Set	Dip/Dip Direction (degrees)				
	I	II	III	IV	V
J1	30/N021	15/N072	23/N072	33/N056	24/N070
J2	70/N236	74/N260	73/N273	67/N246	69/N247
J3	67/N170	74/N162	76/N160	75/N157	73/N152

TABLE 3. Rock Mass Classification

Classification System	Rating Range		Average rating	
	S1	S2	S1	S2
GSI	31-49	32-49	40	41
RMR	35-58	41-59	46	50

PROPERTIES OF ROCK

Properties of intact rock were obtained through laboratory testing of intact rock samples collected from boreholes on both abutment slopes. Average values of these properties for slopes S1 and S2 used for the present study are given in Table 4. Hoek and Brown constant i.e. m_i for the intact rock was assumed to be 9 (Hoek, 2000).

TABLE 4. Properties of Intact Rock for Slopes S1 and S2

Slope	Unit weight γ (kN/m ³)	Poisson's ratio ν	Uniaxial compressive strength σ_{ci} (MPa)	Deformation modulus E_i (GPa)	Hoek-Brown parameter m_i
S1	27.620	0.15	115	65	9
S2	27.270	0.18	110	68	9

For the determination of deformation modulus of the rock mass, three types of in-situ tests i.e. cyclic plate load tests, dilatometer tests and MASW (Multi-channel Analysis of Surface Waves)

tests were performed, since laboratory test results for the rock mass is not considered to be appropriate because of the reduced sample size with fewer discontinuities (Bieniawski, 1978; Palmstrom and Singh, 2001). Additionally, deformation modulus was also estimated from Roclab (Rocscience, 2013) software based on the uniaxial compressive strength, GSI and E_i . Since the values obtained from Roclab were very close to the minimum in-situ value obtained from plate load test, deformation modulus obtained from Roclab was used for the analyses and the same is presented in Table 4. Hoek- Brown strength parameters m_b and s_b for the rock mass were estimated using Roclab. These parameters were estimated using minimum GSI values. Rock mass properties estimated are given in Table 5. Properties of the rock mass was varying with the elevation in slope S1 and this spatial variation in rock mass properties was considered in the analysis, as shown in Table 5. Bearing capacity of the rock mass was estimated using cyclic plate load tests, empirical relations and numerical analyses and by comparing the results and using engineering judgement, a final value of 1 MPa was considered.

TABLE 5. Properties of Rock Mass for Slopes S1 and S2

Slope	Unit weight γ (kN/m ³)	Poisson's ratio ν	Deformation Modulus E_m (GPa)	Hoek-Brown Parameters	
				m_b	s_b
S1 (Below S60)	27.095	0.20	10.40	0.766	0.0005
S1 (Above S60)	25.860	0.20	7.36	0.333	0.0009
S2	26.752	0.20	11.62	0.793	0.0005

STABILITY ANALYSIS OF SLOPES

Stability analysis of the slopes has been carried out using finite element based software Phase² (Rocscience, 2014a) to analyse the global stability of the slopes under static and seismic conditions. 3-noded triangular elements were used to discretise the slopes. Bottom boundary was kept fixed and the roller boundary conditions were used along the lateral boundary. Hoek–Brown failure criterion was used as the strength criterion. Residual strength was assumed to be the same as peak strength i.e. perfectly plastic behaviour has been assumed. Absolute energy criterion was used as the convergence criterion with a tolerance value of 0.1 % (Kanungo et al., 2013). For the stability analysis of slopes under design basis earthquake conditions, pseudo-static analysis was carried out with horizontal and vertical seismic coefficients 0.18 and 0.12 respectively, which were obtained from site specific ground response analysis. According to Hoek and Brown (1997) and Akgun et al. (2014) it is important in any rock slope stability analysis to assess if the orientation of the existing discontinuity sets could lead to the block instability i.e. planar failure, wedge failure, toppling failure. This can be efficiently assessed by stereographic projections. Hence, kinematic analysis has been carried out at each slope sections and possibility of any such failure has been assessed using DIPS (Rocscience, 2014c).

RESULTS AND DISCUSSION

Stability of the slopes was determined by the factors of safety as well as the deformations of the slope at different locations. *Factor of safety* as per the shear strength reduction (SSR) technique (Matsui and San, 1992) in the numerical models is defined as the factor by which the original shear strength parameter is divided in order to bring the slope to the verge of failure. Stability analysis has been carried out under static and seismic conditions. Summary of the factors of safety and deformations for both slopes under static and seismic condition are given in Table 6. Factors of safety were higher than the target factors of safety of 1.50 and 1.20 for static and design basis earthquake conditions respectively. Deformations obtained were small which fall under little or no ground adjustment failure category (Idriss, 1985). It can be concluded from the factors of safety and deformations obtained from numerical analysis that the slopes were globally stable under both static and seismic conditions and there is no need of reinforcement for both the slopes, considering global stability.

TABLE 6. Summary of Results from Equivalent Continuum Analyses

Condition	Factor of safety		Maximum displacement (mm)		Maximum shear strain ($\times 10^{-3}$)	
	S1	S2	S1	S2	S1	S2
Static	2.04	2.12	10.00	6.30	1.40	1.10
DBE	1.67	1.79	15.50	14.50	4.00	1.70

DBE = Design basis earthquake

Kinematic analysis revealed that there was no possibility of any type of block instability along slope S2. However, it was observed that there is a possibility of wedge failure along some sections of slope S1. Stereographic projections and also field observations showed that wedges were forming along the slope S1 with the combination of J1 and J3 joint sets. Further, wedge failure analysis was carried out for all the slope sections of S1 using limit equilibrium based software SWEDGE (Rocscience, 2014b) under static and design basis earthquake (DBE) conditions. Potential wedge failures that could possibly occur in each individual slope sections were determined from this analysis. A combination analysis was performed by entering the attributes of all the three joint sets depending on their location in a particular zone. Shear strength parameters for the joint infill were assessed through laboratory testing and the estimated values of cohesion and friction angle used for the analysis were 0 kPa and 40° respectively assuming that the infill shear strength is equal to joint shear strength. Since, it was not possible to analyse the stability of several wedges formed by the individual combination of joints, stability analysis of the wedge formed by the average joint attributes for each set at different pier locations was performed. It was observed that the least stable wedges are forming at the locations between S50 and S60 foundations (slope sections C1 and D1 in Fig. 3). Factors of safety under static and dynamic conditions obtained for wedges at some locations are lower than the target value of factor of safety, indicating the need for slope reinforcement. Summary of the Swedge analysis is provided in Table 7.

TABLE 7. Summary of Wedge Failure Analysis for Slope S1

Slope Section	Joint Dip/Dip direction (degrees)			Factor of Safety	
	J1	J2	J3	Static	DBE
A1	52/038	48/242	63/149	1.33	0.97
B1	52/038	48/242	63/149	1.33	0.97
C1	41/053	48/235	71/152	1.27	0.92
D1	41/053	48/235	71/152	1.27	0.92
E1	38/048	56/240	70/153	1.50	1.08
F1	38/048	56/240	70/153	1.50	1.08
G1	38/048	56/240	70/153	1.50	1.08
H1	38/048	56/240	70/153	1.50	1.08
I1	47/067	47/244	71/131	-	-
J1	47/067	47/244	71/131	-	-

REINFORCEMENT DESIGN

It was clear from the equivalent continuum modelling that both the slopes are stable and there is no need of reinforcement, considering global stability of slopes. However, stereographic projections and SWEDGE analysis showed that unstable wedges are forming at some locations along slope S1. To avoid wedge failures, both the options of slope flattening and providing rock anchors were considered. Wherever the flattening required to avoid wedge formation was less, slopes were flattened. In all other places, rock anchors were suggested to provide stability against wedge failures. Maximum anchor forces required to achieve target factors of safety under both static and seismic conditions were obtained from SWEDGE analysis. This anchor force was then distributed among the rock bolts using suitable spacing. Anchors are provided in such a way that the desired anchor force is distributed in the area of the wedge, whose co-ordinates and dimensions were obtained from the SWEDGE analysis. Field Pull-out tests were carried out on rock anchors to obtain the pull-out capacity of the rock anchors. Prestressed cable anchors were provided to the required capacity to avoid wedge failure. For the slope S2, since no wedges were forming, nominal reinforcement of 32 mm diameter bolts at 2.5 m spacing was suggested as an additional measure to withstand any surficial failures, considering the importance of the project.

The rock bolts designed using Swedge for slope S1 and nominal reinforcement for slope S2 were installed in Phase2 model. Two types of rock bolts were used - end-anchored and fully bonded. An End Anchored bolt is represented as a 1-D deformable element whose interaction with the finite element meshes is through the endpoints only (Rocscience, 2014a; Wang and Garga, 1992). Fully bonded bolt is modeled by a series of 1 -D deformable elements joined end to end (Rocscience, 2014a; Wang and Garga, 1992). Details of different types of bolts used for the analysis are given in Table 8. Equivalent continuum analysis was carried out on both the slopes with bolts installed in place and the results are presented in Table 9. While there was minimal effect of reinforcement on the global stability of slope S2, some effect on the factor of safety was observed on slope S1. This could be attributed to the fact that the bolts used on slope S1 are longer when compared to those used on slope S2, especially near the toe. Displacement contours for reinforced slopes under static case are shown in Fig. 4 and Fig. 5.

TABLE 8. Properties of Rock Bolts






Bolt No.	Rock Bolt Representation	Bolt Type	Diameter (mm)	Length (m)	Peak Load (MN)	Prestress (MN)
1		End-anchored	32	4.0	0.08	0.02
2		End-anchored	32	11.5	0.23	0.05
3		End-anchored	40	22.6	0.64	0.64
4		Fully-bonded	32	21	0.40	0.00
5		End-anchored	40	30	0.64	0.64

TABLE 9. Factors of safety and maximum displacements for unreinforced and reinforced slopes

Condition	Factor of safety				Maximum displacement (mm)			
	Unreinforced		Reinforced		Unreinforced		Reinforced	
	S1	S2	S1	S2	S1	S2	S1	S2
Static	2.04	2.12	2.24	2.12	10.00	6.30	7.00	6.36
DBE	1.67	1.79	1.76	1.83	15.50	14.50	15.00	12.00

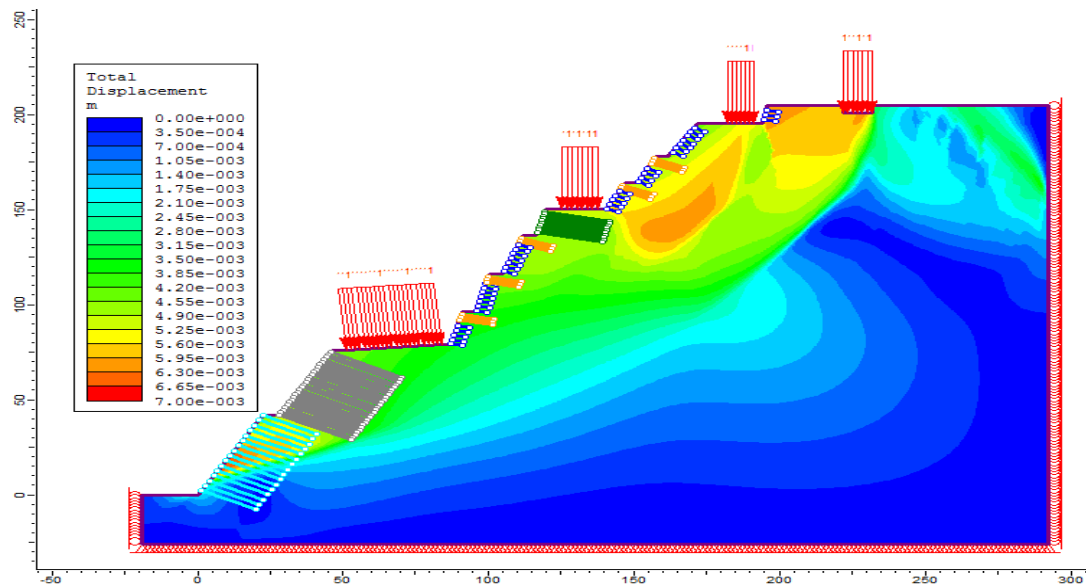


FIG. 4. Displacement contours for reinforced slope S1 under static condition

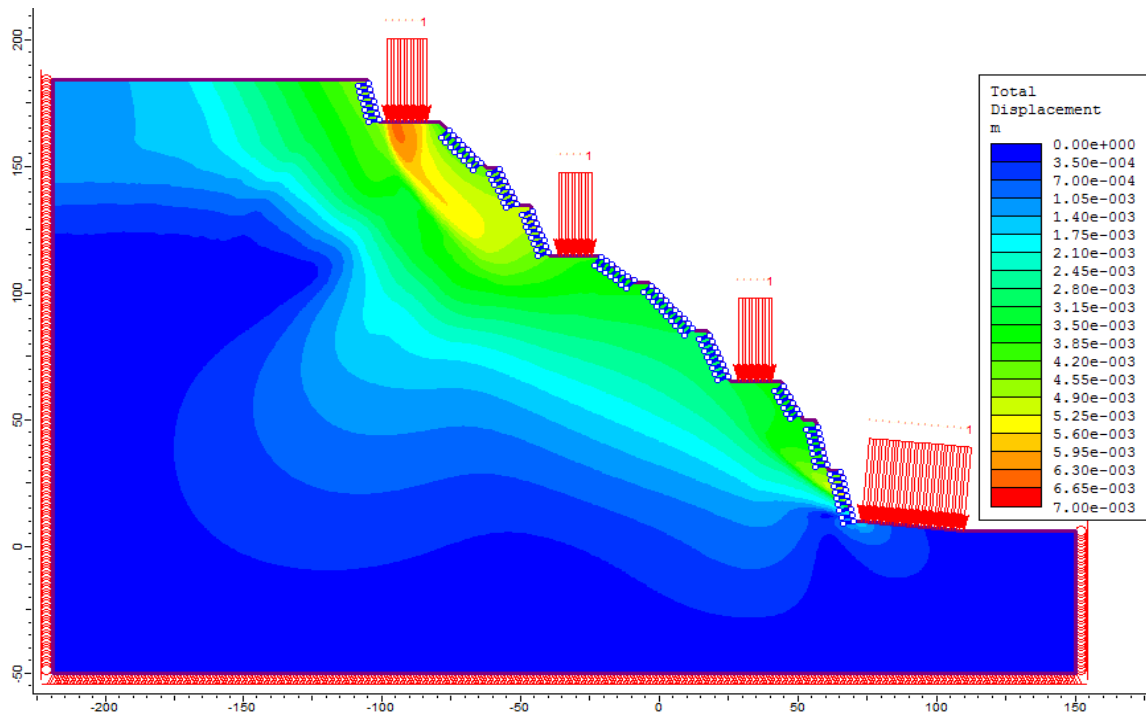


FIG. 5. Displacement contours for reinforced slope S2 under static condition

FIELD MONITORING

The project is under progress and the slope sections are being carefully cut to the required dimensions, without disturbing the strata around. Rock bolts are being installed and to improve the structural effectiveness of rock bolts and also to provide safer working conditions, particularly from rock fall, steel fiber reinforced shotcrete of 100 mm thickness with minimum fibre content of 35kg/cum was recommended and being adopted in the construction. The function of shotcrete is to prevent raveling of zone of fractured rock.

As the excavations are on the slope and river Chenab flowing near the foothill, protecting the river from the falling debris is of high priority. Hence catch trenches were provided to prevent the falling of loose boulders into the rivers. Muck deposited in these trenches is transported to the dump yard created further down the slope, far from the slope profile. Since dump yards are on slope, fencing was provided along the boundary to arrest the falling of excavated muck into the river. Construction of slope S2 as per the recommended reinforcement layout is complete and construction of slope S1 is in progress. A photograph of the completed slope S2 is shown in Fig. 6. Wedges were observed during slope cutting and the rock bolts installed along the slope stabilized these wedges, without any structural collapse. Deformations of the slope at all the points are being continuously monitored using total station and these deformations are well within the values predicted by the numerical analysis.



FIG. 6. Completed slope S2

8. SUMMARY AND CONCLUSIONS

Stability analysis of two rock slopes supporting a railway bridge under construction is presented in this paper. Different methods were used to analyse the stability of slopes under static and seismic conditions. It was observed that the slopes were globally stable with higher factors of safety than the required. However, unstable wedges were identified through stereographic projections and wedge failure analyses, which necessitated rock reinforcement. Anchor force required to stabilize these wedges at different locations was obtained from wedge analysis and the same is provided in the form of rock bolts, whose type and length was designed based on the requirements for any specific slope section. It was observed that the global factor of safety was not significantly affected with the provision of bolts. Construction of slope sections is being monitored continuously.

REFERENCES

- Akgun, H., Serkan, M. and Mustafa, K.K. (2014). "Geotechnical investigations and preliminary support design for the Geçilmez tunnel: A case study along the Black Sea coastal highway, Giresun, Northern Turkey." *Tunn. Undergr. Space Technol.* 40: 277-299.
- Bieniawski, Z.T. (1978). "Determining rock mass deformability: experience from case histories." *Int J Rock Mech Min Sci.* 15(5): 237-247.

- Eberhardt, E., Stead, D. and Coggan, J.S. (2004). "Numerical analysis of initiation and progressive failure in natural rock slopes—the 1991 Randa rockslide." *Int J Rock Mech Min Sci.* 41(1): 69-87.
- Gurocak, Z., Alemdag, S. and Zaman, M.M. (2008). "Rock slope stability and excavatability assessment of rocks at the Kapikaya dam site, Turkey." *Eng Geol.* 96 (1-2): 17–27.
- Hoek, E. (2000). "Practical rock engineering." Balkema, Netherlands.
- Hoek, E. and Brown, E.T. (1997). "Practical estimates of rock mass strength." *Int J Rock Mech Min Sci.* 34(8): 1165–1186.
- Idriss, I.M. (1985). "Evaluating seismic risk in engineering practice." *Proc. 11th Int. Conference on Soil Mechanics and Foundation Engineering*, Vol. 1, Balkema, Rotterdam: 265-320.
- IS 1893 (2002). "Criteria for earthquake resistant design of structures." *Indian Standard Code by Bureau of Indian Standards.* New Delhi, India.
- ISRM (1981). "Rock characterization, testing and monitoring." *ISRM Suggested Methods.* Pergamon Press, New York.
- Kanungo, D.P., Pain, A. and Sharma, S. (2013). "Finite element modeling approach to assess the stability of debris and rock slopes – a case study from the Indian Himalayas." *Nat Haz.* 69(1): 1–24.
- Latha, G.M. and Garaga, A. (2010a). "Seismic stability analysis of a Himalayan rock slope." *Rock Mech Rock Eng.* 43(6): 831–843. Latha, G.M. and Garaga, A. (2010b). "Stability analysis of a rock slope in Himalayas." *Geomech and Eng.* 2(2): 1-16.
- Matsui, T. and Sam, K.C. (1992). "Finite element slope stability analysis by shear strength reduction technique." *Soils Found.* 32(1): 59–70.
- Pain, A., Kanungo, D.P. and Sarkar, S. (2014). "Rock slope stability assessment using finite element based modelling—examples from the Indian Himalayas." *Geomech and Geoeng.* 9(3): 1-16.
- Palmstrom, A. and Singh, R.B. (2001). "The Deformation Modulus of Rock Masses - Comparisons Between In Situ Tests and Indirect Estimates." *Tunn. Undergr. Space Technol.* 16(3): 115 – 131.
- Rocscience (2013). "RocLab Version 1.033. Rock Mass Strength Analysis Program using the Hoek–Brown Failure Criterion." *Rocscience Inc. 31 Balsam Ave., Toronto, Ontario, Canada.*
- Rocscience (2014a). "Phase2 Version 8.020, Finite Element Analysis for Excavations and Slopes." *Rocscience Inc. 31 Balsam Ave., Toronto, Ontario, Canada.*
- Rocscience (2014b). "SWEDGE version 6.003, 3D surface wedge analysis for slopes." *Rocscience Inc. 31 Balsam Ave., Toronto, Ontario, Canada.*
- Rocscience (2014c). "Dips version 6.015, graphical and statistical analysis of orientation data." *Rocscience Inc. 31 Balsam Ave., Toronto, Ontario, Canada.*
- Wang, B. and Garga, V.K. (1992). "A numerical model for rock bolts." *Proc. Intl. Conference on Rock Support in Mining and Underground Construction*, Vol. 1, Balkema, Rotterdam: 57-66.

Development of a Landslide Observation System Using ZigBee Wireless Communication Technology

Y. Kawamura, Ph.D.¹; H. Jang, Ph.D., P.E.²; K. Ohta, P.E.³; and Y. Inagaki, P.E.³

¹Univ. of Tsukuba, Tsukuba, Ibaraki, Japan. E-mail: kawamura@iit.tsukuba.ac.jp

²Curtin Univ., Kalgoorlie, WA, Australia.

³Nippon Koei Co., Ltd., Tsukuba, Ibaraki, Japan.

Abstract: Extensive area of Japan is subjected to threats of potential landslides as roughly 70 percent of Japan consists of a steep mountainous terrain and moreover numerous artificial hill slopes are developed in residential areas. While various types of structural counter measures have been developed and successfully implemented in Japan, significant numbers of areas remain unprotected. Hence, non-structural measures, such as hazard maps and early warning systems, are required to minimize risks. One of the key technologies of the early warning system is the automatic detection system for landslides. In this research, we are developing an automatic detection system for landslides using ZigBee wireless communication technology. A general ZigBee-compliant platform made by Hitachi Co. Ltd. was customized and used in the constructing the wireless landslide detection system. The developed system monitors various environmental data, such as 3-axes acceleration, temperature, humidity, and illumination intensity. It was verified that all measured parameters except humidity were measured properly at an actual slope site with the proposed system.

INTRODUCTION

Japan is prone to landslides because of its geomorphological, geological, climatic and geographical conditions. Not only the public infrastructures but also numerous residential areas are subjected to threats of landslides. Unfortunately, it requires significant time and budgets to protect all these areas. Therefore, it is necessary to develop economical automatic detection system that can be readily installed in extensive areas in order to enhance the early warning systems. To this end, several researchers and companies (Ramesh et al. and Rosi et al.) have developed wireless sensor network systems for landslide detection.

This paper presents development of wireless landslide monitoring system using ZigBee-compliant components and the results of field verification tests. The field test was conducted at the hill slope in Ibaraki prefecture, Japan. The extensometers, previously installed, in the hill slope has recorded movement of approximately 30 mm/month. During the field test, the proposed system acquired data that may be attributed to the potential landslide movements.

LANDSLIDE DETECTION SYSTEM USING ZIGBEE TECHNOLOGY

Figure 1 shows a ZigBee terminal. ZigBee is one of the communication standards for wireless sensor networks developed in recent years. It is mainly used for measurement and control (Tei et al.). Table 1 shows a comparison with other wireless communication standards. From this table it can be seen that ZigBee could be useful in various locations and applications (Nakahata et al. and Moridi et al.). ZigBee can operate on multiple radio frequency bands. However, the regulation of radio waves enforced by the Japanese government, limits ZigBee to use only the 2.4 GHz band in Japan. The data transmission rate is theoretically about 250 kbps. It is possible to communicate with a ZigBee terminal from other ZigBee terminals. Depending on the frequency of transmission, ZigBee devices operate from 100 days to several years using battery power. They can be used to build an extensive network. Theoretically, a maximum of 65,528 ZigBee terminals could be connected in one ZigBee network. ZigBee terminals are composed of three types: coordinator, router, and end device. The ZigBee coordinator is responsible for overall network management. Each network has exactly one coordinator. The coordinator performs the following functions:

- a) Selects the channel to be used by the network
- b) Starts the network
- c) Assigns how addresses are allocated to nodes or routers
- d) Permits other devices to join or leave the network
- e) Holds a list of neighbors and routers
- f) Transfers application packets

A ZigBee router is used in tree and mesh topologies to expand network coverage. The function of a router is to find the best route to the destination for transferring a message. A router performs all the functions of a coordinator except for that of establishing a network. A router can also perform the functions of a ZigBee end device. A ZigBee end device can be connected to a router or a coordinator (parent). It also operates at low duty cycle power, meaning it consumes power only while transmitting information. Therefore, ZigBee architecture is designed so that an end device's transmission time is short. The end device performs the following functions:

- a) Joins or leaves a network
- b) Transfers application packets

ZigBee networks are characterized by multi-hop functionality and large network capacity. Multi-hop is the function of transmitting data via relays when the sending terminal cannot transmit the data to the receiving terminal directly. As a result, this can reduce transmission power. Moreover, if the network capacity is large, a lot of terminals can be configured in one wireless network. Two or more routes for transmitting data can be selected, increasing the success rate of the transmission. This possibility also allows a mesh network to be built. ZigBee terminals are economical as well such that the cost of the landslide detection system can be kept low. Moreover, the operation of the network is automatic and easily maintained. Thus, ZigBee has many advantages as a means for implementing a landslide detection system.

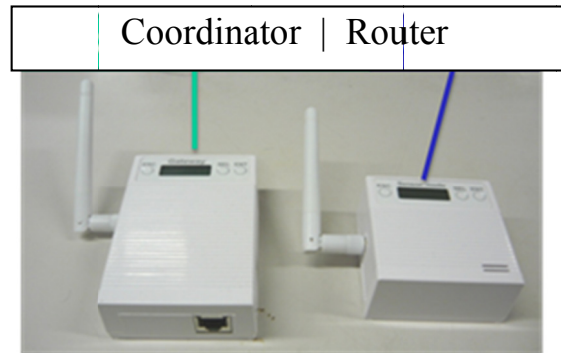


FIG. 1. Picture of ZigBee-Coordinator and router.

Table 1. Comparison with other wireless network standards

Name	Wi-Fi	Bluetooth	ZigBee
Communication distance	100m	10m	10~100m
Communication speed	11Mbps	1Mbps	250Kbps
Network capacity	32nodes	7nodes	65, 536nodes
Battery life	Several hours	Several days	Several months~ years
Application	Wireless LAN	Wireless Sound	Instrumentation control

SYSTEM CONFIGURATION

In this system, AirSenseWare software runs on a PC to collect data via the ZigBee wireless network. The data is transferred wirelessly via the ZigBee method. Figure 2 shows the outline of the system. The ZigBee network communicates by radio between the sensing devices which are connected to ZigBee routers, ZigBee routers which just relay data from router to router, and the base station which is called “ZigBee-Coordinator”. ZigBee-Coordinator communicates to the PC via Ethernet. It is able to send and receive data and commands to and from other equipment via serial communication. This wireless landslide detection system is named “GeoSense”.

ZigBee-Corrdinator used in this research is a modified version of a base station. It has three functions: (1) it constructs the wireless network, (2) it conveys data received from the ZigBee-Router to the AirSenseWare software, (3) it sends the operation period commands to the ZigBee routers. It is necessary to construct a mesh network, as opposed to a network of a different topology, for the detection of landslides, and this requires a ZigBee network composed only of ZigBee routers (and a coordinator) without any ZigBee end devices. (Note that a ZigBee router can also function as a ZigBee end device.) A ZigBee router determines the Received Signal Strength Intensity (RSSI) value of the signal sent to it by another ZigBee router and sends this

value to the ZigBee-Coordinator. The conversion from received signal power to RSSI is performed by Eq. (1):

$$Y=10 \log_{10}X \quad (1)$$

Moreover, a ZigBee route obtains environmental landslide-sensing data from the equipment attached to it, transmits this data to the ZigBee-Coordinator, and then changes its operating mode. The operating mode is the function that optimally manages the ZigBee's power consumption. Figure 3 shows the state transition chart of a GeoSense. The following describes the operating modes of a GeoSense.

The operating mode is changed by a command from the AirSenseWare software as well as by the internal operations of the GeoSense device itself. A GeoSense has the following five operational modes. In power supply OFF mode, the GeoSense's power is OFF. During this mode, the GeoSense cannot measure data and cannot accept wireless commands. In Personal Area Network (PAN) build mode, the GeoSense tries to connect to the PAN which the ZigBee-Coordinator constructed after power was initially turned ON. After connecting to the PAN, the GeoSense displays the wireless network information, such as the PAN-ID and radio channel. In RSSI measurement mode, the ZigBee router sends, to the ZigBee-Coordinator through the wireless network, the RSSI value measured when another ZigBee router communicated with it. The transmitted data is recorded in a log. In data transmission mode, the ZigBee router sends data from an externally connected device to the ZigBee-Coordinator. The transmitted data is recorded in a log. The ZigBee router and the external device exchange data and instructions by serial communication. In Sleep mode, the ZigBee router is running in a power saving mode for a cycle which was set by the operating period command.

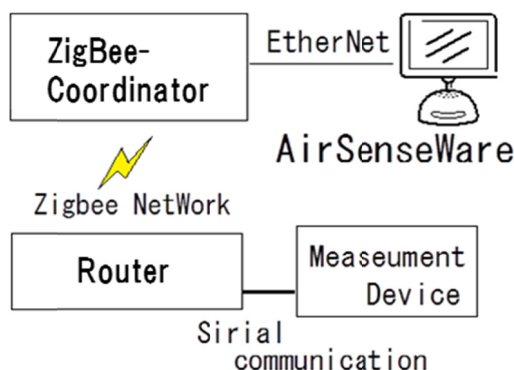


FIG. 2. Outline of the proposed landslide observation system.

DEVELOPMENT AND OUTLINE OF THE SLOPE SENSING DEVICE

The ZigBee router itself does not have the ability to sense environmental conditions. Therefore, a slope sensing device was developed which could communicate with a ZigBee. This sensing device activates cyclically with the same timing as that of a ZigBee router. The sensing device and the ZigBee router communicate with each other via serial communication. The data obtained with the sensing device, 3-axes acceleration, temperature, humidity, and intensity of illumination, is transmitted via the

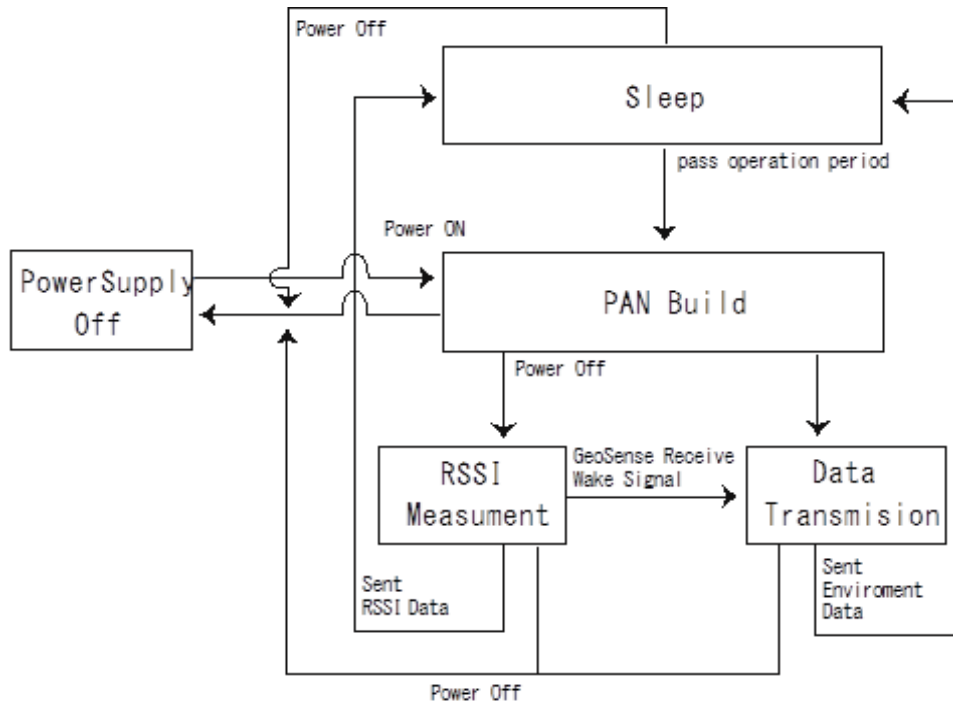


FIG. 3. State transition chart of GeoSense.

ZigBee communication system. Normally, slope monitoring takes more than one month. So, if we monitor it in real time, it requires a very large-capacity battery. Therefore, our system was designed to take measurements only three times per day. The selected monitoring frequency was considered reasonable for the moving rate of the landslide. Furthermore, this measurement cycle significantly reduces electricity consumption. The activation of the sensing device is determined by the status of the ZigBee router. Therefore, when the ZigBee router is active, the sensing device is active, as well. Similarly, when the ZigBee router is sleeping, the sensing device is also sleeping.

This device is composed of the following parts. First, it uses an H8-3052 microcomputer, which controls the sensors and communication with the ZigBee router. It has an A/D converter that can select from eight analog input ports. Slope monitoring requires the measurement of many environmental parameters, such as temperature and acceleration, multiple analog inputs is a useful feature. This microcomputer was also selected because of its widespread availability. The H8-3052 typically draws 40 mA at 5 V, which is not a particularly low level of power consumption. However, this is not a problem since it only operates for 45 seconds for each activation of the ZigBee router. For example, if the ZigBee routers were to activate 24 times per day, this device would only operate for $45 \text{ s} \times 24 = 1080 \text{ s}$ per day. A 9 V / 800 mAh dry cell battery was used for the sensing device. If the ZigBee routers were to activate once a day, the microcomputer would work more than 17 days with one 9 V dry cell. With additional dry cells, longer monitoring periods would be possible.

For monitoring sensors, the KXM52-1050 (triaxial acceleration), LM35DZ (temperature), NJL7502L (illumination), and CHS-GSS (humidity) were selected. Once this device receives an activation signal from the ZigBee router, it activates immediately. Acceleration, humidity, illumination, and temperature are measured sequentially. The obtained data are converted to binary data and then transmitted to the ZigBee router via a serial communication cable. To ensure robust communication, the data are transmitted thrice. This whole process is finished within 45 seconds.

FIELD VERIFICATION TEST OF THE PROPOSED SYSTEM

Field verification test of the system was conducted at the hill slope (Ibaraki Prefecture, Japan), where 30 mm/month of landslide type movement has been recorded by the extensometer that had been previously installed. The objectives of this field monitoring were to verify the system performance, evaluate its durability, and evaluate capability of landslide detection. This field test was carried out during early December of 2010 with measurements continuously taken once every 10 min for 2 days. The 3-axes acceleration is monitored to detect change in inclination induced by potential landslide movements. In addition, humidity and illumination were measured simultaneously to examine the relationship between rainfall and landslide movements.

Figure 4 shows a map of the area around the test site. A total of nine ZigBee routers were used for this test. Six of them were used as relay nodes and three of them were used as sensing devices. The relay nodes were positioned between the ZigBee-Coordinator and the sensing devices in an almost liner fashion. They relayed data from the sensing devices.

The ZigBee-Coordinator is represented as a star in the Figure 4. The red-masked area is the area where signs of landslide activities had been noted. Two sensing devices (171, 175) were located inside of this area and one (170) was set outside of it. The one outside the area was to be a reference point. The ZigBee-Coordinator requires significant electrical power, so it was connected to electricity via an extension cord. Figure 5 shows the setup of ZigBee routers (both relay and sensing devices). As shown in Figure 5, ZigBee routers with sensing device were attached on a stands that were approximately 1 m above the ground. The stands were fixed to the ground using piles which were driven into the ground at least 50 cm. For water and corrosion protection, these devices were covered by plastic boxes with a desiccant agent inside. The monitoring was

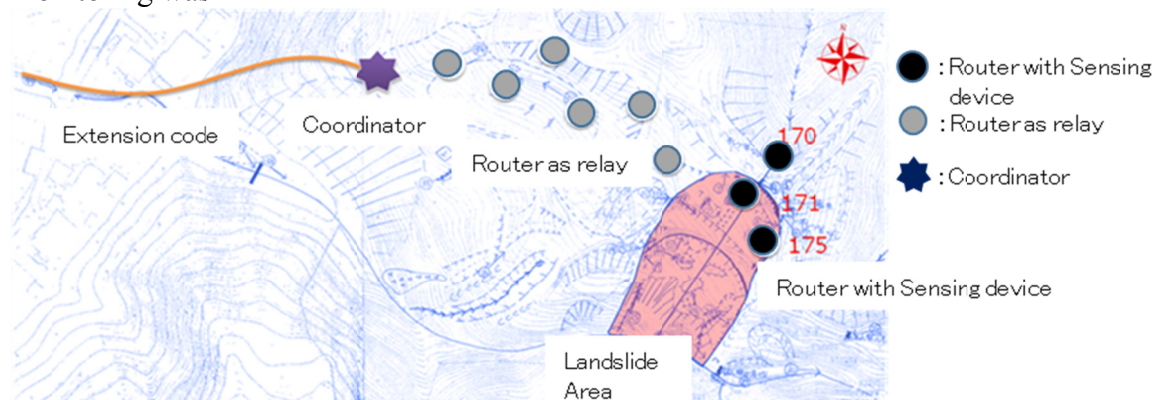


FIG.4. Field verification test area and distribution of the proposed system.

continuously performed for 2 days. Device No.175 failed during the test, so its results were not used. The network activated every 10 minutes (45 seconds: active, 9 minutes and 15 seconds: sleeping).It was confirmed that measurements were successfully taken 321 times during the 2 days 5 hours and 30 minutes of continuous operation. The accelerations, temperatures, humidity and illumination data obtained during the test are presented in Figure 6. Figure 6 shows that the device No.170 and 171 exhibit opposite trend in accelerations in three directions: The increase and decreasing trend is reversed, especially in z-axis, starting at 12/03/04:00. On the other hand, the temperature variations of 170 and 171 are consistent. It is inferred that this trend may be attributed to landslide activity, since the extensometer recorded movement of 1 mm during this period. However, the quantitative verification is not sufficient at this time.



FIG.5. Set up of ZigBee router with sensing device on stands with piles.

Monitoring of temperature and Illumination by the GeoSense (a landslide monitoring system) was successful. As shown in Figure 6, the temperature variations acquired by the GeoSense is the same as those of the Automated Meteorological Data Acquisition System (AMeDAS) of the Japan Meteorological Agency. The Illumination sensor indicated approximately 450 lx during daytime and 0 lx after sundown. The humidity data was partially lost, due to excessive condensation of the sensor covers. Although no particular correlation between rainfall and landslide occurrence could be found during the field test, the system was found to properly perform with the low energy consumption mode.

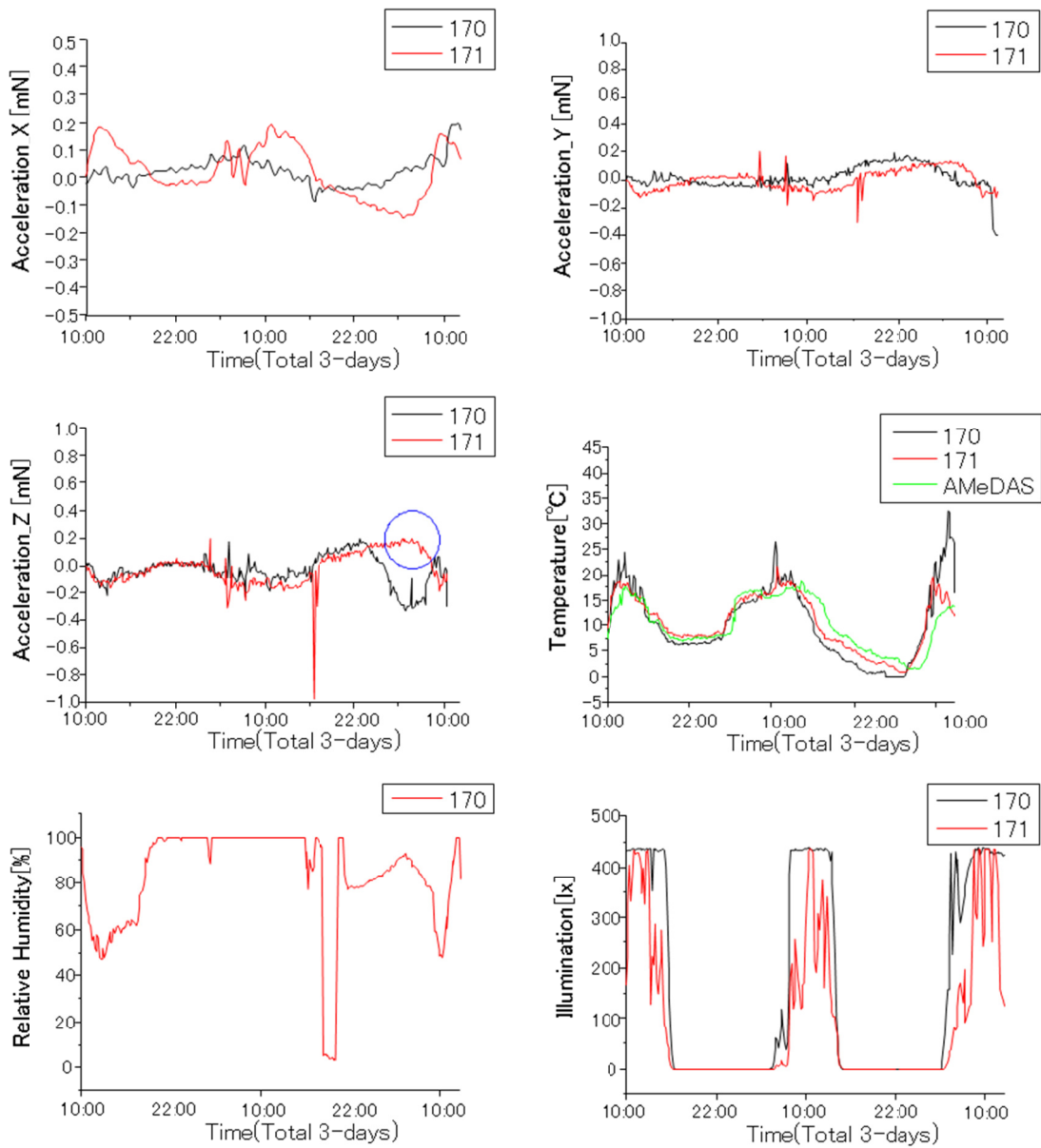


FIG.6. Results obtained by field verification testing.

CONCLUSIONS

It is necessary to detect the onset of a landslide, and therefore the development of an automatic detection system for landslides is urgently required. In general, landslide

detection requires a long monitoring period. Moreover, sufficient accuracy for detecting the threshold, high signal to noise ratio, versatile data acquisition frequency, robustness, easy maintenance, and low cost are required.

In this research, we developed an automatic landslide detection system that meets the requirements for field application, using ZigBee wireless communication technology. The system components are readily available for field implementation. In particular, sleep and timer functions were added to the proposed system to minimize the battery consumption and enable long term monitoring in mountainous and forest regions where access to electricity is difficult. Moreover, a slope sensing device was developed which could communicate with a ZigBee router. It was equipped to measure 3-axes acceleration, temperature, humidity, and intensity of illumination.

A verification test of our proposed system was conducted at a hill slope where movements have been reported. It was confirmed that all measurement items except humidity were measured properly at the actual slope site with this proposed system. In addition, our proposed system detected a small amount of landslide-type behavior. From these results, it can be said that the effectiveness of our proposed system was verified.

REFERENCES

- Ramesh, M. V. (2009). "Real-time Wireless Sensor Network for Landslide Detection." *Proceedings of the third International Conference on Sensor Technologies and Applications, SENSORCOMM 2009, IEEE, Greece*: June 18 - 23
- Rosi, A., Bicocchi, N., Castelli, C., Mamei, M., Zambonelli, F. (2011). "Landslide monitoring with sensor networks: experiences and lessons learnt from a real-world deployment." *International Journal of Sensor Networks (IJSNET)*, Vol.10, No.3, 111-123.
- Tei, R., Masanori, T. (2006). "ZigBee development handbook – Practice introduction network -." *Tokyo : RIC TELECOM*: 19–25, 109-116.
- Nakahata, Y., Kawamura, Y. (2010). "Development of the landslide observation system using ZigBee." *Proceedings of SICE Annual Conference*: CD-ROM (TC10.02).
- Moridi, M. A., Kawamura, Y., Sharifzadeh, M., Chanda, E. K., Jang, H. (2014) "An investigation of underground monitoring and communication system based on radio waves attenuation using ZigBee." *Tunneling and Underground Space Technology*. Vol.43: 362-369.

McCook Reservoir Instrumentation and Monitoring

Georgette Hlepas, Ph.D., P.E.¹; and William Rochford, P.E.²

¹Geotechnical Engineer, US Army Corp of Engineers, Dam Safety Modification and Mandatory Center of Expertise. E-mail: georgette.hlepas@usace.army.mil

²Chief of Geotechnical and Survey Section, US Army Corp of Engineers, Chicago District. E-mail: william.a.rochford@usace.army.mil

Abstract: The McCook Reservoir project is a below-grade reservoir to temporarily store combined sanitary overflow (CSO) water from the city of Chicago and surrounding communities. CSO is stored until it can be treated and then discharged into the Chicago sanitary and ship canal (CSSC). The reservoir is being excavated through approximately 15.2 m (50 ft) of soil and 76.2 m (250 ft) of rock, requiring the installation of earthen retaining walls and rock support measures for the near vertical rock wall to achieve the design depths and geometries. In addition, in order to minimize groundwater infiltration and CSO exfiltration, a perimeter cutoff wall and grout curtain have been installed. Due to the project proximity to adjacent roadways, railways, and waterways as well as for onsite project safety, a potential failure modes analysis was performed on the various project features and a surveillance and monitoring plan was developed to monitor for those failure modes that were deemed credible. This monitoring program consists of a series of piezometers, inclinometers, time domain reflectometry, extensometers, crack meters, survey methods, and visual monitoring. An automated data acquisition system (ADAS) is also installed that permits near-real time access to automated instrumentation data. The purpose of this paper is to discuss the lessons learned regarding design and installation considerations for the design, installation, data management, interpretation, and evaluation of the instrumentation.

INTRODUCTION

The McCook Reservoir Project is being constructed by the U.S. Army Corps of Engineers (USACE) in partnership with the Metropolitan Water Reclamation District of Greater Chicago (MWRD) as part of the Tunnel and Reservoir Plan (TARP) to reduce flooding in the Chicagoland area. Once completed, the project will store combined sewer overflow (CSO) waters from the TARP Mainstream and Des Plaines Deep Tunnel systems until the CSO can be pumped to the Stickney Water Reclamation Plant (Stickney WRP). The design capacity of 38 billion liters (10 billion gallons) will benefit over 3 million people in Chicago and 36 suburbs. To minimize groundwater infiltration and seepage from the Chicago Sanitary and Ship Canal (CSSC) and the Des Plaines River, along with preventing exfiltration of CSO, a

seepage barrier consisting of a double row grout curtain and overburden slurry cut-off wall was installed around the reservoir perimeter.

The reservoir is located adjacent to the I-55 traffic corridor and between the CSSC and the Des Plaines River channel. The perimeter of the reservoir consists of a freight railroad (CSX) at the northeast end, the MWRDGC railway along the southeast length, Interstate 55 (Stevenson Expressway) along the northwest length, and a project access road that runs along the perimeter of the project (refer to Figure 1). In addition, major utilities, such as gas and water lines, are directly adjacent to the site.



Figure 1: Aerial View of the McCook Reservoir Site

In order to achieve the design capacity, the reservoir is constructed by excavating approximately 15.2 m (50 ft) of overburden as well as blast excavation of 76.2 m (250 ft) of rock. The overburden is stabilized with different types of retaining walls including a gabion wall, soil nail wall, and concrete block retaining wall.

A potential failure modes analysis (PFMA) was performed by the project engineering team to determine areas where the project was susceptible to unacceptable risk and where performance monitoring is required both during construction and operational phases of the project. As a result, a Surveillance and Monitoring Plan (SMP) was developed and is currently being used to monitor potential failure modes that may jeopardize project safety, proper functioning of project features, and to provide early warning signs of potential failures. The USACE Engineering Manual “Instrumentation and Monitoring of Embankment Dams and Levees”, EM 1110-2-1908 (draft), was used to guide the development of the SMP. The engineering manual aided the selection of specific instrumentation, the monitoring frequency, establishment of thresholds, data management considerations, and evaluation frequency. The SMP includes discussions on the various monitoring techniques used in concert to monitoring the complete project performance including visual monitoring, survey monitoring, and subsurface instrumentation. The surveying techniques include GPS, Electronic Distance Measurement (EDM), and LiDAR. Subsurface instrumentation includes series of inclinometers, time-domain reflectometry cables (TDR), fully grouted piezometers (PZs), extensometers, and meteorological sensors. In most cases, multiple instruments are used to monitor each failure mode. For example, the slope stability of the rock wall is monitored in multiple locations by extensometers, inclinometers, TDR cables, and crackmeters. This aids the evaluation team in resolving anomalies and more accurately determining the location, extent, and magnitude of any detected displacement. Further, an Automated Data Acquisition System (ADAS) is installed to facilitate a relatively high frequency of data collection and alarm notification of any readings that exceed established alarm thresholds. Instrumentation monitoring frequency was set to 6 hr intervals in order to obtain readings pre- and post blast events. The data is transferred through cellular modem to a hosted server where data can be accessed through the internet.

The SMP is updated as construction progresses, features are constructed, feature stability is evaluated, and lessons are learned regarding the instrumentation and monitoring effectiveness. The SMP will continue to be used through the operations phase of the project. This paper will focus on the lessons learned regarding the following specific surveillance and monitoring methods:

- EDM
- Extensometer
- Combination Units: Inclinometer, TDR, and PZ's

ELECTRONIC DISTANCE MEASUREMENT

EDM has been employed at the site to monitor for potential displacement of various features including the Gabion Wall, the Soil Nail Wall, Vertical Rock Wall, and MWRD Railway. A Total Station, an electronic theodolite that measure the distance from itself to a target point, was used to monitor these features. A GPS unit was also used for the MWRD Railway monitoring.

Gabion Wall Monitoring: The approximately 183 m (600 ft) long Gabion Wall (location shown in Figure 1) has a maximum height of 7.8 m (25.5 ft) at the northernmost end and steps down to a height of less than 1.5 m (5 ft) at the southernmost end. The slope behind the wall showed visual signs of distress and the gabion baskets visually appeared to have displaced. In order to monitor the for wall displacement, 31 reflective targets were installed along the face of the Gabion Wall at the base, center, and top at locations shown in Figure 2. The targets were composed of a plastic tab with the reflective target adhered to it. The targets were attached to the gabion baskets with metal ties.

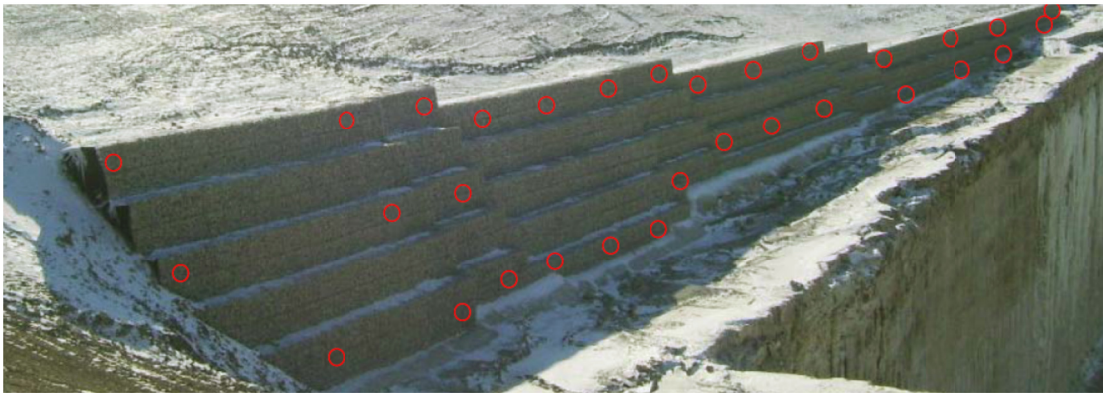


Figure 2: Target locations Gabion Wall at Northeast Corner of Reservoir Site

Monthly EDM surveys began in April 2010. Data indicated that there was progressive movement towards the reservoir and in some locations a magnitude of movement in excess of 15.2 cm (6 in) over the course of 4 years was measured. Figure 3 shows the graphical data of one of the target points, Point 11002 (location identified in Figure 2), over the course of a 4 year period.

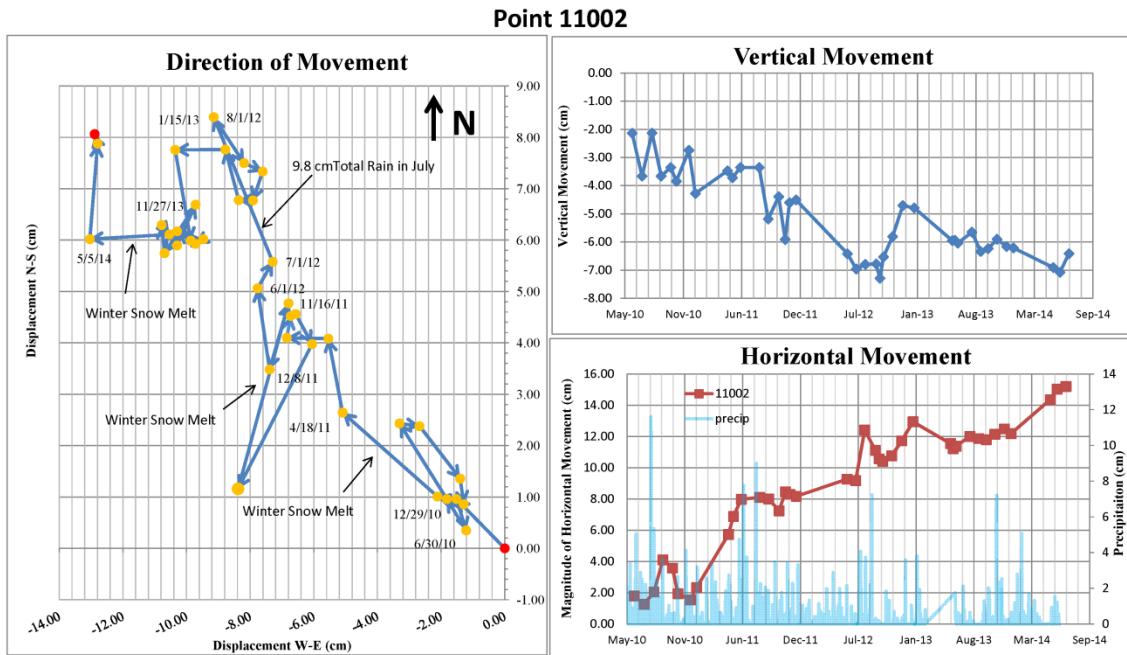


Figure 3: Graphical representation of data for one of the target points on the Gabion Wall

Initial evaluation of the data concluded that movement was primarily in response to precipitation events. However, after site visits were performed to investigate the physical conditions of the slope and gabion wall, it was determined that the wall as a whole was not moving; rather individual wires of the gabion basket mesh were deforming. In addition, the metal ties that attach the survey targets to the gabion baskets were corroding and breaking and permitting the targets to dislocate. Further, the plastic material of several of the targets had broken due to weathering. Figure 4 shows the localized gabion basket deformation and an example of a damaged target with corroded attachment ties.



Figure 4: Gabion Basket Localized Deformation (left) and Target Damage and Tie Corrosion (right)

Soil Nail Wall Monitoring: In order to monitor the performance of the soil nail wall (Figure 5), reflective targets were installed along its face at 3 elevations (base, mid level, and top). This series of targets were metal with the reflective target attached to the soil nail wall face with a single screw and washer as shown Figure 6.



Figure 5: Photo of Soil Nail Wall installation

Initial surveys indicated that there was negligible movement. However, over the course of 2 years, data indicated anomalous readings at various locations along the wall and inability to obtain readings at several locations. Visual inspections of the wall indicated that there were no signs of distress, such as cracking in the shotcrete wall facing. Close inspection of the targets revealed that several targets had rotated about the single screw used to attach the targets, the metal frame of several targets were bent, and the reflective portion of target was detaching from the metal frame in several instances. Corrosion of the screws resulted in the loosening of the attachment and rotation of the metal frame. A second screw and corrosive resistant materials would have prevented rotation. Discussions with construction personnel indicated that some of the frames were damaged and bent during construction activities and the detachment of the reflective material was due to weathering.

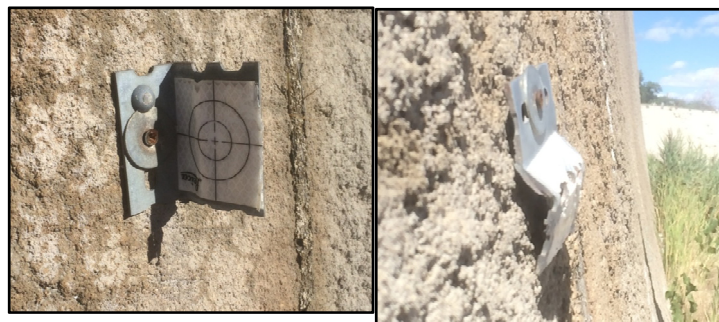


Figure 6: Photos of Reflective Targets on the Soil Nail Wall with Corroded Screw (left) and Rotated and Bent Frame (right)

The EDM method of monitoring was determined to provide accurate results. However, the intent of the monitoring program was not met as the surveys were providing the results of localized displacements of the targets (and gabion wire mesh in the case of the gabion wall) rather than global monitoring of the physical features. Lessons learned are that consideration should be given to the longevity of the monitoring program, the target material, attachment details, and the material susceptibility to environmental and construction impacts. In addition, site visits to visually verify the survey results is of paramount importance.

EXTENSOMETERS

In order to monitor for rock wall stability, LiDAR surveys have been performed periodically and inclinometers, multiple point borehole extensometers (MPBXs), single point borehole extensometers (SPBXs), crackmeters, and time domain reflectometry cables have been installed at critical locations as determined by the potential failure mode analyses. The first three extensometers to be installed were multiple borehole extensometers and were all located on the northwest side of the reservoir. The instruments each extend from the top of rock, at the base of the soil nail wall, and are installed at 15 degrees angles from horizontal. Bladder anchors were used based on the jointed rock condition. In order to prevent damage to the instrument heads from equipment traffic on the adjacent rock surface, the instrument heads were recessed into the rock. The deepest anchors are installed approximately 85.3 m (280 ft) from the instrument head. Figure 7 shows a typical cross-section and installation detail.

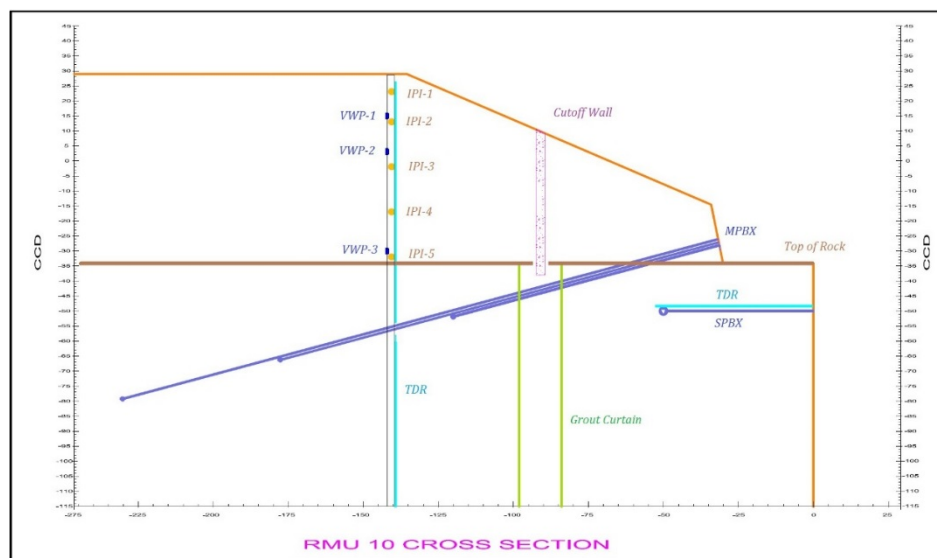


Figure 7: Typical Cross-section Showing Extensometer and Inclinometer Installation

Initial data plots indicated relatively minor rock wall displacement towards the open excavation in two of the extensometers; however the data was questionable. There were inconsistencies between the multiple anchor points at each installation, one

anchor point was measuring both tensile and compressive movement, and one of the anchor points showed intermittent data collection. Data from neighboring instruments, construction activities, and meteorological activities were all reviewed to identify the cause. Evaluations indicated that the readings were somewhat correlated to precipitation events; however a clear pattern behavior and cause could not be identified. Instrumentation data from neighboring instruments did not identify any movement. A site visit to inspect the rock wall slope and extensometer instrument heads revealed that two of the instrument heads were all inundated from recent precipitation events. The original design took inundation into consideration and reasoned that runoff from precipitation events would be drained through joint features in the heavily jointed rock. However, inspections revealed that the joint openings were not sufficient to drain the volume of runoff entering the hole resulting in complete inundation of the instrument heads. This was due to the joints being filled with construction debris preventing drainage and that the amount of runoff was greater than anticipated as drainage from the soil nail wall base infiltrating the extensometer drill hole (refer to Figure 8).



Figure 8: Photo of recessed extensometer head (left) and proximity of soil nail wall drain to recessed head and debris (right)

In addition, the instrument heads were recessed more than 15.2 cm (6 in) into the drill hole making access to service the instrument difficult. Concern of the infiltration freezing and causing damage to the head resulted in the installation of a concrete box with an access hatch to protect the instrument head from further damage. In addition, the flow from the soil nail wall drains was routed away from the instrument heads. However, this did not solve the issue of access to the instrument head assembly. The initial solution was to demolish the concrete boxes and extend the instrument heads. However, during demolition of the concrete, the hole surrounding the instrument head was inadvertently enlarged; permitting much improved access to the instrument heads; negating the need for extension of the instrument head assembly, refer to Figure 9a. A new concrete protective barrier with access hatch was installed over the enlarged hole and instrument head assembly as shown in Figure 9b.

The lesson learned in this case was that the design specifications should consider the geometry of the instrument head and its position within the drill hole. Accessibility to the instrument should have been considered initially and the specifications indicate the need to be able to readily service the instrument. In addition, the extensometer proximity to the soil nail wall drainage system as well as infiltration concerns should have been considered prior to the installation. It is noted that there was no oversight of the installation and only the general location of the instrumentation was provided. It is recommended that oversight for all instrument installations be performed and that exact location of the instrument installation be verified in the field.



Figure 9: (a) Photo of recessed extensometer head enlarged and soil nail wall drain re-routed, (b) Photo of new concrete protective barrier and access hatch

COMBINATION UNITS: INCLINOMETERS, TDR, PZ's

A clay seam within the rock at approximately 64 m (210 ft) below the top of rock is believed to be the cause of identified shear movement in the rock wall. In addition, identified seepage at the rock face and indicators of distress on the roadway caused

concern regarding the overburden slope stability. In order to minimize cost and maximize monitoring techniques, three automated combination units consisting of an in-place inclinometer (IPI), TDR cable, and multilevel PZs were installed extending from the top of ground to below the final design elevation of the reservoir, 97.5 m (320 ft) depth. The TDR and the PZs were attached to the inclinometer casing and the sacrificial grout tube. Figure 7 shows the typical instrument location in cross-section. Figure 10 shows a photo during the installation of the 3 instruments.

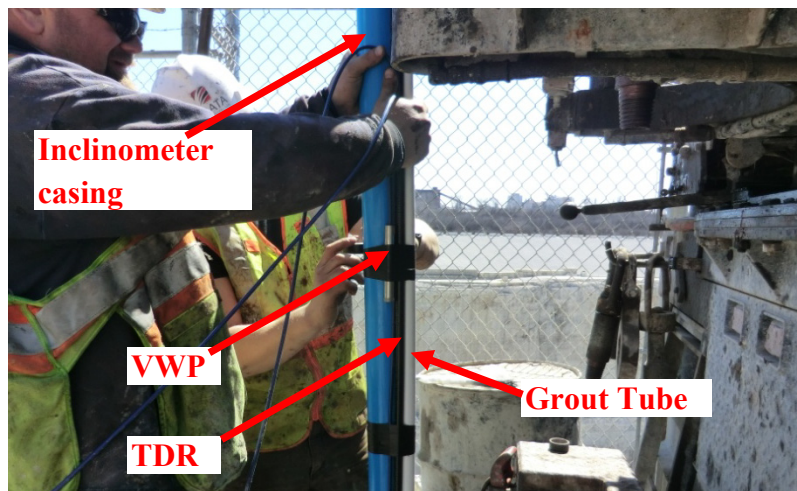


Figure 10: Photo of the Installation of the Combination Unit

Overhead powerlines made drilling the required depths impractical; therefore the instruments were flush mounted in the roadway to protect from traffic. Remote monitoring units (RMUs) containing electronic equipment required for data collection, data storage, and data transfer wirelessly were installed at each location behind the road guard rail with cabling extended through the subsurface to the combination units.

Inclinometers: Seven tilt sensors were installed in each inclinometer casing, 5 of which were installed in the overburden and 2 in the rock (above and below the clay seam). Due to the distance between the sensors above the clay seam and the next closest sensor in the overburden being approximately 27.4 m (90 ft), an extension cable was used. The sensing zones were limited to location of expected movement to reduce the total number of instruments and the cost of the installation. The sensing zones could always be adjusted if a different zone was determined to be more appropriate, however, downtime of the instrument would be required and appropriate spacers would be required to be custom ordered.

TDR: In order to monitor for movement along the entire length of the instrumented borehole, a TDR cable was installed along the exterior of the inclinometer casing. The TDR cable is a cost effective tool that permits detection of location of shear movement; however, the instrument does not provide for determining the magnitude or direction of movement. The design intent was to use the TDR to verify readings

from the inclinometer as well as to adjust inclinometer sensing zones based on more accurately identified locations of movement by the TDR. Although the TDR cable is relatively inexpensive, the unit required to connect the TDR cable to the datalogger (the TDR 100) is costly. In addition, it was anticipated that the TDR cable would be sensitive enough to detect movement of 0.6 cm (0.25 in). However, movement of that magnitude was measured with the inclinometer without any response indicated in the TDR data. Review of installation documentation indicated that the cable was installed adjacent to the grout tube and the inclinometer casing (as shown in Figure 10). In addition, the backfill grout for the combination unit was found to have up to 40% bentonite material. Review of available literature, “Real Time Monitoring of Infrastructure using TDR Technology” (2000) by Charles Dowding and Kevin O’Connor, indicates that the amount of bentonite material used in successful TDR application in the region was limited to less than 5%. The strength and stiffness of the cable, grout, rock, and soil were not taken into consideration prior to installation. It is reasoned that the TDR is unable to detect movement less than 0.5 cm is due to the dampening effect caused by the positioning of the cable and relatively flexible grout used.

Piezometers: Five fully grouted vibrating wire piezometers were installed at various elevations along the combination unit in order to monitor for groundwater elevations behind the grout curtain and aid in identifying potential seepage through the groundwater barrier. These instruments were successful in detecting a decrease in groundwater elevations, as shown in Figure 11 (recorded in Chicago City Datum (CCD)). This decrease was correlated to neighboring seepage flows through the rock wall face, indicative of a breach in the grout curtain.

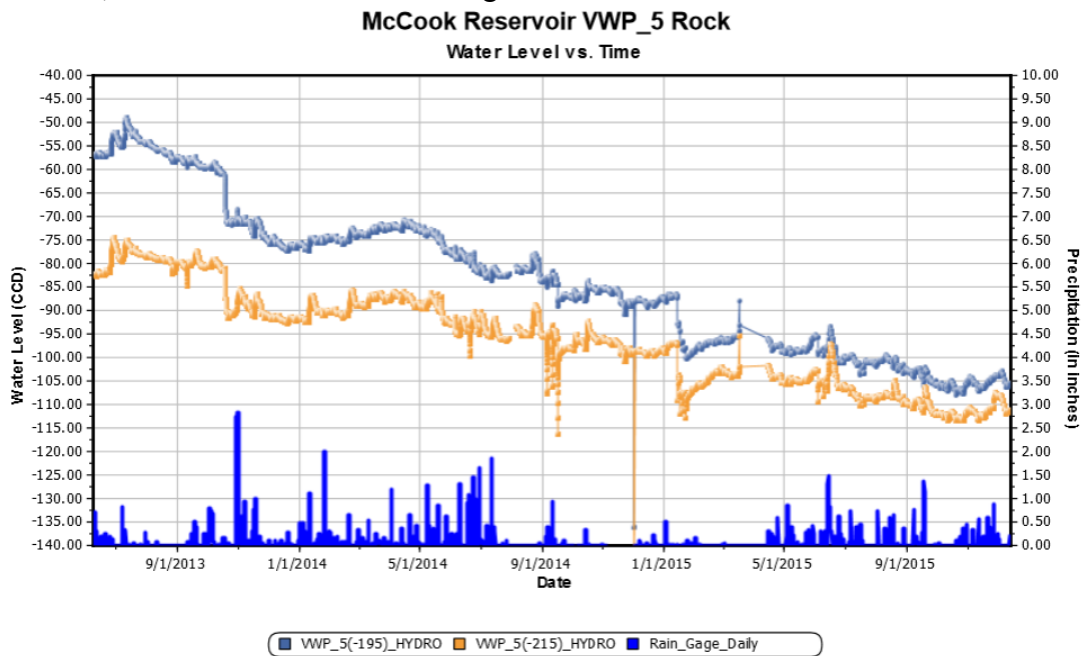


Figure 11: Rock Piezometer at EL -195 (blue) and EL -215 (orange) indicating water level decrease over time.

The combination units were successful in minimizing the cost of instrument installation by permitting the installation of multiple instruments into one borehole. The in-place inclinometers were successful in monitoring movement in the overburden and rock at a higher frequency than what is attainable by manual methods. In addition, it permitted the flexibility of adjusting sensing zones. The TDR units, however, were not as successful as had been anticipated as the magnitude of movement required to be detectable has yet to be achieved. The cable installation along both the inclinometer casing as well as the grout tube along with the type of grout mix used has been determined to result in a dampening effect that increases the required amount of displacement for displacement detection. Future installation details will include consideration to the stiffness and strength of the grout with respect to the instrumentation, rock, soil, and amount of movement required to be detected. The TDR cable positioning will also be modified to reduce the dampening effect of neighboring casing materials.

CONCLUSIONS

After performing a potential failure modes analysis, the project engineering team developed a surveillance and monitoring plan (SMP) to monitor for those potential failure modes that may jeopardize project safety, proper functioning of project features, and to provide early warning signs of potential failures. The USACE Engineering Manual “Instrumentation and Monitoring of Embankment Dams and Levees”, EM 1110-2-1908, was used to guide the development of the SMP. This paper discussed some of the lessons learned during the implementation of the SMP with focus on Electronic Distance Measurements, Extensometers, and Combination Units.

The lessons learned include the importance of instrument and material selection with respect to monitoring longevity, installation location, environmental impacts, and the importance of verifying readings through site visits, as well as oversight during installation. In addition, it was determined that combining multiple instruments in one borehole location can be a cost effective means to monitor potential failure modes with multiple technologies.

REFERENCES

- US Army Corps of Engineers (2016). EM 1110-2-1908, Engineering Manual “Instrumentation and Monitoring of Embankment Dams and Levees”
- Dowding, C.H. and O’Connor, K.O. (2000). “Real Time Monitoring of Infrastructure using TDR Technology”, Structural Materials Technology NDT Conference.
- US Army Corps of Engineers (2014) “McCook Reservoir Instrumentation and Monitoring Design Documentation Report”

Slope Movement in Permafrost near Fairbanks, Alaska

Mohammadhossein Sadeghiamirshahidi, ASCE¹; and Stan Vitton, Ph.D., P.E., ASCE²

¹Graduate Research Assistant, Dept. of Civil and Environmental Engineering, Michigan Technological Univ., Houghton, MI 49931. E-mail: msadeghi@mtu.edu

²Associate Professor, Dept. of Civil and Environmental Engineering, Michigan Technological Univ., Houghton, MI 49931. E-mail: vitton@mtu.edu

Abstract: A section of oil pipeline near Fairbanks Alaska is experiencing hillslope movement. While the pipeline's support system was designed to handle large movements, the slope movements are starting to exceed the anticipated design requirements. The pipeline was constructed on low angle permafrost slopes composed of Fairbanks silt. The silt occurs in three relatively distinct layers; an upper active layer, followed by an *ice-rich silt layer* overlying a *non-ice rich silt layer*. Based on inclinometer data, the slope movement is occurring near the ice-rich layer/non-ice layer interface at a rate of 4.5 cm/year. A traditional slope stability back analysis indicates that for slope instability to develop, the ice-rich layer (assumed the weakest) would require the layer's friction angle to be in the range of about three degrees; much lower than traditional strength values would suggest. While some small underground gold mine shafts are located about 100 meter from the base of the slope movement, it is speculated that an additional factor causing slope creep is the syngenetic formation of the permafrost, which formed in successive frozen layers during freezing. Recent research has also suggest the possibility of cold weather neof ormation of smectic clays developing that could assist in slope creep.

INTRODUCTION AND BACKGROUND

Slope movement is occurring along a portion of the Trans Alaska Pipeline System (TAPS); a 1,270 km long pipeline that conveys oil from the north slope of Alaska to the Port of Valdez on Prince William Sound (Figure. 1). The pipeline crosses more than 800 river and stream crossings and passes through three mountain ranges. In areas with stable rock and soil the pipeline is buried, while in permafrost areas, the pipeline is generally constructed above ground. The pipeline is built in a flexible pattern for the above ground portion and is supported by 78,000 supports 18 m apart. A key design aspect of the pipeline is the ability of the pipeline to withstand large scale earthquakes. There are a couple of locations, however, where slope movements have caused the pipeline to move. One site, located north of Fairbanks, is within the Tanana River valley (a major tributary to the Yukon River) underlain by the Fairbanks silt.

The site is located in continuous permafrost northwest of the US Corps of Engineer's Cold Regions Research and Engineering Permafrost Tunnel Research Facility located in the town of Fox, Alaska (USCOE 2015). This facility has conducted significant research on the behavior of the Fairbanks silt. According to the USCOE, the regional geology of the area is identified as the Yukon-Tanana Upland, and is bounded by the Tanana River Valley and eastern Alaska Range foothills to the south and by the Yukon River Valley to the north. This upland area stretches from western central Alaska into Yukon, Canada. The stratigraphy of Fairbanks silt at the research center is composed of an upper formation called the Ready Bullion Formation approximately 8 m thick forming at the end of the Wisconsin glaciation and the start of the Holocene about 10,000 years ago. Underlying the Ready Bullion Formation is the Goldstream Formation approximately 9 m thick forming between 10,000 and 30,000 years ago during the Late-Pleistocene. Interestingly, the Yukon-Tanana Upland area was not glaciated during the last

glacial episode but was located just southwest of the terminus of final glaciation. Windblown silt from the glacier is believed have formed the Fairbanks silt (Pève 1956).

The TAPS pipeline was designed to allow the pipeline to move laterally along the support system. Since 1990, however, slope movement has resulted in the pipeline pushing up against the vertical support beam as shown in Figure 2. In 2005 ten inclinometers and thermistors were installed along the pipeline. Survey markers were also located normal to the pipeline to indicate the overall extent of slope movement. Figure 4 shows the relative locations of the inclinometers along the cross-section M-M' (red) of the pipeline and the magnitude of movement for each inclinometer. The relative slope movement, since 2009 has averaged about 4.5 cm/year in downslope movement. A well-defined shear zone was noted between the ice-rich silt layer (blue) and the frozen silt layer (green). Overall, the slope movement at the site has an aerial extent of approximately 73 hectare with a maximum length of about 2,200 m.

The slope's stratigraphy is divided into three distinct layer as shown in Figure 3 along cross-section M-M' (direction of cross section shown in Figure 4). The first layer (white) is the active zone, underlain by an ice-rich silt middle layer (blue). The ice-rich layer thickens from less than a 1 m upslope, where movement begins, to approximately 140 m at the valley bottom. Below the ice-rich layer is a frozen silt layer (green) with little to no observable frozen ice. Below the silt is sand and gravel layer, most likely associated with the Fox Gravel, but in some places it is incorporated within the lower frozen silt layer. It is unclear if the two distinct silt layers can be correlated with the Ready Bullion and Goldstream Formations at the CRREL Tunnel Research Facility. As seen in the inclinometer data in Figure 2, the movement is along a shear zone between the ice-rich layers.



FIG 1. Location of the Trans Alaska Pipeline System (TAPS), (taken from Library of Congress), and approximate location of the study area

The reason for the slope movement starting in 1990, some 20 years or so after construction of the pipeline, is not understood. One possibility is due to underground gold mining below the slope where the movement is developing. The mining would have been located in the Fox Gravel below the Fairbanks silt. While two small-scale gold mining operations occur on the opposite slope from the pipeline, they are too far away from the pipeline to have an effect on the slope movement. There are, however, a couple of small mine shafts about 100 to 200 meters from the base of the slope movement. Since there is little to no surface facilities associated with these shafts, such as roads, etc. visible, it is likely shafts were exploratory in nature. The ages of the shafts are not known but it is likely that they were developed before construction of the pipeline in late 1970's.

While some slope movement certainly started before 1990, noticeable movement occurred around 1990 initiating a slope monitoring program. The slope movement clearly indicate a time element caused by some type of soil/ice creep process. It is known that frozen soil properties can change over time, especially under stress or due to changes in chemical and geomicrobiological processes, there appear to be no obvious difference between this location and other similar locations along the pipeline where there is little to no slope movement. To investigate the soil movement, a back analysis was conducted using a standard limit equilibrium method (LEM) slope stability analysis to estimate the strength values required to cause slope instability for the site. The analysis was carried out using Rocscience Slide (Schaefer et al. 2013; Smith et al. 2015). The purpose of the paper is to present the results of this investigation along with a possible hypothesis to explain the slope creep movement.

SLOPE STABILITY ANALYSIS

The magnitude and direction of the horizontal displacements of the support structure at different times are shown in Figure 4. The maximum horizontal displacements along the pipeline have two major overall directions identified as cross-sections A-B and G-H on Figures 4 and 5. The steepest slope at the site, however, is along the K-L direction, also shown in Figures 4 and 5. The slope was analyzed along all three cross-sections. The stratigraphy provided in Figure 3 and identified as cross-section M-M' was assumed to be representative of the soil profile for cross-sections A-B, G-H and K-L. The topography of these cross sections were obtained from a Digital Elevation Model (DEM) (represented as a raster) using ArcMap 10.2.2 and imported to Rocscience Slide 6.0 software for slope stability analyses.

As discussed above, the soil profile has been interpreted as the following three soil layers for input to the slope stability analyses: (1) top active layer composed of unfrozen silt, (2) an ice-rich silt layer and (3) lower frozen silt layer. Strength parameters for the active layer and bottom frozen silt layer were obtained from Wu, 1984, who conducted a slope stability analysis near Fairbanks using a friction angle of 30° for unfrozen silt and 27° for frozen silt.

For the ice-rich silt, the selection of strength parameters was difficult since the ice strength is highly dependent on time, strain rate, temperature and purity of the ice. Figure 6a and Figure 6b (both modified from Fish, 1991) show how the invariant of the deviatoric stress changes with time and strain rate, respectively, implying the change of friction angle and cohesion of ice also with time and strain rate. The changes in ice strength with varying temperature and purity are shown in Figure 7. It can be seen from this figure that cohesion reduces from 16 MPa at -12°C for pure ice to around 0.6 MPa for saline ice at -5°C. Internal angle of friction also decreases from 20° at around -12°C for pure ice to around 6° for saline ice at -5°C (Fish, 1991). Furthermore, Song et al., 2004 show that adding 4 wt. % (1.72 vol. %) silt-sized particles to pure

ice reduces the internal friction angle by about 30%. According to these strength dependencies of ice, the slope stability analysis along each cross sections were analyzed using two scenarios. The first scenario assumed the strength of the ice-rich layer was dominated by “*pure ice*”, while the second scenario assumed the strength of the ice-rich layer was dominated by “*saline ice*”. While there is no evidence that the ice-rich layer is composed of saline ice, it was considered as a “lower bound” assumption, since the strength of saline ice, in general, is a fraction of the strength of pure ice (Anderson and Weeks 1958). For each scenario the safety factors were analyzed with different friction angles and cohesions for ice-rich layer.



FIG 2. Pipeline movement on the pipeline support system at Treasure Creek.

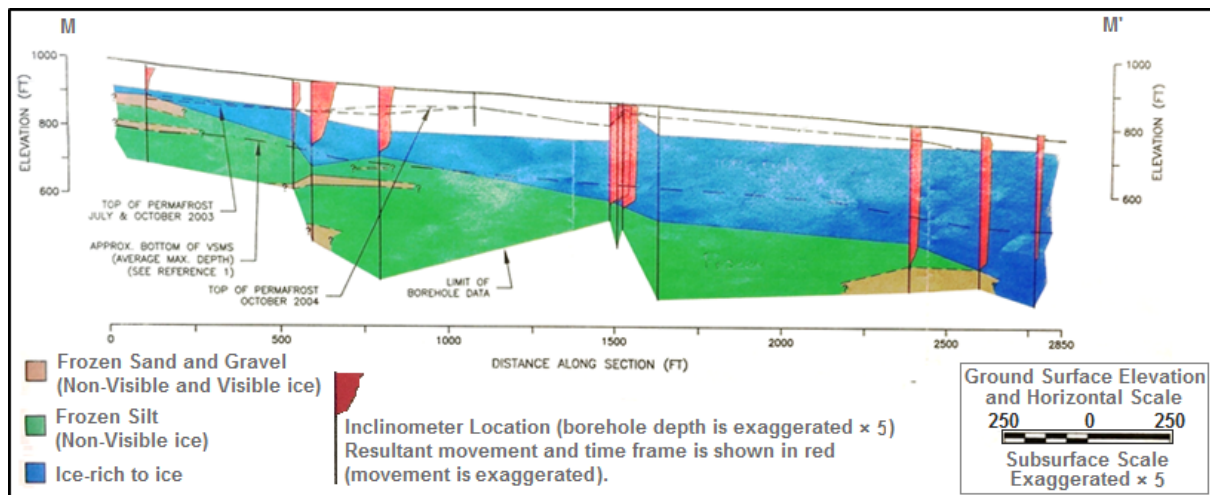


FIG 3. Generalized soil profile along M-M' direction at treasure Creek (modified from 2013 TAPS annual slope stability monitoring report)). Note 1 m = 3.03 ft.

RESULTS

Different limit equilibrium methods including the Bishop simplified, Janbu simplified, Janbu corrected, and Spencer methods were used to analyze the stability of the slope for the three cross sections (A-B, G-H, K-L) using strength values discussed. Different failure surfaces along with different search methods were used for each of the limit equilibrium methods used to find the slip surface having a global minimum factor of safety. The analysis results are summarized in Table 1. The Janbu simplified method produced the lowest factor of safety (“lower bound”) for all scenarios. All of the factors of safety, however, were well above one.

A separate analysis was conducted using the Janbu simplified method assuming the ice-rich layer had 5% by weight salinity with a friction angle of about 6° and cohesion of 100 kPa. The slope geometry and the different soil layers used in the stability analyses are shown in Figure 8. The global minimum factor of safety of the Janbu simplified method and the related failure surface are shown in Figure 9. Results of the stability analysis indicate that even for the “lower bound” case, all three cross-sections were stable with safety factors above one. While the analyses were based on assumed strength values, they clearly represent lower bound strength values for the site.

A back analysis (Duncan and Stark 1992) was then conducted to determine strength values along the shear zone between the middle “ice-rich” silt and the “frozen silt”. This analysis indicated that the ice-rich layer would have to have zero cohesion and friction angle of less than around 3° for the slope represented by A-B cross section for minimal stability (Safety factor =1). For cross-section G-H the “ice-rich” layer should have zero cohesion and a friction angle of less than 2.5° for minimal stability, while K-L cross section would require cohesion of 100kPa and a friction angle of less than 3.5° for minimal stability. A sensitivity chart of friction angle and safety factor of the slope stability for the saline ice-rich layer along the K-L cross section is shown in Figure 10. Clearly, these strength values are much lower than the values for even saline ice.

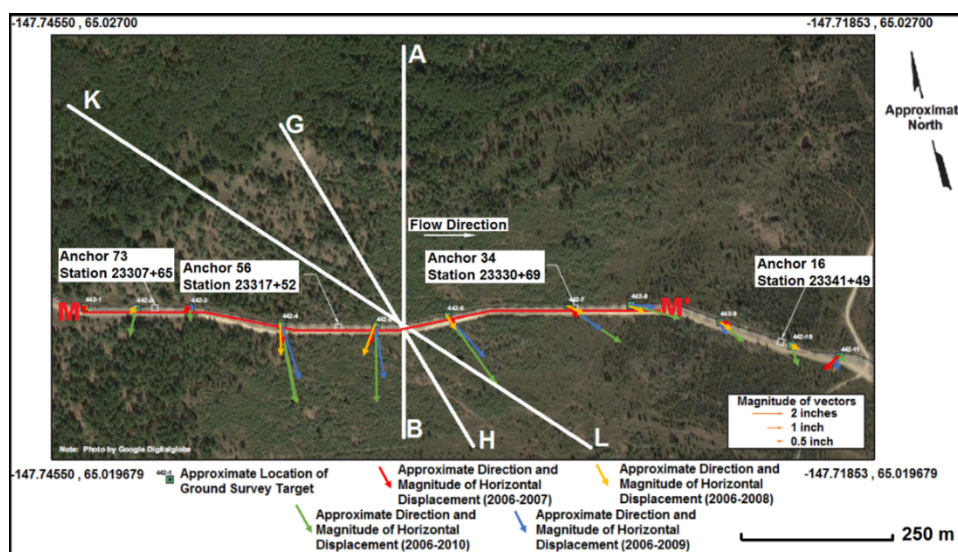


FIG 4. Direction and magnitude of horizontal displacements for cross-sections A-B, G-H and K-L (Site plan modified from 2013 TAPS annual slope report)

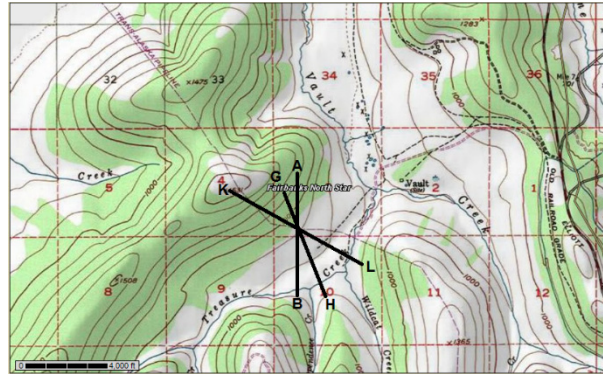


FIG 5. Approximate direction of the A-B, G-H and K-L cross sections on topographical map of the study area (Topographical map is taken from NRCS Web Soil Survey website)

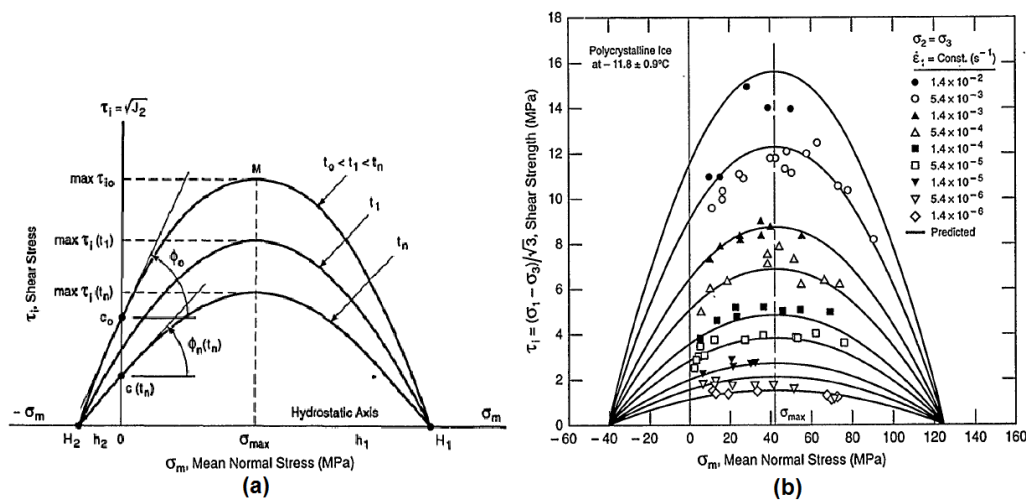


FIG 6. (a) Change of Second invariant of deviatoric stress with time showing shear strength (cohesion and angle of internal friction) of ice changes with time, (b) Shear strength of ice changes with strain rate (modified from Fish, 1991)

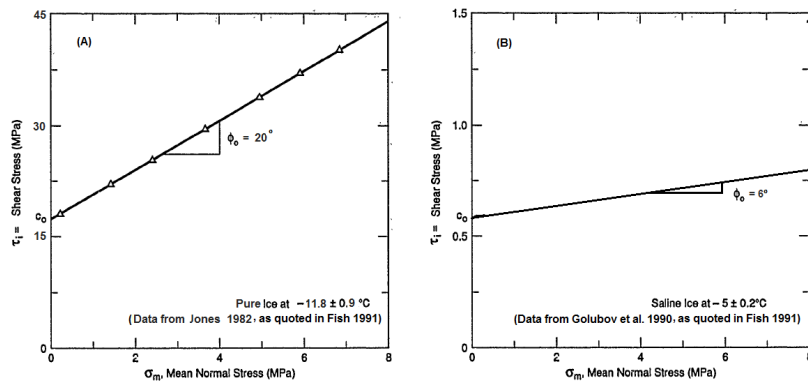


FIG 7. Change of strength parameters of ice by changing temperature and Purity (A: Strength parameters of pure ice at around $-12 \text{ }^\circ\text{C}$ (from Fish, 1991), B: Strength parameters of saline ice at around $-5 \text{ }^\circ\text{C}$)

Table 1. Results of the slope stability analyses using different limit equilibrium methods

Cross section	Ice Layer	Global Minimum Safety factor			
		Janbu simplified method	Bishop simplified method	Janbu corrected method	spencer method
A-B	Pure Ice	3.93	4.01	4.019	4.02
A-B	Saline Ice	1.63	1.65	1.659	1.65
G-H	Pure Ice	5.39	5.47	5.470	5.44
G-H	Saline Ice	1.65	1.67	1.684	1.67
K-L	Pure Ice	2.60	2.65	2.662	2.64
K-L	Saline Ice	1.24	1.28	1.29	1.28

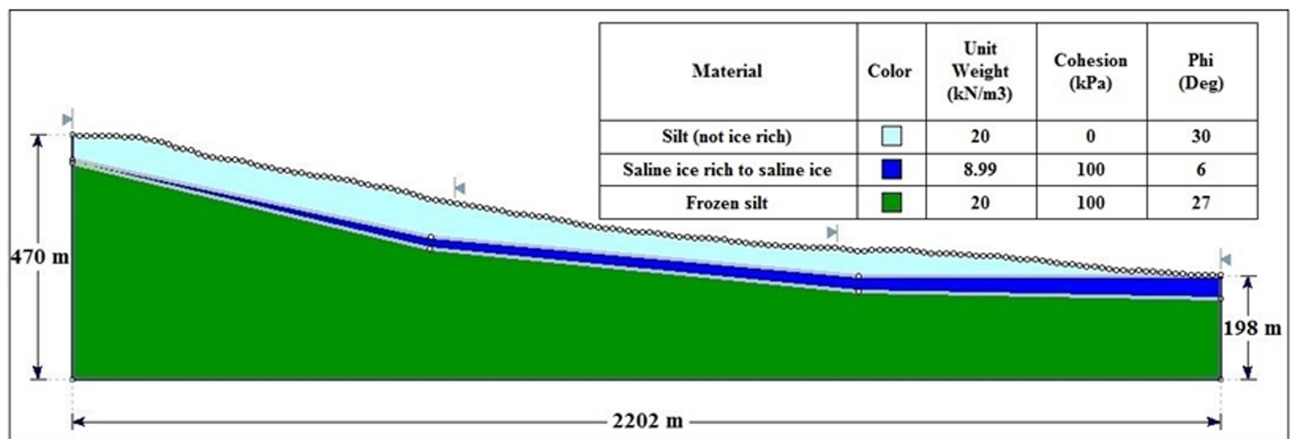


FIG 8. Modeler for the scenario where the Blue layer is saline ice (along K-L cross section)

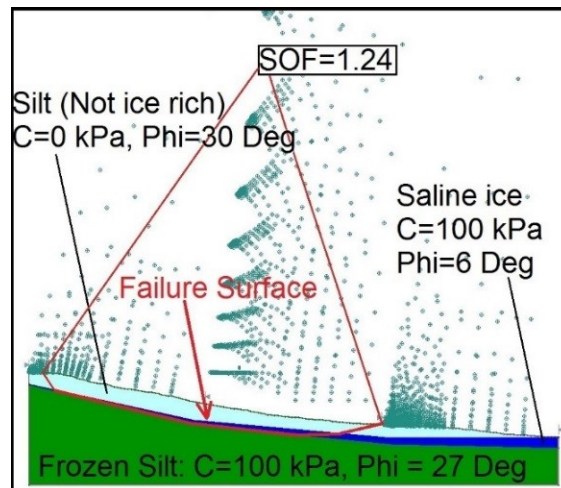


FIG 9. Results of Janbu simplified method for the scenario where the Blue layer is assumed to be saline ice (along K-L cross section)

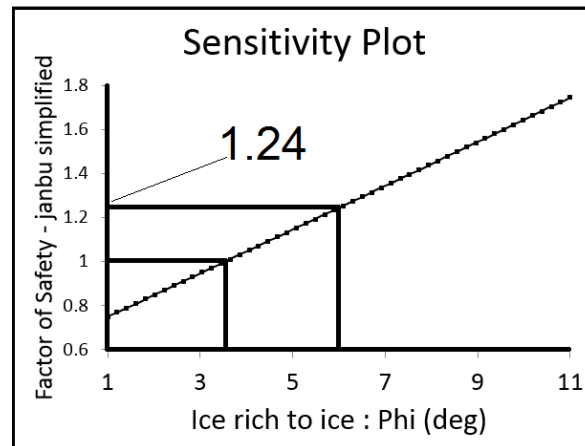


FIG 10. Results of sensitivity analyses based on Janbu simplified method for the scenario where the ice-rich layer is assumed to be saline ice (along K-L cross section)

DISCUSSION

The pipeline was constructed about 15 years before noticeable movements were observed in 1990. Monitoring indicates that the movement is at depth along a distinct shear zone interface between the ice-rich layer and the frozen silt layer. While the effects of the gold mining shaft could certainly be a factor, another possible explanation for slope movement would be due to ice creep at the base of the ice-rich layer. This does not necessarily explain, however, the movement along this section of the pipeline and not along others with similar slope stratigraphy and slope angles. An additional factor that must also be considered is the geomorphological evolution of the slopes.

It can be inferred that the shear zone interface between the two layers formed either as an erosional surface or as an environmental change surface that formed deposition of the silt. According to Pèwè (1975) “*periods of greatest loess deposition in Alaska correspond to glacial maximums. During these periods the source areas, vegetation-free flood plains and outwash plains, were at their greatest extent. In the periglacial areas, such as the Tanana, Yukon, and Kuskokwim valleys, repeated glacial advances with related wind conditions and source areas favorable for loess deposition have created multiple loess blankets.*” The formation of these “blankets” along with the permafrost developing syngenetically, that is, with the silt freezing into permafrost as it was being deposited, could clearly form layers where zones of weakness can develop. This is different than epigenetic permafrost that forms after the soils that have already been deposited and then subjected to a colder climate with continuous freezing. It is also possible that during periods of warming, vegetation grew creating organic layers. High organic layers along with animal remains are well known in the Fairbanks area Pèwè (1975). In addition, it is possible that high moisture zone caused by gelifluction (also known as solifluction) could generate a potential continuous ice-rich layer that could certainly be prone to creep (Shur 2004).

Another possibility is the potential formation of high clay-rich layers in the silt as the silt and permafrost were developing. Pèwè (1975), citing research by Dement (1962), notes that textural bands high in clay-size particles occur parallel to the surface of the silt deposits. Recent research by Vogt and Larque (1998) have found that neof ormation and transformation of clays can occur in a periglacial environment at temperatures far lower than 0 C°. They note that “*permafrost desiccates and indurates soil horizons. During summer, the perennially frozen ground under the*

active thawed layer creates confined conditions, whereas in winter the closed system between the permafrost and the freezing front migrating downwards leads to irreversible changes in the soil structure and to transformation and neoformation of minerals.” They cite a case study in Siberia where a periglacial slope deposit formed on syenite bedrock and containing detrital clays (chlorite, illite) was believed to have undergone neoformation to ferroan smectite. Given that the Fairbanks silt formed syngenetically, it is possible that under certain environmental conditions, along with appropriate minerals present, smectitic clay or other clay minerals could form in continuous layers from neoformation and/or transformation of clays. Vogt and Larque (2002) note that these layers can be used as markers for the study of periglacial environments, while Vogt, Clauer and Larqué (2010) indicate that these layers can also be used to assess global environment change from the authigenesis of clay minerals found in sedimentary rock formations.

At this point in the investigation it is not known what the composition of the shear zone interface between the ice-rich layer and the frozen silt layer are composed of. It is possible, however, that the base of the ice-rich interface layer could consist of either a continuous ice, organic layer or possibly a high clay-rich layer. All three of these materials would be prone to downslope creep. Further investigation, however, is needed to understand the stratigraphy of the site to be able to understand and predict the magnitude of future slope movement and the mitigation of the pipeline movement as well as the possible involvement of the mining shafts.

CONCLUSIONS

Based on the results of the field and slope stability analysis the following conclusions are summarized:

1. Around 1990 slope movements were observed along a section of the TAPS pipeline north of Fairbanks, AK. Due to the magnitude of the movements, inclinometers and thermistors were installed in 2005. Since that time slope movements have averaged 4.5 cm/year and have caused the pipeline to butt up against some of the support structures where the slope movements are occurring.
2. The slope movement is not associated with thawing of the active layer but with a deeper layer along a distinct shear zone at the interface of an ice-rich silt layer and a frozen silt layer.
3. The length of the slope movement is approximately 2,200 m at its longest extent
4. The direction of the slope movement is not along the direction of the steepest section of the slope.
5. Reasonable material strength parameters for the ice-rich layer indicate that the slope should be stable, with safety factors ranging from 2.5 to 4.0 even when considering the ice-rich layer is composed of pure water. When the ice-rich layer is assumed to be composed of a saline ice the factors of safety reduce to 1.2 to 1.7 but still indicate that the slope should be stable.
6. A back analysis indicates that the strength parameters for the ice-rich layer should be even lower to achieve a minimal factor.
7. Ice creep movement is most likely the cause of the slope movement but does not necessarily explain why movement is occurring in one area and not in another.
8. Possible geomorphological explanations include the shear zone surface forming as a periglacial “blanket” or surface that formed syngenetically, that is, with the silt freezing into permafrost as it was being deposited. It is further hypothesized that possible neoformation

and/or transformation of clays during the formation of the “blanket” or surface, generating higher levels of clay minerals such as smectitic clay could have resulted in ice formations with increased ice-creep properties.

ACKNOWLEDGEMENT

This project was funded by the US Department of Transportation (USDOT) through the Office of the Assistant Secretary for Research and Technology. The authors would also like to thank the contribution of Caesar Singh, USDOT program manager, and Alyeska Pipeline Integrity Management team for access to the data used in this paper.

DISCLAIMER

The views, opinions, findings, and conclusions reflected in this paper are the responsibility of the authors only and do not represent the official policy or position of the USDOT/OST-R or any State or other entity.

REFERENCES

- Anderson, D.L. and Weeks, W.F. (1958). “A Theoretical Analysis of Sea-Ice Strength,” *Trans. Act. Am. Geophy. Union*, Vol. 39(4): 632-640.
- Dement, J. A. (1962). The morphology and genesis of the subarctic brown forest soils of central Alaska: Cornell Univ., Ph.D. thesis, 147 p.
- Duncan, M.J. and Stark, T.D. (1992). “Soil Strengths from Back Analysis of Slope Failures”, *ASCE Proc. Stability and Performance of Slopes and Embankments II*, Geotechnical Special Publication (GSP), No. 31: 890-904.
- Fish, A.M. (1991). “Creep and yield model of Ice under Combined Stress” Special Report 91-31, U.S. Army Corps of Engineers, Cold Regions Research & Engineering Laboratory: 1-316.
- Song, M.; Cole, D.M.; Baker, I. (2004). “Initial experiments on the effects of particles at grain boundaries on the anelasticity and creep behavior of granular ice: *Annals of Glaciology*, 39: 397- 401.
- TAPS, (2013). “TARS annual slope stability monitoring report,” 31-1-02353-001, Shannon & Wilson, Inc. Fairbanks, Alaska.
- Pèwè, P.R. (1956). “Origin of the upland silt near Fairbanks, Alaska”. *Bull. Of the Geol. Soc. Of Am.*, VOL. 67: 699-724.
- Pèwè, T.L. (1975). Quaternary geology of Alaska. United States Geological Survey Professional Paper 835: 1-145.
- Schaefer LN, Oommen T, Corazzato C, Tibaldi A, Escobar-Wolf R, Rose WI (2013) Numerical modeling of Volcanic slope instability and related hazards at Pacaya Volcano, Guatemala. *Bull Volcanol* 75:720
- Shur, Y.; French, H. M.; Bray, M.T. and Anderson, D.A. (2004). “Syngenetic Permafrost Growth: Cryostratigraphic Observations”, *Permafrost and Periglac. Process.*, Vol. 15: 339–347.
- Smith, D. M., Oommen, T., Bowman, L. J., Gierke, J. S., & Vitton, S. J. (2015). Hazard assessment of rainfall-induced landslides: a case study of San Vicente volcano in central El Salvador. *Natural Hazards*, 75(3), 2291-2310.

- US Corps of Engineers. (2015). Cold Regions Research and Engineering Laboratory Permafrost Tunnel Research Facility. [ONLINE] Available at: <http://permafrosttunnel.crrel.usace.army.mil/>. [Accessed 2 August 15].
- Vogt, T. and Larque, P. (1998). "Transformations and neoformations of clay in the cryogenic environment: examples from Transbaikalia (Siberia) and Patagonia (Argentina)" *European Journal of Soil Science*, 49: 367-376.
- Vogt, T. and Larque, P. (2002). "Clays and secondary minerals as permafrost indicators: examples from the circum-Baikal region *Quaternary International* 95–96, pp. 175–187.
- Vogt, T, Clauer, N., and Larqué, P. (2010). "Impact of climate and related weathering processes on the authigenesis of clay minerals: Examples from circum-Baikal region, Siberia," *Catena*, Vol. 80, pp. 53–64.
- Wu, T.H. (1984). "Soil movements on permafrost slopes near Fairbanks, Alaska" *Can. Geotech. J.*, Vol. 21(4): 699-709.

Stabilizing Walls Retained by Nailing under Additional Excavations

Majid Taherzadeh Dorobati¹; Alborz Hajiannia²; and Shahrzad Kasaeian³

¹Graduate Student, Dept. of Civil Engineering, Islamic Azad Univ., Najafabad Branch, Esfahan, Iran. E-mail: majid_taherzadeh@yahoo.com

²Assistance Professor, Dept. of Civil Engineering, Islamic Azad Univ., Najafabad Branch, Esfahan, Iran. E-mail: Alborz@aut.ac.ir

³Ph.D. Student, School of Engineering, Univ. of Queensland (UQ), Australia. E-mail: s.kasaeian@uq.edu.au

Abstract: To stabilize slopes and support excavations, soil nailing is known for its low cost, high safety, workability and remarkable performance. Combinatorial anchorages are more effective, and where high safety factors are required, prestressed cables are used with concrete blocks, in-situ concrete piles or double steel profile. Researches on parameters affecting safety factor, stress, settlement and displacement many; however, studies on the effects of additional excavation on excavation walls or methods and mechanisms that preserve the additional depth without compromising the whole wall stability are few. This paper investigates the effects of 7m additional excavation on 23m-deep excavation walls of the Twin Towers project in Shahr-e kord, Iran, retained by soil nailing. To do this, use was made of 2D-FEM and anchorage method with in-situ concrete piles, and the results were validated through comparing the calculated and measured wall displacements. Effects of seven key design factors (pile diameter, horizontal spacing, embedded depth, and anchor angle, prestressing force, bonded/unbonded length of the piles or anchors) have been discussed based on the results of FEM which is quite an efficient method for settlement predictions. Finally, a number of design charts have been prepared for in-situ concrete pile anchorage used in additional excavations.

1-INTRODUCTION

Nailing (started in mid 1980s in Hong Kong (Hossain and Yin 2012). has been widely used in deep excavations in recent years because of its safety, workability, and cost-effectiveness. Wang et al. (2008) concluded that the maximum horizontal displacement occurs mostly at the anchor tip and, then, it decreases from top to bottom. Tang et al. (2008) analyzed the displacement and stress in prestressed anchor cables of the composite nailed structures and showed that the wall displacements (vertical and horizontal) are controlled better when use is made of prestressed anchor cables with the nailing system. Jin et al. (2010) concluded, in their research, that a

combination of nailing and prestressed cables is more appropriate for the protection of the walls of deep excavations. Yan (2012) combined Drucker-Prager's and tensile slip models, carried out the finite element analysis of the composite nailing, and concluded that better results are found. Ma et al. (2013) research results showed that a composite nailed structure has a better seismic performance than a simple one. In general, past researches have shown that composite soil anchorage methods (using steel profiles, concrete piles or concrete blocks) are quite efficient in controlling displacements in excavation walls. Niroumand and Kassim (2010) are only a few among many researches carried out on the subject. The supporting structure (usually called PSN) combines the structures of the scattered row piles and soil nailing wall; soil nailing is used to support the soil between the piles combining the advantages of scattered row piles and soil nailing and improving the soil stability between piles (Song 2010; Wu et al. 2006; Gong and Sun 2005). As far as the soil nail wall is concerned, its deformation is reduced and its supporting depth is expanded by setting scattered row piles. Although PSN structures are widely used in the engineering practice (Yang and Zhang 2006), few researches (only theoretical and numerical simulation analyses) have been done on them so far focusing mainly on the soil arching effect (Jin et al. 2005; Liu et al. 2010; Yang and Liu 2011) and the internal forces between piles and soil (Chen 2009; Song 2010; Tian 2011).

A point common in all the related studies is a constant excavation depth, but if, for any reason, e.g. when the design parameters are not found at the excavation bed alignment, the excavation depth is to be increased and, therefore, its wall protection system (designed based on the former depth) will not work properly; Therefore, it is necessary that proper measures be taken to stabilize the additional depth, maintain the position of the initial slip surface, prevent the displacements to exceed the allowable limits, and, finally, preserve the stability of the whole implemented system. To achieve these goals, use has been made, in the present research, of a combination of in-situ concrete piles and prestressed anchor cables as a stabilization system for the additional depth. Effects of pile diameter, horizontal spacing, embedded depth, anchor angle, prestressing force, and bonded/unbonded length on the lateral displacements have been studied and the results discussed in full details in the sections that follow.

2-A BRIEF STUDY OF THE GEOTECHNICAL CONDITIONS OF THE PROJECT SITE

The excavation depth was 23m, the excavation amounted close to 160,000 m³, and stabilization was done by 11 rows of nails placed 2 meters apart (vertically and horizontally) at an angle of 15° (Fig. 1).

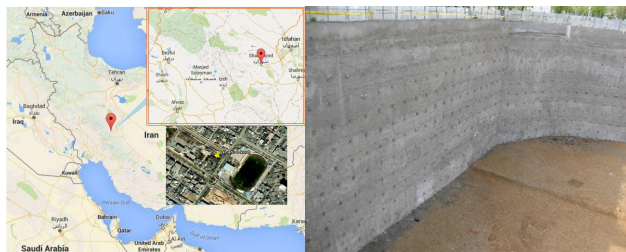


FIG. 1- Site location (red balloons) and a view of nail-stabilized walls

The project in question is situated in Shahr-e Kord, Iran, in a piece of land 7000 m² in area facing streets from three sides and a 1-storey building from the fourth; the site lies in Zagros Zone. Our studies started through drilling three 25m, two 30m, and two 45m deep boreholes none of which met the underground water level. (Table 1).

Table 1- Soil properties used in the FEM simulation

Depth(m)	Soil Type	ϕ (deg)	C(kPa)	γ (kN/m ³)	E(MPa)	Bond stress(kPa)
0-4.5	GC	38	9.8	20	68	250
4.5-12	SC	32	24.5	19	58	200
12-16	GC	38	14.7	20	68	250
16-21.5	GC	40	19.6	20	83	250
21.5-45	SC	38	14.7	20	205	300

3- THE ANALYSIS METHOD

3-1- THE FEM

In this paper, use has been made of Plaxis-2D Ver.8.2 for investigating the wall performance, displacements, settlements, and forces in the members (Brinkgreve 1994 and 2004). Fig. 2a shows an example of the deformed mesh in the software environment for the model being studied. The model boundary conditions have been so defined as to close the horizontal displacements in the left and right boundaries, and all the vertical and horizontal displacements in the lower boundary; the underground water level does not affect the model.

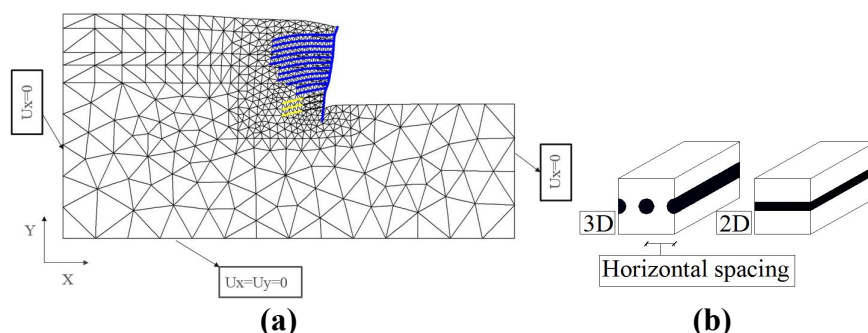


FIG. 2- a)The finite element model, b) 3D to 2D stiffness balancing

3-2- STIFFNESS BALANCING METHOD

For the 3D simulation of a nailing system with 2D software, it is necessary that the members' stiffness be balanced. According to Singh and Babu (2010), the steel bars in grout were modeled using equivalent elasticity modulus (E_{eq}) (relation 1), and the members' stiffness were balanced using the stiffness reduction method based on the members' horizontal spacing (relations 2). Fig. 2b clearly shows such balancing.

$$E_{eq} = E_n \left(\frac{A_n}{A} \right) + E_g \left(\frac{A_g}{A} \right) \text{ and } A = 0.25\pi D_{DH}^2 \xrightarrow{\text{and}} A_g = A - A_n \text{ and } A_n = 0.25\pi d^2 \quad (1)$$

$$EA \text{ (kN / m)} = \left(\frac{E_{eq}}{S_h} \right) \left(\frac{\pi D_{DH}^2}{4} \right) \xleftarrow{\text{and}} EI \text{ (kNm}^2 \text{ / m)} = \frac{E_{eq}}{S_h} \left(\frac{\pi D_{DH}^4}{64} \right) \quad (2)$$

where D_{DH} is the diameter of the borehole, d is the steel bar diameter, E_g is the grout elasticity modulus, E_n is the bar elasticity modulus, EA is the axial stiffness, and EI is the equivalent bending stiffness.

3-3- TYPES OF ELEMENTS USED IN THE SIMULATION

To model the system under investigation, use was made of 15-node triangular elements. Also, to model the longitudinal nail elements, the shotcrete surface and piles, we used the elastic modeling with Plate elements and introducing Interface elements (Song and Chen 1996; Yang 2004). Considering the heave control problems (associated with the pit bottom), and the necessity of studying the soil behavior under loading/unloading, we used the HS (Hardening Soil) model (Liew and Khoo 2006; Singh and Babu 2010), and to model the stabilization system of the additional depth, use was made of prestressed anchors with in-situ concrete piles. To model the prestressed elements, we made use of anchors for the unbounded length and of geogrid elements for the bonded length with axial stiffness (EA) the value of which is a function of the number of the anchors' strands per borehole which, in turn, is a function of the prestressing force required for the design.

3-4- EXCAVATION SIMULATION

To simulate the excavation, use was made of the staged analysis system with 11 separate phases each of which consisted of excavation, nailing at the required level, and applying shotcrete. For the 23 m depth, phase 1 was defined with 2.5 m excavation and the rest with 2 m each. The 7 m additional depth was divided, depending on the number of the rows of anchors, into two phases with 2.5 m and one phase with 2 m excavation (for 2 rows of anchors) or three phases with 2 m and one phase with 1 m excavation (for 3 rows of anchors).

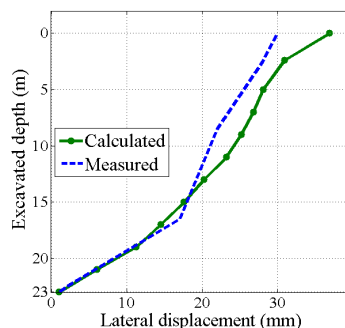


FIG. 3- Comparison of the results of the numerical modeling and field measurements

Fig. 3 shows the wall horizontal displacement found from the field measurements and numerical modeling. As shown, the highest value is at the wall top and decreases with an increase in depth. The numerical results too have shown these variations and it can be claimed that the numerical modeling has had acceptable results.

4- RESULTS AND DISCUSSION

Since the initial depth has been 23 m increasing to 30 m after 7 m of additional excavation, we are to take measures to anchor the additional depth and do not allow the displacements to exceed the permissible limits (δ_h / H and $\delta_v / H < 1/500$) (Lazarte et al. 2003). To achieve these goals, use was made, in this paper, of in-situ concrete piles with anchors, and the effects of the 7 key design parameters (pile diameter, horizontal spacing, embedded depth, anchor angle, prestressing force, and bounded/unbounded length) to be discussed in the following sections were investigated. Fig. 4 shows an overall picture of the wall after additional excavation.

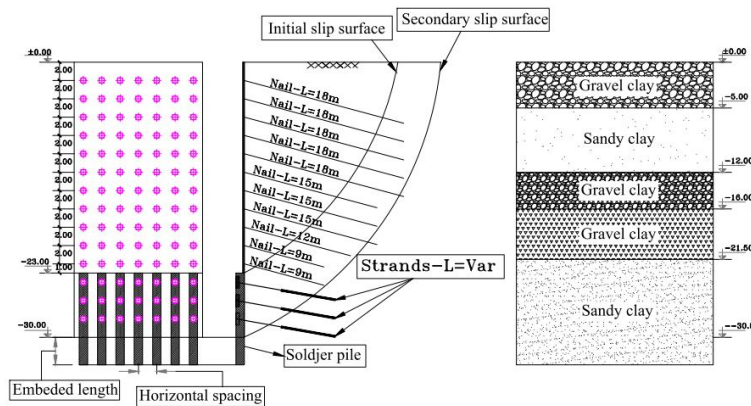
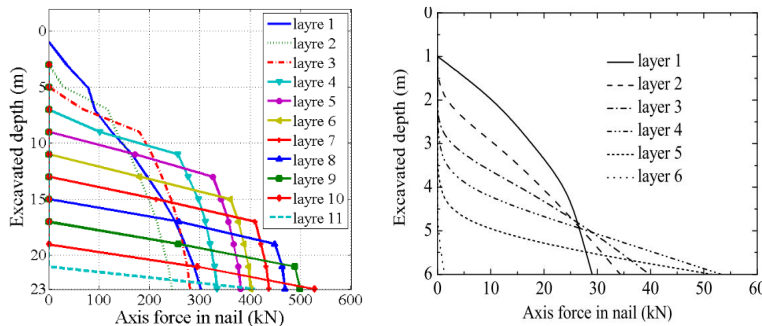


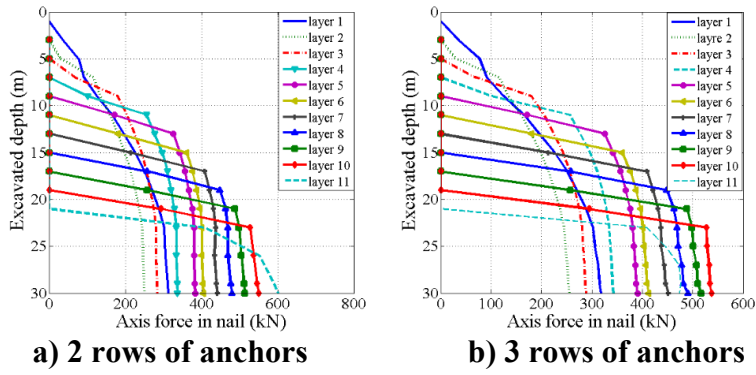
FIG. 4- An overview of the wall after additional excavation

4-1- TENSILE FORCE IN THE NAILS

Figs. 5, 6 show the tensile forces in the nails before and after the additional excavation.



a) Results of this study b) Ma et al.'s results
FIG. 5- Axial force in nails before additional excavation



a) 2 rows of anchors b) 3 rows of anchors
FIG. 6- Axial force in nails after additional excavation

As shown, with an increase in the excavation depth, the displacements increase too causing an increase in the tensile force in the nails; the highest amount is created in row 10. Row 11 experiences less force (compared to row 10) amounting approximately to the force in row 5; the reason could be the cessation of the excavation after this row. This result conforms to those reported by Yang and Song (2004) and Ma et al. (2011). After additional excavation, the force in the nails has not changed considerably; the changes have been considerable in the nails of the last two rows of nails (more intensified when 2 rows of anchors are used).

4-2- EFFECTS OF ANCHOR ANGLE

Effects of the anchor angle on the lateral displacement, were investigated for 2 and 3 rows of anchors at angles of 10, 15, 20, and 25° (and also combinatorial angles according to Tables 2).

Table 2- Combinatorial angles

Number of row	Angle(deg)	Angle(deg)
1	10	15
2	15	20
3	20	25
View	Mixed Angle:1	Mixed Angle:2

Number of row	Angle(deg)	Angle(deg)
1	10	15
2	25	20
View	Mixed Angle:1	Mixed Angle:2

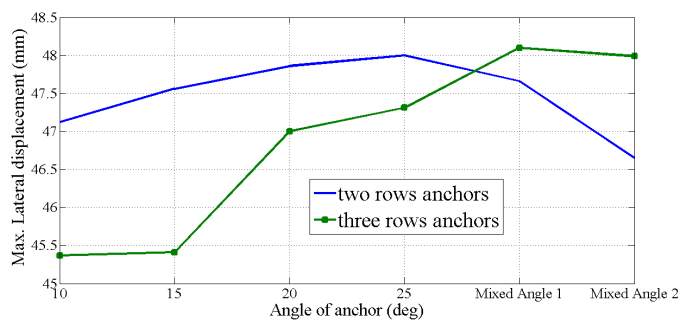


FIG. 7- Effects of anchor angle on the maximum lateral displacement

Fig. 7 shows that when the anchor angle increases from 10 to 25°, the lateral displacements increase too. The effect is quite more if combinatorial angles and 2 rows of anchors are used; the lateral displacement will reduce. If 3 rows of anchors are used, the case related to the combined angles will have the maximum displacement.

4-3-EFFECTS OF HORIZONTAL SPACING OF PILES AND PILE DIAMETER

Any change in this spacing directly affects the performance of the stabilization system; this is clearly shown in Figs. 8a. As shown, when 2 rows of anchors are used for the stabilization of the additional excavation, the maximum lateral displacement (at the excavation edge) caused by an increase in the horizontal spacing, will increase with a greater gradient (compared with 3 rows of anchors). Fig. 8b shows that a change in the pile diameter does not noticeably affect the lateral displacement (for both 2 and 3 rows of anchors).

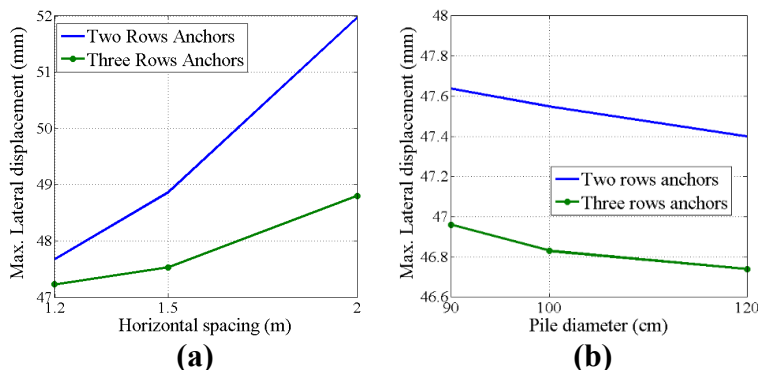


FIG. 8- Effects of horizontal spacing and pile diameter on the maximum lateral displacement

4-4- EFFECTS OF THE PRESTRESSING FORCE AND EMBEDDED PILE DEPTH

To check the effects of the anchors’ prestressing force, different combinatorial forces were studied according to the values in Tables 3 .

Table 3- Anchors’ prestressing forces

Number of row	Preloading(kN) (top to bottem)				
	2Rows	800,800	800,650	650,650	650,500
3Rows	800,800,800	800,650,650	800,650,500	800,500,500	-

Fig. 9a shows that, in general, a decrease in the prestressing force causes an increase in the lateral displacement; for 2 rows of anchors, changes take place with a greater gradient. Fig. 9b shows that the embedded pile depth can affect the lateral displacements.

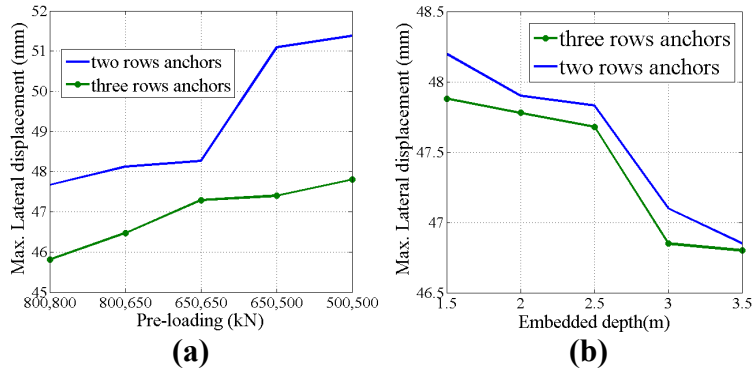


FIG. 9- Effects of prestressing force and embedded pile depth on the maximum lateral displacement

As shown, the effect of the embedded depth of piles from 1.5 to 2.5 m is not too noticeable on lateral displacement. However, the effect of such increase from 2.5 to 3 m is quite noticeable. And increasing the depth to 3.5 m would not greatly influence a reduction in lateral displacement. Thus, 3 m can be take as the optimum depth.

4-5- EFFECTS OF BONDED/UNBONDED ANCHOR LENGTHS

Bonded/unbonded anchor lengths are parameters that affect lateral displacements. Fig. 10 shows that, in general, an increase in the bonded/unbonded anchor lengths will cause (for both 2 and 3 rows of anchors) a decrease in lateral displacements.

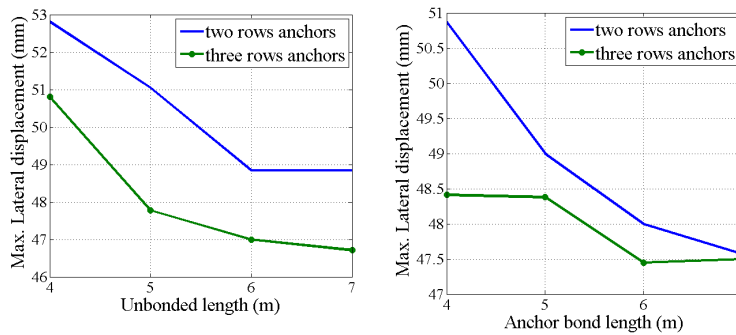


FIG. 10- Effects of bonded/unbonded anchor lengths on the maximum lateral displacement

5- CONCLUSIONS

In this case study, results are as follows:

- 1- FEM results conform well to the field measurements and show that forces created in the nails depend on the nail location; they generally increase with an increase in the excavation depth. The last row is an exception to this rule; it has less force because there excavation has ceased there.
- 2- FEM results show that the additional excavation causes an increase in the force of the existing nails in the lower levels of the initial depth; this increase is much more in

the last two rows (rows 10 and 11). To reduce this force based on the existing capacities, the nails' horizontal spacing in the last two rows may be reduced.

3- Effects of the 7 key design parameters (pile diameter, horizontal spacing, embedded depth, bonded/unbonded length, anchor prestressing force, anchor angle) on the lateral displacements were studied and the results are as follows:

- For 3 rows of anchors (to stabilize the additional excavation), an anchor angle of 10° can be optimal, but for 2 rows, a combination of 15 and 20° would lead to the least lateral displacement.
- A change in the pile diameter does not considerably affect the lateral displacements.
- An increase in the anchors' prestressing force from 500 to 800 kN will lead to a decrease in the lateral displacements.
- An increase in the bonded/unbonded anchor length from 4 to 7 m will cause a decrease in the lateral displacements
- An increase in the embedded depth of the concrete piles will cause a decrease in the lateral displacements and we may consider three meters as the optimum embedding depth.
- It is worth mentioning that the key design parameters studied in this research are somehow interrelated; a change in any one of them will affect the main conditions governing the design; hence, to obtain an optimum design for the project under investigation, use can be made of the graphs found from the results of this research.

REFERENCES

- Brinkgreve, R. B. J. (1994). *Geomaterial models and numerical analysis of softening*, Delft, the Netherlands.
- Brinkgreve, R. B. J. (2004). "PLAXIS-2D user's manual and scientific manual. Version 8[computer program]." *A.A. Balkema: Rotterdam, the Netherlands*.
- Chen, H. T. (2009). "Application and numerical simulation of sparse pile-soil nail wall retaining structure." *Master Dissertation of Jilin University*.
- Gong, B. X., and Sun, Z. (2005). "The design of the retaining support with steel tube piles and soil-nail wall." *Traffic Engineering and Technology for National Defence*, (1): 65-68.
- Hossain, M., and Yin, J. (2012). "Influence of Grouting Pressure on the Behavior of an Unsaturated Soil-Cement Interface." *J. Geotech. Geoenviron, ASCE.*, Vol. 138 (2): 193-202.
- Jin, G. F., Tu, Y. M., and Ruan, C. Q. (2005). "Study on anti-sliding effect of the scattered row piles in soil nailing wall pit-protection." *Rock Soil Mech*, Vol. 26 (4): 577-579. (in Chinese).
- Jin, Q., Li, X., and Hu, B. (2010). "Application of composite soil nailing structure in foundation pit supporting." *Presented at Third International Conference on Information and Computing, ICIC, IEEE*, Jiang Su, China. Vol. 4, 181-184.
- Lazarte, C. A., Elias, V., Espinoza, R. D., and Sabatini, P. J. (2003). "Geotechnical Circular No. 7 – Soil Nail Walls." *FHWA0-IF-03-017. Federal Highway Administration, Washington, D.C.*
- Liew, S. S., and Khoo, C. M. (2006). "Soil nail stabilisation for a 14.5 m Deep excavation at uncontrolled fill ground." *Presented at Proceedings-DFI/EFFC 10th International Conference on Piling and Deep Foundations*, Amsterdam, The Netherlands.

- Liu, B., Yang, M., Yang, Z. Y., and Wu, Z. C. (2010). "Design and practice of composite structure with scattered row piles and soil nailing for pit protection." *China Civil Engineering Journal*, Vol. 43 (10): 106–114.
- Ma, L., Shen, S. L., Du, Y. J., and Sun, W. J. (2011). "A case study of the behavior of soil-nail supported deep mixed wall in the soft deposit of Shanghai." *Lowland Technology International* Vol. 13 (2): 1-8.
- Ma, T., Zhu, Y., and Meng, D. (2013). "Numerical analysis of composite soil nailing retaining wall under earthquake." *Appl Mech Mater*, Vol. 275-277: 1353-1358.
- Niroumand, H., and Kassim, K. A. (2010). "Analytical and numerical studies of horizontal anchor plates in cohesion less soils." *Electron J Geotech Eng*, Vol. 15: 281-292.
- PLAXIS. (2006). "PLAXIS Reference manual." City: Delft University of Technology & Plaxis by The Netherlands.
- Singh, V. P., and Babu, G. L. S. (2010). "2D Numerical Simulations of Soil Nail Walls." *Geotech Geol Eng*, Vol. 28 (4): 299-309.
- Song, E. X., and Chen, Z. Y. (1996). "Soil nailing supported and finite element analysis." *Engineering Investigation.*, (2): 1-5(in Chinese).
- Song, K. X. (2010). *Numerical simulation on combined supporting system consisting of pile-interal-sturct and soil nailing.*
- Tang, L., Song, M., Liau, H., Wu, Z., and Xu, T. (2008). "Analysis of stress and deformation of prestressed anchor cable composite soil nailing." *Chinese J Rock Mech Eng*, Vol. 27 (02): 410.
- Tian, S. W. (2011). "Soil arching effect analysis of the sparse pile-soil nail compound support in foundation." *Master Dissertation of Guangzhou University.*
- Wang, J., Cao, J., Hu, J., and Liu, H. (2008). "Application of FLAC in foundation pit with compound soil nailing wall support." *Presented at Fourth International Conference on Natural Computation, ICNC, IEEE.* Vol. 4,331-336.
- Wu, Z. C., Yang, Z. Y., and Luo, X. M. (2006). "Stability analysis of scattered row pile-soil-nailed wall protection structure." *Chinese Journal of Rock Mechanics and Engineering*, Vol. 25 (S2): 3607-3613.
- Yan, Z. G. (2012). "FEM analysis of composite soil-nailing considering tensile failure." *Appl Mech Mater*, Vol. 105-107 (1488-1491).
- Yang, G. H. (2004). "Practical calculation method of retaining structures for deep excavations and its application." *Rock Soil Mech*, Vol. 25 (12): 1885-1896.
- Yang, J., and Song, E. X. (2004). "Analysis of an underground excavation and recommendation." *Industry Architecture (Supp.)*, Vol.: 333-336. (in Chinese).
- Yang, M., and Liu, B. (2011). "Retaining characteristics of composite structure with scattered piles and soil nailing." *Journal of Building Structures*, Vol. 32 (2): 126–133.
- Yang, Z. Y., and Zhang, J. (2006). "Development and application of composite soil nailing walls in Shenzhen." *Chinese Journal of Geotechnical Engineering*, Vol. 28 (S): 1673-1676.

Understanding the Behavior of Rock-Fall Motion Using Wireless Sensor Technology

Prapti Giri¹; Kam Ng, M.ASCE, P.E.²; Christopher Robinson³; William Phillips⁴; and Marian Phillips⁵

¹Ph.D. Research Assistant, Univ. of Wyoming, Laramie, WY 82071.

²Assistant Professor, Dept. of Civil and Architectural Engineering, Univ. of Wyoming, Laramie, WY 82071. E-mail: kng1@uwyo.edu

³Director of Software Engineering, Silent Solutions LLC, Conifer, CO.

⁴Director of Operations, Silent Solutions LLC, Conifer, CO.

⁵President and CEO, Silent Solutions LLC, Conifer, CO.

Abstract: A recent advancement of technology led to the development of wireless remote sensing devices that can overcome many limitations of some widely used conventional monitoring technologies. This paper is limited to describing the framework of the wireless sensor network (WSN) system that allows wireless communication between the sensors and the remote computer and hence, understanding the motional behavior of the sensors during rock fall. The results from two controlled experiments and a series of free fall experiments where fall was led by rolling and sliding, are presented. Sensor tags were used to indicate slope movement or change in slope behavior leading to failure. A WSN system was developed and installed on a small-scale slope system simulating the free-fall of rock mass. Our experimental results describe different rock fall patterns which facilitate subsequent establishment of failure thresholds. Results obtained from these laboratory experiments will improve potential slope failure prediction and alleviate its hazardous risk through the development of a warning system. Being accurately informed of impending failure is in itself a great achievement; knowing the failure type helps people envision the extent of damage the failure would cause. This advancement increases the safety of lives and properties.

INTRODUCTION

Geotechnical slope stability monitoring has been a serious concern and need of our society for decades after experiencing significant fatalities and loss of properties of significant value. According to the Transportation Research Board (TRB 1996), nearly every state of the United States suffer from landslides, and regions close to water bodies are more vulnerable to such hazard. In Wyoming there has been nearly \$20 million in dam failure damage costs since 1906. Currently, more than 30,000 dams in Wyoming are aging (Wyoming Homeland Security 2011). According to an estimate documented by Highland (2012) of the U.S. Geological Survey, the total direct costs of landslides in Colorado for the year 2010 were over \$9 million,

including nine casualties and four injuries. Many scientific research works have been carried out for decades in the field of hazard monitoring, particularly landslide. The conventional technologies use inclinometers, strain gauges, tilt-meters and extensometers for monitoring slope movement. These methods have many limitations, such as heavy drilling and boring required on unstable slopes for the device installation, vulnerability to harsh weather conditions, lack of real-time data collection and transmission, manual data recording and high cost of devices. A recent advancement of technology led to the development of wireless remote sensing devices that can overcome many limitations of some widely used conventional slope monitoring technologies. However, the wireless sensor network (WSN) system have not been deployed widely in the field of landslide monitoring, especially in USA. Also, this system has been used only as a tool to detect movement irrespective of its type and magnitude. The purpose of this research is to advance the WSN system for identifying different types of slope movement and warning the users of facilities such as transportation, coal mines, and water structures of impending slope failures. This paper particularly focuses on the results of laboratory experiments that were carried out to test the system operation, validate data collected by the sensors, and identify the typical pattern of rock fall led by rolling and sliding.

LIMITATIONS OF CURRENT MONITORING SYSTEMS

In the process of monitoring slope failures and alerting people of impending slope failures, several systems beside the conventional technologies have been recently developed. Amongst all are fiber optic sensors, robotic total station, Ground-Based Interferometric Synthetic Aperture Radar (GB-InSAR) and wireless sensor network system. The fiber optic device designed by Li et al. (2013) is composed of a series of fiber optic sensors, including fiber bragg grating (FBG) strain gauge, FBG inclinometer, and FBG soil-pressure sensor. They are difficult to install in unstable slopes as the sensors need to be placed deep inside the soil/rock mass to monitor movements. Also, the system is vulnerable to rainfall, and the operation cost is high. Likewise, a robotic total station (Fung et al. 2014) may not be applicable to slopes with vegetative coverage that obstructs the view between a target and the total station. According to a recent case study in Børa, Norway, GB-InSAR was incapable of properly monitoring slope movements during snowfall as the coverage of slope face with snow obstructs the recording of exact slope movement (Rouyet 2013). Also, the operation and handling cost is high so use of this system for continuous monitoring could be expensive.

Wireless sensor network system is a recent advancement in this field. It can overcome the shortcomings of many systems mentioned above, such as real-time monitoring, device installation, system installation cost, operation cost, and difficulty in system handling. The Sensor-based Landslide Early Warning System (SLEWS) developed by Arnhardt et al. (2010), and an internet-enabled WSN system consisting of accelerometer and soil moisture sensor in the sensor device by Smarsly et al. (2014), could overcome some of the limitations of conventional monitoring systems. These systems have not been deployed to monitor rock fall, which is more challenging to predict and a common failure mode in a mountainous region. The WSN system has not been pragmatically applied for slope monitoring in USA

because 1) the system was mostly developed by other professions focusing on system development and data collection, 2) slope movement and failure process are not clearly understood from the field data collected by the WSN system, and 3) the successful development of a reliable WSN system for slope monitoring requires a collaborative effort of multidisciplinary experts. The understanding of sensor data is vital for describing the type of slope movement and accurately predicting the time and extent of a slope failure. The application of WSN system in all-weather condition, including snowfall and rain, is necessary to confirm its uninterrupted operation during harsh weather or in a buried condition. To address these limitations, our ongoing research project began with the development of a pragmatic and efficient WSN system through laboratory experiments to understand the association between collected data and slope movement types. Due to space limitation, this paper presents some controlled laboratory experiments and fall experiments.

SENSOR NETWORK SYSTEM FRAMEWORK

Our experiments were conducted using wireless technologies including Bluetooth Low Energy (BLE) or Bluetooth 4.0 communication toolset. With the current need of our laboratory experiments, the distance limitation of 45 m for Bluetooth was adequate for testing only. The communication tools will be switched to different firmware when a longer communication distance is needed, allowing for peer to peer meshing network. It includes 6LOWPAN which stands for IPv6 over Low Power Wireless Personal Area Network that allows low-power devices with limited processing capabilities to be in the network enabling data collection and exchange between the devices (e.g. sensors) and the remote computer. The field tests will make use of these two communication technologies based on the environment, and distance from collection server. The primary software used are Nodejs for collecting data, Node-red for design, and MySQL for data storage. Node-red was used for the primary programming interface to allow ease of learning and understanding the logical flow of functions while programming. Node-red enables us to open a connection using a BLE, Synapse, or standard wireless USB dongle that allows bi-directional communication with the sensors. Currently, the sensors have a maximum data stream at a rate of 1 sample/per approximate 100 ms.

The WSN system consists of Texas Instruments (TI) Sensor tags, having 9 degrees of motion (i.e. 3 degrees of acceleration, 3 degrees of rotation, and 3 degrees of the direction of magnetic field), and BLE wireless network for communication between the ARM based computer (On Site Collector) and with the Sensor tag. The long term off-site database is connected via a USB cellular or satellite Internet Connection. The basic setup configuration for this WSN system is illustrated in FIG. 1. The system is provided with Virtual Private Network (VPN) connected to provide bi-directional secure communication as well as having a private network through the Internet. The accelerometer, gyroscope and magnetometer data in 3-axes are generated by the Sensor Tag sensor. The tag sends data via BLE protocol to an ARM based computer running the node-red Collection program. The Node-red collection program then provides a time stamp, and simple MySQL database to allow a copy of the data to be stored locally, and later transmission to central repository for further study. The ARM based Collection system is very versatile due to its multitude of abilities to transmit

the data back to the long-term storage servers. It can use plain old telephone lines, cellular modems, satellite connections, long range wireless technologies, or basically anything that can give an IP address and route traffic to/through the Internet. The system can be built for field monitoring with higher data frequency up to 10Hz and the communication range between the sensors and the computer of up to 2,200 m.

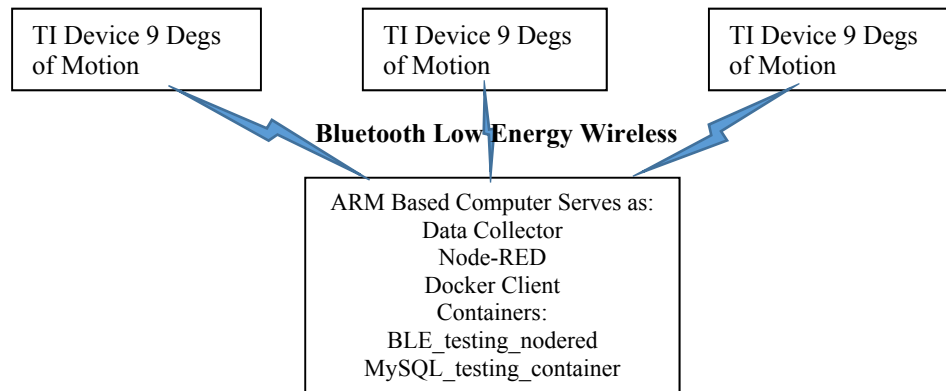


FIG. 1. WSN basic setup configuration.

On any slope to be monitored, the sensor devices will be placed at the locations detected as unstable over the entire slope. The installation of sensor on rock mass involves attaching the sensor to the rock using weatherproof, highly adhesive material such as non-toxic and nature safe epoxies. The sensors could be placed with quad-copter flying machine to help reduce the risk of human life to climb to the location of the monitored rocks. On soil slopes, the sensor devices will be installed such that about 1 to 4 cm diameter protruding anchor attached to the device, is penetrated into the soil to a depth depending on the depth of underlying firm or more stable layer.

SENSOR TESTING

Controlled rotation and controlled fall experiments were setup at the University of Wyoming to understand the data collected by accelerometers. Measured data was compared with theoretical values to verify the accuracy of the sensor. All the tests were conducted with the sensor within a distance of 5 m and the data collection frequency was 10 Hz.

Controlled Rotation Experiment

The main objectives of the controlled rotational experiment are to check the accuracy of the accelerometer readings and to understand the measurements taken by a 3-axis accelerometer. Sensor testing involved comparing the results obtained from the 3-axis accelerometer at various orientations (direction of x, y, and z axes) of the sensor and the theoretical values, determined using mathematical equations, expressed in terms of the gravitational acceleration (g). The experiment helped to understand the motion behavior of the sensor in terms of “ g ” values in three axes.

The experiment was carried out using a model with a platform that could rotate from 0 to 90° (FIG. 2(a)). Sensor device was mounted onto the platform at the center, top right and bottom left corners to understand the effect of sensor positions on the

sensor data. A magnetic-mount angle indicator was used to set the platform at different angles. At the beginning, the rotating platform was set at a horizontal position and levelled using a 2-axis bubble level. After levelling the block, the first rotation test was conducted at 0° by placing the sensor at the center of the platform with +z facing the base in the direction of gravity, +x facing forward in the direction of rotation and y along the axis of rotation (FIG. 2a). About 200 data samples were collected. The platform was rotated to 15° and the data were collected. The experiment was repeated for 30°, 45°, 60° and 90° with respective data collection.



(a) Rotating platform setup (b) Sensor testing at 45° rotation

FIG. 2. Controlled rotation experimental setup and testing.

The x, y and z acceleration values shown in Table 1 are the average of acceleration data collected for about 20 secs at an update speed of 100 ms (i.e. 1 data per 100 ms). A sample of raw data collected for the previously described experiment at 0° rotation are presented in FIG. 3. FIG. 3 shows consistent acceleration values in z-axis with the maximum variation of only about 0.01g along the almost level linear best fit line. Similar small variation of acceleration values in x and y axes were observed. Hence, the average acceleration values in x, y and z-axes were reasonably determined for each experiment as summarized in Table 1. The resultant acceleration (G_R) calculated using Equation (1) is presented in Table 1 to confirm that these values are close to theoretical resultant (G'_R) value of 1g.

$$G_R = \sqrt{G_{x-m}^2 + G_{y-m}^2 + G_{z-m}^2} \tag{1}$$

where, G_{x-m} , G_{y-m} , and G_{z-m} are measured accelerations in x-axis, y-axis, and z-axis, respectively. The measured average accelerometer data were compared with the theoretical values determined using mathematical equations obtained by resolving the resultant acceleration (G_R) into two axes in the plane of rotation. The third axis along the axis of rotation is always zero since there is no change in orientation with respect to rotation. In this case, the sensor device is placed on the platform such that x was facing forward in the direction of rotation, y is parallel to the axis of rotation and z is facing downward. Equations (2) and (3) were established based on this setting to compare the measured results.

$$G_{x-c} = \sin \theta \times G_R \tag{2}$$

$$G_{z-c} = \cos \theta \times G_R \tag{3}$$

where, G_{x-c} is the calculated acceleration in x-axis, G_{z-c} is the calculated acceleration in z-axis, and θ is the degree of rotation with respect to horizontal plane. Comparison of the results in FIG. 4 shows that the theoretical and measured acceleration values are in good agreement.

Table 1. Accelerometer data at different sensor rotations and positions

Sensor Orientation	Rotation, θ (degree)	G_{x-m} (g)	G_{y-m} (g)	G_{z-m} (g)	Resultant Acceleration, G_R (g)
+z facing in the direction of gravity, +x facing forward in the direction of rotation and y along the axis of rotation	Sensor Placed at the axis of rotation				
	0	-0.07	0.03	0.90	0.90
	15	-0.25	0.01	0.88	0.91
	30	-0.50	0.00	0.77	0.92
	45	-0.71	-0.01	0.61	0.93
	60	-0.87	-0.01	0.39	0.95
	90	-1.00	-0.02	-0.13	1.00
	Sensor Placed at the top right corner of platform				
	0	0.01	0.02	0.91	0.91
	15	-0.24	0.01	0.87	0.91
	30	-0.49	0.00	0.78	0.92
	45	-0.71	-0.01	0.61	0.93
	60	-0.87	-0.01	0.39	0.95
	90	-1.00	-0.02	-0.07	1.00
	Sensor Placed at the bottom left corner of platform				
	0	-0.01	0.02	0.91	0.91
	15	-0.27	0.01	0.88	0.92
	30	-0.51	0.01	0.77	0.93
	45	-0.73	0.00	0.60	0.94
	60	-0.88	0.00	0.39	0.97
	90	-1.00	-0.01	-0.12	1.01

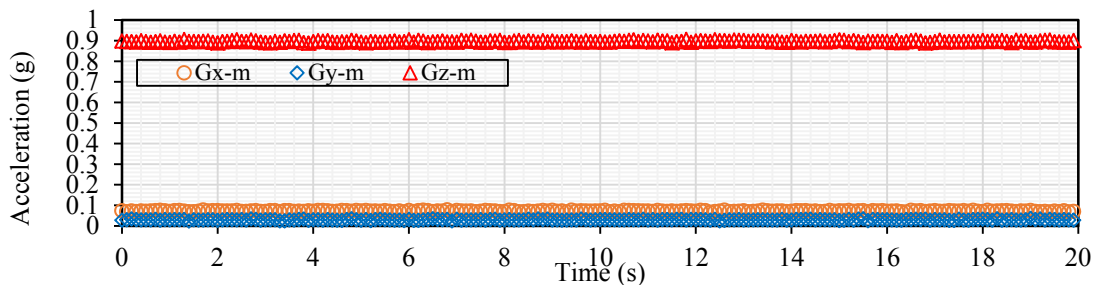


FIG. 3. Acceleration vs time (sec) in x, y and z-axes at 0° rotation.

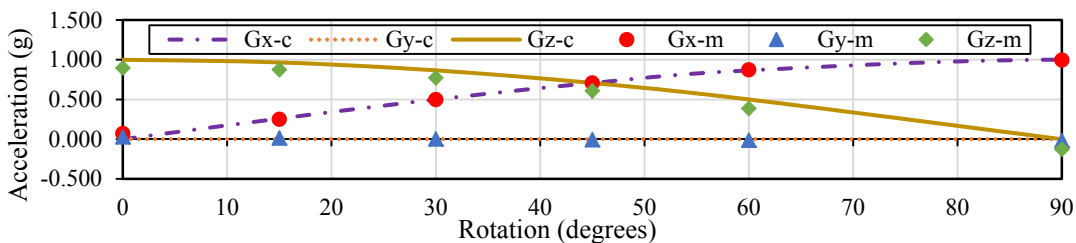
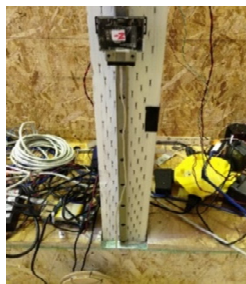


FIG. 4. Comparison of accelerations at rotation angles from 0 to 90°.

Controlled Fall Experiment

Similar to the controlled rotation experiment, the objectives of controlled fall experiment are to further verify the accuracy of sensor and understand the movement in terms of measured acceleration. Here, the measured acceleration is equal to gravity since the motion is constant using a constant 2.5 rpm motor to pull the bearing vertically down. FIG. 5 shows the laboratory experiment setup with the sensor device placed on a vertically positioned linear bearing such that positive x-axis faced vertically downward in the direction of fall, with y-axis and z-axis parallel to horizontal plane. The height of controlled fall was about 45 cm.



(a) Overall setup



(b) Sensor tag attached to the bearing

FIG. 5. Controlled fall experimental setup and testing.

Three test runs, for the same sensor setup as described above, were conducted to check the consistency of the experimental data and to evaluate the acceptance of these data. The expected acceleration value in x-axis is 1g while 0g is expected in y and z-axes. The acceleration values from three similar experimental runs are plotted as a function of time in FIG. 6. The results consistently show that the G_{x-m} values are close to 1g for the x-axis facing in the vertical direction of motion while G_{y-m} and G_{z-m} values are small and often close to zero. Discrepancy between those expected and measured values was attributed to the bearing slide rail not being perfectly vertical to the direction of gravity. The measured data were within 0.05g for G_{x-m} , 0.016g for G_{y-m} and 0.014g for G_{z-m} with respect to their corresponding average acceleration values.

FALL EXPERIMENT

Free fall of rock mass is one of the common slope failure modes, especially in a mountainous region. Fall often associates with a complex landslide at which at least two types of movement involved in the fall activity. In this paper, rock roll-rock fall and rock slide-rock fall were simulated in the laboratory. The purpose of the experiment is to understand the sensor data associated with typical movement patterns prior to and during fall. Beside acceleration measurements, the sensor also equipped with a gyroscope that measures an angular velocity and a magnetometer that identifies its absolute orientation with respect to earth's magnetic north. However, due to space limitation, only acceleration data was presented and discussed in this paper. Two types of fall experiments performed on two object models are described and the results are presented in the following sub-sections.

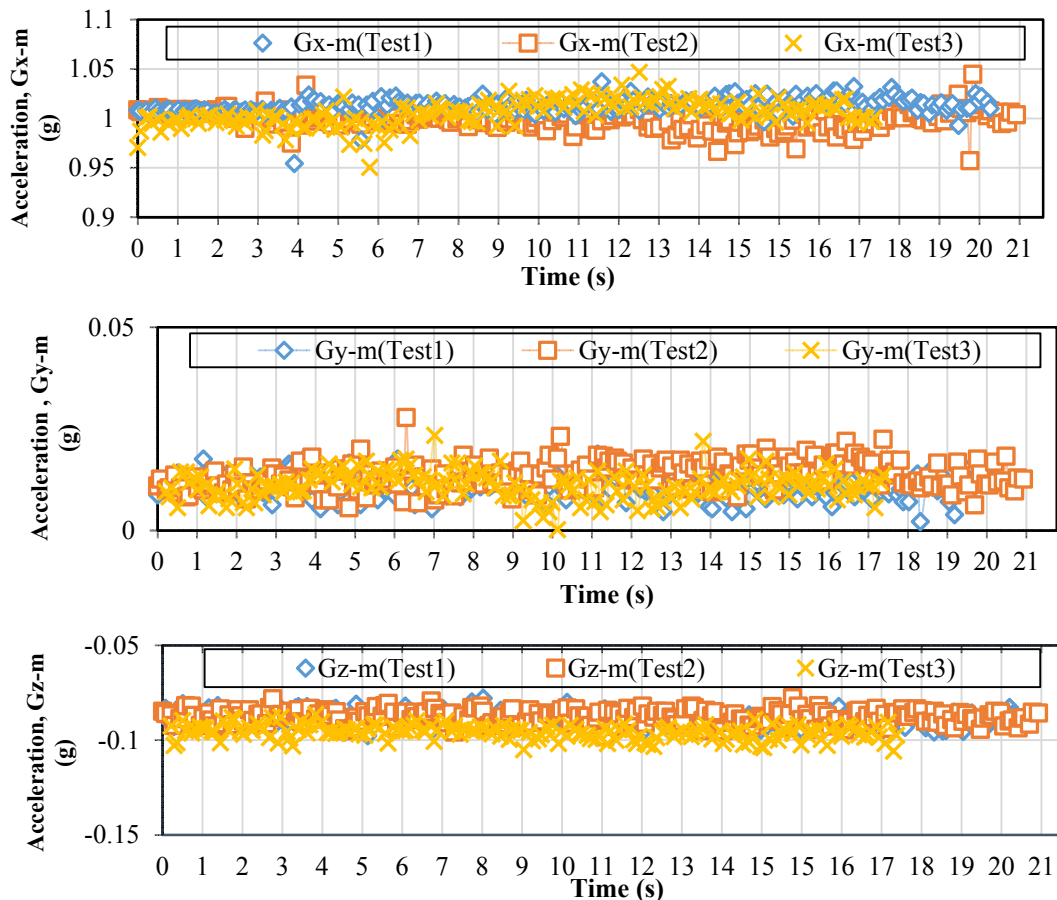


FIG. 6. Comparison of accelerations from three similar experiments with x-axis of the sensor facing in the downward direction of motion.

Both fall experiments used the same laboratory setup as illustrated in FIG. 7 except the two different falling object models used in the roll-fall and slide-fall experiments. The experiment consisted of a wooden box (1.2m×1.2m) with a photoelectric sensor setup at the floor level (FIG. 7(b)) and the platform supported on a wooden post at a height of about 2.2 m above the floor level. The setup was made such that rolling or sliding of the object can be performed on an almost perfectly horizontal platform and in a fixed path guided by two wooden walls along the platform. Two photoelectric sensors are provided on the platform (FIG. 7(a)). The photoelectric sensor-1 at the back activates data collection from TI Sensor tag, the photoelectric sensor-2 on the edge defines the beginning of fall, and the photoelectric sensor-3 at the floor terminates the data collection (FIG. 7(b)).

Roll-Fall Experiment

To simulate the rolling of rock mass before the free fall, a sensor tag was mounted onto a cylindrical object made of a packing tape as shown in FIG. 8. The object was made to roll over the platform using an electric motor at a constant 2.5 revolution per minute, a cable, a wooden wheel and a hollow steel rod. The setup was made such that one end of an inextensible flexible cable was attached to the motor and the other

end was tied to a hollow steel rod that easily slid in the gap provided on the wooden walls (FIG. 8(c)). The wooden wheel with a groove (FIG. 8(d)) was attached to the revolving rod of the motor to increase the pulling speed of the cable. As the cable winds on the wheel, the steel rod at the back of the rolling object moved forward pulling the object towards the edge of the platform and letting it fall. Experiments were carried out at different orientations and starting positions of the sensor shown in FIGs 8(b) and (c). Same experiment was conducted twice to check its repeatability of sensor measurements.

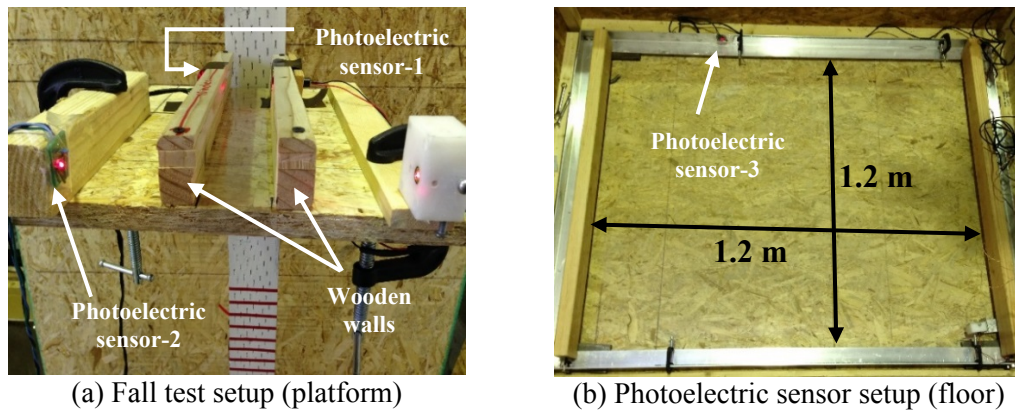


FIG. 7. Experimental setup for fall tests.

The measured acceleration results with respect to time are plotted in FIG. 9 for the test runs 1 and 2. For test runs 1 and 2 shown in FIGs 9(a) and 9(c), respectively, G_{y-m} values were nearly zero since y-axis was oriented parallel to the axis of rotation of the rolling object. G_{x-m} value changed sinusoidally from about $-0.7g$ to 0 , 0 to $1g$, $1g$ to 0 and returned to about $-0.7g$. The result shows that positive x-axis was rotating from about 225° position with horizontal plane when it first reached the photoelectric sensor-1. It began to roll, changing the angle with horizontal from 225 ($-0.707g$) to 270 ($0g$ value) and to 360° ($1g$ value) and so on completing about 495° before the free fall. Likewise, G_{z-m} values also changed in the same way as the G_{x-m} but with different corresponding rotating angles, z-axis being perpendicular to x-axis. At the time 0 sec, the initial G_{x-m} and G_{z-m} values were about $-0.7g$ since both rotations were at 225° with the horizontal plan. When G_{z-m} value changed to about $-1g$ with the negative z-axis faced downward in the direction of gravity, the perpendicular x-axis yielded G_{x-m} value of $0g$.

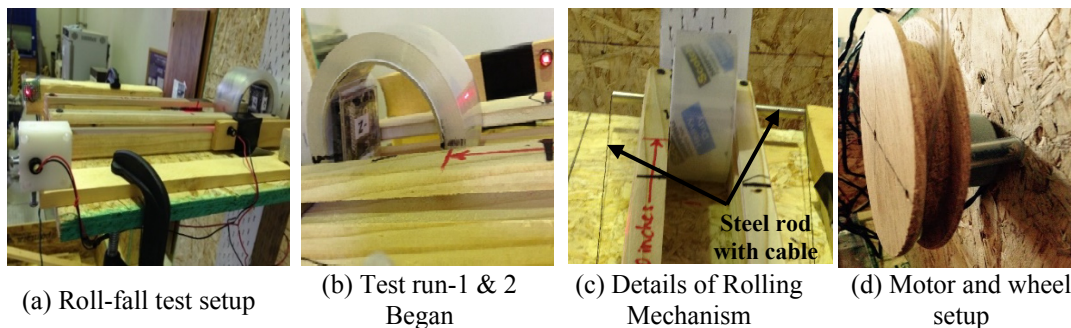


FIG. 8. Experimental setup and positions of sensor tag in a roll-fall experiment.

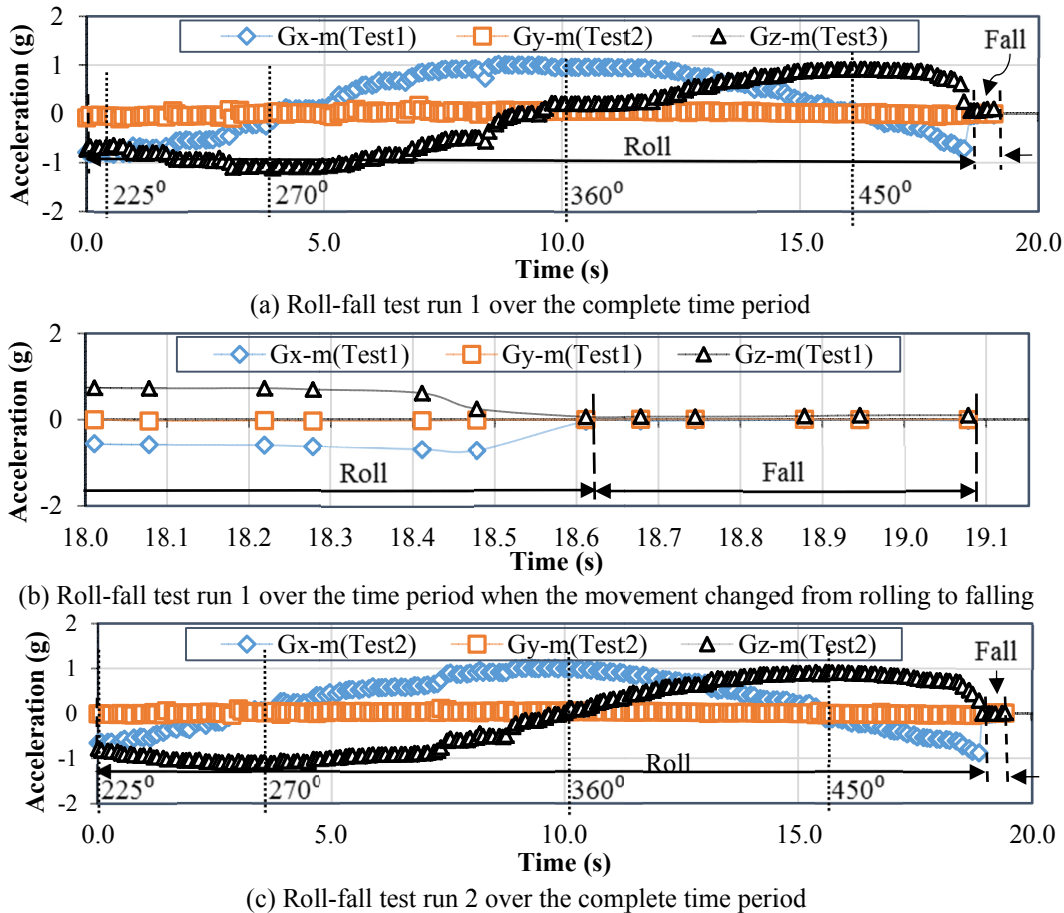


FIG. 9. Acceleration results of the roll-fall test runs 1 and 2.

A clear distinction between rolling data and fall data was observed in FIG. 9. The accelerations in two axes in a plane perpendicular to the platform, drastically changed from +1g or -1g to as close as zero value. This is because the measured acceleration is the vector sum of gravity and motion accelerations. In this case, motion acceleration is almost zero because of nearly constant velocity of the rolling mass. Data from the test runs 1 and 2 were almost the same, confirming the repeatability of the test results, and were comparable to the calculated values for gravity acceleration (FIG. 10).

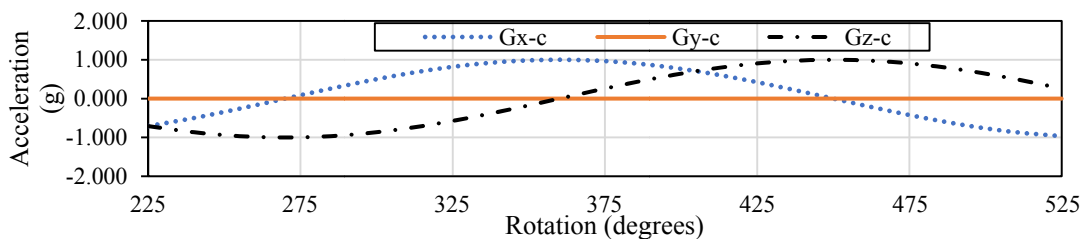


FIG. 10. Calculated acceleration vs rotation for Test runs 1&2.

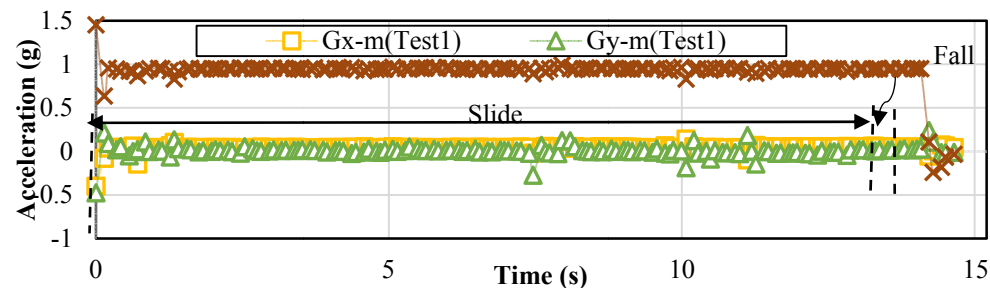
Slide-Fall Experiment

Slide-fall experiment was carried out by using the same setup that was used for the roll-fall experiment. In this experiment, however, the object used was a wooden block

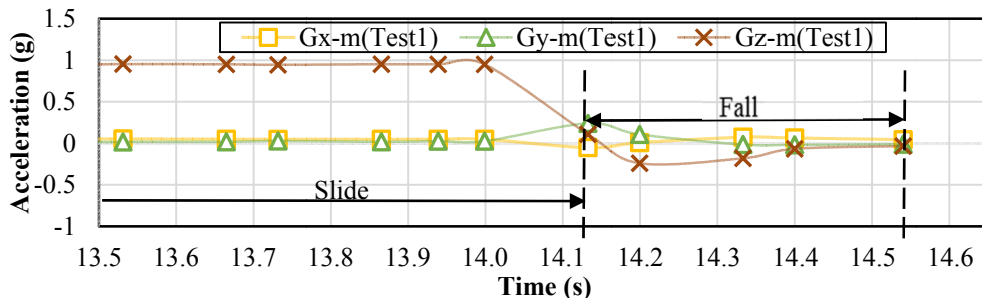
that could slide easily on the platform before falling (FIG. 11). The same motor and cable setup was used to pull the sliding block at a constant speed on the platform to the edge such that measured acceleration equals gravity and allow free fall. A sensor tag was mounted onto this sliding block and the three photoelectric sensors were similarly setup with different functions. The first photoelectric sensor at the back of the platform started the data collection from the sensor tag as soon as the sliding block obstructed the laser beam hitting the photoelectric sensor. Data was stored into MySQL Workbench with fall type “I” representing initial data or the sliding data. As the block slid and obstructed another laser beam hitting the second photoelectric sensor placed on the edge of the platform, the sensor tag data were marked with letter “F” representing fall. As the sliding block hit the ground, it obstructed the third laser beam and stopped data collection from the sensor tag.



FIG. 11. Experimental setup for a slide-fall experiment.



(a) Slide-fall test over the complete time period



(b) Slide-fall test over the time period when the movement changed from sliding to falling

FIG. 12. Acceleration result of the slide-fall test.

Results of the slide-fall experiments for three test runs of the same test, with +x facing backward in the opposite direction of sliding, +y in the direction perpendicular

to x in horizontal plane and +z in the direction of gravity, are presented in FIG. 12. During the sliding phase, +z facing towards gravity yielded acceleration data (G_{z-m}) closer to 1g, whereas x and y-axes being perpendicular to the direction of gravity yielded results (G_{x-m} and G_{y-m}) closer to zero. The discrepancy between expected and measured value was attributed to the wooden platform being not perfectly horizontal. FIG. 12 shows a sudden change or drop of acceleration value in the axis along the direction of gravity from almost constant approximate value of 1g to close to zero. This is because during free fall the gravity and motion acceleration measured by the sensor are equal and opposite resulting is zero measured acceleration.

CONCLUSIONS

A basic setup configuration of WSN system designed for monitoring landslides is presented. Experiments conducted in the laboratory supported the performance and implementation of the WSN system developed for continuous and quasi-real time (1 data per 0.1sec) monitoring of movement processes. All experiments carried out in the laboratory were conducive to confirm the credibility of the sensors used in the WSN system for slope stability monitoring. Laboratory experiments for fall tests confirmed the repeatability of any experiments carried out for multiple runs. Results from this experiment were verified by calculated acceleration at each rotation. The discrepancies in x, y and z-axis data were about 0.7%, 2.9% and 10% of the calculated data for a particular test. Controlled fall experiment was conducted to check the accuracy of the sensor device. The data collected for the experiment were within 0.05g for acceleration in x-axis, 0.016g for acceleration in y-axis and 0.014g for acceleration in z-axis with respect to their corresponding average acceleration values. Laboratory experiments described in this paper improved our understanding of the measurement collected by the sensor devices. These experimental data will provide the basis for establishing failure threshold values that are required in the development of a hazard warning system for slopes.

REFERENCES

- Highland, M.L. (2012). Landslides in Colorado, USA: Impacts and Loss Estimation for the Year 2010. Report 2012-1204, U.S. Geological Survey, U.S. Department of Interior.
- Wyoming Homeland Security. (2011). Wyoming Multi-Hazard Mitigation Plan: Chapter 4 – Dam Failures. June: 4.1-4.10.
- Arnhardt, C., Fern, T.M. & Azzam, R. (2010). "Monitoring and Early Warning of Slope Instabilities and Deformations By Sensor Fusion in Self-Organized Wireless Ad-Hoc Sensor Networks". *International Symposium and the 2nd AUN/Seed-Net Regional Conference on Geo-Disaster Mitigation in ASEAN-Protecting Life from Geo-Disaster and Environmental Hazards*, 2(3): 163–169.
- Li, F., Du, Y., Zhang, W, Sun, B., and Li, F. (2013). "Monitoring system for high steep slope based on optical fiber sensing technology". *Advanced Sensor Systems and Applications V*, 8561: 1-6.
- Smarsly, K., Georgieva, K., and König, M. (2014). "An Internet-Enabled Wireless Multi-Sensor System for Continuous Monitoring of Landslide Processes". *International Journal of Engineering and Technology*, 6(6): 520-529.
- Rouyet, L. (2013). "Monitoring and Characterization of Rock Slope Instabilities in Norway using GB-InSAR". Master Thesis, University of Lausanne, Switzerland.

The Use of LiDAR for Monitoring and Assessing Landslides

Timothy D. Stark, F.ASCE, D.GE¹; and Ahmed K. Baghdady²

¹Professor, Civil and Environmental Engineering, Univ. of Illinois at Urbana-Champaign, 205 N. Mathews Ave., IL 61801. E-mail: tstark@illinois.edu

²Graduate Research Assistant, Dept. of Civil and Environmental Engineering, Univ. of Illinois at Urbana-Champaign, 205 N. Mathews Ave., IL 61801. E-mail: baghdad2@illinois.edu

Abstract: This paper illustrates techniques for assessing the location of past and future landslides using LiDAR. More importantly, this paper will use LiDAR to identify areas susceptible to large landslides which is important for hazard mapping, safe zoning, and public safety. The assessment techniques will be illustrated using the 2014 SR-530 landslide near Oso, Washington. This major and tragic landslide exhibited some important aspects of geo-mechanical behavior that will be discussed and how LiDAR and geotechnical reconnaissance can be used to avoid a future tragedy.

INTRODUCTION

Geohazards due to landslide have caused widespread damage across the United States. According to the U.S. Geologic Survey (USGS), landslides cost the United States between \$1 billion and \$2 billion in damages and kill more than 25 people every year. Improving our understanding of landslide failure mechanisms and triggering factors is crucial to enhancing hazard and risk assessment procedures. The first step towards a reasonable assessment of areas susceptible to landslides is acquiring an accurate topographic survey through which morphological features can be characterized. Light detection and ranging (LiDAR) - also known as airborne laser scanning (ALS), airborne laser swath mapping (ALSM) - is a relatively new technology that helps identifying topography with a reasonably high resolution. Several studies have demonstrated the significance of LiDAR data in identifying landslide prone areas and even locating previously unmapped landslides. (Haneberg et. al, 2009).

In the present case study, a 0.91 m resolution digital elevation model (DEM) acquired with airborne LiDAR has been used to understand the behaviour of the 2014 SR-530 landslide near Oso, Washington. The 2014 landslide provides the industry with some lessons for future mapping of landslide prone areas that are discussed

herein. A separate paper presents the failure mechanism and material properties derived from an investigation into the 2014 SR-530 Landslide (Stark et. al, 2016).

SR-530 LANDSLIDE

On 22 March 2014, a catastrophic landslide destroyed the Steelhead Haven community near Oso along the North Fork of the Stillaguamish River in Snohomish County, Washington. The landslide is referred to as the SR-530 landslide because the slide debris buried Washington State Route 530 (SR-530) that connects Arlington and Darrington, Washington. The landslide is considered the deadliest landslide event in the American history (Keaton et al., 2014), tragically destroying more than 40 homes and killing 43 people. The slide involved approximately 8.3 million cubic meters of glacial deposits and water filled colluvium from prior landslides present along the slope toe. The 2014 slide debris travelled more than 1.5 km to its distal edge on the south side of SR530.

The crest of the SR530 landslide slope is located at approximately elevation 270 m (880 ft) on the north side of the west trending valley of the Stillaguamish River, which is around elevation 75 m (246 ft). The slope is a part of large glacial terrace deposit that developed after the advance of continental ice sheets into the Puget Sound. The width of Stillaguamish River Valley varies from 2.0 km to more than 6.0 km. The 2014 slide occurred at a relatively narrow reach of the river where it flows north then flows west along the slope toe. The river erosion, especially at the eastern part of the slope, has caused a number of shallow landslides in the lower part of the slope including slides in 1937, 1951, 1952, 1967, 1988, and 2006.

Bedrock in the immediate landslide area primary consists of Jurassic metasedimentary, metavolcanic, and ultramafic rocks in the western portion of the valley and Tertiary sedimentary and volcanic rocks in its eastern portion (Dragovich et al., 2002; Keaton et al., 2014). Quaternary-age surficial deposits mantle the bedrock and include glacial-fluvial Outwash, glacial Till, glacial Lacustrine, and abundance of landslide deposits as shown in Figure 1.

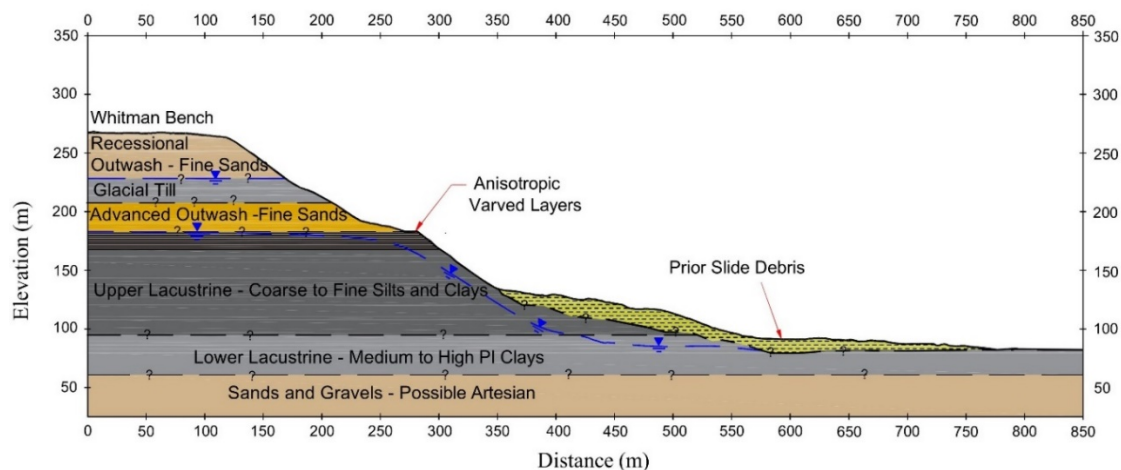


Fig. 1. Geologic cross-section of the landslide area

LiDAR DATA

Topographic conditions before and after the 2014 SR530 slope are documented in a series of high resolution airborne LiDAR surveys taken prior the 2006 landslide event (2003) and prior to and after the 2014 SR530 landslide event. Analysis of the LiDAR topographic relief images shows many large prehistoric landslides including one at the location of the 2014 slide. The significant feature of these prehistoric landslides is they all involve the upper glacial terrace, i.e., the Whitman Bench, and are not just shallow slides along the slope toe caused by river erosion.

The occurrence of an ancient slide at the location of the 2014 slide is important because it created the Ancient Landslide Bench shown in Fig. 2 that supported and protected the Whitman Bench from the shallow slides below caused by river toe erosion. Based on the geometry of neighboring slides shown in Fig. 2, it is anticipated the ancient landslide at this location occurred through the weak varved lacustrine layers in the upper Glacial Lacustrine deposit and involved the overlying Whitman Bench. After this slide, a bench or ledge was created that buttressed the overlying Whitman Bench and protected the Whitman Bench slope from shallow slides and river toe erosion

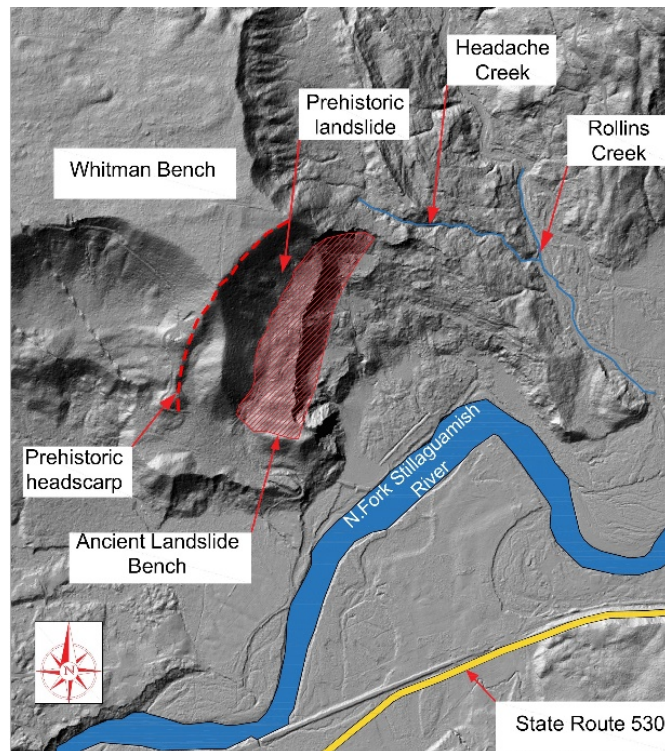


Fig. 2. LiDAR-derived topography showing the SR530 landslide in context with the Ancient Landslide Bench (see shaded area).

HISTORICAL LANDSLIDE DATA

The 2014 SR530 landslide occurred in a slope with a history of prior landslides. Aerial photographs of the 1932 (Thorsen, 1969), 1937, 1951, 1952, 1967, 1988, and 2006 landslide events, show only the lower portion of the slope was involved and the sliding was confined to the Upper and Lower Lacustrine Clay layers. This shallow sliding removed some of the Ancient Landslide Bench but there was still sufficient width of the bench to support the overlying Whitman Bench until 2014. In each of these shallow slides, the slide mass would move the active river channel to the south away from the slope toe. The river would then start eroding the slide debris until the river was again undermining the Lower Lacustrine Clay and overlying slope. Based on the date of prior slides and aerial photographs, it took about 35 to 40 years to erode enough slide debris to initiate another shallow landslide in the Upper and Lower Lacustrine Clay layers that would remove some of the Ancient Landslide Bench especially on the eastern end.

For example, Fig. 3 presents the slope cross-section shown in Fig. 1 and the difference in slope topography in 2003 and 2013 from LiDAR images. Using the difference in topography from 2003 and 2013, the source and accumulation zones for the 2006 slide were determined and are shown in Fig. 3. These zones show the source of the 2006 slide mass is the Upper and Lower Lacustrine Clays and the resulting slide debris moved the river to the southern extent of the accumulation zone. This is important for concluding the Stillaguamish River did not contribute to the 2014 slide because the river was significantly south of the slope toe.

More importantly, Fig. 3 shows the upper portion of the source zone removed about 21 lineal meter of the Ancient Landslide Bench at this cross-section location, i.e., eastern end of the bench. Fig. 3 shows most of the eastern side of the Ancient Landslide Bench was removed by prior shallow slides and provided little support to the overlying Whitman Bench compared to the wide bench at the western end. The eastern portion of the Ancient Landslide Bench was significantly thinner than the western end because the river flows almost directly north into the slope on the eastern end and then runs parallel to the slope toe towards the west. For example, Fig. 4 shows the river cutting deeper into the slope on the eastern end than the western end in 1947, 1951, 1965, and 2006. As a result, more of the Ancient Landslide Bench was removed by the prior shallow slides on the eastern end than the western end, which left the Whitman Bench marginally stable on the eastern end.

Fig. 4 also shows the changes in the Stillaguamish River channel with time and shows the river channel was pushed south after the 1967 and 2006 slides. In each case, these shallow slides were triggered by river erosion undermining the slope toe and the shallow slides removed some of the Ancient Landslide Bench but did not involve the overlying Whitman Bench. Stability analysis of the 1967 and 2006 slopes shows that the factor of safety decreased from 1.18 to 1.02 due to the toe erosion over these 39 years. Therefore, the lower portion of the slope was marginally stable even after a shallow slide event.

Fig. 5 shows the northward progression of the scarps into the Ancient Landslide Bench on the eastern end from 1967 to 2013, which left the Whitman Bench essentially unsupported after the 2006 slide. These recent V-shaped headscarps (see

Fig. 5) show the headscarps are retrogressing towards the Whitman Bench and cutting into the Ancient Landslide Bench that was supporting the upper Whitman Bench. Comparison between the pre- and post- topography of the 2006 landslide extracted from LiDAR datasets also indicates that approximately 21 lineal meters (70 ft) of the bench had been removed by the 2006 landslide (Badger, 2015).

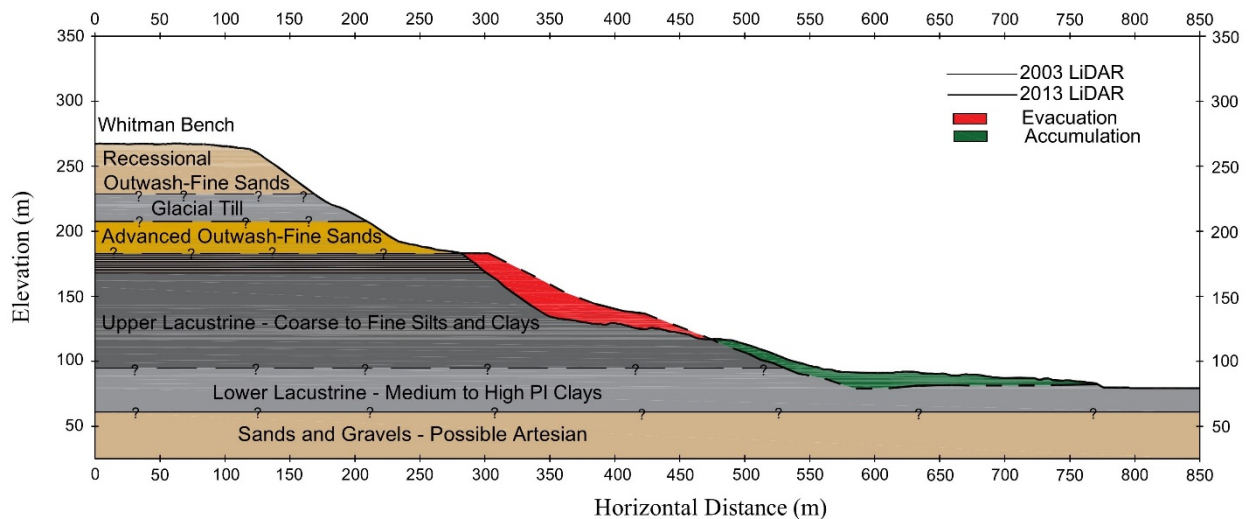


Fig. 3. Differences in surface topography 2003 and 2013 and locations of source and accumulation zones for 2006 slide.

2014 LANDSLIDE

The 2014 landslide is significantly different than the shallow 1937, 1951, 1952, 1967, 1988, and 2006 slides. The slide mass involved in the 2014 slide is much greater than in previous slide and its mobility was much greater resulting in a slide mass travelling more than 1.5 km in comparison to not more than 250 m (820 ft) in previous shallow slides (Iverson, 2015). The main reason behind the 2014 landslide behavior is the Whitman Bench was marginally stable after the 2006 slide, as there was not enough material remaining on the eastern end of the Ancient Landslide Bench to support the Whitman Bench. The 2014 slide mass had a large potential energy because it involved the upper portion of the slope and pushed the water filled and saturated colluvium that had accumulated along the slope toe across the valley enabling it to flow almost 1.5 km (See Fig.1).

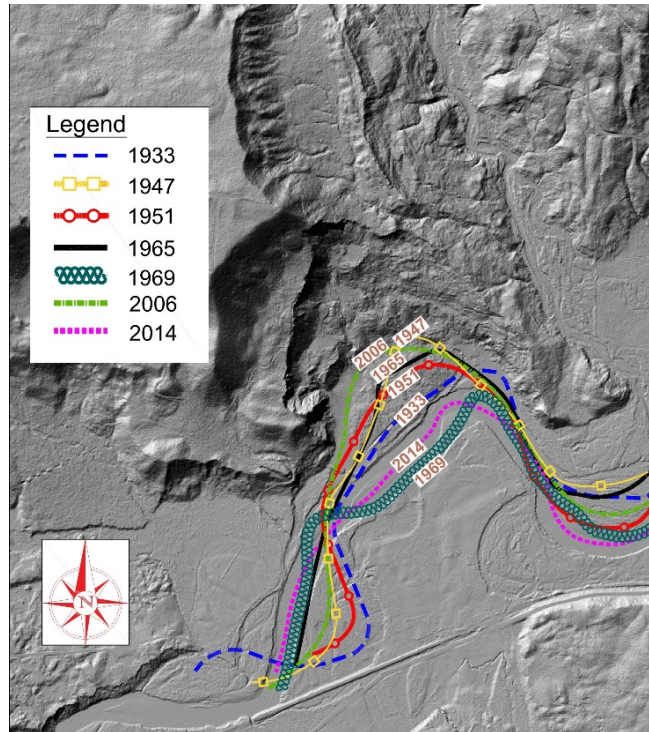


Fig. 4. Changes in Stillaguamish River Channel between 1933 and 2014 due to prior shallow landslides and location of first 2014 slide.

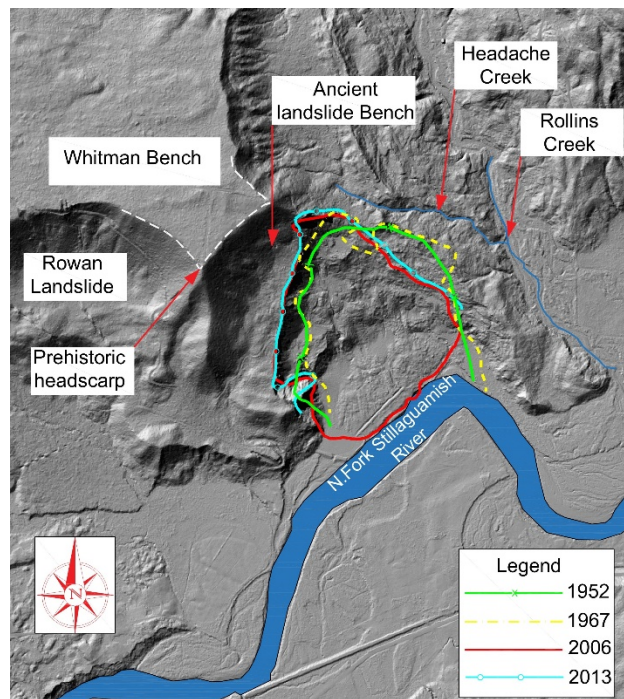


Fig. 5. Historic Landslide Scarps from 1952 to 2013.

LANDSLIDE HAZARD MAPPING

Understanding the failure mechanism for the large landslide in the Stillaguamish River Valley is important for guiding future landslide hazard mapping using LiDAR images, which was expanded by the state legislature after the 2014 landslide. LiDAR images should be used to identify the following two slope configurations that can result in a high elevation landslide that can have a large runout: (1) areas where the entire slope, i.e., upper terrace, has been oversteepened and/or undermined by prior sliding, river erosion, or other activity so they exhibit a steep and high slope and (2) areas that are not steep over the entire slope because of a significant colluvial deposit along the slope toe but do exhibit an ancient landslide bench that is not sufficiently wide to support the upper terrace (2014 landslide). Both of these areas should be identified and labeled as high risk because the upper portion of the slope has high potential energy that can push the involved slope deposits into and possibly across the valley instead of stopping at or near the river as the low elevation landslides do.

Therefore, slope height alone is not a good indicator because many other slopes along the valley have a similar height but the ancient landslide bench supporting the upper terrace, i.e., Whitman Bench, has not been compromised as it was on the eastern end of the 2014 slide area. If the ancient landslide bench is still sufficiently wide to support the upper terrace or Whitman Bench, only shallow slides in the lower portion of the slope will occur which will only impact the river and not the majority of the valley as occurred in 1937, 1951, 1952, 1967, 1988, and 2006.

A slide could involve the Whitman Bench and not impact the valley as occurred in 2014 if the ancient landslide bench is wide enough to slow down or stop the slide mass so it does not cascade off the bench and push or bulldoze the colluvium along the lower portion of the slope across the valley as in 2014. So the key issue for hazard mapping is assessing the width and ability of an ancient landslide bench to support and/or arrest any slide movement that involves the Whitman Bench because it is located about 200 m (650 ft) above the river and has considerable potential energy that could push slope materials into the valley. Figure 6 shows a number of ancient landslide benches supporting the Whitman Bench. The green shaded areas are Ancient Landslide Benches that are currently wide enough to support the upper portion of the slope and they have no potential to create a large and highly mobile landslide similar to the 2014 SR530 Landslide.

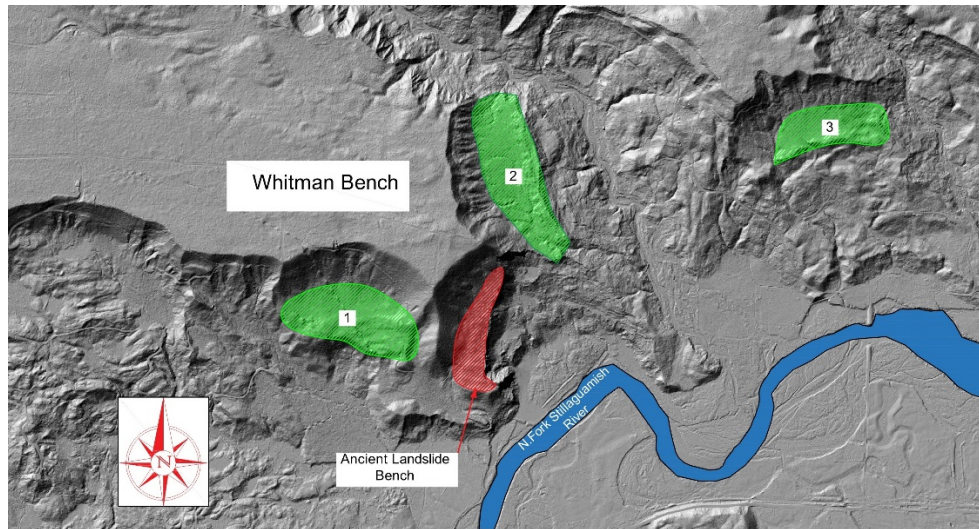


Fig. 6. LiDAR-derived topography showing the SR530 the Ancient Landslide Benches at the vicinity of SR530 landslide (see shaded area).

SUMMARY

This paper provides an overview of the 2014 SR530 landslide history. Imagery derived from LiDAR was used to enhance the understanding of the landslide event and the cause. This case history provides the industry with recommendations for future LiDAR hazard mapping and risk assessments. Areas where the upper terrace or Whitman Bench has been undermined by prior sliding, river erosion, or other activity from LiDAR images should be labelled as high risk because the upper portion of the slope has sufficient potential energy to push lower slope materials across the valley instead of stopping at or near the river as in a shallow slide caused by river erosion.

REFERENCES

- Badger, T.C. (2015). *Geotechnical Report: SR 520 MP 35 to 41 Geotechnical Study, Washington*, unpublished report by the Washington Department of Transportation, 199 p.
- Dragovich, J. D., Logan, R. L., Schasse, H. W., Walsh, T. J., Lingley, W. S., Jr., Norman, D. K., Gerstel, W. J., Lapen, T. J., Schuster, J. E., and Meyers, K. D., (2002), *Geologic Map of Washington-Northwest 167 Quadrant*, Washington Division of Geology and Earth Resources, 1:250,000 scale, Geologic Map GM 50.
- Haneberg, W.C., Cole, W.F., and Kasali, G., 2009, High-resolution LiDAR-based landslide hazard mapping and modeling, UCSF Parnassus Campus, San Francisco, USA: *Bulletin of Engineering Geology and the Environment*, v. 68, p. 273-286 (doi: 10.1007/s10064-009-0204-3).
- Iverson, R.M., Georgea, D.L., Allstadt, K. Reid, M.F., Collins, B.D., J.W.Vallance, J.W., Schilling, S.P., Godt, J.W., Cannon, C.M., Magirl, C.S., Baum, R.L., Coe, J.A., Schulz, W.H., and Bower, J.B. (2015). "Landslide mobility and hazards: implications of the 2014 Oso disaster." *Earth and Planetary Science Letters*, 412, 197–208.

- Keaton, J.R., Wartman, J., Anderson, S., Benoit, J., deLaChapelle, J., Gilbert, R.B., and Montgomery, D. R. (2014). “The 22 March 2014 Oso Landslide, Snohomish County, Washington.” unpublished report by Geotechnical Extreme Event Reconnaissance (GEER), funded by the National Science Foundation, 228 p.
- Stark, T.D., Baghdady, A.K., Hungr, O., and Aaron, J. (2016). “SR530 Landslide – Failure Mechanism and Material Properties.” SUBMITTED TO Journal of Geotechnical and Geoenvironmental Engineering, ASCE, September, 30 p.
- Thorsen, G. W., (1969), Landslide of January 1967 which diverted the North Fork of the Stillaguamish River near Hazel, Memorandum dated November 28, 1969, to Marshall T. Huntting, Department of Natural Resources, Geology & Earth Resources Division, Olympia, WA.

The Use of Electrical and Geotechnical Techniques to Assess a Small Earth Dam

Yara S. Maalouf¹; Naji N. Khoury, Ph.D., P.E., M.ASCE²; and Louis Junior Saad³

¹Laboratory Instructor, Dept. of Civil and Environmental Engineering, Notre Dame Univ.-Louaize, Zouk Mosbeh, Lebanon. E-mail: yara.warde@gmail.com

²Assistant Professor, Dept. of Civil and Environmental Engineering, Notre Dame Univ.-Louaize, Zouk Mosbeh, Lebanon. E-mail: nkhoury@gmail.com

³Engineer/Team Leader, ACTED, Lebanon. E-mail: louisjunior.saad@gmail.com

Abstract: In this study electrical resistivity tomography (ERT) was conducted to assess any anomalous seepage through an earth dam. Two ERT profiles on earth dam crests were recorded using AGI supersting R1/IP equipment - a total of 28 electrodes, spaced at one meter, were used in the resistivity testing - and then analyzed with EarthImager 2D. In addition, dynamic cone penetration (DCP) testing was used to identify various soil strata through the embankment of the earth dam. Correlations (qualitative and quantitative) were established between electrical resistivity and DCP rate which provided useful information for integrating electrical resistivity and geotechnical properties. The DCP testing was conducted in accordance with the ASTM D 6951. Shelby tube specimens were collected for laboratory testing (i.e., shear strength, consolidation, permeability, and soil classification). ERT analysis revealed the presence of clay layers and a saturated zone that could be a seepage zone. Findings showed that higher DCP value was associated with low resistivity value.

INTRODUCTION

Many countries currently regulate dam design, construction and operation in order to increase dam effectiveness and safety. These structures should be designed properly to ensure that failure does not occur during their service period. Poor design and/or monitoring the health of dams can have a severe negative impact on the safety and economics of a region (Zhong et al., 2011 and Hickey and Sabatier, 2011). Dams failure have a significant effect on human lives, social capital, negative environmental consequences and significant expense (Zhong, et al. 2011 The 1979 collapse of the Morvi River Dam in India resulted in a death toll of 15,000. In 1993 the city of Des Moines was devastated when the levee failed. More recently the Ames and New Orleans floods caused serious damage in many communities. Earth dams have failed in other countries including Italy, Nigeria and Lebanon. For example, on May 21, 2015 an earth dam in Aqoura, a village in the Jbeil district, Lebanon, collapsed as a result of internal erosion. This

caused the failure of three other dams (MTV, 2015), flooding the surrounding region and destroying large cultivated areas. This region has been flooded three times in its history due to similar conditions.

Several geotechnical tests have been conducted in order to assess the health of earth dams including geophysical, Standard Penetration Test (SPT), Cone Penetrating Test (CPT), and boreholes (Sudha et al., 2009; Panthulu et al., 2001; Mulabdic., 2013; Ikard et al. 2014; Ikard et al., 2015). Studies have shown a correlation between Electrical Resistivity Tomography (ERT) and geotechnical data for characterization of subsurface soil (e.g., Sudha et al. 2009, Cosenza et al., 2006; Ayolable et al., 2010 and Gay et al., 2006). The correlation between electrical resistivity and other geotechnical testing, however, is still weak (Sudha et al, 2009).

This study focuses on the use of ERT in assessing possible seepage within the structure of an earth dam. DCP tests were also conducted to assess the different types of soil strata in the field. Correlations between the data obtained from ERT and DCP were then established.

METHODOLOGY

The study area (Laqlouq) is a small mountainous village in Jbeil, Mount Lebanon, Lebanon. Laqlouq has an altitude ranging from 1850 m to 2000 m. More than 200 small earth dams are located in the area surrounding s shown in Figure 1.



FIG. 1 Photographic view of the earth dams

The field testing included ERT and DCP testing along with laboratory testing. Two survey lines were conducted on the crest of the earth dam using AGI Supersting R1/IP. A total of 28 electrodes were laid on the crest of the earth dam with 1 m electrode spacing and dipole-dipole array, refer to Figure 2. Data acquired from the field were analyzed using EarthImager 2D.

DCP tests were also conducted at various locations and data was recorded up to a depth of 2.5 meters. Soil samples were obtained from the field for laboratory testing in accordance with the ASTM standards (i.e., sieve analysis, Atterberg limits, Proctor tests, permeability and shear strength). Results showed that the soil was classified as CL according to the Unified Soil Classification System. In addition, the liquid limit obtained was 34% and the plastic limit was 17%. It was also found that the plasticity index was 17%. Findings from the standard Proctor test showed that the dry unit

weight and optimum moisture content were 19 kN/m^3 and 22% respectively. The angle of friction obtained from the direct shear test was 27° and the cohesion 38 kPa. The residual shear strength parameters obtained were: $c' = 35 \text{ kPa}$ and $\phi' = 24^\circ$.



FIG. 2 Field electrical resistivity setup

PRESENTATION AND DISCUSSION OF RESULTS

The 2D ERTs on the dam are shown in Figures 3 and 4. RMS values of 2.6% and 9.5% for the investigated profiles indicated that the data fit with the computed response. The resistivity for profile 1 ranged between approximately $15 \text{ } \Omega\cdot\text{m}$ and $40 \text{ } \Omega\cdot\text{m}$, indicating clay-type soil. This was consistent with borehole soil samples collected, which revealed that the soil consists of clay-type material. Profile 2 provided resistivity values ranging from $18 \text{ } \Omega\cdot\text{m}$ to $47 \text{ } \Omega\cdot\text{m}$. Lower values near the surface represented higher water content due to water infiltration from late spring rainfall. The thickness of the top layer was approximately 2 m along the two profile lines. A layer of drier clay was found between 2 m and 4.5 meters, with wetter clay below 4.5 meters. The resistivity of clayey formation is represented by a resistivity of less than $100 \text{ } \Omega\cdot\text{m}$. ERTs also revealed a saturated zone, which is consistent in the literature (Lin et al., 2013). The authors are currently conducting additional field tests that will help corroborate on this specific potential seepage area.

Dynamic cone penetration profile 1 (DCP1) was conducted between electrodes 15 and 16 (i.e., 15 and 16 meters) along profile 1. Figure 5 shows the variation of DCP and resistivity data with depth for DCP1. It can be noted that for an average DCP index of approximately 6.9 cm/blow, the same resistivity values, $22.2 \text{ } \Omega\cdot\text{m}$, were obtained. For a DCP index of around 8 mm/blow, higher resistivity values, $16 \text{ } \Omega\cdot\text{m}$, were obtained.

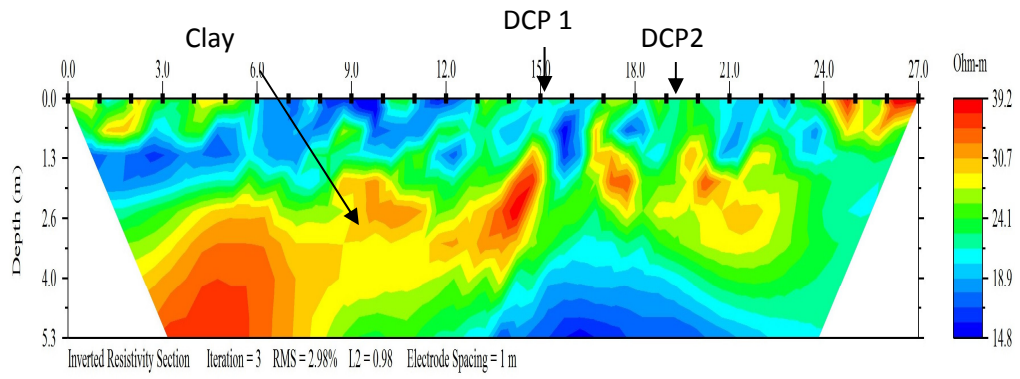


FIG. 3 Modeled resistivity section along the ERT line for crest (location 1)

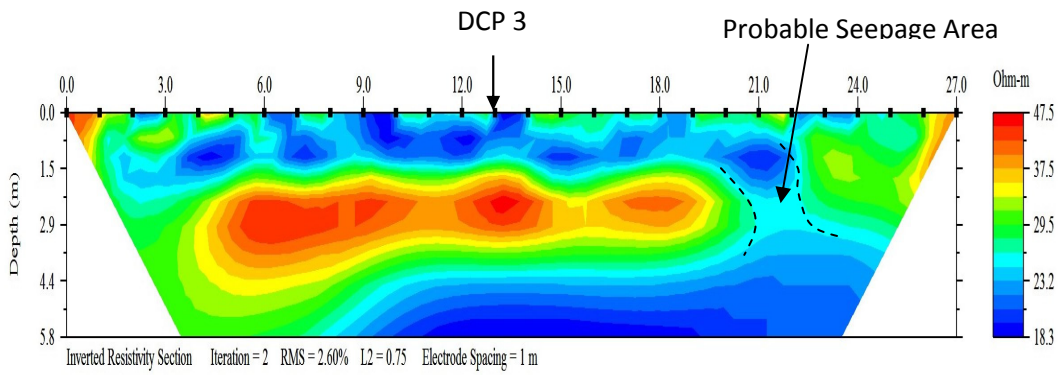


FIG. 4 Modeled resistivity section along the ERT line for crest (location 2)

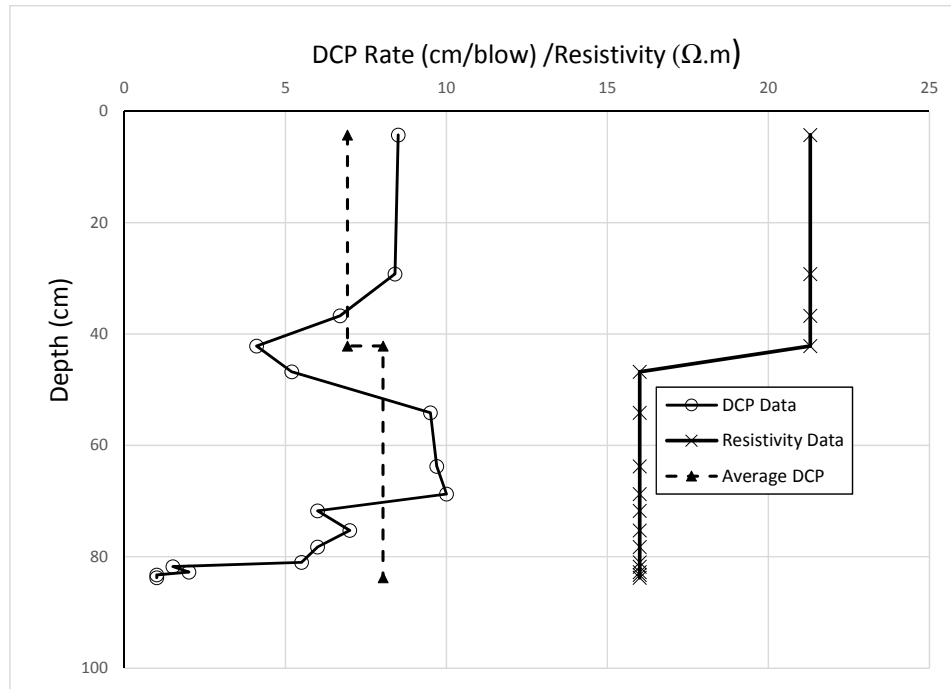


FIG. 5. Variation of DCP and resistivity values with depth for location DCP1

Results for DCP 2 (along profile 1) with resistivity results are depicted in Figure 6. The DCP shows two layers, the top layer had a DCP value of 10.6 cm/blow and the second layer, 4.4. Figure 6 shows that lower DCP values were equivalent to higher resistivity values, which is consistent with the trend shown in Figure 5. A third DCP, DCP 3, was conducted along ERT profile 2, at a distance of 13 m. Results are plotted in Figure 7. DCP and resistivity results showed the existence of three layers. It is also evident that lower DCP values were associated with high resistivity results.

Figure 8 shows a plot of DCP versus inverted resistivity results. Attempts were made to develop a correlation between DCP and resistivity. A linear relationship with a low R-squared value was developed. Results showed no statistically significant correlation, see Figure 8. This is consistent with studies in the literature. The study was conducted based on field results and limited to approximately 7 data points. The authors are currently conducting both field and laboratory studies (under a controlled environment) on a wide range of soils (e.g., sand, silt).

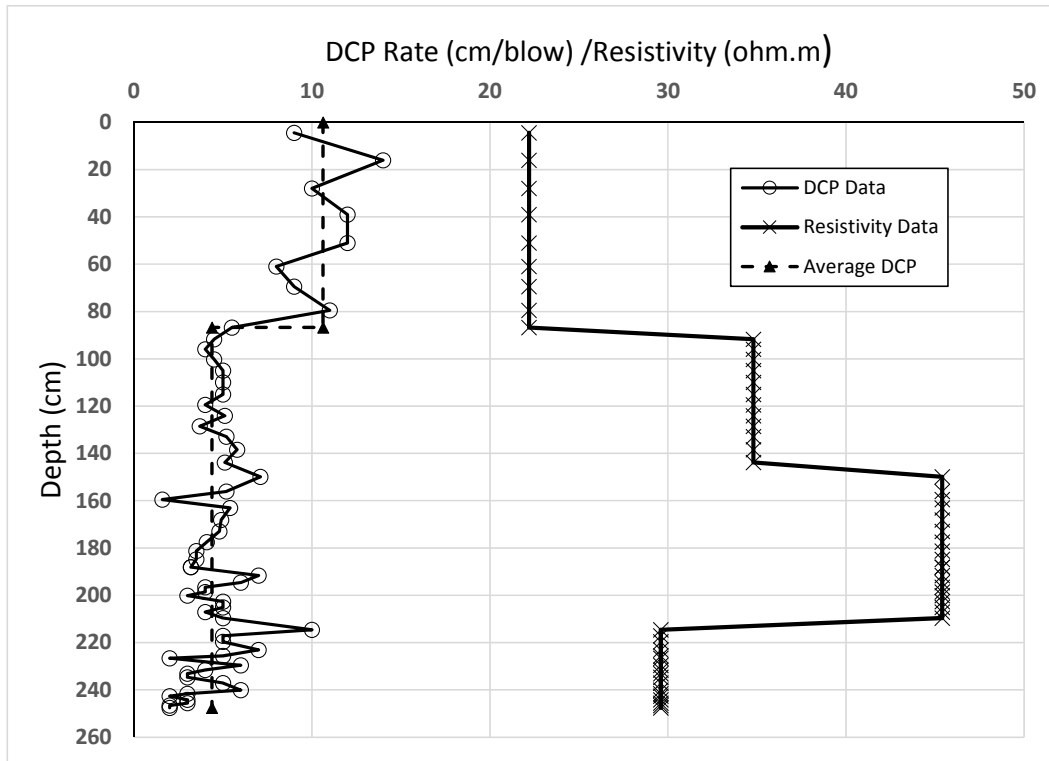


FIG. 6. Variation of DCP and resistivity with depth for location DCP2

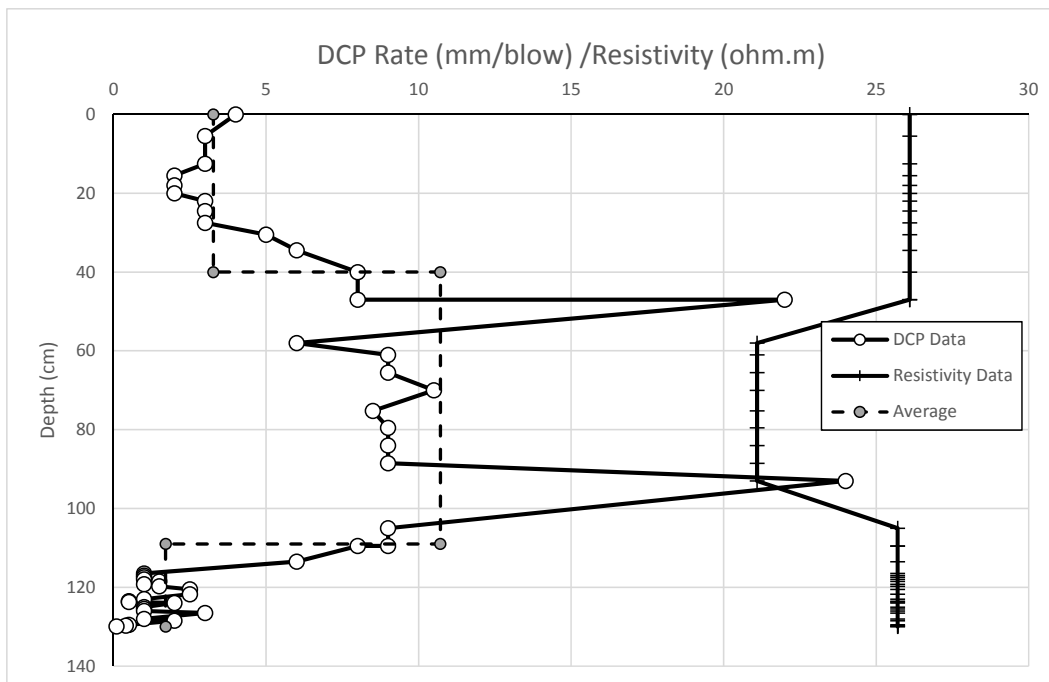


FIG. 7. Variation of DCP and resistivity with depth for location DCP3

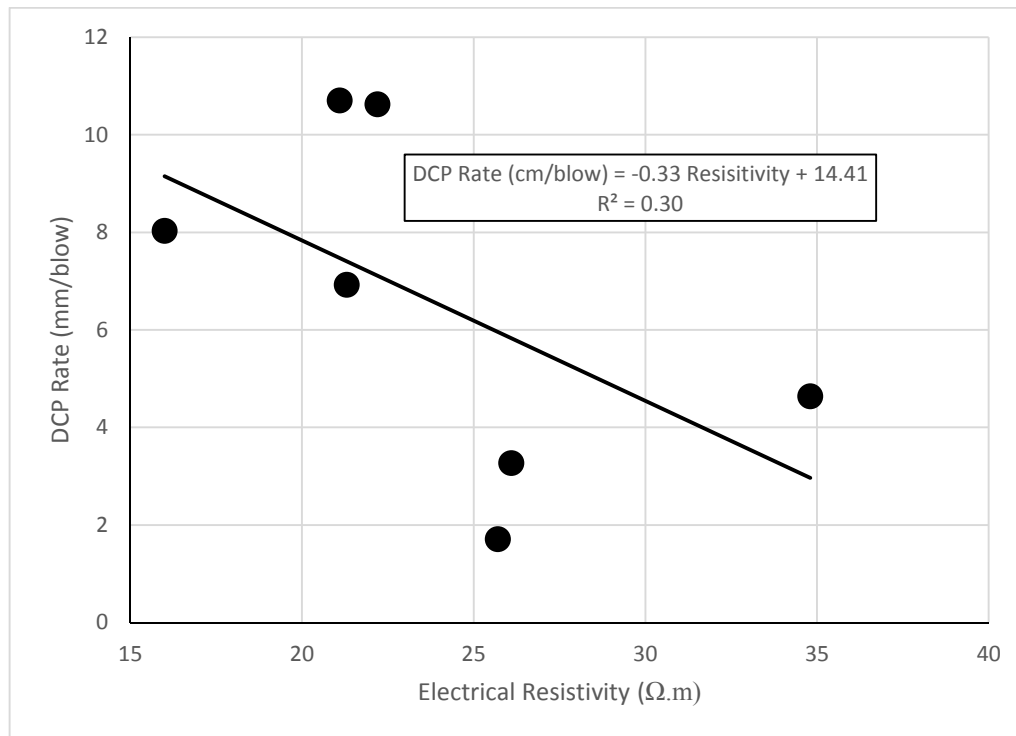


FIG. 8. DCP results versus inverted resistivity extracted from 2D soundings

CONCLUSIONS

This study was undertaken to identify areas of anomalous seepage in an earth dam using ERT. Various layers were identified in the ERTs along profiles 1 and 2. Results showed zones with low resistivity values, which could be associated with high water content – an indication of probable/possible seepage zones within the embankment. Efforts were also made to establish correlations between electrical resistivity and DCP rates. In general, both approaches revealed the same number of layers and provided consistent depths. Quantitative analysis revealed a linear model with a low R-squared, which was not statistically significant, indicating no correlation between electrical resistivity and DCP rates. Additional laboratory and field testing are being conducted by the authors to increase the database on this topic and attempt to develop quantitative relationships between DCP and other geotechnical parameters (e.g., shear strength and N-values from SPT).

ACKNOWLEDGMENTS

This paper is made possible by the generous support of the American people through the United States Agency for International Development (USAID). The contents are the responsibility of the authors and do not necessarily reflect the views of USAID or the United States Government. The authors are thankful for this generous support and would like to acknowledge the students, namely Lukas Farah, Tonia El Hajj, Karine Moudawar, Sarah Moawad, Louis Junior Saad, Karl Feghali,

Roy Hajje, Rayan Fawaz and Mr. Elie Lahoud the lab technician at Notre Dame University-Louaize who assisted in this project.

REFERENCES

- Ayolabi, E. A., Folorunso, A. F., & Oloruntola, M. O. (2010). Constraining Causes of Structural Failure Using Electrical Resistivity Tomography (ERT): A Case Study of Lagos, Southwestern, Nigeria. In *23rd EEGS Symposium on the Application of Geophysics to Engineering and Environmental Problems*.
- Cosenza, P., Marmet, E., Rejiba, F., Cui, Y. J., Tabbagh, A., & Charlery, Y. (2006). Correlations between geotechnical and electrical data: a case study at Garchy in France. *Journal of Applied Geophysics*, 60(3), 165-178.
- Gay, G. D., Morgan, F., Vichabian, Y., and Sogade, J. A., Reppert, P. and Harton, E. (2006): Investigations of andesitic volcanic debris terrains: Part 2 – *Geotechnical Geophysics 71, B9 – B15*
- Hickey, C., and Sabatier, J. (2011). Overview of the Workshop on Monitoring and Failure Detection in Earthen Embankments, *24th EEGS Symposium on the Application of Geophysics to Engineering and Environmental Problems*.
- Ikard, S. J., Rittgers, J., Revil, A., & Mooney, M. A. (2015). Geophysical investigation of seepage beneath an earthen dam. *Groundwater*, 53(2), 238-250.
- Ikard, S. J., Revil, A., Schmutz, M., Karaoulis, M., Jardani, A., & Mooney, M. (2014). Characterization of Focused Seepage Through an Earthfill Dam Using Geoelectrical Methods. *Groundwater*, 52(6), 952-965.
- Lin, C. P., Hung, Y. C., Yu, Z. H., & Wu, P. L. (2013). Investigation of abnormal seepages in an earth dam using resistivity tomography. *Journal of GeoEngineering* 8(2), 61-70.
- Mulabdic, M. (2013). Use of penetration testing for determination of soil properties in earth dam. *Proceedings of the 18th International Conference on Soil Mechanics and Geotechnical Engineering*.
- Panthulu, T. V., Krishnaiah, C., & Shirke, J. M. (2001). Detection of seepage paths in earth dams using self-potential and electrical resistivity methods. *Engineering Geology*, 59(3), 281-295.
- MTV, 2015, Newsfeeds, [online]. Available from <http://mtv.com.lb/News/480452>.
- Sudha, K. Israil, M., Mittal, S. and Rai, (2009), Soil Characterization using Electrical Resistivity Tomography and Geotechnical Investigations, *Journal of Applied Geophysics* 67, 74-79.
- Zhong, D., Sun, Y., & Li, M. (2011). Dam break threshold value and risk probability assessment for an earth dam. *Natural hazards*, 59(1), 129-147.

Assessing the Life Cycle Benefits of Recycled Material in Road Construction

Eleanor F. Bloom¹; Gregory J. Horstmeier²; Angela Pakes Ahlman, P.E., LEED AP³;
Tuncer B. Edil, Ph.D., P.E., D.GE⁴; and Gary Whited, P.E.⁵

¹M.S. Student, Geological Engineering Program, Univ. of Wisconsin-Madison, Madison, WI. E-mail: efbloom@wisc.edu

²Undergraduate Student, Geological Engineering Program, Univ. of Wisconsin-Madison, Madison, WI. E-mail: ghorstmeier@wisc.edu

³Technical Director, Recycled Materials Resource Center, Univ. of Wisconsin-Madison, Madison, WI. E-mail: angela.pakes@wisc.edu

⁴Research Director, Recycled Materials Resource Center, Univ. of Wisconsin-Madison, Madison, WI. E-mail: tbedil@wisc.edu

⁵Senior Administrative Program Specialist, Civil and Environmental Engineering Department, Univ. of Wisconsin-Madison, Madison, WI. E-mail: whited@engr.wisc.edu

Abstract: Life cycle assessments of recycled material use in roadways are currently not well understood or well documented. The Recycled Materials Resource Center's (RMRC) research is aimed at quantitatively determining the environmental and economic benefits of using recycled material in road construction. Two case studies were performed to analyze the impacts of incorporating recycled material in the reconstruction of two major roadways using life cycle assessment (LCA) and life cycle cost analysis (LCCA) tools. Results from both roads show that the use of recycled materials reduces energy and water consumption, greenhouse gas emissions, and cost. Because typical roadway construction projects do not separately track the extensive use of recycled materials, the RMRC was unable to utilize the LCA and LCCA technology in the first roadway's analysis without making significant assumptions for the inputs. To clarify and verify some of these assumptions, the second roadway project was undertaken. This second case study is being studied to determine a better methodology for data collection with fewer assumptions, in addition to assessing the benefits of recycled material use. The methodology for data collection and analysis developed through the second project can be used to conduct LCAs and LCCA for future highway construction projects with greater confidence.

INTRODUCTION

The sustainable roadway construction has become an increasingly popular topic because of global climate change and rising costs of virgin materials. Buildings and infrastructure utilize 40% of all materials extracted in the U.S. (Kilbert 2002), and the construction industry emits approximately 6% of total U.S. industry-related greenhouse

gasses (GHGs) (Truitt 2009). To be sustainable, highways must be designed to reduce their environmental impacts through thoughtful planning, design and construction, including the reduced use of virgin materials.

The goal of this paper is to quantitatively and accurately determine the environmental and economic benefits of using recycled material through the reconstruction of two roadways, thereby further demonstrating the viability of life cycle analyses in evaluating the advantages of sustainable road construction. Life cycle assessments (LCAs) quantify environmental impacts over the lifetime of a product by using a meticulous evaluation methodology. Life cycle cost analyses (LCCAs) outline cost comparisons among design alternatives, denoting economic benefits (Van Dam et al. 2015). For both studies, the environmental and economic savings are evaluated by comparing the actual road designs with recycled materials, “Actual,” to an equivalent design which substitutes conventional virgin materials for all recycled materials, “Reference.”

CASE STUDY: INTERSTATE-94

Background

One life cycle tool, Building Environmentally and Economically Sustainable Transportation-Infrastructure-Highways (BE²ST-in-Highways), uses LCA and LCCA techniques to evaluate the overall impact of highway construction projects. A 1.6 km (1 mi) north-south corridor of Interstate 94 (I-94) in Kenosha County was identified by the Wisconsin Department of Transportation (WisDOT) and the RMRC for a BE²ST-in-Highways analysis. Construction plans outline a multi-year reconstruction, modernization, and expansion of I-94 mainline and ramps, as well as a resurfacing of State Highway (STH) 142 (WisDOT 2015a). Recycled materials used in the project include fly ash, bottom ash, foundry sand, recycled concrete aggregate (RCA), and recycled asphalt pavement (RAP) (N. Schlegal and B. Blum, personal communication, August-January, 2013-2014).

There are three portions of the reconstruction: mainline, ramps, and STH 142. The reconstructed mainline is comprised of layers given in Table 1. The ramps and STH 142 have similar layers, but with slightly different dimensions and no asphalt base layer. The embankment was quantified separately in addition to the three portions of the roadway. Embankment was used in various locations with varying thicknesses in order to elevate roads to design specifications in the mainline and the ramps. A total volume of approximately 180,000 cubic meters of embankment was used for this portion of the I-94 construction. STH 142 underwent resurfacing rather than full reconstruction, therefore needed no SCM or embankment. The embankment was comprised of bottom ash from We Energies (70%), on-site native clays (25%), and foundry sand from Rexnord Sand & Gravel (5%).

TABLE 1. Mainline Materials Layers with Dimensions and Source Distance

Layer	Material	Thickness	Distance	Source
Portland Cement Concrete (PCC) Surface Pavement	Fly Ash	30.5 cm (12")	16 km (10 mi)	We Energies
	Cement		1.6 km (1 mi)	Michels Paving
	Aggregates			
	Water			
Asphalt Base – Hot Mix Asphalt (HMA)	Asphalt Binder Virgin Aggregate	7.5 cm (3")	1.6 km (1 mi)	Payne & Dolan
Base Aggregate	Virgin Aggregate	15 cm (6")	28 km (17 mi)	Bartel Aggregate
	RAP (55%)		0	Recycled On-Site
Select Crushed Material (SCM)	Virgin Aggregate	33 cm (13")	48 km (30 mi)	Franklin Aggregates
	RCA (37.5%)		0	Recycled On-Site

Analysis

BE²ST-in-Highways

Lee et al. (2013) describes the life cycle tool used for the I-94 analysis. BE²ST-in-Highways was created as a tool for quantifying how a highway reduces its environmental impact by incorporating recycled materials in its design. Criteria considered by BE²ST-in-Highways, which were recommended by RMRC stakeholders, include: energy use (MJ), global warming potential (GWP) (Mg), water consumption (kg), social carbon cost (SCC) (\$), hazardous waste (kg), in situ recycling (m³) without transporting from off-site, total recycling (m³), and life cycle cost (\$).

BE²ST-in-Highways utilizes the Pavement Life Cycle Assessment Tool for Environmental and Economic Effects (PaLATE) as a support program to assess the environmental effects of pavement and road construction. Because PaLATE was primarily used to conduct the LCA for the second case study, this program will be discussed in the second case study's analysis later in this paper. The expected lifetime (50 years), maintenance schedule, and rehabilitation procedures for I-94 were provided by WisDOT and incorporated in the LCA and LCCA model.

Assumptions

A significant amount of assumptions were required to perform the LCA and LCCA of the Actual and Reference designs. The assumptions are as follows:

- The Reference design dimensions were assumed exactly the same as the Actual design's dimensions. Virgin aggregate or other traditional material was substituted in place of recycled material in the Reference design. In reality, different dimensions or quantities of virgin material may have been required based on the actual properties of the materials involved.
- The quantities of materials used in each layer were proportional to the volume of

- the layer as calculated from the design plans. Actual purchased quantities for the reconstruction could not be obtained.
- Ranges of percentages of recycled material used in the base aggregate and SCM layers were provided. The average of these ranges was used to calculate the volume of material in these layers
 - The dimensions of roadway fill and embankment could not be accurately quantified from roadway plans. However, the total volume of embankment material volume was provided. This quantity was used in the analysis.
 - The amount of individual material within the surface PCC pavement was calculated from the proportions in the PCC mix design used by the pavement supply company.
 - No recycled materials were included in the HMA mix for the asphaltic base. Therefore, it was assumed there would be no difference in the asphalt base's environmental impact between the Actual and Reference designs.
 - Although the lifetime of the roadway may differ between the Actual and Reference design, the lifetime and maintenance schedule predicted by WisDOT was used for both designs.
 - The material required for maintenance procedures was assumed to have the same designs and mixes as the initial reconstruction.
 - If the designer did not provide a transportation method, it was assumed that the material was transported via dump truck.
 - The transportation distances were based on project-specific data. Transportation distances were calculated from the material suppliers (quarries, pavement mix plants, etc.) to the I-94 reconstruction site.
 - The life cycle costs were estimated from average costs of raw materials provided by suppliers, the Wisconsin Concrete Pavement Association (WCPA), and Engineering News-Record (ENR's Dodge Data and Analytics 2015 report). Transportation costs were not available and, therefore, not used in this analysis.

Results

The results of the BE²ST-in-Highways analysis are summarized in Table 2. The criteria gathered from PaLATE include energy use, GWP (equivalent to carbon dioxide, or CO₂, emissions), water consumption, and hazardous waste. The SCC is based on a unit SCC of 69 \$/MJ of CO₂. The 'percent improved' is calculated by the percent increase or decrease in the results of constructing the Actual as compared to the Reference design. For most criteria, a decrease in impact is desired for the Actual. Since the Reference uses no recycled materials, its values for *in situ* recycling and total recycling are zero. The percent improved for the 'recycling criterion' are based on the fraction of recycled materials over total materials used for the reconstruction. The cost savings are calculated from the difference in the cost of actual quantities of fly ash, RAP and RCA base aggregate, bottom ash, and foundry sand versus the cost of hypothetical, equivalent quantities of cement, virgin base aggregate, granular fill, and sand, respectively.

For all criteria, the Actual result in improved environmental impacts. The greatest percent improved is in total recycling. This is, in large, due to the extensive use of bottom ash for embankment and fill material. Only RAP and RCA contributed to the *in situ*

recycled material, and therefore, the *in situ* recycling improved by a smaller percentage than total recycling. Although the bottom ash was not recycled on site, it was transported from a coal power plant landfill ten miles from the construction site. The second largest percent improvement is in GWP and SCC, both by 39%. This suggests that the Actual design reduced carbon emissions and the associated social cost for the reconstruction project by over one third. Cost savings were calculated by the reduction in material unit costs from using recycled versus virgin material. The project saved over \$770,000. The largest cost savings were attributed to the use of bottom ash (over \$410,000 saved) because of the lower unit cost due in large to the close proximity to the site and the large volume of bottom ash used.

TABLE 2. Results of BE²ST-in-Highways

Criteria	Reference	Actual	Percent Improved
Energy Use (TJ)	141,000	89,000	37%
GWP (Mg)	9,500	5,800	39%
Water Consumption (kg)	38,000	28,000	25%
SCC (\$)	\$ 654,000	\$ 398,000	39%
Hazardous Waste (kg)	237,000	151,000	36%
In Situ Recycling (m ³)	0	19,100	7%
Total Recycling (m ³)	0	154,000	57%
Life Cycle Cost Savings [\$]:		\$771,000	

CASE STUDY: BELTLINE

Background

The Beltline Highway is a multi-lane, urban, and major arterial highway used by a substantial number of local and regional travelers in the Madison, Wisconsin area (WisDOT 2015b). This 2.5-kilometer (1.5-mile) section is a part of the Wisconsin Backbone System (US 151) from Dubuque, IA, to Fond du Lac, WI. Safety and population growth are key reasons the Beltline is being expanded, and increased mobility is crucial to the efficiency of Beltline travelers.

This RMRC analysis focuses on the eastbound half of the Beltline Highway reconstruction from Whitney Way to Seminole Highway, including an expansion from two to three lanes in each direction. This section of highway includes the convergence for major roads: Highways 18/151 and Highways 12/14. The top wearing course was converted from the existing HMA overlay to 28 cm (11") concrete pavement, at times with an asphaltic base. Six ramps were updated and four were added. Construction on the Beltline began in fall of 2014 and is expected to end in late 2015 for eastbound lanes. Recycled materials used in this project include: RAP, recycled asphalt shingles (RAS), RCA, and fly ash. RAP and RAS were used in HMA pavement. Fly ash was used in concrete. RAP and RCA were recycled both onsite from the existing pavement and offsite at a quarry for embankment/fill, SCM, and base aggregate.

Analysis

In addition to determining the life cycle benefits of recycled materials use as in the I-94 analysis, another objective of this study was to determine a methodology for gathering information such that significant assumptions will not be made regarding the LCA and LCCA.

Data Collection

The RMRC worked directly with WisDOT employees and contractors to collect real-time data for this project. As research progressed, the RMRC contacted sub-contractor representatives from various engineering and construction firms to better refine project details. Key, site-specific WisDOT and sub-contractor files, including Item Record Account spreadsheets, Quality Management Plan (QMP) specifications, concrete and HMA pavement mix designs, site plans, and bid item lists, were used to determine the LCA/LCCA inputs. Such files aided in tracking materials, specifically material type, volume, tonnage, unit cost, equipment/processes for installation, and transportation distance. Weigh tickets were also critical in data collection because they described the material, its origin, and its quantity. Additionally, WisDOT provided a maintenance schedule over the 50-year lifetime of the roadway, including material quantities for the rehabilitation processes.

Omitted from weigh tickets were the RAP and RCA recycled from the existing pavement and used for base aggregate and embankment/fill. To determine the amount of RAP and RCA, the site plans were used to calculate the volume of existing HMA and PCC pavement on the road. The average density of the pavements was then used to calculate the weight of the recycled materials. According to the contractor, this estimation method would be valid because almost all onsite-recycled pavements were used in the reconstruction.

The costs for the actual design were gathered from either Beltline-specific bid item prices, WisDOT average bit item prices, or a personal communication with state or national pavement agencies.

PaLATE

PaLATE is an LCA/LCCA program designed by the Consortium on Green Design and Manufacturing from the University of California, Berkeley and commissioned by the RMRC. For this case study, PaLATE was used directly to conduct the LCA and LCCA. PaLATE can be updated by the user to allow for project specific details, such as adding RAS to the list of materials or updating the equipment specifications. Users input the initial design, initial construction materials and transportation, maintenance materials and transportation, equipment use, and cost for a roadway. Bid item data from WisDOT and contractors was separated by raw materials. For example, typical PCC concrete consists of cement, fly ash, aggregates, and water. For each raw material, a transportation distance and unit price were determined. Environmental outputs include (UC Berkeley 2007): energy consumption (GJ), water consumption (kg), CO₂ emissions (kg), nitrous oxide (NO_x) emissions (kg), particulate matter-10 (PM₁₀) emissions (kg), sulfur dioxide (SO₂)

emissions (kg), carbon monoxide (CO) emissions (kg), and leachate information, including Mercury, lead, Resource Conservation and Recovery Act (RCRA) hazardous waste generated, and both cancerous and non-cancerous human toxicity potential (HTP). Economic outputs include the net present value life cycle costs (\$) and annualized costs of the net present values (\$).

For the PaLATE LCCA, costs associated with the initial construction materials and processes were calculated. Costs of maintenance and repairs were entered in the subsequent years when rehabilitation is expected to occur and brought to present value. Actual bid item costs reflect the use of both recycled and virgin material. To determine cost savings for bid item materials, the cost of 100% virgin material was compared to estimated recycled material prices. Unit prices for virgin aggregate and salvaged asphaltic pavement were gathered from WisDOT's average bid item prices (WisDOT, 2015c). The Wisconsin Concrete Pavement Association provided cost estimates of fly ash, cement and RCA. The National Asphalt Pavement Association and the Wisconsin Asphalt Pavement Association provided cost data on RAS and RAP in HMA, respectively.

Assumptions

Although the method of data collection was improved compared to I-94 project, a number of assumptions were needed while performing the LCA, as follows:

- Only the eastbound portion of the construction would be analyzed. However, minor construction on both the west- and eastbound sides occurred in fall 2014, carrying into April 2015. Thus, all material quantities from the start of construction until April 1, 2015 were divided in half to estimate materials for only the eastbound highway more accurately.
- Results presented in this paper reflect the material used for the eastbound Beltline construction up to late October, 2015. At that point in time, the eastbound construction was approximately 80% complete.
- Existing roadway dimensions were used to calculate volumes of RAP and RCA. When ranges of widths were provided, the widths were averaged.
- Unless otherwise stated, the assumed transportation vehicle was dump trucks, with the exception of cement trucks for cement/fly ash.
- Virgin material, Reference, was substituted ton-for-ton for recycled material, Actual. In reality, different quantities of virgin material may be required to construct the Reference design road to meet structural support requirements.
- Recycled aggregate from offsite quarries was designated as RCA.
- Only the total volume of the PCC surface material was provided. The amount of raw material was calculated from the proportions in the PCC mixes used by the pavement supply company. The same process was used for HMA pavement raw material calculations
- Costs for the Reference design or recycled materials not found in the project bid items were estimated from averages based on literature or personal communications.

Results

The LCA results of the Beltline analysis are shown in Tables 3a and 3b. In general, reductions were seen in all PaLATE categories. The PaLATE categories are slightly different than BE²ST-in-Highways, including more parameters that address air and toxic emissions. The greatest reduction is seen in PM₁₀ at 21%. Because more recycled material was used with a smaller transportation distance, less vehicles and equipment were used on and off site, resulting in fewer particulate emissions. The reductions in categories reported in BE²ST-in-Highways indicate reductions or improvements as follows: energy (13%), water consumption (12%), CO₂ emissions (13%), and RCRA hazardous waste (9%).

TABLE 3. PaLATE results of Beltline analysis

	Energy (TJ)	Water Consumption (g)	CO ₂ (kg)	NO _x (g)	PM ₁₀ (g)	SO ₂ (g)
Actual	146,000	40,400	10,000	95,200	33,100	386,000
Reference	167,000	45,900	11,500	98,300	41,600	390,000
Reduction	13%	12%	13%	3%	20%	1%

TABLE 3b. PaLATE results of Beltline analysis

	CO (g)	Hg (g)	Pb (g)	RCRA Hazardous Waste (g)	HTP cancer (kg)	HTP non cancer (Mg)
Actual	36,400	163	9,120	823,000	8,980	24,100
Reference	37,400	173	9,960	903,000	8,750	28,900
Reduction	3%	6%	8%	9%	-3%	17%

LCCA savings from the initial construction were estimated to be \$34,900 from the use of RAP and RAS in HMA, \$130,000 from the use of both onsite and offsite recycled base aggregate and SCM, and \$56,000 from the substitution of fly ash for cement concrete pavement. At present value, the savings from maintenance over the roadways lifetime are \$27,750. The savings total about \$250,000 from the use of all recycled material over the project's lifetime.

DISCUSSION

Comparison of Data Collection Methods

The I-94 and Beltline case studies provided an opportunity to analyze and improve data collection methodology for highway life cycle analyses. The majority of the data for the I-94 analysis was provided post-construction. Post-construction data collection for I-94 led to issues including over-generalization of mix designs and sourcing, averaging market prices for materials, and inability for real-time data collection. Because real-time data was not collected, estimates of material quantities were based on road plan dimensions rather than actual amounts of purchased material. This calculation method

was avoided for the Beltline analysis, because data was collected during construction. Favorable timing, resources, and personnel were available for the Beltline data collection. However, the onsite recycled RCA and RAP were calculated from dimensions, as they were not directly weighed and tracked during Beltline construction.

These case studies also demonstrated the different challenges associated with material tracking and evaluation in urban (Beltline) versus rural (I-94) construction. Although urban construction has time and area constraints not seen in rural construction, urban settings generally have greater access to resources, suppliers, and offsite recycled materials. Rural construction is advantageous for recycling existing roadways due to adequate storage room for RAP and RCA onsite, eliminating additional offsite transportation.

Comparison of LCA Tools

Another objective of these two case studies was to explore LCA and LCCA tools. BE²ST-in-Highways focuses on a few of the impact categories included in the PaLATE analysis that were approved by stakeholders. The variety of categories evaluated by PaLATE can be advantageous when trying to understand the full environmental impact of a roadway. It is important for the public to understand that using recycled materials can improve air quality and reduce waste in addition to more commonly referenced environmental issues such as energy and GHG reduction. PaLATE is also formatted on an unlocked spreadsheet, allowing the user to make adjustments for project specific details. However, adjustments could lead to errors in formulas if the user does not understand the program's complex calculations.

BE²ST-in-Highways is advantageous because it draws from multiple databases and tools to calculate the environmental and economic benefits of recycled materials. It was created for the RMRC, and therefore addresses the impacts requested by member state departments of transportation. Because the program is locked, it does not allow for adjustments, preventing possible errors in spreadsheet formulas.

Comparison of Results

The two case studies demonstrated the environmental and economic benefits of using recycled materials in road construction. For both roadways, the use of recycled materials led to a decrease in energy and water consumption, CO₂ emissions, and hazardous waste generation. Greater reductions are seen for the I-94 analysis as compared to the Beltline. Reductions in the four, shared categories for I-94 range from 25-39%, while Beltline reductions range from 9-13%. This can be attributed to a greater ratio of recycled to virgin material in the I-94 reconstruction compared to the Beltline. The more recycled materials substituted for virgin, the lower the environmental impact.

CONCLUSION

The two studies promoted a better understanding of DOT methods for material tracking, which assisted in developing an improved methodology for collecting input data needed for life cycle analyses. The reduction of the negative environmental impacts due

to recycled material use in highway construction improves the sustainability of roadways and shows good cost savings. Continual use of recycled material in road construction, as well as the tracking and assessment of the benefits of recycled materials use, should be made a priority by state DOTs.

ACKNOWLEDGMENTS

N. Schlegal and B. Blum of CH2M-Hill provided the design information for I-94 project. The cost data for I-94 project was gathered from Mr. Art Covi of We Energies, Mr. Kevin McMullen of WCPA, and from ENR. Dr. J. C. Lee provided support with the analysis. G. C. Courter of Hoffman Construction and Joe Jirsa and Mary Gehrke of WisDOT assisted with the Beltline project data.

REFERENCES

- Dodge Data and Analytics ENR, "Construction Economics," *Engineering News-Record*, p. 26, July 2015.
- Epps, Jon, Presentation at RAP Summit, *National Center for Asphalt Technology*, October 2009
- Kilbert, C.J. (2002). "Policy instruments for a sustainable built environment." *Journal of Land Use and Environmental Law*. 17(2): 379-394
- Truitt, P. (2009) "Potential for reducing greenhouse gas emissions in the construction sector." *U.S. EPA Archive Document*, <<http://www.epa.gov/sectors/pdf/construction-sector-report.pdf>> (July 27, 2015).
- Lee, J.C., Edil, T.B., Benson, C. H., and Tinjum, J.M. (2013). "Building Environmentally and Economically Sustainable Transportation Infrastructure: Green Highway Rating System." *Journal of Construction Engineering and Management*, 130(12), A4013006: 1-10.
- WisDOT. (2015a). "I-94 North-South Freeway Project." *511 Wisconsin Construction Projects*, <<http://projects.511wi.gov/i94northsouth/>> (May 20, 2015).
- WisDOT. (2015b). "Madison Beltline Study." *Wisconsin.Gov-Projects*, <<http://wisconsindot.gov/Pages/projects/by-region/sw/madisonbeltline/default.aspx>> (June 2015).
- WisDOT. (2015c). "Wisconsin Department of Transportation – Average Unit Price List." <<http://wisconsindot.gov/hcciDocs/contracting-info/average-unit-price.pdf>> (Dec. 9, 2015).
- Van Dam, T., et al. (2015). "Towards Sustainable Pavement Systems: A Reference Document." *Federal Highway Administration*, Washington, D.C.
- UC Berkeley. (2007). "PaLATE." *Consortium on Green Design and Manufacturing*, <<http://www.ce.berkeley.edu/~horvath/palate.html>> (Mar. 28, 2014).

Assessment of the Pollution Potential of an Aquifer from Surface Contaminants in a Geographic Information System: A Case Study of Pakistan

Yawar Hussain¹; Sadia F. Ullah²; Adil Dilawar³; Gulraiz Akhter⁴; Hernan Martinez-Carvajal⁵; and Henrique L. Roig⁶

¹Doctorate Student, Dept. of Civil and Environmental Engineering, Univ. of Brasilia, Brazil. E-mail: yawar.pgn@gmail.com

²Doctorate Student, Dept. of Biological Sciences, Univ. of Brasilia, Brazil.

³Student, Dept. of Physics, Univ. of Sargodha, Pakistan.

⁴Chairman, Dept. of Earth Sciences, Quaid-i-Azam Univ., Islamabad, Pakistan.

⁵Professor, Dept. of Civil and Environmental Engineering, Univ. of Brasilia, Brazil.

⁶Professor, Institute of Geosciences, Univ. of Brasilia, Brazil.

Abstract: Thal Doab Aquifer (TDA) lies in Indus Basin has experienced rapid growth of population, livestock and agricultural activities because of easy availability of surface and groundwater. The alarming growth rates of these three interrelated landuse activities are the source of pollution of TDA from non point sources (NPS). So for the managerial purposes an efficient approach for the assessment of groundwater aquifer sensitivity, the DRASTIC model in geographic information system (GIS) environment was applied. GIS layers were developed for each of the DRASTIC parameters and combined into natural sensitivity coverage. The resultant natural vulnerability values were grouped into four categories: low to moderate-indicating that the groundwater aquifer is very well protected and risk of contamination from NPS is very low; high-the groundwater aquifer is much more susceptible to contamination due to several hydrologic conditions; and very high-all hydrologic parameters are conducive to the rapid transport of contamination to the groundwater aquifer. Results indicate that, most part of the study area falls under high to very high vulnerability zone, eastern part 17.2% is under very high vulnerability zone, while a small portion of about 15.6% is under low vulnerability zone at north and northwestern parts.

INTRODUCTION

Pakistan has an agricultural based economy which is suffering from major water related problems due to, overexploitation and uneven distribution of resources at local, national and regional levels. The main source of water is the Indus River System (IRS) which forms a large continuous and well transmissive aquifer (Akram

et al. 2014), with its major portion in the form of four patches of alluvium, usually referred to as Doabs.

Groundwater in TDA is under continuous environmental risk because of rapid growth of agriculture, livestock, and population over the last many years. These three interrelated land use activities are the sources of pollution for TDA. These are called Non- point Sources (NPS) of pollution because, they pollute the water at large spatial extensions. The growth of these NPS has been posing a serious threat to country's most precious Groundwater reservoirs and consequently, the degradation of socioeconomic status of people living there (Hussain. 2014). Although, some of contamination data is available in upper regions of TDA, only limit data is available from the central and lower parts. The impact assessment analysis of these NPSs on TDA is a serious environmental problem.

Ground water vulnerability is defined as the potential for an aquifer to become polluted. In present scenario, the best solution is the use of Groundwater Vulnerability Mapping (GVM) for preventive purposes through prioritization of areas where GW monitoring is critical (Al-Zabet, 2002). Also, with the application of this technique the land-use planning of the projected area can be done on rational probabilistic basis. GVM is based on assumption that hydrogeological settings of a particular area protect GW from surface contaminate, making some parts of land relatively more vulnerable than others (Shirazi et al. 2013). In GVM hydrogeological factors are taken under consideration while marking the study area into different vulnerability zones having relatively different vulnerability potentials.

Scientific history of the world has witnessed many examples of development and applications of Index methods like DRASTIC, GOD, IRIH, AVI, EPIK and SINTTACS but, according, to Muhammad et al. (2015) among these available methods the most famous is the DRASTIC (Acronym seven hydrogeological parameters) model. DRASTIC model was the result of joint efforts of National Water Well Association (NWWA) and U.S. Environmental Protection Agency (EPA). This model has hydrogeological meaning attached to its each letter for example D for depth of water, V is vadose zone, A for aquifer media, S stands for soil types, T, I and C acronym for topography, net recharge and hydraulic conductivity, respectively. Worldwide adoptability of DRASTIC, made it an effective vulnerability tool (Samey and Gang 2008).

Study area

Thal Doab is a triangular piece of land which is divided into upper, middle and lower parts. Indus River marks the eastern boundary throughout the entire length of Doab. Western side is marked by Jhelum River in the upper Doab and Chenab River in the middle and lower parts with Salt Range is at north as shown in figure 1. Thal Doab lies between geographic coordinates $28^{\circ} 57' 46.3''$ to $32^{\circ} 58' 49''$ north and longitudes $70^{\circ} 30' 04''$ to $72^{\circ} 55' 30''$ east (Figure 1). This area covers seven districts (Bakkhar, Jhang, Jhelum, Khushab, Layyah, Mianwali and Muzafargarh) of Punjab province. Topography of Thal Doab is relatively flat but, it has very well defined canal networks which irrigate most of the study area.

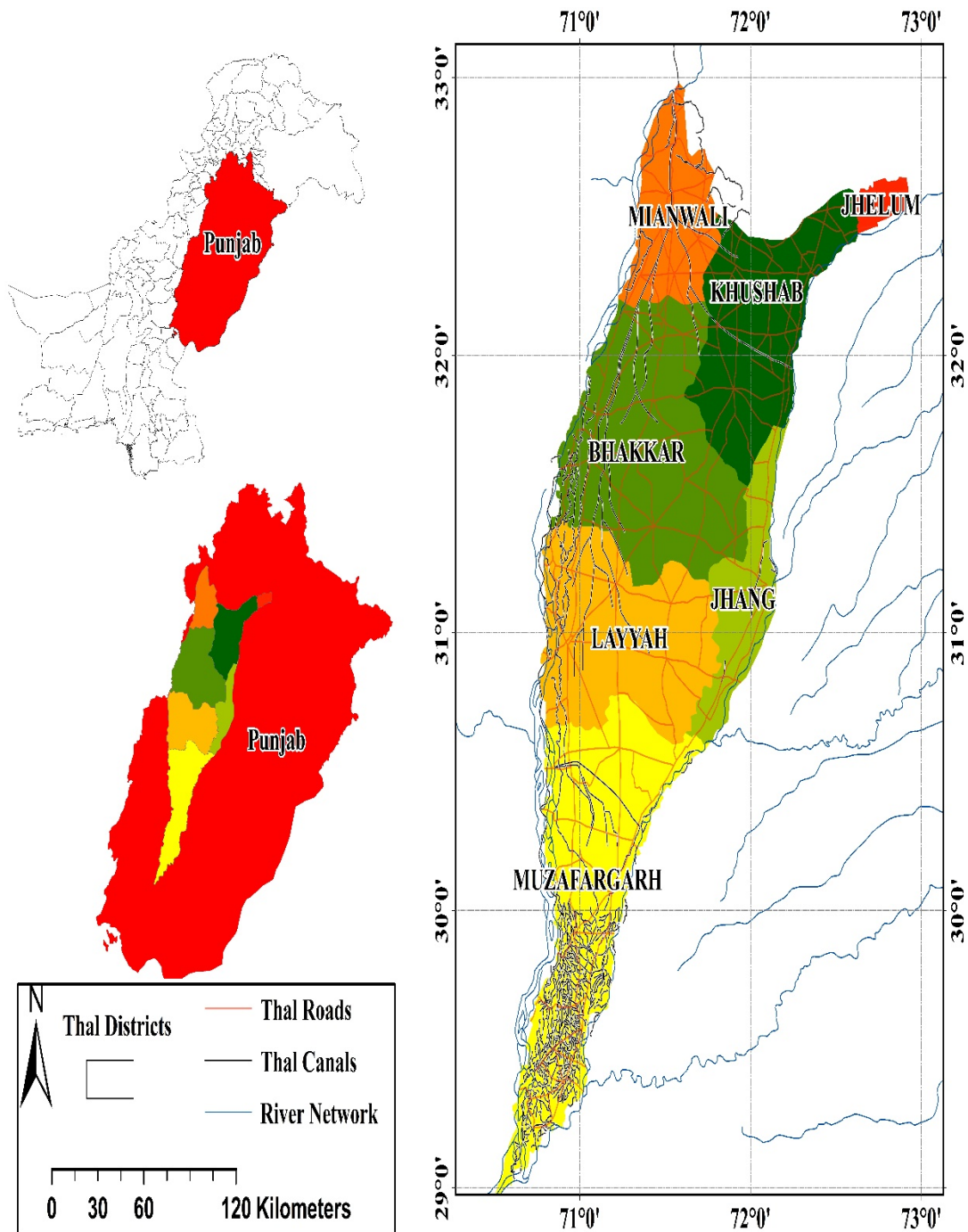


FIG. 1. Location map of the study area showing Rivers, Canals, Roads and Districts of Thal Doab.

It lies in the region of arid climate with very hot summers and mild winters. The maximum recorded temperature is 54⁰C and minimum recorded temperature is -1⁰C. The dust storms are common in this area (Nickson et al. 2005). Soil has less organic nutrients which increase the regions dependency on the use of fertilizers for healthy and productive agriculture (Greenman et al. 1967).

MATERIAL AND METHODS

DRASTIC model was developed by Aller et al. (1987) one of the most commonly used rating methods. The DRASTIC model provides opportunity for aquifer vulnerability analysis with readily available data and future modifications flexibility. Vulnerability is defined as the probability of aquifer getting contaminated. It is a relative term, and all aquifers in the world are more or less vulnerable. This relativity of different aquifers to the surficial contaminants, is the function of variability of DRASTIC parameters that are involved in contaminant movement from surface to groundwater. All these site specific hydrogeological parameters are built in a mathematical rating model which is a categorical rating method like overlay and an index method. In this model the vertical movements of surface contaminants are assumed to be a function of the hydrogeology of that specific area. Each letter in the acronym DRASTIC has a hydrological characteristic of the study area as, Depth of water table (D), Net recharge (R), Aquifer media (A), Soil media (S), Topography (T), Impact of Vadose zone (I) and Hydraulic Conductivity (C) as mentioned in Table 1.

Table 1. Relative Weights Given to DRASTIC Parameters

No	Parameter	DRASTIC Weight
1	Depth of table	5
2	Net recharge	4
3	Aquifer media	3
4	Soil media	2
5	Topographic	1
6	Vadose zone	5
7	Hydraulic conductivity	3

DRASTIC model has three numerical parts i.e. Range, Rating and Weight. The impact of each parameter in contaminant movement is fixed in the model. This relative fixed importance of each parameters in the model is called weight and it is represented as “W” (Khan et al. 2013). Its value varies from 1 to 5, where 5 is most effective while 1 is the least. A value of 5 is given to the vadose zone (unsaturated zone above water table) which makes it most effective parameter in the vulnerability analysis. Table 1 has the details of relative weight of each influence parameter in the vulnerability analysis. But, the value of each parameter is not constant throughout the study area as it varies spatially. This spatial variability of DRASTIC parameters is called Range (Aller et al. 1987). The input parameters are divided into different ranges based on their respective data variability and a subjective rating value is given to each range. This value is variable within the range 1 to 10 and selected based on recommendations from hydrogeologists. Final aquifer vulnerability map is generated based on DRASTIC index “Di” calculated from equation 1. Multiplication of relative specific and general impact factor of each hydrogeological parameters in the DTASTIC gives a final vulnerability index for that parameter and their total sum gives to final required vulnerability map (Aller et al. 1987).

$$DI = DwDr + RwRr + AwAr + SwSr + TwTr + IwIr + CwCr \quad (1)$$

D= Depth of water table

R= Recharge (Infiltration)

A= Aquifer media

S= Topography

I= Impact of vadose zone

C= Hydraulic conductivities

Where DI=DRASTIC Index, 'R' is rating factor and 'W' is relative weight.

All the steps involved in GWVM are carried out in ArcGIS software which provides computerized mapping, and spatial data analysis that enables the manipulation and analysis of spatially referenced information to describe the relationship between landscape features. The preparation of DRASTIC input thematic maps from different data types. GIS has proved an efficient tool for environmental analysis and has superb capabilities in handling large spatial data sets, which has enhanced greatly its applicability since the last many years. GIS can better handle thematic mapping and spatial analysis of attributes. Geodatabase which is a digital representation of the hydrogeologic information prerequisite for the model is used to generate seven DRASTIC thematic maps (as a point, line, or polygon layer) in GIS environment (Rahman, 2008). Final product is the GVM which is obtained by linearly combining each layer with its respective rating and weight and then adding the maps resultant GWV is relative and qualitative (Al-Abadi et al. 2014).

RESULTS AND DISCUSSIONS

Depth of water table map

DWT is the distance in which pollutants move through soil media before reaching groundwater table. Depth of water table is the most important DRASTIC parameter because, if depth of water table is low it leads to high vulnerability and vice versa (Rahman 2008). Data for the depth of water table was derived from Pakistan Council of Research in Water Resources. Database includes the well identification number, depth of water table, latitude and longitude of each well. This information was converted into a thematic map by using IWD interpolation method in ArcGIS 10.1. IWD is a best method for such types of interpolations (Hussain et al, 2016) The DWT map is divided into four zones, then drastic rating was assigned to each class based on vulnerability potentials (Figure 2A). 52 % of study area is under high vulnerability while only 10% is under low vulnerability. The percentage of Thal Doab under very high and moderate vulnerabilities were estimated at 28% and 12%, respectively.

Net recharge map

Net recharge calculation is the main vehicle to quantify transport of both liquid and solid wastes from surface to groundwater. TDA is recharged from both lateral (rivers

and canals seepage) and vertical (rainfall percolations and irrigation) flows. Due to scarcity of such a huge amount of data set at regional scale an alternate approach was adopted to calculate recharge map. Isotopic concentrations of $\delta^{18}\text{O}$ (oxygen isotope) taken from different wells was interpolated. Then on the basis of $\delta^{18}\text{O}$ concentration study area is divided into three categories as Category-1 ($\delta^{18}\text{O} > -5.5\%$), Category-2 (-7.5 to -5.5%) and Category-3 ($\delta^{18}\text{O} < -7.5\%$). The depleting in the isotopic values suggest the decreasing role of rain and increasing role of surface waters in groundwater recharge. These categories are changed in term of recharging sources and rating values are assigned on the basis of contribution of each agent in aquifer recharge mechanism (Personal communication, July17, 2014). Most part of study area is recharged by rivers which, increase its vulnerability probability. Small portion at northern side is recharged by rainfall. A rating factor of 9 is assigned to river recharge which covers most of study area while, rating 5 is used for rainfall recharge areas with low vulnerability (Figure 2B).

Aquifer media map

Aquifer media refers to the consolidated or unconsolidated rock that serves as an aquifer. The larger the grain size and the more fractures or openings within the aquifer, higher the permeability, and thus vulnerability, of the aquifer. In this study alluvium geology is further sub classified on the basis of nature of depositional agents (wind or water). Aeolian deposit on the western part are given high rating because they are continuously being eroded and redeposited. This process increases their porosity and therefore vulnerability. Aquifer media map is reconstructed from geological map (Kazmi and Jan, 1997). This map was digitized and converted into different polygons. These polygons containing different geological material in response of different depositional agents as shown in Figure 2C.

According to Aller et al. (1987), the vadose media for an unconfined aquifer system is the same as the aquifer media. Therefore, aquifer media is used with different weight factor as given in Table 1.

Hydraulic conductivity map

Hydraulic conductivity influences the mobility of contaminants in saturated zone. Higher the value of hydraulic conductivity higher the vulnerability and vice versa. Data of 40 pumping tests conducted by the USGS in late sixties was processed. Area is divided into different zones. Single value of each hydraulic parameter was assigned by taking simple average of all tests falling in particular zone. The developed hydraulic zones are shown in Figure 2D. Most of area is under very high vulnerability.

Topographic map

If slope is low, hydraulic gradient is low which cause water to stay there for longer time thus providing contaminants longer time to percolate through the soil. 1km GTOPO 30 USGS Digital Elevation Model was used to calculate percentage slope of

Thal Doab. Because of flat (0-2) nature of project area's topography a homogenous single slope value is assigned.

Soil map

Soil characteristics of an area effect its vulnerability potential by impacting the recharging potential of the aquifer (Sener and Davraz. 2012). Soil map used in the study based on the FAO-UNESCO Soil Map of the World. Soils are classified based on the topsoil. Thal Doab contains alluvium soil which is categorized on the basis of proportion of its sand particles. Central part of the Doab contains relatively more sand particles than peripheral parts as shown in Figure 2E.

Aquifer vulnerability assessment

A special modified rating system is used for this study. All the seven vulnerability parameters are joined according to equation (1) in ArcGIS 10.1 at fixed scale and with a constant grid value of 100 by 100 meters.

Table 2. DRASTIC Index Values in Thal Doab with Vulnerability Zones and Area Percentage

Vulnerability Classes	DRASTIC Index Value	Area (%)	Settlements
Low	138-164	15.6	Daud Khel, Koruwala
Moderate	164-177	24	Ludawala, Muhib Shah
High	177-191	43.2	Behal, Ghazi Ghat, Jaswal
Very High	191-203	17.2	Ahsanpur, Ghulaman, Kamyab

The resultant vulnerability index values are divided into four vulnerability classes low, moderate, high and very high as projected in Figure 2F. Most part of study area which is under high agricultural activities has high vulnerability risk while eastern parts fall under low vulnerability class. As shown in Table 2. 43.2 % of Thal Doab lies under moderate vulnerability zone while, while 17.2 % having very high vulnerability. Ahsanpur, Ghulaman and Kamyab fall under very high vulnerability and need special attention of the policy makers to have a special type of landuse which cast minimum pollution at the surface.

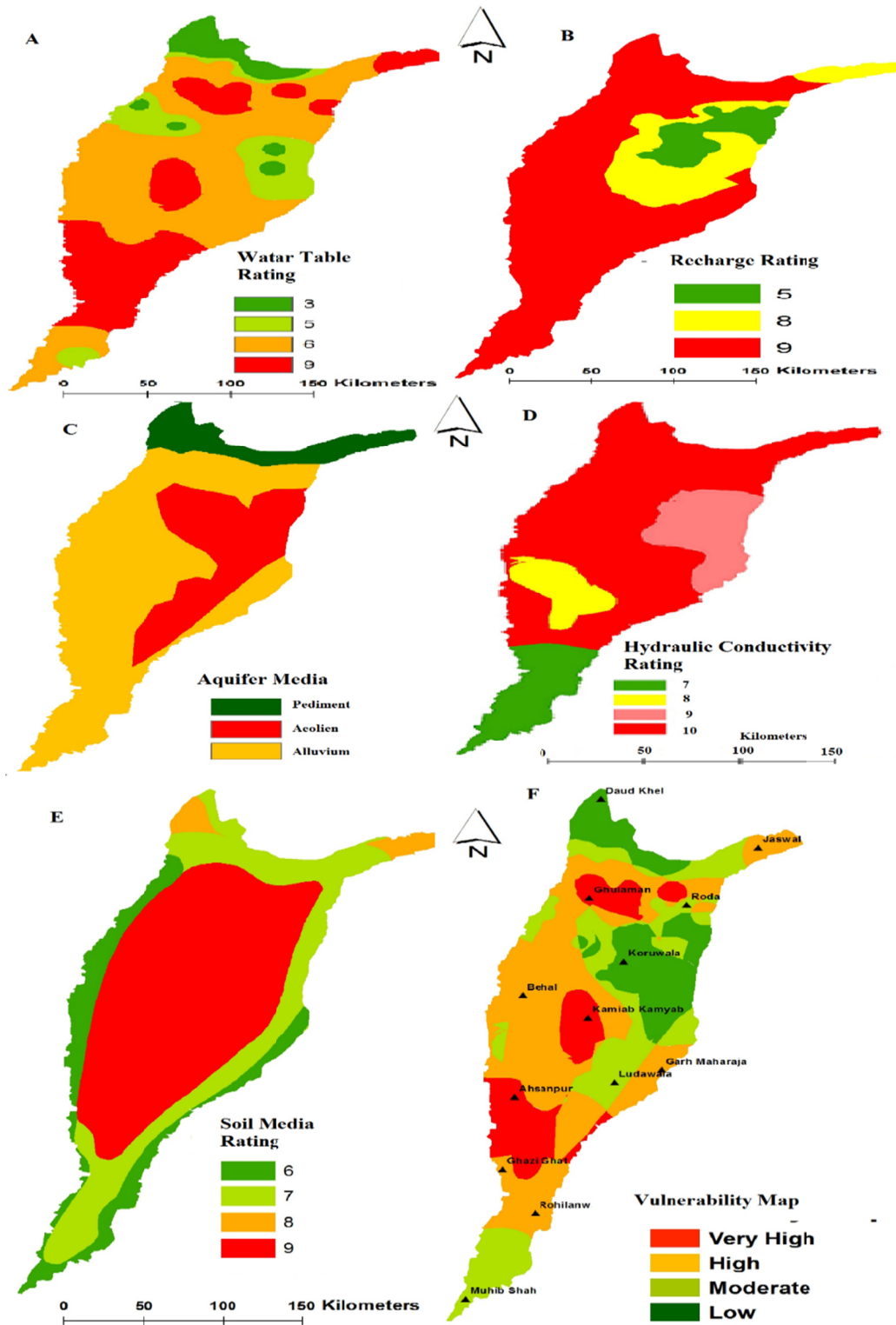


FIG. 2. Evaluation of DRASTIC input thematic layers. (A-F) water table, recharge, soil, aquifer media and hydraulic conductivity and Vulnerability Map of Thal Doab showing different vulnerability zones having different pollution potentials.

CONCLUSIONS

This study was conducted to demarcate study area into different vulnerability zones based on the hydrogeological parameters. The results show that DRASTIC model has very good potential to divide area into different vulnerability zones. It is concluded that vulnerability categories lie in range of very high and high in active and abandoned flood plain of Indus River and areas of Thal Doab where there is high recharge from Indus River. Low vulnerability is found in areas having low recharge.

REFERENCES

- Akram, W., Latif, Z., Iqbal, N and Tasneem, M.A. (2014). "Isotopic investigation of groundwater recharge mechanism Thal Daob." *Nucleus*, Vol. 2(2): 187–197.
- Al-Abadi, A.M., Al-Shamma, A.M. and Aljabbari, M. H. (2014) "A GIS-based DRASTIC model for assessing intrinsic groundwater vulnerability in northeastern missan governorate, southern Iraq." *Appl. Water Sci.*, 1-13.
- Aller, L., Lehr, J. H., Petty, R. and Bennett, T. (1987). "DRASTIC: A standardized system to evaluate groundwater pollution potential using hydrogeologic settings." *U.S. EPA Report 600/2 – 85/018*.
- Al-Rawabdeh, A. and Al-Ansari, N. (2014). "Modeling the risk of groundwater contamination using modified DRASTIC and GIS in Amman-Zerqa basin, Jordan." *Open Eng.*, Vol. 4(3): 264-280.
- Gosal, G. (2004) "Physical geography of the Punjab." *J. P. S.*, Vol. 11(1):19-37.
- Greenman, D. W., Swarzenski, W. V. and Bennett, G. D. (1967). "Groundwater hydrology of the Punjab, west Pakistan with emphasis on problems caused by canal irrigation." US Geol. Survey Water-Supply Paper.
- Hussain, Y. (2014). "Hydrogeophysical investigations and GIS vulnerability mapping of Kot Adhu." Quaid-i-Azam University, Islamabad, Pakistan.
- Hussain, Y., Dilawar, A., Ullah, S.F., Akhter, G., Martinez-Carvajal, H., Hussain, M.B. and Aslam, A.Q. (2016). "Modelling the Spatial Distribution of Arsenic in Water and Its Correlation with Public Health, Central Indus Basin, Pakistan." *J. Geosci. Environ. Protec.*, Vol. 4(2): 18-25.
- Kazmi, A.H. and Jan, M.Q. (1997). "Geology and tectonics of Pakistan." Graphic publishers, Karachi, Pakistan.
- Khan, A. D., Ghoraba, S., Arnold, J. G. and Luzio, M. D. (2014b). "Hydrological modeling of upper Indus Basin and assessment of deltaic ecology." *Int. J. Mod. Eng. Res.*, Vol. 4(1): 73-85.
- Muhammad, A. M., Zhonghua, T. Dawood, A. S. and Earl, B. (2015) "Evaluation of local groundwater vulnerability based on DRASTIC index method in Lahore, Pakistan." *Geofis. Int*, Vol. 54(1): 67–81.
- Neshat, A., Pradhan, B., Pirasteh, S. and Shafri, H.Z.M. (2013). "Estimating groundwater vulnerability to pollution using a modified DRASTIC model in the Kerman agricultural area, Iran." *Environ. Earth Sci.*, Vol. 71(7): 3119–3131.
- Nickson, R. T., McArthur, J. M., Shrestha, B., Kyaw-Myint, T. O. and Lowry, D. (2005). "Arsenic and other drinking water quality issues, Muzaffargarh district, Pakistan." *Appl. Geochemistry*, Vol. 20(1): 55–68.

- Rahman, A. (2008). "A GIS based drastic model for assessing groundwater vulnerability in shallow aquifer in Aligarh, India." *Appl. Geogr.*, Vol. 28(1): 32–53.
- Samey, A.A. and Gang, C. (2008). "A GIS based DRASTIC model for the assessment of groundwater vulnerability to pollution in west Mitidja: Blida city, Algeria." *J. Appl. Sci.*, Vol. 3(7): 500-507.
- Secunda, S., Collin, M.L. and Melloul, A.J. (1998). "Groundwater vulnerability assessment using a composite model combining drastic with extensive agricultural land-use in Israel's Sharon region." *J. Environ. Manage.*, Vol. 54(1): 39–57.
- Sener, E. and Davraz, A. (2012). "Assessment of groundwater vulnerability based on a modified DRASTIC model, GIS and an analytic hierarchy process (ahp) method: the case of Egirdir lake basin (Isparta, Turkey)." *Hydrogeol. J.*, Vol. 21(3): 701–714.
- Shah, Z. U. H. and Ahmad, Z. (2015). "Hydrochemical mapping of the upper Thal Doab (Pakistan) using the geographic information system." *Environ. Earth Sci.*, Vol. 74(3): 1-17.

Carbon Footprint: Liquefaction Effects on a Private Residence

Manasa Vijayakumar¹; Jennifer J. Cheng¹; Murat Küçükvar²; Ahmed Elgamel, M.ASCE³; Kevin R. Mackie, M.ASCE⁴; and Omer Tatari, A.M.ASCE⁴

¹Graduate Student, Dept. of Structural Engineering, Univ. of California San Diego, La Jolla, CA 92093-0085.

²Assistant Professor, Dept. of Industrial Engineering, Istanbul Sehir Univ., Istanbul 34662, Turkey.

³Professor, Dept. of Structural Engineering, Univ. of California San Diego, La Jolla, CA 92093-0085.

⁴Associate Professor, Dept. of Civil, Environmental and Construction Engineering, Univ. of Central Florida, Orlando, FL 32816-2450.

Abstract: In this study, focus is placed on ground improvement in seismic regions, as a geotechnical application of major economic and environmental consequence. To this end, a pilot framework is developed for assessment of related cost and carbon emissions. For a representative residential structure built on potentially liquefiable ground, three options are considered. The first option is to implement a ground modification countermeasure before constructing the structure. The other options include repair of damage, primarily by re-leveling the structure if the earthquake occurs. For the developer/stakeholder, the initial as well as potential post-earthquake cost and carbon emissions are factors of interest. The a priori ground modification considered for this study is vibro stone columns, and the technique for post-earthquake re-leveling of the residence is compaction grouting. Carbon emissions are computed via process-based life-cycle-assessment (P-LCA). The analysis framework is presented along with the underlying calculation procedures. Potential benefits and shortcomings in terms of cost and carbon emission are contrasted, highlighting significance to the process of decision support.

INTRODUCTION

In the last few decades, studies have been conducted on sustainability in the infrastructure industry (Ding 2007, Ortiz et al. 2008). Inclusion of carbon-footprint considerations in the field of geotechnical engineering is becoming of vital importance as a component within the realm of an environmentally-conscious society (Fragaszy et al. 2011, Inui et al. 2011, Basu et al. 2014, Shillaber et al. 2014, Keaton 2014).

In this regard, ground improvement is a significant element of geotechnical work, particularly in areas prone to seismic hazard and associated liquefaction (Cubrinovski

et al. 2011a, Tokimatsu et al. 2012, Yasuda et al. 2012, Bray et al. 2014). Indeed, pervasive liquefaction-induced settlement of houses and similar structures was recently seen (FIG. 1) during the Great East Japan Earthquake (Tokimatsu et al. 2012, Yasuda et al. 2012) and the Christchurch, New Zealand earthquakes (Cubrinovski et al. 2011a, 2011b, 2012). Restoration of these houses by re-levelling was among the main rehabilitation procedures.



FIG. 1. Large settlements and tilting of building due to liquefaction (Yasuda et al. 2012, Ashford et al. 2011).

As such, this study is concerned with carbon emissions incurred during a priori ground improvement, and possible subsequent re-levelling of settled structures. For new construction, potential damage may be mitigated by implementing appropriate ground improvement techniques (Baez and Martin 1995, Adalier et al. 2003, Adalier and Elgamal 2004). Conversely, the damage can be repaired after the anticipated earthquake event occurs. As such, this study investigates the cost, and environmental impact due to carbon emissions for a representative residential building. The a priori ground improvement method for the residence is vibro stone columns and the method for re-levelling post-earthquake is compaction grouting. The analysis for carbon emission follows the process-based life cycle assessment (P-LCA) procedure as presented by Harmouche et al. (2012).

In the following sections, scope and methodology for calculating cost and carbon emissions for a specific earthquake-induced settlement scenario are described. The calculation framework and results are presented, with details reported in Vijayakumar (2015).

GROUND IMPROVEMENT AND RE-LEVELLING TECHNIQUES

Vibro stone columns (Baez and Martin 1995, Adalier et al. 2003, Adalier and Elgamal 2004) are used to improve the bearing capacity of soil and reduce settlement (FIG. 2). Vibro stone columns stiffen the soil by constructing dense stone aggregate inclusions in a grid pattern into the soil.

Compaction Grouting (Boulanger and Hayden 1995) using Low Mobility Grout (LMG) is one of the ground improvement methods recommended by MBIE (2012) to re-level structures (FIG. 3). This method involves injecting thick grout into the soil (Andrus and Chung 1996, MBIE 2012) by inserting a pipe into the ground and injecting bulbs of grout (Haramy et al. 2012). The expansion of the grout mass raises the building and increases the bearing capacity of the soil (Andrus & Chung, 1996).

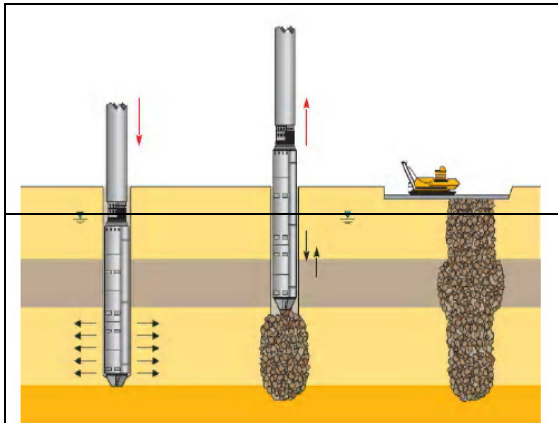


FIG. 2. Stone column installation (Chawla et al. 2010).

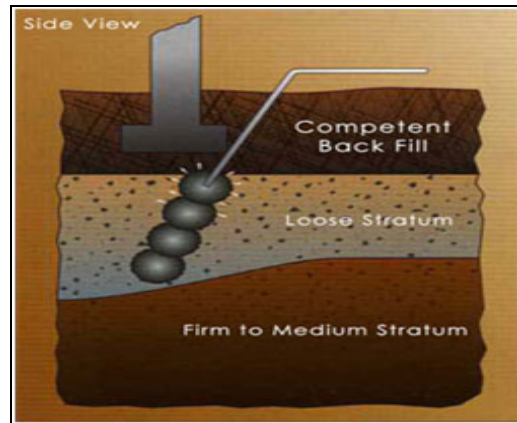


FIG. 3. Compaction grouting (<http://lincolnllc.com/techniques.php>).

LIFE-CYCLE ASSESSMENT

A large volume of research exists about life cycle assessment (LCA) models to quantify the environmental impact for the constructed infrastructure (Ochoa et al. 2002, Bilec et al. 2006, Tatari and Küçükvar 2012, Küçükvar and Tatari 2013).

Carbon emission is one of the many environmental impacts that are addressed by the LCA methodology. Some studies have been already performed to assess the carbon emissions from different ground improvement techniques (Chawla et al. 2010, Pinske 2011, Mitchell and Kelly 2013).

Of the existing LCA models (Bilec et al. 2006), this study reports on results using the process-based life cycle assessment (P-LCA) methodology. For P-LCA, one possible approach for computing the carbon emissions is based on materials used. Carbon emission factors (EF) convert the amount of material used to the associated carbon emissions (Hammond and Jones 2008). The University of Bath's Inventory of Carbon and Energy (ICE) provides a reliable database of these EFs for over 400 construction materials that came from either secondary data resources or were derived from known information (Hammond and Jones 2008). The EFs from ICE only account for emissions due to production and manufacturing. The boundary condition for the EFs is therefore, cradle-to-gate. The emissions due to transportation are computed separately since this can vary from project to project.

SCOPE OF STUDY

For new residential structures that may be built on potentially liquefiable ground, three cases are considered. In the first case, the structure is built, and potential

settlement damage resulting from seismic activity is repaired thereafter (by re-levelling the structure). The other two cases include a ground improvement countermeasure before construction of the structure, to mitigate such potential settlement damage (with repairs still needed in one of these cases). The aim is to develop a pilot framework for the assessment of cost and carbon emissions associated with the three cases. For the stakeholder, the initial as well as post-earthquake cost and carbon emissions are assumed to be factors of interest towards a decision as relates to the potential a-priori countermeasure deployment (and its extent).

The framework is presented along with the necessary underlying computational concerns and representative results. The cost and carbon emissions considered are those due to material production, transportation to and from the site, and on-site construction activity.

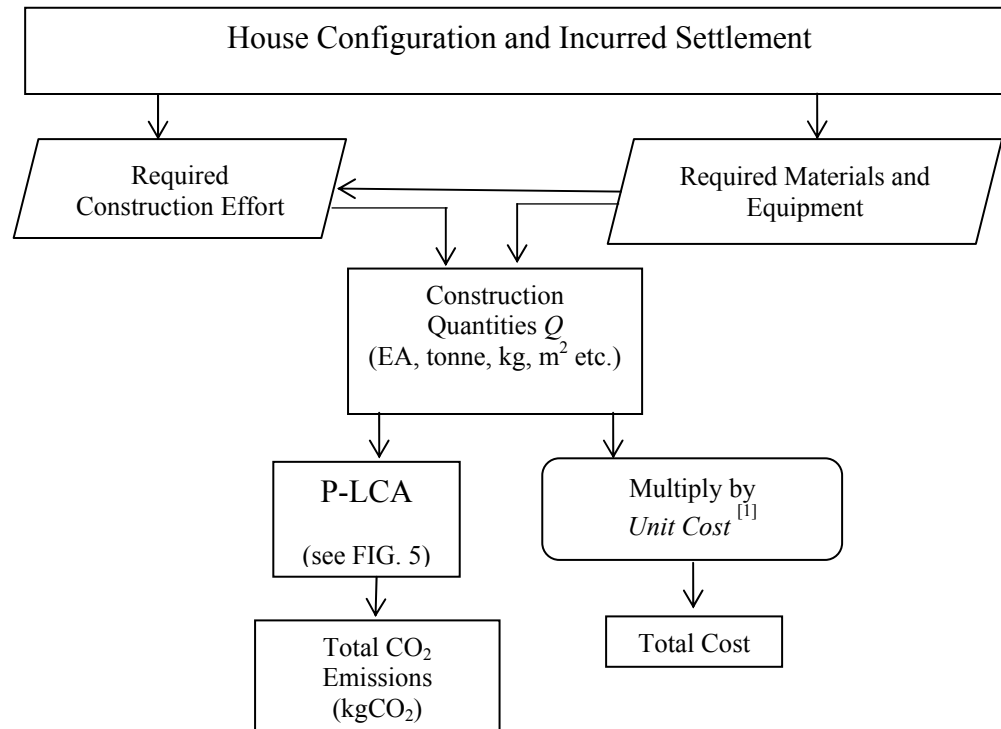
COST AND CARBON COMPUTATION METHODOLOGY

FIGs. 4 and 5 present the steps for computing the cost, and the carbon emissions. Construction items such as materials, equipment, and so forth are first defined. Based on the scope of the construction project, the necessary quantities (Q) of each construction item are computed (Vijayakumar 2015). An item may have more than one quantity and thus, more than one associated cost. For example, re-grading and resurfacing requires two different quantities, concrete, and the associated construction equipment. With the P-LCA methodology based on economic equivalents, the unit cost is needed for all construction items. The RS Means reference (2008-2015) provides national averages for such unit costs. The unit costs used herein only include the material/production cost for the LCA model. To compute the total cost for the project, the quantities (Q) calculated are multiplied by unit costs that include material cost and overhead & profit according to RS Means (2008, 2010, 2013, 2015).

In this P-LCA study, carbon footprint is defined as the amount of carbon dioxide emissions directly and indirectly emitted from cradle-to-site (Hammond & Jones (2008)), and thereafter in the construction and usage (Ochoa et al. 2002). Other greenhouse gas emissions are not considered. As presented in Harmouche et al. (2012), the emissions generated are categorized into three phases: (1) the embodied carbon or the raw material emissions being those generated during production of the material, (2) the construction activity emissions being those generated during construction on site, and (3) the transportation or tail pipe emissions being those generated during transportation of the material. The methods for computing each of these emissions are summarized in FIG. 5. Apart from the above three phases, FIG. 5 shows a separate category to illustrate that the diesel production emissions are related to the combined transportation and construction components. All details related to FIG. 5 are presented in Vijayakumar (2015).

CASE STUDY: RESIDENCE ON LIQUEFIED GROUND

For this study, the considered idealized residence is a two-story wood frame structure supported on a slab-on-grade foundation with a footprint of 10.7 m by 10.7 m (approximately 240 m² area for 2 stories). The hardscape around the residence is



[1] Unit cost includes overhead and profit (RS Means 2008-2015)

FIG. 4. P-LCA carbon and cost computation.

assumed to be 50 m². The following three cases for construction (with or without a priori ground improvement) and post event settlement/repair are considered:

- (1) No ground improvement implemented with a post-event settlement of 0.15 m,
- (2) Ground improvement implemented as a countermeasure against moderate levels of shaking such as those corresponding to a Contingency Level Earthquake (CLE, an event with a 10% chance of exceedance in 50-years (USGS 2007)) with a post-event settlement of 0.06 m, and

(3) Ground improvement implemented as a countermeasure against higher levels of shaking such as those corresponding to a Maximum Considered Earthquake (MCE, an event with a 2% chance of exceedance in 50-years (USGS 2007)) with practically no post-event settlement. Throughout, the term settlement herein is assumed to implicitly also account for any differential settlements.

Ground Improvement (GI) Prior to Construction: The stone columns are presumed to have a unit weight of 1600 kg/m³ and a depth of 8 m for Case 2 and 12 m for Case 3. After the construction of stone columns, a stone bed (depth of 0.54 m for Case 2 and 0.80 m for Case 3) is laid on the ground spread over the entire footprint. The cost and carbon emissions are computed by the process outlined in FIGs. 4 and 5.

Table 1 briefly outlines the GI Quantities for cost and carbon emission calculations. Full details are provided in Vijayakumar (2015), for GI as well as for the Post-event Repair discussed below.

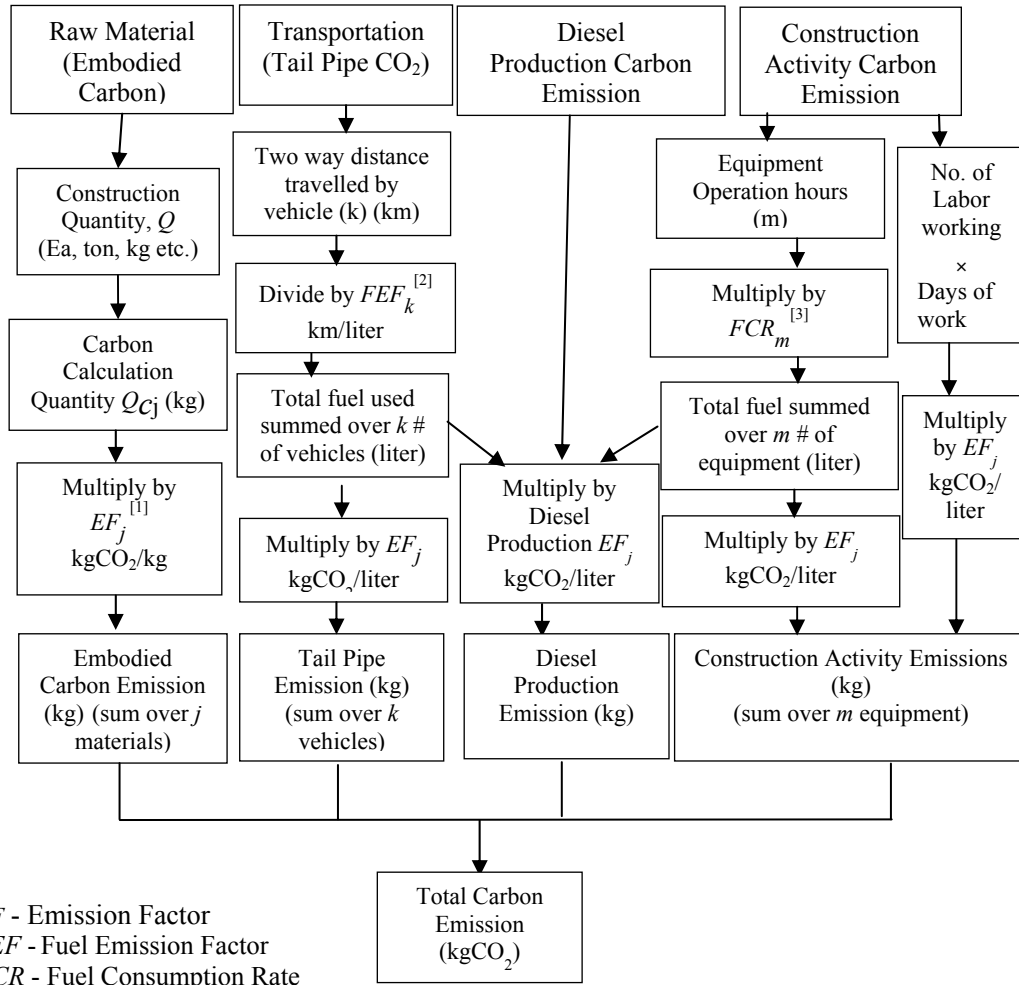


FIG. 5. P-LCA for total carbon emission (full details in Vijayakumar 2015).

Table 1. Outline of GI Quantities (full details in Vijayakumar 2015).

Material	Quantity, Q
Stone Aggregate for Stone Column (SC)	No. of SC x Area of SC x Depth of SC x Unit Weight of Aggregate
Diesel for Equipment – Stone Injector	No. of days of use x No. of hours per day x Fuel Consumption Rate
Diesel for transportation of stone aggregate	No. of trucks x Two Way Distance / Fuel Emission Factor of vehicle

Post-event Repair: Similar to the GI cases, the cost and carbon emissions are computed following the process outlined in FIGs. 4 and 5. For each of the three cases considered, the residence experiences a certain level of settlement, as mentioned above. For each settlement limit, there is an associated repair effort. Each repair effort, similar to the GI cases, has a set of construction items (for Cases 1 and 2, as Case 3 does not require any repair). All the input parameters required to estimate the

quantities of repair items are reported in Vijayakumar (2015). For instance, the estimate for grout volume was taken simply as $2 \times$ house footprint area \times settlement (i.e., a factor of 2 is assumed). The raw materials required to repair the house include grout to re-level the foundation, concrete to re-grade the hardscape area around the house, and reparation or replacement of damaged representative non-structural components.

In this study, emphasis is placed on house re-levelling, and thus only a concise list of non-structural components is included (repair for flooring, doors, and chimney). In the broader perspective, cost and carbon emissions may be associated with a wider range of additional considerations, including potential damage to the wet and dry utilities, and possible temporary relocation of the residents.

CASE STUDY: RESIDENCE ON LIQUEFIED GROUND

Based on the prescribed seismic response scenario, FIG. 6 shows a summary of the total cost calculated for the three considered cases. The Case 3 incurred cost is found to be the least. Costs for Case 1 and Case 2 are comparable and each about 10% higher than Case 3. Similarly, FIG. 7 shows that Case 3 results in the least carbon emissions.

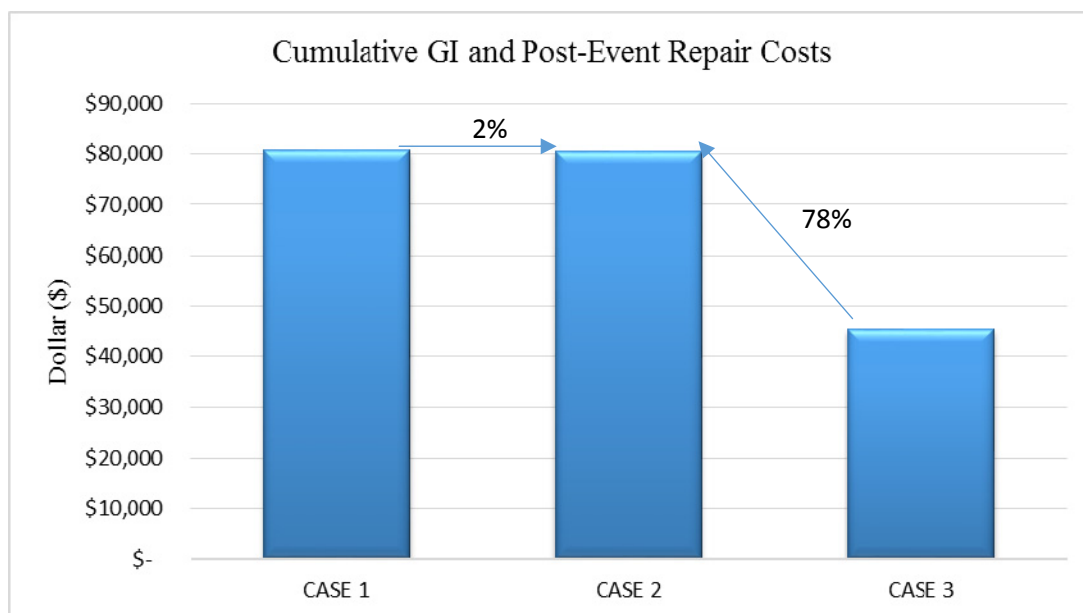


FIG. 6. Cumulative GI and subsequent repair costs for the three cases.

Based on the discussions above, it can be inferred that Case 3 is the most viable option given the postulated seismic scenario occurs. In general, Case 3 may not always be the most appropriate option, as the situation depends on the expected level of seismicity, and the risk that the stakeholder is willing to assume.

Nevertheless, this analysis framework can aid the overall decision-making process such that the stakeholder is able to evaluate the potential benefits and shortcomings in

terms of cost and carbon, in light of their tolerance for risk and disruption of function. Finally, it is noted that in Vijayakumar (2015), an extension of this framework is presented with simple probabilistic representations for the postulated seismic response, cost, and carbon emissions.

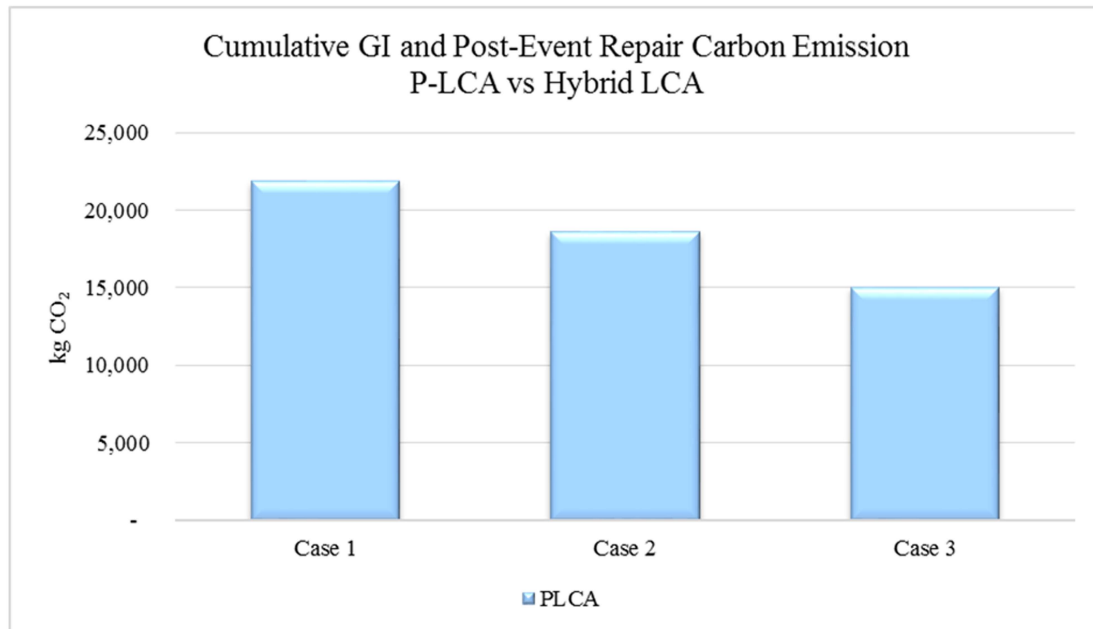


FIG. 7. P-LCA carbon emission from GI and subsequent repairs.

SUMMARY AND CONCLUSIONS

This study is concerned with cost and environmental impact due to carbon emission as metrics in a decision-support assessment framework. In order to define and integrate the salient elements of the framework, three cases of ground improvement and the corresponding overlying residence settlements are considered. Cost estimates are derived from existing databases for construction items. Carbon emissions for each case are computed using the P-LCA model. As such, the above described study introduces and integrates the various components of the framework, in that the incurred settlement as well as the cost and carbon emission computations are all based on specific quantities, within a deterministic framework. While the emphasis was placed on a residential structure scenario, the developed framework can be easily extended to an entire housing development or other similar commercial complex.

ACKNOWLEDGMENTS

The authors appreciate the financial support provided by the National Science Foundation grant no. CMMI-1201195.

REFERENCES

- Adalier, K., & Elgamal, A. (2004). "Mitigation of Liquefaction and Associated Ground Deformations by Stone Columns." *Engineering Geology*, 72(3), 275-291.
- Adalier, K., Elgamal, A., Meneses, J., Baez, J.I. (2003). "Stone Columns as Liquefaction Countermeasure in Non-plastic Silty Soils." *Soil Dynamics and Earthquake Engineering*, Volume 23, Issue 7, October, 571-584, ISSN 0267-7261.
- Andrus, R.D. and Chung, R. M. (1996). "Liquefaction Remediation near Existing Lifeline Structure." *Proc. Earthquake Resistant Design of Lifeline Facilities and Countermeasure against Soil Liquefaction*, National Center for Earthquake Engineering Research, Buffalo, NY.
- Ashford. S., Boulanger. R., Donahue, J., Stewart, J. (2011). "Geotechnical Quick Report on the Kanto Plain Region during the March 2011, Off Pacific Coast of Tohoku Earthquake, Japan." *Geotechnical Extreme Events Reconnaissance (GEER) Association Report No. GEER-025a 2011*.
- Basu, D., Misra, A. and Puppala, A.J. (2014). "Sustainability and geotechnical engineering: perspectives and review." *Canadian Geotechnical J.*, 52(1), 96-113.
- Baez, J. I., & Martin, G. (1995). "Permeability and Shear Wave Velocity of Vibro-Replacement Stone Columns". *Soil Improvement for Earthquake Hazard Mitigation*, ASCE, pp. 66-81.
- Boulanger, R.W. and Hayden, R.F. (1995). "Aspects of Compact Grouting of Liquefiable Soils," *J. Geotechnical Engineering*, ASCE, 121, 12, 844-855.
- Bilec, M., Ries, R., Matthews, S., and Sharrard, A.L. (2006). "Example of a Hybrid Life-Cycle Assessment of Construction Processes." *J. Infrastruc Sys*, 12, 207-215.
- Bray, J., Cubrinovski, M., Zupan, J., & Taylor, M. (2014). "Liquefaction Effects on Buildings in the Central Business District of Christchurch. *Earthquake Spectra*", *Earthquake Spectra*, Vol. 30, No 1, 85-109.
- Chawla, G.R., Raju, V.R., and Krishna, Y.H. (2010). "Some Environmental Benefits of Dry Vibro Stone Columns in a Gas Based Power Plant Project." *GEOtrendz*, Volume I: Contributory Papers, Proceedings of the Indian Geotechnical Conference (IGC – 2010), December 16-18, 2010, IIT Bombay, Mumbai, India
- Cubrinovski, M., Henderson, D., and Bradley, B.A. (2012). "Liquefaction Impacts in Residential Areas in the 2010-2011 Christchurch Earthquakes." Tokyo, Japan: *One Year after 2011 Great East Japan Earthquake: International Symposium on Engineering Lessons Learned from the Giant Earthquake 3-4 March*, <http://ir.canterbury.ac.nz/handle/10092/6712>.
- Cubrinovski, M., Green, R. A., Wotherspoon, L., Allen, J., Bradley, B., Bradshaw, A., and Wood, C. (2011a). "Geotechnical Reconnaissance of the 2011 Christchurch, New Zealand Earthquake." *GEER Assoc. Report No. GEER-027*.
- Cubrinovski, M., Bray, J. D., Taylor, M., Giorgini, S., Bradley, B., Wotherspoon, L., & Zupan, J. (2011b). "Soil Liquefaction Effects in the Central Business District during the February 2011 Christchurch Earthquake." *Seismological Research Letters*, 82(6), 893-904.
- Fragaszy, R.J., Santamarina, J.C., Amekudzi, A., Assimaki, D., Bachus, R., Burns, S.E., Cha, M., Cho, G.C., Cortes, D.D., Dai, S. and Espinoza, D.N. (2011). "Sustainable development and energy geotechnology—Potential roles for geotechnical engineering." *KSCE Journal of Civil Engineering*, 15(4), pp.611-621.

- Haramy, K.Y., Henwood, J.T., Szyrakiewicz, T. (2012). "Assessing the Effectiveness of Compaction Grouting Using Seismic Methods." Proc., Grouting and Deep Mixing, ASCE, 1441-1449. doi. 10.1061/9780784412350.0120
- Harmouche, N., Ammouri, A., Spour, I., Chehab, G., and Hamade, R. (2012). "Developing a Carbon Footprint Calculator for Construction Buildings." Construction Research Congress, ASCE, 1689-1699.
- Hammond, G. and Jones, C. (2008). "Inventory of Carbon & Energy (ICE)." University of Bath, 2008. Version 1.6a.
- Inui, T., Chau, C., Soga, K., Nicolson, D., & O'Riordan, N. (2011). "Embodied Energy and Gas Emissions of Retaining Wall Structures." Journal of Geotechnical and Geoenvironmental Engineering, 137(10), 958-967.
- Keaton, J. (2014). "Sustainability Concepts and Some Examples Common in Geotechnical Engineering." Geo-Congress 2014, Feb., 3817-3825.
- Küçükvar, M. and Tatari, O. (2013). "Towards a Triple Bottom-Line Sustainability Assessment of the U.S. Construction Industry." Int. J. Life Cycle Assessment, 18 (5), 958-972.
- MBIE (2012). Ministry of Business, Innovation & Employment, Building & House Information "Repairing and Rebuilding Houses Affected by the Canterbury Earthquakes, Part A: Technical guidance (TC1 and TC2)" December, Updates: <http://www.building.govt.nz/userfiles/file/publications/building/guidance-information/pdf/canterbury-technical-guidance-technical-guidance-part-a.pdf> (Aug. 14, 2013).
- Mitchell, J. K., and Kelly, R. (2013). "Addressing Some Current Challenges in Ground Improvement." Proc. ICE-Ground Improvement, 166(3), 127-137.
- Ochoa, L., Hendrickson, C., and Matthews, H.S. (2002). "Economic Input-Output Life-Cycle Assessment of U.S. Residential Buildings." Journal of Infrastructure Systems, 8, 4, 132-138.
- Pinske, M.A. (2011). "Life Cycle Assessment of Ground Improvement Methods." MS Thesis, UC Davis, Davis, CA.
- RS Means. (2008-2015). "RS Means 2008, Building Construction Cost Data" RS Means, MA.
- Shillaber, C., Mitchell, J., and Dove, J. (2014). "Assessing Environmental Impacts in Geotechnical Construction: Insights from the Fuel Cycle". Geo-Congress 2014 Technical Papers. February, 3516-3525
- Tatari, O., and Küçükvar, M. (2012). "Assessment of US Construction Sectors: Ecosystems Perspective." J. of Construction Eng & Management, 138(8), 918-922.
- Tokimatsu, K., Tamura, S., Suzuki, H., & Katsumata, K. (2012). Building Damage Associated with Geotechnical Problems in the 2011 Tohoku Pacific Earthquake. Soils and Foundations, 52(5), 956-974.
- Vijayakumar, Manasa (2015). "A Framework for Cost and Carbon Assessment: Liquefaction Effects on Lightweight Structures." MS Thesis, Department of Structural Engineering, Univ. of California San Diego, La Jolla, CA.
- Yasuda, S., Harada, K., Ishikawa, K., & Kanemaru, Y. (2012). "Characteristics of Liquefaction in Tokyo Bay Area by the 2011 Great East Japan Earthquake." Soils and Foundations, 52(5), 793-810.

Design and Construction of the Chicago Riverwalk

Matthew F. Hellenthal, P.E., S.E.¹; and Dan M. Gross, P.E.²

¹Project Engineer, Alfred Benesch and Company, 205 North Michigan Ave. Suite 2400, Chicago, IL 60601.

²Senior Vice President, Alfred Benesch and Company, 205 North Michigan Ave. Suite 2400, Chicago, IL 60601.

Abstract: The Riverwalk is located in the middle of downtown Chicago and extends nearly 2,800 ft. along the main branch of the Chicago River between State Street and Lake Street. The project consists of six themed “rooms” connected by canopied “underbridges” beneath the existing bascule bridges to provide a continuous path. The goal of the project was to provide an area for Chicago’s residents, workers, and visitors to connect with nature in the heart of the city, which led to a wide-ranging theme of sustainability throughout all aspects of the design. This paper presents a case study of the considerations and challenges associated with the design and construction of a sustainable public project in a complex urban environment.

INTRODUCTION

The gritty, working waterfront along the Chicago River in the early 1900s was heavily focused on industry and commerce. As these factories and merchants began to disappear from the banks, the river began to display its resiliency and recover from years of pollution. In recent years, there has been a growing interest in the ecology of the river and its value as a natural resource.

Although the area has been referred to as the Riverwalk for many years, the path was interrupted by each crossing street and was only accessible via stairs at the ends of each block. The site was relatively featureless with a concrete walking surface approximately 7 ft. above the water and only a few park benches to provide seating. There was little attraction to a very valuable piece of land along the river. During reconstruction of the adjacent Wacker Drive Viaduct in the early 2000s, the roadway and structure were configured to facilitate expansion of this pedestrian space along the river. The first phase of the project from Michigan Avenue to State Street was completed in 2009. In 2011, work began to expand the Riverwalk an additional six blocks to the west.

The final plan west of State Street consisted of six themed “rooms” connected by canopied “underbridges” beneath the existing bascule bridges to provide a continuous path along the river. Starting from the east end of the project at State Street, the rooms are referred to as the Marina Plaza, Cove, River Theater, Water Plaza, Jetty, and Boardwalk. From the existing outline of the channel, the build-out extends 20 ft. under each bridge, 25 ft. from State Street to Franklin Street, and 50 ft. between

Franklin Street and Lake Street. The first three blocks from State Street to LaSalle Street shown in Figure 1 were completed in 2015 and the last three blocks from LaSalle Street to Lake Street shown in Figure 2 will be completed in 2016. Funding was provided through a \$99 million Transportation Infrastructure Finance Innovation Act (TIFIA) loan.

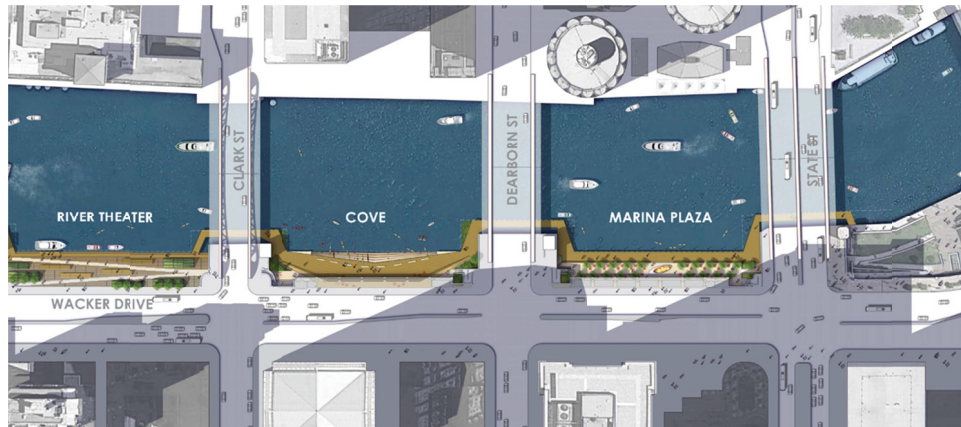


Figure 1 – Map of Marina Plaza, Cove, and River Theater from State Street to LaSalle Street



Figure 2 – Map of Water Plaza, Jetty, and Boardwalk from LaSalle Street to Lake Street

PROJECT GOALS

The goal of the project was to provide an area for Chicago's residents, workers, and visitors to connect with nature in the heart of the city, which led to a wide-ranging theme of sustainability throughout all aspects of the design. Four groups of objectives

were identified to achieve this goal: economic, cultural, recreational, and ecological.

The economic objectives were focused on the ability of the Riverwalk to generate revenue for initial construction and long-term maintenance costs. Leasable space for vendors was incorporated in the design beneath the overhang from the Wacker Drive Viaduct. The height of the dock wall in certain locations was also selected to provide commercial tour boat operators with direct access.

The cultural objectives were intended to bring people together. The Riverwalk provides unique gathering spaces for people to enjoy the river and the history of the site, thereby enhancing community life in the area. Certain rooms such as the Boardwalk and the River Theater provide plenty of ideal space and seating to come together for events on land or water.

The recreational objectives were focused on giving users different ways to enjoy the river. Restaurants and bars in the Marina Plaza and Cove provide a beautiful spot to dine or grab a drink. Kayak rentals offer the opportunity for users to exercise and experience the city from a new perspective. Fishing piers in the Jetty allow people to interact with nature in a hands-on way that is often very difficult in an urban environment. Areas of the Jetty are also intended for teaching, where students can visit the river and learn about the environment. These activities will help foster a continued awareness of the river as an important natural resource.

The ecological objectives were intended to improve the health of the ecosystem and minimize the detrimental aspects of construction. Numerous plantings and trees were added to enrich and diversify the vegetation. Aquatic habitats were attached to the face or underside of the structural elements. Floating gardens were used in the Jetty with native wetland plants. Even a large cistern was placed underneath the River Theater to capture rainwater and reuse it for irrigation.

The project will have a very positive effect on the sustainability of the city and would not be realized without an extensive geotechnical and structural design effort. Due to the sensitivity of the river ecosystem, every design decision required careful consideration of the potential impacts. These considerations were just as important as providing a safe and economical structure.

ROOM DESIGN

Each room between bascule bridges extends the existing walkway 25 ft. into the Chicago River and is approximately 300 ft. long, except for the Boardwalk between Franklin Street and Lake Street that is roughly 50 ft. wide and 600 ft. long. The existing dock wall shown in Figure 3 consists of two rows of round timber piles at 2'-6" spacing along the front row and 5'-0" spacing along the back row. Timber tongue and groove sheeting was used between the two rows of piles to retain the fill. The wall was tied back by concrete encased tie rods that extended back to the drilled shafts supporting the adjacent viaduct. The maximum retained height was approximately 28 ft. based on the permitted dredging elevation in the river. An 8ft. tall concrete cap extended down into the river from the walking surface.

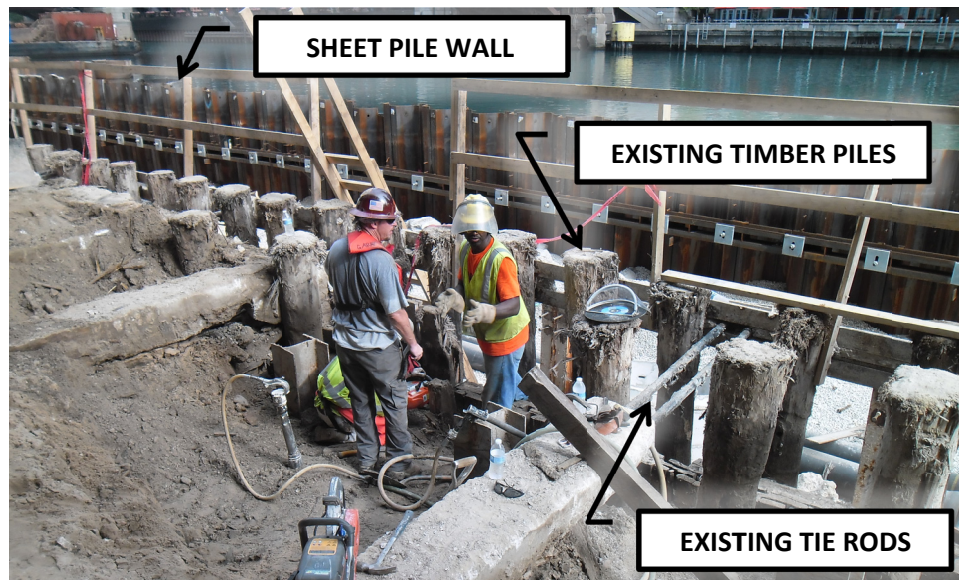


Figure 3 – Existing Dock Wall after Removal of Concrete Cap

The structural systems in the four rooms at the east end of the project are very similar. Numerous alternatives ranging from pile-supported piers to floating docks were considered, but a conventional tied back sheet pile wall was desired for its proven track record and low maintenance costs. However, due to the limited width of the build-out, a new deadman system was not considered practical or cost effective. Instead, the new system is tied back to the location of the existing wall, where a concrete anchor block is cast over the wale and timber piles to connect the new and existing tie rods as shown in Figure 4. By incorporating the existing system in the final design, the amount of new materials required and the carbon footprint were significantly reduced. The new tie rods were spaced at approximately 10 ft. and galvanized for corrosion protection.

Earlier construction of the Riverwalk from Michigan Avenue to State Street revealed that the tie rods were in excellent condition with minimal corrosion when the concrete encasement was removed. While there were not many concerns with the condition of the existing tie rod system, consideration was still given to the redundancy of the system. In the event of an existing tie rod failure, the concrete anchor block and structural slab were designed and detailed with enough strength to redistribute the load to the adjacent tie rods. The structural slab is also able to transfer loads out to the peninsulas at each end of the rooms where additional lateral resistance can be developed.

The riverbed consisted of a thick layer of river muck underlain by soft clays. Due to environmental concerns and the potential cost for transporting and disposing of this material, excavation in the river was not performed in the typical rooms. However, the inclusion of the river muck layer greatly increased the lateral loads on the system. The material had negligible internal stability and vertical surcharge loads were transferred directly to the wall as a lateral load (*i.e.* an earth pressure coefficient of one).

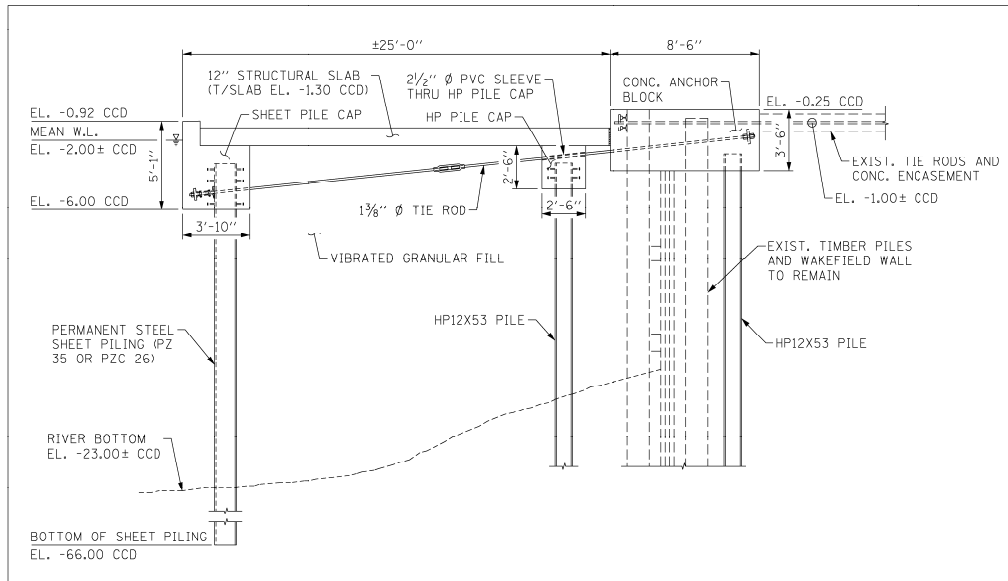


Figure 4 – Section through Structural System in the Marina Plaza, Cove, River Theater, and Water Plaza

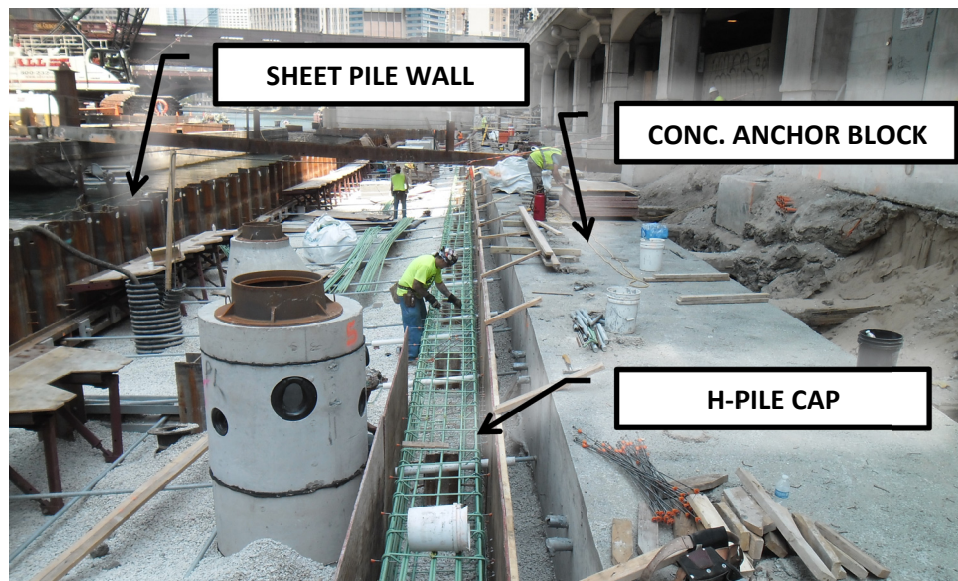


Figure 5 – Construction of Slab Support Beam with H-Piles in the Cove

The river muck and soft clays also had estimated settlements up to a few feet. Remediation methods were considered, but eventually it was decided to support a structural slab on the sheet pile wall and an additional row of H-piles at approximately 10 ft. spacing near the existing dock wall as shown in Figure 5. All drainage components also had to be structurally supported. Drainage structures were installed over precast caps that socketed over H-piles. Depending on the size and depth, pipes were either hung from the structural slab or supported on steel saddles on H-piles.

The Jetty used a unique structural system. The area was designed as a series of piers that project into the river. Since these piers could be susceptible to collisions, the U.S. Coast Guard (USCG) required that the system resist the same design loads as the underbridges described in the following section. These loads, combined with the desire for floating gardens between piers and aquatic habitat on the underside of the structure, led to the use of drilled shafts with a concrete cap. A total of nineteen shafts with a diameter of 5 ft. were used. The drilled shaft cap is 4 ft. thick similar to the underbridges. Since the condition of the timber piles and sheeting in the existing dock wall was questionable, sheet piling was placed to retain the fill as shown in Figure 6. The top of the sheeting bears on the drilled shaft cap, which is tied into the existing tie rods similar to the other rooms. Additional redundancy in this room is provided by the lateral capacity of the drilled shafts.

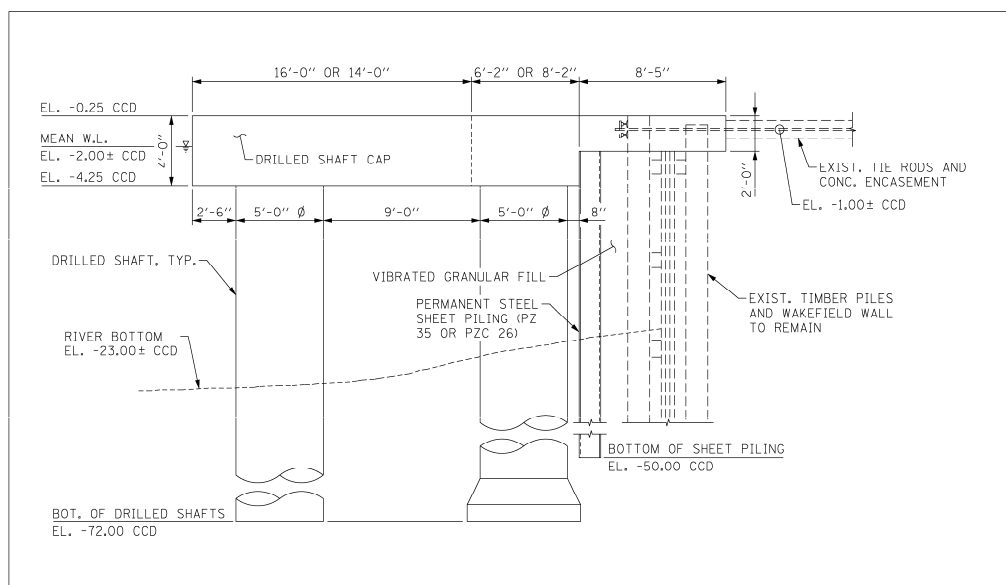


Figure 6 – Section through Structural System in the Jetty

The Boardwalk was put into the Contract as a performance-based specification. The increased width allowed various systems to be used and it was left to the Contractor to determine the most cost effective solution.

UNDERBRIDGE DESIGN

The canopied walkways beneath the bascule bridges are 10 ft. wide and vary in length up to 170 ft. Each structure consists of a 4 ft. deep concrete cap on four drilled shafts ranging from 6 ft. to 8 ft. in diameter as shown in Figure 7. To allow water to flow behind the underbridges and give users a feeling of being closer to nature, steel grating bridges span from the underbridges to the adjacent rooms at each end.

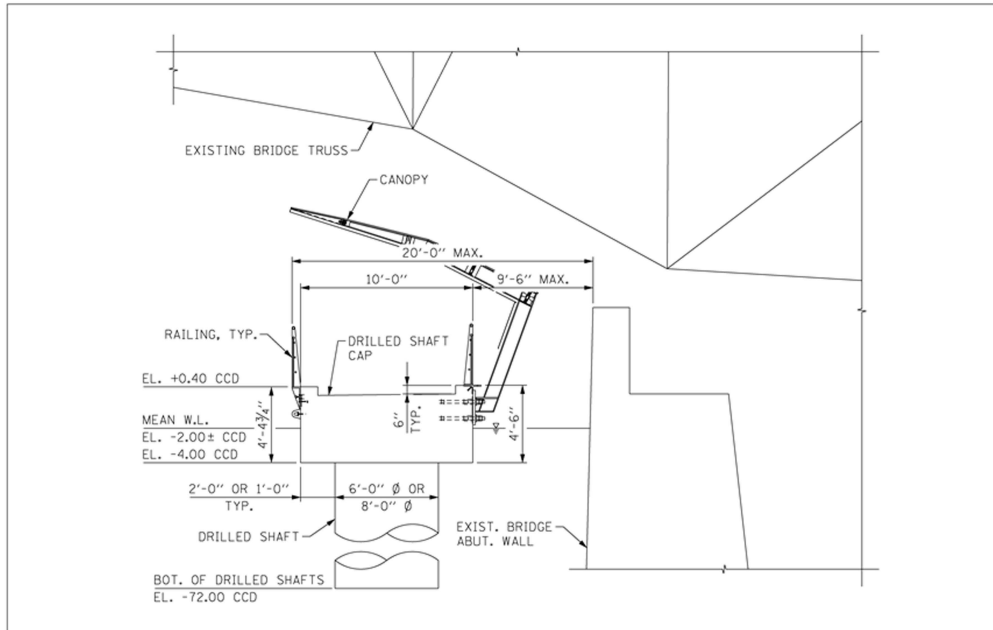


Figure 7 – Section through Structural System used for the Underbridges



Figure 8 – Permanent Casing Installation for the Dearborn Street Underbridge

The two interior shafts at each underbridge are located beneath the bascule bridges and required bridge lifts for installation as shown in Figure 8. Test lifts were

performed during the design phase of the project to determine the maximum opening angle that could be achieved. Existing plans were then used to develop clearance diagrams to aid the Contractor during the bid phase. Temporary closures of approximately one week were used at each street for installation.

Since the underbridges are located at the edge of the navigational channel, detailed analyses for barge collisions were required. The collision loads applied to the underbridge structures were developed in accordance with the AASHTO Guide Specification and Commentary for Vessel Collision Design of Highway Bridges using design vessel criteria set by the USCG. The first design vessel was based on the largest tow that passes the site, the Spartan II barge and tug, at an impact speed of 1.75 mph. The second design vessel was a conventional deck barge and tug at an impact speed of 3.50 mph. Information was also collected from various tour boat operators in the area to verify that the potential impact forces from their boats would not control the design. A summary of the final design forces is shown in Table 1 below.

Table 1 – Design Vessel Collision Load Summary

Design Barge	Total Displacement (tonnes)	Vessel Impact Speed (mph)	Collision Force Parallel to Channel (lbs.)	Collision Force Perpendicular to Channel (lbs.)
Spartan II	11,621	1.75	1,623,000	811,500
Typical Deck	1,901	3.50	1,515,000	757,500

The underbridges were assessed using two separate finite element programs. LUSAS software was used to model the full system and assess overall behavior. LPile software was used to analyze the drilled shafts and capture the nonlinear response of the soil and concrete shafts. LPile was also used to calibrate the support conditions in LUSAS to make sure the two programs were in agreement.

The underbridges were designed to withstand the vessel collision loads without any hinging of the drilled shafts; however, hinging would allow the structure to undergo greater deflections and absorb more energy from a larger or faster vessel. Instability would only occur if two hinges formed per shaft and the load was sustained.

Gravity loads were superimposed with the design vessel collision forces. Pedestrian live load was applied in a patterned fashion in order to capture the maximum force effects. The concrete self-weight loads also had to consider the means and methods of construction.

There were two distinct construction methods that were permitted for the drilled shaft caps. The first method of construction was a “bathtub” approach where an integral precast concrete form would be delivered in three segments via barge as shown in Figure 9 and installed over the top of the drilled shafts. The remainder of the concrete would then be placed into the precast form to complete the underbridge. The objective of this method was to facilitate construction and minimize the disturbance in the river by eliminating the need for underwater formwork. Since there

is no falsework to be removed and the joints between precast segments are located over the interior shafts, this method would not lock in any negative moment over the shafts due to concrete self-weight and would result in an increased positive moment at midspan as shown in Figure 10.

The second method was to construct falsework for the entire shaft cap as an independent system. The falsework would support the entire load of the wet concrete. Upon removal of the falsework, the drilled shaft cap would support the concrete self-weight in a continuous manner as shown in Figure 11.

The drilled shafts and the drilled shaft cap were designed to be adequate regardless of the method of construction selected by the Contractor. Ultimately, the Contractor selected the bathtub approach.

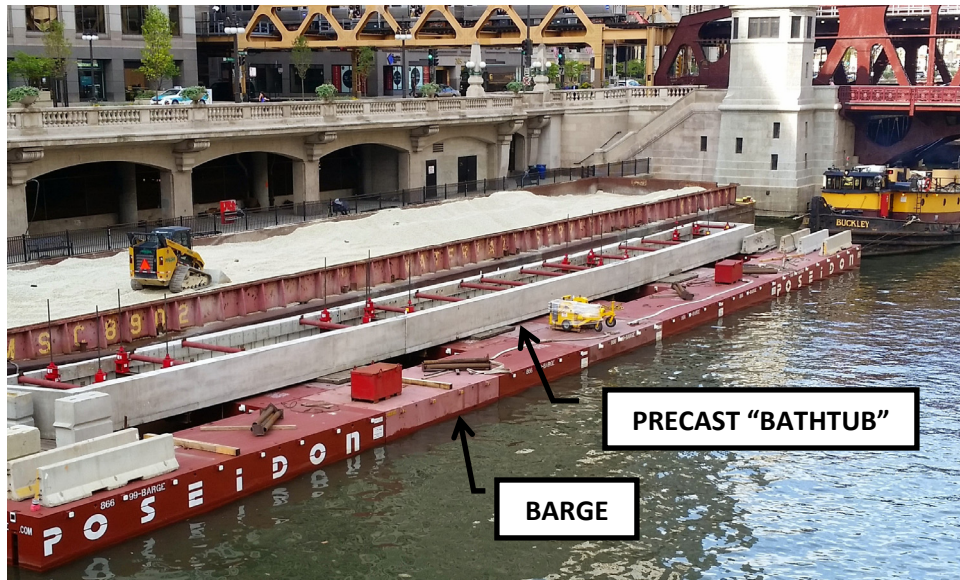


Figure 9 – Precast Bathtub Delivery for Underbridge Construction

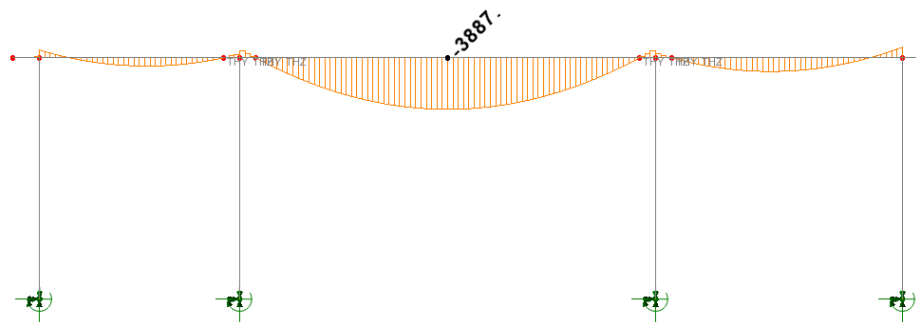


Figure 10 – Bending Moment Diagrams (k-ft) for Precast Bathtub Method of Underbridge Drilled Shaft Cap Construction

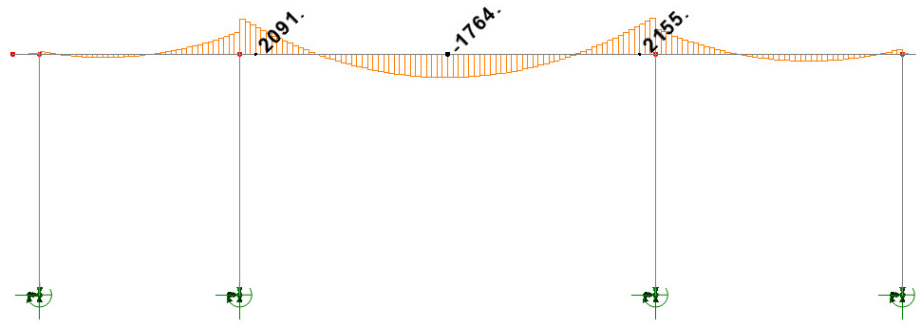


Figure 11 – Bending Moment Diagrams (k-ft) for Shored Method of Underbridge Drilled Shaft Cap Construction

CONSTRUCTION

During construction, a considerable amount of coordination was required with city, state, and federal agencies as well as private businesses and utilities along the river. Each room presented a unique set of construction challenges. Minimizing the impact to the environment was especially important. Excavation in the river was limited to the drilled shafts and all work was performed behind a turbidity curtain.

Extensive existing infrastructure such as utilities, freight and subway tunnels, sewer outfalls, and chiller pipes from nearby buildings required careful installation of numerous deep foundations. The freight and subway tunnels typically run in a north-south direction under the existing bridges and were constructed in the early 1900s. Although bulkheads were once installed to prevent flooding if damage occurred, the tunnels still carry active utilities. The layout of the drilled shafts at each underbridge was often driven by this constraint and the Contractor was required to probe the locations of the tunnels prior to any casing installation or drilling operations. The Contractor was also required to monitor the existing tunnels during construction.

CONCLUSIONS

As Chicago's "second shoreline", the Riverwalk will provide a sustainable public space in the heart of Chicago for generations to come. The project shows how geotechnical and structural engineering can be instrumental in bringing sustainable development to a complex urban environment.

REFERENCES

- AASHTO (American Association of State Highway and Transportation Officials). (2009). Guide Specifications and Commentary for Vessel Collision Design of Highway Bridges, 2nd Edition, with 2010 Interim Revisions. AASHTO, Washington, D.C.

Financial Sustainability as a Metric for Infrastructure Projects

Ranjiv Gupta, Ph.D., P.E., M.ASCE¹; Jeremy W. F. Morris, Ph.D., P.E.²;
and R. David Espinoza, Ph.D., P.E., M.ASCE³

¹Project Engineer, Geosyntec Consultants, Phoenix, AZ. E-mail: rgupta@geosyntec.com

²Senior Consultant, Geosyntec CAT Advisory, Washington, DC. E-mail: jmorris@geosyntec-cat.com

³Senior Principal, Geosyntec CAT Advisory, Washington, DC. E-mail: despinoza@geosyntec-cat.com

Abstract: Various sustainability rating systems have been developed to provide an objective framework for assessing infrastructure projects. Examples include civil engineering environmental quality assessment and award scheme (CEEQUAL), Greenroads™, Envision™, infrastructure voluntary evaluation sustainability tool (INVEST), and infrastructure sustainability (IS). These rating systems aim to help the construction industry identify and quantify sustainable approaches that are beneficial to infrastructure projects. Most of these infrastructure rating systems have their origins in the rating systems developed for evaluating commercial buildings, such as building research establishment environmental assessment methodology (BREEAM), leadership in energy and environmental design (LEED), green globes, and Energy Star®, which poses a few challenges when these types of tools are applied to broader infrastructure projects. Of most significance is the lack of a financial sustainability metric within the tools. This is understandable: buildings generally have a well-defined and relatively short service life for revenue generation, clear redevelopment options to perpetuate the real property value, and few long-term liabilities or legacy issues (e.g., pollution potential). However, other infrastructure projects have much longer service lives and are even expected to remain viable over an indefinite post-service period long after revenue generation has ended. This paper presents a review of sustainability metrics used by various infrastructure rating systems and compare their advantages and disadvantages. Thereafter, the paper discusses the need to engage and encourage decision makers to invest in more sustainable approaches for developing large infrastructure projects with very long term service and post-service lives by including a financial metric to existing rating systems. Finally the paper discusses a few financing options which could help the construction industry transition to more sustainable design approaches while simultaneously protecting their return on investment.

INTRODUCTION

An early and widely accepted definition from the Burtland Report (1987) defines sustainable development as one that meets the needs of the present without compromising the ability of future generation to meet their own needs. According to Basu et al. (2015): “*Sustainability of a system is its ability to survive and retain its functionality over time. In very simple terms sustainability deals with the supplies (capacities) and demands (loads) in a system, and as long as the supply is greater than the demand, the system is sustainable. Time is an inherent aspect of sustainability, and questions related to sustainability must be addressed by considering supplies and demands that change over time*”. The three main parameters which need to be considered during sustainable infrastructure development are economic growth, competitiveness, and social well-being (WEF, 2014), as shown in Figure 1. In general, the main objective of a responsible and sustainable infrastructure development strategy should be to minimize lifecycle depletion of energy, material resources, and financial resources. While significant attention has been paid to environmental protection and material conservation, the financial aspects of sustainable development are not well understood or quantified, leading to a situation where costs for long-term property management and monitoring are passed onto future generations.



FIG. 1. Parameters for Sustainable Development

There is a growing consensus that delivering a sustainable built environment starts with incorporating sustainability thoughts at the planning and design stages of an infrastructure construction project (Basu et al., 2015). Our ability to implement sustainable practices diminishes as the project progresses through the planning, design, construction, operations, decommissioning/closure, and post-closure phases (Figure 2). Civil engineers have an opportunity to implement social, environmental, and financial sustainable practices in infrastructure development due to their involvement in the initial stages of a project and their ability to evaluate projects in a holistic manner, thereby contributing to improving the triple bottom line (i.e., people, planet and profit).

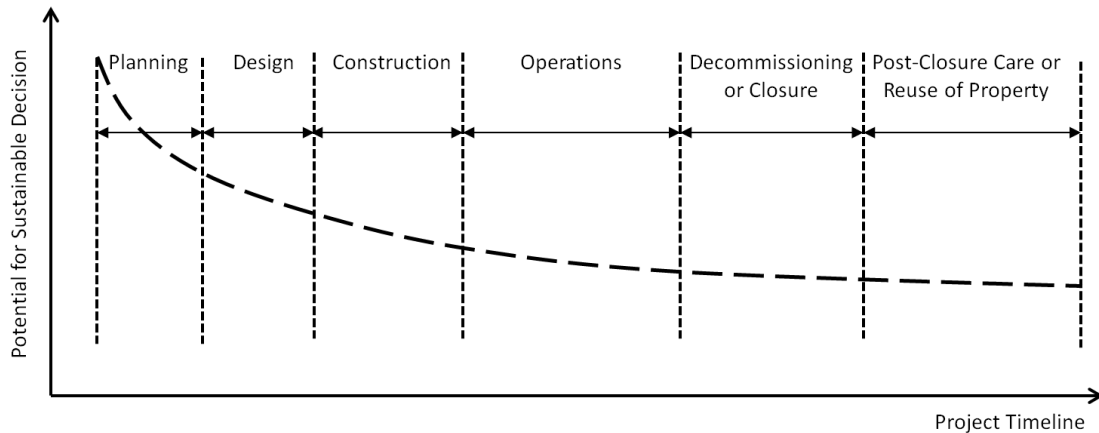


FIG. 2. Potential for making a sustainability related decision during an infrastructure project life-cycle (modified Figure 7 from Basu et al., 2015)

Some of the methods and solutions that should be implemented during planning and development of an infrastructure project include: (1) optimizing designs to utilize energy efficient equipment and processes; (2) incorporating full lifecycle costs in design decisions; (3) employing remote data collection and real time data evaluation reporting; (4) tailoring technical specifications to utilize local materials or reuse site materials; (5) applying sustainable decision criteria for potential remediation requirements or future site closure options; (6) utilizing recycled materials and wastes for energy and production of alternative fuels; (7) performing climate variability assessments to develop design criteria; and (8) maximizing electronic communication to minimize waste generation. Thus, sustainability concepts could be incorporated in infrastructure project by developing an understanding of the sustainability framework to properly quantify the financial and environmental benefits through various stages of the project.

SUSTAINABILITY RATING SYSTEMS

Sustainability rating systems (SRS) provide a framework for assessment, planning, design, operations, maintenance, and monitoring of projects that serves to rapidly assess numerous design alternatives within context of sustainability. Benefits of using a publicly available SRS include enhancement of the design process, increased accountability, reduction of risk, competitive advantage, increased profitability, and improved quality of life and project recognition. Several SRS are available within the U.S. and worldwide, with applicability ranging from general civil engineering works to specific project categories such as buildings, highways and transportation, landscaping, water and wastewater, gas pipelines, electricity transmission and distribution, and communication networks.

The salient features of five common infrastructure SRS are presented in Table 1. These are Civil Engineering Environmental Quality Assessment and Award Scheme (CEEQUAL), Greenroads, Envision, Infrastructure Voluntary Evaluation

Sustainability Tool (INVEST), Infrastructure Sustainability (IS), all of which were developed in the late 2000s. The Greenroads, Envision, and INVEST are national SRS, whereas CEEQUAL and IS are international SRS.

Table 1: Features of Sustainability Rating Systems Applicable to Infrastructure Projects

System Criteria	CEEQUAL and CEEQUAL International	Greenroads	Envision	INVEST	Infrastructure Sustainability (IS)
Year Established	2004	2010	2012	2012	2012
Governing Body	Construction Industry Research and Information Association (CIRIA) and Crane Environmental	Greenroads International	Institute of Sustainable Infrastructure (ISI)	Federal Highway Administration (FHWA)	Infrastructure Sustainability Council of Australia (ISCA)
Geography	Started in UK and available for rest of the World	U.S.	U.S.	U.S.	Australia and New Zealand
Applicable	Civil Engineering, Infrastructure, Landscaping Public Projects and Contracts	Highways and Transportation Projects	Any Infrastructure Project	Highways and Transportation Project	Transportation, Water-Sewerage and Drainage, Energy-Electricity Transmission and Distribution, Gas pipelines, Communication - Networks
Project Phase	Planning, Design and Construction	Planning, Design, Construction, Operations and Maintenance	Planning and Design, Construction, Operations and Maintenance, Deconstruction and Decommission	System Planning Project Development, Design and Construction, Operations and Maintenance	Design, Construction and Operations
Rating	Pass, Good, Very Good, Excellent	Bronze, Silver, Gold, Evergreen	Bronze, Silver, Gold, Platinum	Bronze, Silver, Gold, Platinum	Commended, Excellent, Leading

The assessment process adopted by infrastructure rating systems have their origins in SRS such as Building Research Establishment Environmental Assessment Methodology (BREEAM) and Leadership in Energy and Environmental Design (LEED) that were developed to assess building construction in the 1990s and involve comparing the performance of a project against multiple weighted criteria in order to earn credits (Poveda and Lipsett, 2011). Detailed examination of individual performance criteria and credits is beyond the scope of this paper; however, it is noted that the variability in weighting between each SRS makes it difficult to assess a project consistently across local, national, and international markets (Reed and Bilos, 2013). In practical terms, any review of infrastructure sustainability must include goals for project decommissioning and closure, post-closure care or long-term maintenance (LTM), and reuse of the property because realizing these sustainability objectives requires the owners and operators to focus on proactively reducing environmental and financial liabilities by optimizing design, construction, and management during the operational life of the project (Morris, 2012). As shown in Table 1, all five SRS capture planning, design, construction, and maintenance phases of a project but only one – Envision – includes a deconstruction and decommissioning phase. None of the SRS include considerations for costs incurred during the post-service life, such as LTM and reuse of the property, or assign an economic value to risk reduction achieved by implementing sustainability practices and measures early in the project.

The lack of financial metrics to account for the sustainability of infrastructure projects was inconsequential when such investments were entirely publicly funded. As projects become increasingly funded by the private sector through public/private partnerships (P3s), the need for financial sustainable metrics become more apparent. Absent such considerations, investors may opt for cheaper capital expenditures (CAPEX) in exchange of higher long-term operating expenditures (OPEX). As a result, the initial higher costs required to implement sustainability practices may negatively impact the short-term return on investment (ROI) thereby discouraging decision makers from adopting such methods. Thus, a financial metric that captures the effect of sustainable practices on long-term ROI is required to properly make a go/no-go decision on projects and help prevent investors from penalizing projects which have taken proactive steps to reduce long-term liabilities. Unfortunately, the most common investment valuation tool in use, the net present value (NPV) method, cannot fairly account for such risk reduction measures because the effects of substantial positive impacts to future cash flows are rendered largely irrelevant by discounting.

FINANCIAL EVALUATION OF INFRASTRUCTURE PROJECTS

The NPV method was initially developed to value future cash flows of relatively simple financial instruments, such as treasury and corporate bonds, and only later transferred to value real investment opportunities. The mechanics of calculating the NPV of infrastructure projects is relatively straight forward and typically consists of: (i) estimating the expected project life (e.g., concession period, patent protection period, natural resource availability) (ii) calculating the project

expected annual revenues (V_t) as well as the expected expenses/liabilities (I_t) during the life of the project; (iii) calculating the annual net cash flow ($V_t - I_t$); (iv) selecting a risk-adjusted discount rate, RADR (α) that accounts for the project risk; and (v) calculating the project annual discounted net cash flows as $(V_t - I_t) \times (1 + \alpha)^{-t}$ where $(1 + \alpha)^{-t}$ is the discount factor (DF) and (vi) calculate the project NPV by adding all the annual discounted net cash flows. Projects with positive NPV are considered to have a ROI greater than α whereas projects with negative NPV are generally considered have a ROI lower than α .

Although the NPV method is easy to implement and communicate to decision makers, it fails to capture the value of future cash flows (either positive or negative). Hence, project valuations based on NPV fail to identify the benefits of sustainable decisions that require an upfront capital investment to achieve a long-term reduction in liabilities. In the NPV method, all risks associated with a project are lumped into a single parameter (i.e., the risk premium) that is added to the risk-free interest rate to obtain a RADR (α), that is, the time value of money (represented by the risk free rate) is adjusted to account for risk. However, when dealing with uncertainty, the NPV method may yield results that are not compatible with investor's perception of risk particularly when dealing with negative cash flows (Espinoza and Morris, 2013). For risk-averse investors, risk should always reduce the value of an investment. To capture this sentiment accurately, risk should reduce the value of positive cash flows (i.e., revenues) and have the opposite effect on negative cash flows (i.e., expenditures). The use of a single parameter (the discount factor) to represent the project risk cannot capture this simple fact as any increases in the discount rate to account for revenue risk results in artificial reductions of expenditures. In addition, the discount factor is very sensitive to the selection of the RADR. This feature does not bode well to sustainable decision-making given the rather arbitrary, heuristic nature of RADR selection. The discount factors for 60 years assuming a RADR of 12% (not an unusually high discount rate assumed in practice) are illustrated in Figure 3. As shown in this figure, the value of long-term liabilities on the NPV of a project after 60 years may only be 0.1%. Thus, it follows that the benefits of reducing long-term liabilities by incurring upfront costs for implementing sustainable measures would not be realized by an investor using this valuation technique. Years of continued reliance of NPV techniques in valuation of infrastructure projects have resulted in a myopic investment mindset within corporations and government entities, which has led decision makers to select projects that payoff quickly over those that would be more sustainable and increase long-term stakeholders' value (Lundstrum, 2002; Antia et al., 2010; World Economic Forum, 2011).

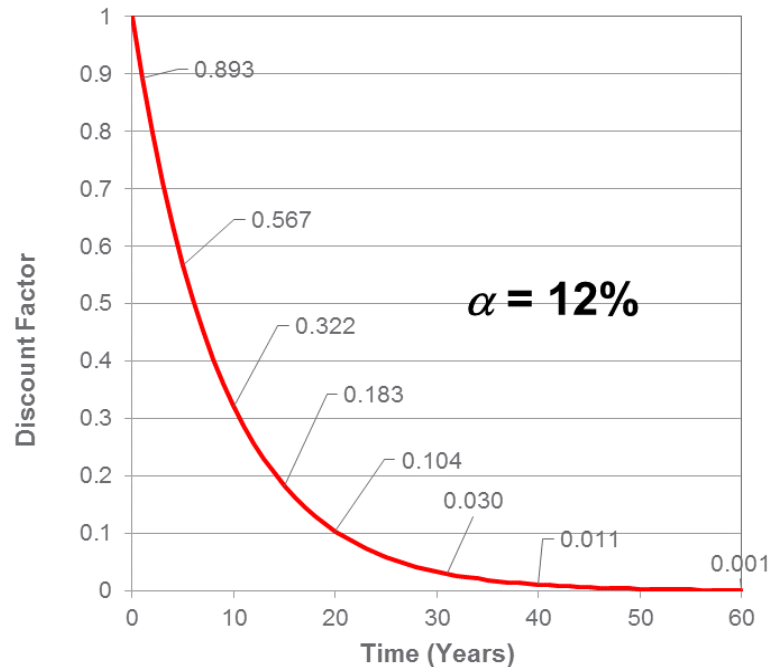


FIG. 3. Influence of Discount factor on NPV of a project

SUSTAINABLE INFRASTRUCTURE INVESTING

Infrastructure investments have typically long-term horizons such that the useful (operational) life of the project created can last several generations. Moreover, the project infrastructure may require care for a long period of time after its useful life. For example, a mechanically stabilized earth (MSE) berm designed to increase landfill disposal capacity must continue to perform for as long as waste is contained at the site, even after the waste filling operation (revenue generation) has ceased. As discussed above, in the past, infrastructure investments were typically made using public funds. As result, society's long-term perspective was only at odds with the short term needs of public officials who may favor projects that would score them more political points in the short-term at the expense of society's long-term well-being. As more infrastructure projects were funded by the private sector through P3s, society also has to reconcile the short-term horizons of equity investors and shareholders. In order to account for financial sustainability, infrastructure projects cannot be evaluated only from the shareholders', investors', even politicians' perspective as their investment horizons are relatively short. For most infrastructure projects, society's longer horizons should be the driving consideration.

Attaining financial sustainability implies that VLT funding requirements have been accurately predicted and appropriate accrual mechanisms have been implemented to ensure that enough funds are available for closure and/or decommissioning along with post-closure OPEX. Understanding how the design and project financials are related is paramount for the selection of the appropriate sustainable design measures.

DECOUPLED NET PRESENT VALUE AS A FINANCIAL SUSTAINABILITY METRIC

The previously described problems with the use of NPV as a tool to account for both the time value of money and as a proxy for risk aversion, particularly when valuing projects with investments made over a period of time (which is the case for most projects), can be avoided if both the uncertainty associated with future cash flows and the investments are decoupled from the discount rate. To better quantify the value of future cash flows and, hence, better assess the effect of sustainability measures, project valuation should be performed using a model that decouples risk from the time value of money. Such a valuation model, the decoupled net present value (DNPV) method, was introduced by Espinoza and Morris (2013). The separation of risk from the time value of money facilitates evaluation of the effects of each source of technical risk (e.g., storm, earthquake) and market risk at different times. Each identified risk is considered as a separate cost to the project and it is conceptually equivalent to the price of a self-insurance policy against that risk. Using this technique allows financial and management mechanisms to be developed that discreetly incorporate both technical and market risks and leads to a more complete evaluation of project sustainability. The expected revenues (V_t) and expected liabilities or expenses (I_t) are similar to the NPV method. Risk is characterized by synthetic insurance premiums that an investor is willing to pay for fixed cost of liabilities (R_l) and guaranteed revenue (R_v). The costs of these premiums are subtracted from the net cash flows to render riskless cash net cash flows. Thus, future cash flows can be discounted only to account for the time value of money.

Because each risk has been accounted for as a cost to the project, future cash flows can be discounted to account the time value of money using the risk-free rate (r_f), thus eliminating the need to arbitrarily select a discount rate as is the case with NPV analysis. Figure 4 shows the expressions for valuation using both methods and also provides a schematic comparison of both approaches.

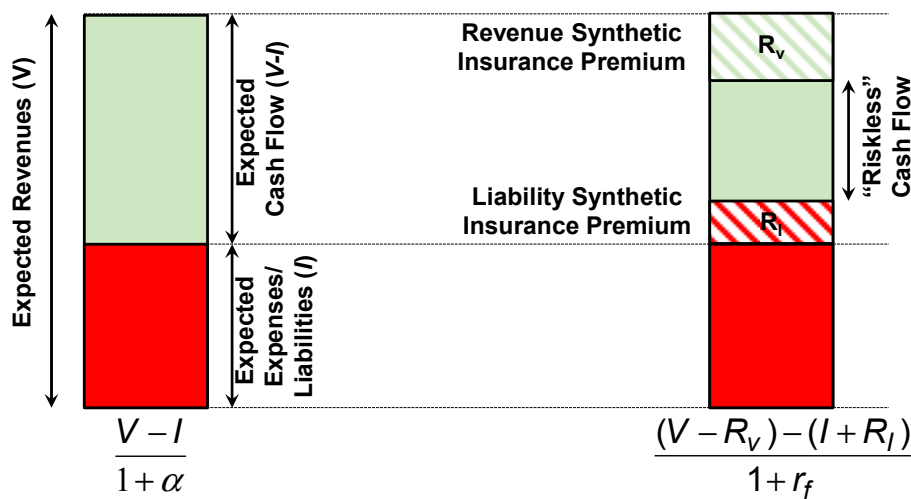


FIG. 4. Framework for financial sustainable modeling using NPV (left) and DNPV (right)

Depending on the source of each risk and the availability of data to evaluate it, these costs could be estimated using: (1) probabilistic/stochastic methods based on probability density functions (PDFs) constructed from available empirical data; (2) subjective industry-specific information obtained from technical experts obtained in a structured and repeatable manner; and/or (3) option pricing techniques developed in the financial industry to estimate the risk of traded commodities (Espinoza, 2014). The cost of risk can then be integrated under the DNPV framework. By identifying individual components of risk, data can be compiled in a repository database in a manner more conducive to analysis (e.g., repair costs per linear foot of roadway embankment for a given factor of safety). This can later serve to improve estimates of the cost of similar risks. This ability to iteratively “learn” from past applications is a key strength of the DNPV method. DNPV analysis can help to properly allocate risk in a contractual setting, can be fully integrated with the concept of a risk register, and results are relatively easy to convey to decision makers. These features far outweigh the drawback of the added complexity in the calculation.

CONCLUSIONS

The SRS for infrastructure projects aim at helping the construction industry identify and receive credit for sustainable approaches to project development. While the SRS capture the planning, design, and operational life of infrastructure projects, they do not fully account for decommissioning or LTM, which is where the benefits and economic risk reductions achieved by adopting sustainable practices early in the project may be best realized. The SRS also lack a financial metric by which to capture these economic risk reductions. Without such a metric, the initial higher costs incurred by implementing measures to improve project sustainability may discourage decision makers from adopting such measures. To better quantify technical and financial risks in allocating costs for sustainability assessment of infrastructure projects without unduly affecting either revenues or liabilities that are far in the future, the DNPV methodology is recommended as a far more robust alternative to NPV. The challenges of estimating future cash flows using NPV analysis are primarily associated with the integration of the time value of money and risk in a single parameter: the discount rate. Traditionally, decision makers have tried to overcome this shortcoming through “thoughtful and reasoned” selection of the discount rate. However, the complexity of cash flow associated with infrastructure projects makes this a futile exercise. DNPV analysis separates risk from the time value of money, facilitating evaluation of the effects of each source of technical risk and market risk at different times and preventing the artificial reduction of long-dated cash flows. Users of existing SRS would benefit from the addition of a financial sustainability metric constructed around a valuation technique such as DNPV, as this would allow objective review of the long-term liability costs (e.g., closure, decommissioning, or LTM) associated with different project development scenarios, and give economic value to risk reduction measures that improve project sustainability.

REFERENCES

- Antia, M., Pantzalis, C., and Park, J.C., (2010), “CEO Decision Horizon and Firm Performance: An Empirical Investigation”, *Journal of Corporate Finance*, 16, 288-301.
- Basu, D., Misra, A., and Puppala, A. J., (2015), “Sustainability and Geotechnical Engineering – Perspectives and Review”, *Canadian Geotechnical Journal*, 52, 96-113
- Burtland, G. H., (1987), “Our Common Future”, World Commission on Environment and Development, 1987, 300pp.
- Espinoza, R.D., and Morris, J.W.F., (2013), “Decoupled NPV: A simple, improved method to value infrastructure investments”, *Construction Management and Economics*, 31, 471-496
- Espinoza (2014), “Decoupling Time Value of Money and Risk: A Step toward the Integration of Risk Management and Quantification,” *International Journal of Project Management*, 32, 1056-1072
- Lundstrum, L., L., (2002), “Corporate Investment Myopia: A Horserace of the Theories”, *Journal of Corporate Finance*, 8, 353-371
- Morris, J.W.F. (2012), “End of life, post-closure care, and the sustainable landfill”, *MSW Management*, May 2012, 46-52
- Poveda, C. A. and Lipsett, M. G., (2011), “A Review of Sustainability Assessment and Sustainability/Environmental Rating Systems and Credit Weighting Tools”, *Journal of Sustainable Development*, 4, December 2011
- Reed, R., and Bilos, A.K., “An Examination of International Sustainability Rating Tool: An Update”, *Proc. 19th Pacific Rim Real Estate Society Conference, Melbourne, Australia, 13-16 January 2013*
- World Economic Forum (2011), “The Future of Long-Term Investing”, prepared in collaboration with Oliver Wyman, 87pp.
- World Economic Forum (2014), “Infrastructure Investment Policy Blueprint”, prepared in collaboration with Oliver Wyman, 43pp.

Groundwater Management for Sustainable Underground Subway Development in Manhattan, New York City

Chu E. Ho, Sc.D., P.E., ENV SP, M.ASCE¹

¹Associate, Arup, 77 Water St., New York, NY 10005. E-mail: chu.ho@arup.com

Abstract: The construction of underground subway facilities will introduce a barrier to the natural groundwater flow due to the presence of permanent structures buried in the ground. This will create a damming effect and cause a rise in the groundwater level in the vicinity of the subway structures. This paper presents an equilibration system that was adopted for the second avenue subway project in Manhattan, New York City to deal with the groundwater accumulation problem. The equilibration system consisted of a network of pipes and manholes that collects water built up on the upstream side of an underground structure to be transferred across and discharged into the ground on the downstream side. The design of the equilibration system was based on the principle of hydraulic flow under a potential energy difference. The system was designed to be self-sustaining and maintenance free.

INTRODUCTION

The Second Avenue Subway Project in New York City is located on the east side of Manhattan Island, consisting of a total of 16 new stations and one renovated station, with 8.5 miles of tunnels extending from 125th Street in Harlem to Hanover Square in Lower Manhattan. The entire project will be constructed in four phases. Phase 1, currently under construction, extends the existing 63rd Street Station on the Lexington Avenue Line to 99th Street where the new construction would link up with an existing tunnel section constructed in the 1970s between 99th and 105th Street (Figure 1). Phase 1 consists of three new underground stations located at 72nd Street, 86th Street and 96th Street (Aksman et al. 2012). The 72nd Street and 86th Street Stations are mined caverns in rock, while the 96th Street Station is a cut-and-cover station in soft ground. Two tunnels, 22 feet (6.6m) in diameter, are excavated by tunnel boring machines (TBM) and will serve as the running tunnels (S1 and S2) between the stations. Two other tunnels (G3 and G4) will split off from the S1 and S2 tunnels respectively beyond 72nd Street Station to connect into the existing bell-mouth stub tunnel at 63rd Street Station. The 63rd Street Station will be retrofitted to accommodate the new facilities. Two turnout caverns (G3/S1 and G4/S2) are located

between 63rd Street and 69th Street, to allow for future extension of the S1 and S2 tunnels further southwards as part of Phase 3 of the project.

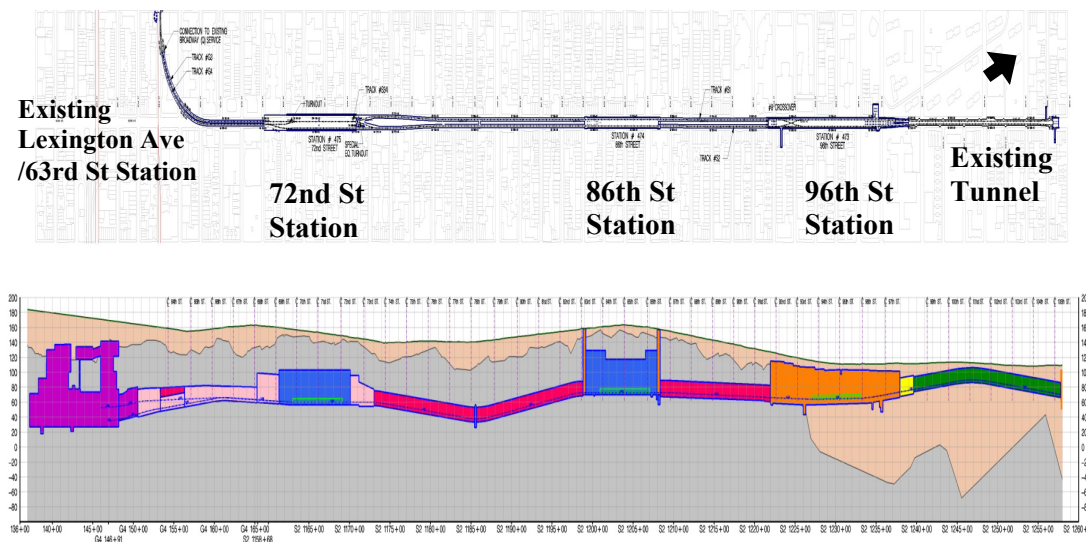


FIG.1 Second Avenue Subway Phase 1 development

The new subway alignment is flanked by buildings consisting mainly of 4 to 6 story brownstone structures with a single basement, with occasional more recent high-rise buildings, as well as some historic buildings and hospitals. A sustainable development of the new facility will require that minimal impact be introduced to the urban environment as a result of the permanent presence of the underground subway structures. This paper reviews the groundwater hydrogeology of the development site and presents the methodology for mitigating potential rise in the water table in the vicinity of the new underground subway facilities.

EXISTING GROUNDWATER CONDITIONS

The relief of Manhattan Island is such that the ground surface elevation is typically higher within the central core of the island and falls away in the direction of the Hudson River, East River and Harlem River along its western, eastern and northern boundaries respectively. The regional groundwater regime on Manhattan Island is controlled primarily by these three rivers. Along Second Avenue, which runs mainly in the north-south direction, the groundwater flow is predominantly from west to east, following the topography of the ground, which generally slopes towards the East River. However on the local scale, the groundwater regime is influenced by several factors, such as temporal and spatial variations in recharge rates; discharge from natural streams, storm water and leaking water pipes; infiltration into existing buried elements such as shafts, tunnels, basements and utility conduits; and variations in the transmissivity of the aquifer due to bedrock topography, man-made features, as well as soil and rock heterogeneity. These factors result in localized deviations from the

general trend of groundwater flow. The area north of 92nd Street is a complex aquifer of predominantly granular material (i.e. highly pervious fill, sand and sand/gravel with varying amounts of silt) seated directly over sound bedrock or decomposed rock (Figure 1). Over a large part of the area, this aquifer is subdivided by an aquiclude of organic silt or silty clay.

For the present Phase 1 development, the majority of the new construction is in rock (i.e. rock caverns for 72nd Street Station and 86th Street Station, with all associated tunneling work carried out in rock). Hence the interference with the natural groundwater flow is minimal over the majority of the subway alignment. Only at the location of 96th Street Station, where it is located within the aquifer, was there a likelihood of potential interference. An array of 8 observation wells and 14 vibrating wire piezometers were installed on the east and west sides of the proposed new construction to provide information on existing groundwater conditions. Observed groundwater levels ranged from approximately EL+97ft near 96th Street to EL+104ft between 94th and 95th Street. The water levels were generally located 8 to 15ft (2.4 to 4.5m) below the ground surface. Fluctuation of ground water levels was typically 2 to 6ft (0.6 to 1.8m) over a period of 4.5 years. The water level fluctuations were not typically seasonal due to the prevalence of impermeable surfaces limiting year round evapotranspiration. Water level fluctuations were more likely to be influenced by localized groundwater flow conditions.

Piezometers installed in borings did not indicate any significant tidal-induced water table fluctuations in the 96th Street Station area. This was possibly due to the large distance between the subway alignment and the East River more than 1000ft (300m) away. Based on the groundwater levels in observation wells along Second Avenue in relation to the mean water level in the East River, it was estimated that the overall groundwater flow across the subway alignment would be about 1ft in 1000ft (0.1m in 100m) in the easterly direction. The normal high water level (HWL) was expected to vary approximately linearly between EL+105ft at 92nd Street and EL+102ft at 95th Street, and to remain unchanged at EL+102ft north of 95th Street. It was determined that the normal low water level (LWL) would be at EL+97ft over the entire length of the station. Approximately half of the basements in the vicinity lie within 1feet below the normal high water line. Flood insurance maps published by the Federal Emergency Management Agency (FEMA, 1983) suggested that the 500-year flood level is at EL+109.4ft for the area under consideration, which was higher than most of the existing basement levels.

UNDERGROUND SUBWAY STRUCTURES

The new 96th Street Station and associated transition tunnel will stretch from 92nd to 99th Street, running along Second Avenue where it will connect into an existing tunnel in the north (Figure 2). The total footprint of the new station and transition tunnel is 1767ft (535m) long, and is constrained within the limits of the curb lines of the existing street approximately 60ft (18m) wide. The sidewalks on each side of the street separating the station walls and the adjacent buildings are approximately 20ft

(6m) wide. The length of the existing tunnel between 99th and 105th Street is 1815ft (550m).

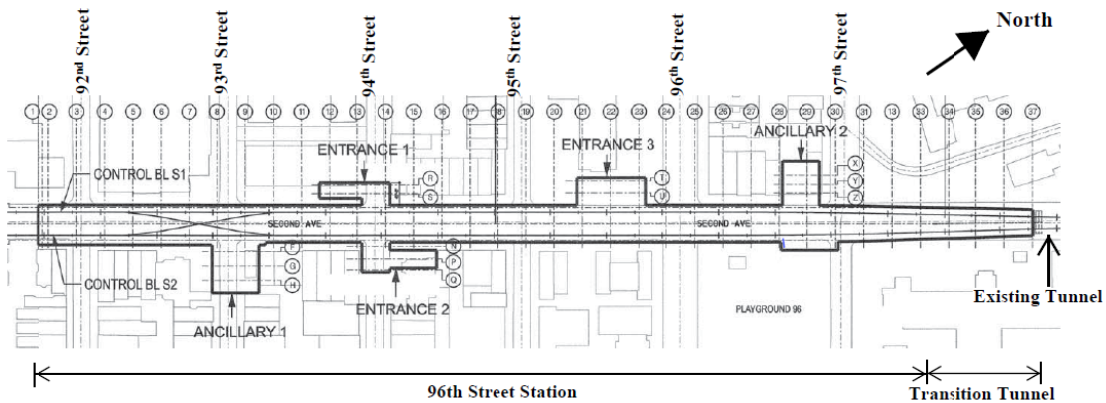


FIG.2 Plan of 96th Street Station and transition tunnel

Construction of the 96th Street Station and the transition tunnel was carried out mainly through fill, organics, silty sands and deep glacial deposits of varved silts and clays, except for the southern section where decomposed rock and high bedrock levels were encountered. The base of the station invert slab was located at about 55ft (16.7m) below ground on average. The facility was constructed using cut-and-cover technique with bottom up sequence (Grigson et al. 2016). Figure 3 shows the typical cross section of the support of excavation (SOE) schemes adopted. At the southern portion, up to about 93rd Street, the station box was constructed from within temporary braced secant pile walls in shallow rock. Beyond 93rd Street, the rock dips away rapidly to great depths below street level and the station box was constructed using permanent diaphragm walls typically installed up to 100ft (30m) deep (Ho and Hu 2014).

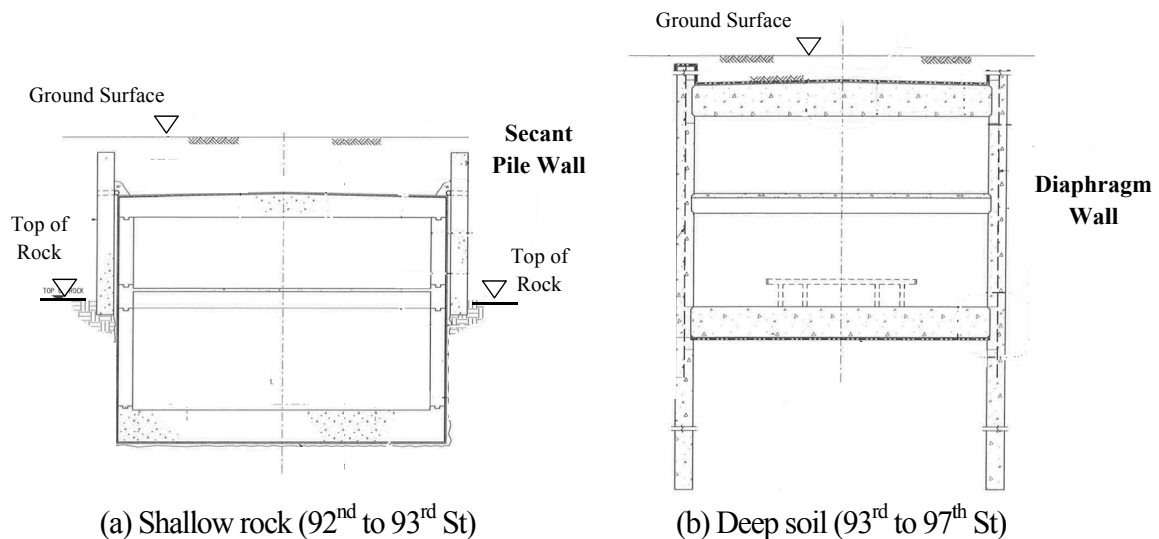


FIG.3 Station box in shallow rock and deep soil

The general elevation of the station roof ranged from EL+114.7ft to EL+101.7ft from south to north, except at two locations where the roof was depressed to approximately EL+97ft to allow the crossing of two 48 inches (1.2m) diameter sewer pipes running transverse to the station box (one at 95th Street and the other at 97th Street). The two depressed roof sections were 13ft (0.4m) wide and 4ft (1.2m) deep at 95th Street, and 8.5ft (2.6m) wide and 5ft (1.5m) deep at 97th Street. It was required in the contract that the top 5 to 6ft (1.5 to 1.8m) of the secant pile walls and diaphragm walls be demolished upon completion of the station construction and backfilled with granular soil to allow for installation of future utilities in the street.

GROUNDWATER CONTROL

Numerical Modeling of Groundwater Flow

A groundwater flow analysis was carried out to assess the impact of the new subway structure on the existing groundwater levels. Two dimensional finite element simulations of the groundwater seepage around the station structure was carried out using SEEP/W assuming a representative soil profile and water table at EL+102ft. Table 1 summarizes the flow parameters for the soil strata adopted in the analysis. The model flow boundaries were established at 500ft (150m) from the centerline of the station, with a bottom no-flow boundary assumed at the bedrock 168ft (51m) below ground. The natural groundwater flow was first modeled without the station box in place and the initial boundary conditions were adjusted to obtain a cross flow gradient of 1:1000, with the downstream head fixed at EL+101.5ft. A flow rate of 0.8 ft³/day (22.3 liters/day) was found to satisfy these conditions.

Table 1. Soil profile and flow parameters

Soil Type	Soil Thickness		Flow Characteristics	Horizontal Conductivity, k_H	Vertical Conductivity, k_v
	(ft)	(m)		(cm/s)	(cm/s)
Fill	16	4.8	Isotropic	1×10^{-3}	1×10^{-3}
Organics	10	3.0	Isotropic	4×10^{-5}	4×10^{-5}
Silty Sand	22	6.7	Isotropic	1×10^{-3}	1×10^{-3}
Varved Silt/Clay	120	36.4	Anisotropic	5×10^{-4}	5×10^{-5}

Using the boundary conditions established above, a subsequent model was set up with the station box in place (Figure 4). In the model, it was assumed that the groundwater will flow over the roof through the gaps in the slurry wall at the two depressed roof sections and also below the slurry walls, but not through the slurry walls. The backfill material in the depressed roof sections was specified as crushed stones (with a basic hydraulic conductivity of 10^{-2} cm/s). In modeling this material in the 2D space above the depressed roof, an equivalent hydraulic conductivity of 1.16×10^{-4} cm/s was assigned. This was based on the assumption that unobstructed flow only takes place through the two depressed roof sections and in the ground 10ft on either ends of the new station and existing tunnel, and no flow occurs through the SOE walls abandoned in the ground.

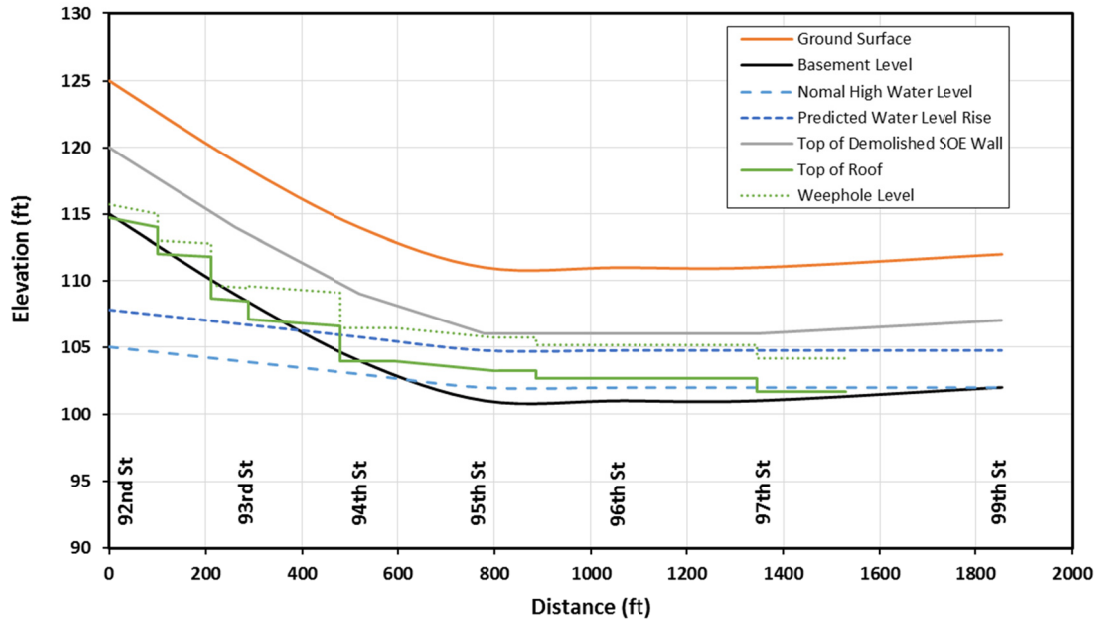


FIG.5 Comparison of raised groundwater levels and basement levels

Groundwater Equilibration System

Figure 6 shows the layout of an equilibration system that was designed to mitigate the groundwater accumulation problem. Essentially, the accumulated water on the upstream side would be captured using a network of collection pipes and manholes, and transferred via solid pipes across the station roof to be dispersed into the ground on the downstream side. This approach makes use of the potential energy of the groundwater head to initiate flow in the system whenever an imbalance in the water

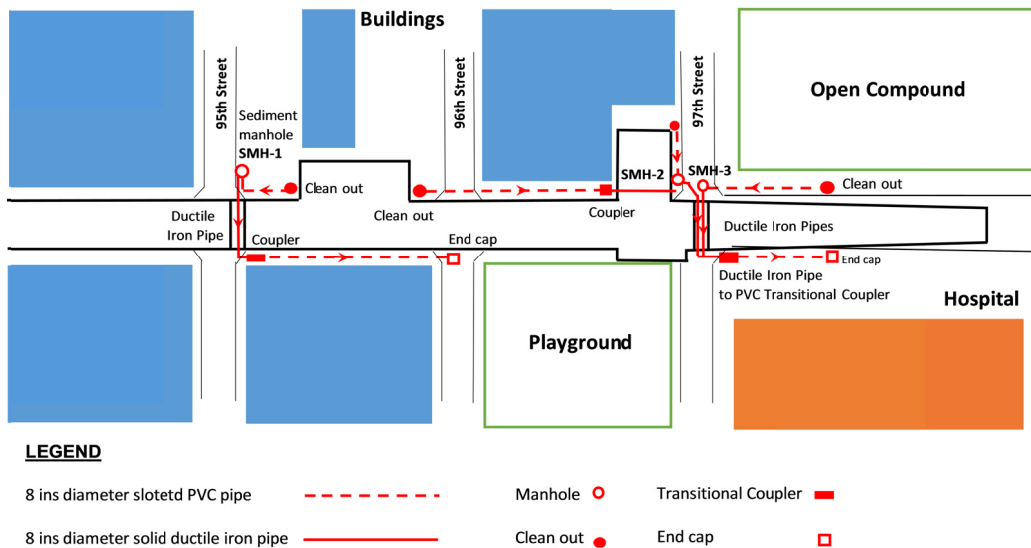


FIG.6 Layout of groundwater equilibration system

levels occur between the upstream and downstream sides. The pipes were sized for a much larger capacity than the required flow in order to avoid the need for regular cleaning due to accumulation of sediments over time. The materials utilized are simple and easily replaceable. The system is self-sustaining and requires minimal maintenance.

Two sets of equilibration systems were designed, one to cater to the flows between 95th and 96th Street and another for the flows between 96th and 99th Street. Flow transfer was effected at the two major sewer crossings at 95th and 97th Street within the depressed roofs (Figure 6). In this project, the layout of the collection and dispersion pipes were severely constrained by the congested utilities in the sidewalk and existing building boundaries. 8 inches (203mm) diameter Schedule 80 slotted PVC pipes were specified for the drainage system. These pipes were surrounded with 1 inch (25mm) graded crushed stones wrapped in a geotextile fabric to keep out fines. The specified fabric was a Mirafi 140N non-woven geotextile with an apparent opening size (AOS) of 0.212mm and discharge capacity of 135 gal/min per square feet of surface area (5500 l/min/m²). The drainage zone was 2ft (0.6m) wide and a minimum of 3ft (0.9m) high, and was required to be embedded at least 2ft (0.6m) within the granular fill above the impervious organics layer (Figure 7).

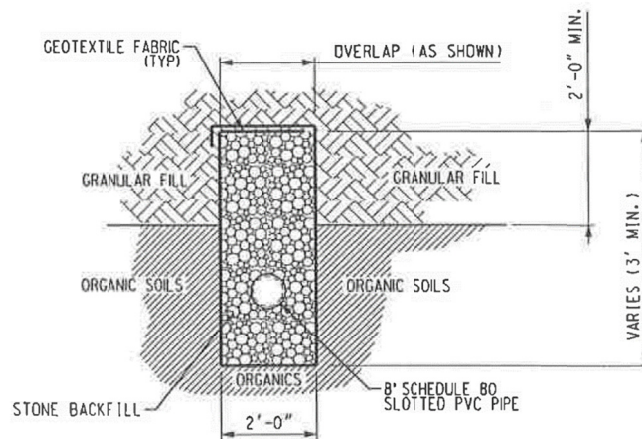


FIG.7 Details of collection and dispersion pipes

The collection pipes drained into a manhole, where fine sediment was trapped before allowing the overflow to be admitted to the solid transfer pipes (Figure 8). The transfer pipes consisted of 8 inches (203mm) diameter ductile iron pipes. Manholes (SMH-1 to SMH-3) were located on the upstream side (west side of the station box) at each junction. Due to congestion of utilities on the east side of the station box, it was not possible to locate manholes on the downstream side. The manhole invert at the 95th Street crossing point (SHM-1) was fixed at EL+95ft, with the collection and transfer pipes located 2ft (0.6m) higher at EL+97ft. The discharge end of the transfer pipe was connected to the dispersion pipe at the same elevation via a transitional coupler. At the 97th Street crossing point, the corresponding elevations of the

manhole inverts (SMH-2 and SMH-3) were fixed at EL+96ft, with the collection and transfer pipes similarly located 2ft (0.6m) higher. The discharge end of the transfer pipe was connected by a 90 degree elbow to the dispersion pipe which was located lower at EL+97ft. The entrances to all the transfer pipes in the manholes were enclosed in a geotextile fabric to keep sediments out. The collection and dispersion pipes were capped at each end.

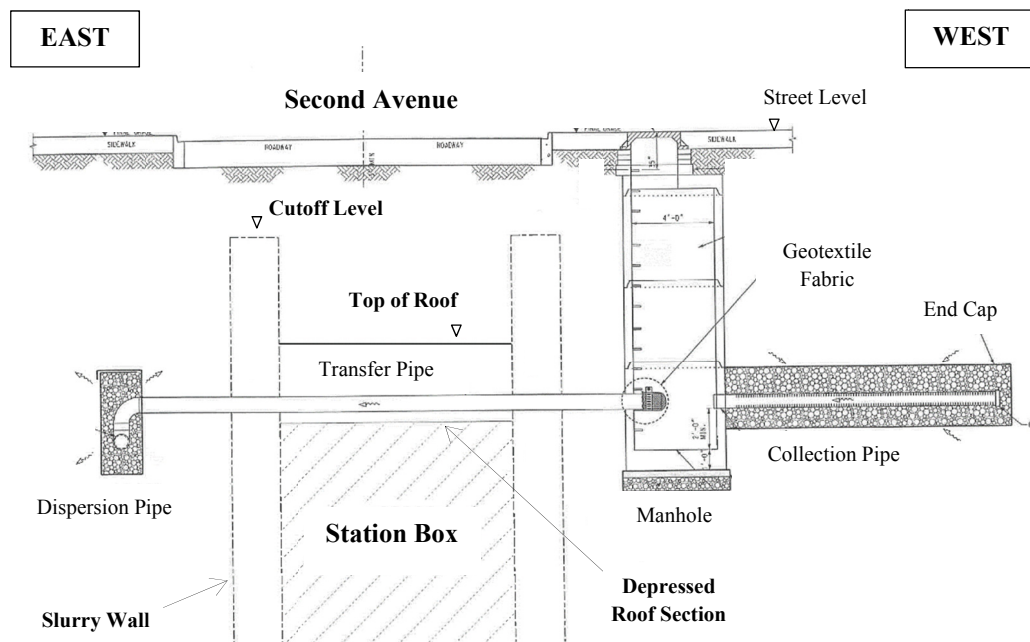


FIG. 8 Manhole and piping scheme

Although the system was designed to be maintenance free, cleanouts were provided at approximately 100ft (30m) intervals along the collection and discharge pipes as a redundant measure for cleaning access if necessary. Figure 9 shows the typical arrangement at the 97th Street crossing point.

CONCLUSIONS

This paper investigates the impact of the construction of a new subway line on the existing groundwater regime. Numerical modeling indicated that a rise of up to 2.8 feet (0.85m) in water table was possible due to the damming effect of the permanent underground subway structure. This potential rise in groundwater level may impact adjacent building basements in the vicinity of the subway structure. An equilibration system was designed to provide relief to the groundwater accumulation problem. The equilibration system consisted of a network of drainage pipes and manholes which collects the water built up on the upstream side of the station to be transferred across the roof of the station and discharged into the ground on the downstream side. The design of the equilibration system was based on the principle of hydraulic flow driven by a potential energy difference. The system is self-sustaining and maintenance free.

This project demonstrated that solutions for sustainable design of groundwater flow problems in urban environments can be simple and yet elegant.

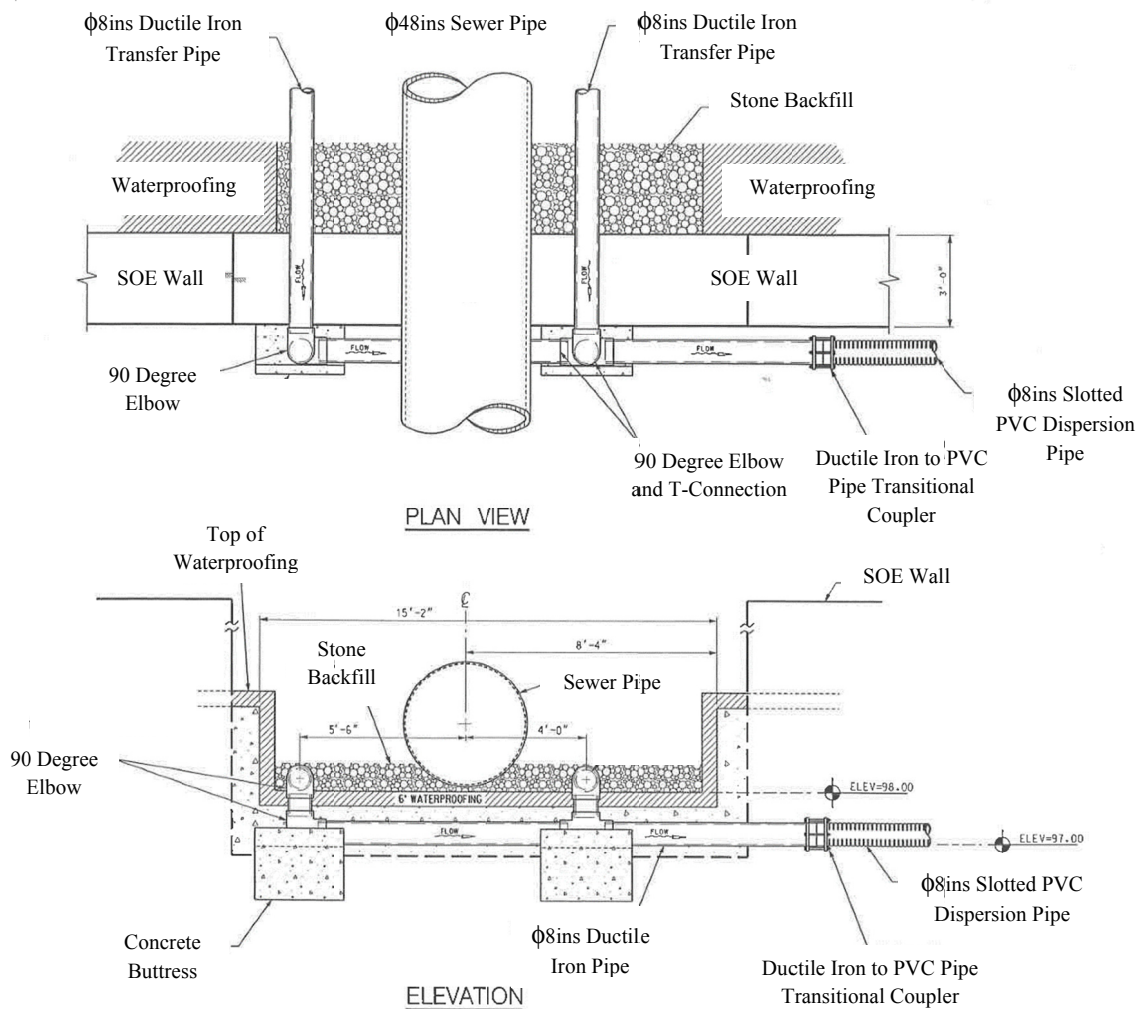


FIG.9 Typical piping configuration at crossing point in depressed roof

REFERENCES

- Aksman B., Grigson, R. and Giffen, R. (2012). "Second Avenue Subway Project, New York: Design of New Underground Stations", *Proc. Structures Congress*, Chicago, ASCE, 12p.
- FEMA (1983). Flood insurance maps.
- Grigson, R., Ho, C., and Lemus, P. (2016). "Second Avenue Subway Project: Deep Excavation Support of a Cut-and-cover Station", *Proc. Geotechnical and Structural Engineering Congress*, Phoenix, AZ, ASCE: 402-415.
- Ho, C. E., and Hu, S. (2014). "Design Optimization of Underground Subway Station Diaphragm Walls Using Numerical Modeling", *Geotechnical Special Publication No.234*, ASCE: 3122-3132.

Impacts of the Design Methods of Drilled Shafts in Sand on the Environment

Mina Lee¹ and Dipanjan Basu, C.Eng., M.ASCE²

¹MASc. Student, Dept. of Civil and Environmental Engineering, Univ. of Waterloo, 200 University Ave West, Waterloo, ON, Canada. E-mail: m65lee@uwaterloo.ca

²Associate Professor, Dept. of Civil and Environmental Engineering, Univ. of Waterloo, 200 University Ave West, Waterloo, ON, Canada. E-mail: dipanjan.basu@uwaterloo.ca

Abstract: Drilled shafts can be designed in various ways depending on the assumptions involved. However, the difference between the different design methods manifests significantly in terms of environmental impacts. In order to study this aspect systematically, drilled shafts are designed using eight different design methods for a homogeneous and a layered sand profile. The environmental impacts of the different designs are evaluated by life cycle assessment (LCA). Parametric studies are performed to study the impact of soil properties on the environmental impacts.

INTRODUCTION

Evaluation of construction projects on the basis of their impacts on the environment is important for sustainable development. Geotechnical engineers can contribute to this effort by estimating the potential environmental impacts of design, construction, and maintenance of geo-structures. Construction activities impact the environment, and the degree of this impact can be roughly estimated by the quantity of materials used in the construction process. The quantity of materials (e.g., concrete and steel) required in a construction project is determined to a large extent during the design. Therefore, the connection between a design and its impact on the environment should be thoroughly investigated. This is particularly important in geotechnical engineering because several geotechnical elements, e.g., foundations, slopes, and retaining structures, have multiple analysis and design methods available as part of the accepted norm, and these different methods lead to different material consumptions. For example, there are multiple methods available for capacity calculation of drilled shafts and different design dimensions ensue by using the different methods, which results in different quantities of material consumption. It is therefore necessary to judiciously choose a design method, which not only ensures serviceability and safety but also causes minimal detrimental impact on the environment.

The objective of this study is to evaluate the environmental impacts of the different available design methods for drilled shafts. Two profiles consisting of sandy soils are considered, and drilled shafts embedded in these profiles are designed for a given

applied load using the available design methods. After obtaining the design dimensions, life cycle assessment of the drilled shaft construction process is performed to determine the environmental impacts each design causes. Subsequently, a parametric study is performed to study the effects of soil properties on the environmental impacts.

DRILLED SHAFT DESIGN

Eight different manuals or textbooks (Budhu, 2008; Canadian Geotechnical Society, 2006; Coduto, 2001; Das, 2011; Federal Highway Administration, 2010; Fleming et al., 2009; Reese et al., 2006; Salgado, 2008) are referred to for identifying the different design methods for drilled shafts available to the profession. The design methods suggested by Budhu (2008) and Reese et al (2006) use the exact same assumptions and equations; therefore, these two methods are considered identical. The equations for drilled shaft capacity calculation prescribed in these manuals and books are used in this study to design the drilled shafts.

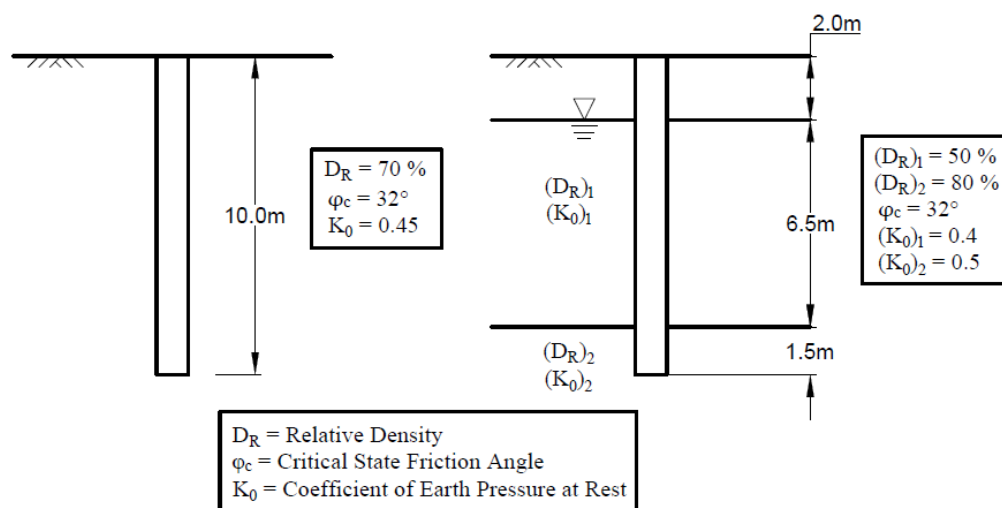


FIG. 1. Subsurface profiles considered: (a) homogeneous soil and (b) layered soil.

Two distinct subsurface profiles consisting of sand layer(s) are considered, as illustrated in Figure 1. The homogenous profile, shown in Figure 1(a), consists of a dry sand layer with relative density $D_R = 70\%$, critical-state friction angle $\phi_c = 32^\circ$, and coefficient of earth pressure at rest $K_0 = 0.45$. The layered profile shown in Figure 1(b) consists of a top sand layer with $D_R = 50\%$, $K_0 = 0.4$, and $\phi_c = 32^\circ$, and it is underlain by a dense sand layer with $D_R = 80\%$, $K_0 = 0.5$, and $\phi_c = 32^\circ$. For this profile, the water table is at a depth of 2 m below the ground surface.

The drilled shafts are designed such that both their lengths are fixed at 10 m. Therefore, the difference in the pile dimensions because of the use of different design methods is manifested in the pile diameter. An axial load of 2000 kN is applied on both the piles, and a factor of safety (FS) of 2.5 is used. The required gross volume of steel reinforcement for the drilled shafts is assumed to be 2.5% of the gross volume of concrete, based on the recommendations of FHWA (2010).

The eight different design methods used in this study are based on different inputs and assumptions. For example, the design methods suggested by Budhu (2008), Coduto (2001), FHWA (2010), Reese et al (2006), and Salgado (2008) are in-situ test based methods that require blow counts (N values) from the standard penetration test (SPT). The standard blow counts corrected at 60% energy, N_{60} , are estimated based on the correlations developed by Meyerhof (1957) and Skempton (1986), as recommended in Salgado (2008):

$$N_{60} = \frac{D_R}{100\%} \left(A + BC \frac{\sigma'_v}{p_A} \right) \quad (1)$$

where D_R is in percentage, σ'_v is the effective vertical stress in kPa, p_A is the reference stress (100 kPa), and A , B , and C are correlation coefficients with $27 \leq A \leq 46$, $B \approx 27$, and

$$C = \frac{1 + 2K_{0,NC}}{1 + 2K_{0,NC}} \quad (2)$$

in which $K_{0,NC}$ is the coefficient of at-rest earth pressure for normally consolidated soils. The peak friction angle φ_p used in design is estimated from the correlations based on N_{60} (De Mello, 1971).

In order to study the effect of the variation of soil properties on the environmental impacts, additional designs were performed. For the homogeneous profile, drilled shafts were additionally designed for $D_R = 50\%$ and 85% . For the layered profile, four different combinations of D_R were considered: (i) 25% and 65%, (ii) 25% and 80%, (iii) 50% and 65%, and (iv) 65% and 90% for the top and bottom layers, respectively. For both the soil profiles, K_0 is varied over a range of 0.4-0.5, and φ_c is varied over 32° - 36° .

LIFE CYCLE ASSESSMENT

Life cycle assessment (LCA) is a useful tool to evaluate potential environmental impacts of a product considering its overall life cycle. It typically consists of two parts: inventory analysis (IA) and environmental impact assessment (EIA). The LCA procedure followed in this study is based on the guidelines by ISO 14044: 2006.

In this study, LCA is conducted for a single drilled shaft embedded in the subsurface profiles shown in Figure 1. The life cycle of a single drilled shaft is bounded from the extraction of raw material up to the completion of the construction work. A complete life cycle usually includes the demolition or recycling stage; however, the stages beyond the end of construction are omitted here because, typically, pile foundations have a long service life, require minimal maintenance, and are rarely dismantled.

Inventory Analysis

Inventory analysis involves compilation and quantification of inputs and outputs for a product throughout its life cycle (ISO 14044: 2006). The inputs for drilled shafts include masses of materials (e.g., steel and cement) and the corresponding embodied energies required to operate the processes. Embodied energy is the summation of all the primary energies (i.e., energies obtained from fossil fuels and renewable sources) consumed to produce a material (or product). The outputs are the environmental consequences of operating the processes. In this study, the environmental consequences are quantified by the amount of emissions released to air. Figure 2 shows the unit processes involved in each life cycle stage of a typical drilled shaft.

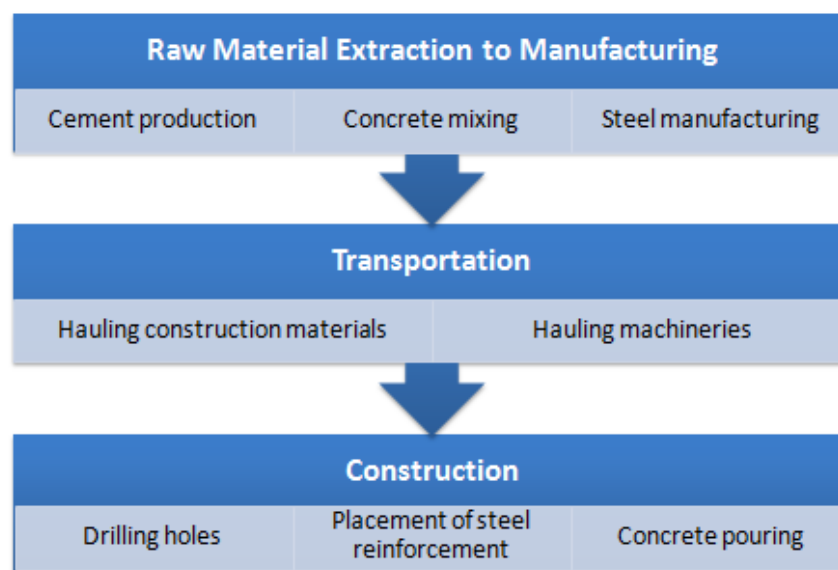


FIG. 2. Life cycle stages of a typical drilled shaft.

The quantity of materials (soil, concrete, steel, and fuel) is determined from the pile diameter and length obtained from the design calculations. The embodied energy of a particular material is estimated as the product of the mass of material used in drilled shaft construction and its respective embodied energy intensity (EEI). Inventory of Carbon & Energy (ICE) provides a list of EEIs for various materials (Hammond and Jones, 2011). The embodied energy consumed from the extraction of raw materials to manufacturing stages represents the primary energy consumed to operate the relevant processes (i.e., extraction, refinery, and manufacturing). For transportation and construction stages, the embodied energy is quantified based on the amount of fuel combusted to operate the hauling trucks and construction machineries. The total embodied energy (TEE) is the summation of embodied energies from all life cycle stages considered within the system boundary.

Air emissions (outputs) are quantified based on the emission coefficients provided by the National Renewable Energy Laboratory (2012). For every unit process, certain air

emissions (e.g., CO₂, CH₄, NO_x, and SO_x) are expected to be released. The mass of a particular air emission is the product of the mass of the material in question and its corresponding emission coefficient.

Environmental Impact Assessment

Environmental impact assessment is conducted to understand and evaluate the magnitude and significance of the potential environmental impacts of a product (i.e., drilled shaft in this case) throughout its life cycle (ISO 14044:2006). The categories of impact considered in this study are (i) climate change, (ii) terrestrial acidification, (iii) photochemical oxidant formation, (iv) human toxicity, (v) terrestrial ecotoxicity, and (vi) freshwater toxicity. The impacts of the air emissions quantified in the inventory analysis are investigated based on these categories. For example, CO₂ and CH₄ are the major contributors to global warming, and fall under the category of climate change. The calculated mass of air emissions is translated into an appropriate measurement to understand its contribution to the relevant environmental impact. For example, the contribution of CH₄ towards climate change is characterized by the global warming potential (GWP) and is quantified in terms of equivalent mass of CO₂. The characterization factors which translate the mass of air emissions into the relevant equivalent unit of a particular impact category are obtained from the ReCiPe database (Goedkoop et al., 2014). Table 1 summarizes the characterization factors and the equivalent measurement units for each impact category.

TABLE 1. Categories of environmental impacts.

Impact Category	Characterization Factor	Equivalent Measurement Unit
Climate Change	Global Warming Potential (GWP)	Kg of CO ₂
Terrestrial Acidification	Acidification Potential (AP)	Kg of SO ₂
Photochemical Oxidant Formation	Photochemical Oxidant Formation Potential (POFP)	Kg of NMVOC ^a
Human Toxicity	Human Toxicity Potential (HTP)	Kg of 1,4-DB ^b
Terrestrial Ecotoxicity	Terrestrial Ecotoxicity Potential (TEP)	Kg of 1,4-DB
Freshwater Ecotoxicity	Freshwater Toxicity Potential (FTP)	Kg of 1,4-DB

^aNMVOC = Non-methane volatile organic carbon compound

^b1,4-DB = 1,4 dichlorobenzene

RESULTS

Effect of Different Design Methods

Table 2 summarizes the means and coefficients of variation (COV) of the pile diameters and concrete volumes for the two soil profiles obtained by using the different

design methods. Considering the fact that the drilled shafts are designed for the same applied load, a COV of 42-44% for the pile diameters is remarkably high. The COV becomes even greater (66-68%) when the volume of concrete instead of the pile diameter is considered.

TABLE 2. Pile diameter and concrete volume.

Soil Profile	Average Pile Diameter (m)	COV of Pile Diameter	Average Concrete Volume (m ³)	COV of Concrete Volume
Homogenous	0.92	0.42	7.66	0.66
Layered	0.97	0.44	8.73	0.68

The average TEE for drilled shafts embedded in the homogeneous profile is 72349 MJ with a COV of 65%, and the average TEE for drilled shafts in the layered profile is 83292 MJ with a COV of 67%. Maximum TEEs of 210335 MJ and 160707 MJ are obtained from the property-based design method of Salgado (2008) for both the homogeneous and layered profiles, respectively, and the corresponding minimum TEEs of 8346 MJ and 8398 MJ are obtained from the design method proposed by Fleming et al. (2009). The COVs of TEE are almost the same as the COVs of concrete volume in Table 2. This is because the majority of calculations in the LCA is related to the volume of concrete.

The trends of variation of the environmental impacts for all the impact categories (given in Table 1) are very similar because of which the results from the EIA are reported only for the category of GWP. The values of the environmental impacts for GWP, as obtained from the different design methods, are normalized with respect to the maximum value (18108 Kg of CO₂ equivalent). Table 3 summarizes the maximum values used for the normalization for all the impact categories and Figure 3 shows the normalized environmental impacts (GWPs) of drilled shafts. The COVs for each environmental impact are close to the COVs of the concrete volumes obtained in Table 2.

TABLE 3. Reference values for normalization.

Impact	Reference Value	Unit
GWP	18108	Kg of CO ₂
AP	56	Kg of SO ₂
POFP	51	Kg of NMVOC
HTP	120	Kg of 1,4-DB
TTP	0.0442	Kg of 1,4-DB
FTP	0.00356	Kg of 1,4-DB

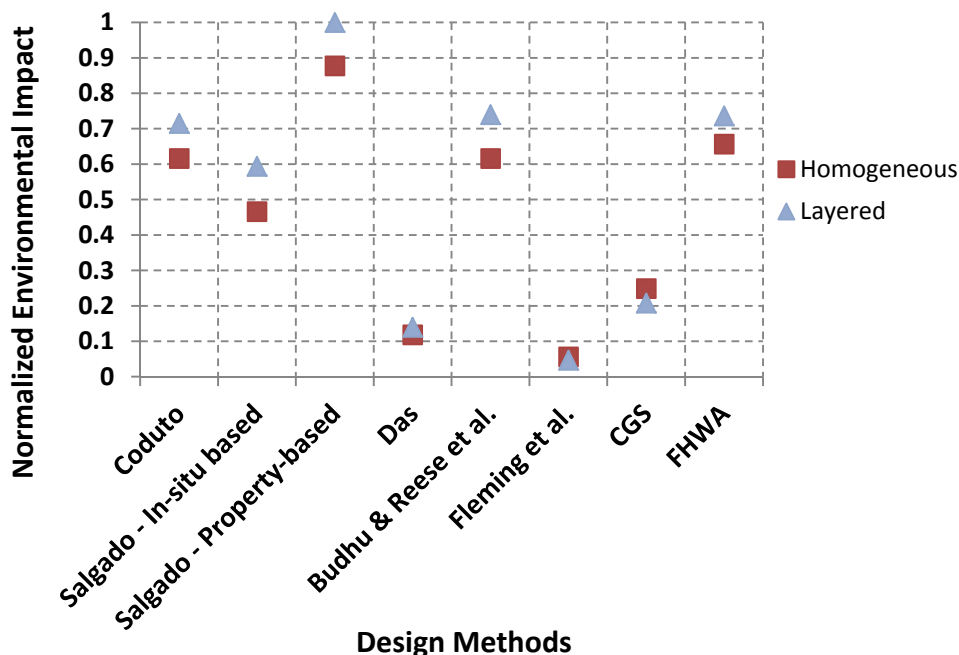


FIG. 3. Environmental impacts of drilled shafts for different design methods.

Effect of Soil Properties

Figure 4 shows the normalized environmental impact (considering only GWP) for various D_R values selected for this study. "H" in the legend of Figure 4 denotes homogeneous layer (Figure 1(a)), and "L" denotes the layered profile (Figure 1(b)). For the range of D_R considered, the COVs of the environmental impacts, considering all the categories mentioned in Table 1, range over 45-70%.

Figure 5 shows the normalized environmental impacts (considering only GWP) as functions of K_0 . There is practically no variation in the environmental impacts because most design methods (except the property-based design method of Salgado (2008)) do not explicitly consider K_0 as a design parameter. For the range of K_0 considered, the COVs of the environmental impacts, considering all the categories mentioned in Table 1, range over 53-70%.

Similar results were obtained when environmental impacts were investigated as functions of φ_c — the variations are very similar to those shown in Figure 5. It was observed that φ_c does not influence the design outcomes much for most of the methods except the property-based method of Salgado (2008). For the range of φ_c considered, the COVs of the environmental impacts for all the categories range over 54-80%.

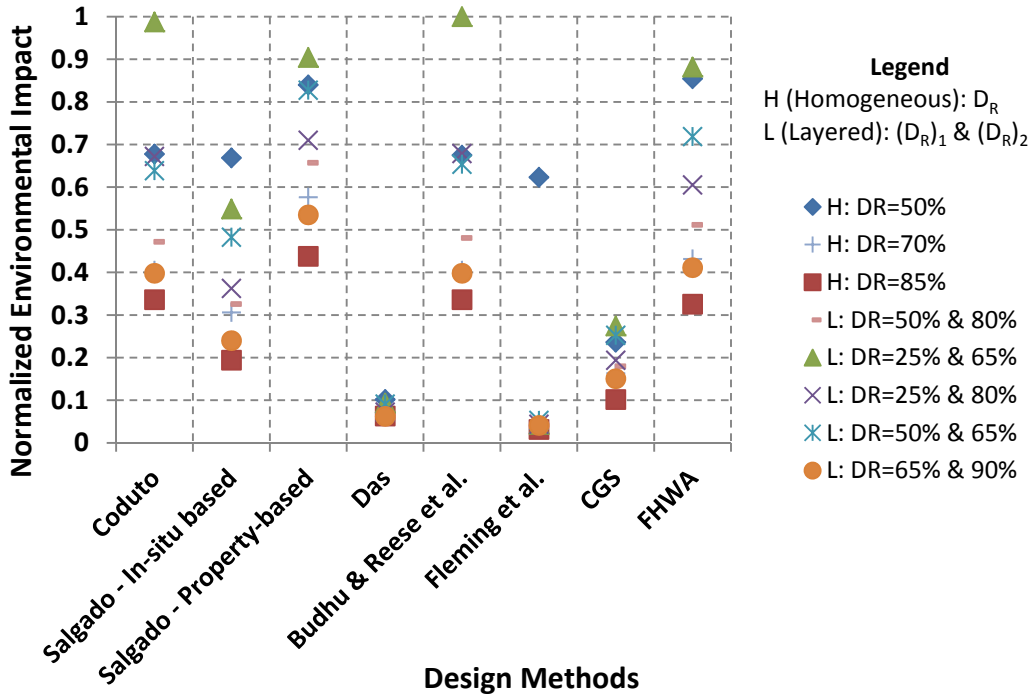


FIG. 4. Environmental impacts for various D_R .

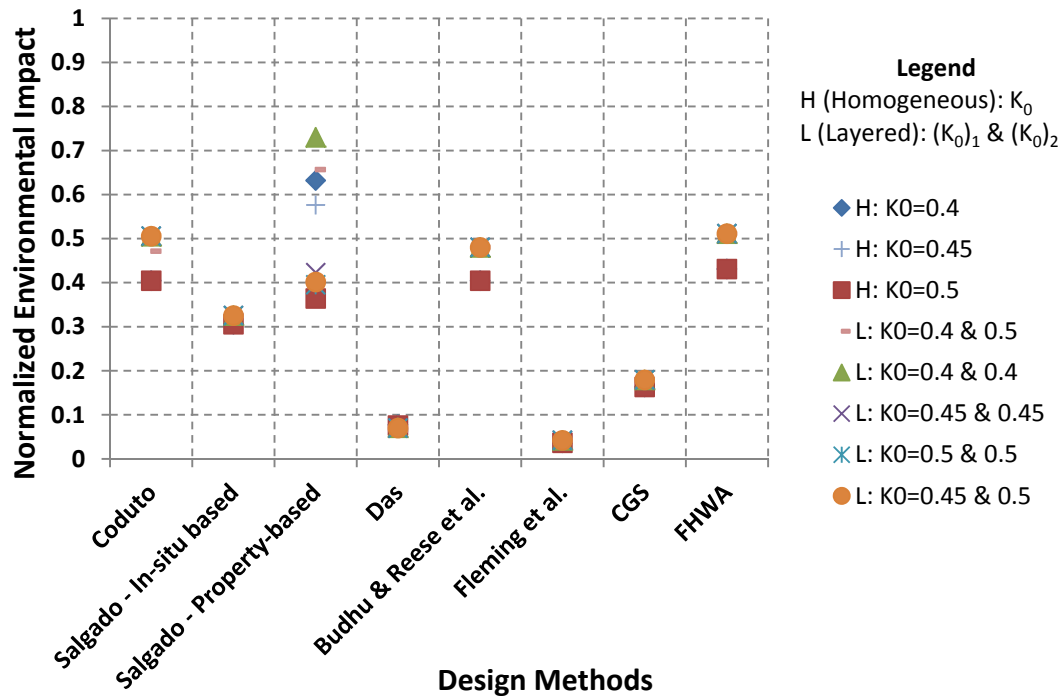


FIG. 5. Environmental impacts for various K_0 .

What do the Environmental Impacts Signify?

In order to understand the implications or severity of the environmental impacts from the different design methods, the national statistics from the Government of Canada are used as reference values. For example, the standard deviation (SD) of GWP (for the homogenous profile) obtained from the different design methods is 3443 equivalent kg of CO₂. According to the Government of Canada (2012), the average annual greenhouse gas (GHG) emission from operating private vehicles per capita is 2149 kg in the year 2007. Thus, the SD of the GWP (caused by the choice of different design methods) exceeds the annual GHG emissions by 60%. Given the fact that the calculations presented in this paper were made considering a single drilled shaft and that thousands of drilled shafts are constructed every year all over the world, choice of a particular design method for drilled shafts may have a significant environmental impact in the world.

CONCLUSIONS

Life cycle assessment was conducted on drilled shafts to obtain the differences in the environmental impacts of drilled shaft design for eight different design methods. Six categories of environmental impact were considered in this study: climate change, terrestrial acidification, photochemical oxidant formation, human toxicity, terrestrial ecotoxicity, and freshwater toxicity. The drilled shafts were assumed to be embedded in homogeneous and layered sand profiles and were designed for a given applied load. Parametric studies were performed by varying the relative density, coefficient of at-rest earth pressure, and critical-state friction angle of soil.

The COVs of the environmental impacts, obtained by using the eight different design methods, range over 45-80%. These variations have a strong correlation with the design results because the calculations in the LCA are mostly related to the concrete volume of the drilled shafts. This suggests that decisions made during the design process can affect the environmental impacts of drilled shaft throughout its life cycle. The standard deviation of global warming potential, as obtained from the different design methods, was found to be 1.6 times the average per capita annual GHG released from private vehicles in Canada. Thus, the differences in terms of the environmental impacts between the design methods are not trivial, and careful selection of design methods is necessary for sustainable development.

REFERENCES

- Budhu, M. (2008). *Foundations and Earth Retaining Structures*. John Wiley & Sons, Hoboken, NJ, USA.
- Canadian Geotechnical Society. (2006). *Canadian Foundation Engineering Manual*, 4th Ed., Canadian Geotechnical Society, Vancouver, BC, Canada.
- Coduto, D. P. (2001). *Foundation Design: Principles and Practices*, 2nd Ed., Prentice Hall, Upper Saddle River, NJ, USA.
- Das, B. (2011). *Principles of Foundation Engineering*, 7th Ed., Cengage Learning, Stamford, CT, USA.

- De Mello, V.F.B. (1971). "Standard Penetration Test.", *4th Proceedings of Panamerican Conference of Soil Mechanics and Foundation Engineering*, ASCE, San Juan, Puerto Rico, 1-86.
- Federal Highway Administration. (2010). "Drilled Shafts: Construction Procedures and LRF Design Methods.", <<http://www.fhwa.dot.gov/Engineering/geotech/foundations/nhi10016/index.cfm>> (March 5, 2015).
- Fleming, K., Weltman, A., Randolph, M. and Elson, K. (2009). *Piling Engineering*, 3rd Ed., Taylor & Francis, Abingdon, OX, UK.
- Goedkoop, M., Heijungs, R., Huijbregts, M., Schryver, A., Struijs, J. and Zelm, R. (2014). "Characterisation and Normalisation Factors", <<http://www.lcia-recipe.net/file-cabinet>> (May 5, 2015).
- Hammond, G. & Jones, C. (2011). "Inventory of Carbon and Energy Version 2.0.", <<http://web.mit.edu/2.813/www/readings/ICEv2.pdf.old>> (Jan. 7, 2015).
- ISO. (2006). "ISO 14044: Environmental Management - Life Cycle Assessment - Requirements and Guidelines." Geneva, Switzerland.
- Meyerhof, G.G. (1957). "Discussion for Session I.", *4th Proceedings of International Conference of Soil Mechanics and Foundation Engineering*, London, UK, Vol. 3: 10.
- National Renewable Energy Laboratory. (2012). "U.S. Life Cycle Inventory Database.", <<https://www.lcacommons.gov/nrel/search>> (April 11, 2015).
- Reese, L.C., Isenhower, W.M. and Wang, S. (2006). *Analysis and Design of Shallow and Deep Foundations*. John Wiley & Sons, Hoboken, NJ, USA.
- Salgado, R. (2008). *The Engineering of Foundations*. McGraw Hill, Boston, MA, USA.
- Skempton, A.W. (1986). "Standard Penetration Test Procedures and the Effects in Sands of Overburden Pressure, Relative Density, Particle Size, Ageing and Overconsolidation.", *Geotechnique*, Vol. 36(3): 425-447.
- Government of Canada. (2012). "Greenhouse Gas Emissions from Private Vehicles in Canada, 1990 to 2007.", <<http://www.statcan.gc.ca/pub/16-001-m/2010012/part-partiel-eng.htm>> (July 15, 2015).

Minimization of Cost and CO₂ Emissions for Drilled Shafts under Axial Loading Using a Big Bang–Big Crunch Algorithm

Andrew Assadollahi, Ph.D., E.I.¹

¹Assistant Professor, Dept. of Civil and Environmental Engineering, Christian Brothers Univ., Memphis, TN 38104.

Abstract: A procedure is developed to minimize cost and CO₂ emissions for the design of reinforced concrete drilled shafts subjected to axial loading, satisfying geotechnical limit states and using a Big Bang–Big Crunch (BB-BC) algorithm. The objectives of this research are to develop low-cost and low-CO₂ emission designs of drilled shafts and to compare low-cost and low-CO₂ emission designs. Cost is based on materials and labor required for the construction of drilled shafts. The CO₂ emissions are associated with the extraction and transportation of raw materials; processing, manufacturing, and fabrication of products; and the emissions of equipment involved in the construction process. The cost and CO₂ objective functions are subjected to soil bearing and displacement limits. A design example is presented to compare low-cost and low-CO₂ emission designs. Results are presented that demonstrate the effects of different magnitudes of applied axial loads, soil properties, factors of safety, and allowable settlements on low-cost and low-CO₂ emission designs.

INTRODUCTION

Low-cost designs of engineering systems have always been a concern in engineering practice. Since the annual emissions of carbon dioxide (CO₂) have grown by about 80% since 1970 and were estimated to be 77% of total anthropogenic greenhouse gas emissions in 2004 (UNIPCC 2007), the consideration of CO₂ emissions in structural concrete design has become a prudent area of research. Large emissions of CO₂ are produced during the manufacturing of Portland cement, the principal binder used in concrete. Due to these large CO₂ productions, efforts have been made to design concrete structures that are more sustainable. In addition, there has been no investigation into the design of drilled shafts for low-cost and low-CO₂ emissions which consider all of the geotechnical limit states using evolutionary methods.

Big Bang–Big Crunch (BB-BC) has been shown to be a computationally efficient heuristic method to solve a variety of optimization problems. Erol and Eksin (2006) proposed the original BB-BC algorithm which involved exploiting the power of the mean of a population using an abstract model of the lifecycle of the universe. In each

“Big Bang” stage, a set of normally distributed solutions is generated about the weighted mean of the solution space. After the solutions are evaluated, a “Big Crunch” stage computes a new center for the next “Big Bang” based on the fitness of the various solutions. Over successive cycles of Big Bangs and Big Crunches, the standard deviation of the normal distribution of new solutions decreases and the search tends to become more localized in the neighborhood of the best solution. When some measure of the averaged solution and/or the best solution ceases to improve over a number of cycles, the optimization is assumed to have converged.

The form of the objective function for this optimization is consistent with that presented by Camp and Assadollahi (2013). Both the cost objective function and the CO₂ emission objective function include the unit emissions associated with excavation, formwork, reinforcing steel, and concrete.

The general form of the optimization problem is given as

$$\text{Minimize: } f_{cost} = \sum_{i=1}^R C_i u_i(x_1, x_2, \dots, x_n) \quad \text{or} \quad f_{CO_2} = \sum_{i=1}^R E_i u_i(x_1, x_2, \dots, x_n) \quad (1)$$

$$\text{Subject to: } p_j(x_1, x_2, \dots, x_n) \leq 0 \quad (2)$$

Where f_{cost} is the cost function and f_{CO_2} is the CO₂ emission function, C_i are the unit costs, E_i are the unit CO₂ emissions, u_i are the amount of material and construction units, x_i are the design variables, n is the number of design variables, R is the number of material and construction units, and p_j are the penalty functions.

DRILLED SHAFTS SUBJECTED TO AXIAL COMPRESSIVE LOADS

Drilled shafts are essentially cast-in-situ concrete piles that may or may not have steel reinforcement and may or may not be belled. There are two load-transferring mechanisms between the shaft and the soil: load-carrying capacity of the shaft point and frictional resistance. Figure 1 shows an axially-loaded drilled shaft where P is the applied axial compressive force, Q_p is the load-carrying capacity at the tip and Q_s is the frictional (skin) resistance. There are two geometric design variables for the optimization: D is the diameter of the shaft and L is the length of embedment of the shaft. The geotechnical limit states include soil bearing capacity and shaft settlement. The soil bearing capacity is computed as the sum of Q_p and Q_s :

$$Q_u = Q_p + Q_s \quad (3)$$

The factor of safety against soil bearing failure is given as:

$$FS = \frac{Q_u}{P + W} \quad (4)$$

where W is the self-weight of the shaft. The total vertical elastic settlement is computed as:

$$s = s_1 + s_2 \quad (5)$$

where s_1 is the elastic deformation of the shaft material and s_2 is the settlement of the shaft caused by the load at the shaft point.

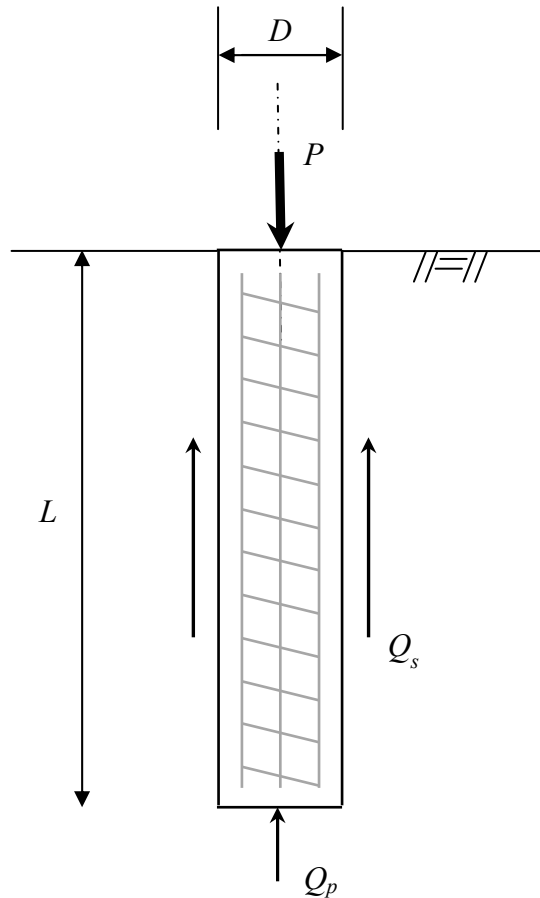


FIG. 1. Drilled Shaft Subjected to Axial Compressive Load

CONSTRAINTS

In order to provide safety and stability against geotechnical limit state failure, constraints are imposed to ensure stability of the geomaterial, as well as geometric limitations. Each design constraint is posed as a penalty on the overall objective function of the design and is non-zero only when violated. In other words, if the design is feasible, the sum of the constraint penalties will be zero. There are three different penalties that are imposed on designs when a constraint is either less than a minimum requirement or greater than a maximum requirement. If the factor of safety against bearing capacity is less than the minimum required factor of safety, the safety factor penalty is given as:

$$p_{FS} = 1 - \frac{FS}{FS_{min}} > 0 \quad (6)$$

Where FS_{min} is the minimum factor of safety against bearing failure. In order for a drilled shaft to be considered a deep rather than shallow foundation, the depth of embedment must be at least four times greater than its diameter. If the depth of embedment is less than four times the diameter, the depth penalty is given as:

$$p_{depth} = 1 - \frac{L}{4D} > 0 \quad (7)$$

If the total vertical settlement is greater than the maximum allowable settlement, the settlement penalty is given as:

$$p_{sett} = 1 - \frac{s_{max}}{s} > 0 \quad (8)$$

where s_{max} is the maximum allowable settlement of the drilled shaft.

A total penalty function is used to enforce the penalties p_j on the objective function. The total penalty for a candidate low-cost or low-CO₂ emission design k is a function of the summation of the stability, capacity, reinforcement configuration, and geometric constraints.

The penalized objective function F_k is a product of the cost or CO₂ objective function of candidate design k and its total penalty:

$$F_k = \left(1 + \sum_{j=1}^3 p_j \right)^\eta f_k \quad (9)$$

where η is a positive penalty exponent. The penalty expression imposes a numerical penalty on the value of the objective function that tends to reflect the degree at which the constraints are violated by a candidate set of design variables.

BIG BANG-BIG CRUNCH OPTIMIZATION

Erol and Eksin (2006) developed the original BB-BC optimization from an abstract model of the lifespan of the universe. In the initial Big Bang stage, solution variables are uniformly randomly distributed throughout the search space. Next, during the contraction of the Big Crunch stage, a center of mass \vec{x}_{cm} is computed from the initial population using penalized objective function values as:

$$\vec{x}_{cm} = \frac{\sum_{k=1}^{NC} \frac{\vec{x}_k}{F_k}}{\sum_{k=1}^{NC} \frac{1}{F_k}} \quad (10)$$

where \vec{x}_k is the position of candidate k in an n -dimensional search space and NC is the candidate population size. For the subsequent iterations of the Big Bang stage, new candidate solution positions \vec{x}_k^{new} are normally distributed around the center of mass by:

$$\bar{x}_k^{new} = \beta_1 \bar{x}_{cm} + (1 - \beta_1) [\beta_2 \bar{x}_l + (1 - \beta_2) \bar{x}_g] + \frac{r\alpha(\bar{x}_{max} - \bar{x}_{min})}{n_{cycle}} \quad (11)$$

where β_1 and β_2 are values in the range [0, 1] that weight the influence of the local best solution \bar{x}_l and the global best solution \bar{x}_g on the center of mass of new population positions, r is a random number from a standard normal distribution, α is a parameter limiting the size of the search space, \bar{x}_{max} and \bar{x}_{min} are the upper and lower limits on the values of the design variables, and n_{cycle} is the number of Big Bang iterations. Depending on where the center of mass is located in the search space, especially during early cycles of the algorithm, it is possible to generate a design variable value that is outside the prescribed range. In this case, values that lie outside the search space limits are reset to the appropriate minimum/maximum values (Erol and Eksin 2006). The global best solution \bar{x}_g is limited to candidates that are feasible, or in other words, designs that have no penalty applied to their objective function values.

Numerical results indicate that a population of 300 initial candidate solutions is adequate to balance computational efficiency and overall algorithm performance. A general stopping criterion of 3,000 analyses is used. Computational results show that $\beta_1 = 0.3$ and $\beta_2 = 0.6$ routinely provide the best footing designs for this example. Using a value of $\alpha = 1$ in Equation (7) enables the initial search to sample the full range of values for each design variable. For all the spread footing design examples, $\eta = 2$ (Camp and Assadollahi 2015).

DESIGN EXAMPLE

The objective of this design example is to investigate the cost and CO₂ emissions impact of drilled shafts subjected to axial compressive forces. All designs will satisfy geotechnical limit states.

The fitness function is defined as:

$$f_{cost} = C_e V_e + C_f A_f + C_r M_r + C_c V_c \quad \text{or} \quad f_{CO_2} = E_e V_e + E_f A_f + E_r M_r + E_c V_c \quad (12)$$

where C_e is the unit cost of excavation, C_f is the unit cost of formwork, C_r is the unit cost of reinforcement, C_c is the unit cost of concrete, E_e is the unit emission of excavation, E_f is the unit emission of formwork, E_r is the unit emission of reinforcement, and E_c is the unit emission of concrete. The computations of the volume of excavation V_e , area of formwork A_f , mass of the reinforcement M_r , volume of concrete V_c , and volume of compacted backfill V_b are consistent with the methodology used by Camp and Assadollahi (2013).

Unit emission values are based on the extraction and the transportation of raw materials; processing, manufacturing, and fabrication of products and machinery; and the emissions of equipment involved in the construction process and are given in Camp and Assadollahi (2013). Table 1 lists the specified loading, footing, and soil design parameters. The parameters are based on typical values of a dry sand, typical factors of safety, and allowable settlements of drilled shafts. Table 2 lists the summary of the low-cost designs developed by the BB-BC procedure based on the

input parameters given in Table 1. Table 3 lists the summary of the low-CO₂ emission designs developed by the BB-BC procedure based on the input parameters given in Table 1. A sensitivity study is done by varying different soil parameters and axial compressive loads and then plotting the average cost and CO₂ emissions.

Table 1. Input Parameters

Input parameter	Unit	Symbol	Value
Internal friction angle of soil	<i>degree</i>	ϕ'	35
Unit weight of soil	<i>kN/m³</i>	γ_s	18.5
Poisson ratio of soil	—	ν	0.3
Modulus of elasticity of soil	<i>MPa</i>	E	50
Applied vertical force	<i>kN</i>	P	5,000
Factor of safety for bearing capacity	—	FS	3.0
Maximum allowable settlement	<i>mm</i>	δ	100
Minimum Shaft Diameter	<i>m</i>	D_{min}	0.3
Minimum Shaft Length	<i>m</i>	L_{min}	1.0

Table 2. Designs Based Low Cost

Design Variables	Value
D (m)	1.155
L (m)	4.645
Excavation (m^3)	7.72
Concrete Formwork (m^2)	16.85
Reinforcement (kg)	144.40
Concrete (m^3)	4.87
Best Cost	\$ 2,224.78
Average Cost	\$ 2,228.22
Std. Dev. Cost	\$ 8.40
Associated CO ₂	1,952.58 kg

Table 3. Designs Based Low CO₂ Emissions

Design Variables	Value
D	1.155
L	4.645
Excavation (m^3)	7.72
Concrete Formwork (m^2)	16.85
Reinforcement (kg)	144.40
Concrete (m^3)	4.87
Best CO ₂	1,952.58 kg
Average CO ₂	1,958.16 kg
Std. Dev. CO ₂	11.31 kg
Associated Cost	\$ 2,224.78

Figures 2 through 7 show a plot of average cost and average CO₂ emissions as the applied axial load, soil elastic modulus, soil Poisson ratio, soil internal angle of friction, factor of safety, and allowable settlement varies, respectively. The purpose of these sensitivity studies is to show how average cost and average CO₂ emissions change as different input parameters are varied. The results summarized in Tables 2 and 3 are based on one particular set of input parameters, which are summarized in Table 1.

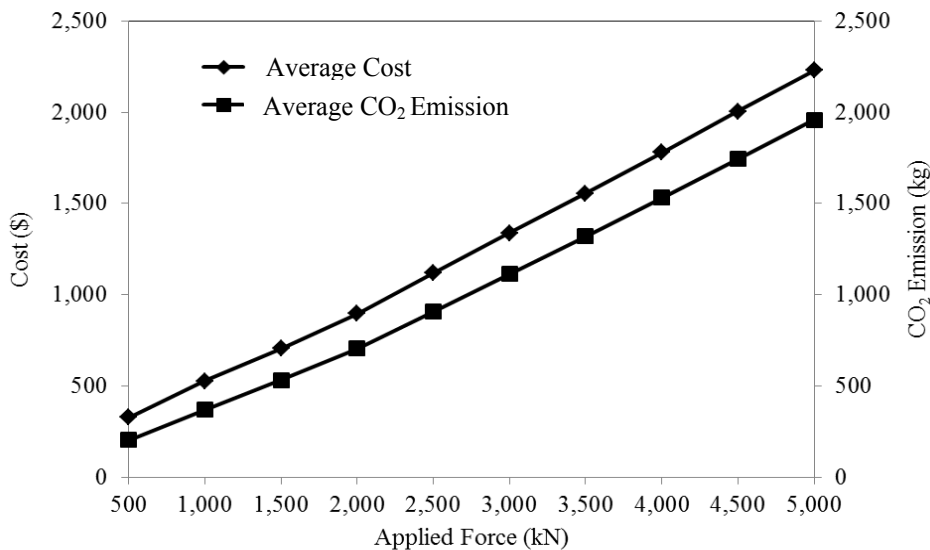


FIG. 2. Average Cost and Average CO₂ Emissions as a Function of Applied Force.

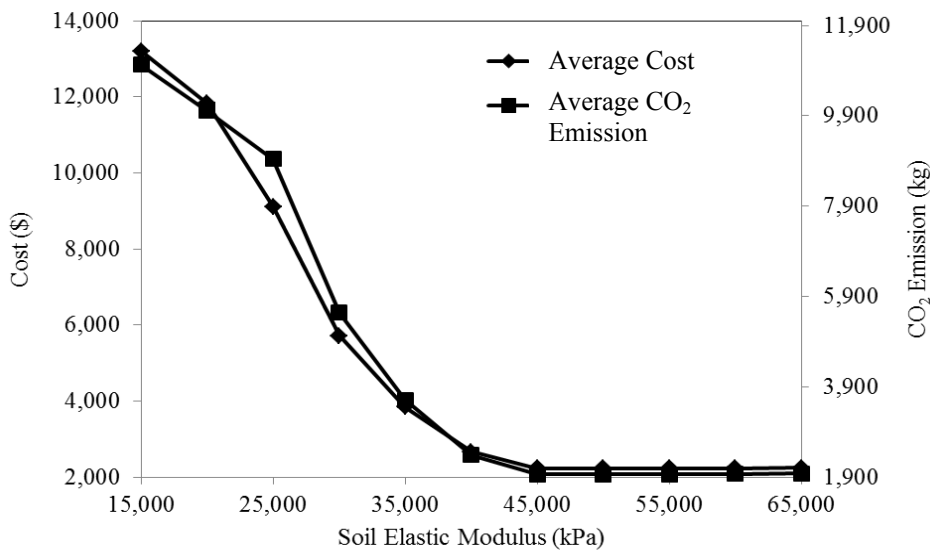


FIG. 3. Average Cost and Average CO₂ Emissions as a Function of Soil Elastic Modulus.

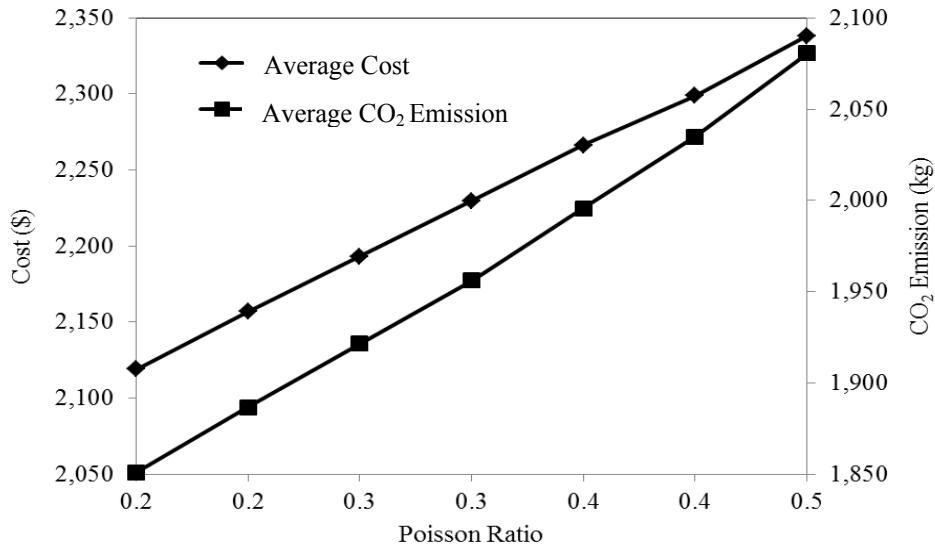


FIG. 4. Average Cost and Average CO₂ Emissions as a Function of Soil Poisson Ratio.

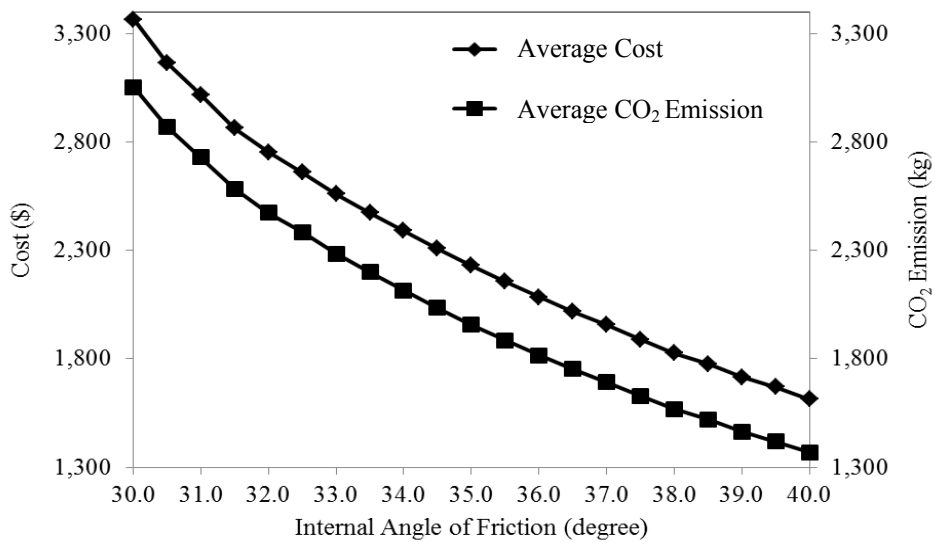


FIG. 5. Average Cost and Average CO₂ Emissions as a Function of Soil Internal Angle of Friction.

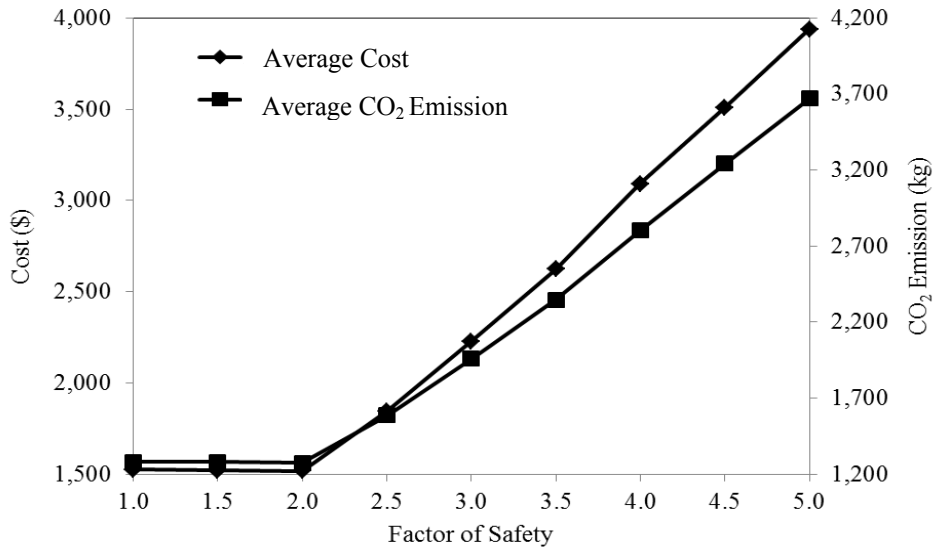


FIG. 6. Average Cost and Average CO₂ Emissions as a Function of Factor of Safety.

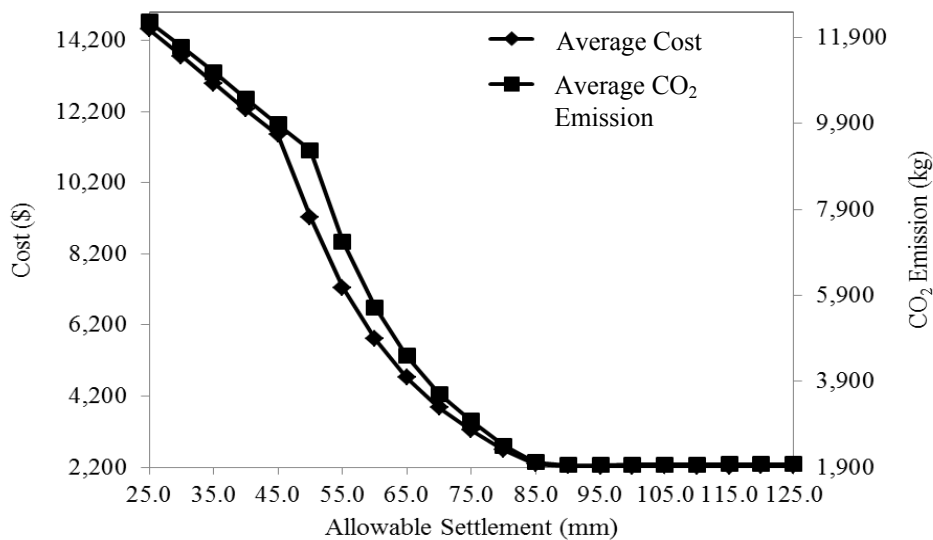


FIG. 7. Average Cost and Average CO₂ Emissions as a Function of Allowable Settlement.

CONCLUSIONS

A procedure is developed to minimize cost and CO₂ emissions for reinforced concrete drilled shaft designs. Evaluations are based on design optimizations using a cost and a CO₂ emission objective function developed with a hybrid multi-phase BB-

BC algorithm. The objectives of this research are to develop low-cost and low-CO₂ emission designs of drilled shafts and to compare low-cost and low-CO₂ emission designs.

Examples show that the best low-cost design is identical to the best low-CO₂ design. The likely reason for this is that both the cost and CO₂ objective functions are built using a weighted aggregate fitness function and have identical forms. Each of these objective functions are being minimized in order to provide low-cost and low-CO₂ emission designs while still adhering to appropriate geotechnical limit states. A sensitivity analysis shows a nearly linear increase in both cost and CO₂ emissions as the applied force is increased. There is a decrease and change in concavity in both cost and CO₂ emissions as the soil elastic modulus is increased. There is a nearly linear increase in both cost and CO₂ emissions as the soil Poisson ratio is increased. There is a decrease in both cost and CO₂ emissions as the internal angle of friction is increased. For factors of safety up to 2.0, there are insignificant changes in both cost and CO₂ emissions. However, for factors of safety greater than 2.0, there is a nearly linear increase in both cost and CO₂ emissions. There is a decrease and change in concavity in both cost and CO₂ emissions as the allowable settlement is increased.

ACKNOWLEDGEMENTS

The author is grateful to Mr. Brian Harris, Ms. Jodie Crocker, Dr. Siripong Malasri, P.E., and Mr. R. Eugene McGinnis, P.E. for providing constructive comments during the course of this study.

REFERENCES

- Camp, C. V. and Assadollahi, A. (2015). "CO₂ and Cost Optimization of Reinforced Concrete Footings Subjected to Uniaxial Uplift." *Journal of Building Engineering*, 3 171-183.
- Camp, C. V. and Assadollahi, A. (2013). "CO₂ and Cost Optimization of Reinforced Concrete Footings Using a Hybrid Big Bang-Big Crunch Algorithm." *Structural and Multidisciplinary Optimization*, 48(2) 411-426.
- Erol, O. K. and Eksin, I. (2006). "A New Optimization Method: Big Bang-Big Crunch." *Advances in Engineering Software*, Vol. 37, 106-111.
- United Nations Intergovernmental Panel on Climate Change (2007). Climate Change 2007: Synthesis Report. Contribution of Working Groups I, II and III to the Fourth Assessment Report of the Intergovernmental Panel on Climate Change [Core Writing Team, Pachauri, R.K and Reisinger, A. (eds.)]. IPCC, Geneva, Switzerland.

State DOT Life Cycle Benefits of Recycled Material in Road Construction

Eleanor F. Bloom¹; Kelly Del Ponte²; Bharat Madras Natarajan³; Angela Pakes Ahlman, P.E., LEED AP, WasteCap AP⁴; Tuncer B. Edil, Ph.D., P.E., D.GE, Dist.M.ASCE⁵; and Gary Whited, P.E.⁶

¹M.S. Student, Geological Engineering Program, Univ. of Wisconsin-Madison, Madison, WI. E-mail: efbloom@wisc.edu

²M.S. Student, Geological Engineering Program, Univ. of Wisconsin-Madison, Madison, WI. E-mail: kdelponte@wisc.edu

³Undergraduate Student, Geological Engineering Program, Univ. of Wisconsin-Madison, Madison, WI. E-mail: madrasnataraj@wisc.edu

⁴Technical Director, Recycled Materials Resource Center, Univ. of Wisconsin-Madison, Madison, WI. E-mail: angela.pakes@wisc.edu

⁵Research Director, Recycled Materials Resource Center, Univ. of Wisconsin-Madison, Madison, WI. E-mail: tbedil@wisc.edu

⁶Senior Administrative Program Specialist, Civil and Environmental Engineering Dept., Univ. of Wisconsin-Madison, Madison, WI. E-mail: whited@engr.wisc.edu

Abstract: The use of recycled materials in highway construction has the potential to achieve significant benefits affecting the triple-bottom line (environment, prosperity and society). Although state departments of transportation (DOTs) have been in the forefront of introducing recycled materials, they have not been able to clearly convey the benefits in a quantitative and transparent manner using easily understood metrics. What is lacking is direct information on sustainability assessment characteristics, i.e. greenhouse gas emissions, energy and water consumption, and waste generation. To determine the benefits of using recycled materials for DOTs, the Recycled Materials Resource Center (RMRC) is undertaking a project with the objective of providing a tool to quantitatively analyze and report the environmental and life cycle benefits of using recycled materials in highway construction. Subsequently, an analysis of the environmental benefits was conducted using PaLATE, a life cycle assessment (LCA) tool developed with RMRC sponsorship. The LCA analysis of four environmental parameters (energy use, water consumption, carbon dioxide emissions, and hazardous waste generation) showed significant environmental benefits when states used recycled industrial byproducts such as fly ash and recycled roadway materials such as recycled concrete aggregate (RCA) and recycled asphalt pavement (RAP).

INTRODUCTION

Over 163,000 miles of highways in the National Highway System form the backbone of our 4-million-mile public road network. These highways are

continuously being constructed and rehabilitated, requiring large amounts of natural raw materials, producing waste, and consuming energy (AASHTO 2008, Gambatese 2005). In order to reduce these economic and environmental costs, state Departments of Transportations (DOTs) have been reusing highway construction materials in various DOT projects.

The Recycled Materials Resource Center (RMRC, <http://rmrc.wisc.edu>), located at the University of Wisconsin-Madison, and many governmental agencies have developed fact sheets on various recycled materials and industrial byproducts for their use in highway construction applications. These fact sheets typically have addressed the engineering properties and environmental suitability issues relevant to various applications, and in some cases have incorporated design guidelines and construction specifications. However, direct information on sustainability assessment characteristics, i.e., greenhouse gas (GHG) emissions, energy and water consumption, and life cycle cost benefits is not yet readily available. Agencies may track system-wide use of quantities for major recycled materials such as fly ash in concrete, recycled asphalt pavement (RAP), recycled concrete aggregate (RCA), etc., but they have not yet calculated the benefits accrued by substitution of these materials for conventional materials. Project by project tracking of recycled materials use post-bid award has been a challenge as well. Although state DOTs have been in the forefront of introducing recycled materials, they have not been able to clearly convey the benefits in a quantitative and easily understood manner.

The objective of this study is to develop a tool by which the state system-wide material use quantities can be used to calculate the life cycle benefits associated with the incorporation of these recycled materials and industrial byproducts to highway pavement construction. In order to realistically quantify the output of such a tool, data on the recycled materials quantities used by each RMRC member state DOT was collected and analyzed. The RMRC member state DOTs that have provided data for this study are: Georgia (GDOT), Illinois (IDOT), Minnesota (MnDOT), Pennsylvania (PennDOT), Virginia (VDOT), and Wisconsin (WisDOT).

EVALUATION OF LCA TOOLS

Life Cycle Assessment Tool Methodology

The first step in developing a quantitative benefit assessment tool was to examine existing publically available pavement life cycle assessment (LCA) tools. An LCA can assist in a better understanding of the environmental impacts of products throughout their life cycle, cradle-to-grave, and provide relevant data in order to make informed decisions (ISO 2006). The International Organization for Standardization (ISO) 14040 series provides general principles and a framework for an LCA study, detailing four phases of an LCA: (i) definition of goals and scope, (ii) inventory analysis, (iii) impact assessment, and (iv) interpretation. In general, LCAs should have defined system boundaries, functioning units, and inputs/outputs. For most pavement LCAs, the defined system boundaries are materials, construction, use, maintenance, and end-of-life (Santero 2011). For the purpose of this study, we examined four existing publically available LCA tools (Table 1), focusing on the

scope of each tool, including the system boundaries and environmental impacts. The four tools were selected based on their availability to the public and the locations where they were developed.

TABLE 1. LCA Tools Researched for this Project, based on Table 1.2 from Santero, et al., 2011 (AASHTO 2010, Horvath 2004, MTU 2011, Santero 2011, TRL 2011)

<i>Tool</i>	<i>Developer</i>	<i>Interface</i>	<i>Pavement Types</i>
asPECT	Transport Research Library	GUI	asphalt only
GreenDOT	AASHTO	spreadsheet	all
PE-2	Michigan Technological University	web-based	all
PaLATE	UC-Berkeley, RMRC	spreadsheet	all

Overview of LCA Tools

Each LCA tool assessed for this study follows the four phases of an LCA defined by the ISO. The goal of using LCA for this study is to calculate the environmental impacts of using recycled materials or industrial by-products in highway pavement. Ideally, the chosen assessment's impacts would include GHG emissions and energy use at a minimum. Additionally, the chosen tool should be able to analyze as many of the DOTs reported recycled materials as possible. The following section discusses and compares each of the tools.

asPECT: The Transportation Research Laboratory (2011) developed the Asphalt Pavement Embodied Carbon Tool to follow the material used in asphaltic pavement from raw material acquisition through the end of life processes of disposing of or recycling the pavement materials. The main goal of asPECT is to calculate GHG emissions based on ten life cycle stages for a road from user inputs such as materials, fuels, transportation modes and distances, and energy use. While this would be advantageous for an individual project, the tool was too specific for the purposes of a system-wide study. Another major disadvantage is asPECT is only capable of analyzing asphaltic pavements, which does not allow for a complete analysis.

PE-2: PE-2, developed by Michigan Technological University (2011), estimates the life cycle emissions associated with construction, maintenance, and roadway use. Unique to this tool, PE-2 has a web-based interface and takes into account the costs of traffic delay caused by construction operations. PE-2 was designed solely for projects based in Michigan and is limited by pre-defined construction operations and fewer materials in its database. While PE-2 was found to be a good tool to use for a quick estimate of environmental costs, it was not considered to be capable of a more in-depth analyses needed for this project.

GreenDOT: GreenDOT, described by AASHTO (2010), was specifically developed for state DOTs to calculate CO₂ emissions from operations, construction, and maintenance projects. GreenDOT includes emissions based on four categories:

electricity, materials, on-road vehicles, and off-road vehicles. GreenDOT is able to calculate project-specific or system-wide emissions. GreenDOT is also unique in that it calculates emissions of the electrical components of a highway, for instance, traffic signals. Overall, GreenDOT was found to be user friendly, but limited in the amount of materials and equipment in its databases.

PaLATE: PaLATE, developed at UC-Berkeley for the RMRC (Horvath 2004), follows the production of materials, construction, maintenance, and end-of-life processes. Initial material inputs are analyzed based on the equipment used to produce and transport them to the construction site. Emissions due to construction, maintenance, and production are calculated from the equipment used in all processes. Many of the outputs of PaLATE are based upon the volumes or weight of materials used and the parameters of equipment used, such as the productivity and fuel consumption of each machine. PaLATE furthers its impact assessment by outputting not only GHG emissions, but also energy use, water consumption, particulate matter, waste generation, and human toxicity potentials. The first and only version of PaLATE was developed in 2004 (Horvath 2004), and while the range of environmental outputs of PaLATE is wide, these are limited by potential out-of-date databases. However, PaLATE can be updated with relative ease, unlike the other LCA tools. Based on the limitations and advantages of each LCA tool, PaLATE was found to be the best suited to accommodate the objectives of this project.

MATERIALS ANALYSES ASSUMPTIONS AND APPROACH

Survey Results

In the first phase (2013) of data collection, a survey was conducted with RMRC six-member state DOTs (GA, IL, MN, PA, VA and WI) in order to determine the degree to which recycled materials were used and tracked by member states. The survey results showed that while many DOTs use commonly recycled materials, most track neither the breakdown of recycled materials used per each pavement layer nor the total annual quantities used. Overall, the six member states agreed that the availability of a recycled materials tracking tool would be useful.

In the second phase of data collection, RMRC member state DOTs were asked to report quantities of recycled materials for the calendar or fiscal year of 2013. The only DOT required to report by law the amount of recycled materials being used is IDOT. Although recycled materials use quantities could not be tracked effectively by most of the DOTs, information on as-let items for projects within the time period for each state was available. In order to calculate the quantities of recycled materials from as-let material quantities, a set of assumptions regarding average design specifications needed to be determined for each state DOT. This was established through interviews and correspondence with engineers from each member state. These assumptions and averages were then used to calculate the amounts of recycled materials used in hot mix asphalt (HMA), concrete mixes, and base course layers.

Assumptions

Because determining specific design parameters (such as pavement thicknesses and fly ash replacement of concrete) for every DOT project over the annual period was challenging, certain standard practice assumptions were made. Table 2 lists the assumptions made in order to calculate the quantities of fly ash used by each member DOT. General assumptions made when running the LCA analysis in PaLATE included:

1. A 1:1 replacement volume or mass of virgin with recycled material was assumed, despite the known varying mechanical properties.
2. Both cement and fly ash were assumed to be delivered by cement trucks over a one-way distance of 200 miles (Gary Whited, personal communication, July 7, 2015).
3. All RAP and RCA was assumed to be processes and reused on site with a transportation distance of zero miles.
4. All other materials, including HMA and ready-mix concrete, were assumed to be delivered by trucks over a one-way distance of 25 miles.
5. For all RAP used in HMA pavement, 6% was assumed to be used as asphalt replacement with the remaining 94% used as aggregate in the mix.
6. For all RAS used in HMA pavement, 20% was assumed to be used as asphalt replacement with the remaining 80% used as aggregate in the mix.
7. Any RAP used in HMA was equated into virgin aggregate and asphalt. However, the RAP specifically identified for base course material was equated only into virgin aggregate.
8. All RCA was assumed to be used in base course, and therefore used as a replacement to virgin aggregate.

TABLE 2. Fly Ash Assumptions and the Data Time Period

<i>State</i>	<i>Material</i>	<i>Calculation Assumptions</i>	<i>Year of Data</i>
<i>IDOT</i>	Fly Ash	All fly ash used as cement replacement	Calendar Year 2013
<i>WisDOT</i>	Fly Ash	For Concrete Pavements and Driveways: Pavement thickness is 25.4 cm (10 in) Unit quantity of fly ash in concrete is 101 kg/m ³ (170 lbs/CY)	Fiscal Year 2013
<i>MnDOT</i>	Fly Ash	Unit quantity of fly ash in concrete is 101 kg/m ³ (170 lbs/CY)	Calendar Year 2013
<i>PennDOT</i>	Fly Ash	Fly ash replacement in cement was 15% Pavement thickness is 25.4 cm (10 in)	Calendar Year 2013
<i>GDOT</i>	Fly Ash	All reported fly ash quantity was used in HMA and none in concrete pavement.	Calendar Year 2013
<i>VDOT</i>	Fly Ash	20% of half the total cementitious material used	Calendar Year 2013

Approach to PaLATE Analysis

The quantities of recycled material used by each member state were analyzed in PaLATE to determine environmental impacts and benefits of the recycled material use. These environmental impacts and resulting benefits were analyzed comparatively by using the same exact volume of virgin material. Four environmental impact factors: energy, water consumption, CO₂ emissions, and RCRA hazardous waste generation were deemed sufficient for evaluation of the state materials. RCRA Hazardous Waste, as stated by the U.S. EPA, is a waste with properties that make it dangerous or potentially harmful to human health or the environment (U.S. EPA 2015). PaLATE determines the environmental impacts based on three categories: material production, material transportation, and processes (equipment). Material production includes the processes associated with extracting or generating the materials, such as RAP milling and virgin aggregate quarrying. Material transportation incorporates the impacts associated with transporting each material the specified distance in the chosen vehicle. Processes (equipment) consist of the impacts associated with installing the material, such as paving, placing, and compaction.

The first step in conducting the PaLATE analysis was to compile the collected recycled material data for all states. Then, equivalent virgin material amounts were calculated for their recycled counterpart. Both the recycled and virgin material quantities were input into a PaLATE sheet, from which the specific environmental impact for each material's production, transportation, and processes were determined. Finally, the environmental impact of recycled versus virgin material was analyzed.

RESULTS

The recycled materials used by all RMRC member-states and analyzed in PaLATE include RAP, RAS, RCA, fly ash, blast furnace slag, and rubber. These recycled materials could be equated to four virgin materials: virgin aggregate in pavement mixes (HMA and concrete), asphalt, cement, and base course aggregate. The distribution of recycled materials is shown in category in recycled material in some capacity. 7.7 million tons of recycled material was used in 2013. It is evident that RAP is the most widely used recycled material, followed by RCA and then fly ash.

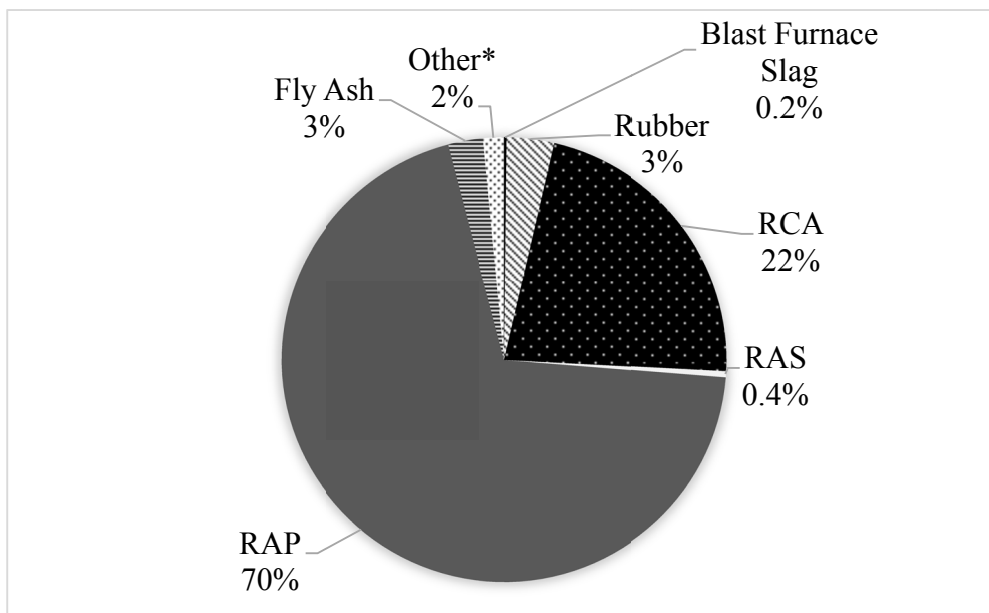


FIG. 1. Distribution of Recycled Material Tracked and Reported by RMRC Member States

Of all the recycled materials used by the six states during the one-year period, only fly ash and RAP were used and tracked by all states. Most states track RAS and RCA as well. One state, Illinois, tracked several other recycled materials including steel slag, by-product lime, glass beads, microsilica, dowel bars, rebar, and welded wire reinforcement, designated by the “Other” category in recycled material in some capacity.

Because they are only used by one state, comprise 1% of the total recycled materials usage, and are not included in PaLATE databases, the “Other” materials were not incorporated in this analysis. It is important to note that even though the states may not be tracking a certain material for the purpose of this study that does not necessarily indicate the state has not used the recycled material in some capacity.

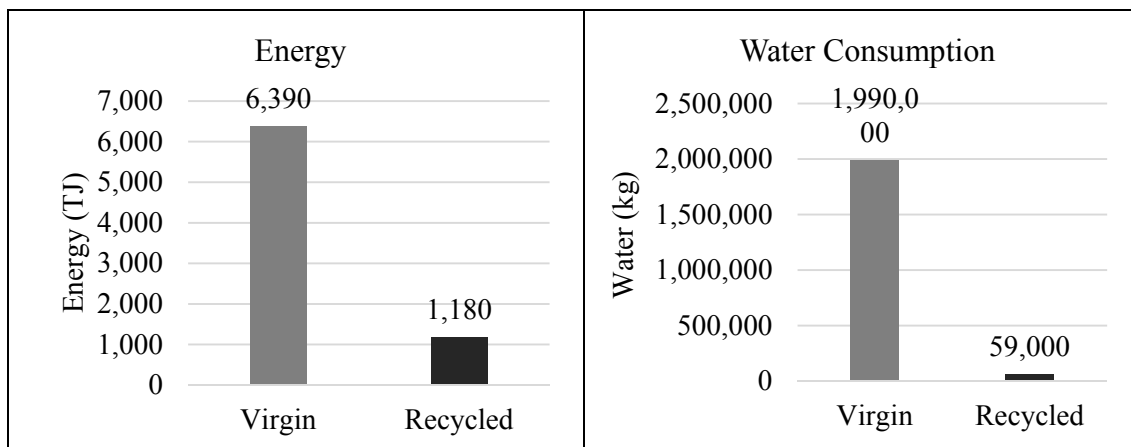
Each state DOT’s data was collected and analyzed separately and the results were combined to determine the total savings due to the use of recycled material. A summary of the environmental impact results are listed in Table 3 and are further demonstrated by Figure 2. In general, the use of recycled material significantly reduced the environmental impact in all four factors: energy, water consumption, CO₂ emissions and RCRA hazardous waste.

TABLE 3. Summary of Environmental Benefits of Six DOTs Use of Recycled Material

Impact Category	Virgin	Recycled	Savings	% Redux
Energy (TJ)	6,390	1,180	5,210	82%
Water consumption (kg)	1,990,000	59,000	1,931,000	97%
CO ₂ (Mg)	355,00	52,600	302,400	85%
RCRA Hazardous Waste (Mg)	68,900	2,180	66,720	97%

Figure 2 aids in the visualization of how the impacts may have been different had virgin materials been used instead of reclaimed recycled materials. The largest reductions by percent are seen in water use reductions. By using recycled materials, state DOTs saved 1.9 million liters of water over a one-year period. This amount would be enough water to fill over 14,000 bathtubs during the one-year period (USGS 2015). The next largest reduction is RCRA hazardous waste, followed by CO₂ emissions. The DOTs reduced their RCRA Hazardous waste generation by almost 67,000 Megagrams and saved over 300,000 Megagrams of CO₂. This is equivalent to the CO₂ emitted by 64,400 cars in one year (U.S. EPA, 2014). Regarding energy savings, the use of recycled material avoided using 5,210 Terajoules of energy, equivalent to the average energy consumption of 133,000 U.S. households in one year (U.S. EIA, 2015).

The results of all participating DOTs recycled material use can be compared based on the type of pavement layers: HMA pavement, concrete pavement, and base course. The greatest savings are associated with HMA. The two main reasons for this are that the most widely tracked/used recycled material is RAP, and asphalt production is environmentally impact-intensive. Although cement is also nearly as environmentally impactful, less fly ash is being used by states compared to RAP. Therefore, we see the majority of the savings stem from the replacement of virgin asphalt and aggregates in HMA mix designs. Base course resulted in the smallest savings, as the equivalent virgin base aggregate impact is not as great compared to impact associated with the pavement surface layers.



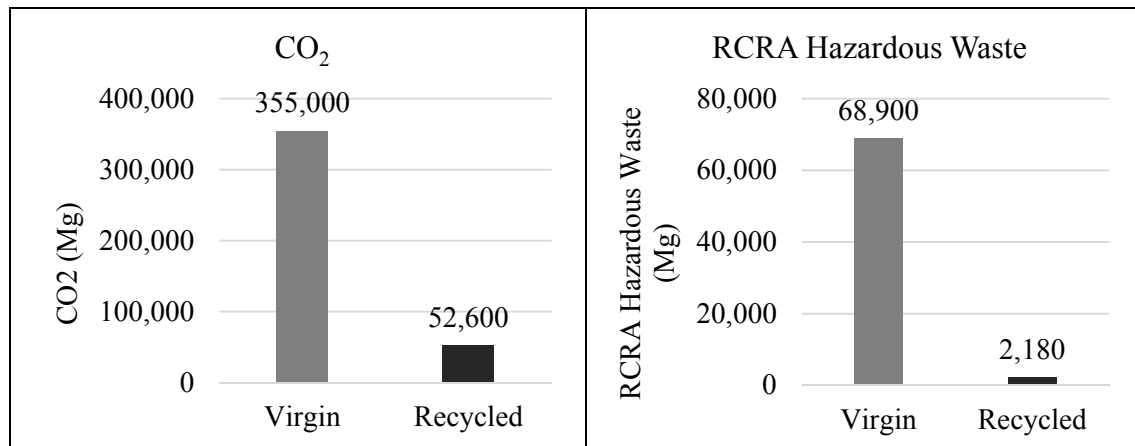


FIG 2. Difference in Environmental Impact for Recycled Versus Virgin Material

The results may also be analyzed in terms of PaLATE assessment categories: materials production, transportation, and processes (equipment). The largest savings are seen in the materials production category, particularly water consumption. Many of the recycled materials require little to no water in their production. Virgin materials, however, require a significant amount of water for processing, particularly asphalt and cement. There are reductions in the transportation category are due in large to the zero-mile transportation distance of material recycled from existing roadways (RAP, RCA).

There is a small (less than 10%) increase in environmental impact due to the processes associated with constructing the roadway. While the paving processes remain the same whether recycled or virgin materials are used, the difference is attributed to placement of base aggregate. In PaLATE's database, recycled base aggregates, mainly RAP and RCA, have a slightly greater density than conventional granular base. Since there is a greater weight of RAP and RCA, more activity and fuel consumption is required for installation. Therefore, the recycled aggregate has a larger impact for the processes category than its virgin counterpart.

DISCUSSION

The four LCA tools researched for this project all had unique advantages and disadvantages. The vast number of materials, equipment, and environmental outputs in the PaLATE database led to it being the LCA tool to be used and further developed in this study. The only version of PaLATE was developed in 2004, making its databases 10 years old at the start of this project. However, the databases could be easily updated as needed.

Six member states (GA, IL, MN, PA, VA and WI) provided the quantities of recycled material used throughout the system over a one-year period. The environmental effects of using recycled material in pavement construction were then analyzed using the LCA tool PaLATE and compared to a reference analysis in which the total volume of recycled material was replaced by an equal volume of virgin material. Overwhelmingly, the use of recycled material in pavement construction

decreased the environmental impacts in all four parameters (energy, water consumption, CO₂ emissions, RCRA hazardous waste), showing average environmental impacts savings between 80-97%.

In the future, the RMRC is developing a recycled material tracking tool for member state DOTs, allowing for more accurate reporting of recycled materials use and environmental benefits. The RMRC also hopes to estimate the economic savings associated with the use of recycled material by conducting a life cycle cost analysis. Additionally, the team will complete an update of the environmental, material, cost, and equipment databases within PaLATE so that RMRC member states and users of PaLATE will have up to date data analyses.

CONCLUSIONS

Using the life cycle assessment tool PaLATE, this study has established the quantitative environmental benefits of using major recycled materials. The environmental impact parameters of energy, water consumption, CO₂ emissions, and RCRA hazardous waste indicated a large increase in environmental benefits. Quantifying these benefits may serve as motivation for more DOTs to actively use and track recycled materials in highway applications. The Recycled Materials Resource Center, with the help of six member DOTs (GA, IL, MN, PA, VA and WI), is working to understand how DOTs can better track recycled materials in order to calculate the life cycle benefits associated with the incorporation of recycled materials and industrial byproducts into highway pavement construction.

ACKNOWLEDGMENTS

The Recycled Materials Resource Center provided funding for this project. UW–Madison staff provided valuable materials use and pavement design experience, and aided in the data collection and analysis. Various materials engineers from each member state DOT provided the required materials use data for this project: Steve Krebs (WisDOT), Winnie Okello (PennDOT), Gerard Geib (MnDOT), Edward Wallingford and Mike Fitch (VDOT), Mathew Mueller (IDOT), Richard Douds (GDOT), and Peter Wu (GDOT).

REFERENCES

- AASHTO. (2008). “Primer on Transportation and Climate Change.” *American Association of State Highway and Transportation Officials*,
<ftp://www.mdt.mt.gov/research/LIBRARY/PCRT-1-OL-PRIMER-TRANSPORTATION-CLIMATE_CHANGE-AASHTO.PDF> (Feb. 24, 2015).
- AASHTO. (2010). “GreenDOT.” *American Association of State Highway and Transportation Officials*,
<<http://144.171.11.40/cmsfeed/TRBNetProjectDisplay.asp?ProjectID=2621>> (Feb. 24, 2015).

- Gambatese, J., & Rahendran, S. (2005). "Sustainable Roadway Construction: Energy Consumption and material Waste Generation of Roadways." *Construction Research Congress 2005*, (pp. 1-13). doi:10.1061/40754(183)21
- Horvath, A. (2004). "PaLATE: Pavement Life-cycle Assessment Tool for Environmental and Economic Effects." *Consortium on Green Design and Manufacturing, University of California, Berkeley*, <<http://www.ce.berkeley.edu/~horvath/palate.html>> (July 22, 2015).
- ISO. (2006a). *ISO 14040: Environmental management -- Life cycle assessment -- Principles and Framework*. Switzerland: International Organization for Standardization.
- ISO. (2006b). *ISO 14044: Environmental management -- Life cycle assessment -- Requirements and guidelines*. Switzerland: International Organization for Standardization.
- Michigan Technological University (MTU). (2011). "PE-2: Project Emission Estimator." *Michigan Technical University*, <http://www.construction.mtu.edu/cass_reports/webpage/> (Mar. 3, 2015).
- Santero, N., Loijos, A., Akbarian, M., & Ochsendorf, J. (2011). "Methods, Impacts, and Opportunities in the Concrete Pavement Life Cycle." *Massachusetts Institute of Technology, Concrete Sustainability*, <http://www.specifyconcrete.org/assets/media/docs/MIT_Pavement_LCA_Report.pdf> (Mar. 3, 2015).
- TRL. (2011). "asPECT: asphalt Pavement Embodied Carbon Tool." *Transportation Research Laboratory*, <<http://www.sustainabilityofhighways.org.uk/>> (Mar. 3, 2015).
- U.S. EIA. (2015). "How much electricity does an American home use?" *U.S. Energy Information Administration*, <<http://www.eia.gov/tools/faqs/faq.cfm?id=97&t=3>> (Aug. 10, 2015).
- U.S. EPA. (2015). "Hazardous Waste Regulations." *Wastes – Laws & Regulations*, <<http://www.epa.gov/osw/laws-regs/regs-haz.htm>> (July 22, 2015).
- U.S. EPA. (2014). "Greenhouse Gas Emissions from a Typical Passenger Vehicle." *Office of Transportation and Air Quality*, <<http://www3.epa.gov/otaq/climate/documents/420f14040a.pdf>> (Jan. 5, 2016).
- U.S. Geologic Survey (USGS). (2015). "Water Questions & Answers: How much water does the average person use at home per day?" *The USGS Water Science School*, <<http://water.usgs.gov/edu/qa-home-percapita.html>> (Aug. 10, 2015).

How Ground Improvement Contributes to the Green Building Movement

Chris Woods, P.E., G.E., D.GE., LEED^{AP} BD+C, M. ASCE¹

¹Vice-President, Densification, Inc., 40650 Hurley Ln., Paeonian Springs, VA 20129.

Abstract: Owing to the tremendous efforts of the United States Green Building Council (USGBC) and the development of the LEED rating system, a mechanism has been created to evaluate construction projects from a “green building” standpoint. Using a free, foundation industry-specific carbon calculator tool for this study, the carbon footprint of a theoretical project was evaluated for four separate foundation options on the given site, using consumption data from real projects. Two methods of ground improvement, dynamic compaction and aggregate piers were the first two options considered, the third option was driven pile foundations, and the final option was a full removal of the unsuitable fill material and replacement with imported structural fill. Results of the study indicated that under the assumed conditions, ground improvement programs can have a carbon footprint on the order of 2 to 6% of the footprint associated with full removal of the fill material to send to a landfill. As such, this paper recommends that further evaluation be given towards establishing a new LEED credit related to geotechnical construction issues, or at minimum, establishing a carbon footprint reduction scorecard that could be incorporated into the existing LEED infrastructure.

INTRODUCTION

As we continue forward in the 21st Century, the concept of sustainability has come to the forefront as a generation of engineers, architects, and scientists wrestle with ways to reduce our impact on the environment, and conserve our natural resources. As part of the LEED Rating System (presently on v4 for Building Design and Construction – the focus of this paper), new structures can achieve varying levels of certification, based on the level of points achieved on the LEED scorecard. Points can be obtained as they relate to the site, transportation access to a site, to the energy features of a building, to water efficiency, the materials and resources used in construction of a building, and to indoor air quality.

From a geotechnical engineering standpoint, however, there are very few ways to directly contribute points towards the LEED certification of a building. Sure, steel piles can count towards material reuse credits if the material is recycled, or energy piles can be considered as part of a geothermal design, but when it comes to what is in the ground or the earthwork aspects of a project, the LEED rating system does not have a clear way to account for sustainable aspects of geotechnical design and construction.

Those familiar with the foundation industry are aware that there are generally two types of foundation conditions which can exist. First, you can have soils with suitable

bearing characteristics on which shallow foundation systems are constructed. Alternatively, if poor soils are present, deep foundation elements can be installed to transfer the structural loads to more suitable bearing layers at depth. In the middle of these two alternatives, however, lies the field of ground improvement. Utilizing a wide variety of ground improvement techniques, marginal soils can be improved to allow for the use of shallow foundation construction with minimal long-term settlements.

When considering sustainable aspects of geotechnical construction, ground improvement is one of the first aspects that comes to mind. The entire intent of ground improvement is to utilize and improve the in situ soils at a site, rather than removing them or installing foundation systems which bypass them. In doing so, it is possible to divert a significant stream of materials from either being removed from a site and sent to a landfill, or cause the need for resources to be expended constructing more substantial and more costly deep foundation systems.

In 2012, the European Federation of Foundation Contractors (EFFC) and the Deep Foundations Institute (DFI), the EFFC-DFI Carbon Calculator Tool, which is used to evaluate the carbon footprint for common foundation-related techniques (both from a ground improvement and deep foundation standpoint) that are used throughout the industry. In creating the calculator, EFFC-DFI developed a way of evaluating geotechnical aspects of construction projects in a manner that could potentially be used to contribute towards LEED certification points on a project, if properly utilized.

LEED v4 FOR BUILDING DESIGN AND CONSTRUCTION

Presently, there are eight main categories which comprise the LEED v4 checklist: Location and Transportation, Sustainable Sites, Water Efficiency, Energy and Atmosphere, Materials and Resources, Indoor Environmental Quality, Innovation, and Regional Priority. Out of the eight categories (which comprise a total of 12 prerequisites and 46 credits), only four prerequisites/credits tangentially touch on geotechnical-related aspects of a construction project, and none relate specifically to the sustainable aspects of ground improvement and foundation design.

A brief summary of each prerequisite/credit that relates to geotechnical aspects of construction is as follows:

- *Energy and Atmosphere Credit – Renewable Energy Production* – This credit is loosely related to geotechnical construction when it comes to geothermal aspects of foundations. A new and emerging technology is the use of “energy piles”, which utilize pile foundations as individual geothermal elements.
- *Materials and Resources Prerequisite – Construction and Demolition Waste Management Planning* – In the materials and resources section, the second prerequisite requires the preparation of a plan as it relates to the reuse and recycling of as much construction and demolition waste as possible on a project.

- Materials and Resources Credit – Construction and Demolition Waste Management – The overall intent of this credit is to recycle and/or salvage nonhazardous construction and demolition materials. It specifically excludes, however, excavated soils and land-clearing debris.
- Innovation Credit – This final credit of the LEED v4 scorecard is a catch-all innovation credit. It allows for points to be earned for achieving “significant, measurable environmental performance using a strategy not addressed in the LEED green building rating system.” At present, this credit presents the only potential option for achieving LEED points related to geotechnical construction.

As can be seen, there are limited opportunities, at best, for geotechnical components of a project to contribute to the LEED certification of a building, as the system is currently comprised.

EFFC-DFI CARBON CALCULATOR TOOL

Over the last 15 years or so, several methods of calculating the carbon footprint of an organization, product, or project have been developed. All methods generally fall into one of two categories: corporate standards or product standards. Corporate standards are more geared towards an organization, whereas product standards are more geared towards a particular project or product. Regardless of the differing standards, all calculators are based on a single underlying principle, as shown in Equation 1:

$$\text{Carbon Footprint} = \sum[(\text{Activity Data}) * (\text{Emission Factors})] \quad (1)$$

In calculating the carbon footprint, the summation of the data represents the boundary condition for which all activities within are included, and then each activity is multiplied by an emission factor which converts the emissions of each activity into an equivalent tonnage of carbon dioxide (CO₂eqv). The difference between standards then boils down to establishment of the perimeter (i.e. which activities are included) and which emissions factors are used.

Presently, there are several entities within the foundation industry that have developed carbon calculator tools for their own uses. The EFFC and DFI, with the assistance of Carbone 4, recently teamed to develop a carbon calculator tool for the foundation industry which uses a sector-specific carbon accounting methodology which can be used in a consistent manner across all foundation-related projects. The initial version of the calculator was made available in 2012; version 2.1, released in 2013, is the most current version of the calculator.

Emissions generally fall into two main categories: primary and secondary emissions. Primary emissions include manufacturing of materials, their transportation to a job site, and then the emissions generated as part of the construction process.

Secondary emissions include items such as transportation of people and equipment to and from a site, depreciation of equipment, and the transportation and treatment of waste materials from a site. As such, six main categories are used as part of the EFFC-DFI calculator tool: materials, energy used on site, people's transportation, freight transportation, assets depreciation, and waste. It should be noted, that the emissions factored into the EFFC-DFI calculator focus on from the manufacturing phase through the installation phase. Emissions factors from the use and end-of-life aspects of the life cycle are not included as part of this specific calculator.

EXAMPLE PROJECT – SINGLE-STORY WAREHOUSE STRUCTURE

In an effort to highlight the contributions that ground improvement can make to a project from a sustainability point of view, a theoretical project was examined using the EFFC-DFI Carbon Calculator Tool, using consumption data from actual projects. This project was based on the construction of a single-story warehouse building having a footprint of 50,000 square feet (4,645 square meters) on a site where 15 feet (4.6 meters) of miscellaneous fill material exists. Four foundation scenarios were evaluated as part of this study:

- Building founded on shallow foundations following dynamic compaction program to improve the fill;
- Building founded on shallow foundations after installing aggregate piers through the fill;
- Building founded on shallow foundations bearing on structural fill placed once the miscellaneous fill was removed and sent to a landfill;
- Building founded on pile foundation system.

Based on actual project information for a similar site, structural loads for the building were assumed to be 150 kips (667 kN) per column, 500 pounds per square foot (psf) (24 kPa) of live load on the floor slabs, and 5,000 pounds per linear foot (plf) (74 kN per meter) around the perimeter footings. Column bays were assumed to be on a 50-foot by 50-foot spacing (15.24-m by 15.24 m). A description of each of the four evaluations, including the input data specific to each case is provided below.

Scenario No. 1 – Dynamic Compaction

In this scenario, the in-place miscellaneous fill was assumed to have been improved using a dynamic compaction program. Fill material typically improved by dynamic compaction consist of sand and gravel materials with generally less than 20% minus 200 type material. Based on sites with similar soil conditions, a program consisting of two passes using a 10-ton weight dropped from a height of 50-feet (15.24 m), with 5 to 7 drops per point on a 12-foot (3.66 m) grid spacing was considered. Based on an average assumed production of 5,000 square feet (465 square meters) a day, a total of 10 working days was estimated to complete the dynamic compaction program.

The equipment used to be as part of a dynamic compaction program described consists of an American 700 series (60-ton) crawler crane and a crew of three men. Average fuel consumption is about 75 gallons of diesel per day, or about 750 gallons

over a two week period. Three low-boy trucks are required to mobilize the crane to the job site, and so a total of six round trips was included for mobilization/demobilization. No raw materials are used during this process, and no waste is generated.

Scenario No. 2 – Aggregate Piers

The second ground improvement scenario considered was to install aggregate piers to improve the fill and provide the necessary vertical support for the structure. For this study, it was assumed that 30-inch diameter piers were installed to a depth of 15 feet (4.57 m) (through the fill material). The aggregate material used in these types of piers generally consists of 2-inch minus well-graded stone material. This material is generally a quarry-processed type aggregate, given the need for relative uniformity of the piers. The vertical working load for each pier was anticipated to be 70 kips, based on project data. Based on the building loads described above, a total of 36 piers would be needed for the twelve columns, 64 piers around the perimeter footing, and using a 12-foot by 12-foot (3.66 m by 3.66 m) spacing for floor slab support, and additional 347 piers for slab support. In total, 450 piers were anticipated to be required for this project. Expecting that 30 piers could be installed per day, a total of 15 working days was estimated to complete the aggregate pier program.

Equipment used to install aggregate piers consists of a backhoe-type machine, fitted with the aggregate pier drilling equipment along with a front end loader to deliver stone to the hopper of the drilling machine. A four man crew is typical for this type of aggregate pier program. Average fuel consumption for the two pieces of equipment is about 75 gallons of diesel per day, for a total of about 1,125 gallons of diesel for the entire job. Each piece of equipment is delivered to the site on a single truck, and so four round trips were included for mobilization and demobilization. From a material standpoint, approximately 2.75 cubic yards (2.1 cubic meters) of stone is required per pier, or approximately 1,250 cubic yards total; however, no waste is generated from this process.

Scenario No. 3 – Driven H-Pile Foundations

The third foundation option for the site being considered was to install driven steel H-piles for structural support. In this case, it was assumed that Grade A36 Steel HP10x42 piles could provide allowable axial capacity of 50 tons (445 kN) per pile for 30-foot (9.1 m) long piles. Based on the estimated building loads, a total of 36 piles were estimated for the column loads, another 45 piles for the perimeter wall footing, and a total of 250 floor slab piles based on the tributary area associated with a 500 psf floor loading. In total, approximately 331 piles would be required for this particular building. Anticipating that 25 piles could be installed per day, a total of 15 working days was estimated for pile installation.

Equipment used in pile driving operations generally consists of a conventional crawler crane with pile leads and hammer attached and a loader to move piles around the site from the stockpile to installation location. Average fuel consumption for the two pieces of equipment was estimated to be about 75 gallons of diesel fuel per day, for a total of about 1,125 gallons of diesel over a three week period. The pile driving rig was assumed to be delivered on three trucks, with the loader requiring a fourth truck. In total, eight round trips were included for the project. HP10x42 piles have a weight of approximately 42 pounds per linear foot. Assuming 331, 30-foot long piles, approximately 417,000 pounds of steel is needed for scenario, and no waste was assumed to be generated.

Scenario No. 4 – Removal of the Miscellaneous Fill and Replacement with Select Fill

The final foundation scenario considered was the complete removal of the miscellaneous fill material for off-site disposal, and replacement with select granular fill material. Following the completion of the removal and replacement program, the building would be founded on typical shallow foundations. For the purposes of this study, it was estimated that this work could be completed in a 15-day span.

Utilizing a treatment footprint of 50,000 square feet, and assuming that the 15 feet of fill is removed, a total of approximately 28,000 cubic yards of material would be exported as waste and then imported for placement as structural fill. In the Carbon Calculator, the trucking associated with the export and import operations is addressed in the waste and materials sections, respectively. During the on-site operation, it is assumed that a bulldozer, a dump truck, and a compactor would be in operation full-time during the 15-day period, and use an average collective fuel consumption of 75 gallons of diesel fuel, for a total of approximately 1,125 gallons of fuel on the project.

Results

Using the assumptions outlined above, the EFFC-DFI Carbon Calculator was used to estimate the total carbon footprint associated with each of the four scenarios. A tabular summary of the pertinent carbon components is provided in Table A.

Table A. Summary of Carbon Output for Each Foundation Scenario

	Dynamic Compaction	Aggregate Piers	Pile Foundations	Removal and Replacement
Materials	0	20	354	453
Energy	10	15	15	15
Freight	0	9	3	195
Mob/Demob	2	1	2	1
Transportation	1	2	3	3
Assets	0	0	0	0
Waste	0	0	0	80
Totals	13	47	380	750

*Note – all values provided are in tons of Carbon Dioxide Equivalent (tCO₂eqv).

The carbon dioxide equivalent for each component was calculated by multiplying the activity data outlined in each of the scenarios by the emission factor included in the calculator tool. The factors chosen by the creators of the calculator were the ones calculated using the most closely aligned methodology to the individual component. Sources included in the calculator database were obtained from Ecoinvent, Bilan Carbone V7, Sustainableconcrete, ICE v2, DEFRA, IEA 2012 and EcoTransit.

It is important to note, that the results for the four cases outlined above are based on real consumption data and boundary conditions from projects similar to the ones described and considered herein. However, given the fact that most projects do not implement multiple foundation systems on the same site, it was not feasible to provide results from a single site for comparison purposes.

CONCLUSIONS

As can be seen in Table A, there is a significant variation in the carbon footprints associated with each of the four foundation scenarios evaluated. At either end of the spectrum, the dynamic compaction program had a footprint that was less than 2% of the footprint associated with a full removal and replacement program, with the aggregate pier and pile options falling in between and representing 6% and 51%, respectively. One conclusion that can clearly be drawn from the data is that the successful implementation of a ground improvement program can significantly reduce the carbon footprint of a project, when compared to a deep foundation system or full removal and replacement.

So what are the next steps with respect to geotechnical construction and sustainability? One option could be to create a new credit in the Materials and Resources section which establishes threshold values for reduction compared to a baseline that, if achieved, can earn points on the LEED scorecard. Alternatively, in the absence of a new credit, a similar type of scoring system could be utilized with some consistency within the Innovation Credit. In doing so, it could ease the process for gaining points, by not having to recreate a job-specific scoring system on every project where ground improvement is being considered.

Regardless of the avenue chosen, it stands to reason that implantation of ground improvement programs can contribute significantly to a project from a sustainability standpoint, and should be considered as part of the LEED scorecard in some manner.

ACKNOWLEDGMENTS

The author would like to acknowledge the ongoing efforts by the USGBC, EFFC, and DFI towards advancement of the foundation industry, while at the same time being considerate of the long-term effects of the construction industry on the planet. Additionally, many thanks are given to the President of Densification, Inc., Joe Drumheller, for his support of endeavors such as this paper, in the best interests of the industry and environment.

KEYWORDS

Sustainability, dynamic compaction, aggregate piers, ground improvement, LEED v4 for Building Design and Construction, Carbon Calculator Tool

REFERENCES

Lemaignan, Benoit and Wilmotte, Jean-Yves (2014). “EFFC DFI Carbon Calculator Tool, Version 2.3”. *The European Federation of Foundation Contractors (EFFC) and Deep Foundations Institute (DFI)*. Web. 31 July 2015. www.geotechnicalcarboncalculator.com.

Skyline Steel. “Steel Foundation Systems Product Manual”. Parsippany, New Jersey. Undated.

Tensar Company. “Course Notes from GeoPier Technical Workshop”. Phoenix, Arizona. 4 to 6 October 2012.

United States Green Building Council (USGBC). “LEED v4 for Building Design and Construction”. Washington, D.C. 1 July 2015.

Sustainable Geotechnical Design for Al-Azhar Park, Cairo

Ahmed Hosny Abdel-Rahman¹ and Salwa Yassin²

¹Professor, National Research Center, Cairo, Egypt.

²Senior Geotechnical Engineer, Dar Al-Handasah Consultancy, Cairo, Egypt.

Abstract: A national park was constructed at Al-Azhar district in the capital of Egypt. The park site was historically covered with several tons of fill and waste material dumped over decades. The fill material was in a dry condition and susceptible to considerable settlement upon wetting. A major potable water network which consists of tanks and pipes, with piled foundations, exists in the site. Considering the existing social and environmental hazards, due to the site location and its constituents, it was decided to transform the site into a national park serving the community. A sustainable geotechnical design was investigated and applied in order to eliminate the anticipated environment and economic hazards due to geotechnical construction works for such large site. Design or construction technique that might cause damage to the existing water tanks and pipes, or pollution to the surrounding environment was avoided. This paper presents case history on the sustainable geotechnical design successfully applied to the site of Al-Azhar park.

INTRODUCTION

Geotechnical engineering is normally regarded as the most resources intensive discipline within civil engineering due to the consumption of a considerable amount of material including re-figuring the landscape and site grading. This paper presents case history for a sustainable geotechnical design for a site in Cairo, which was covered with heterogeneous fill and waste material for decades, shown in Figure 1, then converted to a national park for public use. The site is about 80 acres and the waste material was up to 15m to 40m height formed since the Fatimid Islamic civilization in Cairo (more than 600 years). The site was an environmental hazards as it contributed to carbon emission and dust affecting the heart of Cairo. It was decided to utilize the site and its unique location by transforming it into an attractive green park. The site constraints comprised huge amount of waste material and its constituents, an existing water pipe network and three major potable water tanks founded on piles. All these constraints, represented great challenges for geotechnical design. Sustainable geotechnical design through utilizing site material, recycling, adopting local products and manpower, was adopted. The applied geotechnical design had a major positive economic impact on the project, and also beneficial to the environment by preventing huge amount of excavated waste materials.



FIG. 1. Fill and waste material across the site of Al-Azhar park

LITERATURE

Civil engineering, in general, covers wide range of projects that is in close effect to human society footprint, such as buildings, roads and infrastructures. Geotechnical engineering, in specific, interferes many social, environmental and economic issues (Jefferis 2008). Implementing sustainable approach in geotechnical engineering has been surrounded with difficulties, where the profession is often dominated by financial motivations (Abreu et al. 2008). In addition to budgets constraints, the scarcity of a direct and simple qualitative measures or framework for sustainability in geotechnical engineering makes it more difficult to assess any proposed design (Abreu et al. 2008). For most of the project, there is always a conflict between the economic and environment protection aspects, which always advocates the sustainability of the project.

Sustainability means prudent acknowledgement and application of; (i) robust design and construction that involves minimal financial burden and inconvenience to the society, (ii) minimal use of resources and energy in planning, design, construction and maintenance of geotechnical facilities, (iii) use of materials and methods that cause minimal negative impact on the ecology and environment and (iv) as much reuse of existing geotechnical facilities as possible to minimize waste (Gradel 1997, Kibert 2008).

Most of the available evaluation procedures for sustainability share the same considerations for the effect of the geotechnical design with views of life cycles, environment and economic contributions to the surrounding community. Consideration to the balance between optimum use of the available resources and material with minimum negative impact on the surrounding society would be the optimum approach towards sustainability along with economic and social benefits. The case history in this paper is a geotechnical design that covers the main aspect of sustainability; cost, environment and ecological cycle, without hindering the safety of the geotechnical design.

PROJECT DESCRIPTION AND SITE CONDITIONS

For centuries, since the Fatimid Caliphate, the area designated for Al-Azhar park had been used as a dump area for fill material and rubble of demolished structures. The thickness of the fill layer varies between 15m to nearly 40m. The site is bounded in the East by Salah Salem Highway, in the South by Bab Al-Wazir cemetery, in the West by the historic wall of old Cairo and in the North by Al-Azhar Street. Figure 2 shows a general layout for the park and its boundaries.

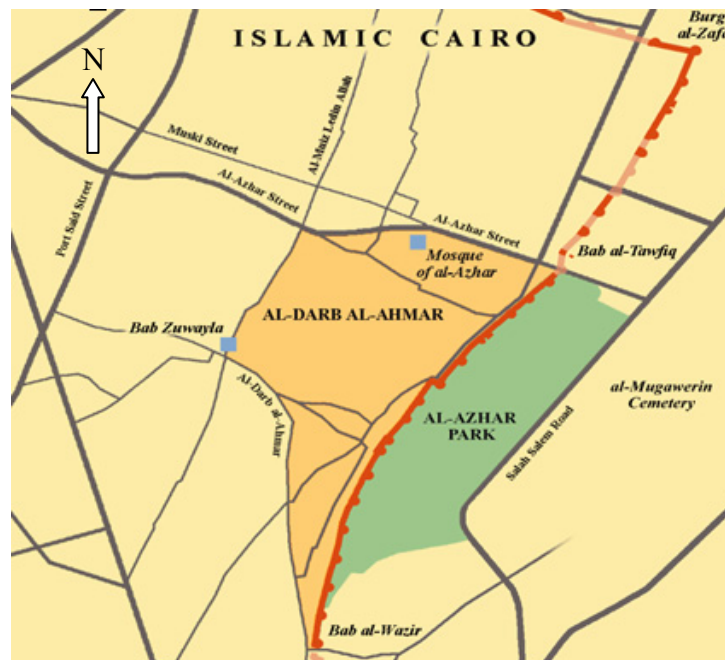


FIG. 2. General layout of Al-Azhar park site

A comprehensive geotechnical investigation program was carried out to identify the properties and extent of the fill material on site. The existing fill material mainly comprised silt and sand size materials, rubble, pottery pieces, and small percentage of waste material. The depth of the investigation extended to 40m from the existing ground level and no ground water was encountered during the investigation. In general, the subsurface profile consisted of a thick layer of dry fill overlying a natural dense sand layer. About 40% of the site are formed from steep slopes as shown in Figure 1.

The site also contains three major tanks of 80 m diameter and 8 m deep for potable water as shown in Figure 3. The tanks are linked with cast iron pipe network distributed across the site. The entire system (tanks and pipes) are supported on piled foundation.



FIG. 3. The existing potable water tanks

GEOTECHNICAL CHALLENGES

The site is situated in the middle of the heavy populated city of Cairo. Moving the existing mountains of fill and waste material was not possible, as it would have required a new dump area outside the city and increase air pollution.

During the geotechnical investigation, a considerable loss of drilling fluid, in many boreholes was observed indicating discontinuities and open skeleton structure within the fill layers and potential for collapse due to additional loads. Silt migration from the fill matrix was observed after wetting, leaving a relatively weak matrix of soil that would severely settle under loading (Abdel-Rahman, 2002). Further investigation and testing revealed that the fill layer would experience settlement upon wetting up to 30 cm.

The existing water tanks and pipe network, founded on piled foundation within the fill material, were expected to experience considerable settlement upon wetting from irrigation process, and consequently additional loads due to negative skin friction that could exceed the design capacity of the existing piled foundation.

Laboratory testing proved that, the existing fill material was not suitable for plantation due to an extremely high salt content.

The approach of the geotechnical design was to isolate the existing fill from the required planting soil by a hydraulic barrier to eliminate irrigation water from reaching the underlying fill material, and hence avoid settlement, in addition to minimizing the differential settlement along the park roads.

Geomembranes and clay liners could be used to prevent water to penetrate the subsurface soil layers (Wissa and Fuleihan, 2000). A comparative study was conducted between geomembrane sheets and clay liner as a hydraulic barrier. The choice between the two types of barrier was based on factors such as cost, construction, availability, local experience, long term performance, maintenance required for the existing pipe network and the required excavation. Based on the comparative study the clay liner was selected and applied with compaction on site.

ECONOMIC CHALLENGES

The required earthwork across the site comprised excavation, disposing, importing, and re-working of onsite fill or engineering fill materials. The amount of excavation work required to reach the final designed grade from the existing level was estimated to be nearly two million cubic meters. It was also required to import nearly 0.5 million cubic meter of approved engineering fill for the construction of roads and embankment within the park, and another 1.0 million cubic meter of planting soil suitable for cultivation and agriculture.

The allocated budget for the required earthwork across the park represented the major part of the overall budget of the project. Also the cost of the required treatment for the subgrade material to overcome the shortcomings of the heterogeneous fill layer and protect the existing pipes network constituted a controlling item in the project budget. Therefore, innovative ideas to reduce the cost of earthwork, and subsequent cost associated with geotechnical treatment and land preparation were required.

ENVIRONMENTAL CHALLENGES

Disposing of nearly two million cubic meters of waste material from Cairo would be a major source of environmental hazard, and would add to the existing traffic problem within the city. In addition, up to 10% - 45% of the existing heterogeneous fill was dry fine material (smaller than 0.075 mm), that would cause dust problems during high winds when mobilized. Figure 4 shows the particle size distribution of different samples of the existing fill with high percentage of fines, mainly silt.

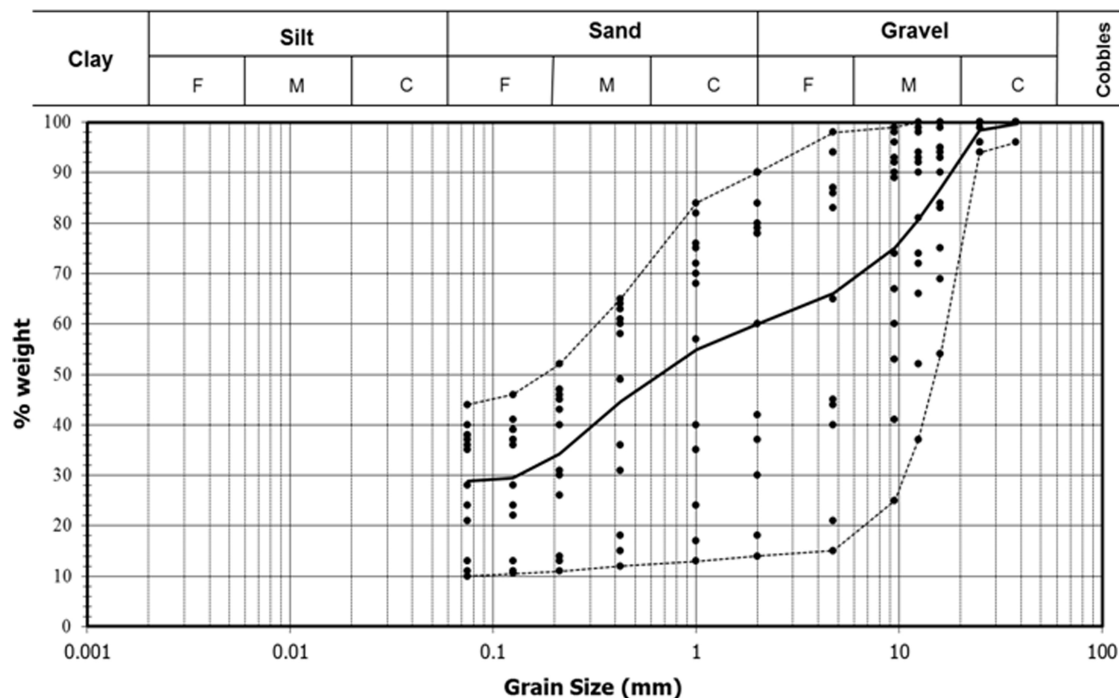


FIG. 4. Particle size distribution for different fill samples across the site

SUSTAINABLE GEOTECHNICAL SOLUTION

The approach adopted to overcome site challenges was applying geotechnical treatment to the fill layer depending on the available site material through recycling. This concept was achieved by recycling the fill material that had to be excavated from the site to reach the final designed grade levels. However, to improve the gradation of the site fill material, it was decided to utilize a uniform sorted material from a near borrow area. The excavated material from the nearby Al-Azhar tunnel project site was used for the park construction. This solution dramatically decreased the amount of material required to be disposed away from the tunnel site, while acting as near borrow area for the park. Consequently, enormous cost saving was realized and the environmental impact was minimized.

Al-Azhar Tunnel Excavated Sand

The park construction was running in parallel to the excavation of Al-Azhar tunnel that is located 100 meters away, on the northern side of the Park (Figure 2). The tunnel is running through well sorted siliceous sand at depth of 25 m below the existing ground level along its alignment. The tunnel construction company exported the excavated sand to the park site for further used. The particle size distribution of the excavated sand from the tunnel is shown in Figure 5.

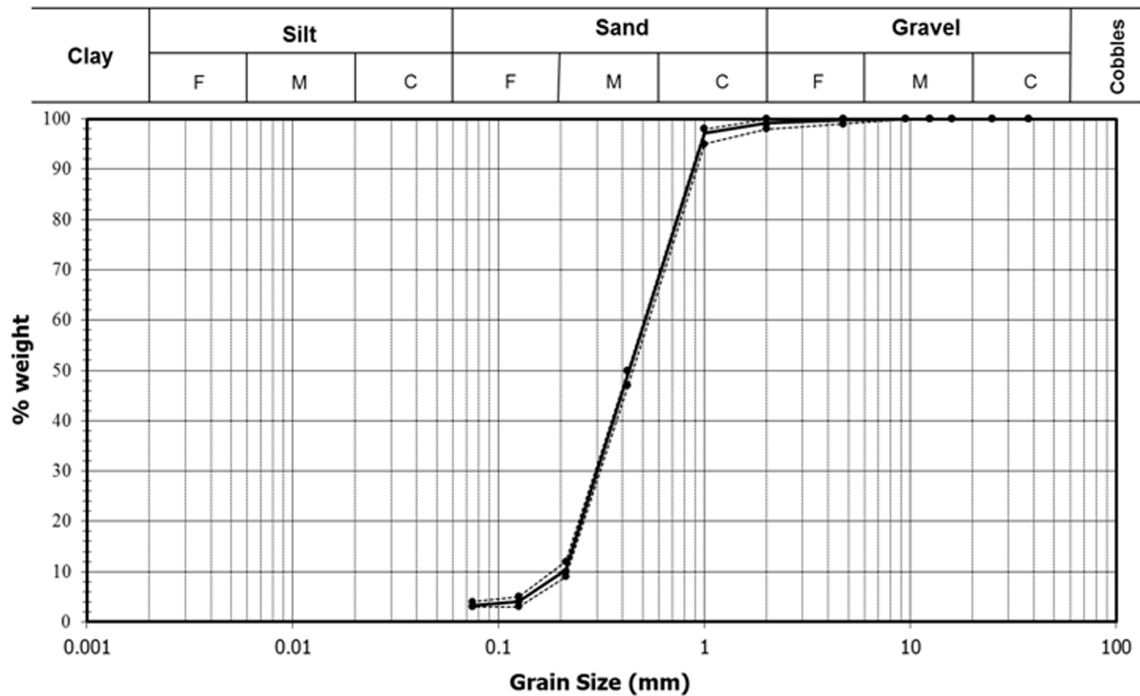


FIG. 5. Particle size distribution of the excavated sand from AL-Azher tunnel

Recycling of the Park Site Fill Material

The heterogeneous fill material at the park site was sieved on three consecutive large sieves, specifically manufactured for the project, with opening sizes of 5 mm, 20 mm, and 40 mm. The retained materials on top of the coarsest sieve was disposed as waste or unwanted out-sized material. The other sieved materials were piled up on separate locations for the re-use. Figure 6 shows the average grain size distribution produced from the sieving process. These materials were re-mixed with the tunnel sand to produce stable materials for geotechnical works and roads embankment as per the new design for the park.

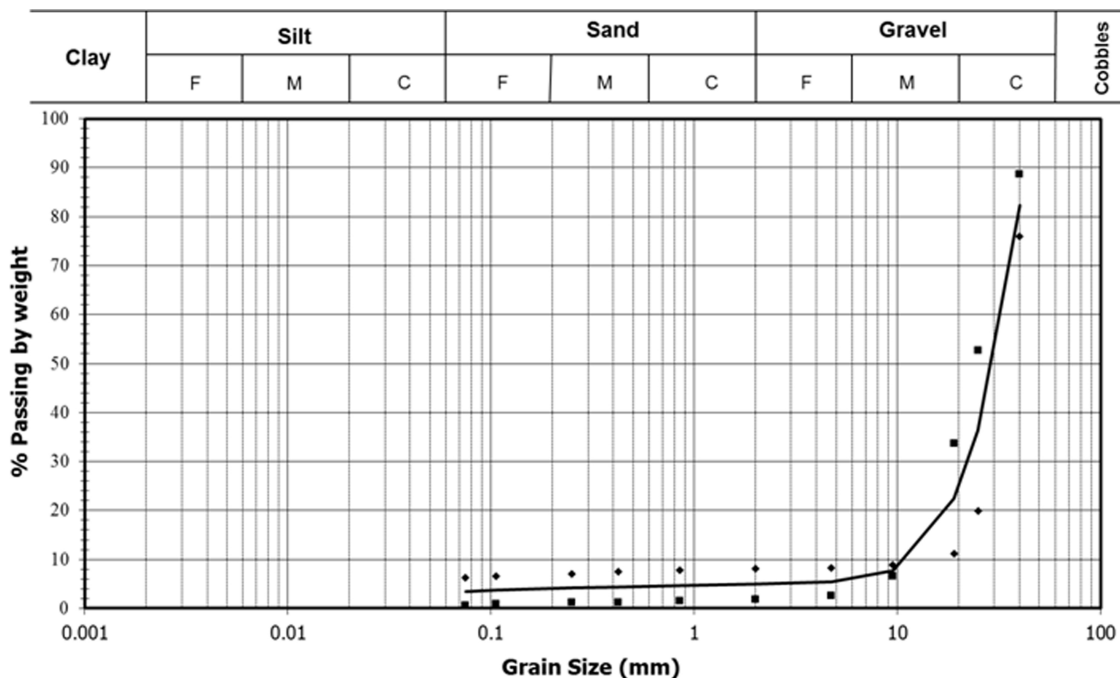


FIG. 6. Average particle size distribution of sieved material on-site

Hydraulic Barrier

The anticipated settlement of the existing fill was prevented by hydraulically isolate the existing fill from the planting soil layer, by applying a relatively impermeable liner on the top of fill layer. Two types of liners, referred to herein as clay liner and slope liner, were designed using a mixture of the sieved material on site and different percentage of an imported clay. Clay liner was designed with low permeability to minimize water infiltration and applied on nearly flat slopes (4H:1V or flatter). For the rest of the slopes on site, which is steeper than 4H:1V and water run-off was expected, slope liner was applied. Finally, a drainage network was installed on top of the liner to collect the excess water and minimize the amount of perched water on the liner.

Clay Liner

Clay liner was produced from a homogeneous mixture of an imported high-plastic clay (CH) and the fill material passing the 5 mm sieve with a mixing ratio of (1:2 by volume) respectively. The clay used in the mixture was imported from a borrow areas near Katamia-Suez road located 40 km from the site. The liner was applied in two layers with total thickness of 30 cm with compaction to a minimum field density of 90% of the maximum dry density measured in a laboratory modified proctor test. Figure 7 shows the results of a comparative study carried out on the clay liner, using field and laboratory test results to confirm the achieved dry density and level of compaction on site.

Finally, an infiltration test was conducted on a tested strip on site to check the overall performance of the liner versus the laboratory permeability tests results. The infiltration test lasted for a week and no water infiltration was observed (Abdel-Rahman, 2001).

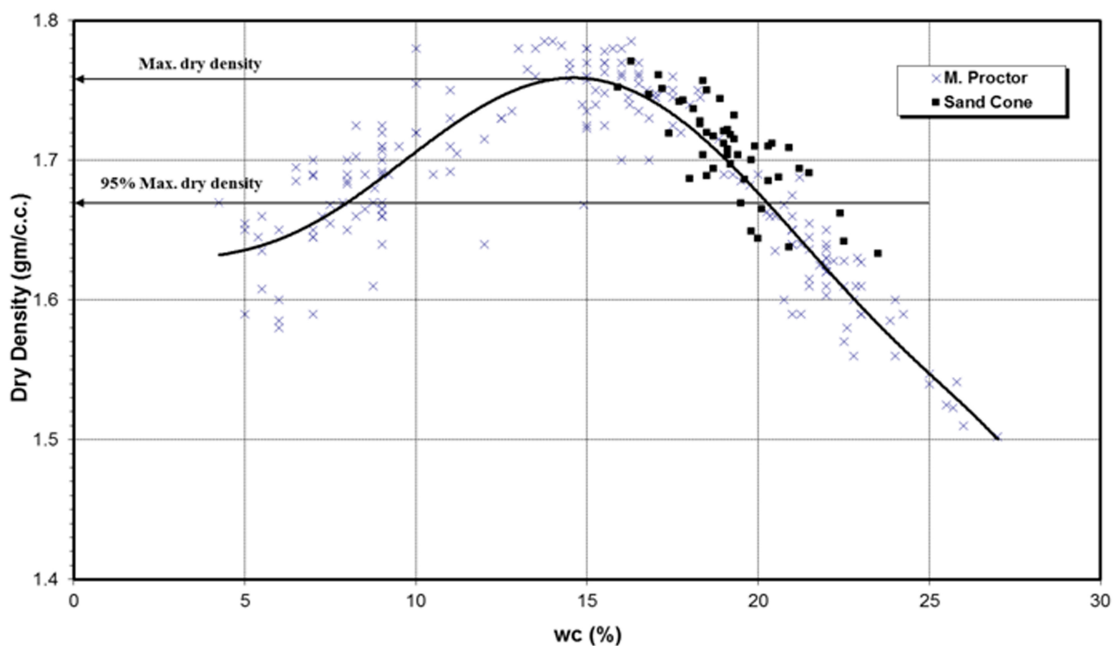


FIG. 7. Field and laboratory compaction test results on clay liner

Slope Liner

Step slopes on the site were designed for a maximum slope of 2H: 1V for stability purposes and to facilitate plantation and maintenance operations. Slope liner was a mixture of the site fill material passing sieve size 5 mm and the imported clay with mixing ratio of (1:1 by volume). The liner was applied in 20 cm thick layer and compacted to a minimum field density of 90% of the maximum dry density measured in a laboratory modified proctor test.

Road Embankment

There was about 22 km length of roads throughout the park and several embankments with varying height from 1.0 m to 2.5 m. In order to reduce the cost of the imported engineering fill material required for roads and embankments, two types of engineering fill were used. First type, which is referred to as site structural fill and represented the major part of the required fill material, is based on a mixture of the sieved site material and the imported tunnel sand. The second type is an imported approved engineering fill material, placed on two sub-layers of 20 cm each and compacted to 95% of the maximum dry density measured in laboratory modified proctor tests.

The structural fill material, constituted of the coarse sieved soils (passing sieve 40 mm and retained on sieve 5 mm), and mixed with the tunnel sand. Following several trials, the general mixing ratios between these materials ended up with 20% of the coarsest sieved materials (passing sieve size 40 mm), 60% of the materials passing sieve size 20 mm, and 20% of the tunnel sand. These ratios were susceptible to slight changes depending on the available grain size distributions produced out of the sieving process. The geotechnical properties of the site structural fill were categorized as non-compressible soil type A-1-b according to AASHTO, with minimum dry unit weight of 1.80 t/m^3 .

Planting Soils

A considerable amount of planting soils was required to be backfilled on top of the liner for agricultural purposes. The existing fill on site was proven to be unsuitable for plantation due to the high salt content. The tunnel sand was found to have a reasonable salt content that could be reduced by washing. Therefore, it was decided to directly use the tunnel sand as planting soil. Figure 8, shows the final layout of planting zones across the park.



FIG. 8. Final layout of the park

CONCLUSION

Geotechnical engineering deals with natural conditions of surrounding environment through producing and/or consuming natural material which affects the surrounding landscape. Therefore, adopting sustainable design at an early stage of planning and design is the key towards sustainability. This paper presented case history and sustainable geotechnical design successfully applied positive economic and environmental impact. The project improved environmental and esthetic hazard of the city and contributed in reducing carbon emission and dust through development of new green area.

ACKNOWLEDGMENTS

The authors appreciate the support of the International Engineering Foundation and the Agha Khan Cultural Services (AKCS).

REFERENCES

- Jefferis, S.A. (2008). "Moving towards Sustainability in Geotechnical Engineering." *Proc. of the Geo Congress 2008*, Geotechnical Special Publication No. 178, 844-851.
- Abreu, D.G, Jefferson, I., Braithwaite, P. A. and Chapman, D. N. (2008). "Why is Sustainability Important in Geotechnical Engineering." *Proc. of GeoCongress 2008*, Geotechnical Special Publication No. 178. 821-828.
- Gradel, T.(1997). "Industrial Ecology: Definition and Implementation." *Industrial ecology and global change*, Socolow, R., Andrews, C., Berkhout, F. and Thomas, V. (eds.) 23-41.
- Kibert, C.J. (2008). *Sustainable Construction*, 2nd Edition — John Wiley and Sons Inc., New Jersey,
- Abdel-Rahman, A.H. and Sayed M., (2002) "Recycling of Heterogeneous Fill into Geotechnically Stable Soils" *Journal of Soil Mechanics and Foundation*, The Egyptian Geotechnical Society, Vol. (13), part (1).
- Wissa, A., and Fuleihan, N., "Protection of Water Resources Using Natural, and Synthetic Liners". *The Fourth International Geotechnical Engineering Conference*, Cairo University, Cairo, Egypt, 2000.
- Abdel-Rahman, A.H., (2001)." Use of Clay Liner as a Barrier to Eliminate Problems Associated with Wetting of Dry Fill" *Civil Engineering Research Magazine*, Al-Azhar Univ., Vol. (23), No. (4), Oct. 2001, pp 1306-1322

Uncertainty in the Estimates of Embodied Energy and CO₂ Emissions for Ground Improvement: The Influence of Material Haul Distance

Craig M. Shillaber, A.M.ASCE¹; Annie R. Pearce, M.ASCE²;
James K. Mitchell, Dist.M.ASCE, P.E.³; and Joseph E. Dove, M.ASCE, P.E.⁴

¹Assistant Teaching Professor, Dept. of Civil and Environmental Engineering, Northeastern Univ., Boston, MA 02115.

²Associate Professor, Dept. of Building Construction, Virginia Tech, Blacksburg, VA 24061.

³University Distinguished Professor Emeritus, Via Dept. of Civil and Environmental Engineering, Virginia Tech, Blacksburg, VA 24061.

⁴Associate Professor of Practice, Via Dept. of Civil and Environmental Engineering, Virginia Tech, Blacksburg, VA 24061.

Abstract: Geotechnical engineers now have the tools to estimate total embodied energy (EE) and carbon dioxide (CO₂) emissions and may use this information in order to better incorporate sustainable development principles into ground improvement projects. In the early stages of a project, uncertainty arises in EE and CO₂ emissions estimates because many details regarding the specific materials and their sources may be unknown. Therefore, the influence of uncertainty on EE and CO₂ emissions estimates may be significant and should be determined. The streamlined energy and emissions assessment model (Shillaber et al. 2015b) is used in this paper to evaluate the influence of material haul distance on total EE and CO₂ emissions. The case history projects analyzed include the construction of 364 rammed aggregate columns for foundation support of Pearson Hall on the Virginia Tech campus and the installation of deep soil mixing columns to support an earthen embankment for levee LPV 111 in New Orleans, LA. The actual material haul distances were 8 km for Pearson Hall and ranged from 3.2 km to 1,130 km for LPV 111. Assuming no change in transportation mode or efficiency with increasing distance, it was determined that for each multiple of the as-built haul distances, total project EE increases by 4.9% for Pearson Hall and 4.5% for LPV 111; total project CO₂ emissions increase by 3.1% for Pearson Hall and 2.7% for LPV 111.

INTRODUCTION

The need to design for sustainable development in civil engineering practice has led to the advent of environmental impact assessment tools tailored to geotechnical practice. These include the Geotechnical Carbon Calculator (Carbone 4 2014) and the Streamlined Energy and Emissions Assessment Model (SEEAM) (Shillaber et al.

2015b). Environmental impact assessment tools such as the Geotechnical Carbon Calculator and the SEEAM provide data which can enable geotechnical engineers to make decisions more consistent with the principles of sustainable development (Shillaber et al. 2015a).

The Geotechnical Carbon Calculator and the SEEAM are rooted in Life Cycle Assessment (LCA) principles. LCA is a method for quantitatively evaluating the environmental impacts of a product or process over its lifetime (EPA 2006). LCAs may be simplified to account for specific impact factors within narrowed boundary conditions by a process known as streamlining (Todd and Curran 1999). The Geotechnical Carbon Calculator and the SEEAM both implement LCA streamlining. The differences between these methods are described by Shillaber et al. (2015b).

Typically, many construction details that are important inputs into environmental assessment methods are not known at the design stage (e.g., the quantities of materials and fuel required for construction, material and waste haul distances). Uncertainty in estimated geotechnical construction quantities arises from variability in the subsurface conditions, the size of construction equipment, the cost and availability of materials from suppliers, and which material suppliers are used during construction. Based on two case history projects, this paper presents an evaluation of the degree to which varying material haul distance influences the results of embodied energy (EE) (i.e., all energy that is consumed to bring something into its current state (Chau et al. 2008)) and carbon dioxide (CO₂) emissions assessments conducted using the SEEAM. Recommendations are made for how to select material haul distances for energy and/or carbon assessments conducted at the design stage.

The SEEAM Method

The SEEAM is a streamlined LCA method that quantifies EE and CO₂ emissions for ground improvement projects, with boundaries extending from the extraction of raw materials through the completion of construction (Shillaber et al. 2015b). In the SEEAM analysis, total EE and CO₂ emissions include those from: 1) materials (from raw material extraction until they are ready for delivery to the construction site), 2) materials transportation (delivery of materials from suppliers to the construction site), 3) site operations (equipment activity on site), and 4) waste transportation (transporting waste from the site to a disposal facility). The methodology primarily consists of multiplying the quantities of materials, transportation, or fuel by corresponding unit coefficients of EE and CO₂ emissions (Shillaber et al. 2015b).

Case History Projects

Two case history projects were analyzed to evaluate the influence of material haul distance on total EE and CO₂ emissions. These were (1) the construction of rammed aggregate columns to support shallow foundations for Pearson Hall on the Virginia Tech campus, and (2) the application of Deep Soil Mixing (DSM) to improve the foundation soils for support of levee LPV 111 in New Orleans, LA. These projects were selected because of their differences in size, ground improvement technology used, number of materials, and the availability of construction data.

Rammed Aggregate Columns - Pearson Hall

Pearson Hall is a new 6 story replacement dormitory building at Virginia Tech. The foundation design called for shallow foundations supported by 0.76 m diameter rammed aggregate columns. In total, 364 rammed aggregate columns were installed, of which 322 were specified to be composed of cement treated aggregate (CTA) and extend to bedrock. The remaining 42 columns were composed of untreated aggregate (UA) and were to extend to various depths based on their location under the structure.

The contractors and university provided records of material and fuel quantities, as well as installation logs for each column. In total, 3,219 m of CTA columns with an average length of 10 m were constructed using 4,185 tonnes of CTA. A total of 752 m of UA columns with an average length of 5 m and the working pad were constructed of a total of 1,193 tonnes of UA. The aggregate materials were delivered from a supplier located 8 km from the site in a total of 331 truckloads. Machinery used for installing the columns consumed a total of 11,250 liters of diesel fuel.

Deep Soil Mixing Columns - Levee LPV 111

LPV 111 is a section of levee in New Orleans, LA that was overtopped and heavily damaged during Hurricane Katrina in 2005 (Cali et al. 2012). Subsequently, the crest elevation of the 8.5 km long levee was raised by about 3 m in order to withstand a 100 year flood event (Cali et al. 2012). The final design consisted of an earthen embankment supported by panels of overlapping 1.6 m diameter DSM columns. The DSM increased the shear strength of the foundation soils to enable minimizing the footprint of the embankment and help limit settlement (Cooling et al. 2012).

DSM construction involved the use of 417,000 tonnes of 75% slag, 25% Portland cement binder and 454,000 m³ of water to treat 1.4 million m³ of foundation soil (Schmutzler et al. 2012). The binder was delivered to the site by 23 tonne cement tankers; it is estimated that over 18,130 truckloads of binder were used for the construction (Schmutzler et al. 2012; Shillaber et al. 2015b). The embankment was constructed of 400,000 m³ of DSM spoil recycled as embankment fill and 441,000 m³ of compacted borrow soil (Druss et al. 2012). Additional embankment stability was provided by 376,000 m² of geogrid with a mass of approximately 395 tonnes (Kelsey 2012; Shillaber et al. 2015b). In total, the equipment consumed about 6.1 million liters of diesel to complete all construction at LPV 111 (Shillaber et al. 2015b).

METHOD

To determine the influence of different material haul distances on total project EE and CO₂ emissions, a parametric study of the Pearson Hall and LPV 111 projects was conducted in which material haul distances via heavy duty truck were varied. For Pearson Hall, four nearby aggregate suppliers were located, and the distance from each to the construction site was determined using Google Maps. Then, conventional SEEAM analyses were performed for the project considering each different supplier.

A different method was followed for LPV 111 because the DSM required materials from more than one source. Instead of locating nearby suppliers of each material, a

series of increasing multiples of the actual haul distances from the suppliers was applied. For example, a multiple of 1 corresponds to the actual distances and a multiple of 2 doubles all the distances. LPV 111 also involved material transportation by barge; however, the barge distances were not adjusted in this analysis.

Assumptions for Analysis

Five assumptions were made in this evaluation for quantifying the influence of material haul distance on total project EE and CO₂ emissions, as follows:

- 1) There is no change in transportation mode or increase in transportation efficiency with increasing material haul distance.
- 2) When used, distance multiples are applied equally to all materials and haul distances when more than one material and material supplier are used for the construction (e.g., LPV 111).
- 3) Only transportation of materials from the location supplying the construction site is considered to be variable in this assessment. Transportation of materials from their production location to a local supplier is not varied in this analysis.
- 4) All vehicles hauling materials to the construction site operate at the average fuel economy for the vehicle class (primarily U.S. Class 8, heavy duty trucks).
- 5) Transportation for mobilization and demobilization, as well as worker commuting was not considered in this assessment.

RESULTS

Pearson Hall

The aggregate suppliers ranged in distance from 8 km to as far as 77 km from the project site, as shown in Table 1. Supplier 1 was used for construction; the distance from Supplier 1 to the construction site is taken as a base distance. The distance multiple, M , shown in Table 1, is the ratio of the supplier distance to the base distance. The distance multiple was determined for each of the possible suppliers for Pearson Hall in order to compare results between the two case history projects.

Table 1. Truck haul distances from potential suppliers of aggregate and cement treated aggregate for Pearson Hall for use in the SEEAM analysis.

Aggregate Supplier	Distance (km)	Distance Multiple, M
1 (actual)	8	1.0
2	25	3.1
3	42	5.3
4	77	9.6

Fig. 1 shows the increase in total EE and CO₂ emissions for the rammed aggregate columns with increasing distance multiple, M . The increase in EE and CO₂ emissions with M is linear, with total project EE and CO₂ emissions increasing by 94 GJ (4.9%)

and 7 tonnes (3.1%) per unit increase in M , respectively. The maximum distance (77 km, $M = 9.6$) resulted in a 42% increase in total EE and a 26% increase in total CO₂ emissions over the minimum distance (8 km, $M = 1.0$). The proportions of the total EE and CO₂ emissions for materials transportation, materials, site operations and waste transportation vs. distance multiple, M , for Pearson Hall are shown in Fig. 2.

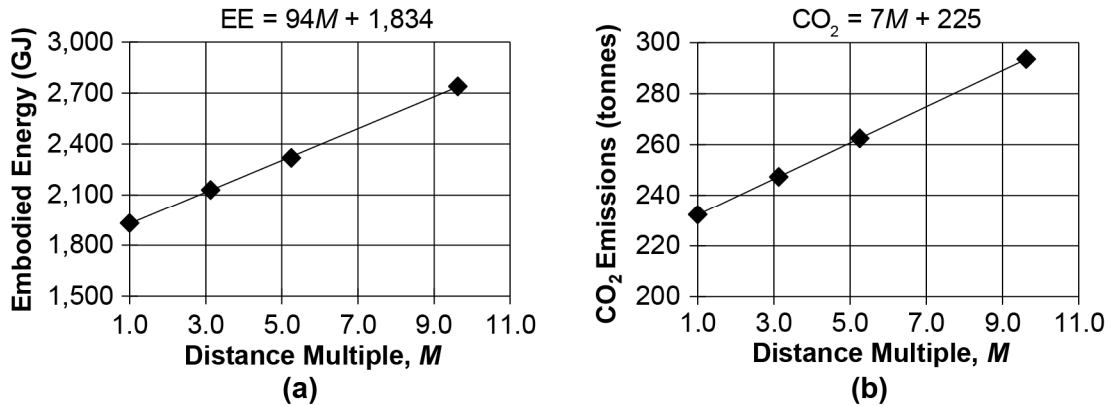


FIG. 1. (a) Increase in total EE and (b) increase in total CO₂ emissions for Pearson Hall with increasing multiples of truck haul distance for materials.

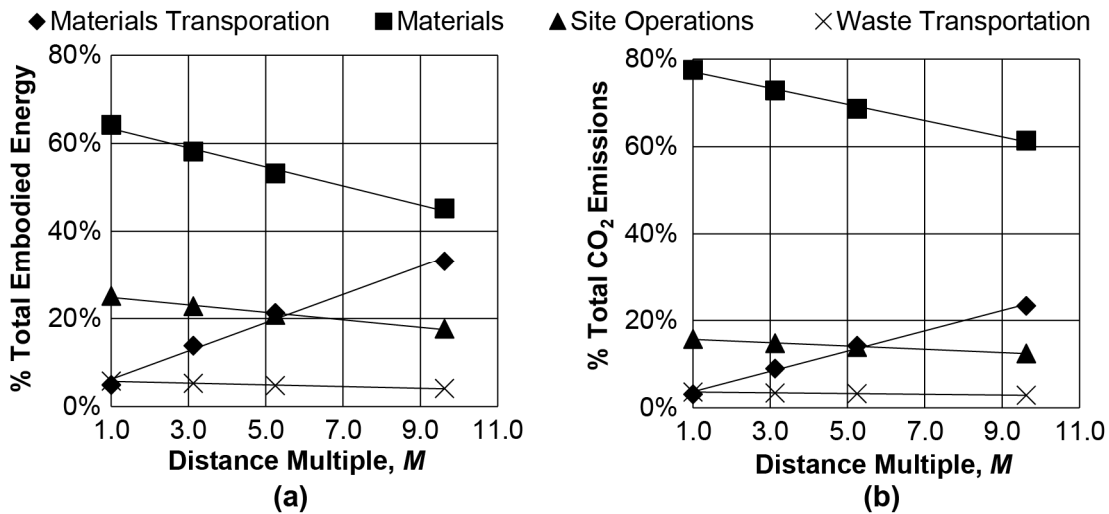


FIG. 2. (a) Proportion of total EE, and (b) proportion of total CO₂ emissions vs. material truck haul distance multiple, M , for Pearson Hall.

Levee LPV 111

Materials were delivered to LPV 111 by more than one mode of transportation. In this analysis, only the variation in trucking distance was considered. The actual truck haul distances were used as base distances. These values were then multiplied by distance multiples of 2, 3 and 4 and the total project EE and CO₂ emissions were determined for each case. Haul distances for each material and each distance multiple, M , are shown in Table 2.

Fig. 3 shows the increase in total EE and CO₂ emissions with each multiple, M , of material haul distances. It was determined that the increase in EE and CO₂ emissions

with M is linear, with total project EE and CO₂ emissions increasing by 53,300 GJ (4.5%) and 4,000 tonnes (2.7%) per unit increase in M , respectively. With all haul distances at 4 times the actual supplier distances, total EE is 14% greater and CO₂ emissions 8% greater than the actual construction case. The proportions of the total EE and CO₂ emissions for materials transportation, materials, site operations and waste transportation vs. distance multiple, M , for LPV 111 are shown in Fig. 4.

Table 2. Truck haul distances used in the SEEAM analysis for each major construction material in the LPV 111 project, by multiple of the actual distances.

Distance Multiple, M	Haul Distance (km)		
	Binder	Geogrid	Borrow Soil
1 (actual)	3.2	1,130	37
2	6.4	2,260	74
3	9.6	3,390	111
4	12.8	4,520	148

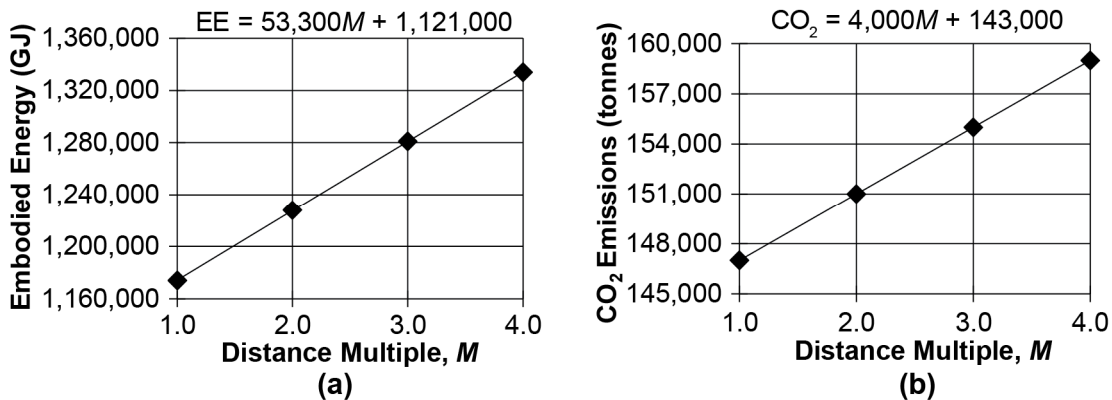


FIG. 3. (a) Increase in total EE and (b) increase in total CO₂ emissions for LPV 111 with increasing multiples of truck haul distances for all materials.

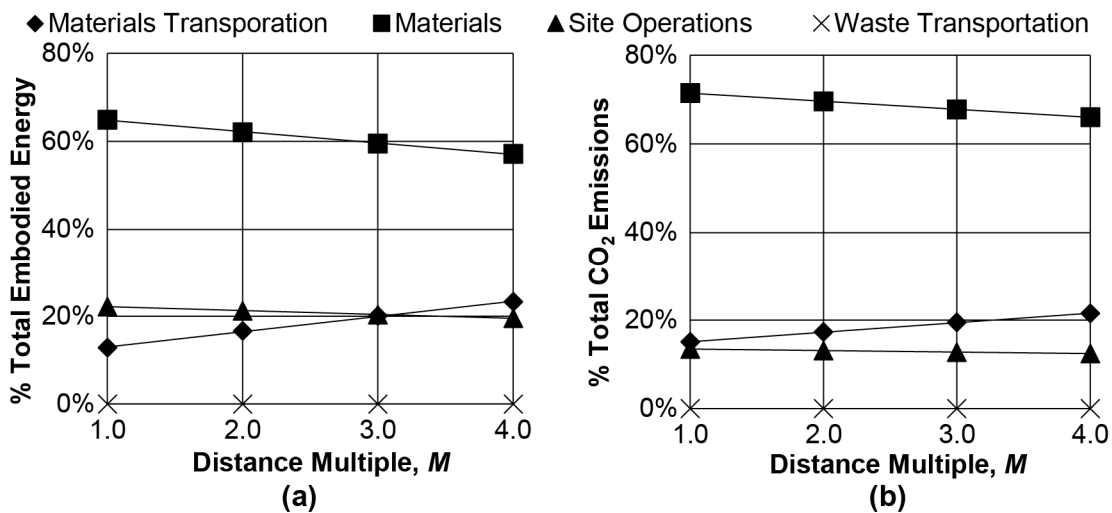


FIG. 4. (a) Proportion of total EE, and (b) proportion of total CO₂ emissions vs. material truck haul distance multiple, M , for LPV 111.

DISCUSSION

The preceding results for the percentage increases in total EE and CO₂ emissions with increasing truck haul distance multiple, M , are similar for Pearson Hall and LPV 111, despite substantial differences between the techniques, materials used and the size of the projects. For instance, the increase in total EE with M is 4.9% for Pearson Hall and 4.5% for LPV 111. Considering both projects, the average increase in total EE with each multiple of material haul distances is 4.7%. The increase in total CO₂ emissions with M is 3.1% for Pearson Hall and 2.7% for LPV 111. Considering both projects, the average increase in total CO₂ emissions with each multiple of material haul distances is 2.9%. Even with the greater percentage increase in total EE and CO₂ emissions with trucking distance associated with the Pearson Hall analysis, tripling the trucking distance ($M = 3$) for all materials results in less than a 10% increase in total EE and less than a 7% increase in total CO₂ emissions.

The linear increase in total EE and CO₂ emissions with increasing distance is attributed to how the SEEAM method accounts for transportation via heavy duty (U.S. Class 8) trucks. For every 1 km distance between a material supplier and the construction site, one round trip made by one heavy duty truck (2 km total distance traveled) is responsible for 0.0355 GJ of EE and 0.0027 tonnes of CO₂ emissions. This is true regardless of whether the truck is fully loaded or empty, as the SEEAM computes EE and CO₂ emissions for trucking based on the amount of fuel consumed by the vehicle given average vehicle fuel economy (Assumption 4). In actuality, there is some variability in vehicle fuel economy based on load, traffic conditions, driver habits, and vehicle age/engine technology. Incorporating additional research regarding the age of the truck fleet, loaded vs. unloaded truck fuel economy and typical local traffic conditions could increase the level of precision in the analysis.

The other assumptions in the assessment will have differing effects on the results. For example, the assumption that there is no change in transportation mode or efficiency with increasing distance will result in overestimating EE and CO₂ emissions compared to accounting for any increases in transportation efficiency with distance, or changes to the mode of transportation from heavy duty trucks to less energy and emissions intensive alternatives, such as rail. In contrast, excluding transportation for mobilization, demobilization and worker commuting results in underestimating the EE and CO₂ emissions associated with the project; however, these activities are common to all ground improvement alternatives and may have similar impacts. Finally, while it is likely that a given material will be transported from the same manufacturing plant to a supplier or distribution center by a constant mode of transportation, a situation could arise where this is not the case. For instance, the plant that normally provides the material to the supplier may not have sufficient capacity to keep up with demand, resulting in the same material being delivered to the supplier from a second plant. Such an occurrence could increase the EE and CO₂ emissions for the project if the second plant is located farther away from the supplier.

As expected, the proportion of the total EE and CO₂ emissions associated with materials transportation increases with increasing haul distance, as shown in Figs. 2 and 4. In conjunction with the increase in the proportion of total EE and CO₂ emissions due to materials transportation, the proportion of total EE and CO₂

emissions associated with all other aspects of the construction decreases. Material transportation is not responsible for the largest proportion of total EE or CO₂ emissions for any of the distances considered in this analysis (up to $M = 9.6$ for Pearson Hall and $M = 4$ for LPV 111). In all cases, the production of the materials from raw material extraction until they are ready for delivery to the site is responsible for the largest proportion of total project EE and CO₂ emissions.

In addition to the uncertainty in the assessment due to unknown material haul distances, there is also uncertainty in the EE and CO₂ emissions coefficients for transportation fuels (e.g., diesel, gasoline) and the construction materials. For example, Venkatesh et al. (2011) report that the whole life emissions for gasoline have a coefficient of variation (COV) of 0.04, where the COV is defined as the ratio of the standard deviation to the mean. Based on statistics in the Inventory of Carbon and Energy database (Hammond and Jones 2011), many common construction materials exhibit COVs between 0.2 and 0.5 for EE, and some have COVs >1.0. This means that in reality, total project EE and CO₂ emissions will follow a distribution, which is shifted higher or lower based on material haul distances. Determining distributions of total EE and CO₂ emissions is beyond the scope of this paper.

RECOMMENDATIONS

When making estimates of total EE and CO₂ emissions at the design stage of ground improvement projects, the actual suppliers for construction materials may not be known. Therefore, it is recommended that a radial distance be established around the project site as a base distance for the trucking of each material. This radial base distance should encompass one or more reasonable suppliers for each material.

Given the results of the deterministic analyses on the Pearson Hall and LPV 111 case history projects presented herein, if the difference between the selected radial base distances used in the EE and CO₂ emissions estimates and the actual haul distances is less than a factor of 3 times the selected radial base distances, it is likely the actual EE and CO₂ emissions will differ by less than 10% from the estimated EE and CO₂ emissions (i.e., the distributions of total EE and CO₂ emissions will likely be shifted by <10% from the estimated distributions). At present, it is not confirmed if other ground improvement technologies and project sizes will exhibit similar results; however, this could be evaluated with data from additional case histories.

It is unlikely that all materials will have actual haul distances at the same multiple, M , of the selected base distances (Assumption 2). Some actual haul distances may result in $M < 1$ for some materials if the base distance encompasses more than one supplier, while others may have $M > 1$. As a result, it is likely that actual differences between the estimated and actual EE and CO₂ emissions will be smaller than the percent increases shown in the analyses of the case histories in this paper.

To contribute to sustainable development, geotechnical engineers should seek to minimize EE and CO₂ emissions by design through selected methods and materials, suppliers, and waste handling procedures. To minimize EE and CO₂ emissions, the nearest material supplier should be used whenever possible. However, substantial differences in price, supplier or material quality (Aretoulis et al. 2010), or a strong relationship between a particular supplier and the contractor or owner (Lu and Yang

2010) can influence supplier selection. Material quality can be particularly important for aggregates, which may have specifications for durability and reactivity that may preclude sourcing aggregate from the nearest supplier in favor of higher quality material from a greater distance (M. Valle, personal communication, 2015).

CONCLUSION

As sustainable development considerations in civil engineering practice continue to mature, quantitative environmental impact assessments will become more common in geotechnical practice. When these assessments are conducted at the design stage in order to estimate environmental impacts such as EE or CO₂ emissions to aid in deciding between alternatives, they involve uncertainty in material, fuel and transportation quantities.

This paper presents deterministic analyses of EE and CO₂ emissions for both a small and a large ground improvement project using the SEEAM method, in order to evaluate the influence of material truck haul distance on the results. It was shown that for each increasing multiple of selected base haul distances, project EE increases by an average of 4.7% and project CO₂ emissions increase by an average of 2.9%.

When conducting environmental assessments at the design stage, it is recommended for geotechnical engineers to locate potential suppliers for each material around the project site, then select a reasonable distance for the transportation of each material to the site for use in estimating the total EE and CO₂ emissions. It is likely that the actual haul distances will result in less than a 10% difference in project EE and CO₂ emissions from the estimate using a selected base distance, unless all the actual distances differ from the base distances by a factor of 3 or more. Analyzing additional case histories with a variety of project sizes and ground improvement technologies could confirm whether or not these conclusions have widespread applicability.

ACKNOWLEDGMENTS

The authors acknowledge the support of the Via Department of Civil and Environmental Engineering and the Institute for Critical Technology and Applied Science at Virginia Tech. The authors are grateful for the efforts of Kenton Martin and Tim Myers of Barton Malow Company, Ryan Goldstein and Kevin Hodges of GeoStructures, Inc., Kord Wissmann of Geopier Foundation Company, and Aaron Curfiss of the Department of University Planning, Design and Construction at Virginia Tech for providing data regarding the construction at Pearson Hall. The authors thank Treviicos for providing construction data from LPV 111. The authors acknowledge Matthew Valle of Oldcastle Materials, Inc., and Kevin Younkin of PJ Keating Company, who provided information regarding the aggregate supply chain.

REFERENCES

- Aretoulis, G. N., Kalfakakou, G. P., and Striagka, F. Z. (2010). "Construction material supplier selection under multiple criteria." *Operational Research International Journal*, 10(2), 209-230.

- Cali, P., Lelong, B., Bruce, D., Valagussa, S., Beckerle, J., Gardner, J., and Filz, G. (2012). "Overview of deep mixing at levee LPV 111, New Orleans, LA." *Proc., 4th International Conference on Grouting and Deep Mixing*, ASCE, Reston, VA, 661-671.
- Carbone 4. (2014). Geotechnical Carbon Calculator, version 2.3, [Software]. EFFC-DFI, Available from <<http://www.geotechnicalcarboncalculator.com/>>.
- Chau, C., Soga, K., Nicholson, D., O'Riordan, N., and Inui, T. (2008). "Embodied energy as an environmental impact indicator for basement wall construction." *Proc., GeoCongress 2008*, ASCE, Reston, VA, 867-874.
- Cooling, T., Boeckmann, A., Filz, G., Cali, P., Evans, J., and Leoni, F. (2012). "Deep mixing design for raising levee section, LPV 111 New Orleans, LA." *Proc., 4th International Conference on Grouting and Deep Mixing*, ASCE, Reston, VA, 672-681.
- Druss, D., Wilding, A., Cooling, T., Beckerle, J., Schmutzler, W., and Gardner, J. (2012). "Use of deep mixing return material for levee construction." *Proc., 4th International Conference on Grouting and Deep Mixing*, ASCE, Reston, VA, 629-639.
- EPA (2006). *Life cycle assessment: Principles and Practice*. Report No. EPA/600/R-06/060. Cincinnati, OH, National Risk Management Research Laboratory, U.S. Environmental Protection Agency.
- Hammond, G., and Jones, C. (2011). "Inventory of Carbon and Energy (ICE)." Version 2.0, Sustainable Energy Research Team (SERT), University of Bath, UK.
- Kelsey, C. (2012). "NOLA levee reconstruction." *CE News*, 24(11), 44-46.
- Lu, M., and Yang, G. (2010). "The selection of construction material suppliers in supplier relationship management." *Proc., 2010 International Conference of Information Science and Management Engineering*, vol. 1, Institute of Electrical and Electronics Engineers Computer Society, Los Alamitos, CA, 189-192.
- Schmutzler, W., Leoni, F. M., Bertero, A., Leoni, F., Nicholson, P., Druss, D., and Beckerle, J. (2012). "Construction operations and quality control of deep mixing at levee LPV 111 New Orleans." *Proc., 4th International Conference on Grouting and Deep Mixing*, ASCE, Reston, VA, 682-693.
- Shillaber, C. M., Mitchell, J. K., and Dove, J. E. (2015a). "Energy and carbon assessment of ground improvement works. I: definitions and background." *Journal of Geotechnical and Geoenvironmental Engineering*, 10.1061/(ASCE)GT.1943-5606.0001410, 04015083.
- Shillaber, C. M., Mitchell, J. K., and Dove, J. E. (2015b). "Energy and carbon assessment of ground improvement works. II: working model and example." *Journal of Geotechnical and Geoenvironmental Engineering*, 10.1061/(ASCE)GT.1943-5606.0001411, 04015084.
- Todd, J. A., and Curran, M. A. (1999). *Streamlined life-cycle assessment: a final report from the SETAC North America streamlined LCA workgroup*. Streamlined LCA Workgroup, Society of Environmental Toxicology and Chemistry.
- Venkatesh, A., Jaramillo, P., Griffin, M. W., and Matthews, H. S. (2011). "Uncertainty analysis of life cycle greenhouse gas emissions from petroleum-based fuels and impacts on low carbon fuel policies." *Environmental Science & Technology*, 45(1), 125-131.